JFPS The Japan Fluid Power System Society

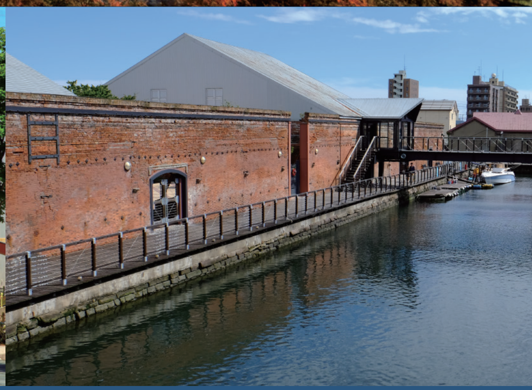

Proceedings of

The 11th JFPS International Symposium on Fluid Power

HAKODATE 2020

Oct. 12-13, 2021

One-off sessions

Opening Ceremony | Ceremony

Opening Ceremony

Chair: Kazuhisa Ito, Shibaura Institute of Technology

[OP-01] Welcome Message
○Kazushi SANADA[1] (1.Yokohama National University)

[OP-02] Opening Address
○Yutaka TANAKA[1] (1.Hosei University)

Invited Lecture | Invited Lectures

Invited Lecture 1

[IL1-Introduction] Introduction
○Kazuhisa Ito[1] (1.Shibaura Institute of Technology)

[IL-01] Piezoelectric pumps for hydraulic actuation
○Andrew Plummer[1] (1.University of Bath)

Invited Lecture | Invited Lectures

Invited Lecture 2

[IL2-Introduction] Introduction
○Kazuhisa Ito[1] (1.Shibaura Institute of Technology)

[IL-02] Research on high performance electro-hydrostatic actuator (EHA) system
○Jiao Zongxia[1] (1.Beihang University)

Invited Lecture | Invited Lectures

Invited Lecture 3

[IL3-Introduction] Introduction
○Kazuhisa Ito[1] (1.Shibaura Institute of Technology)

[IL-03] Fluid Power: from Motion Control to Powertrain Innovation
○Zongxuan Sun[1] (1.University of Minnesota)

Invited Lecture | Invited Lectures

Invited Lecture 4

[IL4-Introduction] Introduction
○Kazuhisa Ito[1] (1.Shibaura Institute of Technology)

[IL-04] Tribology Research on Fluid Power in Japan Review and State of the Art
○Toshiharu Kazama[1] (1.Muroran Institute of Technology)

Organized Session | Organized session

Automobile

[OS1-01] A Study on Rotor Behavior of a Gerotor Pump
○Ryo Kojima[1], Takahiro Takeno[2], Hideki Yanada[1], Hiroshi Yokoyama[1] (1.Toyohashi University of Technology, 2.Toyohashi University of Technology(Currently at Terumo Corporation))

[OS1-02] Modeling of Compact Car Active Suspension with Pneumatically Controlled Variable Damping Force Oil Damper and Variable Rigidity Air Spring
○Yasukazu Sato[1], Shogo Sato[1] (1.Yokohama National University)

[OS1-03] Power Absorber by Air Compression and Release Cycle with Controller for Adjusting Air Release Timing to Obtain Variable Absorbing Capacity (First Report – Basic Concept and Design)
○Takashi Shibayama[1], Toshinori Fujita[1], Sho Ueyama[1] (1.Tokyo Denki University)

[OS1-04] Clarification of Parameters and Development of a Method for Estimating Loading Forces Acting on the Spool Valve of a Hydraulically Controlled Automotive Transmission
○Daisuke Yanagawa[1], Masahiro Kouya[1], Sho Tozuka[1], Masaru Shimada[1], Idris Tengku[1], Naoki Uezono[1] (1.Jatco,Ltd)

Organized Session | Organized session

Functional Fluid

[OS2-01] A Study on a Mathematical Model for AC Electroosmosis Micropump
Yo Makita[1], ○Kazuhiro Yoshida[1], Sang In Eom[1], Joon-wan Kim[1] (1.Tokyo Institute of Technology)

[OS2-02] Multi-Layered Disk Type of Electro-Rheological Braking Device for Small Mobile Robot
○Takanori Togawa[1], Yuta Sato[1], Yutaka Tanaka[1], Jinghui Peng[2] (1.Hosei University, 2.Harbin Institute of Technology)

[OS2-03] Lightweight &Twin-driven MR Fluid Actuator for Haptic Devices
○Tetsumasa Takano[1], Asaka Ikeda[2], Akinori Yamaguchi[1], Isao Abe[2], Takehito Kikuchi[2] (1.Graduate School of Engineering, Oita University, 2.Faculty of Science and Technology, Oita University)

Organized Session | Organized session

Simulation and Modeling

Organized Session | Organized session

Aqua Drive 1

Organized Session | Organized session

Aqua Drive 2

Muscle Considering Load Variation during Experiments
○Satoshi Tsuruhara[1], Ryo Inada, Kazuhisa Ito[1] （1.Shibaura Institute of Technology）

[OS4-2-03] Experimental study on Dual-Layer Type Vortex Cup Driven by Aqua Drive System
○Wataru Kobayashi[1], Tetsuya Akagi[1], Shujiro Dohta[1] （1.Okayama University of Science）

Organized Session | Organized session

Soft Actuator 2

[OS5-2-01] Pneumatic Source Proposal for Improving Portability and Responsiveness of Artificial Muscle via Dimethyl Ether Phase Change and Combustion
○Ryuto Enjo[1], Manabu Okui[1], Taro Nakamura[1] （1.Chuo university）

[OS5-2-02] Development of Six-Legged Mobile Robot Using Tetrahedral Shaped Pneumatic Soft Actuators
○Kenta Hase[1], Tetsuya Akagi[1], Shujiro Dohta[1], Takashi Shinohara[1], Wataru Kobayashi[1], So Shimooka[2] （1.Okayama University of Science, 2.Okayama University）

[OS5-2-03] Development of the Transfer System for Bedridden Elderly and Disabled People using Pneumatic Actuators
○Feifei Cho[1], Keisei Kato[1], Ryota Endo[1], Takumi Kobayashi[2], Tetsuya Akagi[2] （1.National Institute of Technology Tsuyama College, 2.Okayama University of Science）

[OS5-2-04] Development of Pneumatic Drive Pipe Inspection Robot using Radial Bending Type Soft Actuator
○Takashi Shinohara[1], Hikaru Furuya[1], Tetsuya Akagi[1], Shujiro Dohta[1], Takumi Kobayashi[1], So Shimooka[2] （1.Okayama University of Science, 2.Okayama University）

Organized Session | Organized session

Soft Actuator 1

[OS5-1-01] Analysis and Design of Servo Valve Using Buckled Tubes for Desired Operation of Flexible Robot Arm
○Takumi Kobayashi[1], Hideyuki Obayashi[1], Tetsuya Akagi[1], Shujiro Dohta[1], Wataru Kobayashi[1], Takashi Shinohara[1], So Shimooka[2] （1.Okayama University of Science, 2.Okayama University）

[OS5-1-02] Development of Pneumatic Variable Linear Stepping Actuator and Soft Stepping Actuator with Bending Motion for Rehabilitation Device of Hip Joint
○Kota Oe[1], Tetsuya Akagi[1], Shujiro Dohta[1], Takashi Shinohara[1], Wataru Kobayashi[1], So Shimooka[2] （1.Okayama University of Science, 2.Okayama University）

[OS5-1-03] Development of Extension Type Flexible Pneumatic Actuator with Displacement Sensor Using Ring-shaped Magnet and Hall Sensor for Tetrahedral-type Soft Mechanism
○Kenshiro Takeuchi[1], Takumi Kobayashi[1], Tetsuya Akagi[1], Shujiro Dohta[1], Takashi Shinohara[1], Wataru Kobayashi[1], So Shimooka[2] （1.Okayama University of Science, 2.Okayama University）

[OS5-1-04] Development of Highly Durable Straight Fiber Type Pneumatic Artificial Muscle with a Double Structural Air Chamber
○Naoki Saito[1], Daisuke Furukawa[1], Toshiyuki Satoh[1], Norihiko Saga[2] （1.Akita Prefectural University, 2.Kwansei Gakuin University）

[OS5-1-05] Evaluation of Lifting Motion with Non-wearing Type Pneumatic Power Assist Device ~ Comparison of Active and Passive Type ~
○Masashi Yokota[1], Reito Hirabayashi[1], Masahiro Takaiwa[2] （1.Tokushima University, Graduate School Advanced Technology and Science, 2.Tokushima University, Graduate School of Technology, Industrial and Social Sciences）

Genaral Session | Pneumatics

Robotics and Mechatronics 1

[GS1-1-01] Development of a Simple Servo-Pneumatic Three DOF Pick-And-Place Manipulator
Chin-Yi Cheng[1], Jyh Chyang Renn[1], Shyang Jye Chang[1], ○Ilham Saputra[1] （1.National Yunlin University of Science and Technology）

[GS1-1-02] Development of Fingertip Mechanism With Contact Point Estimation
○Kei Mikami[1], Kotaro Tadano[1] （1.Tokyo Institute of Technology）

[GS1-1-03] Development of Outdoor Activity Assist Suit
○Toshihiro Yoshimitsu[1], Rui Matsumoto （1.

Kanagawa Institute of Technology)

[GS1-1-04] Examination on Attitude Control System of Hand Manipulator with Compact Pneumatic Cylinders by E-FRIT
○Shogo Tomita[1], Eiji Murayama[1], Yukio Kawakami[1] (1.Shibaura Institute of Technology)

[GS1-1-05] Design and Fabrication of a Soft Filament-polymer Jamming Actuator
○Peng Qin[1], Zhonghua Guo[1], MengYu Dou[1], Zhongsheng Sun[1], Yan Teng[1], Xiaoning Li[1] (1.Nanjing University of Science and Technology(China))

[GS1-1-06] Robotic Blood Vessel Mechanism for Self-Healing Function of Soft Robots
Kenjiro Tadakuma[1], Shohei Inomata[1], Yuta Yamazaki[2], Fumiya Shiga[2], Masanori Kameoka[2], MD Nahi Islam Shiblee[2], ○Issei Onda[1], Tomoya Takahashi[1], Yu Ozawa[1], Masahiro Watanabe[1], Hidemitsu Furukawa[2], Masashi Konyo[1], Satoshi Tadokoro[1] (1.Tohoku University, 2.Yamagata University)

Genaral Session | Oil hydraulics

Robotics and Mechatronics 2

[GS1-2-01] Design and Manipulability Analysis of a Redundant Anthropomorphic Hydraulically Actuated Manipulator
○Fu Zhang[1], Junhui Zhang[1], Min Cheng[2], Ruqi Ding[3], Bing Xu[1], Shen Zheng[1] (1.State Key Laboratory of Fluid Power and Mechatronic Systems, Zhejiang University, 2.State Key Laboratory of Mechanical Transmissions, Chongqing University, 3.Key Laboratory of Conveyance and Equipment, Ministry of Education, East China Jiaotong University)

[GS1-2-02] Wide Field of View Projection Display for Remote Control of Construction Robot
○Daisuke Kondo[1] (1.Osaka University)

[GS1-2-03] Experimental Implementation of a Hydraulic Turbine Access System with Six-DoF Active Motion Compensation for Taiwan Offshore Wind Farms
Mao-Hsiung Chiang[1], Bo-Yen Chen [1], ○Sheng-Chia Lin[1] (1.National Taiwan University)

[GS1-2-04] Modular Hydraulic Servo Booster for Multi-Axis Robots
Sang-Ho Hyon[1], ○Tomoro Kai[1] (1.Ritsumeikan University)

[GS1-2-05] Comparison of Mechanical Drive System and Hydraulic Direct-Drive System for Motor Power
○Juri Shimizu[1,2], Takuya Otani[2], Kenji Hashimoto[3], Atsuo Takanishi[2] (1.Hitachi, Ltd., 2.Waseda University, 3.Meiji University)

Genaral Session | Oil hydraulics

Energy Saving

[GS2-01] Research on the Characteristics of the Cylinder Exhaust-Return Energy-Saving System
○Yuto Fujiwara[1], Mitsuru Senoo[1], Hiroyuki Asahara[1] (1.SMC Corporation)

[GS2-02] Design Guideline and Investigation of Accumulator Parameters for a Novel Hybrid Architecture
○Seiji Hijikata[1], Kazuhisa Ito[2], Hubertus Murrenhoff[1] (1.Institute for Fluid Power Drives and Systems (ifas), RWTH Aachen University, 2.Department of Machinery and Control Systems, College of Systems Engineering and Science Shibaura Institute of Technology)

[GS2-03] Research Regarding the Energy Saving Conditions of the Air Blow for Removing and Drying Out Water
○Daisuke Kurakami[1], Keiichirou Koga[1], Gohei Harimoto[1] (1.SMC Corporation)

[GS2-04] Energy Regeneration and Reuse of Excavator Boom System with Hydraulic Constantly Variable Powertrain
○Cuong Tri Do[1], Kyoung Kwan Ahn[1] (1.University of Ulsan)

[GS2-05] Efficient Closed Pump Controlled Hydraulic-Gas Balanced Energy Recovery Driving Method for Hydraulic Excavator Boom
○Lianpeng Xia[1], Long Quan[1], Hongjuan Zhang[1], Yunxiao Hao[1], Lei Ge[1] (1.Taiyuan University of Technology)

[GS2-06] Experimental Validation of Improvement of the Overall Efficiency for Electro-hydraulic Drive System using Efficiency Maps
○Ha Tham Phan[1], Yasukazu Sato[1] (1.Yokohama National University)

Genaral Session | Pneumatics

Medical and Welfare

[GS3-01] Development of Silicone Outer Shell Type Pneumatic Soft Actuator
○Yuma Nakanishi[1], Yasuhiro Hayakawa[1], Keisuke Kida[1], Hiroaki Ichii[1] (1.National Institute of Technology (Kosen) , Nara College.)

[GS3-02] Development of Pneumatically Driven Verification System for Ophthalmic Needling Operation
Feng Tao[1], ○Maina Sogabe[2], Taro Ito[3], Tetsuro Miyazaki[2], Toshihiro Kawase[4,1], Takahiro Kanno[5], Yoshikazu Nakajima[1], Kenji Kawashima[2] (1.Tokyo Medical and Dental University, 2.The University of Tokyo, 3.Tottori University, 4.Tokyo Institute of Technology, 5.RIVERFIELD Inc)

[GS3-03] Development of a Whole Body Training Device by Multi-directional Force Input Using Pneumatic Artificial Muscles
Soichiro Ito[1], ○Tetsuro Miyazaki[2], Junya Aizawa[3], Toshihiro Kawase[1,4], Maina Sogabe[2], Takahiro Kanno[5], Yoshikazu Nakajima[1], Kenji Kawashima[2] (1.Tokyo Medical and Dental University, 2.The University of Tokyo, 3.Juntendo University, 4.Tokyo Institute of Technology, 5.RIVERFIELD Inc.)

[GS3-04] Development of Robotic Forceps Driven by Soft Actuator with Built-In Displacement Sensor
○Osamu Azami[1], Takahiro Kanno[1], Toshihiro Kawase[2,3], Maina Sogabe[4], Tetsuro Miyazaki[4], Kenji Kawashima[4] (1.Riverfield Inc., 2.Tokyo Medical and Dental University, 3.Tokyo Institute of Technology, 4.Tokyo University)

Genaral Session | Oil hydraulics

Tribology, Seals, and Contamination Control

[GS4-01] Effect of Sealing Surface Flatness on Leakage Characteristics of Flange-Type Gasket Model Using Oil Viscosity-Temperature Relations
○Song Gao[1], Toshiharu Kazama[1] (1.Muroran Institute of Technology)

[GS4-02] Experimental Analysis of Rotational Motion of Pistons and Slippers of a Swashplate Axial Piston Pump Using Visualization Technique
○Takumi Furuya[2], Toshiki Haga[2], Toshiharu Kazama[1] (1.Muroran Institute of Technology, 2.Graduate School of Muroran Institute of Technology)

[GS4-03] Feasibility and Precision Analysis of a Test Rig with Adjustable Oil Film Thickness
○Haiji Wang[1], Guanglin Shi[1] (1.Shanghai Jiaotong University)

Genaral Session | Pneumatics

Components and Systems 1

[GS5-1-01] Magnetic Sensor Study for Improving Air Turbine Spindle Performance
○Vanisara Kaewnamchai[1], Tomonori Kato[1], Kazuki Kawakubo[1], Kazumasa Yamashita[1] (1.Fukuoka Institute of Technology)

[GS5-1-02] Study on Multi-Cylinder Type Wind Powered Air Compressor
Applied Hypocycloid
○Ryota Tanoue[1], Toshinori Fujita[1] (1.Tokyo Denki University)

[GS5-1-03] Development of Bidirectional Arm Curl Machine Using Pneumatic Artificial Rubber Muscles
○Toshihiro Kawase[1,2], Tomoya Nakanishi[1], Shintaro Yoshida[3], Shingo Ohno[3], Ryo Sakurai[3], Tetsuro Miyazaki[4], Takahiro Kanno[5], Maina Sogabe[4], Yoshikazu Nakajima[1], Kenji Kawashima[4] (1.Tokyo Medical and Dental University, 2.Tokyo Institute of Technology, 3.Bridgestone Corporation, 4.The University of Tokyo, 5.RIVERFIELD, Inc.)

[GS5-1-04] Design of a Pneumatic Oscillator for Paper Machine's Doctor Blade Systems
Stefano Colaiuda[1], ○Michele Gabrio Antonelli[2], Pierluigi Beomonte Zobel[2], Massimiliano Centofanti[1] (1.SMC Italia S.p.A., 2.Department of Industrial and Information Engineering and Economics, University of L'Aquila)

Genaral Session | Oil hydraulics

Components and Systems 2

[GS5-2-01] Leakage Characteristics of a 3-port Pressure Reducing Valve
○Haroon Ahmad Khan[1], Byeong-Il Choi[2], Jung-Ho Park[2], So-Nam Yun[2] (1.University of Science and Technology, Korea, 2.Korea Institute of Machinery and Materials)

[GS5-2-02] Generation Mechanism of Flow Force Acting on Spool Valve
○Fumio Shimizu[1], Kazuhiro Tanaka[1] (1.Kyushu

Institute of Technology)

[GS5-2-03] The Effect of the Spline Coupling on the Rotating Assembly Tilt Behavior in a High-speed Axial Piston Pump
〇Haogong Xu[1], Junhui Zhang[1], Weidi Huang[1], Bing Xu[1], Fei Lyv[1], Xiaochen Huang[1] (1.State Key Laboratory of Fluid Power and Mechatronic Systems, Zhejiang University)

[GS5-2-04] First-order Trajectory Sensitivity Analysis of Multi-level Pressure Switching Control System
Jing Yao[1,2,3], 〇Pei Wang[1], Xinhao Li[1], Yuwang Cheng[1], Xiaoming Cao[1] (1.School of Mechanical Engineering, Yanshan University, 2.Key Laboratory of Advanced Forging &Stamping Technology and Science of Ministry of Education of China, 3.Hebei Key Laboratory of Heavy Machinery Fluid Power Transmission and Control)

[GS5-2-05] A Study on the Pulse Analysis and Vibration Characteristics of Hydraulic System for Prediction of Check Valve Behavior
〇Jeong-Woo Park[1,2], So-Nam Yun[1], Young-Bog Ham[1], Eun-A Jeong[1] (1.Korea Institute of Machinery &Materials, 2.Chungnam National University)

[GS5-2-06] Research on an Oil-hydraulic Component to Reduce Pressure Pulsation
〇Yasuo Sakurai[1], Misaki Hashimoto[2], Moritaka Maehara[3], Norikazu Hyodo[4] (1.Ashikaga University, 2.MITSUBA Corporation, 3.SAWAFUJI ELECTRIC CO., LTD., 4.TOKYO KEIKI INC.)

Genaral Session | Oil hydraulics

Construction, Components and Systems

[GS6-01] Operating Information Presentation for Hydraulic Construction Robot
〇Hironao Yamada[1], Takahiro Ikeda[1], Satoshi Ueki[1], Kazuma Shinkai[2], Katsutoshi Ootsubo[3] (1.Gifu University, 2.Sumitomo Heavy Industries, Ltd., 3.Kinjo Gakuin University)

[GS6-02] Frequency Response Analysis of Parallel Link Mechanism using Oil-hydraulic Cylinders of Tunnel Boring Machines
Ryo Yamamoto[1], 〇Kazushi Sanada[1], Shigeaki Ashikaga[2] (1.Yokohama National University, 2.Komatsu Ltd.)

[GS6-03] A Power-Split Hybrid Transmission to Drive Conventional Hydraulic Valve Controlled Architectures in Off-road Vehicles: The Case of a Mini-Excavator
〇Mateus Bertolin[1], Andrea Vacca[1] (1.Purdue University)

[GS6-04] Control of Air Bubble Content in Working Oil by Swirling Flow
Sayako Sakama[2], 〇Yutaka Tanaka[1], Yasuhiro Kodera[3], Yoshiaki Kitamura[3] (1.Hosei University, 2.National Institute of Advanced Industrial Science and Technology, 3.KYB Corporation)

[GS6-05] Pulse Tests on Additive Manufactured Valve Blocks – Damage Analysis and New Design Possibilities
〇Sebastian Deuster[1], Stefan Aengenheister[1], Gunnar Matthiesen[1], Katharina Schmitz[1] (1.RWTH Aachen University, Institute for Fluid Power Drives and Systems (ifas))

[GS6-06] The Potential in Fluid Power Systems for a Sustainable Future
〇Katharina Schmitz[1] (1.RWTH Aachen University, Institute for Fluidpower Drives and Systems (ifas))

[GS6-07] New Intelligent Hydraulic Power Control System
〇Takahiro Urai[1], Ken Shindo[1] (1.Bosch Rexroth corporation)

Opening Ceremony | Ceremony

Opening Ceremony

Chair: Kazuhisa Ito, Shibaura Institute of Technology

[OP-01] Welcome Message

〇Kazushi SANADA[1] （1.Yokohama National University）

[OP-02] Opening Address

〇Yutaka TANAKA[1] （1.Hosei University）

Welcome Message

On behalf of the Japan Fluid Power System Society, it is my great honor to announce the 11th JFPS International Symposium on Fluid Power HAKODATE 2020 as a major academic international symposium. I present thanks all of you who are involved in the symposium. Academic researchers of fluid power community have a long history of exchanging their friendship and academic information. I believe that we must do our best to take over the history and expand fluid power community for the next generation. Fluid power researchers have academic interests in oil-hydraulics, pneumatics, water hydraulics, and functional fluids. Application of fluid power have spread to broad fields. I believe this symposium is a key conference which summarizes recent trends on fundamental and application of fluid power. This message is devoted to success of the 11th JFPS International Symposium on Fluid Power HAKODATE 2020.

Sincerely yours,

12th, October, 2021

Kazushi SANADA, Dr. Eng., Professor
President, the Japan Fluid Power System Society
Dean of College of Engineering Science
Yokohama National University, Japan

Opening Address

On behalf of Japan Fluid Power System Society (JFPS) and JFPS-HAKODATE2020 committee, I am pleased to welcome you to the 11th International Symposium on Fluid Power Hakodate2020 at Hakodate Arena. We have a trust that you will have a rewarding time at this conference. Hope you and your loved ones are doing fine even under this difficult situation regarding Covid-19 pandemic. Unfortunately, considering the current world situation, we have decided to deliver the symposium basically online with pre-recorded video presentations.

The first this symposium was held at Tokyo Institute of Technology in 1989. Since then, the JFPS International Symposium on Fluid Power has been held every three years. Originally, it was scheduled to be held in October 2020 last year, but it was postponed for one year due to the Covid-19 pandemic. The symposium will address recent developments in fluid power technologies such as hydraulics, pneumatics, water hydraulics and functional fluids, and present basic researches, applications and case studies.

We have received excellent full papers with very interesting topics on fluid power. After the strictly peer-review process, there are 73 accepted papers for the symposium. I would like to thank the 33 reviewers for their cooperation in the symposium. All accepted papers will be presented in 12 sessions for pre-recorded presentations on the website. From these 73 papers, the best paper awards, the best student paper awards, and the GFPS best paper award will be selected and presented in the closing & awards ceremony.

Four invited papers have also been organized by the committee in a two-day period. I would like to thank Prof. Andrew Plummer, University of Bath, Prof. Zongxia Jiao, Beihang University, Prof. Zongxuan Sun, University of Minnesota, and Prof. Toshiharu Kazama, Muroran Institute of Technology.

We have participants that represent academia, industry, and research institutions from Japan, China, Korea, Germany, U.S.A., Taiwan, Italy and U.K. This conference indeed follows the established path of bringing together engineers, scientists, and practitioners that are working on the fundamental aspects of fluid power. Through your participation and interaction with other attendees, this will be a truly exciting, memorable and fruitful symposium.

Hakodate, where the symposium is being delivered this time, is Hokkaido's third largest city and a traditional harbor city. Hakodate has experienced notable influence from overseas. And Hokkaido is a famous place for the Ainu culture. The Ainu are an indigenous people from the northern region of the Japanese archipelago. The Ainu traditional pattern is designed in the header of first page of each paper. I would like to thank Mrs. Nobuko Tsuda and her related people for their cooperation in using the Ainu pattern.

I appreciate to be supported by grant funding from, The Precise Measurement Technology Promotion Foundation, NSK Foundation for the Advancement of Mechatronics, Japan Fluid Power Association, and SMC Corporation.

During several years, all the committee members cannot help but be pleased that they overcame many difficulties and arrived at this opening of the symposium. I would like to thank a member of people who have made it possible to put this conference together, Prof. Toshiharu Kazama and Mr. Hidehiko Shimamura of co-chairperson, Prof. Yukio Kawakami of Steering chair, Prof. Kazuhiro Yoshida of Paper chair, Prof. Kazuhisa Ito of Program chair, Prof. Toshiharu Yoshimitsu of Exhibition chair, Prof. Kenjiro Takemura of Website chair, Prof. Kenji Kawashima of Budget chair, Prof. Yasuo Sakurai of Secretary general, and all the other members of HAKODATE2020 Executive Committee.

I hope you find this symposium stimulating and get some time to get valuable information.

Sincerely yours,

From Hakodate,

Yutaka Tanaka

Yutaka Tanaka
JFPS HAKODATE2020, General Chairperson

October 12, 2021.

.

Invited Lecture | Invited Lectures

Invited Lecture 1

[IL1-Introduction] Introduction

〇Kazuhisa Ito[1] （1.Shibaura Institute of Technology）

[IL-01] Piezoelectric pumps for hydraulic actuation

〇Andrew Plummer[1] （1.University of Bath）

The 11th JFPS International Symposium on Fluid Power HAKODATE 2020 Oct. 12-13, 2021 The Japan Fluid Power System Society

Piezoelectric Pumps for Hydraulic Actuation

Andrew PLUMMER*

* University of Bath
UK

Professor Andrew Plummer received his Ph.D from the University of Bath in 1991, for research into control of electro-hydraulic systems. He worked as a research engineer for Thales from 1990, developing flight simulator control technology, before joining the University of Leeds in 1994. From 1999 until 2006 he was global control systems R&D manager for Instron, manufacturers of materials and structural testing systems. He is now Director of the Centre for Power Transmission and Motion Control, University of Bath, and has published 180 papers in the field of motion and force control, many relating to electro-hydraulic servo-systems. Prof. Plummer is Past Chair of the Institution of Mechanical Engineers Mechatronics Informatics and Control Group and also the UK Automatic Control Council, and is Associate Editor of both the International Journal of Fluid Power and Control Engineering Practice. He is Chair of the Global Fluid Power Society.

ABSTRACT

There is an increasing demand for small-scale hydraulic actuation systems, working at around the one hundred watts range, for example in human-scale robot applications. Pump-controlled actuators, where motion is controlled by varying the flow delivered to an actuator by a dedicated pump, are potentially energy efficient and allow the well-known flexibility in system design and control provided by hydraulics. However, compact and effective variable-displacement or variable-speed pumps for delivering in the region of 1 L/min and 100 bar are not widely available. Piezoelectric pumps are a possible solution. A single-cylinder piezoelectric pump consists of a piezoceramic actuator – either a stack or a bending actuator – vibrating a piston in a pumping chamber connected to suction and discharge lines by valves which rectify flow. Piezopumps have been found to be commercially viable in some low power fluid movement applications (10mW order of magnitude), for example in medicine. However, higher power piezopumps are still a matter of research. In this presentation I describe developments in this field, including reviewing some previous and current research, and describing the technical challenges and possible solutions.

Invited Lecture 2

The 11th JFPS International Symposium on Fluid Power HAKODATE 2020 Oct. 12-13, 2021 JFPS The Japan Fluid Power System Society

Research on High Performance Electro-Hydrostatic Actuator (EHA) system

Zongxia JIAO*

* Beihang University
China

Prof. Zongxia Jiao is from Beihang University, Beijing, China. He is currently director of the Fluid Transmission and Control Branch of the China Mechanical Engineering Society, honorary Director of the Electromechanical Branch of the China Aviation Society, Changjiang distinguished professor, winner of the National Science Fund for Distinguished Young Scholars. He has been engaged in the theory, key technology and equipment research of electro-hydraulic servo systems and basic components. He has also worked in the field of the reliability and high-performance control of the aircraft hydraulic system, the key technology and equipment of high-efficiency braking system, high-reliability hydraulic system and electro-hydraulic servo control. Prof. Jiao has been granted 2 National Technology Invention Awards (2nd class) and 1 National S&T Progress Awards (2nd class) and has established the IEEE/CSAA Aviation Electromechanical Series International Conference. He has published more than 300 papers including 6 ESI high cited papers.

ABSTRACT

More/All-electric aircraft are currently the development trend of aircraft. Electro-hydrostatic actuator (EHA) is a highly integrated actuation in power-by-wire aircraft utility system, including an electrical motor, pump and cylinder. EHA has the advantages of easy maintenance and good controllability. But its dynamic behavior is relatively low and the temperature increment is fast, which restrict the use of EHA. In order to overcome these disadvantages, a new design of EHA which features active load-sensitive has been developed. Active load-sensitive is achieved by using a special pressure control valve to actively control the variable pump. It adjusts the displacement of pump according to load pressure feedback and position feedback intelligently, which keeps the advantage of high efficiency but also overcomes the weakness of low rigidity. Especially in the high load condition, the temperature of the motor can be reduced significantly. Both simulation and experiment results indicate the performance improvement of the EHA.

Invited Lecture | Invited Lectures

Invited Lecture 3

[IL3-Introduction] Introduction

〇Kazuhisa Ito[1] （1.Shibaura Institute of Technology）

[IL-03] Fluid Power: from Motion Control to Powertrain Innovation

〇Zongxuan Sun[1] （1.University of Minnesota）

The 11th JFPS International Symposium on Fluid Power HAKODATE 2020 Oct. 12-13, 2021 The Japan Fluid Power System Society

Fluid Power: from Motion Control to Powertrain Innovation

Zongxuan SUN*

* University of Minnesota
USA

Zongxuan Sun is a Professor at the Department of Mechanical Engineering, University of Minnesota. He received his Ph.D. degree in Mechanical Engineering from University of Illinois at Urbana-Champaign in 2000. He is currently Director of the Engineering Research Center for Compact and Efficient Fluid Power (CCEFP). He was a Staff Researcher (2006-2007) and a Senior Researcher (2000-2006) at General Motors Research and Development Center in Warren, MI. His research interests include controls, fluid power, and mechatronics with applications to automotive and commercial vehicle propulsion systems. Dr. Sun has published over one hundred fifty referred technical papers and received twenty two US patents. Dr. Sun is a recipient of the Charles E. Bowers Faculty Teaching Award, George W. Taylor Career Development Award from College of Science and Engineering, University of Minnesota, NSF CAREER Award, SAE Ralph R. Teetor Educational Award, Best Paper Award from ASME Automotive and Transportation Systems Technical Committee in 2018, Best Paper Award from 2012 International Conference on Advanced Vehicle Technologies and Integration, Inventor Milestone Award, Spark Plug Award, and Charles L. McCuen Special Achievement Award from GM R&D.

ABSTRACT

Fluid power is widely used in off-road vehicles including construction machinery and agriculture equipment for driving and working functions. Given the increasing global focus on energy efficiency and environmental impact, powertrain innovation for off-road vehicles is needed. Inspired by this urgent need, we would like to refocus on the fundamental strengths of fluid power and connect them to the energy conversion, power transfer and motion control. This talk will present the study of motion control using fluid power, including accuracy, efficiency, and control bandwidth. Based on the motion control, we will discuss the powertrain innovation using fluid power. Examples will be provided including free piston engine, camless engine, controlled-trajectory rapid compression and expansion machine.

Invited Lecture | Invited Lectures

Invited Lecture 4

[IL4-Introduction] Introduction

〇Kazuhisa Ito[1] （1.Shibaura Institute of Technology）

[IL-04] Tribology Research on Fluid Power in Japan Review and State of the Art

〇Toshiharu Kazama[1] （1.Muroran Institute of Technology）

The 11th JFPS International Symposium on Fluid Power HAKODATE 2020 Oct. 12-13, 2021 The Japan Fluid Power System Society

Tribology Research on Fluid Power in Japan–Review and State of the Art

Toshiharu KAZAMA*

* Muroran Institute of Technology
Japan

Toshiharu Kazama is a Professor of the Muroran Institute of Technology since 2006. He joined the Institute as an Associate Professor in the department of mechanical engineering in 1994. Prior to coming to the Muroran Institute of Technology, he has done research work as a Research Associate at Yokohama National University, Japan. Dr. Kazama received his BEng, MEng, and PhD degrees from Yokohama National University. Primary areas of research have been tribology and cavitation as related to fluid power systems and components as well as machine elements and design. He has worked in the fields of internal flow of hydraulic pumps and motors, lubrication of hydrodynamic and hydrostatic bearings, sealing of packing and gaskets, and cavitation of liquid jets and erosion.

ABSTRACT

Hydraulic pumps, motors, and cylinders are the major components in hydraulic systems, which achieve transformation between mechanical energy and fluid pressure. The reliability, efficiency, and performance of such a system depend on the tribology at the interface between its sliding, bearing, and sealing parts. This talk briefly describes the short history of research on equipment tribology in Japan and surveys the knowledge and insights obtained in the last couple of decades, including the activities of research committees in Japan Fluid Power Systems Society (JFPS), and Japan Hydraulic and Pneumatic Society (forerunner of JFPS). With the literature review alongside the cutting-edge technology, theoretical and experimental approaches for these systems in Japan are surveyed. Additionally, our results and efforts mainly regarding pump tests and slipper models in terms of thermal effects, including liquid physical properties, thermohydrodynamic lubrication, and elastic deformation, are presented. Results on roughness effects, including mixed lubrication and surface interaction, are also presented. Finally, challenges in fluid power tribology, future development agenda, and vision, with remarks on scope and perspective, are discussed.

Organized Session | Organized session

Automobile

[OS1-01] A Study on Rotor Behavior of a Gerotor Pump

〇Ryo Kojima[1], Takahiro Takeno[2], Hideki Yanada[1], Hiroshi Yokoyama[1] （1.Toyohashi University of Technology, 2.Toyohashi University of Technology(Currently at Terumo Corporation)）

[OS1-02] Modeling of Compact Car Active Suspension with Pneumatically Controlled Variable Damping Force Oil Damper and Variable Rigidity Air Spring

〇Yasukazu Sato[1], Shogo Sato[1] （1.Yokohama National University）

[OS1-03] Power Absorber by Air Compression and Release Cycle with Controller for Adjusting Air Release Timing to Obtain Variable Absorbing Capacity (First Report – Basic Concept and Design)

〇Takashi Shibayama[1], Toshinori Fujita[1], Sho Ueyama[1] （1.Tokyo Denki University）

[OS1-04] Clarification of Parameters and Development of a Method for Estimating Loading Forces Acting on the Spool Valve of a Hydraulically Controlled Automotive Transmission

〇Daisuke Yanagawa[1], Masahiro Kouya[1], Sho Tozuka[1], Masaru Shimada[1], Idris Tengku[1], Naoki Uezono[1] （1.Jatco,Ltd）

The 11th JFPS International Symposium on Fluid Power HAKODATE 2020 Oct. 12-13, 2021 The Japan Fluid Power System Society

A Study on Rotor Behavior of a Gerotor Pump

Ryo KOJIMA*, Takahiro TAKENO**, Hideki YANADA*, Hiroshi YOKOYAMA*

*Department of Mechanical Engineering, Toyohashi University of Technology
1-1, Hibarigaoka, Tempaku-cho, Toyohashi, Aichi, 441-8580 Japan
(E-mail: kojima.ryo.lw@tut.jp)
** Department of Mechanical Engineering, Toyohashi University of Technology
(Currently at Terumo Corporation)

Abstract. In our previous study, rotor behavior of a gerotor pump used for automatic transmissions was measured using gap sensors, but the mechanism of the rotor behavior is yet to be made clear. In this study, in order to reveal the mechanism of the rotor behavior, we measure the pressure distributions on both sides of the inner rotor and numerically simulate the pressure distributions in the side clearances of the rotors. It was revealed that the pressure distributions on both sides of the rotors were different and that such differences in pressure distribution caused axial forces and moments of force being exerted on the rotors. It is concluded that the differences in pressure distribution between two sides of the rotors cause the tilting behavior of the inner rotor and the approach of the outer rotor to the casing sidewall.

Keywords: Gerotor pump, Rotor behavior, Pressure distribution, CFD

INTRODUCTION

In recent years, against the background of global warming, the fuel economy of automobiles has been attracting more attention. Reducing the power loss of automatic transmissions has become more essential to improve fuel economy. The power loss of a hydraulic pump incorporated in an automatic transmission occupies a relatively high proportion of the total power loss of the automatic transmission. Therefore, decreasing the power loss of the pump, especially that resulting from friction torque, is vital to improve fuel economy [1].

The friction torque characteristics of hydraulic pumps have previously been examined [2-11], and a negative resistance regime, in which the friction torque increases with decreasing rotational speed, is typically observed and it becomes wider under increased pressures and temperatures [4, 7]. It is also known that solid-to-solid contact takes place in this regime. However, for internal gear pumps, it has not been determined where the solid-to-solid contact begins to take place.

Pham et al. [12, 13] experimentally investigated the eccentricity and tilt of the outer gear of a crescent internal gear pump/motor and found that the outer gear was in contact with the casing due to its tilt and eccentricity. Uchino et al. [14] experimentally investigated the rotor behavior of a gerotor pump using gap sensors under various operating conditions. They revealed that the inner rotor rotated near the middle of the cover wall and casing sidewall, slightly tilted with respect to them, and behaved in a manner roughly similar to precession, as shown in Figure 1, and that the outer rotor rotated in the vicinity of the casing sidewall and did not vary its attitude with rotational angle. In addition, it was revealed that as the dimensionless parameter $\mu N/\Delta P$ (where μ [Pa $\cdot$ s] is the oil viscosity, N [s^{-1}] is the rotational speed, and ΔP [Pa] is the pressure difference) decreased, the clearance between the outer rotor and the casing sidewall decreased and the eccentricity ratio of the outer rotor increased. However, the mechanism of the rotor behavior has not yet been made clear.

In this paper, in order to reveal the mechanism of the rotor behavior of the gerotor pump, the pressure distributions on both sides of the inner rotor are measured. In addition, numerical simulations are conducted to investigate the pressure distributions in the clearances between the rotors and their surrounding walls under a uniform side

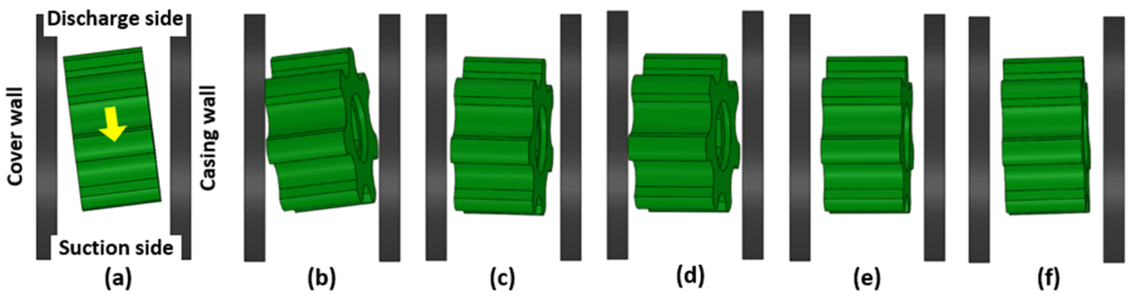

Figure 1. Variation of inner rotor attitude during a single rotation measured at 60°C, 500 min^{-1}, 1 MPa (arrow in (a) indicates the rotation direction), at (a) 0°, (b) 72°, (c) 144°, (d) 216°, (e) 288°, and (f) 342°. [14]

clearance condition and to compare the measured results with simulated ones. Based on the results, a mechanism of the rotor behavior is discussed.

EXPERIMENT

Test Pump

A schematic of the test gerotor pump used for automatic transmissions is shown in Figure 2 and the specifications of the pump are described in Table 1. The displacement of the pump was experimentally determined. The side clearances of the rotors and the diametral clearance of the outer rotor under no pressure were obtained by measuring the widths of the rotors, the outer diameter of the outer rotor, and the depth and internal diameter of the cylindrical hole of the casing. In order to measure the pressure distributions on both sides of the inner rotor, pressure transduces (JTEKT, PYS-3-10-M, pressure range = $0-10$ MPa) were mounted at the same radial and angular positions at the interval of 60 degrees on both the cover and cover-with-ports. Pressures in the side clearances were transmitted to the pressure transduces through 1 mm diameter holes. In Figure 2(b), the angle $\theta = 0^{\circ}$ was defined as the angular position at which a line starting from the center of the outer rotor passes through the center of the inner rotor, and the pumping stroke thus changes from a discharge stroke to a suction stroke at $\theta = 0^{\circ}$. Therefore, oil is sucked in the angular range of $\theta = 0^{\circ} - 180^{\circ}$ and is discharged in the range of $\theta = 180^{\circ} - 360^{\circ}(0^{\circ})$.

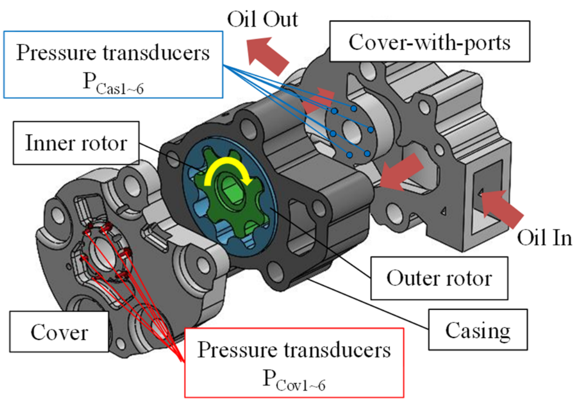

(a) Test pump schematic.

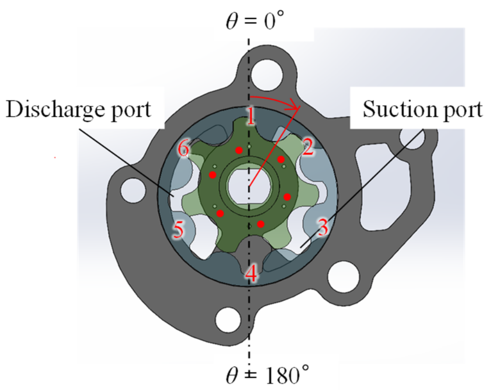

(b) Positions of pressure measurement.

Figure 2. Test pump schematic and positions of pressure measurement.

Table 1. Specifications of the test pump.

Displacement [cm³]	9.94	
Dimensions / number of teeth	Inner rotor	Outer rotor
Width [mm]	19.476	19.479
Tip diameter [mm]	38.0	33.4
Root diameter [mm]	28.2	43.7
Outer diameter [mm]	—	50.649
Total side clearance [μm]	42	39
Diametral clearance [μm]	—	149
Number of teeth	7	8

Experimental Apparatus and Method

Figure 3 shows the experimental apparatus. The test pump was driven by an induction motor at different rotational speeds ($500-4000$ min^{-1}), discharge pressures ($1-3$ MPa), and oil temperatures ($20-100$°C), and the pump discharge pressure was adjusted using a throttle valve mounted at the outlet of the pump. The oil temperature was measured in a reservoir. The viscosity of the oil was 0.0436 Pa · s at 20°C, 0.0106 Pa · s at 60°C, and 0.0043 Pa · s at 100°C. The discharge pressure, suction pressure, and pressures in the side clearances of the inner rotor, rotational speed, discharge flow rate, and shaft torque were measured and recorded using a data logger with a sampling period of 1 ms.

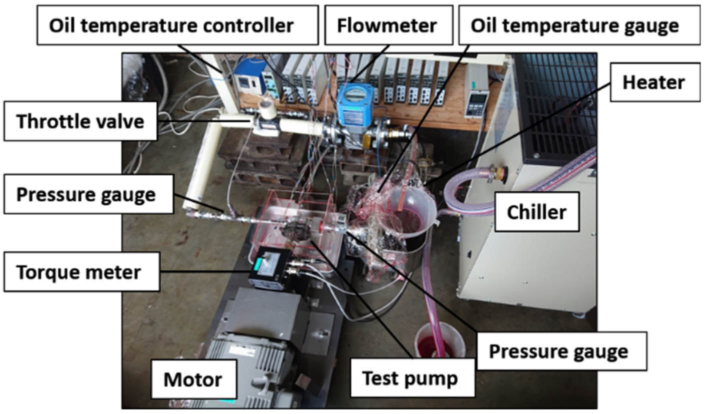

Figure 3. Experimental apparatus.

NUMERICAL ANALYSIS

A simplified model was developed to numerically analyze the pressure distributions in the clearances around the rotors and is shown in Figure 4, in which yellow spaces stand for the flow passages and are divided into six

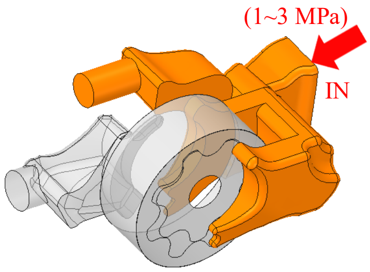

(a) Space between the inlet and suction ports.

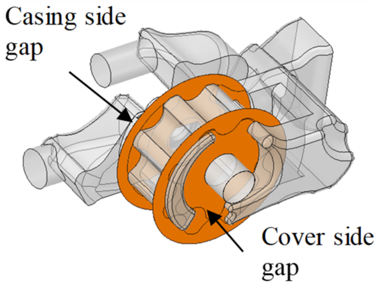

(b) Side gaps of rotors.

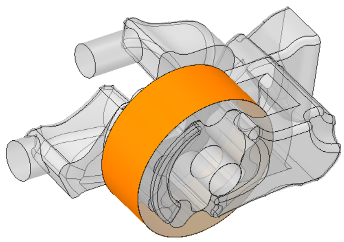

(c) Gap on the outer periphery of the outer rotor.

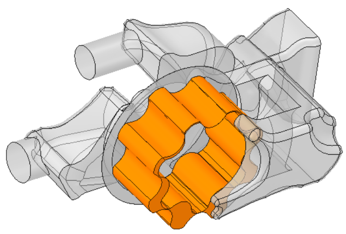

(d) Space between the two rotors.

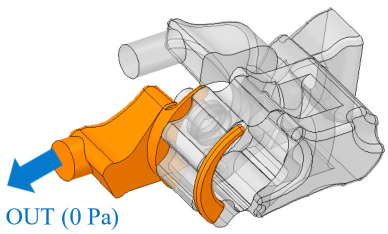

(e) Space between the discharge ports and outlet.

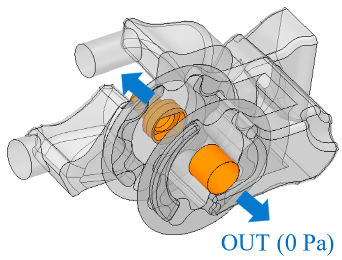

(f) Gaps between the driving shaft and plain bearings.

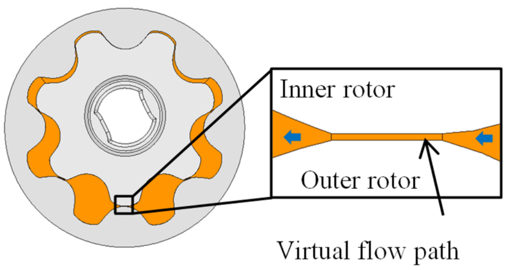

(g) Virtual flow path.

Figure 4. Analytical model.

subspaces. Figure (a) shows the space between the inlet port and the suction ports of the pump, Figure (b) the space between the sides of the two rotors and cover/casing, Figure (c) the space between the casing circular wall and the outer periphery of the outer rotor, Figure (d) the space between the two rotors, Figure (e) the space between the discharge ports of the pump and the outlet, and Figure (f) the space between the driving shaft and plain bearings machined in the cover and cover-with-ports.

The purpose of this numerical simulation is to examine whether some difference in pressure distribution is generated between the two sides of the rotors or not. Therefore, to simplify the simulation, the following conditions (1) to (4) were set: (1) The rotors do not rotate and are stationary in the center between the cover and casing sidewall. (2) The rotors are not eccentric and do not tilt. (3) The pump is operated as a hydraulic motor, though the rotors do not rotate. Therefore, to generate a pressure difference between the inlet and outlet, (4) a flow path is formed between the teeth of the inner and outer rotors situated near the transition zone from the high pressure side to the low pressure side, as shown in Figure 4(g), and pressure in the range of 1 to 3 MPa is applied to the inlet (Figure 4(a)) while 0 Pa is applied to the outlet (Figures 4(e), (f)). The height of the virtual flow path was adjusted so that the theoretical flow rate of the pump corresponding to each rotational speed passed through at each inlet pressure. A CFD software, ANSYS CFX (Ver.18.0), was used for the numerical simulation.

RESULTS AND DISCUSSION

Figure 5 shows the pressures measured at the points 1 to 6 shown in Figure 2(b) under the conditions of 60℃, 3 MPa, $3000\ \mathrm{min}^{-1}$. The highest pressure was observed at point 5 for this condition but was observed at point 6 for some other conditions. The magnitudes of the mean value and fluctuation of the pressure at each point were different at the casing side and cover side. It is considered that such differences result from the difference in the side gap and from the inclination of the inner rotor as shown in Figure 1.

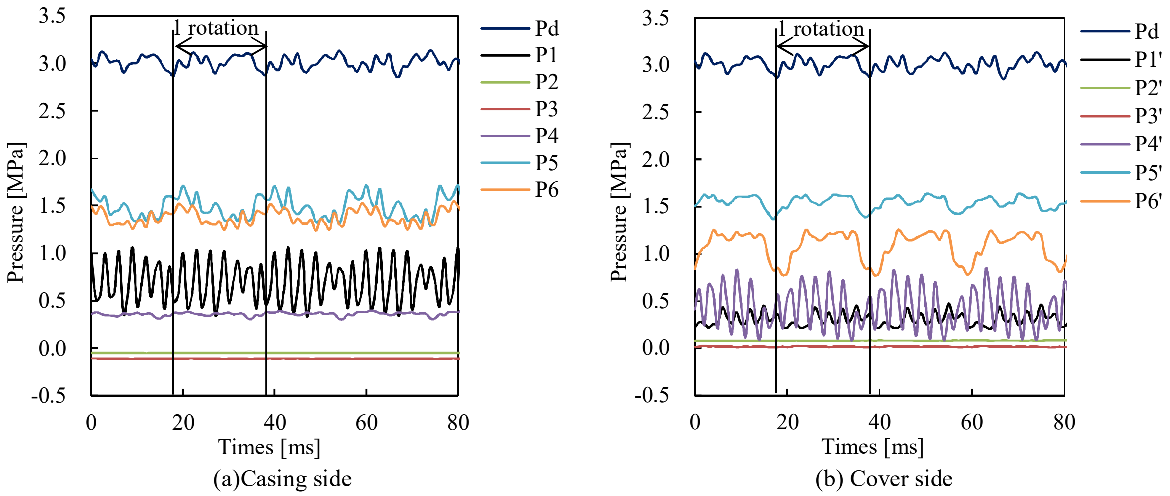

Figure 5. Pressures on the inner rotor sides measured at 60℃, 3 MPa, $3000\ \mathrm{min}^{-1}$ (P_d is the discharge pressure, $P_1(P_1{}')$ to $P_6(P_6{}')$ are the pressures at the points 1 to 6 shown in Figure 2(b)).

Figure 6 provides an example of the pressure distribution on the casing side and cover side of the rotors obtained by the numerical simulation. The pressure distributions on both sides were almost the same, but it can be seen that there is some difference in the area around $\theta = 180^{\circ}$. The length of the flow passage from the branching point downstream the inlet to the casing-side suction port is shorter than that from the branching point to the cover-side suction port, and the former is about a half of the latter (see Figure 4). The pressures at both suction ports are macroscopically the same because the suction ports on both sides are connected through the space between the two rotors. Therefore, the pressure drop must be the same in both flow passages. This means that the flow velocity in the shorter passage is about twice that in the longer passage, which was demonstrated by the numerical simulation. Such a difference in inflow velocity at both suction ports may cause differences in velocity as well as pressure in the two side gaps of the rotors. In addition, all the fluid that have passed through the side gaps of the rotors point toward the outlet. Such an asymmetric flow passage structure downstream the discharge port also may cause asymmetric pressure distributions in the two side gaps of the rotors.

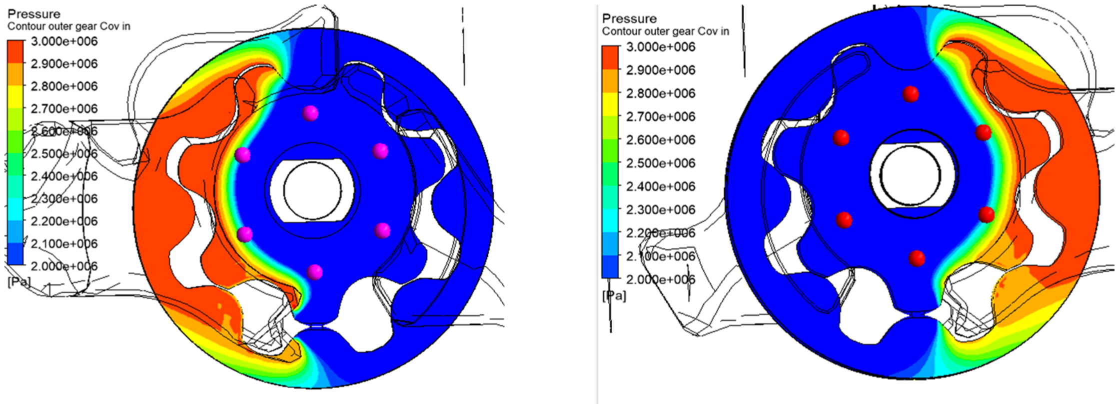

(a) Casing side. (b) Cover side.

Figure 6. Simulated pressure distribution on both sides of rotors at 60℃, 3 MPa, 3000 min^{-1}.

Figure 7 compares the measured pressure distributions on both sides of the inner rotor with simulated ones; for the latter, the pressures at the points symmetrical to the measurement points with respect to the line connecting the angular positions of $\theta = 0^{\circ}$ and $\theta = 180^{\circ}$ are plotted. An error bar attached to each measured value indicates the range of the pressure fluctuation at each measurement point, as shown in Figure 5. It is shown that the simulated pressures were larger than the measured ones but that the tendency of the pressure variation with angle was almost the same in the experiment and simulation. It is considered that the difference in the magnitude of the pressure between the experiment and simulation results from the differences in the axial position and the attitude of the rotor. The inner rotor in the numerical simulation model were situated at the center between the cover and casing sidewall and did not incline, while that in the test pump were not at the middle and inclined. The inclination of the inner rotor causes the variations of the gaps and may increase the leakage flow rate through the gap, which was confirmed by comparing the leakage flow rate between the experiment and numerical simulation. It is considered that a larger leakage flow rate in the experiment than in the numerical simulation generated a larger pressure drop in the side gaps and that the pressures in the side gaps were lower in the experiment than in the numerical simulation.

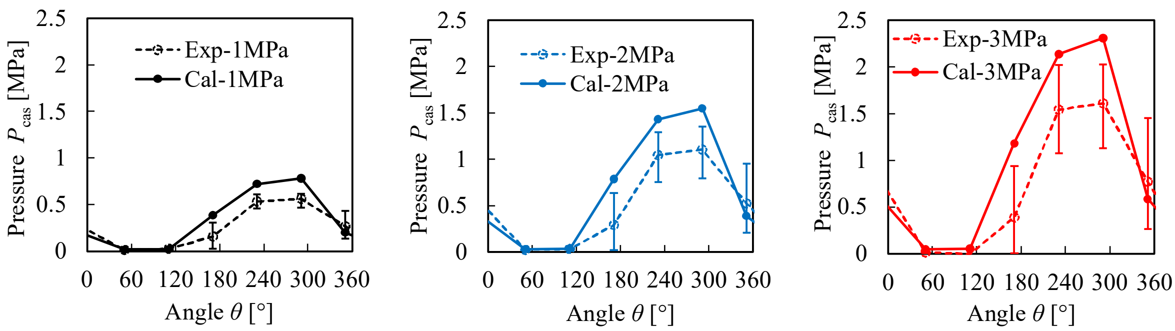

(a) Pressure distribution on casing-side surface.

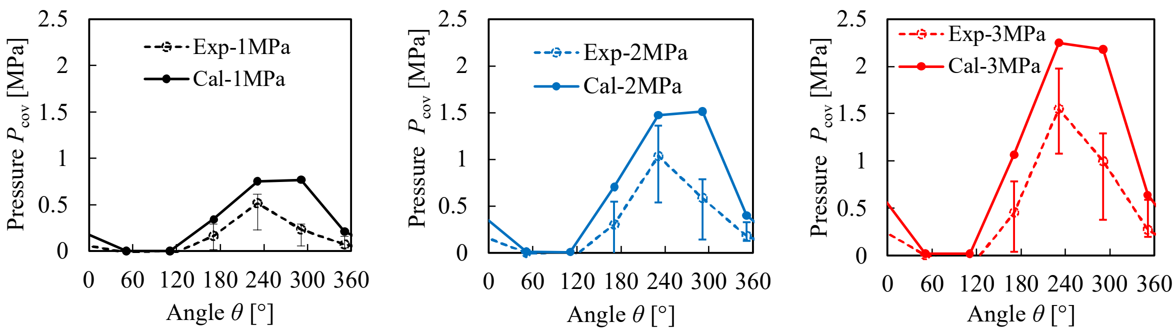

(b) Pressure distribution on cover-side surface.

Figure 7. Comparison of pressure distribution on both sides of the inner rotor between experiment and numerical simulation at 60℃, 3000 min^{-1}.

Figure 8 shows the simulated axial force acting on the inner rotor F_{in} and that acting on the outer rotor F_{out} which were calculated from the simulated pressure distributions. Positive values of the forces mean that the forces act in the direction from the cover to the casing sidewall. The numerical simulations were conducted under different viscosities μ, pressure differences ΔP, and flow rates (corresponding to rotational speeds N), and the calculated axial forces were plotted against the dimensionless parameter $\mu N/\Delta P$. It can be seen that the force F_{in} tends to point to the cover but that the force F_{out} points to the casing sidewall at almost all the values of $\mu N/\Delta P$. The latter result corresponds to the previously measured results [14], which showed that the outer rotor rotated in the vicinity of the casing sidewall. The magnitude of F_{in} was larger than that of F_{out}, which means that the pressure difference between the two sides of the inner rotor is larger than that of the outer rotor. In addition to the axial forces, the differences in pressure distribution on both sides of the rotors generate moments of forces acting on the rotors. The moment of force acting on the inner rotor makes it incline because there was a relatively large diametral clearance (65 μm) between the hole at the center of the inner rotor and the driving shaft. The inclined inner rotor may contact the cover and/or the casing sidewall. The pressure difference between the two sides may vary with rotational angle because the side gaps varied with rotational angle in practice. Therefore, the moment of force acting on the inner rotor varies with rotational angle, which causes the variation of the inclination angle with rotational angle, as shown in Figure 1.

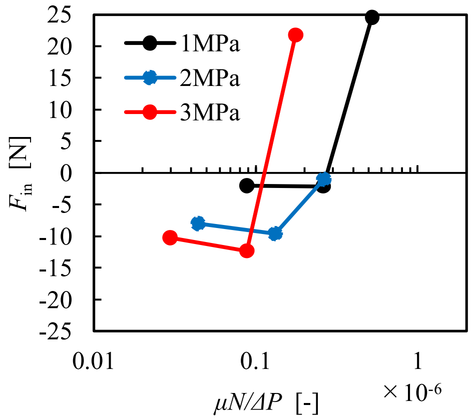

(a) Axial force acting on the inner rotor.

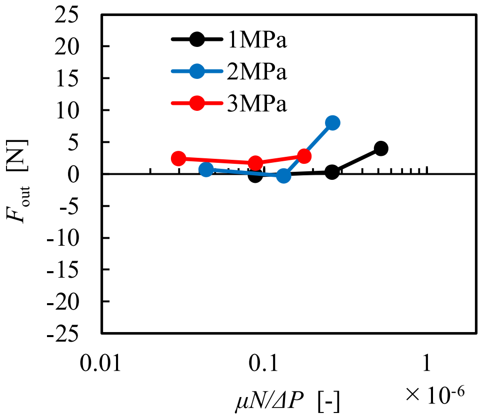

(b) Axial force acting on the outer rotor.

Figure 8. Simulated axial forces acting on the inner and outer rotors ($F_{in} F_{out} > 0$ indicates that the force acts toward the casing sidewall.).

CONCLUSION

In this study, pressure distributions on both sides of the rotors of a gerotor pump used for automatic transmissions were measured and numerically simulated using a simplified model. The measured and simulated pressure distributions agreed qualitatively. The simulations showed that the pressure distributions on both sides of the rotors were different even though the rotors were situated at the middle of the cover and casing sidewall and did not incline, and that an axial force acting on the outer rotor toward the casing sidewall was generated, which agreed with the result of the previous study [14].

ACKNOWLEDGMENTS

This work was supported by the Project for Building Simulation Platforms to Accelerate Development of Next-Generation Vehicles (Transmission Research Association for Mobility Innovation; TRAMI) grant in 2020.

REFERENCES

1. NAKAMURA, T., Improvement of Fuel Efficiency of Passenger Cars by Taking Advantage of Tribology, Journal of Japanese Society of Tribologists, 2016, 61-2, pp.65-70. (in Japanese)
2. WILSON, W., E., Rotary-Pump Theory, Transactions of the ASME, 1946, 68-4, pp.371-384.
3. WILSON, W., E., Performance Criteria for Positive-Displacement Pumps and Fluid Motors, Transactions of the ASME, 1949, 71-2, pp.115-120.
4. INAGUMA, Y., HIBI, A., Friction Torque Characteristics of a Vane Pump, Journal of the Japan Hydraulics & Pneumatics Society, 1994, 25-7, pp.843-849. (in Japanese)

5. KLUGER, M., A., FUSSNER, D., R., ROETHLER, B., A Performance Comparison of Various Automatic Transmission Pumping Systems, 1996, SAE paper 960424.
6. MANCO, S., NERVEGNA, N., RUNDO, M., ARMENIO, G., PACHETTII, C., TRICHILO, R., Gerotor Lubricating Oil Pump for IC Engines, 1998, SAE Paper 982689.
7. INAGUMA, Y., Friction Torque Characteristics of an Internal Gear Pump, Proceedings of the IMechE, Part C: Journal of Mechanical Engineering Science, 2011, 225-6, pp.1523-1534.
8. INAGUMA, Y., Oil Temperature Influence on Friction Torque Characteristics in Hydraulic Pumps, Proceedings of the IMechE, Part C: Journal of Mechanical Engineering Science, 2012, 226-9, pp.2267-2280.
9. INAGUMA, Y., Friction of Outer Rotor Affecting Friction Torque Characteristics in an Internal Gear Pump, Proceedings of the IMechE, Part C: Journal of Mechanical Engineering Science, 2015, 229-16, pp.3013-3026.
10. MANNE, V. H. B., VACCA, A., MERRILL, K., A Numerical Method for Evaluating the Torque Efficiency of Hydraulic Orbit Motors Considering Deformation Effects and Frictional Losses, Mechanical Systems and Signal Processing, 2021, 146, 107051.
11. RITURAJ, R., VACCA, A., RIGOSI, M., Modeling and Validation of Hydro-Mechanical Losses in Pressure Compensated External Gear Machines, Mechanism and Machine Theory, 2021, 161, 104310.
12. PHAM, T. H., MÜLLER, L., WEBER, J., Dynamically Loaded the Ring Gear in the Internal Gear Motor/Pump: Mobility of Solution, Journal of Mechanical Science and Technology, 2018, 32-7, pp.3023-3035.
13. PHAM, T. H., MÜLLER, L., WEBER, J., Theoretical and Experimental Analysis of the Effect of Misaligned Ring Gear on Performance of Internal Gear Motors/Pumps, Journal of Mechanical Science and Technology, 2019, 33-9, pp.4049-4060.
14. UCHINO, T., TAKENO, T., KOJIMA, R., YOKOYAMA, H., YANADA, H., Behaviors of Gears in an Internal Gear Pump for Automatic Transmission, The Proceedings on Autumn Conference of Japan Fluid Power System Society 2019, 2019, pp.35-37. (in Japanese)

The 11th JFPS International Symposium on Fluid Power HAKODATE 2020 Oct. 12-13, 2021 The Japan Fluid Power System Society

Modeling of Compact Car Active Suspension with Pneumatically Controlled Variable Damping Force Oil Damper and Variable Rigidity Air Spring

Yasukazu SATO* and Shogo SATO**

*Department of Mechanical Engineering, Faculty of Engineering, Yokohama National University
79-5, Tokiwadai, Hodogaya, Yokohama, Kanagawa, 240-8501 Japan
(E-mail: sato-yasukazu-zm@ynu.ac.jp)
**Former Graduate Student, Graduate School of Engineering Science, Yokohama National University
79-5, Tokiwadai, Hodogaya, Yokohama, Kanagawa, 240-8501 Japan

Abstract. Active suspension system with a pneumatic linear actuator consisting of airtight devices, an air spring, and a variable damping force damper, has been developed with the aim of controlling the posture of a compact car during turning and acceleration / deceleration. In this active suspension, the air pressure can control both the rigidity of the air spring and the damping force characteristics of the damper. In the variable damping force damper, the relation between the air pressure and the damping force has non-linear characteristics, and it is important to model the variable damping force mechanism at the design stage in order to estimate the performance of the active suspension and the vehicle behavior. In this paper, the model of the fluid resistance element in the variable damping force mechanism is conducted for expressing its non-linear characteristics. This model fits actual damper behavior well.

Keywords: Modeling, Suspension, Air spring, Damper, Automobile

INTRODUCTION

Automobile suspension is a mechanism that generates passive spring force and damping force by coil spring and oil damper, and the specifications of spring and damper determines the suspension performance. Some kinds of active suspension system have an air spring actuator controlled by air pressure or a damper actuator controlled by the auxiliary oil hydraulic power source. However, it is necessary to install control valves to the active suspension system, and there is a problem of difficulty to install them in a small vehicle.

For this issue, the authors proposed a compact and lightweight airtight circuit pneumatic system in which actuators, tanks, compressors, etc. were composed of airtight equipment that has no sliding parts and no leak of gas, and applied it to active suspension using air springs [1]. Figure 1 is a photograph of a small vehicle equipped with an air spring active suspension to control the attitude of roll behavior during turning and pitch behavior during acceleration / deceleration. In this active suspension, the pressure-resistant thin-wall metal bellows developed by the authors is used for the airtight variable volume actuator and compressor. Figure 2 shows the structure of the pressure-resistant thin-wall metal bellows. A viscoelastic ring is inserted in the inner diameter groove of a conventional thin-wall metal bellows to maintain the curvature of the groove against deformation of the bellows and prevent stress concentration and buckling of the groove due to the rise in gas pressure inside the bellows. Therefore, it maintains elasticity of thin-wall metal bellows, and its pressure resistance is 7 times that of conventional thin-wall metal bellows. It is possible to output 7 times power in the same cross-sectional area by supplying higher air pressure. The authors installed a pressure-resistant thin-wall metal bellows air spring on the outer cylinder of the damper to control the spring rigidity instead of the coil spring of the normal suspension, and

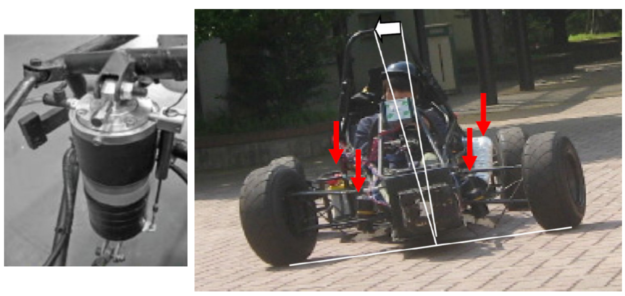

Figure 1. Vehicle posture control using metal bellows air-spring active suspension

also installed a metal bellows of the same structure inside the damper to vary the damping force by air pressure control. As shown Fig.3, an active suspension with pneumatically controlled variable damping force damper has been developed.

Since this variable damping force damper has a non-linear damping force characteristic with respect to the controlled air pressure, for applying it to various vehicles with different specifications, a model of the non-linear damping force characteristic needs to be constructed. is constructed. At the design stage, it is important to estimate the performance of the active suspension and the behavior of the vehicle. In this paper, the authors construct a model of the fluid resistance element of the damping force device, and report that the characteristic representation by the model shows good agreement with the experimentally measured result of the prototype damper. Except for the damping force device, the authors have reported the model of metal bellows air spring and conventional oil damper in the former researches [1],[2].

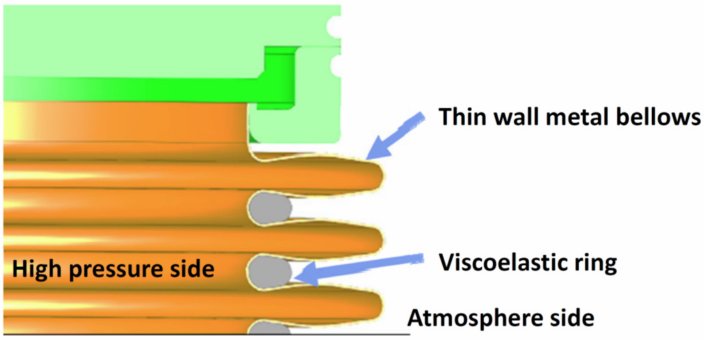

Figure2. Pressure-resistant thin-wall metal bellows

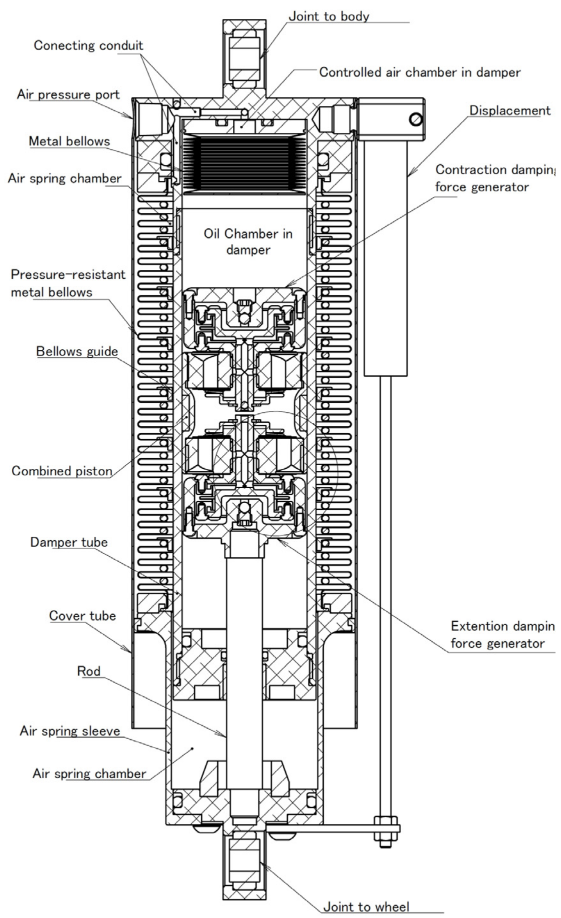

Figure 3. Developed metal bellows air spring with controllable damping force device

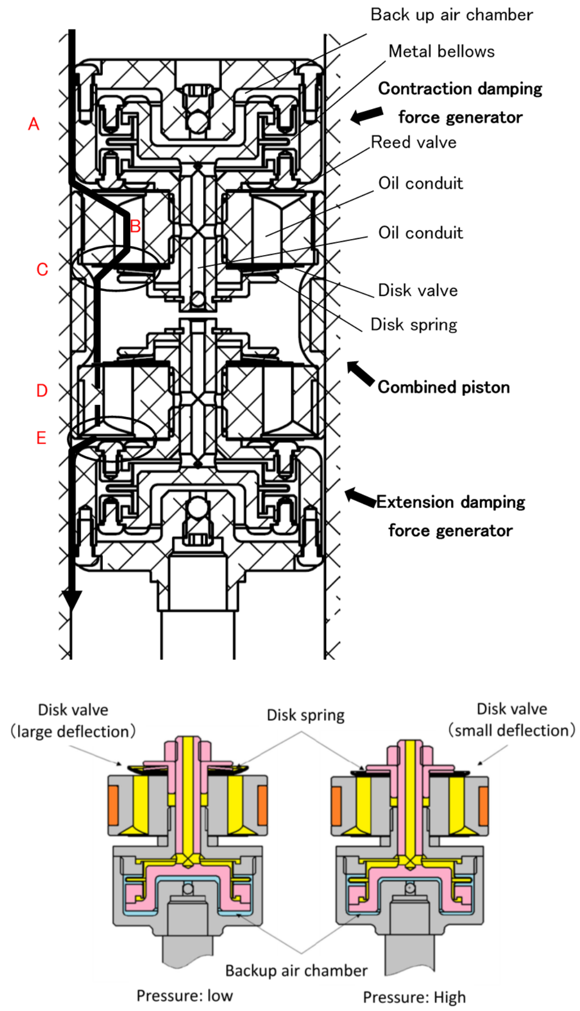

Figure 4. Combined piston with damping force devices

STRUCTURE AND WORKING PRINCIPLE OF VARIABLE DAMPING FORCE CHARACTERISTICS DAMPER

In the variable damping characteristic damper shown in Figure 3, the controlled air pressure is supplied to the thin-wall metal bellows chamber corresponding to the gas chamber of a normal oil damper,. The metal bellows separates the oil inside the damper from the air in the bellows chamber.
With this structure, the controlled air pressure in the bellows chamber can adjust the pressure of the oil inside the damper. The damper piston is a composite piston in which damping force generation mechanisms are installed on the head side and rod side of the piston, respectively. The mechanism installed on the head side generates damping force during contraction, and the mechanism on the rod side generates a damping force during extension. Figure 4 shows the damping force generators. Each contraction and extension damping force generator is symmetrically arranged around the combined piston. The neutral pressure adjusted to the bellows chamber pressure acts as a static pressure on the entire mechanism. The neutral pressure controls the set load of the disc spring by air volume change of the backup air chamber kept airtight with the metal bellows. The set load of the disc spring is applied to press the disc valve. As the neutral pressure rises, the set load of the disc spring increases. For contraction, the oil flow is squeezed by the disc valve (part C) through the gap (part A) and oil passage (part B) on the outer periphery of the damping force generation mechanism to generate a pressure difference. The load is set to the disc spring, and a corresponding damping force is generated. Then, the oil passes through the passage (part D, broken line part in Figure 4) apart from the disc valve passage. The oil flows out from the rectifying valve (part E) with a low set load. Damping force is generated by the same manner of oil flow during extension.

MODEL CONSTRUCTION OF FLUID RESISTANCE ELEMENT OF DAMPING FORCE GENERATOR

Principle of Actuation of Damping Force Generator

Figure 5 shows the measured values of the damping force characteristics. The air pressure of 0.2MPa, 0.4MPa, and 0,6MPa controls the damping force characteristics. In the figure, the vertical axis is converted from the damper piston speed to the flow rate Q passing though the piston, and the horizontal axis is converted from the damping force to the pressure difference ΔP between both sides of the piston.
Based on the actual measurement results and the operating principle, the model of the damping force characteristics of the variable damping force damper is constructed. In the condition that the pressing force on the disc valve by the controlled air pressure is sufficiently large, the disc valve below the cracking pressure does not lift. It is assumed that the thin parallel walls passage flow represents the clearance leakage flow region $Q1$ in this condition. The flow region $Q2$, in which the pressure difference at the piston ΔP increases and the disc valve bends and lifts, is added to the region of $Q1$.

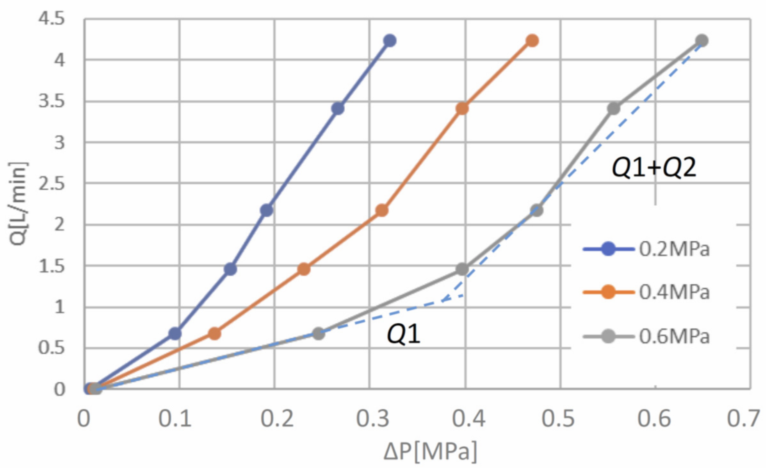

Figure 5. Measured damping force characteristics for damper rod extension
(Damper force and velocity are converted to pressure and flow rates)

Modeling of Fluid Resistance at Damping Force Generator

Leakage flow region – Disc valve in damping force generator does not lift

Both flow regions are expressed as the followings;
For the leakage flow region $Q1$;

$$Q1 = \frac{bh^3}{12\mu l}\Delta P \tag{1}$$

where the leakage flow rate $Q1$ is assumed as laminar flow, and symbols are defined as the clearance width b, clearance height h, the clearance overlap length l, and oil viscosity coefficient μ , respectively. In the flow region $Q1$, the disc valve does not lift. Therefore, all parameters are fixed except the pressure difference ΔP.

Orifice flow region – Disc valve in damping force generator lifts according to pressure difference

The formula of orifice is applied to the estimation of passing flow rate through the orifices consisting of the circular hole and the disc valve in the damper piston. The orifice holes are circularly arranged in equal interval. The orifice flow region $Q2$ is expressed by;

$$Q2 = nC_dA\sqrt{\frac{2\Delta P}{\rho}} \tag{2}$$

where, symbols are defined as the number of orifice holes n, the discharge coefficient C_d, and oil density ρ, respectively. The discharge coefficient C_d is represented by the function of Reynolds number, and the approximate expression in the reference [3] is used. The cross-sectional area of flow path, A, for one orifice hole is assumed as the cylindrical surface with the circumference of hole and the valve lift but bending of the disc valve from the center to the outer circumference is also considered. The thin wall disc valve lifts and bends, since the center of the disc is loaded with pneumatically controlled set force and the outer area of disc receives the pressure at the hole. Considering bending of disc valve, the cross-sectional area A is expressed by;

$$A = \pi d\delta \cdot \frac{1}{\pi} \tag{3}$$

where, symbols are defined as the diameter of the circular hole d, the lift of the disc valve at the outer peripheral side δ, respectively. In Eq.(3), $1 / \pi$ is the correction coefficient of the flow path area due to the disc valve bending. The disc valve lift is expressed by;

$$\delta = \frac{A'\Delta P - F_0}{k} \tag{4}$$

where, A is the equivalent pressure receiving area of disc valve, which is considered not only circular hole but also the pressure distribution around the hole. F_0 is the initial load of the disc valve determined by the set pressure of air pressure control, and k is the combined spring constant of the disc valve and the disc spring. For the orifice flow region $Q2$, t the following equation is derived from Eq. (2) to Eq. (4);

$$Q2 = \frac{n}{\pi}\cdot C_d\pi d\frac{A'\Delta P - F_0}{k}\sqrt{\frac{2\Delta P}{\rho}} = nC_d d\frac{A'\Delta P - F_0}{k}\sqrt{\frac{2\Delta P}{\rho}} \tag{5}$$

EXPERIMENTAL VARIDATION OF DAMPING FORCE GENERATOR MODEL

Figure 6 shows the result of calculation of the variable damping force generator model. The proposed model can express the nonlinear characteristics of the damping force generator for each controlled air pressure. This model fits actual damper behavior well.

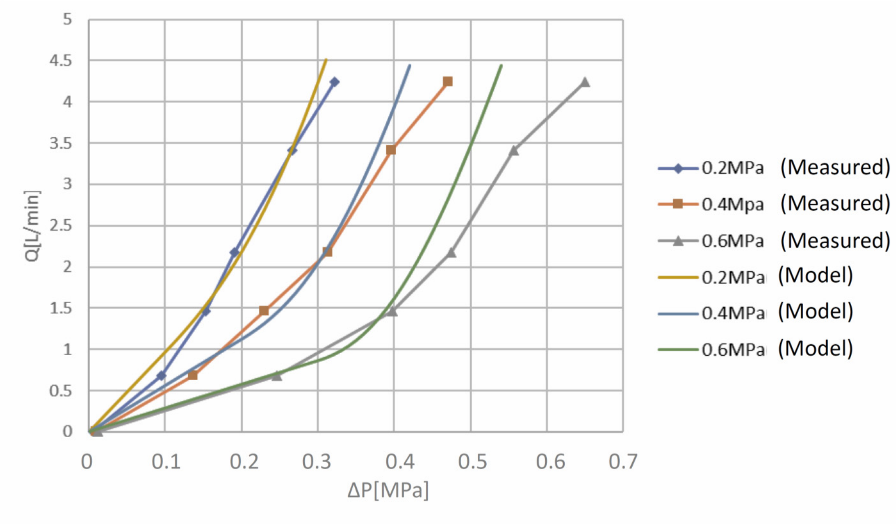

Figure 6. Comparison of measured damping force characteristics and damping force characteristic model for damper rod extension
(Damper force and velocity are converted to pressure and flow rates)

CONCLUSION

In this paper, a model of the nonlinear damping force characteristics of an active suspension for compact cars is constructed, which consists of an air spring using a pressure-resistant thin wall metal bellows and a variable damping force damper. Tools simulating the behavior of vehicles equipped with conventional suspension are widespread at the design stage. By incorporating the proposed model of damping force generator into the damper section, it is expected to estimate the performance and vehicle behavior of the developed active suspension at the design stage.

REFERENCES

1. SATO, Y., MIYAZAWA, J., HIRAYAMA, T., SHIMBORI, T., Pressure Resistance Improvement of Metal Bellows for Pneumatic Actuators, Proceedings of the 9th JFPS International Symposium on Fluid Power Matsue 2014, 2014, pp.284-289.
2. OGAWA, T., SATO, Y., SHIMBORI, T., Air Spring Suspension for Compact Vehicle Posture Control using Metal Bellows Actuator, Proceedings on Autumn Conference of JFPS 2017, 2017, pp. 95-97.(in Japanese)
3. McCLOY, D., MARTIN, H., Control of Fluid Power: Analysis and design 2nd edition, Ellis Horwood Limited, 1980, pp.101-103.

The 11th JFPS International Symposium on Fluid Power HAKODATE 2020 Oct. 12-13, 2021 JFPS The Japan Fluid Power System Society

Power Absorber by Air Compression and Release Cycle with Controller for Adjusting Air Release Timing to Obtain Variable Absorbing Capacity (First Report – Basic Concept and Design)

Takashi SHIBAYAMA*, Toshinori FUJITA* and Sho UEYAMA*

* Department of Advanced Machinery Engineering, Faculty of Engineering, Tokyo Denki University
5 Senju-Asahi-cho Adashi-ku, Tokyo, 120-8551 Japan
(E-mail: t-shiba@f5.dion.ne.jp)

Abstract. To reduce CO2, fuel cell system for heavy duty trucks is under development popularly in the world. For conventional heavy trucks with internal combustion engine (Hereafter ICE), power absorber by air compression and release cycle is widely utilized to obtain effective braking force on long steep down hill road. However, there is no ICE in fuel cell system. Regenerative brake is also effective for those heavy FCV trucks on the condition that battery state of charge (hereafter SOC) is not full. If battery SOC becomes full, the regenerative brake could not be available. Some emergency power absorber is required for such severe situation. In this paper, new power absorber by air compression and release cycle is proposed which includes controller for adjusting air release timing to obtain variable capacity.

Keywords: Automobile, FCV, Brake, Energy absorber, Compressor

INTRODUCTION

The basic principle of proposed power absorber was reported at CTI Berlin conference in 2019[1]. Figure 1 shows the principle how resistance force generated. Air chamber is made by two different diameter pistons. The two pistons are connected to reciprocating rod and the reciprocating rod is connected to rotating shaft similar as crank system of the ICE.（In this figure, rotating shaft and crank system are not drawn） As shown in the figure, air is in-taken at bottom dead center (Hereafter BDC), then air is compressed, and high resistance force is generated by high pressure. At top dead center (Hereafter TDC), the compressed air is released and exhausted. After TDC, air is expanded and negative pressire is generated,and the resistance forece is generated again by the negative pressure. By those resistance forces , power aborption is obtained. As shown in the figure, there is no moving cams which are quite common for ICE.The moving pistons directly open and close the air inlet and air outlet. Such simple system is aimed in this development. At low speed, isothermal calculation according to the formula “PV=const” can be used,. At high speed , adiabatic calculation can be used and compression pressure will become higher. Here, isothermal calculation is applied to keep margin for designning large enough capacity power aborption .

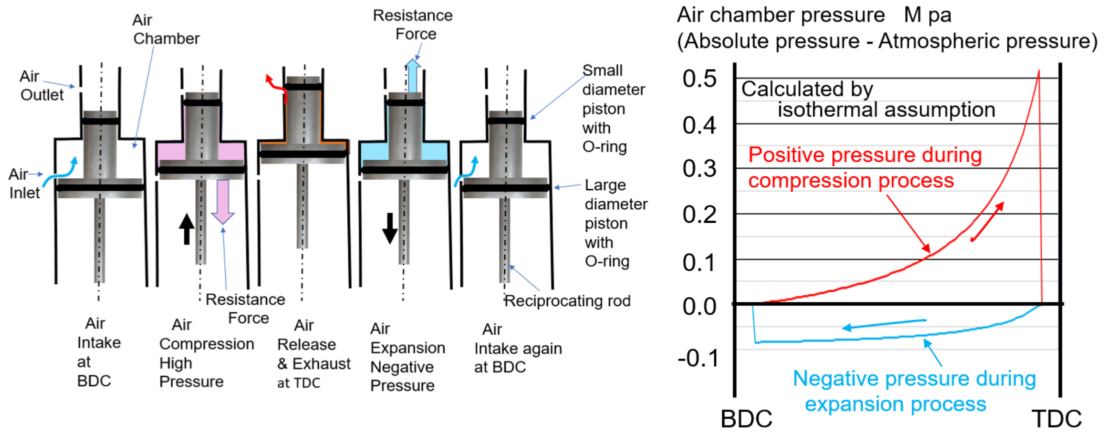

Figure 1. Basic principle of air compression and release cycle power absorber

ADDITIONAL CONTROLLER FOR ADJUSTING AIR RELEASE TIMING

In Figure 2 , new power absorber with controller for adjusting air release timing is shown. Additional controller as shown in the figure 2 is applied. By the screw bolt and nut for adjusting air release timing, distance between the two sliding O-rings becomes variable and adjustable that can be operated by a rotational actuator.

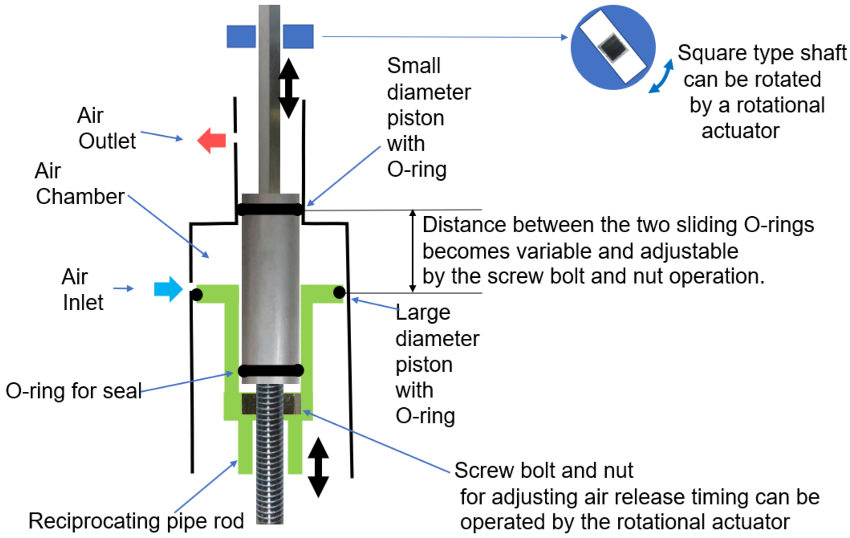

Figure 2. Improved power absorber with air release timing adjusting function.

SOME EXAMPLES OF AIR RELEASE TIMING ADJUSTING

To make the new system more comprehensive, let us see four examples. Figure 3 shows the example when the adjustment makes " No air release" situation. Air outlet could not be opened even at TDC. Positive pressure will remain, and power absorption is not high enough.

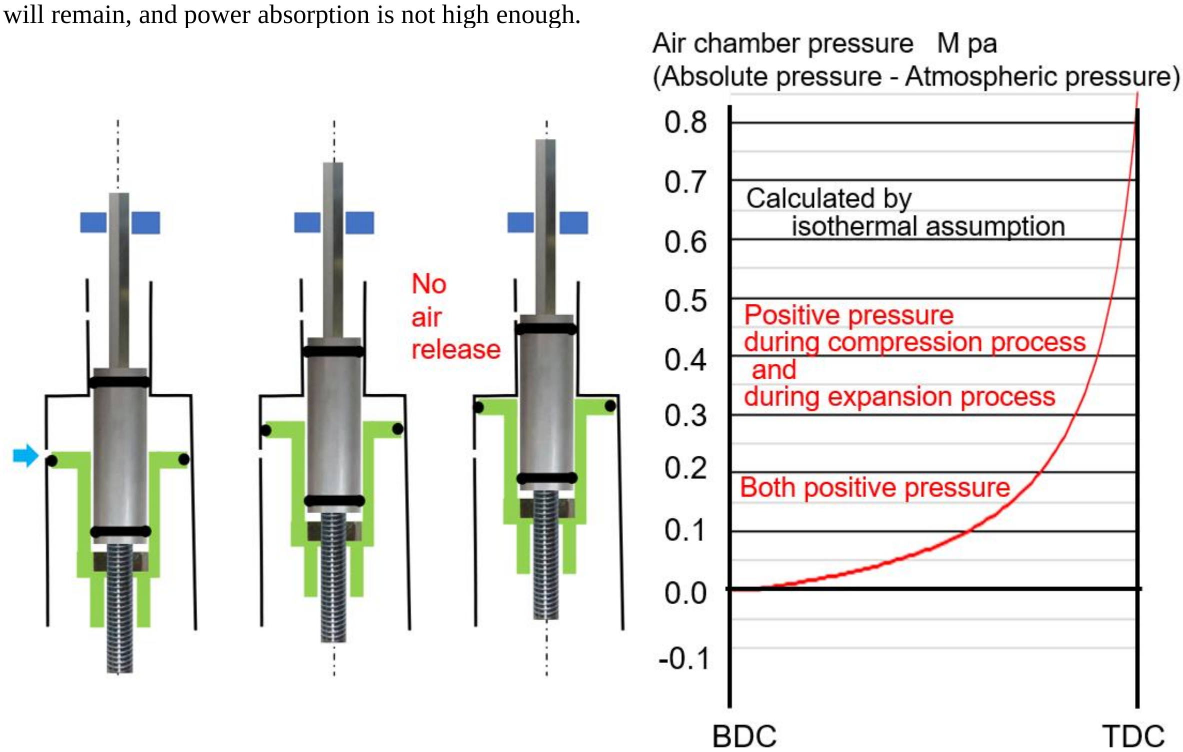

Figure 3. Adjustment Example-1 Air release adjustment makes " No air release " situation

Figure 4 shows the adjustment for maximum power absorption. By this adjustment, power absorber capacity becomes maximum which is equivalent to Figure 1. Compressed air can be released and exhausted at TDC.
And after TDC, negative pressure during expansion process is generated. By both the positive pressure during compression process and the negative pressure during expansion process generate resistance force against the reciprocating axis driving force. Then, maximum power absorption can be executed

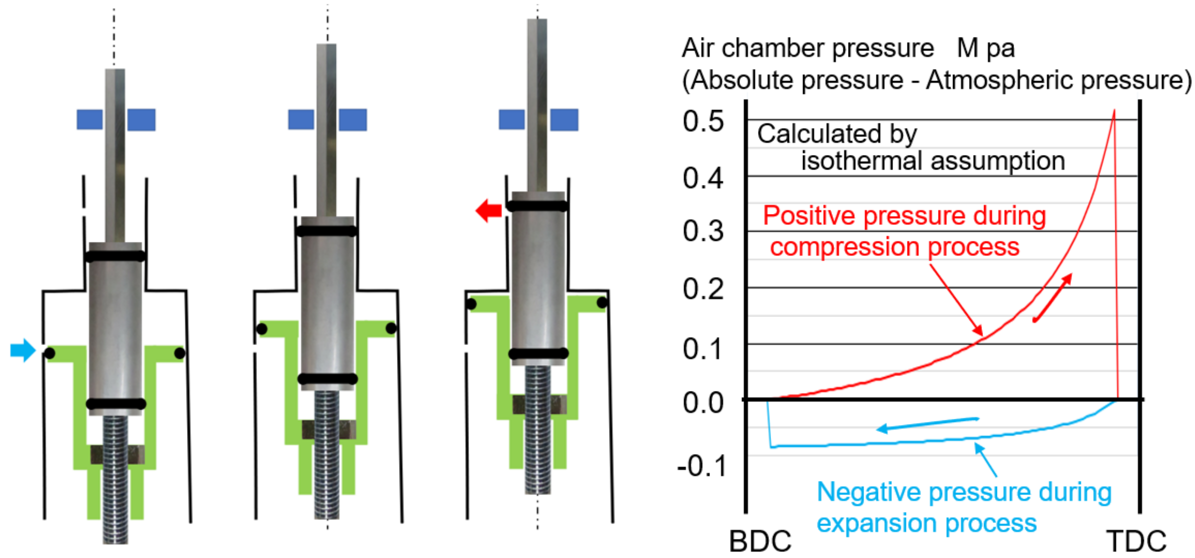

Figure 4. Adjustment Example-2 Power absorber capacity is maximum, equivalent to figure 1

Figure 5 shows the one other example of adjustment for small capacity. Air will be released earlier than figure 4. Because the air release timing is earlier, maximum chamber pressure is lowered and both positive pressure duration length and negative pressure duration length are shortened, that leads to capacity reduction.

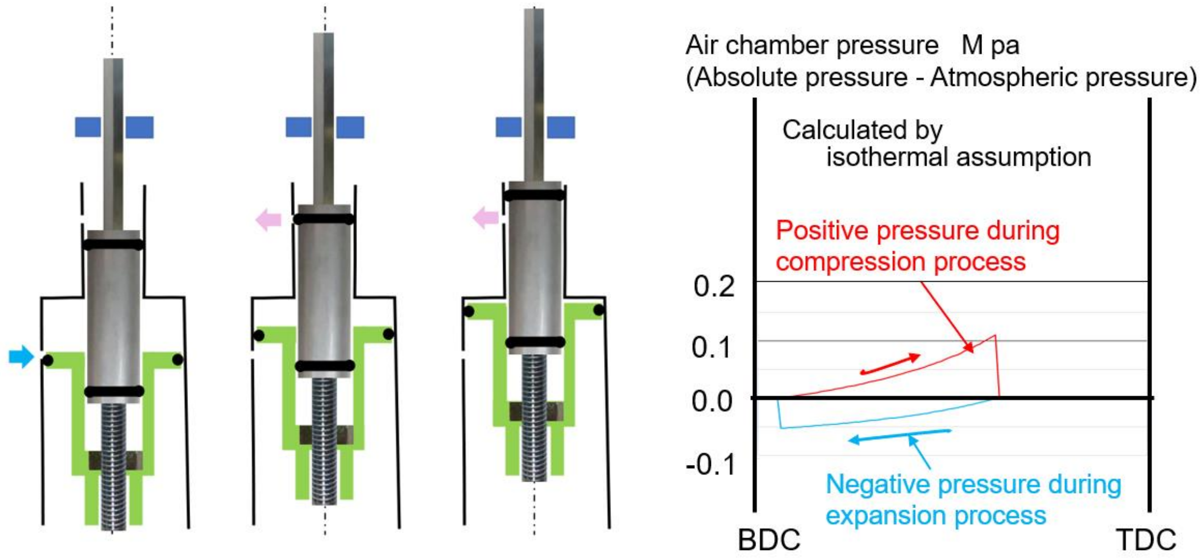

Figure 5. Adjustment Example-3 Power absorber capacity is small

And figure 6 shows the last example. By this adjustment, power absorber capacity becomes very small. If the air release timing would be much earlier than this figure , air release can be started at BDC. By such operation, no absorption situation can be also available.

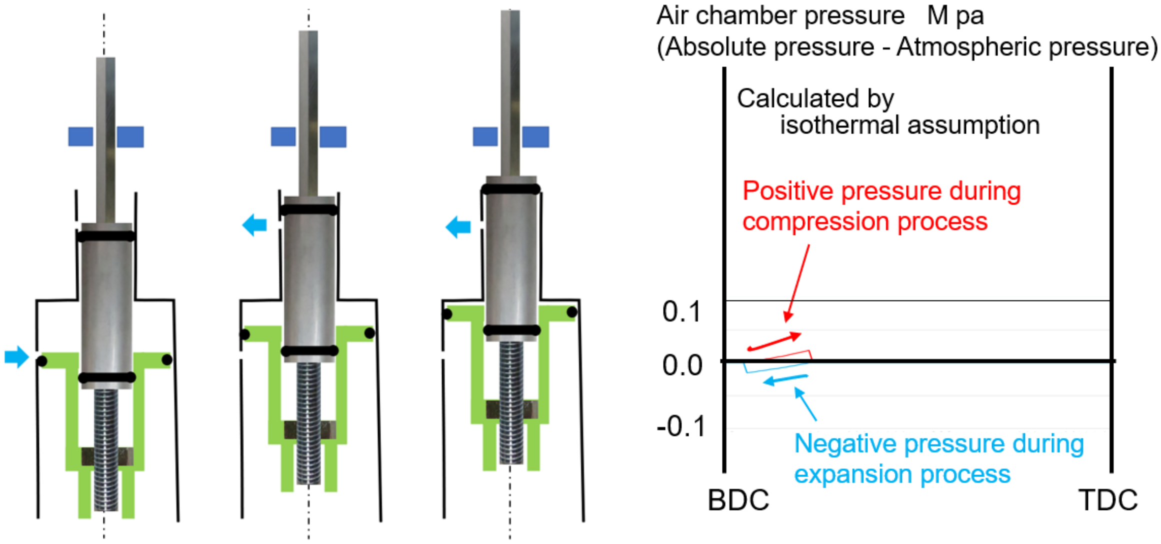

Figure 6. Adjustment Example-4 Powe absorber capacity is very small, almost always released

DESIGN FOR CONFIRMATION TESTING

To make confirmation testing, small desktop size power absorber has been designed and capacity estimation has been executed. Figure 7 shows the result of the capacity estimation. As shown in Figure 7, power absorber capacity can be enlarged by utilizing supercharger for inlet air. If inlet air pressure is larger than atmospheric pressure, pressure of compressed air becomes relatively large, and resistance force also becomes relatively large. The result of planned confirmation testing will be reported at the next report.

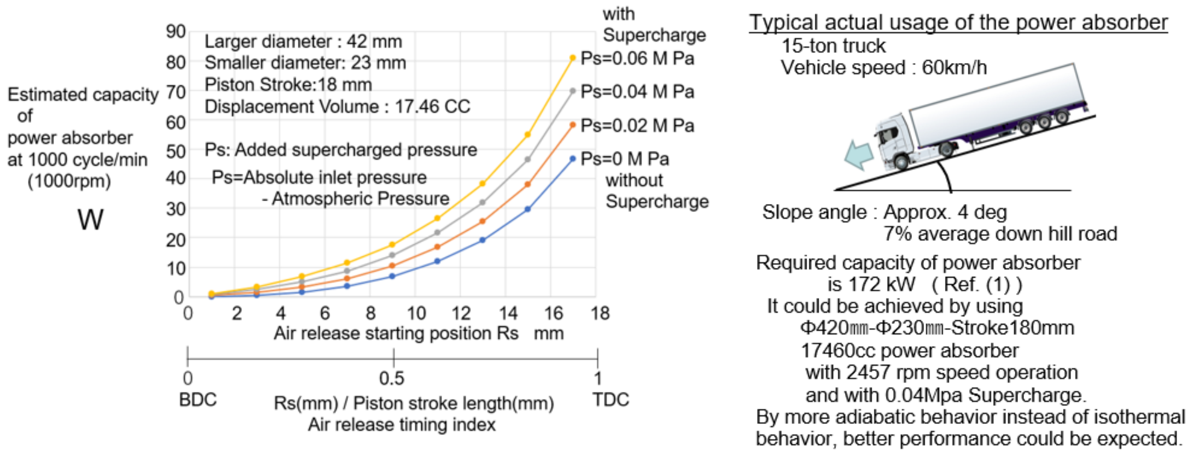

Figure 7. Estimated capacity of the new power absorber prototype for desktop testing.

CONCLUSION

Power absorber by air compression and release cycle with controller for adjusting air release timing has been investigated, and improved power absorber concept is established. Desktop size prototype will be tested and the test result will be reported at the next report.

REFERENCE

1. SHIBAYAMA,T ,How to ensure safety of EV or FCV without reliable, helpful saving functions made by ICE, CTI Berlin conference , 2019, Session G-5

The 11th JFPS International Symposium on Fluid Power HAKODATE 2020 Oct. 12-13, 2021 JFPS The Japan Fluid Power System Society

Clarification of Parameters and Development of a Method for Estimating Loading Forces Acting on The Spool Valve of a Hydraulically Controlled Automotive Transmission

Daisuke YANAGAWA*, Masahiro KOUYA*, Sho TOZUKA*,
Masaru SHIMADA**, Idris TENGKU*** and Naoki UEZONO****

* Department of hardware system development, **CAE group,
Department of experiment, * Experiment Department No. 2
JATCO Ltd
560-2 Okatsukoku, Atsugi, Kanagawa 243-0126, Japan
(daisuke2_yanagawa@jatco.co.jp), (masahiro2_kouya@jatco.co.jp), (sho_tozuka@jatco.co.jp),
(masaru_shimada@jatco.co.jp), (idris2_tengku@jatco.co.jp), (naoki_uezono@jatco.co.jp)

Abstract. The control valve used in hydraulically controlled automotive transmissions contains a spool valve that drains the excess portion of the fluid flow rate while regulating the pressure. The complex flow around the spool valve exerts various loading forces on the valve. These forces can delay valve response owing to increased sliding resistance and also press the valve against the control valve body, giving rise to concern about valve body wear. Although the forces acting on the valve can be calculated by fluid simulations, it has not been known whether the simulation results are correct. Therefore, in this study a load cell was used to measure the loading forces directly. The results confirmed that the tendencies of the calculated results obtained by fluid simulations agreed well with those of the experimental data, thereby verifying the validity of the simulation results.

Keywords: Automatic transmission, Control valve spool, Loading force, Draft angle, Groove depth.

INTRODUCTION

An automotive transmission uses a control valve to supply fluid to multiple hydraulic circuits and to regulate the pressure. Located inside the control valve is a spool valve that drains the excess portion of the fluid flow rate while adjusting the pressure. Loading forces induced by the fluid flow act on the spool valve during the draining process and exert various effects on the valve.

However, heretofore it has been difficult to measure the loading forces acting on the spool valve, although they have been calculated by fluid simulations. Consequently, it has not been known whether the simulation results have been correct. For that reason, judgments about the feasibility of changing transmission specifications have to be based on experimental evaluations of response, wear and other performance parameters. Because specification changes require judgments based on experimentation, a lot of trial and error is involved, which can affect the product development period.

In this work, an experimental setup was built that can directly measure the loading forces acting on the spool valve. This paper presents the results measured with this setup, which confirm the validity of fluid simulations.

SPOOL VALVE STRUCTURE AND CONFIRMATION OF DIMENSIONAL EFFECTS

Fig. 1 shows the structure of the spool valve for which experimental measurements were made in this study. As fluid flows from upstream to downstream, the loading forces produced by the fluid act on the valve to increase friction. That can cause a delay in responsiveness, which is a key characteristic for transmission control. In addition, the loading forces press the spool valve against the control valve body in which it is housed, giving rise to concern about valve body wear.

The experiments measured the effects of two dimensions, the draft angle and the groove depth. It was inferred from fluid simulation results that these two dimensions affect the loading forces.

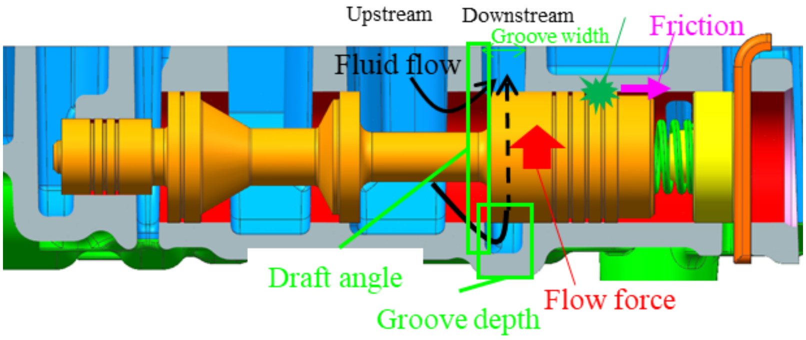

Figure 1 Loading forces acting on the spool valve and their effects

The draft angle refers to the angle of inclination of the valve body wall and is defined as shown in Fig. 2. This inclination is provided to enable easy removal of the mold in the casting process, and the angle is retained by the valve body. The groove depth is defined as shown in Fig. 3.

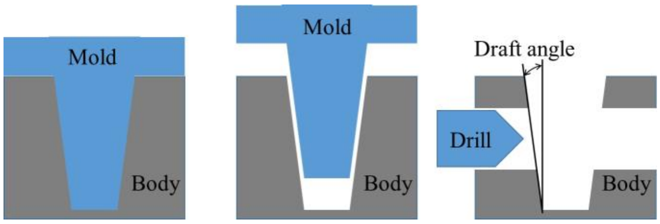

Figure 2 Definition of draft angle

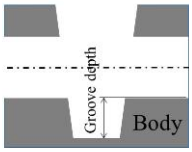

Figure 3 Definition of groove depth

EXPERIMENTAL SETUP

It would be difficult to directly measure the loading force that the spool valve inside the control valve applies to the latter valve body. However, the experimental setup was designed so that the force applied by the spool valve can be measured by a load cell via a rod used as a probe. The position of the rod was determined from simulation results and by confirming the point from wear marks where the spool valve pressed against an actual valve body. A hole was then drilled at that position for installing the rod. The rod passed through a jig to come in contact with the load cell installed above. This structure made it possible to measure the loading forces acting on the spool valve using the load cell via the rod.
The structure of the experimental setup is shown in Fig. 4. The shape of the area around the spool valve in an actual control valve was cut out in the jig, and the attachment parts shown in Fig. 5 enabled the dimensions around the spool valve to be varied. This setup made it possible to determine how the loading forces were affected by the dimensions around the spool valve.
In addition, a screw was provided in the jig at the end of the spool valve for adjusting the amount of stroke from outside the jig so that the pressure would apply force to the rod at the proper stroke position during the experiment.

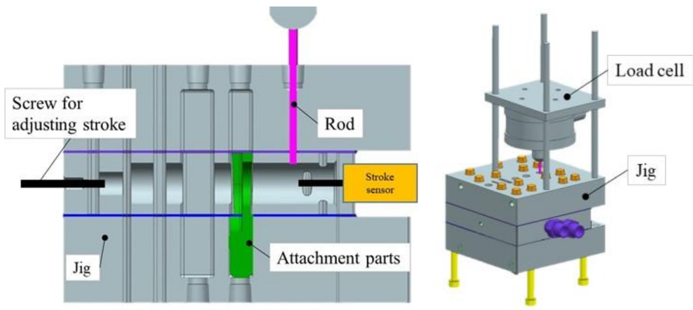

Figure 4 Structure of jig, attachment parts and rod

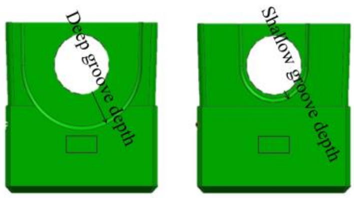

Figure 5 Attachment parts

Fig. 6 shows the measured output of the load cell, representing the loading force applied to it when the upstream pressure was varied using the experimental setup described here. The specifications used in the experiment were a draft angle of 2.0 deg. and a groove depth of 11.5 mm. The vertical axes show the pressure and the loading force applied to the load cell in relation to time on the horizontal axis. The red line is the upstream pressure and the black line is the loading force.

The measured results show that the loading force rose along with the increase in the upstream pressure, indicating that the loading force followed the change in pressure. Presumably, this means that the flow rate increased owing to the differential pressure between upstream and downstream, thereby increasing the loading force produced by the fluid flow. These results confirmed that the experimental setup was capable of measuring the loading force.

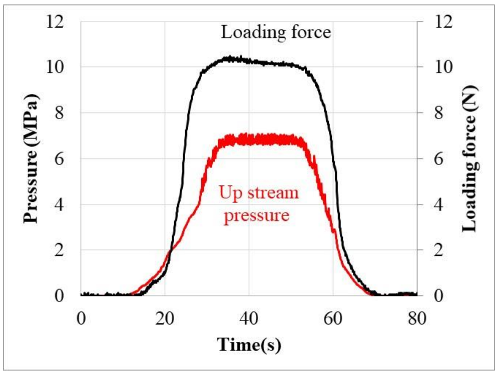

Figure 6 Output of load cell related pressure

SIMULATION MODEL

A 3D model was created of the jig, attachment parts and spool valve described above and used to conduct a fluid simulation of the loading force that was produced by the hydrodynamic force and acted on the position of the rod.

An example of the simulation model is shown in Fig. 7. The loading force simulated in this study acts in the annular clearance between the spool valve and the control valve body as illustrated in Fig. 8. Accordingly, computational accuracy was improved by modeling the annular clearance with a finer mesh.

The simulation conditions were aligned with those of the experiment. In both cases, the upstream pressure was 5.7 MPa, the downstream pressure was 0.7 MPa, the fluid temperature was 50 °C, and the specification of the spool valve diameter was 17 mm.

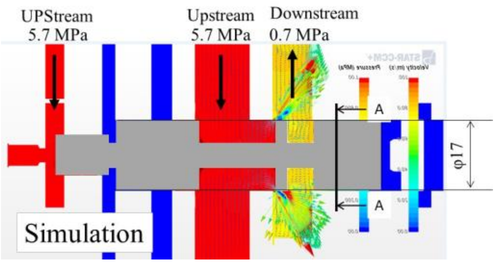

Figure 7 Simulation model

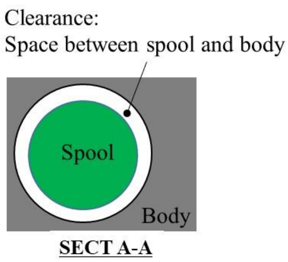

Figure 8 Definition of clearance

COMPARISON OF EXPERIMENTAL AND SIMULATION RESULTS

The results obtained for the effect of the draft angle are shown in Fig. 9. The graph plots the loading force on the vertical axis as a function of the draft angle on the horizontal axis. The blue line is the experimental result and the red line is the simulation result. A loading force of 6.3 N was measured under a condition of a draft angle of 0 deg. It is seen that the loading force increased with a larger draft angle, and a value of 19.3 N was measured at an angle of 2.0 deg. The results of the fluid simulation conducted under the same conditions show a loading force of 14.8 N under a condition of a draft angle of 0 deg. and a value of 24.6 N at an angle of 2.0 deg.

Although there is some discrepancy in absolute values between the experimental and simulation results, both sets of data show the same tendencies and effects on the loading force, thus confirming the validity of the simulation.

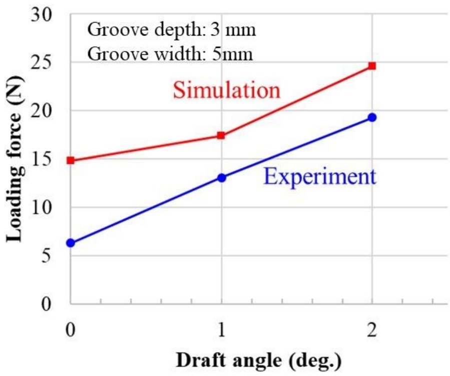

Figure9 Loading force as a function of draft angle

It is assumed that the reason for the effect of the draft angle on the loading force is that it produces a pressure unbalance between the circuit side and the back side, thereby applying force to the circuit side.
As the draft angle increases, a difference occurs in the size of the valve opening between the circuit side and the back side, with the opening becoming larger on the circuit side (Fig. 10). As a result, because the flow rate on the circuit side increases, the flow velocity becomes faster than on the back side. The pressure on the circuit side thus decreases, resulting in a differential pressure. The pressure around the spool valve on the circuit side declines locally to produce the pressure unbalance shown in Fig. 11.

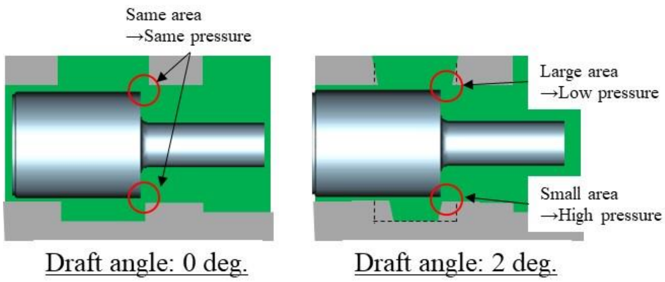

Figure 10 Effect of draft angle

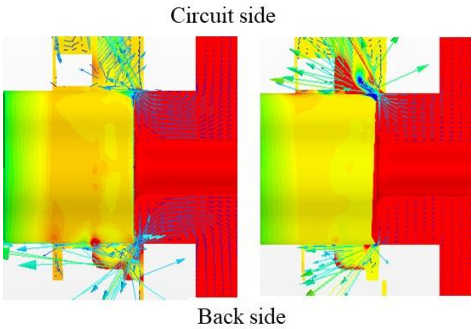

Figure 11 Simulation results for draft angle

Fig. 12 shows the results obtained for the effect of the groove depth. The loading force is plotted on the vertical axis as a function of the groove depth on the horizontal axis. The blue line is the experimental result and the red line is the simulation result. A loading force of 11.2 N was measured at a groove depth of 3.0 mm. The loading force decreased as the groove depth was increased, declining to 3.3 N at a groove depth of 11.5 mm. The simulation results show a loading force of 9.1 N at a groove depth of 3.0 mm and a value of 3.8 N at a groove depth of 11. 5 mm.
Although there is some discrepancy between the experimental and simulation results, both sets of data show the same tendencies, as was seen for the draft angle.

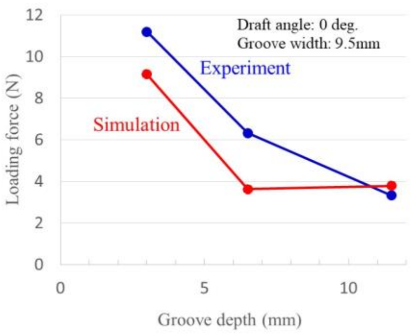

Figure 12 Loading force as a function of groove depth

The action of the following two factors can be considered to explain the reason for the effect of the groove depth on the loading force. (1) The pressure rise induced by the collision of the fluid with the spool valve applies force to the circuit side. (2) The pressure gradient between the back side and the circuit side raises the pressure on the back side, thereby applying pressure to the circuit side.
As shown in Fig. 13, the first factor concerning the collision of the fluid with the spool valve occurs as the fluid in the grooves on the back side flows toward the circuit side (Fig. 14). In the case of a deep groove depth, the flow spreads out before the collision occurs so the effect of the collision is smaller. In contrast, in the case of a shallow groove depth, the effect of the collision is larger so a pressure rise is observed.

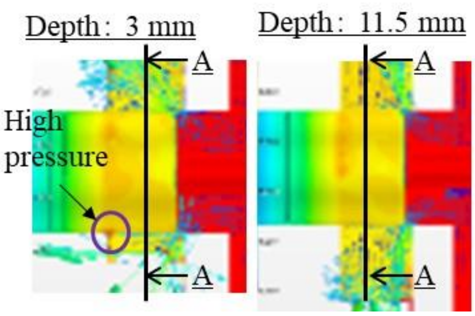

Figure 13 Simulation results for groove depth

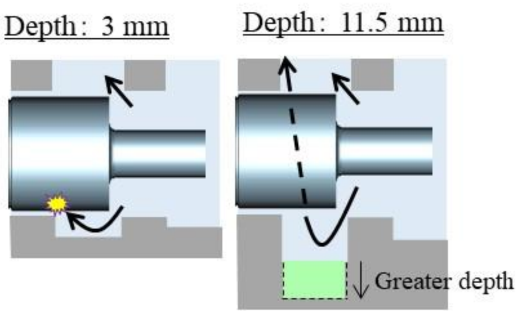

Figure 14 Effect of groove depth

As shown in Fig. 15, the second factor concerning the pressure gradient occurs in the direction of the flow of the fluid between the spool valve and the valve body when the fluid in the grooves on the back side flows toward the circuit side. This is more pronounced for a shallow groove depth because the flow passage is narrower. The influence is small in the case of a deep groove depth (Fig. 16). As a result, the pressure on the back side rises compared with that on the circuit side, thus increasing the loading force.

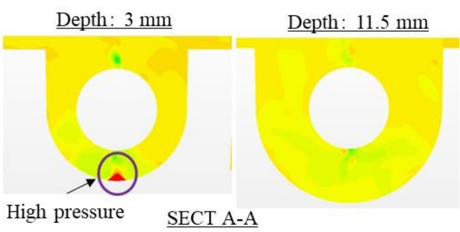

Figure 15 Simulation results for groove depth in sect A-A

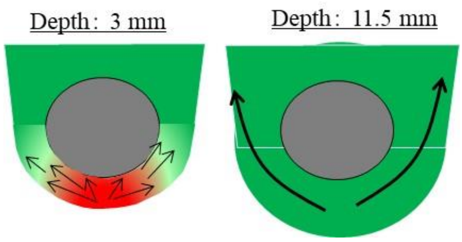

Figure 16 Effect of pressure drop

CONCLUSION

(1) Using a jig cut out in the shape of the area around the spool valve, a rod as a probe and a load cell, the loading forces acting on the valve were measured directly, which has been difficult to do heretofore.
(2) A comparison of the experimental and simulation results revealed that there was some discrepancy in the absolute values, but both sets of data agreed well regarding the tendencies of the dimensional effects on the loading forces. This confirmed the validity of the simulation results.
(3) This has now made it possible to make design judgments of transmission specifications at the development stage before conducting physical tests.

REFERENCES

1. Kenji Sakakibara, ”Development of a hydraulic control system for a new JATCO wide-range CVT”, 10th International CTI Symposium USA. Automotive Transmissions, HEV and EV Drives, USA, 2016, B2_Sakakibara_Jatco_paper, pp. 5-6.
2. Masaru Shimada, ” Application of CFD to develop a control valve spool featuring reduced fluid force” , 2017 JSAE Congress (Autumn), No. 20176045 (2017).

Organized Session | Organized session

Functional Fluid

The 11th JFPS International Symposium on Fluid Power HAKODATE 2020 Oct. 12-13, 2021 JFPS The Japan Fluid Power System Society

A Study on a Mathematical Model for AC Electroosmosis Micropump

Yo MAKITA*, Kazuhiro YOSHIDA**, Sang In EOM** and Joon-wan KIM**

* School of Engineering, Tokyo Institute of Technology
** FIRST, IIR, Tokyo Institute of Technology
4259-R2-42 Nagatsuta-cho, Midori-ku, Yokohama, 226-8503 Japan
(E-mail: yoshida@pi.titech.ac.jp)

Abstract. An AC electroosmosis (ACEO) micropump has been required for lab-on-a-chip to generate a water flow with a miniaturizable simple structure without mechanical moving parts. For design of ACEO devices, an ACEO mathematical model is needed, however, the previous model has large discrepancy between the simulated and measured velocities when physical parameters are used. To overcome the problem, in this study, a new mathematical model was proposed considering the forming time and the nonlinear capacitance of the electric double layer and FEM simulations were performed for a simple ACEO convection generator. The device was fabricated using a MEMS fabrication process and its flow velocities were measured. Through comparison with the simulated values, the effectiveness of the proposed mathematical model was confirmed.

Keywords: AC electroosmosis (ACEO), Mathematical model, Micropump, MEMS, Functional fluid

INTRODUCTION

For lab-on-a-chip, a micropump using AC electroosmosis (ACEO) has been required [1], because it can generate a water flow with simple fixed electrodes. A mathematical model of ACEO has been established theoretically [1, 2], which can estimate the relative variation of the flow velocities, however, the absolute value is far larger than the measured value. In this study, we proposed a mathematical model considering the forming time and the nonlinear capacitance of the electric double layer (EDL). Then we confirmed its validity through comparison between the simulated and the measure flow velocities

PROPOSAL OF MATHEMATICAL MODEL

As shown in Fig. 1, when a container having a pair of plate electrodes on the bottom is filled with liquid like water and applied AC voltage to, charged particles are gathered on the electrode and an EDL is formed. The electric field acts on the charged particles and generates slip velocities on the electrodes. When the polarity of the applied voltage is changed, since the polarity of the electric field is also changed, the direction of the slip velocity is unchanged and convection is generated. This phenomenon is called the ACEO.
In the previous mathematical model of the ACEO [1], the EDL was modelled as a capacitor with a thickness of the Debye length λ_D and the electric field was analyzed. The zeta potential ζ and the electric field component E_t parallel to the electrode were derived. The slip velocity was calculated by the Helmholz-Smoluchowski equation:

$$\bar{u}_s = -\frac{\varepsilon}{\mu}\overline{\varsigma E_t}, \tag{1}$$

where, ε and μ are the permittivity and the viscosity of the liquid and the overbar means the time-averaged value. However, the slip velocity calculated with physical properties was 100 times higher than the measured value, because a delay due to the EDL formation could not be ignored. Hence, in this study, we proposed a new mathematical model considering the forming time and the nonlinear capacitance of the EDL. In this model, the

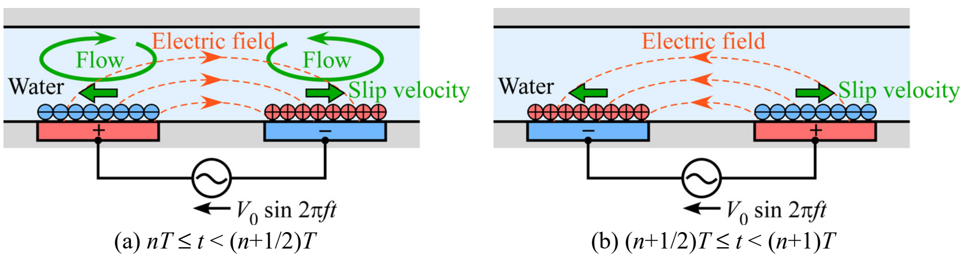

Figure 1. Working principle of AC electroosmosis (ACEO) ($T = 1/f$, $n = 0, \pm1, \pm2, \ldots$)

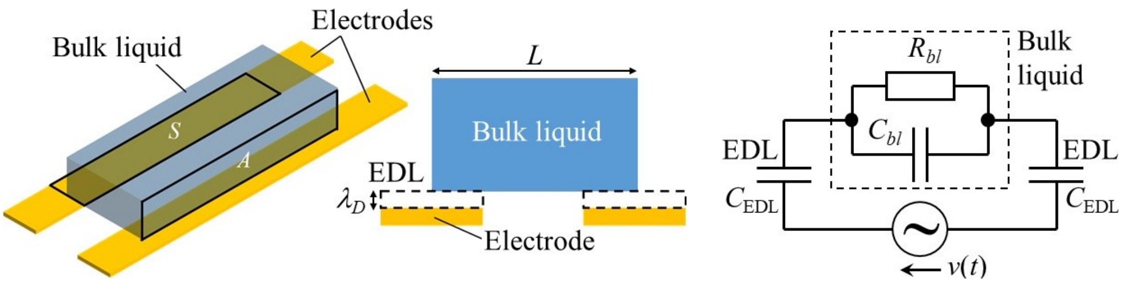

(a) Physical model (b) Equivalent circuit

Figure 2. Proposed model of ACEO convection generator

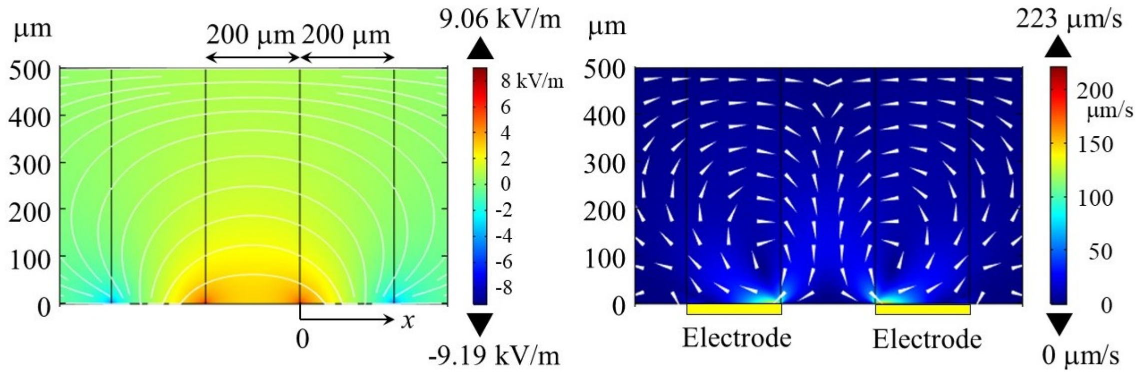

(a) Electric field strength (b) Velocity field

Figure 3. Simulation results of ACEO convection generator

rectangular parallelepiped bulk liquid with a cross section A and length L is modelled as a parallel connection of an electric resistance $R_{bl} = \rho L/A$ and a capacitance $C_{bl} = \varepsilon A/L$ as shown in Fig. 2, where ρ is a specific resistance of the liquid. In addition, the capacitance C_{EDL} of the EDL and the zeta potential ζ are calculated by:

$$C_{EDL} = \frac{\varepsilon S}{\lambda_D}\cosh\left(\frac{z_i e \varsigma}{2kT_a}\right), \varsigma = 0.01V, \tag{2}$$

where, z_i is the valence of the charged particles, e is the quantum of electricity, k is the Bolzmann constant, T_a is the absolute temperature, and V is the applied voltage amplitude. As a result, the slip velocity is calculated as:

$$\bar{u}_s = -\frac{\varepsilon}{\mu}\overline{\varsigma E_t}\cos\theta, \tag{3}$$

where, the phase θ shows the forming time of the EDL.

SIMULATIONS AND EXPERIMENTS

The validity of the proposed mathematical model was examined by FEM simulations and experiments. The ACEO convection generator shown in Fig. 1 was investigated. The electrode width and interval were 200 μm and the 200 μm, respectively, and the diameter and the depth of the cylinder container were 6 mm and 500 μm, respectively. The liquid was water and the simulations were performed using COMSOL Multiphysics™.
Figures 3(a) and (b) show the simulated electric field and the velocity. The convection flows could be generated. Figure 4 left shows the fabricated ACEO convection generator. A 0.5 mm thick silicone plate with a 6 mm diameter hole was attached to a glass wafer with a pair of electrodes. The electrode part was fabricated by a MEMS fabrication process shown in Figs. 4 (a) to (f) as follows: (a) Ti/Au deposition on a glass wafer, (b) positive resist S-1818 (Rohm and Haas Electronic Materials) spin coating, (c) S-1818 patterning, (d) Au etching. (e) S-1818 removal, and (f) Ti etching. The device could be successfully fabricated as shown in Fig. 4 left. Figure 5(a) shows the simulated slip velocities on the electrode. The position x is defined as the distance from the electrode edge as shown in Fig. 3(a). The slip velocity is decreased and the polarity is changed about at x = 150 μm, which is a stagnation point. Figure 5 (b) shows the top view of the fabricated device. The bright line shows the stagnation line. The proposed model can predict the stagnation.
In the experiments, the flow velocities were measured by PTV (particle tracking velocimetry) using fluorescent particles (Sigma Aldrich l9654: diameter 1.0 μm, density 1050 kg/m^3, excitation wave length 470 nm, fluorescence wave length 540 nm. Volume concentration 0.061 %). The movement of the particles was measured with a microscope and analyzed, and the slip velocities were obtained.

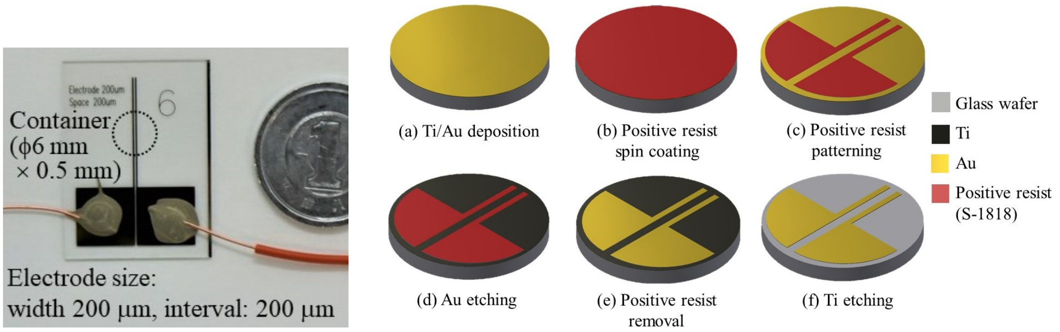

Figure 4. Fabrication process of ACEO convection generator

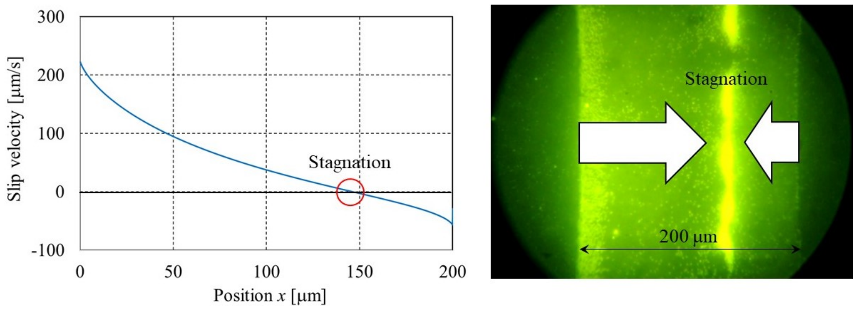

(a) Simulated slip velocity (b) Measured stagnation

Figure 5. Simulated and measured results

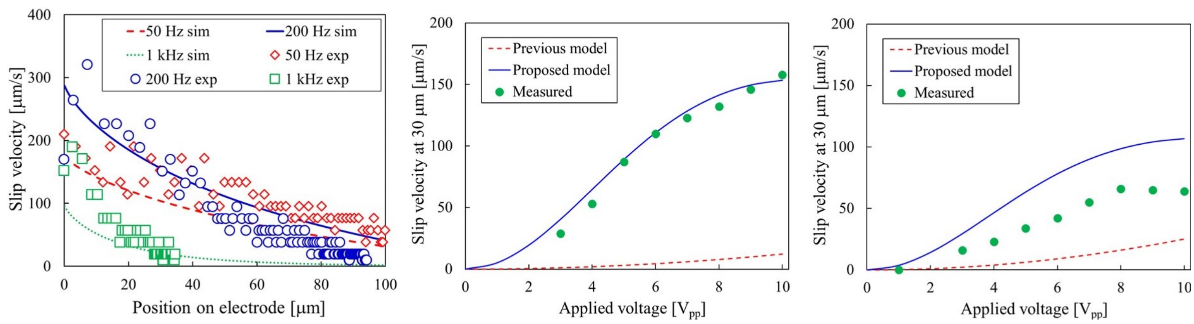

(a) For position on electrode at 7 V_{pp} (b) For applied voltage at 100 Hz (b) For applied voltage at 300 Hz

Figure 6. Simulated and measured slip velocities of ACEO convection generator

The simulation and experimental results were compared. Figure 6(a) shows the slip velocity distribution on the electrode. The simulation results are shown by the dashed, solid and dotted lines. The experimental results are shown by the diamond, circle and square symbols. The applied voltage was 7 V_{pp}. The discrepancy was not so small, however, the same order results were obtained. Figures 6(b) and 6(c) shows the slip velocity at x = 30 μm for the applied voltage. At the applied voltage frequency 100 Hz, good agreement was confirmed (Fig. 6(b)). At 300 Hz, better agreement was obtained than that of the previous model (Fig. 6(c)).

CONCLUSIONS

In this paper, we proposed a new mathematical model of ACEO considering the forming time and the nonlinear capacitance of the EDL and performed the FEM simulations. An ACEO convection generator was fabricated by the MEMS technologies and the slip velocities were measured. As a result of comparisons, the better agreement of the simulation results using the proposed mathematical model was confirmed.

REFERENCES

1. SONI, G., Nonlinear phenomena in induced charge electroosmosis, Dissertation of University of California, Santa Barbara, (2008).
2. YOSHIDA, K., SATO, T., EOM, S. I., KIM, J.-W., and YOKOTA, S., A Study on an AC Electroosmotic Micropump Using a Square Pole - Slit Electrode Array, Sensors and Actuators A, 2017, 265, pp. 152-160.

The 11th JFPS International Symposium on Fluid Power HAKODATE 2020 Oct. 12-13, 2021 JFPS The Japan Fluid Power System Society

Multi-Layered Disk Type of Electro-Rheological Braking Device for Small Mobile Robot

Takanori TOGAWA*, Yuta SATO*, Yutaka TANAKA**, Jinghui PENG ***

* Graduate School of Engineering and Design, Hosei University
2-33 Ichigaya-Tamachi, Shinjuku-ku, Tokyo, 162-0843 Japan
(E-mail: togawa.takanori@gmail.com)
** Faculty of Engineering and Design, Hosei University
(E-mail: y_tanaka@hosei.ac.jp)
*** Harbin Institute of Technology
Harbin, China, 150001
(E-mail: pengjinghui009@gmail.com)

Abstract. In the micromouse competition, small autonomous mobile robots run at high speed in mazes. The robot turns a corner at a steep angle in this competition. However, the recent competition is marked by speeding up. There is a limit to driving performance with motor current control braking. Electro-rheological (ER) fluid actuators have the potential of soft brake function for the small autonomous mobile robot because the ER fluid can quickly control changes in viscosity by changing the electric field. In this research the multi-layered disk type of mechanical brake device using the ER fluid for the micromouse was designed and developed. The performance of the ER braking device was verified through numerical simulation and experiments. Characteristics of on-board power supply for small brake models using the ER fluid was also numerically simulated. A drive electric circuit for boosting applied voltage to the ER fluid and discharging stored electric charge due to high electric voltage for the small autonomous mobile robot was proposed and numerically simulated.

Keywords: Electro-rheological fluid, Braking device, DC motor, Micromouse, Small autonomous mobile robot

INTRODUCTION

Micromouse competition is an event for self-made maze-solving autonomous small robot to compete intelligence and performance [1]. The micromouse as shown in Figure 1 must conform to certain size limitations and needs to solve the maze without outside human intervention. This robot event is held worldwide, especially popular in the U.K., U.S.A., Japan, Singapore, India and South Korea. In this competition, it is required to skillfully control the acceleration and deceleration of a small robot based on its course. However, the acceleration/deceleration control using the electric current control of the robots' mounted motors limits the driving performance improvement. In addition, it is necessary to mount mechanical components in a limited space, and the miniaturization of each element is an important issue. Inspired by the All-Japan Micromouse Competition, the newly designed small scale soft brake aims to promote the driving performance of the micromouse.
Electro-rheological fluids (ER fluids) have characteristics that the viscosity changes due to the change of the electric field between the electrodes, and the viscosity changes reversibly in a short time [2]. Since the viscosity characteristics of the fluid can be controlled by changing the electric field, a braking device suitable for miniaturization with a simple structure without mechanical friction can be realized [3].
Our project team has been proposed and designed a new kind of small-scale soft braking device using ER fluid [4][5]. The innovation of the developed ER brake is that it is easier to miniaturize than mechanical braking

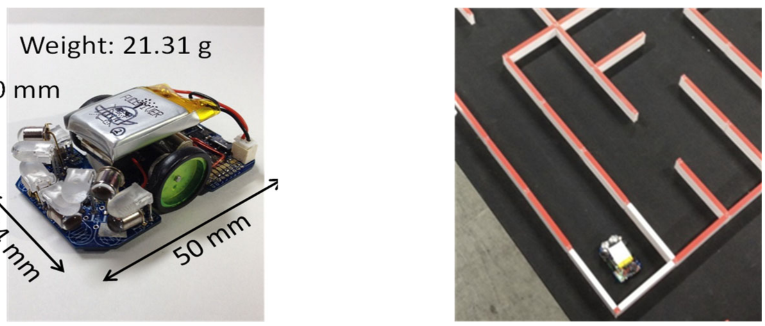

(a) Micromouse (b) Micromouse in a maze
Figure 1. Typical small size of a micromouse and a maze

mechanisms. And because it has less electrical energy, it is environmentally friendly. In addition, the braking performance is improved compared to the electric motor alone, and the controllability and quick response of electric operation is also excellent for autonomous mobile robot. Optimal shape parameter of the disk type of the braking device installed in the small mobile robot were designed and the dynamic characteristics of the braking device were numerically simulated [6].

In this paper, a prototype model of the multi-layered disk type of the small ER braking device was fabricated and the performance characteristics of the braking device were experimentally and numerically verified. Characteristics of on-board power supply for the small braking device using the ER fluid were also numerically simulated. A drive electric circuit for boosting applied voltage to the ER fluid and discharging stored electric charge due to high electric voltage for the small mobile robot was numerically simulated.

ER FLUID AND ER BRAKING DEVICE

Figure 2 shows a configuration of the multi-layered disk type of the ER braking device for small mobile robots such as micromouse. The cylindrical housing body has a diameter of 20.8 mm and a length of 32.0 mm. Three rotating disks of the positive electrodes are supported by a rotating center shaft and bearings. Four disk-shaped negative electrodes are fixed by the cylindrical housing body. The thickness of the electrode is 0.5 mm and made of copper. Gaps of the negative and positive electrodes are kept by conductive spacers at a constant value of 1 mm. The ER fluid is filled between the electrodes. The number of layers between the electrodes was selected as six layers for the simulation of design.

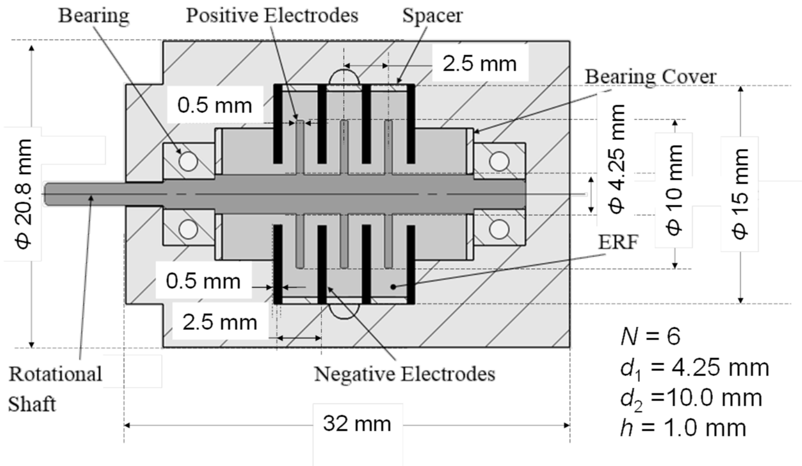

Figure 2. Configuration of ER braking device

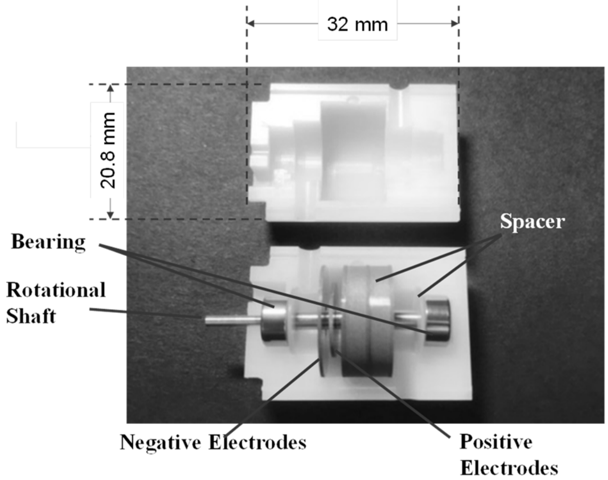

Figure 3. Inner structure view of the prototype ER braking device

Figure 3 shows the internal structure of the designed and prototyped ER braking device. The cylindrical housing was manufactured as a half-split model and made of polyacetal (POM), which has high mechanical strength and

electrical insulating in engineering plastics. The disk electrodes, the shafts, and the spacers was made of conductive metal copper and assembled inside the housing.
The characteristics of the practical ER fluid can be described using the Bingham model as shown in the following equation:

$$\tau = \tau_0(E) + \mu_0\dot{\gamma}\,, \tag{1}$$

where τ is the shear stress, $\dot{\gamma}$ is the shear rate, E is the strength of the electric field between electrodes, $\tau_0(E)$ is the dynamic yield stress varying with the strength of the electric field E, and μ_0 is the base viscosity of the ER fluid without electric field. The dynamic yield stress $\tau_0(E)$ as a function of the applied electric field E and the base viscosity μ_0 is given from preliminary experiments as following equations:

$$\tau_0(E) = 317.5\,E^{1.834}\quad [\mathrm{Pa}]\,, \tag{2}$$

$$\mu_0 = 0.225\quad [\mathrm{Pa\cdot s}]\,. \tag{3}$$

Figure 4 shows the typical relationship between the strength of electric field and the shear stress of the particle type of the practical ER fluid under the shear rate of 400 s^{-1}. As the strength of electric field increases, the share stress increases like an exponential function. By using Eq. (2) and Eq. (3), the approximate curve in Figure 3 could be obtained.

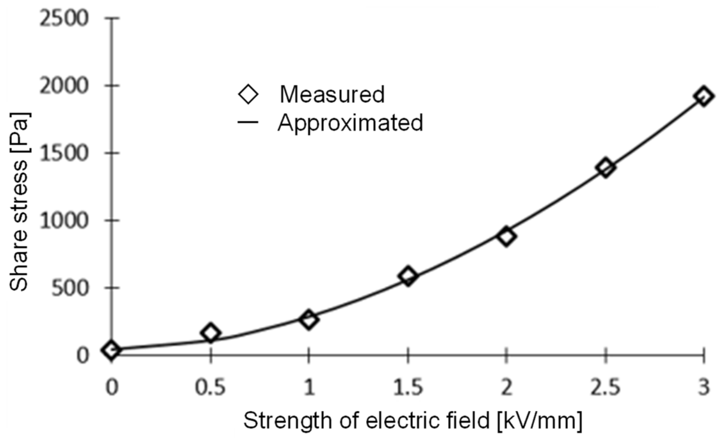

Figure 4. Shear stress vs. strength of the electric field for the ER fluid under the shear rate of 400 s^{-1}

The braking torque T_B can be obtained through the surface integral of the radius r as following equation [5]:

$$T_B = N\int_{\frac{d_2}{2}}^{\frac{d_1}{2}} 2\pi r^2\left(\tau_0(E) + \mu_0\frac{r\omega}{h}\right)dr\,, \tag{4}$$

where N is the number of layers, d_1 and d_2 denote the effective outer and inner diameters of the electrode disks, h is the gap between each pair of positive and negative electrode disks, and ω is the rotational angular velocity.
From Eq. (4), the braking torque of the 6-layer ER braking device shown in Figure 1 is given by the following equation:

$$T_B = \frac{\pi\tau_0(E)}{2}(d_1^3 - d_2^3) + \frac{3\pi\mu_0\omega}{16h}(d_1^4 - d_2^4)\,. \tag{5}$$

The rotational motion equation is expressed by the following differential equation:

$$J\frac{d\omega}{dt} = K_p(\omega_0 - \omega) - T_B\,, \tag{6}$$

where J is the moment of inertia for the entire rotating system, K_p (= 3.6×10^{-6} N m s/rad) is a coefficient determined by the load characteristics of the DC motor, and ω_0 is the initial angular velocity of the system. The dynamic response of the rotating system with the DC motor and the ER braking device can be calculated by the Eq. (5) and Eq. (6).

EXPERIMENTS

Figure 5 shows the configuration of the used equipment in the experiments. Brake characteristics were experimentally measured using the configuration. In the experiment, the DC motor was initially rotating in a steady state with an angular velocity ω_0 (= 500 rad/s). Next, a voltage was applied to the ER braking device, the change in angular velocity was measured by the encoder of the DC motor, and the measured value was stored in the PC through the microcomputer. In these experiments, after starting the ER braking operation, the DC motor has continued to generate torque and the electric short brake was not working.

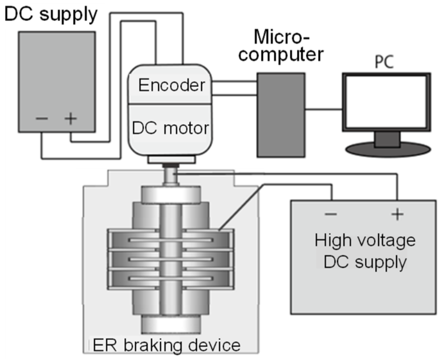

Figure 5. Configuration of experimental setup

Figure 6 shows the experimental and simulation results of the transient response in the rotational angular velocity when the ER braking device is operated. The applied voltage to the ER braking device is 1 kV, 2 kV, and 3 kV, respectively. It can be seen that the ER braking device reduces the rotational angular velocity of the DC motor. There is a slight difference between the experiment and the simulation in the transient state. On the other hand, the final steady-state values of the experiment and simulation were almost the same under the three conditions.

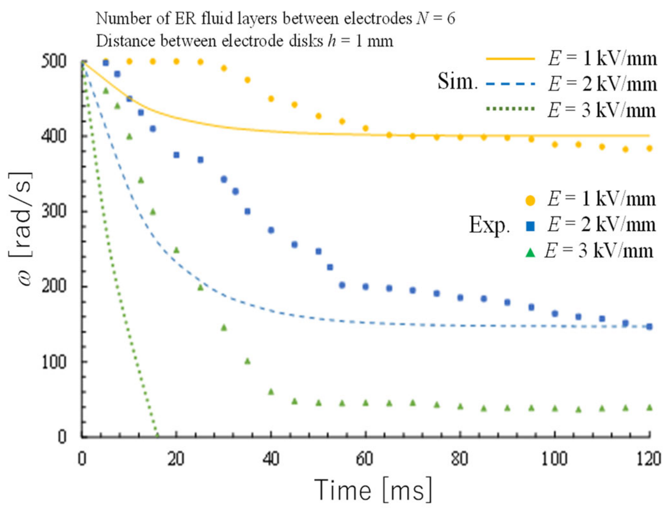

Figure 6. Comparison between the experiment and simulation for angular velocity change of the rotating system

SIMULATION OF DRIVE ELECTRIC CIRCUIT FOR ER BRAKING DEVICE

The power source mounted on the small autonomous mobile robot called the micromouse is two 3.7 volts lithium polymer secondary batteries. A high voltage must be applied between the electrodes to operate the ER braking device. Therefore, it is necessary to design an electric circuit for driving the ER braking device that boosts the voltage of the secondary battery to a high voltage. On the other hand, the condenser of the boosting electric circuit and the ER braking device have a capacitance function. When the micromouse accelerates, it is necessary to quickly discharge the electric charge accumulated by braking mode.

Figure 7 shows the simulation model of ideal boost and discharge electric circuit for the circuit simulator, commercial software LTspice. The voltage of the secondary battery is switched by the power MOSFET S1 on the primary side of the power transformer. The voltage boosted by the power transformer is rectified and smoothed by the diodes D1, D2 and capacitor C1 on the secondary side. As a result, the capacitors are sequentially charged and a high voltage is applied to the ER braking device. Discharge is carried out by switching the electric resistance R1 and the transistor S2.

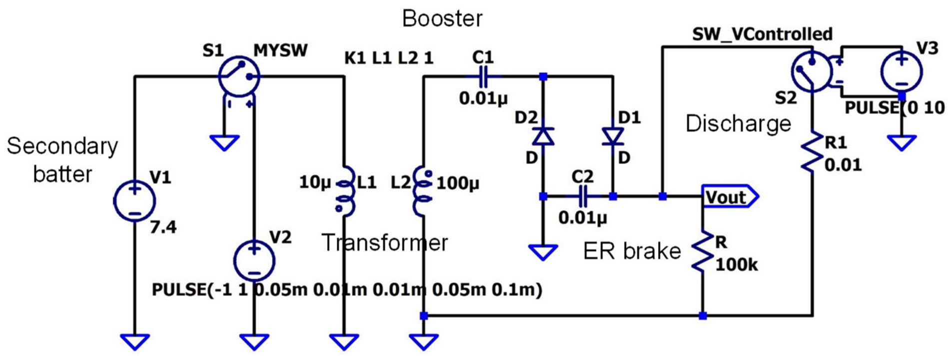

Figure 7. Simulation model of the electrical circuit simulator LTspice

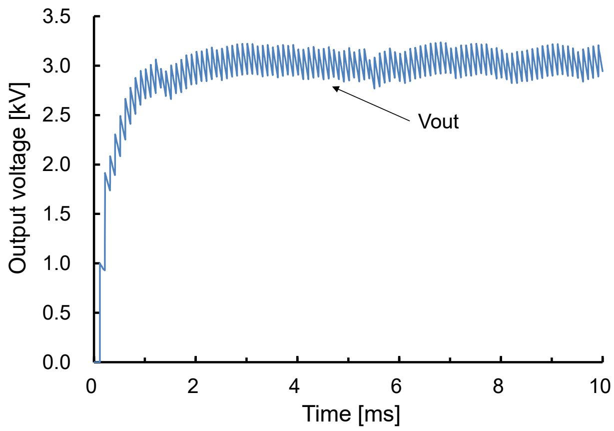

Figure 8. Simulation results of the booster circuit for the ER braking device

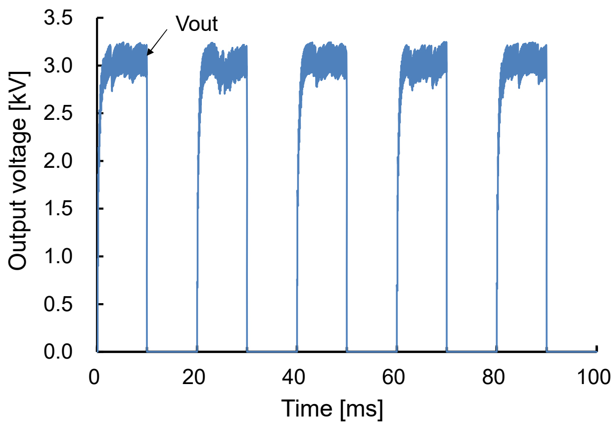

Figure 9. Simulation results of discharge circuit for the ER braking device

The simulation result of the boosted voltage change is presented in Figure 8. The voltage of the secondary battery was set to 7.4 V, and the switch S1 was switched at 10 microsecond intervals. It was confirmed by simulation that the output voltage Vout can be quickly boosted to 3 kV in 1.5 ms.
Figure 9 shows the simulation results of the discharge circuit. The switch S2 was switched at 10 ms intervals. It was confirmed by simulation that the voltage of the ER braking device boosted to 3 kV instantly dropped to 0 V.

CONCLUSIONS

In this paper the multi-layered disk type of the braking device installed in the small mobile robot was proposed and designed. The prototype model of the multi-layered disk type of the small ER braking device was fabricated and the performance characteristics of the braking device were experimentally and numerically verified. The characteristics of the on-board power supply for the small braking device using the ER fluid were numerically simulated. The structure of the drive electric circuit for boosting applied voltage to the ER fluid and discharging stored electric charge due to high electric voltage for the small mobile robot was proposed and the performance of the drive electric circuit was numerically simulated.

ACKNOWLEDGMENTS

We express appreciation the technical support, Mr. Takuma TACHIBANA of the graduate student in the Graduate School of Hosei University and Mr. Mizuki SHIGIHARA of the undergraduate student in Hosei University.

REFERENCES

1. All Japan Micromouse Contest 2020, https://www.ntf.or.jp/?p=340, (accessed on 05 May, 2021).
2. TIAN Y., LI C., ZHANG M., MENG Y., WEN Y., Transient response of an electrorheological fluid under square-wave electric field excitation, Journal of Colloid and Interface Science, Vol. 288, 2005, pp.290-297.
3. TAN, K. P., STANWAY, R., BULLOUGH, W. A., Braking Responses of Inertia/Load by Using an Electro-Rheological (ER) Brake, Mechatronics, Vol.17, No.6, 2007, p.277-289.
4. FAN, X., SAKAMA, S., TOGAWA, T., TANAKA, Y., Design and Fabrication of ER Braking Device for Micromouse, IEEE Proc. 7th Int. Conf. on Fluid Power and Mechatronics (FPM2015), 2015, p.729-733.
5. PENG, J., TOGAWA, T., TACHIBANA, T., TANAKA, Y., Numerical and Experimental Investigation on Braking Characteristics of an Electro-Rheological (ER) Micro Brake, JFPS International Journal of Fluid Power System, Vol.11, No.3, 2018, pp.124-129.
6. TOGAWA, T., TACHIBANA, T., TANAKA, Y., PENG, J., Hydro-Disk-Type of Electrorheological Brakes for Small Mobile Robots, International Journal of Hydromechatronics, 2021, (in press).

The 11th JFPS International Symposium on Fluid Power HAKODATE 2020 Oct. 12-13, 2021 JFPS The Japan Fluid Power System Society

Lightweight & Twin-driven MR Fluid Actuator for Haptic Devices

Tetsumasa TAKANO*, Asaka IKEDA**, Akinori YAMAGUCHI*,

Isao ABE** and Takehito KIKUCHI**

* Graduate School of Engineering, Oita University
Dannoharu 700, Oita 870-1192, Japan
** Faculty of Science and Technology, Oita University
Dannoharu 700, Oita 870-1192, Japan
(E-mail: t-kikuchi@oita-u.ac.jp)

Abstract. We proposed a twin-driven MRF actuator (TD-MRA) using two multi-layered disc-type MR fluid clutches for haptics. We have developed two types of the TD-MRA and compared their torque performances. In our previous works, we designed a 0.6 Nm-class TD-MRA for core components of the haptic interface. However, the size and weight were not suitable for the compact unit. On the other hand, the controllable torque was redundant. From these reasons, we redesigned the TD-MRA, and a 0.3 Nm-class device was developed and evaluated in this study. The specification comparison and results of the mechanical tests were reported in this article.

Keywords: Magnetorheological fluid; haptic device; teleoperation; MR fluid actuator.

INTRODUCTION

Bilateral control concept [1] was proposed as a controlling method for high-fidelity teleoperation systems, e.g. endoscopic surgical robots [2]. However, this concept has not been sufficiently utilized in real systems. For example, owing to the limitations of the present actuator and sensor technology, the da Vinci Surgical System® [3] mainly uses a unilateral controller and, hence, there is less haptic feedback for surgeons. By adding a feedback loop, the machine can support human skills with gravity compensation and friction compensation. In addition, it provides a better haptic perception to the operator while performing a remote operation task. This function is very useful for enhancing operational accuracy and reducing psychological stress from the human operator in very sensitive operation.

Therefore, establishing a high-performance force feedback system for remote-controllable robot systems is necessary to enhance operational accuracy and reduce operators' psychological stresses. Thus, we have developed a twin-driven MR Fluid actuator (TD-MRA) that can control fine haptic feedback [4]. In this actuator, two high-performance MR fluid clutches [5] are used for torque transmission. Fauteux et al. [6] had developed a twin driven MRF actuator using planetary gears, and Song et al. [7] used the same mechanism for a haptic master. The twin-driven mechanism has been used to reduce the basic friction of the actuators, and its low friction characteristics are suitable for haptic devices. However, it is difficult to balance the frictional (and viscous) torque of the normal and reversed rotations of the planetary-gear-based mechanism with the MRF device because of the difference in rotational velocities. Hence, we proposed the TD-MRA using two multi-layered disc-type MR fluid clutches for haptics and a flat gear mechanism.

In our previous works [4], we designed a 0.6 Nm-class TD-MRA for core components of the haptic interface. However, the size and weight were not suitable for the compact unit. On the other hand, the controllable torque was redundant. From these reasons, we redesigned the TD-MRA, and a 0.3 Nm-class device was developed and evaluated in this study. The specification comparison and results of the mechanical tests were reported in this article.

LIGHTWEIGHT MR FLUID DEVICE

We developed some types of compact MR Fluid devices with the basic structure shown in Fig.1. The basic structure is rotational symmetry, and the double bearings hold the rotational shaft. The multi-layered discs were fixed alternately on the housing and the core. The magnetic wire is winded and embedded in the magnetic core. The discs and the magnetic core are made of iron, while the other parts are made of non-magnetic materials. An oil seal is an important component of an MRF device. We used a single lip seal made of fluorocarbon polymer (#31612A, Starlite Co., Ltd.). Figure 2 shows the 0.3 Nm-class MR Fluid device. Table 1 shows the comparison of the specifications for two devices. The 0.3 Nm-class has halves performances and size of the 0.6 Nm-class for almost parameters. The optimal design method was developed in the previous works [5]. We can select optimally designed torque controllable devices on the torque requirements of application.

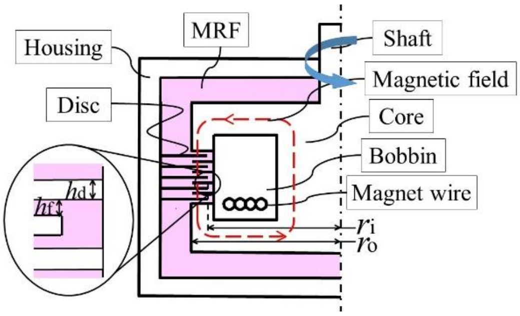

Figure 1. Basic structure

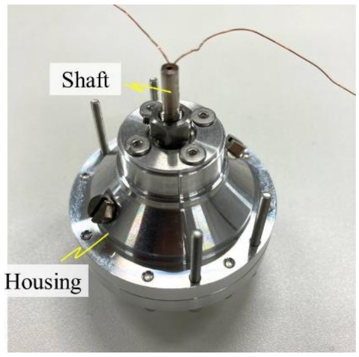

Figure 2. 0.3 Nm-class MR fluid device

Table 1. Specifications of the MR fluid device

Device type	**0.6 Nm-class [4]**	**0.3 Nm-class**
Number of fluid layers	6	6
Thickness of MRF layer	0.2 mm	0.2 mm
Inner radius of disc	12.5 mm	10 mm
Outer radius of disc	15 mm	12 mm
Turning number of the coil	270	154
Rated input current	1.0 A	1.8 A
Rated output torque	0.62 Nm	0.26 Nm
Inertia of output parts	8.76×10^{-6} kgm2	2.47×10^{-6} kgm^2
Mass	183 g	106 g

EVALUTION OF MR FLUID DEVICE

Method

The torque responses of the device were measured with the experimental setup (Fig.3). The device was fixed on an immovable plate and the output shaft was driven at constant speeds with an AC servomotor (SGMAV 08A, Yasukawa) during tests. The torque was measured in real time with a torque sensor (UTMII-5Nm, UNIPULSE). For static torque tests, rotational velocity was controlled at 10, 20, 30, 60, and 120 rpm, to clarify the effects of rotational velocities. In addition, the electric current was controlled at 0.0 ~ 1.8 A for 10 s. The average torques for each condition were calculated. For step tests, the velocity was controlled at 10 rpm, and the current was controlled stepwise with initial and final reference current, e.g., 0.0, 0.3, 0.6 and 0.9 A.

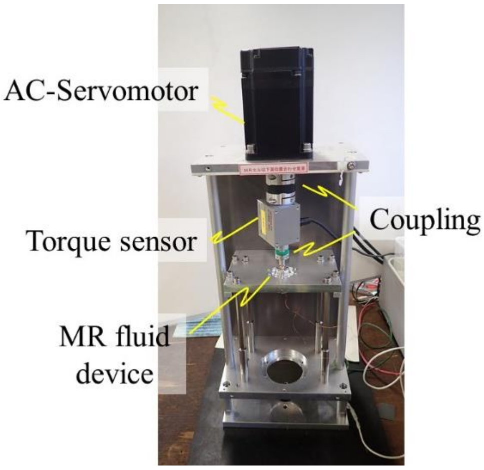

Figure 3. Testing machine for MR fluid device

Result

Experimental results on the static torque are shown in Fig.4. The horizontal axis and vertical axis show the angular velocity in rad/s, and the output torque in Nm, respectively. As shown in the figure, the relation between torque and input current has nonlinearity, and the velocity-dependency of the torque is relatively smaller than the effect of the input current (MR effect).
Figure 5 shows a sample of the step responses. The horizontal axes show the time in seconds, and the vertical axes show the output torque (left) and input current (right). Time constant, which is the time for the step response to reach 63.2% of its final value, is evaluated as a response time. The time constants were about 10 ms for the conditions in which the current starts from zero ampere. On the other case the time constants were less than 5 ms.

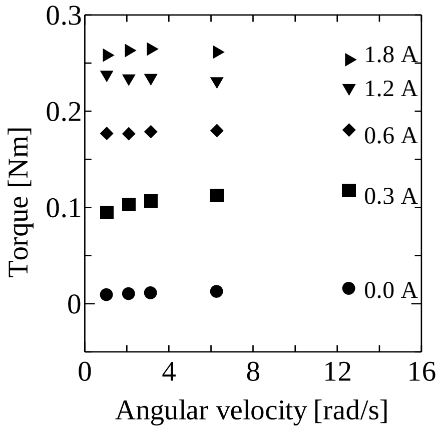

Figure 4. Static torque

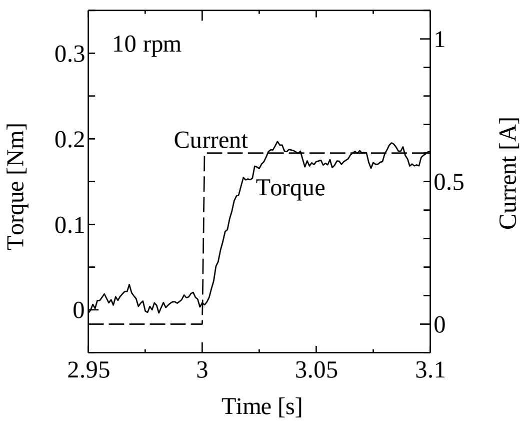

Figure 5. Step response

TWIN-DRIVEN MR ACTUATOR

The basic idea for the TD-MRA was reported in our previous study [4]. A parallel linkage mechanism combines the output shafts of two MR fluid devices to make two directional controllable torques with a one-way motor and a pair of flat gears. To improve the back drivability, the MR fluid device was used as a high-quality torque controllable clutch. In addition, the rotational direction of the input motor was not varied. Two directional output torques were controlled with two MR fluid devices with high torque / inertia ratio. A pair of 0.3 Nm-class MR devices was installed in this structure (Fig.6). Its specifications were listed in Table 2.

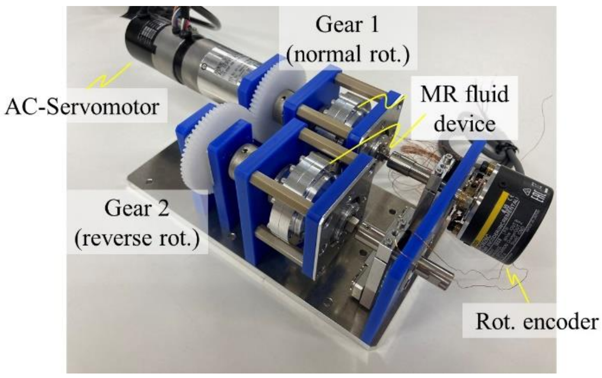

Figure 6. TD-MRA with 0.3 Nm-class MR fluid device

Table 2. Specifications of the TD-MRA

Device type	**0.6 Nm-class [4]**	**0.3 Nm-class**
Inertia of output parts	4.73×10^{-5} kgm^2	2.09×10^{-5} kgm^2
Size (L×W×H)	353×105×85	260×100×80
Mass	1.97 kg	1.28 kg

CONCLUSION

We proposed a twin-driven MRF actuator (TD-MRA) using two multi-layered disc-type MR fluid clutches for haptics. In our previous works, we designed a 0.6 Nm-class TD-MRA for core components of the haptic interface. To reduce the size and weight, we developed 0.3 Nm-class device and installed in the twin-driven mechanism. The performance of the device was evaluated and showed quick responses. As the next stage, we apply this device as core components of the haptic device.

ACKNOWLEDGMENTS

This research was partially supported by Adaptable and Seamless Technology transfer Program through target-driven R&D of the Japan Science and Technology Agency (JPMJTM20HM), Innovative Science and Technology Initiative for Security, ATLA, Japan (JPJ004596), and Grant-in-Aid for Scientific Research of Japan (JP17H03404).

REFERENCES

1. SICILIANO B and KHATIB O (2016) In: Handbook of Robotics (Second Edition, Section 43). Telerobotics. Springer-Verlag. Berlin Heidelberg, pp.1085–1108.
2. TAVAKOLI M, AZIMINEJAD A, PATEL R and MOALLEM M (2007) High-fidelity bilateral teleoperation systems and the effect of multimodal haptics. IEEE Transactions On Systems, Man, And Cybernetics—Part B: Cybernetics 37 (6): 1512–1528.
3. SIMOROV A, STEPHEN OTTE R, KOPIETZ C and OLEYNIKOV D (2012) Review of surgical robotics user interface: what is the best way to control robotic surgery. Surgical Endoscopy 26: 2117–2125.
4. KIKUCHI T, ABE I, NAGATA T, YAMAGUCHI A, TAKANO T (2020), Twin-Driven Actuator with Multi-layered Disc MR Fluid Clutches for Haptics, Journal of Intelligent Material Systems and Structures, DOI: 10.1177/1045389X20943958
5. KIKUCHI T and ABE I (2019) Low inertia torque controllable device using magnetorheological fluid & umbrella-shaped rotor. Engineering Research Express 1 (2): 02502. doi: https://dx.doi.org/10.1088/2631-8695/ab4ecf.
6. FAUTEUX P, LAURIA M, HEINTZ B and MICHAUD F (2010) Dual-differential rheological actuator for high-performance physical robotics interaction. IEEE Transaction on Robotics 26 (4): 607–618.
7. SONG B-K, OH J-S and CHOI S-B (2014) Design of new 4-DOF haptic master featuring magnetorheological fluid. Advances in Mechanical Engineering, 843498.

The 11th JFPS International Symposium on Fluid Power HAKODATE 2020 Oct. 12-13, 2021 The Japan Fluid Power System Society

Investigation of Constant Velocity Motion with Physical Interaction System for Long-Term Stay in Microgravity Space

Tetsuhito FUJITA*, Katsuki MACHIDA, Yusuke SHIMODA,
Manabu OKUI*, Rie NISHIHAMA, Taro NAKAMURA*

* Department of Precision Mechanics, Faculty of Science and Engineering
Chuo University
1-13-27 Kasuga, Bunkyo-ku, Tokyo, 112-8551 Japan
(E-mail: t_fujita@bio.mech.chuo-u.ac.jp)

Abstract. In this study, we developed a wearable device for training and rehabilitation using variable viscoelastic joints and proposed a physical interaction system (PIS) using the device. In addition, the training effect of the developed wearable variable viscoelastic joint unit and the elbow joint using this unit in constant velocity motion was verified experimentally. The elbow joint was flexed and extended under different conditions, and the training effect was verified by measuring the muscle potential. The results confirmed that the magnetorheological brake controlled the elbow joint motion to a constant motion. Furthermore, the increase in muscle potential during the experimental movements and the training effect of this unit during constant velocity movements were confirmed.

Keywords: Magnetorheological fluid brake, Artificial muscle, Training.

INTRODUCTION

A prolonged stay in microgravity or weightlessness causes muscle mass loss and decreased range of motion of joints [1] [2]. Therefore, it is important to prevent these problems through training and rehabilitation during the stay. Currently, the International Space Station (ISS) uses advanced resistive exercise devices (ARED) and other devices to prevent muscle mass loss [3]. However, because of its large size and high weight, the ARED can only be used in facilities such as the ISS, which are constructed through multiple round trips. In addition, the training motions are limited, and rehabilitation to prevent a decrease in the joint range of motion cannot be performed.
Therefore, several studies have been conducted on various devices to maintain the physical functions of astronauts in order to prevent deterioration of their physical functions [5] [6]. However, all of these devices use a motor as the power source, which can be dangerous if the timing of the movement between the device and the person does not match or if the device cannot be left attached and cannot be moved when it is not driven.
In this study, we aim to develop a wearable device that can be used for training and rehabilitation and to realize a physical interaction system (hereinafter referred to as "PIS") using the device, with the objective of applying it to long-term stays in microgravity and weightlessness, including the exploration of other planets. The concept of the proposed PIS is shown in Figure 1. The proposed system has the characteristics of a wearable and unitary system. The wearable design allows astronauts to train without any special preparation. In addition, the system can be used to provide resistance to daily movements to simulate gravity. One unit consists of two antagonistically arranged artificial muscles and a magnetorheological (MR) brake attached to the output shaft. The user can reconfigure the units to accommodate a variety of motions, such as bending and stretching with a wearable unit or using it as an ARED [3] by fixing it on the floor. In this manner, training and rehabilitation can be conducted using a single system, which reduces the system volume and weight, thus reducing costs. To realize the PIS, we focus on the variable viscoelastic joint (hereinafter referred to as "the joint"), which was developed in a previous study [7] [8]. This joint is composed of antagonistically arranged artificial muscles and an MR brake attached to the drive shaft.. The joint is lightweight, has high power, and provides high backdrivability.
This study proposes and develops a wearable variable viscoelastic joint unit (hereinafter referred to as "the unit") and verifies the training effect of isokinetic exercises on the upper limbs using the unit through experiments. The target motions are flexion and extension of the elbow joint, and the training effect is verified by measuring the muscle potentials under each condition of changing the joint viscosity.

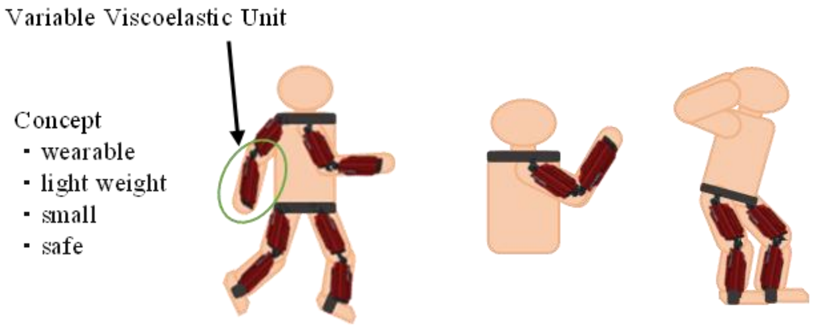

Figure 1. Concept of the physical interaction system and image of the developed unit being freely reconfigured and attached to upper and lower limbs for training

CONCEPT OF PIS

The following functions are required for training and rehabilitation under microgravity.

(1) Support for various motions

In a microgravity environment, it is necessary to be able to respond to a variety of exercises rather than a fixed set of exercises because the entire body will lose its physical functions. This is evident from the functions of the training devices currently in use.

(2) Lightweight and low volume

The space available at manned bases such as the ISS is limited, and the weight of the materials to be transported from the ground to the manned bases greatly affects the cost. For these reasons, lightweight and low volume are necessary features for the PIS.

(3) Application of load in zero gravity

In a microgravity environment, it is difficult to train and rehabilitate using one's own weight or the weight of other devices. Therefore, the PIS needs to function such that it can apply a load to the user even in a gravity-free environment.

(4) Safety

Because the PIS envisioned in this study is a wearable device, safety must be ensured when it is worn by a user.

To satisfy these requirements, the PIS envisioned in this research (1) is capable of various motions depending on the combination of units, (2) weighs less than 3 kg per unit and can be used in a wearable form, (3) controls the rotational torque applied to the joints and uses it as a load, and (4) is a backdrivable and human-friendly system that imitates the principle of the human joint.

Classification of Training and Rehabilitation

Muscle contraction can be classified into eight types of movements, including movement and contraction elements [9], as well as active and passive movements in which humans move proactively and passively in response to the movement of a device (Figure 2). The contraction exercises shown in Figure 2 can be performed individually or in combination with each other to maintain muscle strength and demonstrate the effects of rehabilitation. Therefore, the PIS proposed in this study aims to be a system that can perform all of these exercises comprehensively. Hence, in this study, we first realize active movements in isokinetic contraction using viscous control with this unit and then verify the training effect by measuring muscle potential.

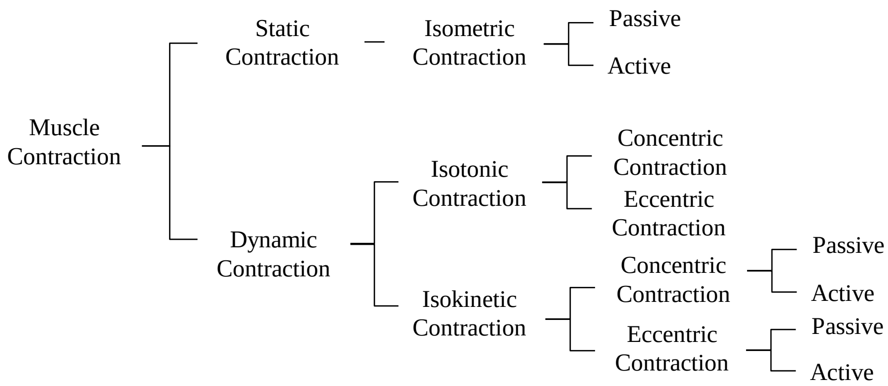

Figure 2. Classification of movements by type of contraction

CONSTANT VELOCITY MOTION WITH VARIABLE VISCOELASTIC JOINTS

Variable Viscoelastic Joint System

In the PIS, high-precision position control is not important, but a structure that does not endanger the user is necessary. In this study, we focused on the variable viscoelasticity property, which is the principle of the human joint.

The principle of the variable viscoelastic joint [7] [8] is shown in Figure 3. The joint is composed of two straight-fiber-type pneumatic artificial muscles [10] (hereinafter referred to as "artificial muscles") and one MR brake, which are antagonistically arranged to mimic the principle of the human joint. The variable elasticity of the joint is achieved by applying air pressure to the artificial muscles. The angle and stiffness of the joint can be controlled independently by controlling the air pressure on the artificial muscles. The MR brake is connected to the output shaft, and the frictional torque of the MR brake is controlled based on the angular velocity of the output shaft to achieve variable viscosity of the joint.

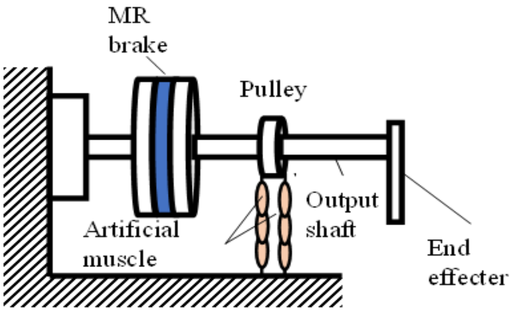

Figure 3. Operating principle of the viscoelastic joint. This joint has antagonistic artificial muscles and magnetorheological fluid brake. The joint stiffness and angle can be changed by applying air pressure to the artificial muscles.

Control Method of MR Brakes

Figure 4 shows an overview of the MR brake control. The control method of the joint viscosity in this joint is described in Eq. (1), where τ_y is the frictional torque of the MR brake, θ_M is the measured joint angle, $d\theta/dt$ is the angular velocity, and D_{jd} is the joint viscosity.

$$\tau_y = D_{jd} \frac{d\theta}{dt} \tag{1}$$

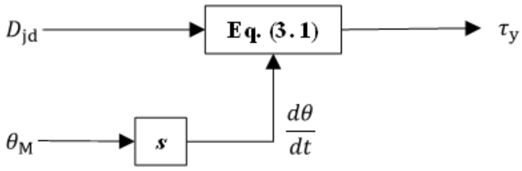

Figure 4. MR brake control overview

PROTOTYPE

Specifications of The Prototype

The following is a description of the prototype "Wearable Variable Viscoelastic Joint Unit" developed in this study to apply variable viscoelastic joints to the PIS.

Figure 5 shows the actual photograph and characteristics of the MR brake (MR brake hollow type No. 505, ER Tech, Japan) used in this unit. The MR brake used in this unit (Figure 5(a)) is 59 mm in diameter, weighs approximately 280 g, and produces 6 Nm of brake torque when the maximum voltage of 8 V is applied.

Figure 5(b) shows the measured brake characteristics. To generate the command torque, an equation that linearly approximates this current-torque relationship is used. In other words, Eq. (2) is used to generate τ_y. Because the dependence of the MR brake on the rotational speed is known to be low [7] [8], the rotational speed is not considered in the calculation of the command value.

$$\tau_y = 15.959I - 0.3283 \tag{2}$$

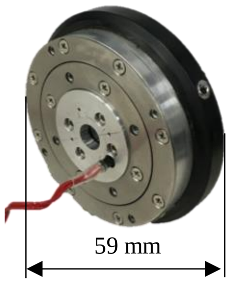

(a) Actual photograph of the MR brake used

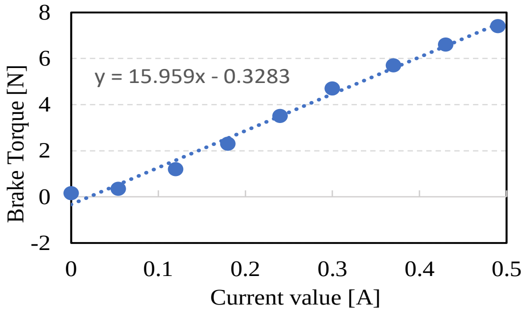

(b) Characteristic graph of the MR brake used

Figure 5. Structure and characteristics of the MR brake installed on the joint

Design

The 3D CAD model of the wearable variable viscoelastic joint unit and the appearance of the manufactured unit are shown in Figures 6 and 7, respectively. Two artificial muscles, a rotary encoder (MES-6-500-PC, Micro-tec, Japan), a pneumatic valve (VDW20GA, SMC, Japan), and a pressure sensor (SEU11-6UA, PISCO, Japan) are installed in each unit. Each unit measures 400 mm in length and 120 mm in width and weighs approximately 2.0 kg. The force from the two artificial muscles is transmitted to the sprocket by a roller chain to generate torque. The diameter of the sprocket used in this unit is 36.6 mm, and the range of motion of this unit is 135 deg. This range of motion can be easily changed by changing the sprocket attached to the unit. In this experiment, only MR brakes were used because the target was an active motion among constant velocity motions, and artificial muscles were not used in the experiment.

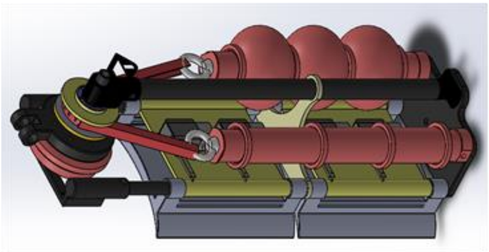

Figure 6. 3D CAD model of the developed variable viscoelasticity unit

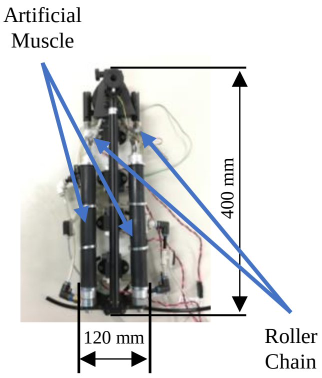

(a) Top View

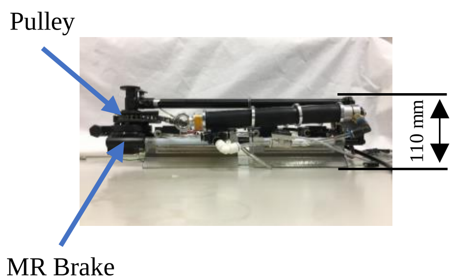

(b) Side View

Figure 7. Actual photograph of the developed unit

EXPERIMENTS WITH THE PROTOTYPE

Purpose of Experiment

The purpose of this experiment was to confirm the training and rehabilitation effects of isokinetic control by joint viscosity and active isokinetic movement in the upper limb unit joints using an MR brake, a viscous element of variable viscoelastic joints. In addition, we verified the effect by measuring the muscle potential of the target area during the flexion and extension movements of the arm.

Experimental Environment and Conditions

The experimental environment is illustrated in Figure 8. The experiment was conducted under the condition of viscous change generated by the MR brake. In the experiment, the subject sat on a chair and moved the handle of the arm attached to the end of the apparatus. In this process, a digital force gauge (RZ-50, Aiko Electric, Japan) was attached to the arm to measure the reaction force applied to the hand when the arm was moved. The subject rotated the arm at the maximum speed at which the MR brake does not slip when a voltage is applied. The rotation speed of the arm, the load applied to the hand, and the electromyography (hereinafter referred to as "EMG")potential of the upper limb were measured at this time. In addition, the subjects practiced each viscosity thoroughly and understood the maximum speed in that viscosity before the experiment. In this experiment, the subject was a healthy male (age, 24 years; height, 175 cm; weight, 55 kg). The upper limit of the voltage applied to the MR brake was set to 8 V.

The target motion of this experiment was the flexion-extension motion of the arm, in which the elbow joint was moved back and forth five times with an amplitude of 90 deg. The maximum flexion angle of the arm was set as 90 deg. In this experiment, the subject first held the handle attached to the arm with the forearm extended (the arm angle was 0 deg at this time). At the start of the experiment, the subject bent the forearm by 90 deg. Immediately after the forearm was bent by 90 deg, the arm was extended by 90 deg. This movement was set as one cycle, and the exercise was performed for five cycles in each trial. The results of three out of five trials were used as the experimental results, and three of the five cycles of arm flexion and extension movements, excluding the first and last cycles, were used. In addition, the load on the hand tip during flexion was measured in this experiment.

Muscle potentials were measured using the Trigno Wireless EMG system (DELSYS). The measurement points were the biceps and triceps muscles. The measured EMG data were band-pass filtered (20–450 Hz), full-wave rectified, and low-pass filtered (10 Hz).

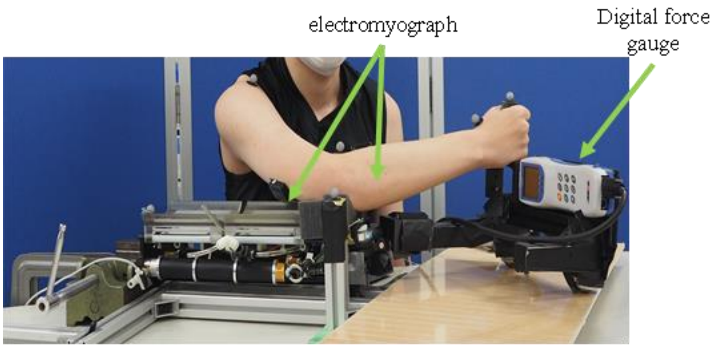

Figure 8. Experimental environment

Results and Discussions

Table 1 shows the angular velocity of the arm and the load applied to the hand during motion with each command viscosity.

The left column of Table 1 shows the joint angular velocity of the elbow during the experimental motion. The vertical axis shows the angular velocity, and the horizontal axis shows the motion time. The solid line represents the mean value of the movement speed, and the dashed line represents the standard deviation. In the graph, when the value is in the positive region, the human forearm moves in the flexion direction, and when it is in the negative region, it moves in the extension direction. The graph shows that the standard deviation value does not deviate significantly from the mean value for any viscosity, and a constant motion is achieved. It indicates that the viscosity of the MR brake can control the joint angular velocity of the arm. When the command viscosity is 0.09 deg/s, which is the highest, the maximum angular velocity is 100 deg/s, and the minimum is -100 deg/s compared with the other viscosities. In the first half of the motion in the bending direction, the angular velocity is controlled to be more constant than when the command viscosity is 0.03 and 0.06 deg/s.

The right column of Table 1 shows the load applied to the tip of the hand during the bending motion. The vertical axis shows the load, and the horizontal axis shows the operation time. The graph shows that the higher the viscosity, the lower the load applied to the tip, and the lower the viscosity, the higher the load. However, the lower the viscosity, the shorter the time in which the load is applied to the tip, and the more temporary the load is.

This is because in the case of low viscosity, the motion speed is high, and the inertia acting on the hand is larger, resulting in a higher value of the load. In contrast, when the viscosity is high, the operating speed is low, and the operating time is long, thus the time when the load is applied is long. It can also be confirmed that the values of the standard deviation of the load do not deviate significantly from the average value from the beginning to the middle of the bending operation for all viscosities. However, at the end of the operation, the values of the standard deviation of the load deviated from the mean value. This is because the subject knew that there was an extension movement after the flexion movement, so he stopped the movement and tried to move to the next movement, which caused the load applied to the hand to be different for each movement.

Table 1. Angular velocity of the elbow joint and load applied to the hand during the experimental motion

		Angular velocity [deg/s]	**Torque [Nm]**
Viscous [Nm s/deg]	0.03	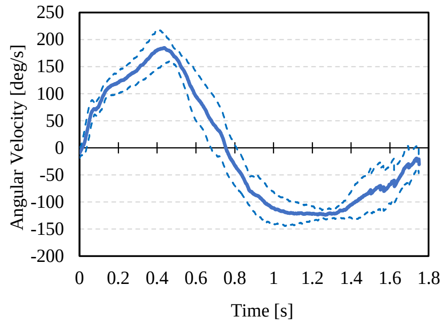	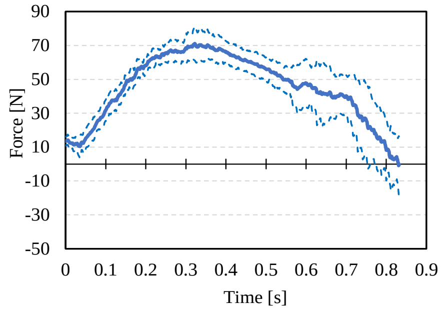
	0.06	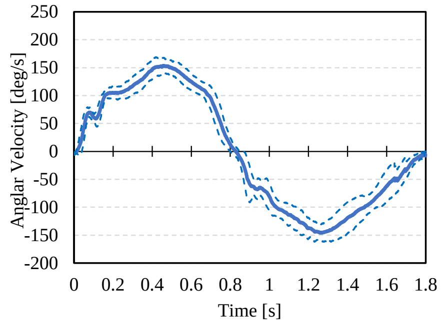	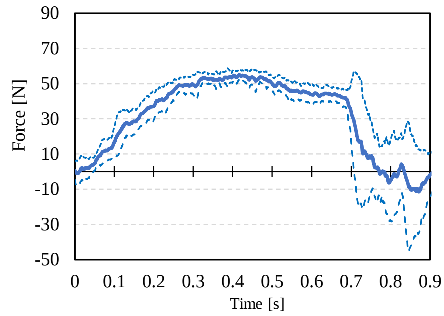
	0.09	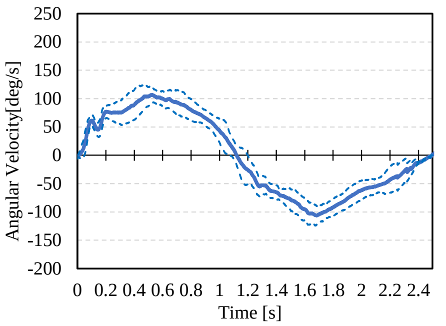	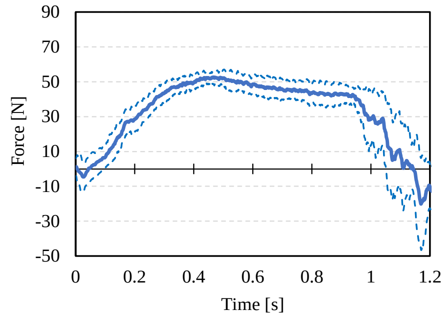

Figures 9 and 10 show the values of EMG potential on the vertical axis and the motion cycle on the horizontal axis for the biceps and triceps muscles, respectively. The orange, gray, and yellow lines represent the commanded joint viscosity of 0.09 deg/s, 0.06 deg/s, and 0.03 deg/s, respectively, and the blue line represents the value when the device is not attached. It can be observed that the biceps muscle is the flexion prime mover and therefore increases in the first half of one cycle during flexion, while the triceps muscle is the extension prime mover and therefore increases in the second half of one cycle during extension. At command viscosities of 0.03 and 0.06 deg/s, the EMG potentials of both biceps and triceps were higher than those without loading.
In this experiment, it was confirmed that there was a training effect when the command viscosity was 0.03 and 0.06 deg/s since the muscle potential increased because of the viscosity change. When the command viscosity was 0.09 deg/s, and when the device was not installed, the EMG potential values did not change compared with the other command viscosities. In addition to the possibility that the inertia force generated during the movement was canceled out, we believe that the subject may have become accustomed to the movement. He might have moved in a way that did not greatly activate the muscles because the movement was performed at 0.09 deg/s viscosity as the last change condition.
In addition, the contraction force of a muscle changes in inverse proportion to the contraction speed. This suggests that the maximum contractile force of the muscle is low for the command viscosity of 0.03 and 0.06 deg/s, which have high operation speeds, and that the value of the muscle potential is larger than that without the device because it is necessary to activate many muscles to operate under the load applied by the viscosity. However, in the case of the command viscosity of 0.09 deg/s, the motion speed was lower than in the other viscosity cases, and the contraction force of the muscles could be higher, thus the number of active muscles was smaller, resulting in lower EMG values. In addition, from the graph of the EMG potential of the triceps brachii muscle shown in Figure 10,

the peak values when the command viscosity was 0.09 deg/s and when the device was not installed were different from those when the command viscosity was 0.03 and 0.06 deg/s. This is because when the viscosity of the MR brake is high, the load applied to the muscle force is changed by canceling out the inertia during operation.

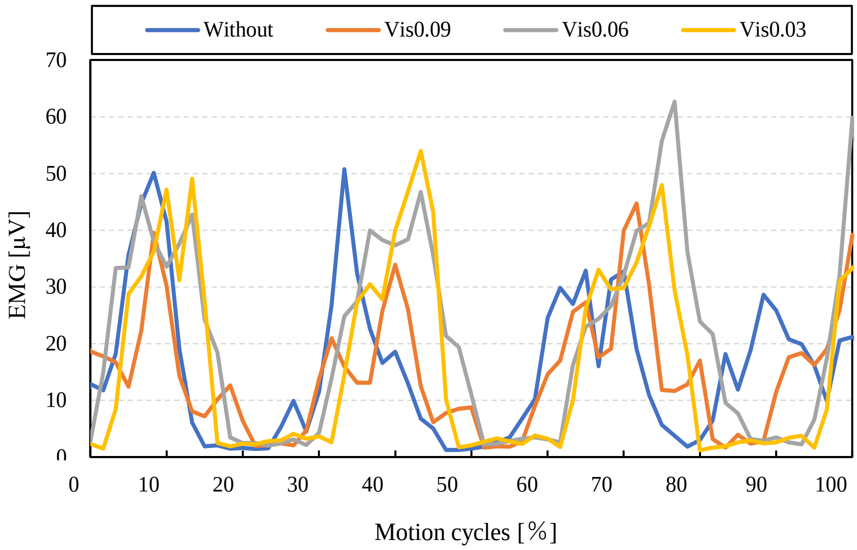

Figure 9. EMG potential values of the biceps brachii muscle

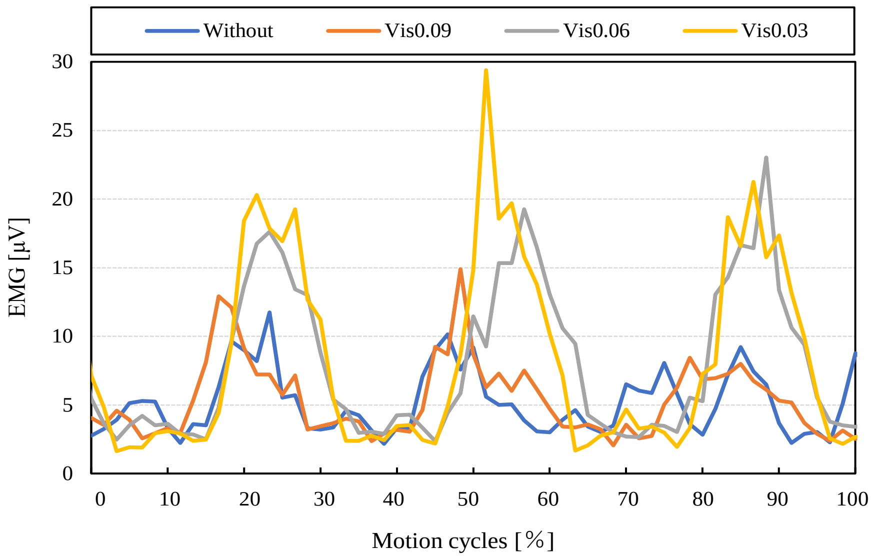

Figure 10. EMG values of the triceps brachii muscle

CONCLUSION

In this study, we developed a wearable device for training and rehabilitation using variable viscoelastic joints and proposed a physical interaction system (PIS) using the device. In addition, the training effect of the developed wearable variable viscoelastic joint unit and the elbow joint using this unit in constant velocity motion was verified experimentally. The elbow joint was flexed and extended under different conditions, and the training effect was verified by measuring the muscle potential. The results confirmed that the MR brake controlled the elbow joint motion to a constant motion. Furthermore, the increase in muscle potential during the experimental movements and the training effect of this unit during constant velocity movements were confirmed.

In the future, we aim to realize various motions with the device attached to a single joint of the lower limb.

REFERENCES

1. OSHIMA, H., MIZUNO, K. and KAWASHIMA, S., Effects of Space Flight on Bone and Muscle, and Astronaut Exercise Program, 2006, The Japanese Journal of Rehabilitation Medicine.
2. KAWASHIMA, S., MIZUNO, Y., WATANABE, Y., OSHIMA, H., Verification about effectiveness of resistance training against changing muscular volume and strength. 2006, JAXA Special Publication: Scientific Report of International Bed Rest Study, JAXA-SP-06-007, pp.34-68.
3. NASA, TEXAS INSTRUMENTS. (n.d.). ARED - RESISTIVE EXERCISE IN SPACE. https://www.nasa.gov/pdf/553871main_AP_ST_Phys_ARED.pdf (accessed on 21 November, 2020, from
4. JAXA (Japan Aerospace Exploration Agency). What will life be like on the International Space Station (ISS)? (JAXA（Japan Aerospace Exploration Agency）) https://fanfun.jaxa.jp/faq/detail/177.html (accessed on 2 June, 2021)
5. NASA. GFE Exercise, https://ntrs.nasa.gov/api/citations/20170009178/downloads/20170009178.pdf6 (accessed on 21 November, 2020)
6. NASA, X1: A Robotic Exoskeleton for In-Space Countermeasures and Dynamometry., https://ntrs.nasa.gov/citations/20140000694 (accessed on 21 November, 2020)
7. Okui, M., Iikawa, S., Yamada, Y. and Nakamura, T., Fundamental characteristic of novel actuation system with variable viscoelastic joints and magnetorheological clutches for human assistance, Journal of Intelligent Material System and Structures, 2018.
8. Okui, M., Iikawa, S., Yamada Y. and Nakamura, T. Variable viscoelastic joint system and its application to exoskeleton, IEEE/RSJ International Conference on Intelligent Robots and Systems, pp. 3897-3902, 2017.
9. ICHIHASHI, N., Basic Knowledge of Strength Training - Factors Affecting Strength and Mechanism of Strength Increase -, 1997, Bulletin of the College of Medical Technology, Kyoto University. Supplement, Health and Human Sciences. http://hdl.handle.net/2433/49548.
10. KOJIMA, A., OKUI, M., HISAMICHI, I., TSUJI, T., Nakamura, T., Straight-Fiber-Type Artificial Muscle Deformation Under Pressurization. 2019, IEEE Robotics and Automation Letters.

The 11th JFPS International Symposium on Fluid Power HAKODATE 2020 Oct. 12-13, 2021 JFPS The Japan Fluid Power System Society

Manufacturing and Evaluation of Similar Micro-Electrohydrodynamic Pumps with Different Scales

Kotaro OKADA*, Masahito NISHIKAWARA*, **, Shunichi NAITO*, Hideki YANADA*, Hiroshi YOKOYAMA*

*Department of Mechanical Engineering, Toyohashi University of Technology
1-1, Hibarigaoka, Tenpaku-cho, Toyohashi, Aichi, 441-8580 Japan
(E-mail: Okada.kotaro.ts@tut.jp)
** Mechanical Engineering Department, Worcester Polytechnic Institute
100 Institute Road, Worcester, MA 01609 USA

Abstract. We investigated the effect of electrode scale on the performance of Electrohydrodynamic (EHD) conduction pumps in this work. Because there are no moving parts in EHD pumps, they can be operated very quietly. Using MEMS technology, we produced micro sized EHD pumps with varying scales and conducted experiments to investigate effect of electrodes scale on EHD pumps. Large pressure was generated with lower flow channels. EHD simulation was conducted with COMSOL Multiphysics to investigate heterocharge layer structure on each scale. When the space between the electrodes was smaller than 50 μm, the positive and negative heterocharge layers overlap. The overlap is needed to be considered in the microscale electrode design.

Keywords: Electrohydrodynamics, EHD pump, MEMS, Scale effect

INTRODUCTION

Electrohydrodynamic (EHD) flow is generated without the use of moving mechanical parts and dielectric fluids are usually used as the working fluid. The EHD flow is promising for pumps, actuators, and heat transport [1-4]. EHD pumps have low vibration and low noise, are easy to miniaturize, and are electronically controllable. Typical phenomena that drive the dielectric fluids are ion drag and conduction. Conduction phenomenon is a flow phenomenon driven by the Coulomb force acting on the electric charges generated by dissociation. In this paper, we treat EHD pumps.

The electrodes widely used for EHD conduction pumps are flush electrode pair with different length. This geometry generates a net flow in the direction to the longer electrode [5-7]. The advantages of this geometry are that it can be used in series to obtain high pressures and can be placed as a part of other device with high flexibility. EHD pumps with several microscale electrodes have been studied so far, as shown in Table 1, and the microscale EHD pump characteristic and the effect of electrode asymmetry on the pump characteristic have been investigated [8-17]. Figure 1 shows the schematic of the EHD conduction pump of this research. The shape, dimensions of the electrodes, L_1, L_3, and the electrode gap, L_2, and the ratio of these dimensions were determined in a previous research [18]. The ratio of L_1, L_2 and L_3 is 1:1:3. The asymmetry of the electrodes generates a Coulomb force unbalance pushing the dielectric working fluid from the narrow electrode to wide electrode [19].

Vázquez et al. [20] have done fundamental numerical simulations of EHD conduction pumping with two-parallel electrodes and introduced two nondimensional numbers, C_0, and β. C_0 is called conduction number which is the ratio of the distance that a dissociation charge migrates during relaxation time to the electrode scale, and β is the parameter that accounts for the electric field enhanced dissociation of dissociative molecules. They have shown two operational regimes of the EHD conduction, called ohmic regime and saturation regime. In the ohmic regime ($C_0 > 1$), positive and negative charges are accumulated on the opposite polarity electrode, respectively, and the layer of the charges with opposite polarity to each electrode is called heterocharge layer. Electric current is proportional to the applied voltage and developed pressure increases with the square of applied voltage. In saturation regime ($C_0 < 1$), on the other hand, as the heterocharge layer is thicker than the electrode spacing, both heterocharge layers overlap. Michel et al. [21] showed that heterocharge layers overlap with asymmetric flush electrodes of L_2=127 μm in EHD conduction pumping used in a flow distribution control device.

Several microscale EHD pumps have been developed. However, The effect of electrode scale on the EHD pump characteristic has not been clarified so far. Therefore, in this study, we use MEMS technology to produce similar EHD pumps with different scales and we investigate the effects of the pump scale on EHD pump characteristics experimentally and numerically.

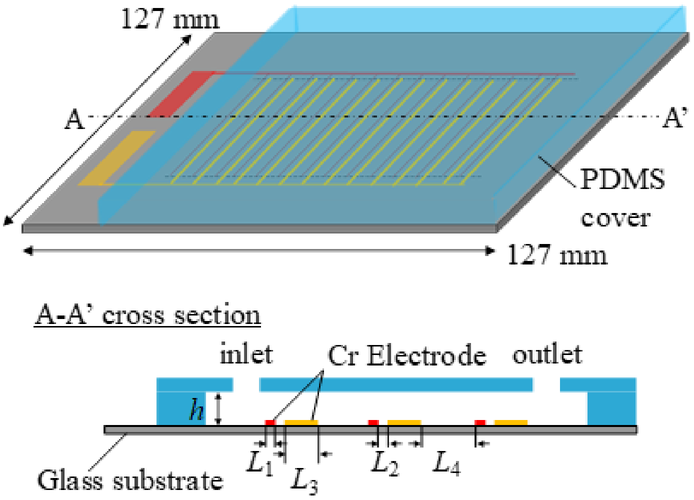

Figure 1. Schematic of EHD pump (not-to-scale).

Table 1. EHD pumps dimensions in previous research [8-17].

Refs.	L_1 µm (narrow)	L_2 µm (gap)	L_3 µm (wide)	L_4 µm (pair pitch)	pair n[0]	Voltage kV	Channel width mm	Channel height mm	Channel length mm
M. K. Russel 2016 [8]	20	30	40	60	100	0.8	-	0.1	-
M.R. Pearson 2014 [9]	1220	970	4060	16510	9	5	57	57	152
M.R. Pearson 2013 [10]	127	127	381	1270	21	0.75	12.7	0.508	40
I. Kano 2013 [11]	120	60	360	480	20	0.5	21	0.1	16
M.R. Pearson 2011 [12]	51	51	178	794	10	0.8	12.7	0.254	11
Y. He 2010 [13]	20	20	20	80	-	0.2	-	0.1-0.15	-
Y. Sakurai 2009 [14]	200	200	200	700	69	2	7	1	90
S. Yokota 2008 [15]	80	200	80	400	108	3	11	0.5	90
J. Darabi 2005 [16]	10	20	10	40	200	0.2	10	0.050	16
S. Moghaddam 2005 [17]	3	10	3	10	-	0.07	32	-	32
This study	5, 50, 500	5, 50, 500	15, 150, 1500	50, 500, 5000	200, 20, 2	0.05, 0.5, 5	18.7	0.02, 0.2, 2	15

EXPERIMENTAL APPARATUS AND METHOD

EHD Pump and Design Electrodes

To generate the net Coulomb force acting on dissociated charges, the electrode configuration was asymmetric. To investigate the effect of electrode scale and channel heights, MEMS fabrication technology was used to produced similar EHD pumps with varying sizes. To examine the impact of channel height, all pumps have a channel height of h = 4L_2 (see Figure 1) and pumps with L_2 = 50 μm have three different channel heights, 1L_2, 4L_2, and 20L_2. β and C_0 are the nondimensional numbers used to define the effects of the scale on EHD pumps, and they are described in the numerical model section. Because the channel length is the same, a pump with smaller electrodes has more electrodes. A fluorinated fluid (Vertrel XF) is filled in the pump as the working fluid. We produced EHD pumps using photolithography, a MEMS technology. For the electrode fabrication, we used a Cr coated glass substrate. The thickness of the Cr coating was 100 nm and the resist (FMR027) was coated on it. For patterning electrodes, we used Electron Beam Lithography Exposure. The electrodes were completed by developing and etching. The flow channel was made of PDMS resin and laminated the substrate and PDMS resin to fabricate the EHD pumps.

Experimental Method

Figure 2 depicts a schematic of the experimental apparatus. EHD pump, a differential pressure gage (Validyne Engineering, DP-15-22-N-1-W4-A), and a flow mater (Sensirion, SLI2000) were used in the experiment. For each component, 1/4 inch tubes were used for the connection. A differential pressure gauge connected to the pump's upstream and downstream was used to measure the pressure generated by the pump. By closing the valve, we were able to conduct experiments with no net flow. The current was measured by the resistor (320 kΩ) inserted between the EHD pump and the power supply. The resistance value of our EHD pump (L_2 = 50 μm) was about 1 MΩ. During the experiments, the pressure and electrical current were monitored at 1-second intervals by a data logger. Stepwise, DC voltage was applied to the electrodes of the EHD pump in the experiment. The maximum apparent electric field strength between the electrodes, defined as the applied voltage divided by the electrode gap, was 6 kV/mm.

NUMERICAL MODEL

Governing Equations for EHD

We used COMSOL Multiphysics for conduct numerical simulation. The flow was assumed to be two-dimensional at steady-state and incompressible in this study, and the flow field was analyzed using the Navier-Stokes equation shown as Eq. (1) as well as the continuity equation of Eq. (2).

$$(\mathbf{u}\cdot\nabla)\mathbf{u} = -\frac{1}{\rho}\nabla P + \frac{\mu_f}{\rho}\nabla^2\mathbf{u} + \mathbf{F} \tag{1}$$

$$\nabla\cdot\mathbf{u} = 0 \tag{2}$$

Where **u** is the velocity vector, P is the pressure, ρ is the fluid density, μ_f is the viscosity coefficient, and **F** is the body force vector. The equation of electric field as shown below must also be solved to calculate the volume force of Coulomb force. Eq. (3) and Eq. (4) are the conservation laws of positive and negative dissociated charges, respectively.

$$\nabla\cdot(q\mu^+\mathbf{E} + q\mathbf{u} - D_i\nabla q) = k_d c - k_r qw = k_r({w_0}^2 F(\omega) - qw) \tag{3}$$

$$\nabla\cdot(-w\mu^-\mathbf{E} + w\mathbf{u} - D_i\nabla w) = k_d c - k_r qw = k_r({w_0}^2 F(\omega) - qw) \tag{4}$$

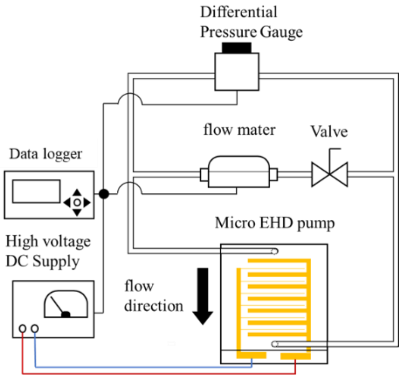

Figure 2. Schematic of experimental apparatus.

Eq. (5) shows Gauss's law. Eq. (6) shows relationship between the electric field and electric potential. Eq. (7) shows Coulomb force. Eq. (8) shows charge density at equilibrium. Eq. (9) and Eq. (10) show the Onsager function representing field-enhanced dissociation. Eq. (11) shows the rate of recombination.

$$\nabla \cdot \mathbf{E} = -\frac{q-w}{\varepsilon} \tag{5}$$

$$\mathbf{E} = -\nabla\phi \tag{6}$$

$$\mathbf{F} = \frac{q}{\rho}\mathbf{E} \tag{7}$$

$$w_0 = \frac{\sigma}{2\mu} \tag{8}$$

$$F(\omega) = \frac{I_1(4\omega)}{2\omega} \tag{9}$$

$$\omega(|\mathbf{E}^*|) = \beta {C_0}^{-1/2}|\mathbf{E}^*|^{-1/2} \tag{10}$$

$$k_r = \frac{2\mu}{\varepsilon} \tag{11}$$

In these equations, μ^+ and μ^- are the ionic mobilities of the positive and negative charges, respectively. Assuming they are equal, we use μ for the ionic mobility. D_i is the ion diffusion coefficient, $\mathbf{E}$ is the electric field strength, ϕ is the electric potential, q is a positive charge density, w is a negative charge density, c is the neutral molecule concentration, k_r is the recombination coefficient, k_d is the dissociation constant, σ is the conductivity, ε is the relative permittivity, and I_1 is the Bessel function of the first kind.

Nondimensionalization of The Governing Equations

The nondimensionalized governing equations derived by using nondimensional parameters are shown in Eqs. (12) to (16). The nondimensional parameters are shown in Eqs. (17) to (21). Eq. (22) represents the dissociation tendency.

$$\frac{\partial \mathbf{u}^*}{\partial t^*} + (\mathbf{u}^* \cdot \nabla)\mathbf{u}^* = -\nabla P^* + \frac{1}{Re^E}\nabla^2\mathbf{u}^* + M^2 C_0(q^* - w^*)\mathbf{E}^* \tag{12}$$

$$\nabla \cdot \mathbf{u}^* = \mathbf{0} \tag{13}$$

$$\nabla^* \cdot (q^*\mathbf{E}^* + q^*\mathbf{u}^* - \alpha\nabla^* q^*) = \frac{{C_0}^2 F(\omega)}{\left(1+\frac{1}{b_r}\right)} - \left(1+\frac{1}{b_r}\right) q^* w^* \tag{14}$$

$$\nabla^* \cdot (-w^*\mathbf{E}^* + w^*\mathbf{u}^* - \alpha\nabla^* w^*) = \frac{{C_0}^2 F(\omega)}{\left(1+\frac{1}{b_r}\right)} - \left(1+\frac{1}{b_r}\right) q^* w^* \tag{15}$$

$$\nabla^2 \phi^* = -C_0(q^* - w^*) \tag{16}$$

$$C_0 = \frac{\sigma_0 L_2}{2\varepsilon\mu E} = \frac{L_2}{2\mu E_0\left(\frac{\varepsilon}{\sigma}\right)} = \frac{1}{2}\frac{L_2}{L_{travel}} \tag{17}$$

$$\alpha = \frac{k_B T}{e_0 E_0 L_2} \tag{18}$$

$$Re^E = \frac{\rho\mu E_0 L_2}{\mu_f} \tag{19}$$

$$M = \frac{\sqrt{\varepsilon/\rho}}{\mu} \tag{20}$$

$$b_r = \frac{\mu^+}{\mu^-} \tag{21}$$

$$\beta = \left(\frac{{e_0}^3 \sigma L_2}{32\pi\varepsilon^2\mu {k_B}^2 T^2}\right)^{1/2} \tag{22}$$

In these equations, E_0 is strength of electric field, e_0 is elementary charge, k_B is Boltzmann constant, and T is the temperature. Conduction number, C_0 is the ratio of the length between the electrodes to the length that the ions can travel by migration within the relaxation time which it takes for the dissociated charges to recombine. α is the diffusion number. Re^E is electric Reynolds number. It includes the ionic drift velocity μE_0 as the representative velocity and is not hydrodynamic Reynolds number. M is mobility number. It is the ratio of hydrodynamic mobility to the ionic mobility. It depends on only liquid properties. These numbers were introduced in a previous research [20]. b_r is mobility ratio of the positive and negative dissociation charges. β is the parameter that accounts for the electric field dissociation of dissociative molecules. The larger β, the more likely it is that dissociated ions are generated. Nondimensional parameters and liquid properties that we used are shown in Table 2. These properties were obtained from [21].

Table 2. Nondimensional quantities and liquid properties for numerical simulation

Nondimensional numbers	L_2 **= 500 μm**	L_2 **= 50 μm**	L_2 **= 5 μm**
Conduction number C_0 (-)	0.50 - 1.50	0.050 - 0.15	0.005 - 0.015
Diffusion number α (-)	0.08×10^{-7} - 0.25×10^{-7}	0.08×10^{-6} - 0.25×10^{-6}	0.08×10^{-5} - 0.25×10^{-5}
Electric Reynolds number Re^E (-)	1.15×10^2 - 3.47×10^2	1.15 ×10 - 3.47×10	1.15 - 3.47
Nondimensional number β **(-)**	0.50	0.16	0.05
Liquid properties (Vertrel XF)			
Density ρ (kg/m^3)	1580		
Conductivity σ (S/m)	3.45×10^{-8}		
Relative permittivity $\varepsilon/\varepsilon_0$ (-)	6.84		
Viscosity μ_f (Pa·s)	6.47×10^{-4}		
Ionic mobility μ (m^2/Vs)	4.64×10^{-8}		
Ion diffusion coefficient D_i (m^2/s)	1.2×10^{-9}		

RESULTS AND DISCUSSION

The time variations of the pressure rise, Δ*P*, and electric current, *I*, of the pump with L_2 = 50 µm and $h = 4L_2$ are shown in Figure 3. The experiment was stopped at 300 V to avoid breakdown of the fluid. The power consumption was 0.1 W at 300 V.

As shown in Figure 4, the pressure rises of all pumps increased with the electric field. Due to differential pressure gage overpressure, the pressure rises of the pump with L_2 = 50 µm were not measured at 6 kV/mm. The maximum generated pressure averaged 727 Pa at the channel height of 50 µm, 463 Pa at 200 µm, and 20 Pa at 1000 µm as shown in Figure 4. The results showed that a higher pressure rise was generated by a lower channel height. The reason for this characteristic is that charges are distributed on a large percentage of cross-section of the channel with a lower height as shown in Figure 5.

Figure 6 depicts the characteristic of the Δ*P* vs Electric field strength. Figure 6 show that the pump with L_2 = 50 µm generated higher pressure than the other pumps. The pump with L_2 = 5 µm is exceedingly small. The manufacturing accuracy of the pump was not accurate due to its exceedingly small scale, and which may have affected the experimental results. In Figure 7, the effects of nondimensional parameters C_0 and β on the generated pressure are shown including the results of the previous research [20], in which the present results are circled (our result of β = 0.05 is not plotted because generated pressure was very small and parallel plate electrode was used in previous research [20]). Figure 6 and Figure 7 shows that our EHD pumps could generate higher pressure than the previous research and generated pressure increase as the electric field strength increase. However, the results of previous research show that there are areas where generated pressure is not proportional to the electric field strength under small C_0 and β conditions. Therefore, we will build a smaller EHD pump than this research and conduct experiments to investigate pump characteristics.

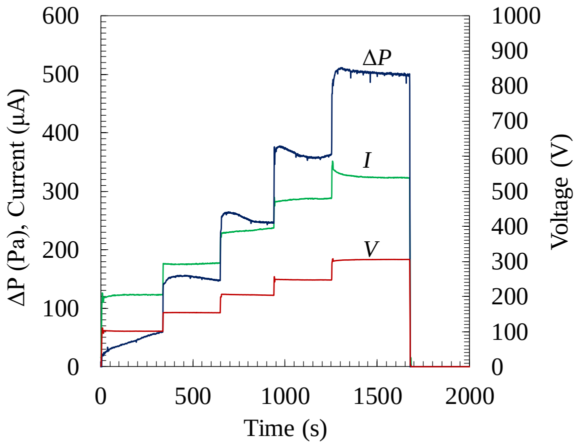

Figure 3. Variations of pressure and electric current of the pump with L_2 = 50 µm and h = 200 µm at zero flow rate.

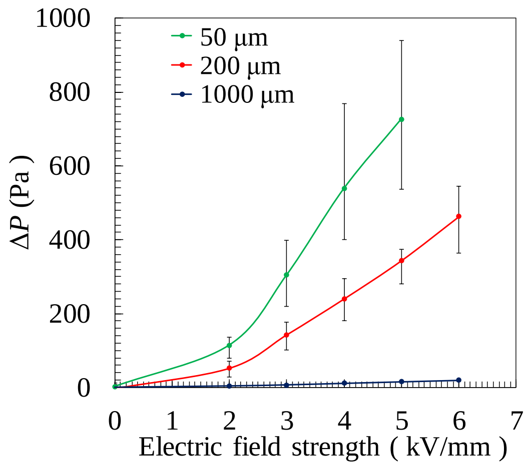

Figure 4. Effect of channel height on pressure rise at zero flow rate of the pump with L_2 = 50 µm.

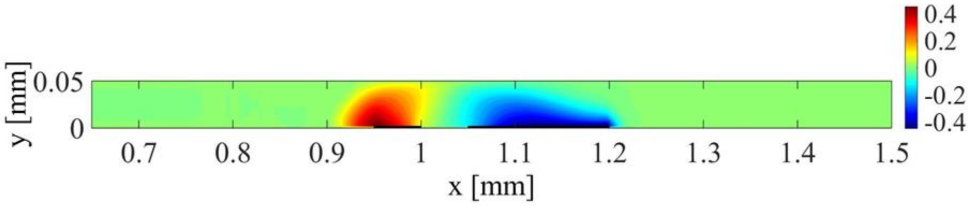

(a) h = 50 μm.

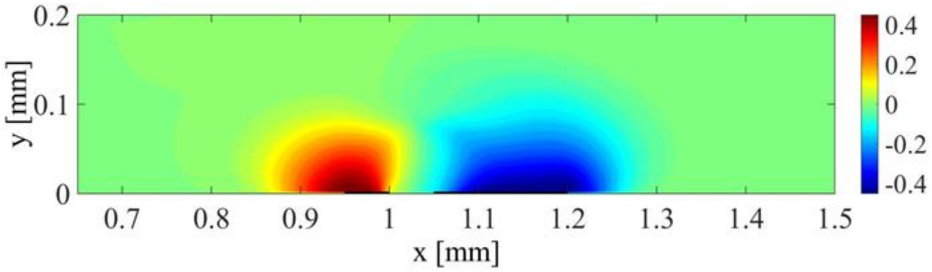

(b) h = 200 μm.

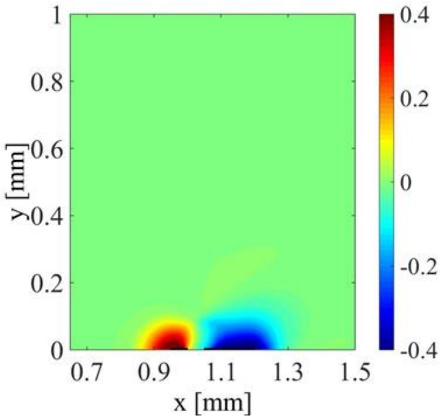

(c) h = 1000 μm.

Figure 5. Charge density distribution at zero flow rate. The unit is C/m^3.

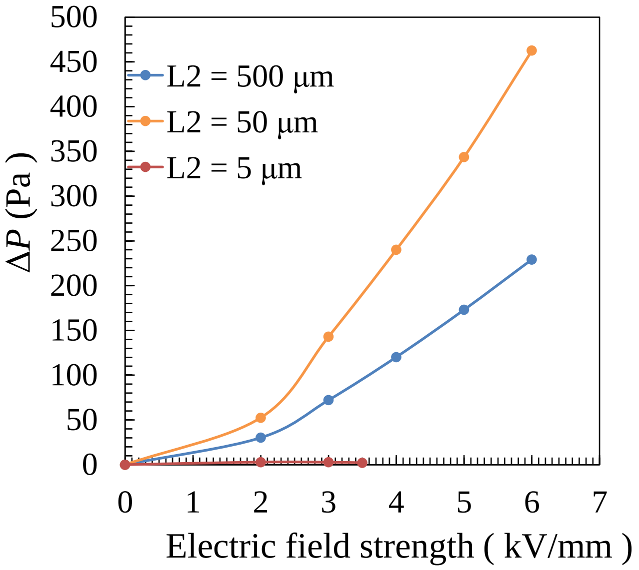

Figure 6. Characteristic of ΔP vs Electric field strength.

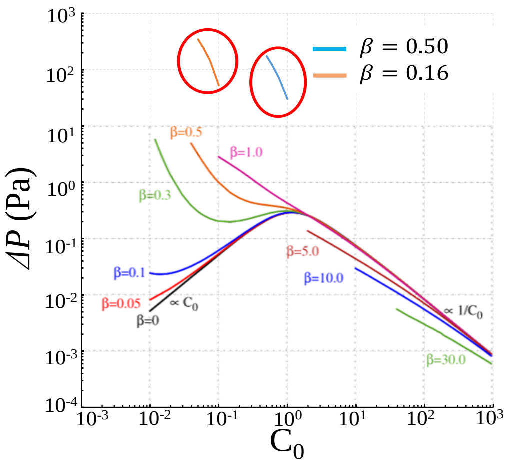

Figure 7. Comparison of C_0 and β between the present research and previous one (present results are circled).

Numerical simulation results are shown in Figures 8 to describe the difference for each similar scale pump. Figure 8 (a) to (c) depict the charge density distribution, while (d) to (e) depict the velocity distribution. In Figure 8 (a) to (c), red and blue lines show the outer lines of each heterocharge layer which is defined as the area where the charge density is higher than equilibrium one, w_0. Here, the overlapping of heterocharge layers and smaller-scale EHD pump have larger area of the overlap. This is because the travel distance of dissociated ions within the relaxation time is independent of electrode scale as shown in Eq. (17). This behavior of the charge distribution on each scale is thought to be related for the difference of the pump characteristic. Also, electric charges of smaller-scale pump distributed on a large percentage of cross-section of the channel. Especially, for the smallest scale pump, the heterocharge layer is over the boundary of the computational domain. Figure 8 (d) to (f) show that the velocity distribution was differed significantly depending on the pump scale. In the pumps with L_2 = 500 μm and L_2 = 5 μm, the vortices were generated near the electrodes only. However, in the pump with L_2 = 50 μm, the vortices were generated at various locations of channel.

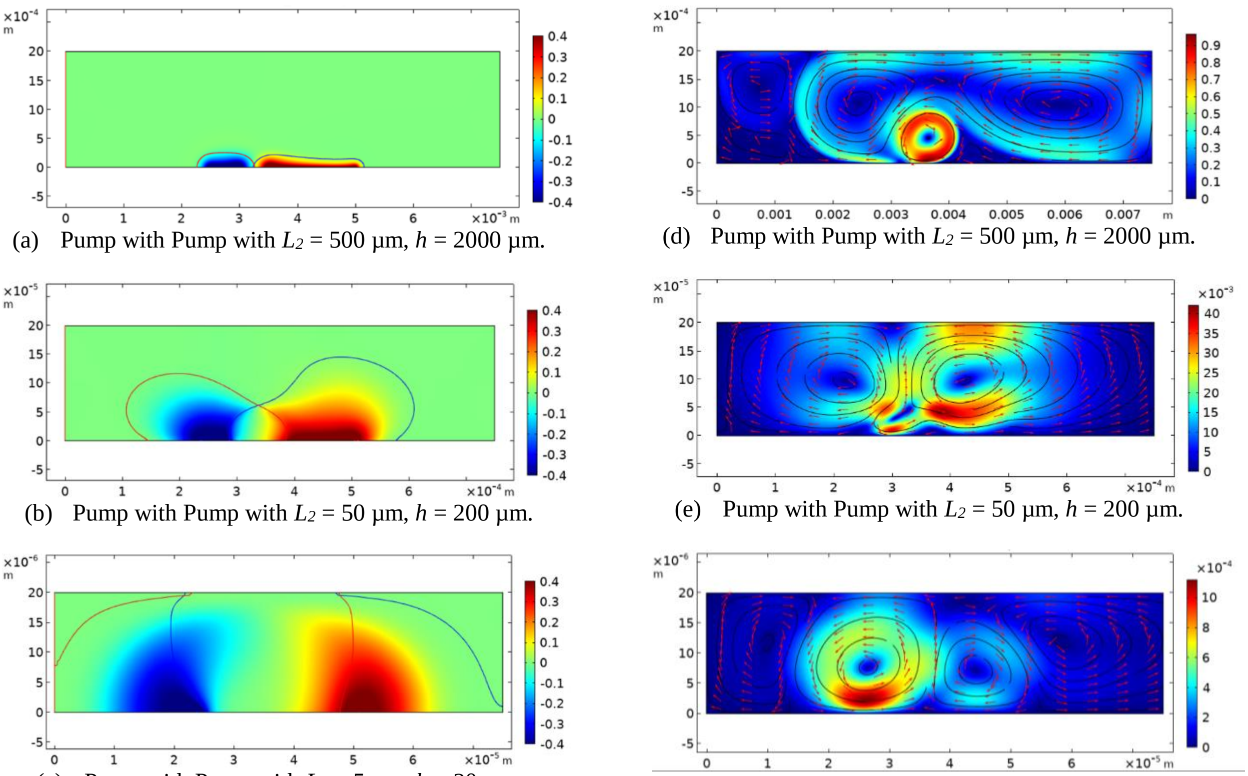

(a) Pump with Pump with L_2 = 500 μm, h = 2000 μm.

(d) Pump with Pump with L_2 = 500 μm, h = 2000 μm.

(b) Pump with Pump with L_2 = 50 μm, h = 200 μm.

(e) Pump with Pump with L_2 = 50 μm, h = 200 μm.

(c) Pump with Pump with L_2 = 5 μm, h = 20 μm.

(f) Pump with Pump with L_2 = 5 μm, h = 20 μm.

Figure 8. (a)~(c) Electric charge density at zero flow rate. The unit is C/m³.
(d)~(f) Velocity distribution at zero flow rate. The unit is m/s.

CONCLUSION

In this research, characteristics of microscale EHD pumps with different channel heights and sizes were investigated. Generated pressure depends on channel height and we could obtain higher pressure by lowering the channel height. The flow rate for lower channel height should be measured because lower channel height may decrease flow rate. By numerical simulation, overlap of the positive and negative heterocharge layers was observed at L_2 = 50 μm or less. Therefore, it is necessary to design the electrode considering the overlap of the heterocharge layer on microscale EHD pumps.

ACKNOWLEDGMENTS

This research was partially supported by Toukai Foundation for Technology, the Yashima Environment Technology Foundation, and the JSPS KAKENHI Grant Number 21K14075. The authors appreciate Mr. T. Hizawa of Toyohashi University of Technology's Evolution of the Electronics-Inspired Interdisciplinary Research Institute (EIIRIS) for his assistance with MEMS fabrication.

NOMENCLATURE

br	Mobility ratio of the positive and negative dissociation charges (-)
c	Neutral molecule concentration (mol/m^3)
C_0	Conduction number (-)
Di	Ion diffusion coefficient (-)
e_0	Elementary charge (C)
$\mathbf{E}$	Electric field strength vector (V/m)
E_0	Electric field strength (V/m)
$\mathbf{F}$	Body force vector (N/kg)
$F(\omega)$	Onsager function (-)
I_1	Bessel function of the first kind (-)
k_B	Boltzmann constant (J/K)
k_d	Dissociation constant (C/mol·s)
k_r	Recombination coefficient (m^3/C·s)
L_2	Electrode gap (m)
L_{travel}	The distance of that ion travel (m)
M	Mobility number (-)
ΔP	Generated pressure (Pa)
q	Positive charge density (C/m^3)
Re^E	Electric Reynolds number (-)
T	Temperature (K)
u	Velocity (m/s)
$\mathbf{u}$	Velocity vector (m/s)
w	Negative charge density (C/m^3)

w_0	Charge density at equilibrium (C/m^3)

Greek

ε	Permittivity (F/m)
μ	Ionic mobility (m^2/Vs)
μ_f	Viscosity (Pa·s)
σ	Conductivity (S/m)
ϕ	Electric potential (V)
α	Diffusion number (-)
β	Nondimensional number with respect to the Onsager function (-)
ρ	Fluids density (kg/m^3)

REFERENCES

1. S. YOKOTA, A Review on Micropumps from the Viewpoint of Volumetric Power Density, Mech. Eng. Rev. 1 (2014) 1–11.
2. M.R. PEARSON, J. SEYED-YAGOOBI, Experimental Study of Linear and Radial Two-Phase Heat Transport Devices Driven by Electrohydrodynamic Conduction Pumping, J. Heat Tran. 137 (2014) 22901.
3. R. ABE, K. TAKEMURA, K. EDAMURA, S. YOKOTA, Concept Of a Micro Finger Using Electro-Conjugate Fluid and Fabrication of a Large Model Prototype, Sensors Actuators, A Phys. 136 (2017) 629–637.
4. T.H. HWANG, Y.J. KIM, H. CHUNG, W.H. RYU, Motionless Electrohydrodynamic (EHD) Printing of Biodegradable Polymer Micro Patterns, Microelectron. Eng. 161 (2016) 43–51.
5. M YAZDANI, J. SEYED-YAGOOBI, Heat Transfer Enhancement of Backstep Flow by Means of EHD Conduction Pumping, International Jounal of Heat and Mass Transfer 73 (2014) 819-825.
6. M YAZDANI, J. SEYED-YAGOOBI, The Effect of Unipolar Charge Injection on EHD Conduction Pumping.
7. ADAMCZEWSKI I, IONIZATION, Conductivity and Breakdown in Dielectric Liquids, London: Taylor and Francis, (1969)
8. M.K. RUSSEL, P.R. SELVAGANAPATHY, C.Y. CHING, Ion Drag Electrohydrodynamic (EHD) Micro-Pumps Under a Pulsed Voltage, J. Electrostat. 82 (2016) 48–54.
9. Y. HE, Y. JIAN, M. CHONGFANG, Design, Fabrication and Experimental Research for an Electrohydrodynamic Micropump, Science China Technological Sciences. 53 (2010) 2839–2845.
10. M.R. PEARSON, J. SEYED-YAGOOBI, Experimental Study of Linear and Radial Two-Phase Heat Transport Devices Driven by Electrohydrodynamic Conduction Pumping, 2014.
11. M.R. PEARSON, J. SEYED-YAGOOBI, Experimental Study of EHD Conduction Pumping at the Meso- and Micro-Scale, 2011.
12. I. KANO, Effect of Electrode Arrangements on EHD Conduction Pumping, 2013
13. Y. SAKURAI, et al., Development of Tube Type ECF-Pump and Its Application to Liquid Cooling System for CPU, Transactions of the Japan Society of Mechanical Engineers, Series B (2009) Vol. 75, no. 753, 966-971.
14. YOKOTA, High-Integration Micro Motor Using Electro-Conjugate Fluid (ECF), the Journal of Robotics and Mechatronics (2005).
15. S. MOGHADDAM, Effect of Electrode Geometry on Performance of an EHD Thin-Film Evaporator, (2005).
16. J. DARABI, H. WANG, Development of an Electrohydrodynamic Injection Micropump and Its Potential Application in Pumping Fluids in Cryogenic Cooling Systems, (2005).
17. M.R. PEARSON, J. SEYED-YAGOOBI, Electrohydrodynamic Conduction Driven Single- and Two-Phase Flow in Microchannels with Heat Transfer, 2013.
18. M.R. PEARSON, J. SEYED-YAGOOBI, Electrohydrodynamic Conduction Driven Single- and Two-Phase Flow in Microchannels with Heat Transfer, Journal of Heat Transfer, 135 (2013) 101701.
19. S. JEONG, J. SEYED-YAGOOBI, and P. ATTEN, Theoretical/ Numerical Study of Electrohydrodynamic Pumping Through Conduction Phenomenon, IEEE Transactions on Industry Applications, vol. 39, no. 2. pp. 355–361, 2003.
20. P.A. VÁZQUEZ, M. TALMOR, J. SEYED- YAGOOBI, et al., In-Depth Description of Electrohydrodynamic Conduction Pumping of Dielectric Liquids: Physical Model and Regime Analysis, Physics of Fluids 31, 113601 (2019).
21. Vertrel Technical Information, Chemours-Mitsui Fluoroproducts Co.,Ltd. https://www.chemours.com/Vertrel/en_US/assets/downloads/pdf/vertrel-xf-technical-information.pdf
22. M. TALMOR, J. SEYED- YAGOOBI, Numerical Study of Micro-Scale EHD Conduction Pumping: The Effect of Pump Orientation and Flow Inertia on Heterocharge Layer Morphology and Flow Distribution Control, Journal of Electrostatics 111 (19), 103548 (2020)

The 11th JFPS International Symposium on Fluid Power HAKODATE 2020 Oct. 12-13, 2021 The Japan Fluid Power System Society

Study on a Low Pressure and Flowrate Driving of Micro Leg Joints for Soft Robots

Koji MICHISHITA*, Kazuhiro YOSHIDA**, and Joon-wan KIM**

* School of Engineering, Tokyo Institute of Technology
** FIRST, IIR, Tokyo Institute of Technology
J3-12, 4259 Nagatsuta-cho, Midori-ku, Yokohama, 226-8503 JAPAN
(E-mail: woodjoon@pi.titech.ac.jp)

Abstract. To aim at developing a micro leg joint driven by low pressure and flowrate, we propose a novel soft actuator composed of extremely soft silicon rubber (Ecoflex) and reinforced by a fiber. Due to two different flexibilities of rubber materials (Ecoflex: stretchable material; PDMS: structural material), the proposed balloon-type actuator generates angular displacement like an insect leg joint at the low applied driving pressure. This actuator is also designed to be driven at a lower flowrate by attaching a fiber to the balloon and restricting its expansion in directions unrelated to the angular displacement. The actuator was successfully fabricated by the molding and curing of rubbers with the attachment of the fiber. To verify the influence of the fiber, we measured the actuation angle and its volume change. The proposed fiber-reinforced actuator achieved the same actuation angle with less volume change compared with one of non-fiber actuators. This study proved the feasibility that the reduction of volume change can increase the dynamic response of the soft actuator.

Keywords: Electro-conjugate fluid (ECF), Soft robotics, Micropump, MEMS, Functional fluid

INTRODUCTION

In recent years, the use of microrobots is expected to search for minute spaces that humans cannot enter, such as under the rubble of disaster sites. It is known that a robot that walks with multiple legs rather than wheels or caterpillars is suitable for moving on rough terrain because of its high adaptability to the ground [1]. The walking of a multi-legged robot composed of rigid materials requires a large number of sensors and complicated controls. On the other hand, soft robots made of flexible materials have the advantage of conformity to objects due to their deformation and the absorption of impact energy, so that they can walk on rough terrain without the need for complicated control. To integrate our ECF micropumps [2] as hydraulic power sources into soft robots, we need to develop their actuators to be driven with low pressure as well as low flow rate.

This study proposes a fiber-reinforced soft microactuator that generates angular displacement like the leg joint of insects with the low pressure and low flow rate driving. The structure and fabrication process of the actuator are described in this study. Also, its characteristics are clarified by the simulations and experiments.

FIBER-REINFORCED SOFT JOINT ACTUATOR

As a way to reduce the driving pressure, we propose to fabricate the soft actuator as a micro leg joint by utilizing two kinds of rubber with different elastic modulus: Ecoflex as a stretchable material and PDMS as a structural material, as shown in Fig. 1(a). This multi-rubber structure is adequate for low pressure driving, but inadequate for low flowrate driving, because a large amount of driving fluid does not contribute to the displacement, as shown in Fig. 1(b).

To satisfy the driving with low flowrate as well as low pressure, this study proposes to limit the deformation that does not contribute to the operating angle by using reinforcing fibers. Fig. 2 shows the structure and working principle of the fiber-reinforced soft joint actuator. The actuator has a hollow structure composed of hard rubber (PDMS), soft rubber (Ecoflex), and reinforcing fibers wrapped around the soft rubber. When the actuator is pressurized, the soft rubber deforms more than the hard rubber. As a result, the hard rubber becomes a displacement constraint and creates an angular displacement. A reinforcing fiber plays a role in suppressing only the deformation of the soft rubber in the vertical direction of the wall surface as shown in Fig. 2(a), reducing the volume change of the hollow portion during the actuator operation. This fiber reinforcement can reduce the amount of working fluid to enter the hollow portion, improving the dynamic characteristics.

Fig. 3 shows the fabrication and assembling process of the fiber-reinforced soft joint actuator. For hard rubber, PDMS (Sylgard 184, Toray Dow Corning) and its curing agent are mixed at a mass fraction of 10: 1. For soft rubber, Ecoflex (Ecoflex00-30, Smooth-On) is used. The lower part and the ceiling are fabricated separately.

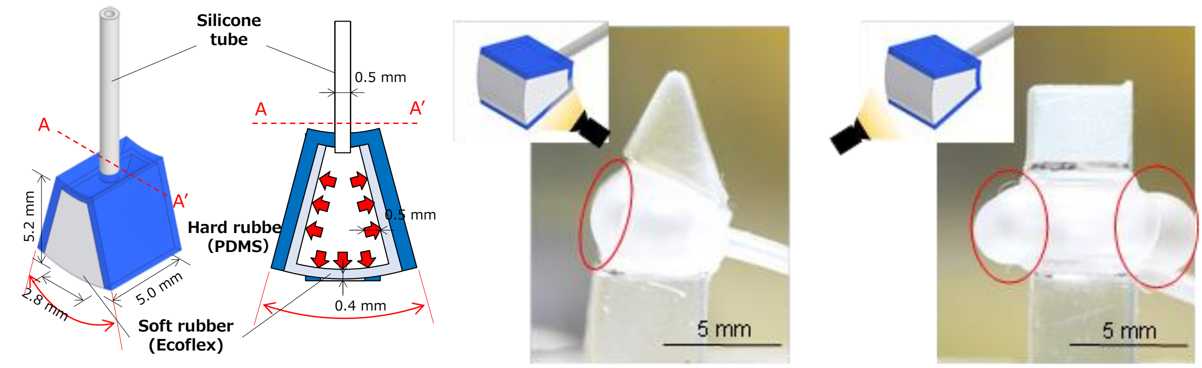

(a) Soft joint actuator composed of two rubber materials (b) Problem of the micro leg joint

Figure 1. Structure, working principle, and problem of the soft joint actuator made of Ecoflex and PDMS

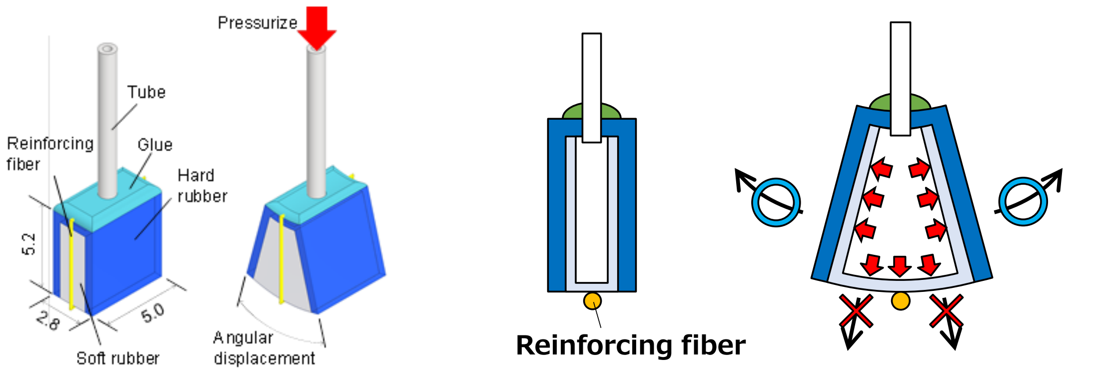

(a) Structure and working principle (b) Limiting the deformation unrelated to the angular displacement

Figure 2. Proposed fiber-reinforced soft joint actuator

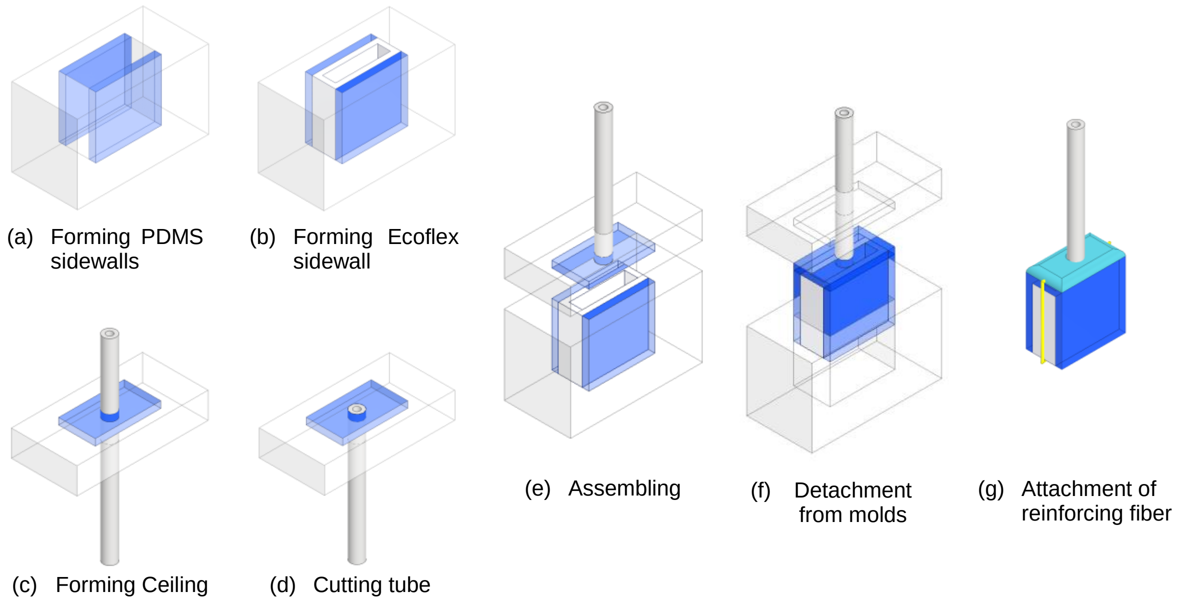

Figure 3. Fabrication and assembling process of the fiber-reinforced soft joint actuator

After bonding the ceiling and the lower part of the actuator, both ends of the reinforcing fiber are fixed to the ceiling of the actuator with a silicone adhesive. There must be no silicone adhesive between the fiber and the sidewall of the actuator not to increase the thickness of the sidewall.

SIMULATIONS AND EXPERIMENTS

Fig. 4 shows the operation of the soft joint actuators at the applied pressure of 30 kPa with a wall thickness of 0.4 mm. Similar to the simulation results, it was confirmed the angular displacement was caused by the difference in elastic modulus between PDMS and Ecoflex. In addition, it can be seen that the Ecoflex part of the non-reinforced soft joint actuator expands in the vertical direction of the wall surface, as in the simulation. On the other hand, in the fiber-reinforced soft joint actuator, it was confirmed that the expansion of the Ecoflex part was suppressed by the reinforcing fiber. Moreover, the deformation form was in good agreement with the simulation by COMSOL Multiphysics^{TM}. Fig. 5(a) shows the simulation and experiment results between the applied pressure and the actuation angle under each fabrication condition. As for the tendency of the change of the actuation angle with respect to the increase of pressure, the experimental value and the simulation result were almost the same. In addition, the angles at the applied pressure of 30 kPa with the wall thickness of 0.4 mm were 24.2 ° and 23.6 ° without and with the fiber reinforcement, respectively. Their actuation angles were almost the same as each other. Fig.5(b) shows the relation between the applied pressure and the volume change of the actuator. Comparing the volume change of the actuator without and with the fiber reinforcement, the volume change of the fiber-reinforced actuator became significantly smaller. The fiber reinforcement makes it possible to drive the actuator with a smaller amount of fluid, improving its dynamic characteristics.

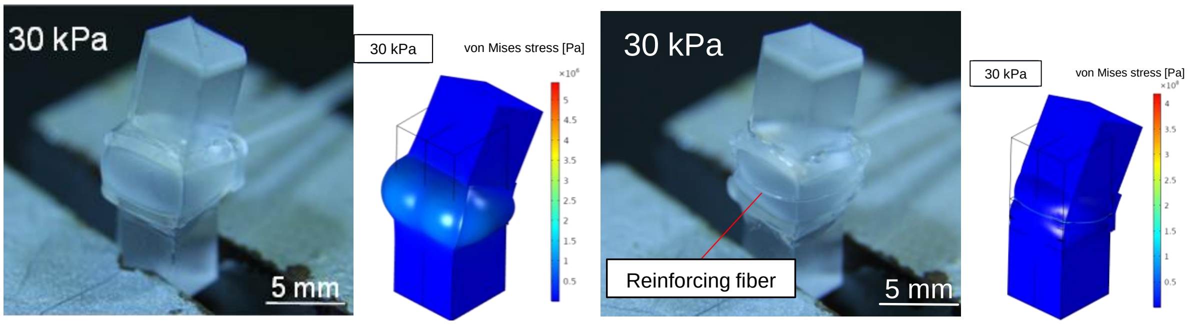

(a) Without the fiber reinforcement (b) With the fiber reinforcement

Figure 4. Comparison of the soft joint actuator without and with a fiber reinforcement

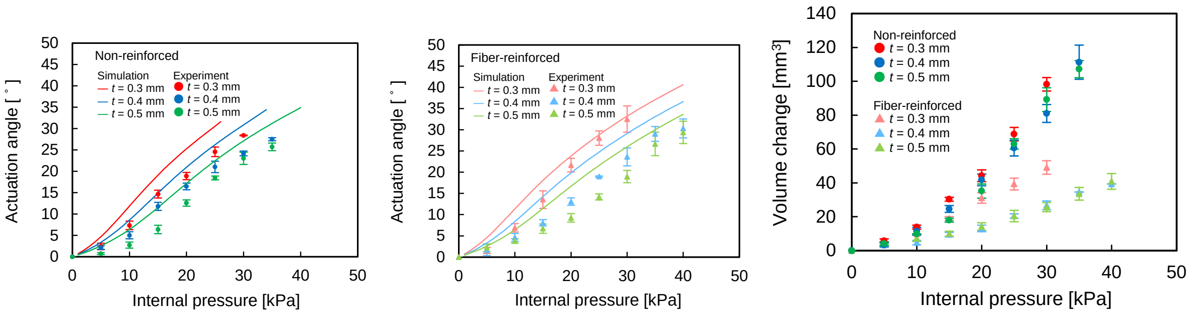

(a) Actuation angle without and with the fiber reinforcement (b) Necessary volume change

Figure 5. Actuation angles and necessary volume changes of the soft joint actuators

CONCLUSIONS

In this study, we proposed the structure and fabrication process of a fiber-reinforced soft joint actuator that generates angular displacement like the leg joint of an insect with low pressure and flowrate driving. The proposed fiber-reinforced soft joint actuator was successfully fabricated and the fiber-reinforcement succeeded in suppressing unnecessary expansion while obtaining the same actuation angle as non-reinforcement.

REFERENCES

1. MAHAPATRA, A., ROY, S. S., PRATIHAR, D. K., Multi-body Dynamic Modeling of Multi-legged Robots, Springer, Singapore, 2020, pp.1-8.
2. KIM, J., TANABE, Y., YOKOTA, S., Comprehending Electro-conjugate Fluid (ECF) Jets by Using the Onsager Effect, Sensors and Actuators A: Physical, 2019, 295-15, pp.266-273.

Organized Session | Organized session

Simulation and Modeling

The 11th JFPS International Symposium on Fluid Power HAKODATE 2020 Oct. 12-13, 2021 The Japan Fluid Power System Society

A Study on the Virtual Simulation Model of an Excavator Equipped with a Tiltrotator Based on Simscape

Seongwoong CHOI*, Kyungsin KWAK*, Yongseok KIM**, Kyoungkwan AHN**, Soonyong YANG**

* Department of Construction Machinery Engineering, General Graduate School, University of Ulsan
93, Daehak-ro, Nam-gu, Ulsan, Republic of Korea
(E-mail: soonyy@ulsan.ac.kr)
** Department of Mechanical Engineering, School of Mechanical Engineering, University of Ulsan
93, Daehak-ro, Nam-gu, Ulsan, Republic of Korea

Abstract. In this paper, we develop a simscape-based simulation model and modeling of excavator with tiltrotator. Dynamic model of excavator 3D models using Simscape Multibody and Hydraulic model of excavator using Simscape Hydraulics were modeled. We apply PID controller to make control system that works along the input angle. Simulation results show that errors occur when comparing input and output angles, but overall, they move along input angles.

Keywords: Construction Machinery, Excavator, Tiltrotator, Simscape, Simulation.

INTRODUCTION

The excavator is a representative equipment working in the construction site. However, it is also used in various fields such as agriculture and forestry, and recently, the scope of use is expanding to the submarine area.[1][2] Typical operations of an excavator include excavation work and leveling work. Excavation work is performed in a variety of workspaces, such as changing field usage, changing drains and pipes, and removing buried soil. The planarization work is performed in a large space such as solidifying the foundation of the field and leveling the equipment access road. This work has a limitation on the working posture of the existing excavator. Therefore, by installing a tiltrotator serving as a wrist, unnecessary operations can be reduced to perform work efficiently and work time can be reduced. Due to this advantage, as the number of excavators equipped with a tiltrotator increases, various studies related to this have been conducted, and research and development on automation, autonomy, and electricization have recently become an issue in relation to excavators.[3] Therefore, in this paper, a study on a virtual simulation model of an excavator equipped with a tiltrotator for automation and autonomy based on Simscape was conducted.

SIMULATION MODEL OF VIRTUAL EXCAVAOR

The simulation model operates the hydraulic valve and actuator of the model by inputting the input angle as shown in figure 1 and receiving the valve control signal through the controller. The excavator model operates by transmitting the force and torque generated by the actuator to the multibody model.

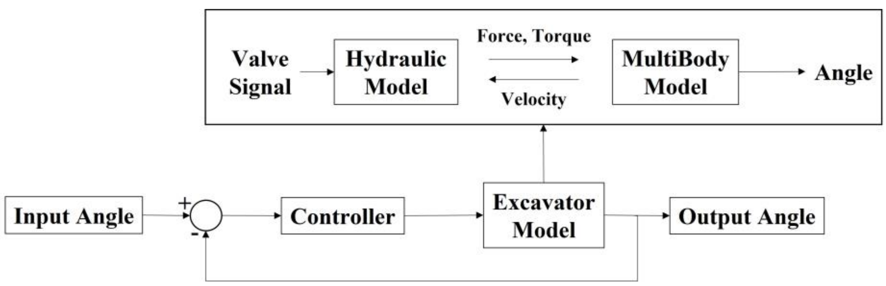

Figure 1. Configuration of Excavator Simulation Model

Excavator Model

To model the hydraulic model, which is the power source of the excavator, and the dynamic model representing the force and torque applied to each joint, it was modeled using Simscape Multibody and Simscape Hydraulics libraries.

3D Model

As shown in Figure 2, the upper body (cabin) and lower body (crawler), boom, arm, bucket, tilt rotator, and cylinder of the excavator were modeled using CATIA.

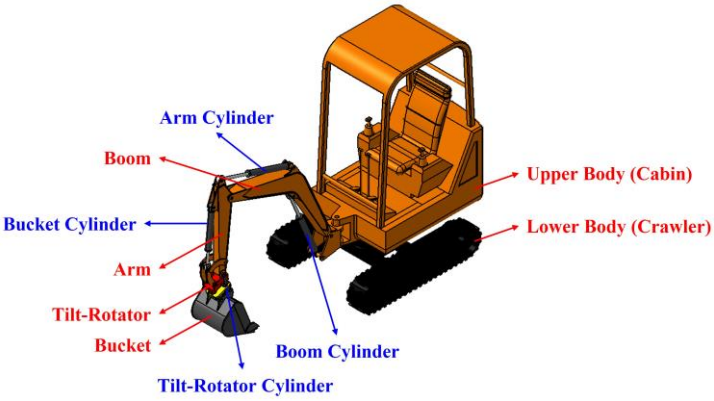

Figure 2. 3D model of excavator with tiltrotator

Multibody Model

The dynamic model representing the excavator's movement was implemented with the force and torque of each joint using Simscape Multibody. The 3D shape of the excavator was modeled using CATIA and Solidworks. To convert to a Simscape Multibody model, create a Simscape Multibody model using the XML file conversion function in Solidworks and create a Data file of the Assembly. The modeled multibody model is shown in Figure 3.[4][5]

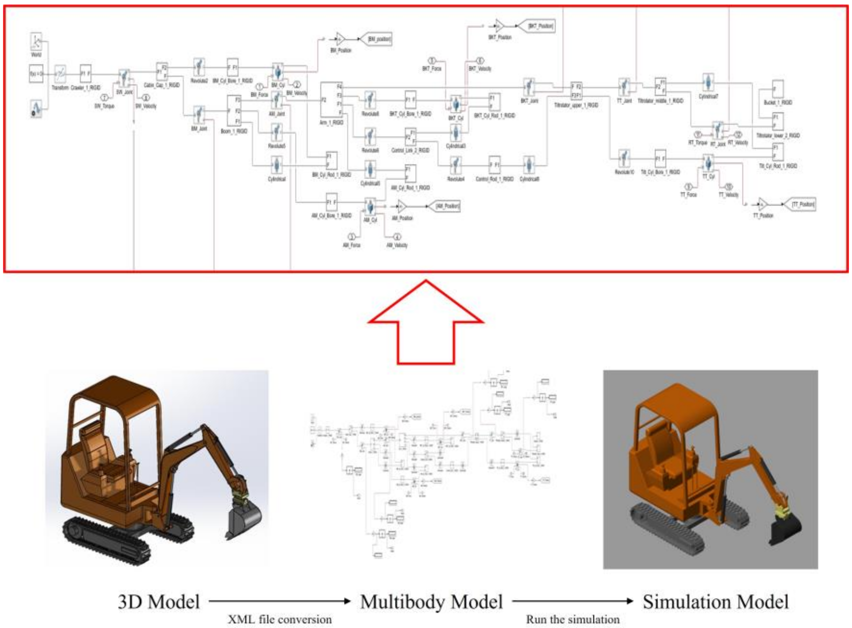

Figure 3. Multibody Model of Excavator

Hydraulics Model

The hydraulic model of the excavator, the main pump, MCV, and actuator (cylinder, motor) were modeled using Simscape Hydraulics. The modeled hydraulic model is shown in Figure 4.[5]

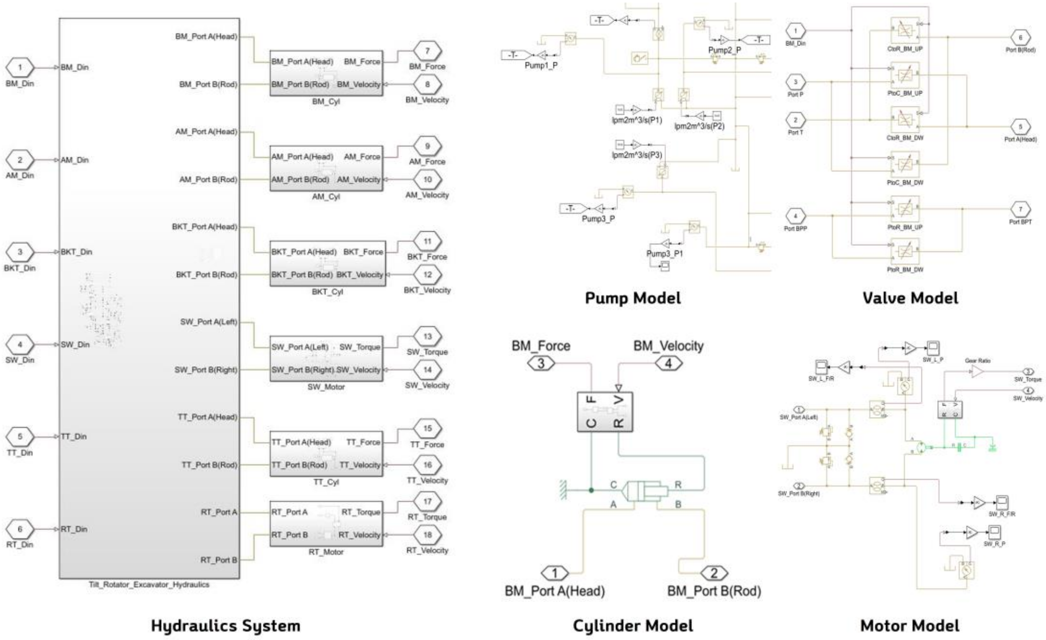

Figure 4. Hydraulics Model of Excavator

Controller & Final Model

It was composed of a feedback controller using the error of each joint input angle and output angle of the excavator. Among the feedback controllers, it was composed of a PID controller, and it was operated using an angle error. An appropriate value was selected by adjusting the gain value of each joint. The controller model is shown in Figure 5. The simulation model was finally completed by combining the previously constructed excavator model and the controller model. The final simulation model is shown in Figure 5.

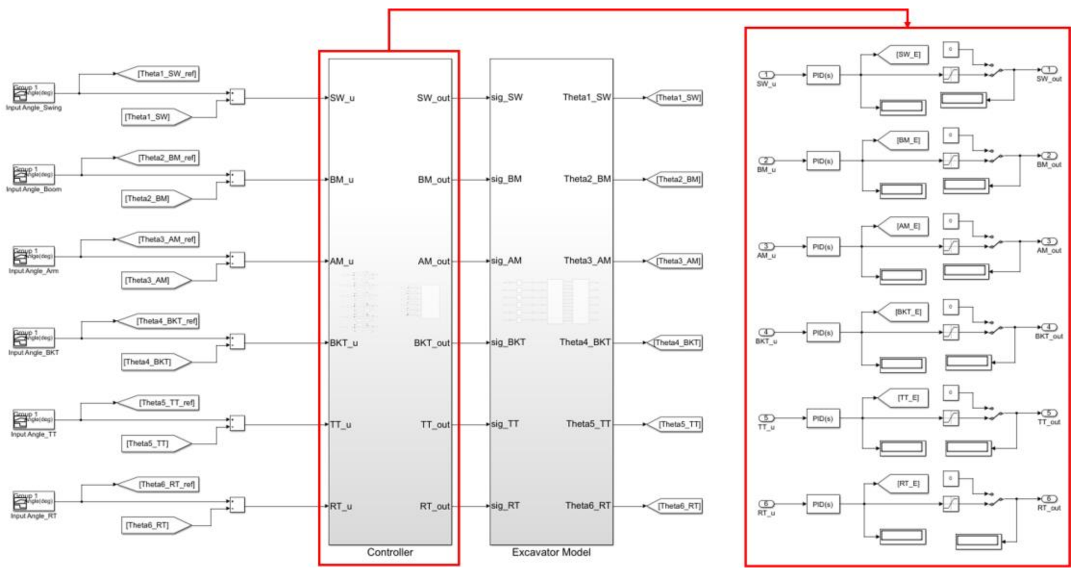

Figure 5. Controller and Final Simulation Model of Excavator

SIMULATION AND RESULTS

The simulation of the completed simulation model proceeded as follows. A simulation was performed for the single motion of the excavator boom, arm, bucket, and tiltrotator, and the input angle of each joint was set as shown in Figure 6. The simulation result for this is shown in Fig. 7, and in the result graph of Fig. 7, the blue line is the input angle and the red line is the output angle. In the resulting graph, you can see that it moves along the input angle over the entire range of motion limit angles, except for differences that occur in some parts. It is expected that the error occurring here will be solved by applying gain adjustment and a control algorithm that complements it.

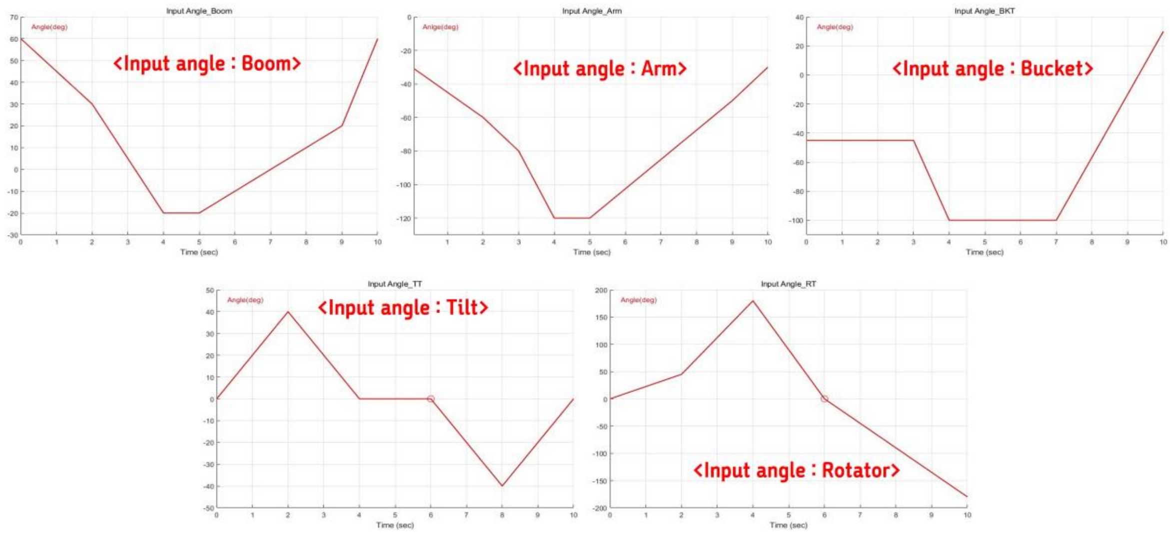

Figure 6. Simulation Input Angle of Excavator Single Operation

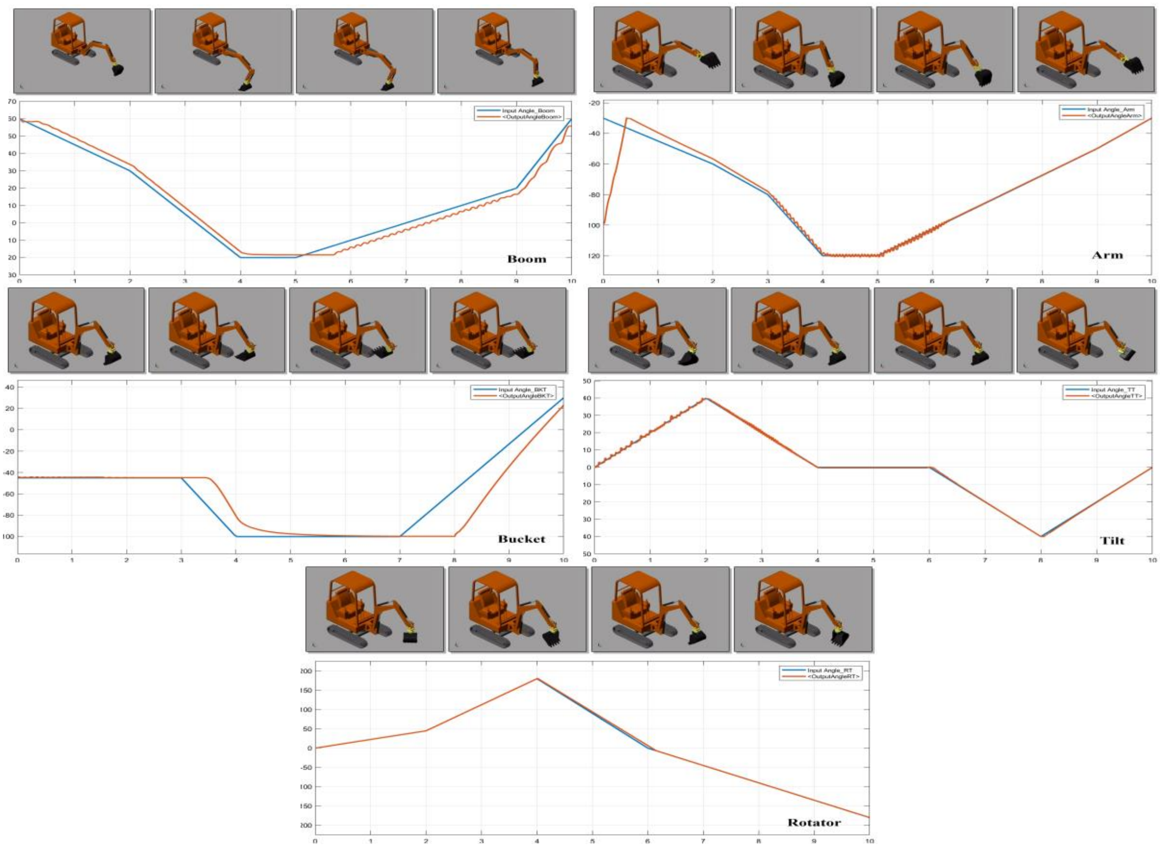

Figure 7. Simulation Results of Excavator Single Operation

CONCLUSION

In this study, a virtual simulation model of an excavator was developed using Simscape of MATLAB. The developed model confirmed the posture and trajectory of the excavator operated by the input angle. The operation of the simulation model was followed according to the input angle, but some slight errors appeared. The error occurring here is thought to be caused by the speed change occurring in the valve direction change. It seems that the error can be solved by applying a control algorithm that can compensate for the gain adjustment of the controller. In future research, we will proceed with research on the control algorithm to improve the developed simulation model.

ACKNOWLEDGMENTS

This paper was supported by Korea Institute for Advancement of Technology(KIAT) grant funded by the Korea Government(MOTIE) (P0012769, The Competency Development Program for Industry Specialist)

REFERENCES

1. T. H. LIM, H. S. LEE and S. Y. YANG, Development of Simulator of Hydraulic Excavator, Journal of Drive and Control, 2005, 2-1, pp.63-68.
2. T. H. LIM and S. Y. YANG, Development and Application of Simulator for Hydraulic Excavator, Journal of the Korean Society for Precision Engineering, 2006, 23-9, pp.142-148.
3. S. W. CHOI, Q. H. LE, T. G. SON and S. Y. YANG, A Study on Construction of Control System for Wireless Remote Control of Small Excavator, Journal of Drive and Control, 2020, 17-4, pp.103-112.
4. D. S. AHN, I. Y. LEE and H. H. KIM, Integrated SolidWorks & Simscape Platform for the Model-Based Control Algorithms of Hydraulic Manipulators, Journal of Drive and Control, 2015, 12-4, pp.41-47.
5. Q. H. LE, Y. M. JEONG, C. T. NGUYEN and S. Y. YANG, Development of a Virtual Excavator using SimMechanics and SimHydraulic, Journal of Drive and Control, 2013, 10-1, pp.29-36.

The 11th JFPS International Symposium on Fluid Power HAKODATE 2020 Oct. 12-13, 2021 The Japan Fluid Power System Society

Modeling, Simulation, and Control of Blade Pitch to Improve the Performance of a Hydrostatic Wind Turbine

Neil GARCIA and Kim A. STELSON

Department of Mechanical Engineering, College of Science and Engineering, University of Minnesota,
111 Church St SE, Minneapolis, MN 55455, USA
(E-mail: garc0408@umn.edu, kstelson@umn.edu)

Abstract. Hydrostatic transmissions are a valuable addition to community-scale wind turbines, reducing maintenance demands and allowing for compact energy storage with comparable efficiency to gearbox transmission units. In this paper we create a model to simulate the performance and improve the control of blade pitching for a wind turbine fitted with a hydrostatic transmission. A model of a 60-kW hydrostatic wind turbine with $K\omega^2$ torque control was previously created in MATLAB Simulink. To add blade pitching into the existing model, a wind turbine blade was digitally recreated, simulated, and used to fit a general equation for the turbine's power coefficient. The model was validated by comparing results with the previous model. A modified proportional controller for blade pitch actuation was added to the system to capture extra energy and dissipate excess energy.

Keywords: hydrostatic transmission, hydrostatic wind turbine, turbine blade pitch

INTRODUCTION

As demand for clean energy alternatives rises around the world, improvements to current strategies for harnessing wind energy have become increasingly valuable. Modern utility-scale wind turbines are equipped with sensors and actuators to adapt to dynamic wind conditions, optimizing power generation and maintaining safe operating conditions with increasingly advanced control schemes.

More sophisticated transmission systems make wind power more reliable and economical. Most wind turbines use transmissions to convert high torque, low speed rotor rotation into high speed, low torque generator rotation. Unlike traditional wind turbine transmissions, which rely on heavy fixed-ratio gearboxes and power electronics [8], a hydrostatic transmission (HST) uses hydraulic lines to transmit power where the rotation of the turbine rotor drives a pump in circuit with a variable displacement hydrostatic motor as shown in Figure 1. The motor then drives a synchronous generator, adjusting its swash plate angle to match the electric grid frequency [6].

A conventional gearbox transmission with a doubly fed induction generator has 95% transmission efficiency, a 96% generator efficiency, and a 97% power electronics efficiency, for a total efficiency of 88.5%. A hydrostatic transmission has an 87% transmission efficiency and a 98% generator efficiency for a total efficiency of 85.2% [10]. However, the continuous variability of a hydrostatic transmission, the elimination of power electronics, the reliability of the components and the improved power-to-weight ratio are all attractive merits of HSTs in wind turbines.

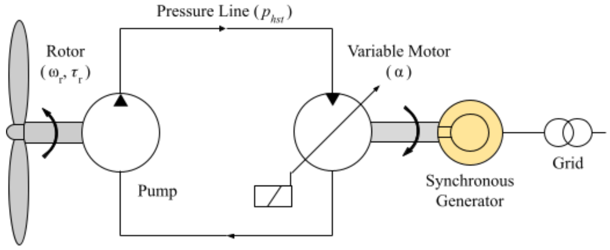

Figure 1. Hydrostatic wind turbine transmission [6].

The Hydraulic Power Transmission Lab at the University of Minnesota has created a simulation of a 60-kW wind turbine (the Polaris P21-60) outfitted with the lab's hybridized hydrostatic transmission, using wind and rotor speed inputs to calculate rotor torque. Current studies in the lab are investigating the use of a hydraulic accumulator to store excess energy otherwise wasted [6] and advanced control strategies such as extremum seeking control to maximize power generation.

While the effect of blade pitching on power generation in conventional wind turbines is well understood, the impact of adding blade pitching to the hydrostatic wind turbine control with hybridization is not fully understood. The goal of this research is to add blade pitching to the existing simulation as a tool to make system performance predictions and improve the hydrostatic wind turbine control strategy.

SYSTEM MODELING

HYDROSTATIC TRANSMISSIONS IN WIND TURBINES

The hydrostatic transmission of a wind turbine is governed by the dynamics of the rotor shaft and HST line pressure as described by Eqs. (1) and (2) [6]:

$$J_r\dot{\omega}_r = \tau_{rot}(\omega_r, u, \beta) - b_r\omega_r - D_{p1}p_{hst} \quad (1)$$

$$\dot{p}_{hst} = \frac{\beta_e}{V}(D_{p1}\omega_r - L_m p_{hst} - \alpha D_m\omega_g) \quad (2)$$

τ_{rot} is aerodynamic torque, a function of rotor speed ω_r, wind speed u, and blade pitch β. b_r is the combined damping of the rotor shaft and pump. D_{p1} is the displacement of HST pump. p_{hst} is the line pressure of the HST. β_e is the effective bulk modulus of the fluid and line, linearized at operating line pressure. V is the fluid line volume. L_m is the sum of losses in the main pump and motor, assuming losses in the line are negligible. D_m is the displacement of the motor. α is the normalized swash plate angle of the motor. ω_g is the generator shaft speed.

FUNDAMENTALS OF WIND TURBINE CONTROL

Wind turbines operate in four regions dependent on wind speed and turbine characteristics [8], shown in Figure 2. In Region 1, wind speed is too low for turbine operation, and blades are pitched to minimize aerodynamic torque. In Region 2, power is generated, but operation is below the rated wind speed. Rotor torque control is the primary mode of power regulation, but turbine blades are also pitched to an angle β to maximize power generation. The power coefficient of the turbine C_p is a function of β and the tip speed ratio (TSR) λ:

$$\lambda = R\frac{\omega_r}{u} \quad (3)$$

where R is turbine blade radius. To maximize power in Region 2, rotor torque is adjusted according to the $K\omega^2$ control law [7], where the turbine operates with torque τ_c to maximize energy capture. Desired torque is given by

$$\tau_c = K{\omega_r}^2 \quad (4)$$

$$K = \frac{1}{2}\rho\pi R^5\frac{C_{p,max}}{{\lambda_s}^3} \quad (5)$$

where ρ is the density of air, $C_{p,\,max}$ is the maximum power coefficient of the wind turbine, and λ_s is the ideal TSR. In Region 3, operation is above rated wind speed and turbine control seeks to maintain safe operating conditions by keeping power constant, pitching the blades out of the wind to dissipate excess energy and keep power generation at rated power. In Region 4, far above rated wind speed, wind speeds are too high for operation, so blades are pitched completely out of wind and the rotor is braked to prevent system damage.

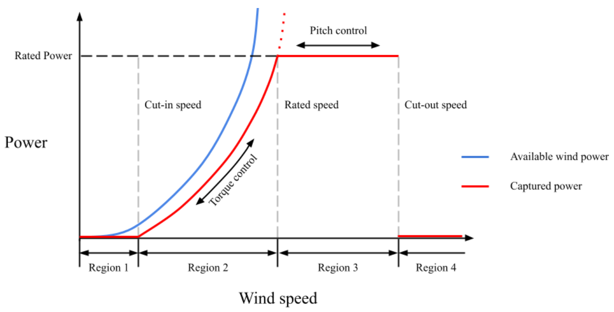

Figure 2. Wind turbine power curve, labeled with regions of operation.

The existing MATLAB Simulink model of the hydrostatic wind turbine includes pressure and rotor dynamics and $K\omega^2$ control (adjusting swash plate angle α to optimize torque for power). Wind inputs and rotor speed are translated to rotor torque by referencing a 2-D interpolation table for τ_{rot} (u, ω_r) shown in Figure 3. A constant blade pitch of 0° is assumed as optimal in Region 2, although additional energy can be captured by using non-zero pitch. In Region 3, blades are pitched to limit power, with the actuation assumed to be instantaneous.

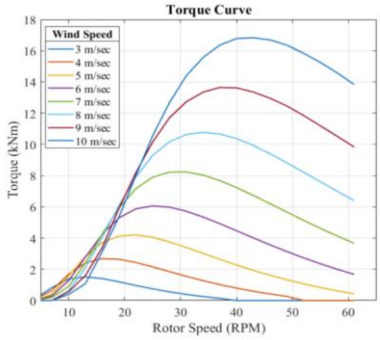

Figure 3. Visualization of the interpolation table for torque for the simulated 60-kW turbine [5].

BLADE PITCH SIMULATION

To accurately include blade pitch in the model, the existing interpolation table needed refinement. To do so, the turbine blades were modeled and simulated in QBlade. QBlade [4] is a blade element momentum analysis program that allows for the construction, visualization, and simulation of wind turbine blades. QBlade uses multi-parameter blade element analysis to simulate blades for a range of wind speeds, rotational speeds, and blade pitches. A general equation incorporating blade pitch can be fit to simulation results and used in dynamic simulation and control models. Ideally, the blade designed and simulated in QBlade would directly emulate the 60-kW turbine of interest to the lab, the Polaris P21-60. But information on blade geometry (airfoils, chord length, twist) is proprietary with no information available online [9]. Instead, blade design is based on the AOC 15/50 wind turbine, a 50-kW turbine well-documented by the National Renewable Energy Laboratory (NREL). Information on blade geometry is provided in Table 1 [2]. Twist is optimized for performance at a blade pitch of 4° by QBlade [4]. The resulting blade geometry is shown in Figure 4.

Table 1. Table of geometric airfoils over blade length (out from a hub of radius 0.305 m) used in QBlade simulation.

Position (%)	Chord (mm)	Twist (°)	Airfoil
5	469	60.7733	S814
15	594	44.8478	S814
25	719	24.766	S814
35	798	16.1283	S814
45	738	11.5355	S814
55	677	9.71968	S812
65	617	7.82523	S812
75	557	6.46623	S812
85	497	5.44484	S813
95	437	5.51314	S813

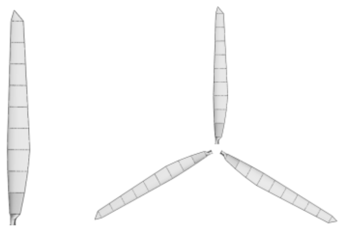

Figure 4. AOC 15-50 turbine blade geometry in QBlade.

Simulations of the blade were conducted under the range of conditions specified in Table 2. A plot of the resulting C_p (λ, β) data is shown in Figure 6. This plot was compared to a sample C_p (λ, β) surface from NREL for a different wind turbine (the CART3 650-kW wind turbine) (Figure 5) for similarity in shape.

Table 2. Ranges of wind speed u, rotational speed ω_r, and blade pitch β for QBlade simulations.

Parameter	Range	Units
u	[0, 13]	m/s
ω_r	[6, 20]	rpm
β	[-10, 10]	°

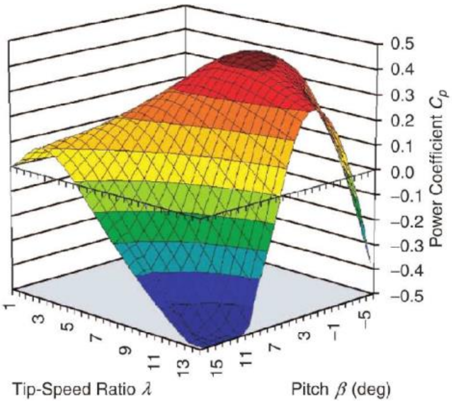

Figure 5. C_p-TSR-β surface for the CART3 60-kW wind turbine [3].

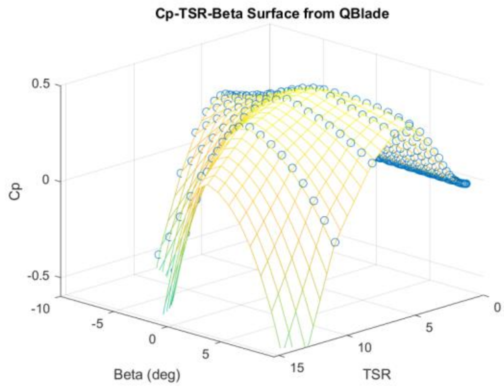

Figure 6. C_p-TSR-β surface for the AOC 15-50 50-kW wind turbine, generated in QBlade.

An existing C_p-TSR curve for an NREL 50-kW turbine at 0° is shown in Figure 7. When plotted on top of the QBlade data shown in Figure 8, the C_p-TSR curve for the 50-kW NREL turbine sits close to the surface and follows the same curvature, overshooting slightly at high TSR values.

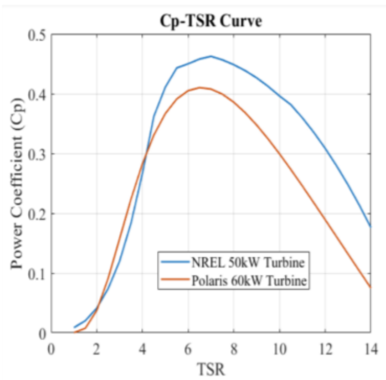

Figure 7. C_p-TSR curves for the NREL 50-kW turbine and the Polaris 60-kW turbine [5].

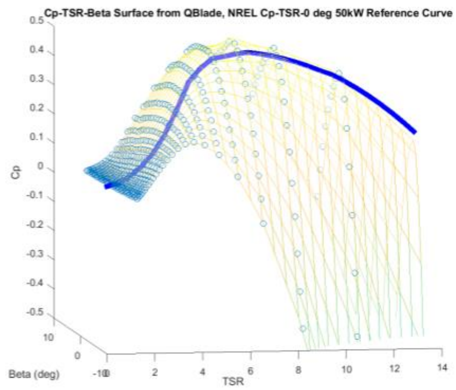

Figure 8. C_p-TSR curve for the NREL 50-kW turbine (blue line) and QBlade data for the AOC 15-50.

BLADE PITCH IMPLEMENTATION

GENERAL EQUATION FOR WIND TURBINE POWER COEFFICIENT

A general equation for modeling the power coefficient of wind turbine rotors is given in Eq. (6) [1]:

$$C_p(\lambda,\beta) = c_1\left(\frac{c_2}{\lambda_i} - c_3\beta - c_4\beta^x - c_5\right)e^{-c_6/\lambda_i} \quad (6)$$

$$\frac{1}{\lambda_i} = \frac{1}{\lambda+0.08\beta} - \frac{0.035}{\beta^3+1} \quad (7)$$

with constants c_1 through c_6 found empirically. x is assumed to be 2 for all calculations. Derived constants are summarized in Table 3 [5].

Table 3. Constants used with Eq. (6) to model turbine performance, with source described.

Source	c_1	c_2	c_3	c_4	c_5	c_6
Existing theoretical 60-kW	0.1564	116	0.4	0	3.5	11.5
Least squares 50-kW	4.8625	3.6654	-0.8531	7.8609	0.1251	10.3240
Scaled least squares 60-kW	4.1534	3.6654	-0.8531	7.8609	0.1251	10.3240

The constants used to produce the 60-kW curve found in Figure 7 were chosen by rescaling the 50-kW curve, based on real data, for a 60-kW turbine, using the nominal maximum C_p of the P21-60 turbine [5]. Assuming a value of $c_4 = 0$ means that C_p does not vary significantly with blade pitch and is thus inaccurate for blade pitches other than 0°. New constants that more accurately represented the relation between C_p and β were needed.

Using the C_p-TSR-β plot generated for the AOC 15/50 in QBlade as a reference, the same methodology was followed to determine new constants: fitting a surface in the form of Eq. (6) for a 50-kW turbine as closely as possible, then scaling that equation for a 60-kW turbine. To achieve a closer fit between the approximate model and the QBlade data, nonlinear regression was performed using MATLAB to minimize error between the model and the data.

The first attempt at fitting the function to the data produced unrealistic results. The data generated by QBlade included negative data points for C_p for large values of λ. After removing points from the QBlade data with negative C_p values, least squares regression was repeated, yielding the constants found in Row 2 of Table 3. The resulting 50-kW surface, compared with QBlade results and experimental NREL 50-kW results, can be seen in Figure 9.

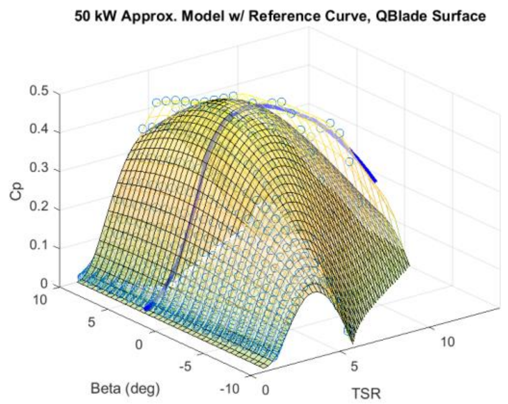

Figure 9. 50-kW C_p-TSR-β surface generated using Eq. (6) (yellow surface) using constants found with least squares regression. QBlade AOC 15/50 results (dots) and the NREL 50-kW C_p-TSR curve (blue) for 0° pitch included for comparison.

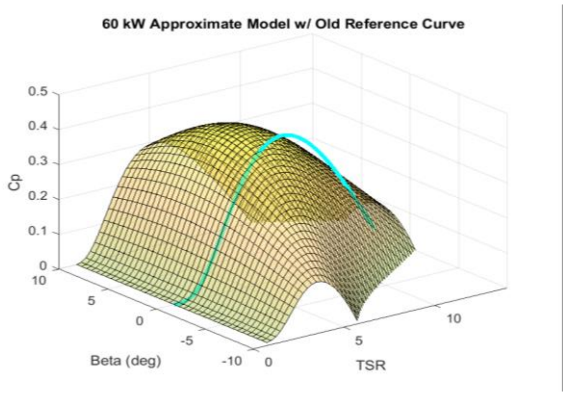

Figure 10. 60-kW C_p-TSR-β surface generated using Eq. (6) (yellow surface) based on scaled-down constants found for a 50-kW turbine. The old C_p-TSR curve (light blue) for 0° pitch is included for comparison.

To scale the 50-kW to match the NREL 60-kW reference curve, constant c_1 for the 50-kW surface was divided by the surface's maximum C_p value and multiplied by the maximum C_p value of the NREL reference curve. The scaled constants can be found in Row 3 of Table 3. The resulting 60-kW surface, compared with the old C_p-TSR curve (light blue) for 0° pitch, can be seen in Figure 10. Because the QBlade design optimized for β = 4° and the old C_p-TSR curve was generated assuming optimum performance at 0°, comparisons to the old curve should be drawn at 4° rather than 0°.

SIMULINK IMPLEMENTATION

After deriving the necessary constants to characterize the 60-kW turbine, Eq. (6) was incorporated into the existing Simulink model. To convert the calculated C_p to rotor torque, the following two additional relations were applied:

$$P = C_p\left(\frac{1}{2}\rho v^3 A\right) \tag{8}$$

$$\tau_{rot} = \frac{P}{\omega_r} \tag{9}$$

where P is power generated, and A is the swept area of the rotor. To test the new system's performance, step wind inputs were fed to the old lookup table system (at β = 0°) and the new system based on Eq. (6) (at both β = 4° and β = 0°). Results are plotted in Figure 11. System performance at optimum blade pitch is indistinguishable between the old and new models.

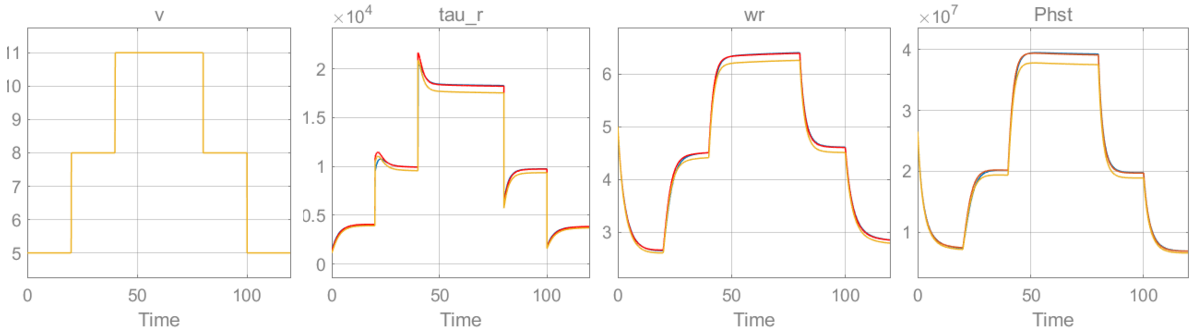

Figure 11. Comparison of system outputs (rotor torque τ_{rot} [Nm], rotor speed ω_r [rad/s] and line pressure p_{hst} [Pa]) for stepped wind input v [m/s]. Results using Eq. (6) and the constants found using least squares regression at a blade pitch of 0° and 4° are shown in yellow and red. Results using the lookup table torque calculation at a blade pitch of 0° are shown in blue and are indistinguishable from those in red (using Eq. (6) and β = 4°).

Dynamic Pitch Control

Following implementation in Simulink, a controller for blade pitch was designed to limit power generation in Region 3, when available power exceeds rated power for the turbine. Actuators for blade pitching were modeled as a first-order system. Experimental time constants ranged between 9.6 and 12.3 seconds, so a time constant of 10 seconds was assumed. The blades were modeled as follows:

$$\dot{\beta} + \frac{1}{\tau_\beta}\beta = f(t) \tag{10}$$

where τ_β is the time constant for blade pitching and $f(t)$ is the input to the system. To control blade pitch based on power generation, a proportional controller comparing current power generation to rated power generation was designed. The proportional controller's output runs through a saturation block allowing only negative signals to pass. If the turbine runs above rated power, blade pitch will drop, limiting power generation. But if the turbine is below rated power, the controller output will be optimal, that is, unchanged by the proportional controller. The controller was tested with a 0.1 Hz sinusoidal wind input, yielding the response found in Figure 12. When overlaid with the response of the uncontrolled pitch system locked at β = 4°, the effect of the controller is evident; power is limited to 60 kW by pitching the blades out of the wind when power would otherwise go above rated.

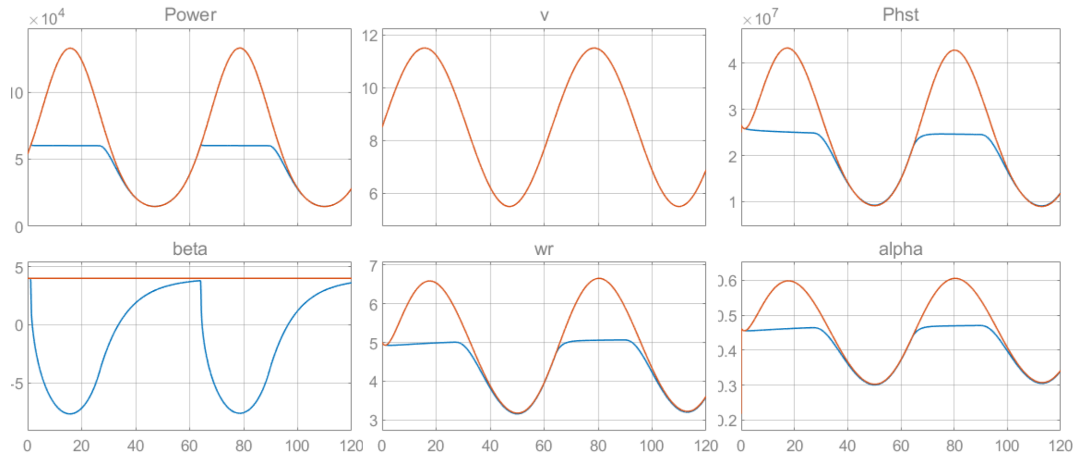

Figure 12. Overlaid comparison of Simulink outputs for system with (blue) and without (orange) pitch control.

CONCLUSION

To improve the dynamic model of a 60-kW hydrostatic wind turbine, blade pitch was added as a variable in rotor torque calculations. This capability was added to a previous MATLAB Simulink model of a hydrostatic wind turbine with $K\omega^2$ control. To incorporate blade pitching, a 50-kW wind turbine blade was recreated according to design specs for the AOC 15/50 wind turbine and simulated using QBlade blade element momentum analysis. Least squares regression was used to fit a general equation for power coefficient C_p to QBlade simulation results; the resulting surface was scaled and compared to trusted experimental data. A proportional controller based on pitch was added to the system to improve power capture and dissipate excess energy, modeling pitch actuators as a first-order system. Further studies in improving wind turbine performance might explore the potential of using stored energy using a hydraulic accumulator to pitch the blades and optimize power capture. There is also the potential to use the simulation to study more sophisticated control methods.

ACKNOWLEDGMENTS

The authors thank the following members of the Hydraulic Power Transmission Laboratory at the University of Minnesota for their help with this research: Justin Chen, Daniel Escobar, Mike Gust, Mark Leinberger, Biswaranjan Mohanty and Eric Mohr.

REFERENCES

1. ACKERMAN, T., Wind Power in Power Systems, Second Edition, John Wiley & Sons, 2012.
2. HUGHES, P., SHERWIN, R., Advanced Wind Turbine Design Studies, Advanced Conceptual Study Final Report, National Renewable Energy Laboratory, 1994.
3. JOHNSON, K. E., PAO, L. Y., BALAS, M. J., FINGERSH, L. J., Control of Variable-speed Wind Turbines: Standard and Adaptive Techniques for Maximizing Energy Capture. IEEE Control Systems Magazine, vol. 26, no. 3, 2006, pp. 70-81.
4. MARTEN, D., LENNIE, M., PECHLIVANOGLOU, G., NAYER, C. N., PASCHEREIT, C. O., Validation and Application of an Unsteady Lifting Line Free Vortex Wake Module Implemented Within the Open-Source Wind Turbine Blade Design Code QBlade, Journal of Engineering for Gas Turbines and Power, 138(7), 2015.
5. MOHANTY, B., "Design and Control of Hydrostatic Continuous Variable Transmission for a Community Wind Turbine," Ph.D. dissertation, University of Minnesota, Minneapolis, MN, USA, 2019.
6. MOHR, E., MOHANTY, B., STELSON, K. A., Short-Term Energy Storage System for Hydraulic Hybrid Wind Turbine Transmission. ASME/Bath Symposium on Fluid Power and Motion Control, Bath, UK, 2020.
7. LAKS, J.H., PAO, L. Y., WRIGHT, A.D., Control of Wind Turbines: Past, Present, and Future, American Control Conference 2009, St. Louis, USA, 2009.
8. PAO, L. Y., JOHNSON, K. E., A Tutorial on the Dynamics and Control of Wind Turbines and Wind Farms, American Control Conference 2009, St. Louis, USA, 2009.
9. Polaris America LLC, P21-60 Specification Sheet, 2015.
10. STELSON, K. A., Hydrostatic Transmissions for Community-Scale Wind Turbines, 2021.

The 11th JFPS International Symposium on Fluid Power HAKODATE 2020 Oct. 12-13, 2021 JFPS The Japan Fluid Power System Society

Internal Flow and Hysteresis Characteristic of the Poppet Type Pressure Control Valve

Seiei MASUDA*, Fumio SHIMIZU**, Masaki FUCHIWAKI**, Kazuhiro TANAKA**

* Control Systems Engineering Department, IHI Corporation
3975-18, Haijima-cho, Akishima-shi Tokyo 196-8686 Japan
(E-mail: masuda.seiei624@mail.kyutech.jp/masuda4361@ihi-g.com)
** Graduate School of Computer Science and Systems Engineering, Kyushu Institute of Technology
680-4, Kawazu, Iizuka-city, Fukuoka, 820-8502 Japan

Abstract. Hysteresis characteristics have emerged in pressure-flow characteristic experiments of poppet valves designed and prototyped by the author. In order to clarify the mechanism of this hysteresis characteristic, we confirmed the reproduction of hysteresis and confirmed the validity of the research policy. Specifically, we investigated the internal flow by CFD analysis and examined the reproduction of hysteresis characteristics by CFD. First, the precision of CFD analysis was verified by confirming that the empirical values of in the reference and calculated values were in good agreement. Furthermore, CFD analysis of the internal flow was performed. As a result, it was clarified that there is a flow pattern that can be roughly divided into two types of internal flow with different flow rates. Then, by changing the flow rate in a time-dependent manner using CFD, we were able to reproduce the hysteresis characteristics that are in good agreement with the empirical results.

Keywords: Poppet valve, Flow force, Hysterics, Pressure control valve, CFD

NOMENCLATUR

A_o	:	Opening area of damping orifice	k	:	Spring constant
A_p	:	Cross-sectional area of poppet piston	m	:	Mass of the valve
C	:	Orifice flow coefficient	*Pressure*	:	Non-dimensional quantity of static pressure at surface of poppet valve (based on pressure at rated conditions)
C_0	:	Critical damping coefficient			
C_d	:	Damping coefficient of the orifice			
C_f	:	Viscous damping coefficient	ΔP	:	Differential pressure at the orifice
D	:	Damping coefficient in the equation of motion of the valve	Q	:	Flow rate
			Q_o	:	Flow rate through the orifice
DB	:	Hole diameter at seat	*Radius*	:	Non-dimensional quantity of r (based on inlet radius)
DL	:	Valve piston diameter			
DS	:	Diameter of poppet valve spool	Re	:	Reynolds number
d	:	Spring displacement	r	:	Radial position
F_f	:	Flow force	t	:	Time
Flow rate	:	Non-dimensional quantity of flow rate (based on rated conditions)	x	:	Valve displacement (based on valve displacement at rated conditions)
$F_{preload}$	:	Spring preload			
$F_{pressure}$	:	Force applied to the valve due to pressure	x_0	:	Initial spring deflection
F_s	:	Spring force	α	:	Poppet cone angle
F_{shear}	:	Shear force on the valve	ρ	:	Fluid density
g	:	Non-dimensional quantity of x (based on bore size)	ND	:	Non-dimensional unit

INTRODUCTION

Poppet valves are the valves that are often used next to spool valves and are often used as pressure control valves or flow control valves for hydraulic systems. Many studies have been conducted. Oshima et al. reported the experimental results of the effect of valve shape on the characteristics of poppet valves [1]. They reported the experimental results of a method to reduce the flow force of a poppet valve by changing the shape of the valve and the shape of the roll downstream of the valve (hereinafter referred to as the collar). Ito et al. measured the pressure distribution and flow force on the valve surface around a poppet valve and compared the results with numerical analysis [2]. Johnston et al. reported the experimental results of flow patterns and flow force in poppet valves without and with collars. In the visualization experiment using a poppet valve without a collar in the report, it was shown that there were three types of flow patterns and that they affected the flow force [3]. Vaugan et al. performed computational fluid dynamics (CFD) around a poppet valve using the finite volume method with a commercial code to analyze the flow field [4], and Rundo et al. performed CFD on a poppet valve used in a relief valve that can set the control pressure and predicted the flow pattern that generates the flow force. They reported on a method to reduce the flow force by using a collar [5]- [6]. Many studies have also been conducted on the stability of poppet-type pressure control valves. Hayashi et al. reported that there are two types of vibration modes depending on whether the poppet is in contact with the valve seat or not [7]. However, no clear stability criterion for poppet-type pressure control valves has been obtained. The motivation for this study was that the pressure-flow characteristics of a prototype poppet valve [10] designed by the author showed a hysteresis characteristic in which the polarity of the pressure gradient changed with respect to the flow rate change with a very long period [10]. This hysteresis characteristic has not been studied before, and to clarify the mechanism of its occurrence, we studied the internal flow by CFD analysis and the reproduction of its characteristics by CFD. The hysteresis phenomenon is one of the typical nonlinear phenomena, and it cannot be denied that it may have a significant influence on the stability of poppet valves and poppet-type hydraulic control valves.

Figure 1 shows the geometry of the prototype pressure control valve, and Table 1 shows its non-dimensionalized main parameters. Figure 2 shows the hysteresis characteristics of the pressure-flow characteristics obtained in the experiment. The arrows (1) to (5) in Figure 2 show the time sequence of the control pressure trajectory. When the flow rate reaches about 80% of the rated value, the pressure in path (3) appears to increase rapidly at a constant flow rate. When the mass flow rate reaches about 80% of the rated condition, however, the pressure in path (3) seems to increase rapidly at a constant flow rate. Even if the flow rate is decreased in the return path after reaching the maximum flow rate, the pressure remains high and decreases gradually. Therefore, the purpose of this study was to reproduce the hysteresis phenomenon of the pressure-flow characteristics by analyzing the internal flow of the test poppet valve using CFD.

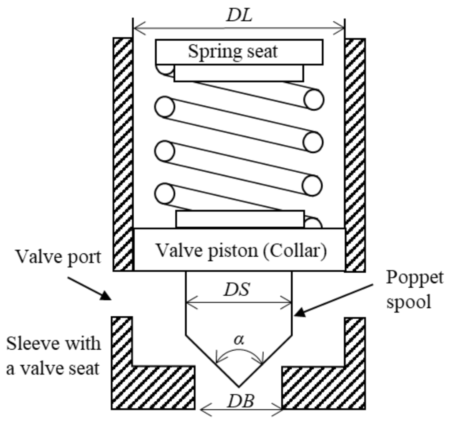

Figure 1. Structure of Pressure Control Valve

Table 1. Specifications of Pressure Control valve

Constants, Dimensions and Rated Performance	Value
Poppet apex angle(α) [degree]	90
Large spool diameter ratio (DL/DB)	1.8
Spool small diameter ratio (DS/DB)	1.07
Valve seat diameter (DB/DB)	1
Resonant frequency [rad/s]	800

Note 1: Re = (Mean velocity at throttle・Distance between poppet and seat) / Kinematic viscosity of working fluid

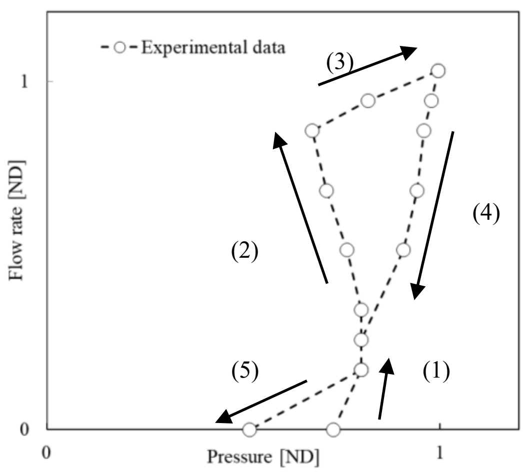

Figure 2. Control Pressure vs. Flow Rate Hysteresis Characteristic

VALIDATION OF ANALYSIS METHOD

At the beginning of the study, we verified whether the CFD analysis of the flow field around the poppet valve could reproduce the real phenomena. The test data used for the verification is the data of Ito et al. [2]. The commercial code Simerics-MP+ is used to analyze the flow field of an incompressible fluid using the finite volume method. Simerics-MP+ is capable of CFD analysis and coupled analysis of the equations of motion of the same body. By applying a sliding mesh to the finite volume method [8], the CFD analysis can reflect the transient changes in valve opening and flow path geometry as the valve is displaced. Figure 3 shows the geometry of the poppet valve of Ito et al. used in the CFD analysis. Figure 4 shows the test apparatus. Figure 5 shows the analysis grid. The mesh type is an orthogonal grid with 8 to 10 grids at the throat, and the minimum mesh size is on the order of 1/100 mm. No special consideration is given to the boundary layer mesh and wall roughness.

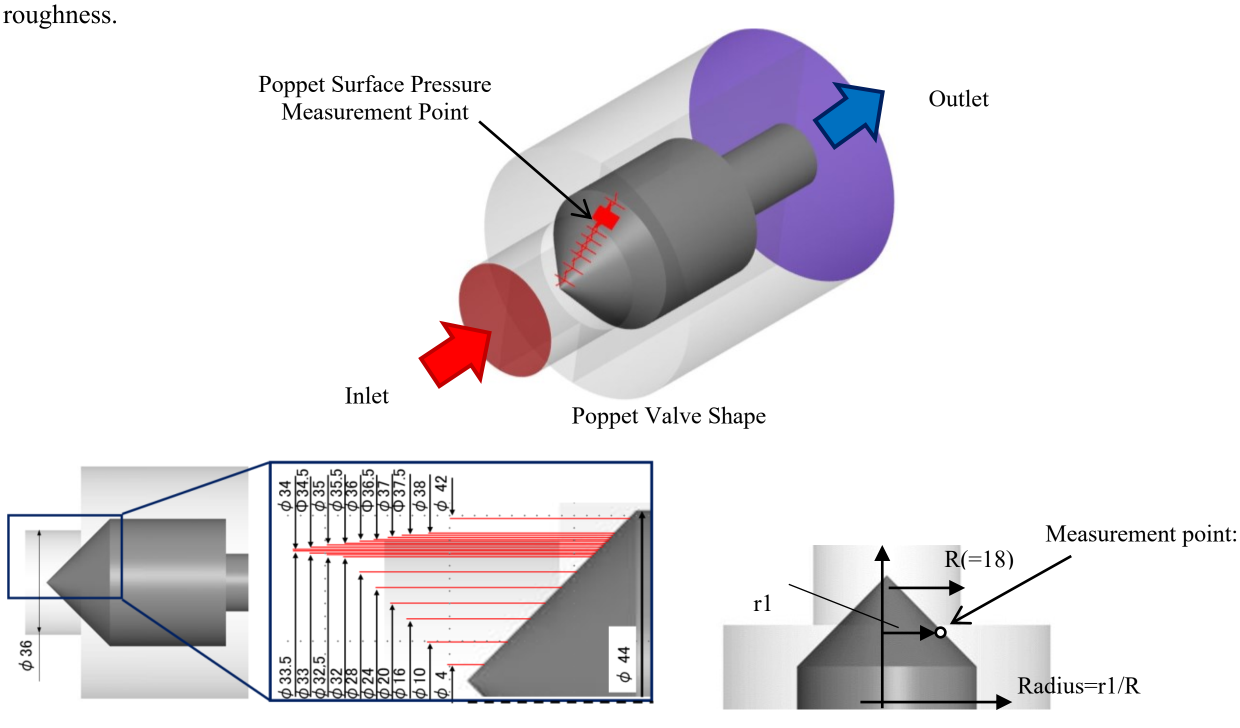

Measurement Point Definition of Non-Dimensional Radius

Figure 3. Shape of Poppet Valve used for Verification of Analysis Method

Table 2. Analysis Conditions for a Simerics-MP+ Model

Software used	Simerics-MP+
Analysis type	Steady state
Turbulence model	standard k-ε
Fluid density [kg/m^3]	863
Fluid viscosity [Pa・s]	0.0267
Entrance boundary condition [l/min]	(a) Q = 42 (Re = 200) (b) Q = 60 (Re = 300) (c) Q = 42 (Re = 200)
Exit boundary condition [Pa]	0 (Static Pressure)
Valve displacement [mm]	(a) 6, (g = 1/6) (1) (b) 6, (g = 1/6) (c) 4, (g = 1/9)
Grid type	Orthogonal grid
Grid number	1,300,000 [-]

Note1: g = Valve displacement / Inlet pipe diameter

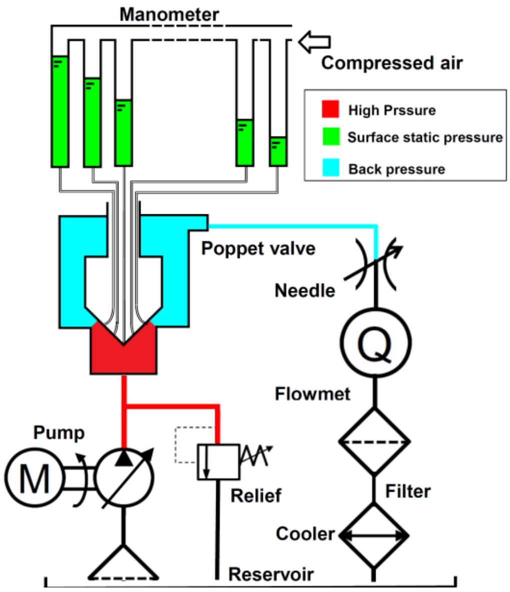

Figure 4. Verification Test Setup

Table 2 shows the three conditions used for verification. Although a cavitation model was incorporated in the CFD calculations, the maximum calculated void fraction was less than$10^{-5,}$ so the effect of cavitation was not significant. We have also confirmed that the calculated results do not differ depending on the location of the outlet boundary and the conditions. A comparison of the static pressure distribution on the surface of the poppet valve between the test results and the CFD analysis is shown in Figure 6. In this figure, the pressure is non-dimensionalized by the valve tip pressure and the radial direction is non-dimensionalized by the inlet port radius. The calculated results are in good agreement with the experimental results of Ito et al. under three different analytical conditions, and the difference between them is small, less than a few percent. In the next section, we attempt to apply the Simerics-MP+ analysis to the flow field around the poppet valve with hysteresis as shown in Figure 1.

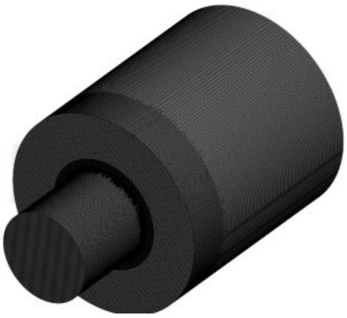
Whole Grid

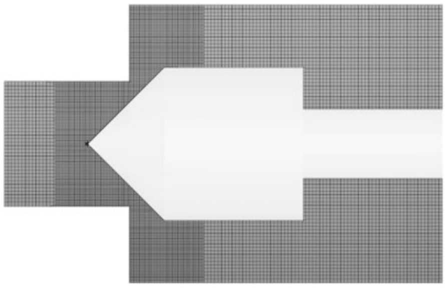
Cross-Sectional Shape

Figure 5. Analysis Grid for Simerics-MP+

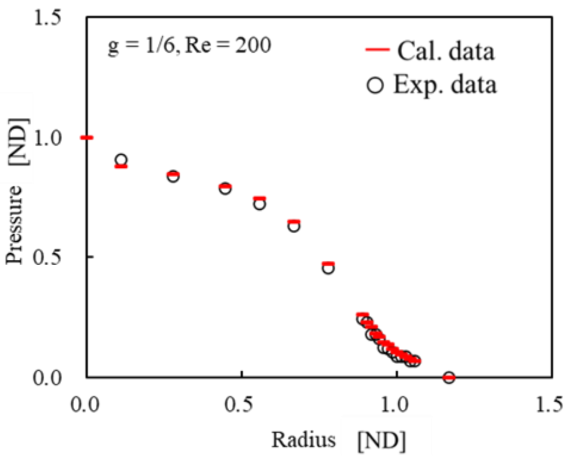

(a) Q = 42

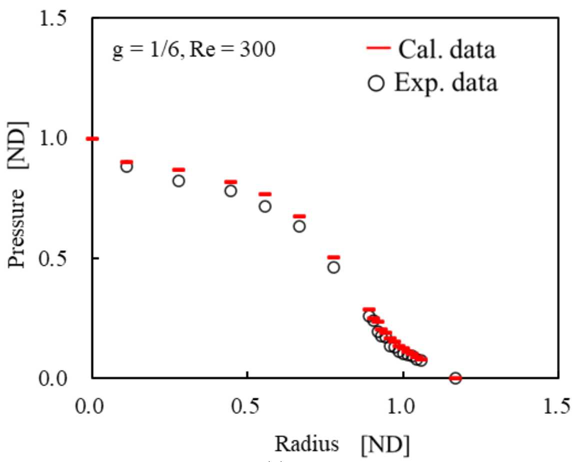

(c) Q = 42

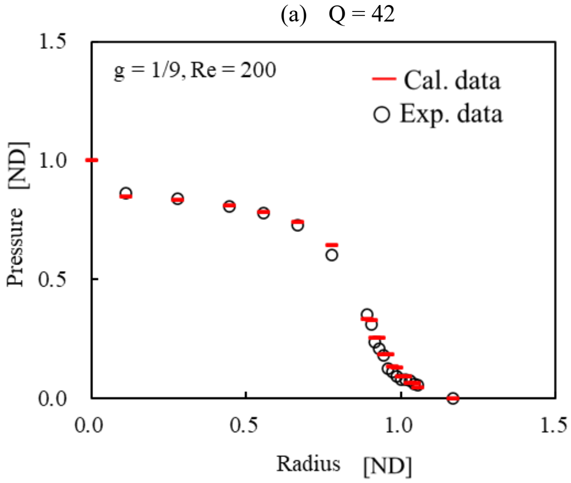

(b) Q = 60

Figure 6. Verification Results

ANALYSIS OF THE FLOW FIELD AROUND A POPPET VALVE AND DISCUSSION

To investigate the flow pattern of the internal flow, a steady-state flow analysis was conducted with the flow rate at the inlet and the pressure (back pressure) at the outlet. As an example of the results of the steady-state flow analysis, the calculation results at the four points shown in Table 3 are illustrated below. Figure 7 shows the analysis grid. The CFD results (velocity contour of the poppet valve cross-section) for conditions (1) to (4) in Table 3 are shown in Figure 8.

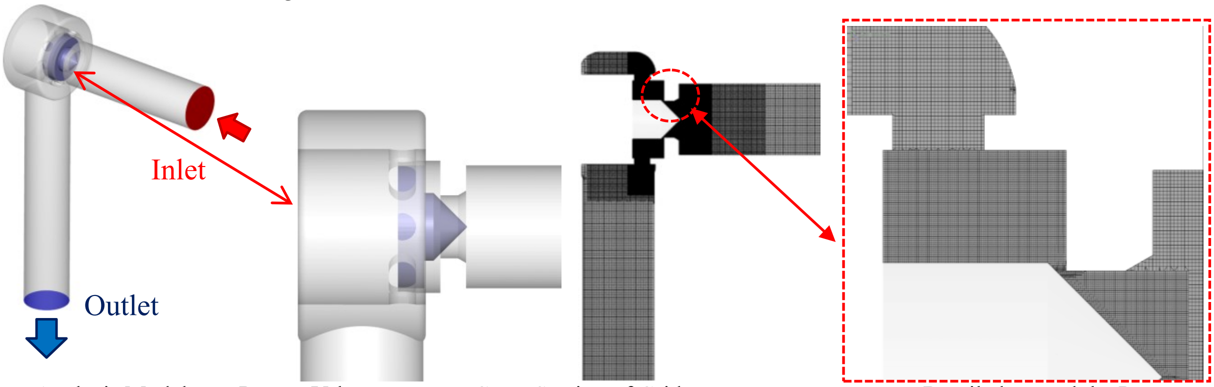

Figure 7. Analysis Grids for Simerics-MP+

Table 3. Analysis Conditions for a Simerics-MP+ Model

Software used	Simerics-MP+
Analysis type	Steady / Transient
Turbulence model	Standard k-ε
Fluid density [kg/m^3]	770
Fluid viscosity [Pa・s]	0.00149
Entrance boundary condition [ND]	Steady: (1) 0.30 (2) 0.49 (3) 0.73 (4) 1.00 Transient: 0.05 - 1
Exit boundary condition [Pa]	0.79 (Static Pressure)
Grid number	4,000,000 [-]
Incremental time	- / 0.000054 [s]

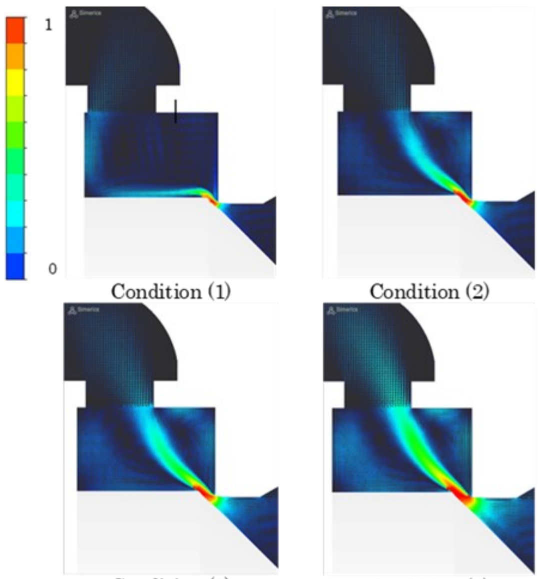

Condition (1) *Flow rate* [ND]=0.30, (g = 0.024, Re = 13000)
Condition (2) *Flow rate* [ND]=0.49, (g = 0.039, Re = 22000)
Condition (3) *Flow rate* [ND]=0.73, (g = 0.058, Re = 34000)
Condition (4) *Flow rate* [ND]=1.00, (g = 0.080, Re = 49000)

Figure 8. Velocity Contours and Flow Patterns under the Conditions shown in Table 7

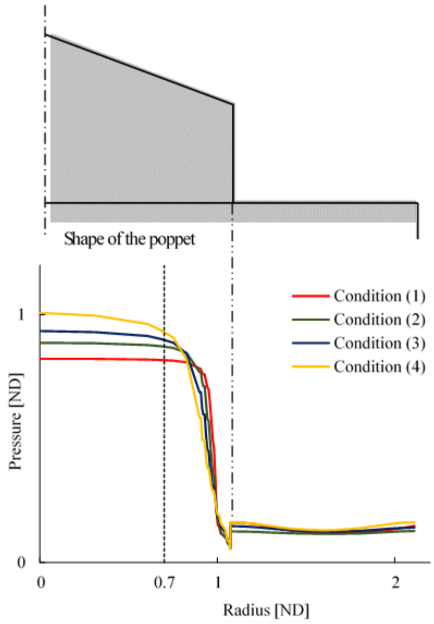

Figure 9. Distributions around the Poppet Valve

When the flow rate at the inlet boundary condition in Table 3 is small (Condition (1)), the velocity vector diagram shows that the jet around the poppet valve flows along the poppet axis and the jet is attached to the spool (hereafter referred to as attaches flow). The jet then decelerates, collides with the spool collar, and turns at a right angle. In Condition (2), (3) and (4), as the flow rate increases, the jet separates near the bottom of the minimum throat of the valve and flows in a straight line toward the port of the sleeve (straight flow). These results indicate that there are two types of flow patterns in the valve: Attached flow and Straight flow.

Figure 9 shows the static pressure distribution at the valve surface for an arbitrary cut plane relative to the poppet valve radial direction. The inlet pressure increases with increasing flow rate due to the increase in pressure at the apex of the poppet valve. In the radial pressure distribution, the pressure gradient changes near the minimum throttle, and there is no significant difference in the large diameter of the valve. Comparing the pressure at a certain point of radius 0.7 ~ 1.0 with the increase of inlet flow rate for each flow rate condition, the pressure tends to be lower for the condition with higher inlet flow rate. The force in the direction of opening the valve decreases. This decrease in force is equal to the increase in force in the direction of closing the valve. Further elaboration is needed in this area.

Figure 10 shows the flow force against the valve displacement. In conditions (2) to (4), the flow force is proportional to the valve displacement, but in condition (1), the flow force is calculated to be small, suggesting that there is a correlation between the flow force and the flow pattern.

When the flow force acts on the valve, the inlet pressure changes due to the change in valve displacement and spring force, and the force due to pressure acting on the valve also changes. The flow force also changes. In other words, the effect of the variation of the force acting on the valve is calculated by the coupled analysis function of Simerics-MP+, and the final balanced spring displacement, inlet pressure, and flow force are calculated at each time. In this way, the force acting on the valve is fed back by the flow force variation, and the valve displacement and inlet pressure are recursively determined. Since the opening area of the poppet valve is proportional to the valve displacement as shown in Equation below [9], the flow force is almost proportional to the valve displacement except for condition (1). The polarity acts in the direction of closing the valve. In condition (1), the flow force is much smaller than the other conditions, and the flow force per displacement is less than 1/5.

$$Ap = \pi \cdot DB \cdot x \cdot \sin\frac{\alpha}{2} \tag{1}$$

Figure 11 shows the valve opening area versus valve displacement, and the results show that the valve opening area is proportional to the valve displacement. Figure 12 shows the calculated flow coefficients for each condition, where the opening area is non-dimensionalized as the opening area under the rated condition. As can be seen from these results, the flow coefficient is constant at about 0.75 regardless of the change in flow rate, indicating that the state of attachment and detachment of the jet does not affect the flow coefficient.

Next, the results of the steady-state flow analysis for the valve with hysteresis characteristics under the boundary conditions (1) to (4) shown in Table 3 are shown in Figure 13, in comparison with the test results.

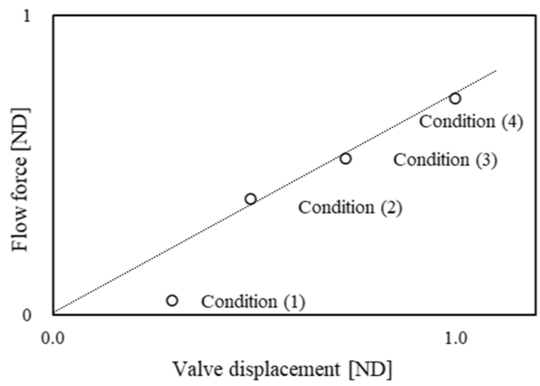

Figure 10. Valve Displacement vs. Flow Force

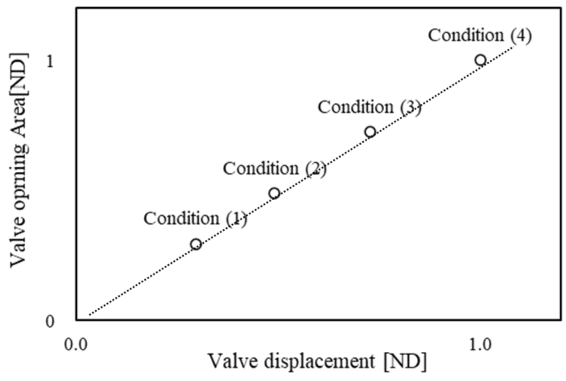

Figure 11. Valve Displacement vs. Valve Opening Area

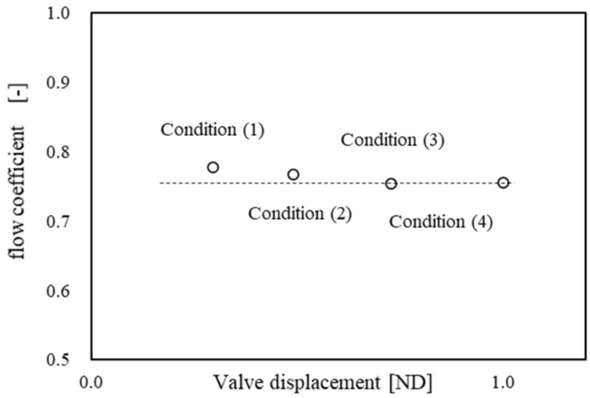

Figure 12. Coefficient of the Flow Rate

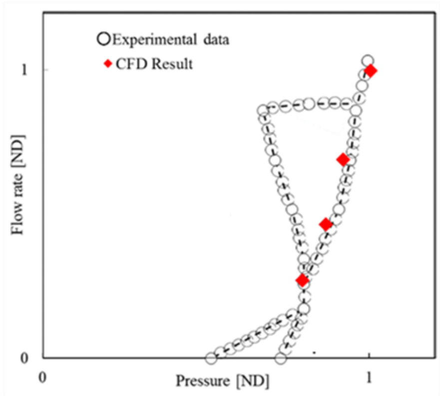

Figure 13. Control Pressure Flow Rate Hysteresis Characteristics of the Pressure Control Valve (Empirical results)

From this comparison, the analytical results agree well with the characteristics of the high-pressure side at the return of the flow characteristics against the control pressure with hysteresis. This point is interesting, but the details of the reason for this are still unknown at this stage, and further research is needed.

RESULTS AND DISCUSSION OF COUPLED ANALYSIS OF VALVE EQUATIONS OF MOTION AND CFD

To reproduce the hysteresis of the flow characteristics against the control pressure of a poppet valve, a coupled analysis between the flow field of the pressure and flow characteristics and the equation of motion of the valve was conducted using Simerics-MP+. The equation of motion of the valve is expressed as Eq. (2) [9].

$$m\frac{d^2x}{dt^2}+D\frac{dx}{dt}+k_d=\sum F_{Pressure}+\sum F_{Shear}-F_{Preload} \tag{2}$$

The external forces acting on the valve are the force due to the pressure to which the valve is subjected, the shear force and the spring preload. In each time increment of the CFD calculation, when the convergence judgment of the flow calculation is completed, the calculation module of the above equation of motion of the valve is activated and the translational motion of the valve is calculated. The damping coefficient D in the above equation of motion can be the sum of the damping coefficient C_f due to the viscosity of the fluid and the damping coefficient C_d due to the damping orifice located behind the valve and can be expressed as "$D = C_f + C_d$". First, we consider the damping force of the damping orifice. The damping force of the orifice as a valve circuit can be equivalent to the force corresponding to the pressure drop ΔP at the orifice as Eq. (3).

$$C_d\cdot\frac{dx}{dt}=\Delta P\cdot A_p \tag{3}$$

From this, it is possible to calculate the damping force. Since ΔP changes transiently in experiments, it is difficult to determine it exactly, but the damping force can be calculated by referring to the value in the experiment. Furthermore, the damping coefficient of the damping orifice is determined. Since the valve velocity is the flow rate through the orifice divided by the poppet piston area, the damping coefficient is can be calculated from Eq. (3) and Eq. (4). The valve velocity can be estimated.

$$\frac{dx}{dt}=\frac{Q_o}{A_p}=\frac{A_o\cdot C}{A_p}\cdot\left(\frac{2\cdot\Delta P}{\rho}\right)^{\frac{1}{2}} \tag{4}$$

Next, we consider the damping force due to the viscosity of the fluid. The largest of these is the viscous frictional force between the outer circumference of the piston, which is the large diameter part of the valve, and the sleeve surface, which is derived from Newton's law of viscosity. This value is less than 1/10 of the damping force generated by the orifice, according to the results of calculations. These results show that the viscous damping force is small compared to the damping force of the damping orifice, indicating that this orifice has a significant influence on the actual damping of the poppet valve. The calculation method of the axial flow force is shown in Figure 14.

Figure 15 shows the temporal variation of the supply flow rate (ramp input). In the experiment, the data was collected at a time that could be considered steady state, but in the CFD calculation, the same real time calculation as in the experiment is not possible due to the condition of the Courant number. Therefore, a larger change in inlet flow rate than in the experiment was input to the calculation.

A comparison between the simulation results and the test results of the flow rate against the control pressure of the pressure control valve is shown in Figure 16. Because of the large computational load of this analysis, the simulation results at the end of the forward journey (under rated conditions) were used as initial values for the return journey. This figure shows the calculation results after the transient condition that occurs at the start of valve opening is settled. The control pressure-flow characteristics, including the hysteresis phenomenon, are in good agreement. Compared with the pressure characteristic curve with empirical hysteresis shown in Figure 16, the numerical results of the forward path with slowly increasing flow rate were almost equal to the empirical pressure value. The numerically calculated pressure was almost equal to the value of the curve for the low-pressure side. The velocity contour diagram was checked for the flow conditions from (1) to (4) in Table 3, and it was found that attached flow occurred in conditions (2) and (3) as in condition (1), and flow force was working in the direction of opening the valve. On the other hand, for the return path, the results of the numerical analysis and the empirical pressure characteristic curve for the high-pressure side are in good agreement in order. And the results are comparable to those calculated under the Steady state condition shown in Figure 13. The flow pattern is strait flow with the jet detached after passing through the minimum opening area of the poppet.

The estimated value of steady-state flow force and the flow force obtained by CFD are in good agreement in order. The flow force in forward path is on order the same as the flow force in return path, but the polarity is reversed.

Axial force acting on the valve body

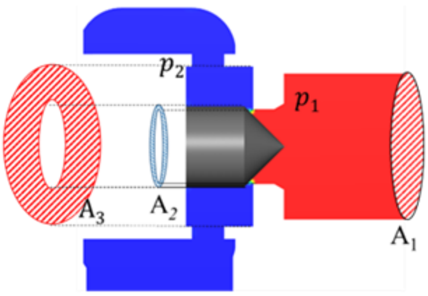

In case of valve closure $F_0 = \int p_1\,dA_1 + \int p_2\,d(A_2 + A_3)$

In case of valve release $F_{cal} = \int p_1\,dA_1 + \int p_2\,d(A_2 + A_3) + \int \tau_0 dA_0$

Axial flow force $\Delta F = F_{cal} - F_0$

Figure 14. Calculation way of flow force

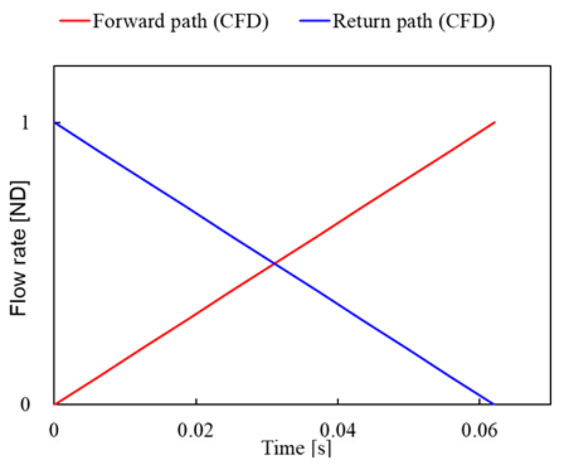

Figure 15. Input Conditions for supply flow rate

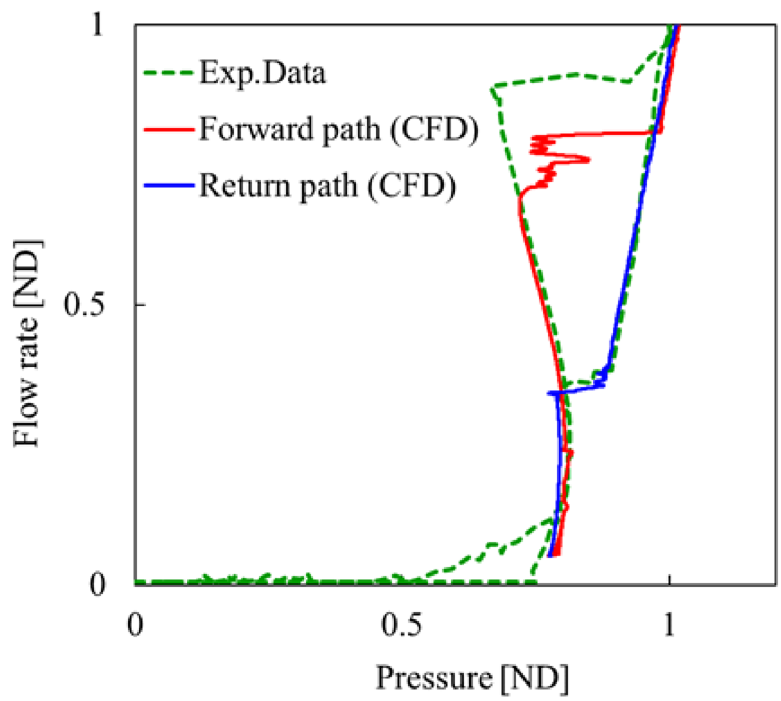

Figure 16. pressure flow Characteristics

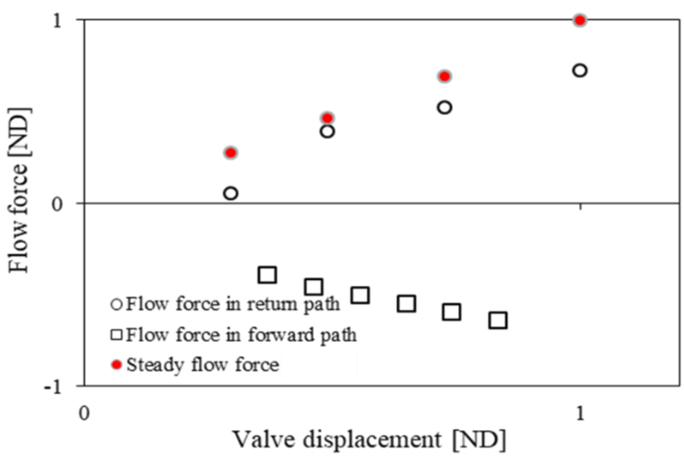

Figure 17. Comparison of Flow Force Characteristics

Figure 17 shows a comparison of the flow forces at six points on the forward path calculated from the results of the coupled analysis, the flow forces at four points calculated under the conditions (1) to (4) in Table 3, and the four calculated values of the steady-state flow force based on the momentum theory at that time. The estimated values of the steady-state flow force and the CFD-derived flow force agree well in terms of order. The order of the flow force in the forward path is the same as that of the flow force in the return path, but the polarity is reversed. The fact that the hysteresis characteristic can be reproduced in the calculation despite the large difference in the flow input condition dQ/dt between the experiment and the numerical calculation may mean that this hysteresis characteristic always occurs regardless of the length of the period. Alternatively, it may mean that the time required for this phenomenon to reach a quasi-steady state is extremely short. Since the damping coefficient is also relevant here, further research is needed.

CONCLUSION

Hysteresis characteristics appeared in the characteristic tests of the prototype poppet valve. It was found that the hysteresis characteristic appeared depending on the operating conditions and valve shape. CFD analysis was used to elucidate the mechanism of this characteristic.
First, CFD analysis of the flow field around the poppet valve was performed using a commercial code, and the validity of the analysis results was confirmed by comparing them with test results. The analysis of a poppet-type pressure control valve, which generates hysteresis in the control flow characteristics against the control pressure, revealed that the flow field around the poppet valve can be classified into two types: attached flow and straight flow. It was found that the flow field around the poppet valve can be divided into two types: adhered flow and detached flow. It was also found that the hysteresis phenomenon that occurs in the control flow characteristic of the poppet-type pressure control valve against the control pressure can be reproduced by the coupled analysis of the CFD calculation of the total pressure around the poppet valve and the equation of motion.
This paper is an English version of the paper [10] submitted by the authors to the Journal of the JFPS 2021 for the 11th JFPS International Symposium.

ACKNOWLEDGMENTS

We would like to express our deep gratitude to Mr. Naoki Hirose (currently working at Voith IHI Paper Technology Co., Ltd.), who was a master's student at Kyushu Institute of Technology, for his cooperation in this research.

REFERENCES

1. OSHIMA, S., AN EXPERIMENTAL STUDY ON THE SEVERAL POPPET VALVES WITH DIFFERENCE IN SHAPE, Proceedings of the JFPS International Symposium on Fluid Power, 1989, pp.361-368
2. ITO, K., TAKAHASHI, K., INOUE, K., Flow in a Poppet Valve: Computation of Pressure Distribution using a Streamline Coordinate System, JSME International Journal Series B Fluids and Thermal Engineering, 1993, 36-1, pp.42-50
3. JOHNSTON, D. N., EDGE, K. A., Experimental Investigation of Flow and Force Characteristics of Hydraulic Poppet and Disc Valves, Proceedings of the Institution of Mechanical Engineers, Journal of Power and Energy, 1991, 205-3, pp.161-171
4. VAUGHAN, N. D., JOHNSTON, D. N., EDGE, K. A., Numerical simulation of fluid flow in poppet valves, Proceedings of the Institution of Mechanical Engineers, Journal of Power and Energy, 1992, 206-2, pp.119-P127
5. ALTARE, G., RUNDO, M., OLIVETTI, M., 3D Dynamic Simulation of a Flow Force Compensated Pressure Relief Valve, ASME International Mechanical Engineering Congress and Exposition, 2016, pp. V007T09A061
6. FINESSO, R., RUNDO, M., Numerical and experimental investigation on a conical poppet relief valve with flow force compensation, International Journal of Fluid Power, 2017, 18-2, pp.111-122
7. HAYASHI, S., Instability of Poppet Valve Circuit, JSME international journal. Ser. C, Dynamics, control, robotics, design and manufacturing, 1995, 38.3: 357-366.
8. Simerics Manual V5.0, 2019, Simerics, Washington
9. New Edition hydraulic and Pneumatic Handbook, Ohm Sha, Tokyo, 1989, pp.69-71 (Book in Japanese)
10. MASUDA, S., SHIMIZU, F., FUCHIWAKI, M., TANAKA, K., Internal Flow and Hysteresis Characteristic of the Poppet Type Pressure Control Valve, Journal of the JFPS, 2021, 52-1, pp.8-15.

The 11th JFPS International Symposium on Fluid Power HAKODATE 2020 Oct. 12-13, 2021 The Japan Fluid Power System Society

Flow Patterns and Hysteresis Characteristic of a Poppet Valve

Naoki HIROSE*, Seiei MASUDA **, Fumio Shimizu***,
Masaki Fuchiwaki***, Kazuhiro TANAKA***

*Paper Machinery Engineering Department, Paper Machine Group,
Voith IHI Paper Technology Co., Ltd.
2-1-6 Tsukuda, Chuo-ku, Tokyo 104-0051, Japan
(E-mail: naoki.hirose@voith.com)
**Control Systems Engineering Department, IHI Corporation
3975-18, Haijima town, Akishima-shi, Tokyo, 196-8686 Japan
(E-mail: masuda4361@ihi-g.com)
*** Graduate School of Computer Science and Systems Engineering,
Kyushu Institute of Technology,
680-4, Kawazu, Iizuka city, Fukuoka, 820-8502 Japan

Abstract. Previous studies on poppet valves have revealed that there are various flow patterns in the flow field around the valve body and that the flow pattern inside the poppet valve has various effects on the poppet valve. Recently, Masuda et al. have reproduced the hysteresis phenomenon on the pressure and flowrate characteristics of a poppet valve by CFD analysis coupled with an equation of motion. Unfortunately, their paper does not describe the detailed relationship between the hysteresis characteristics and the flow pattern. In this study, by succeeding and developing the work of Masuda et al. and including the results of previous studies, we have systematically organized the flow patterns of poppet valves into five types and clarified the relationship between the hysteresis characteristics and flow patterns. In addition, the flow force acting on the poppet valve connecting the hysteresis characteristic and the flow pattern has also been clarified.

Keywords: Poppet valve, Flow patterns, Flow forces, Hysteresis characteristics, CFD

INTRODUCTION

Poppet valves are the second most commonly used control valves in hydraulic systems after spool valves, and have been widely studied [1]. It is well known that the flow pattern in a poppet valve shows more complex changes than that in a spool valve and can be one of the factors that affect the dynamic characteristics of the valve. Masuda et al. [2] showed that the hysteresis phenomenon of the pressure-flow rate characteristics of a poppet valve can be reproduced by calculating the integral of the valve driving force due to the pressure around the poppet using CFD analysis coupled with the equation of motion. Figure 1 shows the geometry of the prototype pressure control valve, Figure 2 shows the experimental circuit, and Figure 3 shows the experimental and CFD results of the pressure-flow rate characteristics. The results of this study are interesting because they show that CFD software can reproduce the hysteresis characteristics of poppet valves. Unfortunately, their study does not describe the detailed relationship between the hysteresis and the flow pattern.

In many previous studies on flow patterns, Schrenk [3] first visualized the flow pattern under the same valve opening, the same supply pressure, and the same flow rate, and reported the existence of five types of flow patterns. Figure 4 shows the schematic diagram of the five flow patterns he showed. Following this, McCloy [4] observed flow patterns in a two-dimensional channel and identified three types of flow patterns. Johnston et al. [5] reported the results of experiments on flow patterns and flow forces in poppet valves with and without collars. In the visualization experiment using a poppet valve without a color, they reported the existence of three types of flow patterns, two of which (Attached flow pattern and Straight flow pattern) occurred stably. They also showed that these flow patterns affect the flow force, and reported that the Attached flow pattern generates a negative flow force and the Straight flow pattern generates a positive flow force. Figure 5 is their visualization resultant diagram showing those three flow patterns. Furthermore, Vaugan et al. [6] performed a CFD analysis of the internal flow of a poppet valve using axisymmetric incompressible flow, steady flow analysis, k-ε turbulence model, and finite volume method using CFD software. They reported that the quantitative prediction of jet reattachment was inaccurate and the Attached flow pattern could not be reproduced. Hayashi [7] summarized the unstable vibration generated in poppet valves based on these studies. Rundo et al. [8] performed CFD analysis of the flow inside a poppet valve used in a relief valve that can set the control pressure, predicted the flow pattern that generates the flow force, and reported a method to reduce the flow force with a collar. Thus, it is understood that there are various flow patterns in the flow field inside the poppet valve and that they are related to the unstable vibration, but a systematic understanding of them has not yet been obtained.

In order to succeed and further develop the work of Masuda et al. [2], this study systematically organizes the flow patterns in the prototype poppet valve used in their research by CFD analysis, and clarifies the relationship between the hysteresis characteristics and the flow patterns, as well as the relationship between them and the flow force. Simerics-MP+ was used as the CFD software.

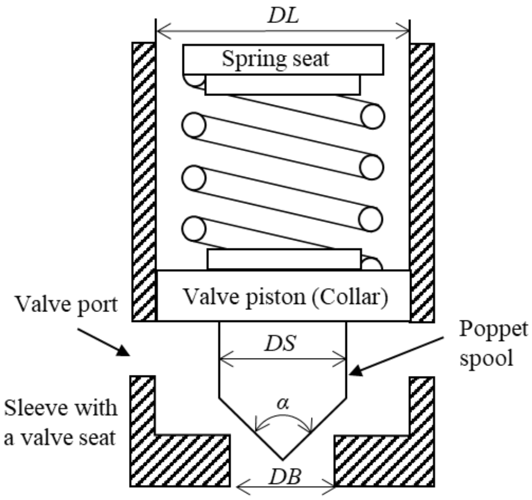

Figure 1. Structure of Pressure Control Valve [2]

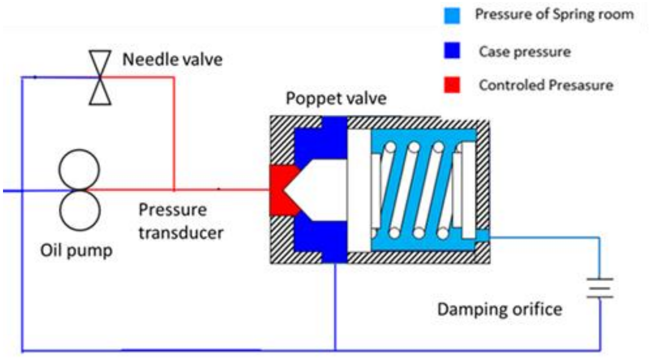

Figure 2. Schematic Diagram of Experimental Equipment [2]

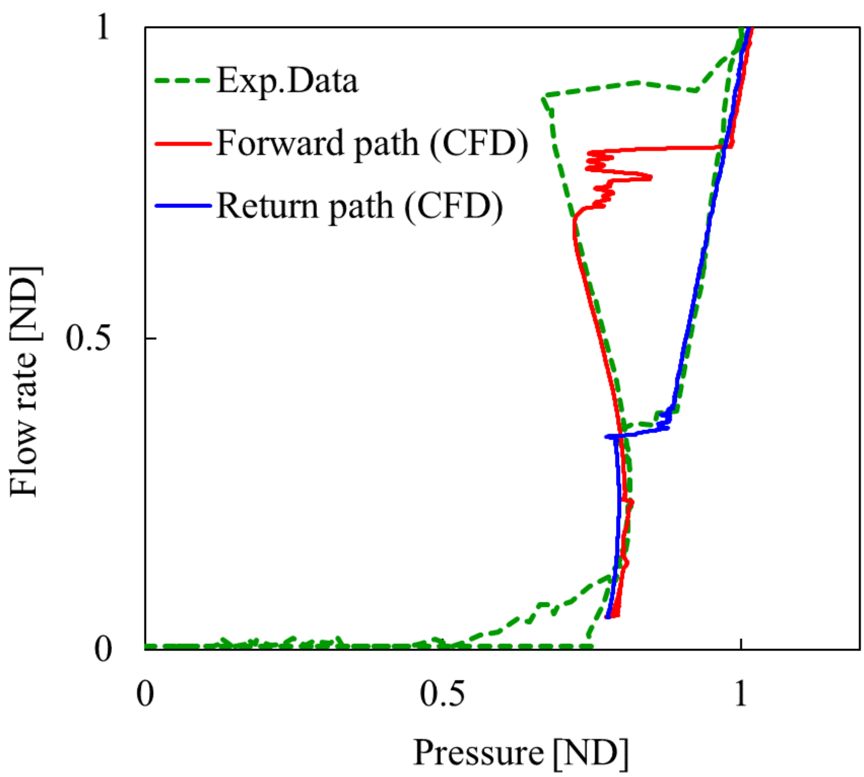

Figure 3. Hysteresis Path in Control Pressure vs. Flow Rate
(Comparison of Experimental and Transient CFD Results) [2]

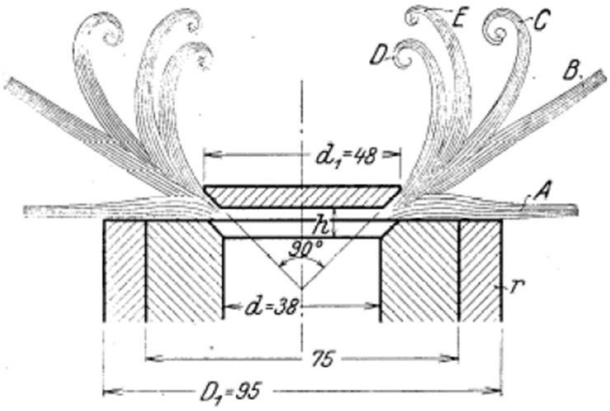

Figure 4. Flow Patterns from Schrenk [4]

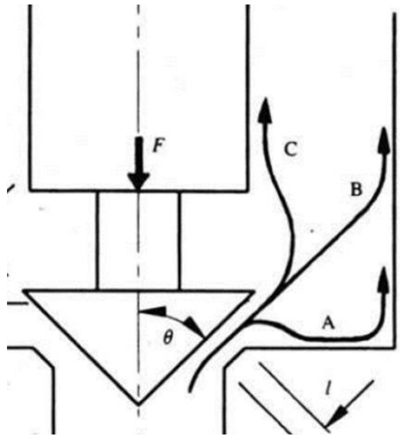

Figure 5. Flow Patterns from Johnston [5]

NOMENCLATUR

D	:	Damping coefficient [N/(m/s)]
DB	:	Sheet section hole diameter (= 13.5 [mm])
DL	:	Valve piston diameter [mm]
DS	:	Poppet valve spool diameter [mm]
F	:	Flow force [ND]
F_{shear}	:	Shear force [N].
$F_{preload}$	:	Spring preload [N]
$F_{pressure}$	:	Pressure force [N]
k	:	Spring coefficient [N/m]
m	:	Poppet valve mass [kg].
ND	:	Dimensionless unit
P	:	Pressure [ND]
Q	:	Flow rate [ND]
t	:	Time [s]
x	:	Valve displacement [ND]
α	:	Poppet cone angle (= 45 [°])
ρ	:	Density [kg/m^3]
μ		Viscosity [Pa・s]

CALCULATION CONDITIONS FOR THE FLOW FIELD INSIDE A POPPET VALVE

In Simerics-MP+, the equations of motion of the valve body can be coupled with CFD analysis. The computational grid is a sliding mesh that can expand and contract to accommodate the translational motion of the valve. By applying the finite volume method to the sliding mesh, CFD analysis can be performed to reflect the transient changes in the valve opening degree and the flow path shape with the valve disc displacement. Figure 6 shows the schematic of the test poppet valve, Figure 7 shows the calculation grid, and Table 1 shows the calculation conditions.

In this study, steady flow and unsteady flow calculations were performed. In the steady flow calculation, the valve was fixed and the condition of constant flow rate was applied. In the unsteady flow calculation, the valve was made movable and the flow rate was increased linearly in the range of Q = 0.05~1.0 [ND], and when the rated flow rate was reached, the flow rate was decreased linearly in the range of Q = 1.0~0.05 [ND].

For the initial conditions of the unsteady flow calculation, the initial value of the flow rate was first determined to be Q = 0.05 [ND], and then the unsteady flow calculation was carried out with the valve body set to be movable, and the valve displacement when the valve motion was settled down was used as the initial value. The valve displacement at this time was x = 0.04 [ND]. The pressure P, flow rate Q, and valve displacement x used are nondimensionalized in terms of rated pressure, rated flow rate, and valve displacement at rated pressure and flow rate, respectively.

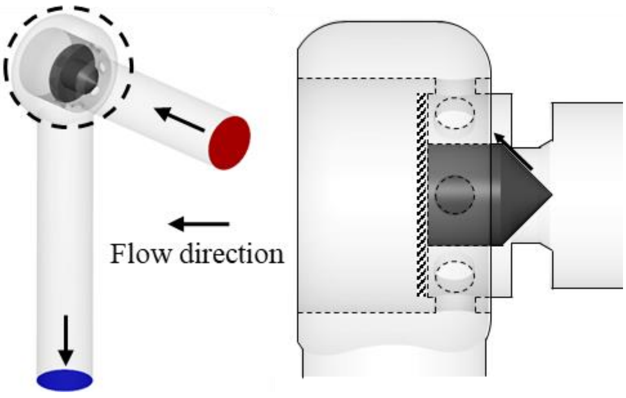

Figure 6. Outline Bird's-Eye and Cross-Section View of the Test Poppet Valve

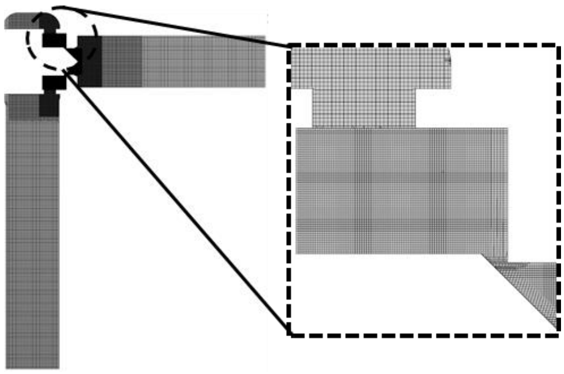

Figure 7. Analysis Grid of the Target

Table 1. Analysis Conditions

Software used	Simerics-MP+	
Analysis type	Steady state	Transient
Turbulence model	standard k-ε	
Fluid density	770	
Fluid viscosity	0.00149	
Entrance boundary condition [ND]	Flow rate = const.	0.05~1 (Flow rate/Rated flow rate)
Exit B.C. [ND]	0.2 (Static Pressure)	
Grid number	4,000,000 [-]	
Incremental time		0.000054 [s]

ANALYSIS RESULTS

Flow Patterns

Figure 8 shows five typical flow patterns obtained from steady-state calculations with a fixed valve and constant flow rate (for example, for a valve displacement x = 0.07 [ND]). Each figure shows the velocity and pressure contour plots for the central cross section including the poppet axis. The flow patterns 2 to 5 were observed even in the case of unsteady calculation under the condition that the valve was movable and the flow rate was changing. In the present study, the initial valve displacement was set to 0.04 [ND] due to the conditions that must be satisfied in order to keep the calculation grid sound. The areas circled by the solid black lines in Figure 8 (a), (b), (d) are enlargements of the pressure distribution in the areas circled by the dashed black lines.

From these results, the flow patterns can be roughly classified as follows.

(a) Flow pattern 1

This is a viscous flow pattern that spreads uniformly through the channel at very low flow rates. Since it appears only at very low flow rates, it does not have a significant effect on the flow in the valve in actual use, such as flow force.

(b) Flow pattern 2

In the low flow rate region, the first point where the jet from the throat separates from the poppet surface is the sleeve corner that constitutes the throat. Because the jet is attracted to the low pressure part of the separated flow region, the jet adheres to the vertical wall of the sleeve inlet. This is a stable flow pattern.

(c) Flow pattern 3

This is an unstable flow pattern that occurs in the low to medium flow rate region. Since the steady flow analysis did not converge, the unsteady flow analysis was conducted. As a result, it was found that the jet flow pattern oscillates between flow patterns 2 and 4, and its frequency is not constant.

(d) Flow pattern 4 (Attached flow)

This is a stable flow pattern that occurs in the medium to large flow rate region. The flow passes through the throat and flows into the valve chamber as a jet, generating a flow that adheres to the surface of the poppet spool due to the Coanda effect. If a collar is not present, the jet flows directly downstream to the outlet. If a collar is present, the jet hits the collar and turns 90 degrees in the radial direction.

(e) Flow pattern 5 (Straight flow)

This is an extremely stable flow pattern that occurs in the medium to large flow rate region. The flow passes through the throat and flows into the valve chamber as a jet, which detaches from the end of the poppet cone and flows directly into the valve chamber as a free jet.

The characteristics of the above five flow patterns are illustrated in Figure 9. The numbers in the figure correspond to the numbers of the flow patterns in Figure 8. Table 2 shows the results of the comparison between the flow patterns shown in Figures 4 and 5 and those obtained from the present analysis.

As for the flow patterns in the poppet valve, there were some research results such as five types or three types of flow patterns from past visualization experiments, but each of them corresponds to one of the five flow patterns shown here. Therefore, based on the numerical results of this study, the flow field in the poppet valve can be systematically classified into five types. Furthermore, flow patterns 4 and 5 are confirmed in all experimental reports and computational results, and these two types of flow patterns can be recognized as stable flows. The hysteresis characteristics in this study are strongly related to the regions of flow pattern 3, 4 and 5.

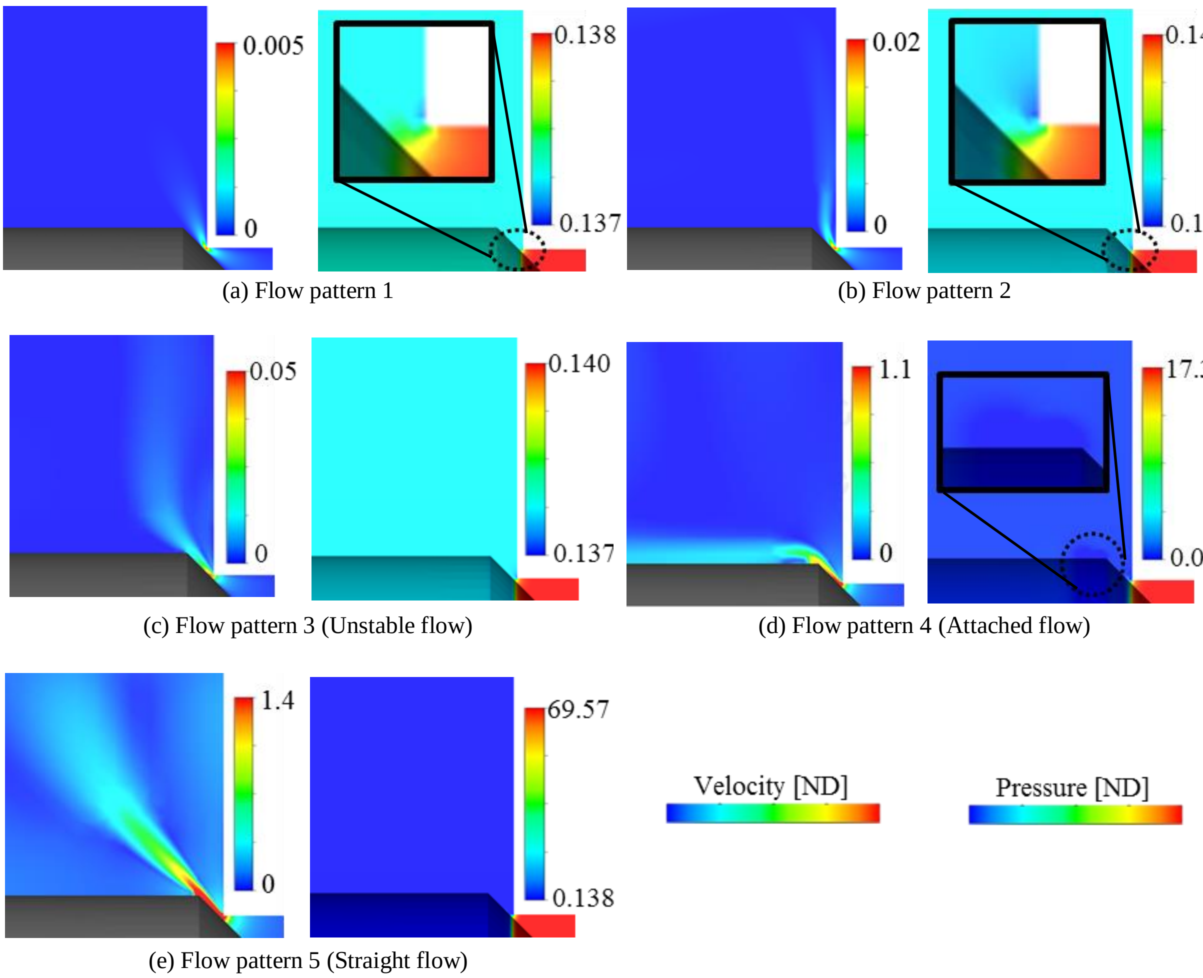

Figure 8. Pressure and Velocity Contour Plots for Five Typical Flow Patterns in Poppet Valve (Obtained from Steady-State Calculations with a Fixed Valve and Constant Flow Rate)

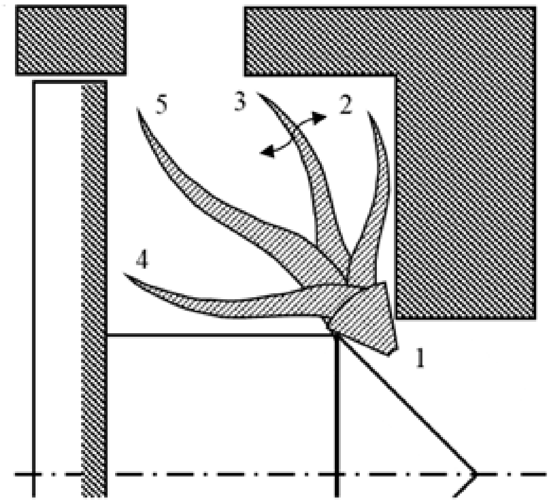

Figure. 9 Illustration of the Calculated Flow Patterns

Table 2. Correspondence Table between Type Number of Flow Patterns Calculated in the Present Work and Flow Patterns from Schrenk [3] and Johnston [5], where Alphabets such (a)-(h) correspond to that shown in Figures 4 and 5

	Flow pattern				
Present work	1	2	3	4	5
Schrenk		A	B	D, E	C
Johnston		A		C	B

Switching Phenomena

In this section, the cause of the transient switching phenomenon from flow pattern 4 to 5 in the trajectory of the hysteresis characteristics shown in Figure 3 is examined on the reference planes ① and ② shown in Figure 10(a), (b). The reference plane ① is set as a vertical cross section that includes the axis of the poppet valve, and the reference plane ② is set as a circular cross section that cuts the separation bubble occurring from the end of the poppet cone to the corner of the poppet spool start.

Contour plots of the eight flow fields (velocity distribution and two types of pressure distribution at the same time), which characteristically suggest the switching mechanism of this hysteresis characteristics, are shown in Figures 11, 12, and 13. Figure 11 is a contour plot of the velocity distribution of the internal flow on the reference plane ①, showing the jet flowing from the throat into the valve chamber. However, the color contours of the poppet cone surface and the poppet spool surface in Figure 11 show the pressure distribution on those surfaces, respectively. Figure 12 shows the pressure distribution contours of the entire valve chamber on the reference plane ①. Figure 13 shows the pressure distribution contours on the reference plane ②. The following alphabetic symbols in (a) ~ (h) correspond to the symbols in Figures 11~13. Summarised by time series, we comment on the results as follows.

(a) t = 0.391 [s].

Both the flow pattern 4 and the pressure distribution are axisymmetric and stable.

(b) t = 0.427 [s].

Flow pattern 4 exists stably as an axisymmetric flow, but the pressure distribution at the reference plane ② is starting to become unstable in terms of axisymmetry with the appearance of a low-pressure part on the left side. Unfortunately, the reason for this remains unexplained.

(c) t = 0.433 [s].

The pressure distribution at the reference plane ② shows that the lower half of the cross section is under low pressure due to the large growth of the low pressure section that had appeared on the left side, and the axisymmetry of the pressure has broken down. The flow pattern of axisymmetric flow 4 is about to detach from the lower part of the valve spool.

(d) t = 0.435 [s].

The low pressure area that grew on the lower side of the pressure distribution in the reference plane ② above repeats its strength and weakness, and is moving downward to the region closer to the outlet port. Due to this effect, the flow pattern 4 of the axisymmetric flow is trying to leave the lower part of the poppet spool. In other words, the transition to flow pattern 5 has begun.

(e) t = 0.448 [s].

The low pressure part of the pressure distribution in the reference plane ② repeatedly becomes larger and smaller, mainly at the bottom. Due to this effect, flow pattern 4 exists only in the upper part of the poppet spool, while the rest of the region is in a separated state (flow pattern 5).

(f) t = 0.461 [s].

The low pressure zone grows larger and expands to the upper half of the poppet spool. As a result, the flow pattern on the upper half of the poppet spool also begins to separate. The flow pattern on the rest around the

poppet spool becomes completely separated and flow pattern 5 appears.
(g) t = 0.463 [s].
The low pressure part of the pressure distribution expands to the entire circumferential area, and the flow is completely separated, completing the flow pattern 5.
(h) t = 0.471 [s].
The flow pattern 5 is complete, and both the flow pattern and the pressure distribution are axisymmetric and stable.
In (a) ~ (h), there are two stable flow patterns 4 and 5, such as Attached flow and Straight flow. As the flow rate increases, there is a transition (switching) between the two flow patterns. This is found to be due to the collapse of the axisymmetry of the flow as a result of the collapse of the axisymmetry of the pressure distribution of the separated bubble (low pressure part) generated in the reference plane ② as the flow rate increases. These results indicate that there is a close relationship between the path of the hysteresis characteristic and the flow pattern.

(a) Plane ① (red surface)
vertical cross section to include the axis of the poppet valve

(b) Plane ② (green surface)
Circular cross section to cut separation bubbles

Figure 10. Reference Planes to Examine the Causes of Transient Switching from Flow Pattern 4 to 5

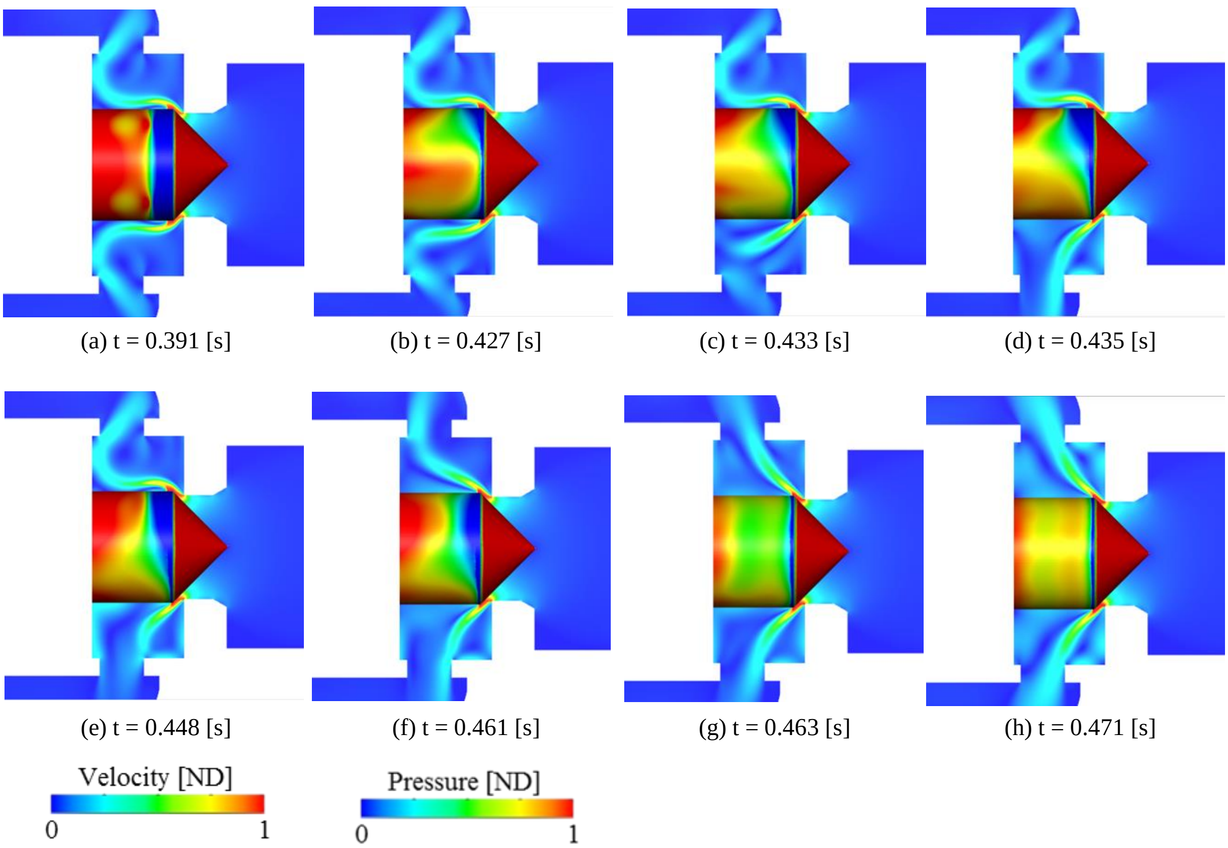

(a) t = 0.391 [s] (b) t = 0.427 [s] (c) t = 0.433 [s] (d) t = 0.435 [s]

(e) t = 0.448 [s] (f) t = 0.461 [s] (g) t = 0.463 [s] (h) t = 0.471 [s]

Figure 11. Velocity Contours in the Plane ① (Pressure Contour on the Poppet Surface)
Time Series Data of the Phenomenon of Transient Switching from Flow Pattern 4 to 5

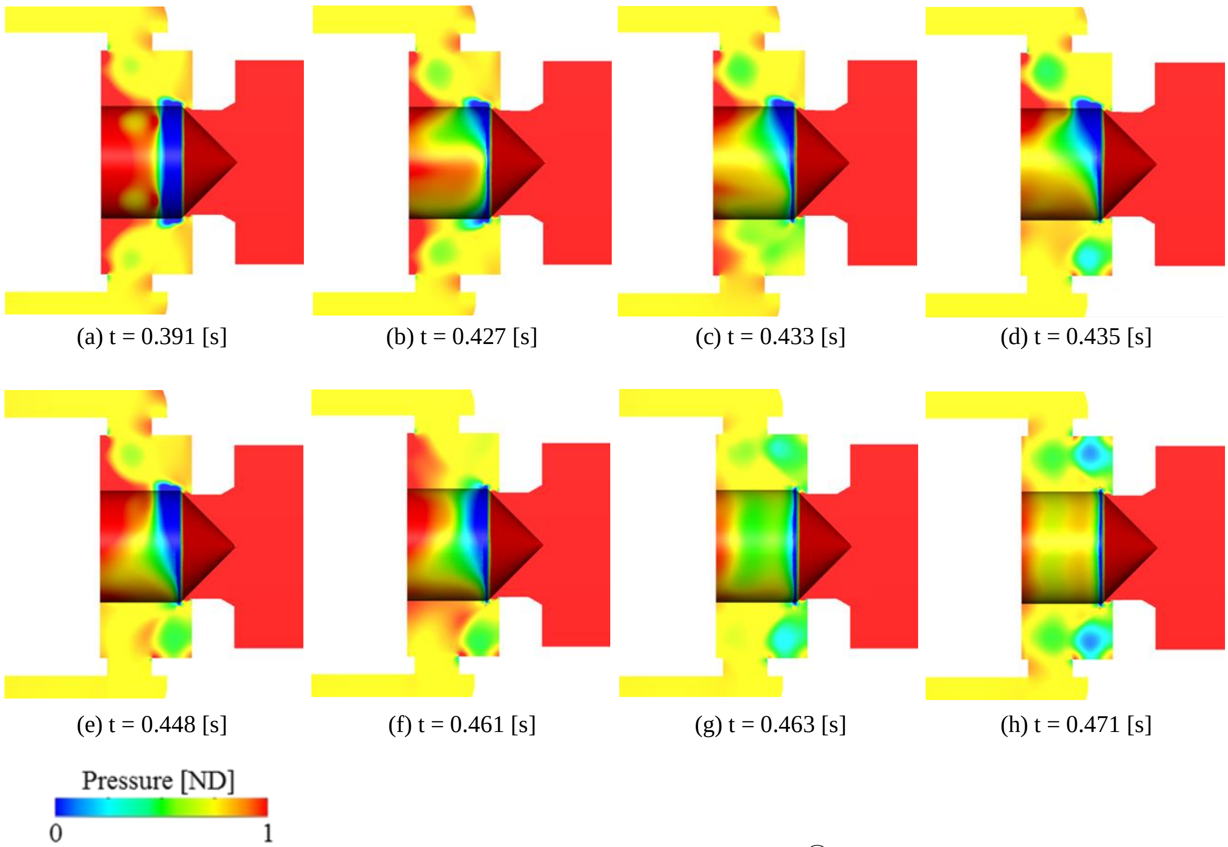

Figure 12. Pressure Contours in the Plane ①
Time Series Data of the Phenomenon of Transient Switching from Flow Pattern 4 to 5

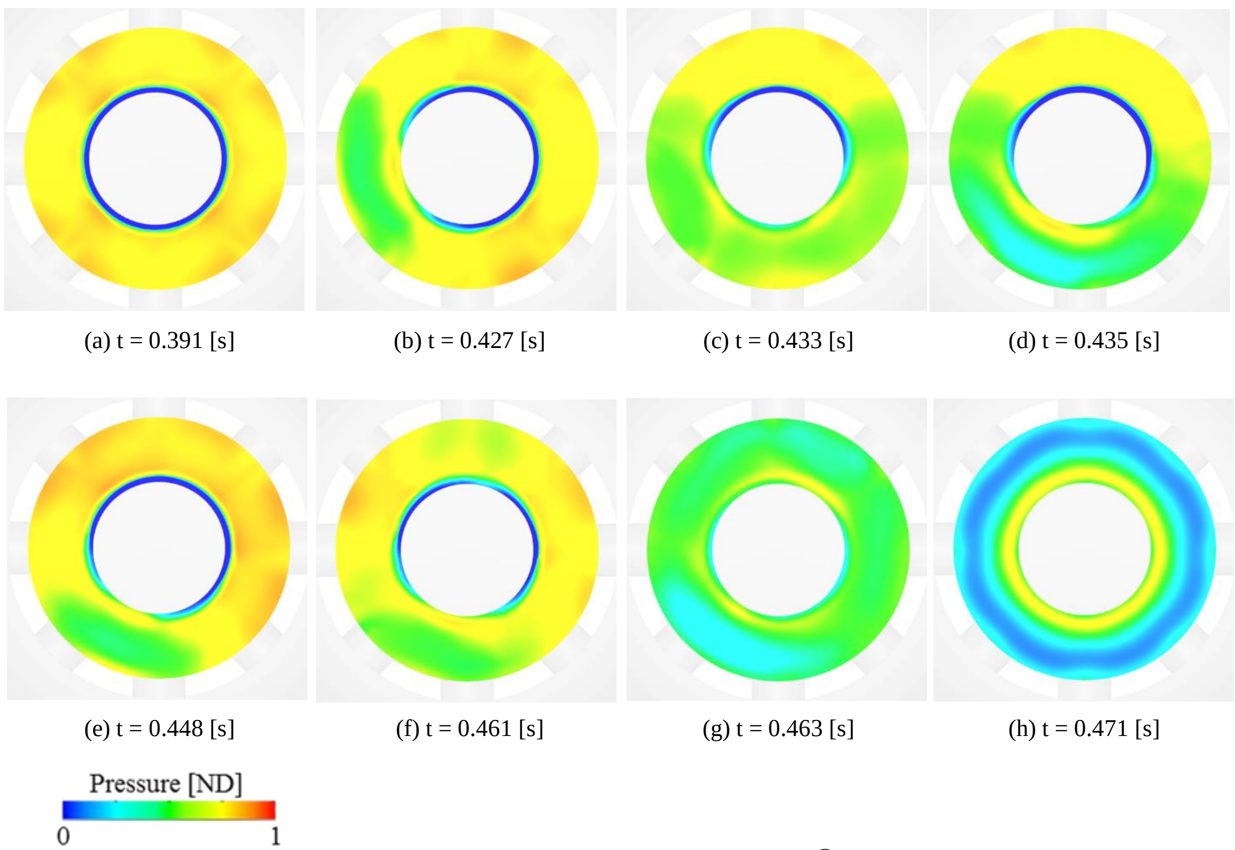

Figure 13. Pressure Contours in the Plane ②
Time Series Data of the Phenomenon of Transient Switching from Flow Pattern 4 to 5

FLOW FORCES ON AXIAL DIRECTION

Coupled Analysis between CFD and Equation of Motion of Valve Body

In order to reproduce the hysteresis characteristics of the flow rate against the control pressure in a poppet valve, a coupled analysis between the flow field of the pressure and flow rate characteristics and the equation of motion of the valve body was conducted using Simerics-MP+. The equation of motion of the valve body in the axial direction is expressed as follows: Eq. (1) [9].

$$m\frac{d^2x}{dt^2}+D\frac{dx}{dt}+k_d=\sum F_{Pressure}+\sum F_{Shear}-F_{Preload} \tag{1}$$

The force acting on the valve body is expressed as the sum of the force due to the pressure, shear force and spring preload that the valve body receives.
In the coupled analysis, within each time increment of CFD calculation, after the convergence judgment of the flow calculation is completed, the module for calculating the above equation of motion of the valve body is activated, and the translational motion of the valve body is calculated.
The damping coefficient D in the above equation of motion can be thought of as the sum of the damping coefficient D_f, which is due to the viscosity of the fluid, and the damping coefficient D_d, which is due to the damping orifice located behind the valve, and can be expressed as $D = D_f + D_d$. Comparing the magnitudes of the two, the damping force due to the viscosity of the fluid is an order of magnitude smaller than the damping force of the damping orifice. That is, $D_f << D_d$. These results indicate that this orifice has a significant influence on the actual damping of the poppet valve. Since the critical damping coefficient is $C_0 = 2\sqrt{mk} = 108$ [N/(m/s)], we consider that a larger value would be acceptable as a setting value in the calculation. Therefore, we set the damping coefficient to 2000 [N/(m/s)], referring to the value that is the smallest case of damping force.

Relationship between Flow Pattern and Flow Force Corresponding to the Path of Hysteresis

Figure 15(a) and (b) show the axial flow force against flow rate change and valve displacement, respectively, in the operating region where hysteresis occurs in the pressure-flow characteristic experiment as shown in Figure 3. The axial flow force, flow rate, and valve displacement are non-dimensionalized by their respective values at the rated flow rate. As in Figure 3, the red solid line indicates the forward path of hysteresis, and the blue solid line indicates the return path of hysteresis. As for the axial flow force against the flow rate change shown in Figure 15, in the forward path, the negative flow force gradually increases as the flow rate starts to increase from around Q = 0 [ND], and unstable fluctuations start around the flow rate Q = 0.69 [ND], and then the flow force suddenly becomes positive around Q = 0.83 [ND]. In the return path, as the flow rate begins to decrease from around Q = 1 [ND], the flow force decreases linearly and quickly drops to around 0 [ND] near the point where the flow rate drops below Q = 0.42 [ND]. The positive and negative flow forces are of the same order.
The relationship among hysteresis, flow pattern, and axial flow force will be discussed. First, flow patterns 1, 2, and 3 appear in the region below Q = 0.25 [ND].Then, as the flow rate increases, flow pattern 4 (Attached flow) appears in the region where the negative flow force increases (Q = 0.3 ~ 0.69 [ND]). In this region (Q = 0.69 ~ 0.83 [ND]), both flow pattern 4 and flow pattern 5 appear in confusion, and the flow pattern is about to make a transition by sensing a slight disturbance. When the flow rate increases until it passes through this region, the stable flow pattern 5 (Straight flow) appears.
In short, we can conclude that severe oscillations occur between flow pattern 4 (Q = 0.3 ~ 0.69 [ND]) and flow pattern 5 (Q > 0.83 [ND]) due to the transition phenomenon. This indicates that the hysteresis characteristic is due to the transition of the flow pattern from 4 (Attached flow) to 5 (Straight flow).
In addition, the magnitude of the flow force becomes negative (-) and positive (+) in flow patterns 4 and 5, respectively, which synchronizes the valve displacement with the change in flow force and thus the flow pattern.
Finally, the three-dimensional calculation results of the parameters ΔP, Q, and x, which are thought to govern this phenomenon, are shown in Figure 16. There are two paths for the valve displacement, one that maintains the linear relationship and the other that deviates from it, only within the region where the hysteresis characteristic occurs. The flow pattern corresponding to this linear relationship is Straight flow, and the flow pattern deviating from it is Attached flow. This result indicates that the Attached flow is caused by a small change in the valve displacement.

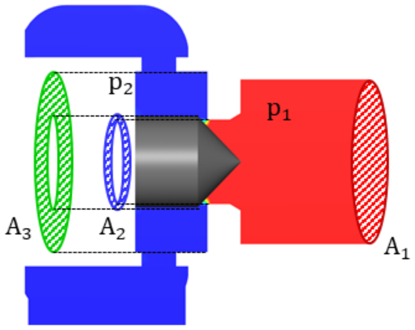

Axial force acting on the valve body

In case of valve closure $$F_0 = \int p_1 dA_1 + \int p_2 d(A_2 + A_3)$$

In case of valve release $$F_{cal} = \int p_1 dA_1 + \int p_2 d(A_2 + A_3) + \int \tau_0 dA_0$$

Axial flow force $$\Delta F = F_{cal} - F_0$$

Figure 14. Calculation Way of Flow Force

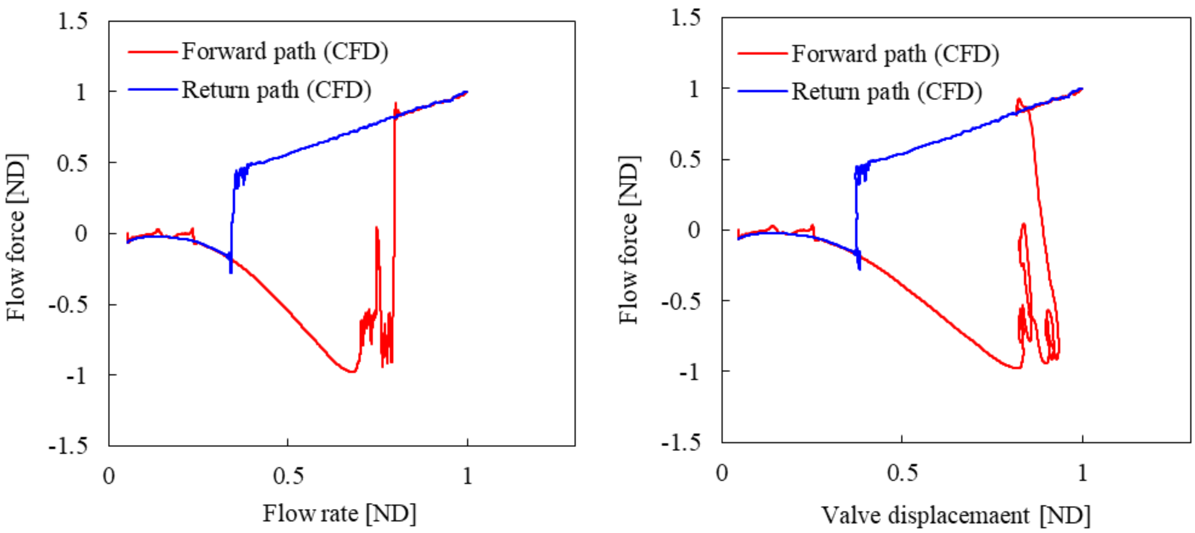

(a) Flow Force vs. Flow Rate (b) Flow Force vs. Valve Displacement

Figure 15. Time Series Data of Axial Flow Forces Corresponding to the Path of Hysteresis shown in Figure 3

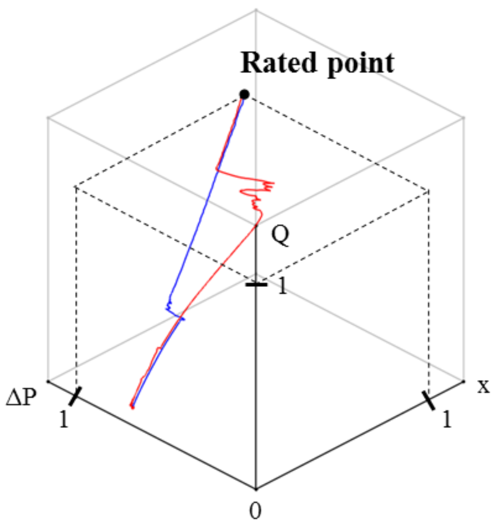

Figure 16. Three-Dimensional Representation of Time Series Data of Pressure P, Flow Rate Q and Valve Displacement x, which Correspond to the Path of Hysteresis shown in Figure 3

CONCLUSION

In this study, CFD software was used to systematically organize the flow patterns in the prototype poppet valve used in the study by Masuda et al. [2] and to clarify the relationship between hysteresis characteristics and flow patterns.
The following points were clarified.

1. The flow patterns in the poppet valve can be classified into five categories.
2. In a poppet valve, a transition in flow pattern occurs between two stable flow patterns 4 and 5 (Attached flow and Straight flow) as the flow rate increases. At that time, large pressure and valve displacement oscillations occur.
3. Attached flow is caused by a small change in valve displacement.
4. As for the axial flow force, in flow pattern 4 (Attached flow), the negative flow force increases as the flow rate increases. On the other hand, in flow pattern 5 (Straight flow), the positive flow force increases as the flow rate increases. And the order of the positive and negative flow forces is about the same.
5. This difference in the polarity of the flow force affects the valve displacement and causes a transition in the flow pattern. The cause was found to be the collapse of the axial symmetry of the flow as a result of the collapse of the axial symmetry of the circumferential pressure distribution in the separated bubble (low pressure part) generated at the cylindrical corner of the poppet cone end as the flow rate increases.

In conclusion, the path of the hysteresis characteristics of the poppet valve is closely related to the flow patterns.

REFERENCES

1. OSHIMA, S., An Experimental Study on the Several Poppet Valves with Difference in Shape, Proceedings of the JFPS International Symposium on Fluid Power, 1989, 1989-1 pp. 361-368.
2. MASUDA, S., SHIMIZU, F., FUTIWAKI, M., TANAKA, K., Internal Flow and Hysteresis Characteristic of the Poppet Type Pressure Control Valve, Transaction of the Japan Fluid Power System Society, 2021, 52-1, pp.8-15.
   (MASUD, S., et al, Internal Flow and Hysteresis Characteristic of the Poppet Type Pressure Control Valve, This paper has also been presented at JFPS International Symposium on Fluid Power hakodate2020.)
3. SCHRENK, E., Disc Valves, Flow Patterns, Resistance, and Loading, British Hydromechanics Research Association, 1957, 547, pp.1-17.
4. MCCLOY, D., MCGUIGAN, R. H., Some Static and Dynamic Characteristics of Poppet Valves, Proc. Instn. Mech. Engrs, 1964, 179, pp199-213.
5. JOHNSTON, D. N., EDGE, K. A., Experimental Investigation of Flow and Force Characteristics of Hydraulic Poppet and Disc Valves, Proc. Instn. Mech. Engrs, Part A, 1991, 205, pp161-171.
6. VAUGHAN, N. D., et. al., Numerical Simulation of Fluid Flow in Poppet Valves, Proc. Instn. Mech. Engrs, Part A, 1992, 206, pp.119-127.
7. HAYASHI, S., Instability of Poppet Valve Circuit, JSME International Journal. Ser. C, Dynamics, Control, Robotics, Design and Manufacturing, 1995, 38-3, pp357-366.
8. ALTARE, G., RUNDO, M., OLIVETTI, M., 3D Dynamic Simulation of a Flow Force Compensated Pressure Relief Valve, Proc. Instn. Mech. Engrs Congress and Exposition IMECE2016 November 11-17, IMECE2016-65624.
9. SIMERICS, Simerics Manual V5.0 (2019).

The 11th JFPS International Symposium on Fluid Power HAKODATE 2020 Oct. 12-13, 2021 JFPS The Japan Fluid Power System Society

Numerical Study on Identification Inputs for Nonlinear Hydraulic Cylinders

Teruo KATO*, Satoru SAKAI*, Ryo ARAI*

*Department of Mechanical Engineering, Shinshu University
4-17-1 Wakasato, Nagano City, Nagano, 380-0928 Japan
(E-mail: 20hs203d@shinshu-u.ac.jp)

Abstract. This short report discusses the identification input for nonlinear hydraulic cylinders. First, we focus on an input-output nonlinearity which exists even in the absence of nonlinear friction and prevents us from observing and measuring the input-output behaviors. Second, we propose a new identification input via a modification that is numerically studied via a nondimensionalization technique. Finally, we confirm the effectiveness of the new identification input via a numerical system identification.

Keywords: Hydraulic cylinder, Identification, Input-output nonlinearity.

INTRODUCTION

Hydraulic robots can achieve high power-weight ratio in comparison with electric robots and also realize a gravity compensation without any control. A new modeling of hydraulic cylinder dynamics will be a foundation to improve control performance against the nonlinearity, uncertainty, parameter perturbation, and so on (e.g., [1] [2] [3]). In general, the modeling procedure (e.g., [4]) in a broad sense may include the identification procedure (e.g., a system identification procedure, a parameter identification procedure [5]). The identification procedure is always needed in the numerical simulation procedure (e.g., [6]) at least in order not only to check the stability and control performance before the experimental procedure and also to search a set of good parameters (e.g., link ratio, control gain). Especially, in the context of learning (e.g., a deep learning) based on Big Data, the parameter identification procedure is gaining importance.

However, in many cases, we are disturbed to observe and measure the input-output behaviors of nonlinear hydraulic cylinders. It is well-known that the piston displacement cannot be small in the steady state even if the standard identification input (e.g., the spool displacement for a servo-valve) such as a sinusoidal amplitude is small [7]. For example, when we implement these sinusoidal signals for a nonlinear hydraulic cylinder, the piston displacement in the steady state reaches and collides with one of the ends (the rod side) of the hydraulic cylinder. This is because an input-output nonlinearity which exists even in the absence of nonlinear friction. Due to this input-output nonlinearity, we cannot get enough observation and measurement to apply many system identification and parameter identification methods. This is a serious problem in the identification procedure.

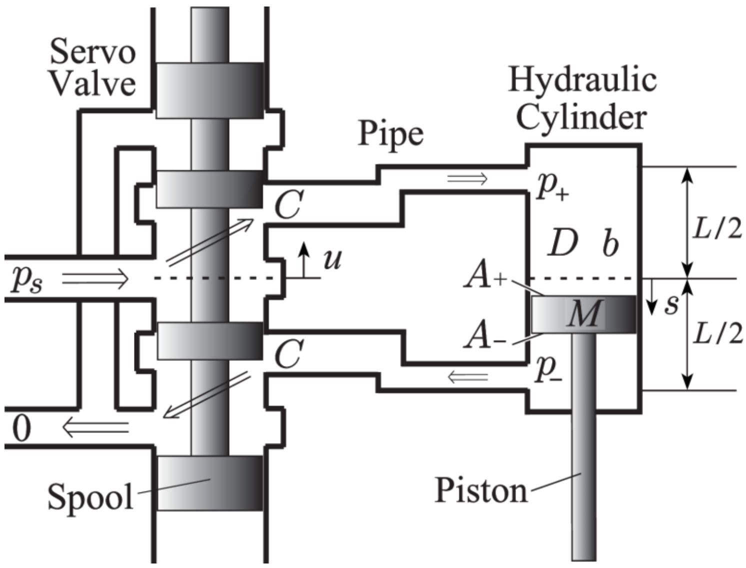

Figure 1. Hydraulic actuator.

NOMINAL MODEL

Figure 1 shows a hydraulic arm and its cylinder. Let us review the conventional nominal model in the original representation: [8] [9] [10] [11].

Consider the conventional nominal model

$$\begin{cases} M\ddot{s} &= -D\dot{s} + A_+p_+ - A_-p_- \\ \dot{p}_+ &= \dfrac{b}{V_+(s)}(-A_+\dot{s} + Q_+) \\ \dot{p}_- &= \dfrac{b}{V_-(s)}(+A_-\dot{s} - Q_-) \end{cases} \tag{1}$$

where the displacement $s(t)$ [m], the cap pressure $p_+(t)$ [Pa], the rod pressure $p_-(t)$ [Pa], and the spool displacement (the input) $u(t)$ [m] are the functions of time t [s]. The subscript $+$ and $-$ denote the cap-side and the rod-side, respectively, and the subscript $\pm$ denotes both sides. The driving force is $f(t) = A_+p_+(t) - A_-p_-(t)$ [N]. The mass M [kg], the damping coefficient D [Ns/m], the piston areas $A_+ \geq A_-$ [m^2], and the bulk modulus b [Pa] are the positive constants. The cylinder volumes $V_+\big(s(t)\big) = A_+(L/2 + s(t))$, $V_-\big(s(t)\big) = A_-(L/2 - s(t))$ [m^3] with the constant stroke L [m] are the functions of the displacement $s(t)$[m]. The input Q_+ and Q_- [m^3/s], are approximated by Bernoulli's principle:

$$Q_+ = Ch_+u,\ Q_- = Ch_-u \tag{2}$$

with

$$h_+ := \sqrt{\left|\mathrm{sgn}(-u)p_+ + \frac{1+\mathrm{sgn}(+u)}{2}p_s\right|}$$
$$h_- := \sqrt{\left|\mathrm{sgn}(+u)p_- + \frac{1+\mathrm{sgn}(-u)}{2}p_s\right|}$$

where the flow gain C [$\sqrt{\mathrm{m}^5/\mathrm{kg}}$] and the source pressure P [Pa] are the positive constants. The conventional nominal model introduces the restricted domain $s \in (-L/2, L/2)$ and $p_\pm \in [0, p_s]$ and the absolute notation within the square root functions (2) is dropped. The conventional nominal model (1) (2) in the original representation is not our result but well-known. The equations (1) ignore the nonlinear friction effect and also the internal and external leakage effects at least. Indeed, only the linear friction $D\dot{s}(t)$ is taken into account in the nominal model. The equations (2) assume the steady flow and the negligible servo dynamics of the zero-lapped spool valve.

On the other hand, the stroke L can include the pipe length effect and the bulk modulus b includes the pipe (or tube) flexibility effect. Of course, the difference (e.g., the nonlinear friction effect by the actual sealing) between the conventional nominal model and the experimental setup exists and depends on each experimental setup but would change continuously. In the context of robust control [12] [13], the difference is taken into account in the controller design procedure in many controller design procedures (e.g. [14] [15] [16] [8] [9] [10]) as uncertainty.

One of the linearized models of the nominal model is given as:

$$\begin{cases} M\ddot{\hat{s}} = -D\dot{\hat{s}} + A_+\hat{p}_+ - A_-\hat{p}_- \\ \dot{\hat{p}}_+ = \dfrac{b}{V_+(0)}\left(-A_+\dot{\hat{s}} + C\sqrt{p_s/2}\ u\right) \\ \dot{\hat{p}}_- = \dfrac{b}{V_-(0)}\left(+A_-\dot{\hat{s}} - C\sqrt{p_s/2}\ u\right) \end{cases} \tag{3}$$

whose state $\hat{x}(t) := (\hat{s}(t),\ \dot{\hat{s}}(t), \hat{p}_+(t), \hat{p}_-(t))^{\mathrm{T}}$ starts from the same state $\hat{x}(0) = x(0)$ in the presence of the same input $u(t)$.

INPUT-OUTPUT NONLINEARITY

We focus on an input-output nonlinearity which always exists even in the absence of nonlinear friction. Suppose the sinusoidal signal:

$$u(t) = A_u \sin(2\pi f t) + 0 \tag{4}$$

is applied as the standard identification input. Even if the sinusoidal amplitude A_u is small, it is well-known that the piston displacement $s(t)$ cannot be small in the steady state and reaches and collides with one of the ends (the rod side) of the cylinder $s(t) \to L/2$ eventually [7]. Due to this input-output nonlinearity, we cannot get enough observation and measurement to apply many system identification and parameter identification methods. This is a serious problem in the identification procedure.

The following proposition is useful to understand this problem explicitly from a familiar linear approximation point of view. Here, let us introduce the nondimensionalization in order to discuss comprehensively [17] [18] [19].

• Proposition 1 : Consider the original representation (1) (2) in the original representation. Then, there exists a set of a time scaling $t^* = (1/T)t$, a variable scaling$(s^*,\ p_+^*,\ p_-^*)^{\mathrm{T}} = ((1/S)s, (1/P_+)p_+, (1/P_-)p_-)^{\mathrm{T}}$, and an input scaling $u = (1/U)u^*$ by which the standard sinusoidal signal:

$$u^*(t^*) = A_u^* \sin(2\pi f^* t^*) + 0$$

causes the piston displacement in the steady state:

$$s^*(t^*) = B_u^* \sin(2\pi f^* t^* + \phi) + 0$$

where

$$B_u^* = A_u^* \sqrt{\frac{8P^*}{\omega^{*6} + (D^{*2} - 4(A^* + 1))\omega^{*4} + 4(A^* + 1)^2 \omega^{*2}}}$$

$$\phi = \tan^{-1}\left(\frac{\omega^{*2} - 2(A^* + 1)}{-D^* \omega^*}\right)$$

with $\omega^* = 2\pi f^*$

Let us recall the set of the time transformation $t^* = (1/T)t$ with $T = \sqrt{ML/(bA)}$, the state transformation $x^* = (\,s^*,\ \dot{s}^*,\ p_+^*,\ p_-^*)^{\mathrm{T}} = X_s^{-1}x$ with

$$X_s := \begin{bmatrix} S & 0 & 0 & 0 \\ 0 & MS/T & 0 & 0 \\ 0 & 0 & P_+ & 0 \\ 0 & 0 & 0 & P_- \end{bmatrix} = \begin{bmatrix} L & 0 & 0 & 0 \\ 0 & \sqrt{MLbA_+} & 0 & 0 \\ 0 & 0 & b & 0 \\ 0 & 0 & 0 & b \end{bmatrix},$$

and the input transformation $u^* = (1/U)u$ with $U = (\sqrt{A_+^3 L/M}/C)$. The original representation (1) (2) in the original representation is transformed to the following nondimensional representation:

$$\begin{cases} s^{*\prime} &= -D^* s^{*\prime} + p_+^* - A^* p_-^* \\ p_+^{*\prime} &= \dfrac{1}{1/2 + s^*}(-s^{*\prime} + Q_+^*) \\ p_-^{*\prime} &= \dfrac{1}{1/2 - s^*}(+s^{*\prime} - (1/A^*)Q_-^*) \end{cases}$$

and

$$Q_+^* = Ch_+^* u,\ \ Q_-^* = Ch_+^* u$$

with

$$h_+^* := \sqrt{\left| \mathrm{sgn}(-u)p_+^* + \frac{1 + \mathrm{sgn}(+u)}{2} P^* \right|}$$

$$h_-^* := \sqrt{\left| \mathrm{sgn}(-u)p_-^* + \frac{1 + \mathrm{sgn}(-u)}{2} P^* \right|}$$

where $T,\ S,\ P_+,\ P_-,U$ are the constants and D^*, A^*, P^* are the nondimensional parameters defined as $D^* \coloneqq D\sqrt{L/(MbA_+)}$, $A^* \coloneqq A_-/A_+(\leq 1)$, $P^* \coloneqq p_s/b$. The notation $\bullet'$ denotes the derivative with respect to the nondimensional time t^*. Simultaneously, the linearized models (3) after the standard linear approximation has the following transfer function matrix the nondimensional transfer function matrix:

$$\frac{\sqrt{8P^*}}{p^2 + D^*p + 2(1 + A^*)}\begin{bmatrix}(+p^2 + D^*p - 2(1 - A^*))/(2p)\\(-p^2 - D^*p - 2(1 - A^*))/(2A^*p)\\p + D^*\\1/p\end{bmatrix} \tag{5}$$

from the input u^* to the estimated outputs $\hat{y}_0^* = (\hat{p}_+^*,\ \hat{p}_-^*,\ \hat{f}^*,\ \hat{s}^*)^{\mathrm{T}}$ of the linearized model (3) in the nondimensional version. Here, the notation s denotes the derivative operator in the Laplace transform with respect to the nondimensional time $t^* = (1/T)t$. This immediately brings the explicit formula on the gain and phase. Note that the above proposition (5) uses the similar technique in our paper [19] but the explicit formula on the gain and phase has never reported. Note that the obtained formula:

$$\frac{\sqrt{8P^*}}{p^3 + D^*p^2 + 2(1 + A^*)p}$$

with the restricted parameter $2(1 + A^*) \leq 4$ is different from the familiar formula:

$$\frac{K}{p^2 + 2\zeta w_n p + {w_n}^2}\frac{1}{p}$$

with the unrestricted parameter ${w_n}^2 < \infty$. This difference implies a link to the conservative control performance [13] based on the familiar formula. In a word, the familiar formula is too large and is not used here in this paper. Based on Proposition 1, we can explicitly design a standard identification input with the amplitude A_u^* to achieve that the piston displacement with the amplitude B_u^* does not reach and collide with one of the ends (the rod side) of the cylinder comprehensively. However, this is for the linearized model. We should design a certain identification input to achieve for nominal model of nonlinear hydraulic arms. This is an understanding of the serious problem from a familiar linear approximation point of view.

NEW IDENTIFICATION INPUT

As the main contribution of this paper, in this section, we propose a new identification input modification for nonlinear hydraulic cylinders.

• Condition 1 : The new identification input should be defined not in the feedback manner but the feedforward manner. In general, in identification procedure (in modeling procedure in a broad sense), it is of importance to observe and measure the input-output behavior as it is. However, in many cases, control inputs constructing some closed-loop systems change the input-output behaviors even when the linear approximation is not needed. We should define the identification input only use a feed-forward manner.

• Condition 2 : The new identification input should close to the standard identification input (e.g., the standard sinusoidal input) in some senses. This is because, in many cases, we already have a few knowledge of the system and we cannot confirm the safety of the system. In other words, we should avoid a large modification from the standard identification input.

As one of the simplest new identification inputs, we propose the following modification:

$$u^*(t^*) = A_u^* \sin(2\pi f^* t^*) + u_0^*(D^*, A^*, P^*, f^*) \tag{6}$$

where u_0^* is the nondimensional constant. The first term is nothing but the standard sinusoidal input (4), and the second term is a special constant depending on the three nondimensional parameters as well as the frequency appeared in the first term. Clearly, the proposed identification input (6) is given in a feed-forward manner and the only difference between them is just the existence of the constant u_0^*. The above 2 conditions (Condition 1 and Condition 2) are satisfied in these senses. The remaining problem is how to search the constant u_0^*. Now let us define the best constant u_0^* as a minimization of u_0^* to achieve the following formula:

$$J(u_0^*) = \frac{s^*(0) - \min_{0\le t^*\le T_u^*} s^*(t^*)}{0.01\left(\max_{0\le t^*\le T_u^*} s^*(t^*) - \min_{0\le t^*\le T_u^*} s^*(t^*)\right)} > 1$$

as an objective function in this paper. Here T_u^* is the test time. Since the search space of the constant u_0^* is just the 1 dimensional space, we apply an advanced direct search method in which we repeat the nonlinear dynamics computations and the parameter updates in the only 3 dimensional parameter space ($\theta^* := (D^*, A^*, P^*) \in \mathbb{R} \times [0,1] \times \mathbb{R} \subset \mathbb{R}^3$). Unfortunately, many experimental conditions are often restrictive in terms of the scale and cannot be comprehensive. On the other hand, the usual numerical conditions are also restrictive when the parameter space is too large. However, the advanced direct search method is quite efficient than the conventional direct search method with the 8 dimensional parameter space($\theta := (M, D, L, A_+, A_-, b, C, p_s) \in \mathbb{R}^8$). Due to the parameter reduction (8 to 3), the computational time complexity of the advanced direct search method has $\mathcal{O}(n^3)$ and that of the conventional one has $\mathcal{O}(n^8)$(we see $n = 10$ case in the next section). Furthermore, instead of the original state, the Casimir functions reduce the computational time [20]. In the nonlinear dynamics computations, the Casimir functions are applied to compute the non-dimensional state $x^*(t^*)$ starting from the initial state $x^*(0) = (0, 0, P^*/2, A^*P^*/2)^T$ in the presence of the new identification input $A_u^* \sin(2\pi f^* t^*) + u_0^*$ with the amplitude $A_u^* := A_u/U_s$ and the frequency $f_u^* := T_s f_u \in \{0.002, 0.15\}$. The test period is defined as $[0, T_u^*]$:=$[0, 3/f_u^*]$ and the Adams-Moulton method with the variable step is applied (MATLAB 2015a, Simulink ver.8.6, 64 [bit], CPU 1.60 [GHz], Memory 8.0 [GB]).

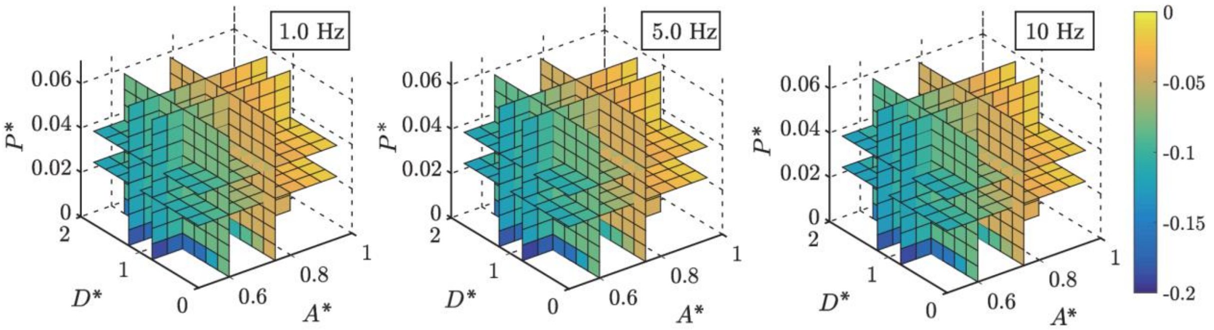

Figure 2. The best constant u_0^* in $D^*A^*P^*$-space ($D^* = D\sqrt{L/(MbA_+)}$, $A^* = A_-/A_+$, $P^* = p_s/b$).

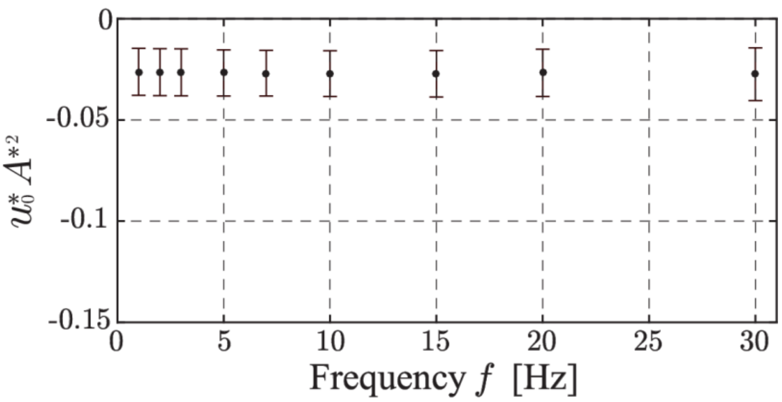

Figure 3. The value of $u_0^* A^{*2}$ in $D^*A^*P^*$-space ($D^* = D\sqrt{L/(MbA_+)}, A^* = A_-/A_+, P^* = p_s/b$).

Figure 2 shows a part of the searched constant u_0^* in the 3 parameter-space for each frequency. As an unexpected result, the constant u_0^* mainly depends on the nondimensional area A^* only and less sensitive to the other nondimensional physical parameters. **Fig. 3** shows the value of $u_0^* A^{*2}$ in the 3 dimensional parameter space for each frequency. One of the simplest approximation is numerically obtained as follows:

$$u_0^* \approx u_0^*(A^*) := -0.0266/A^{*2} \tag{7}$$

EXPERIMENTS

Figure 4 shows an appearance of the experimental setup and **Fig. 5** shows the signal diagram. The experimental setup consists of a manipulator (the arm length 315 [mm]), a pump (DAIKIN, NDR081-071H-30, 11.7 [L/min], $p_s = 7$ [MPa]), a tank 7 [L], four pipes (YOKOHAMA, SWP70-6, 1/4 [inch]), a valve (YUKEN KOGYO, LSVG-01EH-20-WC-A1-10), two cylinders asymmetric cylinder (JPN, KW-1CA30×75, L=75 [mm]), a filter (Taisei Kogyo, UM-03-20U-1V) and an oil (ISOVG32, 860 [kg/m^3], 40 ± 2 [°C]).

The output signals $p_\pm$ are measured by a pressure sensor (KEYENCE, AP-15S), the output s is measured by a potentiometer (MIDORI, LP-100F-C) and the identification input u is measured by the LVDT. These output and input signals are detected by an AD converter (Interface, PCI-3155, 16 [bit]) and recorded by a control PC (EPSON, LX7700, Linux [21], 2.53 [GHz]) by a sampling time 1.0 [ms]. In order to identify the parameters, a chirp-like input with the amplitude $A_u = 1.2$ [V], the frequencies $f = 0.5 + (5.0 - 0.5)/36 \cdot t$ [Hz] is applied via a DA converter (Interface, PCI-3325, 12 [bit]). The identified and measured parameters are $(M,\ D,\ L,\ A_+,\ A_-,\ b,\ C,\ p_s) = (14,\ 3200, 0.075,\ 7.0 \times 10^{-4},\ 5.4 \times 10^{-4},\ 5.3 \times 10^{8},\ 1.6 \times 10^{-4},\ 7.0 \times 10^{6})$[5]. Since the parameter identification is in the off-line world, the time derivative of the piston displacement s and the pressures $p_\pm$ are sufficiently calculated via the first or second difference approximation and the standard moving average.

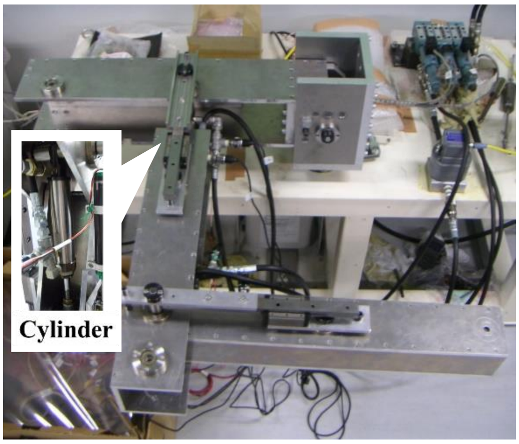

Figure 4. The experimental setup (photo).

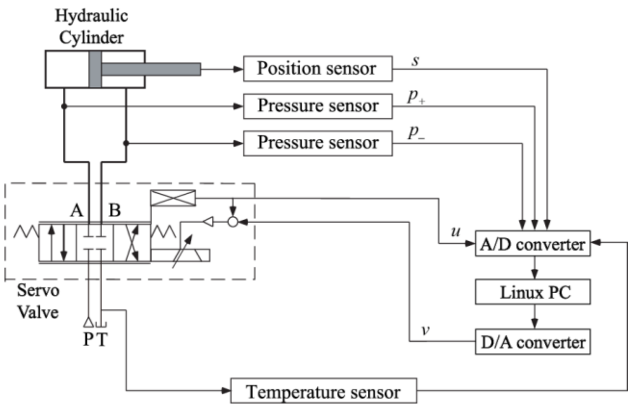

Figure 5. The experimental setup (signal flow).

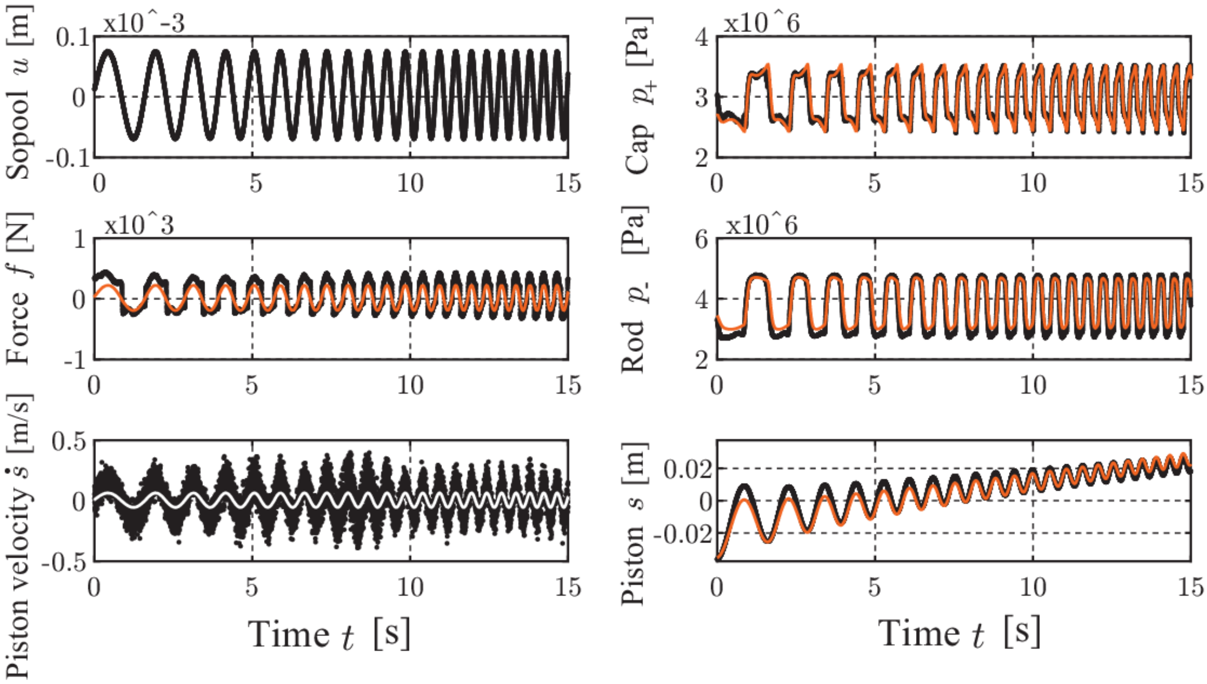

Figure 6. Experimental setup (Black) vs. Nominal model (Red) (only piston velocity of Nominal model is not Red but White)[11].

Figure 6 shows a long time cross validation in which the experimental outputs (Black) were never used in the parameter identification procedure. Nevertheless, with respect to the nonlinearly-shaped responses in the cap pressure, the nominal model has an accuracy that any linearized model (transfer function) cannot have. **Fig. 7** and **Fig. 8** are simulation results and experimental results. Those results show the time response of the piston displacement in the presence of the conventional chirp-like input and also shows the time response of the piston displacement in the presence of the same chirp-like input with the proposed constant u_0^* in the presence of same initial states. Even though the applied constant u_0^* is 0.046 and very tiny (about 4.6 [%] compared with the input sinusoidal amplitude A_u^*), the input-output nonlinearity is almost disappeared. Eventually, the proposed constant u_0^* avoids the collision with the end of the cylinder $s(t) \nrightarrow L/2$. Now we can fully observe and measure the input-output behaviors. On the other hand, in case of the conventional chirplike input without the constant u_0^*, not only the identification procedure but also the model validation procedure can fail. The second impact of the proposed constant u_0^* is small. This means that our approach using the new identification input (7) is very effective to solve the problem.

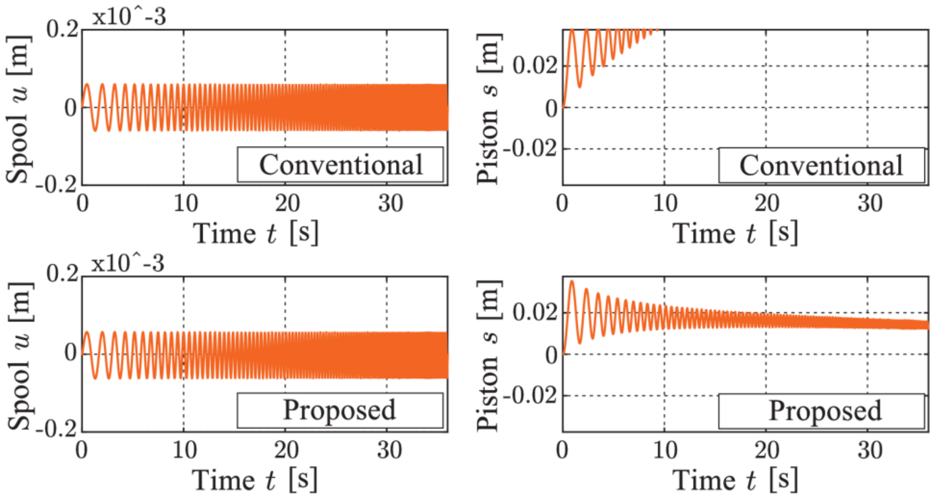

Figure 7. Simulation results.

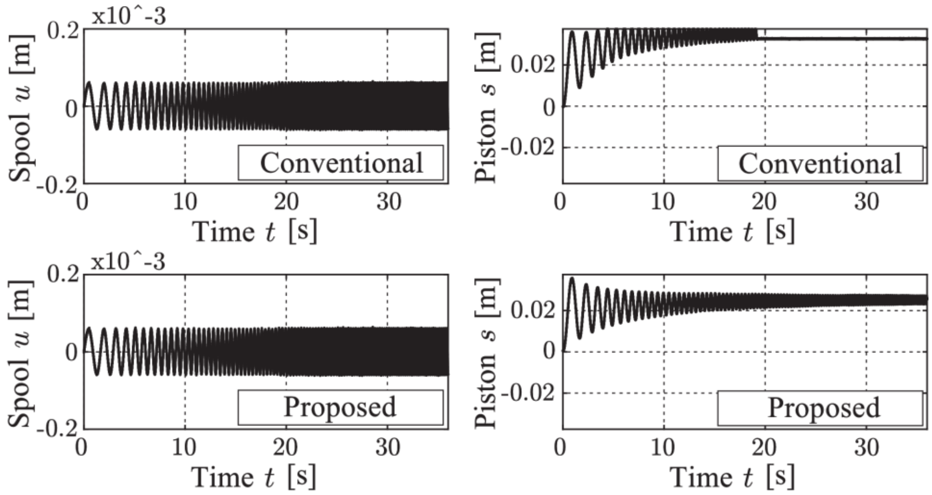

Figure 8. Experimental results.

NUMERICAL SYSTEM IDENTIFICATION

Figure 9 shows the bode diagram of the nominal model. Because of new identification input, we can fully observe and measure the input-output behaviors to apply a numerical system identification, numerically.

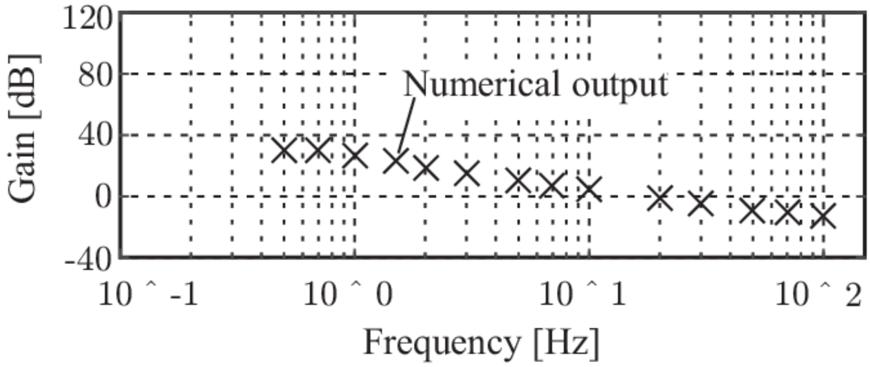

Figure 9. The identified bode diagram of the nominal model. X markers are numerical outputs (gain of input-put) which are observed.

CONCLUSION

The report provides a very simple but comprehensive modification of the standard identification input for nonlinear hydraulic cylinders. Due to the input-output nonlinearity, we cannot observe and measure the input-output behaviors to apply many system identification and parameter identification methods. This is a serious problem in the identification procedure. We propose a new identification input via the modification consisting of a very simple but comprehensive constant u_0^*. We show the effectiveness of the proposed identification input. The piston displacement can be small even in the steady state and we can fully observe and measure the input-output behaviors and can success the numerical system identification.

REFERENCES

1. H. Merritt. Hydraulic Control Systems. John Willey and Sons, 1967.
2. J. Watton. Fluid Power Systems. Prentice-Hall, 1989.
3. M. Jelali and A. Kroll. Hydraulic Servo Systems, Springer, 2002.
4. P. C. Breedveld. Bond Graph Modeling of Engineering Systems: Theory and Application (edited by Wolfgang Borutzky), 2011, Chapter 1. Springer.
5. S. Sakai and Y. Maeshima. A new method for parameter identification for n-dof hydraulic robots. In Proc. of IEEE ICRA, 2014, pp. 5983-5989.
6. S. Sakai. Further results on fast computation of a class of hydromechanical system. In Proc. of IFAC Lagrangian and Hamiltonian method for Nonlinear control, 2018, pp. 7-12.
7. Edouard Richard and Jean C. Vivalda. Mathematical analysis of stability and drift behavior of hydraulic cylinder driven by a servovalve. ASME Journal of Dynamic systems, Measurement and Control, 2002, 124(1), pp. 206-213.
8. A. Kugi and W. Kemmetmuller. Impedance control of hydraulic piston actuators. In IFAC Symposium on Nonlinear Control Systems, 2004, pp. 1241-1246.
9. G. Grabmair and K. Schlacher. Energy-based nonlinear control of hydraulically actuated mechanical systems. In Proc. of IEEE CDC, 2005, pp. 7520-7525.
10. P. Y. Li and M. R. Wang. Natural storage function for passivity-based trajectory control of hydraulic actuators. IEEE/ASME Transactions on Mechatoronics, 2014, 19(3), pp. 1057-1068.
11. S. Sakai, and Stefano Stramigioli. Visualization of hydraulic cylinder dynamics by a structure preserving nondimensionalization. IEEE/ASME Transactions on Mechatoronics, 2018, 23(5), pp. 2196–2206.
12. A. J. van der Schaft. L2-Gain and Passivity Techniques in Nonlinear Control. Originally published as volume 218 in the series: Lecture Notes in Control. Springer-Verlag London, London, 2000.
13. K. Zhou, J. C. Doyle, and K. Glover. Robust and Optimal Control. Prentice-Hall, Inc., Upper Saddle River, N.J., 1996.
14. B. Yao, F. Bu, J. Reedy, and G. T.-C. Chiu. Adaptive robust motion control of single-rod hydraulic actuators: Theory and experiment. IEEE/ASME Transactions of Mechatoronics, 2000, 5, pp. 79–91.
15. T. Boaventura, M. Focchi, M. Frigerio, J. Buchli, C. Semini, G. A. Medrano-Cerda, and D. G. Caldwell. On the role of load motion compensation in high-performance force control. In Proc. IEEE/RSJ IROS, 2012, pp. 4066-4071.
16. Jouni Mattila, Janne Koivumaki, Darwin G. Caldwell, and Claudio Semini. A survey on control of hydraulic robotic manipulators with projection to future trends. IEEE/ASME Transactions on Mechatoronics, 2017, 22(2) pp. 669-680.
17. I. Nezu and H. Nakagawa. Turbulence in Open Channel Flows. CRC Press, 1993.
18. W. D. Curtis, J. David Logan, and W. A. Parker. Dimensional analysis and the pi theorem. Linear Algebra and Its Applications, 1982, (47) pp. 117-126.
19. E. Buckingham. On physically similar systems. Physics review, 1931, 4, pp. 354-376.
20. S. Sakai. Casimir based fast computation for hydraulic robot optimizations. In Proc. IEEE/RSJ IROS, 2013, pp. 2874-2881.
21. S. Sakai, K. Osuka, T. Maekawa, and M. Umeda. Robust control systems of a heavy material handling agricultural robot: A case study for initial cost problem. IEEE Transactions on Control Systems Technology, 2007, 15, pp. 1038-1048.

The 11th JFPS International Symposium on Fluid Power HAKODATE 2020 Oct. 12-13, 2021 The Japan Fluid Power System Society

On the Analysis of Energy Behaviors in Hydraulic Cylinder Dynamics via Modeling of Experimental Excavators

Ryo ARAI *, Satoru SAKAI*, Akihiro TATSUOKA**

*Department of Mechanical Engineering, Shinshu University
4-17-1 Wakasato, Nagano city, Nagano, 390-8553 Japan
(E-mail: 20w4001g@shinshu-u.ac.jp, satorus@shinshu-u.ac.jp)
**Mitsubishi Heavy Industries

Abstract. The paper partially discusses an analysis of the nominal model of hydraulic cylinder dynamics. The pump pressure dynamics is especially focused. First, we review hydraulic cylinder dynamics and apply our physical parameter identification method to agriculture scale experimental excavators. Second, we analyze the energy behaviors by one of the Hamiltonians that is different from the previous Hamiltonian with the exponential terms.

Keywords: Hydraulic Machinery, Physical Parameter Identification, Energy, Port-Hamiltonian Theory

INTRODUCTION

Unmanned hydraulic machineries are gaining popularity and a new generation of model based control of hydraulic machinery is coming (e.g., [1][2][3][4][5]). In this paper, we discuss energy behaviors of hydraulic cylinder dynamics which is important for model based control of agriculture scale excavators. In agriculture scale, the most widely used controls are PID or PID-like control. However, model based control has the possibility to achieve better performance than PID control [6][7][8]. Especially, even against modeling errors, the robust control theory such as the port-Hamiltonian theory guarantees robustness [9][10]. In the paper, in agriculture scale, we discuss the experimental, numerical, and analytical energy behaviors of a Hamiltonian in hydraulic cylinder dynamics. The paper has two main results. As the first main result, our previous physical parameter identification method [11][12] is applied to experimental excavators that have a pump pressure dynamics. As the second main result, we discuss the experimental, numerical, and analytical energy behaviors in hydraulic cylinder dynamics from the port-Hamiltonian point of view by one of the Hamiltonians that is different from the previous Hamiltonian with the exponential terms [13].

NONLINEAR NOMINAL MODEL

Let us consider a hydraulic arm whose nonlinear nominal model is a coupling of the hydraulic cylinder dynamics [14] and a pump pressure dynamics defined later. First, the hydraulic cylinder dynamics is described by

$$\left\{ \begin{array}{rcl} \dot{x} &=& f_0(x) + g_0(x)u \\ y &=& x \end{array} \right. \tag{1}$$

with

$$x = [(q_1\ q_2)\ (\dot{q}_1\ \dot{q}_2)\ (p_{+1}\ p_{+2})\ (p_{-1}\ p_{-2})]^{\mathrm{T}},\ u = [u_1\ u_2]^{\mathrm{T}}$$

where the subject $i = 1$ or 2 is the joint number and the subject $+$ or $-$ is denotes the cap side and the rod side. The joint angle $q_i(t)$ [rad], the joint angle velocity $\dot{q}_i(t)$ [rad/s], the cap side pressure $p_{+i}(t)$ [Pa], the rod side pressure $p_{-i}(t)$ [Pa], and the orifice area $u_i(t)$ [m^2] are the functions of time t [s]. The drift term $f_0(x)$ and the input term $g_o(x)u$ are the functions of the state x. Second, the pump pressure dynamics is described by

$$\dot{p}_p(t) \;=\; \frac{b_p}{V_p}\left(Q_p - \sum_{i=1}^{2} Q_i - Q_t\right) \tag{2}$$

where the pump pressure $p_p(t)$ [Pa] and the pump flow rate Q_p [m^3/s] are the function of time. The pump bulk modulus b_p [Pa] and the pipe volume V_p [m^3] are the physical parameter. The input flow rate Q_i [m^3/s] and the tank flow rate Q_t [m^3/s] are the function of the tank pressure $p_t(t)$ [Pa] and approximated by Bernoulli's principle as hydraulic cylinder dynamics.

PHYSICAL PARAMETER IDENTIFICATION AND VALIDATION

In this section, we update our physical parameter identification method [11][12] to agriculture scale excavators. Suppose that $[q_2(t), \dot{q}_2(t), \ddot{q}_2(t), p_{\pm 2}(t), \dot{p}_{\pm 2}(t), p_p(t), \dot{p}_p(t), p_t(t), u_2(t)]$ is obtained at each time $t = t_1, \cdots, t_N$. From the project theorem in Hilbert space [15], the set of the unknown physical parameter $\hat{a}_1$ and $\hat{a}_2$ are identified uniquely as the following values:

$$\hat{a}_1 = (X_{1N}^{\mathrm{T}} X_{1N})^{-1} X_{1N}^{\mathrm{T}} Y_{1N}\ ,\ \hat{a}_2 = (X_{2N}^{\mathrm{T}} X_{2N})^{-1} X_{2N}^{\mathrm{T}} Y_{2N} \tag{3}$$

where the matrices X_{1N}, Y_{1N}, X_{2N}, and Y_{2N} are obtained from the experimental outputs.
The experimental setup consists of an agriculture scale excavator (ZX30U-5A), pipes (PFH06, 3/8 inch), and a servo open-center valve only. The excavator is driven by the servo open-center valve whose the orifice area $u_2(t)$ is measured by a displacement sensor (LP-20F) and a DC servo motor (T720-0.12EL8), a rack and a pinion (reduction ratio 1/25), an AD board (PCI-3155, 16 bit), a control PC (Linux, 3.8 GHz, 4.0 GB), and a DA board (PCI-3325, 12 bit). The outputs of the excavator are a piston displacement measured by a piston displacement sensor (CPP-45-150LS), the cap, rod, pump, and tank pressures measured by the pressure sensors (AP-16S). Since the physical parameter identification is in the off-line case, the time derivative of the piston displacement $\dot{s}_2(t)$ and the cap and rod sides pressures $\dot{p}_{\pm 2}(t)$ are sufficiently estimated via the first difference approximation. In order to identify the physical parameters, the ideal sinusoidal signal $r_2(t) = 100\sin(2\pi 0.5t)$ [m^2] is applied in a period $(t = 2.0 - 20.0)$ [s].

Table 1. Identification result for the nominal numerical simulator.

Symbol	Parameter	Value	Unit
J_2	Moment of inertia	2.3×10^2	$\mathrm{kg \cdot m^2}$
F_{d2}	Damping coefficient	1.3×10^4	$\mathrm{N \cdot s/m}$
F_{c2}	Coulomb friction coefficient	1.3×10^2	N
W_2	Gravity coefficient	1.9×10^2	$\mathrm{kg \cdot m}$
b	Bulk modulus	9.4×10^8	Pa
b_p	Pump bulk modulus	6.0×10^7	Pa
C_{f+2}	Flow gain	4.6×10^{-3}	$\mathrm{m/(s \cdot \sqrt{Pa})}$
C_{f-2}	Flow gain	4.0×10^{-3}	$\mathrm{m/(s \cdot \sqrt{Pa})}$
Ci_2	Internal leakage coefficient	1.3×10^{-11}	$\mathrm{m^3/(s \cdot Pa)}$
Ce_{+2}	External leakage coefficient	4.7×10^{-12}	$\mathrm{m^3/(s \cdot Pa)}$
Ce_{-2}	External leakage coefficient	3.6×10^{-12}	$\mathrm{m^3/(s \cdot Pa)}$
C_{ft}	Tank flow gain	1.1×10^{-2}	$\mathrm{m/(s \cdot \sqrt{Pa})}$

Table 1 shows the results of the identification. All the identified physical parameter values were positive without any restrictions on the sign or value range of the parameters
This section also discusses the validation. First, the nominal numerical simulator is constructed with the physical parameters on the laptop (2.2 GHz, 4.0 GB, MATLAB R2015a, Simulink). Second, by the Adams-Bashforth method (ode113) the numerical outputs are generated by an experimental input $u_2(t)$. Third, the experimental outputs and the corresponding numerical outputs are generated by the same experimental input and are compared with each other. The frequency of the ideal sinusoidal signal for validation is $f = 0.5$ [Hz]. Here the initial state values of the nominal numerical simulator is given from the measured values except the initial piston velocity $\dot{s}_2(t)$ that is not measured but estimated by the just first order differentiation.

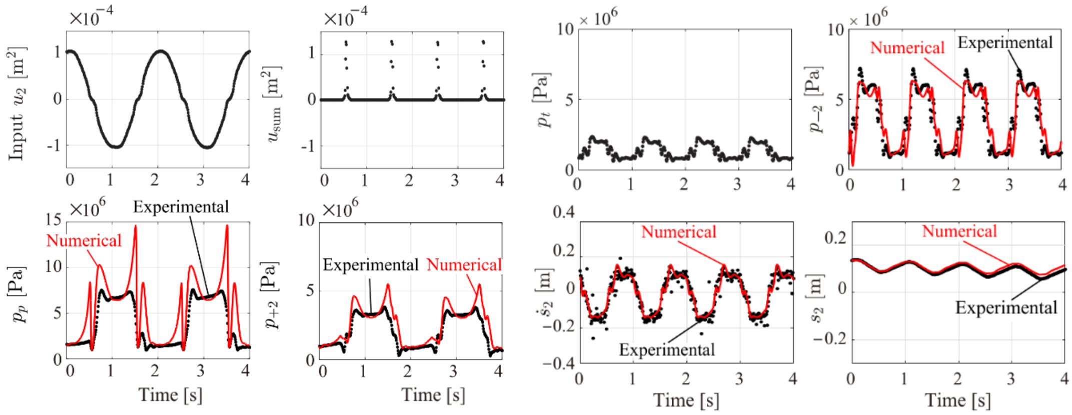

Figure 1. Input and the outputs (Validation, f =0.5 [Hz], Joint 2).

Figure 1 shows the results of the validation. In Figure 1, against modeling errors, not only the cap and rod sides pressures $p_{+i}(t)$ and $p_{-i}(t)$ but also the pump pressure $p_p(t)$ are generated sufficiently. The amplitude error of the pump pressure can be observed but the phase and the number of the peaks were very similar.

ENERGY BEHAVIOR ANALYSIS

In this section, we compare the experimental, numerical, and analytical energy behaviors of the excavator in agriculture scale. One of the most famous representations is the following input-state-output representation [9][10]

$$\left\{ \begin{array}{rcl} \dot{z} & = & (J(z) - R(z))\nabla_z H(z) + g(z)\bar{u} \\ \bar{y} & = & g(z)^{\mathrm{T}}\nabla_z H(z) \end{array} \right. \tag{4}$$

where $z \in \mathbf{R}^n$ is the state, $\bar{u} \in \mathbf{R}^m$ is the input and $\bar{y} \in \mathbf{R}^m$ is the corresponding output. $J(z) = -J^{\mathrm{T}}(z) \in \mathbf{R}^{n \times n}$ is a skew symmetric matrix and $R(z) = -R^{\mathrm{T}}(z) \in \mathbf{R}^{n \times n}$ is a symmetric matrix. The notation ∇_z is the partial derivative with respect to z. In case of hydraulic cylinder dynamics, $H(z)$ are given as:

$$H(z) = \frac{1}{2}J_2\dot{q}_2^2 + V_{+2}(s_2)(-b - p_{+2}) + V_{-2}(s_2)(-b - p_{-2}) - W_2 g\cos(q_{1const} + q_2) \tag{5}$$

which is one of the Hamiltonians and different from the previous Hamiltonian with the exponential terms [13]. For the Hamiltonian in the paper, the first term is the kinetic energy. The second and third terms are the internal energy. The fourth term is the potential energy. The cap and rod side pipe volumes $V_{\pm 2}(s_2)$ are the functions of the piston displacement $s_2(t)$. The moment of inertia J_2, the gravity coefficient W_2, the joint angle q_{1const} , and the gravity acceleration g, and the bulk modulus b are the physical parameters. The time derivative of the Hamiltonian $\dot{H}(z)$ from the port-Hamiltonian point of view is given as:

$$\dot{H}(z) = \nabla_z^{\mathrm{T}} H(z)R(z)\nabla_z H(z) + \bar{y}^{\mathrm{T}}\bar{u}. \tag{6}$$

Now we can compare the experimental, numerical, and analytical time responses of the time derivative of the Hamiltonian $\dot{H}(z)$ of the hydraulic cylinder dynamics with the identified physical parameters. The experimental time responses of the time derivative of the Hamiltonian is derived directly from the measured Hamiltonian and its derivative, while the numerical and analytical time responses of the time derivative of the Hamiltonian are derived indirectly by Equation (6). In the paper, we analyze the two cases, that is, the slowest case $f = 0.5$ [Hz] and the fastest case $f = 1.0$ [Hz].

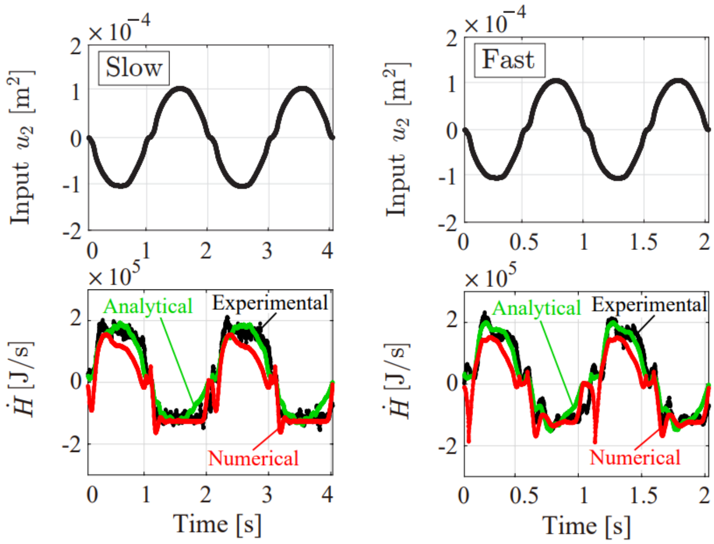

Figure 2. Experimental (black) vs. Numerical (red) vs. Analytical (green) time responses of the time derivative of the Hamiltonian. (Energy behavior analysis, Slow: $f = 0.5$ [Hz], Fast: $f = 1.0$ [Hz]).

Figure 2 shows the experimental, numerical, and analytical time responses of the time derivative of the Hamiltonian in the slow case and fast case. The experimental, numerical, and analytical energy behaviors were close to each other. One of the most important features is the asymmetric behavior of the time derivative Hamiltonian even though input is symmetric in the sense of the standard sinusoidal signal. This asymmetrical behaviors comes from drift of the piston displacement $s_2(t)$ in Figure 1. This result implies that the port-Hamiltonian point of view will be applicable in agriculture scale against modeling errors.

CONCLUSIONS

In this paper, a method for identifying physical parameters of an open-centered multi-degree-of-freedom hydraulic arm is proposed, and the effectiveness of the proposed method is verified by model validation and energy analysis for a 1-DOF real construction machine arm. By calculating the output of the Hamiltonian, the validity of updating the model to the Port-Hamiltonian system of an open-centered hydraulic arm was evaluated. In all, via the experimental, numerical, and analytical energy behaviors, the applicability of the port-Hamiltonian theory is confirmed in agriculture scale against modeling errors. Future work will be to verify the model and with simultaneous motion of two axes, and to analyze the energy.

ACKNOWLEDGMENTS

This work was partially funded by JSPS KAKENHI Grant Number 21K03934. This funding is highly appreciated. The authors are also grateful for the technical help provided by Yusuke Nabana, Yuki Nishimura, and Kazuki Nagai.

REFERENCES

1. Zhang, Q., Basics of Hydraulic Systems, Taylor & Francis, 2008.
2. Huang, Y., Zhang, Q., Agricultural Cybernetics, Springer. 2021.
3. Sakai, S., Iida, M., Osuka, K., Umeda, M., Design and control of a heavy material handling manipulator for agricultural robots, Autonomous Robots, Vol. 25, No. 3, 2008, pp. 189-204.
4. Mattila, J., Koivumaki, D., Caldwell, D. G., Semini, C., A survey on control of hydraulic robotic manipulators with projection to future trends, IEEE/ASME Trans. Mechatronics, Vol. 22, No. 2, 2017, pp. 669-680.
5. Raibert, M., Blankespoor, K., Nelson, G., Playter, R., BigDog, the rough-terrain quadruped robot, In Proceedings of the IFAC World Congress, 2008, pp. 10822-10825.
6. Merritt, H., Hydraulic Control Systems, John Willey & Sons, 1967.
7. Watton, J., Fluid Power Systems, Englewood Cliffs, New Jersey, USA, 1989.
8. Mohieddine, J., Andreas, K., Hydraulic Servo-Systems, Springer, 2003.
9. Duindam, V., Macchelli, A., Stramigioli, S., Bruyninckx, H., Modeling and Control of Complex Physical Systems: The Port-Hamiltonian Approach, Springer, 2009.
10. van der Schaft, A. J., L_2-gain and passivity techniques in nonlinear control, Springer-Verlag, 2000.
11. Maeshima, Y., Sakai, S., Nakanishi, M., Osuga, K., A Base Parameter Identification Method and Model Validation for Hydraulic Arms, Journal of JFPS, Vol. 43, No. 1, 2012, pp. 16-21.
12. Sakai, S., Maeshima, Y., A New Method for Parameter Identification for N-DOF Hydraulic Robot, In Proceedings of IEEE International Conference on Robotics and Automation (ICRA), Hong Kong, China, 2014, pp. 5983-5989.
13. Arai, R., Sakai, S., Tatsuoka, A., Zhang, Q., Analytical, Experimental, and Numerical Investigation of Energy in Hydraulic Cylinder Dynamics of Agriculture Scale Excavators, Energies, submitted.
14. Sakai, S., Stramigioli, S., Visualization of Hydraulic Cylinder Dynamics by a Structure Preserving Nondimensionalization, IEEE/ASME International Transactions on Mechatronics, Vol. 23, No.5, 2018, pp. 2196-2206.
15. Luenberger, D., Optimization by vector space method, Wiley interscience, 1968.

Organized Session | Organized session

Aqua Drive 1

[OS4-1-01] Consideration of Thermal Stability of the Ultra-Precision Water-Lubricated Spindle

○Dmytro Fedorynenko[1], Yohichi Nakao[2] （1.Tohoku University, 2.Kanagawa University）

[OS4-1-02] Multidisciplinary Design Optimization of a Tortuous Path Trim for a Labyrinth Control Valve

○Runlin Gan[1], Xukang Li[1], Song Liu[1], Baoren Li[1] （1.Huazhong University of Science &Technology, FESTO Pneumatic Technology Center）

[OS4-1-03] Design of Magnetostrictive Power Generation Device from Pulsating Pressure in Hydraulic Pipeline by Using Water Hydraulic Cylinder

○Kaito Miyashita[1], Shouichiro IIO[1], Tsuyoki TAYAMA[2], Ryuichi ONODERA[2], Shyota ABE[2] （1.Shinshu University, 2.Tohoku Steel Co., Ltd.）

[OS4-1-04] Flow Characteristics of a Cavitating Jet through a Small Rectangular Orifice with Different Aspect Ratios

○Hironori Takei[1], Kohei Terakawa[1], Shouichiro Iio[1], Kotaro Takamure[2], Tomomi Uchiyama[2], Futoshi Yoshida[3] （1.Shinshu University, 2.Nagoya University, 3.KYB Corporation）

The 11th JFPS International Symposium on Fluid Power HAKODATE 2020 Oct. 12-13, 2021 The Japan Fluid Power System Society

Consideration of Thermal Stability of the Ultra-Precision Water-Lubricated Spindle

Dmytro FEDORYNENKO*, Yohichi NAKAO**

* Department of Aerospace Engineering, Tohoku University
6-6-01 Aramaki-Aza-Aoba, Aoba-ku, Sendai, 980-8570 Japan
(E-mail: fedorynenko.dmytro.b3@tohoku.ac.jp)
** Department of Mechanical Engineering, Kanagawa University
3-27-1 Rokkakubashi, Kanagawa-ku, Yokohama 221-8686, Japan
(E-mail: nakao@kanagawa-u.ac.jp)

Abstract. In this study, the thermal stability of the spindle with water-lubricated hydrostatic bearings was investigated via simulation. The simulation study was divided into two separate tasks. As the first stage, the temperature distribution in the flowing part of spindle bearings was determined utilizing the SolidWorks Flow Simulation. The experimentally gathered temperature of lubricant and spindle surfaces was used as boundary conditions for a finite volume problem. Then, the thermal analysis of the spindle was performed using the obtained temperature field in the first stage. The pattern of gap variation in journal and thrust bearings due to the thermal deformation of bearing surfaces was established. The thermal stability of a spindle under the influence of an external temperature field is analyzed using a bearing film force and stiffness as indicators.

Keywords: water-lubricated bearing, thermal deformation.

INTRODUCTION

Thermal deformation of ultra-precision spindles is the main limiting factor for improving machining accuracy and productivity. The primary sources of heat in machine tool spindles are bearings. Aerostatic and hydrostatic spindle bearings are widely used for ultra-precision machine tools [1]. High thermal stability at high speeds is the main benefit of aerostatic bearings. However, they have very low damping and stiffness characteristics compared to oil bearings. Oil hydrostatic bearings are advantageous for ultra-precision spindles in terms of achieving high accuracy of machining. When lubricating oil hydrostatic bearings, power losses due to oil flow cause heat generation, especially at high speeds [2]. The pressure power losses are caused by the pressure drop in the bearing supply system and cannot be avoided. The power losses on viscous friction, especially at high speeds, lead to the temperature rise of lubricating fluid and, consequently, to spindle deformation. Accordingly, it decreases machining accuracy.

In contrast to oil, water has relatively low viscosity, higher specific heat, and thermal conductivity. Thus, it is considered that higher thermal stability can be achieved by using water as lubricating fluid for ultra-precision spindles. A spindle with water-lubricated hydrostatic bearings was proposed to cope with the disadvantage of both the aerostatic and oil hydrostatic bearings [3]. Static characteristics and dynamic behavior of the water-lubricated spindle were then studied [4]. The patterns of the change in a spindle temperature field and the thermal stability of spindles with different rated rotational speeds were experimentally investigated [5]. However, the influence of thermal deformations on the water-lubricated spindle accuracy has not been thoroughly investigated yet.

This paper aims to investigate the influence of thermal deformations on the thermal stability of the water-lubricated spindle. The simulation studies reveal the influence of the thermal deformations on the linear expansion of the spindle bearing surfaces, the gap change in bearings, and their stiffness.

STRUCTURE OF THE WATER-LUBRICATED SPINDLE

The investigated ultra-precision spindle with water-lubricated hydrostatic bearings [5] is schematically presented in Fig. 1. The spindle has four recessed journal bearings and four recessed opposed-pad thrust bearings with short pipe restrictors for each recess. The mentioned restrictors are designed and installed to achieve the highest static stiffness for water-lubricated bearings [5]. The thrust bearing has an outer diameter of 89 mm and an inner diameter of 51 mm. The nominal gap size in the thrust bearing is 10 μm. Journal bearings are located at both ends of the rotor. The journal diameter and the journal bearing's axial length are 50 mm and 49 mm, respectively. The nominal gap size in the journal bearing is 12 μm.

The spindle rotor is made of stainless steel. Diamond-like carbon is plated onto the outer surfaces of the rotor and the inner surfaces of the casing to prevent undesirable contact between them during spindle rotation [5]. The rated supply pressures are 2.5 MPa and 2.1 MPa for journal and thrust bearings, respectively. The highest rotational speed of the spindle is 3000 min^{-1}.

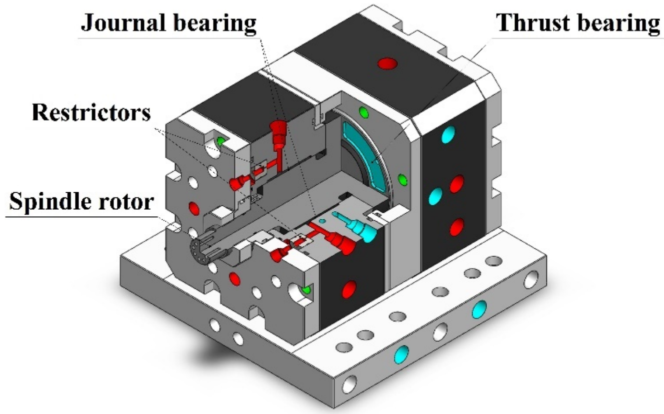

Figure 1. Structural Diagram of Water-Lubricated Hydrostatic Spindle

LUBRICATION TEMPERATURE FIELD

Temperature distribution and the resultant deformation of the spindle are keys of importance to develop an effective temperature control technique aimed at achieving higher thermal stability of the ultra-precision spindle. Temperature changes of the water flow and spindle have been evaluated via calculations and experiments. A commercially available CFD is used for solving a heat transfer task in the spindle with internal fluid flow. The temperature distribution inside a spindle-flowing part was derived by numerical simulation using experimentally obtained data as boundary conditions to enhance the validity and accuracy of numerical analysis.
The simulations were carried out in two stages. At the first stage, the temperature field of lubrication in the spindle was determined using the SolidWorks Flow Simulation, including heat transfer to a solid body. The data obtained experimentally were used as the initial and boundary conditions: inlet water temperature, supply pressure, and outlet flowrate (Tab. 1). As the outer wall temperature and initial solid temperature, the experimentally obtained outer casing temperature and outer rotor temperature were taken, respectively. Finally, experimentally gathered values of the outlet water temperature were used to evaluate the accuracy of numerical simulation.

Table 1. Boundary Conditions

Inlet Parameters	
Supply water temperature, [°C]	23.72
Supply pressure (journal bearing), [MPa]	2.5
Supply pressure (thrust bearing), [MPa]	2.1
Outlet Parameters	
Total water flowrate, [l/min]	4.2
Additional Parameters	
Outer wall temperature, [°C]	23.93
Initial solid temperature, [°C]	22.88
Surface roughness, [μm]	0.8

Figure 2 presents the water temperature distribution on the bearing surfaces of a left journal bearing and the left side of an opposed-pad thrust bearing, as it is depicted in a cross-section view in Fig. 1. High fluid temperature is formed on bearing lands achieving the maximum value of 24.9 °C on inter-recess lands of the thrust bearing. This phenomenon is due to a relatively small gap in the thrust bearing resulting in temperature rise when liquid flows under pressure through narrow slots between recesses. On the contrary, the minimum temperature of lubricant is observed in such areas of a bearing as recesses (24.33 °C) and drainage channels (24.21 °C) due to their relatively high depth comparable to lands.

THERMAL ANALYSIS OF SPINDLE

At the second stage, the thermal analysis of the spindle was performed employing the SolidWorks Simulation. The mentioned analysis was aimed at defining the spindle displacement caused by thermal deformations. The influence of the rotor deformation caused by an external load and water pressure in bearing recesses did not consider this stage. The temperature field on the spindle surfaces obtained at the first stage was used as the boundary conditions of a finite element problem. The initial solid temperature (T_s=22.88 °C), defined at the first stage when flow simulation, is further used as the reference temperature at zero thermal strain for thermo-elastic analysis. It is established that the spindle rotor ends elongate by around 2.7 μm due to the influence of thermal deformations. Consequently, the pointed rotor deformation affects the positioning accuracy of a clamping device, thereby deteriorating the machining accuracy of linear dimensions of a workpiece.

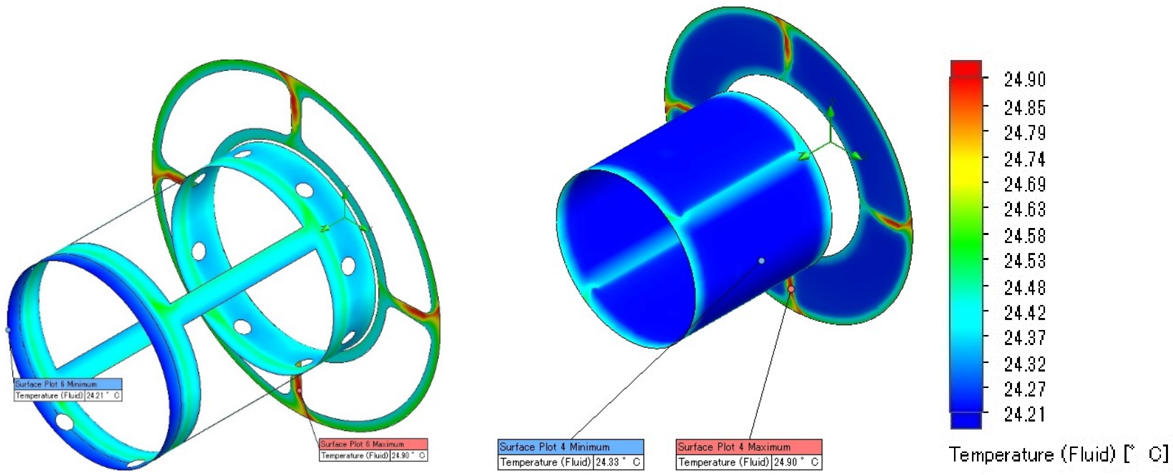

(a) (b)

Figure 2. Fluid Temperature Distribution on the Bearing Surfaces of the Casing (a) and Rotor (b)

The thermal deformation of bearing surfaces results in the change of initial design gaps for the journal and thrust bearings. A thrust gap variation resulting from the thermal deformation is shown in Fig. 3, (a). The gap variation from the initial (design) gap size of 10 μm is represented in a circumferential direction along two diameters of the thrust bearing surfaces: the lowest (inner) and the highest (outer) positions. It is established that the highest thermal displacements are taken place at the thrust inner diameter. On average, the mentioned gap size decreases by around 14 % compared to its design value. Minor deviations up to 0.12 μm of the thrust gap from average values (dashed lines in Fig. 3, (a)) are observed along the bearing circumferential direction at both inner and outer positions. On the contrary, in the radial bearing direction, the average gap variation picks 0.26 μm as depicted in Fig.3, (a).

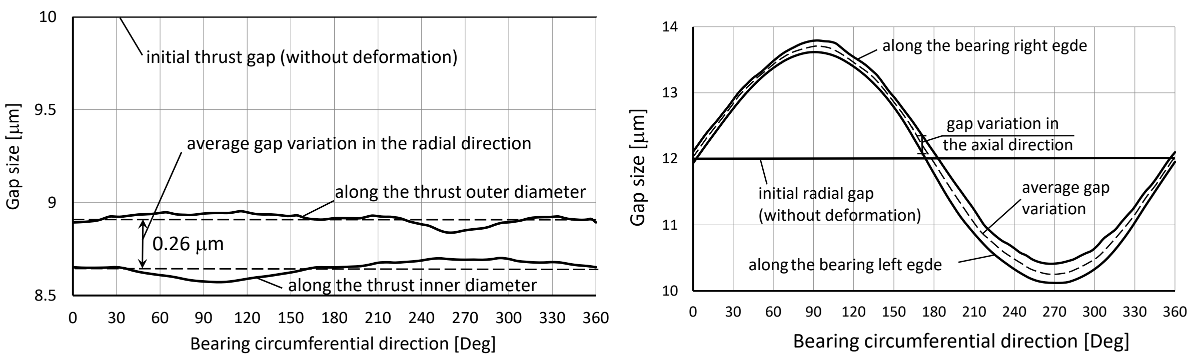

(a) (b)

Figure 3. Gap Variation in the Thrust (a) and Journal (b) Bearings Caused by Thermal Deformations

The thermal deformation of bearing surfaces also leads to the significant variation of the radial gap in the journal bearing (Fig. 3, (b)). Unlike the deformation pattern in the thrust bearing, the conjugated journal surfaces' thermal displacements cause an alternate decrease and increase in the radial gap against the initial (design) gap value of 12 μm. Note that the average gap variation in the axial direction in the journal bearing is relatively minor, reaching a value of 0.22 μm. The primary influence on the bearing gap size for both the thrust and journal bearings is caused by the thermal deformation of the bearing casing. Moreover, the deformation causes the form deviation of bearing surfaces: flatness deviation for thrust bearing surfaces and roundness deviation for journal surfaces.

INFLUENCE OF THERMAL DEFORMATION ON SPINDLE CHARACTERISTICS

This section presents the influence of bearing gap variation on a spindle film force and stiffness.
As shown in Fig. 4, (a), the thrust bearing surface's thermal deformation causes a decrease in both bearing film force and stiffness. This phenomenon is due to the bearing surfaces' thermal expansion, causing a decrease in the gap and, consequently, to an increase in recess pressure. While a supply pressure is keeping constant, this results in increasing the pressure ratio β between supply p_s and recess pressure p_r ($\beta = p_r/p_s$) and thus causes a decrease in the film force and stiffness for an opposed-pad thrust bearing.

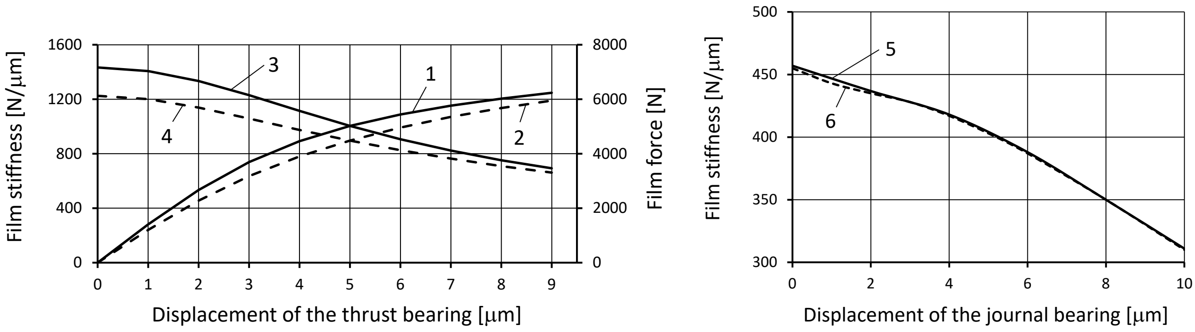

(a) (b)

Figure 4. Thrust Bearing Film Force (curves 1, 2) and Stiffness (curves 3, 4) vs Thrust Bearing Displacement (a) and Journal Bearing Film Stiffness vs Journal Bearing Displacement (curves 5, 6) (b): Solid Curves Correspond to a Bearing without Thermal Deformation; Dashed Curves – Bearing Surfaces Subjected to Thermal Deformation

The effect of non-uniformity of the gap on the journal bearing's output characteristics was then investigated. The non-uniformity of the radial gap leads to the redistribution of pressures in bearing recesses and forming the change in a resultant force supporting a rotor. As a result, the rotor is shifted to a new equilibrium position along the vertical axis by 1.726 μm under the influence of the unbalanced film force. Accordingly, this affects the accuracy of machining diametrical dimensions of the workpiece. Then, the influence of thermal deformation on the stiffness of the journal bearing is investigated and presented in Fig. 4, (b). The thermal effect decreases the stiffness of the journal bearing, but a comparative glance between curves 5 and 6 shows only a little quantitative difference in the stiffness. For example, in the range of the journal bearing displacement up to 1 μm, a decrease in stiffness does not exceed 0.5%.

CONCLUSION

The present study considered the influence of thermal effect on a machine tool spindle with water-lubricated hydrostatic bearings. The study shows that when thermal effects account for, both the film force and stiffness decrease. However, this trend is quantitatively different for spindle bearings: it is relatively minor for the recessed journal bearings, and it causes the stiffness drop up to 14% for the opposed-pad thrust bearings. This also contributes to the decrease in the accuracy of linear dimensions of machined parts.

ACKNOWLEDGMENTS

The presented results are a part of projects Invitational Fellowships for Research in Japan and Grant-in-Aid for Scientific Research (C) of the Japan Society for the Promotion of Science.

REFERENCES

1. WARDLE F., Ultra Precision Bearings, 1st ed. Woodhead Publishing, 2015.
2. FEDORYNENKO D, et al., Increasing of Energy Efficiency of Spindles with Fluid Bearings, Acta Mechanica et Automatica, 2017, Vol. 13, No. 3(41), pp. 204-209.
3. NAKAO Y., et al., Feasibility Study on Design of Spindle Supported by High-Stiffness Water Hydrostatic Thrust Bearing, International Journal of Automation Technology, 2014, Vol. 8(4), pp. 530-538.
4. FEDORYNENKO D, at al., Dynamic characteristics of spindle with water-lubricated hydrostatic bearings for ultra-precision machine tools, Precision Engineering, 2020, Vol. 63, pp. 187-196.
5. NAKAO Y, et al., Thermal Characteristics of Spindle Supported with Water-Lubricated Hydrostatic Bearings, Int. J. Automation Technol., 2019, Vol.13, No.5, pp. 602-609.

The 11th JFPS International Symposium on Fluid Power HAKODATE 2020 Oct. 12-13, 2021 JFPS The Japan Fluid Power System Society

Multidisciplinary Design Optimization of a Tortuous Path Trim for a Labyrinth Control Valve

Runlin GAN*, Xukang LI, Song LIU, Baoren LI

* FESTO pneumatic Technology Center, Huazhong University of Science & Technology,
Luoyu Road 1037, Wuhan, 430074, China
(E-mail:grlhappy@126.com)

Abstract. The labyrinth control valve has the advantages of low noise, low vibration, low flow velocity, good cavitation resistance, and long maintenance intervals. It is widely used in petrochemical, nuclear energy and electric power industries. A multi-disciplinary and multi-objective optimization design framework for the realization of labyrinth flow control valve discs is proposed, and the results of flow field analysis and stress analysis are used as design evaluation index. Based on the design premise of the flow rate, the optimization of the system aims to reduce the maximum velocity of the media and the stress of the disc. From the perspective of fluid and structure, the presented method has important practical significance to improve the research level of labyrinth flow control valves.

Keywords: Multidisciplinary optimization, NSGA-II, Labyrinth valve

INTRODUCTION

In the industrial automation fluid control system, the control valve is one of the widely used fluid control equipment that used to adjust the system parameters such as flow, pressure and temperature. The work performance directly affects the production quality of the product and the benefit of the enterprise, and has great significance in the entire industrial process system. With the technology and the large-scale industrial production field improvement, enterprises have continuously expanded their demand for control valves. The industrial process parameters have increased accordingly. The labyrinth control valve has put forward requirements for high pressure drop, high temperature, high pressure, low vibration and low noise [1-2].

Up to now, there are quite a few documents related to the improvement of the structure of the labyrinth flow control valve. For example, Miller et al. [3] determined the outlet kinetic energy of the throttle plate as an important parameter for evaluation the flow control valve based on engineer practice experience, and believed that the outlet kinetic energy of the labyrinth channel should not exceed 275kpa in multi-phase flow. Tae-sig et al. [4] analyzed the flow characteristics in a single labyrinth channel at different expansion angles. The results showed that the larger the rotation angle, the greater the pressure gradient. Na et al. [5] reduced the flow resistance and increased the flow coefficient through added connect grooves in the labyrinth disc.

The relationship between the various parameters is coupled with each other. Univariate analysis takes a long time and inefficient, and it is impossible to obtain the optimal structure and performance parameters from a global perspective. Therefore, relevant scholars have conducted the research on multi-objective optimization. Corbera et al. [6] optimized the structure of the butterfly valve based on topology optimization and genetic algorithm to obtain a light butterfly valve disc that satisfies the structural safety and flow requirements. Laudon et al. [7] proposed a method to optimize the flow of the Tesla valve. The design was optimized through determined the complete optimization design parameters of the valve and combined the related optimization algorithms. Based on the computer-aided and multi-objective optimization method, Ganesh et al. [8] carried out a parameterized design on the valve plate of the axial piston pump, the fluid noise and structural noise was reduced, and the effectiveness of the optimization process was proved through experiments. It is necessary to study the multi-objective optimization method of the labyrinth valve to obtain better flow field and mechanical performance.

This paper proposes the application of an optimization method, based on the NSGA-II algorithm for the multi-objective optimization solution of the flow velocity and stress of the labyrinth control valve under the restrictions of the flow rate and the structure sizes. In order to achieve the goal, the main influence parameters that affect the flow characteristics and stress characteristics of the disc is analyzed, and parametric modeling is carried out. Then, combined with CFD and FEM software to analyze the flow field and stress field respectively. Based on NSGA-II algorithm to optimize the target.

MATHEMATICAL MODEL

To describe the flow phenomenon in the labyrinth valve, the standard k-ε turbulence model and the incompressible flow model are adopted in ANSYS Fluent. The continuity, momentum equations to be solved are:
Continuity equation:

$$\frac{\partial(\rho)}{\partial t}+\nabla\bullet(\rho U)=0. \quad 1)$$

In the formula, ρ is the density, kg/m^3. U is the velocity vector. ∇ is the Hamilton operator.
Momentum equation:

$$\frac{\partial(\rho u_i)}{\partial t}+\nabla\bullet(\rho u_i\vec{u})=-\frac{\partial p}{\partial i}+\frac{\partial(\tau_{xi})}{\partial x}+\frac{\partial(\tau_{yi})}{\partial y}+\frac{\partial(\tau_{zi})}{\partial z}+\rho f_i. \quad 2)$$

In the formula, p represents the static pressure of the medium, Pa. f_i represents the force of gravity along diverse directions, m/s^2. τ represents the viscous tensor, Pa.
The Zwart-Gerber-Belamri cavitation model based on transport-equation is used in numerical simulation. The mass transport equation is given as follows:

$$\frac{\partial(\alpha\rho_v)}{\partial t}+\nabla\bullet(\alpha\rho_v\vec{U})=R_e-R_c. \quad 3)$$

$$R_e=F_v\frac{3\alpha_{nuc}(1-\alpha_v)\rho_v}{\rho R_B}\left(\frac{2}{3}\frac{|P_v-P|}{\rho_l}\right)^{\frac{1}{2}}. \quad 4)$$

$$R_c=F_c\frac{3\alpha_v(1-\alpha)\rho_v}{\rho R_B}\left(\frac{2}{3}\frac{|P_v-P|}{\rho_l}\right)^{\frac{1}{2}}. \quad 5)$$

Where R_e and R_c are the mass transfer source terms between the liquid and vapor phase in cavitation. α_{nuc} is the nucleation site volume fraction. ρ_l and ρ_v are the density of liquid and vapor. $\vec{U}$ is the velocity of the vapor phase. R_B is the radius of bubble. P_v represents the saturated liquid vapor pressure in 300K and P is the local fluid pressure. F_v and F_c represent the evaporation and condensation coefficient in cavitation.

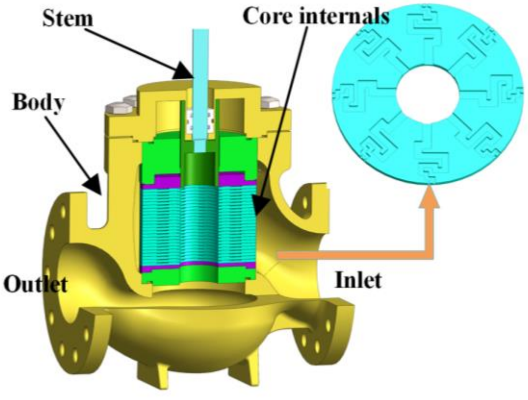

Figure 1. The structure of the labyrinth control valve

COMPUTATIONAL MODEL

Since the valve core of labyrinth control valve bears the main pressure drop and plays a major role in the fluid pressure and velocity variations, only the inlet and outlet accessories of the labyrinth disc flow channels are considered in the calculation. Considering the symmetry of the valve plate, 1/8 of the flow channel in Fig.1 is selected as the calculation model.
The inlet surface and the outlet surface are provided as smooth and no-slip walls. The working conditions of fluid analysis are shown in Table.1. Considering the phenomenon of cavitation, the medium is composed of water and water vapor. The inlet pressure is 10.0MPa and outlet pressure is 2.0MPa. The temperature is 300K and there is no heat transfer. Standard k-ε turbulence model is adopted. The material of the labyrinth disc is stainless steel and

the yield stress is 250MPa. Reference to the industrial valve pressure test (ISO5028), apply a pressure of 15MPa to all positions on the inner wall of the valve, and limit the axial displacement of the labyrinth disc.
The grids of these areas have been divided, as shown in Fig.2. The number of grids affects calculation accuracy and efficiency, and the grid sensibility analysis is performed. When mesh number varies from 101,232 to 1,223,599, the flow rate of the labyrinth control valve is calculated. It can be seen from Fig.3 that the mesh number 766,722 is appropriate.

Table 1. The working conditions

Working condition	
Valve diameter (mm)	100
Upstream pressure (MPa)	10.0
Downstream pressure (MPa)	2.0
Temperature (K)	300
Flow rate (m^3/h)	≥150
Phase 1 medium	Water
Phase 1 density (kg/m^3)	998.2
Phase 1 dynamic viscosity (kg/(m·s))	0.001003
Phase 2 medium	Water-vapor
Phase 2 density (kg/m^3)	0.5542
Phase 2 dynamic viscosity (kg/(m·s))	0.0000134
Stainless steel	
Young modulus	189GPa
Yield stress	270MPa

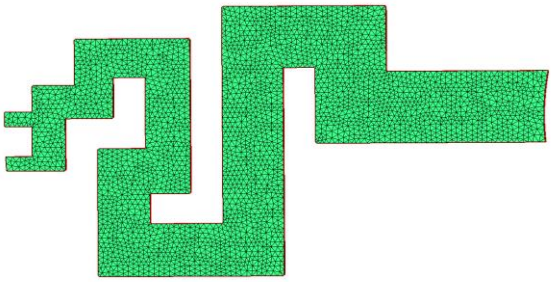

Figure 2. Mesh of the labyrinth control valve

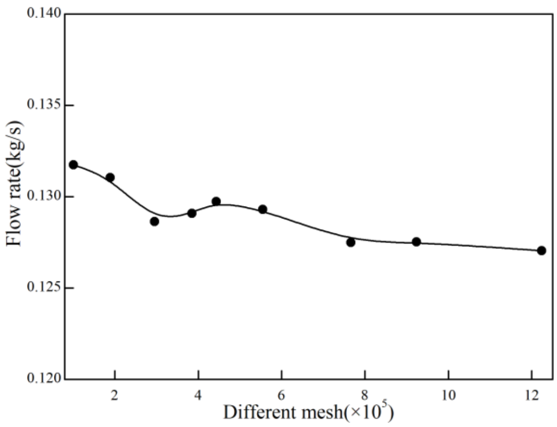

Figure 3. Grid sensibility analysis

DESIGN DESCRIPTION

Miller et al. [3] proposed the valve trim outlet speed and kinetic energy limit criteria, the multi-phase flow outlet kinetic energy under various working conditions cannot exceed 275kpa. Otherwise noise and vibration will be generated, so the fluid speed is selected as the design variable one. At the same time, considering the influence of the labyrinth channel structure on the safety of the disc structure design, the stress of the disc is taken as another design variable. In this paper, the maximum velocity of the flow channel and the stress of the structure are optimized simultaneously under the constraints of flow rate and structure sizes. In this case, the NSGA-II optimization algorithm is used for path optimization. The optimization problem of the labyrinth control valve can be defined as the following equation:

$$\begin{cases} \textit{Minimized}：V(x),S(x) \\ \textit{Subjected}：Q(x) \geq \textit{Flowrate} \\ x \in C(x) \end{cases} \tag{6}$$

Where $V(x)$ is the maximum velocity in the fluid path, $S(x)$ is the maximum stress in the labyrinth channel structure, and $Q(x)$ is the flow rate. $x = [x_1, x_2, \ldots, x_n]$ is the variable element group, and $C(x)$ is the value range.
For incompressible fluids, under the premise of constant flow rate, the flow velocity of the medium is inversely proportional to the size of the flow area. The larger the flow area, the smaller the flow velocity. When the flow area of the flow channel is constant, the effective flow area will be reduced and the flow velocity will increase

due to the "occupy" effect of the vortex in the flow channel. Therefore, the width of the labyrinth channel should be expanded step by step along the flow direction, which can effectively control the speed of the incompressible fluid.

The cross-sectional structure of a single labyrinth flow channel is shown in the Fig.4. The depth direction of the flow channel is perpendicular to the paper surface, and the depth is constant along the flow direction. The width of the flow channel entrance is W_1. The form expands step by step along the flow direction, and the width at number n is $W_n=W_{n-1}\times R$. R is the expansion coefficient and n is the number of quarter turn. Meanwhile, H is the depth of the flow. L_1, L_2, L_3 are the length of the transition part, and $L_1=L_2=L_3$. C_1 is the size of the chamfer. Considering the structure characteristics, the range of parameter values are defined in Table 2. In additional, the number of valve disc and the flow channel in each valve disc are also determined. There are 24 discs inside the inner core and each disc has 8 flow channels.

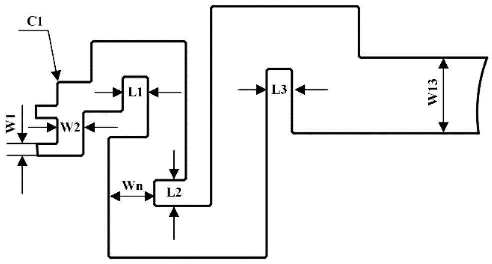

Figure 4. Chosen design parameters for flow path optimization

Table 2. Design parameters for flow path optimization

Parameters(mm)	Initial value	Lower boundary	Upper boundary	Optimized value
W_1	1.264	1	2	1.40
H	1.611	1	3	1.716
L_1	2.591	1	3	2.975
C_1	0.255	0.1	0.5	0.305
R	1.083	1	1.2	1.005

OPTIMIZATION ANALYSIS AND RESULTS

This article has two optimization goals, for multi-objective optimization problems, there is no unique optimal solution in theory, but a set of optimal solutions called Pareto. According to the actual demand, select the appropriate result from the Pareto optimal solution.

The population size, number of iterations, number of variables, and the number of objective functions all affect the optimization effect of the NSGA-II algorithm. The small number of populations and the iterations lead to local optimal solutions and error solutions. A large number of populations and iterations improve the optimization effect. However, it also leads to a decrease in calculation efficiency. In this paper, the population size is 30 and the number of iterations is 20. The first 40 sample points are obtained through the Optimal Space-Filling (OSF) method. The maximum allowable Pareto percentage is 95 and the convergence stability percentage is 2.

Fig.5 is the evolution curve of the overall optimization iteration. It shows that after 10 iterations, the maximum allowable Pareto percentage has reached 96.67, and the convergence stability percentage has reached 6.63. Compared with the initial setting conditions, the number of iterations is saved by 50.70%.

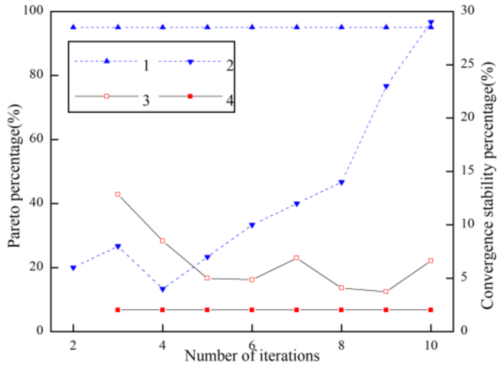

Figure 5. The number of iterations (1. Maximum allowable Pareto percentage=95, 2. Pareto percentage, 3. Stability percentage, 4. Convergence stability percentage=2)

Fig.6 is the set of all solution sets. Based on the correlation Pareto optimal ranking, two candidate points are selected. Candidate points 148, 278. The flow rate difference of the two candidate points is not big. The maximum velocity of candidate points 148 has a greater advantage, although its maximum stress value is slightly increased compared to the candidate point 278. But at the temperature of 300K, the maximum yield strength of the disc is 270MPa, and the safety factor of the candidate point is 3.26, which is much higher than the 1.5 value of the general design. Within the stress range of the disc, the maximum velocity of the flow channel should be reduced as much as possible to reduce vibration and noise. Therefore, candidate point 148 is selected as the optimization result from the two candidate points.

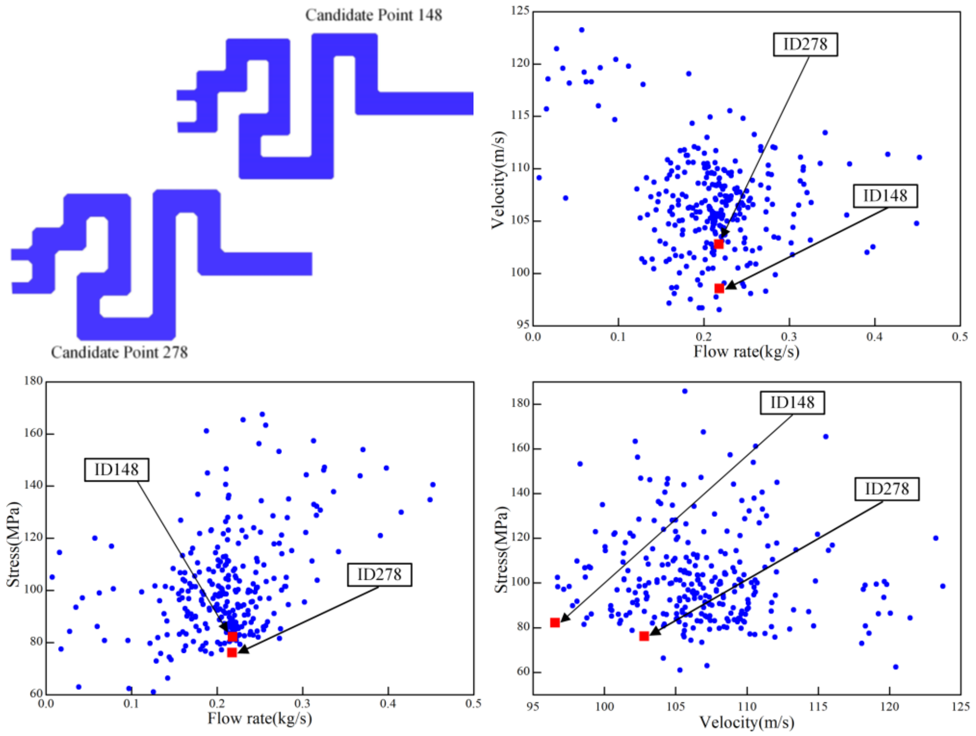

Figure 6. Best two solutions of the optimization process and their position along the all results.

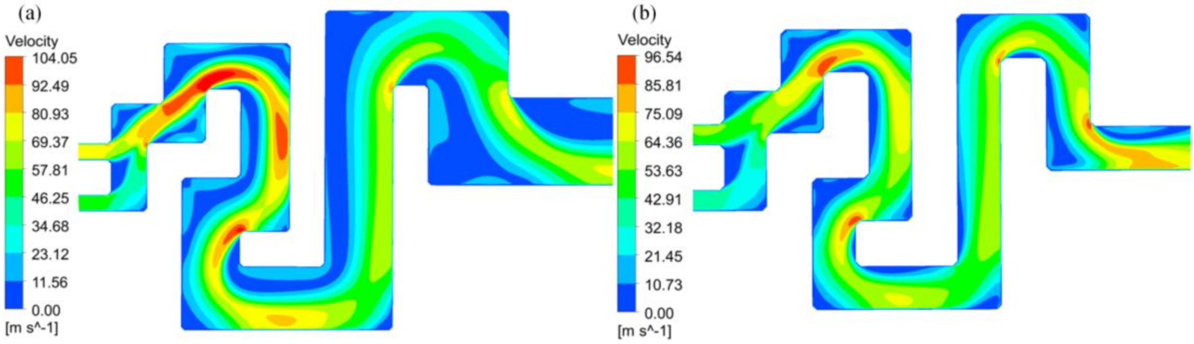

Figure 7. Comparison of the velocity between different valve plate design

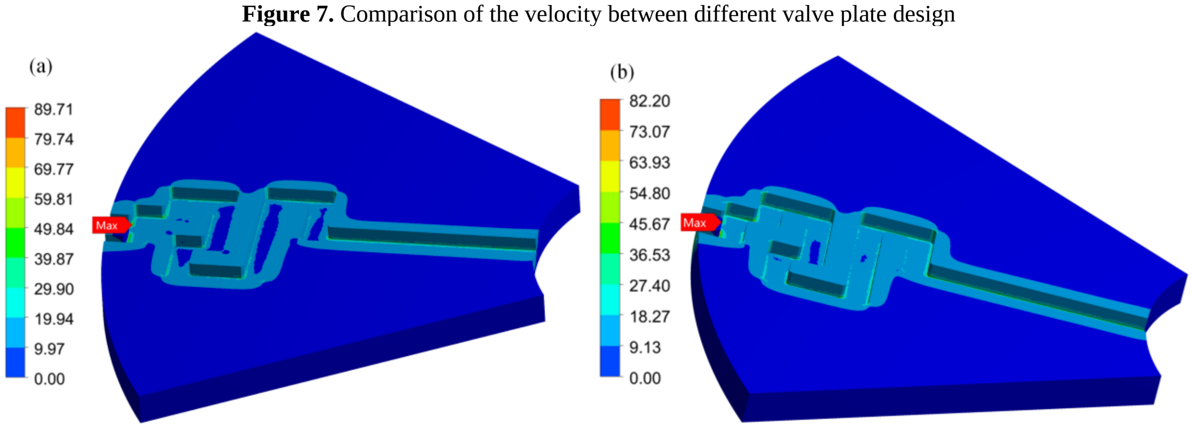

Figure 8. Comparison of the stress between different valve plate design

Table 2 compares the original values with the optimized values. After the flow path optimization process, Fig.7 and 8 show the comparison between the initial design structure and the optimized design structure in terms of fluid performance and disc stress distribution. Before optimization, the high flow velocity mainly appeared in the first few turns of the labyrinth channel. At the same time, due to the large expansion coefficient *R*, it can be seen from Fig.7(a) that a considerable part of the flow channel has a low velocity, indicating that the flow in the flow channel is uneven and the space utilization rate is insufficient. It can be seen from Fig.7(b), after optimized, the proportion of high velocity areas is significantly reduced. The flow in the back section of the runner is more uniform. It can be seen from Fig.8(a) and (b) that the maximum stress basically appears at the corner of the labyrinth channel, where stress concentration is easy to occur, and it needs to pay attention in design. Table 3 shows the performance improvement between the initial structure and the optimized structure. The flow rate is 150.68m^3/h, which meets the design flow rate. Compared with the initial structure flow rate 154.83m^3/h, there is little change. The maximum velocity is decreased from 104.10m/s to 96.54m/s, which is reduced by 7.26%. The maximum stress is 82.20MPa. Compared with the initial design, the maximum stress is 89.71MPa, which is increased by 8.37% after optimization.

Table 3. Objective improvement results

Parameter	Initial design	Optimized design	Improvement (%)
Flow rate (m^3/h)	154.83	150.68	-2.68
Velocity (m/s)	104.10	96.54	7.26
Stress (MPa)	89.71	82.20	8.37

CONCLUSIONS

In order to obtain the best flow field parameters, a parametric model of the labyrinth valve is established. The labyrinth valve system is decomposed into two goals of flow field and structural strength, which realizes the integration of parametric modeling, finite element analysis and multi-objective optimization. The optimization results show that, on the premise of ensure the flow rate, the maximum velocity of fluid path is decreased. At the same time, the stress of the disc structure is reduced, and its safety and reliability are improved. From the perspective of fluid and structure, the realization of multidisciplinary design optimization and multi-objective have important practical significance to improve the research level of labyrinth flow control valves.

ACKNOWLEDGMENTS

The authors would like to acknowledge the support of FESTO Pneumatics Center in HUST.

REFERENCES

1. KWON W C., KIM G R., PARK S C., et al., Design of a tortuous path trim for a high-pressure turbine bypass valve, Proceedings of the Institution of Mechanical Engineers Part E Journal of Process Mechanical Engineering, Vol.224, No.2, 2010, p.149-153.
2. YONEZAWA K., OGAWA R., OGI K., et al., Flow-induced vibration of a steam control valve, Journal of Fluids & Structures, Vol.35, 2012, p.76-88.
3. MILLER HL., STRATTON LR. Fluid Kinetic Energy as a Selection Criteria for Control Valves, ASME Fluids Engineering Division Summer Meeting, 1997, pp.1-8.
4. TAE-SIG G., KUISOON K. The Effect of Divergence Angle on the Control Valve Trim Characteristics, The KSFM Journal of Fluid Machinery, Vol.16, No.1, 2013, p.32-39.
5. LV Z., Na Z., JING H., et al., Study on the improvement of flow characteristics for the optimal design of minimum flow valve with labyrinth channel, 6th International Symposium on Fluid Machinery and Fluid Engineering, 2014, pp.1-4.
6. CORBERA S., OLAZAGOITIA J L., Lozano J A. Optimization of a butterfly valve disc using 3D topology and genetic algorithms. Structural and Multidisciplinary optimization, Vol.56, 2017, p.941-957.
7. TRUONG TQ., NGUYEN NT. Simulation and optimization of tesla valves. Nanotechnology Conference and Trade Show, Vol.1, 2003, p.178-181.
8. SEENIRAJ G K., IVANTYSYNOVA M. A Multi-Parameter Multi-Objective Approach to Reduce Pump Noise Generation, International Journal of Fluid Power, Vol.12, No.1, 2011, p.7-17.

The 11th JFPS International Symposium on Fluid Power HAKODATE 2020 Oct. 12-13, 2021 JFPS The Japan Fluid Power System Society

Design of Magnetostrictive Power Generation Device from Pulsating Pressure in Hydraulic Pipeline by Using Water Hydraulic Cylinder

Kaito MIYASHITA*, Shouichiro IIO**,
Tsuyoki TAYAMA***, Ryuichi ONODERA***, Shota ABE***

*Graduate School of Science and Engineering, Shinshu University
**Department of Mechanical Systems Engineering, Shinshu University
4-17-11 Wakasato, Nagano, 380-8553 Japan
(E-mail: 20w4065c@shinshu-u.ac.jp)
*** Tohoku Steel Co., Ltd.
23 Nishigaoka, Murata, Shibata, Miyagi, 989-1393 Japan

Abstract. This study focuses on a magnetostrictive power generator that converts pulsating pressure in a water hydraulic circuit to electric power through mechanical vibrations to suppress pressure pulsation. This study uses a water hydraulic cylinder as a pressure to force converter. Fluctuation force on the cylinder rod acts on a magnetostrictive piece. The authors measured the pressure, flow rate passing water, and the thrust force on a rod. The pressure fluctuation frequency and the initial cylinder volume is the significant parameter. As a result, the pressure absorption characteristics strongly depend on the pressure pulsation frequency and the initial volume. Several magnetostrictive generators designed and investigated the mechanical strength by structural analysis.

Keywords: Pressure Pulsation, Water hydraulics, Vibration, Generator, Performance

INTRODUCTION

Pressure pulsation often occurs in fluid power systems, causing vibration, noise, and reduced life of connected equipment. Accumulators are commonly used as pressure pulsation suppression devices in water hydraulic circuits, and several other pulsation reduction devices had been proposed[1), 2)]. All of these devices suppress pulsation by dissipating the energy of pressure pulsation into the atmosphere as thermal energy or elastic strain energy. Suppose both suppressions of pressure pulsation and electric power generation can achieve. In that case, it will be possible to supply power to sensors and other devices used in pipelines, and it expects to apply to the IoT, which has been attracting attention in recent years. Therefore, the authors have proposed a Pulsation Absorbing Device (PAD) that absorbs pressure pulsation in a water hydraulic circuit and generates electricity, and have investigated its basic characteristics[3), 4)]. Since the energy loss of the conventional diaphragm type PAD is significant and the transmission of vibration to the power generation device is not easy, the authors start to investigate the magnetostrictive power generation device using a water hydraulic cylinder. In this paper, the authors report the results of the preliminary performance tests for the realization of a power generation device using a water hydraulic cylinder type PAD. In particular, the frequency of the pressure pulsation in the circuit and the effect of the internal volume of the water hydraulic cylinder type PAD on the pressure pulsation absorption characteristics report. In addition, the characteristics of the force generated in the cylinder rod investigate. Besides' the authors reports investigating results of the optimal shape of magnetostrictive materials for magnetostrictive power generation based on structural analysis.

EXPRTIMENTS AND ANALYSIS

Experimental Equipment and Methods

The authors investigate the effects of the frequency of the pressure pulsation in the circuit and the initial volume of the water hydraulic cylinder on the pressure pulsation absorption characteristics and the characteristics of the force generated on the cylinder rod experimentally. Figure 1 shows the water hydraulic circuit. Table 1(a) shows the experimental conditions when the initial volume is constant and the pump rotation speed change to confirm the pulsation absorption performance when the pulsation frequency change. Table 1(b) shows the experimental conditions when the pump rotation speed is constant and the initial volume change to confirm the pulsation absorption performance when the initial volume change. The working fluid is tap water. Swash-plate type piston pump unit (KYB Corp., 16MPa max., 22.5L/min@1500rpm), six cylinders, use. The water from the pump regulate to the desired pressure by a relief valve and passed through an upstream High response transducer (JTEKT, PMS-8M-2), a water hydraulic cylinder type PAD, a downstream High response transducers (JTEKT, PMS-8M-2), an ultrasonic flow meter, a needle valve, a chiller unit(ORION, RKS1503J-MV-01000), and a filter before returning to the tank. Semiconductor pressure sensors (KEYENCE, upstream side: GP-M100, downstream side: GP-M10) measure the other two pressures between a needle valve. For the piping of the experimental circuit, 10A Sch/80 stainless steel pipes use and connect in a straight line at the length shown in the figure. Connect the water Hydraulic cylinder type PAD to the pipe with a T-junction so that Fill the cylinder piston side with working water. The cylinder stroke can fix at any position by installing a fixed wall at the rod end. The initial volume defines as the volume on the piston side of the cylinder. When a pressure pulsation acts on the piston, a thrust force generate in the rod. In magnetostrictive power generation, a magnetic field generate when the magnetostrictive material distort, which is then used to generate electricity. So that the force sensor (small compression type load cell, Kyowa Dengyo, LMC-A-20KN) by install between the rod tip and the fixe wall measure the force acting on the magnetostrictive material. The rod side of the cylinder is opened to the atmosphere. Using the data logger record the pressure, flow rate, and force values a sampling frequency of 1 kHz for 5 seconds.

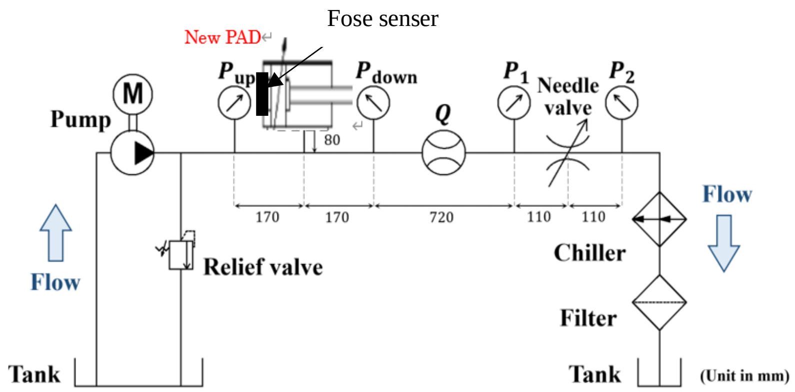

Figure 1. Testing water hydraulic circuit.

Table 1. Experimental condition.

(a) When the initial volume is constant Initial volume.

Fluid medium	Tap water
Fluid temperature[°C]	20
Average pressure $\overline{P_{up}}$ [MPa]	3.2
Average pressure $\overline{P_2}$ [MPa]	0.715
Pump rotation speed[rpm]	1200, 1400, 1600, 1800
PAD Initial volume $V_0 \times 10^{-3}$ [m^3]	0.467

(b) When the pump rotation speed is constant.

Fluid medium	Tap water
Fluid temperature [°C]	20
Average pressure $\overline{P_{up}}$ [MPa]	3.2
Average pressure $\overline{P_2}$ [MPa]	Varies with pump rotation speed
Pump rotation speed[rpm]	1800
PAD Initial volume $V_0 \times 10^{-3}$ [m^3]	0.62, 0.467, 0.317, 0.166, 0.0015

Analysis Conditions and Methods

First, Figure 2 shows how the model introduces into the actual machine. In the future, the authors will refer to Figure 2(a) with the neck as Model A and Figure 2(b) with the notch as Model B. In addition, Figure 2(c) shows the state of the manufactured power generation device.In this figure, the magnetostrictive material shows in red, the coil wind as shown in black, and the magnet attaches as shown in blue. In this device, the magnetostrictive material strains to generate a magnetic field, and the magnets and coils is attached to the device induce electromagnetic induction to generate electricity. In the actual machine the magnetostrictive material will not fixe but only sandwiched between the cylinder cover and cylinder rod.
The optimal shape of the magnetostrictive material must incorporate elements that make it easy to wind coils and easy to attach magnets. Hence, the author conducts a structural analysis to find a new shape. Table 2 shows the physical properties of the magnetostrictive material. As the analysis software use the inventor, and the mesh size set to 0.01 of the model size ratio for both analysis time and accuracy. The load set to 17,000 N, which is slightly higher than the maximum load, in order to find a shape that would not fracture even if the maximum load, which has been confirmed in a water hydraulic cylinder type PAD, was applied. The restraint conditions fixe restraint, and magnetostrictive materials use.

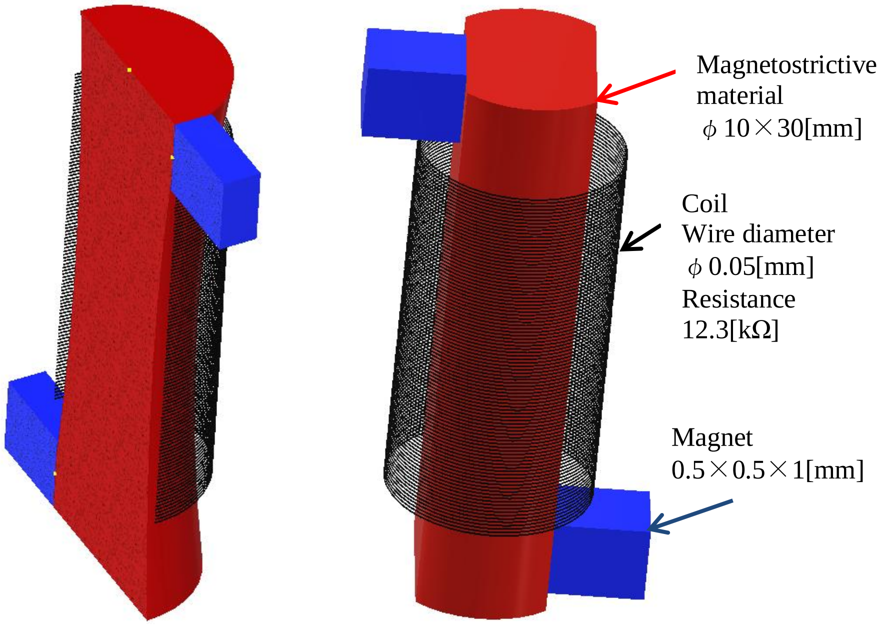

(a) model A. **(b)** model B.

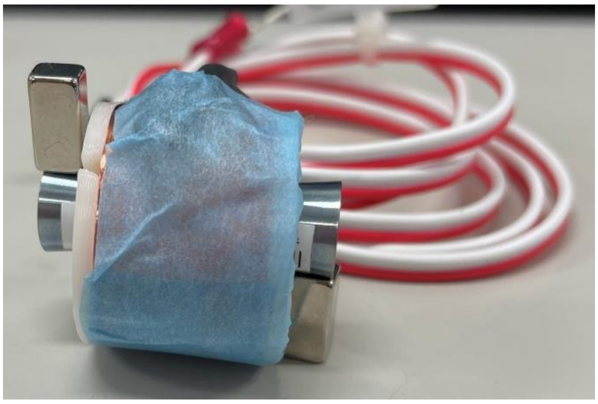

(c) Photo of the testing power generation device.

Figure 2. Materials used in the experiment.

Table 2. physical properties of magnetostrictive material.

Young's modulus	205[GPa]
Poisson's ratio	0.33
Shearing modulus	77[GPa]
0.2% proof stress	397[MPa]
Tensile strength	659[MPa]
Density	8.41[g/cm^3]

DISCUSSION OF THE EXPERIMENTAL RESULTS AND ANALYTICAL RESULTS

Thrust of the Cylinder Rod

Figure 3 shows the experimental results when the initial volume is kept constant. This figure shows versus pump rotation speed for the pressure pulsation absorption efficiency η and the difference between the p-p values of thrust force ΔF. η is the difference between the upstream energy and the downstream energy divided by the upstream energy. Figure 3(a) shows that η increases with the pump rotation speed up to 1600 rpm, and at 1800 rpm, the value is almost the same as at 1600 rpm. Figure 3(b) shows that ΔF reaches its maximum value at 1600 rpm and decreases after that, but there is no significant difference in ΔF between 1600 rpm and 1800 rpm. These results suggest that in the pump rotation speed range in which this experiment was conducted, the efficiency is high at high pump rotation speeds of 1600 rpm to 1800 rpm. The force acting on the magnetostrictive material may be significant.

Figure 4 shows the experimental results when the pump rotation speed keep constant. This figure shows versus initial volume for the pressure pulsation absorption efficiency η and the difference between the p-p values of thrust force ΔF. From Figure 4(a), the authors can see that η increases with V_0. On the other hand, figure 4(b) shows that ΔF decreases as V_0 increases. These results show that there is a trade-off between η and ΔF. This phenomenon occurs because the water hydraulic cylinder type PAD does not absorb the pressure pulsation only by the vibration of the rod, but also by the vibration of the water, molecules in the cylinder are elastic and absorb the pressure pulsation at the same time as the rod. Therefore, when the water in the cylinder increased due to the initial volume increase, the ratio of water in the cylinder absorbing pressure pulsation increased, and the ratio of pressure pulsation transmitted to the rod decreased, so ΔF decreased and η increased.

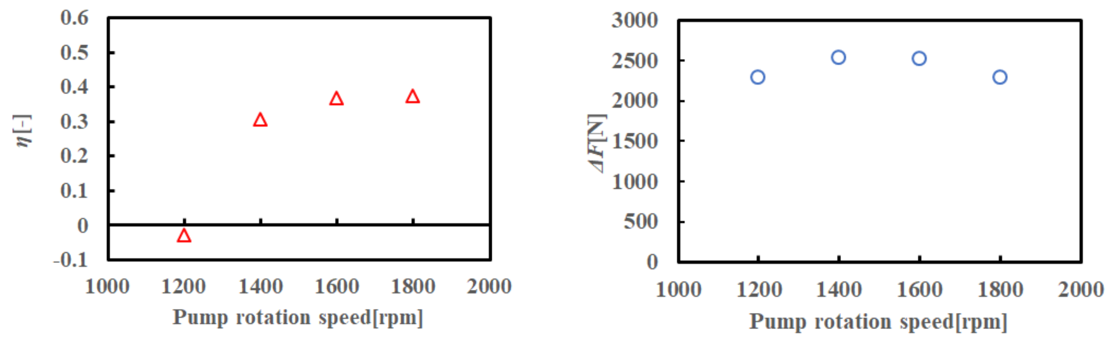

(a) Pressure pulsation absorbing efficiency. **(b)** Differential thrust force ΔF.

Figure 3. pulsation absorbing performance versus Pump rotation speed. (V_0=0.467×10^{-3}[m^2])

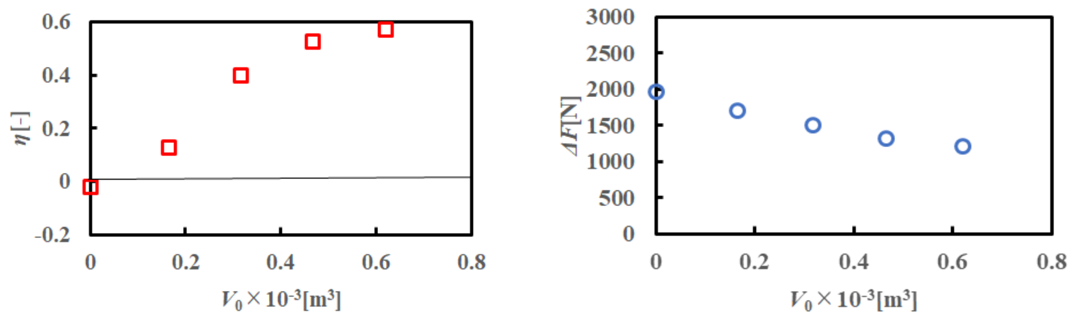

(a) Pressure pulsation absorbing efficiency. **(b)** Peak to peak of thrust force ΔF.

Figure 4. pulsation absorbing performance versus initial volume. (1800[rpm])

Investigating of the Magnetostrictive Material Shape

In the present analysis, the authors investigated the neck model, which is easier to strain and winding a coil, and the notch model, which is easier to attach magnets, and obtained two types of shapes. First, figure 5 shows the results of the analysis for the mesh and von Mises stress of Model A. In order to increase the strength of the model, there are one notch, one in the load part and one in the fixed part, and these two notches are located at 180 degrees symmetry. From this figure, the stress considers concentrating at the neck, and the maximum von Mises is about 350 MPa. The authors believe that this value is sufficient to strain the magnetostrictive material, and from the standpoint of safety factor, no rupture will occur, so practical application is possible.

Next, the authors conduct a structural analysis using a simple structure with only a notch, in order to experimentally confirm the properties of the magnetostrictive material in a simple shape. Figure 6 shows the results of the analysis for the mesh and von Mises stress of Model B. The maximum von Mises stress is about 150 MPa, which is also sufficient to strain the magnetostrictive material, and from the viewpoint of safety factor, it is possible to put it into practical use because it is thought that rupture will not occur.

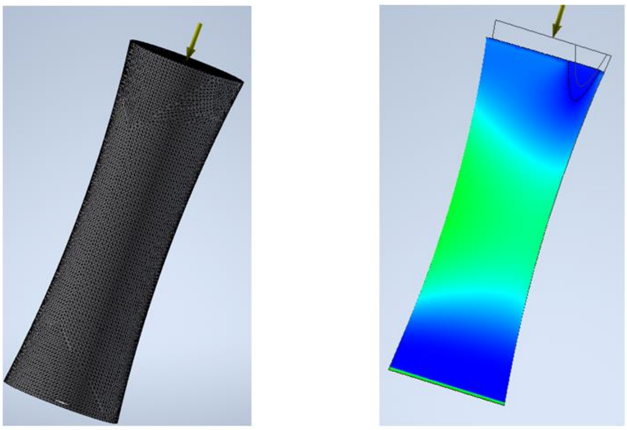

(a) Mesh. **(b)** von Mises stress.

Figure 5. Analysis results of model A.

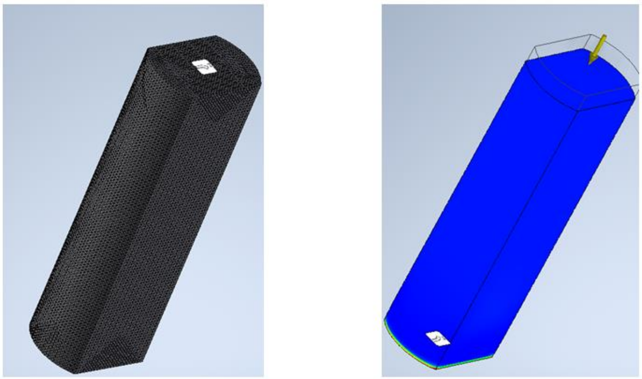

(a) Mesh. **(b)** von Mises stress.

Figure 6. Analysis result of model B.

CONCLUSION

The authors experimentally investigate the relationship between pressure pulsation absorption efficiency and rod thrust force in a new type of PAD using a water hydraulic cylinder. As a result, the authors confirm the absorption effect of pressure pulsation, and show the relationship between pressure fluctuation waveform and thrust force. These characteristics find to be strongly dependent on the initial volume and pump rotation speed. Also' based on the relationship between the pressure pulsation absorption efficiency and the thrust force, structural analysis of the magnetostrictive material was performed to realize the power generation device, the optimum shape of the magnetostrictive material was determined. The results of the power generation test will report at the meeting.

REFERENCES

1. Ken Ichiryu, “Development of accumulator (Hi-Pulsober) for high-frequency ripple absorption of hydraulic system,” Bulletin of JSME, Vol. 15, No. 88, pp.1215-1227, 1972.
2. Yasuo Sakurai, Norikazu Hyodo, and Kenichi Aiba, “Component to reduce pressure pulsation,” Japan Fluid Power System Society, pp. 41-44, April 2017.
3. K. Mori, S. Iio：Feasibility Study on a Pulsation Absorber for Vibration Power Generation, Proc. the 8th International Conference on Fluid Power and Mechatronics, FPM2019-408(2019), pp.1-3.
4. K. Mori, S. Iio：Development of a Liquid Flow Pulsation Damper which Works as Power Generator, The Proceedings on Spring Conference of Japan Fluid Power System Society 2019（2019）, pp.95-97.

The 11th JFPS International Symposium on Fluid Power HAKODATE 2020 Oct. 12-13, 2021 JFPS The Japan Fluid Power System Society

Flow Characteristics of a Cavitating Jet through a Small Rectangular Orifice with Different Aspect Ratios

Hironori TAKEI*, Kohei TERAKAWA*, Shouichiro IIO**,
Kotaro TAKAMURE***, Tomomi UCHIYAMA***, Futoshi YOSHIDA****

* Graduate School of Science and Technology, Shinshu University
** Department of Mechanical Systems Engineering, Shinshu University
4-17-1 Wakasato, Nagano-shi, Nagano, 380-8553 Japan
(E-mail: shouiio@shinshu-u.ac.jp)
*** Institute of Materials and Systems for Sustainability, Nagoya University
Hurou-cho, Tikusa-ku, Nagoya-shi, Aiti, 464-8601 Japan
**** KYB Corporation
1-12-1, Asamizodai, Minami-ku, Sagamihara-shi, Kanagawa, 252-032 Japan

Abstract. Cavitation is one of the significant issues for water hydraulic components. The authors focus on a cavitating jet flow and jet noise characteristics from a rectangular orifice for various aspect ratios. This study deals with the cavitation region in the jet to reveal the relation between the cavitation and vortex structure issuing from a rectangular orifice. The experimental results show that the vortex in the jet shear layer corresponds with the cavitation generation region. No cavitation occurs in the jet center region just downstream of the exit. The cavitation bubbles grow and dissipated at almost the same normalized downstream position for the lower aspect ratio orifices. The cavitating planar jet behavior differs from those for the other lower aspect ratios. The lower aspect ratio jet shows axis switching.

Keywords: Cavitation, Jet, Rectangular Orifice, Water Hydraulics, Visualization

NOMENCLATURE

AR	: jet exit aspect ratio [-]
C	: flow coefficient [-]
De	: equivalent diameter [mm]
DO	: disolved oxigen concentration [ppm]
P_1	: upstream pressure [$\times 10^6$ Pa]
P_2	: downstream pressure [$\times 10^6$ Pa]
Re	: Reynolds number [-]
x	: distance from orifice [mm]
σ	: Cavitation number [-]

INTRODUCTION

Aqua drive system (ADS), which uses tap water as the working fluid, has recently been attracting attention as a clean and environmentally friendly system(1)-(3). ADS is superior to hydraulic systems in terms of hygiene and environment, compliant with various standards such as HACCP and ISO 22000. For this reason, ADS is increasingly being used in manufacturing processes that require cleanliness, such as food, pharmaceuticals, and semiconductors, and in equipment that requires environmental compatibility, such as elevators for nursing care and gates for storm surge protection. However, due to the physical properties of water, the working fluid in ADS is more prone to cavitation than hydraulic oil. So, noise and vibration problems occur apparently.
The previous researches by the authors showed that the cavitation phenomena in a water hydraulic spool valve depend on the width and the opening area of the control orifice and the differential pressure between the orifice. Furthermore, the variation of vibration and noise with downstream pressure shows a peak when the pressure becomes around 0.1 MPa(4). The control orifice in a water hydraulic spool valve is rectangular, and the width and aspect ratio of the orifice changes simultaneously. Therefore, it is essential to check the dependency of cavitation on the width or the aspect ratio individually. The authors made and used a small rectangular orifice, the area is approximately 1.6mm, for evaluating these influences independently. Although some previous studies on rectangular orifices, such as micro-orifices(5), there is insufficient knowledge on the cavitating jet, whose conditions of actual orifice size, Reynolds number, and cavitation number are in this study. The orifice area is constant and almost the same as the control port area of the spool valve. Thus, the experiment parameters are aspect ratio, differential pressure, downstream pressure, and dissolved oxygen concentration. The authors reported that the orifice aspect ratio significantly influences the origin of the cavitation jet, and for a higher aspect ratio,

the less cavitation and noise(6). However, the detail of the cavitation jet is unknown. Therefore, this study aims to grasp the origin and growth of the cavitation jet by visualization.

EXPERIMENTAL EQUIPMENT AND METHOD

Figure 1 shows the testing water hydraulic circuit and the arrangement of visualization devices. The working water pressures, P_1, P_2, are monitored by pressure transducers and adjusted by relief valves. The water passes an accumulator for pulsation suppression and into the test section and returns to a reserver. The water temperature was maintained constant by a chiller. Through the experiment, the dissolved oxygen concentration (*DO*) and the temperature were measured at the inlet of the test section. The *DO* and temperature range from 6.43 to 7.06 ppm and 22.3 to 22.5 °C, respectively. Table 1 lists experimental conditions.
Figure 2 illustrates a schematic view of the test section. The section is a transparent acrylic vessel to observe the cavitation jet directly. Stainless steel plates sandwich the vessel for easy connection to the pipe. An orifice plate is screwed at the center of the bottom plate, as shown in Fig. 2. Figure 3 shows four types of orifice plates used in this study. A type has a circular hole of 1.46 mm diameter, and the other types with rectangular openings with aspect ratios of *AR*=1.00, 6.76, and 52.0. All plates have the same opening area of 1.69mm^2.
The backlighting method with a halogen lamp captures the whole jet image viewing from the front of the test section. On the other hand, the laser light sheet with CW laser (Kanomax, CW532-10-3W) can slice the cavitating jet to grasp cross-sectional images viewing from the top of the test section. A high-speed camera is FASTCAM SA-X2, Photron with a lens (Nikon, NIKKOR 50mm f/1.4). The frame rate of the high-speed camera was 30 kfps, the power of the halogen lamp was 500 W. The time-averaged images were using Image-J software.

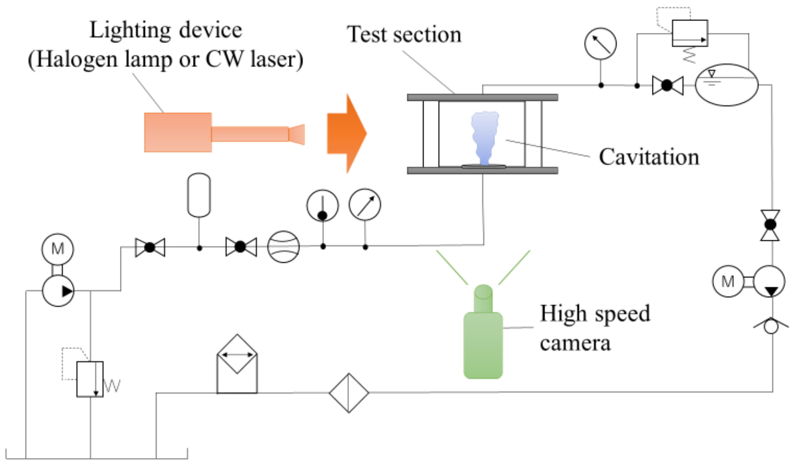

Figure 1. Experimental Circuit

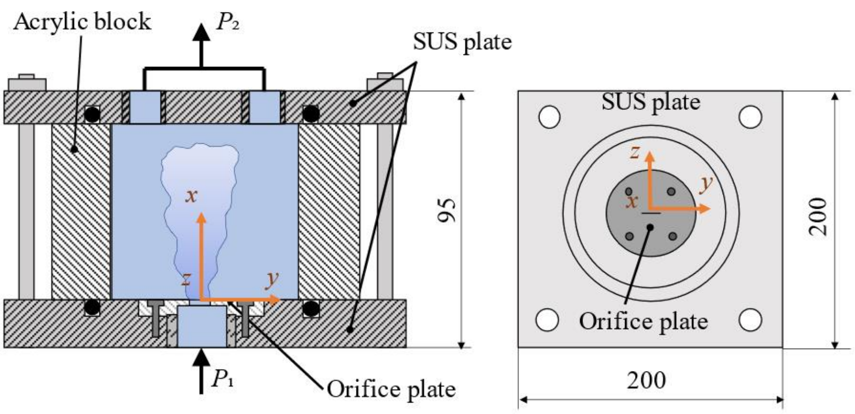

Figure 2. Test Section

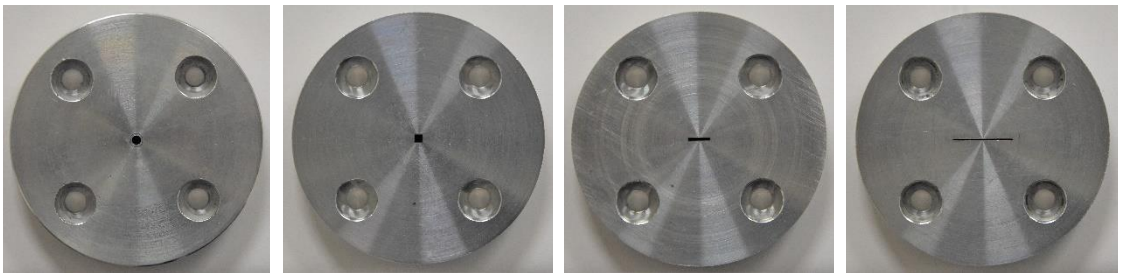

1.30 mm × 1.30 mm 3.38 mm × 0.50 mm 9.36 mm × 0.18 mm

(a) φ1.46 mm (b) AR=1.00 (c) AR=6.76 (d) AR=52.0

Figure 3. Orifice plates

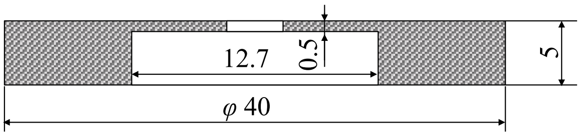

(unit in mm.)

Figure 4. Cross-section of the orifice plate

Table 1. Experimental condition

Fluid medium	Tap water
Temperature [deg. C.]	22.3～22.5
Upstream pressure P_1 [$\times10^6$ Pa]	0.50～3.00
Downstream pressure P_2 [$\times10^6$ Pa]	0.00
Disolved Oxigen concentration DO [ppm]	6.43～7.06
Orifice types	φ1.46mm (circle) AR=1.00, 6.76, 52.0 (rectangle) thickness is 0.5 mm

EXPERIMENTAL RESULTS AND DISCUSSION

Figure 5 shows the front views of the cavitating jet at different upstream pressures. We can easily recognize that the jet generates at the exit and dissipates downstream. The size of the jet is different between two pressure conditions; cavitation jet forms near the jet exit for P_1=0.5×10^6 Pa. In contrast, the jet grows until far from the exit for P_1=3.0×10^6 Pa. Compare the length of the jets between the exit condition. The length for AR=52.0 is shorter than that for other exit shapes. The previous research focused on cavitation type based on bubble diameter. There are two types of cavitation; large diameter bubble cavitation originates from the gas cavitation by the concentration of dissolved gas in the water, and tiny cloud-like bubble by the local pressure drop(4)(6). The bubble cavitation occurs at P_1=3.00×10^6 Pa, especially in cases of φ1.46 mm, AR=1.00, and 6.76. In the case of AR=52.0 shown in Fig. (d), the cavitation region is small around the jet exit.

Figure 6 illustrates instantaneous cross-sectional slicing images of the cavitating jet at the different downstream positions. The brighter region is a higher density of cavitation bubbles. For the circular jet in Fig. (a), a ring shape cavitation can be observed at x/De≈0, and the ring is in the jet shear layer. This fact indicates the cavitation produced by the intense shear stress. The circle shape bubble distribution is not uniform and fluctuating, that confirmed from the movie. The ring shape becomes unclear at x/De≥3.43. The cavitation ring disappears far downstream for the circular jet in Fig. (a). For the rectangular jet of AR=1.00 in Fig. (b), a diamond shape cavitation appears at x/De≈0. The shape rotates at approximately 45 degrees from the jet exit shape. Thus, rapid axis switching will occur because of a rectangular orifice with a low aspect ratio(7)(9). the cavitation shape at x/De≈0 for rectangular jets of AR=6.76, 52.0 shows the exact shape of each exit. The difference between these cavitation patterns is that the jet of AR=52.0 keeps its shape far downstream, as shown in Fig. (d).

Time-averaged images of cross-sectional cavitation patterns are in Fig. 7. These images could get from an average of a thousand images for 33msec. Thus, we can precisely catch the significant phenomenon mentioned above shown in Fig. 6. For the circular jet in Fig. (a), the circle shape remains for x/De≤4.11, and cavitation bubbles do not penetrate near the jet centerline, the x-axis. The cavitation region in the rectangular jet of AR=1.00 deforms, and switching phenomena at x/De≈0 and covers on the jet center area at x/De=3.85, due to enhancement of jet mixing(7)-(9). The cavitation distribution pattern in the jet of AR=6.76 in Fig.(c) appears typical deformation process of a coherent structure of a non-cavitation jet. It means the deformation process due to the self-induced velocity of a vortex ring. The corners of the vortex ring with a small curvature move faster downstream. These cavitation patterns at x/De≈0 and 3.44 shown in Fig. (c) are similar with deformed vortex rings in a non-cavitation jet from the same exit shape. The cavitation region in a two-dimensional jet of AR=52.0 does not penetrate the jet center area regardless of the tiny gap.

Figure 8 illustrates the variations of flow coefficient with the change of cavitation number. The upstream pressure of $P_1=3.00\times10^6$ Pa was constant, and only the downstream pressure was changed. From the results, the flow characteristics improve in the order of φ1.46mm, AR=1.00, AR=6.76, AR=52.0, almost independent on the cavitation number. As the cavitation number decreases, the flow coefficient starts decreasing at some cavitation number drawn in the red circles in Fig. 8. The choked flow by the cavitation will happen from the point. The equivalent diameter of the orifice is De=0.87mm for AR=6.76, De=1.30mm for AR=1.00, and De=1.46mm for φ1.46mm. Under the conditions of AR=6.76, AR=1.00, and φ1.46mm, the larger the equivalent diameter shows the smaller inception cavitation number. On the other hand, no significant cavitation blockage was observed for AR=52.0. The reason for this phenomenon is under investigation.

CONCLUSION

Visualization of cavitating jets with different aspect ratios was performed in this study. The obtained cavitation images indicated that the cavitation is produced in the jet shear layers. The jet exit shape significantly influences cavitation formation and pressure-flow coefficient characteristics. The growth and collapse positions normalized by the equivalent diameter of the cavitation in rectangular jets of AR=1.00, 6.76, φ1.46mm are almost the same. Future work is to grasp the relation between the cavitation phenomenon and flow discharge characteristics.

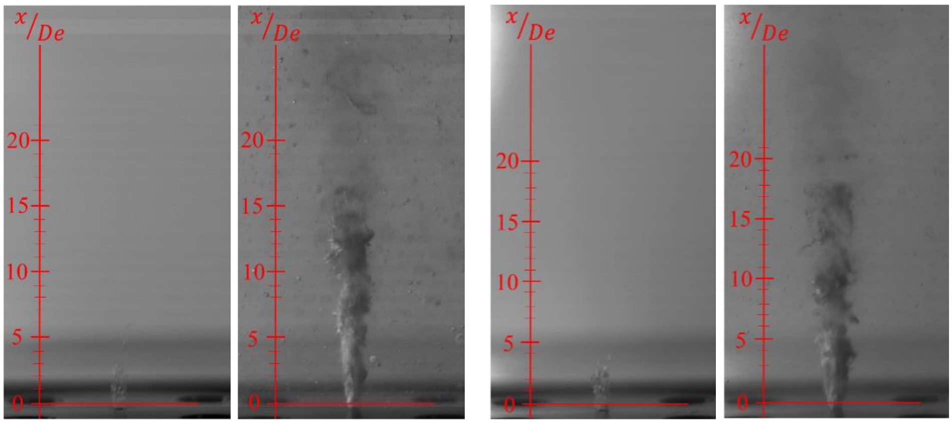

$P_1=0.50\times10^6$ Pa $P_1=3.00\times10^6$ Pa
(a) φ1.46 mm

$P_1=0.50\times10^6$ Pa $P_1=3.00\times10^6$ Pa
(b) AR=1.00

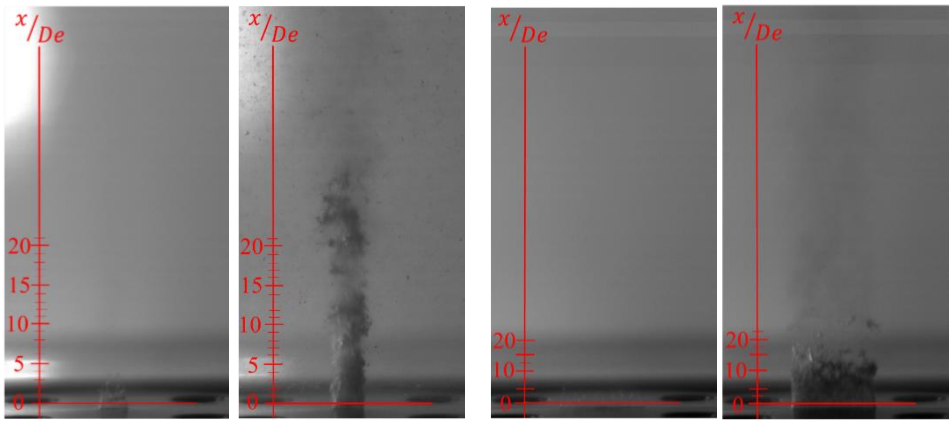

$P_1=0.50\times10^6$ Pa $P_1=3.00\times10^6$ Pa
(c) AR=6.76

$P_1=0.50\times10^6$ Pa $P_1=3.00\times10^6$ Pa
(d) AR=52.0

Figure 5. Instantaneous front views along with the z-axis of a cavitating jet

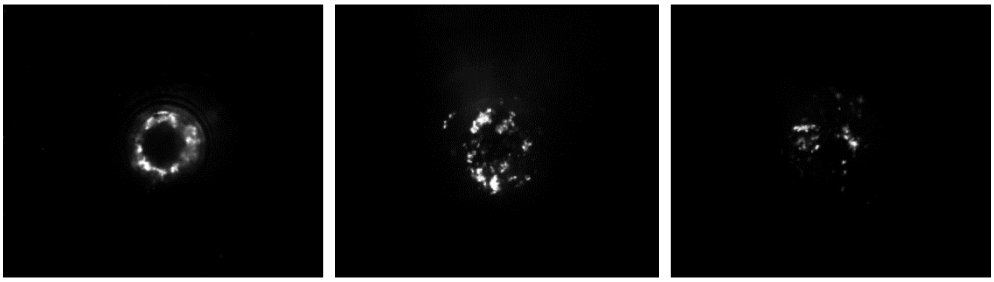

$x/De \fallingdotseq 0$ $x/De=3.43$ $x/De=4.11$

(a) φ1.46 mm, Re=29900

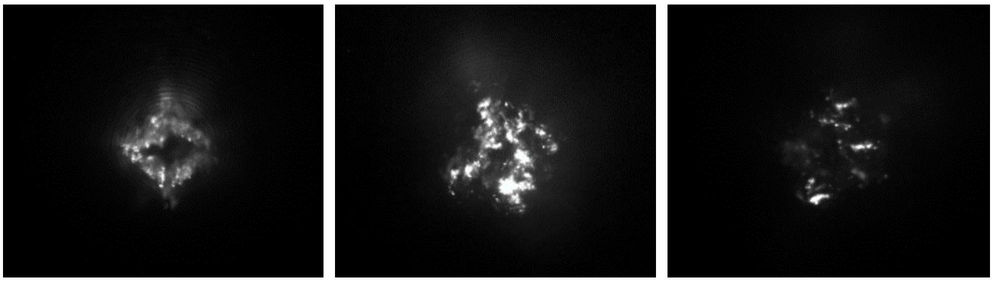

$x/De \fallingdotseq 0$ $x/De=3.08$ $x/De=3.85$

(b) AR=1.00, Re=28700

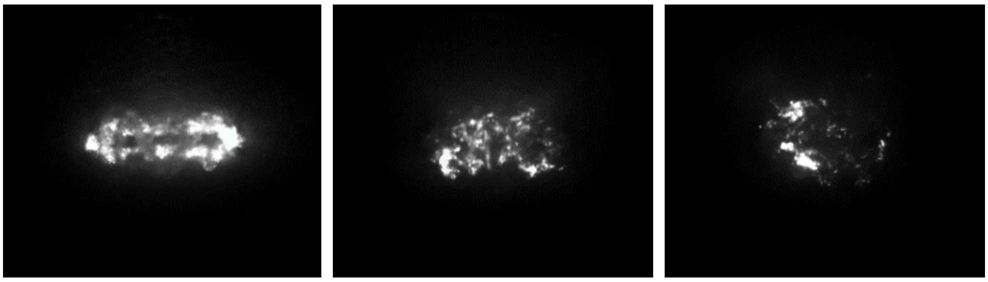

$x/De \fallingdotseq 0$ $x/De=3.44$ $x/De=4.59$

(c) AR=6.76, Re=20900

$x/De \fallingdotseq 0$ $x/De=5.66$

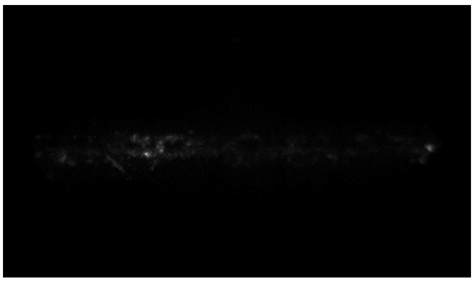

$x/De=8.49$

(d) AR=52.0, Re=11500

Figure 6. Instantaneous cross-sectional slicing images of a cavitating jet at the different downstream position

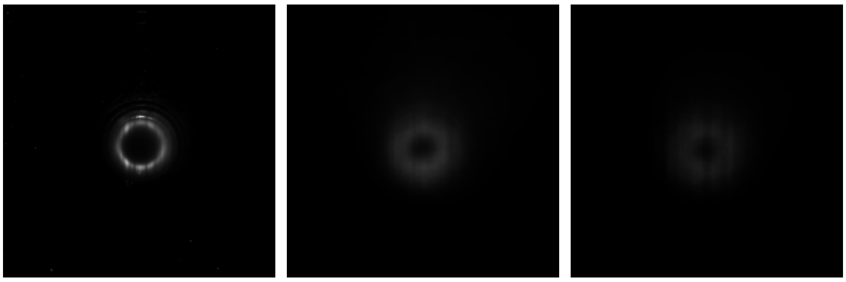

x/*De*≒0 *x*/*De*=3.43 *x*/*De*=4.11

(a) φ1.46 mm, *Re*=29900

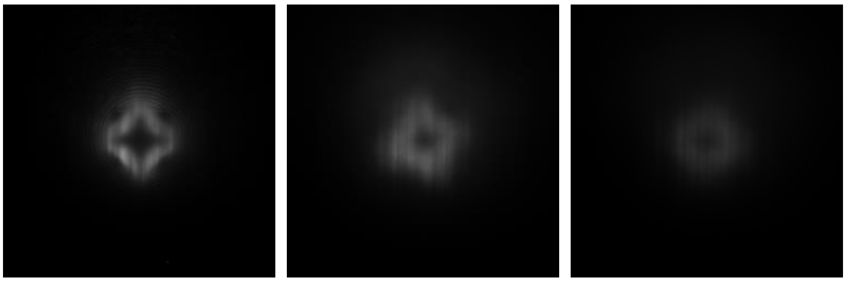

x/*De*≒0 *x*/*De*=3.08 *x*/*De*=3.85

(b) *AR*=1.00, *Re*=28700

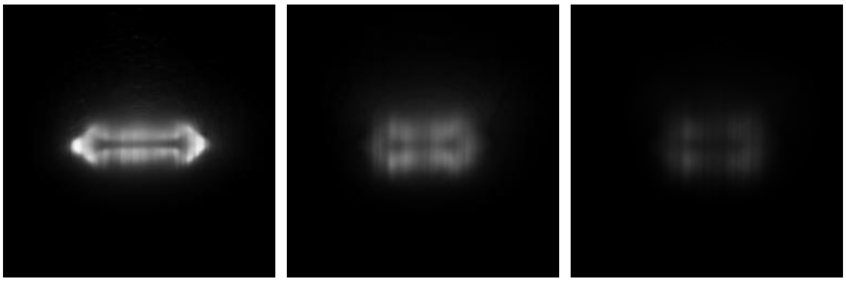

x/*De*≒0 *x*/*De*=3.44 *x*/*De*=4.59

(c) *AR*=6.76, *Re*=20900

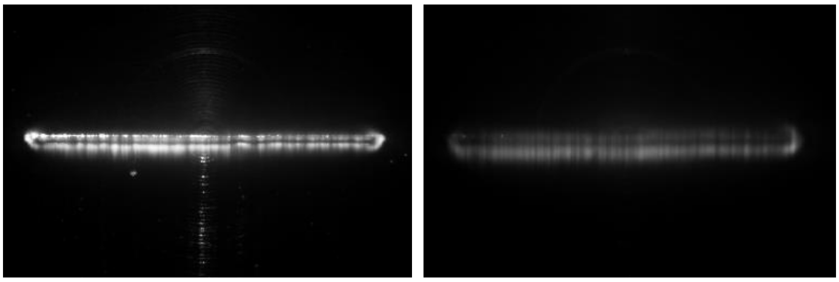

x/*De*≒0 *x*/*De*=5.66

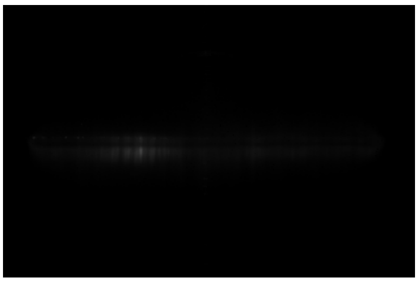

x/*De*=8.49

(d) *AR*=52.0, *Re*=11500

Figure 7. Time-averaged cross-sectional images of a cavitating jet viewing from the downstream

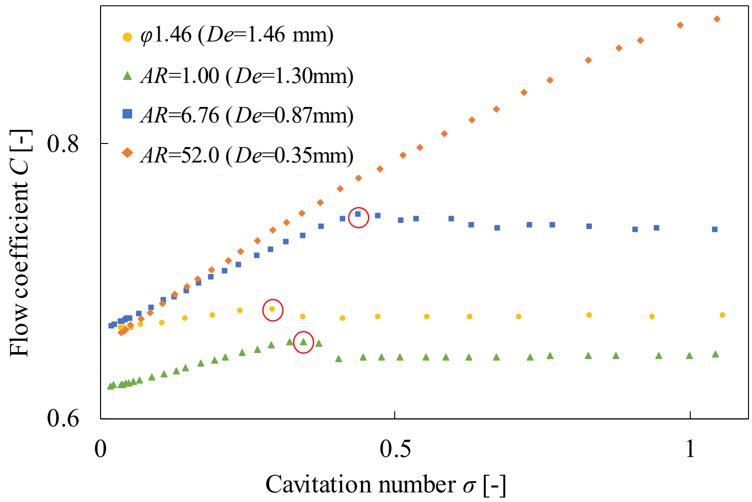

Figure 8. σ- C curves of orifices with various aspect ratios (P_1=3.0×10^6 Pa)

ACKNOWLEDGMENT

This work was carried out by the joint research program of the Institute of Materials and Systems for Sustainability, Nagoya University.

REFERENCES

1. Z. Y. Li, Z. Y. Yu, X. F. He, S. D. Yang, "The development and perspective of water hydraulics", Proc. JFPS International Symposium on Fluid Power, 1999(4), 1999, pp.335–342.
2. E. Trostmann, Water Hydraulics Control Technology, CRC Press, 1995.
3. Progress of Aqua Drive technology (Japan Fluid Power System Society establishment 40th anniversary publication), The Japan Fluid Power System Society, 2011.
4. H. Okabe, Y. Tanaka, A. Watanabe, F. Yoshida, S. Iio, Y. Haneda, "Cavitation in a spool valve for water hydraulics", IOP Conf. Series: Earth and Environmental Science, 240, 062029, 2019.
5. S. Cassineri, et al., "Experiments on liquid flow through non-circular micro-orifices", Micromachines 2020, 11(5), 510, 2020.
6. A. Watanabe, H. Okabe, F. Yoshida, S. Iio, "On cavitating jet issuing from a rectangular orifice", Proc. the 8th International Conference on Fluid Power and Mechatronics (FPM2019), Wuhan, FPM2019-406, 2019.
7. K. Toyoda, "Vortices in jets", Journal of Japan Society of Fluid Mechanics, 24, 2005, pp.151-160.
8. A. K. M. F. Hussain, "Coherent structures and turbulence", J. Fluid Mech., 173, 1986, pp.303-356.
9. K. Toyoda, A. K. M. F. Hussain, "A study of the vortical structures of noncircular jets", Transactions of the JSME Ser.B, 55(514), 1989, pp.1542-1545.

Organized Session | Organized session

Aqua Drive 2

The 11th JFPS International Symposium on Fluid Power HAKODATE 2020 Oct. 12-13, 2021 The Japan Fluid Power System Society

Switching Control of Latex Balloon Expansion by using Fluidic Switching Valve mediated with Coanda Effect

Keita KANEKO* and Kenjiro TAKEMURA**

* Graduate School of Science and Technology, Keio University
3-14-1, Hiyoshi Kohoku-ku, Yokohama, Japan
(E-mail: keitakanekomsazb@keio.jp)
** Department of Mechanical Engineering, Keio University
3-14-1, Hiyoshi Kohoku-ku, Yokohama, Japan
(E-mail: takemura@mech.keio.ac.jp)

Abstract. Soft robots have advantages in terms of safety, softness and compliance. However, fluid driven soft actuators often employed in soft robots require corresponding numbers of pressure supply/valve to drive. Here, we take notice of a fluidic valve which can control flow without mechanically moving parts from the viewpoint of simplifying the driving system of soft actuators. We develop a system which consists of a pump, a fluidic switching valve, and two latex balloons to demonstrate the feasibility of introducing the fluid valve to soft robotics. Since the valve can switch the flow between two outlets when the pressure difference between outlets is under several kPa, we have employed the latex balloon connected to each outlet, which has a peak in its PV diagram. The system can control each balloon's expansion by switching the flow from the pump. Experimental results proved that the system could actuate each balloon at will.

Keywords: Soft robot, Fluidics, Coanda effect.

INTRODUCTION

In recent years, there has been a demand for robots that can operate in the environment close to human. They could be used as nursing care robots, entertainment robots, and customer service robots etc. [1]. Such robots are expected to be safe enough against human to reduce possible physical harms when they become into contact with humans, flexible enough to behave like living organisms, and compliant enough to cope with unexpected situations and environments [2-4]. For these reason, soft robots, in which the structure and actuators themselves are flexible, have been attracting wide attentions [5]. Soft robots are often constructed and actuated by means of fluid-driven flexible rubber actuators [6]. Then, there arises a critical issue. When developing a multifunctional soft robot, the mass and volume of the entire system increase because multiple pressure sources/valves are required according to the number of degrees of freedom of motion required in the robot. A number of researches have been reported on the application of fluidics technology to pneumatic soft robots, where multiple motions can be generated from a single input, suggesting the possibility of fluidics to increase the number degree-of-freedom with simple configuration [7-9]. Compared to pneumatically driven soft robots, hydraulic systems for soft robotics have not been greatly explored yet. Many of the previously reported hydraulic soft robots employ rigid and bulky fluid control components [10, 11].
In light of the above background, we focused on a fluidic valve, which is one of the important elements of fluidics. The idea it to realize a multi-degree-of-freedom motions by appropriately switching the pressure flow generated by a pressure source by using a simple fluidic switching valve. To demonstrate this concept, this study aims to realize a fluid-driven system that can selectively expand balloons by using a simple fluidic switching valve.

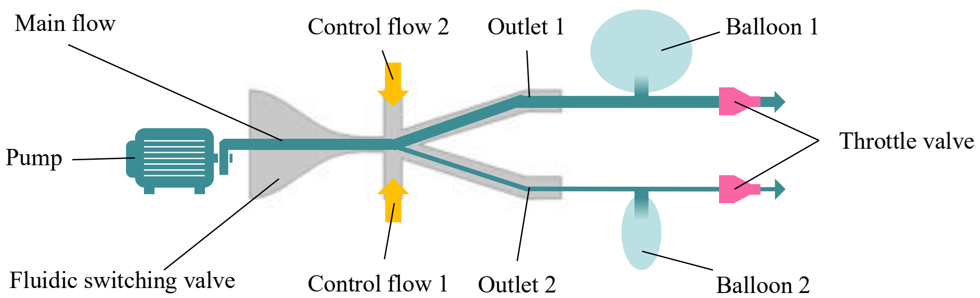

Figure 1. A schematic of the proposed drive system.

SELECTIVE DRIVE OF SOFT ACTUATORS USING A FLUIDIC VALVE

Figure 1 shows a proposed drive system capable of selectively expand each of two balloons at will using a simple fluidic switching valve. The proposed drive system consists of a fluidic switching valve that switches the direction of a main flow discharged from a pump by using control flow. A balloon is attached to each of the two outlet channels. The main flow flows into one outlet according to the control flow input, and a throttle valve located downstream of the balloon increases the gauge pressure of the balloon to inflate the corresponding balloon. By switching the control flow, the other balloon can be selectively inflated. By doing so, selective drive of multiple balloons with a relatively simple configuration can be achieved, contributing to the downsizing of entire system.

FLUIDIC SWITCHING VALVE

Figure 2 shows the schematics of the fluidic switching valve, which has been considered as an important fluidic element in *fluidics*. Fluidics intends to construct a logic circuit with fluid flow like an electrical circuit. For such purpose, the Coanda effect in which fluid flow along a channel wall [12], has been employed to develop a fluidic logic element. We take advantage of this digital switching function in driving soft actuators. The fluidic switching valve can switch the outlet flow which is discharged from the pump (main flow) by inputting control flow from the side (control flow). In other words, the main flow can be directed into the outlet 1 by inputting the control flow 1, and vice versa (see Figure 2).

BALOON

As shown in Figure 2, directing the main flow to the outlet 1 (2) creates a difference in the discharge flow rate between the outlets. This flow difference causes the internal pressure increase of the balloon connected to the outlet 1 (2) thanks to the throttle valve (cf. Figure 1). Therefore, the difference in deformation between the two balloons can be achieved by the pressure difference, ΔP, which depends on the difference in flow rate between the outlets.
Figure 3 shows the PV diagram of a balloon with (a) linear and (b) nonlinear relation between internal pressure and volume. In the case of a balloon with linear PV diagram (a), ΔP must be large to produce a sufficient deformation or expansion. On the other hand, a balloon with a peak in PV diagram (b) deforms little up to a threshold pressure and deforms significantly with the threshold pressure and above. In other words, the balloons having peaks in their PV diagram do not require high pressure for obtaining large deformation. Even if ΔP is small, it is possible to generate a sufficient difference in balloons deformation. Therefore, a latex balloon (polka dot balloon, Tiger Rubber Co., Ltd., Japan) was employed in this study.

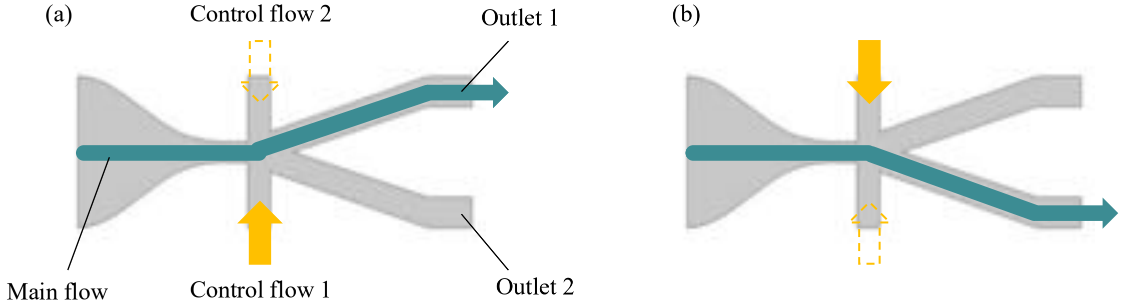

Figure 2. A schematic of a fluidic switching valve. The main flow is directed to (a) the outlet 1, and (b) the outlet 2.

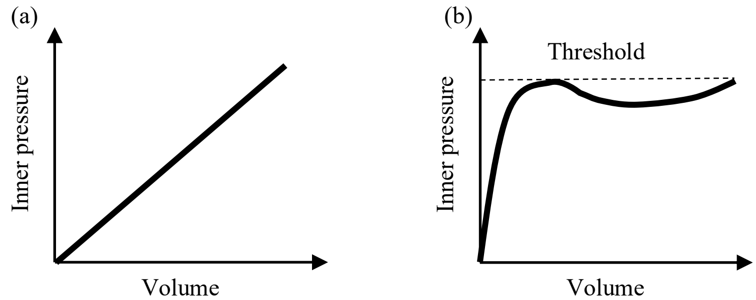

Figure 3. A PV diagrams of a balloon.
(a) Linear PV diagram, (b) Nonlinear PV diagram with a peak.

FABRICATION AND EVALUATION OF COMPONENTS

Fabrication of Fluidic Switching Valve

We developed a fluidic switching valve made of acrylic resign as shown in Figure 4. The diameters of main flow inlet, control flow inlet, and outlet are 13 mm, 3 mm, and 3 mm, respectively. The cross-section of an orifice part where the main flow and the control flow collide is a rectangle with width of 2 mm and thickness of 3 mm. The employed working fluid is water.

Evaluation

For the evaluation of each component, (i) switching characteristics of the fabricated fluidic switching valve and (ii) PV diagram of the latex balloon were experimentally obtained.
Figure 5 shows the experimental setup for switching characterization. A positive displacement pump (V-15, Iwaki Corporation, Japan) was connected to the main flow inlet of fluidic switching valve, and the control flow inlet 2 was closed. A syringe (SS-50ESZ, Terumo Corporation, Japan) was connected to the control flow inlet 1 to direct the main flow to the outlet channel 1. A flowmeter (SEN-HZ06K, Uxcell, China) was connected to each outlet to measure the flow rate along each outlet channel. The flow rate of the main flow was varied from 0 to 25.7 mL/s by 20 equal intervals. Also, the cross-section ratio of the throttle valve (KT-6, Cole-Parmer LLC, USA) connected to the outlets was varied from 59% to 100% (fully closed) by 5 intervals. Figure 6 shows the flow rate difference of the outlet 1 against the outlet 2 ($Q_{out\ 1}$ - $Q_{out\ 2}$). From this result, the volumetric flow rate discharged from the outlet 1 was about 0.25 mL/s higher than that from the outlet 2 in almost all conditions. Note that, there is a leakage from the outlet 2.

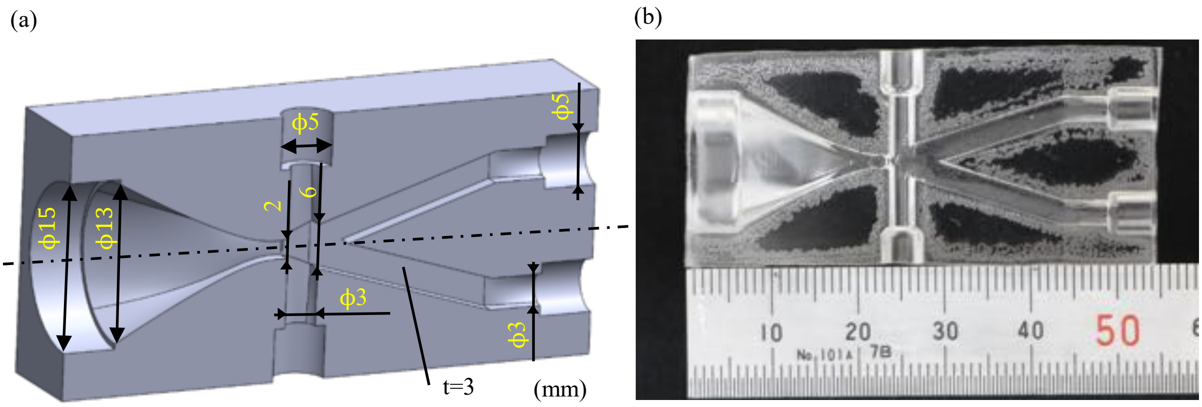

Figure 4. The developed fluidic switching valve.
(a) Cross-section and dimensions, (b) Actual view of the valve.

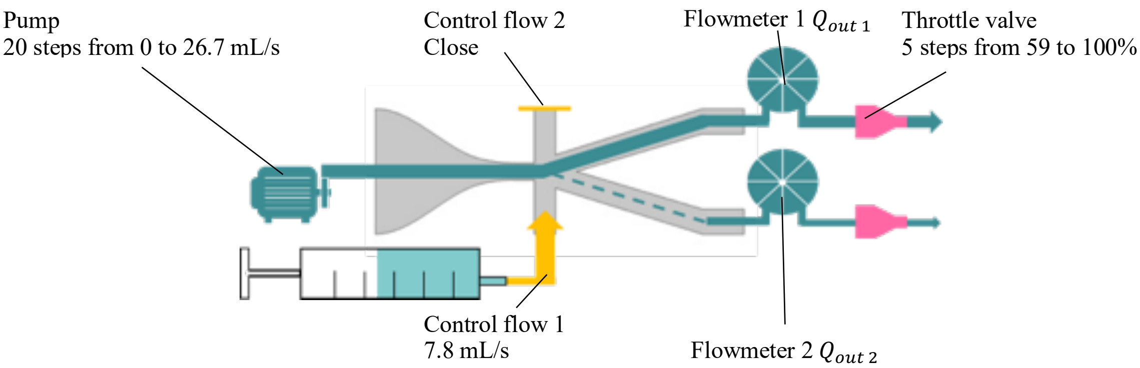

Figure 5. A schematic of evaluation experiment of fluidic switching valve.

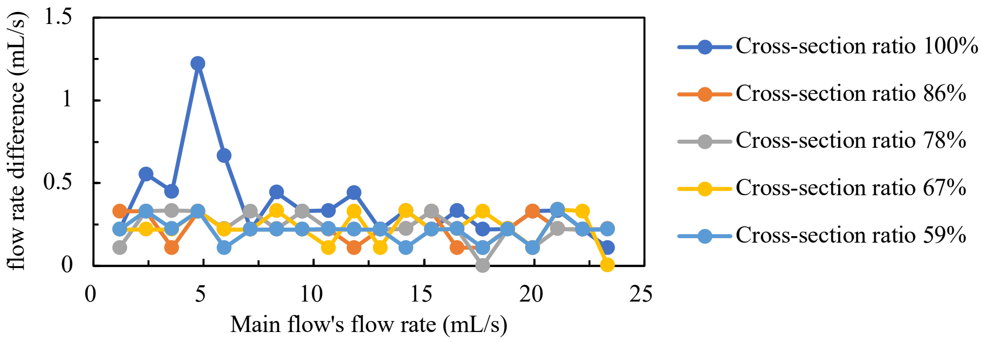

Figure 6. The difference of flow rate of the outlet 1 against the outlet 2.

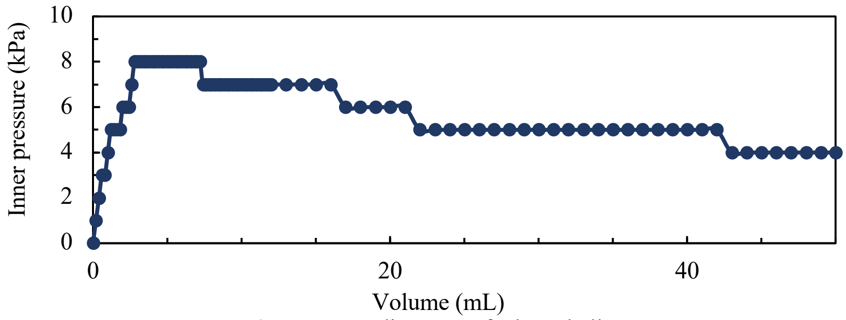

Figure 7. PV diagrams of a latex balloon.

Figure 7 shows the PV diagram of the balloon. The PV diagram was measured by injecting water into the balloon with syringes (SS-50ESZ and SS-10ESZ, Terumo Corporation, Japan). With the balloon volume up to 12 mL, the injection volume step was 12 mL. After that, the water was injected with the step of 1 mL. The internal pressure of balloon was measured with a pressure gauge (GC-31-174, NAGANO KEIKI CO., LTD., Japan) at each balloon volume. The peak internal pressure on the PV diagram was 8 kPa when the volume of the balloon was around 5 mL. Beyond this, the internal pressure decreased as the volume increased. It was confirmed that the balloon deformed greatly at a threshold value of about 8 kPa and higher.

FABRICATION AND EVALUATION OF THE ENTIRE SYSTEM

Fabrication

Figure 8 shows the fabricated system. The system consists of a positive displacement pump (V-15, Iwaki Corporation, Japan), the fluidic switching valve developed in this study, syringes (SS-50ESZ, Terumo Corporation, Japan), tubing connectors (TPX Tubing Connector 3549, Sanwaplatec Co., Ltd., Japan), balloons (polka dot balloon, Tiger Rubber Co., Ltd., Japan) and throttle valves (KT-6, Cole-Parmer LLC, USA). The balloons are connected to the fluidic switching valve via the tubing connector. We employed water as the working fluid in the following experiments.

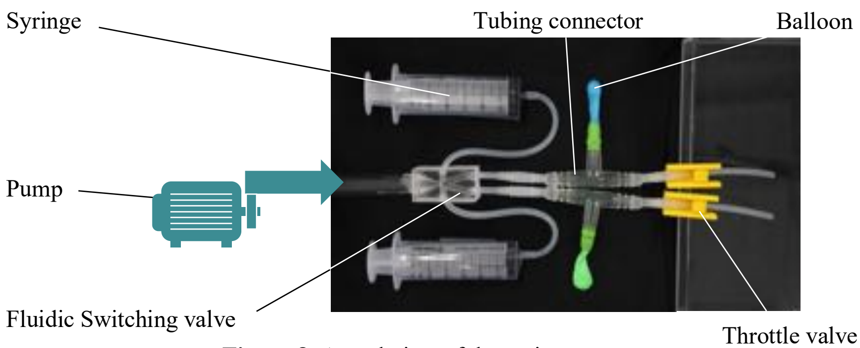

Figure 8. Actual view of the entire system.

Evaluation

Just as mentioned in the previous section, the flow rate of main flow was varied from 0 to 26.7 mL/s with 20 equal intervals. Also, the cross-section ratio of the throttle valve was from 59% to 100% with 5 intervals. The flow rate of control flow 1 was set to 7.8 mL/s, and the control flow 2 was closed. The main flow and control flow 1 was introduced at t = 0 s, and after a sufficient time (8 s: time for the syringe to be empty), the flow was stopped. The deformation of the balloon was visually recorded with the different combination of parameters of the main flow rate and the cross-section ratio of the throttle valve.
Figure 9 summarizes the experimental result. We categorized the behavior of the balloon as follows: (a) both of the balloons are always inflated with or without control flow, (b) any of the balloon inflates but not deflates when the control flow is stopped, (c) any balloon inflates and deflates when the control flow is stopped (desired behavior), (d) one or both of the balloons did not inflate much, and (e) both of the balloons did not inflate at all. Figure 10 shows the deformation of the balloons at a cross-section ratio of 59% and a main flow rate of 9.5 mL/s. The time required for balloon deflation under this condition was 4 s for the blue balloon and 6 s for the yellow balloon. Figure 11 shows the deformation of the balloon at a cross-section ratio of 59% and a main flow rate of 10.8 mL/s. Under this condition, the time required for balloon deflation was 12 s for the blue balloon and 83 s for

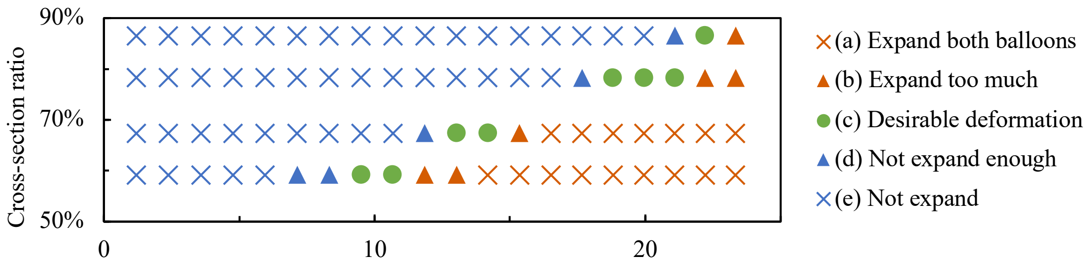

Figure 9. The experimental result.

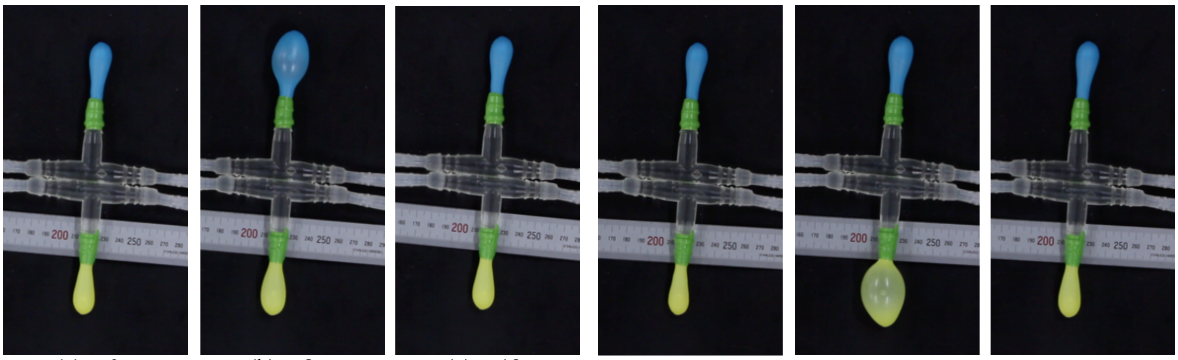

(a) t=0 s (b) t=8 s (c) t=12 s (d) t’=0 s (e) t’=8 s (f) t’=14 s

Figure 10. Balloon’s deformation under cross area: 59%, main flow: 9.5 mL/s.
(a) t=0 s: inflow started, (b) t=8 s: control flow 1 was stopped, (c) t=12 s: balloon contracted,
(d) t’=0 s: inflow started, (e) t’=8 s: control flow 2 was stopped, (f) t’=14 s: balloon contracted.

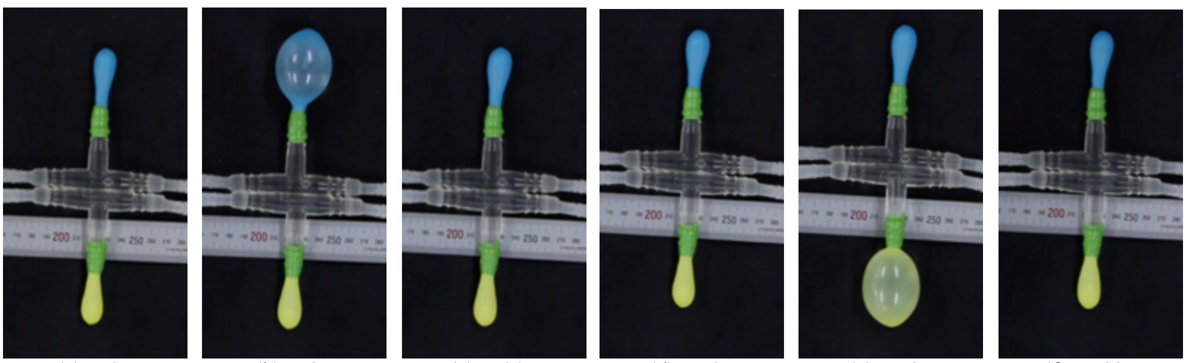

(a) t=0 s (b) t=8 s (c) t=20 s (d) t’=0 s (e) t’=8 s (f) t’=83 s

Figure 11. Balloon’s deformation under cross area: 59%, main flow: 10.8 mL/s.
(a) t=0 s: inflow started, (b) t=8 s: control flow 1 was stopped, (c) t=20 s: balloon contracted,
(d) t’=0 s: inflow started, (e) t’=8 s: control flow 2 was stopped, (f) t’=83 s: balloon contracted.

the yellow balloon. In Figures 10 and 11, (a/d) shows the initial state of the balloons at t = 0. When the water in syringe is fully injected at t = 8s, the balloons appear as shown in (b/e). After a sufficient time for deflection, the balloons restore their initial appearance as shown in (c/f). Time required for the balloons to be fully deflected depends on the flow experimental condition. Note that (a-c) are for the blue balloon to be expanded, and (d-f) are for the yellow balloon to be. These experimental results indicate that balloons can be selectively driven by setting appropriate inflow conditions.

Here we discuss why the appropriate flow conditions (c) are distributed diagonally in Figure 9, and why there is a difference in time required to restore the initial appearance among the different conditions as shown in Figures 10 and 11. As the main flow rate increases, the inner pressure of the balloon increases because the velocity difference between upstream and downstream of the balloon increases. Since the balloons required the threshold pressure, 8 kPa, to largely deform, the flow rate of the main flow should be high enough to produce this threshold pressure or higher. In other words, if the main flow rate is too low, the inner pressure of the balloon will not be high enough to inflate the balloon sufficiently. To avoid this, the cross-section area ratio of the throttle valve should increase to obtain the desired deformation. Therefore, the plots of desired deformation locate diagonally in Figure 9.

When the flow rate of main flow is high and the balloon is inflating ((a) to (b), and (d) to (e) in Figures 10 and 11), the inner pressure of the balloon once increases and then decreases by ΔP_{def} according to the deformation of the balloon, due to the nonlinear PV diagram shown in Figure 7. The smaller the ΔP_{def} is, the easier it is for the balloon to deflate ((b) to (c), and (e) to (f) in Figures 10 and 11) when the control flow is stopped. In other words, the deformability of the balloon depends on ΔP_{def}, which depends on the deformation of the balloon when the control flow is stopped. Then, the deformation of the balloon depends on the main flow rate. Therefore, it is considered that the time required for balloon's deflation became longer as the main flow rate increased.

CONCLUTION

In this study, in order to simply realize the multi-degree-of-freedom motion of a soft robot, we proposed a method to selectively inflate a balloon using a valve that can be operated by control flow input. The developed valve is capable of generating a flow difference of approximately 0.25 mL/s between two outlets, and selective inflation of balloons is realized with a simple configuration for balloons having peaks in their PV diagram. This shows the possibility of a new driving method for soft actuators, and shows that a multi-degree-of-freedom soft robot can be driven only by fluid elements.

REFERENCES

1. NISHIOKA, Y., Pneumatic Soft Robot Arm, Journal of the Robotics Society of Japan, Vol.33, No.9, 2015, p.664-667.
2. KIM, S., LASCHI, C. and TRIMMER, B., "Soft robotics: a bioinspired evolution in robotics", Trends in Biotechnology, Vol.31, No.5, p.287-294, 2013.
3. SHEPHERD, F. R., ILIEVSKI, F., CHOI, W., MORIN, A. S., Stokes, A. A., MAZZEO, D. A., CHEN, X., WANG, M. and WHITESIDES, M. G., Multigait Soft Robot, Proceedings of the National Academy of Sciences, Vol.108, No.51, 2011.
4. KATZSCHMANN, R., MARCHESE, A., RUS, D., Exploration of underwater life with an acoustically controlled soft robotic fish, Science Robotics, Vol.3, No.16, 2018.
5. TAKEMURA, K., Soft Robotics using Electro-Conjugate Fluid (in Japanese), Measurement and control, Vol.57, No.11, p.775-779, 2018.
6. CACUCIOLO, V., SHINTAKE, J., KUWAJIMA, Y., MAEDA, S., FLOREANO, D. and SHEA, H., Stretchable pumps for soft machines, Nature, Vol.572, p.1-4, 2019.
7. GORISSEN, B., MILANA, B., BAEYENS, A., BROEDERS, E., CHRISTIAENS, J., COLLIN, K., REYNAERTS, D. and DE VOLDER, M., Hardware Sequencing of Inflatable Nonlinear Actuators for Autonomous Soft Robots, Advanced Materials, Vol.31, No.3, 2019.
8. ZATOPA, A., WALKER, S., and MENGUC, Y., Fully Soft 3D-Printed Electroactive Fluidic Valve for Soft Hydraulic Robots, Soft Robotics, Vol.5, No.3, p.258-271, 2018.
9. WEHNER, M., TRUBY, R., FITZGETALD, D., MOSADEGH, B., WHITESIDE, G., LEWIS, J., WOOD, R., An integrated design and fabrication strategy for entirely soft, autonomous robots, Nature, Vol.536, No.7617, p.451-455, 2016,
10. GALLOWAY, K., BECKER, K., PHILLIPS, B., KIRBY, J., LICHT, S., TCHERNOV, D., WOOD, R., GRUBER, D., Soft Robotic Grippers for Biological Sampling on Deep Reefs, Soft Robotics, Vol.3, No.1, p.23-33, 2016.
11. POLYGERINOS, P., WANG, Z., GALLOWAY, K., WOOD, R., WALSH, C., Soft robotic glove for combined assistance and at-home rehabilitation, Robotics and Autonomous System, Vol.73, p.135-143, 2015.
12. TESAŘ, V., Fluidic Valve for Reactor Regeneration Flow Switching, Chemical Engineering Research and Design, Vol.82, No.3, p.398-408, 2004.

The 11th JFPS International Symposium on Fluid Power HAKODATE 2020 Oct. 12-13, 2021 JFPS The Japan Fluid Power System Society

Comparison of Model-Free Adaptive Displacement Control and Model Predictive Displacement Control for Tap-Water-Driven Muscle Considering Load Variation during Experiments

Satoshi TSURUHARA* and Ryo INADA** and Kazuhisa ITO***

*Graduate School of Mechanical Engineering, Shibaura Institute of Technology
307 Fukasaku, Minuma-ku, Saitama, 337-8570 Japan
(E-mail: md21074@shibaura-it.ac.jp)

** MEng, Graduate School of Mechanical Engineering, Shibaura Institute of Technology

*** Department of Machinery and Control Systems, Shibaura Institute of Technology
307 Fukasaku, Minuma-ku, Saitama, 337-8570 Japan
(E-mail: kazu-ito@shibaura-it.ac.jp)

Abstract. The muscle is well known to have strong asymmetric hysteresis characteristics and its characteristics depend on the load applied to the muscle. This makes it difficult to design a controller for high-performance displacement control considering load variations. In a previous study, model predictive control with a servomechanism combining an inverse optimization algorithm and adaptive model matching, and model-free adaptive control were applied to muscles, and high tracking control performance was achieved in the presence of static modeling errors due to load variations in both control methods. However, the results for the load variation during the experiment have not been discussed yet. Therefore, by comparing the two control methods, the robustness to load variations during the experiment was evaluated. The experimental results show that both methods have high tracking control performance equivalent to 0.013 mm in steady-state response after load variations, and that MFAC is more robust than MPCS with AMM.

Keywords: Model-free adaptive control, Data-driven control, Model predictive control, McKibben-type artificial muscle, Aqua-drive system

1. INTORODUCTION

The McKibben-type artificial muscle is widely researched in biorobotic engineering, medical engineering, and industrial applications, owing to its many advantages including high flexibility, high power density, low weight, low cost, and simple structure [1]. In particular, tap-water-driven muscles do not require any special power source such as compressor and pump and can be directly actuated by typical water supply network [2][3]. In addition, they have advantages such as no fire hazards and a small burden on the environment, because tap-water is used as the working fluid instead of pneumatic. Therefore, the tap-water-driven muscles are expected to be used in the above-mentioned application that requires a high degree of cleanliness. However, the muscle is well known to have strong asymmetric hysteresis characteristics caused by nonlinear contraction behavior and friction between components. In addition, its characteristics depend on the load applied to the muscle. Therefore, it is difficult to derive a precise muscle model describing its behavior and to design a controller for high-performance displacement control.

The purpose of this study is to propose a control method to solve this problem and to evaluate and examine its robustness through experiments. In a previous study, model predictive control with servomechanism combining inverse optimization and adaptive model matching (MPCS with AMM) is proposed, and high tracking control performance was achieved even in the presence of static modeling errors for load variation applied to the muscle [4]. However, the method requires a complex mathematical model using an asymmetric Bouc-Wen model, which is a quite time-consuming to be derived, identified, and evaluated. Moreover, in the presence of modeling errors, the stability of the control system of the conventional method cannot be guaranteed. To solve these problems, model-free adaptive control (MFAC) [5], which does not require prior information about the mathematical model of the control target and controller structure, was introduced, and high tracking control performance was achieved while reducing the modeling effort [6]. In [4] and [6], the robustness of each control method to initial load variation was confirmed, but their robustness to load variation during the experiments has not yet been discussed. Therefore, in this paper, the robustness to load variation during the experiments is evaluated and compared for MFAC and MPCS with AMM.

The rest of this paper is organized as follows. First, the concept and structure of the MPCS with AMM is described. Next, introducing a full form dynamic linearization (FFDL) data model, the derivation of the MFAC controller and the controller structure are described. Finally, experimental results of the proposed and conventional controllers for load variation are presented to evaluate their effectiveness and robustness.

2. Model Predictive Control with Servomechanism by an inverse optimization algorithm with adaptive model matching (MPCS with AMM)

In this section, a previous study, the model predictive control system with servomechanism by inverse optimization with adaptive model matching, is briefly described using the block diagram in Figure 1 [4]. The system was designed to provide robust control over the loads applied to the muscle. In the green region, the error is calculated from the muscle system, and model which is a highly accurate mathematical model using the asymmetric Bouc-Wen model, and the adaptive algorithm is updated. Then, adaptive linearization and adaptive model matching are performed using the obtained estimated parameters to control the linearized muscle model to match the predictor output of the MPCS controller. On the other hand, in the blue region, the MPCS controller is designed by carrying out inverse optimization to achieve the pre-specified desired poles. Therefore, the control performance is expected to be robust against load variations, and the robustness against static load variations was confirmed.

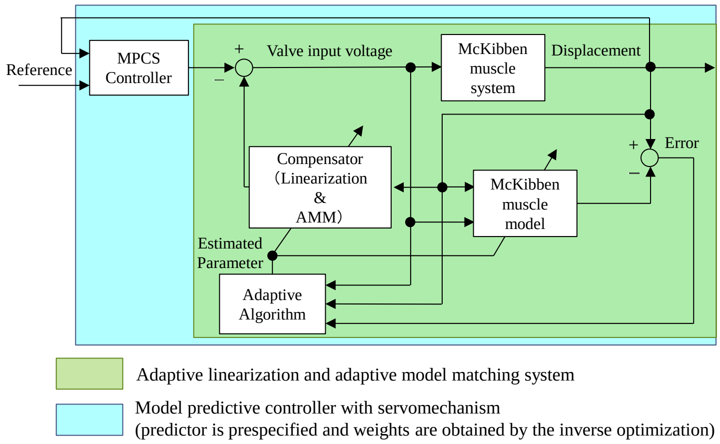

Figure 1. Block diagram of MPCS with AMM

3. Model-Free Adaptive Control (MFAC)

In this section, the MFAC system design is presented. The control system has many advantages, such as its applicability to nonlinear discrete-time systems and its ability to guarantee rigorously asymptotic stability without Lyapunov stability theory or key-technical lemma. After explaining the dynamic linearized data model, a pair of the estimation and control law for MFAC is derived.

3.1 Introduction to Dynamic Linearization Data Model

In this section, the dynamic linearization data model, which is a fully equivalent to the unknown nonlinear discrete-time system, is introduced to design the MFAC controller. In particular, the FFDL data model, which is one of the most common dynamic linearization models is explained. First, the unknown scalar nonlinear discrete-time system is defined as follows.

$$y(k+1) = f\left(y(k), y(k-1), \cdots, y\left(k-n_y\right), u(k), u(k-1), \cdots, u(k-n_u)\right) \tag{1}$$

where $u(k), y(k) \in R$ represent the control input and output of the system for time k, respectively, and $f(\cdot): R^{n_u+n_y} \to R$ is an unknown nonlinear function. Also, $n_y, n_u \in Z_+$ are two unknown orders of output and input, respectively. The system represented by equation (1) can be rewritten as a dynamic linearization data model (in particular, the FFDL data model) by the following theorem. Here, in order to introduce the theorem, the nonlinear discrete-time system needs to satisfy the following two assumptions.

Assumption 1
The partial derivatives of $f(\cdot)$ with respect to all variables are continuous. □

Assumption 2
The nonlinear discrete-time system (1) satisfies generalized Lipschitz condition: There exists a real constant $b \geq 0$ such that

$$|y(k_1+1) - y(k_2+1)| \leq b \left\| \boldsymbol{H}_{L_y+L_u}(k_1) - \boldsymbol{H}_{L_y+L_u}(k_2) \right\| \tag{2}$$

for all $k_1, k_2 \geq 0$. where $H_{L_y,L_u}(k) = \left[y(k), \cdots, y\left(k - L_y + 1\right), u(k), \cdots u(k - L_u + 1)\right]^T \in R^{L_y+L_u}$ is a vector consisting of all outputs and inputs of the system up to pseudo-order L_u $(1 \leq L_u \leq n_u)$, $L_y (1 \leq L_y \leq n_y)$, which is smaller than the order of system (1) such as n_u, n_y. The theorem for the FFDL data model is shown as follows. □

Theorem (FFDL data model)
Assume that system (1) satisfies Assumption 1 and 2 given above. Moreover, assume that the norm of the change in vector $\boldsymbol{H}_{L_y,L_u}(k)$, which consists of the changes in the inputs and outputs of the system, is nonzero, this is $\left\| \Delta\boldsymbol{H}_{L_y,L_u}(k) \right\| \neq 0$ where $\Delta\boldsymbol{H}_{L_y,L_u}(k) \triangleq \boldsymbol{H}_{L_y,L_u}(k) - \boldsymbol{H}_{L_y,L_u}(k-1)$. Then, there exists a time-varying pseudo-gradient vector (PG vector) $\boldsymbol{\phi}_{f,L_y,L_u}(k) \in R^{L_y+L_u}$ such that the following equation (3) is satisfied.

$$\Delta y(k+1) \triangleq y(k+1) - y(k) = \boldsymbol{\phi}^{\boldsymbol{T}}_{f,L_y,L_u}(k) \Delta\boldsymbol{H}_{f,L_y,L_u}(k) \tag{3}$$

where $\boldsymbol{\phi}_{f,L_y,L_u}(k) \triangleq \left[\phi_1(k), \cdots, \phi_{L_y}(k), \phi_{L_y+1}(k), \cdots, \phi_{L_y+L_u}(k)\right]^T$. Furthermore, from Assumption 2 and equation (3), we can say that $\left\| \boldsymbol{\phi}_{f,L_y,L_u}(k) \right\| \leq b$, which implies that the PG vector is bounded. □

In the following sections, the FFDL data model derived by the above theorem is used to design the control system.

3.2 Design the model-free adaptive controller based on the FFDL data model

First, it is necessary to estimate the PG vector to construct the FFDL data model at each time step, because the PG vector cannot be obtained analytically. For this purpose, the following evaluation function is introduced as follows.

$$J_e\left(\widehat{\boldsymbol{\phi}}_{f,L_y,L_u}(k)\right) = \left|\Delta y(k) - \widehat{\boldsymbol{\phi}}^T_{f,L_y,L_u}(k)\Delta\boldsymbol{H}_{L_y,L_u}(k-1)\right|^2 + \mu \left\| \widehat{\boldsymbol{\phi}}_{f,L_y,L_u}(\mathrm{k}) - \widehat{\boldsymbol{\phi}}_{f,L_y,L_u}(\mathrm{k}-1) \right\|^2 \tag{4}$$

The evaluation function expressed by equation (4) represents, in the first term, the difference between the change in output and the change in output represented by the FFDL data model using the estimated PG vector, and in the second term, the change in the PG vector with the weighting factor $\mu > 0$. Then, minimizing the evaluation function (4) with respect to the estimated PG vector, the following update law can be derived.

$$\widehat{\boldsymbol{\phi}}_{f,L_y,L_u}(k) = \widehat{\boldsymbol{\phi}}_{f,L_y,L_u}(k-1) + \frac{\eta\Delta\boldsymbol{H}_{L_y,L_u}(k-1)\left(\Delta y(k) - \widehat{\boldsymbol{\phi}}^T_{f,L_y,L_u}(k)\Delta\boldsymbol{H}_{L_y,L_u}(k-1)\right)}{\mu + \left\|\Delta\boldsymbol{H}_{L_y,L_u}(k-1)\right\|^2} \tag{5}$$

where $\eta \in (0,2]$ represents the step factor of the PG vector modification terms.
On the other hand, to derive the control law for MFAC, we consider the following 1-step ahead evaluation function of control input as follows.

$$J_c\left(u(k)\right) = |y_d(k+1) - y(k+1)|^2 + \lambda|u(k) - u(k-1)|^2 \tag{6}$$

where $y_d(k+1)$ represents the reference signal and $\lambda > 0$ represents the weighting factor for the change in the input. The evaluation function (6) represents in the first term, the difference between the reference and output of the system, and in the second term, the change in the input. Substituting FFDL data model (2) into this evaluation function (6), and minimizing (6) with respect to the control input signal $u(k)$, and by replacing the PG vector with an estimate, the following control law can be derived as follows.

$$\Delta u(k) = \frac{\rho_{L_y+1}(k)\widehat{\boldsymbol{\phi}}_{L_y+1}(k)\big(y_d(k+1)-y(k)\big)}{\lambda + \left\|\widehat{\boldsymbol{\phi}}_{L_y+1}(k)\right\|^2} - \frac{\widehat{\boldsymbol{\phi}}_{L_y+1}(k)\left(\sum_{i=1}^{L_y}\rho_i\widehat{\boldsymbol{\phi}}_i\,\Delta y(k-1-i)\right)}{\lambda + \left\|\widehat{\boldsymbol{\phi}}_{L_y+1}(k)\right\|^2} \tag{7}$$

where $\rho \in (0,1], i = 1, \cdots, L_y + L_u$ represents the step factors for each PG vector element to make the controller algorithm more flexible., and $\widehat{\boldsymbol{\phi}}_i$ represents the i-th element of the PG vector.

The block diagram of the above algorithm is shown in Figure 2. The MFAC performs the update law in equation (5) and the control law in equation (7) in online using only the change in input and output of the system. This allows us to control nonlinear systems without explicitly using the mathematical models.

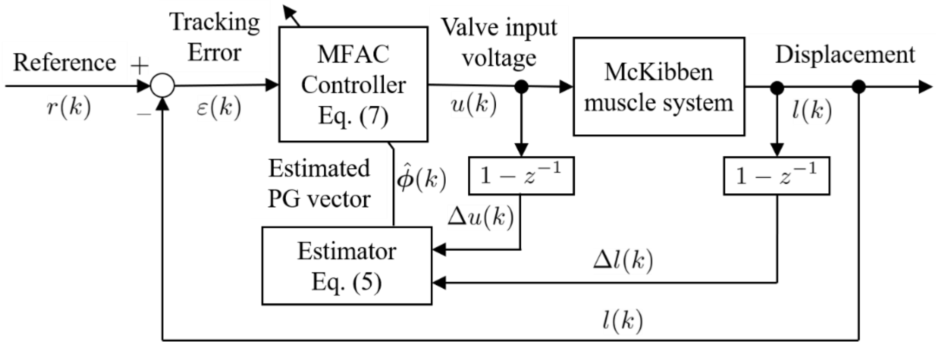

Figure 2. Block diagram of Model-Free Adaptive Control

4. Experimental results

In this section, the experimental conditions are described and a comparison between MFAC and MPCS with AMM based on the experiment results is presented in order to evaluate the robustness to load variations during experiments.

4.1 Experimental conditions

The experimental conditions for MFAC and MPCS with AMM are shown in Table 1 and 2, respectively, and switching the load applied to the muscle from 44 N to 68 N when experimental time is about 60 s to examine the load variations during the experiments. In additions, the experiment is conducted using the experimental circuit shown in Figure 3 and reference signal is set step signal for 50 mm.

Table 1. Experimental conditions for MFAC

Item	Value	Unit
Sampling time T_s	0.01	s
Weighting factors μ, λ	1	-
Step factors ρ, η	1	-
Order of PG vector L_y, L_u	1	-
Initial value of PG vector $\widehat{\boldsymbol{\phi}}_{f,L_y,L_u}(1)$	$[1\ 0.05]^{\mathrm{T}}$	-

Table 2. Experimental conditions for MPCS with AMM

Item	Value	Unit
Sampling time T_s	0.1	s
Predictive horizon H_p	5	step
Control horizon H_u	5	step
Coefficient of forgetting parameter λ_0	0.99	-
Initial value of forgetting parameter $\lambda(0)$	0.95	-
Covariance matrix $P(0)$	$1000I_{16}$	-
Desired pole	{0.6 0.7 0.8}	-

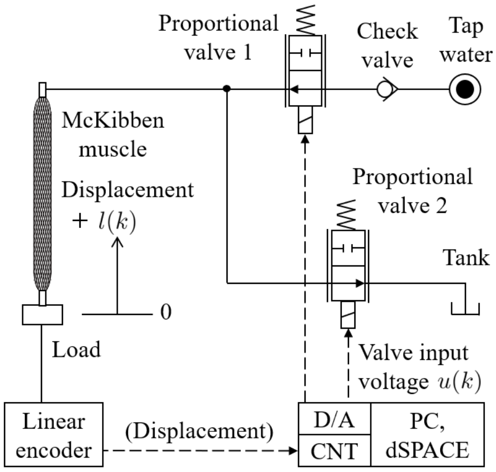

Figure 3. Experimental circuit

4.2 Comparison of MFAC and MPCS with AMM by Experiments

Based on the above conditions, Figure 4 shows the comparison results of the control performance of MFAC and MPCS with AMM considering the load variation during the experiments. From this figure, it can be confirmed that although the control performance deteriorates around 60 s for the load change, high tracking control performance is achieved for both control methods in the steady-state response after 100 s. In addition, this figure and Table 3 show that the tracking control performance of MFAC and MPCS with AMM is found to be almost equal in the steady-state response. These results imply control performance that is generally close to the performance limit of the sensor is obtained because the adaptive systems are introduced in both control methods. On the other hand, from the evaluation of the maximum absolute error of Table 3, the control performance of MFAC in the transient response immediately after load variation is better that that of the MPCS with AMM.

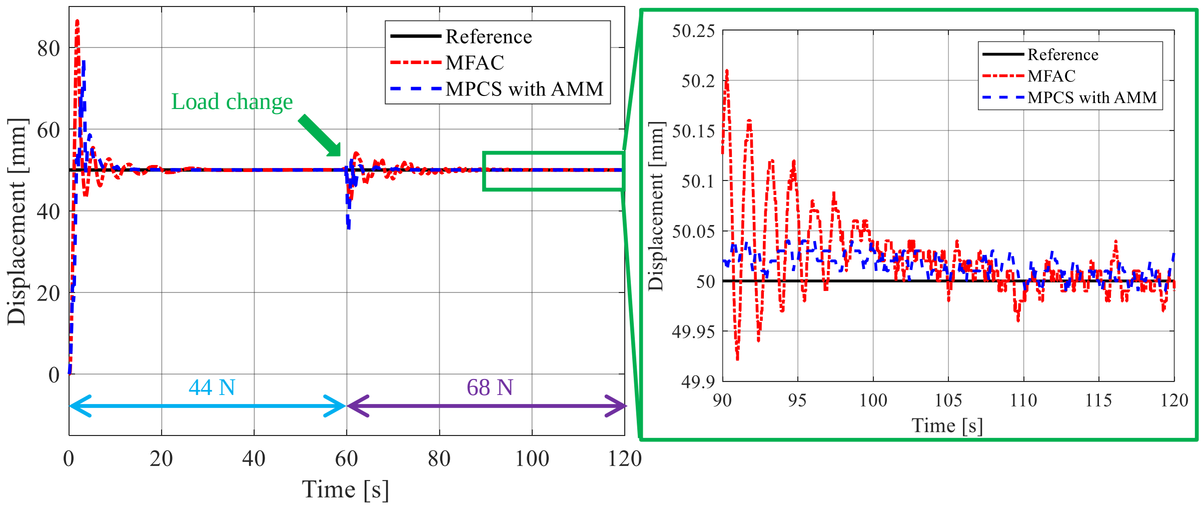

Figure 4. Comparison MPCS with AMM and MFAC for load variations during experiments

Table 3. Evaluation results of the control performance for Figure 4

Evaluation method and interval	MFAC	MPCS with AMM
Mean absolute error (100 ~ 120 s) [mm]	0.013	0.013
Max absolute error (50 ~ 120 s) [mm]	7.85	15.2

Figure 5 shows the results of tracking error in the steady-state response using 13 samples of data, (a) the transient response after the load variation, (b) the steady-state response before (35 ~ 55s) and after (100 ~ 120s) the load variation. Figure 5 (a), it can be seen that there is not much difference between the control performance of MFAC and MPCS in the transient response immediately after the load is changed. On the other hand, the results after load variation of Figure 5 (b) shows that the MFAC and the MPCS with AMM have almost the same control performance in terms of the minimum value, however, the MFAC has a narrower quartile range and a narrower maximum-minimum range than the MPCS with AMM. In addition, comparing the control performance before and after the load variation, it can be seen that MPCS with AMM has higher control performance before the load variation, while MFAC has higher control performance after the load variation. Therefore, these results show that the MFAC is clearly more robust to load variation than the MPCS with AMM. The reason for this is that these results implies that the MFAC has a higher ability to sustain the adaptive capability of the PG vector. Moreover, MFAC is a reasonable result because of its guaranteed asymptotic stability. On the other hand, although MPCS with AMM can sometimes achieve high tracking control performance, it cannot reduce the modeling error due to the lack of persistent adaptive capability, resulting in bad control performance in some cases. Furthermore, MPCS with AMM is a reasonable result because stability is not guaranteed in the presence of modeling errors.

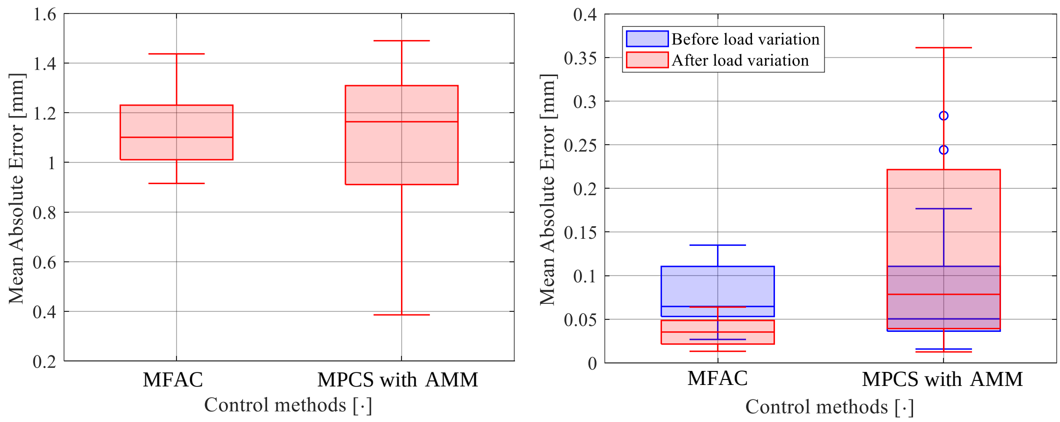

(a) The transient response (b) The steady-state response (before and after load variation)

Figure 5. Box plots of experimental results for load variations during experiments (13 samples each)

5. Conclusion and Future work

In this paper, model predictive control with servomechanism combining inverse optimization and adaptive model matching, one of the model-based control, and model-free adaptive control, one of the data-driven control, are applied to tap-water-driven muscle, and the control performance and robustness against load variations during experiments are described. First, the previous study, MPCS with AMM is briefly described. Then, the full form dynamic linearization data model, which is different from the mathematical model, is introduced and describes the design of a model-free adaptive control system based on this model. The experimental results show that both MPCS with AMM and MFAC have high tracking control performance of about 0.013 mm in steady-state response after load variations, but MFAC is more robust than MPCS with AMM even though no exact mathematical model is used. In the future, we will propose a method for adjusting parameters and initial values based on an optimization algorithm.

REFERENCES

1. Andrikopoulos, G., Nikolalopoulos, G., Manesis, S., A Survey on Applications of Pneumatic Artificial Muscles, Proceedings of 19th Mediterranean Conference on Control and Automation, 2011, pp. 1439-1446.
2. Conrad, F., Trends in Design of Water Hydraulics – Motion Control and Open-Ended Solutions, Proceedings of the 6th JFPS International Symposium of Fluid Power, 2005, pp. 420-431.
3. Miyakawa, S., Aqua Drive System: A Technology Using Tap Water and Its Applications, Proceedings of the 8th JFPS International Symposium on Fluid Power, 2011, pp. 26-37.
4. Tsuruhara, S., Inada, R., Ito, K., Model Predictive Displacement Control Tuning for Tap-Water-Driven Muscle by Inverse Optimization with Adaptive Model Matching, Proceedings of the 10th International Conference on Fluid Power Transmission and Control -ICFP2021, 2021, pp. 286-292.
5. Hou, Z., Xiong, S., On Model-Free Adaptive Control and Its Stability Analysis, IEEE Transactions on Automatic Control, Vol. 64, No. 11, 2019, pp. 4555-4569.
6. Tsuruhara, S., Ito, K., Design of Model-Free Adaptive Displacement Control System for Tap-Water-Driven Muscle, Proceedings of the Conference on Japan Fluid Power System Society in 2021 Spring, 2021, (*in Japanese*, Submitted).

The 11th JFPS International Symposium on Fluid Power HAKODATE 2020 Oct. 12-13, 2021 JFPS The Japan Fluid Power System Society

Experimental study on Dual-Layer Type Vortex Cup Driven by Aqua Drive System

Wataru KOBAYASHI*, Tetsuya AKAGI* and Shujiro DOHTA*

*Department of Intelligent Mechanical Engineering, Faculty of Engineering, Okayama University of Science
1-1 Ridai-cho, Kita-ku, Okayama city, Okayama, 700-0005 Japan
(E-mail: kobayashi@are.ous.ac.jp)

Abstract. This paper concerns with experimental study on a vortex cup. The cup has a vortex chamber inside the cup and it can generate a swirl flow causing negative pressure in the chamber. There exists problems of the cup to be solved: improvement of the suction force and application of other working fluids. This study applies aqua drive system as a driving source to the cup to validate the performance of the cup. In addition, a modification of the shape of the cup is considered. The approach adopts a folding flow path inside the cup. Experiments of a prototype dual-layer cup are carried out to validate the performance of the cup with change of designed parameters: a chamber height, a flow path width and a gap height. As a result, it is confirmed that the cup with redesigned parameters can achieve four times as large as that of the conventional cup.

Keywords: Vortex cup, Aqua drive system, Dual-layer, Swirl flow, Optimal design

INTRODUCTION

A vortex cup is a new non-contact type handling method by using vortex levitation [1]. Traditional methods to convey semiconductor and glass substrates adopt a contact type handling method which use pneumatic end effectors to hold them. This method, however, has some problems as follows: 1) it causes static electricity between end effectors and substrates, 2) it has a potential risk to hurt substrates directly, 3) its handling force is inadequate to convey large, heavy and extra-thin substrates [2].

To solve the problems described above, a Bernoulli-chuck type end effector shown in Figure 1 was developed. The end effector can convey substrates with non-contact method. Compressed air is exhausted from bottom-side nozzles and then exhausted air from clearance between the end effector and floor surface which ejects in a radial direction discharges into the atmosphere [3]. This makes the center area of the end effector, which is in vortex chamber, negative pressure. Thus, the end effector with the vortex chamber can hold substrates by negative pressure, and exhausted air prevent the end effector from touching with floor surface. The end effector, however, requires relatively large flow rate and has small suction force [4].

On the other hand, some studies showed that swirl flow can also make negative pressure in the center of flow [5]. Then a new non-contact type end effector using swirl flow, which called vortex cup shown in Figure 2, was developed [6-10]. The air consumption of the vortex cup can be one fourth of that of the Bernoulli-chuck type end effector. Thus, it indicates that the cup with swirl flow can solve the problems mentioned above. There exist additional studies about swirl flow in the cup. Li [11] reported a flow analysis on the cup, especially in the vortex chamber. It was shown that the center of swirl flow in the vortex camber moved and this phenomenon decreased velocity of swirl flow. This also caused reduction of suction force of the cup. Kawakami [12] introduced cylindrical/circular- truncated-cone shaped guides into the vortex chamber to prevent movement of the center of swirl flow. It was confirmed that height and diameter of the guides affect to suction force of the cup. Bonaccorso [13] also installed an electric motor into the center of the vortex chamber and the motor can generate a swirl flow without supplied air.

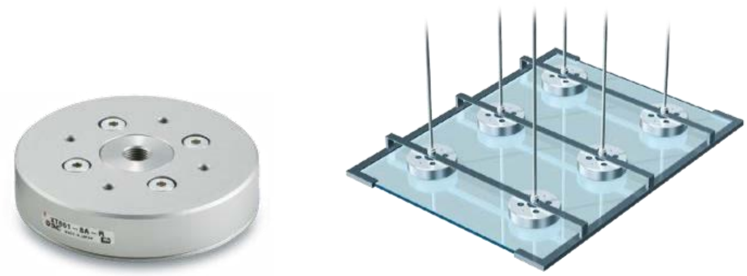

Figure 1. Bernoulli-chuck type end effector (XT661, SMC corporation).

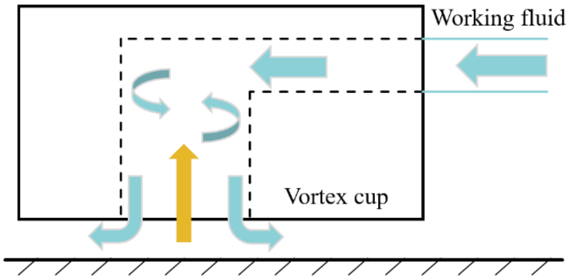

Figure 2. Schematic diagram of vortex cup using swirling flow.

This study concerns with a modification of the shape of the cup to improve the suction force of the cup and an application of aqua drive system using tap-water as a working fluid. Although the conventional pneumatic cup is applied to a conveyor of semiconductor as mentioned above, an aqua drive cup described in this paper can be applied to a holding mechanism of underwater systems. Other driving sources without aqua drive system are unsuitable in underwater environment because of their waterproof performance. On the other hand, if the aqua drive cup is available, holding mechanism in underwater environment with no waterproofing can be realized. The conventional vortex cup mentioned above has simple cylindrical vortex chamber and some improvements applied inner guides in the chamber. On the other hand, the authors introduce a folding flow path inside a vortex cup and make second-layer in order to increase the flow velocity and reduce the radius of a vortex chamber. The detail of the cup is described later. Experimental analysis of a prototype new-shaped cup is also conducted and effects of designed parameters of the cup on the suction force are validated to show an optimal design of the new-shaped cup. Moreover, additional experiments show the difference of driving sources: aqua drive and pneumatic systems.

AQUA DRIVE VORTEX CUP

Vortex cups mentioned above are generally driven by pneumatic systems to mount them on the non-contact type handling devices such as end effectors. The cups can overcome the problems that the conventional handling methods mentioned above have. Moreover, an expansion their application range to other driving sources is relatively easy because the working principle of the cups is simple. The cups have no limitation of working fluids. There are, however, few studies concerning with any other working fluids such as oil, water, and functional fluids. This study focuses on water as working fluid of the cup and aims to show the difference between pneumatic and aqua drive cups.

First of all, an aqua drive system is applied to a vortex cup. The shape of the vortex cup is a cylinder with a simple vortex chamber and an inlet port on side surface of the chamber. Figure 3 shows a tested aqua drive cup made by 3D printer (AFINIA H800+, Microboards Technology Inc). The diameter of the vortex chamber r and the height of the vortex chamber h in Figure 3(b) are 70 mm and 40 mm, respectively. The inner diameter of inlet port is 8 mm. Inlet flow from the port runs along the inner surface of the vortex chamber and forms swirl flow.

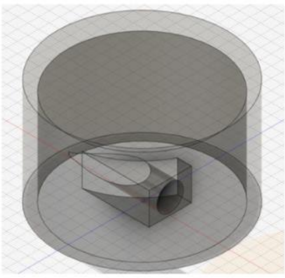

(a) Schematic view of tested cup

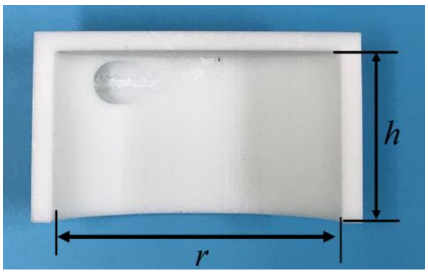

(b) Cross-sectional view of tested cup

Figure 3. Tested aqua drive vortex cup.

To validate its performance, which means a suction force of the cup, an experimental setup shown in Figure 4 is constructed. The experimental setup consists of the tested cup, a jig to hold the cup, a force gauge (FGC-5, NIDEC-SHIMPO CORPORATION) to measure the suction force of the cup, and a wire to connect the cup with the force gauge. Its driving source is from tap-water in the author's laboratory of which pressure is approximately 280 kPa: almost average pressure of tap-water in Japan. Experiments here are carried out by changing the diameter and the height of the cup to show the effect of them to the suction force of the cup. Measurements are carried out

2

eight times and the average of them are shown in Figure 5. Additional experiments which change only driving source from aqua drive to pneumatic system are also carried out and Figure 5 plots the results: blue lines and dots show the results of the aqua drive cup and green lines and dots show the results of the pneumatic cup. Note that both driving sources used same supplied pressure of 280 kPa.

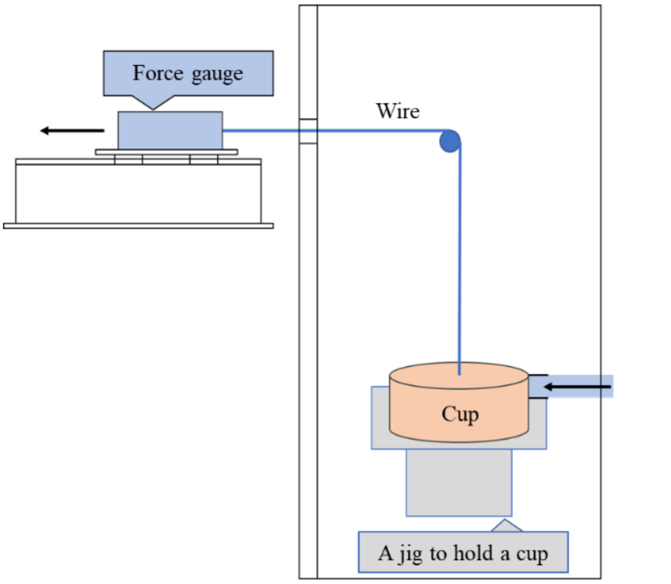

Figure 4. Schematic diagram of experimental setup for suction force measurement.

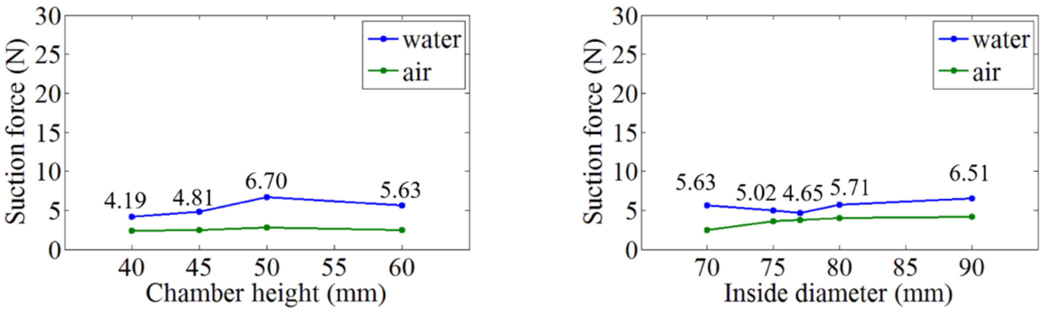

(a) Suction force vs. camber height (b) Suction force vs. chamber diameter

Figure 5. Experimental results of single-layer type vortex cup.

The experimental results showed that the tested cup generates approximately 5 N of the suction force and little difference exists when the diameter of the cup is changed from 40 to 60 mm and the height of the cup is changed from 70 to 90 mm. In particular, the cup with the chamber diameter of 50 mm generates the maximum suction force but the difference between the maximum and minimum suction forces is only 2.5 N.
On the other hand, the results also showed the difference of driving sources. It is confirmed that the suction force of the aqua drive cup was larger than that of the pneumatic cup under all conditions in these experiments. In particular, the suction force of the pneumatic cup was less than 4 N under all conditions. Notice here that the size of the cup was designed with consideration for application of the aqua drive system: the diameter of the inlet port, the diameter and height of the vortex chamber. In other words, the tested cups were specialized in aqua drive system and their dimension might be too large to apply to the pneumatic cup. The important point in these experiments is that we can apply other driving sources such as aqua drive system same as the conventional pneumatic system. This suggests that application range of vortex cups can be expanded.

DUAL-LAYER TYPE VORTEX CUP

The foregoing experiments showed a possibility of a vortex cup driven by aqua drive system. The cup, however, had insufficient suction force in practical. In addition, the cup constantly requires swirl flow in the vortex chamber

to keep negative pressure when it works. Then, it is considered to modify the shape of the cup in order to improve the performance of the aqua drive vortex cup. The shape of the conventional cup was simple cylinder and some studies inserted cylindrical/circular- truncated-cone shaped guides as mentioned above. In this study, flow path inside a vortex cup is folded to increase flow velocity of the swirl flow and also the suction force of the cup.
This approach was applied to the micro-bubble generator (Aqua air, idea-techno Co., Ltd.) shown in Figure 6. The micro-bubble generator adopted a swirl flow way and it can generate bubbles with diameter of 1 - 60 µm. The inlet flow runs along with inner side surface of the chamber of the generator and negative pressure occurs at the center of the chamber. At the moment, micro-bubbles can be generated due to supplied gas to the center of the camber. Thus, the operating principle of the generator is similar to that of the vortex cup. As seen in Figure 6, the flow velocity inside the generator can increase by folding the flow path at its turn-round points: it is shown as arrows in the figure.
On the other hand, the centrifugal force in the vortex chamber relates to swirl flow which also relates to the suction force of the vortex cup. A centrifugal force F in general is expressed as Eq. (1) where m, ω, and r are a mass, an angular velocity and a radius, respectively. It is clear that a reduction of the radius and increase of the angular velocity lead to gain of the centrifugal force. Thereby, if a radius of a vortex chamber is reduced by folding flow path in a vortex cup as the micro-bubble generator did, the suction force of the cup can be gained without any modifications of outer dimensions of the cup.

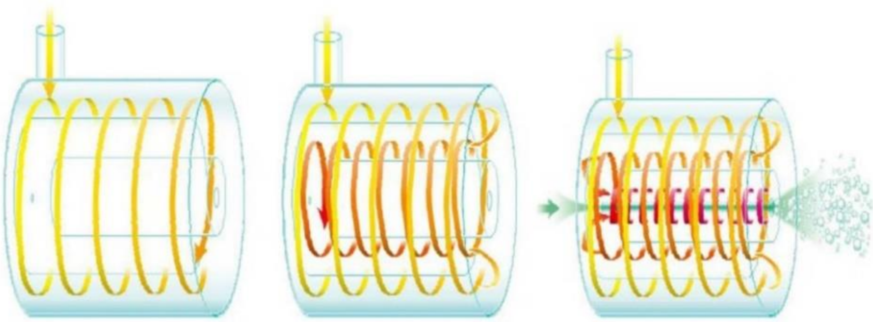

Figure 6. Operating principle of micro-bubble generator (Aqua air, idea-techno Co., Ltd.).

$$F = m\omega^2 r. \tag{1}$$

A prototype of a vortex cup with a folding flow path is made to validate the effectiveness of the forementioned approach. Figure 7 shows the comparison of conventional single-layer and proposed dual-layer type vortex cups. As seen in the cross-sectional view of Figure 7, the structure of the right cup has dual-layer flow path inside the cup and parameters r_i, r_o, h_c and h_i exist. The parameters indicate an inner diameter of the vortex chamber, a width of the flow path in a second-layer, a height of the flow path at the turn-around point, and a height of the vortex chamber, respectively. Figure 8 shows the schematic view of the prototype dual-layer cup and its cross-sectional view. The prototype cup realizes a dual-layer flow path inside the cup by assembling two parts made by 3D printer mentioned above. Figure 9 shows the assembly parts of the prototype cup and the assembled structure enables the parameters r_i, r_o, h_c and h_i to be modified easily by replacing the parts although details of the modifications are described below.

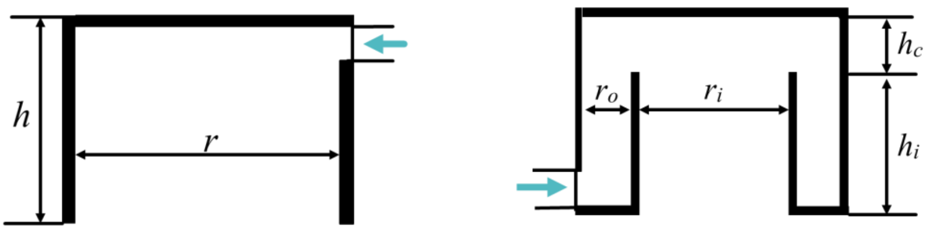

(a) Single-layer (b) Dual-layer

Figure 7. Comparison of single-layer and dual-layer type vortex cups.

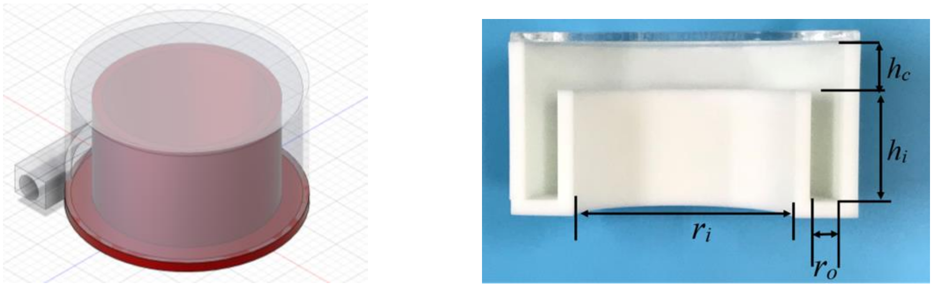

(a) Schematic view of dual-layer cup (b) Cross-sectional view of dual-layer cup

Figure 8. Schematic diagram of tested dual-layer cup.

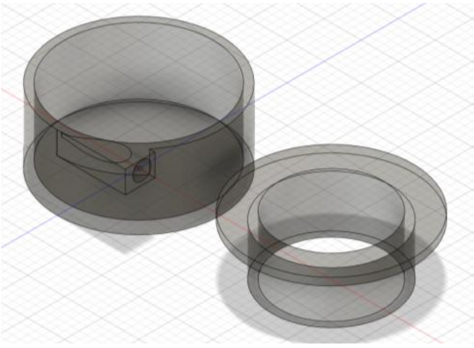

Figure 9. Assembly parts of tested dual-layer cup.

EXPERIMENTAL ANALYSIS OF DUAL-LAYER TYPE VORTEX CUP

The dual-layer cup has additional parameters such as a flow path width r_o in the first-layer and a gap height h_c, that is, there exist four design parameters to optimize the performance in the suction force of the cup: a chamber diameter r_i, a chamber height h_i, a flow path width r_o and a gap height h_c. Note that only the chamber diameter in following experiments is fixed so as not to change the vortex chamber area of the cup from that of the conventional single-layer cup. In addition, other parameters such as a diameter of the inlet flow port, an outer diameter of the cup and a height of the cup are also same as the parameters of the single-layer cup mentioned in previous chapter in order to compare the performance of the dual-layer cup with the single-layer cup. Experiments to measure the suction force of the cup are carried out by using the experimental setup shown in Figure 4 and measurement conditions and procedure are also same as them of the previous experiments. Table 1 shows the designed parameters of a benchmark dual-layer cup of which outer dimension is almost equivalent to the one of the single-layer cup.

Table 1. Designed parameters of benchmark dual-layer cup.

Parameters	**Symbols**	**Value [mm]**
Flow path width	r_o	10
Gap height	h_c	10
Chamber height	h_i	50
Chamber diameter	r_i	70
Inlet port diameter	-	8

First experiment evaluates an effect of changing the flow path width r_o on the suction force of the cup. Figure 10 shows the experimental results. The suction force was measured with changing of only the flow path width from 5 to 15 mm. The difference between aqua drive and pneumatic cups were also examined and the both results are plotted in Figure 10: blue lines and dots show the results of the aqua drive cup and green lines and dots show the results of the pneumatic cup. As seen in Figure 10, the suction force of the aqua drive cup was drastically increased due to the dual-layer structure. It is experimentally confirmed that the cup with the flow path width of 10 mm can generate the maximum suction force of approximately 22 N, which is almost three times larger than that of the single-layer cup. Nevertheless, the suction force of the pneumatic cup with dual-layer showed little change from that of the single-layer cup and also change of flow path width had little effect on the suction force.

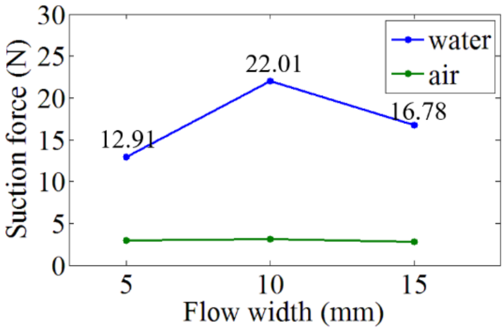

Figure 10. Experimental result on flow path width.

Second and third experiments evaluate effects of changing the gap height h_c and the chamber height h_i on the suction force of the cup, respectively. Figures 11 and 12 show the experimental results. The suction force was measured with changing of the gap height from 5 to 15 mm in the second experiment and with changing of the chamber height from 50 to 70 mm in the third experiment. Note that the second experiment used the redesigned flow path width of 10 mm and the third experiment used the redesigned flow path width of 10 mm and gap height of 15 mm taking account of the results of the first and second experiments. The difference between aqua drive and pneumatic cups were also examined and the both results are plotted in Figures 11 and 12: blue lines and dots show the results of the aqua drive cup and green lines and dots show the results of the pneumatic cup.
The cup with the gap height of 5 mm generates the maximum suction force of approximately 22 N. The gap height in the second experiment means the difference between the height of the first-layer and that of the second-layer in the cup. The force difference in the experiment was only 1.7 N and this means change of the gap height had little effect on the suction force of the cup. On the other hand, it is clear that the chamber height had strong relationship with the suction force of the cup. The cup with the chamber height of 60 mm generates the maximum suction force of approximately 25 N. There existed a large difference between the result with 60 mm chamber height, which showed the maximum suction force, and that with 50 mm chamber height, which showed the minimum suction force. Nevertheless, the suction force of the pneumatic cup showed little change in both experiments. The size of the tested cups was designed with consideration for application of aqua drive system as mentioned above. In particular, the diameter of the inlet port was designed for application of aqua drive system. Hence, the experimental results here showed same tendencies regardless of designed parameters and experimental conditions.
Table 2 shows the parameters for the aqua drive dual-layer cup which mean the combination of the parameters generating the maximum forces on each previous experiment. The maximum suction force of the redesigned cup, which is approximately 25 N, can achieve four times as large as that of the conventional single-layer cup. Thus, the modification with second-layer can increase the velocity of swirl flow in the chamber and then it can also increase the suction force. To analyze the relationship between the designed parameters and the suction force in detail, theoretical consideration based on mathematical models of the cup and computational analysis are required and it will be a next step of this study.

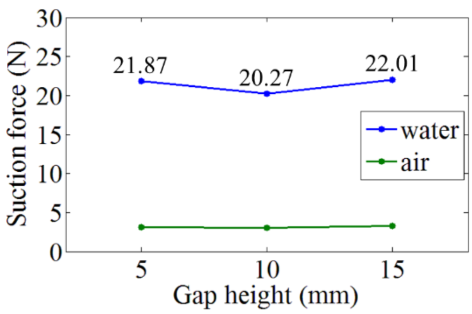

Figure 11. Experimental result on gap height.

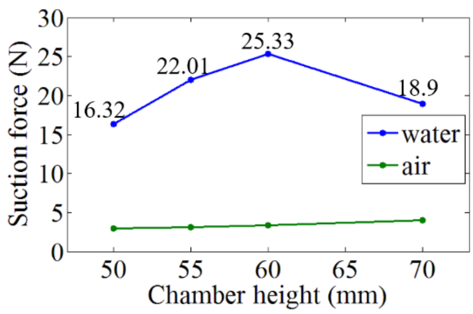

Figure 12. Experimental result on chamber height.

Table 2. Combination of designed parameters for dual-layer cup.

Parameters	Symbols	Value [mm]
Flow path width	r_o	15
Gap height	h_c	10
Chamber height	h_i	60
Chamber diameter	r_i	70
Inlet port diameter	-	8

CONCLUSIONS

This paper concerns with experimental study on a vortex cup which is a new non-contact type handling method by using vortex levitation. The cup has a vortex chamber inside the cup and it can generate swirl flow. The generated swirl flow makes negative pressure in the center of the vortex chamber. This is the working principle of the cup and considerable points of the cup are 1) improvement of the suction force of the cup, 2) application of other working fluids such as oil, water and functional fluids.

This study applies aqua drive system as a driving source to the cup in order to validate the performance of the cup compared with that of the conventional pneumatic driven cup. The experiment of the tested aqua drive cup made by 3D printer was carried out and the relationship between the parameters of the cup and the suction force was shown. Moreover, the additional experiments also showed the difference of two driving sources.

On the other hand, a modification of the shape of the cup was considered. The approach of the modification adopted a folding flow path inside the cup, that is, there existed a second-layer on an outer side of a first-layer of the cup. The experiments of prototype dual-layer cup were carried out to validate the performance of the cup with change of designed parameters: a chamber height h_i, a flow path width r_o and a gap height h_c. As a result, it is confirmed that the cup with redesigned parameters can achieve four times as large as that of the conventional single-layer cup.

Future work of this study is to analyze the relationship between the designed parameters and the suction force in detail, especially for both aqua drive and pneumatic cups. Theoretical analyses based on mathematical models of the cups and computational analyses will be conducted.

REFERENCES

1. BRANDT, E. H., Levitation in physics. Science, 1989, 243-4889, pp. 349-355.
2. MORISAWA, T., et al., A non-contact holder using airflow, JFPS International Journal of Fluid Power System, 2019, 11-3, pp. 104-109.
3. WALTHAM, C., BENDALL, S., KOTLICKI, A., Bernoulli levitation, American Journal of Physics, 2003, 71-2, pp. 176-179.
4. DINI, G., FANTONI, G., FAILLI, F., Grasping leather plies by Bernoulli grippers, CIRP annals, 2009, 58-1, pp. 21-24.
5. LI, X., KAWASHIMA, K., KAGAWA, T., Analysis of vortex levitation, Experimental Thermal and Fluid Science, 2008, 32-8, pp. 1448-1454.
6. IIO, S., Research on a non-contact handling system using swirling flow (influence of cup-to-work gap thickness on swirling flow characteristics), SICE Trans Ind Appl, 2008, 7-12, pp. 79-84.
7. FALLAH, A., et al., Numerical analysis of a non-contact surface adhesion system based on vortex cup for wall climbing robots, 2013 First RSI/ISM International Conference on Robotics and Mechatronics (ICRoM). IEEE, 2013, pp.368-373.
8. ZHAO, J., LI, X., Effect of supply flow rate on performance of pneumatic non-contact gripper using vortex flow, Experimental Thermal and Fluid Science, 2016, 79, pp. 91-100.
9. LI, X., KAWASHIMA, K., KAGAWA, T., Dynamic characteristics of vortex levitation, 2008 SICE Annual Conference. IEEE, 2008. pp. 1175-1180.
10. WU, Q., YE, Q., MENG, G., Particle image velocimetry studies on the swirling flow structure in the vortex gripper, Proceedings of the Institution of Mechanical Engineers, Part C: Journal of Mechanical Engineering Science, 2013, 227-9, pp. 1927-1937.
11. LI, X., et al., Computational fluid dynamics study of a noncontact handling device using air-swirling flow, Journal of engineering mechanics, 2011, 137-6, pp. 400-409.
12. KAWAKAMI, C., NAKAO, M., NISHIMURA, Y., KONDO, E., Increased sucking force of Vortex Cup attached a Cylinder in the Vortex Chamber, Proceedings of JFPS Autumn Conference, (2015), pp.56-58.
13. BONACCORSO, F., BRUNO, C., LONGO, D., MUSCATO, G., Structure and model identification of a vortex-based suction cup, Advances in Mobile Robotics, 2008, pp. 303-310.

Organized Session | Organized session

Soft Actuator 2

[OS5-2-01] Pneumatic Source Proposal for Improving Portability and Responsiveness of Artificial Muscle via Dimethyl Ether Phase Change and Combustion

〇Ryuto Enjo[1], Manabu Okui[1], Taro Nakamura[1] （1.Chuo university）

[OS5-2-02] Development of Six-Legged Mobile Robot Using Tetrahedral Shaped Pneumatic Soft Actuators

〇Kenta Hase[1], Tetsuya Akagi[1], Shujiro Dohta[1], Takashi Shinohara[1], Wataru Kobayashi[1], So Shimooka[2] （1.Okayama University of Science, 2.Okayama University）

[OS5-2-03] Development of the Transfer System for Bedridden Elderly and Disabled People using Pneumatic Actuators

〇Feifei Cho[1], Keisei Kato[1], Ryota Endo[1], Takumi Kobayashi[2], Tetsuya Akagi[2] （1.National Institute of Technology Tsuyama College, 2.Okayama University of Science）

[OS5-2-04] Development of Pneumatic Drive Pipe Inspection Robot using Radial Bending Type Soft Actuator

〇Takashi Shinohara[1], Hikaru Furuya[1], Tetsuya Akagi[1], Shujiro Dohta[1], Takumi Kobayashi[1], So Shimooka[2] （1.Okayama University of Science, 2.Okayama University）

The 11th JFPS International Symposium on Fluid Power HAKODATE 2020 Oct. 12-13, 2021 The Japan Fluid Power System Society

Pneumatic Source Proposal for Improving Portability and Responsiveness of Artificial Muscle via Dimethyl Ether Phase Change and Combustion

Ryuto ENJO*,Manabu OKUI*,Taro NAKAMURA*

*Department of Precision Mechanics, Faculty of Science and Engineering
Chuo University
1-13-27 Kasuga, Bunkyo-ku, Tokyo, 112-8551 Japan
(E-mail: r_enjo@bio.mech.chuo-u.ac.jp)

Abstract. Pneumatic drive systems are widely used in assistance devices and flexible drive robots owing to their various characteristics. Compressed air generated by engine compressors and large motors drives these devices, but such large and heavy air pressure sources limit the mobilization of pneumatic drive devices. Herein, we propose a two-stage system using dimethyl ether (DME) phase change and combustion to develop the mobilization of pneumatic drive devices. Also, the artificial muscle driven by DME combustion is introduced and prototyped to improve responsiveness. Besides, we experimentally investigated DME combustion characteristics. The result shows a range of combustible air-DME fuel ratios and an air-DME molar ratio of 0.07% that generated the highest pressure. Furthermore, we measured the response time and displacement of the artificial muscle when DME burned in the device. The results indicate that this device drives rapidly than that of previous research.

Keywords: Air-pressure source, artificial muscle, combustion, pneumatic actuators, pneumatic systems

INTRODUCTION

Pneumatic drive systems are widely used in assistance devices [1] and flexible drive robots [2] due to their lightweight, high output, and excellent flexibility characteristics. However, the problems of pneumatic drive systems are air pressure sources and low responsiveness. Compressed air generated by engine compressors and large motors is mainly used to drive these devices, but such large and heavy air pressure sources are barriers to mobilizing pneumatic drive devices. Thus, the construction of a portable air pressure source can expand the application range of such devices.

Along these lines, many mobile pneumatic drive systems have been developed. Among them is an air pressure source used by three points of dry ice [3] that can silently release gas at 0.42 MPa. However, at normal temperatures, the energy required to produce compressed air cannot be safely stored because vaporization could inadvertently occur at any time. Our previous research evaluated an air pressure drive system to develop a portable air pressure source. However, no portability method could be identified [4] (Figure 1). In addition to previous methods, we developed a hybrid pneumatic source [5], which combines the phase changes of liquid carbon dioxide and dimethyl ether (DME). The prototype is able to provide much more amount of compressed gas compared to existing method, but DME had problems, such as flammability and thermal drop problems.

Here, the responsiveness of pneumatic actuators is investigated. The compressed air must activate pneumatic actuators, but the compressible of the air causing the response delay. Also, compressed air is generally supplied through the narrow tube, which causes a response delay.

To improve the response of pneumatic actuators, pneumatic artificial muscles and Magneto-rheological (MR) fluid method has been developed [6]. In this method, elastic uses artificial air muscle, and instantaneous force is generated using MR fluid brake that can change the viscosity. Although this method can generate great force instantly, it needs advanced preparation to drive the devices.

Therefore, the study aims to improve the portability and responsiveness of pneumatic drive systems. To do so, we focus on the physical properties of flammable DME and consider obtaining energy by DME combustion. Also, we consider obtaining energy in two stages via phase change and DME combustion. The proposed method, which uses the gas–liquid phase change of DME at a high flow rate per mass, does not require complicated auxiliary systems and equipment.

Besides, we think that DME combustion can solve the problems of the hybrid pneumatic source, which is the flammability or thermal drop. To improve the responsiveness of the pneumatic drive system, we proposed the pneumatic system driven by DME combustion. This method can generate large instantaneous force using DME combustion inside the pneumatic system. Herein, we proposed the concept of a two-stage pneumatic source and investigated DME combustion characteristics. Also, we proposed a pneumatic system driven by DME combustion and investigated its responsiveness when air-DME mixed gas burned inside the artificial muscle.

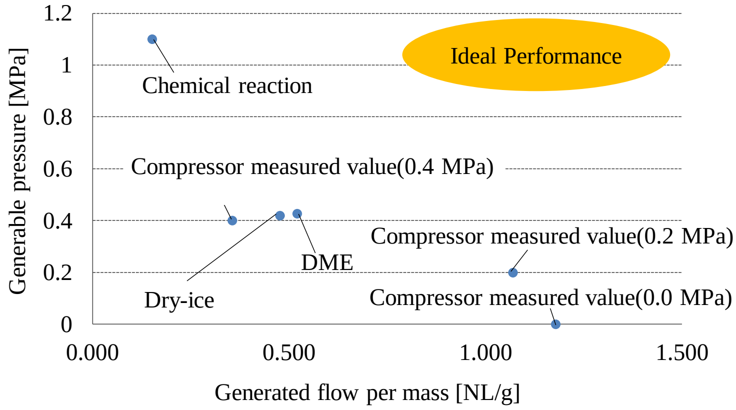

Figure 1. Mobility of pneumatic source flowchart [4]

TWO-STAGE DME USAGE SYSTEM PHASE CHANGE AND COMBUSTION

An overview of the proposed system is shown in Figure 2. Pressurization and decompression occur at regular intervals, and a leveraged pneumatic artificial muscle is used as a pneumatic actuator. The main components of a two-stage usage system are explained below.

(a) Pneumatic actuators are driven via the phase change of DME

(b) After driving the actuators, DME exhaust gas is collected and put into a container

(c) Energy is obtained via combustion, where the DME is ignited using a spark plug in the container.

DME gas-liquid phase change can generate 0.4 MPa of pressure stably. DME does not release particulate pollutants and smoke because it is oxygenated fuel and has no carbon bonds. Additionally, DME is a gas at normal temperatures, and its saturated vapor pressure is low (= 0.6 MPa), so it can easily be stored as a liquid. Based on these properties, DME can be suitably used in a two-stage system.

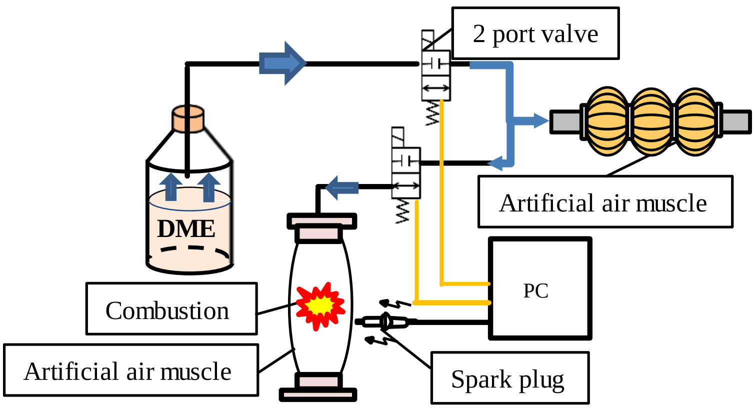

Figure 2. Outline of two-stage application system of phase change and combustion of DME

COMBUSTION EXPERIMENT

Experimental Purpose

The experiment aims to verify the air-DME fuel ratio range for combustion via spark plugs and measure the pressure.

Experimental Method

Figure 3 shows the schematic representation and photo of the experimental device. A tank, pressure sensor (MPS-R33RC-NGAT, MYOUTOKU, Japan), regulator (RVUM6-6, PISCO, Japan), two-port valve (MVP62, PISCO, Japan), spark plug (Hirano giken, Japan) were used. A gas mixture of air-DME fuel was stored in the tank in advance and was injected into a semi-closed container for 3 s using a pressure gauge, a regulator, and a two-port valve. The mixed gas was ignited via a spark plug 2 s after the injection. When the mixed gas burned, the pressure was measured by changing the mixing ratio. The molar ratio parameter, which was set to 0.03%–0.14%, was based on the theoretical air-DME ratio (0.067%). The experiment was conducted in a room maintained at 25°C, and an atmospheric pressure of 0.1013 MPa was used in the calculations. Each measurement was performed thrice. A 1.0 × 1.3-cm^2 hole was created above the semi-closed container because the container's pressure rapidly rises when mixed gas is burned.

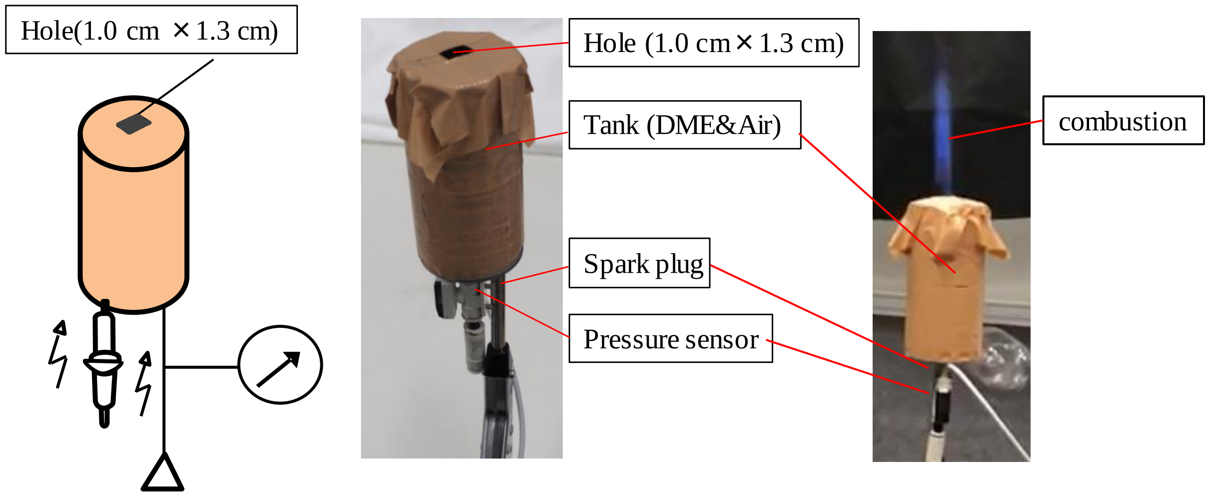

Figure 3. Image of experimental device

Experimental Results and Discussion

Figure 4 shows the pressure variation with the mole ratio parameter when mixed gas burned. The timescale in this graph is unsynchronized. The error bars in Figure 4 represent the standard deviation. The result shows the range of combustible air-DME fuel ratios. The pressure increment occurred due to combustion in the combustible range, and the air-DME molar ratio of 0.07% generated the highest pressure. Considering the theoretical air-DME ratio (0.067%), the highest pressure was generated when air and DME reacted in appropriate proportions.

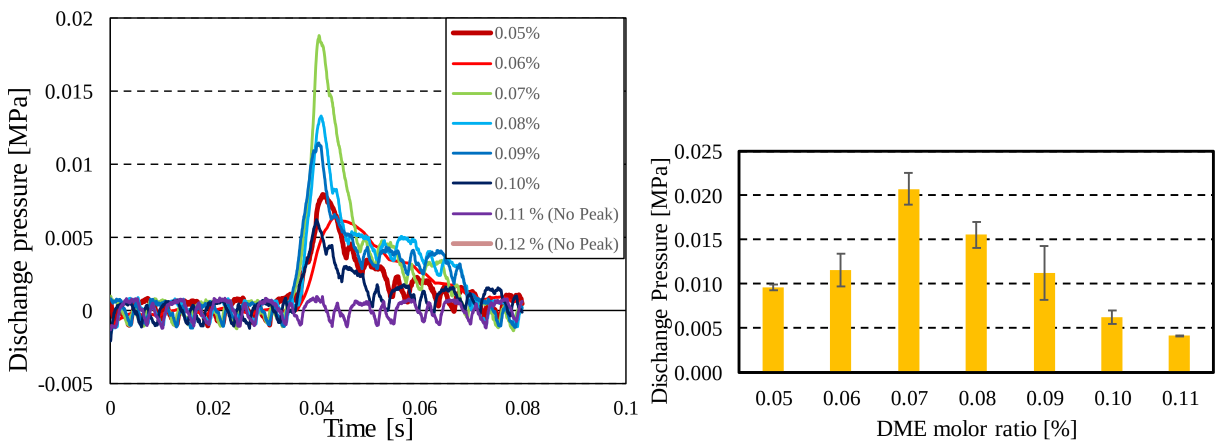

Figure 4. Pressure variation of mixed gas when burned

ARTIFICIAL MUSCLE DRIVEN BY DME COMBUSTION

Figure 5 shows the outline of the artificial muscle driven by DME combustion. The McKibben pneumatic artificial muscle was used as the pneumatic system. The artificial muscle driven by DME combustion is explained below.

① The mixed gas was injected into the artificial muscle
② The gas mixture was ignited by the spark plug in the artificial muscle
③ The rapid pressure increment drove the artificial muscle due to combustion

The method's responsiveness was explained using a simple model (Figure 5). We assumed that the artificial muscle (length and diameter of 100 and 12 mm, respectively) was used and sparks at its center. The distance from the spark point to the surface of the artificial muscle is 6 mm. The air propagates to the surface of the artificial muscle in 1.9 ms after the mixed gas combustion because DME propagates at a speed of 3.1 m/s [7]. Therefore, based on the above, this method effectively improves the responsiveness of pneumatic drive systems.

Experiment

The pressure and displacement were measured when the air-DME mixed gas burned to confirm the proposed method's displacement responsiveness.

Figure 6 shows the experimental setup. Here, the McKibben pneumatic artificial muscle (length and diameter of 100 and 12 mm, respectively), which was used as the pneumatic artificial muscle, was filled with air-DME mixed gas in advance. The mixture ratio of the mixed gas is 0.07%, which generated the highest pressure in the previous experiment. One end of the artificial muscle is attached to a fixed end, whereas the other end to the slide rail, which moves freely along with the displacement of the artificial muscle. Sparks are generated inside the artificial muscle, which ignites the mixed gas. When the mixed gas burned, the pressure was measured using a pressure sensor (MPS-R33RC-NGAT, MYOUTOKU, Japan). Also, the artificial muscle's displacement was measured using a laser displacement meter (HG-C1200, Panasonic, Japan). Each measurement was performed thrice.

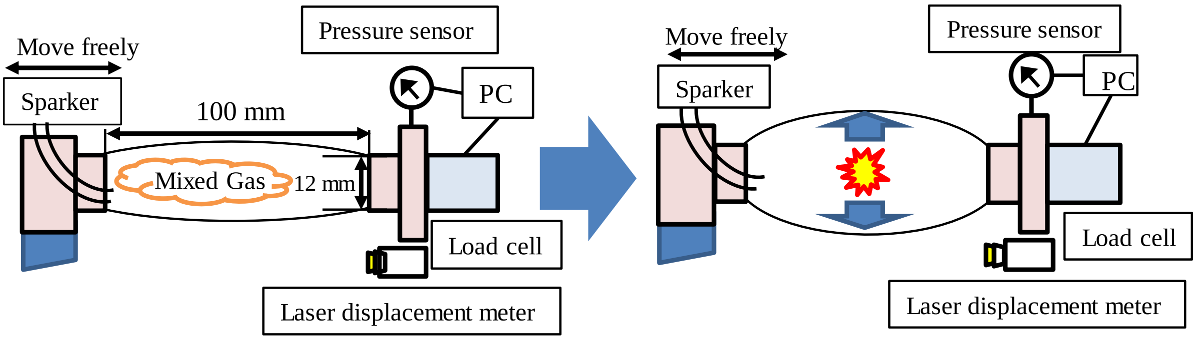

Figure 5. Image of artificial muscle driven by DME combustion

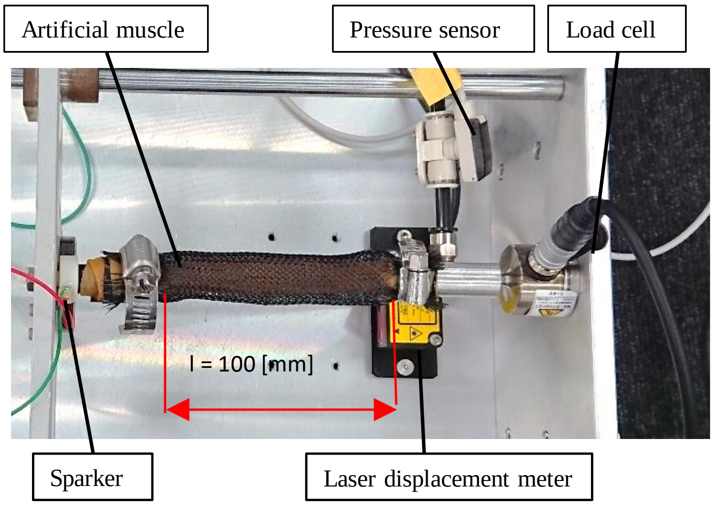

Figure 6. Experimental setup for displacement and contraction force measurement

Experimental Results and Discussion

Figure 7 shows the responsiveness of pressure and displacement of the artificial muscle in DME combustion. The horizontal axis represents the time from the spark, the first vertical axis represents the artificial muscle's internal pressure, and the second vertical axis represents the artificial muscle's displacement. The delay time of displacement was 0.028 s and the reference value of the time constant was 0.037 s (different from the original meaning). Therefore, these results indicate that this system improves responsiveness compared to the conventional pneumatic drive system.

From Figure 6, it takes 0.02 s for the artificial muscle to shrink after the pressure increases. It can also be confirmed that the artificial muscle's displacement oscillates like a damped wave. Besides, it is thought that the McKibben artificial muscle has an elastic component because it is made of a rubber tube.

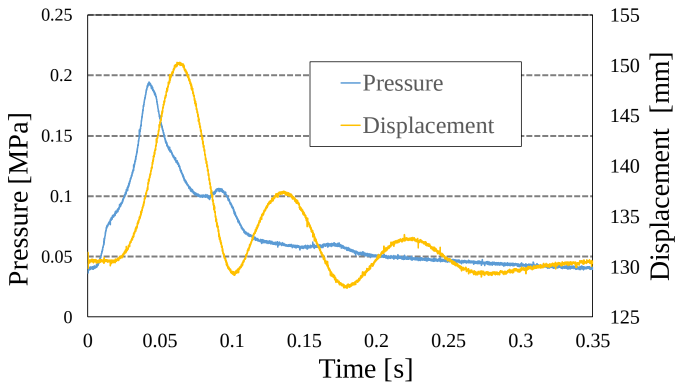

Figure 7. Pressure and displacement of artificial muscle in DME combustion

EXPERIMENT ON CONTRACTION FORCE RESPONSIVENESS OF DME COMBUSTION

The pressure and force were measured when the air-DME mixed gas burned to confirm the proposed method's force responsiveness.

Experimental Method

Figure 6 shows the experimental setup. Just as in the displacement experiment, the McKibben pneumatic artificial muscle (length and diameter of 100 and 12 mm, respectively) was used here and was filled with the air-DME mixed gas in advance. The mixture ratio of the mixed gas is 0.07%, which generated the highest pressure in the previous experiment. To keep the artificial muscle's length constant, both ends of the artificial muscle are fixed. Sparks are generated inside the artificial muscle, which ignites the mixed gas. When the mixed gas burned, the pressure was measured using a pressure sensor (MPS-R33RC-NGAT, MYOUTOKU, Japan), and the artificial muscle's contraction force was measured using a load cell (LUX-B-ID, KYOWA, Japan).

Experimental Results and Discussion

Figure 8 shows the responsiveness of pressure and contraction force of the artificial muscle in DME combustion. The horizontal axis represents the time from spark, the first vertical axis represents the artificial muscle's contraction force, and the second vertical axis represents the artificial muscle's internal pressure. It was confirmed that it takes 0.0057 and 0.0154 s for the pressure increment and the contraction force effect after spark, respectively. Therefore, these results indicate that this system improves responsiveness, as well as the displacement responsiveness.

From Figure 8, it can be confirmed that there is a time lug caused between the increased pressure and contraction force. It is thought that the McKibben artificial muscle has an elastic component. The maximum contraction force was about 44 N. In the future, we will investigate different diameters and lengths of the artificial muscle to produce artificial muscle that can generate high output.

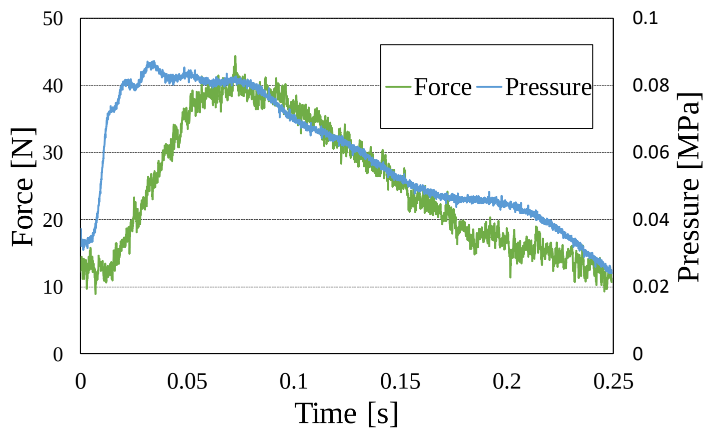

Figure 8. Pressure and force variation with time of artificial muscle in DME combustion

CONCLUSIONS

Here, we proposed a two-stage system using DME phase change and combustion to improve the portability of pneumatic drive systems. Also, we confirmed the range of the air-DME fuel ratio for combustion. Furthermore, we proposed an artificial muscle driven by combustion to improve responsiveness. Besides, we measured the responsiveness of displacement and contraction force when the air-DME mixed gas burned. Consequently, high responsiveness (the delay time of displacement and contraction force were 0.028 and 0.015 s, respectively) was achieved.
In the future, we will investigate the responsiveness driven by combustion by changing different diameters and lengths of the artificial muscle.

ACKNOWLEDGMENTS

Research supported by Yashima Environment Technology Foundation.

REFERENCES

1. SASAKI, D., NORITSUGU, T., TAKAIWA, M., Development of Active Support Splint Driven by Pneumatic Soft Actuator (ASSIST), In Proceedings of the 2005 IEEE International Conference on Robotics and Automation, 2005, pp.520-525.
2. WANG, Z., POLYGERINOS, P., OVERVELDE, J. T., GALLOWAY, K. C., BERTOLDI, K., WALSH, C. J., Interaction Forces of Soft Fiber Reinforced Bending Actuators, IEEE/ASME Transactions on Mechatronics, 2017, 22-2, pp.717-727.
3. WU, H., KITAGAWA, A., TSUKAGOSHI, H., PARK, S. H., Development and Testing of a Novel Portable Pneumatic Power Source Using Phase Transition at the Triple Point, Proceedings of the JFPS International Symposium on Fluid Power, 2005, 223-6, pp.310-315.
4. OKUI, M., NAGURA, Y., ISHIIKAWA, S., YAMADA, Y., NAKAMURA, T., A Pneumatic Power Source Using a Sodium Bicarbonate and Citric Acid Reaction with Pressure Booster for Use in Mobile Devices, In 2017 IEEE/RSJ International Conference on Intelligent Robots and Systems (IROS), 2017, pp.1040-1045.
5. OKUI, M., NAGURA, Y., YAMADA, Y., NAKAMURA, T., "Hybrid Pneumatic Source Based on Evaluation of Air Compression Methods for Portability," IEEE Robotics and Automation Letters, 2008, 3, pp.819-826
6. TOMORI, H., MAJIMA, T., ISHIHARA, H., NAKAMURA, T., "Throwing Motion with Instantaneous Force Using a Variable Viscoelastic Joint Manipulator", Journal of Intelligent Material Systems and Structures, 2017, 28, pp.999-1009 .
7. MOGI, T., OKADA, K., WADA, Y., HORIGUCHI, S.,YOSHIDA, M.,IKEDA, K.,NANBA, M., "Hazards of Large Scale Pool Fire of Dimethyl Ether" Japan Society for safety Engineering, 2007, 46

The 11th JFPS International Symposium on Fluid Power HAKODATE 2020 Oct. 12-13, 2021 JFPS The Japan Fluid Power System Society

Development of Six-Legged Mobile Robot Using Tetrahedral Shaped Pneumatic Soft Actuators

Kenta HASE*, Tetsuya AKAGI*, Shujiro DOHTA*, Takashi SHINOHARA**, Wataru KOBAYASHI* and So SHIMOOKA***

*Department of Intelligent Mechanical Engineering, Faculty of Engineering, Okayama University of Science
**Science Dream lab., Okayama University of Science
1-1,Ridai-cho, Kita-ku, Okayama 700-0005, Japan
(E-mail: akagi@are.ous.ac. jp)
*** Graduate School of Natural Science and Technology, Okayama University
3-1-1, Tsushima-naka, Kita-ku, Okayama 700-8530, Japan

Abstract. Based on elderly society and decreasing birth rates in Japan, the rehabilitation device that can be used in home or hospital without assistance has been desired. In the previous study, a tetrahedral shaped flexible actuator using three extension type flexible pneumatic actuators was proposed and tested as a wrist rehabilitation device. The tetrahedral shaped actuator can extend longitudinally and bend toward any radial direction. In this study, a mobile robot using six tetrahedral shaped actuators that can use a core training and amusement for patients and elderly is proposed and tested. In this paper, the construction and operating principle of the tested robot was described. The control system using a micro-computer and 18 on/off valves was also described. In addition, the walking and rotating tests using the tested robot was carried out.

Keywords: Tetrahedral shaped pneumatic soft actuator, Extension type flexible pneumatic actuator, Mobile robot, Home-based compact 3D simulator

INTRODUCTION

In 2020, the ratio of the Japanese elderly became more than 26 % [1]. In 2040, according to the statistical prediction, the ratio will be growing up to 36%. Under these circumstances, various assisting and rehabilitation devices to help welfare work for the elderly and disabled using pneumatic soft actuators[2] have been actively developed[3-10]. As a pneumatic power assisting device, the wearable power assist suit for nursing care using bellows type actuators was reported by K. Yamamoto [3]. T. Noritsugu and H. Kobayashi also developed power assisted wears using McKibben type pneumatic artificial muscles to increase the force for welfare workers and heavy labors[4-7]. A pneumatic soft actuator is useful for, not only power assisted system but also a rehabilitation device. According to Japanese law, Occupational Therapist (“OT” for short) and Physical Therapist (“PT” for short) can perform the rehabilitation to the patient for just 30 minutes per day. Some of them recommend patients to execute voluntary rehabilitation and exercise at home. According to a medical report, a voluntary rehabilitation might prevent bedridden state, various disease and disuse syndrome[8]. Therefore, it is necessary to develop a home-based rehabilitation device that can safely give a passive exercise to patients. As research on such a rehabilitation device, H. Taniguchi and H. Kawasaki developed a rehabilitation device for inhibiting contracture of finger joints [9-10]. In the previous study, the washable portable rehabilitation device using Extension type Flexible Pneumatic Actuators (we call it “EFPA” for short) that can provide passive exercise was proposed and tested[11]. The attitude control of the device based on the model without position sensor was carried out. As a rehabilitation device using the same EFPA, W. Tian developed the tetrahedral-shaped soft robot arm for wrist rehabilitation was developed[12]. Usually, a pneumatic actuator was often used for wearable and rehabilitation devices because it has advantage of compliance based on air compressibility. Especially, a pneumatic soft actuator is more suitable because it has more advantages such as lighter weight and more compliance based on flexibility. In the next step, we consider to develop the rehabilitation device that includes an amusement element. Typical amusement device at home is a video game. Especially, Japanese game maker “Nintendo” produced the fitness device with video game “Wii Fit™” in 2007. The device was also used as a rehabilitation device of outpatients following total knee replacement[13]. It seems that the rehabilitation device with amusement is useful to carry out the medical treatment while a patient is enjoying. In consideration of application of rehabilitation into the video game, most of video game device only gives vibration as feedback signal to a user from a virtual space. If a device that can safely give physical feedback movement to a patient can be realized, it is truly useful. It is also useful as an amusement device. As a feedback device from a virtual space, a 3-dimantional simulator such as a flight simulator and an automobile drive simulator had been developed as an arcade game device. However, the typical 3D simulator is bulky and expensive. If a compact and safe home-based 3D simulator can be realized, the device will be valid for both rehabilitation and amusement. In this study, we imagine a “mobile cushion” as a target device. It is because it does not need bulky frame and can be used by just seating. In this paper, a compact 3D simulator that can give radial inclined angle, rotational and translational motions and vibration to a seat with patient is proposed. In detail, the development of a low height mobile robot that can rotate and translate toward radial direction using EFPAs will be described.

PREVIOUS TETRAHEDRAL-SHAPED SOFT ROBOT ARM USING EFPAS[12]

To realize a compact cushion type mobile robot, a compact soft actuator with a long stroke motion is required. In the previous study, as a low-cost soft actuator with long stroke, the EFPA sing this type of hose was proposed and tested[11,12]. Figure 1 shows the view and schematic diagram of the EFPA. The EFPA consists of a silicone rubber tube with inner diameter of 8 mm, outer diameter of 11 mm and covered with a bellows type nylon sleeve (The Fit Life Co. Ltd., Hose Reel). The original length of EFPA is 200 mm, and the mass is 50 g. The actuator can be constructed at low cost, the material cost of the EFPA is about 5 US dollars per 1 m. The EFPA can extend about 2.5 times of its original length. The maximum pulling force of the EFPA is about 60 N[11]. The pushing force of the original EFPA is not available because the bending stiffness is too low.

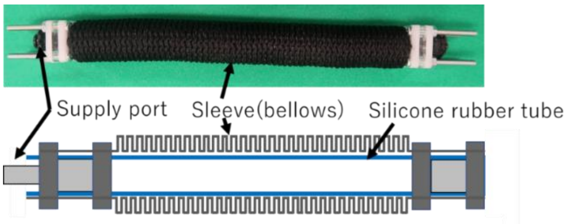

Figure 1. View and schematic diagram of EFPA[11].

Figure 2 (a) shows the appearance of the tetrahedral-shaped soft robot arm for wrist rehabilitation developed in the previous study. In the design of the robot arm, it was intended to realize a robot arm that can bend 90 deg. and generate sufficient torque. The tetrahedral-shaped soft robot arm consists of three EFPAs with an original length of 200 mm and 22 PET sheets with a 1 mm thickness as a restraint plate. Three EFPAs are set on the three sides of the tetrahedron except at the bottom, and they are restrained by 22 PET sheets to increase the bending stiffness. Figure 2 (b) shows the drawings and dimensions of each reinforced PET sheet. The position of the holes for placing the EFPA on the PET sheet are changed between 11 mm at the minimum radius and 126.5 mm at the maximum radius from the center of each PET sheet. Each EFPA can be placed so that the EFPA can have an elevation angle of 45 deg. with respect to the base. By restraining the three EFPAs each other with an elevation angle of 45 deg. by many PET sheets, the axial elastic force of the rubber tube in each EFPA can be shared in the horizontal and vertical directions. Consequently, the stiffness in both directions can be enhanced.

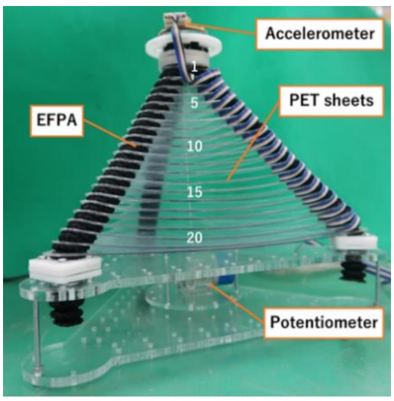

(a) Tetrahedral-shaped soft robot arm

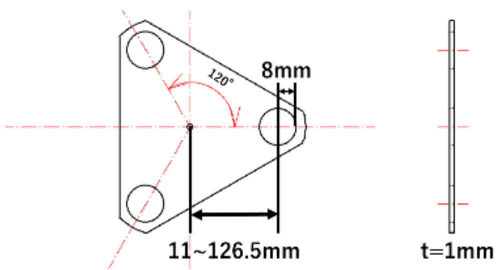

(b) Reinforced PET sheet

Figure 2. Appearance of the tetrahedral-shaped soft robot arm and drawing and dimensions of a PET sheet[12].

Figure 3 shows the view of bending motion using the previous robot arm. The operating principle of the robot arm is as follows. When one or two EFPAs are pressurized, driven EFPAs can extend and the bending motion toward various directions along a certain sphere can be realized as shown in Figure 3. Furthermore, when all three EFPAs are pressurized, the robot arm can extend approximately twice their length in the vertical direction. From a preliminary experiment, the tested robot arm can bend more than 90 deg. and generate a torque of 7 Nm that can be obtained from the experiment based on the law of virtual work.

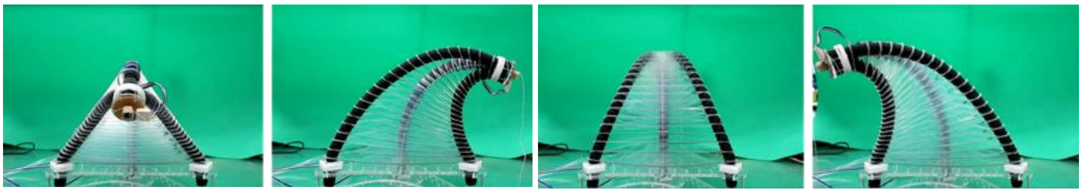

Figure 3. View of bending motion using the previous robot arm. [12].

IMPROVED SOFT ACTUATOR AND FUNDAMENTAL CHARACTERISTICS

In this study, we consider to develop a mobile robot that uses the tetrahedral-shaped soft robot arm as a leg. In order to apply the robot arm mentioned above to the leg, it is necessary to make the size of the actuator smaller to decrease the height of the mobile robot, and the generated torque was investigated as a fundamental characteristic. Figure 4 (a) and (b) show the improved Tetrahedral-shaped soft Actuator (we call it "TSA" for short) and the shape of restraint PET sheets with the setting angle of EFPA of 45 and 60 deg. from the base stage, respectively. In order to get higher stiffness and generated force, compared with the previous soft robot arm, the shorter EFPA with the original longitudinal length of 180 mm was used for TSA. Each TSA has 10 restraint PET sheets. As shown in Figure 4, the setting position of each EFPA are changed so that the setting angle of EFPA from the base can keep 45 and 60 deg. Each PET sheet is installed every three pitches. The lengths of one side of an equilateral triangle-shaped base stage using the setting angle of 45 and 60 deg. are 230 and 135 mm, respectively. The heights of TSA using the setting angle of 45 and 60 deg. are 120 and 145 mm, respectively.

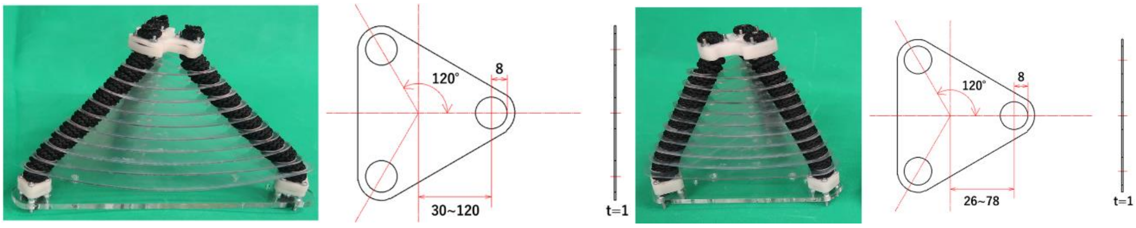

(a) EFPA setting angle 45 deg. (b) EFPA setting angle 60 deg.

Figure 4. Tetrahedral-type soft actuator and shape of restraint PET plates.

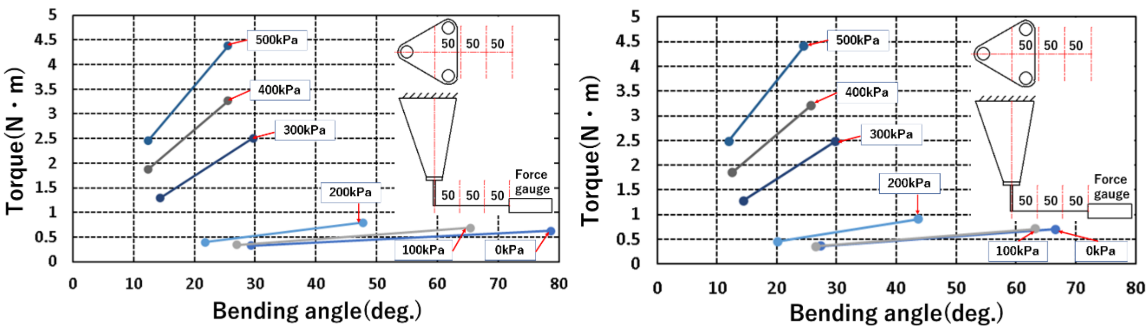

(a) EFPA setting angle 45 deg. (b) EFPA setting angle 60 deg.

Figure 5. Relation between bending angle and bending torque of TSA.

Figures 5 (a) and (b) show the result of bending stiffness according to applied pressure by using the TSA with EFPA setting angle of 45 and 60 deg., respectively. In the experiment, under the condition when the base stage was locked on a table, the horizontal pulling force was applied to the top of the tetrahedral-type soft actuator until

a certain bending angle occurs as shown in right figure on the graph. Each graph in Figures 5 shows the relation between the bending angle and bending torque of TSA. The torque was calculated by the height of TSA and the measured horizontal pulling force at the top of the TAS. In Figure 5, each line shows the difference of applied pressure for three EFPAs. From Figure 5 (a) and (b), it can be seen that the bending stiffness corresponding to the slope of each line is almost same in both TSAs. It can also be confirmed that bending stiffness is increasing according to applied pressure.
Figures 6 shows the relation between the applied pressure for two EFPAs and generated torque of both TSAs. In Figure 6, the red and blue lines show the results using TSAs with EFPA setting angle of 45 and 60 deg., respectively. In the experiment, the generated torque was calculated by measured force using the experimental setup as shown in left upper figure on graph. From Figure 6, it can be seen that the generated torque of TSA with the setting angle of 60 deg. is superior than the case using TSA with the setting angle of 45 deg. As a result of fundamental experiment using both TSAs, it can be concluded that the TSA with EFPA setting angle of 60 deg. is suitable to apply the mobile robot from view point of almost same bending stiffness, larger generated torque. In addition, we confirmed that TSA with the setting angle of 60 deg. can give larger bending angle and displacement from preliminary experiments. In addition, we also confirm that a TSA can lift up the load with more than 130 N, that is enough lifting force for the target robot, under the condition when three EFPAs are pressurized. It means that the TSA can be used as a leg of the robot, because the TSA can bend while lifting a load when one or two EFPAs are pressurized.

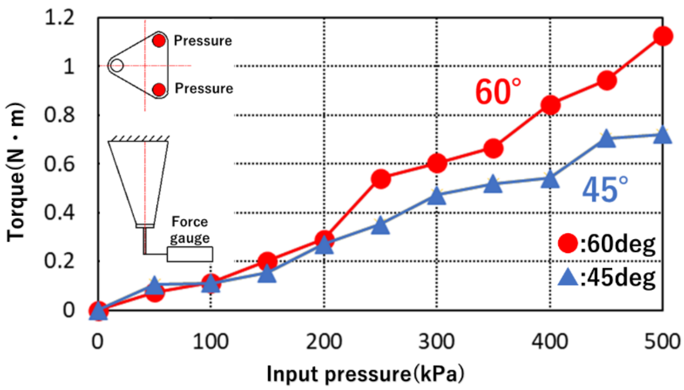

Figure 6. Relation between applied pressure and generated torque.

6-LEGGED MOBILE ROBOT USING TSAS

Figure 7 shows the side and behind view of a 6-legged mobile robot using TSAs. The mobile robot consists of six TSAs. Six TSAs are connected each other so that they can shape regular hexagon. In detail, each corner of triangle-shaped base stage of TSA is connected each other by being sandwiched and screwed by two POM plates in order to be connected surely. Adjacent TSA vertices are connected by a plastic connector. The tested robot has the length of 410 mm, the width of 360 mm and the height of 115 mm. The planer shape of the mobile robot is the regular hexagon with a side of 210 mm. The mass of the robot is 2.85 kg including 18 valves, an embedded controller and so on. In Figure 7, three-character Alphabet symbols indicate the location of EFPA.

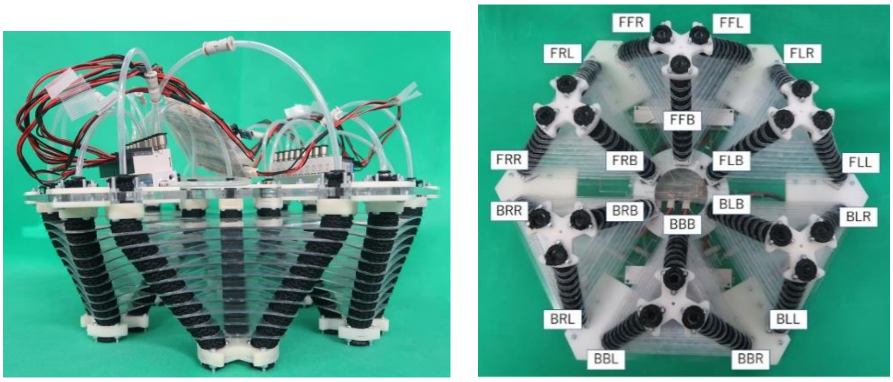

Figure 7. Appearance of 6-legged mobile robot using TSAs (side and behind views)

Figure 8 shows the schematic diagram of the control system using the tested mobile robot and motion pattern of one leg. The control system consists of the tested robot, 18 on/off valves (Koganei Co. Ltd., G010E-1), an embedded controller (Renesas electronics Co. Ltd., SH7125) and a serial communication unit (FTDI Co. Ltd., FT234X). The operation of the mobile robot is as follows. First, an operator sends a character cord to the embedded controller through PC and the serial communication unit. The embedded controller selects the sequential program according to the received character cord. The controller also drives on/off valves according to the selected sequential program through I/O ports. The right side figure on Figure 8 shows the moving patterns of one leg in the robot. In the figure, the red marked circle and arrow show the pressurized EFPA and bending direction, respectively. By changing the pressurized EFPA, the leg can bend in six radial directions every 60 deg. By pressurizing all EFPAs, it can also extend about double toward the longitudinal direction for lifting the robot.

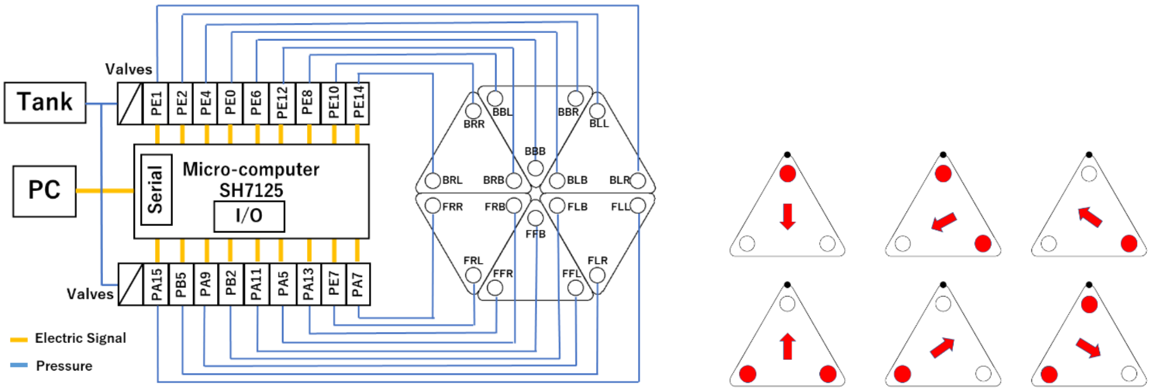

Figure 8. Schematic diagram of control system on the tested mobile robot and motion patterns of one leg.

DRIVING TEST OF THE MOBILE ROBOT USING TSAS

In order to realize the propulsion of the mobile robot, it is necessary to adjust the driving pattern of each TSA. The method of propulsion is as follows. While lifting the whole robot body by extending three TSAs (Support legs), other TSAs bend toward the propulsion direction as a free leg. After that, while lowering the robot body by contracting the extended TSAs, the other TSAs are bending toward the opposite direction. By this method, the robot can move toward six directions based on the motion patterns of the leg as shown in Figure 8. In addition, as three legs works for lifting up the load, the robot can convey a mass with about 40 kg theoretically.

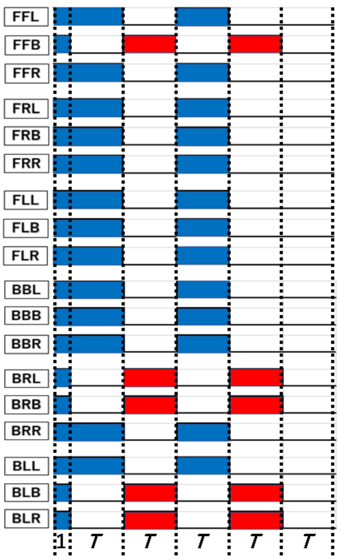

(a) Time chart of driving pattern.

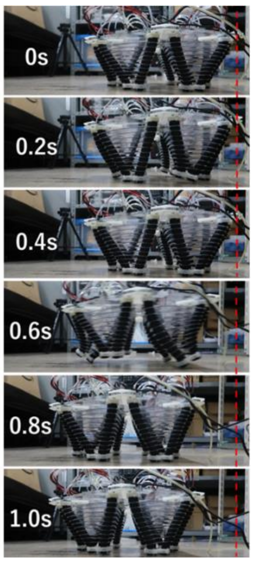

(b) Transient view of movement.

Figure 9. Time chart of driving pattern of each EFPA and transient view of movement of the robot for moving forward.

Figure 9 (a) shows the time chart of sequential driving pattern of each EFPA and transient view of movement of the robot for moving forward. In the time chart, blue bars show the driving pattern for lifting the robot body. Red bars show the bending motion. In this sequence, the combination of the motion with lifting and swing motion for a free leg and the motion with lowering and swing motion for kicking are repeating two times. In addition, each motion is carried out for the time interval *T*. In the case of moving forward, EFPAs related to moving forward are five in three TSAs, that is FFB, BRL, BRB, BLB and BLR. Figure 9 (b) shows the transient view of movement of the robot in the case of moving forward. In the experiment, switching timing of each motion *T* of 360 ms was used. From Figure 9 (b), it can be seen that the robot can move forward smoothly.
Figure 10 show the driven EFPAs for swing motion of legs in moving toward six directions, circled number shows the moving direction of the robot. Symbols ● show the driven EFPA. From Figure 10, it can be seen that six different EFPAs are driven every moving direction.

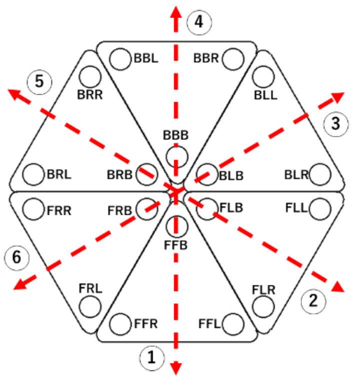

	Driving pattern					
	①	②	③	④	⑤	⑥
FFL			●			
FFB	●		●		●	
FFR					●	
FRL		●				
FRB		●		●		●
FRR				●		
FLL				●		
FLB		●		●		●
FLR						●
BBL						●
BBB		●		●		●
BBR		●				
BRL	●					
BRB	●		●		●	
BRR			●			
BLL					●	
BLB	●		●		●	
BLR	●					

Figure 10. Driven EFPAs for swing motion of legs in moving toward six directions.

In order to obtain the optimal switching time *T*, the driving test of the robot for moving forward with various switching timing was carried out. In the experiment, the averaged moving distance for one driving pattern and the averaged velocity of the robot, when the moving pattern as shown in Figure 9 was repeated three times, were investigated. As a preliminary experiment, the moving distance and the velocity of the robot were investigated when the switching time *T* was changed from 50 to 500 ms every 50 ms. In addition, to obtain the optimal switching time, both distance and velocity were also investigated more detail between 300 and 400 ms every 10 ms. Figures 11 (a) and (b) show the relation between switching timing *T* and the moving distance for one driving pattern and velocity of the mobile robot in case when the timing *T* is from 50 to 500 ms every 50 ms and the timing *T* is from 300 to 400 ms every 10 ms, respectively. In both figures, the red and blue lines show the moving distance and velocity of the robot, respectively. It can be seen that the maximum moving distance can be obtained by using the switching timing of 370 ms. About a velocity, it can be seen that the velocity becomes peak around both switching times of 310 and 360 ms. From the view point of longer stroke and higher velocity, it can be concluded that the switching timing *T* of 360 ms is more suitable to the moving forward.

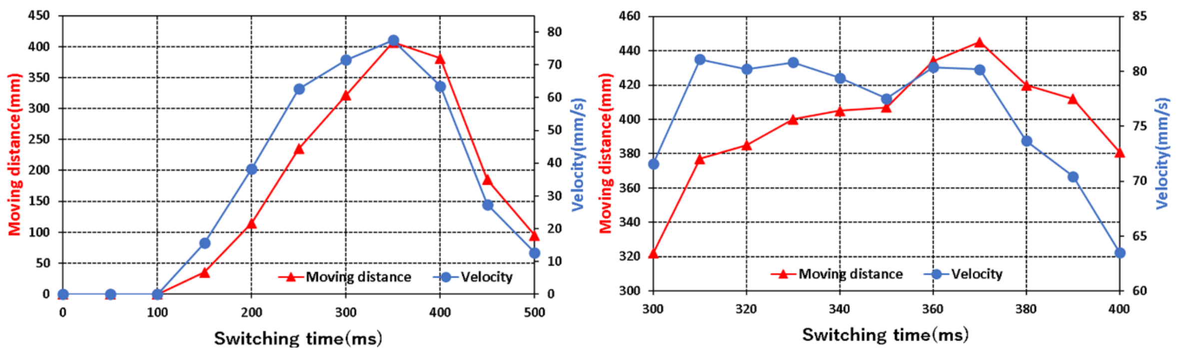

(a) *T* is from 50 to 500 ms every 50 ms. (b) *T* is from 300 to 400 ms every 10ms.

Figure 11. Relation between switching timing *T* and moving distance for a driving pattern and velocity of the mobile robot.

Figures 12 (a) and (b) show time charts of driving pattern of each EFPA when the robot rotates in clock-wise and counter clock-wise, respectively. The switching timing T_1 and T_2 were adjusted by trail and errors. In the experiment, T_1 of 400 ms and T_2 of 350 ms were used, respectively. As a same manner of moving forward, in the rotational operation, three TSAs work to rotate the robot. Figure 13 shows the transient view of rotational motion

6

of the mobile robot when the robot rotates in counter clock-wise. In the experiment, the rotational speed of 15 deg. can be obtained. As a result, it can be concluded that the mobile robot for a home-based compact 3D simulator that can give rotational and translational motions can be realized. In addition, we also confirm that the robot can change the radial inclined angle of the robot and give a vibration.

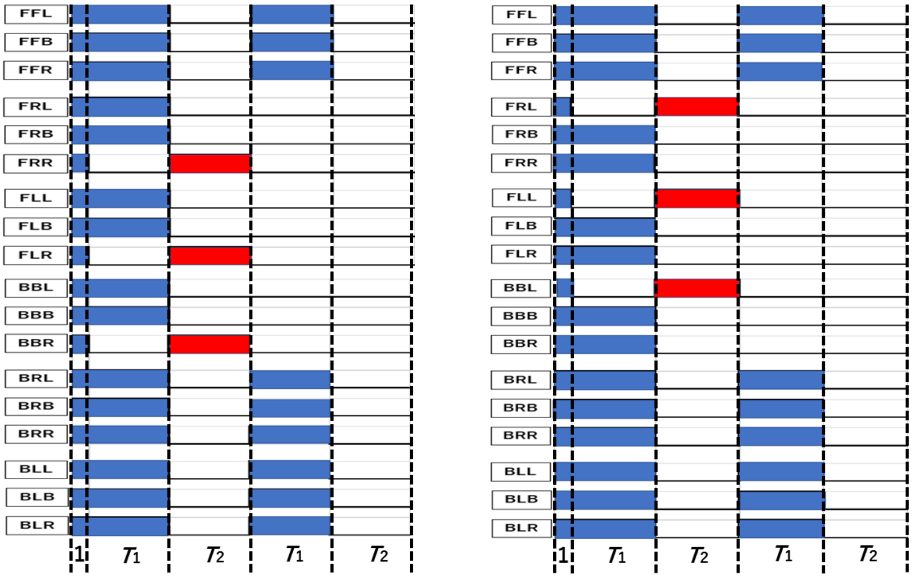

(a) Clock-wise. (b) Counter clock-wise.

Figure 12. Time chart of driving pattern of each EFPA for rotational motion in clock-wise and counter clock-wise

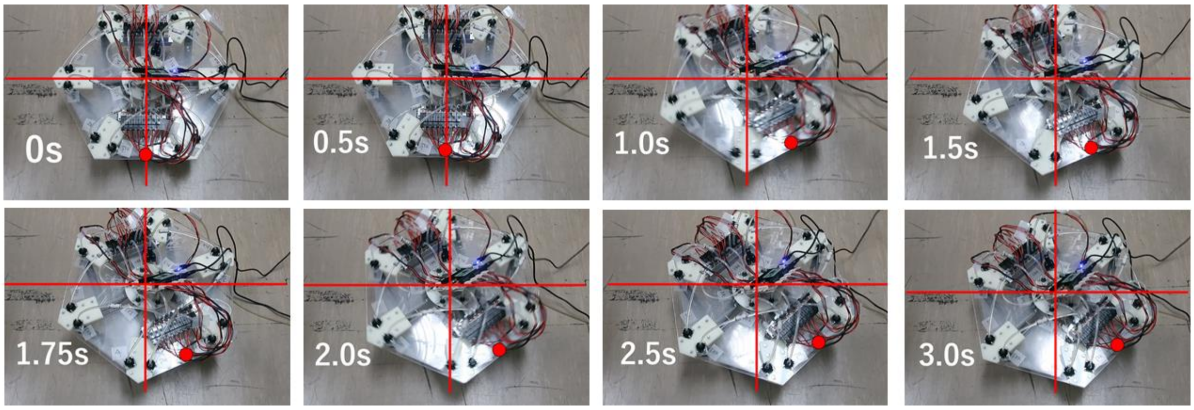

Figure 13. Transient view of movement of the robot for rotational motion.

CONCLUSIONS

This study that aims to develop the mobile robot that can be used for core training and rehabilitation can be summarized as follows.

In order to investigate the suitable Tetrahedral-Shaped soft Actuator (TSA) for the desired mobile robot, two types of TSAs with EFPA setting angle of 45 and 60 deg. were proposed and tested. The bending stiffness and generated torque using both TSAs were investigated. As a result, it can be concluded that the TSA with setting angle of 60 deg. is suitable to the mobile robot because of larger stroke and higher torque. The mobile robot that consists of six TSAs was proposed and tested. The control system that consists of the tested robot and 18 on/off valves was also proposed and tested. The sequential driving pattern for moving forward and rotating in clock-wise and counter clock-wise was investigated. As a result, it can be confirmed that the tested robot can move toward six directions and rotate toward both clock-wise and counter clockwise. In addition, the optimal switching timing for moving forward was investigated. As a result, it was found that the switching timing of 360 ms is suitable to a moving forward. In the tested robot, the maxim velocity of 80 mm/s and the rotational speed of 15 deg/s can be obtained.

ACKNOWLEDGMENTS

This work was supported by JSPS KAKENHI Grant Numbers 16K06202 and 19K04265.

REFERENCES

1. Annual Report on the Ageing Society [Summary] FY 2019 from, https://www8.cao.go.jp/kourei/english/annualreport/2019/pdf/2019.pdf, June 2021.
2. NAGATA, Y., Soft Actuators, Forefront of Development. NTS Ltd., 2004, pp. 291–335.
3. ISHII, M., YAMAMOTO, K. and HYODO, K., Stand-Alone Wearable Power Assist Suit (Development and Avail ability). Journal of the Japan Society of Mechanical Engineers, 2006, 72-715, pp. 175–182.
4. NORITSUGU, T., Pneumatic Soft Actuator for Human Assist Technology. In: Proceedings of the 6th JFPS International Symposium on Fluid Power, Tsukuba, Japan, 2005, pp. 11–20.
5. SASAKI, D., NORITSUGU, T., YAMAMOTO, H., and TAKAIWA, M., Development of Power Assist Glove using Pneumatic Artificial Rubber Muscle. Journal of the Robotics Society of Japan, 2006, 24-5, pp. 640-646.
6. NORITSUGU, T., TAKAIWA, M. and SASAKI, D., Development of Power Assist Wear Using Pneumatic Rubber Artificial Muscles. Journal of Robotics and Mechatronics, 2008, 21-5, pp. 27–31.
7. KOBAYASHI, H., SHIBAN, T., and ISHIDA, Y., Realization of all 7 motions for the upper limb by a muscle suit. Journal of Robotics and Mechatronics, 2004, 16-5, pp. 504–512.
8. Council of Bureau of Social Welfare and Public Health Tokyo Metropolitan Government from, https://www.fukushihoken.metro.tokyo.lg.jp/iryo/sonota/riha_iryo/kyougi01/rehabiri24.files/siryou242.pdf; February 2013 (in Japanese).
9. TANIGUCHI, H., WAKIMOTO, S., SUZUMORI, K., Development of a hand rehabilitation system to prevent contracture for finger joints based on the therapy of occupational therapists (Massage a hand and range of motion exercises using pneumatic soft actuators). Journal of the Japan Society of Mechanical Engineers, 2014, 80-820, TRANS0348.
10. KAWASAKI, H., ITO, S., ISHIGURA, Y., NISHIMOTO, Y., AOKI, T., ABE, T., SAKAEDA, H., OJIKA, T., MOURI, T., UEKI, S., Hand Rehabilitation Assist Robot Designed with Assistance for Thumb Opposability. Journal of the Japan Society of Mechanical Engineers, 2008, 74-748, pp. 3019-3027.
11. SHIMOOKA, S., HANE, Y., AKAGI, T., DOHTA, S., KOBAYASHI, W., SHINOHARA, T., and MATSUI, Y., “Development and Attitude Control of Washable Portable Rehabilitation Device for Wrist without Position Sensor”, JFPS International Journal of Fluid Power System, Vol.13, No.3, 2020, pp. 25-34.
12. TIAN, W., JHAN, C., INOKUMA, M., AKAGI, T., DOHTA, S., and SHIMOOKA, S., ”Development of a Tetrahedral-Shaped Soft Robot Arm as a Wrist Rehabilitation Device Using Extension Type Flexible Pneumatic Actuators”, Journal of Robotics and Mechatronics, Vol.32, No.5, 2020, pp. 931-938.
13. FUNG, V., HO, A., SHAFFER, J., CHUNG, E., GOMEZ, M., “Use of Nintendo Wii Fit™ in the rehabilitation of outpatients following total knee replacement: a preliminary randomised controlled trial”, Physiotherapy. 2012, 98-3, pp. 183-8.

The 11th JFPS International Symposium on Fluid Power HAKODATE 2020 Oct. 12-13, 2021 The Japan Fluid Power System Society

Development of the Transfer System for Bedridden Elderly and Disabled People using Pneumatic Actuators

Feifei CHO[*] , Keisei KATO[*], Ryota ENDO[*] ,
Takumi KOBAYASHI[**] and Tetsuya AKAGI[**]

[*] Dept. Mechanical Systems, National Institute of Technology Tsuyama College
624-1,Numa, Tsuyama City, Okayama, 708-8509, Japan
(E-mail: cho@tsuyama-ct.ac.jp)
[**] Dept. Intelligent Mechanical Engineering, Okayama University of Science

Abstract. In recent years, as the birthrate declines and the population ages in developed countries, the demand for caregivers has been increasing. However, nursing care often involves a physical burden on the caregiver, especially in transfer assistance, which places a burden on the entire body. To solve this problem, this study aims to develop a novel support system such as automatic pneumatic transfer sheets, which can help caregivers to move bedridden elderly people bed-to-bed and bed-to-fully reclining wheelchair. In addition, by using a pneumatic actuator in the roller part and controlling the air pressure in time, this device can not only change the installation surface between the sheet and the back, but also can be expected to prevent bedsores. So far, we have built a prototype, which is half the size of the actual transfer device by using a low-cost servo valve using buckled tubes.

Keywords: Air pressure, Flexible artificial muscle, Transfer system, Servo valve using buckled tubes

INTRODUCTION

In recent years, the number of bedridden elderly people in the world has been increasing remarkably due to the aging of society, and the number of disabled people who fall into severe physical disabilities due to various diseases is not small. In addition, caregivers at home are aging in Japan, as exemplified by the elderly care system[1]. In caring for these elderly and disabled people, transferring them from bed-to-bed and bed-to-fully reclining wheelchair is a heavy physically demanding task for caregivers. Also when caring for bedridden persons, caregivers have to change their posture every two hours because it is necessary to prevent bedsores. In some cases, the heavy burden on caregivers' back and arms might make them uncomfortable, and then increases their mental burden[2].

The above physical and mental burdens are major factors that lead to violence and harassment in nursing homes and home care. These problems return to society as the burden on long-term care insurance premiums, and thus have a significant impact on economy. In order to solve the above problems, the transfer devices and power assist devices are in high demand. However, most of developed devices such as floor traveling lifts, which require large amount of power to lift the care receiver, are expensive and moreover they require the time to wear belts and the labor to hold the care receiver's body. There are also practical low-cost sliding seats sed in homes and narrow facilities, but they require two or more people to support the care receivers, and require a lot of energy to slide them. The same as the floor traveling lifts, caregivers have to take lots of time to prepare the seat under the care receivers. Those answered by more than 50% of the respondents were mental burden 74.3%, temporal restriction 62.5%, and physical burden 53.3%[3]. Figure 1 shows the difficulties in providing care at home.

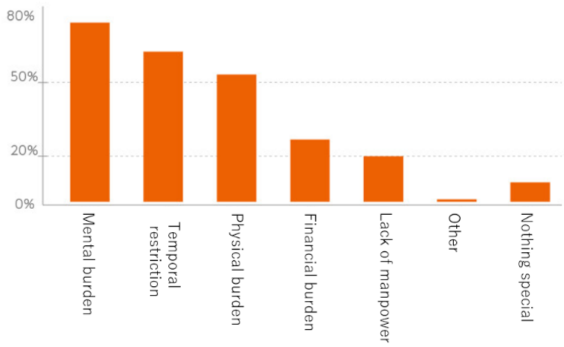

Figure 1. Difficulties in providing care at home[3]

Therefore, in this study, we aim to develop the low-cost flexible transfer and repositioning system for bedridden elderly and disabled people, which can be used for the bed sheet ordinarily. This system also can generate a large transfer force using soft actuator. They consists of a microcomputer, servo valves using buckled tubes[4-5] and soft pneumatic actuators.

OVERALL IMAGE OF THE DEVICE

In this study, we aimed at the improvements of the floor traveling lifts and the slide seat, which were described in the previous chapter, and designed the transfer system for bedridden elderly and disabled people using pneumatic actuators. Figure 2 shows the overall image of the device. The design concept is as follows:

(1) One caregiver can support a care receiver by herself/himself.
(2) No more physical burden on the caregiver.
(3) Easy to prepare, and it will not take long time.
(4) No need to change the bedridden elderly people posture every two hours.

An explanation of the concept is given below. In most cases of floor traveling lifts and sliding seats, one caregiver has to transfer the bedridden elderly people and the other caregiver has to support the care receiver to make sure that the movement will be safe. Therefore, we proposed the powered sliding seat that can transfer automatically. Then, by using the McKiben actuator for the roller part, it will be realized. Because, when the actuator is pressurized, the actuator becomes stiff such as the roller. Then, when the actuator is exhausted, the actuator returns to the flexible state. It does neither take much time to prepare, nor need a lot of space. The principle of operation of this system is as follows. We put the electric motors at both ends of each actuator, then, by rotating the motors, the actuators also rotate, and the sheet moves simultaneously. The bedridden elderly people will be transferred in the manner of the roller conveyor. In order to maintain the flexibility, we used soft materials for a sheet. The operating principle is as follows: when the McKibben actuator is pressurized, the actuator is expanded in radial direction, and it changes from the flexible state to the slightly stiff roller. By controlling the actuators in time, the contact surface between the human back and the bed sheet can be changed, thereby reducing the steaminess of the back and suppressing bedsores. This system can be expected to not only reduce the frequency of repositioning but also reduce the burden on caregivers. Figure 3 shows the construction of the connector part of the actuator. Because of the possibility of contact with the care receiver body, most of ordinary connectors are made of metal, which is inferior in terms of human affinity. The muscle is also contracted about 25% of the original length in axial direction. The average height of elderly people over 70 years old is about 1.6m, therefore, when transferring the caregivers, their knees should be bent.

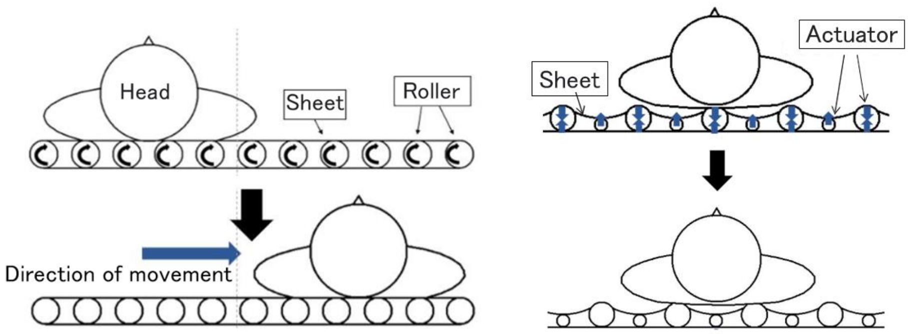

Figure 2. Overall image of the device

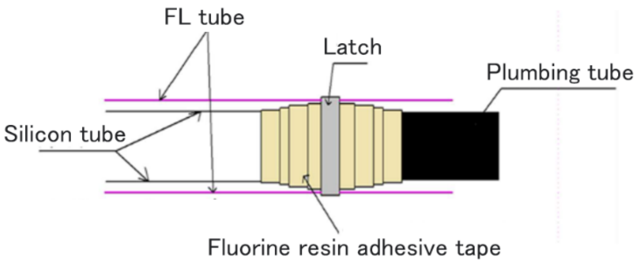

Figure 3. Construction of the connector part of the actuator

First, the internal pressure required for one actuator is determined. The number of actuators supporting the back is obtained from Equation (1), the external pressure applied to one actuator is obtained from Equation (2). Determine the internal pressure and external pressure of the hose is obtained from relational Equation (3). The required torque is obtained by Equation (4). This value does not include the internal pressure required to expand the silicon tube. As shown inTable 1, the parameters used in the calculations are h=0.411m, W=53.4kg, d=0.03m, r=0.03m, and l=1.4m. Where, W and h are the average weight and shoulder width of the care receivers over the age of 70, respectively. The value of W was calculated by back calculating the value of BMI(Body Mass Index), which is the maximum possible external pressure. We used the maximum value 30 of BMI and the average height of the care receivers over the age of 70. As a result, W_{MAX}=77.8kg. Table 1 shows the symbols and parameters used in the calculation of theoretical values.

$$n = \frac{h}{(d+r)} \tag{1}$$

$$Pe = \frac{Wg}{nld} \tag{2}$$

$$Pi = \frac{2Pet}{d} \tag{3}$$

$$T = \frac{1}{2n}d(Wg) \tag{4}$$

Table 1. Symbols and parameters be used in the calculation of theoretical values[6-7].

Actuator(Pressurized)					**The care receivers(Over 70 years old)**		
Diameter	d	0.03m	Number	n	Average weight	W	53.4kg
Thickness	t	0.003m	Internal pressure	Pi			
Length	l	1.4m	External pressure	Pe	Average shoulder width	h	0.411m
Spacing	r	0.03m	Torque	T			

As a result, assuming the average shoulder width of bedridden elderly people who require nursing care over the age of 70, we used eleven McKiben actuators to support the human body, the external pressure applied to one actuator will be about 2MPa, and the required internal pressure was about 0.4MPa. The pressure resistance of the silicon tube is about 0.4 MPa with thickness of 0.003m, and this value is sufficient to withstand the pressure. Then, the torque required for one actuator was calculated to be 1.31N・m. This value does not take into account the friction of the sheets and gears. Figure 4 shows the device of the transfer system.

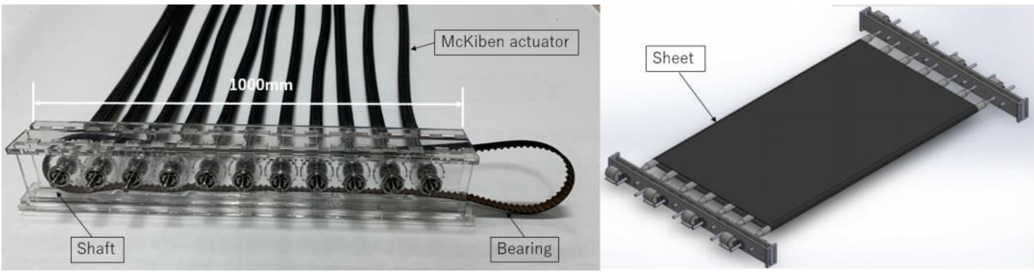

Figure 4. The device of the transfer system

CONTROL SYSTEM

In this system, it is necessary to apply the air to the pneumatic actuators during transferring, rotate the motors, and control pressurizing the actuators in time because it can reduce back steaminess and suppress bedsores for bedridden elderly people. The SH7125 microcontroller is used for this system. Figure 5 shows the schematic diagram of the control system. The control system consists of a tested actuator, a control valve, a pressure sensor and an embedded controller. In consideration of controlling multiple pneumatic valves, we expanded the number of pins capable of PWM output from 4 to 8 that will be allowed for more output. In addition, pneumatic valves are required to operate the pneumatic actuators. However, the pneumatic control valve is the most expensive control device in the fluidic drive system, and it is the big obstacle to make the support device usable at home. Therefore, we used the servo valve using buckled tubes as shown in Figure 6. The valve consists of two buckled soft polyurethane tubes (SMC, TUS0425), two one-touch connectors (Koganei, US4M), one Y-shaped one-touch connecters (Koganei, UY4M), a small-sized RC servo motor (Asakusa Giken, ASV-15: Max. torque of 1.6kgf-cm, Max. speed of 480deg./s, band width frequency of 3 Hz in experiment) and an acrylic rotational disk with connecter holders. The mass of the valve is 40g. The valve has a length of 45 mm, a width of 79 mm and height of 53 mm. Finally, we checked the response of the inner pressure of the actuator by using PI control scheme and the servo valve using buckled tubes. Figure 7 shows the transient response of the pressure. From the figure, it can be seen that the response is close to the stepwise target pressure of 400KPa.

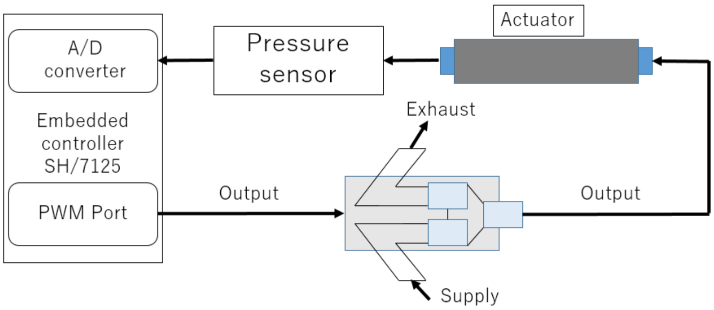

Figure 5. Schematic diagram of the control system

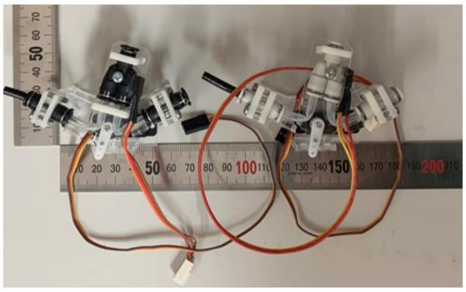

Figure 6. Servo valve using buckled tubes

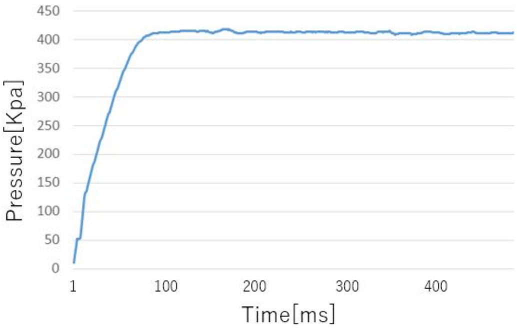

Figure 7. The result of PI control

CONCLUSIONS

In this study, we aimed to develop the transfer system for bedridden elderly and disabled people using pneumatic actuators and we also constructed the control system. In the prototype, we have tried the method of transmitting power from the motor using the bearing to rotate the actuators. We also used SH7125 microcomputer to control the system. In the future work, we plan to improve the device with the new transport method. Finally, we have got confirmation about the movement of this transfer system by using the low-cost servo valve using buckled tubes.

REFERENCES

1. Cabinet Office, Government of Japan: White Paper on the Aging Society, 2009, Section 1: Status of Aging, https://seniorguide.jp/article/1207592.html
2. Fujimoto T., Higashi Y., Takahashi S., Yasuda T., Tamura T., Current status and future of nursing care equipment in facilities, J-STAGE, 2000,14-2, 36-45.
3. LIFULL: The Burden of Struggling with Residential Care, https://kaigo.homes.co.jp/manual/voice/kentou/kurou/
4. Kbayashi H., Akagi T., Dohta S., Kobayashi W., Matsui Y., Shimooka S., Shinohara T, and Aliff M., "Development of Portable Rehabilitation Device Driven by Low-Cost Servo Valve Using Tap Water" International Journal of Mechanical Engineering and Robotics Research, Vol. 9, No. 3, pp. 353-359, March 2020. DOI: 10.18178/ijmerr.9.3.353-359
5. Shimooka S.,Akagi T., Dohta S., Matsui Y., Shinohara T, Hane Y.,and Aliff M., "Development of Reinforced Extension Type Flexible Pneumatic Actuator with Circumferential Restraints and Its Application for Rehabilitation Device" International Journal of Automotive and Mechanical Engineering. 17(3), 8116-8127. July-September 2020.DOI: https://doi.org/10.15282/ijame.17.3.2020.05.0609.
6. Ministry of Economy, Trade and Industry: Average of key dimensions by age group,http://warp.da.ndl.go.jp/info:ndljp/pid/286890/www.meti.go.jp/press/20071001007/004_bessi.pdf
7. Ministry of Health, Labour and Welfare: Results of Physical Condition Survey, https://www.mhlw.go.jp/content/000451760.pdf

The 11th JFPS International Symposium on Fluid Power HAKODATE 2020 Oct. 12-13, 2021 The Japan Fluid Power System Society

Development of Pneumatic Drive Pipe Inspection Robot using Radial Bending Type Soft Actuator

Takashi SHINOHARA*, Hikaru FURUYA**, Tetsuya AKAGI **, Shujiro DOHTA **, Takumi KOBAYASHI** and So SHIMOOKA***

*Science Dream lab., Okayama University of Science
**Department of Intelligent Mechanical Engineering, Faculty of Engineering, Okayama University of Science
1-1, Ridai-cho, Kita-ku, Okayama, 700-0005 Japan
(E-mail: shinohara@pub.ous.ac.jp)
*** Graduate School of Natural Science and Technology, Faculty of Engineering, Okayama University
1-1-1 Tsushima-naka, Kita-ku, Okayama, 700-8530 Japan

Abstract. In this paper, for the purpose of developing a pipe inspection robot that can catch pipes whose diameter has changed due to rust generated inside, the pipe holding mechanism that can flexibly catch various size of pipes was prototyped. A novel pipe holding mechanism using three extension type flexible pneumatic actuators (EFPAs) that holds the pipe while bending radially was proposed and tested. Also, the holding characteristics for various pipes of the tested mechanism is investigated. Furthermore, the inchworm-type robot using the tested holding mechanism was also proposed and tested. As a result, it could be confirmed that the robot could travel on the straight pipes and complicated pipes that consists of different pipes. In addition, a novel propulsion mechanism using only two holding mechanisms was also proposed and tested. It was also confirmed that a speed of 4.5 mm/s was obtained and that it could travel in a curved pipe.

Keywords: Pneumatic Drive Pipe Inspection Robot, Extension type flexible pneumatic actuator, Radial bending type soft actuator, Radial curved type pipe holding mechanism.

INTRODUCTION

In 2014, about 12.1% of the total length of water supply pipeline (660,000 km) in Japan has already passed the endurance period of 40 years [1]. As only 0.76% of the total pipe is changed every year, it will need more than 130 years to renewal the whole pipeline. In addition, water pipelines are complicated and consist of numerous corners and joints. An excavation work to inspect the entire pipes is expensive and time consuming. Therefore, various inspection methods such as a fiber scope, a dowsing and a wheel type inspection robot have been proposed and developed. However, a manipulated fiber scope cannot travel with long distance because of limitation of pushing force. Consequently, various companies and researchers have developed various self-propelled pipe inspection robots [2]-[8]. By using these robots, the cost of pipe inspection can also be reduced. Hence, inspection robots are required to have high mobility in the pipe. In ideal, the shape of the robot body changes naturally in order to consume less energy and shorten the travel time. Therefore, several researchers developed inchworm type pipe inspection robots using pneumatic soft actuators such as pneumatic artificial muscles and flexible cylinders [5]-[8]. In addition, a fluidic actuator does not use electricity as the primary energy, and because there is no risk of electric leakage or short circuits, they can be safely used in damp area such as in water supply pipe [5]-[12]. Based on this concept, we have proposed and tested an inchworm type pipe inspection robot that consists of a sliding propulsion mechanism and a holding mechanism using extension type flexible pneumatic actuators (it is called "EFPAs" for short) in our previous study [13]-[14]. The robot was able to move smoothly in a complex pipe with the inner diameter of 100 mm [14].
However, the tested pipe holding mechanism can only hold a pipe with a certain diameter [14]. In the next step, for developing a pipe inspection robot that can travel in various sized pipes by using only one type pipe holding mechanism, a novel pipe holding mechanism that can flexibly catch pipes with various inner diameters is proposed in this paper. In detail, a radial curved type pipe holding mechanism using three EFPAs that can catch the pipe while bending radially is proposed and tested. Also, the holding characteristics for each pipe (150A, 100A, 75A standards) of the prototyped pipe holding mechanism is investigated. In addition, the inchworm-type pipe inspection robot using the tested holding mechanisms is proposed and tested. Furthermore, we propose a novel propulsion method using only two radial curved type holding mechanisms arranged back-to-back, and investigate the optimal driving timing of the front and rear holding mechanisms for propulsion by experiments.

PREVIOUS INCHWORM TYPE PIPE INSPECTION ROBOT

In the previous study, the inchworm type pipe inspection robot using EFPAs was developed [13-15]. Figure 1 shows the construction of the extension type flexible pneumatic actuator (EFPA) [16-18]. The EFPA consists of a silicone rubber tube with an inner diameter of 8mm and outer diameter of 10mm covered with a bellows-shaped fabric sleeve made of nylon strings and two end connectors made of acrylic with a supply port. The operating principle of the EFPA is as follows. When the supply pressure is applied to the chamber, the inner rubber tube expands toward radial and axial directions. As the bellows-shaped sleeve prevents to expand toward radial direction, the EFPA extends longitudinally. The EFPA can extend more than about 2.5 times from its original length.

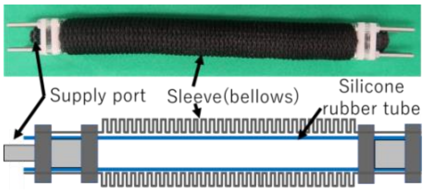

Figure 1. The construction of the extension type flexible pneumatic actuator (EFPA).

Figure 2 shows the construction of sliding/bending mechanism using three EFPAs developed in the previous study [14]. In the mechanism, three EFPAs are set in parallel between both disks in every 120 degrees and have a radius of 12 mm from the central axis of the robot. The operating principle is as follows. The expansion and contraction operation are realized as follows; the mechanism is extended when three EFPAs are pressurized at the same time. And the mechanism is returns to the original shape due to the elasticity of them when three EFPAs are exhausted simultaneously. In addition, the bending motion is applied by pressurizing one or two EFPAs in the sliding/bending mechanism.

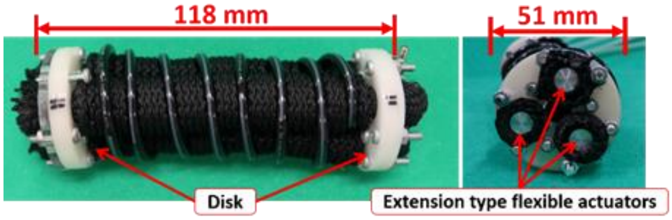

Figure 2. The construction of Sliding/bending mechanism using three EFPAs.

Pipes with smaller inner diameter of 75 and 50 mm that are commonly used as main pipe diameter were selected as a tested pipe in this experiment to a tire wheel type pipe holding mechanisms. In the previous study, in order to get a larger contact area with pipe without a larger volume change, a tire wheel type pipe holding mechanism for 75A standard pipe as shown in Figure 3 (a) is proposed and tested. The mechanism consists of a tire wheel type cylindrical rubber tube holder made by laminated acrylic plates, the rubber tube with outer diameter of 60 mm and two disk shaped holding plates and clamping rings for rubber tube. In the mechanism, the rubber tube is set over the wheel type holder. Both ends of the tube are clamped by the tube holder and disk-shaped holding plates through two clamping rings. By this method, the volume change of inner chamber surrounded by rubber tube for input pressure is limited toward only radial direction of the mechanism. The mass of the tested mechanism is 68.8 g.

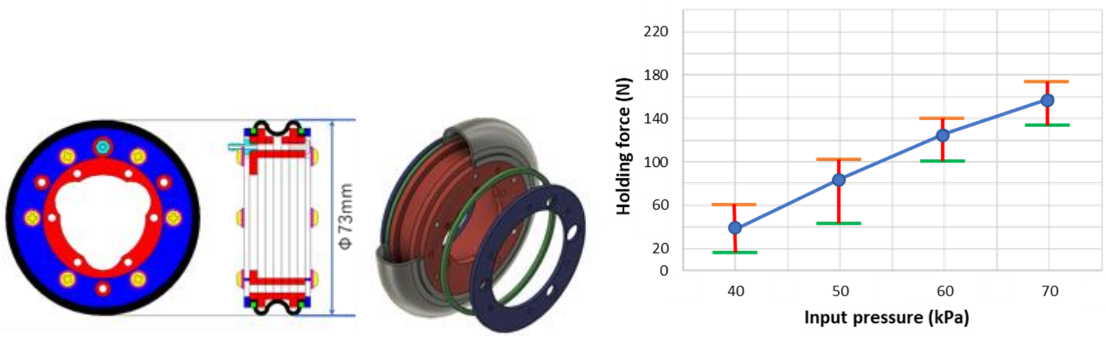

(a) Construction (b) Pipe holding characteristics

Figure 3. The construction and pipe holding characteristics of the tire wheel type pipe holding mechanisms.

Figure 3 (b) shows the relation between supplied pressure and pipe holding force of tested mechanism for pipe diameter of 75A. In the experiment, the pipe holding force is measured as a pulling force when the slip has occurred under the condition when the mechanism in the pipe is pulled. In the figure, symbol shows the average values of holding force of 20 times measurements. The vertical bar shows the measured data distribution. It can be seen that the tested mechanisms can generate pipe holding force of about 160 N. This is enough to apply to pipeline inspection robot using EFPAs, because the maximum generated pulling force of the sliding/bending mechanism in the robot is about 60 N.
Figure 4 shows the construction of the improved pipe inspection robots using the improved holding mechanism. Two holding mechanisms are set to both ends of the sliding/bending mechanism. In both sides of the holding mechanism, there are plastic arc-shaped guide to prevent stacking at a corner as shown in Figure 4.

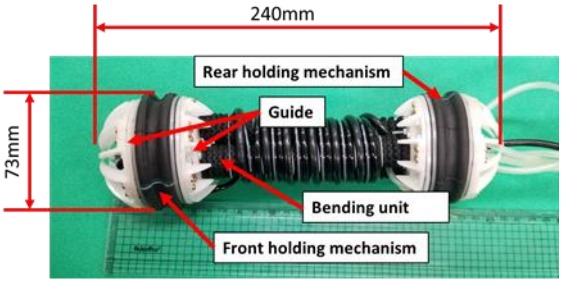

Figure 4. The construction of the tire wheel type pipe holding mechanisms.

The operating principle of the robot is as follows. First, the pipe holding mechanism at the end of the robot expands so that it can hold the pipe. In the condition, the sliding mechanism is extended by pressurizing three EFPAs. When the sliding mechanism extends up to a maximum length, the top pipe holding mechanism expands to hold the pipe. After that, the end pipe holding mechanism and the sliding mechanism contracts by exhausting input pressure, and end holding mechanism moves forward. By repeating these operations, the robot can move forward as an inchworm. The backward motion can also be realized by applying the opposite operation mentioned above. To steer the robot toward desired direction in a pipe joint, after bending motion is applied by pressurizing one or two EFPAs in the sliding/bending mechanism, it can be realized by all three EFPAs are pressurized. By this method, the robot can select six radial directions by pressurized one or two EFPAs in the sliding/bending mechanism.
Figure 5 shows the schematic diagram of control system to drive the tested pipe inspection robot. The system consists of the tested robot, five on/off control valves and an embedded controller. Three valves are used for the sliding mechanism, and they are operated through transistor and I/O port in the embedded controller. Two valves are used for pipe holding mechanisms and operated through transistor and PWM control port in the controller. In order to use the same supplied pressure of 500 kPa for both sliding and holding mechanisms, the holding mechanisms are driven by lower duty ratio signal of 50 % so as to reduce operating pressure of the mechanism. The control procedure is as follows. The operator sends digital code through a serial communication cable using a personal computer. The embedded controller selects to drive suitable valve according to the sequential program that is preinstalled into the controller. The timing of valve operation is adjusted by using a timer function in the embedded controller.

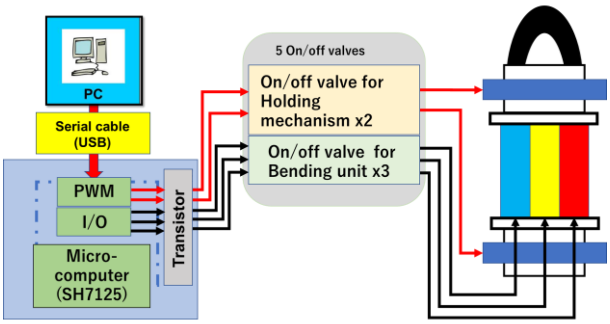

Figure 5. Schematic diagram of control system to drive the mechanism.

Figure 6 shows the results of driving test when the tested inspection robots pass through a complex pipe. In the experiment, three straight pipes with a length of 1 m and a corner and a tee joint were used. In addition, the valve unit was located on outside of pipes. Between the robot and valve unit, there is parallel arranged five small pipes with outer diameter of 4 mm and inner diameter of 2.5 mm. From Figure 6, it can be seen that the robot can pass through smoothly the complex pipe with a total length of 3 m within 4 minutes. Interestingly, through observation, robots are not stuck in corner and tee joints. This is mainly because of the improved higher holding force.

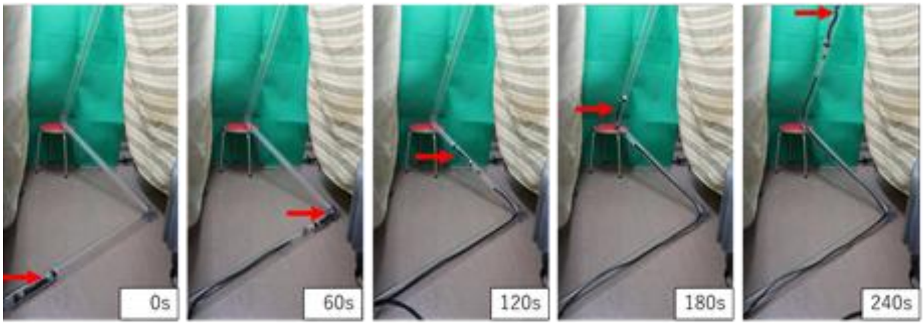

Figure 6. The results of driving test when the tested robots pass through a complex pipe with 75A pipe [14].

RADIAL BENDING TYPE HOLDING MECHANISM

The robot using the tire wheel type pipe holding mechanisms could travel in complex pipes with inner diameters of 75 mm. However, it could only travel in pipes with a certain diameter. The tested holding mechanism can not use for pipes with different diameters such as from 100 mm to 75 mm or to 150 mm. When the holding mechanism catches larger pipe with more than 75 mm, the mechanism doesn't work and occurs explosion. In this study, we aim to develop the pipe inspection robot that can travel in different diameter pipes of 150A, 100A and 75A (inner diameters of 150, 100 and 75mm), they are typical water supply pipes (excluding household branch pipes). We also aim to develop a holding mechanism that can hold various sized pipes or multiple pipes. The design concept of the holding mechanism for different diameter pipes is as follows. In order to hold several different diameter pipes by using only one holding mechanism, the mechanism needs to increase the radial expansion. Although balloon type mechanism that expands seems to be suitable, it consumes a large amount of air. Also, if the expansion due to elastic deformation of material is applied in it, it needs to worry about bursting. Therefore, we apply the method that the length of the material required to change in the radial direction is secured in advance in the direction of the pipeline axis with a margin. In detail, we consider a mechanism that it can change in the radial direction like a flower. The mechanism can hold the inside pipe wall when the actuator expands radially from the initial condition of no pressure. In the initial condition, the actuator extends in the axial direction of the pipe. In addition, this holding mechanism needs to have some flexibility for traveling in curved pipes. Figure 7 shows the construction of a radial bending type pipe holding mechanism prototyped based on the design concept. In the holding mechanism, three EFPAs with a natural length of 75 mm are placed in parallel at a radius of 11 mm from the center every 120 deg. In each EFPA, outer side of EFPA is restrained by connecting both ends through plastic beam like a cantilever beam.

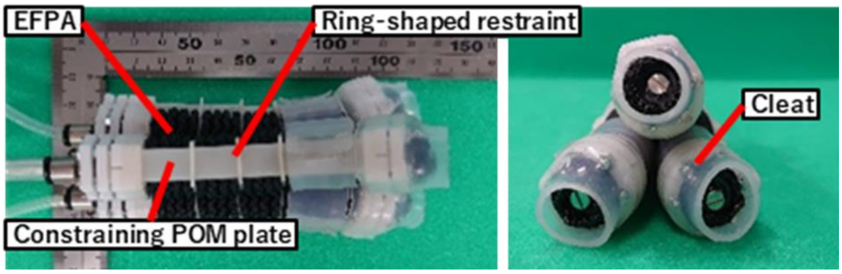

Figure 7. The structure of the radial bending type holding mechanism.

Figure 8 shows the attachment parts for the base that fastens the three EFPAs and the ring-shaped restraint plate at the bellows of each EFPA. The base plate mounted on three EFPAs has three holes with an inner diameter of 8 mm that are located on a radius of 11 mm from the center every 120 deg. Four small holes (for M3 screw) are set on a radius of 7 mm from the center of each large hole so that each EFPA can be easily removed from the mechanism. The ring-shaped restraint has a groove of 1 mm in length and 11 mm in width as shown in Figure 8 A POM restraint plate (thickness of 1 mm, width of 10 mm) is installed into the groove of ring-shaped restraint plates on the outer peripheral side of each EFPA so that the outer side longitudinal length does not change. This ring-shaped restraint plates are installed every four bellows so that the bending motion can occur when EFPAs extend. In addition, each end of EFPA is covered with a silicone rubber tube (with the inner diameter of 15 mm, outer diameter of 18 mm and length of 20 mm) to prevent a slipping. The mass of the holding mechanism is 110 g.

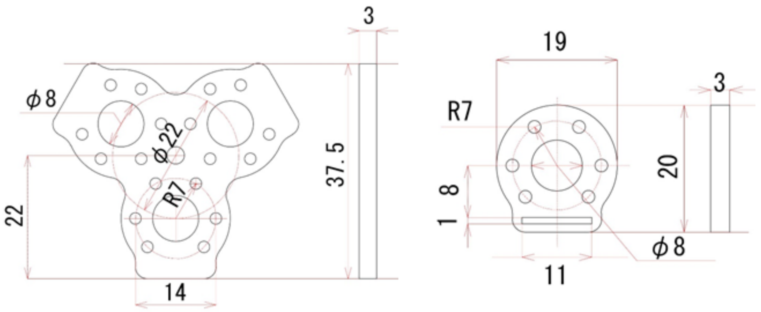

Figure 8. Mechanical drawing of the base plate (Left side) and ring-shaped restraint plate (Right side).

Figure 9 shows the appearance of the radial curved holding mechanism when supply pressure of 500 kPa is applied. It can be seen that the restraint plate can change the extension of each EFPA into a bending motion, and the three EFPAs can be bent radially. The maximum diameter for the applied pressure of 150 kPa is 200 mm. When the applied pressure becomes higher that is more than 200 kPa, each EFPA warps further if the end of EFPA does not reach the inner wall, and the outer diameter of the mechanism become smaller. Therefore, the diameter of the holding mechanism is maximized when the applied pressure is 150 kPa. If it is used in a pipeline with diameter of 200 mm or less, it is not necessary to adjust the pressure.

Figure 9. The appearance of the radial curved holding mechanism when 500 kPa is applied.

The relations between the applied pressure and the holding force using various sized holding mechanisms are shown in Figure 10. Figure 10 (a) shows an experimental setup using prototype holding mechanisms. Figures 10 (b), (c) and (d) show results using the restraint plate with length of 40 mm (thickness of 1 mm, width of 10 mm), 75 mm (thickness of 1 mm, width of 10 mm) and 100 mm (thickness of 2 mm, width of 10 mm), respectively. In each graph, symbols ●, ▲, and ♦ are the average values of the holding force measured 20 times in the case of the pipe of standards 75A (inner diameter of 79 mm), 100A (inner diameter of 105 mm), and 150A (inner diameter of 155 mm), respectively. In the experiment, the holding mechanism inserted into the pipe, and the EFPAs was pressurized. Also, it was pulled through a force gauge (Nidec-Shimpo Corporation; FGPX-100) that is connected in series with the holding mechanism as shown in Figure 10 (a). And the force at the time when the slip occurs is defined as a holding force. Based on 20 times measurements, the average value and distribution of holding force were calculated. From Figure 10, It can be seen that the holding mechanism with the length of 40 mm cannot hold the pipe of 150 A, and the mechanism with length of 75 mm or more can hold all three types of pipes. Also, the holding force using the mechanism with length of 40 mm is larger than the case using others. On the other hands, the holding mechanism with a length of 75 mm has a good holding force that can hold three types of pipes. Therefore, it seems that a holding mechanism with a length of 75 mm is suitable for all three types of pipes. For 100A and 75A standard pipe, the holding mechanism with length of 40mm is suitable, because it has the larger holding force and compact body for curved pipe. In addition, it can be seen that all types of tested holding mechanisms have enough holding force to support the mass of the robot (less than 1 kg), except for the combination that holds the pipe 150A with the holding mechanism of 40 mm.

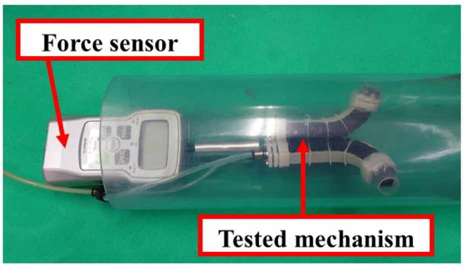

(a) Experimental setup for holding force.

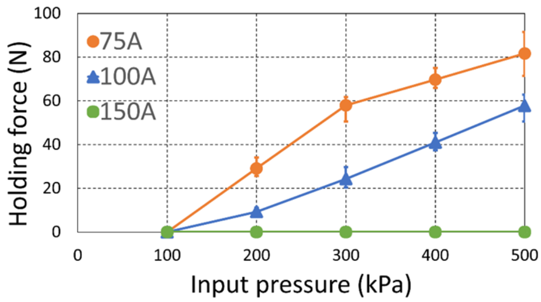

(b) Result using the mechanism with length of 40 mm.

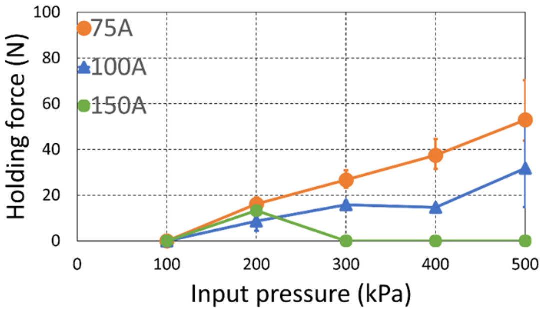

(c) Result using the mechanism with length of 75 mm.

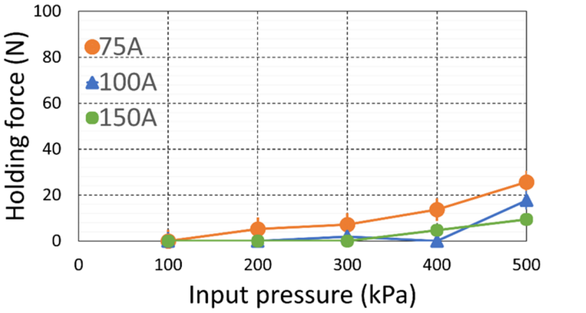

(d) Result using the mechanism with length of 100 mm.

Figure 10. Experimental setup for holding force and relation between input pressure and holding force using various pipe holding mechanisms.

Figures 11 (a), (b) and (c) show the appearance of a pipe inspection robot using the holding mechanism with length of 75 mm, the construction of an omni wheel mechanism in the robot, and the appearance of a shared pipeline plate for the pipe holding mechanism, respectively. The tested robot consists of a propulsion mechanism using the extension / bending mechanism and two radial curved type pipe holding mechanisms with length of 75 mm. The end of both holding mechanisms connected to both ends of the propulsion mechanism. Also, the omni wheel mechanism to reduce the friction and prevent stacking on the curved pipe is installed between the pipe holding mechanism and the propulsion mechanism. Since the holding mechanism needs three EFPAs to bend radially at the same time, it is necessary to share a supply pipeline into three outlets. The shared piping plate as shown in Figure 11(c) has branches for three outlets for EFPAs from a supply port. And it can be compactly integrated. The pressurized air to the front pipe holding mechanism is supplied from the rear side by using a coil type tube (inner diameter of 2.5 mm, outer diameter of 4 mm). The robot has a length of 520 mm, an outer diameter of 73 mm, and the total mass of the robot is about 1 kg.

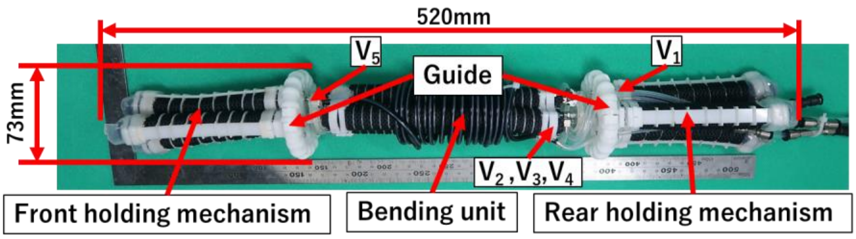

(a) The appearance of the pipe inspection robot using the pipe holding mechanism with length of 45 mm.

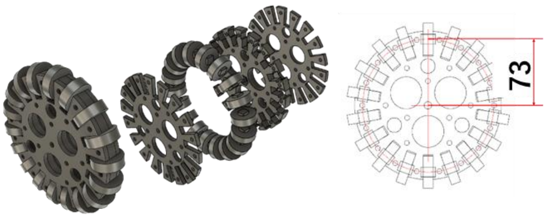

(b) Construction of omni wheel mechanism.

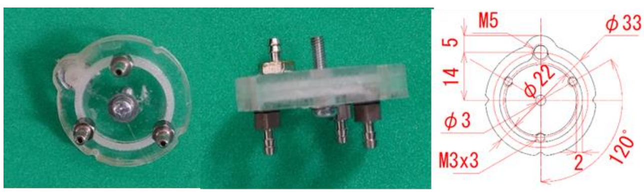

(c) The construction of shared pipeline plate.

Figure 11. The structure and components of the pipe inspection robot.

The control system of the tested robot is the same as the previous one as shown in Figure 5. Figures 12 (a) and (b) show the time chart of each valve for the robot moving forward and moving forward with bending, respectively. In Figure 12, V_1 means the valve to drive the front holding mechanism. V_2, V_3, and V_4 mean valves to drive three EFPAs in the sliding / bending mechanism. V_5 means the valve for the rear holding mechanism. By repeating the operation of moving forward that one cycle requires 11 s as shown in Figure 12 (a), the robot can move forward continuously. The moving backward can be realized by reversing the operation of the front and rear holding mechanism. In the propulsion in the curved pipe, that is the operation for moving forward while bending as shown in Figure 12 (b), one or two of the three EFPAs are pressurized in order to create a bending motion in a certain direction before the extension operation of the sliding / bending mechanism. After that, the three EFPAs are pressurized to extend. The timing of holding is almost the same as the case of moving forward, and one cycle for traveling curved pipe is 11.25 s.

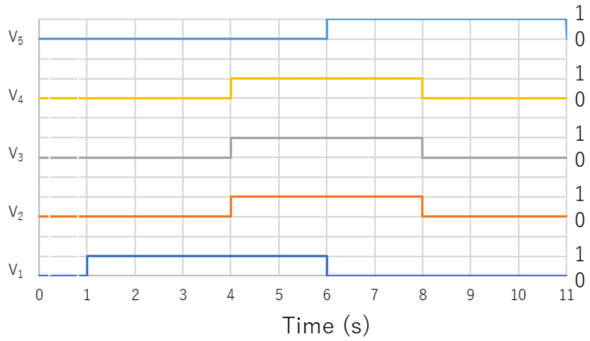

(a) For moving forward (straight pipe).

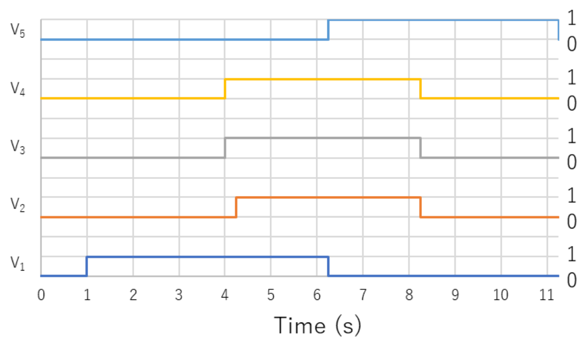

(b) For moving forward while bending (carved pipe).

Figure 12. Time chart of each valve of the robot for moving in straight and curved pipes.

Figures 13 (a) and (b) show a schematic diagram of a pipeline in which different straight pipes are connected in series and a transient view of movement of the robot in traveling test of the pipe inspection robot, respectively. From Figures 13 (b), it can be seen that the tested robot can travel smoothly even if the pipe diameter changes under the condition when the pipeline is set horizontally. It was found that the total travelling time of the pipeline of about 3 m was 210 s, and the average speed of the robot was 14.3 mm/s.

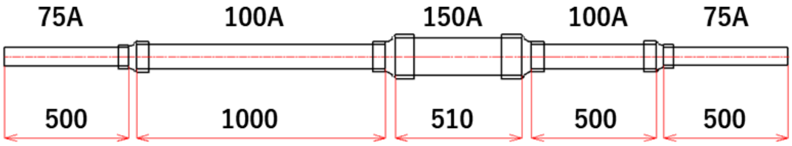

(a) A schematic diagram of a pipeline with different straight pipes.

(b) Transient view of movement of the robot.

Figure 13. Transient view of movement of the robot in traveling test of straight pipe.

In addition, Figure 14 (a), (b) and (c) show the schematic diagram of the complex pipeline, the transient view of the movement of the robot when the robot travels in a hairpin pipeline and L-shaped pipeline with a different diameter pipe, respectively. In the experiment, the short radial curved holding mechanism with length of 40 mm was used because of easy traveling in curved pipe. The supply pressure is 500 kPa. From Figure 14 (b), it was found that the robot could travel in hairpin pipeline with total length of about 3 m within 240 s. From Figure 14 (c), it was found that straight movements in T-shaped pipe were possible. It can be confirmed that the tested robot can run through a pipe with a total length of 2.5 m in 150 s. In addition, it was also found that the propulsive force could be generated when the EFPA bent further after contacting with the pipe. In the next chapter, a novel propulsive method that utilizes this phenomenon as a radial bending type soft actuator will be described.

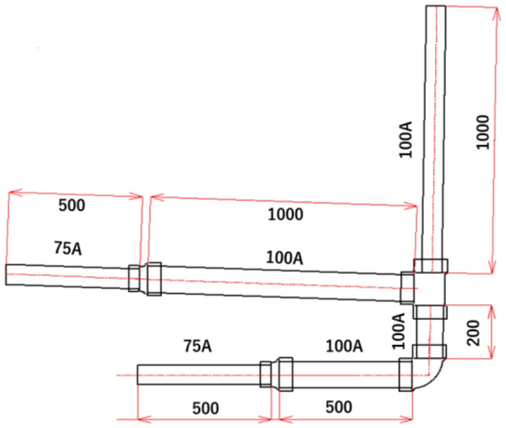

(a) Schematic diagram of the complex pipeline pipe.

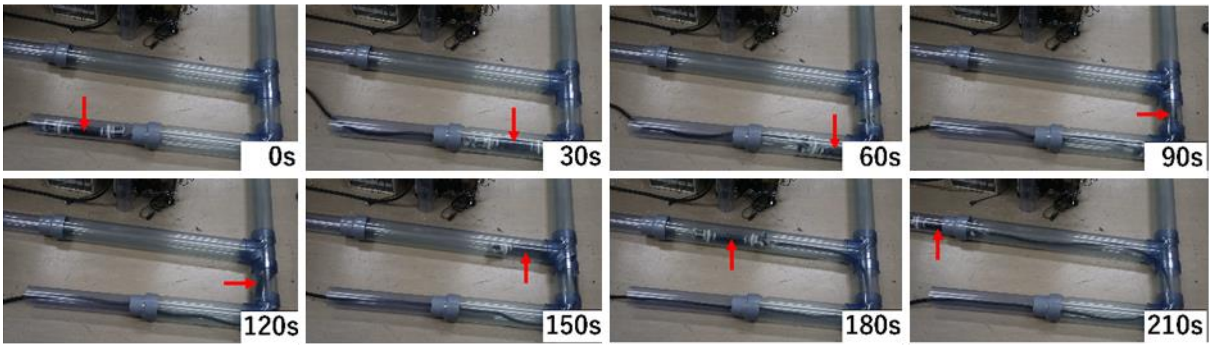

(b) Transient view of the movement of the robot in travelling in hairpin pipe line.

(c) Transient view of the movement of the robot in travelling in L-shaped pipeline

Figure 14. Results of travelling test using the tested robot in the complex pipe.

PROPULSION MECHANISM USING RADIAL BENDING TYPE SOFT ACTUATOR

Figure 15 shows the pipe propulsion mechanism using the radial bending type soft actuators by using the unique phenomenon mentioned above. The propulsion mechanism consists of a back-to-back combination of two radial bending type soft actuators with length of 40 mm, two shared pipeline plates and an omni wheels. It is noted that there is no bending unit compared with the mechanism in Figure 11(a). In the shared pipeline, the same pressure and flow rate will be applied to three EFPAs in each holding mechanism. The size of the robot is 73 mm in outer diameter, 200 mm in length, and 244 gf in weight.

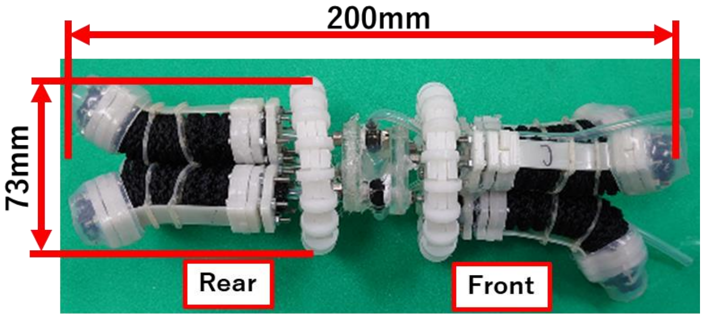

Figure 15. The pipe propulsion mechanism using the radial bending type soft actuators.

Figure 16 shows the transient view of the propulsion of the robot in the preliminary experiment. The operating principle of the propulsion mechanism is as follows. At the beginning of movement of the propulsion mechanism, the holding mechanism on the left side B does not hold the pipe, that is, the actuator is not pressurized. In the repeated operation from the second time, as shown in 1, the holding mechanism B is driven and the robot repeats the operation from the state of holding the pipe. Next, as shown in 2, when the holding mechanism on the right side A is driven, the robot holds the pipe wall with the tip of the EFPAs of the holding mechanism by contacting with the pipe. Next, as shown in 3, when the EFPAs are further pressurized, an entrainment operation of the EFPAs occurs at the contact point of the pipe wall as a fulcrum to give propulsion to the propulsion mechanism. At this time, the holding mechanism B is contracted so as not to interfere with the propulsive force generated by the holding mechanism A. Next, as shown in 4, EFPAs of the holding mechanism B are pressurized, the tips of the holding mechanism B contacts with the pipe wall, and both holding mechanisms hold the pipe. Next, as shown in 5 and 6, if the holding mechanism A is exhausted while the holding mechanism B is pressurized, the position of the holding mechanism A returns slightly. However, this reverse propulsion operation is prevented by adjusting the holding force of the holding mechanism B. After that, as shown in 7, while the holding mechanism B is exhausted, the holding mechanism A is pressurized again, and both holding mechanisms hold the pipe wall. Finally, as shown in 8, by exhausting the holding mechanism B and further pressurizing the holding mechanism A, the force in the propulsion direction is generated to the propulsion mechanism with the tip of the EFPA in contact with the pipe as a fulcrum, such as shown in 3. After that, it returns to the operation 4 after the operation 8. The propulsion mechanism can travel in pipe by repeating the operation from 4 to 8. The propulsion distance is the distance traveled by the operation from 2 to 3 or the operation from 7 to 8. As a result, it can be confirmed that the tested propulsion mechanism can travel in the straight pipe without sliding mechanism by only using entrainment operation of the EFPAs in the holding mechanism. As a future work, it is necessary to investigate the optimal operating switching timing between holding mechanism A and B.

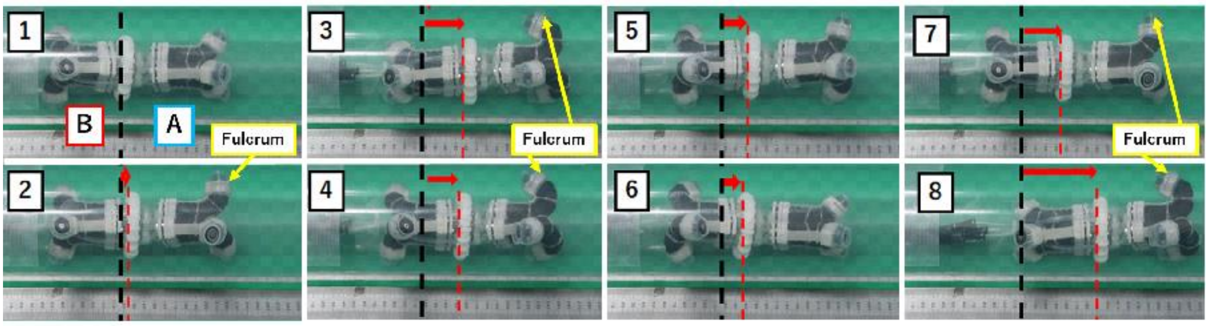

Figure 16. The appearance of the operating principle of the robot.

CONCLUSIONS

This study aiming to develop the pipe inspection robot that can travel in various sized pipes by using only one type pipe holding mechanism can be summarized as follows.

The bending soft actuator that the outer side of EFPA is restrained by connecting both ends through plastic beam was proposed and tested. The radial bending type pipe holding mechanism using three bending actuators based on EFPAs that can hold the pipe while bending radially was also proposed and tested. The holding

characteristics using the prototyped holding mechanisms with a length of 40, 75 and 100 mm were investigated. As a result of experiments for 75A, 100A and 150A standards pipes, the holding mechanism with a length of 75 mm has effective holding force for the 75A and 100A pipes. It was found that the holding force with a length of 40 mm was largest and effective.
The inchworm-type robot using two radial bending type pipe holding mechanisms with a length of 75 mm was proposed and tested. The traveling test in different-diameter straight pipes of 75A, 100A, and 150A was carried out. As a result, it was confirmed that the robot could travel in each pipe. It was also confirmed that the robot using the holding mechanism with a length of 40 mm can travel in complex pipes including 75A and 100A.
The unique propulsion mechanism using only two radial bending type pipe holding mechanisms arranged back-to-back was proposed and tested. As a result of the preliminary driving test, it could be confirmed that the tested propulsion mechanism could travel in the straight pipe by only using entrainment operation of the EFPAs in holding mechanisms.
As a future work, we are going to investigate the optimal operating switching timing between both holding mechanisms in the tested propulsion mechanism.

ACKNOWLEDGMENTS

This work was supported by JSPS KAKENHI Grant Numbers 16K06202 and 19K04265.

REFERENCES

1. Current situation of water supply in japan (in Japanese), https://www.mhlw.go.jp/seisakunitsuite/bunya/topics/bukyoku/kenkou/suido/newvision/chiikikondan/10/suishin_kondan10-1.pdf.
2. YUAN J., WU X., KANG Y., HUANG C., Development of an Inspection Robot for Long Distance Transmission Pipeline on-site Overhaul, International Journal of Industrial Robot, Vol.36, 2009, p.546-550.
3. DERTIEN E., STRAMIGIOLI S., PULLES K., Development of an Inspection Robot for Small Diameter Gas Distribution Mains, IEEE International Conference on Robotics and Automation, Shanghai, China, 2011, pp. 281-294.

SUZUKI, I., MATSUI, H., MATSUZAKA, D., Fundamentals of Water Hydraulic Control, New York Press, 1970, pp.123-124.

4. NAGATANI, K., KUZE, M., YOSHIDA, K., Development of a Transformable Mobile Robot with a Variable Wheel Diameter, Journal of Robotics and Mechatronics, Vol. 19, No.3, 2007, p. 252-257.

JOHNSON, H., et al., A Study of Performance Improvement of a Compressor, Transaction of the Japan Fluid Power System Society, Vol.3, No.4, 2001, p.56-62.

5. YASUI, T., MANO, Y., ITO, F., NAKAMURA, T., Development of Joint Attachment for Passing Curved Pipe of Peristaltic Motion Robot for In-pipe Inspection, Proc. of the 22nd International Conference on Climbing and Walking Robots and the Support Technologies for Mobile Machines (CLAWAR), 2019, pp.45-52.
6. YAMAMOTO, T., KONYO, M., TADAKUMA, K., TADOKORO, S., High-speed Sliding-inchworm Motion Mechanism with Expansion-type Pneumatic Hollow-shaft Actuators for In-pipe Inspections, Mechatronics, vol. 56, 2018, p. 101-114.
7. MIYASAKA, K., KAWANO, G., TSUKAGOSHI, H., Long-mover: Flexible Tube In-pipe Inspection Robot for Long Distance and Complex Piping, IEEE / ASME International Conference on Advanced Intelligent Mechatronics (AIM), 2018, pp. 1075-1080.
8. IKEUCHI, M., NAKAMURA, T., MATSUBARA, D., Development of an In-pipe Inspection Robot for Narrow Pipes and Elbows using Pneumatic Artificial Muscles, IEEE / RSJ International Conference on Intelligent Robots and Systems, 2012, pp. 926-931.
9. KAWASAKI, T., AKAGI, T., DOHTA, S., HARIAHARA, K., Development of a Flexible Sliding Mechanism Using Flexible Pneumatic Cylinder for Rescue Robot, FLUCOME 11th International Conference on Fluid Control, Measurements, and Visualization, Keelung, Taiwan, 2011, 41.pdf, pp. 1-6.
10. AKAGI, T., DOHTA, S., WANG, L., KAWASAKI, T., Development of Sliding Type Inspection Robot using Flexible Pneumatic Cylinder, International Journal of Advanced Mechatronic Systems, Vol. 5, 2013, pp. 87-94.
11. AKAGI, T., DOHTA, S., QIU, H., Pipe Inspection Robot using Flexible Pneumatic Cylinder Built-in Pneumatic Driving System, International Forum on Systems and Mechatronics, Tainan, Taiwan, 2014, pp. 1-6.
12. CHOI, K., DOHTA, S., AKAGI, T., NINOMIYA, S., Development of Pipe Holding Mechanism for Pipe Inspection Robot using Flexible Pneumatic Cylinder, International Conference on Mechanical, Manufacturing, Modeling and Mechatronics, Kuala Lumpur, Malaysia, 2016, pp. 529-536.
13. KUSUNOSE, K., AKAGI, T., DOHTA, S., KOBAYASHI, W., NAKAGAWA, K., Development of Pipe Holding Mechanism and Bending Unit using Extension Type Flexible Actuator for Flexible Pipe Inspection Robot, International Journal of Mechanical Engineering and Robotics Research, Vol. 8, No. 1, 2019, p. 129-134.
14. HAYASHI, K., AKAGI, T., DOHTA, S., KOBAYASHI, W., SHINOHARA, T., KUSUNOSE, K., ALIFF, M., Improvement of Pipe Holding Mechanism and Inchworm Type Flexible Pipe Inspection Robot, International Journal of Mechanical Engineering and Robotics Research, Vol. 9, No. 6, 2020, p. 894-899.

15. KUSUNOSE, K., AKAGI, T., DOHTA, S., KOBAYASHI, W., SHINOHARA, T., HANE, Y., HAYASHI, K., ALIFF, M., Development of Inchworm Type Pipe Inspection Robot using Extension Type Flexible Pneumatic Actuators, International Journal of Automotive and Mechanical Engineering, Vol. 17, No. 2, 2020, p. 8019-8028.
16. SUZUKI, Y., AKAGI, T., DOHTA, S., KOBAYASHI, W., TAMAKI, H., MATSUI, Y., SHIMOOKA, S., Development of Tetrahedral Type Rehabilitation Device using Flexible Pneumatic Actuators, International Journal of Mechanical Engineering and Robotics Research, Vol. 7, No. 4, 2018, p. 409-414.
17. SHIMOOKA, S., DOHTA, S., AKAGI, T., KOBAYASHI, W., YONEDA, M., Development of Portable Rehabilitation Device using Flexible Extension Type Soft Actuator with Built-in Small-Sized Quasi Servo Valve and Displacement Sensor, JFPS International Journal of Fluid Power System, Vol. 11, No. 2, 2018, p.18-25.
18. SHIMOOKA, S., DOHTA, S., AKAGI, T., KOBAYASHI, W., SHINOHARA, T., Improvement of Home Portable Rehabilitation Device for Upper-Limbs, JFPS International Journal of Fluid Power System, Vol. 12, 2019, No. 1, 2019, p. 10-18.

Organized Session | Organized session

Soft Actuator 1

[OS5-1-01] Analysis and Design of Servo Valve Using Buckled Tubes for Desired Operation of Flexible Robot Arm

〇Takumi Kobayashi[1], Hideyuki Obayashi[1], Tetsuya Akagi[1], Shujiro Dohta[1], Wataru Kobayashi[1], Takashi Shinohara[1], So Shimooka[2] （1.Okayama University of Science, 2.Okayama University）

[OS5-1-02] Development of Pneumatic Variable Linear Stepping Actuator and Soft Stepping Actuator with Bending Motion for Rehabilitation Device of Hip Joint

〇Kota Oe[1], Tetsuya Akagi[1], Shujiro Dohta[1], Takashi Shinohara[1], Wataru Kobayashi[1], So Shimooka[2] （1.Okayama University of Science, 2.Okayama University）

[OS5-1-03] Development of Extension Type Flexible Pneumatic Actuator with Displacement Sensor Using Ring-shaped Magnet and Hall Sensor for Tetrahedral-type Soft Mechanism

〇Kenshiro Takeuchi[1], Takumi Kobayashi[1], Tetsuya Akagi[1], Shujiro Dohta[1], Takashi Shinohara[1], Wataru Kobayashi[1], So Shimooka[2] （1.Okayama University of Science, 2.Okayama University）

[OS5-1-04] Development of Highly Durable Straight Fiber Type Pneumatic Artificial Muscle with a Double Structural Air Chamber

〇Naoki Saito[1], Daisuke Furukawa[1], Toshiyuki Satoh[1], Norihiko Saga[2] （1.Akita Prefectural University, 2.Kwansei Gakuin University）

[OS5-1-05] Evaluation of Lifting Motion with Non-wearing Type Pneumatic Power Assist Device ~ Comparison of Active and Passive Type ~

〇Masashi Yokota[1], Reito Hirabayashi[1], Masahiro Takaiwa[2] （1.Tokushima University, Graduate School Advanced Technology and Science, 2.Tokushima University, Graduate School of Technology, Industrial and Social Sciences）

The 11th JFPS International Symposium on Fluid Power HAKODATE 2020 Oct. 12-13, 2021 JFPS The Japan Fluid Power System Society

Analysis and Design of Servo Valve Using Buckled Tubes for Desired Operation of Flexible Robot Arm

Takumi KOBAYASHI*, Hideyuki OBAYASHI *, Tetsuya AKAGI*, Shujiro DOHTA*, Wataru KOBAYASHI*, Takashi SHINOHARA** and So SHIMOOKA ***

*Department of Intelligent Mechanical Engineering, Faculty of Engineering, Okayama University of Science
**Science Dream lab., Okayama University of Science
1-1, Ridai-cho, Kita-ku, Okayama, 700-0005 Japan
(E-mail: akagi@are.ous.ac. jp)
***Graduate School of Natural Science and Technology, Okayama University
3-1-1 Tsushima-naka, Kita-ku, Okayama 700-8530, Japan

Abstract. A Pneumatic soft actuator has many advantages of a higher ratio of generated force and lightweight and inexpensive. It is also attracting attention because of its intrinsic safety due to compliance based on air compressibility. However, in a system using pneumatic soft actuators, a servo valve is most heavy and expensive. Therefore, in the previous study, a low-cost and small-sized servo valve using buckled tubes was proposed and developed. In this paper, a static analytical model for designing the valve was proposed. In order to decrease the cost and size of valves, a multi-port servo valve that can operate three pneumatic actuators of the flexible robot at the same time was proposed. The design method of the valve based on the analytical model to get desired sinusoidal motion of the robot was described. The driving test of the robot arm using the designed valve based on the model was carried out.

Keywords: Analytical model, Model based design, Servo valve using buckled tubes, Flexible robot arm, Extension type flexible pneumatic actuator

INTRODUCTION

A driving system using pneumatic soft actuator have gained considerable attention and many studies have been carried out [1-4]. They were developed as power assisting devices for nursing care [1], elderly [2] and worker [3] using pneumatic artificial muscles [4]. In this study, we aim to develop a low-cost home rehabilitation device driven by pneumatic actuators. In a pneumatic driving wearable or portable device, the size and cost of a servo valve becomes a serious issue. Typically, the most expensive and heavy control equipment in the pneumatic soft mechanism is a servo valve. A typical electro-magnetic servo valve on the market has a complex mechanism for moving its spool while keeping a seal. The complex mechanism makes the valve bulkier and more expensive.

Therefore, a miniaturization and low-cost fabrication of a servo valve is a challenging issue. In order to decrease mass, size and cost of the valve, a simple mechanism for valve opening is required [5-10]. Zhao developed a quasi-servo valve using small-sized on/off valve [5]. Many researchers developed small-size valves driven by vibration. One is a valve using a piezoelectric actuator [6]. The other is a valve using sound [7,8]. In the previous study, a valve driven by a vibration motor was developed [9]. They were on/off type valves, not servo valves. As a small-sized and low-cost servo valve, a servo valve using buckled tubes was proposed and tested in the previous study [11-13]. The position control of the pneumatic rubber artificial muscle using the tested valve was carried out [12]. A multi-port type servo valve was also developed to drive a double-acting type typical pneumatic cylinder [13].

In the next step, to realize more compact valve, we consider developing a valve that can operate many actuators at the same time so that the device using soft actuators can be work according to desired periodical motion. In this paper, an analytical model of the servo valve to design the configuration of buckled tubes to get desired static characteristics is proposed. As a driving target for design of the valve using the proposed model, we select a flexible robot arm using three extension type flexible pneumatic actuators (we call it “EFPA” for short) developed in the previous study [14]. Because the motion of the tested robot arm is often required periodical rotational motion as a rehabilitation device to give a passive exercise for arm and shoulder. In addition, to get the desired operation of three EFPAs in the flexible robot arm by using simple operation of the valve, multi-port control valve using buckled tubes is designed based on proposed model. The driving test of the robot arm using the designed valve is carried out.

SERVO VALVE USING BUCKLED TUBES

Figure 1 shows the construction of multi-port type servo valve using buckled tubes to drive a double-acting type pneumatic actuator developed in the previous study [13]. The valve consists of four buckled tubes, a rotational disk with two Y-shaped connectors (for outlet), four fixed straight connectors (for supply or exhaust port) and a RC servo motor. Each buckled tube is connected between Y-shaped connector and fixed connector. Figure 2 shows the operating principle of the valve. By changing the rotational angle of the disk by motor, the buckled angle of each tube is decreasing or increasing. By increasing the buckled angle of the tube, the sectional area of the tube increases to flow. In the opposite case when the buckled angle is decreasing, the sectional area in the tube decreases and is closed surely below the threshold angle. Because the sectional area in the tube is related to the rotational angle, the valve can realize to switch supply or exhaust for two outlets and control analog flow rate from both outlets.

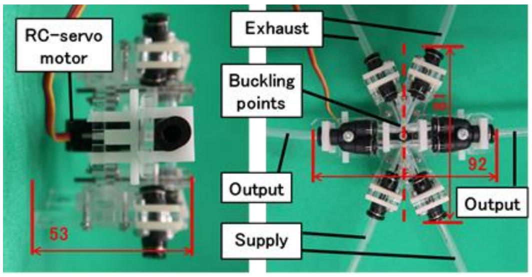

Figure 1. Construction of the servo valve using buckled tubes for double-acting type pneumatic actuator [13].

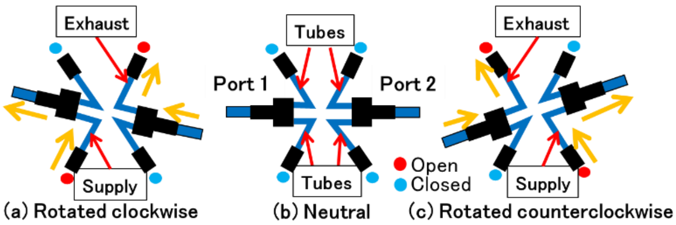

Figure 2. Operating principle of the servo valve using buckled tubes for double-acting type pneumatic actuator [13].

Figure 3 shows the relationship between the motor rotational angle and output flow rate from two outlets of the tested valve. In Figure 3, the horizontal axis shows the incremental rotational angle of a rotation from the initial angle of the motor (= 0 deg.), and the vertical axis shows the output flow rate from the left and right output ports. The negative value shows exhaust flow rate, the positive value shows supply flow rate. The experimental results in Figure 3 show the average value of three repeated measurements. And the red and blue symbols show the output flow rates from Port 1 and Port 2, respectively, which correspond to the left and right side ports in Figure 2. In the experiment, the supply air pressure of 500 kPa was used. The discharge flow rate from each output port is measured with a digital flow meter (SMC Co., Ltd. PFMB7201-C8-AM). From Figure 3, it can be seen that the flow rates from both outlets can change in supply and exhaust symmetrically according to the rotational angle of the servo motor changes. It can also be confirmed that the valve has an overlap that the valve can maintain the output pressure of the valve. The maximum flow rate of 50 l/min and more can be obtained from both ports. The overlap area of the rotational angle is about ± 2 deg.

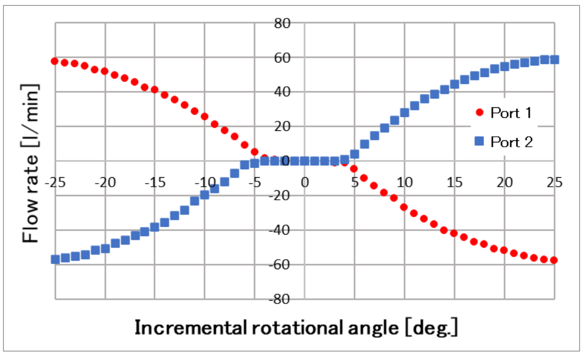

Figure 3. Relationship between motor rotational angle and output flow rate of the servo valve using buckled tubes.

ANALYTICAL MODEL TO DESIGN THE VALVE

Figure 4 shows a simple analytical model of the servo valve using buckled tubes that is related to one side outlet port based on geometrical configuration of tubes and connectors. The model consists of two buckled tubes for supply and exhaust, a Y-shaped connector and two fixed straight connectors. In the model, the Y-shaped connector can rotate around the origin O, a motor shaft, in Figure 4. By using the model, the location of the connected point of tubes in Y-shaped connector after rotational motion can be calculated. As assuming the buckled tube keeps straight except for the buckled point, the buckled point and buckled angle of each tube can also be calculated by using law of cosines. In addition, by the investigated empirical formula of relation between buckled angle and sectional area of the tube described later, it can be calculated the static characteristics of flow rate according to motor rotational angle for the initial buckled angle of each tube.

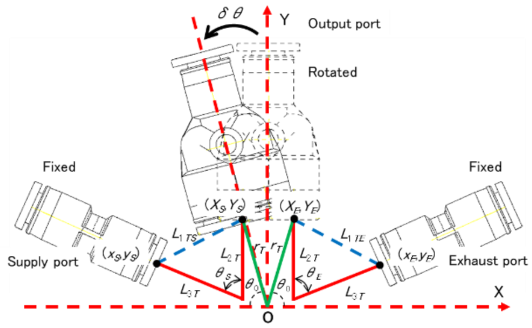

Figure 4. Model of the servo valve using buckled tubes.

From the geometric relationship, the bending angles $\boldsymbol{\theta_S}$ and $\boldsymbol{\theta_E}$ of two tubes change according to the rotation of the rotating disk to which the Y-shaped connector is attached. If the initial angle from the motor rotational axis (origin) to the central axis of the Y-shaped connector is $\boldsymbol{\theta_0}$, the coordinates $\{X_S, Y_S\}$ and $\{X_E, Y_E\}$ of both tubes connected points with the Y-shaped connector to which the tube is attached are given by the following equations.

$$X_S = -r\cos(\theta_0 - \delta\theta) \tag{1}$$
$$Y_S = r\sin(\theta_0 - \delta\theta) \tag{2}$$
$$X_E = r\cos(\theta_0 + \delta\theta) \tag{3}$$
$$Y_E = r\sin(\theta_0 + \delta\theta) \tag{4}$$

where, $\boldsymbol{r}$ is the radius from the motor rotational axis to the end of Y-shaped connector, $\boldsymbol{\delta\theta}$ is the motor rotational angle, and subscript $\boldsymbol{S}$ and $\boldsymbol{E}$ show the supply and exhaust side buckled tube connectors, respectively.
From Equations (1) to (4), the distances between the Y-shaped connector and supply or exhaust connector $\boldsymbol{L_{1TS}}$ and $\boldsymbol{L_{1TE}}$ are given by the following equation.

$$L_{1Ti} = \sqrt{(X_i - x_i)^2 + (Y_i - y_i)^2} \quad (i = S, E) \tag{5}$$

where, $\{x_S, y_S\}$ and $\{x_i, y_E\}$ are the coordinates of the center end of fixed supply and exhaust straight connectors, respectively. In addition, as the supply and exhaust connectors are fixed, and these coordinate $\{x_S, y_S\}$ and $\{x_i, y_E\}$ are constant. Therefore, from law of cosines, the bending angles $\boldsymbol{\theta_S}$ and $\boldsymbol{\theta_E}$ of the two buckled tubes can be obtained by using Equation (5) and the distances $\boldsymbol{L_{2T}}$ and $\boldsymbol{L_{3T}}$ from each connector to the buckled point and are given by the following equation.

$$\theta_i = \cos^{-1}\frac{\left(L_{2T}{}^2 + L_{3T}{}^2 - L_{1Ti}{}^2\right)}{2L_{2T}L_{3T}} \quad (i = S, E) \tag{6}$$

The flow rates $\boldsymbol{Q_S}$ and $\boldsymbol{Q_E}$ from the buckled tubes on supply and exhaust side are given by the following equations.

$$Q_S = A_S \cdot P_S\sqrt{\frac{2}{RT}} \cdot f\left(\frac{P_O}{P_S}\right) \tag{7}$$

$$Q_E = A_E \cdot P_O \sqrt{\frac{2}{RT}} \cdot f\left(\frac{P_A}{P_O}\right) \tag{8}$$

where, A_S and A_E are the opening areas of the buckled tubes and are expressed as a function of the tube bending angles θ_S and θ_E [rad]. P_A, P_O and P_S indicate the atmospheric pressure, output pressure, and supply pressure, respectively, and R is the gas constant, T is the absolute temperature, and the function $f\ (z)$ is the function indicating the flow state, which is expressed by the following equation.

$$f(z) = \sqrt{\frac{\kappa}{\kappa-1}(z^{2/\kappa} - z^{(\kappa+1)/\kappa})}(0.528 \le z \le 1) \tag{9}$$

$$f(z) = \sqrt{\frac{\kappa}{\kappa+1}\left(\frac{2}{\kappa+1}\right)^{2/(\kappa-1)}} \quad (0 \le z \le 0.528) \tag{10}$$

where, κ indicates the specific heat ratio. z means a pressure ratio between downstream and upstream.

In order to know the relationship of the opening area of the buckled tube with respect to the bending angle of the buckled tube, the relationship of the flow rate with respect to the bending angle as shown in Figure 5 was investigated. In the experiment, the same bending tube (SMC Co. Ltd, TUS0425) as the tube used in the tested valve, the supply pressure of 500 kPa was applied. In the measurement, the discharge flow rate from the output port to the atmosphere was measured with a digital flow meter (SMC Co. Ltd., PFMB7201-C8-A-M, resolution 1 l/min) according to the bending angle change of the tube. The bending angle of the tube was measured from the photograph of the tube. In Figure 5, the vertical axis shows the mass flow rate calculated from the volumetric flow rate measured with the flow meter, and the horizontal axis shows the bending angle of the tube. In addition, from the repetition bending test of buckled tube, it has been confirmed that the durability of the buckled tubes is about 15,000 to 100,000 times under the critical condition of fast bending repetition. The durability of buckled tube is related to the generated heat by bending it. In typical use, we can also confirm that the valve using buckled tubes can be used in more than three years.

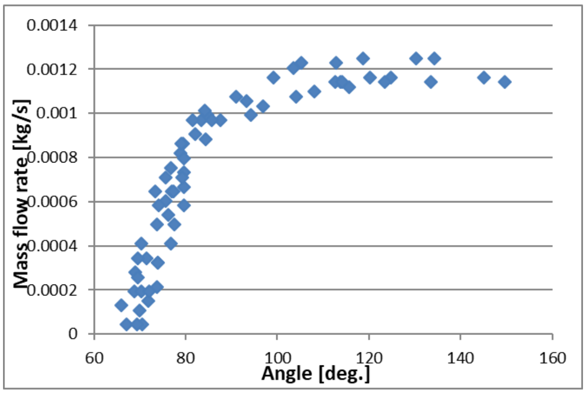

Figure 5. Relation between angle of buckled tubes and mass flow rate.

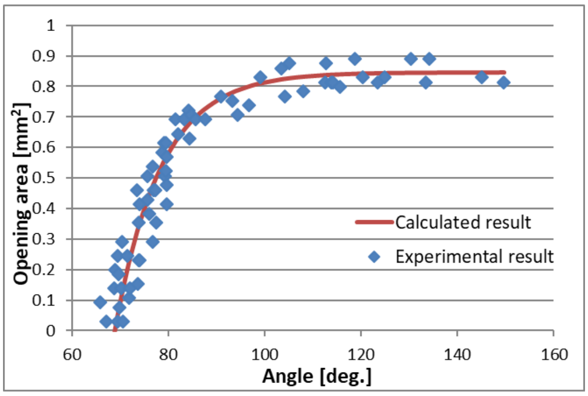

Figure 6. Relation between buckled angle and opening area of buckled tube.

From the result as shown in Figure 5, the opening area (sectional area) A_i of the tube was calculated by using Equations (7), (8), and (10). Figure 6 shows the relation between the bending angle and the calculated sectional area of the buckled tube. In Figure 6, the symbol shows the calculated value of the opening area obtained from the measured flow rate. The red line shows the result by using the approximate model described later (Equation (11)).

From the results as shown in Figure 6, the opening sectional area of the buckled tube with respect to the bending angle is given by the following approximate equation.

$$\boldsymbol{A_i = 0.845\left(1 - e^{-0.105(\theta_i - 68.9)}\right) \quad (i = S, E)} \tag{11}$$

Table 1 lists identified system parameters of the prototype valve. Using the proposed analytical model and identified parameters mentioned above, it is possible to calculate the flow rate characteristics with respect to the motor rotational angle when the position of each connector and the length of each buckled tube are changed.

Table 1. Identified system parameters.

Parameter	Value
P_A [Pa]	101.3×10^3
P_S [Pa]	500×10^3
R [J/(kg・K)]	287
T [K]	300
r_T [m]	0.01353
θ_0 [deg.]	72.8
x [m]	0.01734
y [m]	6.051×10^{-3}
L_{2T} [m]	0.013
L_{3T} [m]	0.015
κ	1.4
ρ [kg/m^3]	1.293

In order to confirm the effectiveness of the proposed model and the identified system parameters, the experimental and calculated static characteristics of output flow rate were compared. Figure 7 shows the comparison between the experimental and calculated results of the output flow rate with respect to the motor rotational angle. In this figure, the symbols ● and ■ indicate the measured flow rate from the outlet Port 1 and 2 of the valves, respectively. In addition, ○ and □ show the calculated results based on the model. From Figure 7, the calculated overlap zone within ± 3deg. is almost same as the experimental results that Port 1 has the overlap zone within ± 2deg. and Port 2 has the overlap zone from -4 to 3 deg. It can also be seen that the analytical model can predict the characteristics of output flow rate relative well, although there is a slight difference in the maximum flow rate. It seems that it is because the relationship between the actual output flow rate (opening area) and the bending angle as shown in Figure 6 has some gaps, it appears as an error. As a result, it can be confirmed the validity of the proposed model that can calculate from the motor rotational angle to the valve output flow rate can be confirmed. In addition, the dynamics of the valve depends on the dynamics of the RC servo motor with buckled tubes, that is a band width frequency of 3.0 Hz.

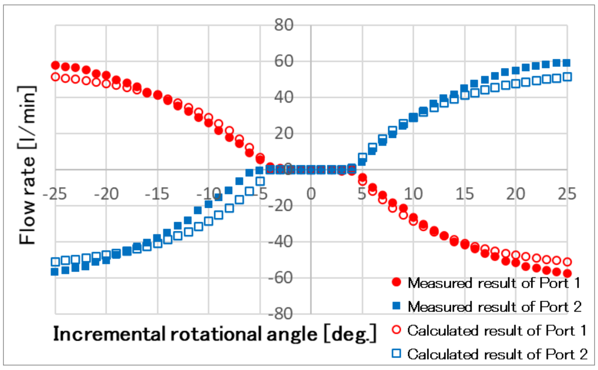

Figure 7. Relation between motor rotational angle and output flow rate of the valve.

DESIGN PROCEDURE OF MULTI-PORT SERVO VALVE AND TARGET DEVICE

As a design of the valve using the analytical model described above, we try to design a multi-port servo valve that can operate three pneumatic actuators at the same time with one RC servo motor. As a driving object using the designed valve, a flexible robot arm using extension type flexible pneumatic actuators (we call it "EFPA" for short) was selected. Figure 8 shows the appearance and structure of EFPA used in the flexible robot arm. The EFPA consists of the silicone rubber tube (inner diameter: 8 mm, outer diameter: 11 mm) is covered with a bellows type sleeve (Swiftrans Co. Ltd., Stretching hose) to restrain its movement to the longitudinal direction. In EFPA, the minimum and maximum diameter of the bellows are 12 and 20 mm, respectively. When the supply pressure is applied to the EFPA, the silicone rubber tube expands in all directions, but the sleeve does not expand in the circumferential direction and extends only toward the longitudinal direction. EFPA can extend until 2.5 times of its original length. This large extension ratio is one of most important advantages of EFPA.

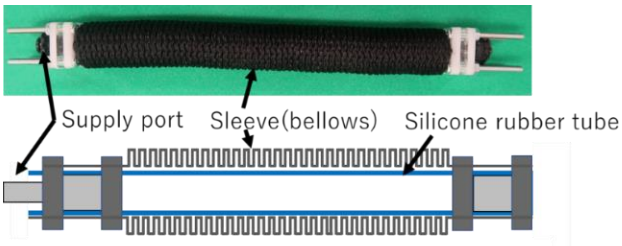

Figure 8. Appearance and schematic diagram of EFPA [14].

Figure 9 shows the appearance and construction of the flexible robot arm using EFPAs. The flexible robot arm consists of 20 Y-shaped restraint PET plates and three reinforced EFPAs that is parallel arranged three EPPA restrained with small restraint PET plates [14]. Three reinforced EFPAs set parallel with a radius of 70 mm every 120 deg. from the center axis by using Y-shaped restraint PET plates with thickness of 1 mm. The robot arm can bend toward radial direction by changing pressurized reinforced EFPA. The robot arm had been developed for rehabilitation device that can give passive exercise to patient's arm and shoulder by its rotating motion while bending. Therefore, the target motion of the robot arm is the rotating motion while bending.

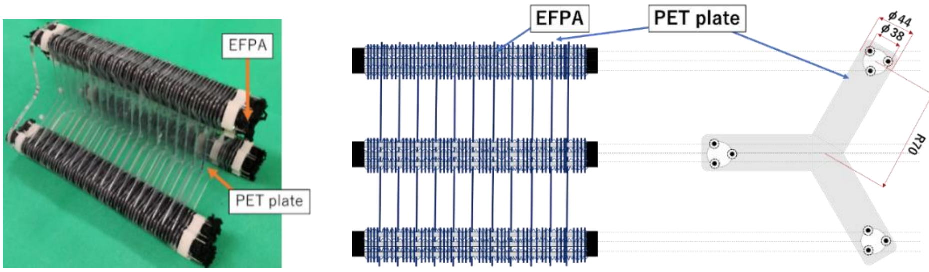

Figure 9. Appearance and construction of reinforced EFPA with circumferential restraints [14].

As a specification of the designed valve, the valve needs three supply, exhaust and output ports. In addition, it is necessary to realize the target motion of the robot arm by simply rotating the RC servo motor in the valve with a rotational range of 60 deg., that is from 0 (neutral position) to -30 deg. (toward counterclockwise) and from 0 to +30 deg (toward clockwise). By using this rotational motion of the motor, each port in the valve to drive each EFPA so that the robot arm can rotate with the bending directional angle from 0 to 360 deg. while bending. The design procedure to realize these specifications mentioned above is as follows.

(1st) Obtain the time-series data of the length of each EFPA based on the analytical model of the robot arm model from the target movement of the robot arm.

(2nd) Match the calculated time-series data of each EFPA length to the time-series data of the rotational angle of the RC servo motor.

(3rd) From time-series data of EFPA length, determine the switching timing from supply to exhaust and from exhaust to supply of valve.

(4th) The expected initial bending angles of the supply and exhaust buckled tubes connected to each actuator are decided. The calculated area for supply and exhaust using the decided initial bending angles and the model of the valve draws on time-series data of EFPA length.

In this procedure, (4th) process is repeating until that the calculated area based on the model meets to the switching timing determined by (3rd) process.

MODEL OF ROBOT ARM AND DESIGN OF MULTI-PORT SERVO VALVE

Next, as a design based on proposed models, the initial bending angle of the buckled tube of the multi-port servo valve is calculated. First, according to the (1st) process in design procedure, the time-series data of the length of each EFPA with respect to the target trajectory is calculated by using the analytical model of the flexible robot arm [14]. Figure 10 shows the analytical models of the robot arm. Figure 10 (a) shows the definition of the bending directional angle $\boldsymbol{\alpha}$ and the bending angle $\boldsymbol{\beta}$ of the robot arm, and Figure 10 (b) shows the definition of length of each EFPA, that is projected length of each EFPA on the plane according to the bending directional angle. The reinforced EFPA located on the X axis is defined as EFPA 1. The other reinforced EFPAs arranged in a counterclockwise direction from the position of EFPA 1 are defined as EFPA 2 and 3, respectively. $\boldsymbol{l_1}$, $\boldsymbol{l_2}$, and $\boldsymbol{l_3}$ as shown in Figure 10 (b) are lengths of the reinforced EFPA 1, 2 and 3, respectively. Assuming that the shape of each EFPA in the robot arm is a circular arc, the lengths $\boldsymbol{l_1}$, $\boldsymbol{l_2}$, and $\boldsymbol{l_3}$ of each EFPA are given by the following equations.

$$\boldsymbol{l_1 = (R - r \cdot cos\,\alpha) \cdot \beta} \tag{12}$$

$$\boldsymbol{l_2 = (R - r \cdot \cos(\frac{2\pi}{3} - \alpha)) \cdot \beta} \tag{13}$$

$$\boldsymbol{l_3 = (R - r \cdot \cos(\frac{4\pi}{3} - \alpha)) \cdot \beta} \tag{14}$$

$$\boldsymbol{R = \frac{l}{\beta}} \tag{15}$$

where, $\boldsymbol{l_i}$ ***(i = 1, 2, 3)*** is the length of each EFPA, $\boldsymbol{R}$ is the radius of curvature of the robot arm, $\boldsymbol{r}$ is the radius from the center to the circumference where the EFPA is located, respectively. From Equations (12) to (15), the central length $\boldsymbol{l}$ of the robot arm is expressed by the following equation.

$$\boldsymbol{l = \frac{l_1 + l_2 + l_3}{3}} \tag{16}$$

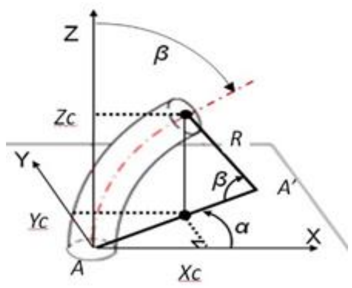

(a) Definition of angles $\boldsymbol{\alpha}$ and $\boldsymbol{\beta}$.

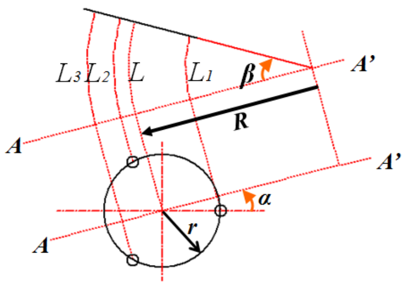

(b) Definition of length of each EFPA.

Figure 10. Analytical model of the flexible robot arm [14].

In addition, to measure the bending directional angle $\boldsymbol{\alpha}$ and bending angle $\boldsymbol{\beta}$ of the robot arm, an accelerometer (Kionix, Inc., KXM52-1050) was attached on the center tip of the robot arm. Both angles $\boldsymbol{\alpha}$ and $\boldsymbol{\beta}$ obtained from that accelerometer output voltage can be obtained from the following equations.

$$\boldsymbol{\alpha = \cos^{-1}\frac{V_x}{\sqrt{{V_x}^2 + {V_y}^2}}} \tag{17}$$

$$\boldsymbol{\beta = \cos^{-1}\left(\frac{V_z}{V_{zmax}}\right)} \tag{18}$$

where, V_x, V_y, and V_z are the differential voltages from the initial values (horizontal state) of the accelerometer in the x, y, and z directions, respectively. V_{zmax} is the maximum difference voltage of V_z when the center tip (accelerometer) is changed from horizontal and vertical.

Next, each desired length of EFPA for the target trajectory of the robot arm is calculated using the analytical model of the robot arm. Here, the target trajectory was set so that the bending angle β was 120 deg. (2π / 3) and the bending directional angle α was 0 to 360 deg. (0 to 2π) in 60 seconds. Figures 11 (a), (b) and (c) show the calculation results of the time-series changes in the displacement of EFPA 1, 2 and 3 with respect to this target trajectory, respectively. In the calculation (experiment), the natural length of each EFPA constructing the robot arm was set to 230 mm under the condition when each EFPA was arranged at a radius of 70 mm from the center of the robot arm.

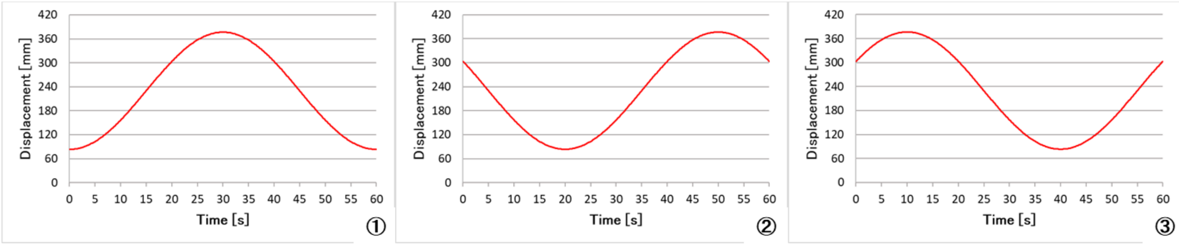

(a) EFPA 1 (b) EFPA 2 (c) EFPA 3

Figure 11. Transient response of calculated length of each EFPA using the analysis model.

According to the (2nd) process in the design procedure, the time series data of the calculated lengths matches to the time series data of the rotational angle of the RC servo motor (0 → -30 → 0 → 30 → 0 deg.). Figure 12 shows data set of the desired length of each EFPA and rotational angle of the RC servo motor.

According to (3rd) process in design procedure, and valve switching timing for supply or exhaust is decided. In detail, the timing at maximum length of each EFPA is regarded as a switching timing from supply to exhaust. The timing of minimum length of each EFPA, it is also regarded as a switching timing from exhaust to supply. Because the motion of EFPA while exhausting is slower than the motion while supply, the switching timing from exhaust to supply is also changed a little later. In (4th) process, by paying attention to these switching points, the initial bending angle of both supply and exhaust buckled tubes so that supply and exhaust motion area can agree with the desired switching timing by using the model of valve mentioned above.

By repeating (4th) process, the initial bending angle of each valve was determined. In Figure 12, the red, blue and green broken lines indicate the supply, exhaust and holding area that are calculated by the designed initial bending angle of each buckled tube, respectively. In addition, designed initial bending angle for each valve is also indicated on right side of each figure. From Figure 12, it can be seen that the calculated valve operation based on the model and the determined initial bending angle almost meet the desired switching timing, although there is some area that cannot be realized due to restrictions on repetitive motor operation.

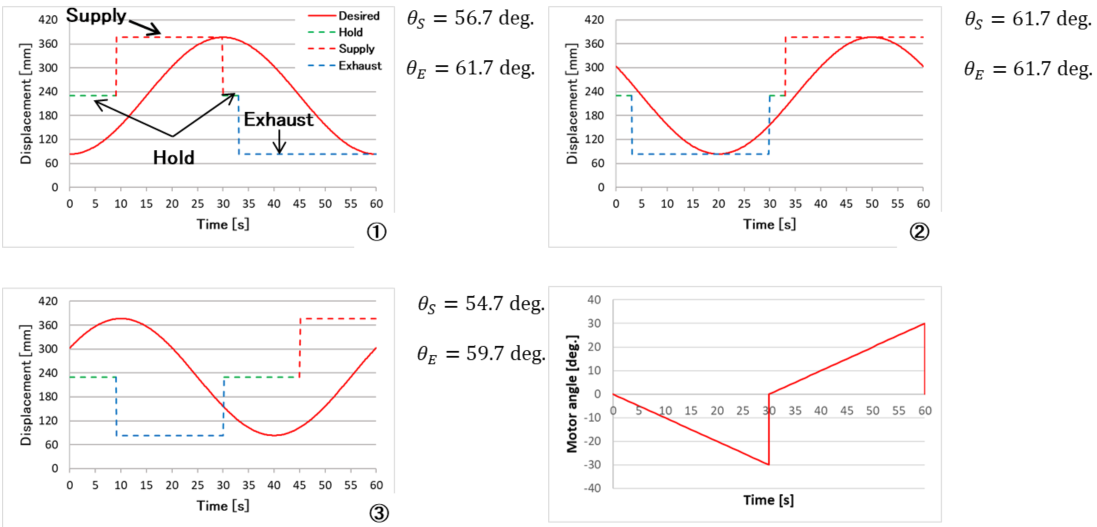

Figure 12. Data set of the desired length of each EFPA and rotational angle of the RC servo motor.

8

Figures 13 (a), (b) and (c) show the calculated static relations between the motor rotational angle and the output flow rate of each designed valve connected to EFPA 1, 2 and 3 using the analytical model of the valve and designed initial bending angles of buckled tubes, respectively. From these results, it can be seen that the output flow rate of the valve for EFPA 1 is inverse to others. It is found that the overlap zone of each valve is different, that are overlap from -9 to 3 deg. for EFPA 1, the overlap from -3 to 3 deg. for EFPA 2 and the overlap from -9 to 15 deg. for EFPA 3, respectively.

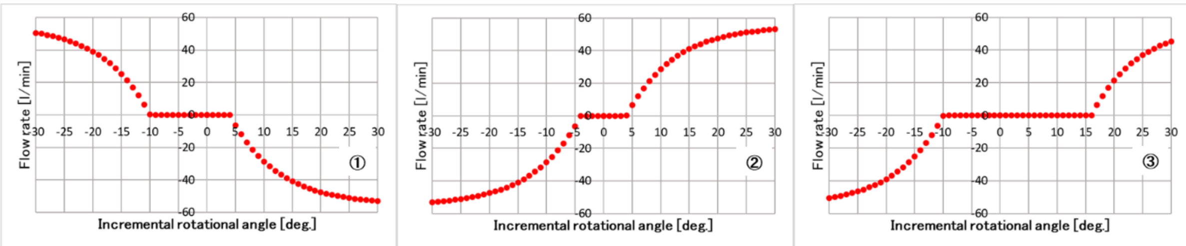

(a) Valve for EFPA 1 (b)Valve for EFPA 2 (c)Valve for EFPA 3

Figure 13. Calculated relations between the motor rotational angle and the output flow rate of each designed valve.

DRIVING TEST OF ROBOT ARM USING THE DESIGNED VALVE

Figure 14 show the tested multi-port servo valve using buckled tubes based on design using the proposed model. The valve has three 3-port type valve units that each valve unit consists of two buckled tubes for supply and exhaust. These are arranged in parallel. Three rotational disks of valve units are driven by a RC servo motor at the same time. Then, the designed initial buckled angle for each valve is shown in Figure 12. The tested valve also has a rotational potentiometer to monitor the rotational angle of the motor. The size of the valve becomes compact compared with the amount volume of three original 3-port type valves. The valve has the length of 90 mm, the width of 81mm and height of 105 mm.

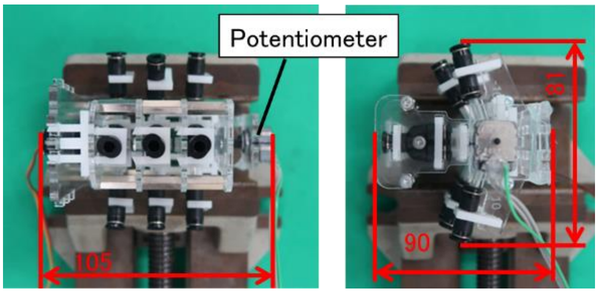

Figure 14. Tested multi-port servo valve using buckled tubes.

Figures 15 shows the schematic diagram and appearance of a control system using the designed multi-port servo valve and the flexible robot arm. The control system consists of the flexible robot arm using three reinforced EFPAs, the designed multi-port servo valve, an accelerometer (Kionix, Inc., KXM52-1050) and an embedded controller (Renesas Electronics Co. Ltd., H8 / 3664F). The accelerometer is attached to the center tip of the robot arm and is used to measure the bending directional angle $\boldsymbol{\alpha}$ and the bending angle $\boldsymbol{\beta}$ of the arm. The RC servo motor of the valve is operated by changing the duty ratio with respect to the preset target angle via the PWM port in the embedded controller. The output signals from the accelerometer are monitored via a recorder (Graphtec Corporation, GL900). In the experiment, the supply pressure of 300 kPa was applied to the multi-port servo valve. The RC servo motor in the valve was repeated to rotate from 0 to -30 to 0 to +30 to 0 deg. every 1 deg. per second.

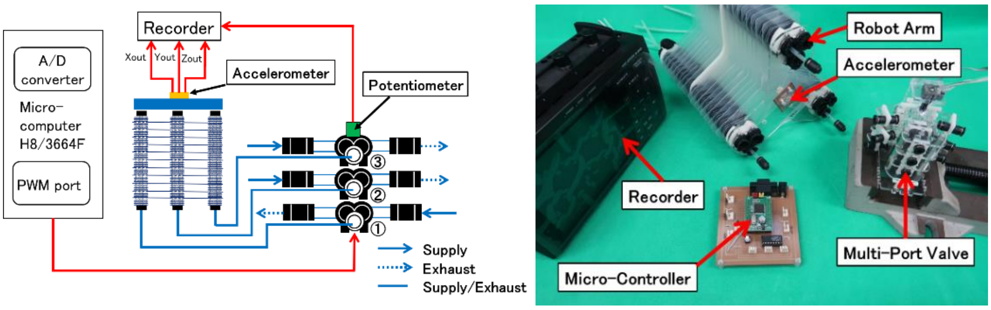

Figure 15. Schematic diagram and appearance of the control system using the designed valve and the flexible robot arm.

Figure16 shows the transient view of motion of the flexible robot arm using the tested valve. It can be confirmed that the robot arm can move according to the desired motion by giving the swing motion of RC servo motor as shown on the lower right of Figure 12.

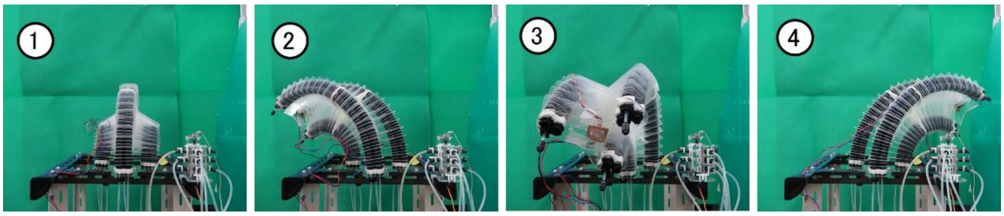

Figure 16. Transient view of motion of the flexible robot arm using the tested valve.

Figures 17 (a) and (b) show the transient response of the measured bending directional angle $\boldsymbol{\alpha}$ and bending angle $\boldsymbol{\beta}$ of the flexible robot arm by using the accelerometer when the robot arm moves according to sequential operation using the tested valve, respectively. Figure 18 shows the transient response of the measured rotational angel of the RC servo motor by using the potentiometer attached on the valve. In both results, a low-pass filter with 1.5 Hz was used to avoid noise. In Figure 17, the solid red line shows the experimental result, and the broken blue line shows the desired bending directional angle and bending angle. From Figure 17, it can be confirmed that the robot arm can almost keep constant bending angle of 120 deg., that is the desired bending angle. It can also trace the desired bending directional angle with the rotation from 0 to 360 deg. It seems that the error is caused by the sequential control without feedback control. In addition, by adjusting the swing speed (rotational speed) of RC servo motor, we believe that the tracking error will be improved. As a result, it can be confirmed that the developed valve can operate three EFPAs in the robot arm at the same time with simple repeating rotational motion using one RC servo motor, and the robot arm can roughly trace the target orbit.

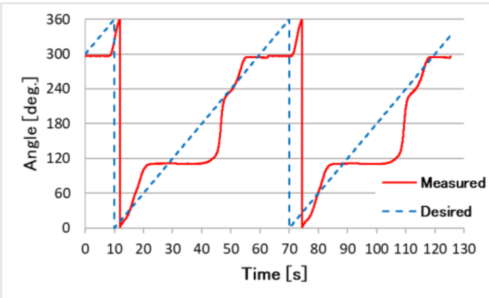

(a) Bending directional angle $\boldsymbol{\alpha}$.

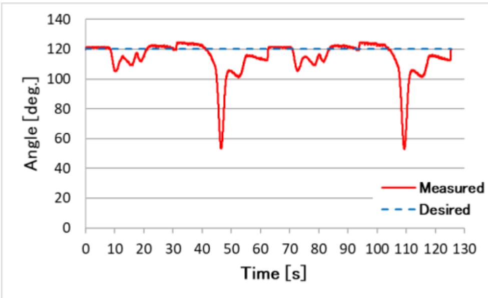

(b) Bending angle $\boldsymbol{\beta}$.

Figure 17. Transient response of the measured bending directional angle $\boldsymbol{\alpha}$ and the bending angle $\boldsymbol{\beta}$ of the robot arm.

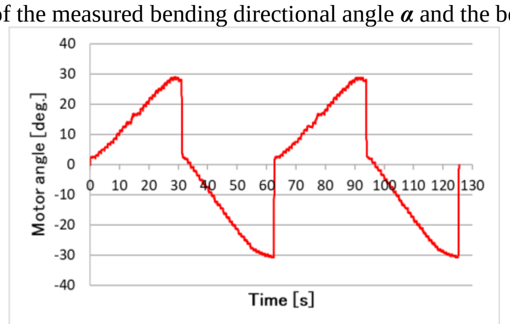

Figure 18. Transient response of the measured rotational angel of the RC servo motor.

CONCLUSIONS

In this paper, the analytical model of the servo valve using buckled tubes to design the configuration of buckled tubes and to get the desired static characteristics was proposed. The flexible robot arm using parallel arranged three EFPAs was also tested. In order to get the desired motion of the robot arm by giving simple swing motion of the valve, the initial bending angle of buckled tubes for each port of the valve was designed based on the proposed model. And the multi-port servo valve using buckled tubes with the designed initial bending angle was developed. The driving test using the tested valve was carried out. As a result, the robot arm could move according to the desired motion. It can be confirmed that the proposed model is valid to design the valve using buckled tube and is useful to design the valve with the special purpose of use.

ACKNOWLEDGMENTS

This work was supported by JSPS KAKENHI Grant Numbers 16K06202 and 19K04265.

REFERENCES

1. ISHII, M., YAMAMOTO, K., HYODO, K., Stand-Alone Wearable Power Assist Suit -Development and Avail-ability-, Journal of Robotics and Mechatronics, Vol.17, 2005, pp.575-583.
2. NORITSUGU, T., TAKAIWA, M., SASAKI, D., Development of Power Assist Wear Using Pneumatic Rubber Artificial Muscles, Journal of Robotics and Mechatronics, Vol.21, 2009, pp.607-613.
3. KOBAYASHI, H., ISHIDA, Y., HASHIMOTO, T., Muscle Suit Development and Factory Application, International Journal of Automation Technology, Vol.3, No.6, 2009, pp.709-715.
4. NAGATA, Y. ed., Soft Actuators -Forefront of Development-, Tokyo: NTS Ltd., 2004, pp.291-335.
5. ZHAO, F., DOHTA, S., AKAGI, T., Development and Analysis of Small-Sized Quasi-Servo Valve for Flexible Bending Actuator, Transactions of JSME, Series C, Vol.76, No.772, 2010, pp.3665-3671.
6. JIEN, S., HIRAI, S., HONDA, K., Miniaturization Design of Piezoelectric Vibration-Driven Pneumatic Unconstrained Valves, Journal of Robotics and Mechatronics, Vol.22, No.1, 2010, pp.91-99.
7. JING, S. et al., A Study on a Sound Operated Valve for a Wearable Pneumatic System: 1st Report: Development of a Pilot Valve a Sound Operated Direction Control Valve, Journal of the Japan Fluid Power System Society, 39(3), 2008, pp.54-60 (in Japanese).
8. NISHIOKA, Y. et al., A New Pneumatic Control System using Multiplex Pneumatic Transmission, Proceedings of 7th JFPS International Symposium on Fluid Power Toyama, 2008, pp.439-442.
9. AKAGI, T., DOHTA, S., KATAYAMA, S., Development of Small-sized Flexible Pneumatic Valve using Vibration Motor and Its Application for Wearable Actuator, Journal of Computer Applications in Technology, 39(1/2/3), 2010, pp.86-92.
10. AKAGI, T., DOHTA, S., Development of Wearable Pneumatic Actuator and Multiport Pressure Control Valve, Journal of Robotics and Mechatronics, 17(5), 2005, pp.529-536.
11. NASIR, A. et al., Development of Low-Cost Wearable Servo Valve Using Buckled Tube, Applied Mechanics and Materials, 393, 2013, pp. 532-537.
12. NASIR, A. et al., Development of Small-sized Servo Valve Controlled by Using Buckled Tube and Its Application, Journals of the Japan Society of Mechanical Engineers, 7(4), 2013, pp. 516-527.
13. OBAYASHI, H. et al., Development of 5–Port Type Low–Cost Servo Valve Using Buckled Tubes, International Journal of Mechanical Engineering and Robotics Research, Vol. 7, No. 6, 2018, pp. 669-673.
14. SHIMOOKA, S. et al., Development of Reinforced Extension Type Flexible Pneumatic Actuator with Circumferential Restraints and Its Application for Rehabilitation Device, International Journal of Automotive and Mechanical Engineering, 17(3), 2020, 8116-8127.

The 11th JFPS International Symposium on Fluid Power HAKODATE 2020 Oct. 12-13, 2021 JFPS The Japan Fluid Power System Society

Development of Pneumatic Variable Linear Stepping Actuator and Soft Stepping Actuator with Bending Motion for Rehabilitation Device of Hip Joint

Kota OE*, Tetsuya AKAGI*, Shujiro DOHTA*, Takashi SHINOHARA**, Wataru KOBAYASHI* and So SHIMOOKA***

*Department of Intelligent Mechanical Engineering, Faculty of Engineering, Okayama University of Science
**Science Dream lab., Okayama University of Science
1-1,Ridai-cho, Kita-ku, Okayama, 700-0005 Japan
(E-mail: akagi@are.ous.ac. jp)
*** Graduate School of Natural Science and Technology, Okayama University
3-1-1 Tsushima-naka, Kita-ku, Okayama 700-8530, Japan

Abstract. Based on elderly society in Japan, the rehabilitation device that can be used in home or hospital without care person's assistance has been desired. In the device, a soft actuator that can move with both longer strokes and larger force is useful. In the previous study, a Pneumatic Linear Stepping Actuator ("PLSA" for short) that can push and pull the flexible rod while changing the gripping position of the tube was developed. In this study, a variable step type PLSA is proposed and tested. And the development of a rehabilitation device for hip joint that using three PLSAs and one connecter connected with three flexible rods and a knee supporter. The tracking position control of knee supporter based on an analytical model is also described. To make simpler rehabilitation device, a soft stepping actuator with bending motion is also proposed and tested. The control system using developed actuators is also introduced.

Keywords: Pneumatic variable linear stepping actuator, Soft stepping actuator with bending motion, Rehabilitation device for hip joint, Backdrivability, Passive exercise.

INTRODUCTION

In 2020, the ratio of the Japanese elderly becomes more than 26 % [1]. In 2040, the ratio will be expected about 36%. Under such a critical society condition, various pneumatic drive soft mechanisms to assist welfare work for the elderly and disabled[2] have been actively developed[3-10]. As a pneumatic soft actuator, a McKibben type pneumatic artificial muscle (PAM for short) is well known and used for soft mechanism. The PAM can generate larger force of more than 300 N by contracting toward the longitudinal direction. However, the contract ratio is very small, that is less than 25 % of the original length. As a soft mechanism using PAM, T. Noritsugu and H. Kobayashi developed power assisted wears[3-6] to increase the force for welfare workers and heavy labors. As an application using other pneumatic soft actuator, H. Taniguchi and H. Kawasaki developed a rehabilitation device for inhibiting contracture of finger joints [7,8]. As a soft mechanism using rigid pneumatic actuator, M. Takaiwa also developed a rehabilitation device for contracture patients using pneumatic parallel manipulator by realizing softness using controller[9]. In these mechanisms, a pneumatic soft actuator was often used because it has an advantage of compliance based on air compressibility. However, most of soft actuator can not realize long stroke motion because of its flexibility. Based on the issue, in the previous study, the Pneumatic Linear Stepping Actuator (we call it "PLSA" for short) that can realize both large force of more than 300 N and long stroke motion was proposed and tested[10,11]. The tested actuator can push or pull the flexible rod with a certain step by changing the gripping point of the flexible rod. It means that the stroke of the actuator has no limit, it depends on length of the flexible rod. The flexible robot arm using three PLSAs that can extend like a robot of Dr. Octopus in cartoon "Spider-man" was also developed [12]. The holding mechanism in PLAS was improved so as to hold the flexible rod surely[13]. In addition, a simple rehabilitation device using PLSA for upper limb was also developed[14]. However, the tested PLSA moves only every certain stroke. Therefore, the positioning accuracy depends on its stroke.

In this study, a novel pneumatic linear stepping actuator that can change the stroke for one step freely is proposed and tested. The construction and operating principle of the tested actuator are described in this paper. As an application using proposed these actuators, rehabilitation devices using three previous PLSAs and renewed PLSAs for hip joint are also described. The control method to improve positioning accuracy was also introduced.

PREVIOUS PNEUMATIC LINEAR STEPPING ACTUATOR

Figure 1 shows the construction of the previous PLSA. The PLSA consists of three double acting type pneumatic cylinders with the stroke of 50 mm and the inner diameter of 16 mm (Koganei Co., PBDA 16×50-M), two pneumatic chucks and a flexible soft polyurethane tube with the outer diameter of 12 mm and the inner diameter of 10 mm as a rod. The ends of three cylinders are connected with a base stage with the pneumatic chuck. They are set every 120 degrees with radius of 25 mm from the center of the base stage. The rod ends of three pneumatic cylinders are also connected with the moving stage with the pneumatic chuck. The flexible linear stepping actuator has a length of 150 mm and an outer diameter of 68 mm. The mass of the actuator is 0.7 kg. The actuator can realize a flexibility at the point of working rod end. The actuator also has a backdrivability while the pneumatic chuck is not driven.

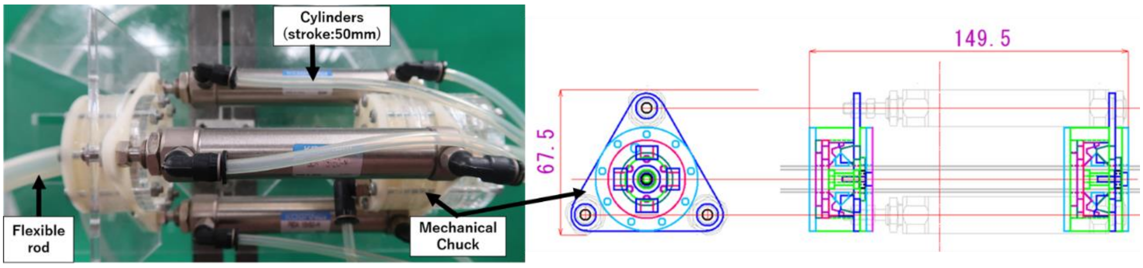

Figure 1. View and schematic diagram of the previous pneumatic linear stepping actuator.

Figure 2 shows the schematic diagram of a magnetic core type pneumatic chuck developed in our previous study[13]. The pneumatic chuck consists of two ring-shaped neodymium magnets, I-shaped cylindrical plastic core in the flexible tube, a doughnut-shaped diaphragm (that is made of a rubber film with a thickness of 1 mm, an inner diameter of 24 mm and an outer diameter of 36 mm) and a mechanical chuck. The mechanical chuck consists of two claws, fixed and moving bases with a slope angle of 45 degrees. The cylindrical plastic core consists of ring-shaped plastic disks and a ring-shaped neodymium magnet with the outer diameter of 8.5 mm and the inner diameter of 5.5 mm. They are penetrated by a screw and a nut. In the mechanical chuck, the ring-shaped neodymium magnet with the outer diameter of 20 mm and the inner diameter of 12 mm is set on the flexible tube to attract the magnet of the moving core. By attracting both magnets of the chuck and the core each other, the core can automatically track the movement of the chuck. When the supplied pressure is applied to the diaphragm, the flexible tube is clamped from both inner and outer sides by claws and moving core. By this method, the chuck can hold the tube (rod) surely.

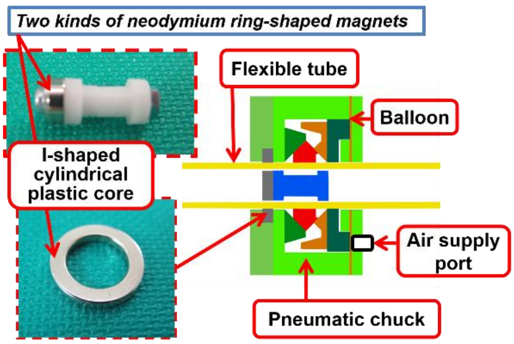

Figure 2. Schematic diagram of inner construction of magnetic core type chuck.

Figure 3 shows the operating principle of the PLSA. The operating principle is as follows: First, the base side chuck is driven to hold the tube as shown in Figure 3 (1). In this condition, as shown in Figure 3 (2), the right-side chambers of cylinders are pressurized. A moving stage with the pneumatic chuck moves toward right. When the moving stage reaches at the right side stroke end, the chuck on the stage is activated to hold the tube as shown in Figure 3 (3). After that, as shown in Figure 3 (4), the chuck on the moving stage is driven and the chuck on the base stage is released. Under the condition that the chuck on the moving stage holds the flexible tube, the air in the right side cylinder chamber is exhausted. At the same time, as shown in Figure 3 (5), the left side chambers of the cylinders are pressurized. While the chuck on the moving stage keeps holding the tube, the flexible tube is pushed toward left as shown in Figure 3 (6). By repeating this procedure, the tube can move toward left every certain stroke. As a result of measurement of generated force, the maximum generated force of 260 N could be obtained.

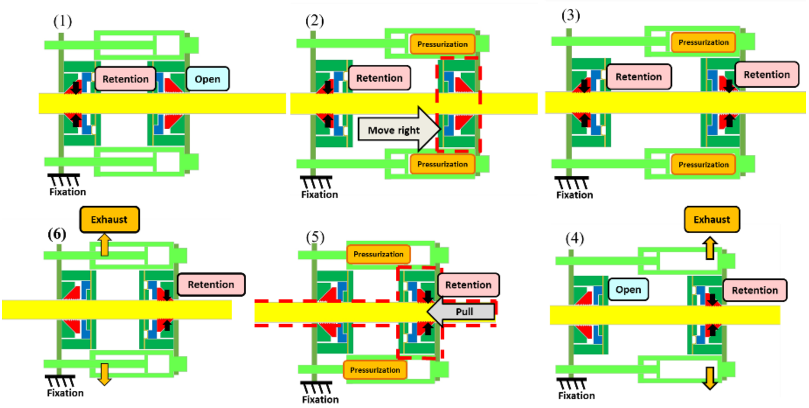

Figure 3. Operating principle of the flexible linear stepping actuator.

REHABILITAION DEVICE FOR HIP JOINT USING PLSA

As an application of PLSA, we select a rehabilitation device for hip joint. The reason why our target is to develop a rehabilitation device for hip joint is as follows. Now the rehabilitation device for hip joint on the market is a device that a patient drives it by him/herself. Therefore, it seems that the device that can give passive exercise for hip joint is useful as a voluntary rehabilitation. In the typical rehabilitation of a hip joint, a Physical Therapist ("PT" for short) moves a patient's knee so that its moving orbit can draw ellipse. By this method, the PT gives a passive exercise to the patient's hip joint. By taking account of moving orbit of the knee, a prototype rehabilitation device for hip joint using PLSA is proposed and tested. Figure 4 shows the construction of the prototype rehabilitation device of hip joint using three PLSAs. The device consists of three PLSAs with flexible rods, a knee supporter and an experimental base frame. Three PLSAs are set on the base frame so that each PLSA is located every 120 degrees from the center, that is the initial position of knee supporter as shown in Figure 4. Each flexible rod is connected to each corner of a triangle-shaped moving stage. The knee supporter is connected with the moving stage by a screw. The operating principle of the tested device is as follows. By changing rod length from each PLSA at the same time, the position of the knee supporter can be changed. In addition, as the rod is flexible, the position of the knee supporter can be controlled while each rod is bending. However, to control the knee position, the bending rod becomes uncertain element. In addition, in the case when the rod bends sharply at the end of mechanical chuck, it was found that the frictional force becomes rapidly large.

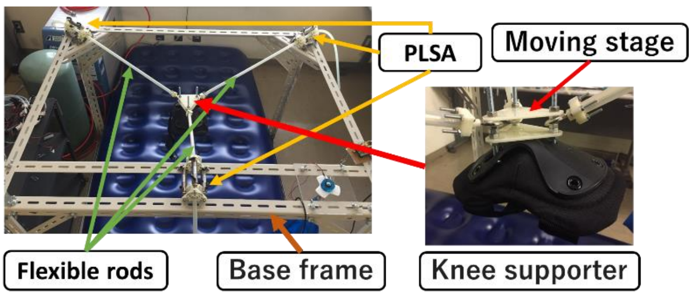

Figure 4. Construction of the prototype rehabilitation device for hip joint using 3 PLSAs.

Therefore, to decrease uncertainness based on bending rods and affection of friction, a universal-joint-type stage for PLSA is proposed and tested. Figure 5 shows the construction of the universal stage with PLSA. The universal stage consists of a rotational type universal joint with radial bearings and a wire-type linear potentiometer[15]. The universal stage can rotate around pitch and yaw axes. Several small balls between lower base and stage work as a thrust bearing. The wire-type linear potentiometer is used to measure the rod length between the PLSA and the moving stage with knee supporter.

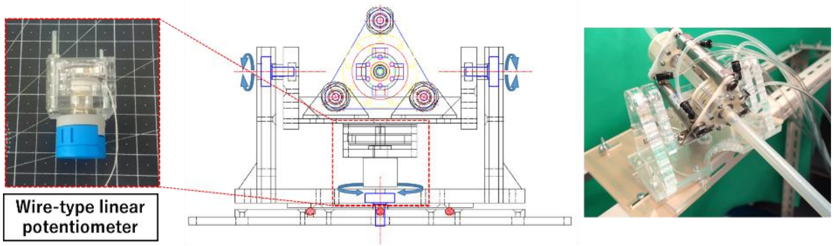

Figure 5. View and schematic diagram of the universal stage with PLSA.

Figure 6 (a) and (b) show the appearance of improved rehabilitation device for hip joint using PLSAs with universal stages and the schematic diagram of control system using three PLSAs and an embedded controller, respectively. In the improved rehabilitation device, the rigid aluminum pipe is installed into the flexible rod in each PLSA, because the universal stage adjusts the suitable direction of PLSA naturally. The aluminum pipe with the outer diameter of 8 mm works as an inner core instead of the moving core. The mechanical chuck grasps the rod surely. The control system of rehabilitation device as shown in Figure 6 (b) consists of 12 on/off valves (Koganei Co. Ltd., G010E-1), the embedded controller (Renesas electronics Co. Ltd., SH7125) and the wire-type linear potentiometer. Each PLSA is driven by four on/off valves. Two valves are used to drive three pneumatic cylinders for pushing and pulling. Each mechanical chuck is driven by an independent on/off valve. Each on/off valve is driven through transistor and I/O ports of the embedded controller. The end of the wire connected to the stage with the knee supporter in order to measure the rod length through A/D converter for monitoring.

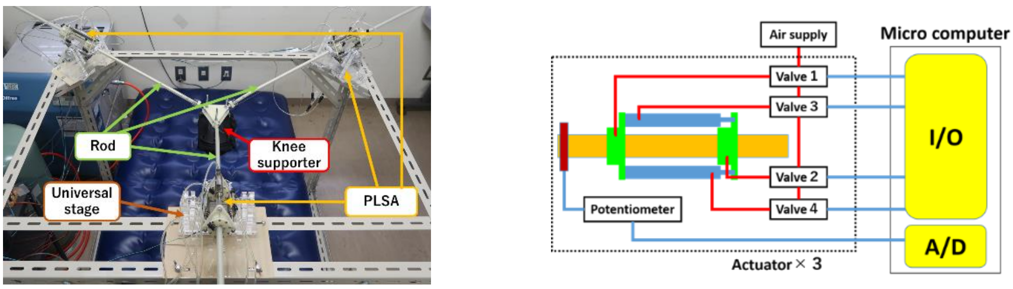

(a) the improved rehabilitation device for hip joint. **(b)** Schematic diagram of control system.

Figure 6. Appearance of the improved rehabilitation device for hip joint using PLSAs with universal stages and the schematic diagram of control system.

ANALYTICAL MODEL AND CONTROL BASED ON STEPPING MOTIONS

In order to control the position of knee supporter by controlling the length of three rods of PLSAs, it needs an analytical model that can calculate rod lengths of three PLSA 1, 2 and 3 from the desired position of the knee supporter. Figure 7 shows the simple analytical model of the rehabilitation device for hip joint. In the model, the position of the knee supporter can be obtained as an intersection of three circles from each center of PLSA. The initial position of knee supporter is defined as an origin of moving area. Three PLSAs, that is Actuator 1, 2 and 3, were located on the coordinate (0, -*b*, 0), (*a*, *b*, 0) and (-*a*, *b*, 0), respectively.

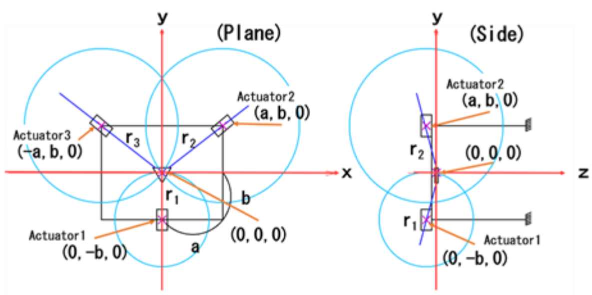

Figure 7. Simple analytical model of the rehabilitation device for hip joint.

From geometric relations in the model, the length of each rod, that is each radius r_1, r_2 and r_3, can be calculated by the following equation.

$$r_1 = \sqrt{x^2 + (y+b)^2 + z^2} \quad (1)$$

$$r_2 = \sqrt{(x-a)^2 + (y-b)^2 + z^2} \quad (2)$$

$$r_3 = \sqrt{(x+a)^2 + (y-b)^2 + z^2} \quad (3)$$

where (x, y, z) means the desired coordinate. a and b show the distance from the origin to the center of PLSA toward x and y direction, respectively. In the experiment, a of 48 mm and b of 38 mm were used. The position control of the knee supporter is carried out as follows. First, the embedded controller calculates the desired length of each rod (radius) from the desired position of the knee that had installed into memory on the embedded controller based on the model mentioned above. The controller also calculates the error e_i between the desired length r_i and the resent length of each rod $L_{i(k)}$. Based on the following equation, each PLSA is driven based on error.

$$e_i = r_i - L_i \qquad (i = 1,2,3) \quad (4)$$

$$e_i \geq \frac{S_t}{2}: \qquad n_i = 1 \qquad \text{(Push)} \quad (5)$$

$$e_i \leq -\frac{S_t}{2}: \qquad n_i = -1 \qquad \text{(Pull)} \quad (6)$$

$$-\frac{S_t}{2} \leq e_i \leq \frac{S_t}{2}: \quad n_i = 0 \qquad \text{(hold)} \quad (7)$$

where S_t and n_i mean the stroke of the cylinder (that is the displacement of 50 mm for one step motion), a motion index for push(= 1), pull(= -1) or hold(= 0), respectively. In the control, each PLSA is selected “push”, “pulls” or “hold” based on error is within a half of one step motion of 50 mm. Then, the current length of each rod L_i can be obtained by the integral of step motion based on the motion index n_i, and given by the following equation.

$$L_i = L_{i0} + S_t \Sigma n_i \quad (8)$$

where L_{i0} shows the initial length of each PLSA. By utilizing the characteristics of the stepping actuator, the controller can calculate the current length of each PLSA from the previous motion of each PLSA without senor. In order to drive three PLSA at the same time based on each motion index, 27 set of driving patterns for 12 on/off valves were prepared in the embedded controller for the position control of the device. Figure 8 shows a sample of time chart in the case when Actuator 1 is pushing (n_1 = 1), Actuator 2 is pulling (n_2 = -1) and Actuator 3 is holding (n_3=0). The Valves 1 to 4 in Figure 8 were shown in Figure 6 (b). The Valves 5 to 8 were used for Actuator 2 and Valves 9 to 12 were for Actuator 3. All driving patterns is carried out every 2.6 s. Figure 9 shows the transient view of movement of the knee supporter while the position of the knee supporter is tracing to an elliptical target trajectory with the major axis length of 400 mm and the miner axis length of 320 mm. From Figure 9, it can be seen that the position of the knee supporter can trace the elliptical target trajectory relatively well.

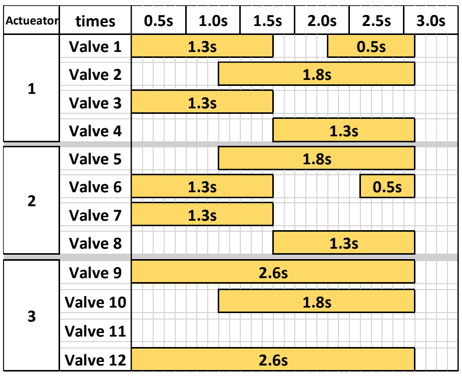

Figure 8. Time chart of pattern(n_1=1, n_2=-1, n_3=0).

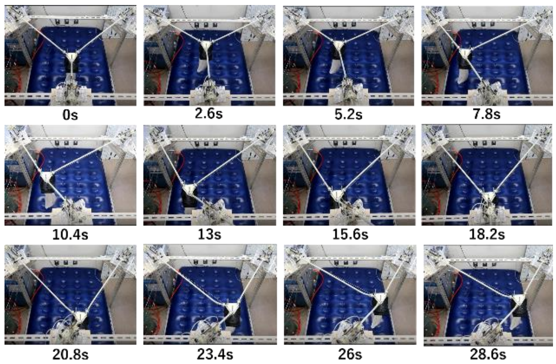

Figure 9. Transient view of movement of knee supporter in control.

CONTROL SCHEME FOR VARIABLE LINEAR STEPPING ACTUATOR

However, the PLSA pushes and pulls every a certain stoke of 50 mm. In other words, the position of the knee supporter has always error within 50 mm. In addition, in the case when a slipping of the rod occurs at the mechanical chuck by some disturbance, the error becomes larger. Therefore, it needs feedback control by using displacement senor. Based on this issue, the improved PLSA with universal stage equipped wire-type linear potentiometer. However, even if the feedback controller is equipped in the system, it still has a problem that the PLSA moves every 50 mm because it is a stepping actuator. Therefore, the method to adjust the step stroke arbitrarily using PLSA is proposed. Namely, we tried the method that both mechanical chucks are used as a brake. The proposed method is as follows. During the pushing and pulling operation of PLSA, either mechanical chuck holds the rod certainly. In the other word, the opposite mechanical chuck is available to use as a brake. In detail, in the pushing operation, the opposite mechanical chuck is driven when the error becomes positive to negative. To realize the operation, the embedded controller detects the rod length through A/D converter and the linear potentiometer every 0.5 s. In the opposite case when pulling, the chuck is driven when the error becomes negative to positive.

Figure 10 (a), (b) and (c) show the transient responses of the rod length of Actuator 1, 2 and 3 when the rehabilitation device moves the knee supporter according to the elliptical target trajectory, respectively. In Figure 10, green triangles and red circles show the results using the previous and proposed control scheme. The blue lines show the desired length. It can be seen that the controlled length using the proposed method can trace the desired length well. The standard deviation of tracking control error using the previous and proposed methods are 19.1 mm and 4.7 mm, respectively.

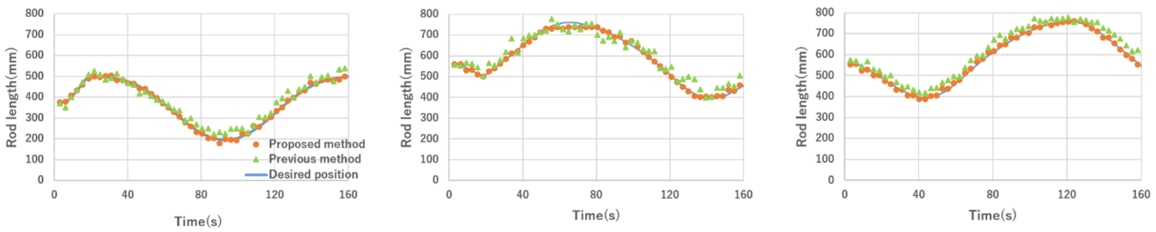

(a) Actuator 1 (b)Actuator 2 (c) Actuator 3

Figure 10. Transient response of each rod length in 3 PLSA when the rehabilitation device moves the knee supporter according to the elliptical target trajectory.

SOFT STEPPING ACTUATOR WITH BENDING MOTION

The rehabilitation device for hip joint using PLSA was successfully developed mentioned above. However, from view of home-based rehabilitation device, the device requires larger setting area and moving area, because the opposite side rod moves according to the motion of knee supporter. In ideal, a compact rehabilitation device that can be used by hanging is necessary. As a hanging type rehabilitation device, the device needs the following functions.

1) Function to adjust the hanging position of knee supporter.
2) Function to rotate the knee supporter according to target orbit.

In order to satisfy both specifications, the actuator needs to adjust the longitudinal length of rod. In addition, the actuator must bend toward radial direction to realize the rotational motion of knee supporter, that is to require soft mechanism. In this study, in order to reconstruct the ordinal PLSA to soft mechanism, we use an Extension type Flexible Pneumatic Actuator (we call it “EFPA” for short) instead of the rigid pneumatic cylinder. Figure 11 shows the view and schematic diagram of EFPA [16,17].

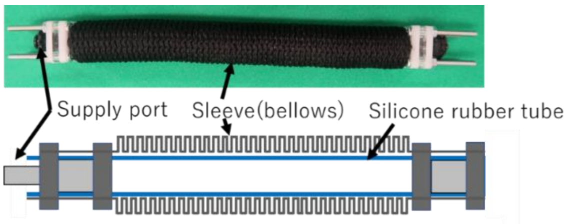

Figure 11. View and schematic diagram of EFPA[16,17].

6

The EFPA consists of a silicone rubber tube with inner diameter of 8 mm, outer diameter of 11 mm and covered with a bellows type nylon sleeve (The Fit Life Co. Ltd., Hose Reel). The EFPA can extend about 2.5 times of its original length. The maximum pulling force of the EFPA is about 60 N[16,17]. The EFPA is very lightweight, the mass is 50 g for the original length of 200 mm. The material cost of EFPA is low, it is about 5 US dollars per 1 m.

In order to construct the sliding mechanism such as a parallel arranged pneumatic cylinders, a cross arranged reinforced EFPA is proposed and tested. Figure 12 shows the construction of the improved PLSA with the cross arranged reinforced EFPA. The improved PLSA consists of the sliding mechanism using the reinforced EFPA, two mechanical chucks and the flexible rod. The cross reinforced EFPA consist of six EFPAs, seven restrain PET sheets and two base connectors. In the cross reinforced EFPA, each three EFPAs are used to construct a tetrahedral-shaped actuator. And two tetrahedral-shaped actuators are set so as to unite both actuators face to face with rotational difference of 60 degrees from the center. Both side of six EFPAs are connected to two base connectors. By this cross reinforced arrangement, the reinforced EFPA can push and pull according to the center axis, the PLSA using the soft actuators can be realized.

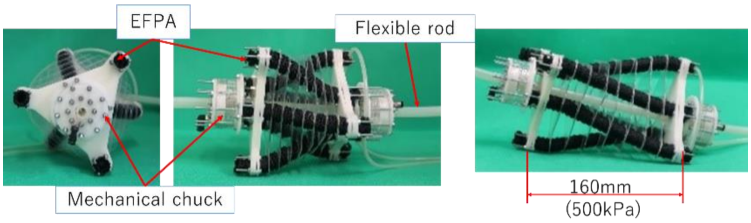

(a) Initial state (b) Pressurized(500kPa)

Figure 12. View of the improved PLAS with cross reinforced EFPAs.

In order to realize a bending operation for rotating the knee supporter according to the target orbit, a soft actuator that can change the bending direction of the flexible rod while pushing and pulling the rod is proposed and tested. Figure 13 (a) shows the construction of a soft stepping actuator with bending motion. The soft stepping actuator consists of a bending unit and the improved PLSA with cross reinforced EFPAs. The bending unit and the improved PLSA are connected in serial. The bending unit consists of six EFPAs with a natural length of 110 mm, ten restrain PET sheets and two donut-shaped end connectors. In the bending unit, six EFPAs are set parallel on the position with radius of 40 mm every 60 degrees from the center, the flexible rod passes through the center hole in restrain PET sheets. The tested soft stepping actuator with bending motion has the outer diameter of 80 mm and the natural length of 380 mm without the flexible rod. The mass of the soft stepping actuator is about 1.8 kg. Figure 13 (b) shows the schematic diagram of control system of the tested actuator. The control system consists of the tested stepping actuator, ten on/off valves and an embedded controller. In the soft stepping actuator, the improved PLSA is driven by four on/off valves, that are Valve 7 to 10, and the bending unit is driven by six on/off valves, that are Valve 1 to 6. The Improved PLSA pushes and pulls the flexible rod toward the bending unit. The bending unit works to change the direction of the pushing or pulling rod. The bending unit can bend toward 12 radial directions by driving three or four adjacent on/off valves.

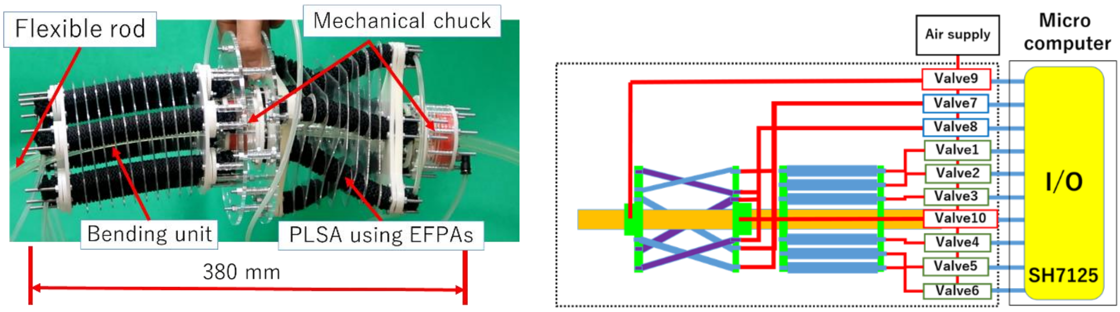

(a) Construction of soft stepping actuator (b) Schematic diagram of control system

Figure 13. Construction of soft stepping actuator with bending motion and schematic diagram of control system.

In order to realize similar operation using the rehabilitation device for hip joint using PLASs, the preliminary experiment using the tested soft stepping actuator with bending motion was carried out. In the experiment, the tested actuator was set vertically on base frame so that the bending unit set toward lower. The end flexible rod connected with the moving stage with the knee supporter. Figure 14 shows the transient view of movement of the tested actuator with knee supporter while the actuator moves the knee supporter according circular motion. In detail, after adjusting the length of rod by using the improved PLSA, the bending unit bends so that the bending directional angle of the unit can change from 0 to 360 degrees every 30 degrees per 2 s. From Figure 14, it can be seen that the tested actuator can realize the rotational motion of knee supporter so as to trace a desired orbit, even if the more compact size of the device is used compared with the case using the previous one as shown in Figure 9. In addition, as the tested soft stepping actuator can adjust the pushing, pulling force and bending force by changing supply pressure to EFPAs, it seems that the tested actuator can apply to other rehabilitation device that is necessary to adjust the applied force to a patient as a future work.

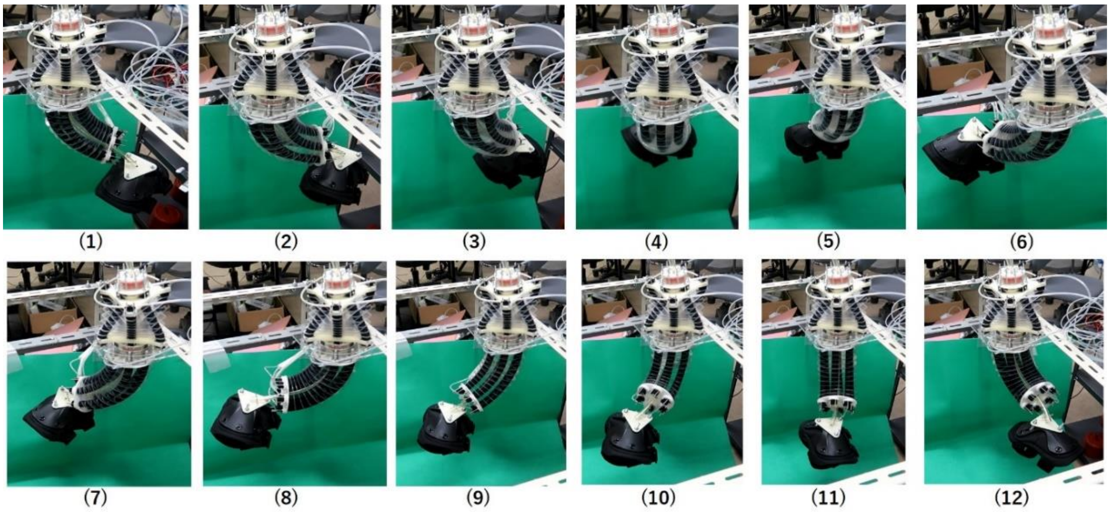

Figure 14. Transient view of movement of tested soft stepping actuator while it moves the knee supporter according circular motion.

CONCLUSIONS

In this study, a prototype rehabilitation device for hip joint that consists of three PLSAs with flexible rods and a knee supporter was proposed and tested. The universal stage for PLSA that consists of a rotational type universal joint with radial bearings and a wire-type linear potentiometer was also proposed. For attitude control, the analytical model that can calculate rod lengths of three PLSAs from the desired position of the knee supporter was proposed. In addition, the method that both mechanical chucks are used as a brake in order to realize variable PLSA was proposed. The position control system of the knee supporter using variable PLSA and the embedded controller based on the proposed method was carried out. It could be concluded that the controlled length using the proposed method could trace the desired length well. The standard deviation of tracking control error was improved from 19.1 mm to 4.7 mm compared with the method using ordinal constant step motion.
To realize a compact rehabilitation device that can be used by hanging, a soft stepping actuator with bending motion that consists of a bending unit and the improved PLSA with cross reinforced EFPAs was proposed and tested. The control system that consists of the tested PLSA, ten on/off valves and an embedded controller was also proposed and tested. As a result, it could be confirmed that the tested PLSA can realize the rotational motion of the knee supporter so as to trace a desired orbit, even if the more compact size of the device is used than the previous one.
As a future work, it is necessary to investigate the suitable force to give a passive exercise for patient with various degrees of physical disability. After that, it is needed to apply a force control to the tested rehabilitation device.

ACKNOWLEDGMENTS

This work was supported by JSPS KAKENHI Grant Numbers 16K06202 and 19K04265.

REFERENCES

1. Annual Report on the Ageing Society [Summary] FY 2019 from, https://www8.cao.go.jp/kourei/english/annualreport/2019/pdf/2019.pdf, June 2019.
2. NAGATA, Y., Soft Actuators, Forefront of Development. NTS Ltd., 2004, pp.291–335.
3. NORITSUGU, T., Pneumatic Soft Actuator for Human Assist Technology. In: Proceedings of the 6th JFPS International Symposium on Fluid Power, Tsukuba, Japan, 2005, pp.11–20.
4. SASAKI, D., NORITSUGU, T., YAMAMOTO, H., TAKAIWA, M., Development of Power Assist Glove using Pneumatic Artificial Rubber Muscle. Journal of the Robotics Society of Japan, 2006, 24(5), 640-646.
5. NORITSUGU, T., TAKAIWA, M., SASAKI, D., Development of Power Assist Wear Using Pneumatic Rubber Artificial Muscles. Journal of Robotics and Mechatronics, 2008, 21(5), 27–31.
6. KOBAYASHI, H., SHIBAN, T., ISHIDA, Y., Realization of all 7 motions for the upper limb by a muscle suit. Journal of Robotics and Mechatronics, 2004, 16(5), 504–512.
7. TANIGUCHI, H., WAKIMOTO, S., SUZUMORI, K., Development of a hand rehabilitation system to prevent contracture for finger joints based on the therapy of occupational therapists (Massage a hand and range of motion exercises using pneumatic soft actuators). Journal of the Japan Society of Mechanical Engineers, 2014, 80(820), TRANS0348.
8. KAWASAKI, H., ITO, S., ISHIGURA, Y., NISHIMOTO, Y., AOKI, T., ABE, T., SAKAEDA, H., OJIKA, T., MOURI, T., UEKI, S., Hand Rehabilitation Assist Robot Designed with Assistance for Thumb Opposability. Journal of the Japan Society of Mechanical Engineers, 2008, 74(748), 3019-3027.
9. TAKAIWA, M., NORITSUGU, T., SASAKI, D., Wrist Rehabilitation Using Pneumatic Parallel Manipulator ~ Proposal of Rehabilitation Based on EMG signal ~. Transactions of the Japan Fluid Power System Society, 2012, 43(3), 85-91.
10. EGUCHI, Y., AKAGI, T., DOHTA, S., “Preliminary Design of Flexible Linear Stepping Actuator Driven by Pneumatic Balloons and Brakes”, MATEC Web of Conferences, Vol.51, No.02004, 2016, pp.1-4.
11. EGUCHI, Y., AKAGI, T., DOHTA, S., KOBAYASHI, W., “Improvement of Flexible Linear Stepping Actuator Driven by Pneumatic Balloons and Brakes”, MATEC Web of Conferences, Vol.82, No.01005, 2016, pp.1-6.
12. FUKUKAWA, N., AKAGI, T., DOHTA, S., KOBAYASHI, W., EGUCHI, Y., “Development of Flexible Robot Arm with Backdrivability Using Flexible Linear Stepping Actuators”, International Journal of Mechanical Engineering and Robotics Research, Vol.6, No.5, 2017, pp.373-377.
13. FUKUKAWA, N., AKAGI, T., DOHTA, S., KOBAYASHI, W., EGUCHI, Y., “Improvement of Pneumatic Chuck in Flexible Linear Stepping Actuator with Backdrivability”, International Journal of Mechanical Engineering and Robotics Research, Vol.8, No.3, 2019, pp.437-442.
14. INOUE, R., AKAGI, T., DOHTA, S., KOBAYASHI, W., EGCHI, Y., FUKUKAWA, N., SHINOHARA, T., “Development of Simple Rehabilitation Device Using Flexible Linear Stepping Actuators”, International Journal of Mechanical Engineering and Robotics Research, Vol.8, No.2, 2019, pp.316-322.
15. MATSUI, Y., AKAGI, T., DOHTA, S., KOBAYASHI, W., TAMAKI, H., Development of Flexible Spherical Actuator with 3D Coordinate Measuring Device. Journal of Flow Control Measurement & Visualization, 2018, 6-2, pp.95–106.
16. SUZUKI, Y., AKAGI, T., DOHTA, S., KOBAYASHI, W., TAMAKI, H., MATSUI, Y., SHIMOOKA, S., Development of Tetrahedral Type Rehabilitation Device Using Flexible Pneumatic Actuators. International Journal of Mechanical Engineering and Robotics Research, 2018, 7-4, pp.409-414.
17. SHIMOOKA, S., AKAGI, T., DOHTA, S., KOBAYASHI, W., SHINOHARA, T., Improvement of Home Portable Rehabilitation Device for Upper-Limbs. JFPS International Journal of Fluid Power System, 2019, 12-1, pp.10-18.

The 11th JFPS International Symposium on Fluid Power HAKODATE 2020 Oct. 12-13, 2021 The Japan Fluid Power System Society

Development of Extension Type Flexible Pneumatic Actuator with Displacement Sensor Using Ring-shaped Magnet and Hall Sensor for Tetrahedral-type Soft Mechanism

Kenshiro TAKEUCHI*, Takumi KOBAYASHI*, Tetsuya AKAGI*, Shujiro DOHTA*, Takashi SHINOHARA**, Wataru KOBAYASHI* and So SHIMOOKA***

*Department of Intelligent Mechanical Engineering, Faculty of Engineering, Okayama University of Science
**Science Dream lab., Okayama University of Science
1-1, Ridai-cho, Kita-ku,Okayama, 700-0005 Japan
(E-mail: akagi@are.ous.ac. jp)
***Graduate School of Natural Science and Technology, Okayama University
3-1-1 Tsushima-naka, Kita-ku, Okayama 700-8530, Japan

Abstract. A soft mechanism that has large moving area and compliance are attractive. This study aims to develop a pneumatic drive soft actuator with 3-dimensional large moving area. Based on the concept that a tetrahedron is a minimum element of solid body, the tetrahedral-type soft actuator that consists of six reinforced Extension type Flexible Pneumatic Actuators (EFPA) and four connectors for vertices was proposed and tested. Each EFPA is set at the position of side of tetrahedral frame. Both ends of each EFPA are connected to connectors in vertices. In addition, to measure the displacement of the EFPA, a non-contact type displacement sensor using a ring-shaped magnet and a hall sensor was proposed. The measurement of the attitude of the tested actuator was carried out. As a result, it could be confirmed that the tested EFPA with displacement sensor could measure whole length of the EFPA by measuring a part of displacement of the actuator.

Keywords: Extension type flexible pneumatic actuator, Tetrahedral-type soft mechanism, Non-contact type displacement sensor using ring-shaped magnet and hall sensor, Measuring system using embedded controller.

INTRODUCTION

In Japan, the ratio of the elderly became more than 26 % in 2020[1]. The ratio will be expected about 36% in 2040. Based on this issue, various human friendly pneumatic devices to assist welfare work for the elderly and disabled using pneumatic soft actuators[2] have been actively developed[3-10] As a human friendly pneumatic drive system, K. Yamamoto developed a wearable power assist suit for nursing care using bellows type actuators[3]. As a system using McKibben type pneumatic artificial muscle (PAM for short), T. Noritsugu and H. Kobayashi also developed power assisted wears [4-7] to increase the force for welfare workers and heavy labors. A rehabilitation device that can enhance to recover their physical ability early after injury and surgery is also required. Now, Occupational Therapist (“OT” for short) and Physical Therapist (“PT” for short) can perform the rehabilitation to the patient for just 30 minutes per day according to Japanese law. Some of them recommend patients to execute voluntary rehabilitation and exercise at home. According to a medical report, voluntary rehabilitation might prevent bedridden state, various disease and disuse syndrome [8]. Therefore, a home-based rehabilitation device that can safely give passive exercise to patients is strongly required. As research on such a rehabilitation device, a rehabilitation device for inhibiting contracture of finger joints were developed by H. Taniguchi and H. Kawasaki [9-10]. M. Takaiwa also developed a rehabilitation device for contracture patients using pneumatic parallel manipulator [11]. In the previous study, the portable rehabilitation device using flexible spherical actuator that can provide passive exercise for the wrist by changing the position of holding hands was proposed and tested [12-14]. In these devices, a pneumatic actuator was often used because it has advantage of compliance based on air compressibility. A pneumatic soft actuator has more advantages that are lighter weight and more compliance based on flexibility. However, a device using soft actuators is usually difficult to realize larger moving area because of their lower stiffness. Especially, 3-dimensional motion with flexibility is more difficult to realize.

In this study, as a final target of the study, we aim to realize a home-based rehabilitation device that can give passive exercise and be safely used at home with non-specialist. We assume that the home-based rehabilitation device is used as a voluntary rehabilitation by patient, and not be used as a medical treatment by PT and OT. We aim to keep the moving range of the recovered joint after medical treatment by giving passive movement. In order to use it at home for a personal user, the device must be constructed compactly and at low-cost. In the previous study, to realize a compact home-based rehabilitation device, a compact soft mechanism that can give 3-dimensional large moving area was proposed and tested. In addition, to control the attitude of the device, a soft actuator in the soft mechanism needs a function to measure its displacement. In this paper, we propose an extension type flexible pneumatic actuator with non-contact type displacement sensor using a ring-shaped magnet and a hall sensor. An attachment type displacement sensor that can be applied to the already assembled soft mechanism using EFPAs is also proposed. The measuring test using the tested mechanism with sensor is carried out by using an unexpansive measuring system using an embedded controller.

EXTENSION-TYPE FLEXIBLE PNEUMATIC ACTUTOR

To realize a soft mechanism with a large moving area, a compact soft actuator with a long stroke motion is required. As a pneumatic soft actuator, a McKibben type artificial muscle is well known. However, the moving area of the McKibben type muscle is very small, the stroke is less than 25 % of its original length. Based on this issue, T. Noritsugu developed an extension type pneumatic artificial muscle by using bellows type nylon mesh and rubber tube [6]. The extensional performance of the muscle depends on bellows. Recently, a superior bellows type sleeve is easily obtained as an ordinal water supply hose. In the previous study, an Extension-type Flexible Pneumatic Actuator (we call it "EFPA" for short) using this type of hose was proposed and tested [14-16]. Figure 1 shows the view and schematic diagram of EFPA. The EFPA consists of a silicone rubber tube with inner diameter of 8 mm, outer diameter of 11 mm and covered with a bellows type nylon sleeve (The Fit Life Co. Ltd., Hose Reel). The original length of EFPA is 200 mm, and the mass is 50 g. The actuator can be constructed at low cost, the material cost of the EFPA is about 5 US dollars per 1 m. The EFPA can extend about 2.5 times of its original length. The maximum pulling force of the EFPA is about 60 N [16-17]. The pushing force of the original EFPA is not available because the bending stiffness is too low.

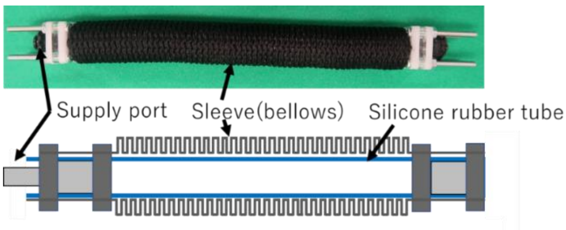

Figure 1. View and schematic diagram of EFPA [14-16].

Therefore, to increase the stiffness of EFPA, a reinforced EFPA was also proposed and tested in the previous study [18]. The left figure on Figure 2 shows the schematic diagram of the reinforced EFPA with circumferential restraints, we call it "reinforced EFPA" for short [18]. The reinforced EFPA that consists of parallel arranged three EFPAs as shown in the right figure on Figure 2 has restrained each other by using restraint PET plates with thickness of 1 mm at the point of sleeve. Each EFPA keeps so as to arrange every 120 deg. at radius of 12.5 mm from the center of the reinforced EFPA. By this method, the bending stiffness of the actuator increases, and the reinforced EFPA can generate the pushing force of 130 N [18].

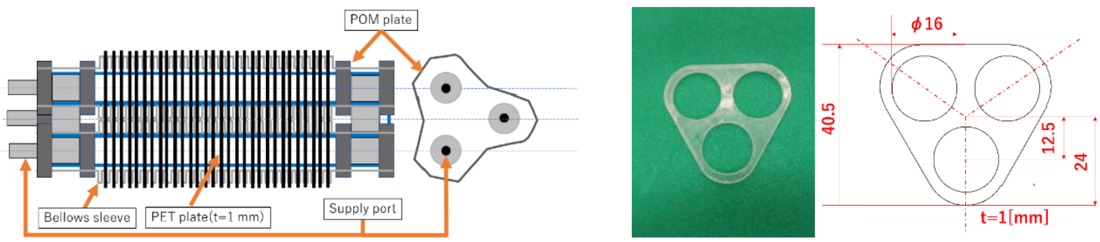

Figure 2. Schematic diagram of reinforced EFPA on the left and Shape of reinforced PET plate on the right.

TETRAHEDRAL-TYPE SOFT MECHANISM

By paying attention to the fact that a tetrahedron is a minimum element of a solid body, a tetrahedral-shaped soft actuator using EFPAs that can form an arbitrary shape by extending each side of the tetrahedron was also proposed and tested. Figure 3 shows a view of a tested tetrahedral-type soft mechanism. The tested mechanism consists of six reinforced EFPAs with a natural length of 130 mm and four connectors for vertex. The vertex is made of ABS resin. Each reinforced EFPA is set at the position of side of the tetrahedral frame. Both ends of each reinforced EFPA are connected to connectors in vertices. Three EFPAs in the reinforced EFPA are connected in series by a supply tube and operated simultaneously. Since the reinforced EFPA has flexibility, it can be naturally curved even if the rigid connector for vertex is used. By this method, the shape of the tested mechanism can change to various shape of tetrahedron.

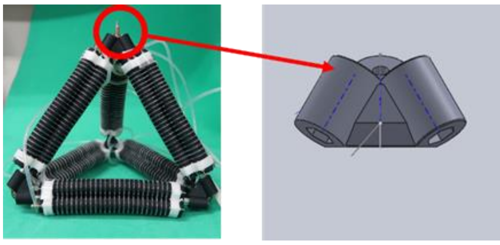

Figure 3. Tetrahedral-type soft mechanism using reinforced EFPAs.

Figure 4 shows the configuration of the sequential control system of the tested mechanism. The system consists of the tested mechanism, six sets of operating valves that consists of two on/off valves (Koganei Co. Ltd., G010E-1), and an embedded controller (Renesas Electronics Co. Ltd., SH7125). In each operating valve, the output port of the switching three port on/off valve is connected to supply port of two-port on/off valve for holding. Each on/off valve is driven through I/O ports in the embedded controller and transistors and can perform three operations, that is to "supply", "exhaust" and "hold".

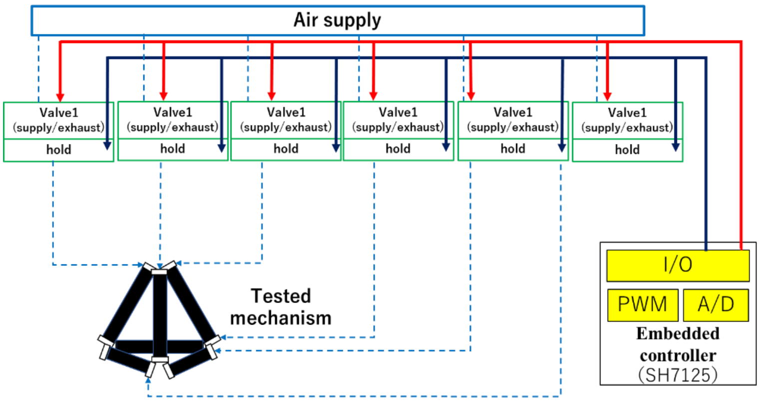

Figure 4. Control system of the tetrahedral-type soft mechanism.

Figure 5 shows the view of movement of the tested mechanism when the sequential operation was applied. As shown in Figure 5 (2), when the three reinforced EFPAs connected with top vertex connector was pressurized, the mechanism extends until 350 mm in height. In opposite case when the three reinforced EFPAs on the bottom were pressurized as shown in Figure 5 (3), the mechanism contracts toward vertical direction. In this case, the minimum height of the mechanism of 195 mm can be realized. In addition, as shown in Figure 5 (5), the mechanism can bend toward six radial directions by pressurizing one or two reinforced EFPAs connected with the top vertex connector. As an application using the mechanism, we think that it can be used as a portable rehabilitation device. By a patient holding the two vertexes connector while the mechanism deforms to various shapes, the actuator can give passive exercise to patient's wrist and upper limbs. Furthermore, by combining more tetrahedral-type soft mechanisms to construct polyhedron, a polyhedral mechanism can give complex passive exercise to a patient.

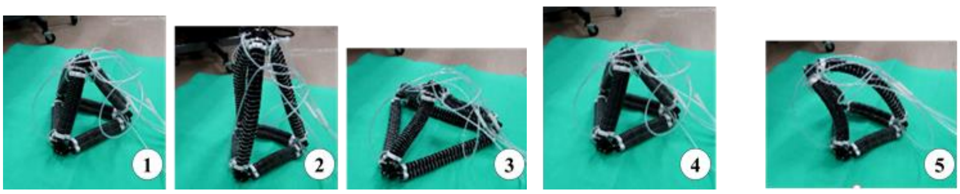

Figure 5. View of movement of the tested actuator when sequential operation was applied.

MEASUREMENT OF MECHANISM

To measure the shape of the mechanism, several trials for measurement were carried out. In one of them, by paying attention that the shape of tetrahedron can be roughly imaged by the position of top vertex, a measuring device to recognize the position of top vertex is proposed and tested. The left figure on Figure 6 shows the construction of the tested measuring device. The device consists of a rotational type two axis universal joint with two potentiometers and wire-type potentiometer [14]. The end of wire of three potentiometers are connected to the behind of the top vertex connector. The operating principle is as follows. In ideal case of no friction, under the condition when the top vertex connector is always pulled by the linear potentiometer, the universal stage is always directed toward the top vertex. In the universal stage, the bottom side potentiometer can measure the directional angle, that is bending directional angle of the mechanism. The side potentiometer can measure an elevation angle, that is bending angle of the mechanism according to the position change of the top vertex. In addition, the length from the measurement origin can be detected by the wire-type linear potentiometer. By obtaining two kinds of bending angle and a distance, the three-dimensional coordinate can be recognized. The right schematic diagram on Figure 6 shows the measuring system that was reconstructed on the previous sequential control system as shown in Figure 4.

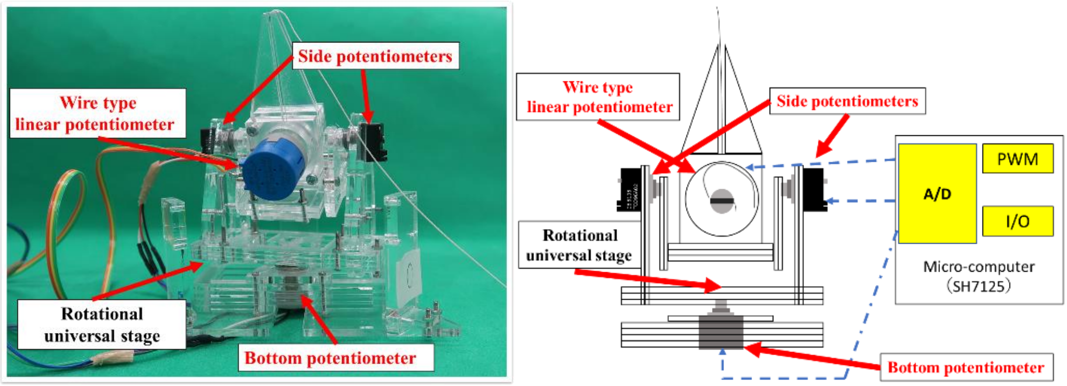

Figure 6. View and system of measurement device using rotational universal stage and wire type linear potentiometer.

Figure 7 (a) and (b) show the transient response of bending angles and the length from the measurement origin, respectively. In Figure 7 (a), red and blue lines show results of the bending directional angle and the bending angle, respectively. It can be seen that the tested measuring device can detect enough information to calculate the coordinate based on polar coordinate system. However, because the real tested device has friction, the measuring error is occurred. Especially the measuring error of bending directional angle is easily occurred because the inertia of universal stage is large. In addition, because the liner potentiometer always is pulling the top vertex connector, the deformation of the mechanism is always affected by the measuring device.

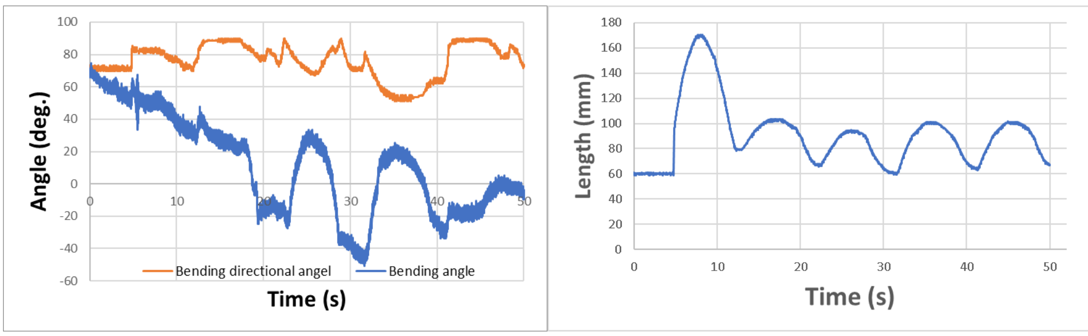

(a) Bending directional angle and bending angle. **(b)** Length from measuring origin.

Figure 7. Transient response of bending directional angle, bending angle and length from measuring origin.

NON-CONTACT TYPE DISPLACEMENT SENSOR

Therefore, a non-contact type displacement or position sensor is required. As a measuring method, the visual camera is one of available methods. However, the camera detecting system depends on light condition and camera position. In addition, such a measuring system using camera requires a superior personal computer for calculation and it is very expensive. It is also very difficult to realize a mounted measuring system using camera. In this study, we tried to develop of a non-contact type displacement sensor of each EFPA. As a specification of the sensor, because EFPA is so flexible, the required sensor needs an ability to measure the displacement of EFPA even if EFPA bends and twists. Therefore, a novel non-contact type displacement sensor that can measure a longitudinal displacement under the condition when the radial directional deviation is occurred is proposed. The left figure on Figure 8 shows the fundamental construction of the proposed sensor. The sensor consists of a hall sensor (Allegro Co. Ltd., A1324LUA-T) and a ring-shaped neodymium magnet with the outer diameter of 15 mm, the inner diameter of 9 mm and the height of 1 mm. The hall sensor is set on the longitudinal axis of the ring-shaped magnet. By using the ring-shaped magnet, the stable cylindrical magnetic field not related to radial directional position change can be used. The right graph on Figure 8 shows the relation between the longitudinal position (displacement) and the output from the hall sensor. The displacement of 0 mm shows the position where the S pole side surface of the ring-shaped magnet meets the surface of the hall sensor. In this figure, each symbol shows the radial directional deviation from the center axis. From Figure 8, it can be seen that the small radial deviation of less than 2 mm is not affected to measure longitudinal displacement. It means that the tested sensor can measure the longitudinal displacement even if EFPA bends or twists. However, it can also be seen that the measuring area of hall sensor is not so large, that is less than 7 mm. Therefore, we apply the tested sensor to measure the displacement of one bellows in EFPA.

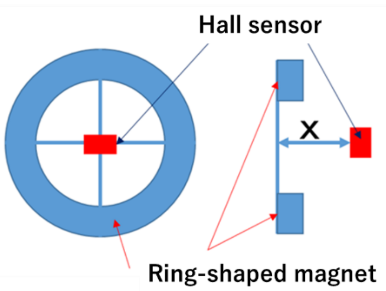

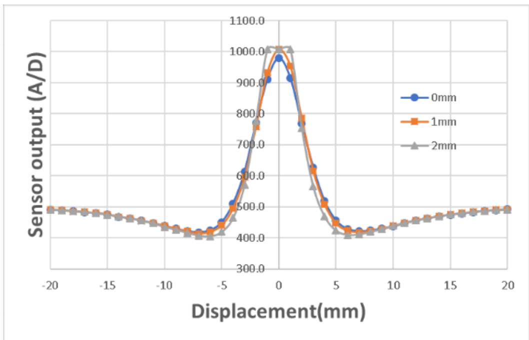

Figure 8. Fundamental construction and static characteristics of non-contact type displacement sensor using ring-shaped magnet and hall sensor.

In the same manner of the previous experiment, the relations between the longitudinal position (displacement) and the output from the hall sensor using various ring-shaped magnets were investigated. Table 1 shows the result, that is the measuring area of the hall sensor using various ring-shaped magnets. In the experiment, 16 types of ring-shaped magnets were used. In order to measure the displacement of one bellows in EFPA, it is necessary more than 7 mm as a measuring area. In addition, it is better to use small-sized magnet, because it must be attached on the EFPA. From view point of wider measuring area and small size magnet, we select the magnet with the outer diameter of 15 mm, the inner diameter of 9 mm and width of 1 mm.

Table 1. Measuring area of hall sensor for various ring-shaped magnets.

Size of magnet	Range	Size of magnet	Range
ϕ7.0×ϕ4.4×5.0	2mm	ϕ13.0×ϕ9.1×1.5	6mm
ϕ7.9×ϕ5.3×3.0	2mm	ϕ28.0×ϕ24.0×1.5	7mm
ϕ10.6×ϕ7.8×5.0	4mm	ϕ30.0×ϕ26.0×1.0	7mm
ϕ13.0×ϕ9.2×5.0	4mm	ϕ15.0×ϕ9.0×1.0	7mm
ϕ11.0×ϕ7.2×2.0	4mm	ϕ22.0×ϕ12.0×1.5	8mm
ϕ11.9×ϕ8.6×2.1	5mm	ϕ38.0×ϕ20.0×1.5	8mm
ϕ19.5×ϕ14.8×1.0	6mm	ϕ24.0×ϕ17.7×1.0	9mm
ϕ20.0×ϕ12.2×3.0	6mm	ϕ28.0×ϕ18.0×1.0	9mm

EFPA WITH NON-CONTACT TYPE DISPLACEMENT SENSOR

Figure 9 shows the construction and the schematic diagram of a reinforced EFPA with the non-contact type displacement sensor. The hall sensor is set at the position with radius of 24 mm from the center of the restraint plate in the reinforced EFPA. The ring-shaped magnet is also set on anther restraint plate at the same position. Both restraint plates for the ring-shaped magnet and the hall sensor are set on reinforced EFPA through one bellows. As assuming that the behavior of each bellows is same at any points, the sensor can estimate the whole displacement by measuring the displacement of one bellows.

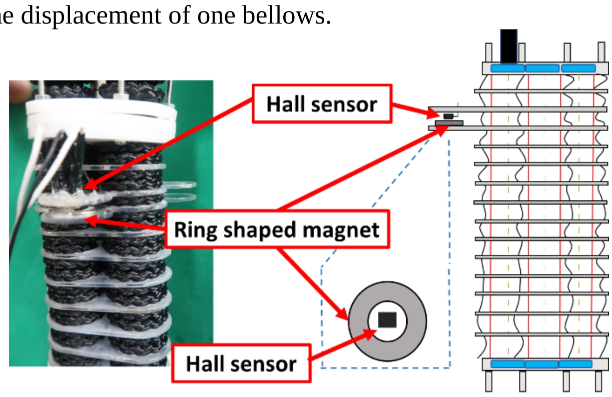

Figure 9. Construction and schematic diagram of reinforced EFPA with non-contact type displacement sensor.

In order to calculate the displacement from sensor output, the calibration test of the tested sensor was carried out. Figure 10 (a) shows the relation between the hall sensor output and the whole displacement of the reinforced EFPA. In the experiment, so as to get increasing output value according to increasing displacement, the pole of the ring-shaped magnet was inversed compared with the previous case as shown in Figure 8. The output voltage from the hall sensor was detected through A/D converter in the embedded controller (Renesas electronics Co. Ltd., SH7125). Based on this relationship, the following approximate equation can be obtained.

$$x = 8.91 \times 10^{-7} s^3 - 7.75 \times 10^{-4} s^2 + 0.326 s - 9.63 \tag{1}$$

where s and x mean the A/D value of hall sensor output voltage through 10-bit A/D convertor in the embedded controller and the whole displacement of the reinforced EFPA, respectively. This cubic equation is selected as approximate equation in order to be easily calculated by a tiny embedded controller.
Figure 10 (b) shows the transient response of the displacement of the reinforced EFPA when the supply pressure is changed from 0 to 500 to 0 kPa manually. In Figure 10, the blue solid line and red broken line show the true displacement that is measure by the connected linear potentiometer (Copal Co. Ltd, JCL100B) in serial and the measure displacement using the sensor output and the approximate model, respectively. From Figure 10, it can be seen that the measured displacement using the tested sensor is relatively good agreement with the true displacement although the small error exists while exhausting. The standard deviation of measuring error is about 4.5 mm, that is about 5 % error of full range. It seems that the error is occurred by uneven contracting of the rubber tube under the condition of large frictional force based on higher pressure. As a result, it can be confirmed that the proposed method to measure whole displacement of EFPA by measuring a part of EFPA using the tested sensor is valid.

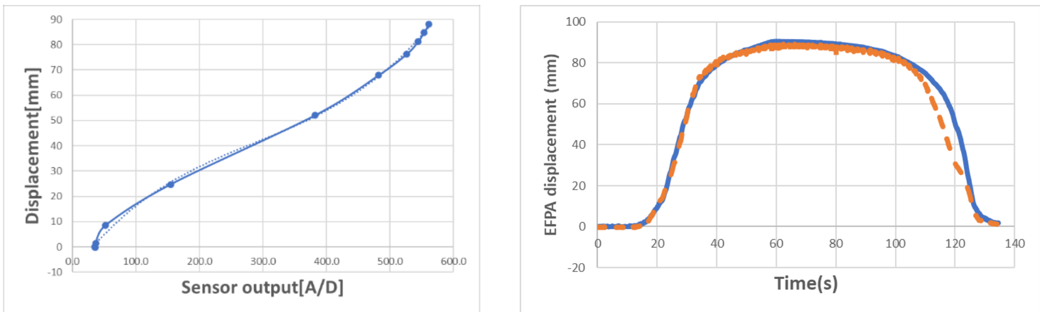

(a) Result of calibration test using the tested sensor. (b) measuring result using tested sensor.

Figure 10. Relation between sensor output and whole displacement of the reinforced EFPA and transient response of the displacement of the EFPA when the supply pressure is changed from 0 to 500 to 0 kPa.

The previous measuring method mentioned above requires the calibration from the sensor output to the whole displacement of the EFPA, each time EFPA changed. In order to improve versatility of displacement measurement, the method to estimate the whole displacement from the measured displacement of one bellows by using the tested sensor is carried out. From the fundamental relationship between sensor output and displacement as shown in Figure 11(a), the following approximate equation can be obtained.

$$x = n \times \{4.70 \times 10^{-8}s^3 - 3.84 \times 10^{-5}s^2 + 1.56 \times 10^{-2}s - 0.517\} \quad (2)$$

where *s*, *x* and *n* mean the sensor output (A/D value) and the whole displacement of EFPA and number of bellows in the EFPA, respectively.Figure 11 (b) shows the relation between the supply pressure and the calculated and true displacement of the reinforced EFPA. In Figure 10, symbols and broken line show the calculated and true whole displacement of the reinforced EFPA, respectively. The calculated displacement is based on the sensor output and the approximate equation mentioned above. The true displacement is the measured displacement by using linear potentiometer that connected to the reinforced EFPA in serial. Symbols ● and ▲ show the case when number of bellows in EFPA is estimated as 21 and 20, respectively. In the experiment, although the number of bellows is 20, the number of 21 was used as a calculated value in consideration of looseness of bellows and rubber tube length. From Figure 11 (b), it can be seen that the calculated displacement almost meets the true displacement even if the relation between the supply pressure and displacement has a large hysteresis. It can also be seen that there is relative larger measuring error while exhausting because of same reason mentioned above. Overall, it can be seen that the calculated displacement can predict the true displacement relative well.

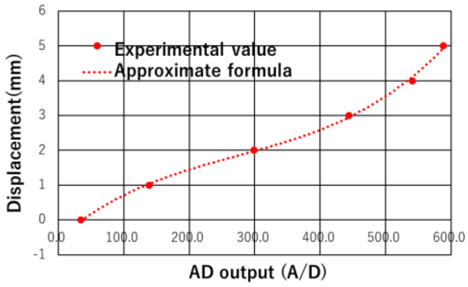

(a) Result of calibration test using the tested sensor.

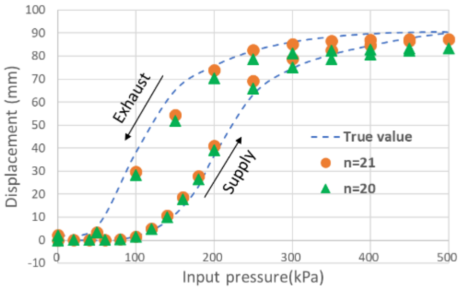

(b) Measured result using tested sensor.

Figure 11. Relation between the supply pressure and displacement of the reinforced EFPA.

CONCLUSIONS

As an attitude sensor for the tetrahedral shaped soft mechanism, the non-contact type displacement sensor using a hall sensor and a ring-shaped magnet was proposed and tested. As a result of fundamental experiment, it found that the ring-shaped magnet with outer diameter of 15 mm and the inner diameter of 9.1 mm and width of 1 mm is suitable to use as a displacement sensor of EFPA from view point of small size and larger measuring area. It also found that the tested sensor can measure the longitudinal displacement even if a radial deviation of less than 2 mm is occurred by using the stable cylindrical magnetic field. The measuring system using the tested sensor and the embedded controller was proposed and tested. The reinforced EFPA with the tested sensor for measuring the displacement of one bellows was proposed and tested. The measuring methods to measure whole displacement of EFPA by measuring a part of EFPA using the tested sensor were proposed. The measuring system using the tested sensor and the embedded controller was also developed. As a result, by using the method to use the approximate equation from sensor output to the whole displacement, it can be confirmed that the measured displacement using the tested sensor was relatively good agreement with the true displacement with the standard deviation of measuring error of about 4.5mm, that is corresponding to about 5 % error of full range. As a more versatile measuring method, the method to estimate the whole displacement from the measured displacement of one bellows was also carried out. As a result, it can also be confirmed that the calculated displacement almost meets the true displacement even if the relation between the supply pressure and displacement has a large hysteresis.

In the future work, we are going to develop an unite type displacement sensor for EFPA. The attitude control of the tetrahedral shaped soft mechanism using the improved EFPAs with sensor was carried out. In addition, it is necessary to investigate the measuring error under the condition of load.

ACKNOWLEDGMENTS

This work was supported by JSPS KAKENHI Grant Numbers 16K06202 and 19K04265.

REFERENCES

1. Annual Report on the Ageing Society [Summary] FY 2019 from, https://www8.cao.go.jp/kourei/english/annualreport/2019/pdf/2019.pdf, June 2019.
2. NAGATA Y. Soft Actuators, Forefront of Development. NTS Ltd., 2004, pp 291–335.
3. ISHII M, YAMAMOTO K and HYODO K. Stand-Alone Wearable Power Assist Suit (Development and Avail ability). Journal of the Japan Society of Mechanical Engineers, 2006, 72-715, pp175–182.
4. NORITSUGU T. Pneumatic Soft Actuator for Human Assist Technology. In: Proceedings of the 6th JFPS International Symposium on Fluid Power, Tsukuba, Japan, 2005, pp11–20,
5. SASAKI D, NORITSUGU T, YAMAMOTO H and TAKAIWA M. Development of Power Assist Glove using Pneumatic Artificial Rubber Muscle. Journal of the Robotics Society of Japan, 2006, 24-5, pp640-646.
6. NORITSUGU T, TAKAIWA M and SASAKI D. Development of Power Assist Wear Using Pneumatic Rubber Artificial Muscles. Journal of Robotics and Mechatronics, 2008, 21-5, pp27–31.
7. KOBAYASHI H, SHIBAN T and ISHIDA Y. Realization of all 7 motions for the upper limb by a muscle suit. Journal of Robotics and Mechatronics, 2004, 16-5, pp504–512.
8. Council of Bureau of Social Welfare and Public Health Tokyo Metropolitan Government from, https://www.fukushihoken.metro.tokyo.lg.jp/iryo/sonota/riha_iryo/kyougi01/rehabiri24.files/siryou242.pdf; February 2013 (in Japanese).
9. TANIGUCHI H, WAKIMOTO S, SUZUMORI K. Development of a hand rehabilitation system to prevent contracture for finger joints based on the therapy of occupational therapists (Massage a hand and range of motion exercises using pneumatic soft actuators). Journal of the Japan Society of Mechanical Engineers, 2014, 80-820, TRANS0348.
10. KAWASAKI H, Ito S, ISHIGURA Y, NISHIMOTO Y, AOKI T, ABE T, SAKAEDA H, OJIKA T, MOURI T, UEKI S. Hand Rehabilitation Assist Robot Designed with Assistance for Thumb Opposability. Journal of the Japan Society of Mechanical Engineers, 2008, 74-748, pp3019-3027.
11. TAKAIWA M, NORITSUGU T, SASAKI D. Wrist Rehabilitation Using Pneumatic Parallel Manipulator ~ Proposal of Rehabilitation Based on EMG signal ~. Transactions of the Japan Fluid Power System Society, 2012, 43-3, pp85-91.
12. MATSUI Y, AKAGI T, DOHTA S, ALIFF M, LIU C. Development of Portable Rehabilitation Device Using Flexible Spherical Actuator and Embedded Controller. Lecture Notes in Electrical Engineering, 2014, 293-1, pp231-238.
13. MATSUI Y, AKAGI T, DOHTA S. Development and Control of Flexible Spherical Actuator for Portable Rehabilitation Device. International Journal of Materials Science and Engineering, 2015, 3-1, pp49-54.
14. MATSUI Y, AKAGI T, DOHTA S, KOBAYASHI W, TAMAKI H. Development of Flexible Spherical Actuator with 3D Coordinate Measuring Device. Journal of Flow Control Measurement & Visualization, 2018, 6-2, pp95–106.
15. SHIMOOKA S, DOHTA S, AKAGI T, KOBAYASHI W and YONEDA M. Development of Portable Rehabilitation Device Using Flexible Extension Type Soft Actuator with Built-in Small-Sized Quasi Servo Valve and Displacement Sensor. JFPS International Journal of Fluid Power System, 2018, 11-2, pp18-25.
16. SUZUKI Y, AKAGI T, DOHTA S, KOBAYASHI W, TAMAKI H, MATSUI Y, and SHIMOOKA S. Development of Tetrahedral Type Rehabilitation Device Using Flexible Pneumatic Actuators. International Journal of Mechanical Engineering and Robotics Research, 2018, 7-4, pp409-414.
17. SHIMOOKA S, DOHTA S, AKAGI T, KOBAYASHI W and SHINOHARA T. Improvement of Home Portable Rehabilitation Device for Upper-Limbs. JFPS International Journal of Fluid Power System, 2019, 12-1, pp10-18.
18. SHIMOOKA S, DOHTA S, AKAGI T, SHINOHARA T. HANE Y and ALIF M. Development of Reinforced Extension Type Flexible Pneumatic Actuator with Circumferential Restraints and Its Application for Rehabilitation Device. International Journal of Automotive and Mechanical Engineering, 2020, 17-3, pp8116-8127.

The 11th JFPS International Symposium on Fluid Power HAKODATE 2020 Oct. 12-13, 2021 The Japan Fluid Power System Society

Development of Highly Durable Straight Fiber Type Pneumatic Artificial Muscle with a Double Structural Air Chamber

Naoki SAITO*, Daisuke FURUKAWA*, Toshiyuki SATOH* and Norihiko SAGA**

*Department of Intelligent Mechatronics, Akita Prefectural University
84-4, Ebinokuchi, Tsuchiya, Yurihonjo, Akita, 015-0055, Japan
(E-mail: naoki_saito@akita-pu.ac.jp)
** Department of Human System Interaction, Kwansei Gakuin University

Abstract. In this paper, we describe a straight fiber type pneumatic artificial muscle with high durability. The air chamber has a double structure of a high strength airbag which has been investigated in Rubber Less Artificial Muscle and rubber tube. The relationship between the internal pressure and contraction displacement, and inner pressure and contraction force was experimentally investigated, and it was confirmed that the hysteresis was less than that of the conventional Rubber Less Artificial Muscle. In addition, position control by this proposed artificial muscle was performed and good characteristics was obtained.

Keywords: Pneumatic, Actuator, Pneumatic Artificial muscle, Basic characteristics, Position control

INTRODUCTION

The development and application of pneumatic artificial muscles, one of the soft actuators, have been promoted in the new mechatronics field such as soft robotics [1-4]. While general pneumatic rubber artificial muscles are lightweight, and it can generate a large contraction force. However, it is considered that the practicality as actuators is poor because of their short durability due to softness of the rubber material.

On the other hand, the Rubber Less Artificial Muscle (RLAM) proposed by Saito et al. [5] has shown durability of more than 200,000 cycles under practical loads and driving pressures [6], indicating its potential as a practical actuator.

However, since RLAM only actuate in the direction of contraction, constraints such as the antagonistic placement of two artificial muscles are necessary [6], it is difficult to use for control involving extension and contraction.

In addition, in the extension and contraction behavior against a load, it contracts when the inner pressure increases, but it does not extend easily when the pressure is decreased. Therefore, it is known to have a hysteresis characteristic [7]. This characteristic makes the design of the control system very difficult, so it is desirable to eliminate the hysteresis characteristic.

Therefore, in this study, we propose a pneumatic artificial muscle with a double structural air chamber consisting of a high strength airbag, which has been developed in RLAM, and a rubber tube, which is expected to reduce hysteresis caused by extension movements due to elastic deformation. This artificial muscle will be fabricated, and the reduction of hysteresis and control performance will be verified to confirm the usefulness of the actuator.

STRUCTURE OF PROPOSED ARTIFICIAL MUSCLE

In this study, we fabricate a pneumatic artificial muscle called the straight fiber type [8, 9], as shown in Figure 1. This pneumatic artificial muscle has a relatively large contraction ratio. In addition, this type has a structural disadvantage in that the deformation of the rubber is larger and more prone to tearing or rupture because of the fibers used to constrain the deformation of the pneumatic artificial muscle are arranged along the axial direction. As shown in Fig. 2, the inside of the air chamber is composed of a high strength airbag, and the outside is covered with a rubber tube to form a double structured air chamber. The axial fibers were used of Kevlar fiber, and eight fibers were arranged so that they were evenly distributed in the circumferential direction as shown in Fig. 2 and attached to the inner airbag so that they slid in the axial direction. A ring made of Kevlar fiber equal to the circumferential length was attached at two axial locations. The amount of axial contraction caused by circumferential expansion increases and enables deformation with a higher contraction ratio. In this way, the Highly Durable Straight Fiber type pneumatic Artificial Muscle (HD–SFAM) was fabricated. The actual fabricated HD-SFAM is shown in Figure 3, and the main parameters are listed in Table 1. By applying a high

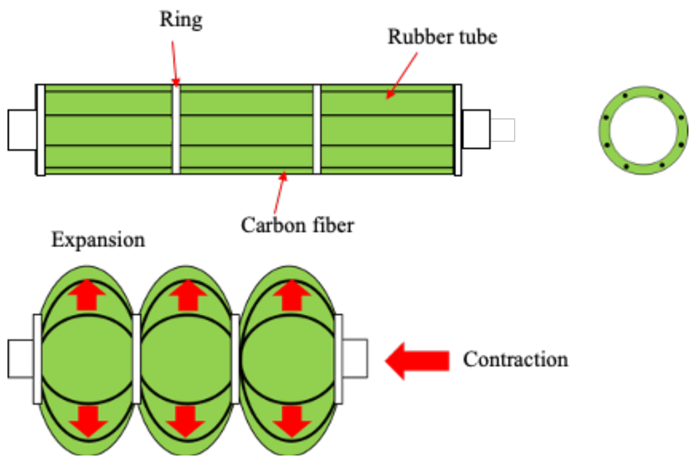

Figure 1. Basic mechanism and drive principle of the straight fiber type pneumatic artificial muscle

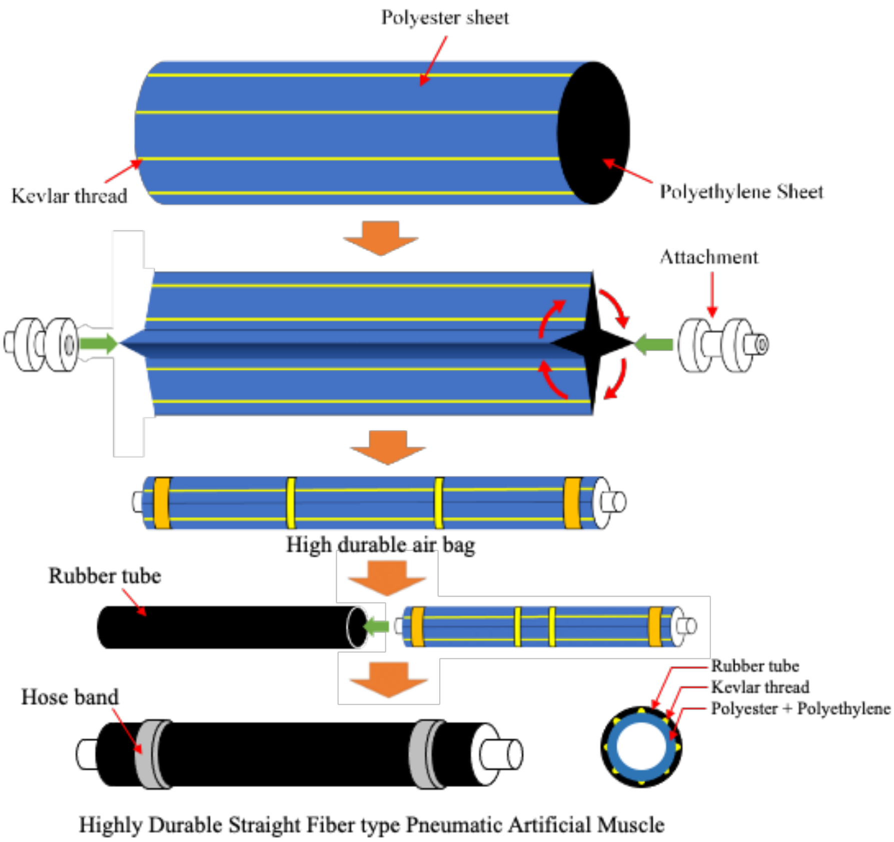

Figure 2. Detailed structural diagram of the HD-SFAM

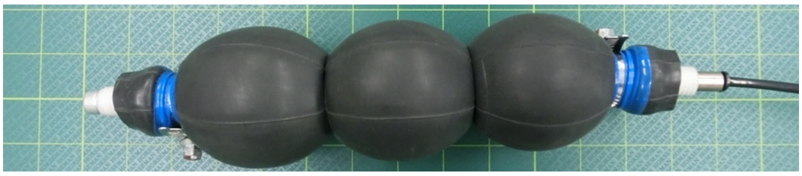

contraction

extension

Figure 3. Prototype HD-SFAM

2

Table 1. Parameters of prototype HD-SFAM

Outside diameter of Rubber tube	23.5
Inside diameter of Rubber tube	22.5
Diameter of High strength air bag	57.3
Length	210.0

strength airbag on the inner side, the HD–SFAM is considered to be able to stretch and contract about 200,000 times [6], basically the same as RLAM.
In the next chapter, we will examine the basic characteristics of this HD–SFAM.

BASIC CHARACTERISTICS

Relationship between inner pressure and contraction ratio

In this section, we first investigate the relationship between inner pressure and contraction ratio as a basic characteristic. The experimental system is shown in Fig. 4. The inner pressure is applied to HD–SFAM with the load suspended, and the contraction ratio is measured. The inner pressure is increased from 0 MPa to 0.2 MPa by 0.02 MPa every 5 seconds, and then decrease to 0 MPa under the same conditions. The average contraction ratio at constant pressure is shown in Fig. 5. From the results, it can be seen that the hysteresis loop becomes smaller as the load increases. Especially at 200 N, the hysteresis loop almost disappears.
Figure 6 shows the comparison of the pressure contraction characteristics between the conventional RLAM and the proposed HD-SFAM when the load is 200N. This result shows that the rubber tube is effective in reducing the hysteresis. On the other hand, in Fig. 5, when the load is 50 N, the hysteresis loop is large, and the HD-SFAM does not sufficiently reduce the hysteresis characteristics depending on the conditions. This may be due to the insufficient contraction force of the rubber tube. The thickness of the rubber tube used in this study is 0.5 mm, and we believe that using thicker rubber tube would increase the elastic force for stretching HD–SFAM and improve the characteristics.

Relationship between inner pressure and contraction force (Isometric contraction characteristic)

Next, we investigate the relationship between inner pressure and contraction force when the contraction ratio was kept constant. The experimental system is shown in Fig. 7. The experimental conditions are as follows: the

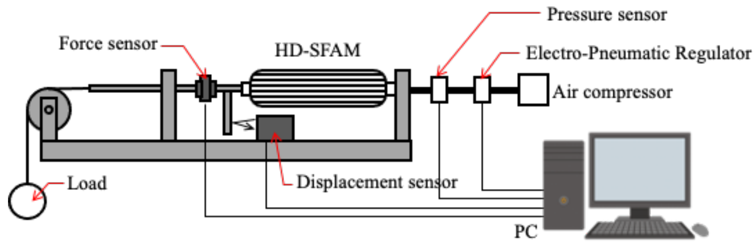

Figure 4. Experimental setup for measuring the relationship between inner pressure and contraction ratio

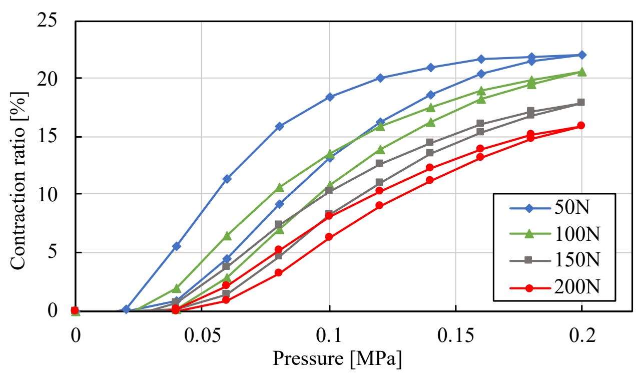

Figure 5. relationship between inner pressure and contraction ratio

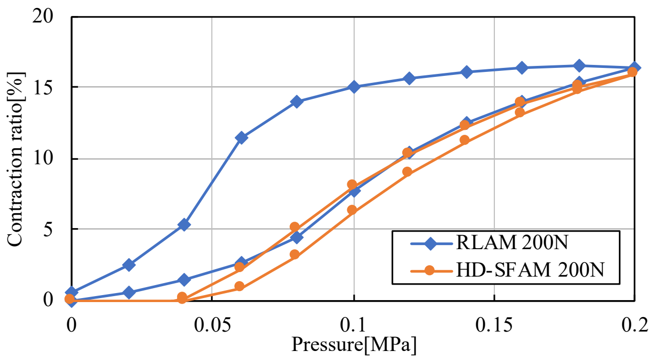

Figure 6. Comparison result of inner pressure and contraction ratio of RLAM and HD-SFAM

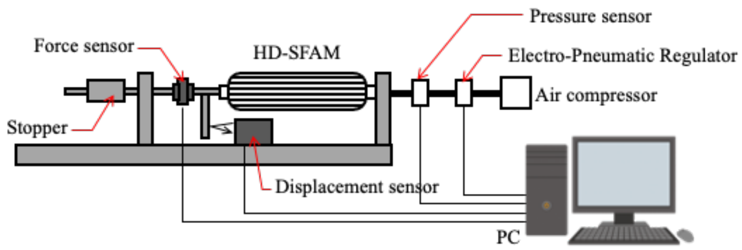

Figure 7. Experimental setup for measuring the relationship between inner pressure and contraction force

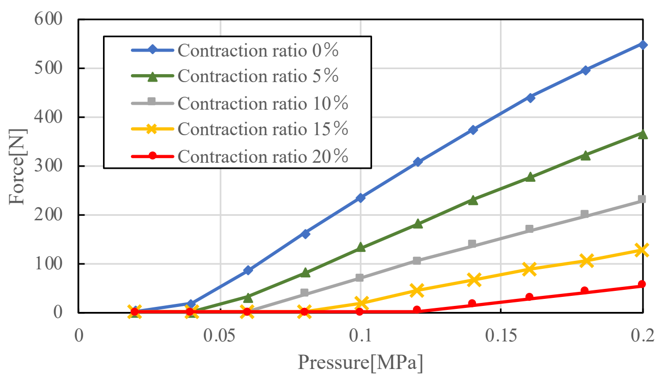

Figure 8. relationship between inner pressure and contraction force

contraction ratio is set from 0% to 20% at 5% intervals, and the inner pressure is applied from 0 MPa to 0.2 MPa at 0.02 MPa intervals. The results are shown in Fig. 8. From the results, it can be seen that the contraction force decreases with increasing contraction ratio. This trend is similar to that of other pneumatic artificial muscles. In the natural length, a force of about 540 N can be output at a pressure of only 0.2 MPa. In addition, this high strength airbag is capable of applying a pressure of 0.6 MPa [6], which means that a large maximum contraction force can be expected by carefully considering the strength of the components such as the hose band.

POSITION CONTROL

In this section, we evaluate the control performance of the developed HD-SFAM. Considering the HD-SFAM as a mass-spring-damper system, the equation of motion becomes as follows:

$$m\frac{d^2x(t)}{dt^2} + c\frac{dx(t)}{dt} + kx(t) = F(t) \tag{1}$$

where $x(t)$ is the amount of contraction, m is the mass at which the force acts, k is the elastic coefficient that describes the spring characteristics of the rubber tube, and c is the damping coefficient. The relationship between the force $F(t)$ and the pressure $P(t)$ can be expressed by the following equation, using the coefficient A:

$$F(t) = P(t)A \tag{2}$$

From Eq. (1) and Eq. (2), the following equation is obtained:

$$X(s) = \frac{A}{ms^2 + cs + k} P(s)\,, \tag{3}$$

This result suggests that the proposed artificial muscle is a typical second-order delay system. Therefore, for position control, it is necessary to incorporate an integrator in the feedback controller to eliminate the steady-state position error, in this paper, position control is basically performed by using PI controller.

The experimental system is the same as in Fig. 4, but with two different suspending loads. One is a suspending load of 200 N, which minimizes the effect of hysteresis. The other is a suspending load of 100 N, and the effect of hysteresis remains a little. The PI controller gain is adjusted by trial and error considering the amount of overshoot and the settling time, and the same gain is used in the two experiments. Figure 9 shows the step response of the position control by the PI controller with a suspending load of 100 N. And Figure 10 shows the step response of the position control by the PI controller with a suspending load of 200 N. Both results show that no steady-state error and no overshoot, and the settling time is about 3 s. The settling time is slightly shorter when the suspending load is 100 N. This result indicates that since the controller gain is the same, the smaller load has less work to interfere with the motion and thus reaches the target position faster. Figure 11 shows the result of changing the suspension load during position control. This result shows that the position control is properly performed even when the external load is changed, and the amount of contraction converges to the target value.

These results confirm that the HD-SFAM has almost no hysteresis effect and is useful as an actuator for systems such as robot joints that require continuous position control.

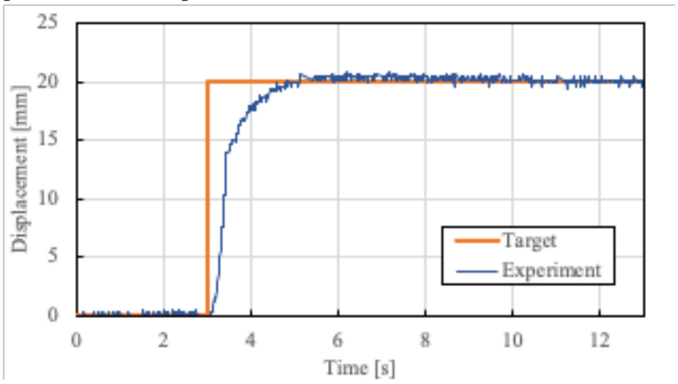

Figure 9. Step response of the position feedback control with PI controller and suspending load of 100 N

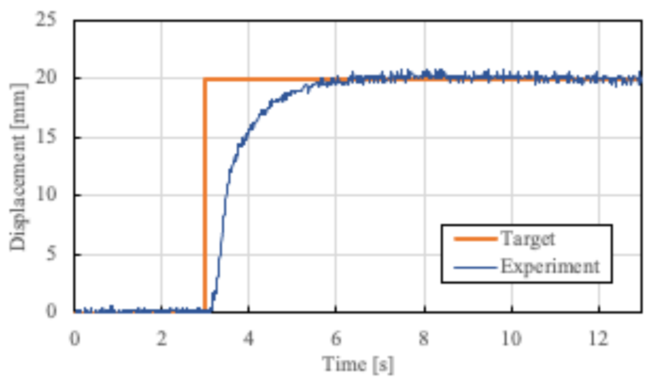

Figure 10. Step response of the position feedback control with PD controller and suspending load of 200 N

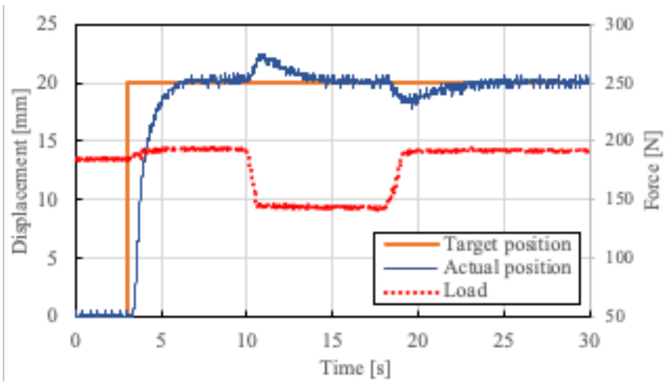

Figure 11. Step response of the position feedback control with PI controller when suspending load changes

CONCLUSION

In this study, we proposed and fabricated a highly durable straight-fiber type pneumatic artificial muscle (HD-SFAM) with a double structure of high-strength airbag and rubber tube. The results obtained are summarized as follows:

1. From the relationship between the inner pressure and the contraction ratio, it was found that the hysteresis decreased as the load increased and almost disappeared when the load is about 200N. The hysteresis tended to be smaller than that of rubberless artificial muscle which we proposed in previous research. However, hysteresis still occurs depending on the load conditions. In this prototype, we were not able to eliminate the hysteresis.
2. The isometric contraction characteristics were similar to those of general pneumatic artificial muscles, and the contraction force decreases with increasing in the contraction ratio.
3. From the results of position control, good position control results were obtained with PI controller. The control system was hardly affected by changes in the magnitude of hysteresis due to changes in the external load, and the response converged quickly to the target value even when the external load was changed during position control.

These results suggest that the proposed HD-SFAM is useful as an actuator for soft robotics.
Further reduction of the hysteresis by re-examining the parameters such as the thickness of the rubber tube and the material of the high strength airbag of the HD-SFAM is our future work.

REFERENCES

1. TAKAOKA, M., SUZUMORI, K., WAKIMOTO, S., IIJIMA, S. and TOKUMIYA, T., Fabrication of thin McKibben artificial muscle with various design parameters and their experimental evaluations, Proceedings of 5th International Conference on Manufacturing, Machine Design and Tribology (ICMDT2013), 2013, p.82.
2. YANAGIDA, T., ADACHI, K. and NAKAMURA, T., Development of Bellows-Type Artificial Rubber Muscle and Application to Peristaltic Crawling Endoscopic Robot, Journal of Robotics and Mechatronics, 2013, 25-4, pp. 748-754.
3. LI, W., NABAE, H., ENDO, G. and SUZUMORI, K., New Soft Robot Hand Configuration with Combined Biotensegrity and Thin Artificial Muscle, IEEE Robotics and Automation Letters (RAL), 2020, 5-3, pp. 4345-4351.
4. KADOWAKI, Y., NORITSUGU, T., TAKAIWA, M., SASAKI, D. and KATO, M., Development of Soft Power-Assist Glove and Control Based on Human Intent," Journal of Robotics and Mechatronics, 2011, 23-2, pp. 281-291.
5. SATO, T., SAITO, N., OGASAWARA, T. and SATO, T., Development of Rubberless artificial muscle and fundamental characteristics, Proceedings of the 37th Annual Conference of the IEEE Industrial Electronics Society (IECON2011), 2011, pp. 2051-2056.
6. SAITO, N. and SATOH, T., Structure of Rubberless Artificial Muscle and Evaluation of a Lifetime, Proceedings of the 42th Annual Conference of the IEEE Industrial Electronics Society (IECON2016), 2016, pp.648-653.
7. SAITO, N., SATO, T., OGASAWARA, T., TAKAHASHI, R. and SATO, T., Mechanical equilibrium model of rubberless artificial muscle and application to position control of antagonistic drive system Industrial Robot: An International Journal, 2013, 40-4, pp. 347-354.
8. TOMORI, H. and NAKAMURA, T., Theoretical Comparison of McKibben-Type Artificial Muscle and Novel Straight-Fiber-Type Artificial Muscle, International Journal of Automation Technology, 2011, 5-4, pp. 544-550.
9. FRANCESCO, D., MICHELE, G. A., PIERLUIGI, B. Z. and TERENZIANO, R., Development of a Straight Fibers Pneumatic Muscle, International Journal of Automation Technology, 2018, 12-3, pp. 413-423.

The 11th JFPS International Symposium on Fluid Power HAKODATE 2020 Oct. 12-13, 2021 The Japan Fluid Power System Society

Evaluation of lifting motion with non-wearing type pneumatic power assist device ~ comparison of active and passive type ~

Masashi YOKOTA*, Reito HIRABAYASHI*, and Masahiro TAKAIWA**

* Graduate School Advanced Technology and Science, Tokushima University
** Graduate School of Technology, Industrial and Social Sciences, Tokushima University
2 1 Minami Johsanjimacho, Tokushima, 770 8506 Japan
(E-mail: c501942002@tokushima-u.ac.jp)

Abstract. In Japan, we are facing an aging society. Securing the young labor force is a serious problem especially in the nursing field to support care recipients and in an industrial field to support heavy labor. In the lifting motion, there are roughly 2 types that are the squat method and the stoop one. The squat method is recommended because the burden on the waist is lowered than the stoop one. Many types of power assist devices are developed at research institutes around the world. However, most of them are wearable types and they promote the stoop method from their mechanical property. In a previous study, we developed a non-wearing type pneumatic power assist device that takes the squat method into consideration and evaluated a lifting motion with a position control system. In this study, we developed a passive assist device as well as an active one and evaluate the effectiveness in lifting motion between them.

Keywords: Pneumatic actuator, Power assist device, Force control, Disturbance observer, Human support.

INTRODUCTION

In Japan, we are facing an aging society, where the shortage of young labor causes a serious problem, especially in the nursing field and primary industrial one. In both working fields, we focus on a lifting motion. A back pain is the most common occupational disease by research of the Japan Ministry of Health, Labor and Welfare (hereinafter referred to as "MHLW") [1]. There are roughly 2 types in the lift motion, a squat method and a stoop one. The former involves lifting with a bent knee and the latter involves only the waist, as shown in **Figure 1**. When humans lift the object more than 15% of their body weight, they unconsciously shift from the squat method to the stoop one [2, 3]. MHLW recommends the squat method because the burden on the waist is lower than the stoop one [4]. The power assist device is one of the solutions to cope with this problem, and many types of devices have been developed at research institutes around the world. A wearable power assist device, which is the most types of devices, decreases the burden on the waist [5~7]. But it is not easy to bend the knee since it pushes the front part of the thigh backward to generate extension torque around the waist joint. Therefore, it is not too much to say, a wearable power assist device may promote the stoop method. Moreover, the wearer is burdened by the total weight of the device. In the meanwhile, an exoskeleton type device unloads the weight of the device to the ground [8~10]. But it takes time to wear the device and become large scale as well as introduction cost.
In the previous study, we have developed a non-wearing type pneumatic power assist device that takes the squat method into consideration and evaluated a lifting motion with a position control system [11]. In this study, we developed a passive type assist device as well as active one. Since the energy consumed by an active type device is greater than that of a passive one, it's not easy to simply compare them. However, we evaluate the effectiveness in both types of the devices from view of reducing physical burden. After presenting the schematics of both types of assist devices, the effectiveness in lifting motion was evaluated through some experiments.

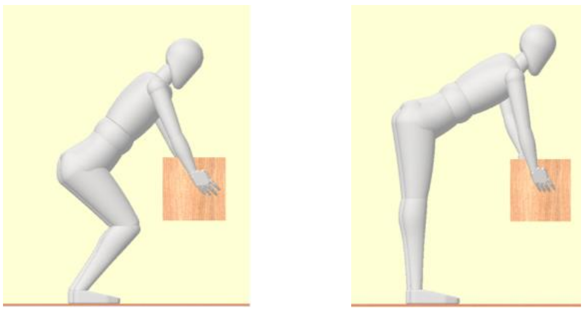

(a) Squat method (b) Stoop method
Figure 1. Lifting motion type.

NON-WEARING TYPE PNEUMATIC POWER ASSIST DEVICE

Overview of the developed device

The 2 types of developed power assist device (hereinafter referred to as "the assist device") is shown in **Figure 2** and **3**. As you see that, both assist devices contact with wearer at just 2 points. One is shoe side and contact with aground and the other pushes up wearer's armpit. Consequently, the wearer does not have physical constraints with the assist device and can lift an object by the squat method. The average height of Japanese persons in their 20s to 50s is approximately 1.65 m [12] and the armpit is located at approximately 82% of the height [13]. Therefore, the supporting position (armpit) of the assist device is approximately 1.35 m. Since a parallel link mechanism is introduced as shown in **Figure 4**, the assist device behaves as one D.O.F link mechanism.
The active type power assist device shown in **Figure 2** is using wire-type pneumatic cylinders. The maximum rotational torque of the actuator is 55.8 Nm at a cylinder pressure of 450 kPa. The total weight of the device is approximately 5.0 kg. **Figure 5** shows the pneumatic driving circuit for active type. The rotational angle of the pulley θ and pressure in the cylinder chambers (p_1, p_2) are detected by a potentiometer and pressure sensors (Keyence Corp., AP-C43), respectively. The output voltages from these sensors are fed back to an A/D converter. A flow type servo valve (FESTO, KMPYE-5) regulates the pressures p_1 and p_2 in the cylinder. The control system is implemented using RTAI, a real-time extension of Linux, and the sampling period is set to 5 ms.
The passive type power assist device shown in **Figure 3** has just a spring instead of an actuator. The support force depends on the number of a spring. The total weight of the device is approximately quite light of 1.8 kg. Since the device consist of only passive element of springs, a subject has a burden when they are crouching.

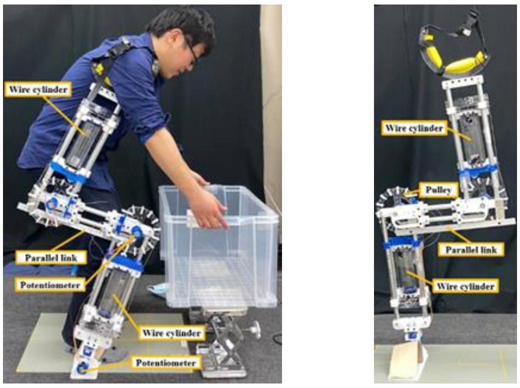

(a) Appearance of motion (b) Appearance of device
Figure 2. Active type power assist device

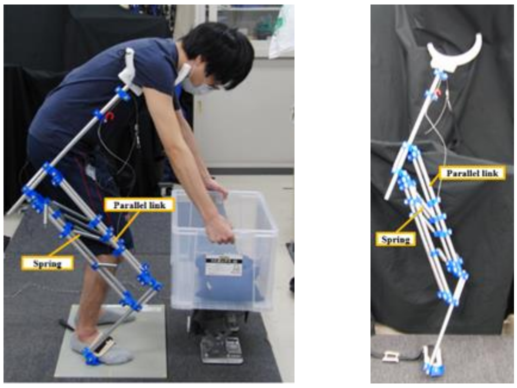

(a) Appearance of motion (b) Appearance of device
Figure 3. Passive type power assist device

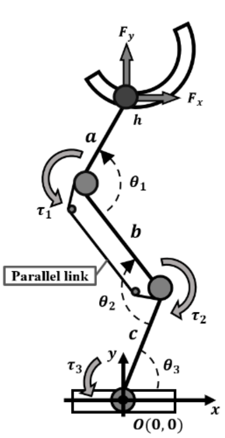

Figure 4. Kinematic model

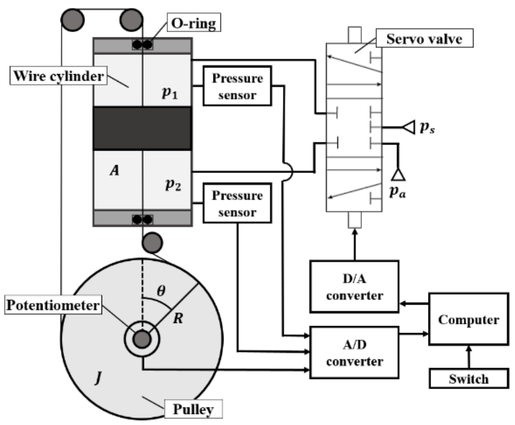

Figure 5. The pneumatic driving circuit for active type

Kinematic analysis

Figure 4 shows the kinematic model of the assist device where a base coordinate system O is set at the lower end and hand vector (the relative position of armpit to the base coordinate system) and joint vector is defined as $h = [x, y]^T$ and $\theta = [\theta_1, \theta_2, \theta_3\,]^T$, respectively. Forward kinematics $h = I(\theta)$ is described as follows.

$$\begin{cases} x = a\cos(\theta_1 + \theta_3 - \theta_2) - b\cos(\theta_2 - \theta_3) + c\cos(\theta_3) \\ y = a\sin(\theta_1 + \theta_3 - \theta_2) \ + b\sin(\theta_2 - \theta_3) + c\sin(\theta_3) \end{cases} \tag{1}$$

Due to the introduced parallel link mechanism, a joint angle is constrained as $\theta_1 = \theta_2$. Consequently, the forward kinematics is rewritten as follows.

$$\begin{cases} x = a\cos(\theta_3) - b\cos(\theta_1 - \theta_3) + c\cos(\theta_3) \\ y = a\sin(\theta_3) \ + b\sin(\theta_1 - \theta_3) + c\sin(\theta_3) \end{cases} \tag{2}$$

The relation between a torque vector $\tau = [\tau_1, \tau_2\,]^T$ a torque around each joint and an applying force vector at the supported position (contact point with armpit) $F = [F_1, F_2\,]^T$ is written in the following equation using a Jacobian matrix J_{aco} from a principle of virtual work.

$$\tau = {J_{aco}}^T F \tag{3}$$

Expanding Eq.3 gives the following statics balance equation.

$$\begin{cases} \tau_1 = a\{-F_x\sin(\theta_3) + F_y\cos(\theta_3)\} \\ \tau_2 = b\{\,F_x\sin(\theta_1 - \theta_3) + F_y\cos(\theta_1 - \theta_3)\} - \tau_1 \end{cases} \tag{4}$$

CONTROL SYSTEM FOR ACTIVE TYPE

Force control system

In the lifting motion, a force control system is applied on the assist device, as shown in **Figure 6** (a). Parameter of force control system is shown in **Table 1**. A reference joint torque vector $\tau = [\tau_1, \tau_2\,]^T$ is calculated from a reference force vector $F = [F_1, F_2\,]^T$ through Eq.4 and the torque control system is constructed as shown in **Figure 6** (b). A disturbance observer is introduced in the torque control system, where $P_\tau(s)$, $P_{\tau n}(s)$ and $Q_\tau(s)$ are plant, the nominal model of the plant and low-pass filter, respectively [14]. Time constant of filter $T_{\tau q}$ and nominal model T_n are set to 0.005 s and 0.001 s, respectively. The output of $Q_\tau(s)$ is the estimated disturbance, including the influence of a joint angular velocity and the influence of a parameter perturbation between a plant $P_\tau(s)$ and its nominal model $P_{\tau n}(s)$ at the same time. If these estimated disturbances are completely compensated, the robustness against the disturbance and parameter perturbation is highly improved. Since a lifting motion in rehabilitation is a relatively slow motion, the influence of inertial moment and viscosity are supposed to be ignored, so that we employ open loop force control without force feedback.

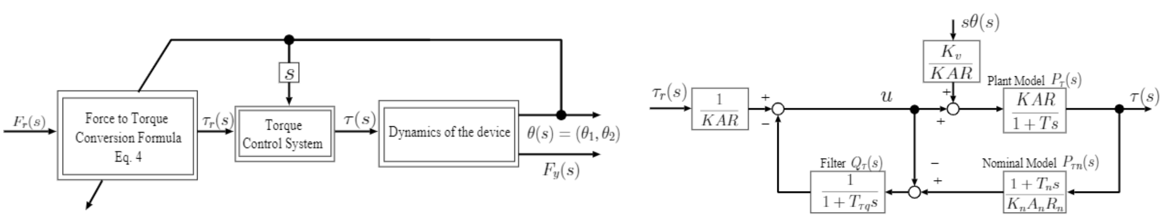

(a) Whole view of force control system. (b) Inner torque control system.

Figure 6. Force control system.

Table 1. Parameter of force control system.

F_r	Reference of generation force vector	[N]
F	Measured force vector	[N]
τ_r	Reference of generation torque vector	[Nm]
τ	Measured torque vector	[Nm]
θ	Joint angle vector	[rad]
F_y	Force at the supported position (y axis)	[N]
K	Flow gain	[−]
K_v	Velocity gain	[−]
T, T_n	Time constant and it's nominal value	[s]
$T_{\tau q}$	Time constant of filter	[s]
A	Effective sectional area of cylinder	[m^2]
R	Radius of pulley	[m]

Force control performance

We confirm the force control system on the active type assist device. As shown in **Figure 7**, the assist device is put on a force plate and the top of the device pushes up an aluminum frame fixed on the ground. In **Figure 8** shows the ramp response in the proposed force control system. The blue dotted line shows the estimated force F_y with Eq. 4 (F_x is set to be 0) based on the torque that is calculated with the measured pressure in the cylinder. The black dashed line indicates the reaction force from the assist device detected by a force plate. A force generated by the assist device roughly follows the reference. The error is mainly caused by an open loop force control. In the lifting motion, it does not require precise force control performance, so we think the obtained force control response shows enough in our lifting motion.

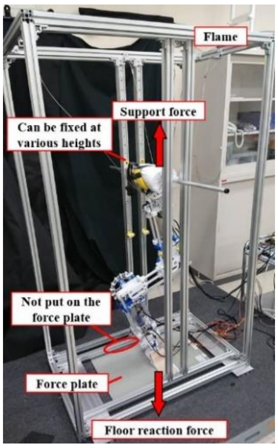

Figure 7. Experiment environment

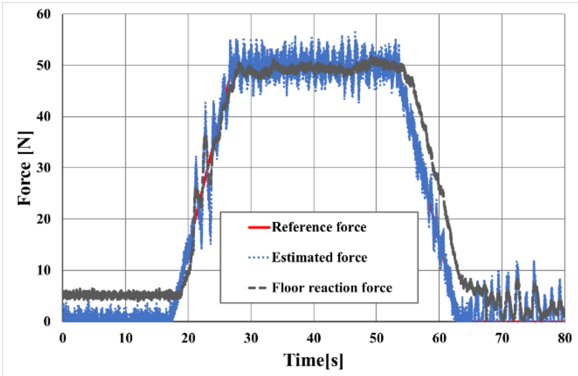

Figure 8. Force control response

SUPPORT EXPERIMENT

Support effect in a lifting motion

We evaluated the support effect during a lifting motion using the 2 types of assist devices. In the case of active type as shown in **Figure 9** (a), the assist device is attached on subject's right side and he performs a lifting motion on a force plate using force control. When the touch switch on the carry case is pushed, the force control starts supporting the subject with a ramp signal in the y direction as the reference in **Figure 6** (a). The reference velocity in the ramp signal is set by trial and error based on the actual lift motion. In the case of passive type, the experimental situation is the same with that in the case of active. As shown in **Figure 9** (b), a subject lifts an object of 10 kg in weight up and down without bending the elbow using the squat method. The subjects are two healthy adult males (173±5 cm in height, 55±1 kg in weight) and four trials are performed with each subject. The raw EMG data measured with myoelectric sensors (Oisaka Electronics Co.) placed on the dominant muscle shown in **Figure 10**, are processed to IEMG with an integration time of 0.2 s.

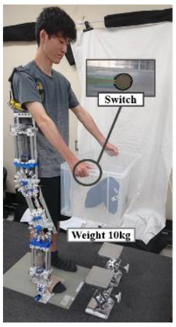

(a) State of lifting motion.

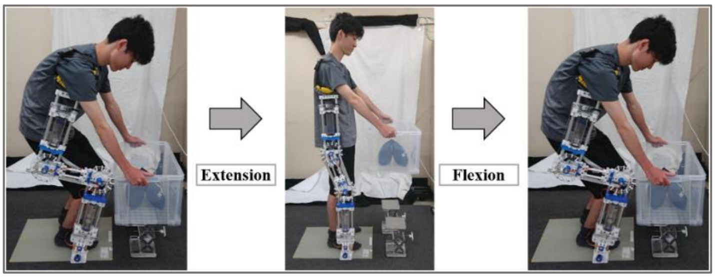

(b) Series of lifting motions.

Figure 9. Evaluation in support experiment.

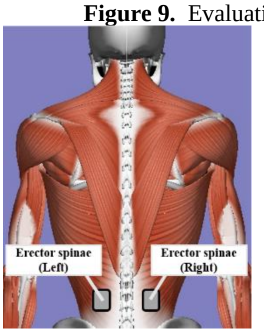

(a) Upper body.

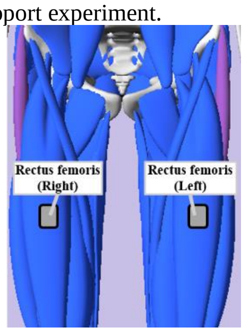

(b) Upper legs.

Figure 10. The place of electrodes on the dominant muscles.

Figures 11 and **12** show the muscle burden of each dominant muscle shown in **Figure 10**, for one subject during the lifting up and down motion with active type and passive one, respectively. The horizontal axis represents the normalized time, which is the interval between lifting and putting off the object based on the signal from the floor reaction force and the situation of the switch. **From Figures 11** and **12**, we can confirm the large decrease in muscle burden of Rectus femoris by using both devices comparing with no device. The muscle burden of Erector spinae is decrease, though not as much as muscle burden of Rectus femoris.

Figure 13 summarizes all the experimental results for the two subjects. The average value of IEMG with a payload of 10 kg without the device is set as the standard (100%). From **Figure 13**, we can confirm that there is a large decrease in the muscle activity ratio of Rectus femoris by using both devices with a significant difference ($p<0.01$). In generally, in the squat method, a larger burden is imposing on the muscle in the upper leg compared to that in the upper body. We can only confirm the decrease in the muscle activity ratio of the right side Erector spinae by using the passive type device with a significant difference ($p<0.01$). But muscle activity of upper legs with passive type is not decreased as much as that of active one. We think the reason is due that the passive type device becomes a resistance when the subject lifts down. In the future work, we will design a burden reduction mechanism in lifting down motion, as well as investigate the influence and effect against one side support with both devices.

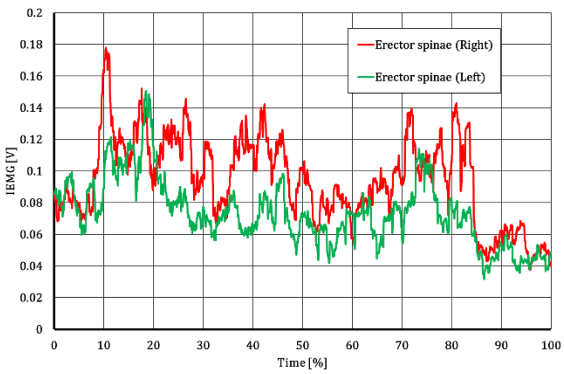

(a) Erector spinae without device.

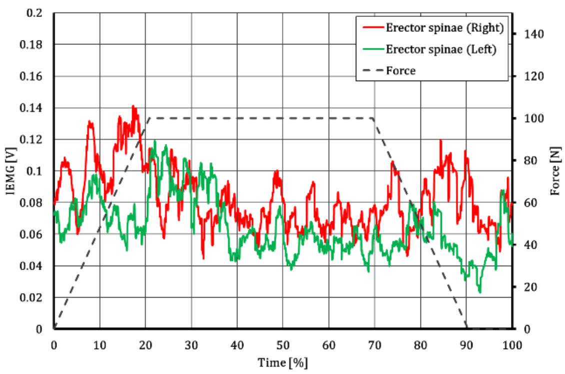

(b) Erector spinae with device.

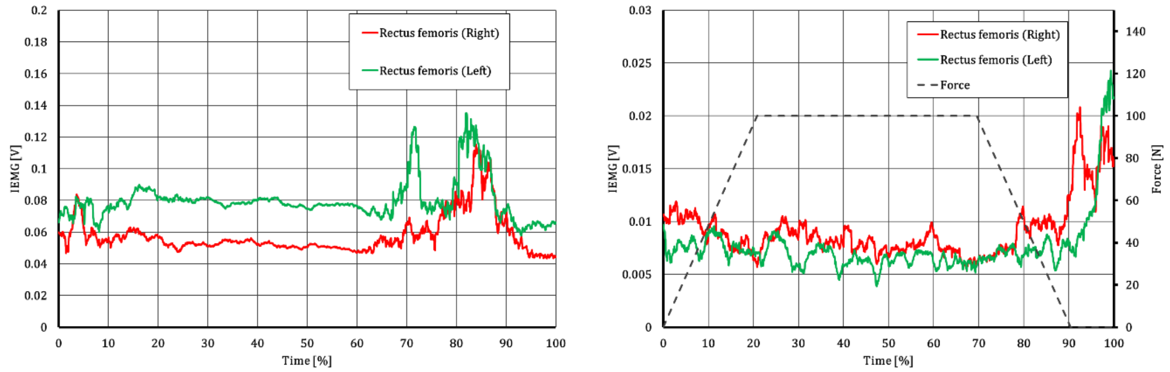

(c) Rectus femoris without device. (d) Rectus femoris with device.

Figure 11. IEMG with active type.

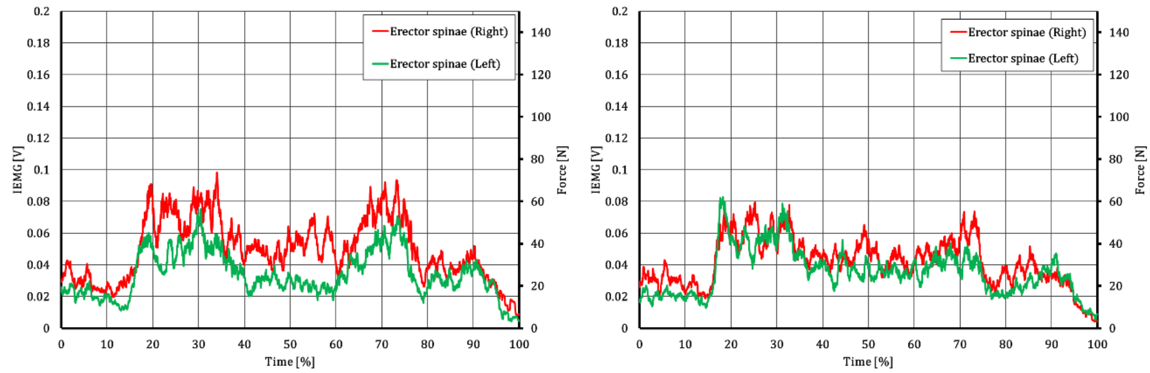

(a) Erector spinae without device. (b) Erector spinae with device.

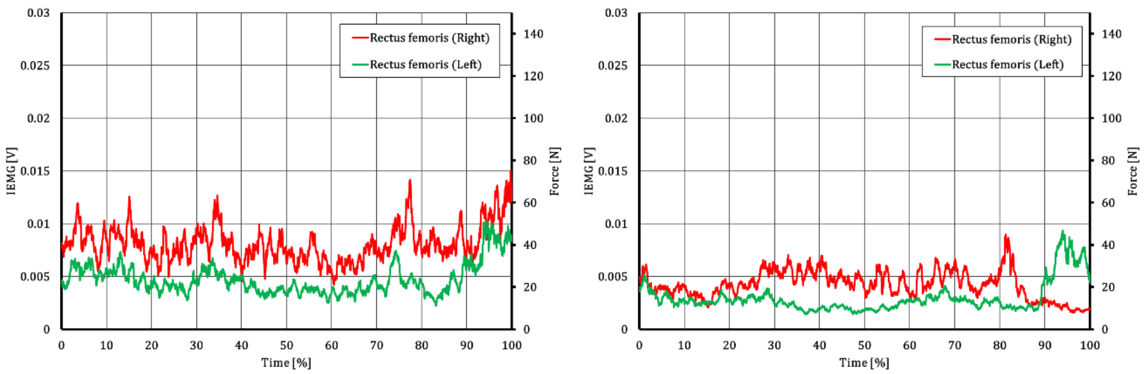

(c) Rectus femoris without device. (d) Rectus femoris with device.

Figure 12. IEMG with passive type.

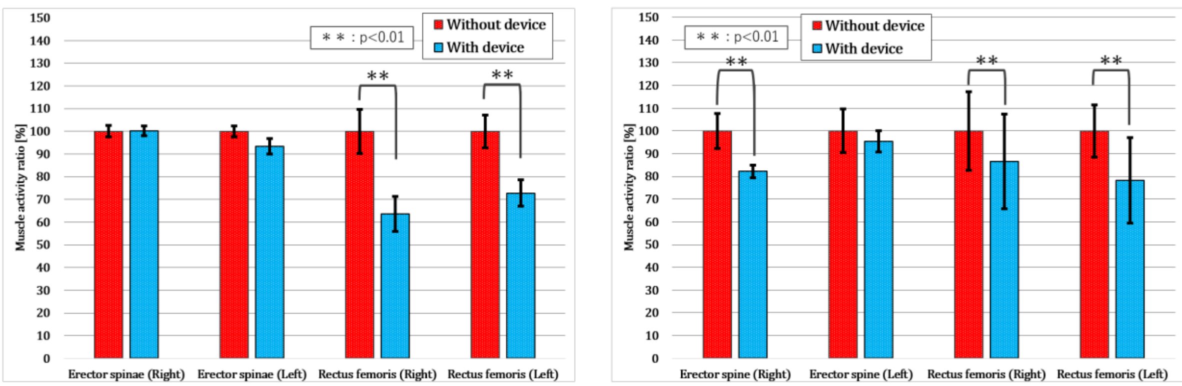

(a) Active type. (b) Passive type.

Figure 13. Comparison of muscle activation.

6

CONCLUSION

In this study, we developed a passive type assist device as well as active one. We conducted experiments to verify the support effect in both of the assist device during a simple lifting motion with a payload by measuring the EMG on the dominant muscle. In generally, in the squat method, a larger burden is imposing on the muscle in the upper leg compared to that in the upper body. From the experimental results, we can confirm that there is a large decrease in the muscle activity ratio in Rectus femoris by using both devices with a significant difference ($p<0.01$) which shows the effectiveness of the developed power assist devices. In the future, we will analyze the state of various muscle activities in lifting motion with a musculoskeletal simulator.

REFERENCES

1. Ministry of Health, Labor and Welfare, Occupational Disease Occurrence Survey Report, 2018 (in Japanese).
2. NAMINOHIRA, K., FUJIMURA, M., Electromyographic and Kinematical Study of Human Lifting Motion -Effect of Mass of Heavy Object on Motion Methods-, Japanese society of occupational medicine, 2010, Vol.58, pp. 234-239 (in Japanese).
3. NAMINOHIRA, K., FUJIMURA, M., SHINKODA, K., Electromyographic and Kinematic Study of Lifting Motion in Male Adults -Effects of Mass of the Object on Motion Patterns (The Second Report)-, Japanese society of occupational medicine, 2011, Vol.59, pp. 245-250 (in Japanese).
4. FUJIMURA, M., NORA, I., The influence on lumbago in lifting weights measured by electrocardiography, Japanese society of occupational medicine, 2004, Vol.52, pp. 341-347 (in Japanese).
5. LI, S., NORITSUGU, T., TAKAIWA, M., SASAKI, D., Design of Wearable Power Assist Wear for Low Back Support Using Pneumatic Actuators, Journal of Robotics and Mechatronics, 2013, Vol.7, No.2, pp. 228-236.
6. KAWAI, S., NARUSE, K., YOKOI, H., KAKAZU, Y., An Analysis of Human Motion for Control of a Wearable Power Assist System, Journal of Robotics and Mechatronics, 2004, Vol.16, No.3, pp. 237-244.
7. NARUSE, K., KAWAI, S., YOKOI, H., KAKAZU, Y., Design of Wearable Power-Assist Device for Lower Back Support, Journal of Robotics and Mechatronics, 2004, Vol.16, No.5, pp. 489-496.
8. MAMIYA, S., TAKAHASHI, T., UCHIYAMA, N., Design and Experimental Verification of a Pantograph-Based Mechanism for Lower Limb Load Reduction by Compensating for Upper Body Weight, Journal of Robotics and Mechatronics, 2018, Vol.30, No.1, pp. 33-42.
9. NARUOKA, Y., HIRAMITSU, N., MITSUYA, Y., A Study of Power-Assist Technology to Reduce Body Burden During Loading and Unloading Operations by Support of Knee Joint Motion, Journal of Robotics and Mechatronics, 2016, Vol.28, No.6, pp. 949-957.
10. NORITSUGU, T., SASAKI, D., KAMEDA, M., FUKUNAGA, A., TAKAIWA, M., Wearable Power Assist Device for Standing Up Motion Using Pneumatic Rubber Artificial Muscles, Journal of Robotics and Mechatronics, 2007, Vol.19, No.6, pp. 619-628.
11. YOKOTA, M., TAKAIWA, M., Development of Non-Wearing Type Pneumatic Power Assist Device -Basic Concept and Performance Evaluation-, Journal of Robotics and Mechatronics, 2020, Vol.32, No.5, pp. 1052-1060.
12. MINISTRY OF HEALTH, LABOR AND WELFARE, National Health and Nutrition Survey Report, 2017 (in Japanese).
13. CHAFFIN, D. B., ANDERSSON, G. B. J., Occupational Biomechanics, 1984, Wiley.
14. TAKAIWA, M., NORITSUGU, T., Positioning control of pneumatic parallel manipulator, International Journal of Automation Technology, 2008, Vol.2, No.1, pp. 49-55.

Genaral Session | Pneumatics

Robotics and Mechatronics 1

[GS1-1-01] Development of a Simple Servo-Pneumatic Three DOF Pick-And-Place Manipulator

Chin-Yi Cheng[1], Jyh Chyang Renn[1], Shyang Jye Chang[1], ○Ilham Saputra[1] (1.National Yunlin University of Science and Technology)

[GS1-1-02] Development of Fingertip Mechanism With Contact Point Estimation

○Kei Mikami[1], Kotaro Tadano[1] (1.Tokyo Institute of Technology)

[GS1-1-03] Development of Outdoor Activity Assist Suit

○Toshihiro Yoshimitsu[1], Rui Matsumoto (1. Kanagawa Institute of Technology)

[GS1-1-04] Examination on Attitude Control System of Hand Manipulator with Compact Pneumatic Cylinders by E-FRIT

○Shogo Tomita[1], Eiji Murayama[1], Yukio Kawakami[1] (1.Shibaura Institute of Technology)

[GS1-1-05] Design and Fabrication of a Soft Filament-polymer Jamming Actuator

○Peng Qin[1], Zhonghua Guo[1], MengYu Dou[1], Zhongsheng Sun[1], Yan Teng[1], Xiaoning Li[1] (1.Nanjing University of Science and Technology(China))

[GS1-1-06] Robotic Blood Vessel Mechanism for Self-Healing Function of Soft Robots

Kenjiro Tadakuma[1], Shohei Inomata[1], Yuta Yamazaki[2], Fumiya Shiga[2], Masanori Kameoka[2], MD Nahi Islam Shiblee[2], ○Issei Onda[1], Tomoya Takahashi[1], Yu Ozawa[1], Masahiro Watanabe[1], Hidemitsu Furukawa[2], Masashi Konyo[1], Satoshi Tadokoro[1] (1.Tohoku University, 2.Yamagata University)

The 11th JFPS International Symposium on Fluid Power HAKODATE 2020 Oct. 12-13, 2021 JFPS The Japan Fluid Power System Society

Development of a Simple Servo-Pneumatic 3-DOF Pick-and-Place Manipulator

Chin-Yi Cheng*, Jyh-Chyang Renn**, Shyang-Jye Chang***, Ilham Saputra****

*Department of Mechanical Engineering
National Yunlin University Science & Technology, Taiwan
(E-mail: zezheng@yuntech.edu.tw)
**Department of Mechanical Engineering
National Yunlin University Science & Technology, Taiwan
(E-mail: rennjc@yuntech.edu.tw)
***Department of Mechanical Engineering
National Yunlin University Science & Technology, Taiwan
(E-mail: changjye@yuntech.edu.tw)
***Department of Mechanical Engineering
National Yunlin University Science & Technology, Taiwan
(E-mail: ilhamsaputra2109@gmail.com)

Abstract. The purpose of this paper is to develop a brand new parallel-connected servo-pneumatic 3-DOF manipulator for automatic pick-and-place purpose. The kinematic design shown in this paper is different from the commercially available DELTA or EXPT pick-and-place manipulators, which are mostly controlled by electric servomotor. The servo-pneumatic manipulator presented in this paper consists of three single-rod pneumatic cylinders, three linear position transducers and three pneumatic proportional directional valves. In addition to the hardware development, a software PID controller is also implemented. To achieve the basic movement of pick-and-place as well as two additional path tracking controls, the closed-loop PID control scheme is utilized. Finally, various experiment results successfully verify the validity of the overall system design.

Keywords: Pneumatics, 3-DOF Manipulator, Industry 4.0, Pick-and-Place, Automation

1. INTRODUCTION

Industrial 4.0 was proposed by Germany in 2011. It was aimed to promote and integrate the modern industrial technology, after-sale service and product manufacturing. Three important foundations include Intelligent Sensing System, Internet of Things (IoT) and Big Data Analysis [1, 2]. On the other hand, pneumatic systems have the characteristics of fast speed, precise control and easy maintenance. Therefore, it is currently widely used in modern automation industry. It is also believed that pneumatic control systems have been playing a very important role to implement the Industrial 4.0. The automatic pneumatic control systems can be divided into two types, one is open loop control scheme and the other is closed-loop control system. The former focuses on the automatic sequence control. However, the fast and accurate position or velocity controls are the significant merits of the latter.

This paper is aimed to develop a brand new parallel-connected servo-pneumatic 3-DOF manipulator for automatic pick-and-place purpose. The kinematic design shown in this paper is different from the commercially available DELTA or EXPT pick-and-place manipulators, which are generally controlled by electric servomotor. The servo-pneumatic manipulator presented in this paper mainly consists of three single-rod pneumatic cylinders, three linear position transducers and three pneumatic proportional directional valves. Figure 1 shows the hardware structure of the proposed servo-pneumatic manipulator. It is worth mentioning that the design idea proposed in this paper arises actually from the well-known 3-DOF ship or yacht simulator [3]. However, the new design is trying to rotate the structure of the simulator upside down and relocate the originally upper movable platform at the new lower position. In the following, the design details of the kinematic hardware will firstly be outlined

2. Hardware Design

The proposed new servo-pneumatic 3-DOF manipulator possesses a closed and parallel-connected kinematic structure, which can further be divided into three parts. They are the main body, constraints and the movable platform with a recording pen as shown in Fig. 1. Figure 2 shows the side-view of the manipulator without the recording pen. The most important components in the whole design are the three actuating units consisting of

three single-rod pneumatic cylinders with three linear position transducers. These three actuating units are interconnected by six universal joints between the fixed upper platform and the lower movable platform at a suitable inclined angle. This inclined angle eventually determines the maximal working space of the lower movable platform. In addition, to maintain the lower movable platform always at the horizontal attitude during the pick-and-place movement, two necessary constrains are also interconnected between the fixed upper platform and the lower movable platform as shown in Fig. 2. The design scheme of the constraint is depicted in Fig. 3. Obviously, such a constraint offers only 2-DOF movements which are the slide and rotation along the axis of ball bearings as shown in Fig. 3. Furthermore, from Fig. 1, there are two constraints placed at two different vertical faces, which will successfully limit the movement of lower platform always at the horizontal attitude.
Finally, the lower movable platform is equipped with a vertical pen located at the center position. This pen can be used to record the actual trajectory of the platform center point. However, in the future real applications, this pen can be easily replaced by a common pneumatic suction pad or other tools to accomplish the automatic pick-and-place assembly. After real experiments, the maximal reachable working space of the proposed manipulator is found to be W100mm x D100mm cm x H220mm. Finally, to accurately control the movement of the lower platform, the inverse kinematic model will be used and discussed in the following section.

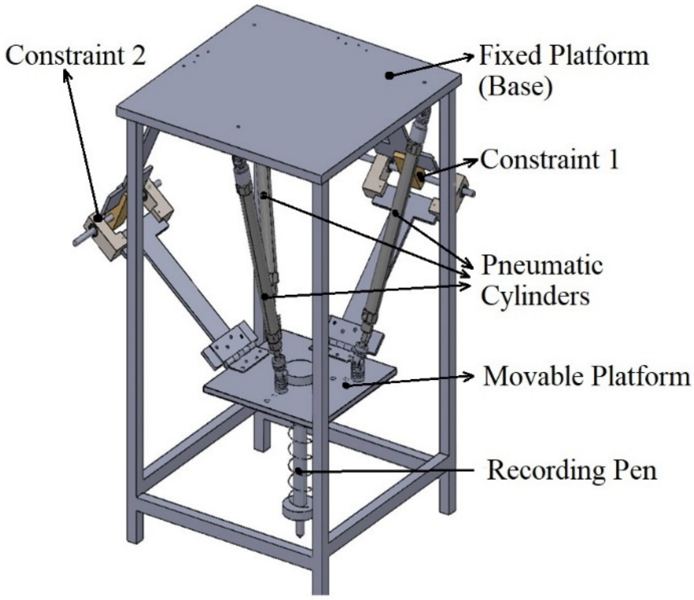

Figure 1. Hardware structure of the servo-pneumatic manipulator.

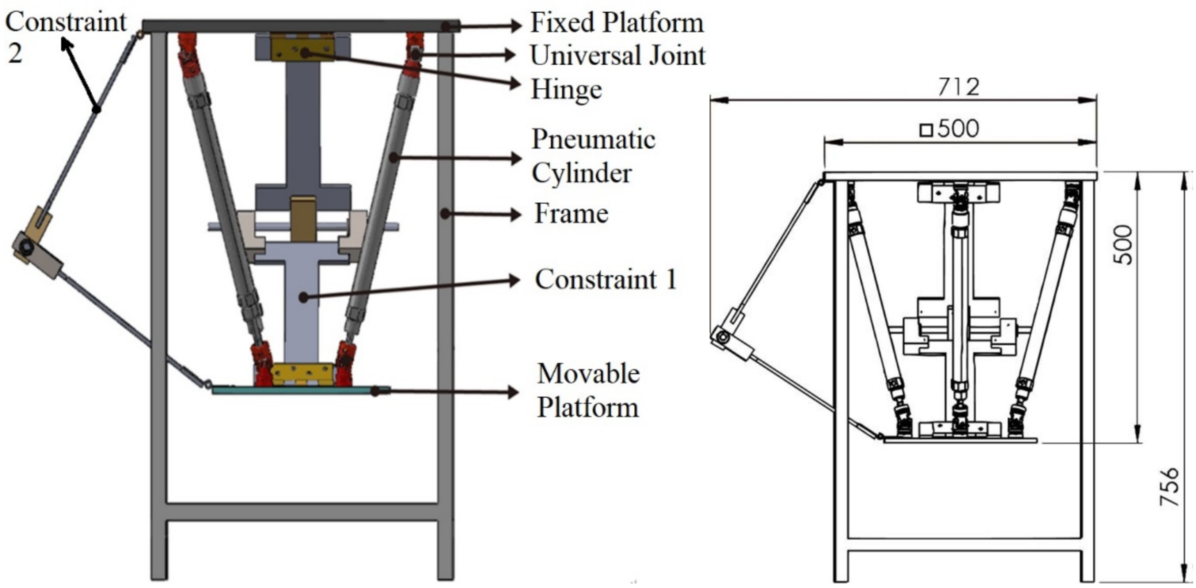

Figure 2. Side-view of the servo-pneumatic manipulator.

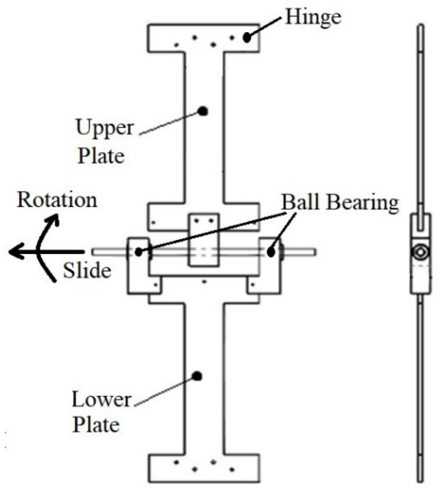

Figure 3. Design scheme of the constraint.

3. Inverse Kinematic Model

The inverse kinematics that maps Cartesian space into joint space is inevitably necessary for the attitude control [4, 5]. Using Cartesian coordinate, the coordinate system {B} for the upper base and coordinate system {P} for the lower movable platform can be defined as shown in Fig. 4. Obviously, from the vector diagram shown in Fig. 4, the following Eq. (1) holds.

$$\boldsymbol{S_i} = {}^B\boldsymbol{P_i} - {}^B\boldsymbol{B_i}, \tag{1}$$

where the vector ${}^B\boldsymbol{B_i}$ is readily known from the hardware design geometry. In addition, the vector ${}^B\boldsymbol{P_i}$ can be calculated by

$$ {}^B\boldsymbol{P_i} = \boldsymbol{T_v} + \boldsymbol{R} \times {}^P\boldsymbol{P_i}, \tag{2}$$

where the vector ${}^P\boldsymbol{P_i}$ is also known from the design geometry. The most important vector in inverse kinematic model is the vector $\boldsymbol{R}$, which is called the attitude orientation matrix and can be formulated by the Eq. (3) [4].

$$\boldsymbol{R} = R_\gamma R_\beta R_\alpha = \begin{bmatrix} c\gamma & -s\gamma & 0 \\ s\gamma & c\gamma & 0 \\ 0 & 0 & 1 \end{bmatrix} \begin{bmatrix} c\beta & 0 & s\beta \\ 0 & 1 & 0 \\ -s\beta & 0 & c\beta \end{bmatrix} \begin{bmatrix} 1 & 0 & 0 \\ 0 & c\alpha & -s\alpha \\ 0 & s\alpha & c\alpha \end{bmatrix}, \tag{3}$$

where $c\alpha$ denotes $cos(\alpha)$, $s\alpha$ denotes $sin(\alpha)$, and so on. The angles of pitch, roll and yaw motions at the center point of movable platform relative to the base coordinate are denoted by γ, β and α. However, these three angles are all equal to zero because of the two additional constraints in the kinematic design as shown in Fig. 1. Therefore, the attitude orientation matrix can be simplified as

$$\boldsymbol{R} = \begin{bmatrix} 1 & 0 & 0 \\ 0 & 1 & 0 \\ 0 & 0 & 1 \end{bmatrix}. \tag{4}$$

Finally, the length L_i of every pneumatic cylinder is actually the scalar length of the vector ***Si***. From Eq. (1), the vector ***Si*** can be rewritten as

$$\boldsymbol{s_i} = \begin{bmatrix} u_i \\ v_i \\ w_i \end{bmatrix} - \begin{bmatrix} b_{ix} \\ b_{iy} \\ b_{iz} \end{bmatrix} = \begin{bmatrix} \bar{x} \\ \bar{y} \\ \bar{z} \end{bmatrix} \ (i = 1, 2, 3) \tag{5}$$

Thus, the length L_i of every pneumatic cylinder can be d

$$L_i = \sqrt{\bar{x}^2 + \bar{y}^2 + \bar{z}^2} \qquad (i = 1, 2, 3) \qquad (6)$$

This is exactly the closed-form solution of the proposed parallel-connected servo-pneumatic 3-DOF manipulator.

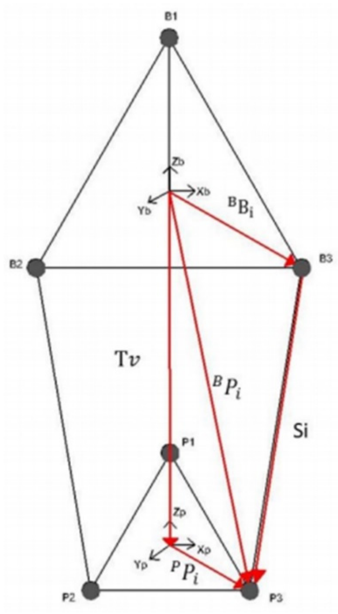

Figure 3. Vector diagram between two working spaces.

4. Closed-loop PID Position Control and Hardware Design

In this paper, traditional but effective PID controller is utilized to control the proposed servo-pneumatic 3-DOF manipulator. Figure 5 shows the control block diagram of a single pneumatic cylinder. The schematic hardware layout of the closed-loop position control of one pneumatic cylinder is depicted in Fig. 6. It is worth mentioning that the whole manipulator system consists of three parallel-connected pneumatic cylinders. Thus, simultaneous control of these three cylinders is necessary. From Fig. 6, two most important components can be observed. The first one is the proportional directional control valve (FESTO, MTYPE-5-1/8LF-010-B) and the second one is the potentiometer for measuring the actual position of the cylinder rod. Finally, the PC-based controller is implemented by using the LabView software. Figure 7 shows the real picture of the developed servo-pneumatic 3-DOF manipulator.

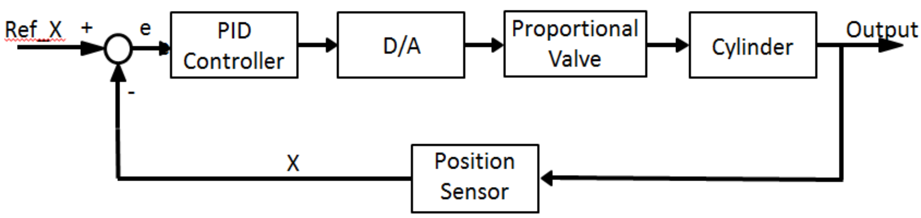

Figure 5. Control block diagram of a single pneumatic cylinder.

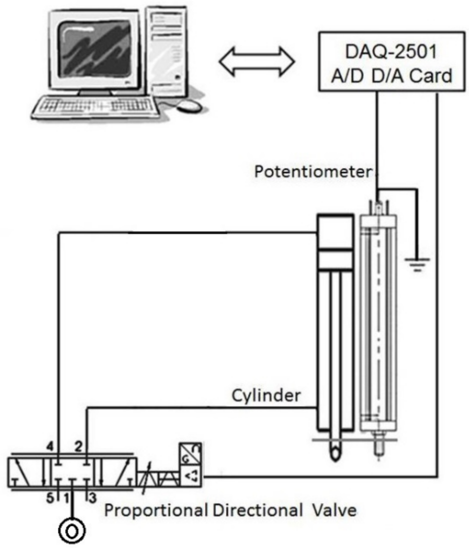

Figure 6. Schematic hardware layout of the closed-loop position control of a single pneumatic cylinder.

Figure 7. Real picture of the developed servo-pneumatic 3-DOF manipulator.

5. Experimental Results and Discussion

5.1 Position control of one single cylinder

In this paper, the trial-and-error approach is utilized to acquire the most suitable gains for the PID controller. Figure 8 and Figure 9 show two experimental results of 60 mm and 120 mm position control for one cylinder, respectively. Obviously, the position control results are satisfactory. However, the dead-zone at the beginning of the position control is also observed. This is chiefly because of the nonlinearity inherent in the proportional directional valve as well as the static friction effect. The percentage steady-state position control error is less than 1%.

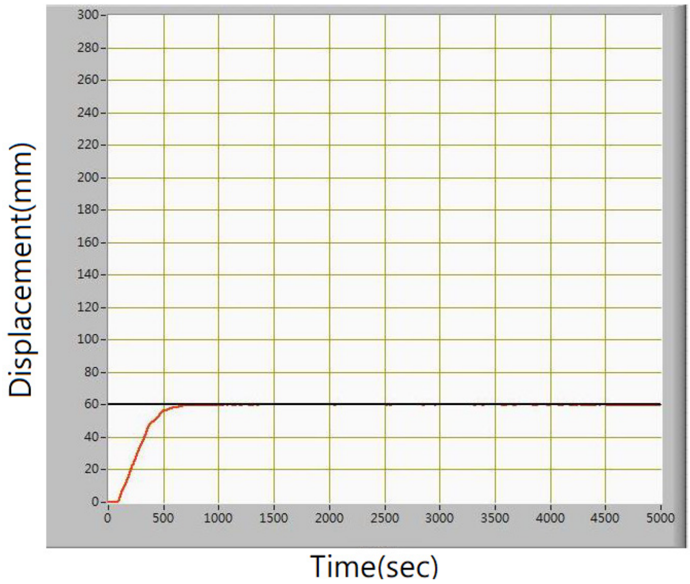

Figure 8. Experimental result of 60 mm position control for one cylinder

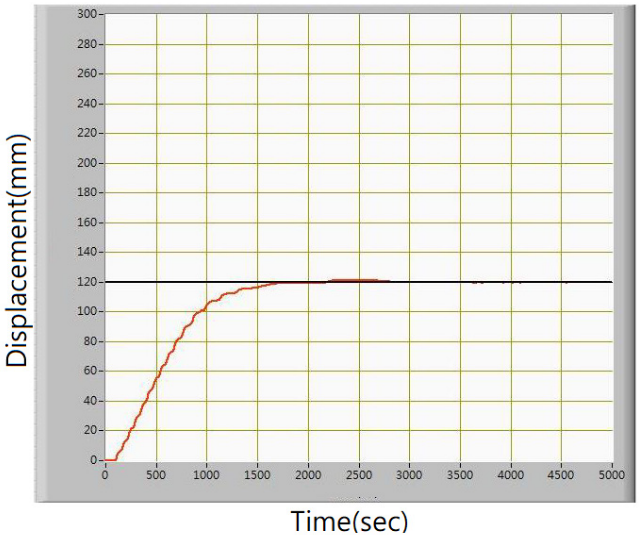

Figure 9. Experimental result of 120 mm position control for one cylinder

5.2 Path Tracking Control

In this paper, two different paths are used to evaluate the performance of the developed servo-pneumatic 3-DOF manipulator. The first one is a circle and the second one is an isosceles triangle. Figure 10 shows the experimental result of tracking a circle of diameter 48 mm. The maximal and minimal percentage tracking error are found to be 8.3% and 0.0052%, respectively. However, the overall average percentage tracking error is 4.2%. On the other hand, the experimental result of tracking an isosceles triangle is shown in Fig. 11. The side length of the isosceles triangle is 100 mm. After calculation, the overall average percentage tracking error is found to be 6.4%.

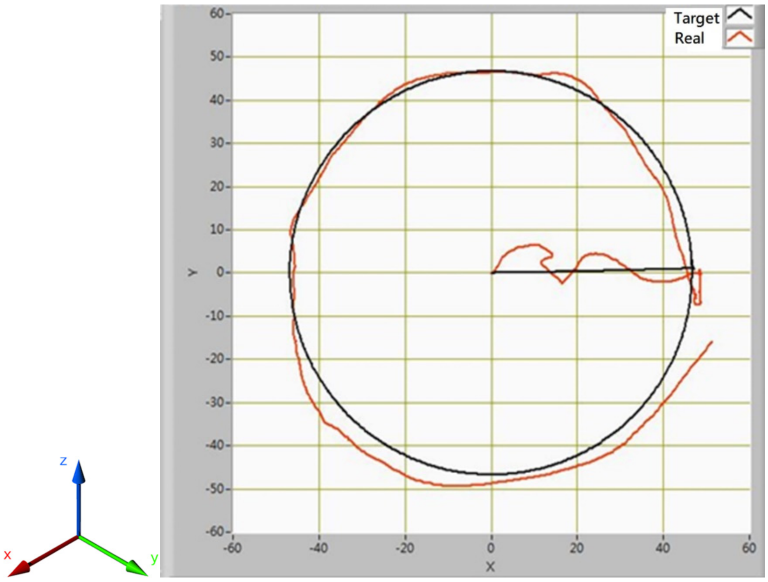

Figure 10. Experimental result of tracking a Circle (φ: 48 mm)

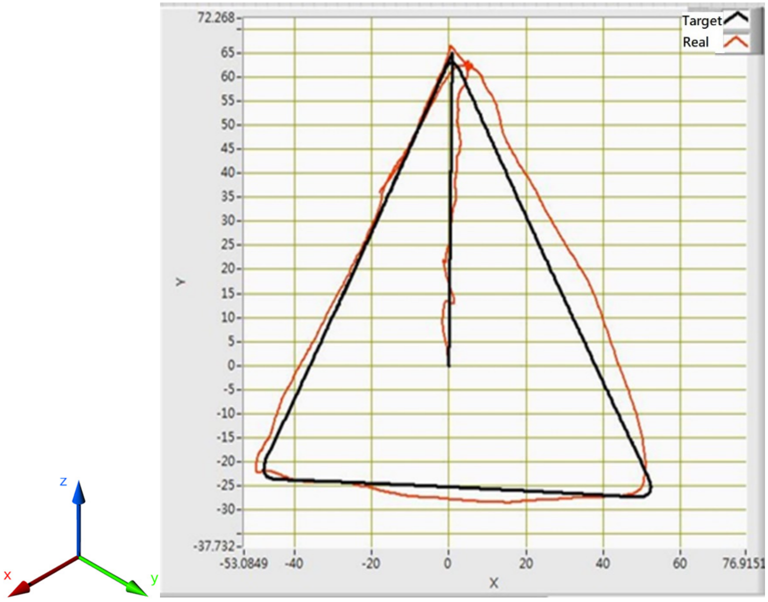

Figure 11. Experimental result of tracking an isosceles triangle (side length: 100 mm)

6. Conclusion

In this paper, a new parallel-connected servo-pneumatic 3-DOF manipulator for automatic pick-and-place is successfully developed and realized. In addition to the basic movement of pick-and-place, two additional path tracking controls, including the tracking of a circle and an isosceles triangle, are also used to evaluate the performance of the developed servo-pneumatic 3-DOF manipulator. Obviously, compared to some commercially available servomotor-controlled manipulators, the experimental percentage control errors appear in this paper are quite large. One main reason for these large errors is that the construction and assembly of the whole manipulator system are accomplished in the laboratory. Therefore, inaccurate manufacturing of components as well as imprecise assembly are both inevitable. In the future, however, the developed servo-pneumatic 3-DOF manipulator may find more potential applications in the field of automation and Industrial 4.0.

ACKNOWLEDGMENTS

The financial supports from the Ministry of Science and Technology under grant number MOST 107- 2622- E-224- 017- CC3 is greatly appreciated.

REFERENCES

1. S.M. Song and C.D. Zhang, "Forward Kinematics of a Class of Parallel (Stewart) Platforms with Closed Form Solutions ,," Prof. of IEEE International Conference on Robotics and Automation, Vol. 2, 1991, pp. 2676 2681.
2. D. Stewart , "A Platform with Six Degrees of Freedom," Proceedings of the Institution of Mechanical Engineers, vol. 180, part 1, no. 5, 1965, pp. 371-386.
3. M. H. Chiang, W. H. Chou and Y. N. Chen, "Analysis and Control of a Three-Axial Pyramidal Pneumatic Parallel Manipulator," Proceedings of 9th JFPS International Symposium on Fluid Power, Matsue, Japan., 2014.
4. C. T. Chen, J. C. Renn and Z. Y. Yan, "Experimental Identification of Inertia and Friction Parameters for Electro-hydraulic Motion Simulator," J. of Mechatronics, Vol. 21, Issue 1, 2011, pp. 1-10.
5. J. C. Renn, B. H. Li, "A Robot Arm Based on Parallel Pneumatic Flexible Muscle Actuators," MATEC Web of Conferences, Vol. 123, 2017, No. 00020.

The 11th JFPS International Symposium on Fluid Power HAKODATE 2020 Oct. 12-13, 2021 JFPS The Japan Fluid Power System Society

Development of Fingertip Mechanism With Contact Point Estimation

Kei MIKAMI* and Kotaro TADANO**

*Department of Mechanical Engineering, School of Engineering, Tokyo Institute of Technology
4259 Nagatsuta-cho, Midori-ku, Yokohama 226-8503, Tokyo, Japan
(E-mail: mikami.k.ac@m.titech.ac.jp)
** Institute of Innovative Research, Tokyo Institute of Technology
4259 Nagatsuta-cho, Midori-ku, Yokohama 226-8503, Tokyo, Japan
(E-mail: tadano.k.aa@m.titech.ac.jp)

Abstract. With the aim of achieving stable grasping with a robot hand, research has thus far been conducted on detecting the slip and contact conditions as well as adjusting the grasping force. However, fault tolerance is a noteworthy concern because the robot hand is expected to come into frequent contact with objects when the tactile sensor is positioned at the fingertip. Therefore, in this paper, a method is proposed for slip detection and contact point estimation that does not require a tactile sensor. This method involves the combination of a pneumatically driven parallel link finger module and a fingertip mechanism using a pneumatic cylinder. Through experiments, the ability to estimate the contact point position via the proposed finger mechanism is confirmed. Therefore, this method is expected to improve failure resistance and help realize a robot hand that can grip stably.

Keywords: finger mechanism, pneumatic, grasping control, slipping, tactile sensor-less system

1. INTRODUCTION

In recent times, the concept of human–robot coexistence in environments such as factories as well as in medical and service fields has been actively researched. Given the presence of robots in such environments, it is important to consider the performance and movement of the robot's hand, which comes into contact with objects during the robot's operation; moreover, the complicated movements and grasping forces of the robot should also be appropriately controlled. These aspects are being actively investigated [1] [2]. In the current industrial robot system, the robot's functions are divided between grasping an object via the hand and manipulating it via the arm. If the robot is to operate while maintaining the orientation of the object once grasped, the object should be positioned such that it can be picked up easily. This is possible in a structured environment such as a factory in the manufacturing industry, but very difficult in an unstructured environment such as in medical and agricultural fields. If the object can be manipulated, its orientation can be changed after it is picked up, which greatly increases the number of applicable tasks that can be performed with the object in hand. In addition, through compensation for the grasping force immediately when slipping occurs, the object can be gripped and prevented from falling down. Through measurements of the slip and compensation for the grasping force, the robot hand can be enabled to stably grip objects even when their properties (shape, mass, coefficient of friction, etc.) are not constant, or when an external force is applied to the object owing to a sudden stop in movement of the arm during transportation of the robot. Therefore, during manipulation of an object in hand, it is important to be able to detect the points at which the object is in contact with the finger.

To this end, some studies have used a contact sensor to detect the grasping state from the contact surface information. In addition, other studies have been conducted to adjust the grasping force by detecting the slip and contact state using a tactile sensor. Melchiorri proposed a method to control the grasping force via detection of the translational / rotational slip using a force / torque sensor with a strain gauge and a distributed tactile sensor [3]. However, despite their usefulness, these methods require the coefficient of static friction to be known. Maeno et al. proposed an elastic finger for detection of distribution, using a strain gauge with a curved surface, and they showed that any object with an unknown weight and friction coefficient can be lifted at any speed [4][5][6]. Their studies have employed tactile sensors to detect the slip. However, fault tolerance is a key concern because the robot's hand is expected to make frequent contact with objects when the tactile sensor is fixed at the fingertip. In addition, when a large number of sensors and distributed tactile sensors are mounted on the robot hand, issues concerning wiring processing and amplifier placement are presented. The higher the resolution is, the longer it takes to acquire sensor information and process data, which becomes a constraint during real-time control.

In this context, it is also possible to employ vision to obtain non-contact slip and contact information [7][8]. However, the processing speed depends on the frame rate of the vision camera. In addition, high resolution is required to detect minute displacements. Even when a high-speed camera is used, the placement of the camera becomes a problem, as space is often restricted around the hand, and a fixed camera may give rise to a camera

blind spot. It is also often necessary for adjustments to be made each time depending on the surrounding environment in terms of factors such as brightness.
To address these drawbacks, a pneumatically driven finger module is proposed in this paper. By means of driving the five-bar link using two pneumatic cylinders, the grasping force can be estimated without employing a force sensor, and a high grasping force-weight ratio can be achieved. Moreover, tactile sensor-less slip detection and contact point estimation are possible through the combination of the finger module and the fingertip mechanism via a pneumatic cylinder. By means of monitoring the contact point oscillation within the control cycle, it is expected that the slip can be detected at high speed.
When an external force is applied to the pneumatic cylinder with the compressed air supply valve closed, the internal pressure of the cylinder changes. The contact point can then be obtained by means of the estimated grasping force from the finger module and the variation in internal pressure of the cylinder. As the proposed mechanism does not involve a tactile sensor, it has an advantage in terms of the fault tolerance not being an issue.
The remainder of this paper is organized as follows. In Section 2, an outline of the proposed fingertip mechanism and contact point estimation method are presented. In Section 3, the control system of the fingertip mechanism and finger module is explained. In Section 4, the experimental results are presented. Finally, Section 5 summarizes the study and presents the concluding remarks.

2. FINGERTIP MECHANISM FOR CONTACT POINT ESTIMATION

2.1 Overview

Figure 1 shows the configuration of the developed fingertip mechanism and each variable thereof, and Figure 2 shows the layout of the proposed fingertip mechanism with the finger module developed in this study. The fingertip mechanism employs a pneumatic cylinder. The supply valve is opened, and compressed air is sent to one of the air chambers through the tube. Then, the supply valve is closed. The change in internal pressure within the pneumatic cylinder is measured using a pressure sensor. The other air chamber is open and under atmospheric pressure. The grasping force F_{grip} is the vertical force on the grasping surface of the tip link. The state corresponding to F_{grip} = 0 N is defined as the initial state. When F_{grip} and the position of the contact point are changed, the load applied to the pneumatic cylinder changes, followed by the cylinder length l_s.

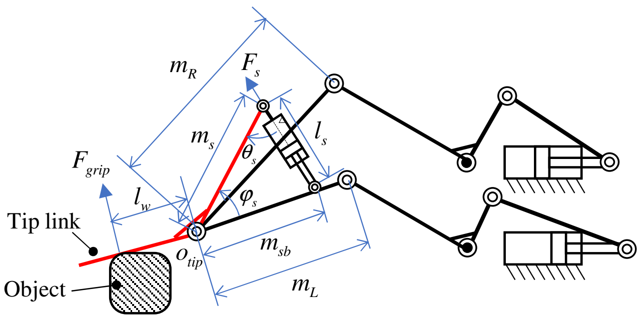

Figure 1. Finger module configuration

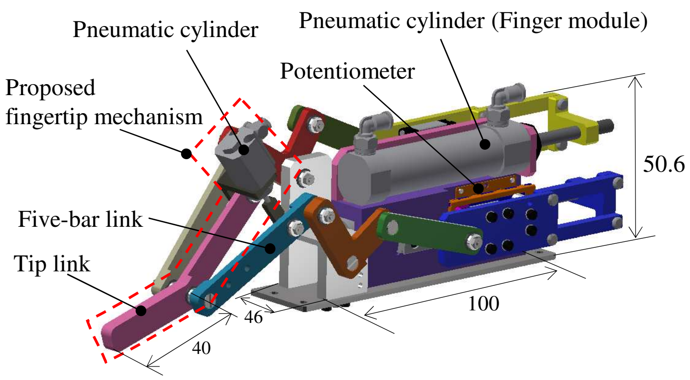

Figure 2. Layout of proposed fingertip mechanism with finger module

2

2.2 Contact Point Estimation Method

This section describes the proposed contact point estimation method via the fingertip mechanism. The torque around the fingertip joint o_{tip} is represented by the following relationship.

$$F_{grip} l_w = F_s \sin\theta_s \cdot m_s . \tag{1}$$

Here, l_w is the distance between the contact point at the object and o_{tip}, F_s is the reaction force of the pneumatic cylinder, θ_s is the angle between the pneumatic cylinder and fingertip link, and m_s is the distance between the rod end of the pneumatic cylinder and o_{tip} as shown in Figure 1. F_s is obtained as follows:

$$F_s = PA . \tag{2}$$

Here, P is the internal pressure (gauge pressure) of the pneumatic cylinder, and A is the area subjected to the pressure. θ_s can be obtained from the cosine theorem using the following equation.

$$\theta_s = \cos^{-1}\left(\frac{m_s^2 + l_s^2 - m_{sb}^2}{2 m_s l_s}\right) . \tag{3}$$

Here, m_{sb} is the distance between the base of the pneumatic cylinder and o_{tip}. Assuming an isothermal change, the estimated cylinder length $\hat{l}_s$ can be obtained from the changes in the internal pressure and volume of the pneumatic cylinder according to Boyle's law as follows:

$$\hat{l}_s = l_{s0} - \left(\frac{V_0 - V}{A}\right) \tag{4}$$

$$V = \frac{P_0 + 101.325}{P + 101.325} V_0 . \tag{5}$$

Here, V is the volume of the cylinder and pipeline together; and P_0, V_0, and l_{s0} are respectively the pneumatic cylinder internal pressure, volume, and cylinder length under no load. On substitution of Eq. (2)–(5) into Eq. (1), the estimated value of l_w is expressed as follows.

$$\hat{l}_w = \frac{PA}{F_{grip}} \sin\left(\cos^{-1}\left(\frac{m_s^2 + \left(l_{s0} - \left(1 - \frac{P_0 + 101.325}{P + 101.325}\right)\frac{V_0}{A}\right)^2 - m_{sb}^2}{2 m_s l_s}\right)\right) m_s . \tag{6}$$

F_{grip} is obtained from the external force F^{ext} at the tip of the finger module and the fingertip link angle ϕ_s. The fingertip link angle ϕ_s can be obtained from the cosine theorem using the following equation.

$$\phi_s = \cos^{-1}\left(\frac{m_s^2 + m_{sb}^2 - l_s^2}{2 m_s m_{sb}}\right) . \tag{7}$$

As this calculation process does not require consideration of parameters related to the properties of the object, it is useful even in an unstructured environment.

The external force F^{ext} can be measured directly using a force sensor; however, in the case of the finger module proposed herein, F^{ext} can be estimated from the differential pressure of the pneumatic cylinder and the kinematics model without a force sensor being required. This approach can potentially reduce costs and improve fault tolerance. In this study, the estimated value $\hat{F}^{ext}$, which is described later, is considered as the external force at the tip of the finger module.

2.3 Proposed Fingertip Mechanism

Figure 3 shows the developed fingertip mechanism with finger module. The total mass is 0.29 kg. This mechanism employs a pneumatic cylinder (SMC, CP2B4-5D). The drive cylinders of the finger module are the low-friction pneumatic cylinders (SMC, CJ2XB16-30Z) and were controlled via a five-port pneumatic proportional valve (FESTO, MPYE-M5-B) with an operating band of approximately 100 Hz. A linear potentiometer was used to detect the position of the cylinder rod, and the intake and exhaust of the pneumatic cylinder were controlled via a pneumatic solenoid valve (SMC, VQZ312-5M1-C6). The supply pressure to the proportional valves was set to 500 kPa, and the initial supply pressure of the pneumatic cylinder was set to 100 kPa. A semiconductor pressure sensor (SMC, PSE540) was used to measure the pressure of each port and the pneumatic cylinder.

3. STRUCTURE OF CONTROL SYSTEM

Figure 4 shows a block diagram of the grasping force compensation control and the compliance control system of the finger module. It can be applied to a pneumatically driven surgery support robot that estimates and controls external force without a force sensor, and also to the proposed mechanism. The reference force F^{ref} was generated from the position error of the tip and transformed into the reference driving force F_{cy}^{ref} for each cylinder using the Jacobian J_a. Moreover, F_{cy}^{ref} was controlled using a PI controller with a feedback force F_{cy}, calculated from the pressure difference in the cylinder. The control signal u was sent to the pneumatic proportional valve, and the force was generated by charging the compressed air into the actuator.
For a grasping task to be executed successfully, compliance and adaptability of the robot hand must be ensured for stable grasping. In this study, the method proposed by Tadano and Kawashima [9] was adopted for the control system. This control system has been applied to pneumatically driven surgery robots that perform external force estimation and force control without force sensors, and it is suitable for the proposed finger module.

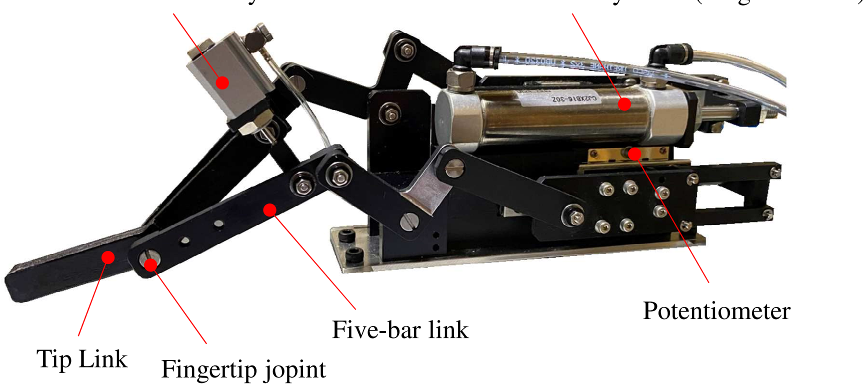

Figure 3. Overview of proposed fingertip mechanism with finger module

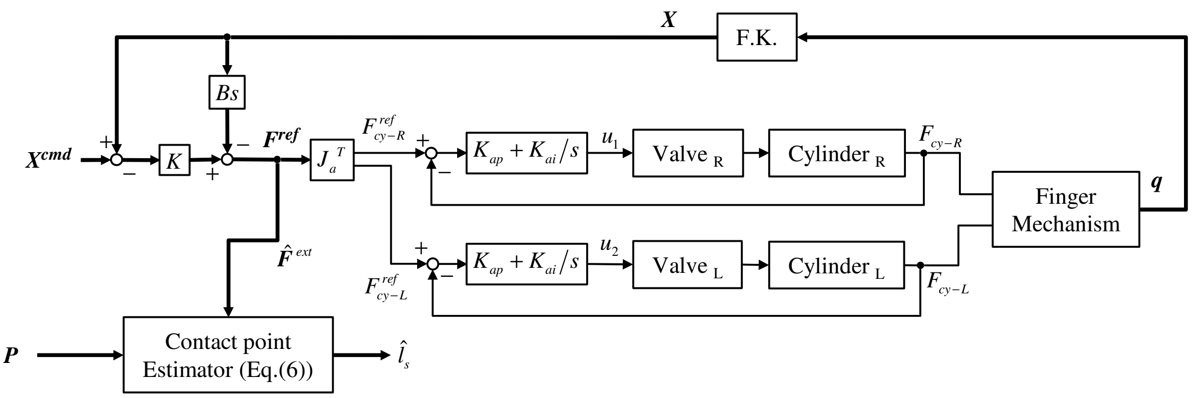

Figure 4. Block diagram of control system

The fingertip was designed as per the motion characteristics described in Eq. (8), where B is the viscosity and K is the stiffness.

$$\hat{F}_{ext} = \begin{bmatrix} B_x & 0 \\ 0 & B_z \end{bmatrix} \begin{bmatrix} \dot{x} \\ \dot{z} \end{bmatrix} + \begin{bmatrix} K_x & 0 \\ 0 & K_z \end{bmatrix} \begin{bmatrix} x^{cmd} - x^{res} \\ z^{cmd} - z^{res} \end{bmatrix}. \tag{8}$$

We constructed a control system to drive the developed finger module. An ADC board was used to capture the signals of the potentiometer and pressure sensor. Additionally, a voltage signal was input from the DAC board to the proportional valves. The control cycle was set to 1 ms.

4. EXPERIMENTAL RESULTS AND DISCUSSION

4.1 Experiment for Assessing Maintenance of Cylinder Internal Pressure

Accurate estimates via the proposed method cannot be obtained if an air leak is present. Therefore, it was necessary to confirm the airtightness of the experimental system. After the solenoid valve was closed under the internal pressure of the pneumatic cylinder, the cylinder rod was moved 10 times with a full stroke within 60 seconds. Then, l_s was measured using a potentiometer attached as shown in Figure 5.

Figure 6 (a) shows the measured value of the cylinder internal pressure, and Figure 6 (b) shows the measured value of l_s. Before and after the experiment, the internal pressure was held at 100 kPa. The amount of air leakage from the experimental system was deemed small enough to be neglected. However, in practical use cases, the internal pressure of the cylinder may gradually decrease when the cylinder is operated continuously for a long time. However, there is a period of time when the robot is not in contact with the object during the work cycle. At this time, if the internal pressure can be held for approximately 60 seconds, the solenoid valve can be opened so as to restore the cylinder pressure when the fingertip is not in contact with the object.

4.2 Experiment for Contact Point Estimation

As part of the study, we conducted an experiment to estimate the contact point using the developed fingertip mechanism and finger module. The object—an arc-shaped resin—was positioned on a linear stage so as to be movable horizontally. The displacement of the linear stage was measured using a potentiometer. An overview of the experimental system is depicted in Figure 7. The experimental parameters are listed in Table 1.

After the fingertip link was pressed against the object, the linear stage was moved to the left, as shown in Figure 7. Figure 8 (a) shows the internal pressure of the cylinder, and Figure 8 (b) shows the comparison between the measured cylinder length l_s (dotted line) and the estimated cylinder length $\hat{l}_s$ (solid line). The displacement of the initial length of the pneumatic cylinder from 14.5 mm to 11 mm could be estimated from the pressure change.

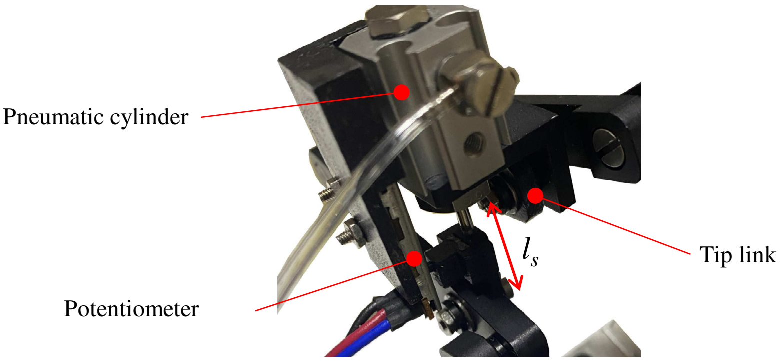

Figure 5. Potentiometer for air cylinder of fingertip mechanism

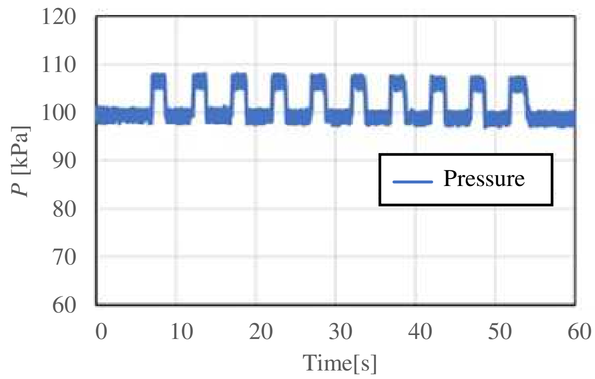

(a) Cylinder internal pressure

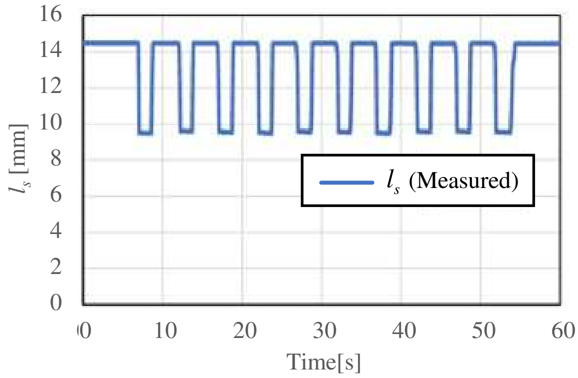

(b) Cylinder length

Figure 6. Results of experiment for assessing maintenance of cylinder internal pressure

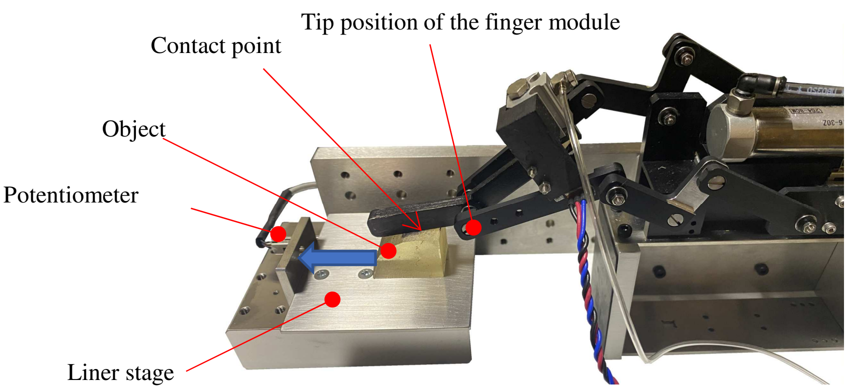

Figure 7. Overview of experimental system

Table 1. Parameters of experimental system

l_{s0}	14.5 [mm]	K	10.0 [N/mm]
V_0	967.6 [mm^3]	B	0.01 [Ns/mm]
P_0	100 [kPa]		

6

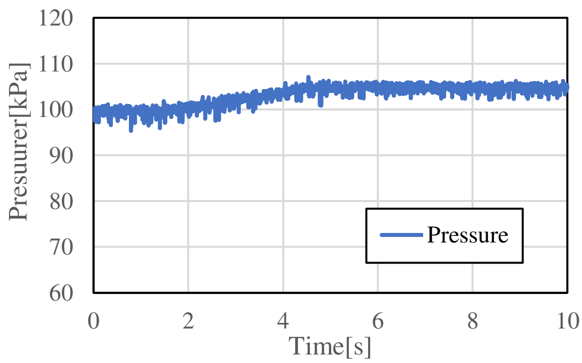

(a) Result of measuring cylinder internal pressure

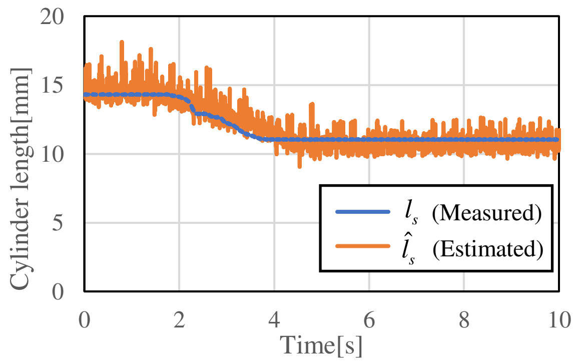

(b) Results of measuring cylinder length

Figure 8. Experimental result for cylinder length estimation

Figure 9 (a) shows the movement distance of the object measured using the potentiometer (Figure 7). Figure 9 (b) shows the comparison between the measured contact point l_w and the estimated contact point $\hat{l}_w$. The measured contact point l_w was obtained via geometric calculations based on the moving distance of the linear stage, cylinder length, and fingertip joint position, which were obtained from each potentiometer. The measured contact point $\hat{l}_w$ was obtained using Eq. (6)

The error between the measured and estimated values was approximately 3 mm or less, which was reasonable. As the estimated cylinder length adequately agreed with the measured value, the estimated grasping force used in the estimation calculation was supposed as the cause of the error. Although there were improvements in the grasping force estimation, changes in the contact position could be detected. Therefore, the estimated the contact position can be used for slip detection.

In the case of detection of slip, it was assumed that the slip could be suppressed by compensating for F_{grip} proportionally to the amount of fluctuation of l_w from the no-load state. By means of calculating the compensation force based on the amount of fluctuation l_w, the grasping force can be appropriately compensated even if there is an error in the absolute value of l_w. The static friction and hysteresis of the mechanism were determined to be the main factors affecting the error of the grasping force estimation. Ultimately, by means of improving the accuracy of the friction model, the error in l_w can be minimized.

CONCLUSION

In this study, we proposed a finger mechanism employing a pneumatic cylinder for contact point estimation. It was experimentally confirmed that the proposed finger mechanism could yield an accurate estimate of the position of the contact point without the requirement for a tactile sensor. Furthermore, by means of combining this mechanism with the finger module developed in this study, a low-cost robot hand with excellent fault resistance can be realized. Overall, the proposed finger mechanism is an elemental technology prototype of the robot hand, whereby stable grasping can be achieved.

In future work, we will consider the F_{grip} compensation method for stable grasping. In addition, we plan to manufacture a multi-finger hand based on the proposed finger mechanism and evaluate its functionality.

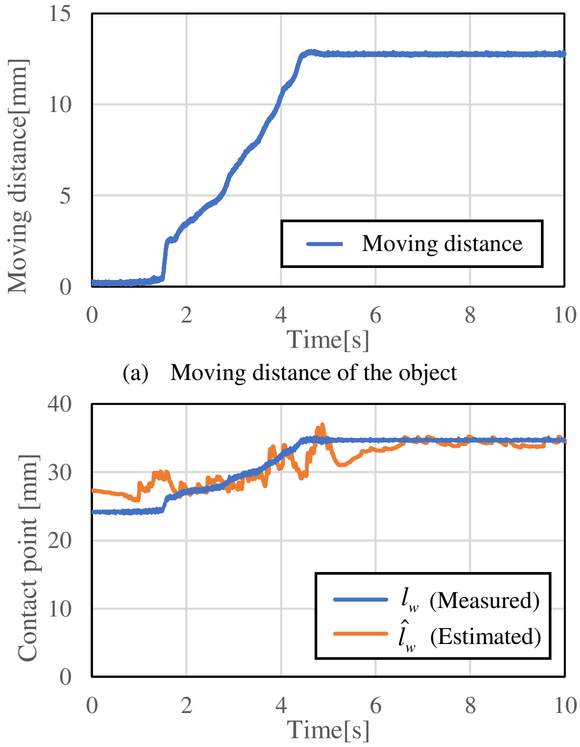

(a) Moving distance of the object

(b) Results of estimating contact point

Figure 9. Experimental result for contact point estimation

REFERENCES

1. KAWASAKI, T., et al., Dexterous Anthropomorphic Robot Hand with Distributed Tactile Sensor: Gifu Hand II, IEEE/ASME Trans. on Mechatronics, Vol.7, No. 3, pp.296-303 (2002)
2. MIZOGUCHI, Y., et al., Development of Intelligent Robot Hand Using Proximity, Contact and Slip Sensing, Trans. Soc. Instrum. Control Eng., Vol.46, No.10, pp.632-640 (2010) (in Japanese)
3. C. Melchiorri, Slip Detection and Control Using Tactile and Force Sensors, IEEE/ASME Transaction on Mechatronics, vol.5, no.3, pp.235-243, 2000.
4. MAENO, T., et al., Control of Grasping Force by Detecting Stick/Slip Distribution at the Curved Surface of Elastic Finger, Proceedings of IEEE International Conference on Robotics and Automation, pp. 3896-3901, 2000
5. YAMADA, D., et al., Artificial Finger Skin having Ridges and Distributed Tactile Sensors used for Grasp Force Control, Journal of Robotics and Mechatronics, Vol. 14, No. 2, 2002, pp. 140-146
6. MAENO, T., et al., Grip Force Control by Detecting the Internal Strain Distribution Inside the Elastic Finger Having Curved Surface, Trans. JSME C, Vol.64, No.620, pp.1258-1265 (1998) (in Japanese)
7. IKEDA, Y., et al., Grip Force Control for an Elastic Finger Using Vision-Based Incipient Slip Feedback, Proceedings of IEEE/RSJ International Conference on Intelligent Robots and Systems, pp.810-815, 2004
8. IKEDA, A., et al., Grip Force Control of the Elastic Body based on Contact Surface Eccentricity During the Incipient Slip, Journal of Robotics Society of Japan vol. 23, no. 3, 2005, pp. 337-343. (in Japanese)
9. TADANO, K., et al., Development of a Master Slave Manipulator with Force Display using Pneumatic Servo System for Laparoscopic Surgery, Proceedings of 2007 IEEE International Conference on Robotics and Automation, pp. 947–952, 2007

The 11th JFPS International Symposium on Fluid Power HAKODATE 2020 Oct. 12-13, 2021 The Japan Fluid Power System Society

Development of Outdoor Activity Assist Suit

Toshihiro YOSHIMITSU *, Rui MATSUMOTO *

* Department of Robot mechatronics, Faculty of Engineering
Kanagawa Institute of technology
1030 Shimo-oghino,Atsugi ,Kanagawa 243-0292
(E-mail: yosimitu@rm.kanagawa-it.ac.jp)

Abstract. In recent years, loss of lives and rescue has increased for nature disaster. In rescue operations what active “long hour”, “outdoor” and “hill”, is broken out exhaustion and injury. Then, we invented to Assist Suit for outdoor activities because it’ll be effective in preventing injury and tired. Assist Suit we invented uses a pneumatic cylinder different of a lot of Assist Suit including HAL the representative Assist Suit made by Cyber Dyne use an electric motor helped joint torque. Using pneumatic cylinder for Assist Suit, it has advantaged at weight and long hour activities we thought. In this study, we putted stress to making control system for Assist Suit and inserting a spring element in power source experimentally. The purpose of this study is to develop a lightweight assist suit actuator system with lower joint motion range and suitable for outdoor activities.

Keywords: Pneumatic, Power assist, Ejector, Regenerator

INTRODUCTION

In recent years, natural disasters such as eruptions have caused an increase in human damage and rescue activities. In rescue activities, there are many cases in which "long hours", "outdoors", "rough terrain", and "sloping areas" are performed, so that the load applied to the lower limbs increases. It is feared that the rescuer may suffer fatigue and injuries due to burden on lower limbs.
The mechanisms used in indoor assist suits are classified as either "there is a small degree of freedom and there is a function to support the direction in which assistance is needed" or "the joint has some flexibility but no function to support the joint" It is. On terrain and sloping terrain, it is necessary to implement conflicting effects such as free movement that does not hinder the activity and assisting the movement of the joint to prevent injuries and sprains. In this study, we develop an actuator system for assist suits that has joint range of motion and reduces the weight of the mechanism and is suitable for outdoor activities.

Outdoor Activity Assist Suit

In situations such as mountain rescue or landslide disasters where work must be continuously performed on uneven or sloping terrain, we develop a power assist suit for lower limbs for the purpose of reducing physical load, extending activity time and preventing injuries to the rescuer himself. The functions required for the lower limb assist suit include weight reduction, lower limb burden on slopes, prevention of injuries, and long-term activities.

Figure 1 shows the outline of the outdoor activity assist suit created in this study. The impact applied to the knee joint is greater when descending than when climbing, which may cause fatigue and injuries due to it.
The aim of outdoor activity assist suit is to absorb the impact applied to the knee joints when descending a slope with an assist unit such as a pneumatic cylinder. Specifically, the rod speed of the cylinder controls the flow rate of compressed air discharged from the head side. It is characterized by aiming for shock absorption.

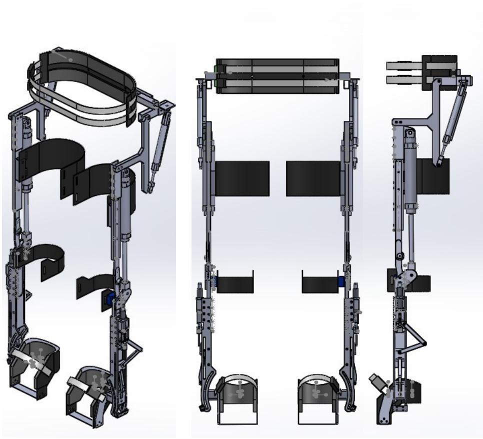

Figure 1. Outdoor Activity Assist Suit

Table1 Assist Suit Elements

Size [mm]	973×475×266
Weight	7.1kg
Power Source	Pneumatic Cylinder(ϕ 32)
Knee range of motion	120Degrees

REGENERATIVE ACTUATORS

This assist suit is a passive actuator that absorbs the impact force applied to the knee joint when going downhill. In previous research, the impact force was absorbed by controlling the opening of the speed controller with a servomotor for flow control. The speed controller controls the outflow speed by the throttle mechanism, but the energy is dissipated as resistance and cannot be used.

In this study, we use an ejector instead of a speed controller for flow control to absorb the impact force when descending and to regenerate energy when descending.

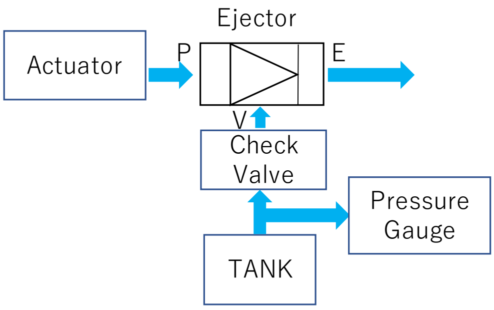

Fig.2 Energy regeneration system

ACTUATOR REGENERATIVE FORCE

The energy regeneration by the ejector includes an ejector cycle circuit. In this study, the vacuum pressure generated by the ejector is used as regenerative energy to drive the actuator while controlling the speed during high-speed movement of the cylinder by the throttle of the ejector. In order to confirm the effectiveness of this mechanism, two types of ejectors of different sizes, cylinder speed-load experiment, cylinder operation-vacuum pressure experiment, were performed and the effectiveness was confirmed.

The experimental results are shown in Fig. 3,4. The flow rate was controlled by the nozzle of the ejector, and the load increased as the effective area of the ejector was smaller, and the cylinder speed was faster.

As an energy regeneration experiment, a small pressure vessel (capacity: 18.0 cc) was connected to the ejector, and the number of reciprocations of the cylinder and the pressure in the pressure vessel were measured. The experimental results show that the smaller the effective area of the ejector, the higher the energy regeneration effect.

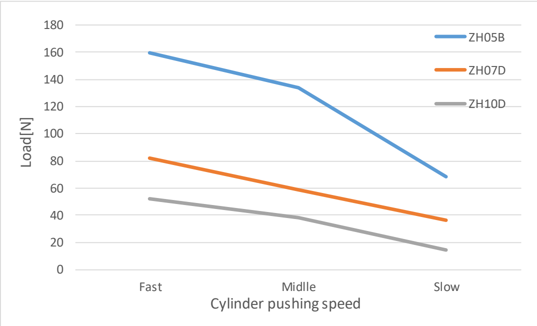

Fig.3 Actuator load experiment

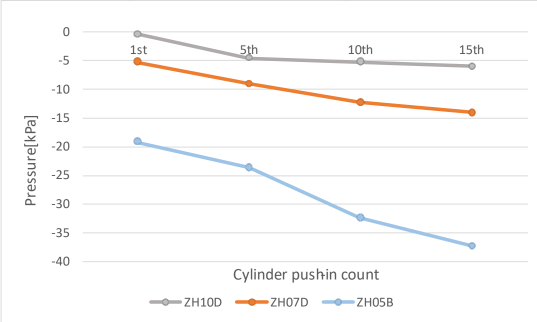

Fig.4 Ejector vacuum pressure experiment

CONCLUSION

In this study, we proposed a mechanism using a pneumatic cylinder and an ejector as an actuator for an outdoor activity assist suit that can save energy and be active for a long time. The mechanism proposed by this study uses a throttle of a vacuum generation mechanism to absorb the impact of a physical load during outdoor activities on a downhill, and to reduce the vacuum pressure generated when compressed air passes through the ejector. The effectiveness of the system that can be used secondarily by accumulating it in the tank was confirmed.

REFERENCES

Yoshimitsu T., Shoji T., DEVELOPMENT OF POWER ASSISTING SUIT FOR ASSISTING RESCUE CREW , Proc. of jfps2017 , 2D32 (2017)

2. Sankai Y., Kawamura Y., Study on Hybrid Power Assist System HAL-1 for Walking Aid using EMG, JSME Proceedings of the Ibaraki Lecture Meeting, pp.269-270(2000)
3. Sano K., Yagi E. : Study on a Power Assist System for Overhead Harvesting / Slope Walking, Proc. of 54th Automatic Control Alliance Lecture , pp.827-829 (2011)
4. TAKEUCHI .H, et al., High Efficiency "EJECTOR CYCLE" Refrigerator , Refrigeration 79(920), pp. 431-432(2004)

The 11th JFPS International Symposium on Fluid Power HAKODATE 2020 Oct. 12-13, 2021 The Japan Fluid Power System Society

Examination on Attitude Control System of Hand Manipulator with Compact Pneumatic Cylinders by E-FRIT

Shogo TOMITA*, Eiji MURAYAMA** , Yukio KAWAKAMI**

*Graduate School of Science and Engineering, Shibaura Institute of Technology
307 Hukasaku, Minuma-ku, Saitama, 337-8570 Japan
(E-mail : md20061@shibaura-it.ac.jp)
** Faculty of Science and engineering, Shibaura Institute of Technology
307 Hukasaku, Minuma-ku, Saitama, 337-8570 Japan

Abstract. Pneumatic system has some merits that being strong against overload and safe for humans because it drives by air, a compressible fluid. Taking advantage of that merits, some research about robots that are used pneumatic actuator have been conducted. In the context of that, we have developed hand manipulator which is driven by compact pneumatic cylinder. Although pneumatic actuators are more difficult to control precisely than electric motor used conventionally, for this problem, we are studying the application of control using E-FRIT (Extended Fictitious Reference Iterative Tuning), which is a PID gain adjustment method based on experimental data. In this paper, we show the result of applying controller design with E-FRIT to developed manipulator.

Keywords: Hand manipulator, Pneumatic cylinder, E-FRIT, PID control, Control system

INTORODUCTION

Today, robots are intervening many of fields such as not only industry but also, care, entertainment, etc. While the distance between human and robots will be close, it will be more required that we develop the robot which is safe to humans. That kind of field of research is named “soft robotics” and pneumatic actuator is collecting a lot of attention as a safe actuator [1] [2].

There are some studies of manipulator with pneumatic actuator. In generally, using pneumatic rubber artificial muscle [3], using bursiform actuator which drive putting in and out air [4], and so on. Our team focuses on using compact pneumatic cylinder at robot hand’s joint. Because pneumatic cylinder drives linearly, we have to convert the linearly motion to rotational motion to adjust robot hands, on the other hand, there is a merit that it can be controlled more easily than other pneumatic actuators because of its simple construction.

We have continued research of manipulator using pneumatic cylinder. In previous researches, some control methods were suggested to pneumatic robotics system (e.g. Simple Adaptive Control, Sliding Mode Control) [5]. They achieved results, but there is a problem that it takes time and effort to identify the system. Also, the manipulator didn’t have reproducibility because of hardware problems. So, we made a new manipulator which can improve the hardware problems, and we are trying to apply E-FRIT, one of the PID gain adjustment methods to force control and attitude control. We achieved force control accuracy of ±0.3[N] by using estimated force in previous research (Figure 1)[6], so in this study, we focus on the attitude control.

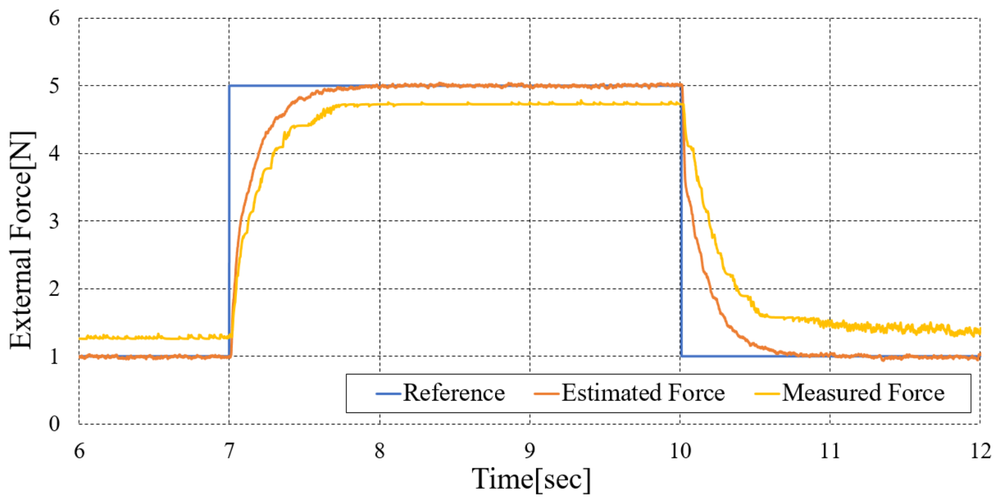

Figure 1. Achievements about force control of manipulator[6]

MANIPULATOR OVERVIEW

Figure 2 shows overview of developed manipulator. It has three joints as with human and it is driven by compact pneumatic cylinder. Table 1 shows the pneumatic cylinder's specifications. In this manipulator, slider lever mechanism makes it possible to convert linearly motion to rotational motion. Figure 3 shows that mechanism overview and Figure 4 shows that manipulator's range of motion. At the mechanical part, we use bearings and bush made of resin to smoothly convert.

This manipulator has potentiometers and pressure sensors to control attitude and force. It is driven by pneumatic cylinder, so we can control the force without using force sensors. If we try to control the force using force sensors (etc. strain gauge), it may not be able to do because of the shape of the object that the sensors do not touch (Figure 5), so force control using pressure difference in the pneumatic cylinder do not depend on the shape of object.

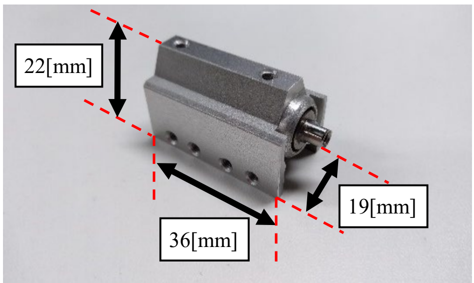

(a) Pneumatic cylinder size

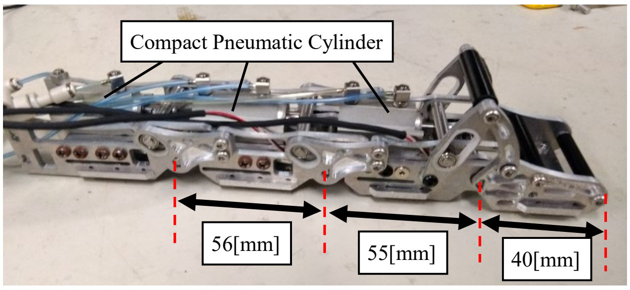

(b)Used manipulator in this study

Figure 2. Developed manipulator

Table 1. Specification of compact pneumatic cylinder

Manufacturer	KOGANEI(Custom order)
Action	Double acting
Fluid	Air
Bore size	10[mm]
Maximum operating pressure	1.0[MPa]
Minimum operating pressure	0.03[MPa]
Standard Strokes	20[mm]
Weight	23.9[g]

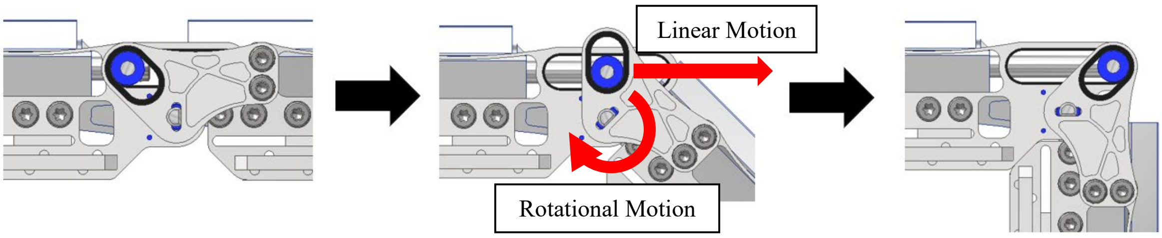

Figure 3. The mechanism of manipulator's joint

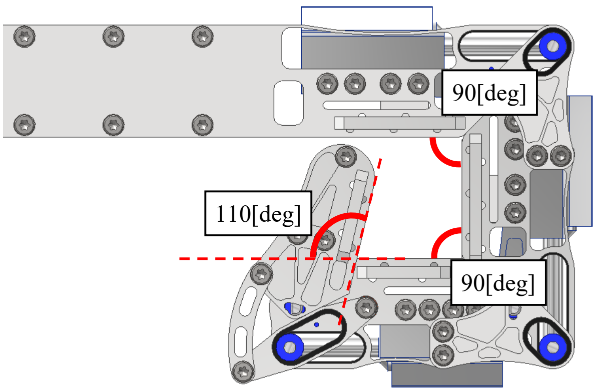

Figure 4. Manipulator's joint angle

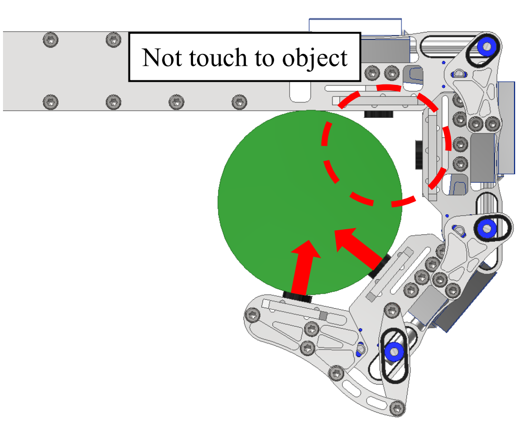

Figure 5. Manipulator's state when grasping (not touch force sensor)

THE EXPERIMENTAL DEVICE OF MANIPULATOR

Figure 6 shows the pneumatic circuit of manipulator used in this study. The manipulator has three kinds of sensor, potentiometers, pressure sensors, and load cells. Potentiometers are used for feedback of manipulator's joint angle to control its attitude. Pressure sensors are used for feedback of pressure inside the pneumatic cylinders to control manipulator's joint torque.

In this manipulator, the control targets are electro-pneumatic regulators which are connected compact pneumatic cylinders at manipulator's joints. Electro-pneumatic regulator is proportional control valve, and it continuously control air pressure in proportion to the input electric signals. Figure 7 shows the response of electro-pneumatic regulator (SMC: ITV0051-3MS). We control them in order to control the manipulator's attitude and joint torque (it's same to control manipulator's gripping force). Incidentally, this time, we control air pressure only head-side of cylinders. Rod-side pressures are fixed about 0.09[MPaG] (that value is electro-pneumatic regulator's output pressure when input 1[V]).

We used MATLAB/Simulink® to design controller and implemented using Simulink Real-Time™.

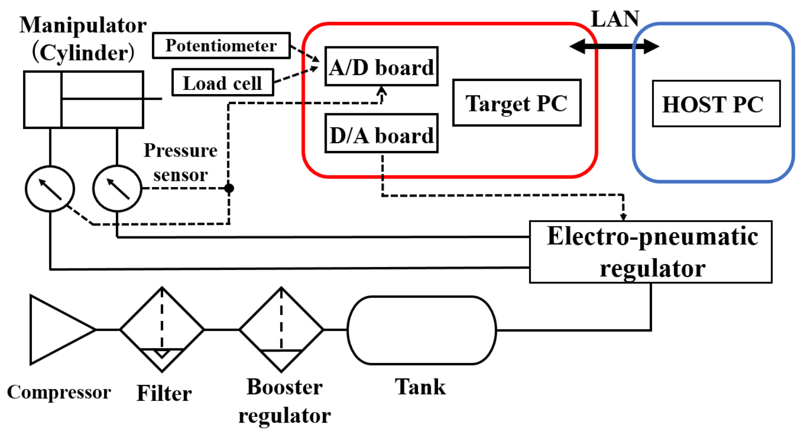

Figure 6. Pneumatic circuit used in this study

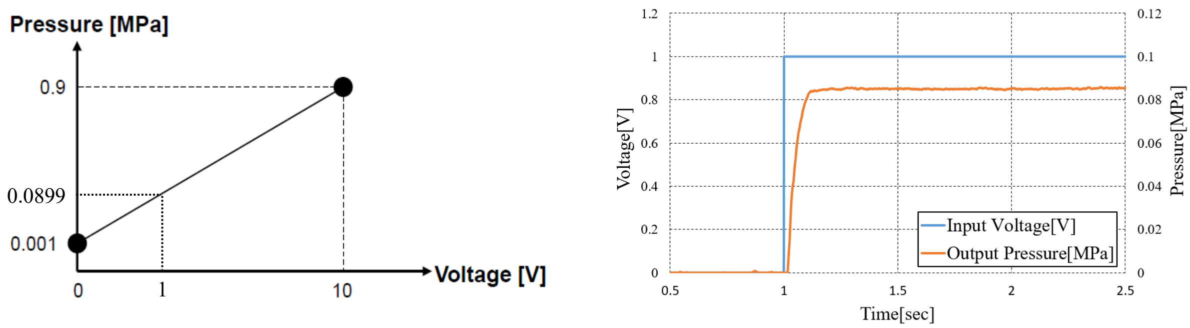

(a) Relationship between Voltage and Pressure (b) Step Response

Figure 7. Electro-pneumatic regulator response

PID GAIN TUNING BY E-FRIT [7]

The manipulator controls attitude and force. For each, we adopted PID control about control method. PID control refers only target value and output value so that we can control the system if we don't know the internal model of the plant, but it has demerit that the difficulty of gain tuning. So in recent years, method of auto gain tuning is under intense investigation. E-FRIT is one of the suggested method of auto gain tuning. It doesn't have to construct simulation models. It needs only stable closed loop data and settling time we specify.
Eq.(1)-Eq.(3) are some parts of relational expressions used in E-FRIT. Eq.(1) shows expression PID controller, Eq.(2) shows expression of reference model, and Eq.(3) shows variable which it optimize. In Eq.(2), the value of n is 2 if the controller is PID control or PI-D control (if you use I-PD control, the value of n is 3). T_{99} is settling time which user can determine arbitrarily. E-FRIT optimize L at Eq.(2) and PID parameter at the same time.

$$C(s) = K_p + \frac{K_i}{s} + K_d s \tag{1}$$

$$M(s) = \frac{1}{(\tau s + 1)^n} e^{-Ls}, \tau = \frac{T_{99}}{4.4n^{0.6}} \tag{2}$$

$$\emptyset = (K_p, K_i, K_d, L) \tag{3}$$

ATTITUDE CONTROL

We performed attitude control experiment on the manipulator's second joint using E-FRIT explained above.
First, we performed a proportional control closed loop experiment (only P control) as preliminary experiment for E-FRIT. Figure 8 shows the result. It is the step input response which reference value is 45[deg].
Table 2 shows the result of E-FRIT calculated gain. Based on this result, we tuned PID gain. Figure 9 shows the step input response as the target value is 45[deg] using the tuned gain. According to this result, we were able to confirm that manipulator's joint angle followed reference value smoothly and overshoot was not seen. It is thought that E-FRIT is valid method for manipulator which drives compact pneumatic cylinder.
Figure 10 shows the result of step response which target is 60[deg] using the same gain as the target value is 45[deg]. It can be seen relaxation oscillations around target value. We found from these results that we have to tuning the gain every time that we change the target value because it has low robustness. There is a small difference about delay time in Figure 9 and Figure 10, this is due to the backlash of the manipulator.

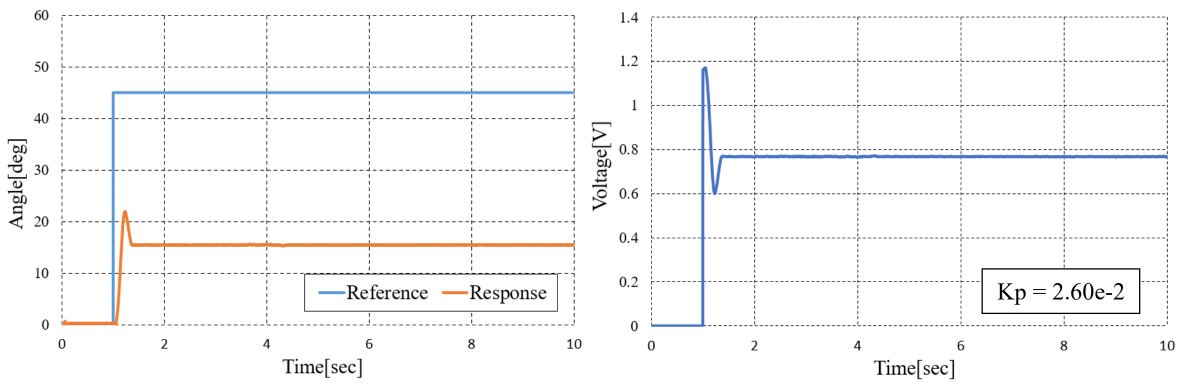

(a)Process variable (manipulator's angle) (b) Manipulated variable(electro-pneumatic regulator)
Figure 8. Preliminary experiment result(P control)

Table 2. E-FRIT calculated result

Kp	2.792e-2
Ki	2.693e-2
Kd	1.000e-3

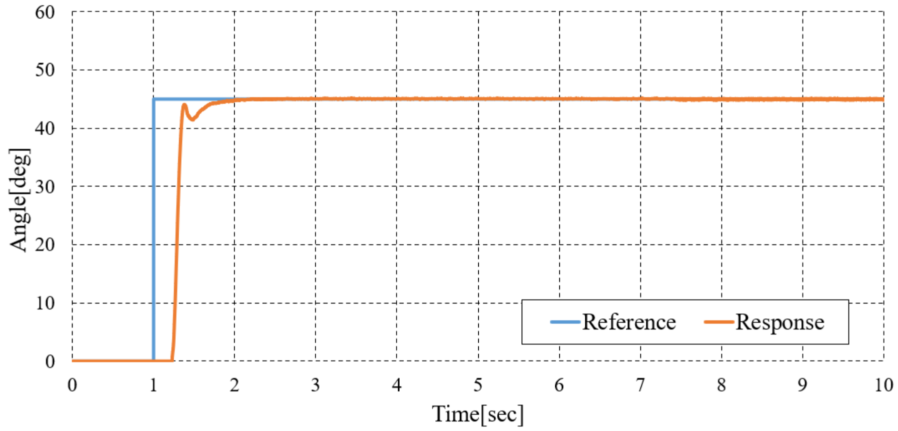

Figure 9. Step response as the target value is 45[deg] (PID control)

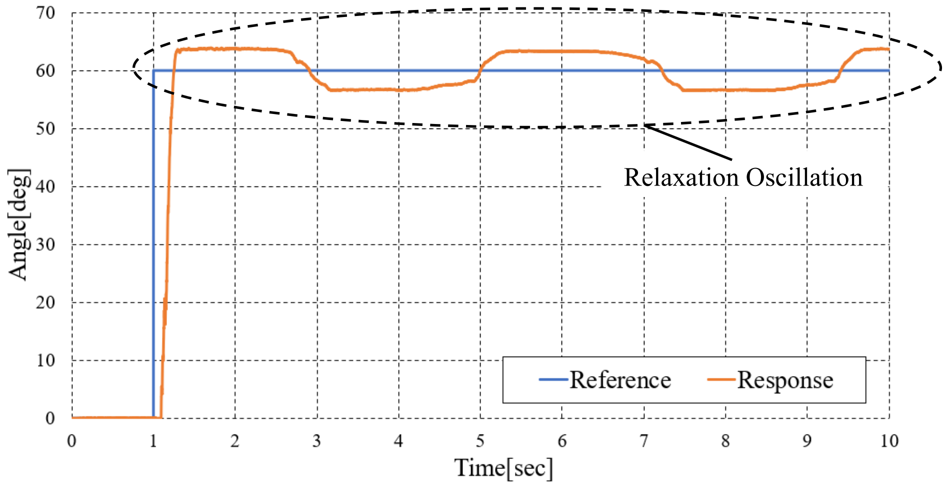

Figure 10. Step response as the target value is 60[deg] (same gain in Figure 9.)

SUGGESTION DISTURBANCE OBSERVER FOR ATTITUDE CONTROL

In attitude control, there is a problem that low robustness to the target value. It is thought that the cause of some disturbances such as frictions. To achieve higher control performance, we thought to apply disturbance observer for attitude control system. Generally, positioning control performance of pneumatic servo system is related to the nonlinear friction characteristics, and there are some previous researches that disturbance observer used as compensation [8] [9].

To design disturbance observer, we have to identity the system of control target to obtain nominal model. To identify the system is a very difficult task, so we lost the advantage of E-FRIT that we can significantly reduce the time and cost required for controller design. There, we calculate the nominal model to use model matching of E-FRIT.

In feedback control, the transfer function P(s) from input to output can be expressed as Eq.(4).

$$\mathrm{P(s)} = \frac{C(s)G(s)}{1+C(s)G(s)} \tag{4}$$

In this control system, C(s) is PID controller calculated by E-FRIT, and G(s) is manipulator's plant model which we want to know. E-FRIT defines closed loop reference model as M(s) showed Eq.(2). If E-FRIT satisfy the model matching, we can think that Eq.(2) is equal to Eq.(4) and Eq.(5) is established. We can estimate the plant model to solve Eq.(5) for G(s).

$$\frac{1}{(\tau s+1)^2}e^{-Ls} = \frac{C(s)G(s)}{1+C(s)G(s)} \tag{5}$$

Figure 11 shows the result of E-FRIT model matching. In this result, there is less difference between actual manipulator's response (blue line) and E-FRIT designed model's response (red line). Therefore, we considered that it satisfied model matching, and we designed disturbance observer from the result.
Figure 12 shows that the control system of manipulator's attitude controller with disturbance observer. The inverse model of nominal model is non proper, so we add Butterworth filter (F) to change to proper. Also, we add the low pass filter (L) in estimated disturbance because potentiometer contains measurement noise.
By the use of disturbance observer made from E-FRIT, we performed manipulator's attitude control experiment with inputting disturbance. Manipulator's joint angle is made to follow a target value (45[deg]), and 10 seconds later, we input 0.5[V] to electro-pneumatic regulator's manipulated voltage as disturbance.
Figure 13 shows the result of comparison with disturbance and estimated disturbance. From this result, we found that the disturbance observer made by E-FRIT can roughly estimate disturbance. Figure 14 shows actual manipulator response. It can be seen that the response with using disturbance observer is less affected by disturbance and it more quickly converges to the target value than not using.

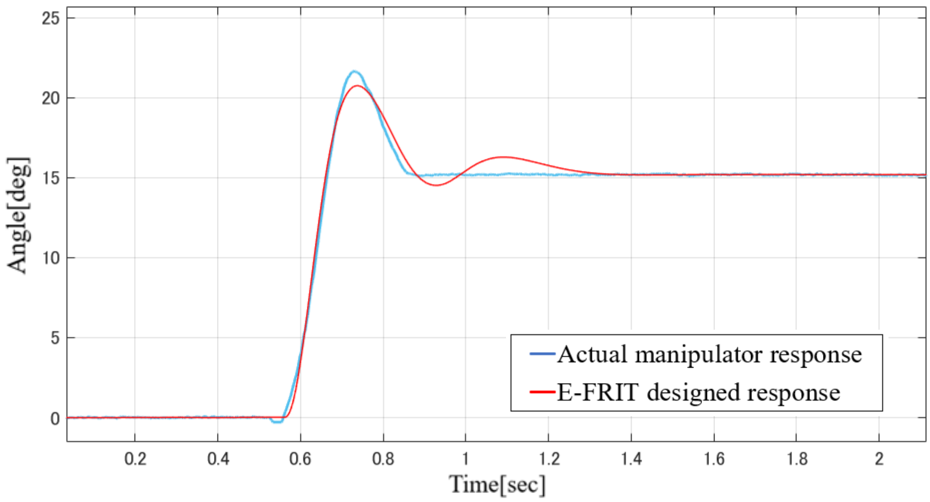

Figure 11. Model matching result by E-FRIT

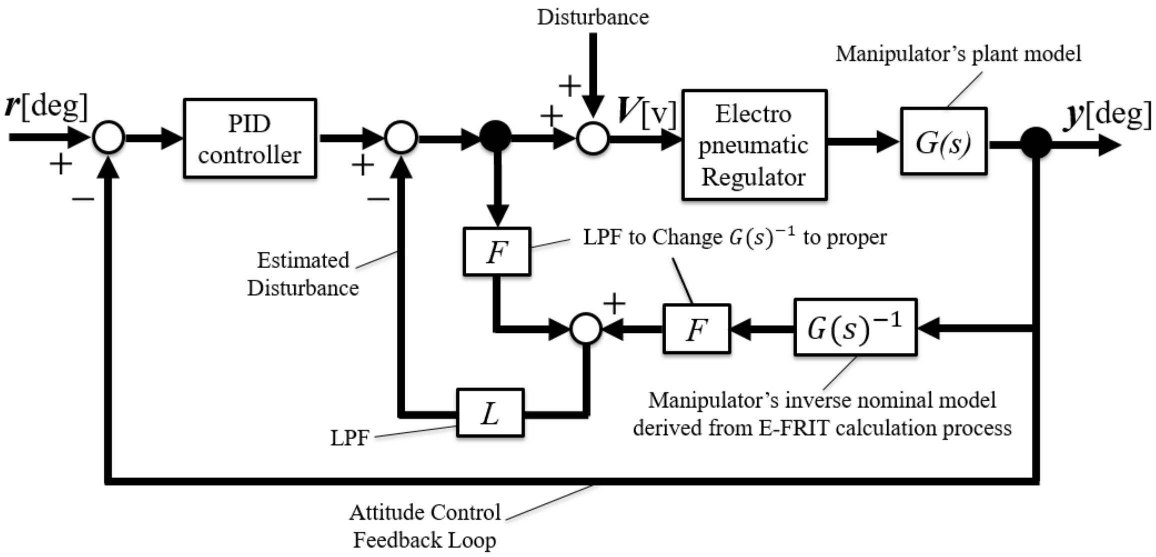

Figure 12. Disturbance observer

6

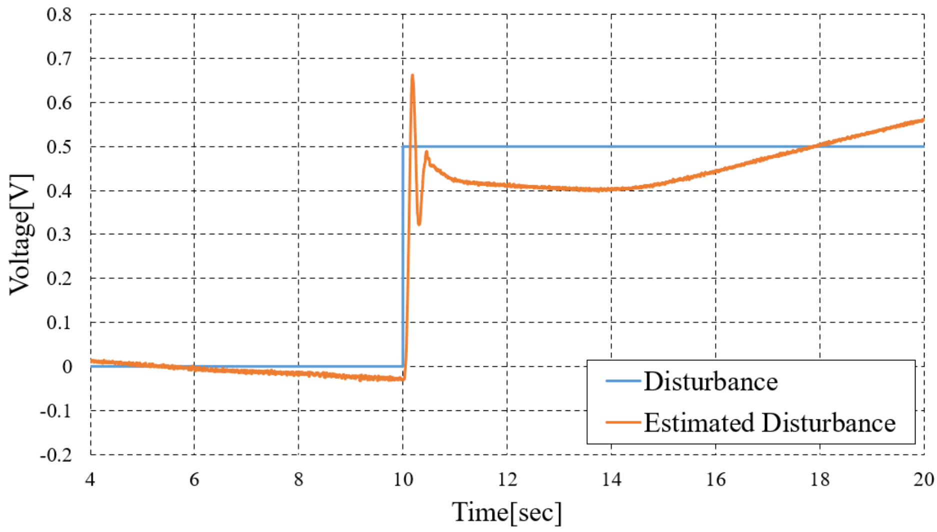

Figure 13. Comparison input disturbance and observed disturbance

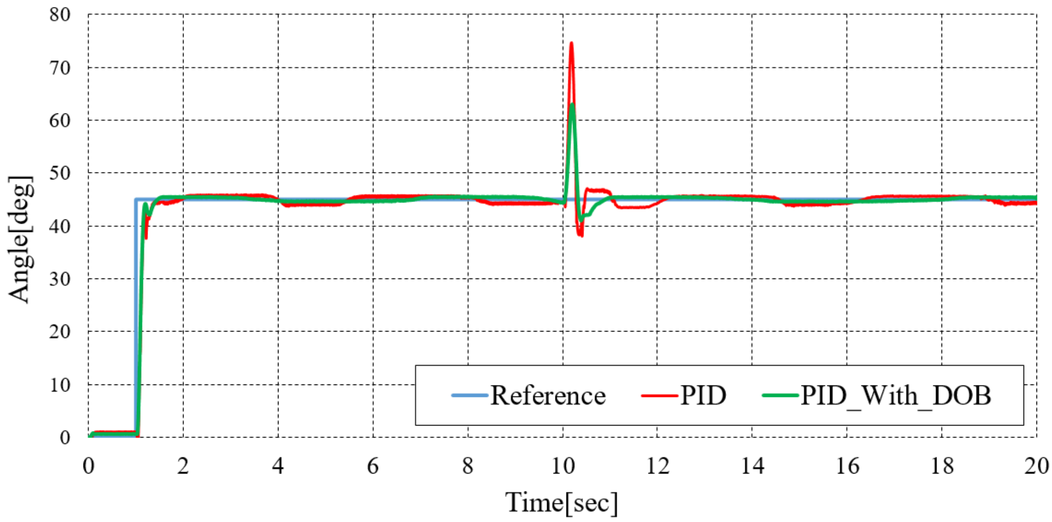

(a) Whole response

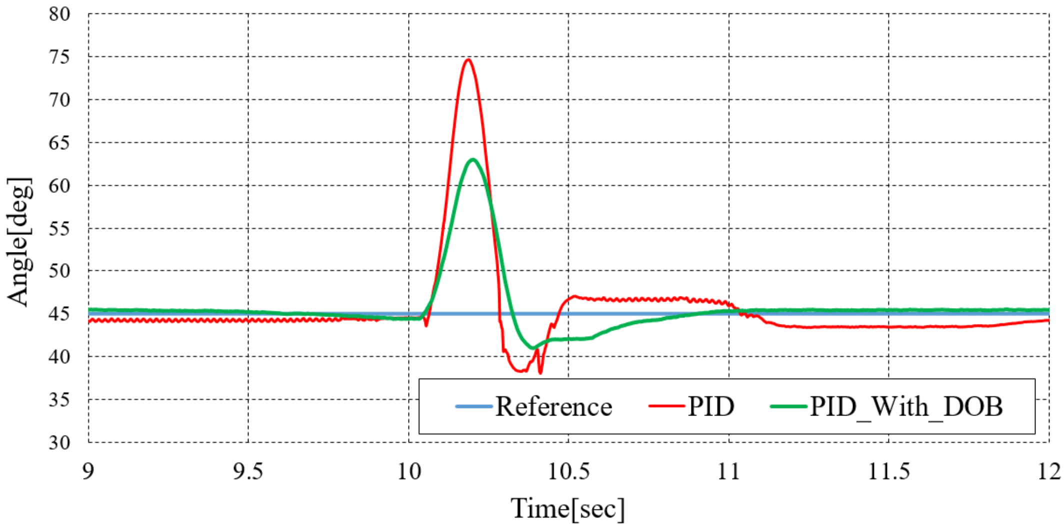

(b)Response around disturbance

Figure 14. Comparison of manipulator's response to disturbances

CONCLUSION

In this study, we developed hand manipulator which is driven by some compact pneumatic cylinders and assess about attitude and force control performance. In previous research, we could achieve a certain result about force control, we focused on attitude control in this study. We designed the attitude control system by PID control whose gain tuned by E-FRIT that one of the method of experimental data auto gain tuning. We could design it to reach the target value quickly and no over shoot, but we found the problem that the control performance deteriorates when we change the target value. There is a need to tuned suitable PID gain every time we change the target value, so we have to another approach to design the control system.
In order to improve the control system of attitude, we considered apply disturbance observer. In usual, we have to identify the system because we need to know the plant nominal model to design disturbance observer, but we focused on the model matching of E-FRIT and we devised that to derive the plant nominal model from result of E-FRIT calculation process.
We made a manipulator's model as described above and built the disturbance obsever. It could estimate disturbance to some extent, and be able to improve the attitude control performance of the manipulator.
In future, we will evaluate the performance of the manipulator as a whole, not just only one joint.

REFERENCES

1. Uchiyama, M., Soft Robotics, Journal of the Robotics Society of Japan, Vol.17, No.6, 1999, pp.756-757.
2. Takaiwa, M., Status and Prospects of Pneumatic Systems, Journal of the Society of Instrument and Control Engineers, Vol.56, No.4, 2017, pp.241-242.
3. Yasunori, O., Development of a Human Safe, Multi-Degree-of-Freedom Robot Arm Technology using Pneumatic Muscles, Robotics Society of Japan, Vol.28, No.3, 2010, pp.302-310.
4. Nishioka, Y., Pneumatic Soft Robot Arm, Journal of the Robotics Society of Japan, Vol.33, No.9, 2015, pp.10-13.
5. Murayama, E., Model-Based Design Approach for Bipedal Robot, Hydraulics and pneumatics, Vol.55, No.3, 2016, pp.23-29.
6. Tomita, S., Development of Hand Manipulator with Compact Pneumatic Cylinder, The Proceeding on Autumn Conference of Japan Fluid Power System Society, 2020, p.21.
7. Kano, N., Actual use of operational data in the process industry, IEEJ Transactions, Vol.131, No.4, 2011, pp.710-717.
8. Noritsugu, T., Design of Pneumatic Positioning Control System Using Disturbance Observer, Transactions of the Society of Instrument and Control Engineers, Vol.31, No.1, 1995, pp.82-88.
9. Iwasaki, M., Optimal Control of Pneumatic Cylinder with Disturbance Observer, Journal of the Japan Hydraulics and Pneumatics Society, Vol.27, No.6, 1996, pp.769-802.

The 11th JFPS International Symposium on Fluid Power HAKODATE 2020 Oct. 12-13, 2021 The Japan Fluid Power System Society

Design and Fabrication of a Soft Filament-polymer Jamming Actuator

Peng QIN, Zhonghua GUO, Mengyu DOU, Zhongsheng SUN, Yan TENG, Xiaoning LI

School of Mechanical Engineering, Nanjing University of Science and Technology
Xiaolingwei 200, Nanjing, Jiangsu Province, P. R. China
(E-mail of corresponding author Zhonghua GUO: gzh@njust.edu.cn)

Abstract: In order to enhance the performance of soft actuator and overcome the problems existing in former soft actuator, a new type of filament-polymer jamming actuator is proposed. The variable stiffness is realized by filament and polymer combination and mix structure with jamming technology. By using such actuator, the large-scale variable-stiffness gripper is proposed and the bending stiffness are measure through experiments. The variable stiffness grippers successfully take the gripping operation while those grippers without variable stiffness fail to grasp the movable objects. The results show that soft filament-polymer jamming actuator has better dynamic characteristics and they are the better choice for fabricating the gripping ends.

Keywords: Pneumatic soft actuator, Fiber filament, Stiffness, Jamming

INTRODUCTION

Due to the advantages of soft material actuators, such as good deformation ability, unlimited freedoms, and adaptability to variable environments, it becomes an important element in automatic robots in recent years. As the core components of soft robots, the performance of the soft actuators is critical for the whole performance of the robots. The deformation ability of the actuators has been extensively studied, such as the deformation of soft actuators in artificial elephant trunk, jellyfish, and worms[1-5].

Stiffness is the important parameter of the soft actuator and it has the great influence on the dynamic performance of the actuator and gripping ends. It is essential to study the stiffness characteristics of soft polymer actuators. The difference in the material and structure of the soft actuator will result in changes in the stiffness of actuator, which will complicate the actuator stiffness study.

In this study, new structure is proposed by using silicone and filament. Influences on bending stiffness from the material parameters are studied, such as diameter, coverage, inner wall thickness and air pressure of composite fiber filament chamber. The results show that the bending stiffness increases with the increment of coverage ratio and inner wall thickness. Although there is not monotonic function of the relationship between bending stiffness and filament diameter, there is a maximum value in the experimental figure. The fiber material type has little effect on the bending stiffness, and the bending stiffness increases with the increment of the air pressure. Moreover, the soft structure is combined with jamming element[6], and the characteristics are increased significantly during experiments. The proposed new actuator and gripper provides useful gripping ends for automatic transferring devices especially dynamic transferring applications.

DESIGN AND FABRICATION OF SOFT FILAMENT-POLYMER ACTUATOR

The purpose of this study is to change the bending stiffness in the driving direction of a rectangular section software actuator, adjusting the bending stiffness of the actuator by winding it with fiber filaments. To change the fiber material type, filament diameter, cover ratio and composite layer position, a rectangular composite actuator is designed, as shown in Figure 1.

The actuator is made of Ecoflex-0020 silica gel and filament. The filament refers to the polyester wax fiber (hard) or cotton fiber (soft). The total length of the actuator is 130mm, where one end is the fixed end of 15 mm, and the other end is the sealed end of 10 mm. The middle part of 105 mm is the curved end of the actuator, the cross section is a rectangle of 10 mm by 10 mm, and the thickness of the wall is 5.5 mm. The composite filament actuator is composed of a linear actuator, a fiber composite layer and an encapsulation layer. The encapsulation layer is to improve the stability of the actuator. Considering that the fiber has a good adhesion to the material of silicone, we use hard polyester waxy fiber and soft cotton fiber, diameter of separately 0.15 mm, 0.3 mm, 0.55 mm, 0.80 mm and 1.00 mm; and the cover ratio is from 0 to 100%. The Inner wall thickness of the actuator is 2 mm, 3 mm and 4 mm.

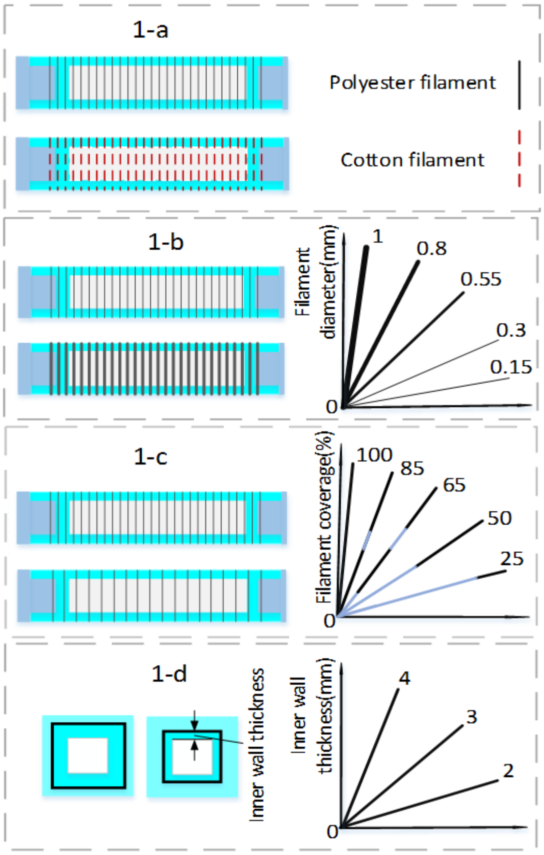

Figure 1. Actuator with different parameters

As shown in Figure 2, the process for fabricating FRSA can be divided into three phases. At the first stage, assemble 3D printed molds(including the side end caps, the inner core, the casing and the upper cover). Then, pour ecoflex-0020 silica gel into a mold, which is cured at the room temperature. At the second stage, the manufactured inner core of the actuator is wound with filament. For effective winding of filaments, an experimental device is designed by the authors to complete controllable filament coverage work. The device is composed of a winding part and an outlet part. The winding part is fixed on the test bench, and the outlet part is fixed on a speed control rail. Combine the stepping motor to control the winding speed and the filament coverage ratio is controlled according to the variable speed of the guide rail. At the third stage, the inner linear filament is accomplished by another process of casting and packaging. The physical model when the package is completed.

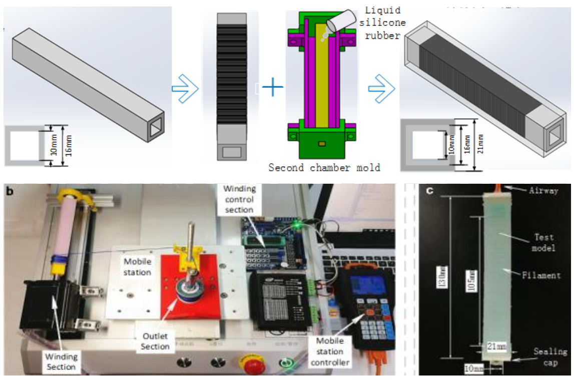

Figure 2. Fabrication of a composite fiber filament soft actuator

2

EXPERIMENTAL RESULT OF BENDING STIFFNESS

It is important to study the effect of composite fiber on the bending stiffness of actuators. However, it is difficult to establish a mathematical model because of the non-linearity of soft materials.
The experimental data show that the bending stiffness increases with the increment of filament cover ratio. However, when the cover ratio reaches the value of 85%, the bending stiffness tends to be stable. In addition, the bending stiffness also increases with the inner wall thickness. Under the same cover ratio, the bending stiffness of FRSA increases firstly and then decreases with the increment of the filament diameter. When the diameter of the filament is 0.55mm, the bending stiffness gets the largest value.

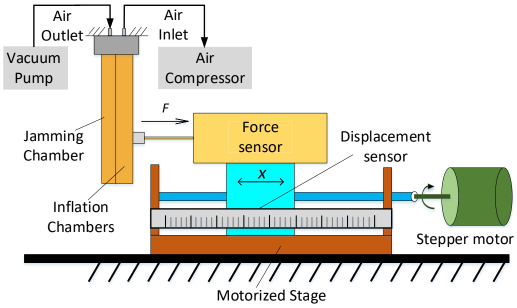

Figure 3. Bending stiffness test platform

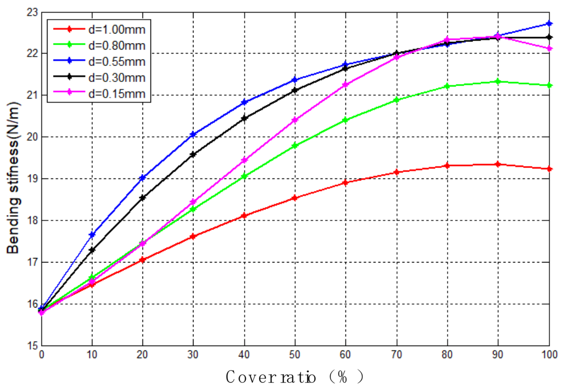

Figure 4. Bending stiffness with variable cover ratios and filament diameters

SOFT FILAMENT-POLYMER JAMMING ACTUATOR AND EXPERIMENT

By the former research, the soft filament-polymer actuator with the diameter of the filament 0.55mm has the largest scale of bending stiffness. Using such parameters, we combine the polymer structure with jamming element. Jamming element is a useful approach to change the actuator stiffness for soft element. As shown in Figure 5, we made the soft filament-polymer and jamming element separately, and combined them together.
The fabricated gripper is made of three Filament-Polymer Jamming Actuators. We put them underwater and did some experiments. As shown in Figure 6, we prepared a large transparent water tank. We put the gripper in the water to grasp the object. After that, we moved the gripper inside the water and recorded the gripping operation. Without variable stiffness, the grasping operation could be successful under static situation, while the object fell off when the gripper was moved. However, the gripper with variable stiffness had better adaptation to dynamic operations and the grasping operation was successful.

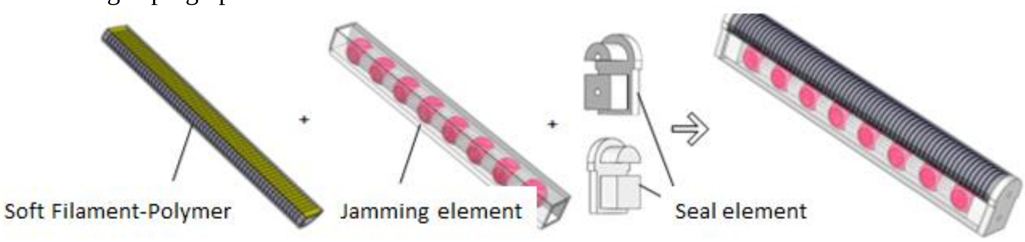

Figure 5. Soft Filament-Polymer Jamming Actuator

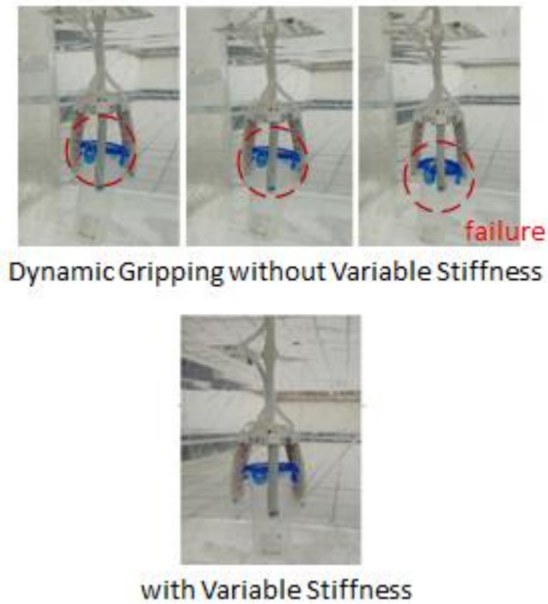

Figure 6. Comparison between actuator with and without variable stiffness

CONCLUSION & FURTHER WORK

The variable stiffness grippers successfully take the gripping operation while those grippers without variable stiffness fail to grasp the movable objects. The results show that soft filament-polymer jamming actuator has better dynamic characteristics and they are the better choice for fabricating the gripping ends.

Our lab continue to study the enhancement of the stiffness and others characteristics of soft actuators and grippers. We recently proposed a new type of bio-actuator and fabricated it successfully. It is inspired by twinning plant. There are lots of twinning plant in the nature. As shown in Figure 7, the morning glory bends around the branch as spiral motion and gets a good performance of gripping. We realized the artificial soft actuator in our lab and found it a good way to increase the soft actuator characteristics. The gripping operations are successfully for different objects shown in Figure 8. In future, we will get more new pneumatic soft elements with better characteristics.

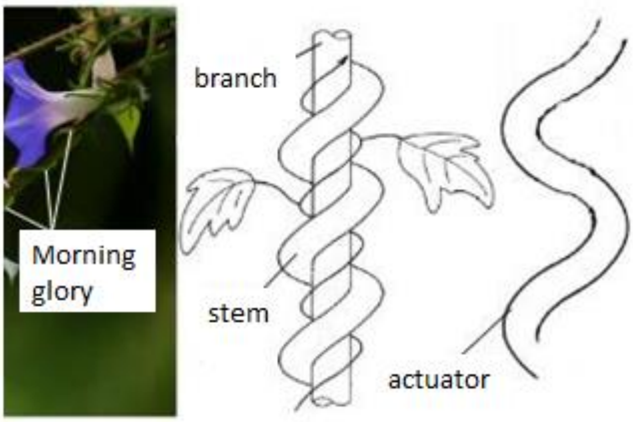

Figure 7. twinning plant

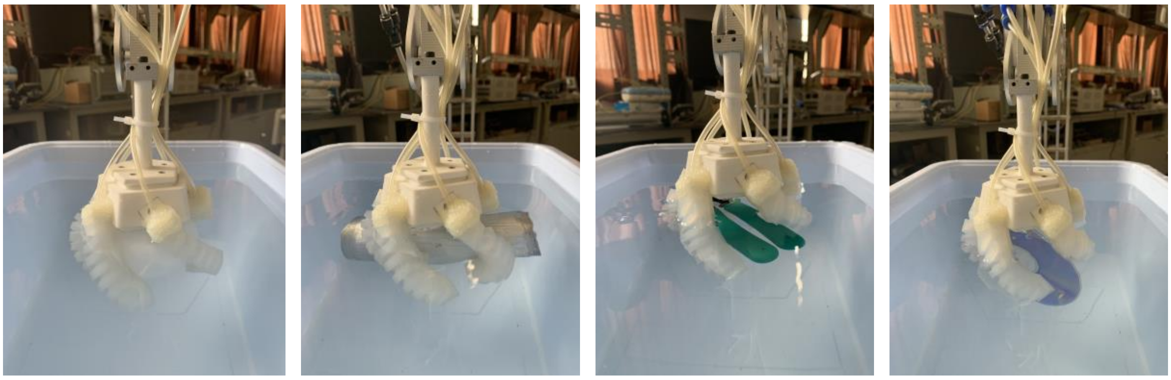

(a) ball above 200g (b) Hollow iron pipe (c) wire plier (d) disk

Figure 8. Objects grasped by bio-gripper of our lab

ACKNOWLEDGMENTS

The authors acknowledge Postgraduate Research & Practice Innovation Program of Jiangsu Province (NO. KYCX20_0364), and Student Extracurricular Academic Research Fund Project of Nanjing University of Science and Technology.

REFERENCES

1. POLYGERINOS P, WANG Z, OVERVELDE JT, et al. Modeling of soft fiber-reinforced bending actuators. IEEE Transaction of Robot.31.778–789.
2. AGARWAL G, BESUCHEt N, AUDERGON B. Stretchable materials for robust soft actuators towards assistive wearable devices.Sci Rep. 6.34224.
3. WANG L, IIDA F. Deformation in soft-matter robotics: A categorization and quantitative characterization. IEEE Robot Automation Mag.22.125–139.
4. CHO K-J, KOH J-S, KIM S. Review of manufacturing processes for soft biomimetic robots. Int J Precis Eng Man. 10.171.
5. SUN Y, SONG S, LIANG X. A miniature soft robotic manipulator based on novel fabrication methods. IEEE Robot Autom Lett.1.617–623.
6. GUO Z, LI X, SUN Z, et al. Soft shaping gripper inspired by marine animals. The 10th JFPS International Symposium on Fluid Power Fukuoka 2017

The 11th JFPS International Symposium on Fluid Power HAKODATE 2020 Oct. 12-13, 2021 JFPS The Japan Fluid Power System Society

Robotic Blood Vessel Mechanism for Self-Healing Function of Soft Robots

Kenjiro TADAKUMA*, Shohei INOMATA*, Yuta YAMAZAKI†,
Fumiya SHIGA†,Masanori KAMEOKA†, MD Nahin Islam SHIBLEE†,
Issei ONDA*, Tomoya TAKAHASHI*, Yu OZAWA*, Masahiro WATANABE*,
Hidemitsu FURUKAWA†,Masashi KONYO*, Satoshi TADOKORO*
* Department of Information Science Tohoku University, † Faculty of Science, Yamagata University
6-6-01 Azaaoba, Aramaki, Aobaku, Sendai Miyagi, 980-8579 Japan
(E-mail: tadakuma@rm.is.tohoku.ac.jp)

Abstract. Soft robots, made of elastomers and gels tend to easily break, punctured, or torn by contact with sharp and thin objects. To deal with this problem, we had proposed a robotic blood vessel mechanism that has a self-healing function by inserting liquid-filled tubes in the body. The liquid flows out and is cured which makes the would heal when the body breaks. In this research, we have improved the healing performance by attaching a liquid-absorbent material on the robot surface. Through experiment, it has confirmed that the self-healing ability can be improved by attaching the absorbent material.

Keywords: Mechanism, Self-Healing, Blood Vessel

1. INTRODUCTION

In recent years, research and development on soft robots have been actively promoted in the field of robotics. Soft robots can be expected to be very useful from the viewpoint of application compared to conventional robots, as they can be softly contacted with the contact target and can be deformed flexibly according to the environment. However, many soft robots have their bodies composed of balloon shaped, membrane structures, and because of their flexible body structure, membranes are easily damaged by contact with the external environment. This fatal issue such as breaking of bodies were still left.
On the other hand, various researches and developments have been promoted from the viewpoint of self-healing materials[1]-[7], and examples of sheets[8] or tires[9] that can be repaired with only small scratches have appeared. However, there are still many studies at the conceptual stage, and self-healing itself takes several hours, and self-healing is impossible if the wound is damaged at the level where the wound opens up[10]-[14].
In view of the above problems, we propose a basic concept of robot blood vessels as shown in the next section.
In this paper, the effect of the proposed basic principle was confirmed by explanation of the basic concept, realization of the actual prototype models, and basic experiments were conducted with them.

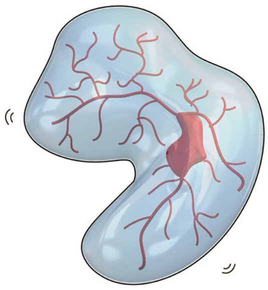

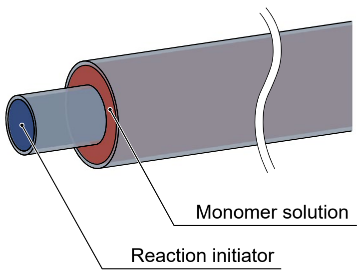

(a) whole body healable robot with robotic blood vessels (b) co-axial type of robotic blood vessel
Figure 1. Concept of the Robotic Blood Vessels

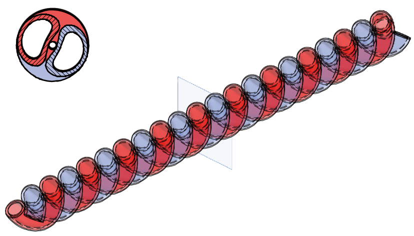

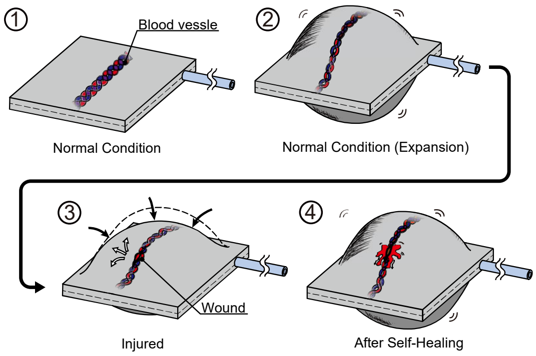

Figure 2. Blood Vessels Mechanism with Twisted Configuration
and Pouch Type Actuator Healable to Re-expanding by Robotic Blood Vessels

2. BASIC CONCEPT

Fig.1 shows the basic concept of a robotic blood vessel. As shown in Fig. 1, blood vessels are stretched to every corner of a soft robot with a flexible body, and even if a part is damaged, blood oozes from the wound, as if it were platelets. The concept is to close the wound and repair it. As shown in Fig. 1 (b), in the cross section, a concentric arrangement of a two-liquids mixture type liquid, a monomer solution and a reaction initiator, was considered. However in actuality, because of the difficulty in connecting to the pipe joint in the above concentric structure, in the first stage of the trial prototyping, the structure was adopted in which two pipes were arranged in a spiral shape as shown in Fig. 3. And table 1 shows the specification of the prototype model.

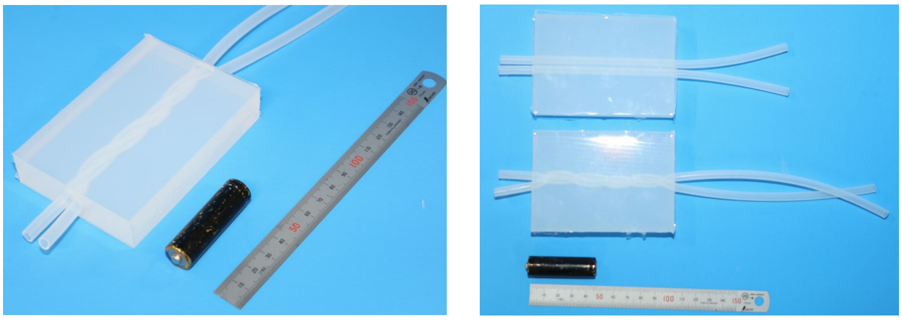

(a) (b)

Figure 3. (a) Prototype Model of the Blood Vessel Mechanism with Twisted Configuration, (b)Straight Type and Twisted Type of the Blood Vessel Mechanism

Table 1. Specification of the First Prototype Model

Width	70 [mm]
Length	100 [mm]
Tickness	20 [mm]
Material	Silicone rubber hardness 30
Diameter of the Tube	Inner: 4 [mm], Outer: 6 [mm]

3. BASIC EXPERIMENTS

3-1. Basic Mixing Experiment

As shown in Fig.4, two syringes containing two liquids stained in red and blue, respectively, were connected to the tubes of the respective vascular mechanisms shown in figure. An experiment was conducted to observe the mixing of two liquids.

First, when a cut was made in the direction perpendicular to the blood vessel, there was almost no difference between the straight type and the helical twist type in the degree of mixing of the two liquids. Next, an experiment was performed to observe the mixing of the two liquids when a wound was made in the direction parallel to the axial direction with respect to the blood vessel(Fig. 5 and Fig. 6).

From the results of the experiments, it was confirmed that the proposed helical twisted type blood vessel mechanism that was devised mixed more liquids through this experiment with the real prototype. For soft robots, there is a method of arranging an infinite number of infinitesimal small blood vessels. However in reality, if the finite number of blood vessels are arranged, this helical twisted type robot blood vessel devised is considered to be very effective and useful in mixing the monomer solution and the reaction initiator for repairing the membrane structure.

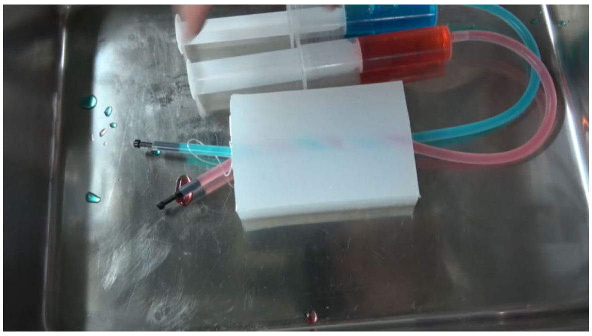

Figure 4. Basic Experimental Setup

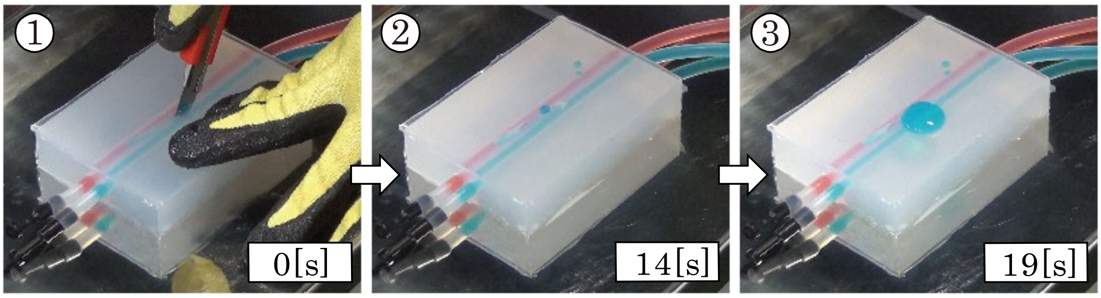

Figure 5. Experiment of mixing of two liquids when scratched in the axial direction (Straight Version)

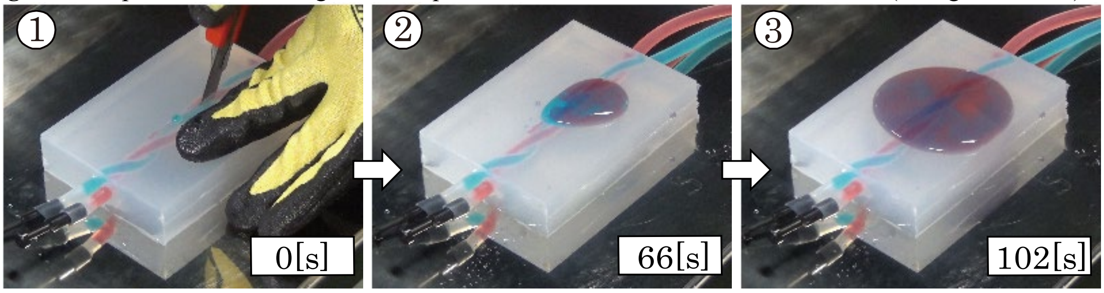

Figure 6. Experiment of mixing of two liquids when scratched in the axial direction (Twisted Version)

3-2. Basic Healing Function Experiment

Based on the above experimental results, assuming that the sheet on the surface of the pouch-shaped structure shown on the right of figure 2 is damaged, one surface of the sealed box which take internal pressure was set to confirm the basic healing function. The sheet with a built-in blood vessel developed this time was put at the upper part of the sealed box. The appearance of the experimental equipment is shown in the figure 7. The same amount of each solution was secreted from two syringe pumps. In addition, in order to make it easier to create a mixed state by keeping the exuded solution in one place, a cloth equivalent to gauze used in case of injury was placed on the surface of the sheet containing the blood vessels even if the direction of the gravity is changed during healing process. If the surface of the sheet containing the blood vessels is injured, the two liquids that correspond to the blood are mixed to close the wound on the sheet, and if it can withstand the internal pressure and expand, the repair will be successful.

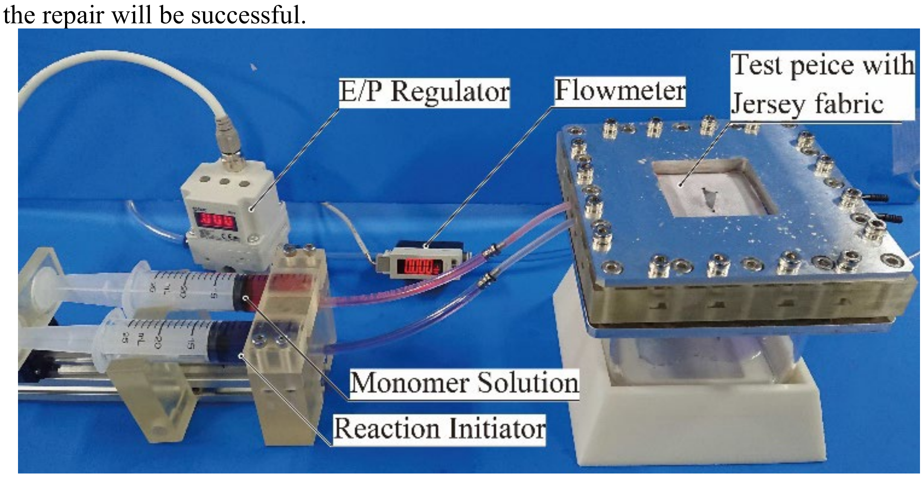

Figure 7. Experimental equipment of Pressure Test

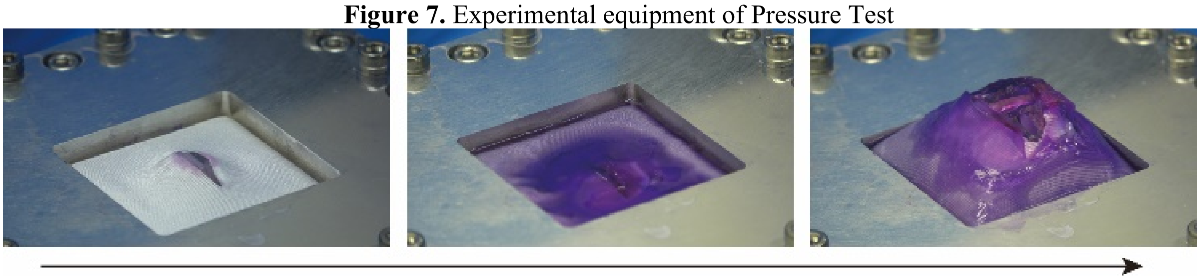

Figure 8. Self-Hearing Process of the Robotic Blood Vessel Mechanism
and Expanding motion after healing without any leakage of the inner air

Figure 8 shows the state of self-repair of the robot vascular mechanism with a cloth having a liquid-absorbing function on the surface, and the state of expansion after self-repair by applying internal pressure without causing air leakage.
As a result of the experiment, it was confirmed that the flexible sheet mounted on the upper surface of the sealed box expanded without causing air leakage even when an internal pressure of 10 kPa was applied. From the above, the basic self-repairing function of the devised robot blood vessel was confirmed by an experiment using a prototype.

4. CONCLUSIONS AND FUTURE WORKS

In this paper, the basic concept of a robotic blood vessel for body repair of a soft robot was proposed. In addition, in the helical twisted type vascular mechanism that was suggested, the effect of mixing in comparison with the conventional method when the wound was made in the axial direction was confirmed through the experiments with actual prototype models. In the future, considering the direction of gravity with respect to the wound, it is conceivable to add viscosity to the liquid and install a gauze structure on the surface, so that much effective healing can be performed without dripping the two liquids.

APPENDIX

The study of this robotic vascular mechanism is from the viewpoint of how to actively repair the body when it is damaged. On the other hand, we are also conducting research and development with the cut resistance gripper mechanism from the viewpoint of taking measures to prevent damage itself as much as possible by equipping it with higher durability. In the durability performance test of this cut-resistant cloth against external contact, we have devised a test device that basically emphasizes the method of "repeated contact at the same place". The tip of the cutting edge to be contacted is replaced with a sharp object (point contact plate, line contact plate) that can be regarded as a very small R, and the extent to which it can withstand different external contacts is investigated. In addition, the cloth tension and the contact position with the cloth can be adjusted by the two rollers on the left and right shown in the figure. The one shown in the figure A is a method with a constant angle, but the one with a variable angle as the next step can be set as a stricter contact state from the viewpoint of cut resistance.

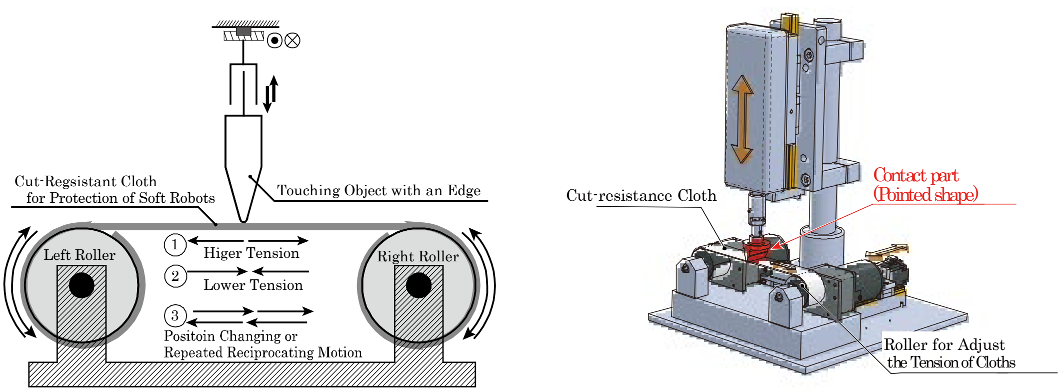

Figure A. Durability Test Equipment for Contact Resistant Cloth

ACKNOWLEDGMENTS

This work was supported by JSPS KAKENHI Grant in Aid for Scientific Research on Innovative Areas "Science of Soft Robot" project under Grant Number JP18H05471

REFERENCES

1. TERRYN, Seppe, et al. Self-healing soft pneumatic robots. science Robotics, 2017, 2-9: eaan4268.
2. WHITE, Scott R., et al. Autonomic healing of polymer composites. Nature, 2001, 409-6822, pp.794.

3. CHEN, Xiangxu, et al. A thermally re-mendable cross-linked polymeric material. Science, 2002, 295-5560, pp.1698-1702.
4. CHENG, Nadia G., et al. Thermally tunable, self‐healing composites for soft robotic applications. Macromolecular Materials and Engineering, 2014, 299-11, pp.1279-1284.
5. BILODEAU, R. Adam, KRAMER, Rebecca K. Self-healing and damage resilience for soft robotics: A review. Frontiers in Robotics and AI, 2017, 4, pp.48.
6. MARTINEZ, Ramses V., et al. Soft actuators and robots that are resistant to mechanical damage. Advanced Functional Materials, 2014, 24.20: 3003-3010.
7. TERRYN, Seppe, et al. Development of a self-healing soft pneumatic actuator: A first concept. Bioinspiration & biomimetics, 2015, 10.4: 046007.
8. TERRYN, Seppe, et al. Toward self-healing actuators: A preliminary concept. IEEE Transactions on Robotics, 2016, 32-3, pp.736-743.
9. NAGAYA, K., et al. Tire with self-repairing mechanism. JSME International Journal Series C Mechanical Systems, Machine Elements and Manufacturing, 2006, 49-2, pp.379-384.
10. TOOHEY, Kathleen S., et al. Self-healing materials with microvascular networks. Nature materials, 2007, 6-8, pp.581.
11. TOOHEY, Kathleen S., et al. Delivery of two‐part self‐healing chemistry via microvascular networks. Advanced Functional Materials, 2009, 19.9, pp.1399-1405.
12. BLAISZIK, Benjamin J., et al. Self-healing polymers and composites. Annual Review of Materials Research, 2010, 40, pp.179-211.
13. HANSEN, Christopher J., et al. Accelerated self‐healing via ternary interpenetrating microvascular networks. Advanced Functional Materials, 2011, 21.22, pp.4320-4326.
14. DEAN, Leon M., et al. Enhanced Mixing of Microvascular Self-Healing Reagents Using Segmented Gas–Liquid Flow. ACS applied materials & interfaces, 2018, 10.38, pp. 32659-32667.

Genaral Session | Oil hydraulics

Robotics and Mechatronics 2

The 11th JFPS International Symposium on Fluid Power HAKODATE 2020 Oct. 12-13, 2021 JFPS The Japan Fluid Power System Society

Design and Manipulability Analysis of a Redundant Anthropomorphic Hydraulically Actuated Manipulator

Fu Zhang*, Junhui Zhang*, Min Cheng**, Ruqi Ding***, Bing Xu*, and Shen Zheng*

* State Key Laboratory of Fluid Power and Mechatronic Systems, Zhejiang University, China.
(E-mail: benzjh@zju.edu.cn)
** State Key Laboratory of Mechanical Transmissions, Chongqing University, China.
*** Key Laboratory of Conveyance and Equipment, Ministry of Education.
East China Jiaotong University, China.

Abstract. Heavy-duty rescue manipulator, replacing humans in dangerous working conditions, has the characteristic of higher robustness and a significantly larger power-to-weight ratio compared. The hydraulic driven robotic manipulator, applied to the heavy-duty rescue manipulator, should have the characteristic of high capability of load, high accuracy, and high dexterity of action, while the existing hydraulic-driven robotic manipulators can hardly satisfy because of the low system pressure, large moment inertia, the installed position of the control valve, and structure. We develop a new type of spherical wrist joint to improve the flexibility of the robotic manipulator. And we design a type of servo-controlled hydraulic-driven robotic manipulator to achieve heavy load and high control accuracy. Then a performance index of the hydraulic manipulator is proposed based on constrained manipulability polytope (CMP).

Keywords: Hydraulic manipulators, Manipulability

INTRODUCTION

Natural disasters and major emergencies seriously threaten the safety of human life and property, so the rapid post-disaster emergency work and safe rescue have become an essential task in the field of public security in recent years. However, the unstructured environment of the disaster scene makes it difficult for the rescue workers to carry out the rescue work quickly, efficiently, and safely. Disaster rescue robots can replace human beings to carry out rescue tasks in a dangerous environment, with solid manipulability and high rescue efficiency, which has been highly valued by all countries [1].

The large heavy-duty robot with rescue operation ability must have the capability of lifting, expanding, grasping, carrying, and other actions. Whether such actions are realized or not depends on the manipulator loading capacity, action flexibility, and control accuracy. The hydraulically driven manipulator has the advantages of high power-to-weight ratio and high robustness. It is suitable for the heavy load conditions of damaged roads, building repair, collapse structure separation, etc. The heavy-duty robot with a hydraulic manipulator system plays an irreplaceable role in the disaster scene [2].

In order to meet the needs of complex tasks in the rescue scene, the rescue manipulator must have the ability to precise operation and good interaction with the operator. Following the configuration of the human arm, we designed a complete hydraulic servo-controlled heavy-duty manipulator with integrated DOF joints [3-5].

Quantifying the manipulator's performance from the perspective of manipulability is especially important for analyzing and designing new manipulator mechanisms and selecting appropriate manipulator configuration in the grasping and operating environment. For the rescue manipulator system, the ability to monitor its motion is crucial to the successful execution of the task. Therefore, the system must be equipped with methods to measure its performance, accuracy, or success rate. In this case, the manipulability measurement is a common technique to determine the manipulability of the workspace [6].

However, unlike an electric manipulator, due to the characteristics of a single-pump-with-multi-actuators system, the velocities of different joints are coupled, and the joint velocity limits are variable. The velocity constraints of various joints are determined by the area parameters of the hydraulic cylinder or the displacement of the swing cylinder. Not only that, more precisely, velocity limits interact [7-9]. Therefore, it isn't easy to evaluate the manipulability of hydraulic manipulators by existing methods.

Yoshikawa analyzed the manipulability of the end effector of the manipulator and proposed an evaluation method of the manipulability, an index related to the volume of the control ellipsoid [10]. Togai suggested using the reciprocal of the condition number of the Jacobian matrix of the manipulator to evaluate the manipulability, which represents the velocity isotropy of the end effector [11]. These local performance indicators cannot reflect the overall performance of the manipulator. For example, the limit of joint position is not considered, and the accessibility is not included in the evaluation. The global performance can also be evaluated by adding local performance indicators of the penalty function. The penalty function of the joint position is introduced into the scaling of manipulation ellipsoid. The ellipsoid axis near the joint limit is reduced so that the global position accessibility index can be evaluated by local manipulation ellipsoid [12-13]. Abdel Malek et al. put the joint position constraint into the augmented Jacobian matrix and optimized the placement of the manipulator by analyzing the augmented matrix [14].

The manipulability ellipsoid cannot transform the velocity limits of the joint into task space, so it may not be able to give an accurate maneuverability evaluation index. Lee proposed scaling Jacobian matrix and steerable polyhedron to consider the constraint of joint velocity. The former can't convert joint velocity into task space velocity accurately [15]. Lee proposed scaling Jacobian matrix and steerable polyhedron to consider the constraint of joint velocity. The former can't convert joint velocity into task space velocity accurately. The polyhedron-based analysis is more accurate [16-17]. The same conclusion is obtained in the study of parallel robots [18-19]. Philip long proposed a new metric called constrained manipulability polyhedron (CMP), which considers the kinematic structure of the system, including closed chain or composite sub mechanisms, joint limits, and the existence of obstacles [20].

Due to the complex and significant velocity constraints of the hydraulic manipulator, it is difficult to evaluate the manipulative performance of the manipulator by traditional ellipsoid analysis. Because of the velocity limit of the joint coupling of the hydraulic manipulator, it is very suitable to use constrained manipulability polyhedron to analyze the operability. Therefore, it is very meaningful to propose a performance index by analyzing CMP.

In this paper, we first introduce the rescue robot we designed, then present a new index to evaluate the manipulability of a hydraulic manipulator by using CMP and show an application example of a two degree of freedom manipulator.

DESIGN OF THE MANIPULATOR

In this part, we first introduce a hydraulically actuated spherical wrist joint and then introduce a seven degree of freedom hydraulic manipulator designed according to the configuration of a human arm. For a serial manipulator, a separate actuator can drive each degree of freedom of the serial mechanism without coupling with other degrees of freedom mechanisms or driving units, which not only provides the convenience of simple control strategy and a small number of actuators but also brings the disadvantages of limited control accuracy, low utilization of axial space of the whole machine and single local actionability. The advantages and disadvantages of the parallel mechanism are opposite to those of serial mechanism. Considering the advantages and disadvantages of the two mechanisms, the full hydraulic drive servo heavy-duty manipulator is proposed to adopt a hybrid scheme.

Design of the Spherical Wrist

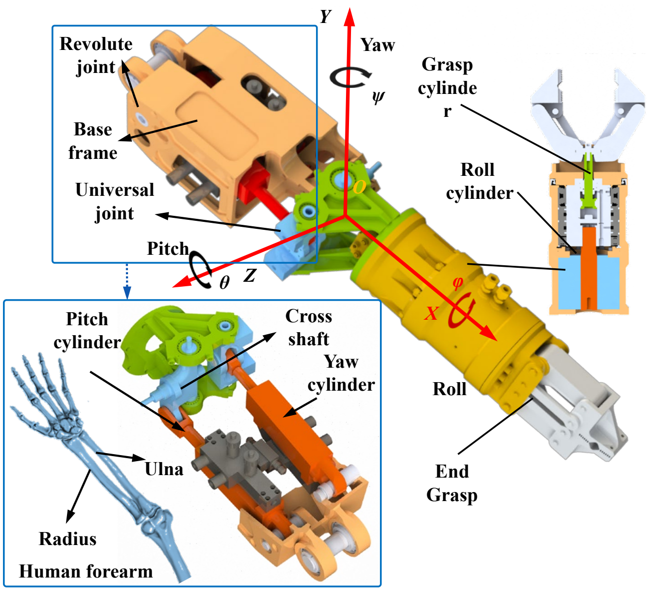

Figure 1. Structure of the roll-pitch-yaw spherical wrist.

The push-rod mechanism is considered a proper transmission way. Unlike electrically actuated areas, the use of pure 3-DOF parallel wrist is limited in hydraulic areas since its size is too large to be installed on a serial manipulator, especially in compact environments. As shown in Fig. 1, Inspired by the human forearm that uses radius and ulna to achieve wrist deviation, we use the hybrid serial-parallel concept to design the wrist as a revolute-universal chain, adopting two parallel linear cylinders to achieve pitch/yaw motion. The wrist structure is designed, as shown in Figs. 1 and 2.

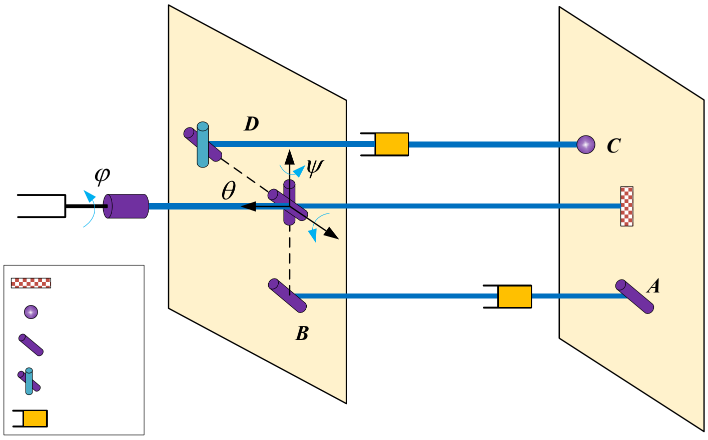

Figure 2. Kinematic diagram of the roll-pitch-yaw spherical wrist.

Points A and B denote the kinematic pair centers of the pitch cylinder, while points C and D denote the kinematic pair centers of the yaw cylinder. The spherical RPY wrist is driven by two parallel linear cylinders for the pitch/yaw motion and a rotary hydraulic cylinder for the roll motion. The pitch cylinder is connected to the base frame and the cross shaft by two revolute pairs. The yaw cylinder is connected to the base frame by a spherical pair and a wrist plate via a universal joint. Moreover, the cross shaft is connected to the base frame via a revolute pair to construct a closed-loop subchain with a four-bar linkage. Besides, the cross shaft is connected to the wrist plate via a revolute pair. In Fig. 1, it should be noted that Point D is on the OZ axis, and Point B is on the YOZ plane at the zero position.

Design of the Overall Manipulator

Based on the proposed RPY wrist, a 7-DOF anthropomorphic redundant hydraulic manipulator is then designed. Except for wrist pitch/yaw/roll, the other 4 DOFs for a human arm are shoulder pitch/yaw/roll and elbow pitch. The 1st joint is determined as a revolute one. The motion of the 2nd joint is usually achieved by a linear hydraulically driven component like the boom cylinder of the excavator's arm. Thus, the basic configuration is given in Fig. 3(a), in which the wrist joints are considered as the 5th, 6th, and 7th joints (R_5 , R_6 , R_7). Referring to the human arm layout, there are two selected configurations of the joints 2-4 (R_2 , R_3 , R_4) shown in Fig. 3(b) and (c). A typical spherical-revolute-spherical (SRS, R_1-R_3) redundant structure is formed for the configuration in Fig. 3(b), which has been applied in electrically driven areas extensively, but resulting in that large installation space and unnecessary axial length are difficult to avoid. Comparatively, the HRM shown in Fig. 3(c) is more like a human arm.

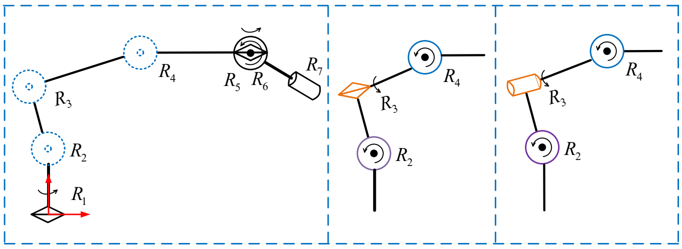

Figure 3. Selected configurations of the 7-DOF hydraulic robotic manipulators

Through this configuration, the HRM and its three-dimensional model are designed as Fig. 4. It is pointed out that the configuration of our designed hydraulic manipulator is different from that in Fig. 3 (c). In Figure 3 (c), the first three joints are perpendicular to each other and intersect, while the first three joints of our designed hydraulic manipulator are perpendicular but not intersect, which is caused by the layout space of the hydraulic cylinder and swing cylinder.

The axis of the 3rd joint goes through the wrist center to easily conduct self-motion manifolds of the 4th joint. A small offset between the 1st and 2nd joints is thereby allowed and assigned for layout consideration. The 1st, 3rd, and 7th joints are driven by hydraulic swing cylinders, and the others by hydraulic linear ones. A high-speed swing cylinder can drive the 1st joint with a gearbox due to its ample installation space.

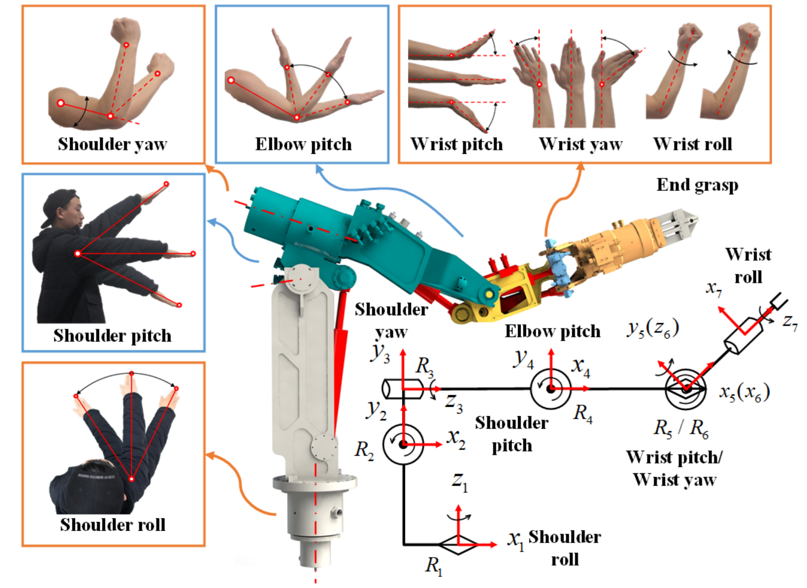

Figure 4. Configuration and three-dimensional model of the proposed hydraulic robotic manipulators

PERFORMANCE INDEX OF HYDRAULIC MANIPULATOR

Previously, we introduced the design of a 7-DOF humanoid hydraulic manipulator. The manipulability of the manipulator affects whether the task can be completed successfully, and it is an essential index of manipulator evaluation. In this part, we introduce the classical manipulability ellipsoid and introduce how to use the reciprocal of the condition number to evaluate the manipulability of the manipulator in operation space. It's introduced how to construct the joint velocity polyhedron according to the pump and valve parameters. The joint velocity polyhedron is constrained considering the joint position limits. The constrained manipulability polyhedron is obtained through an affine transformation. An index is presented which is similar to the reciprocal of the condition number, and it is used to evaluate the manipulator maneuverability based on the constrained manipulability polyhedron.

Manipulability Ellipsoid

The differential kinematics of an n-DOF manipulator can be written as

$$\mathbf{v}_n = \begin{bmatrix} \mathbf{v} \\ \mathbf{w} \end{bmatrix} = \mathbf{J}_n \dot{\mathbf{q}} \tag{1}$$

where n is the degree number of freedom, $\mathbf{v}_n$ is velocity vector in operation space, $\mathbf{v}$ is linear velocity vector in operation space, $\mathbf{w}$ is linear velocity vector in operation space, $\mathbf{J}_n \in \mathbb{R}^{6\times n}$ is the Jacobian matrix, $\dot{\mathbf{q}} = [\dot{q}_1, \dot{q}_2, \ldots, \dot{q}_n]^T$ is the joint velocity vector.

In joint space, the unit hypersphere can be written as

$$\dot{\mathbf{q}}^T \dot{\mathbf{q}} \le 1. \tag{2}$$

After affine transformation of the Jacobian matrix, the unit hypersphere of joint velocity becomes ellipsoid of operation space. It can be given as

$$\varepsilon = \left\{ \mathbf{v}_n^T \left(\mathbf{J}_n \mathbf{J}_n^T \right)^{-1} \mathbf{v}_n \le 1 \right\} \tag{3}$$

The manipulability index of the manipulator can be written as

$$\gamma = \frac{1}{\mathrm{cond}(\mathbf{J})} \tag{4}$$

where γ is a dimensionless quantity denoting the isotropy of velocity, $\mathrm{cond}(\bullet)$ denotes condition number for $\bullet$.

Manipulability Polytope

A polytope, $\mathcal{P}^V$ can be represented as the convex hull of its vertex set (V-representation), i.e.,

$$\mathcal{P}^V = \left\{ \mathrm{x}: \mathrm{x}=\sum_{i=1}^{n} \alpha_i \mathrm{y}_i \,\middle|\, \alpha_i \geq 0,\ \sum_{i=1}^{n} \alpha_i = 1 \right\}\ i = 1,\ldots,n \tag{5}$$

where y_i is the i-th vertex of the polyhedron, and x is the point in the polyhedron. This polyhedral point set can be written as

$$\mathcal{P}^H = \mathbf{Ax} \leq \mathbf{b} \tag{6}$$

where $\mathbf{A} \in \mathbb{R}^{j \times k}$, j is the number of half spaces, k is the dimension of space.

In the form of $\mathcal{P}^H$, we can easily construct the joint velocity polyhedron according to the joint velocity range of the manipulator. It can be written as

$$\mathcal{Q}^H = \begin{bmatrix} \mathbf{I}_n \\ -\mathbf{I}_n \end{bmatrix} \dot{\mathbf{q}} \leq \begin{bmatrix} \dot{\mathbf{q}}_{\max} \\ -\dot{\mathbf{q}}_{\min} \end{bmatrix} \tag{7}$$

where $\mathbf{I}_n$ is the $n \times n$ identity matrix, $\dot{\mathbf{q}}_{\max}$ and $\dot{\mathbf{q}}_{\min}$ are joint velocity limits.

The joint velocity polyhedron in the form of vertices can be defined by vertices as

$$\mathcal{Q}^V = \left\{ \dot{\mathbf{q}}_1^v,\ \dot{\mathbf{q}}_2^v, \ldots,\ \dot{\mathbf{q}}_{2n}^v \right\} \tag{8}$$

where $\dot{\mathbf{q}}_i^v$ is the i-th vertex of the joint velocity polyhedron.

The joint velocity polyhedron matrix can be written as

$$\mathbf{Q} = \begin{bmatrix} \dot{\mathbf{q}}_1^v \\ \dot{\mathbf{q}}_2^v \\ \vdots \\ \dot{\mathbf{q}}_{2n}^v \end{bmatrix} = \begin{bmatrix} \dot{q}_1^{\min} & \dot{q}_2^{\min} & \cdots & \dot{q}_{n-1}^{\min} & \dot{q}_n^{\min} \\ \dot{q}_1^{\min} & \dot{q}_2^{\min} & \cdots & \dot{q}_{n-1}^{\min} & \dot{q}_n^{\max} \\ \vdots & \vdots & & \vdots & \vdots \\ \dot{q}_1^{\max} & \dot{q}_2^{\max} & \cdots & \dot{q}_{n-1}^{\max} & \dot{q}_n^{\max} \end{bmatrix} \tag{9}$$

An affine transformation transforms the joint velocity polyhedron, and the vertex of the polyhedron is transformed by the Jacobian matrix to get a new manipulability polyhedron vertex. The new polyhedron is called manipulability polyhedron. It can be written as

$$\mathcal{P}^V = \{\mathbf{v}_1^v, \ldots, \mathbf{v}_{2n}^v\} = \{\mathbf{J}_n \mathbf{v}_1^v, \ldots, \mathbf{J}_n \mathbf{v}_{2n}^v\} \tag{10}$$

Velocity limits of the hydraulic manipulator

For hydraulic manipulator, the above results are extended. The hydraulic manipulator is a single-pump-multi-actuator system, and the velocity limits of the actuator are affected by the direction of the velocity of the actuator. Here we use the simplification method to simplify the system. The single pump is divided into several virtual pumps, and the flow of each pump is distributed in proportion to the rated flow of the generator. It can be written as

$$Q_{i,\max} = \frac{Q_{i,\mathrm{nom}}}{\sum_{i=1}^{n} Q_{i,\mathrm{nom}}} Q_{\max} \tag{11}$$

where $Q_{i,\mathrm{nom}}$ is the norm flow rate of the i-th control valve, $Q_{i,\max}$ is the maximum flow rate of the i-th joint control valve, $Q_{\max}$ is the maximum flow rate of the pump.

In the quasi-steady state, regardless of the pressure dynamics, the relationship between the joint angular velocity and the flow rate of the hydraulic cylinder is followed as

$$\dot{q}_n = \begin{cases} \dfrac{Q_i \eta_v}{V_{i,g}}, & i\text{-th joint is driven by a swing cylinder or motor}, \\[2ex] \dfrac{\partial q_i}{\partial x_i} \dfrac{Q_i \eta_v}{S(\dot{q}_i)}, & i\text{-th joint is driven by linear cylinder}, \end{cases} \tag{12}$$

$$S(\dot{q}_n) = \begin{cases} A_{1,i},\ \dot{q}_i \geq 0, \\ A_{2,i},\ \dot{q}_i < 0, \end{cases} \tag{13}$$

Where η_v is the efficiency coefficient, Q_i is the flow rate of the i-th joint, $V_{i,g}$ is the displacement of the i-th joint driver, $A_{1,i}$ is the area of the i-th joint cylinder without the rod, $A_{2,i}$ is the area of the i-th joint cylinderwith the rod, $\frac{\partial q_i}{\partial x_i}$ is angular-linear coefficient of the i-th joint.

The velocity limits can be determined by the following equations as

$$\dot{q}_{i,\max} = \begin{cases} \dfrac{Q_{i,\max}\eta_v}{V_{i,g}}, & i\text{-th joint is driven by a swing cylinder or motor,} \\ \dfrac{\partial q_i}{\partial x_i}\dfrac{Q_{\mathrm{i},\max}\eta_v}{S(\dot{q}_n)}, & i\text{-th joint is driven by a linear cylinder,} \end{cases} \tag{14}$$

$$\dot{q}_{i,\min} = \begin{cases} -\dfrac{Q_{i,\max}\eta_v}{V_{i,g}}, & i\text{-th joint is driven by a swing cylinder or motor,} \\ -\dfrac{\partial q_i}{\partial x_i}\dfrac{Q_{i,\max}\eta_v}{S(\dot{q}_i)}, & i\text{-th joint is driven by a linear cylinder,} \end{cases} \tag{15}$$

By substituting Equation (14-15) into Equation (7), the joint velocity polyhedron of the hydraulic manipulator can be obtained.

Positional Joint Limit Constraints

The joint velocity polyhedron obtained above does not consider the joint position limit, so it is necessary to introduce the scaling factor of the joint limit penalty. The velocity polyhedron is constrained before converting to the workspace. The influence of joint position limitation on maneuverability is considered. The scaling factor can be written as

$$\varphi_i^{\max} = 1 - \left(\frac{\max(\overline{q}_i, q_i) - \overline{q}_i}{q_i^{\max} - \overline{q}_i} \right) \tag{16}$$

$$\varphi_i^{\min} = 1 - \left(\frac{\min(\overline{q}_i, q_i) - \overline{q}_i}{q_i^{\min} - \overline{q}_i} \right) \tag{17}$$

$$\overline{q} = \frac{q_i^{\min} + q_i^{\max}}{2} \tag{18}$$

Where $\varphi_i^{\max}$ is the scaling factor of the upper boundary of the i-th joint velocity, $\varphi_i^{\min}$ is the scaling factor of the lower boundary of the i-th joint velocity.

Constrained Manipulability Polytope

Equations (16-17) are introduced into Equation (7) to obtain the constrained joint velocity polyhedron. It is given as

$$\begin{bmatrix} \mathbf{I}_n \\ -\mathbf{I}_n \end{bmatrix} \dot{\mathbf{q}} \le \begin{bmatrix} \boldsymbol{\varphi}^{\max}\dot{\mathbf{q}}_{\max} \\ -\boldsymbol{\varphi}^{\min}\dot{\mathbf{q}}_{\min} \end{bmatrix} \tag{19}$$

Where $\boldsymbol{\varphi}^{\max} = \mathrm{diag}([\varphi_1^{\max}, \varphi_1^{\max}, \ldots, \varphi_n^{\max}])$, $\boldsymbol{\varphi}^{\min} = \mathrm{diag}([\varphi_1^{\min}, \varphi_2^{\min}, \ldots, \varphi_n^{\min}])$.

The constrained joint velocity polyhedron is substituted into Equation (10) to obtain the constrained manipulability polyhedron.

In the constrained manipulability polyhedron, an index similar to the reciprocal Jacobian condition number is used to evaluate the manipulator's manipulability. It is given as

$$\mu = \frac{w_q^*}{w_q} \tag{20}$$

Where w_q^* is the shortest distance from the end of a manipulator to the hyperplane of a constrained manipulability polyhedron, w_q is the longest distance from the end of the manipulator to the vertex of constraint manipulability polyhedron.

ILLUSTRATIVE 2-DOF PLANAR ROBOT CASE

Two hydraulic cylinders drive the joints of shoulder pitch and elbow pitch of the hydraulic manipulator. The performance index of the proposed manipulator is illustrated in Fig 5. The kinematics model of the two degrees of freedom of the hydraulic manipulator is established as

$$(L_{12}^2 + L_{22}^2 - (x_2 + x_{02})^2) / 2L_{12}L_{22} = \cos(\zeta_2) \tag{21}$$

$$(L_{14}^2 + L_{24}^2 - (x_4 + x_{04})^2) / 2L_{14}L_{24} = \cos(\zeta_4) \tag{22}$$

$$\boldsymbol{\zeta} = \mathbf{q} + \boldsymbol{\zeta}_0 \tag{23}$$

$$\frac{\partial q_2}{\partial x_2} = -L_{12}L_{22}\sin(q_2 + \zeta_{02}) / (x_2 + x_{02}) \tag{24}$$

$$\frac{\partial q_4}{\partial x_4} = -L_{14}L_{24}\sin(q_4 + \zeta_{04}) / (x_4 + x_{04}) \tag{25}$$

where L_{12}, L_{14} and L_{22}, L_{24} denote the link lengths, ζ_2 and ζ_4 are angles changing with the displacement of the hydraulic cylinders, $\mathbf{q} = [q_2, q_4]$ is the joint angle vector, $\boldsymbol{\zeta} = [\zeta_2, \zeta_4]$ is the angle vector, $\boldsymbol{\zeta}_0 = [\zeta_{02}, \zeta_{04}]$ is the angle vector in the initial position, x_2 and x_4 are hydraulic cylinder displacements, x_{02} and x_{04} are lengths of hydraulic cylinders in the initial position.

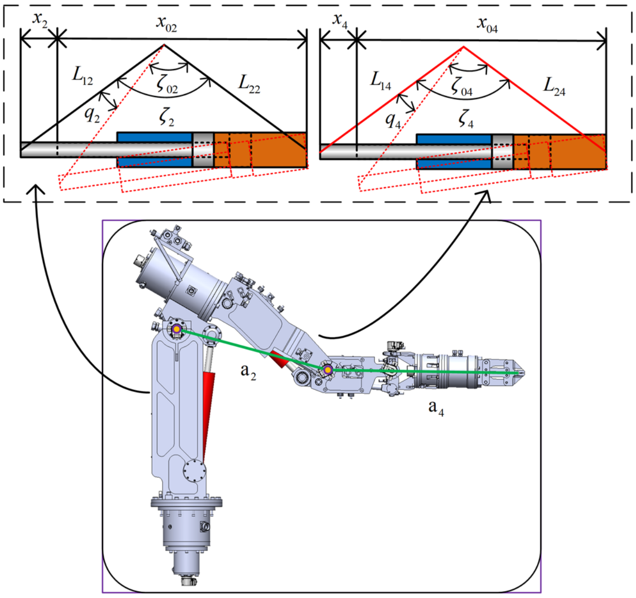

Figure 5. Shoulder pitch and elbow pitch.

In the table, we show the values of the parameters needed.

Table 1. The values of the parameters.

Parameter	Value (Unit)	Parameter	Value (Unit)
a_2	0.87541 (m)	ζ_{02}	1.5348 (rad)
a_4	1.061 (m)	ζ_{04}	0.6430 (rad)
L_{12}	0.8013 (m)	$A_{1,2}$	0.003117 (m^2)
L_{14}	0.6732 (m)	$A_{1,4}$	0.002155 (m^2)
L_{22}	0.2000 (m)	q_2	-0.7873-0.6090 (rad)
L_{24}	0.1500 (m)	q_4	-0.2599-1.8345 (rad)

The two degree-of-freedom mechanism is analyzed based on the manipulation ellipsoid and the manipulability polyhedron.

The manipulability ellipsoids of the manipulator are shown in Fig 6(a). The manipulability analysis of the manipulator workspace is shown in Fig 6(b).

Based on manipulability ellipsoid, a hypersphere in joint space is transformed into the operation space through the Jacobian matrix. It can be considered that the 2-norm of joint velocity is less than 1. This focuses more on the configuration of the manipulator than on the actual velocity limits of the joint. Using this method to analyze the operability of hydraulic manipulators will cause serious problems because the velocity limits of different joints of the hydraulic manipulator are significantly different and coupled.

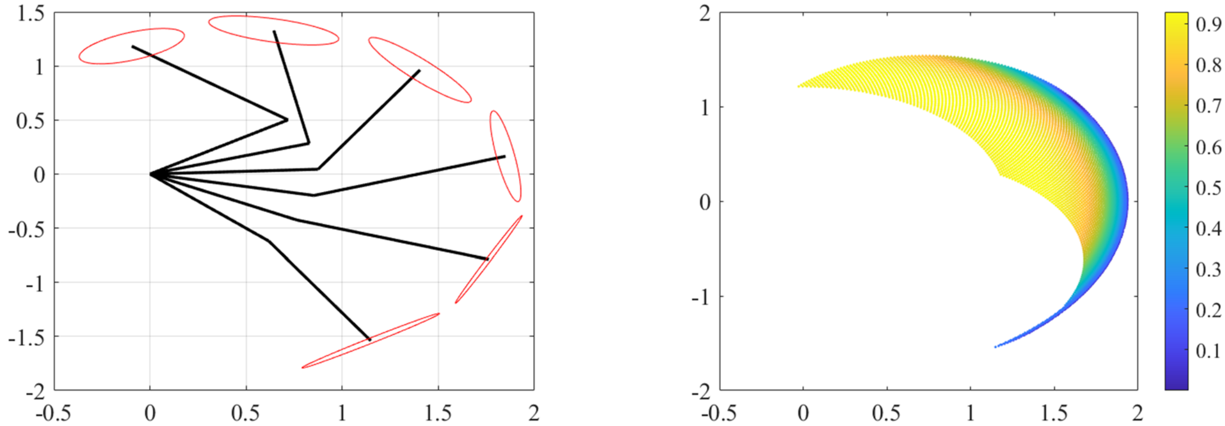

(a) Constrained manipulability polyhedron of the hydraulic manipulator, and the ellipsoid is scaled by 0.2

(b) Performance index of the hydraulic manipulator based on manipulability ellipsoid

Figure 6. Manipulability analysis based on the ellipsoid.

The manipulability polyhedrons of the manipulator are shown in Fig 7(a). The manipulability analysis of the manipulator workspace is shown in Fig 7(b).

Based on manipulability polyhedron, a polyhedron in joint space is transformed into the operation space through the Jacobian matrix. It can be considered that the maximum norm of joint velocity is less than the velocity limit. Velocity limits are considered directly. Therefore, the manipulability polyhedron can more accurately describe the velocity characteristics of the end of the hydraulic manipulator.

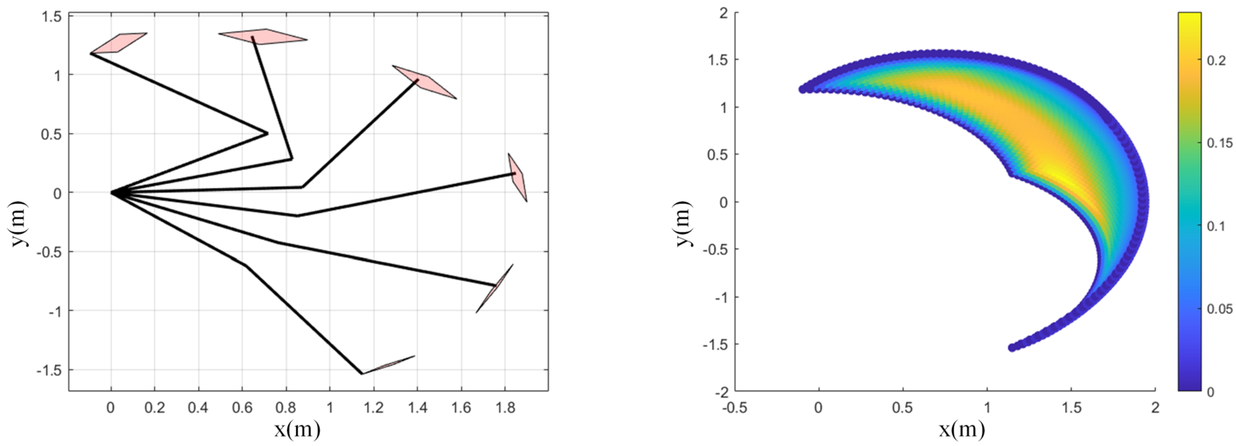

(a) Constrained manipulability polyhedron of the hydraulic manipulator, and the polyhedron is scaled by 0.2

(b) Performance index of the hydraulic manipulator based on manipulability polyhedron

Figure 7. Manipulability analysis based on the polyhedron.

DISCUSSION AND CONCLUSION

In this paper, a kind of hydraulic spherical wrist joint is designed and applied to the humanoid hydraulic manipulator. Then, we review the evaluation methods of manipulator manipulability.

A method of calculating the velocity limits of the hydraulic manipulator is proposed. Manipulability polyhedron analysis is developed, so a performance evaluation index for hydraulic manipulators is obtained. This index can evaluate the isotropy of the end of the manipulator. Finally, two joints of the manipulator are taken as examples to compare the analysis results of the manipulability ellipsoid and the manipulability polyhedron. The results show that the manipulability polyhedron is more suitable for the performance evaluation of the hydraulic manipulator.

The manipulability polyhedron can also be applied to the performance analysis of the two arms, adding the penalty function of the obstacle. Moreover, manipulation polyhedron analysis has excellent potential for mechanism design and task learning of hydraulic manipulators, such as task learning, selection of hydraulic components, and linear hydraulic cylinder structure optimization (in Fig 5). This is a very potential analytical tool. This paper only shows an example of a 2-DOF mechanism. In the future, we will analyze the designed 7-DOF humanoid manipulator thoroughly.

ACKNOWLEDGMENTS

This work was supported in part by the National Natural Science Foundation of China under Grant 91748210, the National Outstanding Youth Science Foundation of China (Grant No. 51922093), and Jiangxi Provincial Excellent Young Funding Program (Grant No. 20192BCBL23005).

REFERENCES

1. HONG S, PARK G, LEE Y, et al., Development of a tele-operated rescue robot for a disaster response, International Journal of Humanoid Robotics, 2018, 15-4, 1850008.
2. CHEN K, KAMEZAKI M, KATANO T, et al., Fundamental development of a virtual reality simulator for four-arm disaster rescue robot OCTOPUS, 2016 IEEE international conference on advanced intelligent mechatronics (AIM). IEEE, 2016, pp.721-726.
3. KIVELÄ T, MATTILA J, AND PUURA J., A generic method to optimize a redundant serial robotic manipulator's structure, Automation in Construction, 2017, 81, pp.172-179.
4. LIANG X, WAN Y, ZHANG C., Robust position control of hydraulic manipulators using time delay estimation and nonsingular fast terminal sliding mode, Proceedings of the Institution of Mechanical Engineers: Part I- Journal of Systems and Control Engineering, 2018, 232-1, pp.50-61.
5. LUO X, LI L, XIE L, et al., Compliance Control Using Hydraulic Heavy-Duty Manipulator, IEEE Transactions on Industrial Informatics, 2019, 15-2: pp.1193-1201.
6. JOHNS JIN L, LI S, LA H M, et al., Manipulability optimization of redundant manipulators using dynamic neural networks, IEEE Transactions on Industrial Electronics, 2017, 64-6, pp.4710-4720.
7. LAMPINEN S, NIEMI J, MATTILA J., Flow-bounded trajectory-scaling algorithm for hydraulic robotic manipulators, 2020 IEEE/ASME International Conference on Advanced Intelligent Mechatronics (AIM). IEEE, 2020, pp.619-624.
8. HULTTINEN L, MATTILA J., Flow-limited path-following control of a double Ackermann steered hydraulic mobile manipulator, 2020 IEEE/ASME International Conference on Advanced Intelligent Mechatronics (AIM). IEEE, 2020, pp.625-630.
9. WANNER J, SAWODNY O., Tool-center-point control of a flexible link concrete pump with task space constraints using quadratic programming, 2020 IEEE/ASME International Conference on Advanced Intelligent Mechatronics (AIM). IEEE, 2020, pp.565-570.
10. YOSHIKAWA T., Manipulability of robotic mechanisms, The international journal of Robotics Research, 1985, 4-2, pp.3-9.
11. TOGAI M., An application of the singular value decomposition to manipulability and sensitivity of industrial robots, Siam journal on algebraic discrete methods, 1986, 7-2 pp.315-320.
12. CHAN T F, DUBEY R V., A weighted least-norm solution based scheme for avoiding joint limits for redundant joint manipulators, IEEE Transactions on Robotics and Automation, 1995, 11-2, pp.286-292.
13. DARIUSH B, HAMMAM G B, ORIN D., Constrained resolved acceleration control for humanoids, 2010 IEEE/RSJ International Conference on Intelligent Robots and Systems. IEEE, 2010, pp.710-717.
14. ABDEL-MALEK K, YU W, YANG J., Placement of robot manipulators to maximize dexterity, International Journal of Robotics and Automation, 2004, 19-1, pp.6-14.
15. LEE J., A study on the manipulability measures for robot manipulators, Proceedings of the 1997 IEEE/RSJ International Conference on Intelligent Robot and Systems. Innovative Robotics for Real-World Applications. IROS'97. IEEE, 1997, 3, pp.1458-1465.
16. SEKIGUCHI H, OHNISHI K., Force capability evaluation methods for bilateral controlled manipulators, 2017 IEEE International Conference on Mechatronics (ICM), IEEE, 2017, pp.111-116.
17. FINOTELLO R, GRASSO T, ROSSI G, et al., Computation of kinetostatic performances of robot manipulators with polytopes, 1998 IEEE International Conference on Robotics and Automation (Cat. No. 98CH36146). IEEE, 1998, 4, pp.3241-3246.
18. KRUT S, PIERROT F., Velocity Performances Indexes for Parallel Mechanisms with Actuation Redundancy, Robotica, 2004, 22-2, pp.129-139.
19. MERLET J P., Jacobian, manipulability, condition number, and accuracy of parallel robots, 2006.
20. LONG P, PADIR T., Constrained manipulability for humanoid robots using velocity polytopes, International Journal of Humanoid Robotics, 2020, 17-1, 1950037.

The 11th JFPS International Symposium on Fluid Power HAKODATE 2020 Oct. 12-13, 2021 JFPS The Japan Fluid Power System Society

Wide Field of View Projection Display for Remote Control of Construction Robot

Daisuke KONDO*

*Dept. of Mechanical Engineering, School of Engineering, Osaka University
2-1 Yamadaoka, Suita, Osaka, 565-0871 Japan
(E-mail: kondo@jrl.eng.osaka-u.ac.jp)

Abstract. A construction robot for disaster relief and its remote control platform is developed as a part of the Impulsing Paradigm Challenge through Disruptive Technologies Program (ImPACT)'s Tough Robotics Challenge Program. Unlike traditional remote-controlled construction equipment, the robot has two arms and many cameras. For remote control the robot, a portable immersive projection screen is proposed. The screen which is in the shape of a part of cylinder, has very simple and portable structure. The shape of screen derives the wide field of view. And it allows to display various camera images in arbitrary arrangement.

Keywords: Rescue Robot, Remote Control, Immersive Projection Technology, ImPACT

INTRODUCTION

The use of unmanned construction machinery will enable workers to avoid the dangerous conditions of the occurrence of natural disasters. Under the Impulsing Paradigm Challenge through Disruptive Technologies Program (ImPACT)'s Tough Robotics Challenge, an innovative construction robot for rescue was developed [1][2]. Fig. 1 shows the outer appearance of a construction robot.
The construction robot has dual arms for carrying out effective rescue activities in the disaster site and has many cameras. And it can be completely remote controlled from the teleoperation cockpit in distant site.

Figure 1. A construction robot.

The teleoperator of the construction robot visually identifies the surrounding situation to perform work appropriately. The operations are performed based on the images transmitted from the many cameras settled on the robot. In conventional remote-control system, the multi-monitor system is used for displaying multiple images. However, the size and layout of images are fixed, so it is not comfortable to understand many images for operator. In this paper, we propose a display designed for handling a number of images, and has panoramic wide field of view.

THE DESIGN OF THE WIDE-FOV PROJECTION SCREEN

The teleoperation cockpit needs to be structed temporary in remote location near the disaster site. To facilitate transportation and installation, we propose a method of forming a projection screen by elastically deforming a flexible plastic panel and fixing it to a frame. The structure is shown in Fig. 2. The projection screen was a 3-mm-thick plastic plate. And it has a sand-blasted surface suitable for projection screen. The plate was elastically deformed into a semi-cylindrical shape, and the upper both-side ends were fixed to the screen stand using clamps and bolts. plastic guides were provided at nine points on the back, and metal stoppers were provided at the bottom to further stabilize the shape. The restorative force of elastic deformation makes a seamless curved surface. The semi-cylinder had a radius of 900 mm and a height of 1500 mm. To increase the downward view angle, the semi-cylinder was inclined toward the back from the observer's point of view. The angle was set as 26° to the vertical.

In general, most wide FOV screens have a concave spherical shape to give the user an immersive feeling. By contrast, the proposed method involved a simple semi-cylindrical shape [3], which afforded a sufficient FOV angle. The horizontal FOV angle at the assumed viewpoint was 133°. The semi-cylinder inclination reduced the less important upper FOV but provided a 56° downward field of view. When an immersive image is presented, the ground conditions are viewed clearly. The viewing distance from the viewpoint to the screen was 1400 mm in the front, which was sufficient.

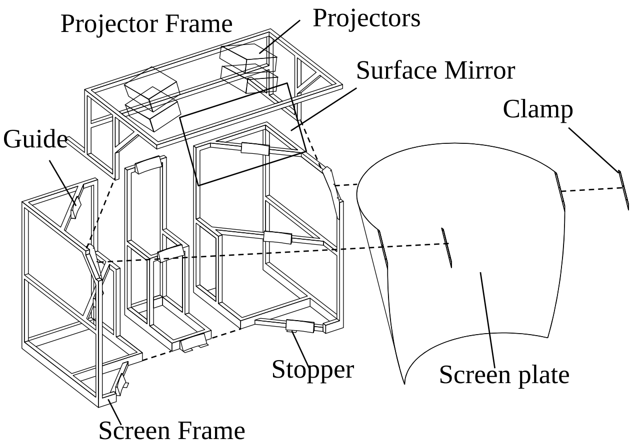

Figure 2. Image depicting assembly of screen and frames.

For image projection, four projectors were used. The projectors used were NEC NP-P451WJL. The screen surface was partitioned into four areas (upper left, upper right, lower left, and lower right) and assigned to each projector. Front projection was used, and the projection was performed from above to avoid shadows caused by the operator. To reduce the height of the system, the projected ray was folded using a surface mirror. Edge blending was applied to the boundary of the area.

A PC is implemented for video processing. The PC can capture up to eight external video signals in HDMI format or others and display them onto screen surface in real time. Generally, the image projected on a curved surface is distorted, this distortion must be removed. Hence, free-form projection display technology 4] was used to compensate the distortion. This technology generates images to be input to each projector by inverse transforming the distortions caused by the relationship among the positions of the projectors, screen shape, and viewpoint position with very low latency. Finally, a unified correct image is displayed on the entire screen.

ARBITRARY ARRANGEMENT OF IMAGES

The various image data acquired by construction robot are transmitted to teleoperation cockpit. In conventional multi-monitor system, because a number of images are displayed in fixed size and layout, it is not suitable to check the images. In our system, each screen is virtually arranged three-dimensionally in the space that can be seen through the field of view of the screen. They are compensated so that they appear as the correct plane and are oriented so that they are facing to the operator. Or it can be oriented at any angle. It is possible to arrange to optimize usability by changing the size according to the importance.

The following eight channels of video were input to the display system.

(1) Front(Main View) (360 degrees camera)
(2) Back View(360 degrees camera)
(3) Arm camera
(4) Gripper
(5) Gripper (side)
(6) Drone
(7) AroundView
(8) Robot's posture

(1) to (7) were transmitted wirelessly from the construction robot, (8) is an image generated in local computer to indicate the robot's joint angles and orientation in real time. The operator can choose some of these eight videos as needed, and are displayed on the screen. the size and layout of images are switched arbitrary with a gamepad. In addition, the arrangement according to the robot's task can be stored in the system as a preset and can be freely recalled and used. Some of the presets used are shown in fig.3. (a) is for traveling on rough terrain, (b) is for manipulation using dual-arm and finding the survivor to rescue. The image necessary in each situation were chosen based on the opinions of the operator. Effective presets can be added according to the various work purpose.

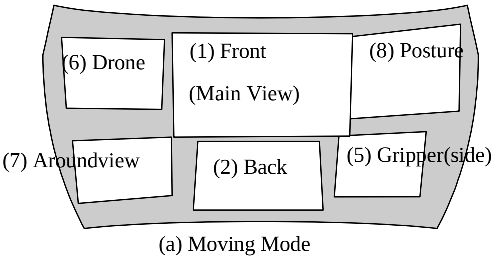

Figure.3 Example of screen arrangement.

FIELD EXPERIMENT

Evaluation experiment was conducted in test field simulating a disaster site. The construction robot demonstrates a scenario in which it was moving on the rough ground, after that find the survivor needs to help under a collapsed house. As shown in fig.4, the proposed wide-FOV projection display was applied as the remote-control cockpit for the evaluation experiment. The teleoperator completely performed remote control using multi-screen.

The moving mode layout(fig.3(a)) was used during robot's traveling, and manipulation mode layout(fig.3(b)) was used at situation that robot seeks a survivor. The main view (1) for checking the front of the robot is a wide field of view image taken by the omnidirectional camera (Point Grey Research LADY BUG 5+) installed at the front of the vehicle body. In order to reduce the amount of data transmission, images in the required directions were cut out by image processing on the PC mounted on the robot, and the results were transmitted by wireless video system(AMINMON CONNEX). The gripper view (4) rotates automatically on the screen to cancel the apparent rotation due to the angle of the robot's gripper. The video delay on the main view is not small at 380ms. The teleoperator can be adapted to the delay by practice. For further improvement of operability, this delay This delay can be reduced by improving video transmission method or using the projector with a low delay mode.

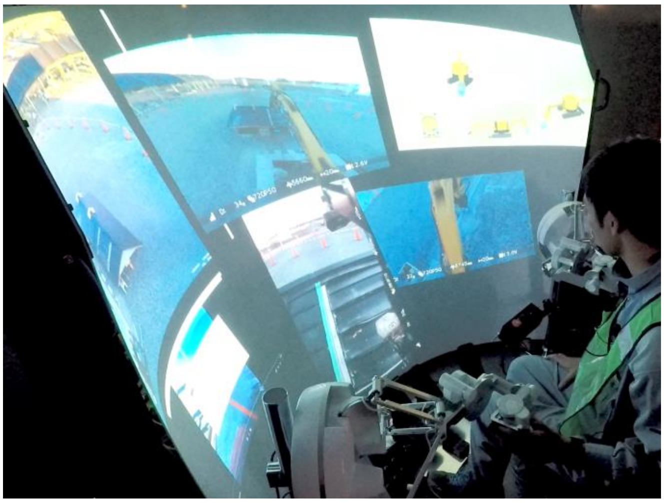

Figure 4. Remote control cockpit.

CONCLUSIONS

As a display system suitable for remote robot operation, we designed and implemented a simple and portable projection-type wide-field display with a semi-cylindrical screen that is elastically deformed from a flat plate. The display has portability to allow it to be installed in disaster areas in case of emergency. And it can display the multiple images which is captured by many cameras settled on the robot, at arbitrary positions. Introducing this display into the remote-controlled cockpit of the construction robot platform in the ImPACT Tough Robotics Challenge, and confirming that it can be used as a wide-field display as a wide-field display for remote-controlled operation.

ACKNOWLEDGMENTS

This study was supported by ImPACT Program “Tough Robotics Challenge” of the Council for Science, Technology, and Innovation (Cabinet Office, Government of Japan).

REFERENCES

1. Yoshinada, H., Kurashiki, K., Kondo, D., et al., Dual-Arm Construction Robot with Remote-Control function, in Tadokoro, S.(ed.), Disaster Robotics, Tracts in Advanced Robotics, vol. 128, Springer, 2019, pp.195-264.
2. Kurashiki, K., Yoshinada, H., Nagatani, K., Tanaka, M., Yamashita, A., Yokokohji, Y., and Konyo, M., A Teleoperated Hydraulic Rescue Robot Integrated With Elemental Technologies, The 10th JFPS international symposium on flued power, 1C12, 2017.
3. Kurokawa, M., Furukawa, M., Kondo, D., Ando, H., Maeda,T.,“Work efficiency for Remote Control with High Frame Rate,” Proc. of the 2017 JSME conf. on Robotics and Mechatronics, 2A1-I08, 2017 (in Japanese).
4. Kondo , D. and Kijima, R., “Proposal of a Free Form Projection Display Using the Principle of Duality Rendering,” Proceedings of Eighth International Conference on Virtual Systems and MultiMedia, pp.346-352,2002.

The 11th JFPS International Symposium on Fluid Power HAKODATE 2020 Oct. 12-13, 2021 JFPS The Japan Fluid Power System Society

Experimental Implementation of a Hydraulic Turbine Access System with Six-DoF Active Motion Compensation for Taiwan Offshore Wind Farms

Mao-Hsiung CHIANG[1], Bo-Yen CHEN[1], Sheng-Chia LIN[1]

[1]Department of Engineering Science and Ocean Engineering, National Taiwan University
No.1, Sec. 4, Roosevelt Rd., Taipei 106, Taiwan

TEL: +886-2-3366 3730
FAX: +886-2-2392 9885
(E-mail: mhchiang@ntu.edu.tw)

Abstract. This study aims to investigate a new turbine access system (TAS) for offshore wind farms in the Taiwan Strait under sea conditions with a wave period of 7.5sec and a significant wave height of 0.5m. The proposed system includes the novel system integration of mechanism design and a hydraulic driving system. The dynamic co-simulation of TAS is achieved firstly to confirm the system design and parameters. The dynamic modelling of the mechanism is implemented by ADAMS software. The hydraulic driving system and control system are derived mathematically and implemented via MATLAB. Then, the dynamic simulation of TAS is achieved through the co-simulation of ADAMS and MATLAB to verify the active compensation control performance of TAS. After that, a full-scale test rig is set up for experimental verification. The vertical height, roll angle and vertical acceleration of the TAS end effector can be reduced effectively through active motion compensation control, thus, improving the access safety of the offshore wind turbine.

Keywords: Offshore wind turbine access system, Active motion compensation, Motion compensation control, Kinematics, Experiment.

INTRODUCTION

As the intensifying greenhouse effect and climate change, people began to pay attention to environmental protection and renewable energy. In recent years, Taiwan achieved good results with rapid construction of onshore wind farm, while its installation area has gradually become saturated. Relatively, typically out at sea, there is a much higher wind speed allowing for more energy to be created at a time. Therefore, Taiwan is planning to develop 5.5GW of offshore wind farm in Taiwan Strait by 2025. Maritime engineering has become one of the important localization technologies in Taiwan. Assuring the safe maintenance of offshore wind turbines has become a significant issue. This study aims to investigate the active compensation system suitable for Taiwan Strait and applies to turbine access systems (TAS).

Maintenance staff enter the tower of offshore wind turbines 10 to 20 times per year. Assuring the safe maintenance of offshore wind turbines has become a significant issue. In order to protect maintenance staff from dangers when getting in and out offshore wind turbines, turbine access systems (TAS) are essential equipment. TAS for offshore wind turbines not only ensure safety during maintenance, but also can effectively enhance the attendance of maritime ships and reduce the installation costs of maritime works.

In general, the docking methods for docking vessels at turbines primarily influence the design of TAS. Different docking methods for connecting ship and wind turbines may lead to different design concepts for TAS. The main categories [1] include:

I. pushing the vessel against the tower through propeller thrust,
II. tying the vessel to the tower,
III. keeping the vessel at a short distance from the tower.

Docking methods (I) and (II) rely on the propeller thrust to maintain vessel stability. Docking method (III) requires a dynamic positioning system to determine vessel positioning. The additional equipment needs to be installed on the tower although docking methods (I) and (II) can effectively reduce the degree of freedom (DOF) of vessel motion caused by waves. The TAS in docking method (III) can compensate six-DOFs vessel motion caused by waves without additional equipment [2].

This study aims to investigate a new six-axial turbine access system for offshore wind farms in the Taiwan Strait, under sea conditions with a wave period of 7.5 sec and a significant wave height of 0.5m. This study describes novel system integration of the mechanism design, hydraulic driving system, and control system. The dynamic co-simulation of TAS is carried out firstly to confirm the system design and parameters through the co-simulation of ADAMS and MATLAB/SIMULINK. Through this co-simulation, we verify the effect of the active compensation control system for TAS. Next, a full-scale test rig is set up for experimental verification. Through the active compensation control experiment in the full-scale test rig, the 6-DOF motion of the TAS end effector can be reduced and verified by practical experiments.

LAYOUT OF TAS

For the docking method that keeps the vessel at a short distance from the tower, this study applies Stewart platform to TAS to compensate the motion caused by waves in six degrees of freedom. It consists of six extensible actuators. Each actuator is connected to the moving platform by a set of joints consist of a universal joint and a revolution joint. And the base platform is connected by a universal joint. The linear extension and retraction of the six actuators gives the platform six degree of freedoms positioning capabilities, including three translational and three rotational degrees of freedoms. The actuators labelled by 1 to 6 with anticlockwise, as shown in Fig. 1. The length of the actuator by zero extension is 1.3 m and the length of maximum elongation is 1 m. The material of the platform is A36 steel which is a standard steel alloy that is a common structural steel in mechanical industry. It has density of 7800 kg/m^3 and yield strength of 252 MPa and an allowable bending stress of 154 MPa. The properties of ASTM A36 steel allow it to deform steadily as stress is increased beyond its yield strength.
The system configuration of the six-DOFs TAS test rig is shown in Fig. 2. The position sensors are set in hydraulic cylinders to measure the cylinder position. In the control system, the D/A interface card sends out the control signal to drive the hydraulic servo valve, and the A/D interface card receives the feedback signals from position sensors. Moreover, a hydraulic power unit with supply pressure of 70 bar is set up.

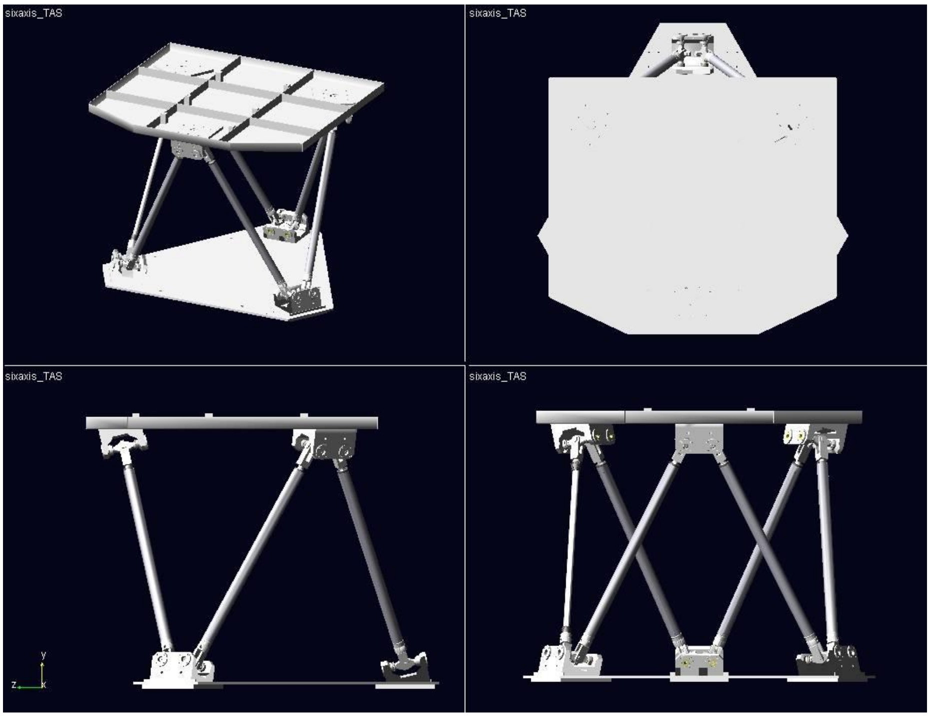

Figure 1 ADAMS model of TAS

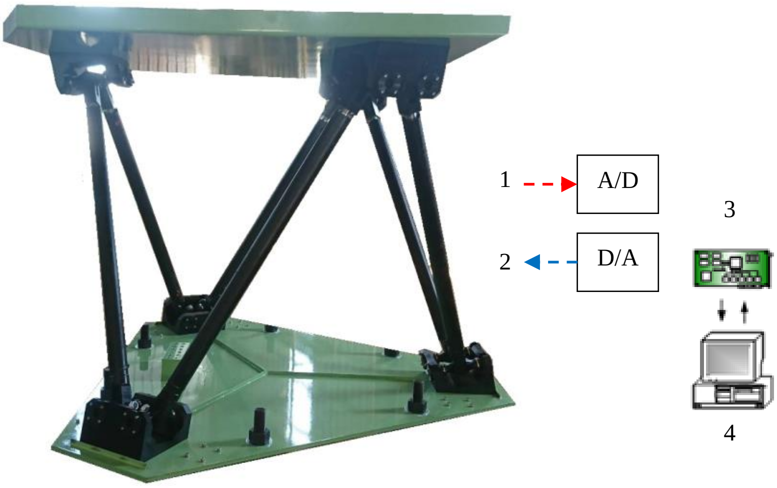

Figure 2 System configuration of TAS test rig

KINEMATICS OF TAS

This section introduces the kinematics of TAS, including inverse kinematics and forward kinematics. Here, both the inverse and forward kinematics of TAS are solved by MATLAB.

The inverse kinematic transformation for the TAS determines the required actuator lengths for a given configuration composed of Cartesian position and orientation of the moving platform with respect to the base platform. As shown in Fig. 3, the origins P and O are the corresponding geometric center of the moving platform and the base one. The Cartesian coordinates of the moving platform are given by the position of origin P with respect to the fixed frame, designated by $[\, p_x \;\; p_y \;\; p_z \,]^T$, and the orientation of the moving platform is usually represented by three standard Euler angles $[\, \alpha , \beta , \gamma \,]^T$, where p_x, p_y, p_z represent the longitudinal (surge), lateral (sway), and vertical (heave) motions, respectively, whereas α, β, γ represent the roll, pitch, and yaw motions. Each leg i links the attachment points $\mathbf{P}_i$ and $\mathbf{B}_i$ on the moving platform and the base, respectively. In this configuration, the attachment points $\mathbf{P}_i$ and $\mathbf{B}_i$ can be expressed as [3]

$$\mathbf{P}_i = \begin{bmatrix} r_P \sin(\lambda_{Pi}) \\ -r_P \cos(\lambda_{Pi}) \\ 0 \end{bmatrix} \equiv \begin{bmatrix} P_{ix} \\ P_{iy} \\ P_{iz} \end{bmatrix}, \quad \begin{aligned} \lambda_{Pi} &= \frac{i\pi}{3} - \frac{\phi_P}{2} & i &= 1,3,5 \\ \lambda_{Pi} &= \lambda_{P(i-1)} + \phi_P & i &= 2,4,6 \end{aligned} \tag{1}$$

$$\mathbf{B}_i = \begin{bmatrix} r_B \sin(\lambda_{Bi}) \\ -r_B \cos(\lambda_{Bi}) \\ 0 \end{bmatrix} \equiv \begin{bmatrix} B_{ix} \\ B_{iy} \\ B_{iz} \end{bmatrix}, \quad \begin{aligned} \lambda_{Bi} &= \frac{i\pi}{3} - \frac{\theta_B}{2} & i &= 1,3,5 \\ \lambda_{Bi} &= \lambda_{B(i-1)} + \theta_B & i &= 2,4,6 \end{aligned} \tag{2}$$

where r_P and r_B denote the length between attachment points and the center of the moving and the base platforms, respectively. As shown in Fig. 3, θ and ϕ are the angles from the center of platforms to the adjacent attachment points on the moving and the base platforms, respectively.

The inverse kinematic problem of the TAS is to determine six link-lengths of the manipulator for particular position (p_x, p_y, p_z) and orientation (α , β , γ) of the moving platform of the manipulator. Given a set of position and orientation of the moving platform, the necessary link-vectors, denoted by $\mathbf{l}_i$ (i = 1,2,…,5,6), can be straightforwardly computed by using the following formula

$$\mathbf{l}_i = \mathbf{R}_{\alpha\beta\gamma}\mathbf{P}_i + \mathbf{D} - \mathbf{B}_i \tag{3}$$

where

$$\mathbf{R}_{\alpha\beta\gamma} = \mathbf{R}_\alpha \mathbf{R}_\beta \mathbf{R}_\gamma = \begin{bmatrix} C_\alpha & 0 & S_\alpha \\ 0 & 1 & 0 \\ -S_\alpha & 0 & C_\alpha \end{bmatrix} \begin{bmatrix} 1 & 0 & 0 \\ 0 & C_\beta & -S_\beta \\ 0 & S_\beta & C_\beta \end{bmatrix} \begin{bmatrix} C_\gamma & -S_\gamma & 0 \\ S_\gamma & C_\gamma & 0 \\ 0 & 0 & 1 \end{bmatrix} \triangleq \begin{bmatrix} r_{11} & r_{12} & r_{13} \\ r_{21} & r_{22} & r_{23} \\ r_{31} & r_{32} & r_{33} \end{bmatrix} \tag{4}$$

is the rotation matrix of the platform and $\mathbf{D}=[\ p_x\ \ p_y\ \ p_z\ ]^T$ which is the translation vector of the platform. $\mathbf{P}_i$ and $\mathbf{B}_i$ are the translational offset vectors of link i on the moving platform and the base respectively. S_α and C_α are defined as sin(α) and con(α). The relation between the vectors can be seen in Fig.3.
The norm of $\mathbf{l}_i$, i.e., $\|\mathbf{l}_i\|$, represents six link-lengths of the current pose, using Eqs. (1), (2) and (4). Thus, Eq. (3) can be written as

$$\begin{aligned} &\|\mathbf{l}_i\|^2 = p_x^{\ 2} + p_y^{\ 2} + p_z^{\ 2} + r_P^{\ 2} + r_B^{\ 2} + 2(r_{11}P_{ix} + r_{12}P_{iy})(p_x - B_{ix}) \\ &+2(r_{21}P_{ix} + r_{22}P_{iy})(p_y - B_{iy}) + 2(r_{31}P_{ix} + r_{32}P_{iy})p_z - 2(p_x B_{ix} + p_y B_{iy}) \\ &\text{for} \quad i = 1,2,\ldots,5,6 \end{aligned} \tag{5}$$

As shown in Eq. (5), for a particular pose of the moving platform there will be an unique solution $\mathbf{l}_i$ (i = 1,2,…,5,6), namely, six link-lengths, thus the inverse kinematic problem of the TAS is nearly straightforward.
When six-DOFs ship motion caused by waves are determined as θ_{roll}, θ_{pitch}, θ_{yaw}, Z_{surge}, Z_{sway} and Z_{heave}, the motion of the base platform of TAS in 6-DOF compensation θ_{broll}, θ_{bpitch}, θ_{byaw}, Z_{bsurge}, Z_{bsway} and Z_{bheave}, can be calculated by DH method [4]. In order to let the moving platform stable, the particular position (p_x , p_y , p_z) and orientation (α , β , γ) of the moving platform of TAS in 6-DOF compensation must be determined as

$$\begin{aligned} p_x &= -Z_{bsurge}, \quad p_y = -Z_{bsway}, \quad p_z = -Z_{bheave} \\ \alpha &= -\theta_{broll}, \quad \beta = -\theta_{bpitch}, \quad \gamma = -\theta_{byaw} \end{aligned} \tag{6}$$

The forward kinematic problem is a very difficult and challenging one that has initiated much research attentions during the past decade. The problem is to determine the position (p_x , p_y , p_z) and orientation (α , β , γ) of the moving platform from six given actuator lengths $\mathbf{l}_i$ (i = 1,2,…,5,6), it is difficult to solve the problem because of the inherent nonlinearity and complexity. The general form of the problem can be obtained from Eq. (5) as follows:

$$\begin{aligned} &p_x^{\ 2} + p_y^{\ 2} + p_z^{\ 2} + r_P^{\ 2} + r_B^{\ 2} + 2(r_{11}P_{ix} + r_{12}P_{iy})(p_x - B_{ix}) \\ &+2(r_{21}P_{ix} + r_{22}P_{iy})(p_y - B_{iy}) + 2(r_{31}P_{ix} + r_{32}P_{iy})p_z - 2(p_x B_{ix} + p_y B_{iy}) - \|\mathbf{l}_i\|^2 = 0 \\ &\text{for} \quad i = 1,2,\ldots,5,6 \end{aligned} \tag{7}$$

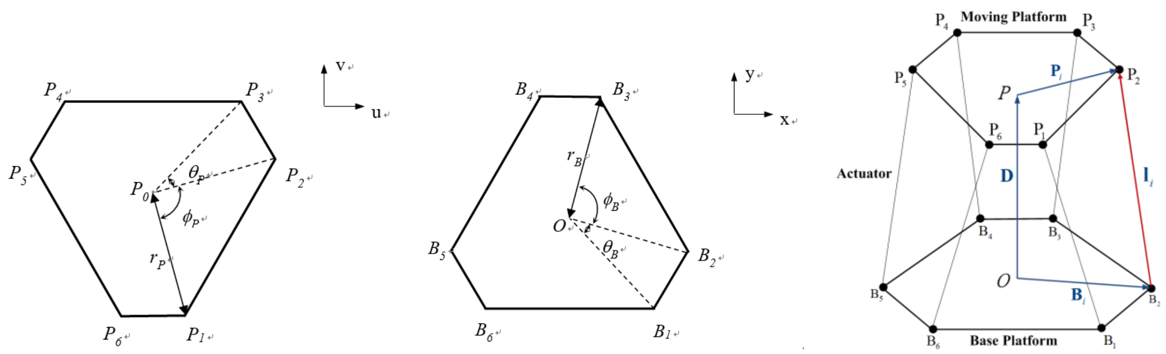

Figure 3 Geometry of moving and base platform and vector representation of TAS

Eq. (7) is multivariate polynomial equations set with respect to the moving platform position parameters (p_x , p_y , p_z) and trigonometric functions of orientation parameters (α , β , γ). Therefore, the solution to the forward kinematic problem involves the solution of a system of highly nonlinear coupled algebraic equations in variables describing the moving platform pose. The Newton-Raphson method is often used to solve the problem, but the duplicate steps before solution convergence cause the real-time application inaccessible. Furthermore, such method may cause infinite loops provided selection of wrong initial values.

RESULTS AND DISCUSSION

This section contains an experiment of the test rig to verify the TAS control performance. To compensate for the wave-induced motion of the end effector, the required displacement of each hydraulic cylinder is determined by the inverse kinematics, which become the target position of each hydraulic cylinder for the closed-loop position control of the hydraulic system. Furthermore, the PID algorithm is used to design the controllers making the hydraulic cylinders generate force correspondingly to drive the TAS.

Figure 4 shows the block diagram of the overall TAS control system in the experiment. The control input from the controllers designed by PID is given to the hydraulic systems to drive the test rig, and the position of each hydraulic cylinder is measured by position sensors and fed back to the controllers. Furthermore, based on the measured position of the hydraulic cylinders, the position of the TAS end effector can be calculated according to the forward kinematics.

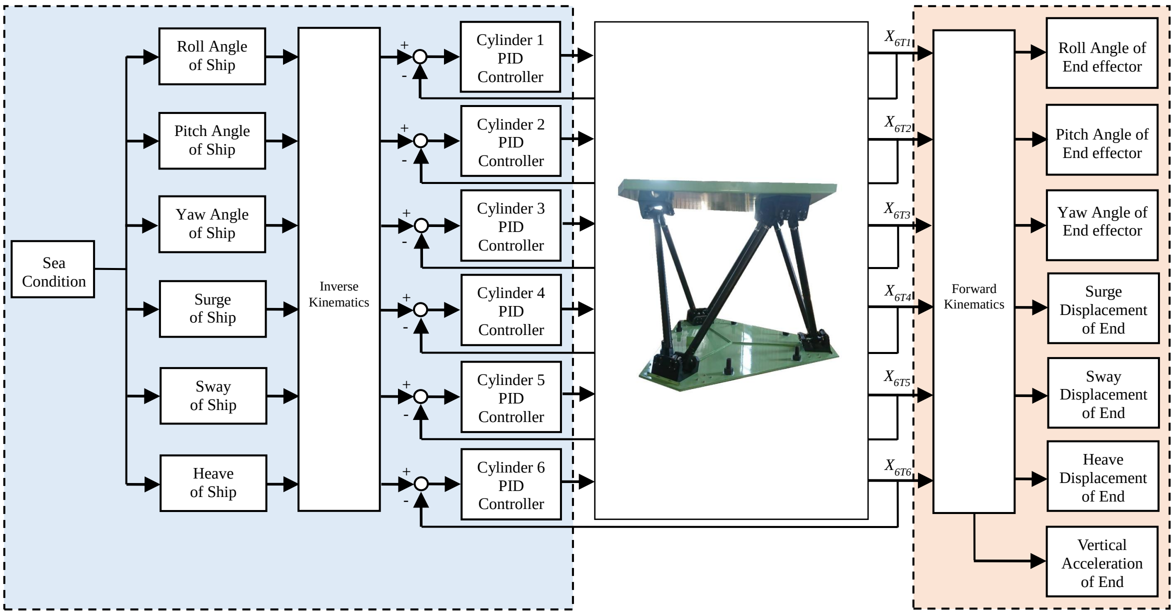

Figure 4 Block diagram of overall TAS control system in experiment

The direction relation between the ship and the wave is shown in Fig.5. Since the sea wave condition influences the ship motion, the motion variation of the ship's center of gravity caused by the given sea wave conditions of the offshore wind farm in Taiwan, with a wave period of 7.5 sec, significant wave height of 0.5m and wave direction of 45 degree is shown in Fig. 6. The wave data in this study is provided by Ship and Ocean Industries R&D Center. Furthermore, the PID controller are designed by Ziegler and Nichols method.

According to the ship motion in Fig. 6, the desired position of the six hydraulic cylinders to compensate for the motion of the end effector (the center of moving platform) can be calculated by the inverse kinematics, which are given as the target position trajectory of each cylinder. Figure 7 shows the position control responses and control errors of the hydraulic cylinders in the simulation and experiment, where the control errors of the six hydraulic cylinders are all within ±0.08m in the simulation and ±0.11m in the experiment.

Furthermore, the active motion compensation response at the TAS end effector can be compared and confirmed through the motion of six-DOF of the end effector. Figures 8 and 9 show the active motion compensation results at the TAS end effector, including three displacement responses and three angle responses of the end effector. In the condition without compensation, the roll, pitch and yaw angle significantly change within ±3.6°, ±3.3° and ±1.2°, respectively; the surge, sway and heave displacement significantly change within ±0.23m, ±0.23m and ±0.36m, respectively. After the active motion compensation, the surge, sway and heave displacement and the roll, pitch and yaw angle and the vertical acceleration change of the end effector can be respectively reduced to 1.4°, 1°, 0.39°, 0.04m, 0.04m, 0.1m in simulation and can be respectively reduced to 2°, 1.5°, 0.5°, 0.05m, 0.05m, 0.12m, in experiment. Therefore, through the verification and comparison in the simulation and experiments, both controls can achieve motion compensation effects.

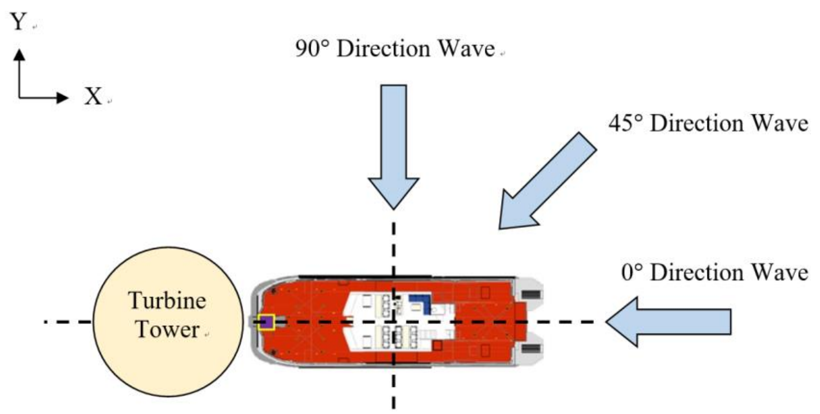

Figure 5 Direction of wave

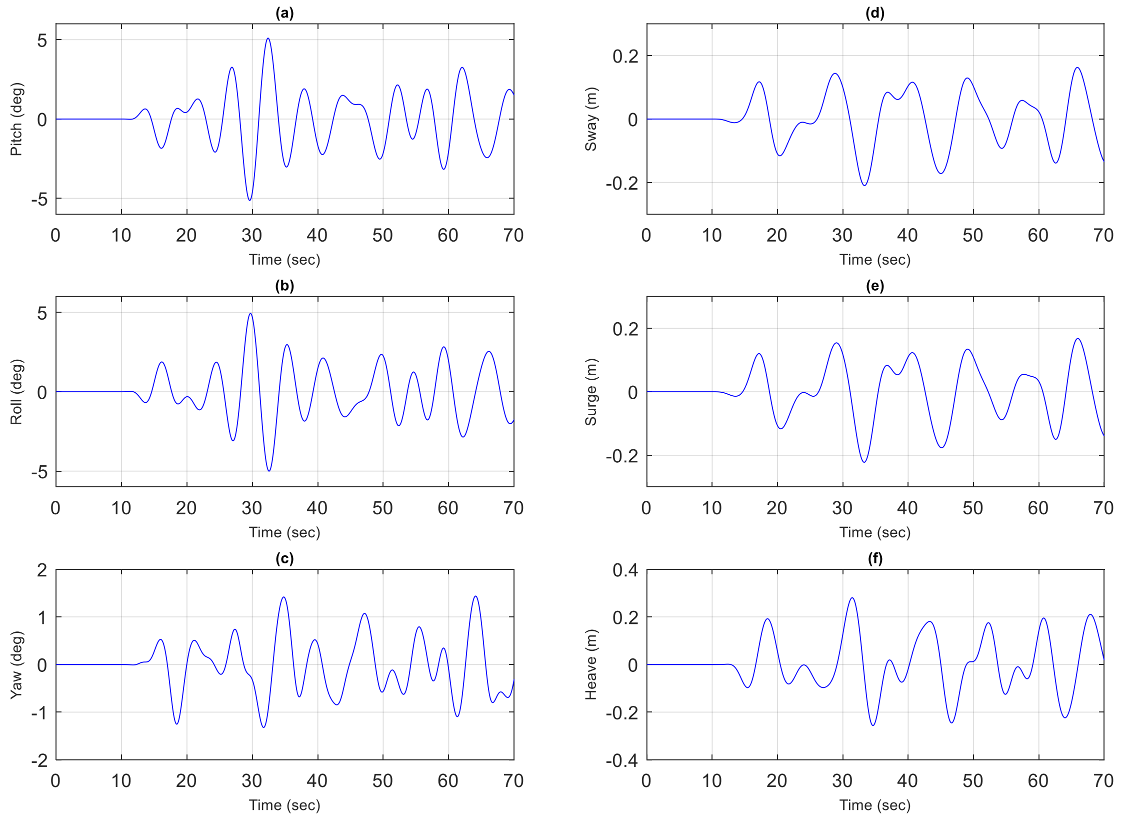

Figure 6 Ship motion caused by sea wave of 7.5 sec period, significant wave height 0.5m and wave direction 45 degree (a) Pitch angle, (b) Roll angle, (c) Yaw angle, (d) Sway position, (e) Surge position, (f) Heave position

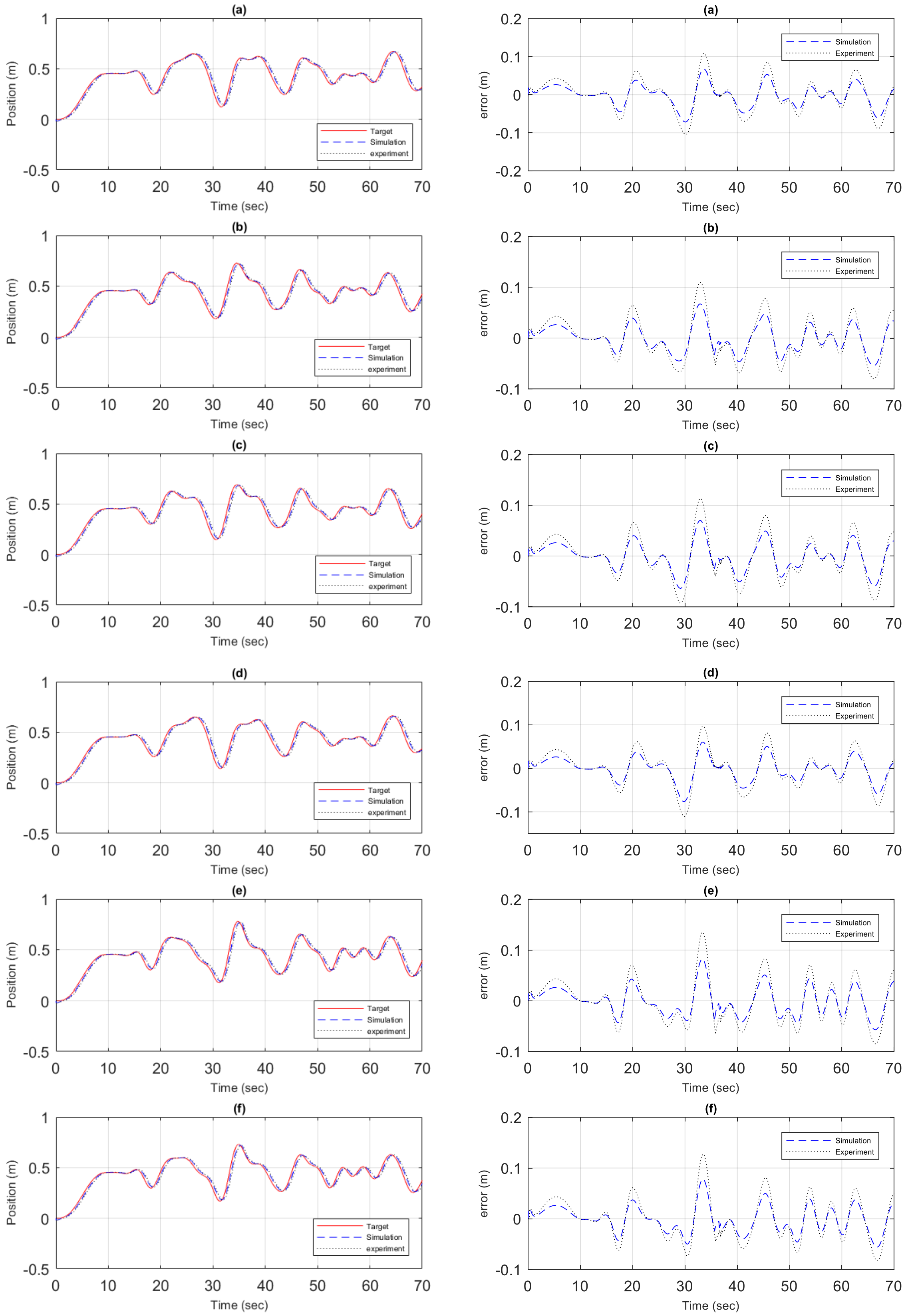

Figure 7 Hydraulic cylinder position control response and control errors
(a) 1st hydraulic cylinder position response, (b) 2nd hydraulic cylinder position response,
(c) 3rd hydraulic cylinder position response, (d) 4th hydraulic cylinder position response,
(e) 5th hydraulic cylinder position response, (f) 6th hydraulic cylinder position response

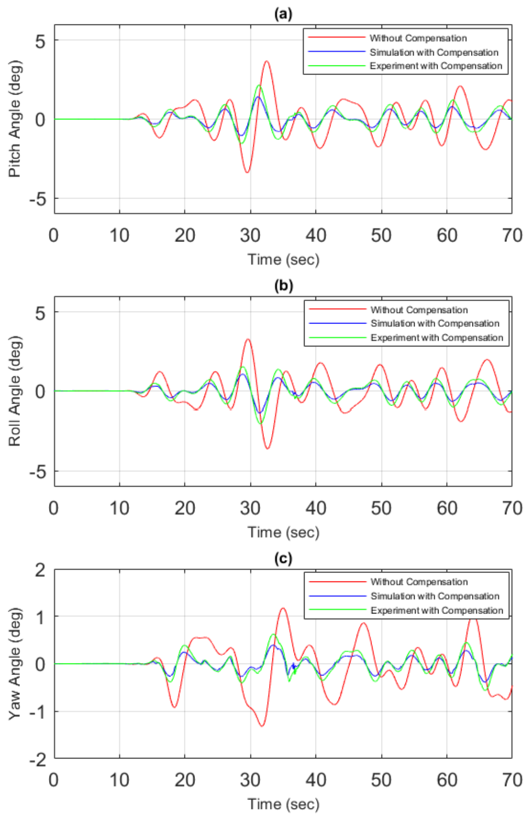

Figure 8 The motion compensation angle response at end effector
(a) Pitch angle response of end effector,
(b) Roll angle response of end effector,
(c) Yaw angle response of end effector

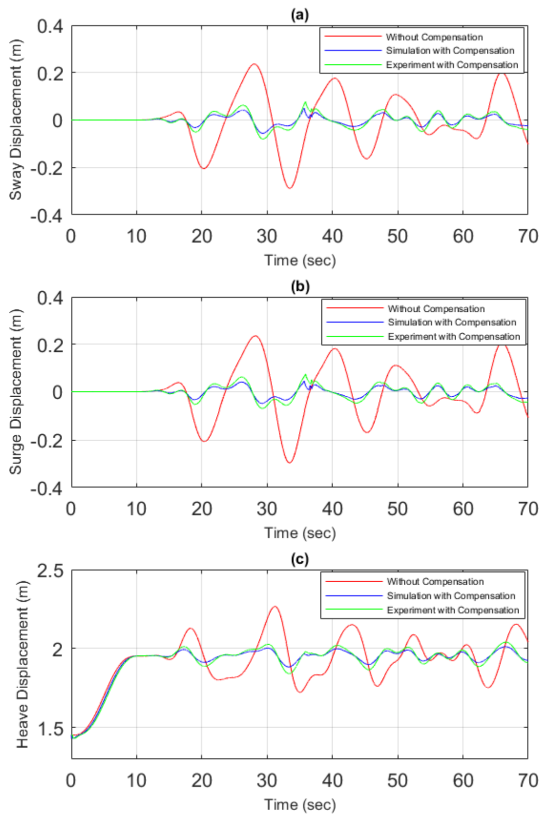

Figure 9 The motion compensation displacement response at end effector
(a) Surge displacement response of end effector,
(b) Sway displacement response of end effector,
(c) Heave displacement response of end effector

CONCLUSIONS

This study developed a TAS with a 6-DOF active motion compensation system for offshore wind farms in the Taiwan Strait, under sea conditions with a wave period of 7.5 sec and significant wave height of 0.5m. The system is driven by active motion compensation control systems using PID. The dynamic co-simulation of TAS via ADAMS and MATLAB/SIMULINK were achieved to confirm the system design and parameters. In addition, a full-scale test rig combined with the Real-time Workshop of MATLAB/SIMULINK was set up for experimental verification. Under the sea conditions of the Taiwan Strait with a wave period of 7.5 sec and significant wave height of 0.5m, the motion in 6-DOF of the TAS end effector can be reduced effectively through active compensation control in both the simulation and experiments. Finally, the TAS proposed in this study has been verified in simulation and experiments with satisfactory active motion compensation performance.

ACKNOWLEDGMENTS

This research was sponsored in part by Ministry of Science and Technology Taiwan under the grant MOST MOST 110-3116-F-002-001.

REFERENCES

1. Twidell, J. and Gaudiosi, G., "Offshore Wind Power", 1 ed., Multi-Science Publishing Co. Ltd., 2014.
2. Cerda Salzmann, D. J., "Development of the Access System for Offshore Wind Turbines," Ph.D. dissertation, Delft University of Technology, 2007.
3. Harib, K. and Srinivasan, K., "Kinematic and dynamic analysis of Stewart platform-based machine tool structures," Robotica, vol. 21, pp. 541-554, 2003.
4. Hartenberg, R. S. and Denavit, J. "Kinematic synthesis of linkages [M]." New York: McGraw-Hill 1964.

The 11th JFPS International Symposium on Fluid Power HAKODATE 2020 Oct. 12-13, 2021 The Japan Fluid Power System Society

Modular Hydraulic Servo Booster for Multi-Axis Robots

Sang-Ho HYON* and Tomoro KAI*

*Department of Robotics, Ritsumeikan University
1-1-1 Noji Higashi, Kusatsu, Shiga, 525-8577 Japan
(E-mail: sangho@ieee.org)

Abstract. A new modular hydraulic circuit suitable for multi-axis robots is proposed. The circuit is characterized by modular design, pressure boost, flow summing, and high response. The main module, called Boost Servo Pump Module (BSPM), is composed of a servo pump and switching valves. The circuit can be simply plugged into conventional servovalve systems, and improves the energy efficiency significantly. The paper presents the realization of the circuit and possible operating modes, then presents the control method for each mode. The simulation results on position control of two-link serial manipulator validate the proposed method by its clear improvement of tracking performance especially in the shared boost mode, where small pumps work together to generate high pressure and flow to the actuator.

Keywords: Modular, Hydraulics, Robot control, Flow summing, Pressure boost

BACKGROUND

To date, most high-performance multi-axis hydraulic manipulators have been equipped with servovalves, which are great inventions, nevertheless present shortcomings related to cost and energy efficiency. In this conventional method, the supply pressure must be set to the highest pressure for the axis of the highest load, which causes throttle loss at other axes. Electric hydrostatic actuators (EHAs) can solve this problem completely [1]. The method is called volume control as opposed to throttle control. Each actuator provides fluid power by itself, which allows decentralized power management. However, the servomotor must be larger as the required power becomes higher. This can pose a severe obstacle against EHA applied to multi-axis robot control.

In 2013, the authors invented a new hydraulic circuit, referred to as the Hydraulic Hybrid Servo Booster (H2SB) [2]. As shown in **Fig. 1**, the circuit has a main pump, four valves (V1 to V4), and a servomotor-controlled pump (SP), which are connected to the inlet/outlet of the cylinder. It embeds a small SP into the valve bridge so that the high-speed (up to valve size) and precision (up to the resolution of SP) are achieved in a hybrid and cost-effective manner. However, this method had three problems:

(P1) Low dynamic response at the “open-circuit mode” due to low-cost cartridge valves
(P2) Increased system size due to many independent valves,
(P3) Low speed at the “closed-circuit mode” and the “boost mode” due to the small volume of SP

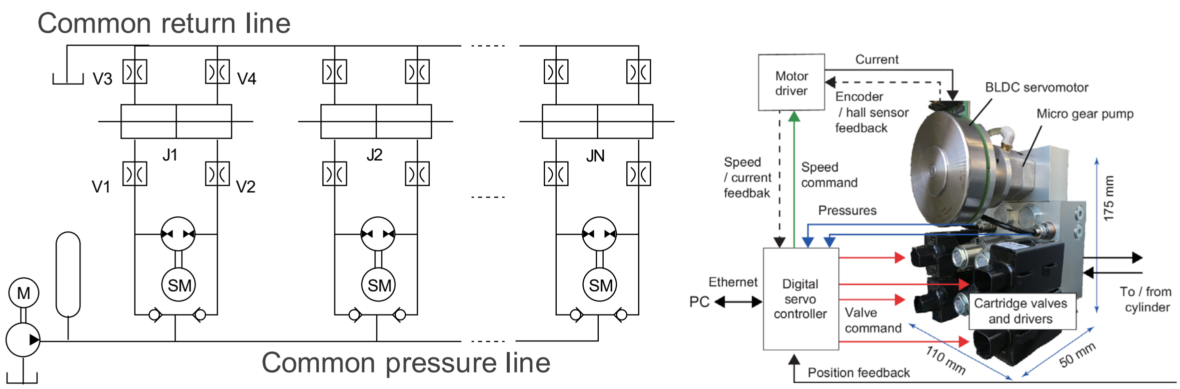

Figure 1. (Previous) Hydraulic Hybrid Servo Booster (H2SB) [2] for multi-axis robot. If the SPs are removed, the circuit just works as the *independent metering valve* system [3,4,5] by controlling four proportional valves V1 to V4. When the outlet valves, V3 and V4, are closed, then it works as independent EHAs with pre-loaded pressure. Moreover, SPs can boost the pressure to obtain higher force and high-resolution flow *independently* by opening the diagonal set of valves.

This experience led us to invent a new *modular* hydraulic servo system suitable for multi-axis robots in this paper, where small servovalves and small servo-pumps are both utilized. By doing so, we can keep the high response of the servovalves while reducing the throttling loss at the valves as much as possible even for the low-pressure operation. Instead, we have abandoned the closed-circuit configuration.

The new circuit is designed to have a modular structure that meets three conditions: 1) the modules are one-to-one connected to the actuators of the robot joints by hoses; 2) servovalves are directly mounted to the actuators; 3) modules are connected to a common pressure source (pump) and reservoir. Thus we solve (P1).

Then, how about (P2) and (P3)? This question is related to what kind of circuit should be implemented in the module. This led us to an idea of *shared boosting*, as opposed to *decoupled boosting* (already achieved in the previous circuit in Fig. 1).

PROPOSED MODULAR HYDRAULIC CIRCUIT

Overview

Figure 2 shows the hydraulic circuit first proposed in this paper. The system has servovalves, two kinds of pumps (the main pump and SPs), and switching valves, which are organized in modular configuration. The main module is called ***Boost Servo Pump Module*** (**BSPM**), composed of a servo pump and a switching valve (normally opened, three-positions, four-ports valve in this specific realization). There is also a special module called Power-Take-Off Module (**PTOM**). The BSPMs work in the following five operation modes, while PTOMs operate at either N-mode or PTO-mode.

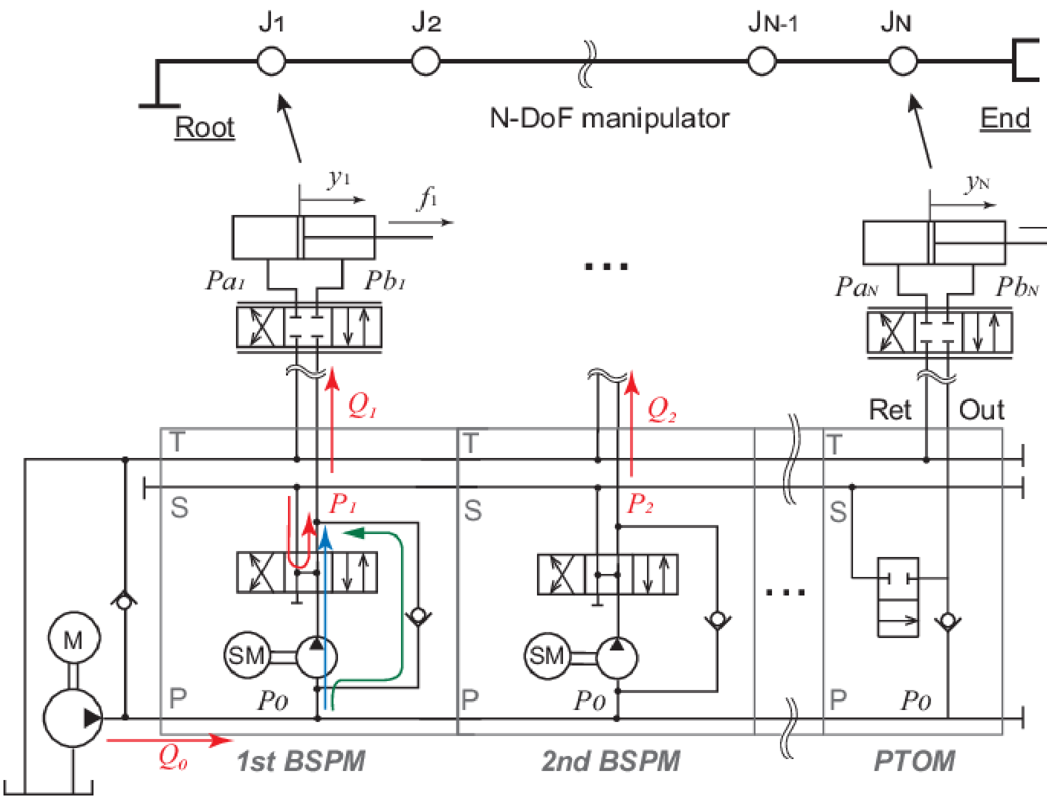

Figure 2. (New) *Modular Hydraulic Servo Booster*. The circuit is stacked together in one unit, and connected by hoses to the actuators, to which the servovalves are directly mounted. The return lines may be combined to a single hose. Each BSPM has a servo pump and a switching valve, but PTOM does not have SP because high-pressure flow may be provided by some BSPMs. Basically, the number of modules is assumed to be N, which is the same as the number of the actuators, but the numbers of BSPMs and PTOMs can be determined according to the motion tasks of the robot. Note that he robot does not need to be a serial manipulator. Each module has P (common pressure), T (tank), S (shared) rails and Outlet/Return ports. When the valves are OFF state, all the outlet of the SPs and the inlet of the servovalves in this circuit are connected through the S rail (called *shared boost* mode). This figure shows a specific realization employing commercial four-ports cartridge valves, but one can replace them with multiple two-ports valves or custom-made three-ports valves. Without SPs and switching valves, the circuit merely serves as a manifold for conventional servovalve systems (upper compatible). Note that the main pump could be powered-off because each SP can directly sack the oil from the reservoir through the line connecting P and T through the check valve.

Operation Modes

1) At low load conditions, the servovalves ensure a high response within the common supply pressure P_0 and maximum flow rate of the valves. Let us call this *normal mode* (**N-mode**). This mode can be achieved by commanding +1 to the switching valves (right position). The main pump controls the common pressure to some value P_0 , for example, to keep some stationary posture of robots.
2) At higher load conditions, each SP boosts the pressure locally. This is called *decoupled boost mode* (**DB-mode**), where we can set independent pressures, $P_1, P_2, \ldots$, for each module. This mode also can be achieved by commanding +1 to the switching valves (right position).
3) Some SPs can share the output flow by summing, where the pressure is determined to the common pressure larger than P_0. This is called *shared boost mode* (**SB-mode**). This mode can be achieved by commanding 0 to the switching valves (normal position).
4) Some SPs "devote" their flow to other modules by commanding -1 to the switching valves (left position). This is called *assisted boost mode* (**AB-mode**). This mode is useful to have higher flow to specific actuator groups.
5) The last mode is trivial, *power-take-off mode* (**PTO-mode**). It just stops the SP (e.g. for cooling purpose) and take flow from other modules through the S rail.

[Note] It is impossible to achieve two different pressures in SB mode. In that case, we just separate the modules into two groups, then block the S ports between the group (e.g. by inserting plugs).

One can operate the circuit in aforementioned five modes according to the loading conditions of robots. One drawback of the circuit is that the meter-out control for the negative load (second and fourth quadrants) causes the energy loss by throttling. This is the expense of holding dynamic response of servovalves for high-performance robots. Therefore, it is important to set the common pressure as low as possible for some given robotic tasks. In this case, the noise and temperature can be reduced significantly by using low-pressure quiet pumps (commercially available) for the main pump.
In our previous local report [6], we have presented a single-axis version of this circuit and verified the reduction of energy loss compared with conventional servovalve systems without scarifying the accuracy. But the previous circuit had no flow routing valves, nor the modular structure. When we apply this circuit to serial manipulators, where the volume of the proximal actuators is usually larger than the distal ones, we need to use larger pump and servo motors to the proximal joints. Mixture of pumps and motors of different sizes prevents the system from being compact and modular. The solution to this problem is to introduce the switching valves to transfer the flows from the distal pump to proximal actuators (or vice-versa) as necessary. This report presents the modified circuit and simulation results.

Related Study

The idea of using multiple power sources to drive multiple actuators is of course not new. Theoretically, one can use many On/Off valves to distribute the flow from multiple power sources to realize desired pressure/flow of the actuators. This is the very attractive feature of the hydraulic drive systems that the electric counterparts do not have. There are many possible combinations, but one of the extremes would be *digital hydraulics*, which is extensively surveyed in [7]. Although the impressive invention would be the novel components such as digital valves, there are still many variants relying on conventional (low-cost) components such as cartridge valves. For example, in [8], the authors proposed N-by-N (conventional) On/Off valves and (conventional) proportional valves for N-DoF excavator. However, the system size and complexity of the controller are increasing as the DoF increases. In [9], the authors combined an EHA with meter-out valve, then applied to 2-DoF robot motion control, wherein the throttle loss is reduced by transferring the flow from one actuator to other actuator. In [10], an interesting example of an excavator is shown, where the flow from bucket and arm cylinders is transferred to the boom cylinder to increase the speed.
All these studies are related to our work, but our circuit in Fig.2 uses servovalves and boosted pressure supplied by multiple servo pumps, which are stacked in a modular configuration. Also, it is ensured that no actuators are blocked because the N-mode is always available. The authors think these points are unique, and attractive for high-performance dynamic hydraulic robots such as humanoid robots, whose joints are driven by many servovalves [11].

CONTROL FOR TWO-LINK MANIPULATOR

This section presents an illustration of the basic control scheme for the proposed circuit. For simplicity, we show the N=2 case and explain how the circuit is utilized to a 2-DoF serial robot shown in **Fig.3, left**. Specifically, we restrict ourselves to a vertical lifting motion of the payload, where five phases exist as indicated in **Fig.3, right**. Details of the modes and control laws, according to the temporal phase transition of the robot motion, are explained as follows.

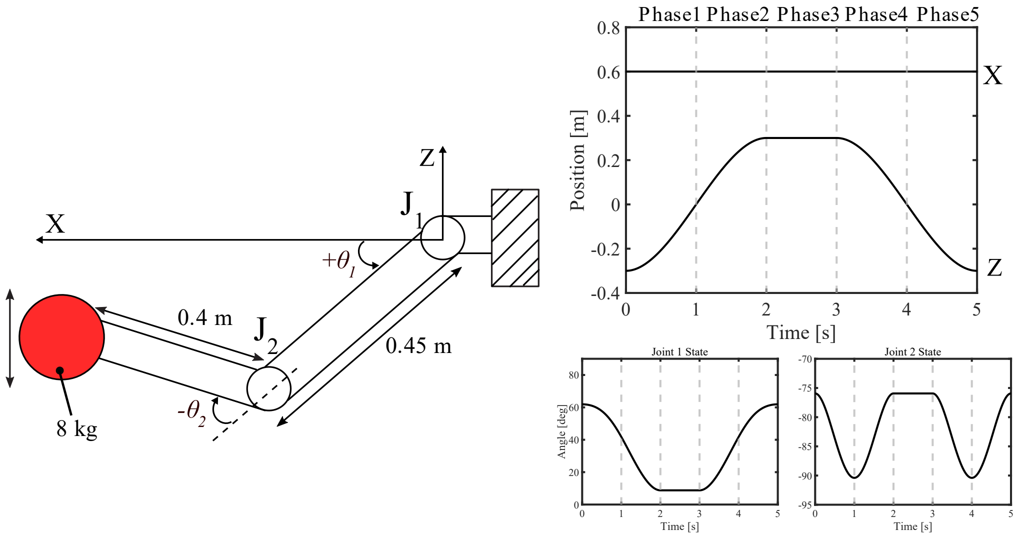

Figure 3. A two-link manipulator and its target trajectory of the tip position

Phase 1 (0~1 [s]):

The both actuators operate at DB-mode because the high pressure is required for both joints. Instead of merely generating high-pressure by boosting, each SP and servovalves coordinately control the position of cylinder to reduce the throttling loss. That is, SP generates the necessary inlet flow to achieve the desired velocity of the cylinder, while the servovalve control the outlet flow by using the actual (measured) pressure drop (meter-out control). This is same as the classical load sensing hydraulic systems.

Let $\bar{v}$ be the desired speed of the cylinder, which can be obtained by differentiating the desired position $\bar{y}$. The target value for the inlet flow $\overline{Q_{in}}$ and outlet flow $\overline{Q_{out}}$ are computed by

$$\overline{Q_{in}} = \begin{cases} A_a \bar{v}, & \bar{v} \geq 0 \\ A_b \bar{v}, & else \end{cases} \tag{1}$$

$$\overline{Q_{out}} = \begin{cases} A_b \bar{v}, & \bar{v} \geq 0 \\ A_a \bar{v}, & else \end{cases} \tag{2}$$

with the piston area of the cap-side A_a and rod-side A_b. Therefore, the commanded speed of the SP $\overline{\omega_2}$ should be

$$\bar{\omega} = \frac{\overline{Q_{in}}}{D_p \cdot \eta} \tag{3}$$

where D_p and η are the volume and efficiency of the SP, respectively. For position tracking purpose, we modify this by

$$\bar{\omega} = \frac{\overline{Q_{in}} + \Delta Q_p}{D_p \cdot \eta} \tag{4}$$

where

$$\Delta Q_p = \begin{cases} K_p(\bar{y} - y) & v \geq 0 \\ -K_p(\bar{y} - y) & else \end{cases} \tag{5}$$

is the feedback term with the proportional gain K_p.

The commanded input to servovalves are given by

$$i = \begin{cases} \dfrac{\overline{Q_{in}} + \Delta Q_{vin}}{C_v \sqrt{|\Delta P_{in}|}}, & \bar{v} \geq 0 \\ \dfrac{\overline{Q_{out}} + \Delta Q_{vout}}{C_v \sqrt{|\Delta P_{out}|}}, & else \end{cases} \tag{6}$$

where C_v is the flow coefficient of the servovalve, and ΔP_{in}, ΔP_{out} are the pressure drop across the inlet and outlet edges, respectively of the spool, which can be measured by pressure sensors. The feedback terms ΔQ_{vin}, ΔQ_{vout} are computed by the same equation (5) with different gains. Although not shown in the equations, we may consider additional flow *in advance* to compensate leakage rather than relying on feedback only.

Phase 2 (1~2 [s]) :
The joint J1 needs high positive power, while J2 need high negative power for breaking. SB-mode is suitable for J1 because single SP cannot provide enough flow. Contrary, N-mode is enough for J2 because the power is provided by the external load, and the servovalve can easily generate back pressure by throttling.
Therefore SP1 uses Eq.(4), where the feedforward term may hit the maximum flow of the SP. The missing flow is made up by SP2. The same equation (5) is used, but only the feedback term is used.

Phase 3 (2~3 [s]):
The both cylinders stop the motion, but still need high force (anti-gravitational force). Therefore, the robot should operate at DB-mode as in Phase 1.

Phase 4 (3~4 [s]) :
The same situation as Phase 2 except for that the polarity of the velocity and load just reverses.

Phase 5 (4~5 [s]):
The all SPs stop (in reality, they may rotate at slow speed to compensate for the leakage), and each servovalve controls the position of each cylinder at (low) common pressure.

Figure 4 shows the operation range of the pressure and flow in this example. **Table 1** summarizes the control law for each phase.

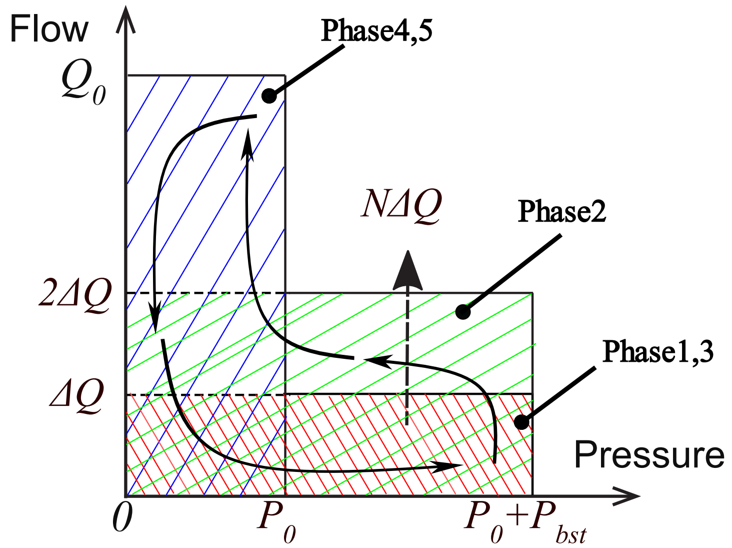

Figure 4. Operating region of the proposed circuit with two modules during the motion of the weight lifting task. The curve shows the trajectory of J1 joint only.

Table 1. Operation modes and control

	J1	J2	Control of SPs	Control of switching valves
Phase 1, 3	DB-mode	DB-mode	SP1 : J1 Position SP2 : J2 Position	V1 : -1 V2 : -1
Phase2	**SB-mode**	AB-mode	SP1 : J1 Position SP2 : J1 Position	V1 : 0 V2 : +1
Phase4	AB-mode	**SB-mode**	SP1 : J2 Position SP2 : J2 Position	V1 : +1 V2 : 0
Phase5	N-mode	N-mode	SP1 : Stop SP2 : Stop	V1 : +1 V2 : +1

POSITION TRACKING SIMULATION

This section shows the simulation result of the position tracking control of the 2-link robot, where the desired task and trajectory were already illustrated in Fig.3. Note that this task is typical for heavy load manipulators. The simulation is conducted by combining AMEsim and MATLAB/Simulink. The arm position is controlled by cylinder position feedback through the inverse kinematics of the four-bar linkage. The cylinder has the piston of the diameter 25 mm, rod of the diameter 12 mm, and 100 mm stroke. The common pressure value is set to 4.0 MPa, which is slightly higher than the pressure for the gravity compensation of the arm itself. For comparison, we set the following two conditions: (a) using DB-mode only; (b) using all modes. The result is shown in **Fig. 5**. Each panel shows, from the top, the position, pressure, and flow of the outlet port of the modules for the J1 (left) and J2 (right).

The position tracking failed in J1 for the condition (a) during Phase 2. This is because of the shortage of the flow and hence, pressure. The error is recovered in Phase 3. On the other hand, in condition (b) the inlet flow, hence the pressure, is timely increased by SB and AB mode during Phase 2, resulting in better tracking performance. Although the flow of SP2 is transferred to J1 actuator, J2 works well with the throttling control for the negative load. Therefore, there is no need to supply flow to J2 except for the make-up flow. However, when the phase transit from Phase 2 to Phase 3 around 2 [s], a small overrunning can be seen in J2 joint due to the transmission delay of the flow.

We computed the power consumption of this simulation, and compared with a conventional servovalve drive system of the supply pressure 14 [MPa], that is, the highest pressure required to achieve the same task. The score of the proposed system was J1 : 35.8 [J], J2 : 21.14 [J], over the conventional one J1 : 92.88 [J], J2 : 70.45 [J]. These results show the clear advantage of the proposed circuit not only over the conventional servo systems, but also against the decoupled load sensing servo systems as we expected.

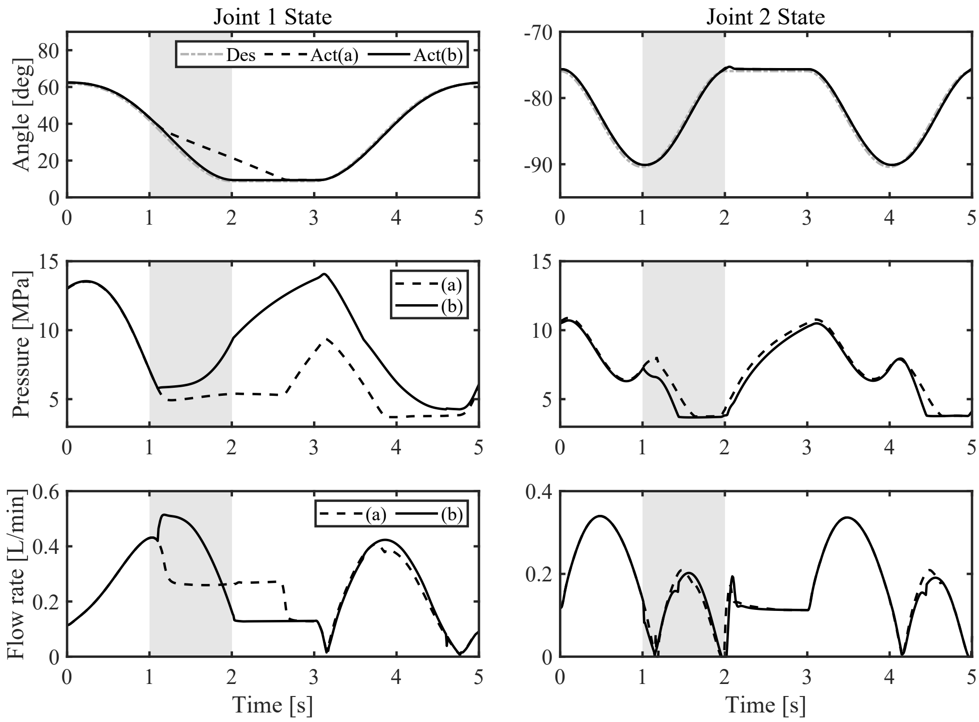

Figure 5. Simulation results on position tracking of two-link robot arm. The shaded region indicates Phase 2 of the motion sequence (see Fig.3).

CONCLUSION

We proposed a new modular hydraulic circuit suitable multi-axis robots. This circuit is characterized by modular, pressure boost, flow summing and high response. We have shown the realization of the circuit and possible operating modes, then presented the control method for each mode. The proposed circuit was numerically evaluated on a two-link serial manipulator. The position control result validated the proposed method by its clear improvement of tracking performance especially in the shared boost mode, where small pumps work together to generate high pressure and flow. The energy consumption is significantly reduced from the conventional servovalve system. Notably, the circuit can be installed to the old servovalve systems with little modification because it is upper compatible. Comparison with existing hydraulic circuits is left for future work. Besides the theoretical analysis, application to real robotic arm with joint torque control [2] is ongoing.

ACKNOWLEDGMENTS

This work was supported by KAKENHI under Grant 21H01297 (PI: S. Hyon).

REFERENCES

1. HABIBI, S., Design of new high-performance electrohydraulic actuator, IEEE/ASME Trans. Mechatronics, Vol. 5, no. 2, 2000, pp. 158-164.
2. HYON, S., TANIAI, Y., HIRANUMA, K., YASUNAGA, K., MIZUI, H., Overpressure compensation for hydraulic hybrid servo booster applied to hydraulic manipulator, IEEE Robotics and Automation Letters, Volume: 4, Issue: 2, 2019, pp.942-949.
3. JANSON, A., PALMBERG, J., Separate controls of meter-in and meter-out orifices in mobile hydraulic systems, SAE Transactions, Vol. 99, no. 2, 1990, pp. 377-383.
4. MATTILA, J., TAPIO, V., Energy-efficient motion control of a hydraulic manipulator, IEEE International Conference on Robotics and Automation, 2000, pp. 3000-3006.
5. YAO, B., LIU, S., Energy-saving control of hydraulic systems with novel programmable valves, 4th World Congress on Intelligent Control and Automation, 2002, pp. 3219-3223.
6. KAI, T., MIZUI, H., HYON, S., Hydraulic Hybrid Servo System H2SB+ for Multi-axis Robots, The 38th Annual Conference of the Robotics Society of Japan, 2020, 1F2-03.
7. LINJAMA, M., Digital Fluid Power – State of the Art, Proceedings of the 12th Scandinavian International Fluid Power Conference Vol3, 2011.
8. RUIKAI, B., TAO, W., QINGFENG, W., A multi-pump multi-actuator hydraulic system with on-off valve matrix for energy saving, IEEE/ASME International Conference on Advanced Intelligent Mechatronics, AIM, 2019, pp. 1110-1115.
9. SHIMIZU, J., OTANI, T., HASHIMOTO, K. and TAKAHASHI, A., Downsizing the motors of biped robot using a hydraulic direct drive system", IEEE-RAS Humanoids, 2018, pp.580-586.
10. BUSQUETS, E., IVANTYSYNOVA, M., A Multi-actuator displacement-controlled system with pump switching – A study of the architecture and actuator-level control, JFPS International, Volume: 8, Issue: 2, 2014, pp. 66-75.
11. HYON, S., SUEWAKA, D. TORII, Y., OKU, N., Design and experimental evaluation of fast torque-controlled hydraulic humanoid robot, IEEE/ASME Transactions on Mechatronics, Vol. 22, no. 2, 2017, pp. 623-634.

The 11th JFPS International Symposium on Fluid Power HAKODATE 2020 Oct. 12-13, 2021 JFPS The Japan Fluid Power System Society

Comparison of Mechanical Drive System and Hydraulic Direct-Drive System for Motor Power

Juri SHIMIZU*, Takuya OTANI**, Kenji HASHIMOTO***, Atsuo TAKANISHI**

* The Graduate School of Advanced Science and Engineering,
Waseda University, and Hitachi, Ltd.
832-2 Horiguchi, Hitachinaka, Ibaraki, 312-0034 Japan
(E-mail: juri-shimizu1112@asagi.waseda.jp)
** The Department of Modern Mechanical Engineering, Waseda University
17 Kikui-cho, Shinjuku-ku, Tokyo, 162-0044 Japan
*** The School of Science and Technology, Meiji University
1-1-1 Higashimita, Tama-ku, Kawasaki, Kanagawa, 214-8571 Japan

Abstract. In biped robots with serial links driven by an electric motor, a motor and transmission are installed in each joint, causing the legs to become very heavy. Therefore, a high-power motor is required at the root of each leg. To overcome this problem, the use of a hydraulic system has been proposed since it would reduce the required output at the root joint by placing the relatively heavy pressure source at the root and adopting lightweight cylinders at each joint. We previously proposed a hydraulic direct-drive system (HDD) based on a flow-based control system by a pump that uses a single-rod cylinder for biped humanoid robots. In this study, an HDD with an interlocking circuit is applied to a walking simulation. The simulation results demonstrate that the motor output of the proposed system is comparable to that of the mechanical drive system.

Keywords: Hydraulics, Humanoid, Biped locomotion, Flow-based control, Simulation

INTRODUCTION

The products people use need to undergo safe quantitative assessments. However, the main method currently used for this purpose (user rating) provides only qualitative results. Therefore, our research group proposes using biped humanoid robots instead of humans to evaluate products. WABIAN-2R (WAseda Biped humANoid-No. 2 Refined) developed by our group can walk with its knees extended by introducing a pelvic mechanism as shown in Fig. 1 [1]. In addition to WABIAN-2R, we have developed a robot that can evaluate various products. It runs as well as walks. The robot requires a high-power actuator in order to move, but due to the robot's size limitation, a high-power electric motor is difficult to implement. To solve this problem, we proposed a method to generate a large torque by using the vibration of the pelvis and the elasticity of the legs [2, 3].

Urata et al. developed a method to improve the continuous output torque in a liquid cooling system in order to increase the output of an electric motor [4]. Other robots have two or three motors on the drive shaft [5–7]. These approaches have led to the development of high speed, high torque, and highly mobile joints for humanoid legs.

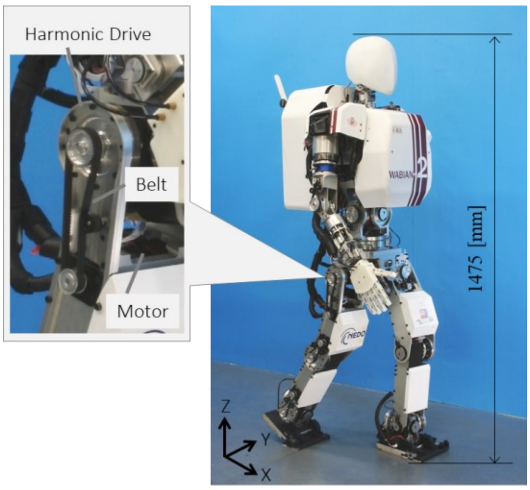

Figure 1. WABIAN-2R

The hydraulic system can realize a robot that is the same size as a human. For example, Boston Dynamics developed ATLAS [8]. Hyon et al. developed a hydraulic humanoid robot [9] called TaeMu, which has the same leg link ratio and weight distribution as humans. TaeMu can directly control the torque of each joint by adjusting the pressure of the actuator by using a servo valve. However, in its intended use, TaeMu needs to reproduce a predetermined motion pattern in order to evaluate a product. This requires a system that can directly control the joint angle.
Previously, we proposed a hydraulic direct-drive system (HDD) based on a displacement control system that uses a single-rod cylinder for a biped humanoid robot [10, 11]. In HDD, the meter-in flow rate of a single-rod cylinder is controlled by the pump discharge flow rate, and the cylinder meter-out flow rate is controlled by a proportional valve. The proposed system showed excellent energy transfer efficiency and excellent speed tracking capability in the evaluation bench system. In addition, the results show that bipedism can be achieved with an HDD that uses a collaborative simulation model of hydraulics and machines [12].
However, the HDD is mounted individually at each joint. This caused the problem of needing to increase the output of each pump to meet the maximum required output of each joint. To solve this problem, an interlocking circuit was proposed that focuses on the symmetry structure of the vibe mechanism and the symmetry of motion [13]. The proposed system reduced the maximum motor output by 27.3% in an evaluation bench device that simulated the load during walking compared with the case without the system.
In addition, comparing the performance in a walking simulation with the performance of a stand-alone HDD, we find that the interlocked HDD reduces the output power of the motor by 34.1% [14].
In this study, HDD with an interlocking circuit and conventional mechanical drive system is applied to a biped humanoid robot simulation model. The results of the performance comparison with conventional mechanical transmission verify the effectiveness of the proposed interlocked HDD.
The remainder of this paper is organized as follows: Section 2 introduces the features of the conventional mechanical drive system and the interlocked HDD for biped humanoid robots. Section 3 describes the experimental setup, procedures, and results. Section 4 discusses future prospects and concludes the paper.

COMPARISON OF DRIVE SYSTEMS

This section describes the features of the mechanical drive system that has been implemented in our biped humanoid robots and the proposed HDD.

Mechanical drive system

As shown in Fig. 1, our developed WABIAN-2R amplifies the motor torque by a harmonic drive connected by a timing belt to achieve high torque [1]. The harmonic drive has a high reduction gear ratio and no backlash. For example, the WABIAN-2R hip joint pitch axis exerted torque with a harmonic drive with a reduction ratio of 1/100. Although high torque and precise control can be achieved, the harmonic drive tends to have low back drivability, which is the ease of following an operation against an external force from the load side, and transmission efficiency is also lower than that of general gear systems.
Fig. 2 shows the characteristics of the transmission efficiency of the harmonic drive SHD17 used in the hip pitch joint of WABIAN-2R [15]. The harmonic drive has the characteristic that efficiency deteriorates at the lower rated torque ratio because there is mechanical loss due to dragging torque caused by friction.

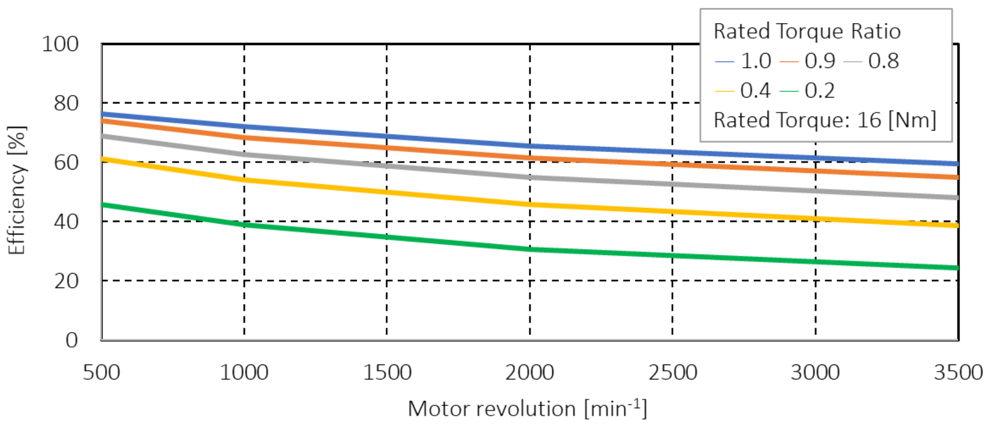

Figure 2. Efficiency of the harmonic drive (SHD17)

Hydraulic direct-drive system

This section describes the features of the hydraulic system and the mechanical link for our proposed HDD for biped humanoid robots.

Hydraulic system

Our proposed HDD controls the flow rate of the actuator by pump derived flow. The proposed circuit is shown in Fig.3. The drive velocity and direction of the cylinder can be controlled by the pump derived flow rate and direction. The cylinder meter outflow rate can be controlled by the proportional valves installed between the pump and the cylinder in a negative load situation when the cylinder drive direction and load direction are the same.
Furthermore, by providing a valve that connects two pump outputs and two valves that connect two cylinders, it is possible to concentrate the pump derived flow rate on the cylinder with a higher load and drive the cylinder with a lower load by the discharge flow rate of the higher load cylinder. The interlocking circuit can reduce the output power of the motor for the pumps.
In this study, Valve 3c that connects the cap side of Cylinders 1 and 2 is added to a previously proposed circuit [13]. A method has already been proposed to control Valve 3b, which connects the rod-side cylinder [13]. Valve 3c can also be controlled on the basis of the proposed control method by reversing the relationship between the meter-in flow and meter-out flow of Cylinders 1 and 2 at an interlocking mode.
The conversion efficiency from the motor output to the cylinder output of the proposed system is determined by the efficiency of the pump shown in Fig. 4. As shown in Fig. 4, high pump revolution and high pump discharge pressure improve pump efficiency. Therefore, in this study, we aim to improve the efficiency of the hydraulic system by increasing the pump revolution by reducing the pump displacement and increasing the pressure by reducing the cylinder diameter.

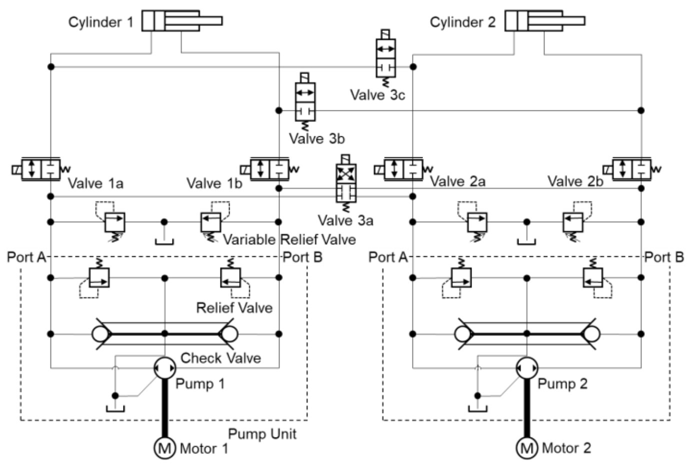

Figure 3. Proposed hydraulic circuit with interlocking drive circuit

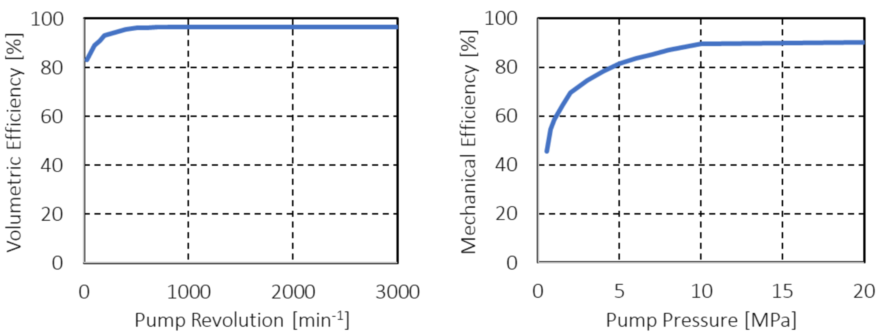

Figure 4. Efficiency of the pump (TFH-080-U-SV)

Mechanical link

The proposed system uses a cylinder as a highly efficient hydraulic actuator. The cylinder is linearly driven, and to use it to drive the rotary joints of biped humanoid robots, a link mechanism is used to convert linear motion into rotary motion. The proposed system can directly control the cylinder speed by the pump revolution. The cylinder speed is easier to control if the joint angular velocity can be determined by the pump revolution. To achieve this, the linear stroke and rotation angle must be linear. Therefore, a linear characteristic was obtained by optimizing the parameters using the 4-bar linkage mechanism shown in Fig. 5 [11]. Table 1 shows the actually designed link parameters. Fig. 6 (a) shows the relationship between the cylinder stroke and the joint angle.

A simulation showed that walking can be achieved by the feedforward flow rate control by pump and proportional valves and the simple proportional control that compensates for the error with the target angle by this linkage mechanism [12].

To improve the efficiency of the drive system, the conversion efficiency of the cylinder output force and joint torque should be focused on. Fig. 6 (b) shows the relationship between cylinder stroke and joint torque at a cylinder output force of 100N. This characteristic indicates that the conversion rate from the cylinder output force to joint torque varies greatly depending on the cylinder stroke.

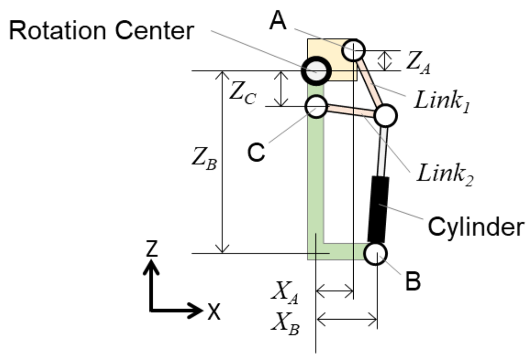

Figure 5. Four-bar linkage mechanisms

Table 1. Four-bar linkage mechanisms parameters

Link 1 [mm]	119
Link 2 [mm]	113
X_A [mm]	59
Z_A [mm]	34
X_B [mm]	100
Z_B [mm]	300
X_C [mm]	0
Z_C [mm]	57

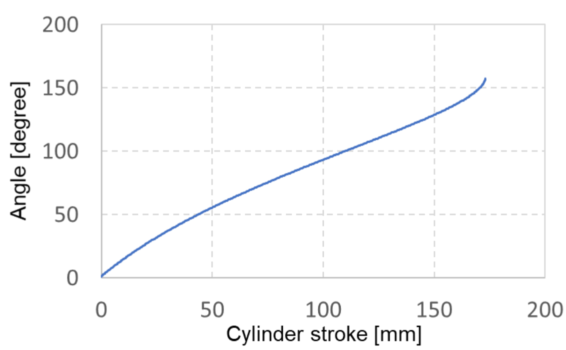

(a) Cylinder stroke and joint angle

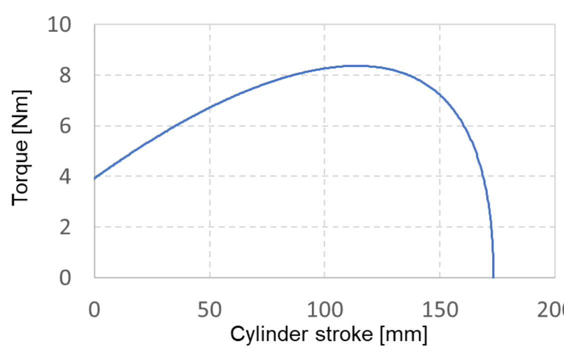

(b) Cylinder stroke and joint torque (Cylinder output: 100 [N])

Figure 6. Link characteristics

Evaluation

The required motor powers of the proposed interlocked HDD and conventional mechanical drive system were compared experimentally. The mechanical hydraulic co-simulation model was used to determine whether the maximum output of the motors can be reduced by the walking pattern. The maximum output of the motor during walking with the mechanical drive system was compared with the situation when the HDD and interlocked HDD were applied. The details are presented in the next section.

SIMULATION

Simulation setup

To compare the proposed HDD with the conventional machine drive system, we developed a simulation model of a biped humanoid robot that implements each system. We used the physical modeling tool LMS Imagine.Lab Amesim™ (Siemens K.K.) to evaluate the proposed system.

Mechanical Drive system

A model for evaluating the motor output of a mechanical drive system was constructed using the three-dimensional mechanical analysis library. The construction of the mechanical model was based on the link mechanism and mass distribution of WABIAN-2R [1]. Since the proposed hydraulic system is applied to the hip pitch joint, we applied the harmonic drive efficiency shown in Fig. 1 to this joint. In the constructed model, the efficiency was determined from the motor revolutions and torque, and the motor output power was calculated by considering this efficiency with respect to the joint output.

Hydraulic direct-drive system

To evaluate the proposed interlocked HDD, we have developed a mechanical hydraulic co-simulation model of a biped humanoid robot. As the mechanical model, the model constructed for the mechanical drive system was used. This mechanism model and the proposed interlocked HDD hydraulic model were coupled. Our proposed hydraulic system was applied to the hip pitch joint. The hip joint required high torque and joint density, and space limitations make it difficult to install large drive systems. The other joints in the model were the same as those in the mechanical drive system. Fig. 7 shows a co-simulation model of hydraulics and machinery, and Fig. 8 shows the details of a hydraulic model. The hydraulic model was based on the circuit shown in Fig. 3 and reflects the valve characteristics and motor responsiveness based on the experiments performed in a previous study [11]. Furthermore, for the efficiency of the pump, the characteristics shown in Fig. 4 were implemented. The corresponding parameters are shown in Table 2. The four-bar linkage mechanism installation angle was adjusted so that the maximum torque shown in Fig. 6 (b) could be exerted in the joint range used in the walking pattern performed in the experiment.

Table 2. Hydraulic circuit model parameters

Pump displacement [cc/rev]		0.8
Pump relief pressure [MPa]		21
Cylinder stroke [mm]		132
Cylinder piston diameter [mm]		15
Cylinder rod diameter [mm]		10
Variable relief valve set pressure [MPa]		15
Hose inner diameter [mm]		6.4
Hose length [mm]	**Pump to Valves 1a, 1b, 2a, 2b**	1000
	Pump to Valve 3a	300
	Valves 1a, 1b, 2a, 2b, to Cylinder 1, 2	2000
	Valves 3b and 3c to Cylinder 1, 2	300
Valves 1a, 1b, 2a, 2b : Nominal flow rate [L/min/MPa]		5
Valves 3a, 3b, 3c : Nominal flow rate [L/min/MPa]		10
Oil kinematic viscosity [mm^2/s]	**40 [deg C]**	14.7
	100 [deg C]	3.7
Experimental oil temperature [deg C]		25

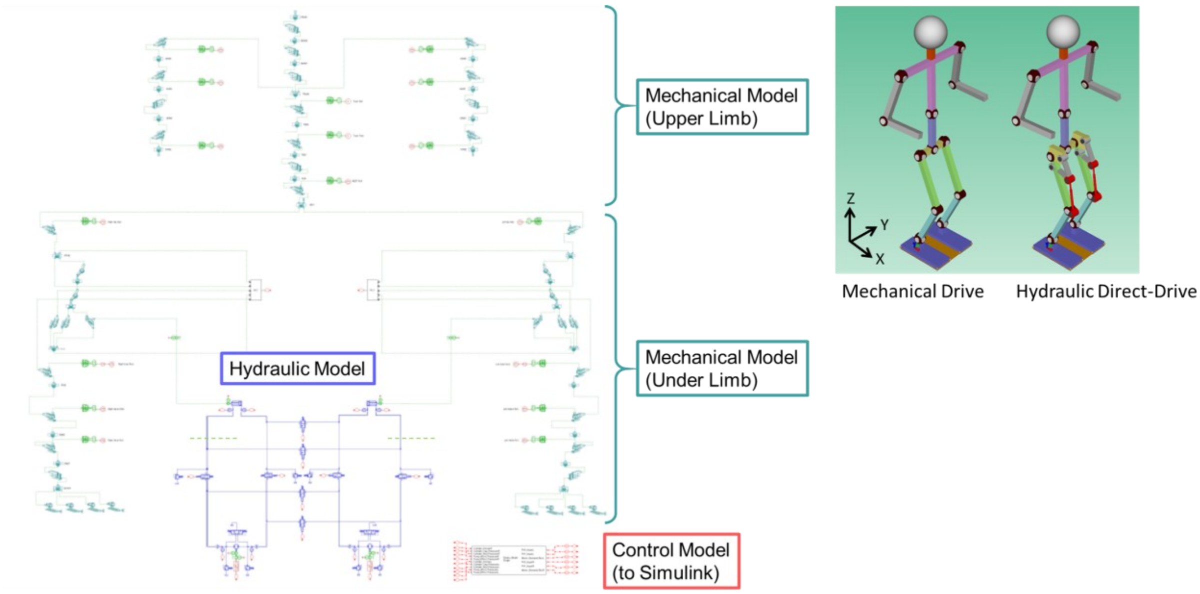

Figure 7. Co-simulation model

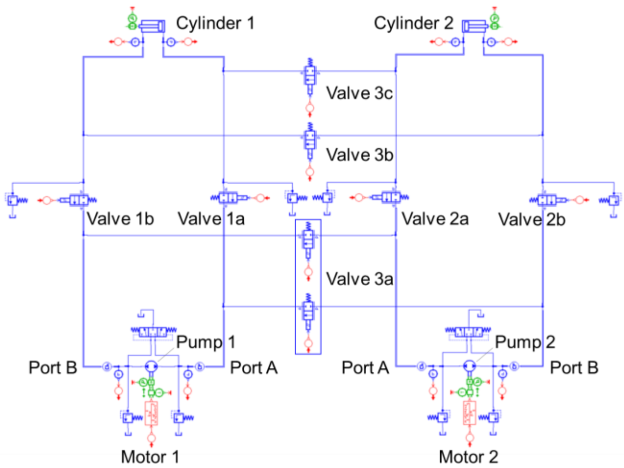

Figure 8. Hydraulic model

Simulation procedure

First, a walking simulation was executed when the mechanical drive system and HDD were applied. From the results, the phase in which the motor output increased during walking was determined. If the output of the motor for driving one leg is high and the output of the motor on the opposite side is low, the output of the motor should be able to be suppressed by using an interlocking circuit.

From the analysis results, the timing of applying the interlocking circuit was determined, and a walking simulation was performed. In addition, the results of the gait simulation will be used to evaluate how much the proposed interlocked HDD reduces the motor output. To verify the effectiveness of the proposed system, we compared it with the results of the walking simulation of the mechanical drive system reported in a previous study [1].

By reducing the output of the motor, the motor can be shrunk. The motor is selected on the basis of the required output. The goal is to achieve the maximum output required for each axis. If the peak output of each motor is reduced by the interlocking method, a smaller motor can be selected, which will contribute to the reducing the weight of the robot. This means that by installing a motor with the same output as before, higher performance than before can be achieved. Therefore, the comparative experiment evaluated the peak output of the motor during walking.

The walking pattern of the simulation experiment was generated using the offline pattern generation method proposed by our research group. The group has a proven track record of walking with WABIAN-2R [1], the basis of the mechanism model. In this study, we applied the walking pattern with knee bending, which is a walking pattern of most biped robots.

Simulation results

Fig. 9 shows the simulation results for the walking motion of the biped humanoid robot model with the HDD. The results show that the proposed HDD can follow the specified trajectory under the walking motion load, thereby achieving biped walking.
Fig. 10 shows the power of Motors 1 and 2 with the HDD and mechanical drive system. As shown in Fig. 10, the power of Motor 1 for the right leg increased at a single stance left phase, such as at 2.7–3.4. In this phase, Motor 1 must raise the right leg quickly. Thus, the output of Motor 1 increased, as shown in Fig. 10. The maximum power was 177.8 W in the HDD and 87.7 W in the mechanical drive system.

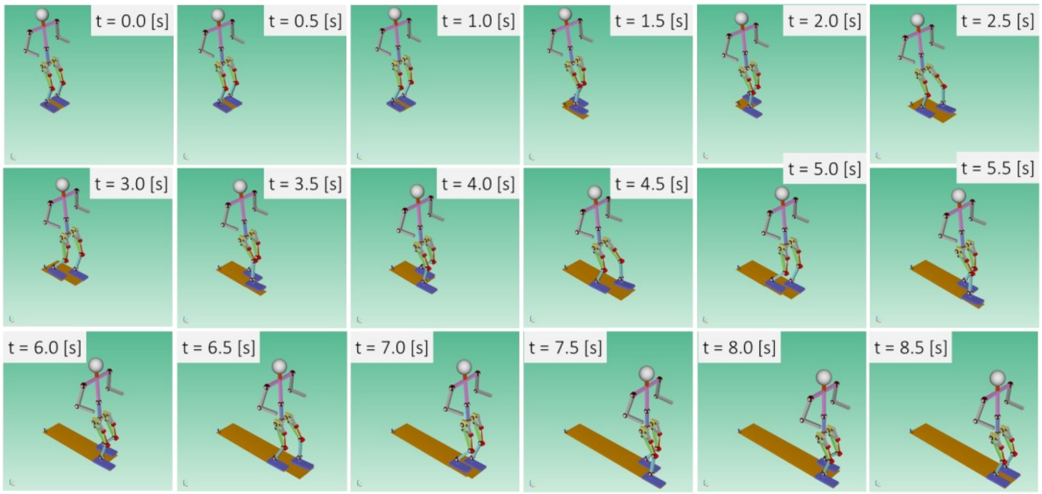

Figure 9. Walking motion of co-simulation model

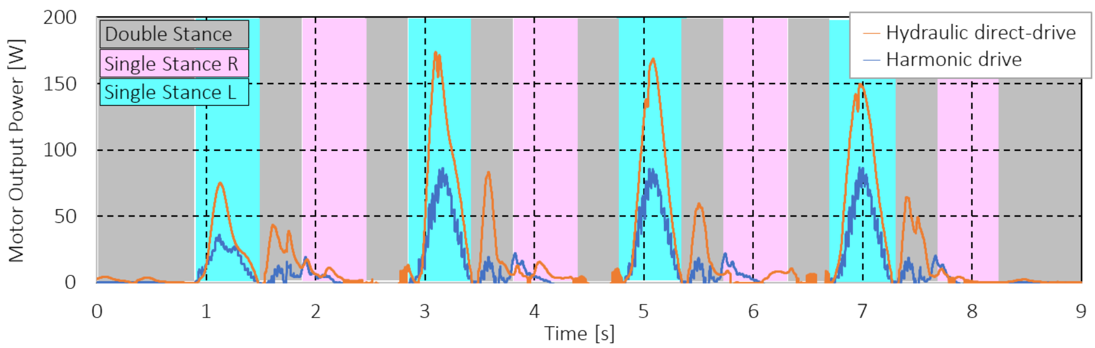

(a) Right leg side

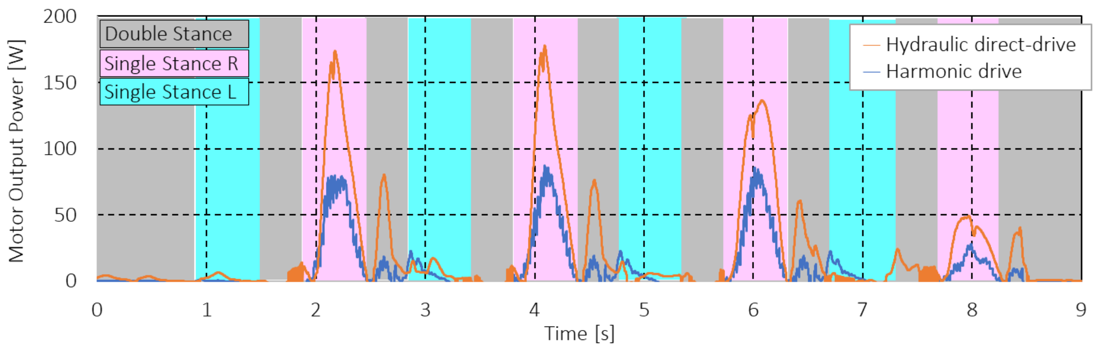

(b) Left leg side

Figure 10. Motor output power

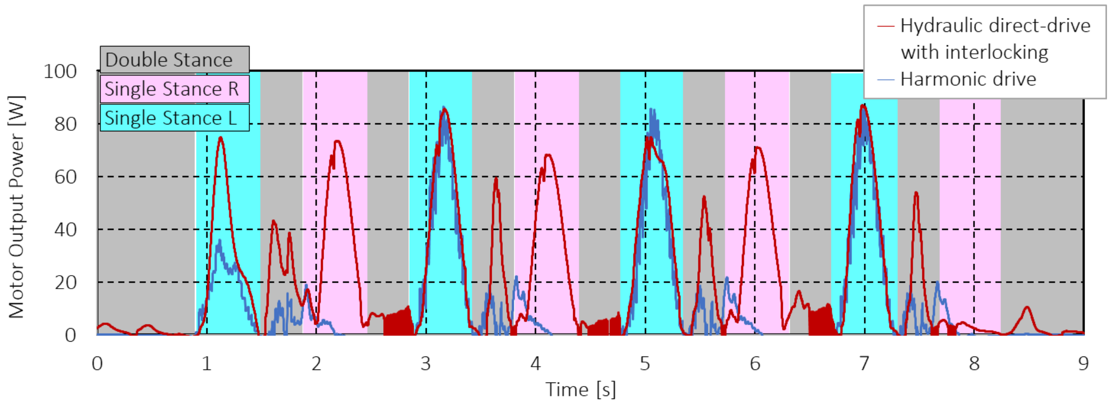

(a) Right leg side

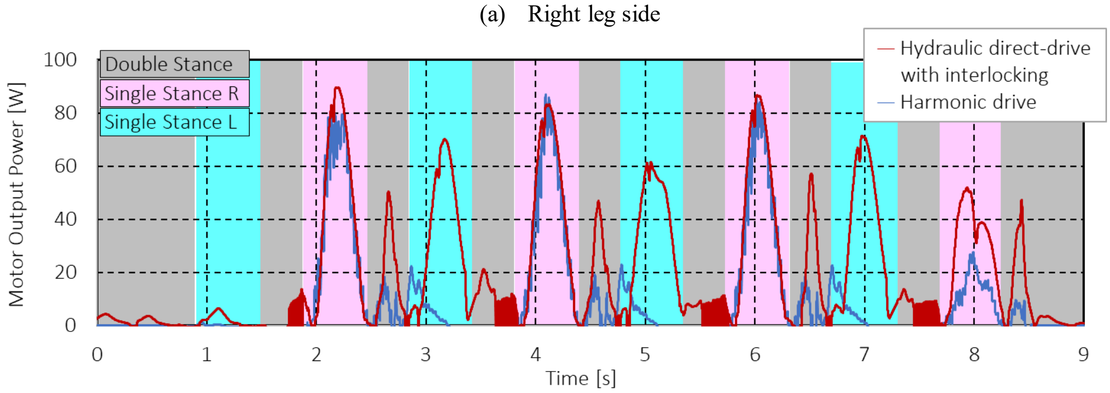

(b) Left leg side

Figure 11. Motor output power

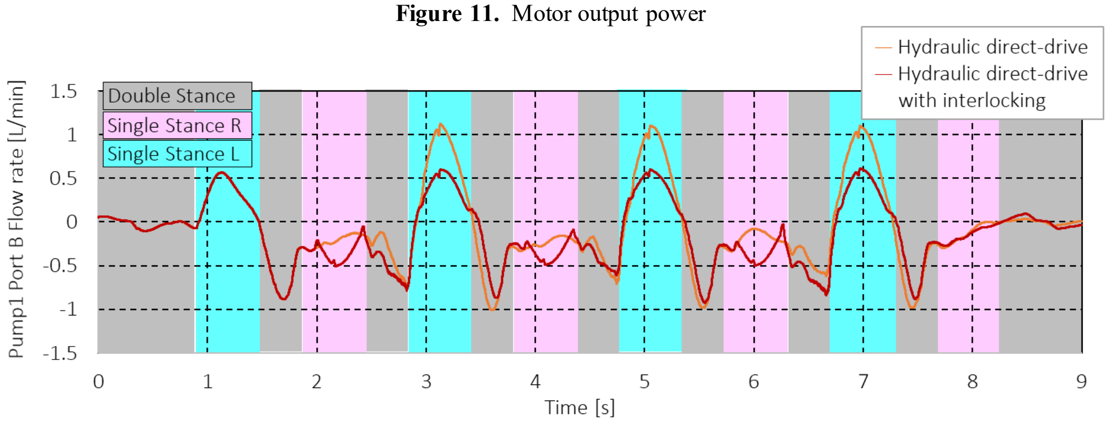

(a) Flow rate

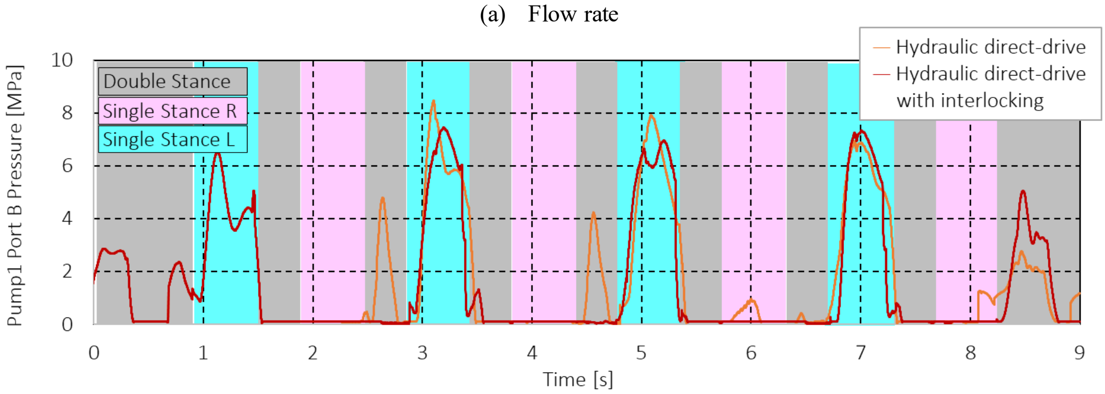

(b) Pressure

Figure 12. Pump1 port B condition

Fig. 11 shows the power of Motors 1 and 2 when the interlocking drive mode was applied. This mode was applied during the single stance phase, and outputs of Pumps 1 and 2 connect to the swing leg side cylinder by

opening Valves 3a and 3c. As shown in Fig. 11, the peak power of Motor 1 was reduced to 89.7 W. Therefore, the maximum motor power can be comparable to that of the mechanical drive system.
Fig. 12 shows Pump1 port B the flowrate and the pressure with the HDD and the interlocked HDD. As shown in Fig. 12, although the pressure was comparable, the flowrate decreased by interloking system at a single stance left phase, such as at 2.7–3.4. Therefore, the peak power of Motor 1 at the phase shown in Fig. 11 (a) was reduced compared to the result shown in Fig 10 (a).

Discussion

As shown in Fig. 10, when comparing the mechanical drive system and a single HDD, the HDD had a higher motor output. This is not a problem with the hydraulic system, but a problem with the link mechanism. Fig. 13 compares the output of the joint when the efficiency of the harmonic drive is not taken into consideration and the output of the cylinder when the efficiency of the hydraulic circuit is not taken into consideration. The maximum outputs of the joint and cylinder were 58.4 and 125.8 W, respectively.
As shown in Fig. 13, the cylinder that drives the joint via the link mechanism required a larger output even when the same walk was performed. This can be improved by searching for energy-efficient link parameters by optimizing the link mechanism. However, since there is a trade-off between the cylinder stroke and the linear characteristics of the joint angle shown in Fig. 6 (a), the optimum link ratio needs to be determined from the viewpoints of controllability and efficiency. In addition, if the hydraulic motor has higher efficiency than the link, an approach should be considered that converts linear motion into rotary motion by a method other than linking.
However, even in that case, the effect of reducing the maximum motor output by the interlocking circuit does not change. Therefore, the effectiveness of the proposed system is not lost. In addition, it would be effective to have an approach that maximizes the effect of the interlocking circuit by controlling the output peaks of the left and right legs to shift by creating a walking pattern.

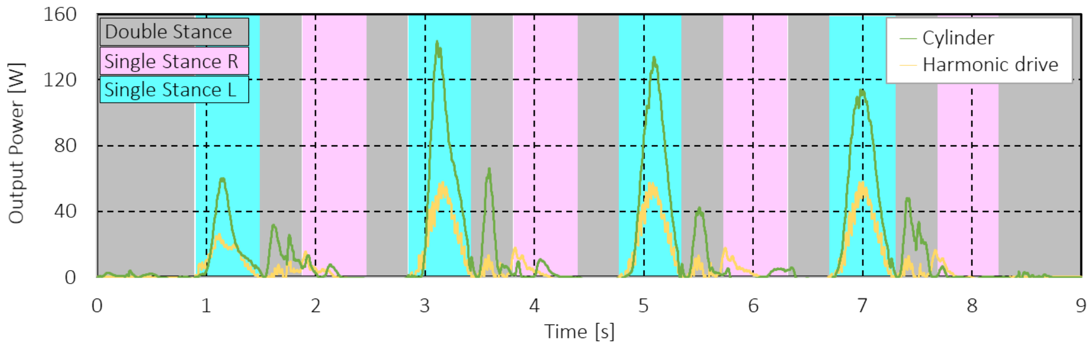

(a) Right leg side

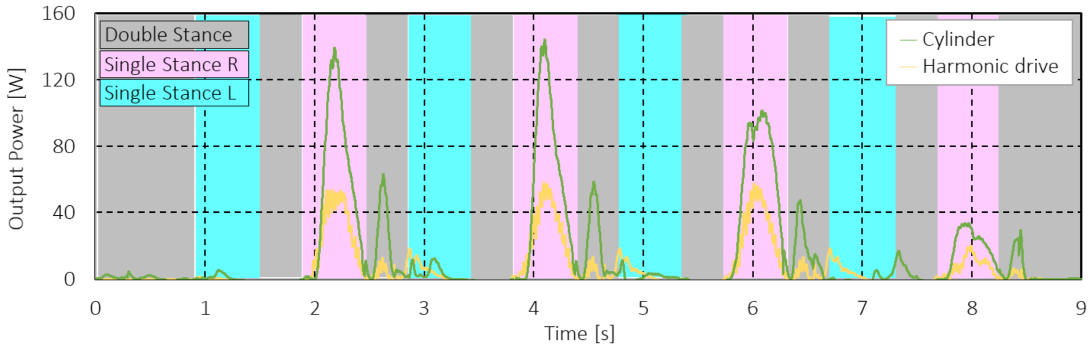

(b) Left leg side

Figure 13. Actuator output power

CONCLUSION AND FUTURE WORKS

In this study, the performances of a hydraulic interlocking drive system with a conventional hydraulic direct-drive system (HDD) and a mechanical drive system were compared to verify the motor output power. A hydraulic and mechanical co-simulation model was used for the evaluation. Simulation results showed that the motor output peaked during the swing leg in walking, and the timing of interlocking was adjusted on the basis of the experimental results.
The results also showed that the motor output in the interlocked HDD could be reduced to the level of a mechanical drive system and that the proposed system contributes to reducing the size of the installed motors for biped humanoid robots.
In the future, linkage mechanism efficiency will need to be improved for energy saving, and the proposed HDD will be applied to a biped humanoid robot to conduct a walking experiment.

ACKNOWLEDGMENTS

This study was conducted with the support of the Research Institute for Science and Engineering of Waseda University and the Future Robotics Organization of Waseda University. This study was part of the humanoid project at the Humanoid Robotics Institute of Waseda University.

REFERENCES

1. OGURA, Y., SHIMOMURA, K., KONDO, H., MORISHIMA, A., OKUBO, T., MOMOKI, S., LIM, H., TAKANISHI, A., Human-like Walking with Knee Stretched, Heel-Contact and Toe-Off Motion by a Humanoid Robot, IEEE/RSJ Int Conf on Intelligent Robots and Systems, 2006, p.3976–3981
2. OTANI, T., HASHIMOTO, K., HAMAMOTO, S., MIYAMAE, S., SAKAGUCHI, M., KAWAKAMI, Y., LIM, H., TAKANISHI, A., Knee Joint Mechanism that Mimics Elastic Characteristics and Bending in Human Running, IEEE/RSJ Int Conf on Intelligent Robots and Systems, 2015, p.5156–5161
3. OTANI, T., HASHIMOTO, K., MIYAMAE, S., UETA, H., SAKAGUCHI, M., KAWAKAMI, Y., LIM, H., TAKANISHI, A., Angular Momentum Compensation in Yaw Direction Using Upper Body Based on Human Running, IEEE Int Conf on Robotics and Automation, 2017, p.4768–4775
4. URATA, J., NAKANISHI, Y., OKUDA, K., INABA, M., Design of High Torque and High Speed Leg Module for High Power Humanoid, IEEE/RSJ Int Conf on Intelligent Robots and Systems, 2010, p.4497–4502.
5. ITO, Y., NOZAWA, S., URATA, J., NAKAOKA, T., KOBAYASHI, K., NAKANISHI, Y., OKADA, K., INABA, M., Development and Verification of Life-Size Humanoid with High-Output Actuation System, IEEE Int Conf on Robotics and Automation, 2014, p.3433–3438.
6. PARK, I., KIM, J., LEE, J., OH, J., Mechanical Design of the Humanoid Robot Platform, HUBO, Advanced Robotics, Vol.21, No.11, 2007, p.1305–1322.
7. KANEKO, K., KAMINAGA, H., SAKAGUCHI, T., KAJITA, S., MORISAWA, M., KUMAGAI, I., KANEHIRO, F., Humanoid Robot HRP-5P: An Electrically Actuated Humanoid Robot with High Power and Wide Range Joints, IEEE Robotics and Automation Letters, Vol.4, No.2, 2019, p.1431–1438.
8. https://www.bostondynamics.com/atlas, (accessed on 1, June, 2021)
9. HYON, S., SUEWAKA, D., TORII, Y., OKU, N., Design and Experimental Evaluation of a Fast Torque-Controlled Hydraulic Humanoid Robot. IEEE/ASME Transactions on Mechatronics, Vol.22, No.2, 2017, p.623–634
10. SHIMIZU, J., OTANI, T., MIZUKAMI, H., HASHIMOTO, K., TAKANISHI, A., Experimental Validation of High-Efficiency Hydraulic Direct-Drive System for a Biped Humanoid Robot, IEEE Int Conf. on Robotics and Automation, 2019, p.9453–9458.
11. SHIMIZU, J., OTANI, T., HASHIMOTO, K., TAKANISHI, A., Evaluation of Tracking Control for Hydraulic Direct-drive System, JFPS International Journal of Fluid Power System, Vol.13, No. 3, 2020, p.17-24.
12. SHIMIZU, J., OTANI, T., HASHIMOTO, K., TAKANISHI, A., Simulation of a Hydraulic Direct-Drive System for a Biped Walking Robot, 16th Scandinavian Int Conf on Fluid Power, 2019, B6.1.
13. SHIMIZU, J., OTANI, T., MIZUKAMI, H., HASHIMOTO, K., TAKANISHI, A., Experimental Validation of Hydraulic Interlocking Drive System for Biped Humanoid Robot, IEEE/RSJ Int Conf on Intelligent Robots and Systems, 2019, p.7163–7169.
14. SHIMIZU, J., OTANI, T., HASHIMOTO, K., TAKANISHI, A., Simulation of an Interlocking Hydraulic Direct-Drive System for a Biped Walking Robot, 12th International Fluid Power Conference, 2020, p.211-220.
15. http://www.takako-inc.com (accessed on 1 June, 20219)
16. https://hds-tech.jp/pdf/hd01_sougou_0204.pdf (accessed on 1 June, 2021)

Genaral Session | Oil hydraulics

Energy Saving

The 11th JFPS International Symposium on Fluid Power HAKODATE 2020 Oct. 12-13, 2021 JFPS The Japan Fluid Power System Society

Research on the Characteristics of the Cylinder Exhaust-Return Energy-Saving System

Yuto FUJIWARA*, Mitsuru SENOO*, Hiroyuki ASAHARA*

* SMC Corporation Tsukuba Technical Center, 4-2-2,
Kinunodai, Tsukubamirai-shi, Ibaraki-ken, 300-2493 Japan
(E-mail: fujiwara.yuto@smcjpn.co.jp)

Abstract. In recent years, as part of efforts toward SDGs (Sustainable Development Goals), energy-saving orientation has become stronger. In addition, it is said that compressed air generation is responsible for approximately 20% of the power consumption in a factory, so energy-saving systems are required to reduce the air consumption of pneumatic cylinders used in various applications. Therefore, the authors have developed an exhaust-return energy-saving system as a new energy-saving actuation system. This system reuses the compressed air normally exhausted after the end of the working stroke, as an air pressure source during the return stroke of the cylinder drive. In other words, no compressed air is consumed in return stroke, so approximately 50% of the air consumption can be reduced per operating cycle. This paper introduces this system and describe the results of calculating the characteristics of the system by simulation.

Keywords: Energy-Saving, Pneumatic System, Exhaust-Return System, Simulation, Characteristic Calculation.

INTRODUCTION

In recent years, as part of efforts toward SDGs (Sustainable Development Goals), energy-saving orientation has become stronger. In addition, it is said that compressed air generation is responsible for approximately 20% of the power consumption in a factory, so energy-saving systems are required to reduce the air consumption of pneumatic cylinders used in various applications.

Normally, in cylinder drive, the same supply pressure is supplied and exhausted in an operating cycle. However, in general applications such as transport and clamping, only the working stroke requires thrust, and a low pressure is often sufficient for the return stroke. Therefore, in order not to impede practicality, the mainstream of energy-saving was the return stroke that does not require thrust. For example, two-pressure actuation and double power operation mechanisms were adopted in accordance with the energy-saving actuation system [1] for reducing the thrust of the cylinder.

However, when pursuing energy-saving by reducing the thrust, there is a limit to the reduction because it is necessary to supply at least enough compressed air to the cylinder to satisfy the required thrust.

Therefore, the authors have developed an exhaust-return energy-saving system as a new energy-saving actuation system. This system reuses the compressed air normally exhausted after the end of the working stroke, as an air pressure source during the return stroke of the cylinder drive. In other words, no compressed air is consumed in return stroke, so approximately 50% of the air consumption can be reduced per operating cycle.

This paper introduces exhaust-return energy-saving system, and describe the results of calculating the characteristics of the system by simulation.

EXHAUST-RETURN ENERGY-SAVING SYSTEM

This system reuses the compressed air supplied to the working stroke that should be exhausted to the return stroke and reuses it for the return stroke as an air pressure source. Therefore, the return stroke does not require an additional compressed air supply. In other words, no compressed air is consumed in return stroke, so approximately 50% of the air consumption can be reduced per operating cycle. The thrust of the working stroke does not change.

As shown in Figure 1, the head side and rod side are connected through the check valve and solenoid valve. The flow path connecting the head side flow path and the rod side flow path is called a return flow path.

In the working stroke, compressed air is supplied to the head side and exhausted from the rod side the same as the general circuit.

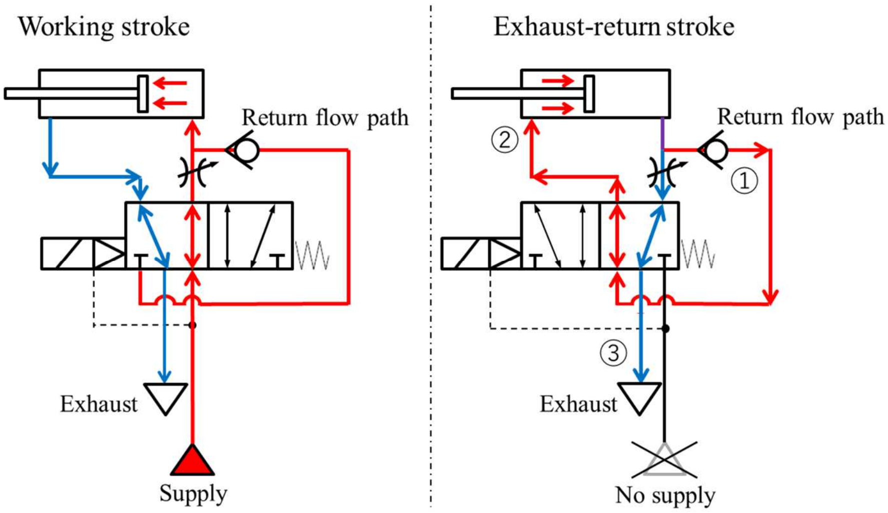

Figure 1. Compressed Air Flow During Operation.

On the other hand, on the exhaust-return stroke, the compressed air supplied to the head side flows as shown below so it can be reused.

(1) Return flow path: The compressed air supplied to the head side is returned to the rod side through the check valve.

(2) Rod side flow path: The returned air is reused and redirected to supply pressure to the rod side port.

(3) Head side flow path: At the same time as the return, the compressed air supplied to the head side is exhausted to the atmosphere and the head side pressure drops.

With this operation, the piston operates with the pressure difference between the rod side and head side. Thus the amount of compressed air supplied in the return stroke is zero.

MODELING and VALIDATION

In order to clarify the characteristics of this system, a simulation model was created. Figure 2 shows the simulation model for the exhaust-return stroke, and Table 1 shows the parameters used for the calculation. For the sake of calculation simplicity, state change of air is assumed to be isothermal change.

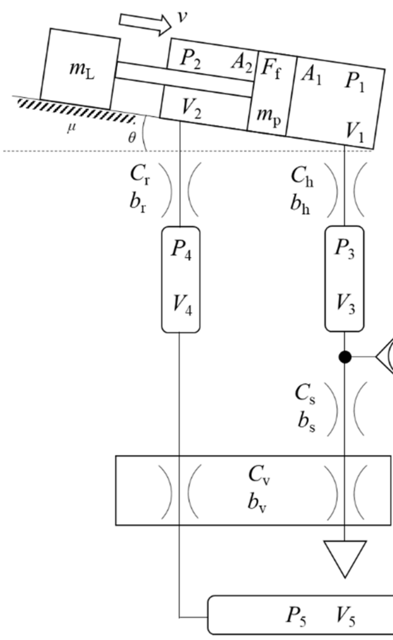

Figure 2. Simulation Model (Exhaust-Return Stroke)

Table 1. Simulation Parameters

Parameter	Name	Unit	Subscript	
P	Absolute pressure	MPa	1	Cylinder head side
V	Volume	m^3	2	Cylinder rod side
C	Sonic conductance	dm^3 / (s･bar)	3	Head side flow path
b	Critical pressure ratio	-	4	Rod side flow path
A	Piston area	m^2	5	Return flow path
θ	Mounting angle	rad	h	Head side port
F_f	Friction force of piston rod	N	r	Rod side port
m_p	Mass of cylinder movable parts	kg	s	Speed controller
m_L	Load mass	kg	k	Check valve
μ	Friction coefficient	-	v	Solenoid valve
T	Temperature	K		
v	Velocity	m / s		
t	Time	s		
R	Gas constant (= 287)	J / (kg･K)		
ρ	Standard reference atmosphere density (= 1.185)	kg / cm^3		
g	Gravitational acceleration (= 9.8)	m / s^2		

Based on this model, the flow of compressed air between each volume is calculated.
For example, the mass flow rate G_{13} flowing from the cylinder head side to the head side flow path is represented by the flow rate equation (1), and the puressure change dP_1 in the cylinder head side pressure due to this is represented by the state equation (2). Then, from the obtained pressure difference in the cylinder, the velocity change dv of the cylinder is represented by the equation of motion (3).

$$G_{13} = \frac{\rho C_h P_1}{100}\sqrt{1-\frac{(\frac{P_3}{P_1}-b_h)^2}{(1-b_h)^2}}\sqrt{\frac{293}{T}}. \qquad [\tfrac{P_3}{P_1} > b_h \ : \text{subsonic} \quad \text{flow}]$$

$$G_{13} = \frac{\rho C_h P_1}{100}\sqrt{\frac{293}{T}}. \qquad [\tfrac{P_3}{P_1} \le b_h \ : \text{choked} \quad \text{flow} \ ] \tag{1}$$

$$\frac{dP_1}{dt} = -\frac{(RTG_{13} + P_1\frac{dV_1}{dt})}{V_1}. \tag{2}$$

$$\frac{dv}{dt} = \frac{P_2A_2 - P_1A_1 - F_f + (m_p + m_L)g\sin\theta - \mu m_L g\cos\theta}{m_p + m_L}. \tag{3}$$

These parameters are repeatedly calculated at time step to reproduce the behavior of the system.
Figure 3 shows the results of confirming the reproducibility of the model for the experiment, and Table 2 shows the conditions for the experimental and calculation.

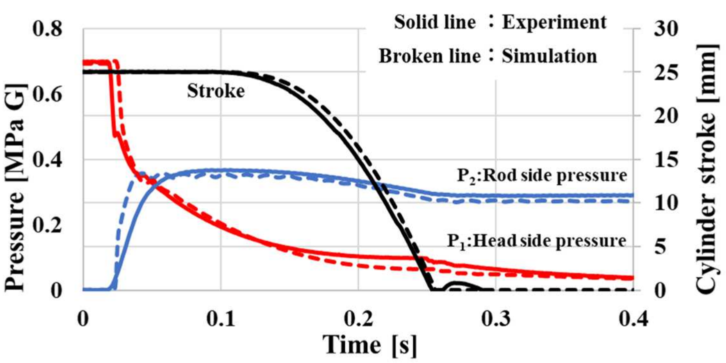

Figure 3. Reproduction of the Simulation Model (Exhaust-Return Stroke).

Table 2. Experimental and Calculation Conditions

Name	Condition
Cylinder (bore – stroke)	Ø 20 mm – 25 mm
Head side flow path (I.D. – length)	Ø 4 mm – 2000 mm
Rod side flow path (I.D. – length)	Ø 4 mm – 2000 mm
Return flow path (I.D. – length)	Ø 4 mm – 100 mm
Supply pressure	0.7 MPa G
Mounting angle	0 rad (horizontal)
Load mass	11 kg

Since the simulation results were in good consistency with the experimental results, the validity of the model was confirmed. Therefore, the characteristics of the system will be clarified using this model.

SIMULATION and DISCUSSION

This system reuses compressed air already supplied into the system compressed air instead of supplying new compressed air, if the return air pressure is not sufficient, operation may not acceptable for the application. Therefore, it is necessary to estimate the remaining pressure after the stroke (hereinafter called return pressure), and the optimum conditions were calculated by simulation.
As a result, it was clarified that two factors affect the return pressure.
The first factor is control of the exhaust. The exhaust-return stroke velocity should be adjusted with a meter out speed controller. Therefore, the larger the exhaust flow rate by increasing the opening in the speed controller, the faster the exhaust-return stroke velocity will be, however, the amount of compressed air flowing from the branch to the return flow path is reduced, which decreases the return pressure. This means that in the exhaust-return stroke, the velocity and thrust are in an inverse correlation relationship as shown in Figure 4.

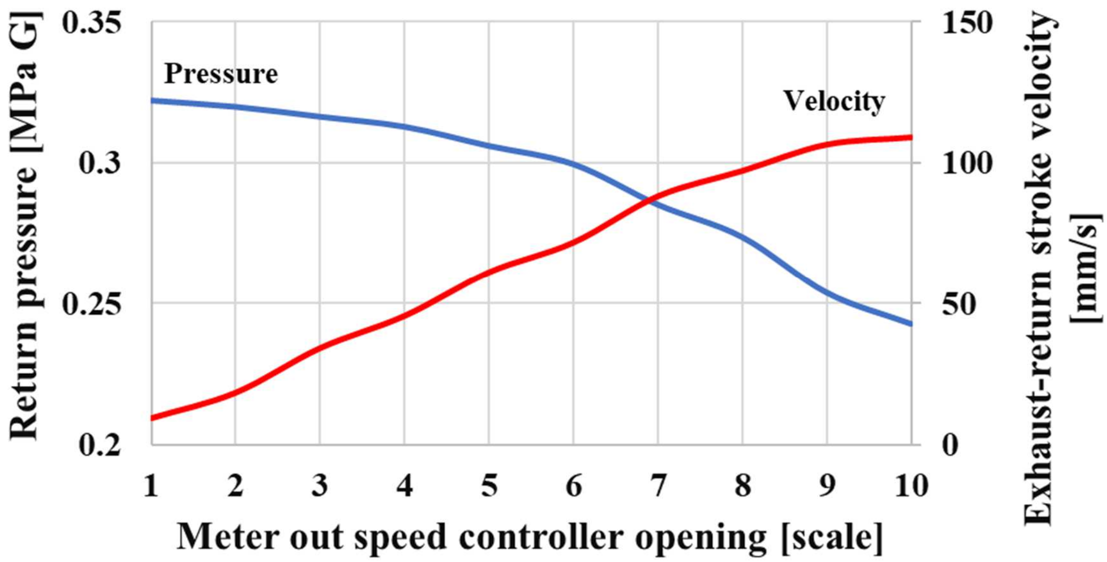

Figure 4. Relationship between the Exhaust-return stroke velocity and return pressure.

The second factor is the volume ratio before and after the exhaust-return stroke. Here, it is the ratio of "the volume that stores the pressure supplied after the working stroke ($V_1 + V_3 + V_5$) " to "the volume in which the returned air flows in during the exhaust-return stroke ($V_2 + V_4 + V_5$) ".
If this ratio is too small, the amount of compressed air that can be returned will be reduced and sufficient pressure will not be maintained during the stroke. On the other hand, if the ratio is too large, the returned air expands and the pressure drops.
From these two factors, the characteristics of the return pressure are shown in Figure 5.

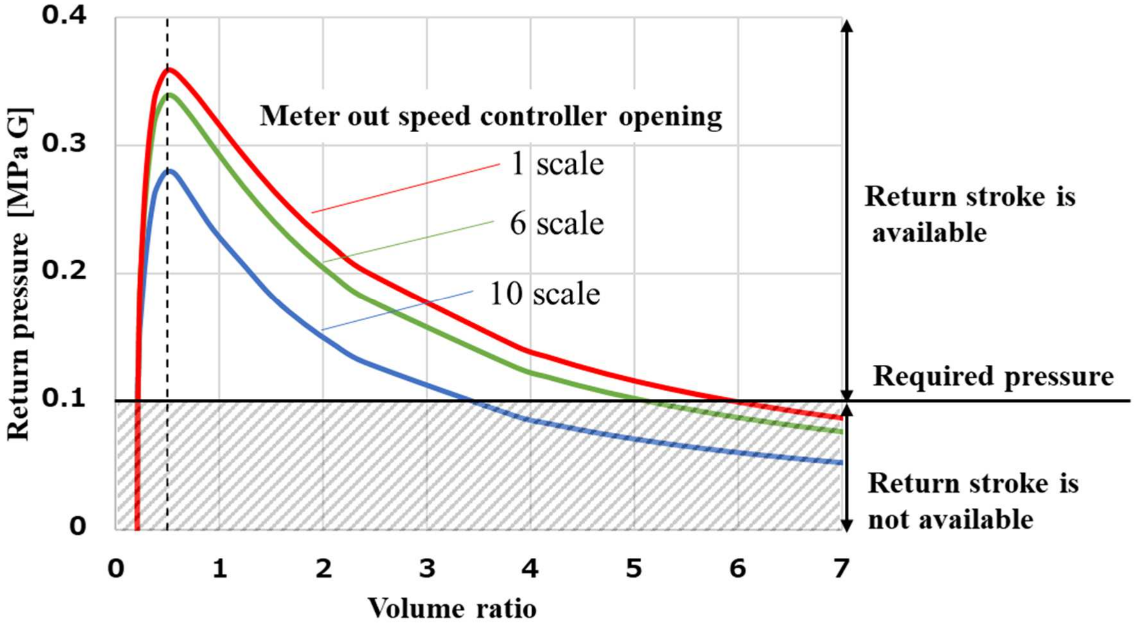

Figure 5. Characteristics of the Return Pressure

As shown in Figure 5, the return pressure peaks at a volume ratio of approximately 0.5. Then, it can be seen that it is necessary to be within a certain volume ratio range in order to satisfy the required pressure.
For example, if the required pressure is 0.1 MPa G, the availability of exhaust-return stroke is as follows:
- If the volume ratio is 3, it is available at all openings.
- If the volume ratio is 5.2, the speed control is limited because it is not available with openings of 6 or more.
- If the volume ratio is 6 or more, it is not available at all openings.

From this simulation result, it was clarified that the characteristics of the exhaust-return energy-saving system are affected by the volume ratio and speed control, and that they should be used under appropriate conditions.

CONCLUSION

(1) The exhaust-return energy-saving system can save approximately 50% of the air consumption by recycling the exhausted air.
(2) Calculation was performed with the simulation model, which turned out that the volume should be in an appropriate range and the relationship between the exhaust-return stroke velocity and return pressure are inverse correlation relationship.

The product development and selection software will be established by taking advantage of these factors.

REFERENCES

1. ONEYAMA, N., Energy Saving for Pneumatic System, 2003, pp.289-309.

The 11th JFPS International Symposium on Fluid Power HAKODATE 2020 Oct. 12-13, 2021 The Japan Fluid Power System Society

Design Guideline and Investigation of Accumulator Parameters for a Novel Hybrid Architecture

Seiji HIJIKATA*, Kazuhisa ITO** and Hubertus MURRENHOFF*

*Institute for Fluid Power Drives and Systems (ifas), RWTH Aachen University
Campus-Boulevard 30, 52074 Aachen, Germany
(E-mail: Seiji.Hijikata@ifas.rwth-aachen.de)
** Department of Machinery and Control Systems, College of Systems Engineering and Science
Shibaura Institute of Technology, 307 Fukasaku, Minuma-ku, Saitama-shi, 337-8570 Japan

Abstract. In order to enhance energy efficiency of excavators for global environment conservation, an Open Center System (OC-System) as a power source has been improved in the world. However, total system efficiency including the internal combustion engine (ICE) has not been thoroughly considered. On the other hand, a Constant Pressure System (CP-System) enabling the engine to be driven optimally is developed but is not accepted in the industry due to the complexity of the required components. Thus, in this research, a hybrid system combining an OC-System with a CP-System is proposed by using a proposed design guideline and analyzing measurement data of a dig and dump cycle. It is indispensable to consider the nominal gas volume and pressure level for an accumulator in terms of energy saving and initial cost. Therefore, the influences of accumulator volume and pressure level are also discussed in this paper.

Keywords: Hydraulic hybrid, accumulator, mobile hydraulics, excavators

INTRODUCTION

To improve the efficiency of excavators many types of different hydraulic architectures have been developed during recent years [1-5]. One of the most common valve controlled architectures is an Open Center System (OC-System). In conventional OC-Systems, however, throttling losses are unavoidable when a single pump supplies fluid to some actuators simultaneously due to the mismatch of the required pressure levels. To eliminate these losses, a Three Pump Open Center System (TPOC-System) based on an OC-System was developed [6]. This system is shown in figure 1. Using three pumps all three hydraulic actuators are powered by individual pumps, and therefore throttling losses are almost negligible if flow rate from the pumps to the tank is small enough by fully tilted joystick operation. Another advantage of this system is simple configuration with hydraulic valves commonly used for excavators. However, in this system, the internal combustion engine (ICE) is not driven optimally resulting in decreased total energy efficiency.

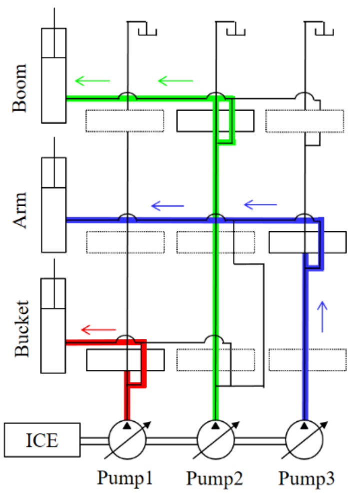

Figure 1. Outline of hydraulic system for TPOC-System

To improve the total efficiency ifas at RWTH Aachen University proposed a Constant Pressure System (CP-System), called STEAM [7, 8], see figure 2. This system consists of a large number of switching valves, two accumulators used for driving actuators and a pump for charging the accumulators. The most important feature is that the rotational speed of the ICE is fixed in its high-efficiency region. Moreover, by using switching valves, installed at the piston and rod side of a cylinder and connected to the accumulators, this system can generate power by utilizing different cylinder forces which contribute to the reduction of throttling losses and recuperate actuator energy. There are, however, some disadvantages; since a high number of switching valves are needed, widespread application in the industry is prevented.

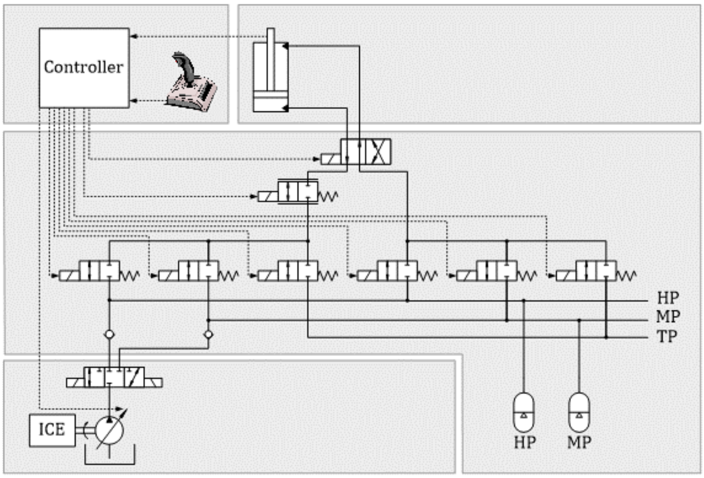

Figure 2. STEAM-System

To solve this problem, the authors propose a new hybrid system combining an OC-System and a CP-System [9-11]. However, previous papers were only discussed for a levelling cycle. Therefore, including a dig and dump cycle which is the most standard cycle for excavators, this paper proposes a design guideline to develop the new hybrid system. In addition, the influence of the nominal gas volume and pressure level for an accumulator is discussed because it is expected that accumulator parameters affect energy saving and initial cost for the new hybrid system. In this research the TPOC-System is used as a reference system to compare fuel consumption.

NEW HYBRID ARCHITECTURE

This system is designed based on three basic principles from the perspective of energy efficiency and a simple configuration. First, to design the simple hydraulic circuit of the new system, open center valves are used as a basic hydraulic system, see figure 3. The new system consists of open center valves, two accumulators, which are set to medium pressure (MP) and high pressure (HP), and a minimum of required components which are used as constant pressure valves. Second, boom potential energy and swing brake energy can be recuperated using MP and HP, and they can be provided to actuators. Thus, the power of the pumps for this system can be reduced by using this stored energy.

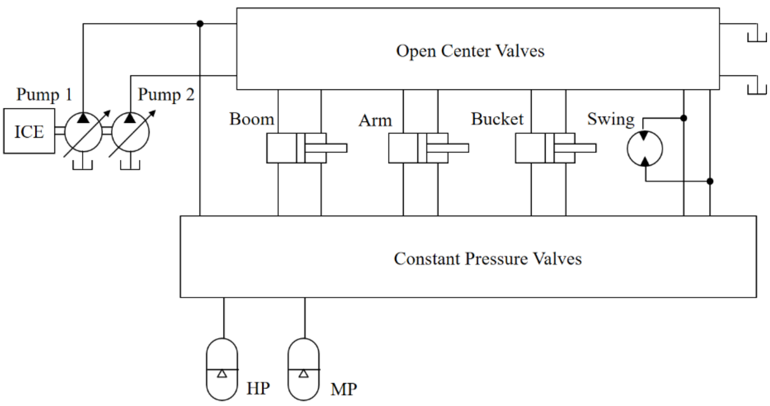

Figure 3. Outline of new hybrid system

Third, the ICE can be operated in the high efficiency region like the STEAM-System. For explanation, a simple relative efficiency map of the ICE is represented in figure 4. The horizontal axis shows ICE's rotational speed n, and the vertical axis indicates ICE's torque T. The values in figure 4 means relative efficiency which is the ratio of total to ICE's maximum efficiency. Generally, the high efficiency region extensively appears at lower rotational speed than that are used in today's conventional excavators. Moreover, the ICE's friction depending on rotational speed can be reduced at lower rotational speed than higher speed. Therefore, the ICE is set to a low rotational speed. The reduction of the ICE's power resulting from altering the high rotation speed into the low rotation speed is compensated by the accumulators. Next, the design guideline to develop the minimum of required components is discussed.

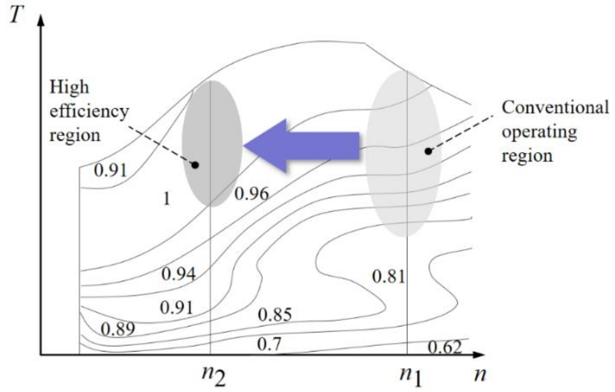

Figure 4. Schematic relative efficiency map of ICE

DESIGN GUIDELINE OF NEW SYSTEM

In order to explain the design guideline of the new hybrid system, the excavator's actuator status is explained at first. Figure 5 describes the load situation for the actuators. The x-axis shows the flow required by each actuator (Q_L), the y-axis shows load pressure (p_L) of the actuator. Herein F_L is the load force, and v is the actuator speed. p_B is the actuator pressure of the cylinder's bottom side, and p_R is the actuator pressure of the cylinder's rod side. A_B is the area of the cylinder's bottom side, and A_R is the area of the cylinder's rod side. α is the actuator area ratio which is A_R / A_B for the cylinder and 1 for the swing. Depending on the movement, each actuator experiences either a resistive force opposing its motion (Q I and Q III) or an assistive force aiding its motion (Q II and Q IV). Consequently, in quadrants I and III the actuator must be actively supplied with power, while in quadrants II and IV, the actuators can actually supply power to the system.

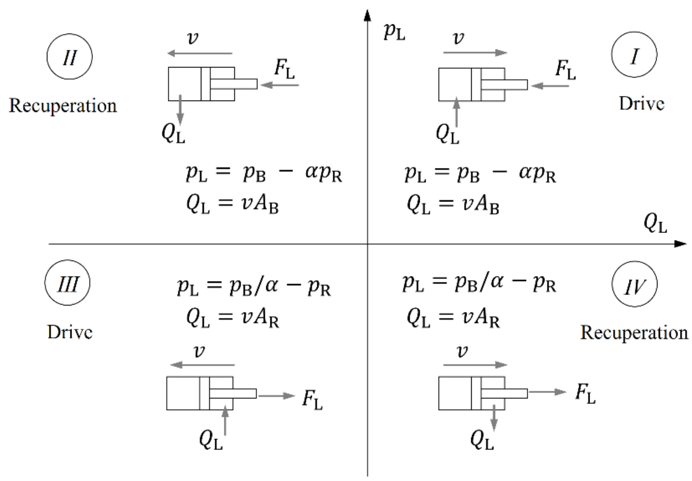

Figure 5. Definition of load pressure and load flow

STEAM has operating modes which have different ways of connecting an actuator to the three pressure rails, as shown in figure 6. The switching valves, which are installed at the piston and rod sides of the cylinders and connect to the three pressure rails, generate nine modes leading to nine different cylinder forces.

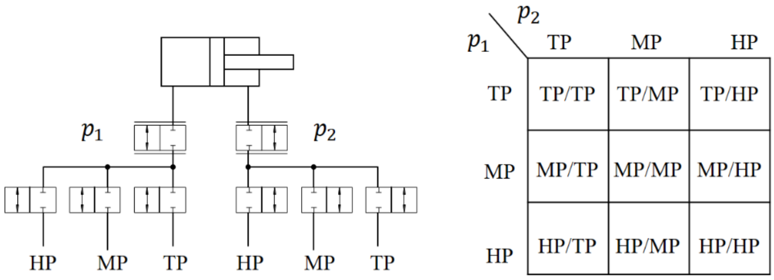

Figure 6. System operating modes

Figure 7(a) describes all nine modes labelled in load quadrants of the hydraulic cylinder for STEAM. For example, the first label of MP/HP shows that the medium pressure is connected to the piston side and the second label of that indicates that the high pressure is connected to the rod side. The position of the modes depends on the HP, MP and TP pressure levels as well as the piston area ratio α. The lines passing through quadrants one and three can be used to actively supply an actuator with flow, while the lines passing through quadrants two and four allow energy to be recovered from the actuator and stored in one of the accumulators. According to switching modes, when a resistive force occurs such as OP_1 in figure 7(a), mode HP/HP lying directly above the current operating point is selected so as to minimize throttling losses. When an assistive force occurs such as OP_2, MP/MP lying directly below the current operating point is selected. In this way, throttling losses of the CP-System can be reduced by using the three pressure rails, however the usage of the three pressure rails cannot promise sufficient total energy efficiency. Normally the higher pressure level of HP must be set to be equal to the maximum operating pressure of the conventional machines to keep the same performances. This results in large throttling losses due to expanding pressure differences between respective modes. Thus, high efficiency for the total system is not expected due to throttling losses.

To overcome this problem, the basic principle of the new system shown in the previous paper [9] has proposed to reduce the pressure level of HP, as can be seen in figure 7(b). By changing HP from p_{HP1} to p_{HP2}, it is possible to reduce throttling losses occurring in regions of respective modes. A problem of the system is that the HP cannot supply to loads requiring higher pressure levels than p_{HP2}. In such a case the main pump can supply the fluid to the loads directly. Additionally, the flow rate to the actuators with quite lower pressure level than the accumulator pressure level is provided directly from the pumps. For example, if the actuator with a low pressure level is driven by the accumulator with a middle pressure level, a large differential pressure resulting in relatively large throttling losses will occur. Thus, the flow rate with a low pressure level is provided by the pump directly.

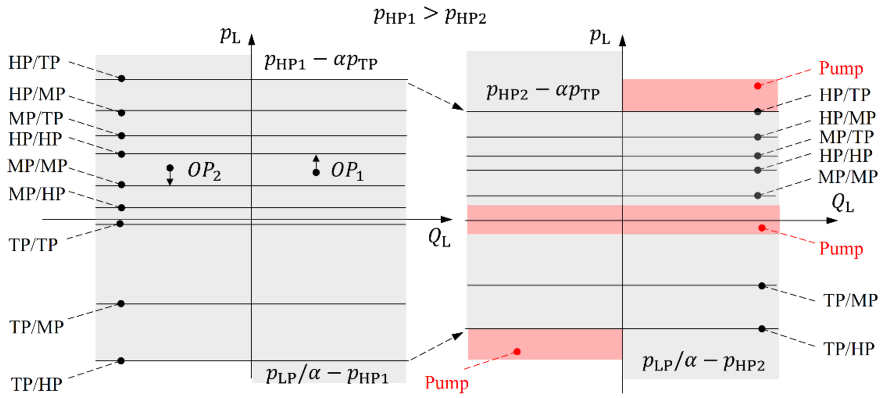

(a) STEAM (b) New system

Figure 7. Comparison of regions of operation against HP

This basic principle of the new system was confirmed in the previous paper [9, 11] by a simulation. However, the simulation results showed effectiveness of the new system for only the levelling cycle in which actuators are not driven with large power but with small or middle power. According to a cycle including motions with large power, it is obvious that system efficiency becomes poor when the accumulator provides flow rate to the actuator with large power. For example, when the accumulator provide flow rate to the actuator of 10 kW, which is not large power, with 50 % of efficiency, losses of 5 kW occur. However, even though efficiency is 80 %, when the accumulator provides flow rate to the actuator of 100 kW, losses of as much as 20 kW occur. In this way, throttling losses resulting from driving the actuator with large power by the accumulator, are likely to affect system efficiency more. In the levelling cycle used in previous discussion, such a case has not appeared, but in the dig and dump cycle where actuators are driven with large power, this matter becomes more prominent.

In order to overcome this problem, as can be seen in figure 8(a), the authors propose that actuators with large power are provided by pumps directly. The region of large power driven by the pumps can be determined based on the boom power during swing boom lift up motion with the soil because this power is the largest actuator power required in the dig and dump cycle. In this manner, throttling losses can be reduced. In addition, the ICE can be driven in high efficiency region when pumps provide large power to the actuators directly, as shown in figure 8(b). The hydraulic circuit of the new system can be designed based on analysis for measurement data of dig and dump cycle and levelling cycle with this design guideline shown in figure 8(a). Therefore, the new system can be operated in most motions required by operators because their cycles account for most actual operation of excavators in the real market.

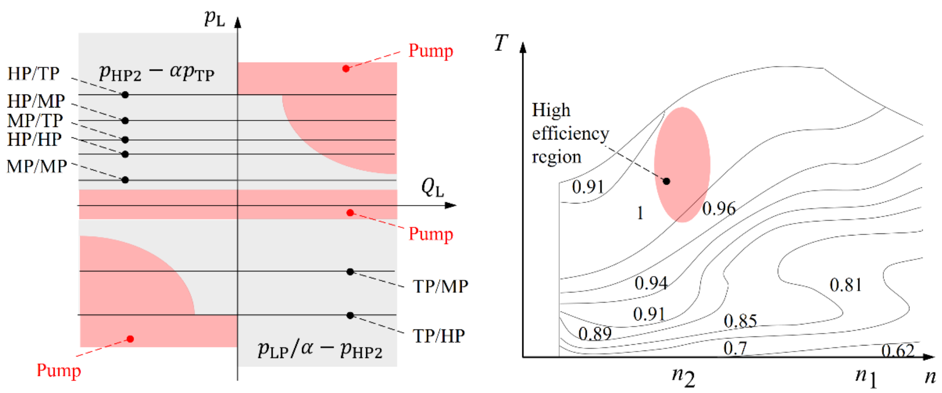

(a) Design guideline (b) Operation of ICE

Figure 8. Design guideline for new hybrid architecture

NEW SYSTEM DESIGN

Figure 9 shows an outline of dig and dump cycle consisting of four motions. In the digging motion, the arm and bucket are pulled to the machines side to dig and the boom is lifted slightly. Next motion which is swing boom lift up motion , the boom is largely lifted and the upper structure is rotated 90 degree. In the bucket dump motion, the bucket is operated to release soil in the bucket. The last motion is to return the initial position, so called swing boom down motion. These figures show the strokes and angle of each actuator. The cycle time is about 12 seconds.

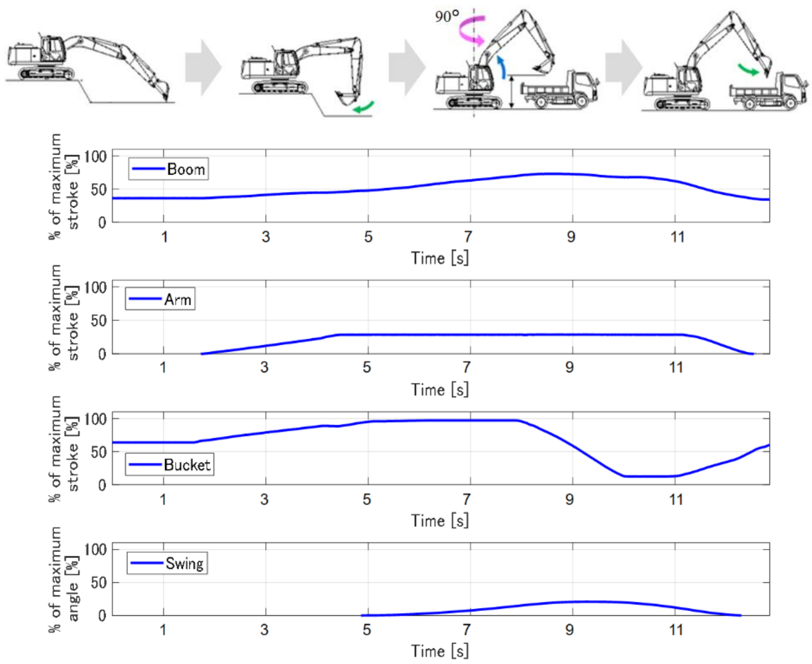

Figure 9. Dig and dump cycle

5

Figure 10 shows histograms of load flow rate and load pressure for each actuator of dig and dump cycle in quadrants presented in figure 5. The horizontal axis indicates load flow for each actuator and the vertical axis shows load pressure. The color bars represents frequency of the actuator motions which means the ratio of total to the operation point of the highest frequency. Additionally, red region indicates area of large power and high pressure level. In these region, as shown in design guideline of figure 8(a), the actuators should be powered by pumps directly. By analyzing measurement data of dig and dump cycle with the design guideline, the hydraulic circuit can be designed. In order to judge the magnitude of the actuator's powers, constant power hyperbolas are added to the diagram. In figure 10(a), power of the boom during boom up motion in quadrant one appears in high power region. Thus, boom up motion is powered by the pump, and accumulator also provide flow rate to the boom so as to compensate flow rate. On the other hand, boom potential power in the boom down motion can be recuperated by the MP accumulator. In figure 10(b), power of the arm extending the piston in quadrant one doesn't appear in high power region mainly. In order to reduce switching pump drive and accumulator drive which results in complexity for the hydraulic circuit of the new system, the arm extending the piston should be driven by only the accumulators. The arm contracting the piston in quadrant three is operated in low power region. Therefore, flow rate to the arm in quadrant three can be provided by accumulators. In figure 10(c), the load pressure levels of the bucket extending the piston in quadrant one appear in high pressure level and in small power area. Thus, the bucket with high pressure level is powered by the pump, and the bucket with small power is driven by the accumulators. According to swing, figure 10(d) shows that swing drive motions in quadrant three are driven in high pressure levels. Therefore, the swing is powered by pumps directly, and the swing brake energy can be recuperated by the HP. From the above, table 1 shows which actuators are powered by the pumps or the accumulators.

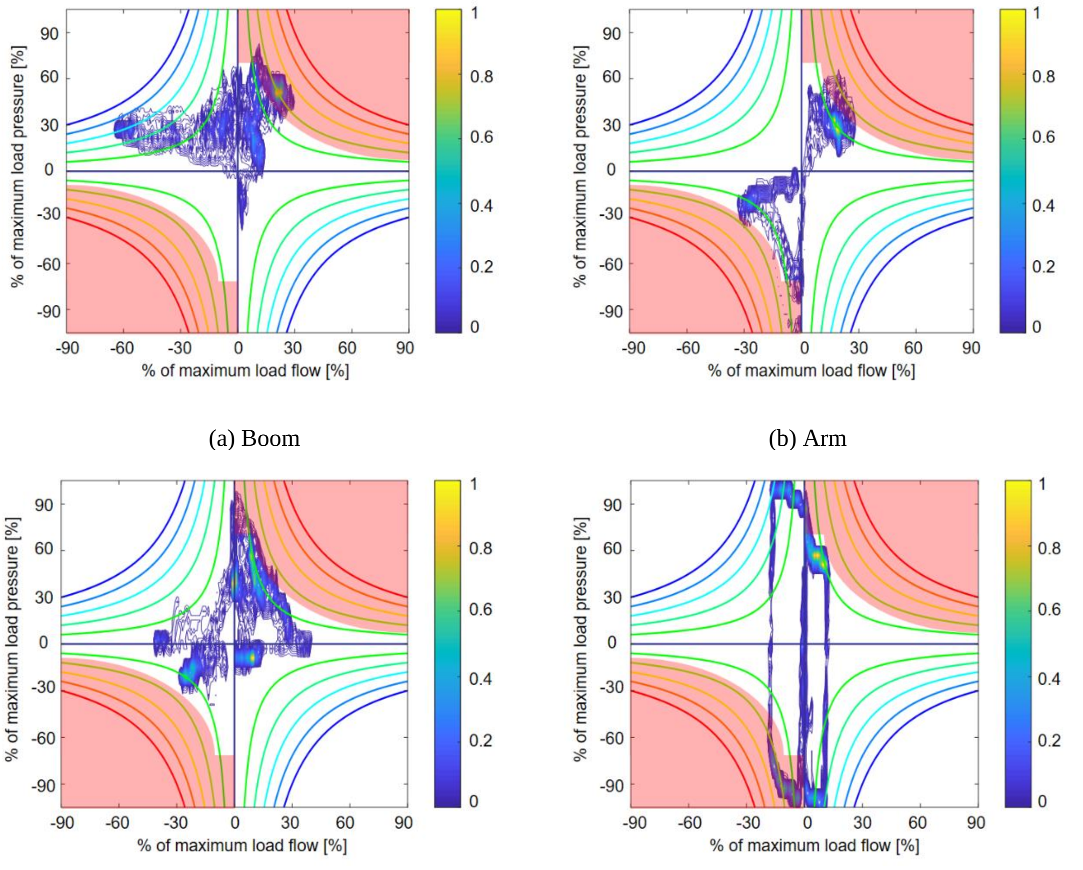

(a) Boom (b) Arm

(c) Bucket (d) Swing

Figure 10. Data analysis of dig and dump cycle

Table 1. Flow distribution matrix in dig and dump cycle

	Pump	Accumulator
Boom	Drive	Drive/Recuperation
Arm	-	Drive
Bucket	Drive	Drive
Swing	Drive	Recuperation

Figure 11 shows the hydraulic circuit of the new system made by analysis of measurement data of dig and dump cycle based on the design guideline. The upper area, framed with the dashed line, shows the open center valves, and the lower area, framed with the dashed line, shows the constant pressure valves. Since the cylinders can be connected to the pumps and the tank by using the open center valves, the number of constant pressure valves can be reduced compared to STEAM. The bottom sides of all cylinders can be connected to HP, and the bottom sides and rod sides of all cylinders can be connected to MP.

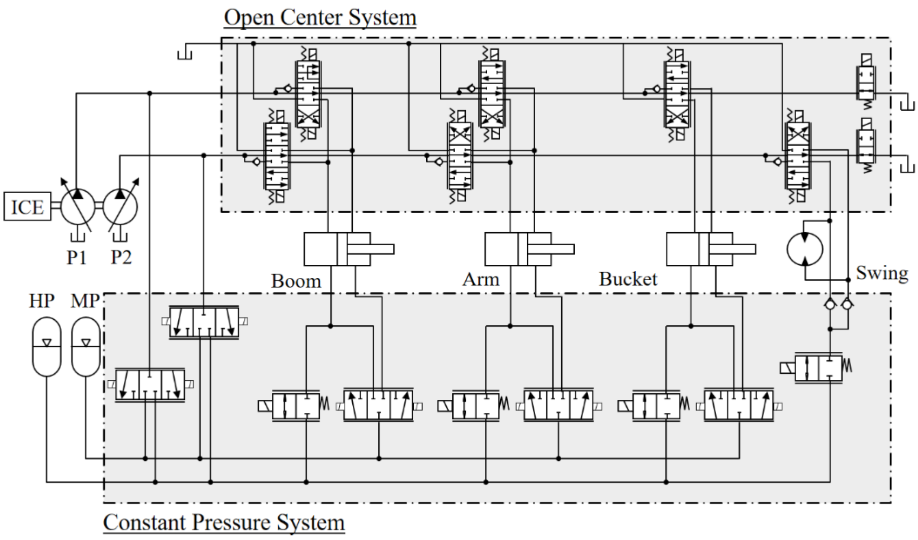

Figure 11. Hydraulic circuit of new system

In figure 12, operations of the new system are presented in the dig and dump cycle. In figure 12(a), about the digging motion, the pump 1 provides flow rate to the bucket with high pressure levels and the pump 2 provides flow rate to the boom with high power. The arm with middle power is driven by MP. In swing boom lift up motion, figure 12(b) shows that the boom and the swing are powered by pump 1 and pump 2, respectively. Furthermore, the flow rate to the boom is provided by HP so as to compensate flow rate to the boom. When the rotational speed of the swing motor decreases, HP can recuperate swing brake energy. In figure 12(c), according to the bucket dump motion, the bucket with small power is powered by MP, and at the same time MP and HP can be charged by the pumps. As can be seen in figure 12(d), in swing boom down motion, pump 2 provides flow rate to the swing and pump 1 charges accumulators, and also, MP provides flow rate to the arm and the bucket. The boom potential energy and swing brake energy can be recuperated by MP and HP, respectively.

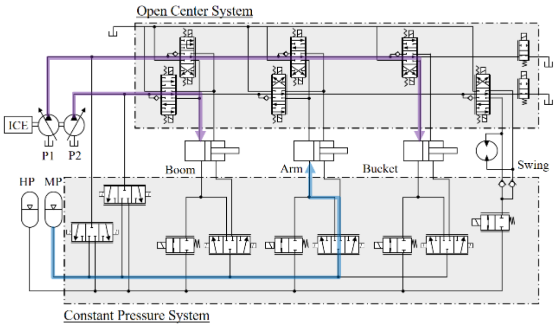

(a) Digging motion

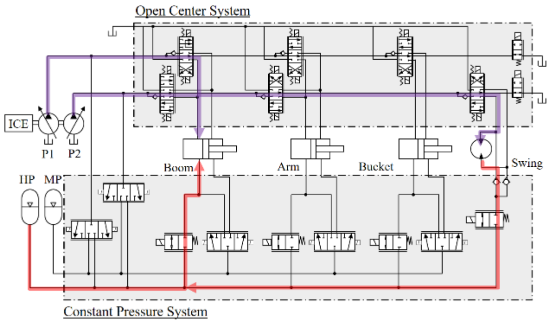

(b) Swing boom lift up motion

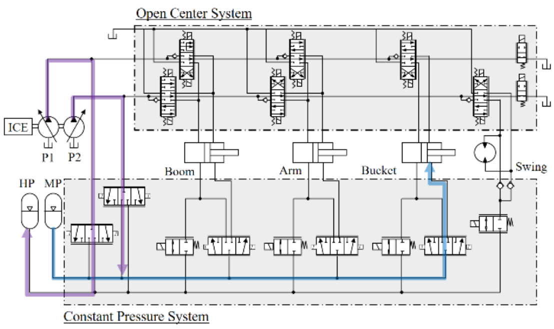

(c) Bucket dump motion

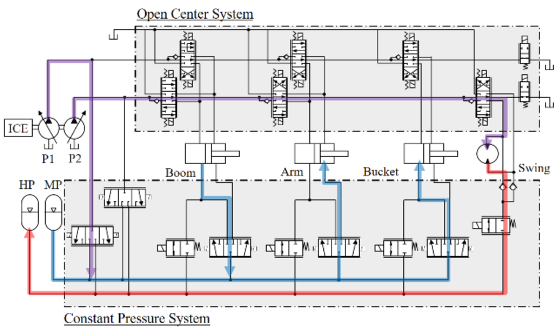

(d) Swing boom down motion

Figure 12. Operations of the new system for dig and dump cycle

SIMULATION MODEL

Figure 13 depicts the simulation model. The input signal and control logic are modelled using Simulink, the hydraulic circuit is simulated by AMESim, and a multi-body dynamic model is programmed in Simulation X. All three programs are run in co-simulation. Measurement data were used as input signals.

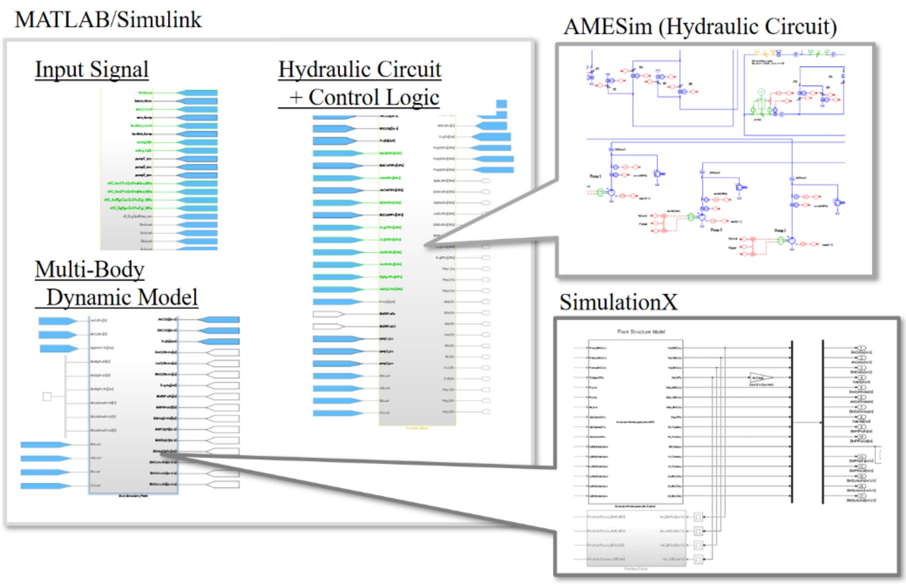

Figure 13. Simulation model

For the new hybrid system, considering parameters of the accumulator is crucial since they affect the system efficiency, initial cost and ease of layout for a real machine. For that, parameter study of accumulator for the accumulator volume and operating pressure is conducted. Table 2 shows parameters of the accumulators. According to parameters of MP, the same parameters shown in previous paper [11] are used in this paper. Parameters of operating pressure levels can be decided based on the pressure levels of actuator which should be powered by MP. For example, about the operating pressure of MP, 150 bar, 160 bar, and 170 bar can be chosen because the maximum pressure level of the actuators is approximately 130 bar. Therefore, a little higher pressure levels than 130 bar are selected for operating pressure levels of MP. According to the volume, if the volume of the accumulator is too small, pressure levels of accumulator will decrease, and moreover, fluid of the accumulators will run out. Thus, 100 L for MP is selected to keep the pressure levels of the accumulator higher than actuator pressure level which is 130 bar. According to the volume of 300 L, it can almost be used as constant pressure in the simulation. The accumulator volume 200 L is set as a middle volume between the small volume of 100 L and large volume of 300 L. On the other hand, according to parameters of HP, the accumulator volumes are same for MP. Furthermore, the operating pressure of HP are set to 230 bar, 240 bar and 250 bar because the maximum pressure levels of the boom are approximately 220 bar when the boom is powered by HP in dig and dump cycle.

Table 2. Parameters of volumes and pressure levels for accumulators

	Operating pressure levels [bar]	Accumulator volumes [L]
MP	150, 160, 170	100, 200, 300
HP	230, 240, 250	100, 200, 300

Table 3(a) shows nine patterns of parameters' combination about MP from No 1 to No 9. In these patterns, HP is set to 230 bar and 100 L. On the other hand, table 3(b) shows nine patterns of parameters' combination about HP from No 1 to No 9. In these patterns, MP is set to 150 bar and 100 L.

Table 3. Parameter combinations of volumes and pressure levels

(a) MP

No	Operating pressure levels [bar]	Accumulator volumes [L]
1	150	100
2	150	200
3	150	300
4	160	100
5	160	200
6	160	300
7	170	100
8	170	200
9	170	300

(b) HP

No	Operating pressure levels [bar]	Accumulator volumes [L]
1	230	100
2	230	200
3	230	300
4	240	100
5	240	200
6	240	300
7	250	100
8	250	200
9	250	300

SIMULATION RESULT

First, the simulation is conducted setting MP to 150 bar and 100L, and HP to 230 bar and 100L. Verifying simulation quality, results of the stroke of cylinders and angle of hydraulic motor are presented in figure 14. They show boom, arm, bucket strokes and swing angle, respectively. The black lines indicate measurement data of the TPOC-System, and the pink lines indicate the simulation results of the new system. The simulation results match stroke and angle course quite well.

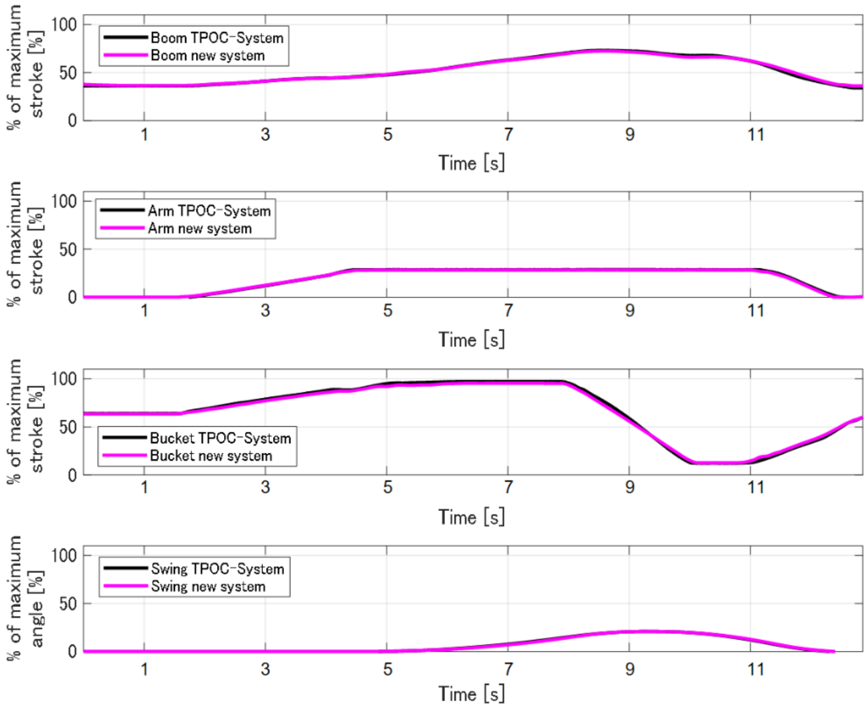

Figure 14. Simulation result for stroke and angle

Figure 15 indicates simulation results of cylinder forces and torque of hydraulic motor. They show boom, arm, bucket forces and swing torque, respectively. The simulation results of the force and torque are in agreement with measurement data of TPOC-System. But approximately 5.3 second, swing torque are a little bit different. The reason is that inertia of soil in the bucket dose not completely correspond to measurement data. However, as shown in figure 14, the simulation results of the swing angle is same behavior to measurement data, and also, the simulation results of the swing torque are almost same. Therefore, to compare system efficiency, this simulation result is useful sufficiently.

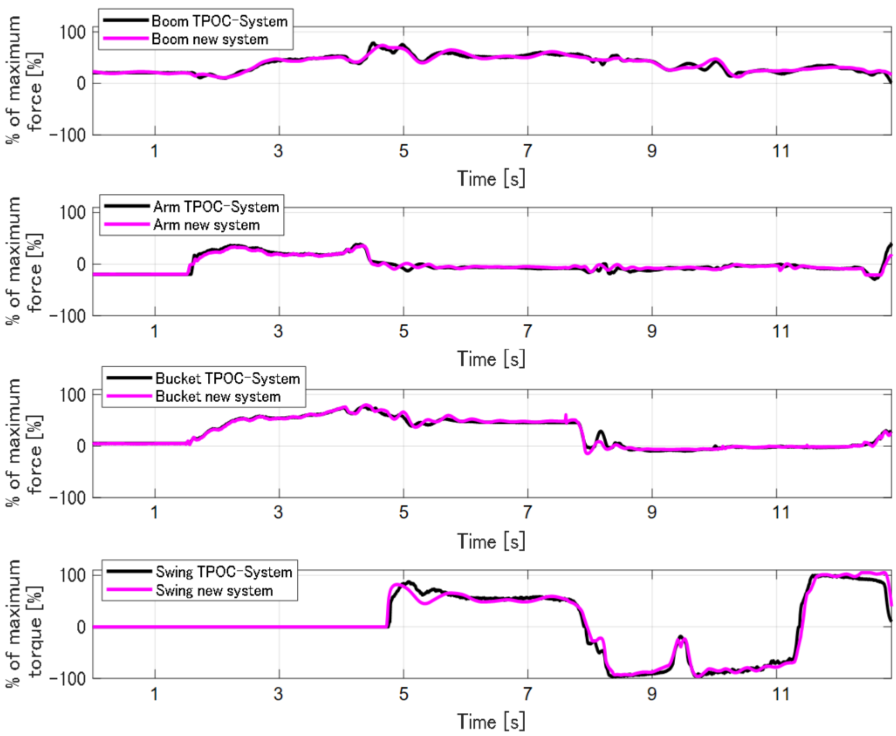

Figure 15. Simulation result for force and torque

Figure 16 depicts different power courses over time during dig and dump cycle for simulation results only. In figure 16, from above, power of pump 1, pump 2, HP and MP are presented. During digging motion, pump 1 provides flow rate to the bucket and pump 2 provides flow rate to the boom. The arm is driven by MP. In swing boom lift up motion, boom and swing are powered by pump 1 and pump 2, respectively. In addition, the boom is driven by HP. According to the bucket dump motion, the bucket is powered by MP, and at the same time MP is charged by two pumps. In swing boom down motion, pump 2 provides flow rate to the swing and pump 1 charges MP and respectively, MP provides flow rate to the arm and the bucket. At the same time, the boom potential energy is recuperated by MP. Since HP recuperates the swing brake energy, it is not necessary to charge HP by the pumps. It is recognized that the pump and the accumulator are powers distributed to cylinders as shown in table 1.

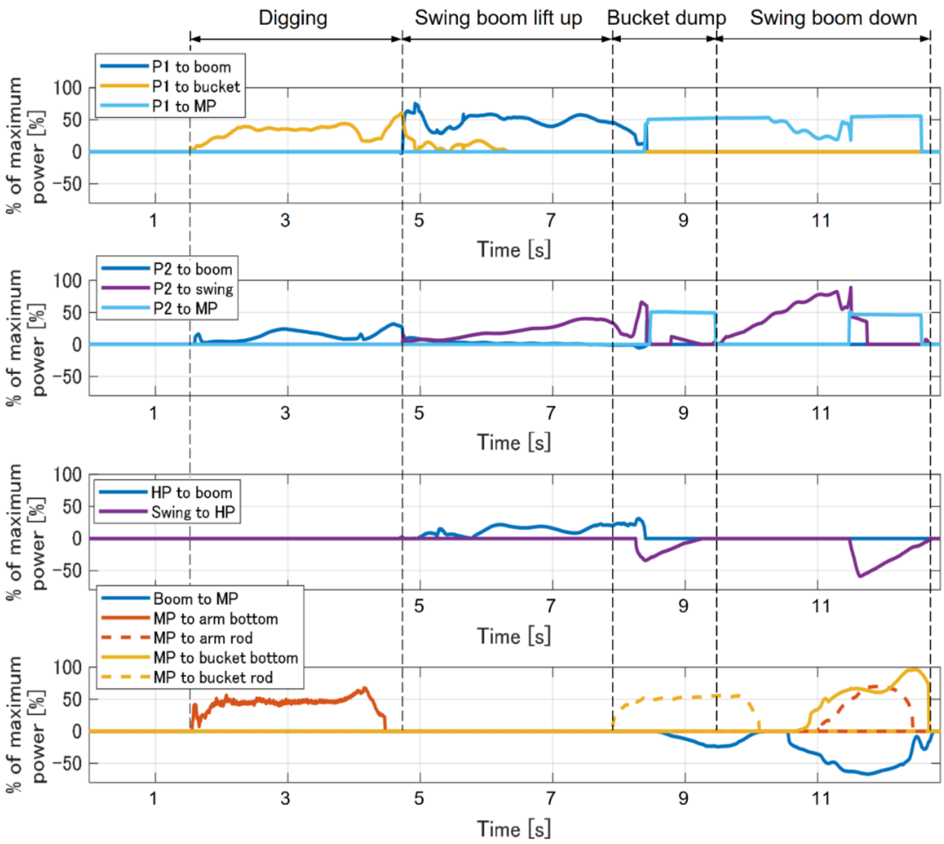

Figure 16. Simulation result for power

In figure 17, a sankey diagram is represented to compare the system efficiency of the TPOC-System with the new hybrid system. The diagram indicates how much energy of diesel fuel was used for driving actuators and how much dissipated as heat losses in the machine. Energy of fuel consumption E_{Diesel} can be calculated by ICE's efficiency map and ICE's shaft energy which can be derived based on pump torque, pump rotational speed, pump efficiency and auxiliary energy. Moreover, a difference between energy of fuel consumption E_{Diesel} and ICE's shaft energy is calculated as ICE losses $E_{\mathrm{loss.Eng}}$. Auxiliary energy E_{aux} and pump losses $E_{\mathrm{loss.pump}}$ can be described by a difference between ICE's shaft energy and pump energy which is calculated based on pump pressure level and pump flow rate. Actuator energy E_{act} and recoverable energy $E_{\mathrm{recoverable}}$ can be derived by load pressure and load flow in quadrants one and three of figure 5 and in quadrants two and four, respectively. A difference between pump energy and sum of E_{act} and $E_{\mathrm{recoverable}}$ is described as throttling losses in the valves and hoses $E_{\mathrm{loss.valve}}$. Recovered energy by the accumulators $E_{\mathrm{recovered}}$ can be calculated based on accumulator flow from the actuators and accumulator pressure level. A difference between recoverable energy $E_{\mathrm{recoverable}}$ and recovered energy $E_{\mathrm{recovered}}$ is described as recovery losses $E_{\mathrm{loss.recovery}}$. According to the TPOC-System in figure 17(a), 63.6 % of diesel fuel is dissipated as ICE losses $E_{\mathrm{loss.Eng}}$, and also 5.7 % are auxiliary energy E_{aux} and pump losses $E_{\mathrm{loss.pump}}$. Moreover, 12.0 % are throttling losses in the valves and hoses $E_{\mathrm{loss.valve}}$. The TPOC-System can not recuperate actuator energy, and therefore recoverable energy $E_{\mathrm{recoverable}}$ is also dissipated as losses. Thus, 11.1 % of diesel fuel energy is used for driving actuators. On the other hand, for the new system in figure 17(b), 14.6 % of diesel fuel energy could be used in order to power actuators. Reasons for the system efficiency improvement are the efficient operation of the ICE and recuperation of boom potential energy and swing brake energy. The new system shows potential of 24 % less fuel compared to TPOC-System.

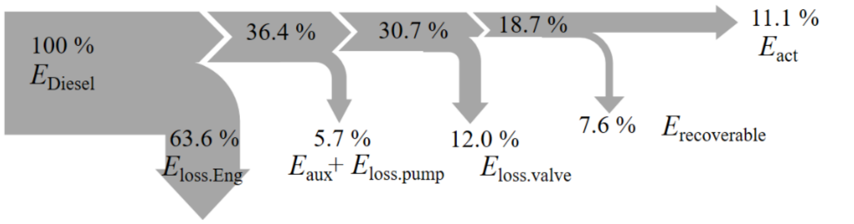

(a) TPOC-System

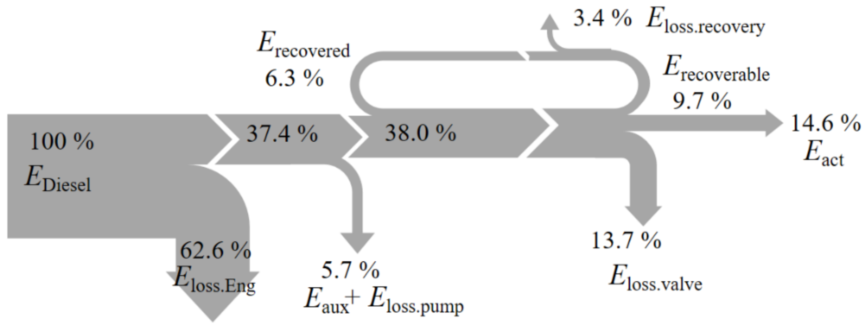

(b) New system

Figure 17. Sankey diagram for system efficiency

Figure 18(a) presents the simulation results of the accumulator pressure levels for parameters of MP which are No 1, No 4 and No 7 in table 3(a). The horizontal axis indicates time, and the vertical axis shows accumulator pressure levels. All pressure levels which are 150 bar, 160 bar and 170 bar decrease with almost same vales and then increase due to charging the accumulators by the pumps and recoverable energy. However, according to 160 bar and 170 bar, at the end of the cycle, the accumulator pressure levels are lower than the start of accumulator pressure levels, especially 170 bar. The reason is that throttling losses resulting from driving the actuator by 170 bar accumulator is lager than using 150 bar accumulator because pressure difference is larger. This causes increase of energy to charge the accumulator. However, the pump energy to charge the accumulator is not enough in lower rotational speed of the ICE. Therefore, at the end of cycle, the accumulator pressure level is lower. Figure 18(b) indicates simulation results of pressure levels for No 1, 2, and 3 in table 3(a). In figure 18(b), the pressure change of the accumulator for 100 L increases, and the pressure change of the accumulator for 300 L decreases. These characteristics will be discussed later.

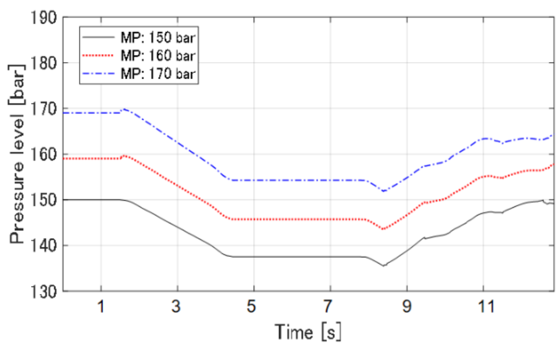

(a) MP: 150 bar, 160 bar and 170 bar

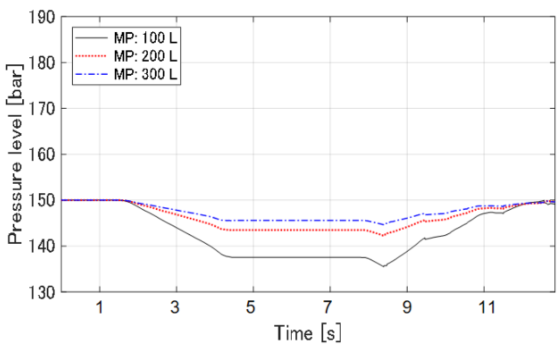

(b) MP: 100 L, 200 L and 300 L

Figure 18. Simulation result for MP accumulator pressure level

Figure 19(a) depicts the simulation results of the accumulator pressure levels for parameters of HP which are No 1, No 4 and No 7 in table 3(b). As with the simulation result of MP, all pressure levels decrease with almost same vales, and then increase. Furthermore, the start and end of the pressure levels are almost same because swing brake energy is enough to charge the accumulator. Figure 19(b) presents simulation results of pressure levels for No 1, 2, and 3 in table 3(b). In figure 19(b), the pressure change of the accumulator for 100 L increases, and the pressure change of the accumulator for 300 L decreases.

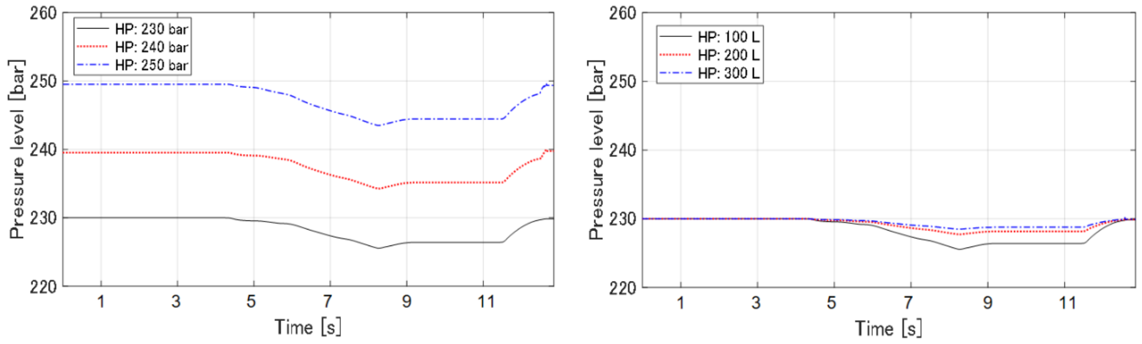

(a) HP: 230 bar, 240 bar and 250 bar

(b) HP: 100 L, 200 L and 300 L

Figure 19. Simulation result for HP accumulator pressure level

The pressure change of the accumulator against the change in volume can be explained with figure 20. Figure 20 shows the different operating states of the accumulator. p_0 is the pre-charge gas pressure, and V_0 is the maximum gas volume at p_0. p_1 is the lower operating pressure, and p_2 is the higher operating pressure. The change in state of the accumulator can be shown by Eq. (1).

$$p_0 \cdot V_0^k = p_1 \cdot V_1^k = p_2 \cdot V_2^k = \mathrm{const} \tag{1}$$

A cycle time of the dig and dump cycle which is about 12 second. This means that the liquid is removed quickly from the accumulator during dig and dump cycle. The change of state of the accumulator, thus, is defined as adiabatic changes of state. The adiabatic index k is set to 1.4. From the above, Eq. (2) can be derived from Eq (1).

$$\Delta p = p_0 \cdot V_0^k \left[\left(\frac{1}{V_2}\right)^k - \left(\frac{1}{V_1}\right)^k \right] \tag{2}$$

When the volume of the accumulator V_0 is sufficiently large (300 L) and changed from V_2 to V_1 , the pressure change Δp becomes small because the change in volume ΔV is quite small compared to the accumulator volume V_0. On the other hand, in a case where the volume of the accumulator V_0 is not large (100 L) and it changes from V_2 to V_1, the pressure change Δp become larger than that of the accumulator with a large volume. If the accumulator volume V_0 is large, the pressure change Δp will be small because the volume change ΔV is relatively small compared to the large accumulator volume V_0. If the accumulator volume V_0 is small, the pressure change Δp will be large because the volume change ΔV is relatively large compared to the small accumulator volume V_0. From the above scenarios, the simulation result with 100 L has the largest pressure change.

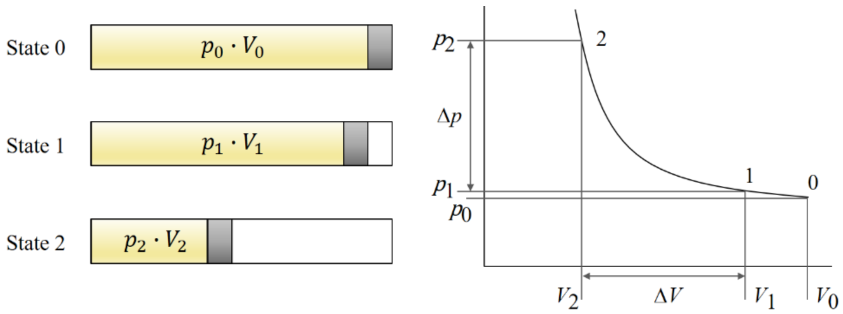

Figure 20. Parameters of an accumulator

According to MP parameters, to compare the system efficiency at pressures of 150 bar and 170 bar, a Sankey diagram of the 170 bar pressure level is presented in figure 21(a). Compared to the 150 bar accumulator pressure shown in figure 17(b), throttling losses in the valves at 170 bar increase because the differential pressure between the accumulator and actuators is larger. Therefore, the system efficiency of 170 bar become worse. The Sankey diagram of the 300 L is shown in figure 21(b). Compared to the 100 L accumulator shown in figure 17(b), system efficiency is almost equal because throttling losses are same as well.

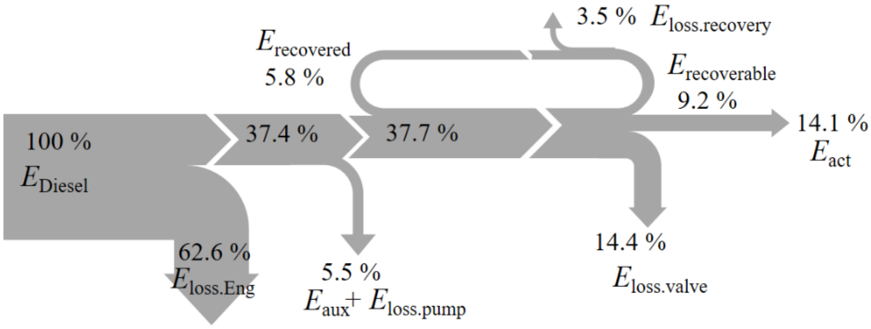

(a) MP: 170 bar (No 7 in table 3(a))

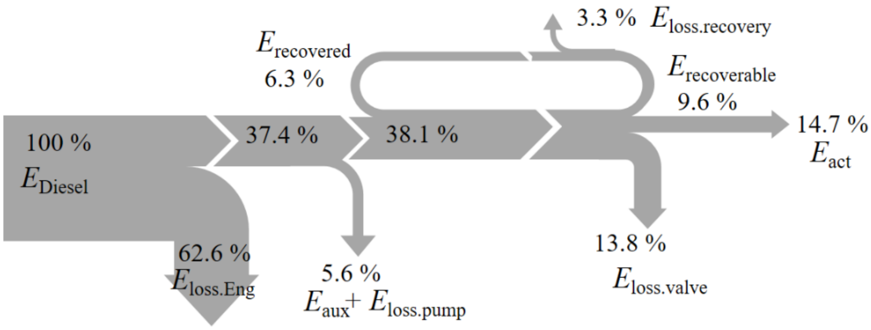

(b) MP: 300 L (No 3 in table 3(a))

Figure 21. Sankey diagram for MP parameters

According to HP parameters, to compare the system efficiency about pressures and volumes, Sankey diagrams of the 250 bar pressure level with 100 L and 300 L with 230 bar are shown in figure 22(a) and figure 22(b), respectively. Compared to the simulation results in figure 17(b), the system efficiency of 250 bar and 300 L is almost same because throttling losses are in agreement with the simulation results in figure 17(b).

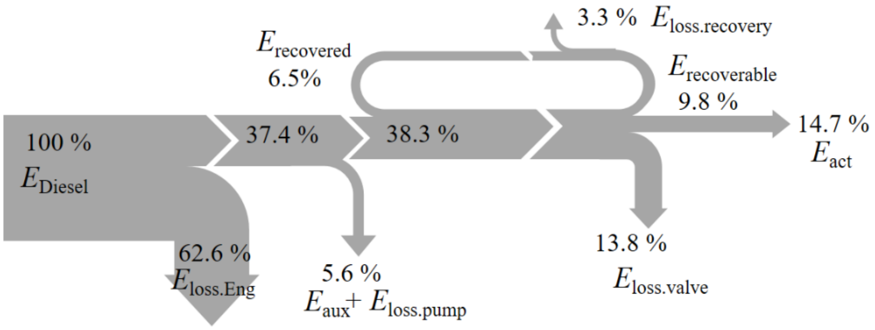

(a) HP: 250 bar (No 7 in table 3(b))

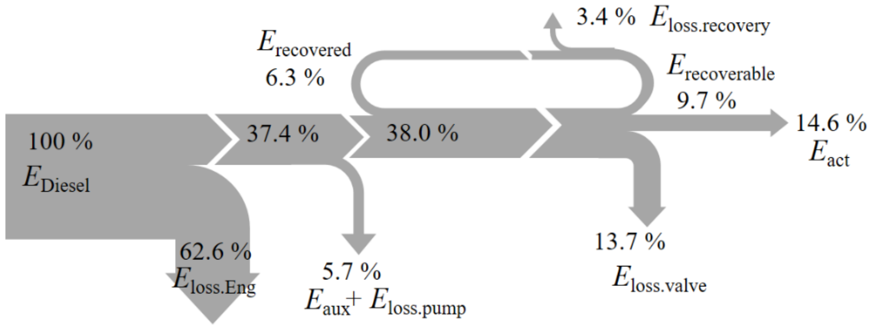

(b) HP: 300 L (No 3 in table 3(b))

Figure 22. Sankey diagram for HP parameters

Figure 23(a) shows the influence of changing parameters for MP from No. 1 to 9 in table 3(a), in terms of energy savings, reduction in fuel consumption against the volumes, and the pressure level. These values compare the fuel consumption of the new system with that of the reference TPOC-System. If the volume of the accumulator is set to a smaller volume, the reduction in fuel consumption is slightly improved. On the other hand, changing the pressure level has a greater effect on the system efficiency of the new hybrid system than changing the volume of the accumulator. Thus, from the perspective of improving energy saving, it is quite important that the pressure level of the accumulator is set as low as possible.

Figure 23(b) shows the influence of changing parameters for HP from No. 1 to 9 in table 3(b), in terms of energy savings, reduction in fuel consumption against the volumes, and the pressure levels. Parameters of HP do not largely affect the system efficiency because discharged and charged power of HP is smaller than MP as shown in figure 16.

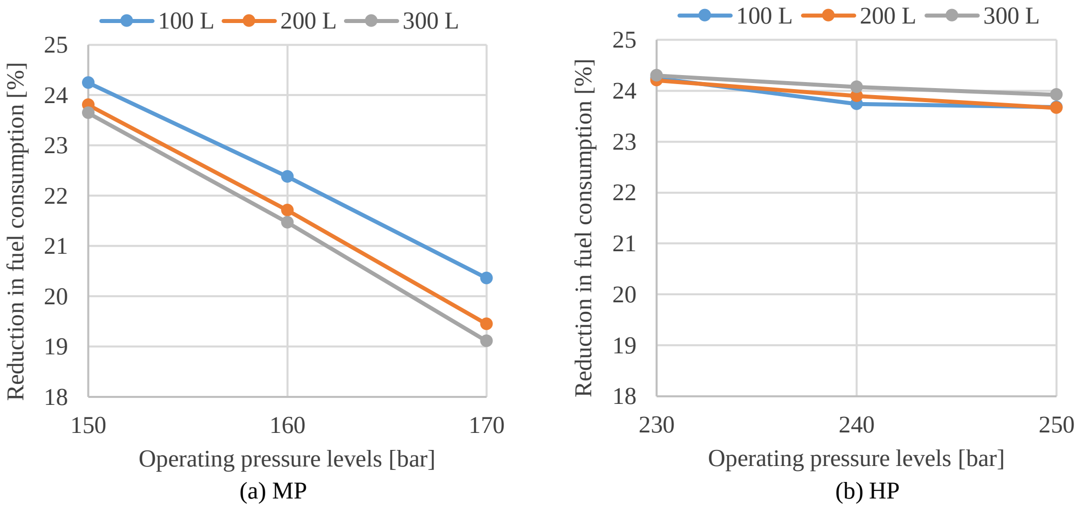

Figure 23. Reduction in fuel consumption for all simulation results

ACKNOWLEDGMENTS

This research work was supported by Hitachi Construction Machinery Co., Ltd.

CONCLUSION

In order to develop the hydraulic circuit of the new hybrid system, the design guideline was proposed from the perspective of energy efficiency and a simple configuration for dig and dump cycle. Moreover, the hydraulic circuit for the new system was designed based on measurement data of the dig and dump cycle with the design guideline. As a result, in simulation, the new system consumes 24 % less fuel than a conventional system which is TPOC-System. Furthermore, the parameters, which are the accumulator volume and pressure level, are discussed in this paper because they have a significant effect on fuel energy savings and initial cost. Through simulation, it can be recognized that setting the MP accumulator pressure level as low as possible is quite effective for energy saving. Furthermore, parameters of HP do not largely affect the system efficiency because discharged and charged power of HP is smaller than MP.

REFERENCES

1. EGAWA, H., KAWASAKI, H., Study of Electro-Hydraulic Energy Saving System (EHESS) for Construction Machinery,12th Scandinavian International Conference on Fluid Power (12. SCIFP), Tampere, Finland, 2011.
2. BUSQUETS, E., IVANTYSYNOVA, M., Toward Supervisory-Level Control for the Energy Consumption and Performance Optimization of Displacement-Controlled Hydraulic Hybrid Machines, 10th International Fluid Power Conference (10. IFK), Dresden, Germany, 2016.
3. SIEBERT, J., GEIMER, M., Reduction of System Inherent Pressure Losses at Pressure Compensators of Hydraulic Load Sensing Systems, 10th International Fluid Power Conference (10. IFK), Dresden, Germany, 2016.
4. DENGLER, P., GEIMER, M., BAUM, H., SCHUSTER, G., WESSING, C., Efficiency Improvement of a Constant Pressure System using an Intermediate Pressure Line, 8th International Fluid Power Conference (8. IFK), Dresden, Germany, 2012.
5. PÖTTKER, A., Mechanic – hydraulic co-simulation on mining excavators, 5th International Fluid Power Conference (5. IFK), Aachen, Germany, 2006.
6. NAKAMURA, T., NAKAMURA, K., OKANO, Y., ISHIKAWA, K., SATO, K., AZUMA, H., KANEHAMA, M., KAJITA, Y., Hydraulic Drive Device for Working Machine, Japan Patent, 2012, WO 2012/157705 A1, JP 2012-241803A.
7. VUKOVIC, M., MURRENHOFF, H., STEAM – A Mobile Hydraulic System with Engine Integration, ASME/BATH 2013 Symposium on Fluid Power & Motion Control, Sarasota, Florida, USA, 2013.
8. VUKOVIC, M., LEIFELD, R., MURRENHOFF, H., STEAM – a hydraulic hybrid architecture for excavators, 10th International Fluid Power Conference (10. IFK), Dresden, Germany, 2016.
9. HIJIKATA, S., WEISHAAR, P., SUGIMURA, K., SCHMITZ, K., MURRENHOFF, H., A hydraulic hybrid architecture combining an open center with a constant pressure system for excavators, 11th International Fluid Power Conference (11. IFK), Aachen, Germany, 2018.
10. HIJIKATA, S., WEISHAAR, P., LEIFELD, R., SCHMITZ, K., Efficiency for a hydraulic hybrid architecture of excavators, MM science journal, 2018, DOI:10.17973/MMSJ.2018_10_201831.
11. HIJIKATA, S., ITO, K., MURRENHOFF, H., Investigation of Accumulator Parameters for a Novel Hybrid Architecture, J. Robot. and Mechatronics, 2020, Vol.32 No.5, pp. 876-884.

The 11th JFPS International Symposium on Fluid Power HAKODATE 2020 Oct. 12-13, 2021 The Japan Fluid Power System Society

Research Regarding the Energy Saving Conditions of the Air Blow for Removing and Drying Out Water

Daisuke KURAKAMI*, Keiichirou KOGA*, Gohei HARIMOTO*

*Technology Research Division, SMC Corporation
4-2-2, Kinunodai, Tsukubamirai-shi, Ibaraki-ken, 300-2493 Japan
(E-mail: kurakami.daisuke@smcjpn.co.jp)

Abstract. One example of the use of air blow is drying workpieces after cleaning. The surface shape of some workpieces is complicated and there are various holes and dents. Hence it can't be dried well, even if a large amount of compressed air is used. If may be the cause of the increased power consumption of the air compressor. Therefore, we have been conducting research on air blow with the aim of establishing a method for selecting appropriate air blow conditions. In this research, we conducted a flat plate drying experiment using an air blow using a convergent nozzle, and summarized the relationship between blow time and the dried range. From the results, we have created a diagram that can select the air blow conditions in which the air consumption is the least according to the required dried range, and we will introduce it.

Keywords: Air blow, Convergent nozzle, Drying, Energy saving

INTRODUCTION

Air blow is used in various applications and adopted in most of the factories. It is considered that approximately 50% of the compressed air used in the factory is occupied by air blow. Therefore, the improvement of the existing air blow equipment is cost-effective, and the user's interest and awareness of it is high [1]. If a discharge pressure of an air compressor can be reduced by efficient air blow, it will lead to reduction of power consumption and energy saving.

One example of the use of air blow is drying workpieces after cleaning. The surface shape of some workpieces is complicated and there are various holes and dents. Hence it can't be dried well, even if a large amount of compressed air is used in the drying process after cleaning. This is the problem for many users. Therefore, it is an issue to remove water and improve drying efficiency by air blow. Based on the above, we have been conducting research on air blow with the aim of establishing a method for presenting appropriate air blow conditions. Here, air blow conditions include nozzle diameter, nozzle inlet pressure, and distance from a workpiece.

In this paper, we will introduce the diagrams to select appropriate blow conditions when drying a flat plate.

EXPERIMENT DRYING FLAT PLATE

Experimental device

Fig. 1 shows the diagram of experimental device. The nozzle inlet pressure (hereinafter referred to as "P_2 [MPa]") is regulated by the pressure regulator. The set pressure of the pressure regulator (often equal to the discharge pressure of the air compressor) is P_1 [MPa]. P_2 is measured by the pressure sensor. The flow rate (hereinafter referred to as "Q [L/min(ANR)]") consumed during air blow is measured by the flow sensor. The position of the nozzle is adjusted by electric actuators. The size of the aluminum plate mounted under the nozzle is 500 mm square.

Before conducting the experiment, some preliminary experiments were conducted and the following was confirmed. Firstly, the nozzle-plate distance has little effect on the dried diameter in the range of 50 mm to 160 mm. Secondly, when P_2 is less than 0.1 MPa, that is, in the case of subsonic flow, it is necessary to increase both the blow time and the air consumption in order to obtain the same drying effect as the choked flow. Consequently, in this experiment, the distance between the nozzle and the plate is 120 mm and P_2 shall be 0.1 MPa or more.

Tab. 1 shows experimental conditions. In this experiment, a nozzle called a convergent nozzle is used. Fig. 2 shows the cross-sectional shape of a convergent nozzle.

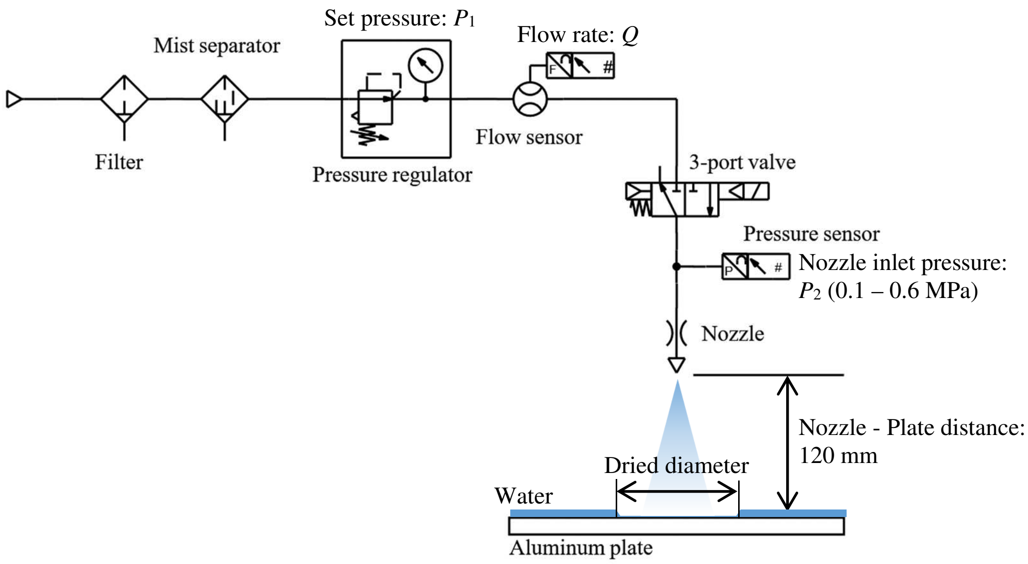

Figure 1. Experimental device diagram

Table 1. Experimental conditions

Nozzle diameter: *d* [mm]	**Nozzle inlet pressure: P_2 [MPa]**					
	0.1	0.2	0.3	0.4	0.5	0.6
1	○	○	○	○	○	○
2	○	○	○	○	○	○
3	○	○	○	○	○	○
4	○	○	○	○	-	-
6	○	○	-	-	-	-

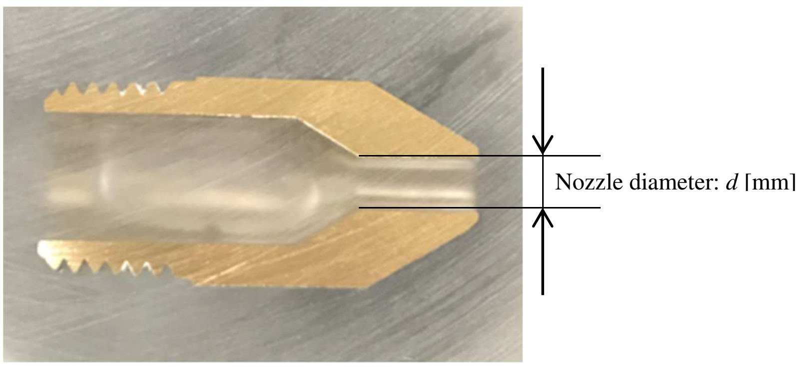

Figure 2. Cross-sectional shape of convergent nozzle

Experimental method

First, spread water evenly on the flat plate. Next, the surface is dried by air blowing. The time keeping air blow is 60 seconds. This situation is recorded as a video with a digital camera. From the video, the image after a certain period of time from the start of air blow is acquired. Use image processing software to measure the dried diameter from the acquired image.
Fig. 3 shows an example of an image taken from a video. For each experimental condition, record the relationship between the time from the start of blowing (hereinafter referred to as “blow time: t [s]”) and the dried diameter (hereinafter referred to as “D [mm]”).

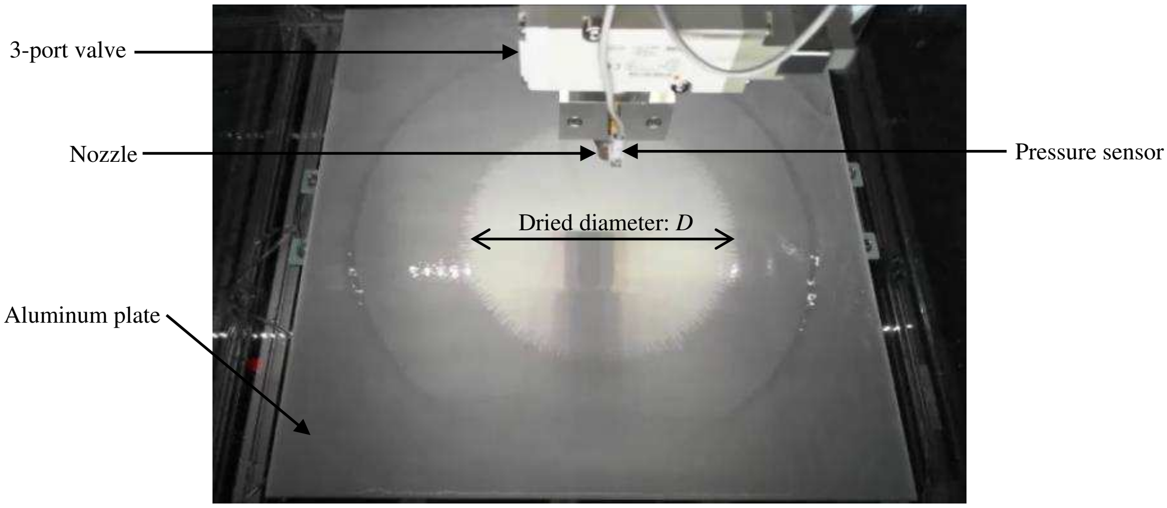

Figure 3. Dry image example

Experimental results

As an example of the experimental results, Fig. 4 shows the relationship between D and t when d = 1 mm, P_2 = 0.2 MPa. D significantly changes immediately after starting the air blow, however the rate of the change of it reduces over time.

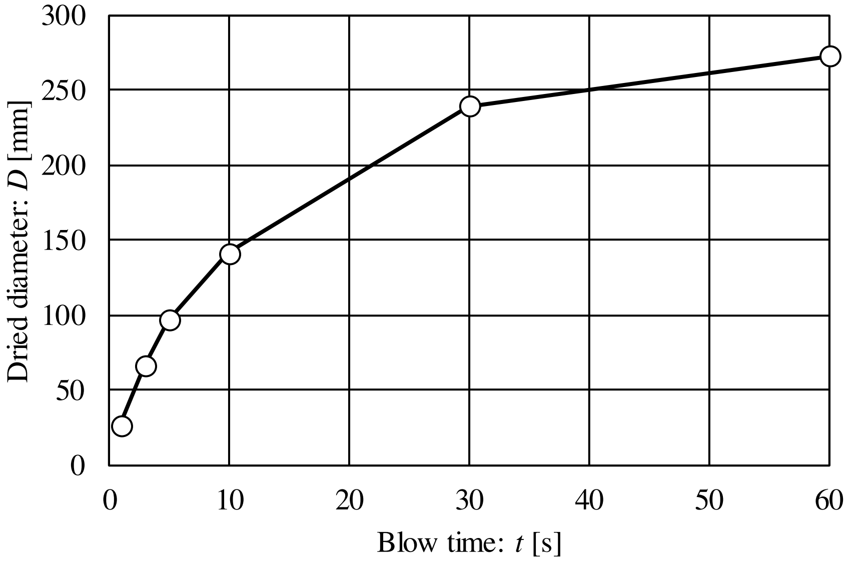

Figure 4. Relationship between dried diameter and blow time
(d =1 mm, P_2 = 0.2 MPa)

CREATION OF THE NOZZLE SELECTION DIAGRAM BASED ON THE ENERGY SAVING CONDITIONS

Relationship between the maximum dried diameter and flow rate

Fig. 5 shows a plot of the experimental values for the relationship between Q and the maximum dried diameter (hereinafter referred to as "D_{max} [mm]"). The shape of the markers is changed for each d. Here, D_{max} means the D after the end of the air blow. From the graph, it is estimated that when using a convergent nozzle, D_{max} is determined by Q, regardless of d or P_2. The relationship between D_{max} and Q can be approximated by Equation 1. The solid line in Fig. 5 shows the value calculated by Equation 1.

$$D_{max} = 125 \times Q^{0.245} \tag{1}$$

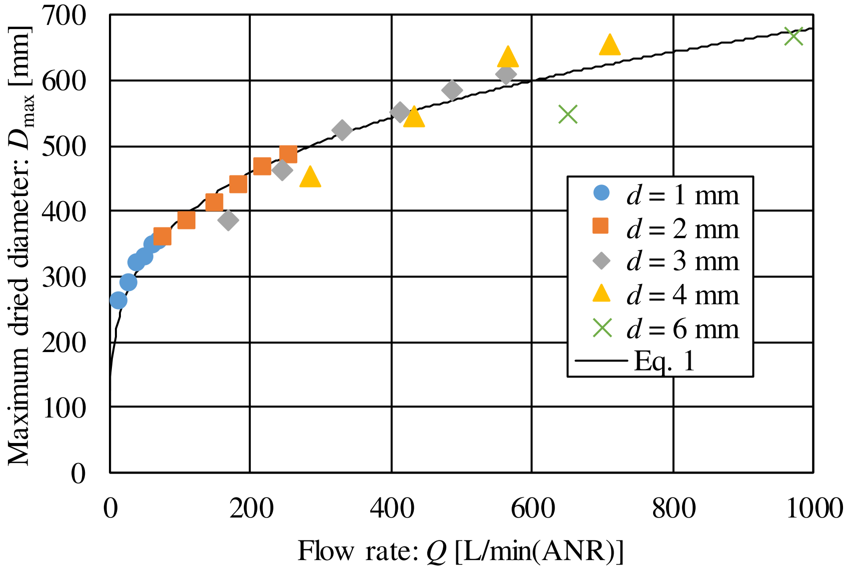

Figure 5. Relationship between maximum dried diameter and flow rate

Relationship between the dried diameter and blow time

Based on the experimental results under all the conditions shown in Tab. 1, the relationship between D and t can be expressed by an equation such as the exponential function shown in Equation 2. D_0 [mm] represents the initial D, and it is calculated by Equation 3.

$$D = D_0 + \left(D_{max} - D_0\right)\left(1 - e^{-\frac{t}{12}}\right) \tag{2}$$

$$D_0 = 12d + 9 \tag{3}$$

Fig. 6 shows the relationship between t and D when d = 2 mm, P_2 = 0.2 or 0.5 MPa. The experimental values are represented by markers, and the values calculated by Equation 2 are represented by solid lines.

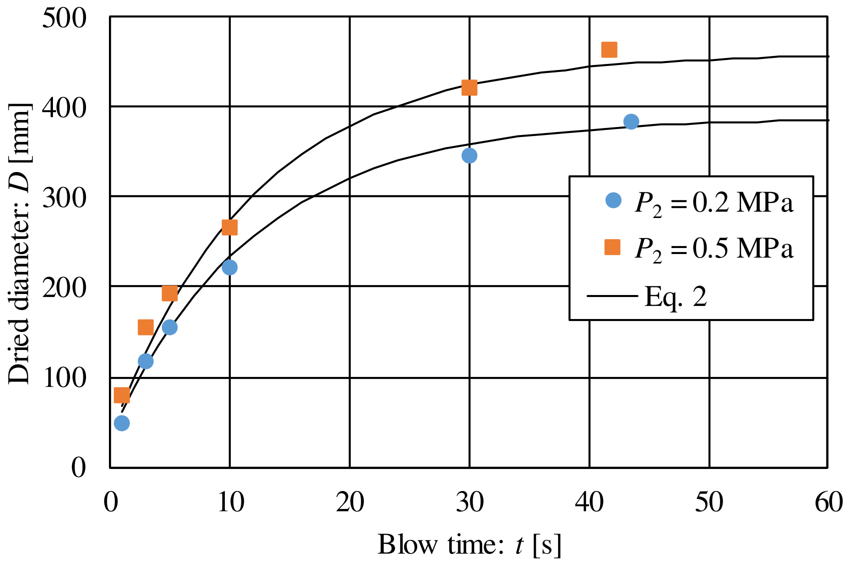

Figure 6. Relationship between dried diameter and blow time
(d = 2 mm, P_2 = 0.2 or 0.5 MPa)

Air-saving blow condition selection diagram

Using Equation 1 to 3, t on which D is reached to Φ200 to Φ600 and the air consumption (hereinafter referred to as "q [L(ANR)]") at that time are calculated. Fig. 7 shows the result. Comparing the air blow conditions when D is the same, the following tendencies can be read. When d is the same, the lower P_2 is, the less q is, however the longer required t is. Similarly, when t is the same, the larger d is, the lower P_2 is and the less q is.
As a selection example, consider the case of drying a range with a diameter of Φ500. The marker on Fig. 7 with the least q in markers indicating air blow conditions in which D is reached to Φ500 is circled in red. The conditions indicated by this marker are d = Φ3, P_2 = 0.5 MPa, and t = 25 s. In this way, the air blow conditions with the least q can be selected according to the desired D. The least q means that the best condition for Energy saving.

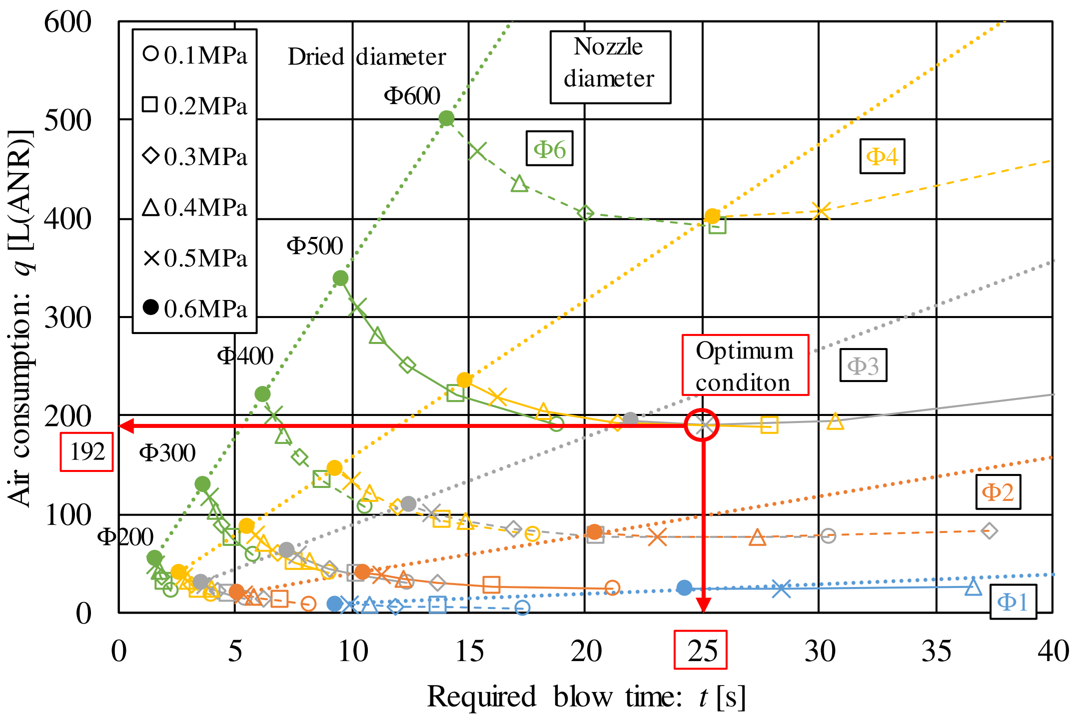

Figure 7. Diagram for selecting the nozzle for drying the flat plate

Energy saving nozzle selection diagram according to set pressure of compressor

In the selection diagram shown in Fig. 7, it is possible to select the air blow conditions in which q is the least, according to the desired D. Incidentally, a discharge pressure of an air compressor varies from factory to factory. Therefore, in order to set to the P_2 selected by using Fig.7, the discharge pressure must be reduced by a pressure regulator. However, if the pressure adjustment range is large, energy loss will occur. Thus, it is efficient that P_2 is as close as possible to a discharge pressure of an air compressor. From the above, it is better to compare q for each d under the same P_2. Consequently, a nozzle selection diagram for each P_2 has been created so that the optimum d can be easily selected for each P_2. Fig. 8 (a) to (d) respectively show the relationship between D and q for each d when P_2 is 0.3 to 0.6 MPa.
Using these diagrams, it is possible to choose d with the least q, depending on P_2 and the desired D. For example, assume that P_2 = 0.5 MPa. In this case, see Fig. 8 (c). From this diagram, d with the least q according to the desired D is determined. Tab. 2 shows the correspondence table between D and the appropriate d when P_2 = 0.5 MPa. In this way, since the appropriate d differs depending on the pressure used and the desired D, it is necessary to use different nozzles according to the blow conditions.

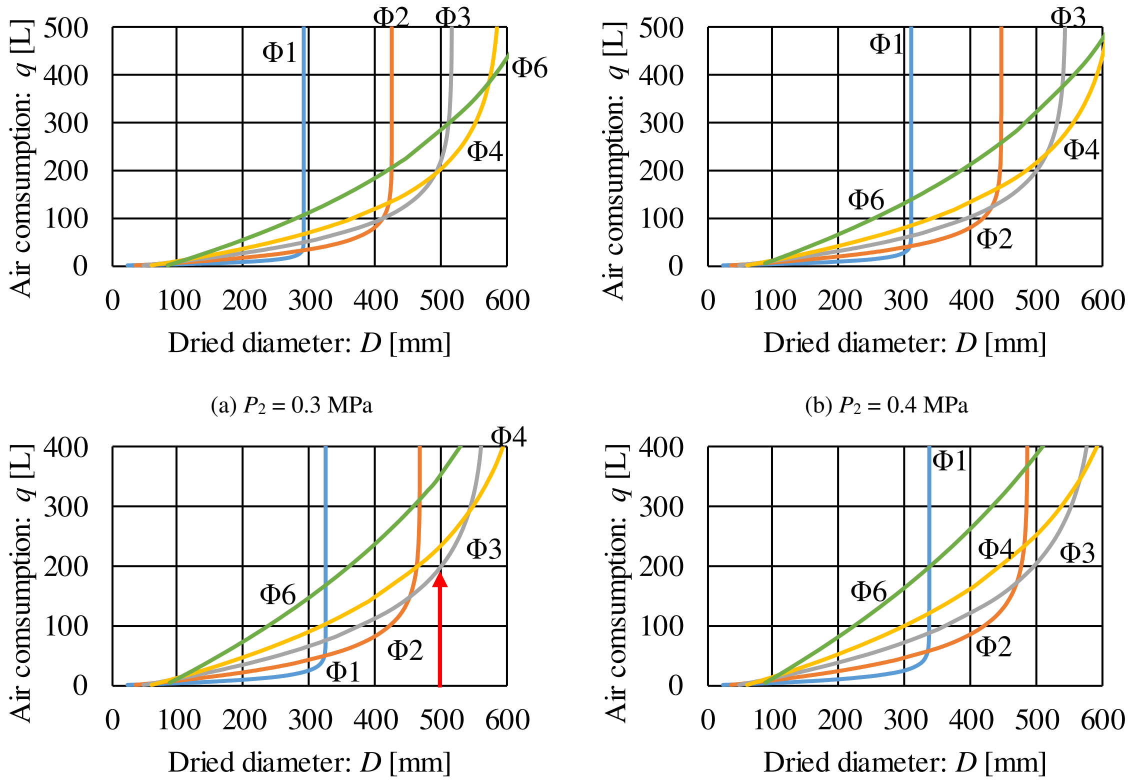

(a) P_2 = 0.3 MPa (b) P_2 = 0.4 MPa

(c) P_2 = 0.5 MPa (d) P_2 = 0.6 MPa

Figure 8. Relationship between dried diameter and air consumption (P_2 = 0.3 to 0.6 MPa)

Table 2. Correspondence table of dried diameter and nozzle diameter (P_2 = 0.5 MPa)

Desired dried diameter [mm]	Appropriate Nozzle diameter [mm]
- 320	Φ1
320 - 460	Φ2
460 - 550	Φ3
550 -	Φ4

CONCLUSION

Based on the experimental results, equations have been established to calculate the dried diameter from flow rate, nozzle diameter, and blow time when drying a flat plate with a convergent nozzle.
Using the established equations, two types of diagrams were created to select the appropriate air blow conditions according to the desired dried diameter.
In the first type of diagram, the air blow condition with the least air consumption can be selected from the all pressure conditions. This type of diagram can include blow time as a selection condition.
In the second type of diagram, the nozzle with the least air consumption can be selected for each pressure. If the pressure to be used is decided, it is suitable to use this type of diagram.

REFERENCES

1. ONEYAMA. N., Energy Saving for Pneumatic System, Energy Conservation Center, 2003, pp.11-12, 97, 195-196.

The 11th JFPS International Symposium on Fluid Power HAKODATE 2020 Oct. 12-13, 2021 The Japan Fluid Power System Society

Energy Regeneration and Reuse of Excavator Boom System With Hydraulic Constantly Variable Powertrain

Tri Cuong DO* and Kyoung Kwan AHN**

* Graduate School of Mechanical and Automotive Engineering, University of Ulsan, Ulsan, Korea
** School of Mechanical and Automotive Engineering, University of Ulsan, Ulsan, Korea
(E-mail: kkahn@ulsan.ac.kr)

Abstract. A new design of an energy recovery system is presented in this paper for regenerating and reusing potential energy in a boom cylinder. The proposed system integrates an electrical hydraulic continually variable powertrain which the main pump is supplied power from both engine and an electric motor/generator. During moving down process, the potential hydraulic energy of boom cylinder is stored in a battery as electricity through a hydraulic motor and an electric motor/generator. Then, during acceleration process, the stored electrical energy can be reused to the electric motor/generator (motor mode) to support the engine. To demonstrate the effectiveness of the proposed system, a real test bench is built. The experiment results indicated that the energy regeneration efficiency could reach up to 37%. Besides, the energy consumption was also reduced.

Keywords: Boom system, constantly variable powertrain, energy recovery system.

INTRODUCTION

In recent years, with the development of industry, pollution and global warming have become extremely serious problems. One of the most popular and widely used equipment is the hydraulic excavator because of its benefits such as moving heavy objects, dig, and demolition. However, like other construction machinery, hydraulic excavators consume a lot of fossil fuels and release harmful gases into the environment [1-4]. To solve this problem, there are two main directions that are to reduce energy consumption and reuse the potential energy in the excavator.

To reduce energy consumption, conventional hydraulic excavators (HE) with internal combustion engines (ICEs) are gradually being replaced by hybrid HE that combines the ICE with an electric motor or electric HE using electric motor and battery. The first structure of hybrid HE is proposed by Kanezawa [5]. After that, a full-scale commercial hybrid HE namely PC200-8 is released from Komatsu [6]. In this hybrid HE, the potential energy in the swing system is recovered through a generator and stored in the battery. The results showed that the energy consumption was reduced 25% compared with conventional HE. Lei Ge proposed an electric HE configuration [7]. In this research, a speed variable electric motor was used as the main power source to drive a variable displacement pump. Besides, a control strategy was designed to adjust the pump displacement and motor speed to ensure these components working in highly efficient areas. The experiment results indicated that the energy consumption reduced from 28.5 to 33%. However, the electric HE still has limitations such as low durability and not suitable for dusty environments.

In HE, there are some places where the energy can be recovered such as in the boom cylinder during the moving down or flow rate of the swing system during deceleration process. In which, potential energy in boom cylinder accounts for 51% of the total recoverable energy [8]. Therefore, energy recovery systems (ERSs) for HE focuses on the recovery of energy in boom cylinder. Yu et al. [9] placed a hydraulic motor at the outlet port of bore chamber to reduce the energy losses. In addition, a flow control valve was integrated to regulate the flow rate through the hydraulic motor. Hence, the hydraulic motor's working point is ensured in the high-efficiency area. The experiment result showed that the energy regeneration efficiency can achieve 57,4%. Based on this research, Do et al. [10] proposed a ERS which can not only recover but also reuse the energy in the boom cylinder system. The proposed system used energy conversion components which combined a hydraulic pump/motor and an electric motor/generator. The boom hydraulic energy is converted to electrical energy and stored in the battery. Then, the stored energy can be reused to the electric motor/generator (motor mode) in the next cycles. However, this system required large device sizes to perform the above functions. This leads to increased manufacturing costs and payback times. Besides, when applying this ERS to the hybrid HE, the system has to integrate an additional electric motor/generator to recover energy, leading to an increase in the cost of the hybrid HE.

Based on the above analysis, this paper proposes a new ERS using an electrical hydraulic continually variable powertrain which contains an engine and an electric motor/generator to drive the main pump. The proposed

system can study not only the problem of reducing energy consumption at the power sources but also the problem of energy recovery in the boom cylinder which have often been studied independently in previous systems. During the moving down process, the potential energy of the boom cylinder is recovered through a hydraulic motor and the electric motor/generator (generator mode) and stored in the battery. Therefore, it is possible to overcome the weakness of previous research [10] with only one electric motor/generator in the powertrain of the hybrid configuration for energy recovery and energy reuse. During the lifting up, the main pump is driven by the ICE and the electric motor/generator (motor mode) which is supplied power from the battery. With the proposed structure, the system is not only recover but also reuse the energy in the boom cylinder system. To prove the effectiveness of the proposed system, a real test bench is built. Several experiments are conducted with the different working modes of the system. The experiment results indicate that the energy regeneration efficiency could achieve 40%. Besides, energy consumption is reduced.
The rest of this paper is organized as follows: Section 2 presents the structure and working principle of the proposed system. The experiment results are presented in section 3. Conclusions are given in the final section.

SYSTEM DESIGN

The proposed system consists of a boom cylinder, an electric motor which is used to emulate the ICE, an electric motor/generator, a variable displacement pump, two proportional control valve 4/3, and some auxiliary valves for safety as shown in Fig. 1. In details, the motor (1) and the electric motor/generator (5) drive the main pump (10) via a planetary gear (3). The rotation speed from the electric motors is connected or disconnected by clutch and brake devices (2, 4, 9). Besides, the double clutch (8) is used to switch the connection between the main pump (10), hydraulic motor (14) and the planetary gear (3). Based on the structure, the proposed system can operate with three main modes: normal working, energy regeneration and energy reuse.

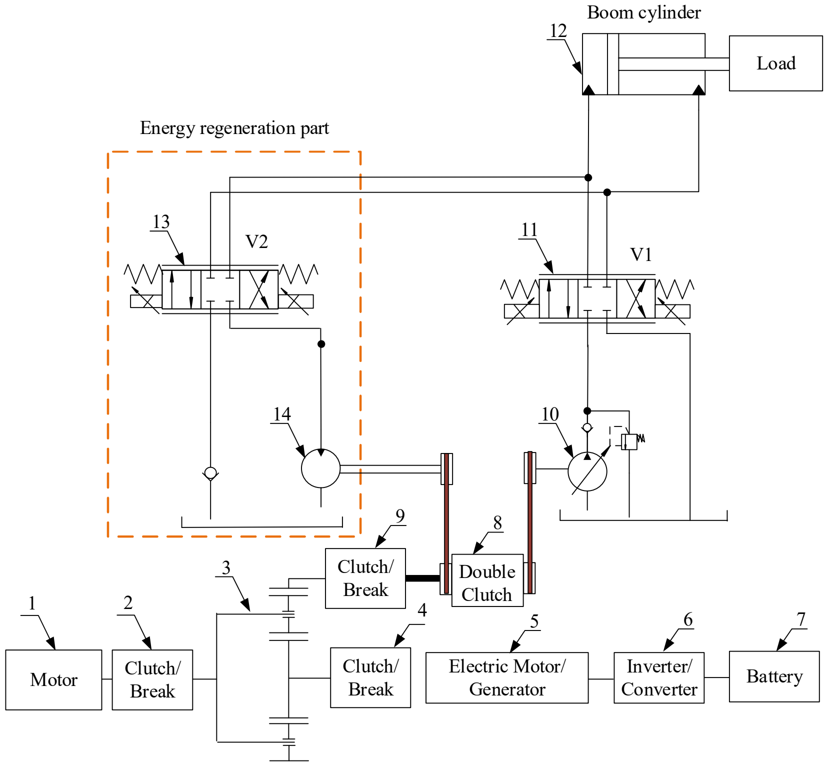

Figure 1. The proposed boom ERS.

In the proposed system, the planetary gear (3) is one of the key components for transferring the power from electric motors (1, 5) to the main pump (10). The planetary gear (3) contains sun, carrier and ring gears as shown in Fig. 2. The electric motor (1) is connected to the sun gear, the electric motor/generator (5) and the main pump (10) are connected with the carrier gear and the ring gear, respectively.

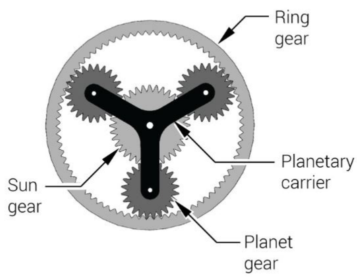

Figure 2. Structure of planetary gear.

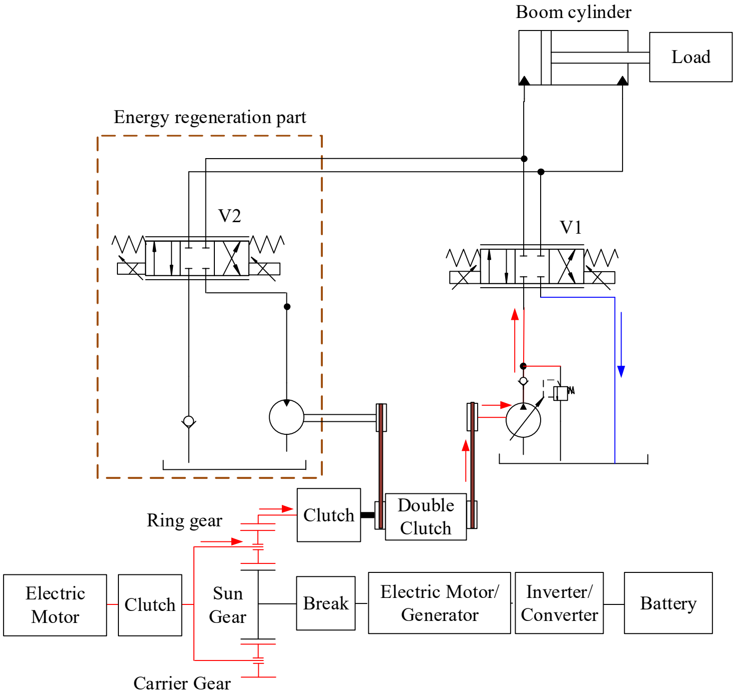

Figure 3. Working principle of normal mode.

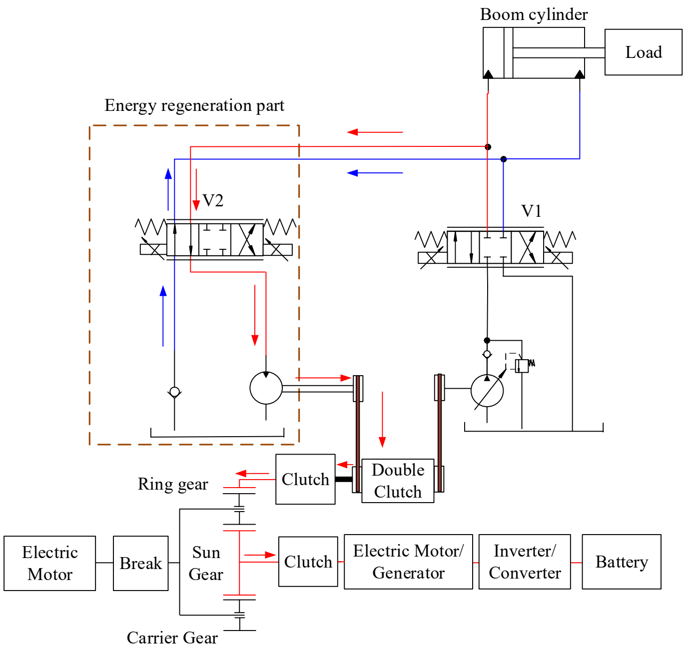

Figure 4. Boom cylinder moves down in the energy regeneration mode.

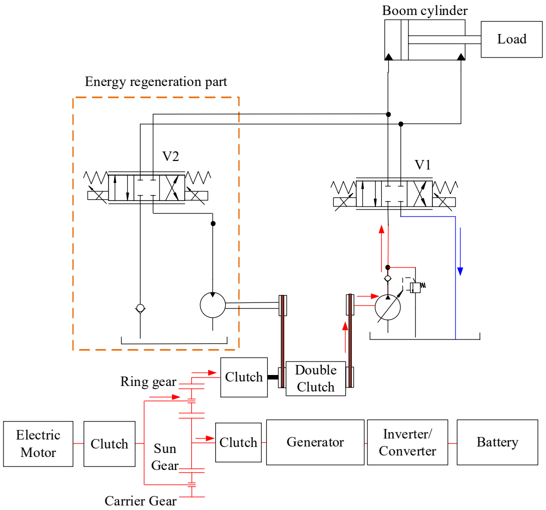

Figure 5. Boom cylinder moves up in the hybrid mode.

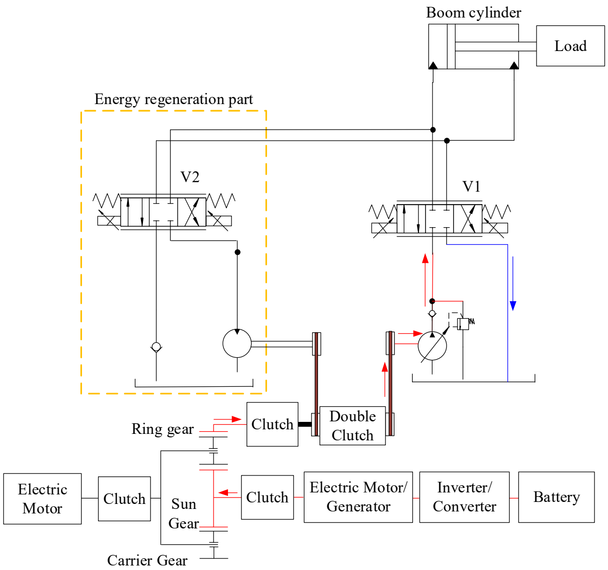

Figure 6. Boom cylinder moves up in the energy reuse mode.

In the normal working mode, the main pump (10) is driven by the electric motor (1) and supply the flow rate to the boom system. The movement of the boom cylinder (12) is controlled by the state of valve V1 (11). When the boom cylinder moves down under the influence of gravity, it can automatically move down without suppling the flow from the power source. The flow rate from the tank can go directly to the rod chamber via valve V1 (11) as shown in Fig. 3.

In the energy regeneration working mode, the boom cylinder (12) moves down by the gravitational force. Instead of going straight to the tank as in normal working mode, the directional valve V2 (13) is adjusted to the left position allowing flow from the bore chamber to pass through a hydraulic motor (14) as shown in Fig. 4. Then, the hydraulic energy is converted to electrical energy through the electric motor/generator (5) and store in the battery (7).

In the hybrid mode, three clutches/brakes (2, 4, 9) work in the clutch function and connect two power sources to planetary gear. During this operation, the electric motor (1) supplies the power to both the main pump (10) and electric motor/generator (5). The cylinder (12) moves up by the flow rate from the main pump (10). Besides, the electric motor/generator (5) works in generator function and convert the mechanical energy to the electric energy and store in the battery (7) as shown in Fig. 5.

In the energy reuse mode, the stored energy in the battery (7) is reused and supplied to the electric motor/generator (5). Then, the electric motor/generator (5) works as motor mode and drives the main pump (10). The flow rate from the tank is supplied to the boom cylinder (12) and lift the load. The flow rate in the rod chamber goes to the tank as shown in Fig. 6.

Table 1. Proposed system configuration.

Components	**Parameter**	**Value**	**[SI unit]**
Cylinder	Bore diameter	50	mm
	Rod diameter	28	mm
	Length	0.75	m
Pump	Displacement	35	cm3/rev
Electrical motor	Power	7.5	kW
Hydraulic motor	Displacement	20	cc/rev
Generator/ motor	Power	5.5	kW

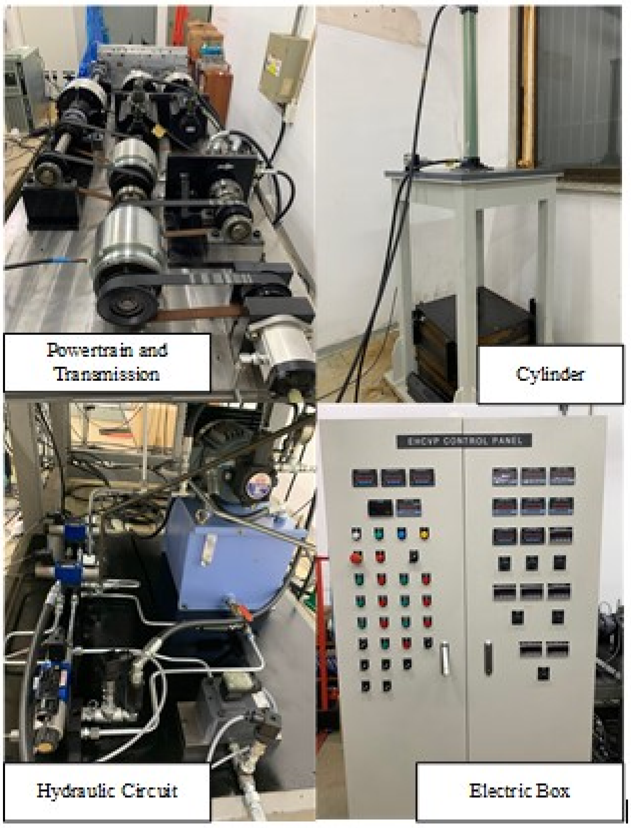

Figure 7. Experiment apparatus of proposed system

EXPERIMENT RESULTS

The experimental setup was built to verify the effectiveness of the proposed system. The detail structure of the experimental system using electrical hydraulic constantly variable powertrain is presented in Fig. 7. The total system includes the main parts such as the cylinder, powertrain, hydraulic circuit and control box. The parameters of the experimental system are shown in Table 1. As presented above, the ICE was emulated by the 7.5kw electric motor. The system is controlled on the computer within real-time Window Target Toolbox of MATLAB 2013b under a sampling time of 0.01 seconds.

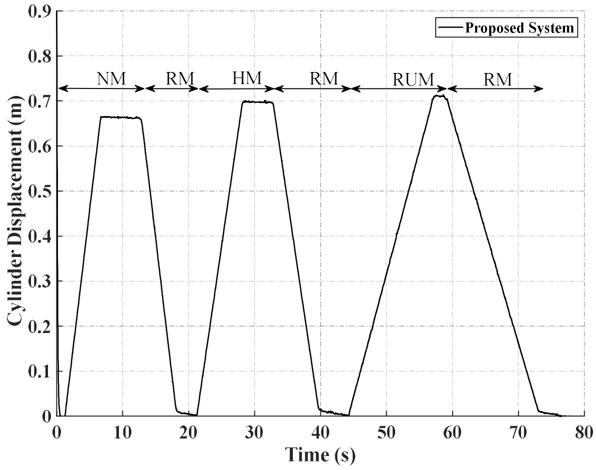

Figure 8. Displacement of the boom cylinder. (NM: normal mode, RM: regeneration mode, HM: hybrid mode, RUM: Reuse mode)

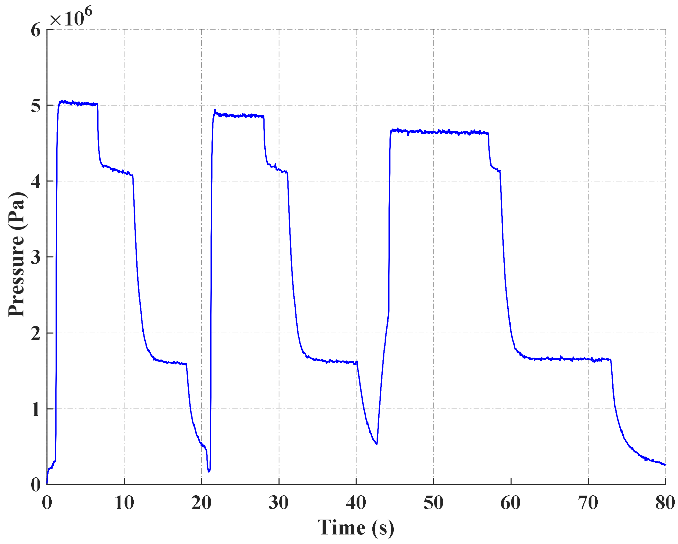

Figure 9. Pressure of the boom cylinder.

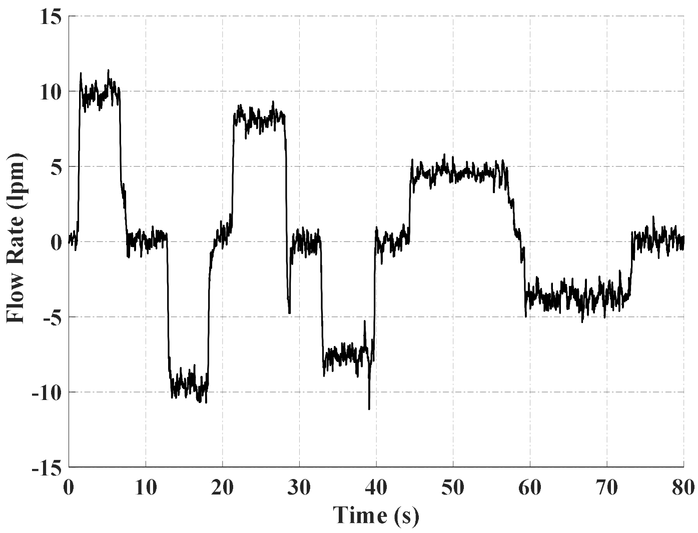

Figure 10. Flow rate of the main pump.

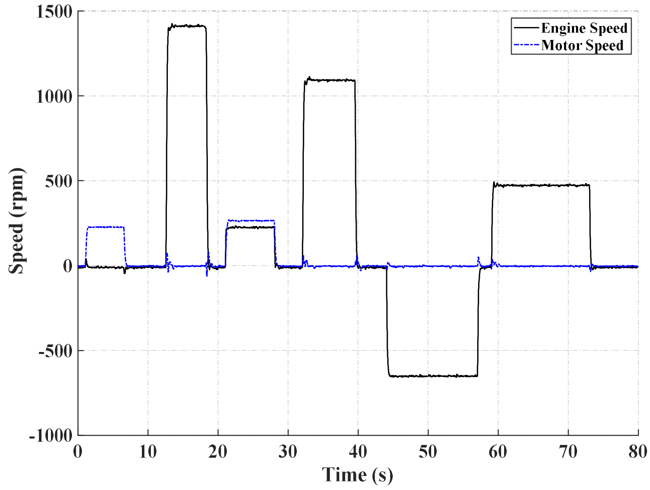

Figure 11. Speed of electrical motor/generator and ICE.

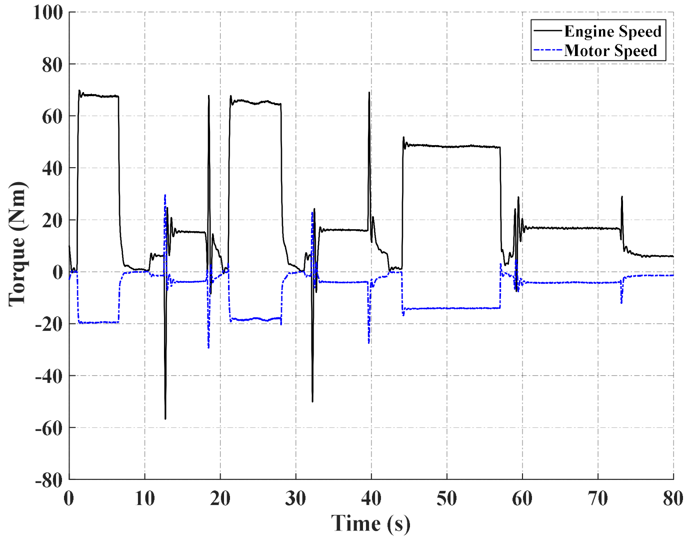

Figure 12. Torque of electrical motor/generator and ICE.

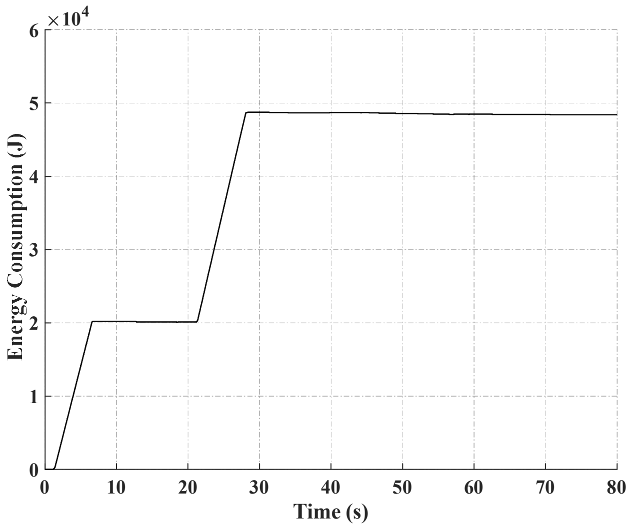

Figure 13. Speed and torque of electrical motor/generator.

Fig. 8 presents the displacement of the boom cylinder in three cycles. From the 0s to 10s, the system run in the normal mode. The boom cylinder took 5 seconds to reach 0.68 m. From the 20s to 30s, the hybrid mode is activated. During this operation, the ICE supplied the power to both cylinder and electric motor/generator. From the 42s to 58, the system operated in the reuse mode with the main pump driven by the electric motor/generator without power from the ICE. During the moving down process, the pressurized flow rate from the cylinder is converted to electric energy through the hydraulic motor and electric generator in energy regeneration mode. Fig. 9 and Fig. 10 shown the pressure and flow rate of the main pump, respectively.
The speed and torque of the electrical motor/generator and engine were presented in Fig. 11 and 12, respectively. In the regeneration mode, the electric motor/generator worked in the generator function. Therefore, the torque and speed were different signs. From the 42s to 58, the speed and torque were the same signs because the electric motor/generator was working in the motor functions and driving the main pump in the energy reuse mode. The highest torque and speed of the electric motor/generator were 20 Nm and 320 rpm during three cycles. Fig. 13 shows the energy consumption of the proposed system. From the 30s, the system could work without the power from the ICE. Hence, energy consumption could be reduced.
The potential energy in the boom cylinder can be estimated based on the pressure (p_c) and flow rate (q_c) as

$$E_p = \int p_c q_c dt \tag{1}$$

The regenerated energy can be estimated as shown in Eq. (2).

$$E_r = \int T_r \omega_r dt \tag{2}$$

where the E_r, T_r, and ω_r are the regenerated energy, torque and speed of the electric motor/generator, respectively. The energy regeneration efficiency of the proposed system can be estimated as follow:

$$\eta = \frac{E_r}{E_p} \tag{3}$$

From the above results, the energy regeneration efficiency of the proposed system was 37%.

CONCLUSION

This paper presented a new energy regeneration system using the electrical hydraulic constantly variable powertrain. In details, the proposed contained a hydraulic motor that could regenerate the energy from the boom cylinder and stored in the battery. In addition, the drive system includes an ICE and an electric motor / generator allowing it to reuse energy during operation. A test rig was developed to prove the effectiveness of the proposed system. The results indicated that the system could work well with designed modes. The energy recovery efficiency of the proposed system could achieve 37%. Besides, the energy consumption was decreased because of energy reuse mode.

ACKNOWLEDGMENT

This research was supported by Basic Science Program through the National Research Foundation of Korea (NRF) funded by the Ministry of Science and ICT, South Korea (NRF-2020R1A2B5B03001480).

REFERENCES

1. DO, T. C., TRUONG, H. V. A., DAO, H. V., HO, C. M., TO, X. D., DANG, T. D., and AHN, K. K., Energy Management Strategy of a PEM Fuel Cell Excavator with a Supercapacitor/Battery Hybrid Power Source, Energies, vol. 12, no. 22, 2019.
2. DANG, T. D., DO, T. C., TRUONG, H. V. A., HO, C. M., DAO, H. V., XIAO, Y. Y., JEONG, E. J. and AHN, K. K., Design, Modeling and Analysis of a PEM Fuel Cell Excavator with Supercapacitor/Battery Hybrid Power Source, Journal of Drive and Control, 16(1), 45-53, 2019.
3. TRUONG, H. V. A., DAO, H. V., DO, T. C., HO, C. M., TO, X. D., DANG, T. D., and AHN, K. K., Mapping Fuzzy Energy Management Strategy for PEM Fuel Cell–Battery–Supercapacitor Hybrid Excavator, Energies, 13(13), 3387, 2020.
4. DINH, T. X., THUY, L. K., TIEN, N. T., DANG, T. D., HO, C. M., TRUONG, H. V. A., DAO, H. V., DO, T. C., and AHN, K. K., Modeling and Energy Management Strategy in Energetic Macroscopic Representation for a Fuel Cell Hybrid Electric Vehicle, Journal of Drive and Control, 16(2), 80-90, 2019.
5. KANEZAWA, Y., DAISHO, Y., and KAWAGUCHI, T., Increasing efficiency of construction machine by hybrid system. Society of Automotive Engineers of Japan. Vol. 100. 2001.
6. INOUE, H., Introduction of PC200-8 Hybrid Hydraulic Excavators. Komatsu technical report 2008, Vol. 54 No.161.
7. GE, L., QUAN, L., ZHANG, X., ZHAO, B., YANG, J., Efficiency improvement and evaluation of electric hydraulic excavator with speed and displacement variable pump. Energy Conversion and Management 2017, 150, 62-71.

8. LIN, T., CHEN, Q., REN, H., HUANG, W., CHEN, Q., FU, S., Review of boom potential energy regeneration technology for hydraulic construction machinery. Renewable and Sustainable Energy Reviews 2017, 79, 358-371.
9. YU, Y. X., AHN, K. K., Optimization of energy regeneration of hybrid hydraulic excavator boom system. Energy Conversion and Management 2019, 183, 26-34.
10. DO, T. C., NGUYEN, D. G., DANG, T. D.; AHN, K. K., A Boom Energy Regeneration System of Hybrid Hydraulic Excavator Using Energy Conversion Components, Actuators, 2021.

The 11th JFPS International Symposium on Fluid Power HAKODATE 2020 Oct. 12-13, 2021 JFPS The Japan Fluid Power System Society

Efficient Closed Pump Controlled Hydraulic-Gas Balanced Energy Recovery Driving Method for Hydraulic Excavator Boom

Lianpeng XIA*, Long QUAN*, Hongjuan ZHANG**, Yunxiao HAO*, Lei GE*

* College of Mechanical and Vehicle Engineering, Taiyuan University of Technology
79 Yingzexi Street, Taiyuan, Shanxi, 030024 China
(E-mail: Quanlong@ tyut.edu.cn)
** College of Electrical and Power Engineering, Taiyuan University of Technology
79 Yingzexi Street, Taiyuan, Shanxi, 030024 China

Abstract. To reduce the energy consumption and pollution emissions of hydraulic excavators, an innovative speed variable pump controlled and gravitational potential energy recovery integrated boom driving scheme is proposed. Firstly, the working principle of the proposed system is analyzed. To verify the feasibility and energy saving effect of the proposed system, the test bench of the proposed system are built. The operating and energy efficiency characteristics of the proposed system are tested and analyzed. The testing results show that, the new system has good motion characteristics and high positioning accuracy. By using the proposed system, the gravitational potential energy is recovered as high as 75.3%; compared with the traditional load sensing system, the energy consumption is reduced by up to 72.4% for lifting and lowering boom each time. In view of good fuel saving and economic performance, the proposed system can be applied to all kinds of heavy-duty manipulator which is driven by hydraulic cylinders.

Keywords: hydraulic excavator, three-chamber cylinder, pump controlled system, energy recovery

INTRODUCTION

Hydraulic excavator and other engineering machinery has huge possession around the world, and has become a major fuel consumption source and pollution emitter [1,2]. With the shortage of fossil fuel, global warming and strict emission standard implementation, how to reduce the fuel consumption and emissions of the hydraulic excavators has become a research hotspot in this field. The electric hybrid power system compensates the load fluctuation by the added electric motor/generator, smoothes the engine output torque, and maintains the engine in an high efficient area for a long time, which provides an effective way to solve this problem [3-6]. However, the hydraulic circuit still uses the conventional valve control system to drive multiple actuators. To complete the same work, compared with the original internal combustion engine power system, the hybrid power system still needs to provide the same amount of energy [7]. Moreover, the use of the hybrid power system increases the investment cost of the hydraulic excavator and the investment cost recovery cycle is long, which limits the promotion and application of this technology. If the energy efficiency of the hydraulic circuit is improved, the fuel consumption of the hydraulic excavator can be further reduced and the cost recovery cycle can be shortened, and the barrier that restricts the application of hybrid power system can be broken.

In recent decades, the proposed load-sensing [8-9], independent metering [10-11] and other technologies can improve the energy efficiency of the hydraulic system to a certain extent. However, the large throttling loss of the valve control system can't be resolved radically. Taking the hydraulic excavator using load sensing system as an example, about 45%-50% of the pump output energy is wasted through the throttling effect of the control valves, and the wasted gravitational potential energy is about 15% of the hydraulic pump output energy [12]. Compared with the valve control system, the pump controlled system doesn't need control valves and can eliminate throttling loss, and the system has high energy efficiency [13, 14]. Therefore, using pump controlled systems and efficiently regenerating gravitational potential energy can greatly improve the energy efficiency of the hydraulic system.

Recovery and reutilization of the gravitational potential energy is an important way to improve the energy efficiency of hydraulic excavators. Currently, there are mainly electric and hydraulic two energy recovery schemes. In the electric energy recovery scheme where the hydraulic circuit is valve control system, the gravitational potential energy is converted to electrical energy by a separately added hydraulic motor-electric generator, and stored in supercapacitor or battery [15]. In the hybrid hydraulic excavators designed by Komatsu Ltd [16], Hitachi Ltd [17] and Zhejiang University [18], the gravitational potential energy of the boom is recovered by the separately added hydraulic motor- electric generator, which has good energy recovery effect. By setting additional electrical energy storage element, using pump controlled system can realize the unthrottled loss recovery of gravitational potential energy. Jong et al. studied the characteristics of the excavator's boom driven by a single pump controlled system, in which the potential energy is recovered and stored in supercapacitor and battery. The energy consumption is reduced by 47.8% [19]. In the hybrid hydraulic excavator developed by the Kobe Steel Ltd, the boom's hydraulic cylinder is controlled by a pump controlled system driven by electric motor. When the boom lowers, the hydraulic pump works in 'hydraulic motor' mode and the electric motor works in 'electric generator' mode. In this way, the potential energy is converted into electrical energy and stored in supercapacitor [20]. Chen et al. studied the characteristics of a variable speed pump controlled excavator's boom scheme in which the hydraulic accumulator and supercapacitor are used to recovery the gravitational potential energy. The results show that the energy consumption is reduced by 33.1% [21].

In the hydraulic energy recovery schemes, hydraulic accumulator is used as energy storage element. Due to that the accumulator' pressure varies with the volume of oil charged, the accumulator has obvious nonlinear pressure characteristics [22]. To compensate this nonlinearity, during the energy recovery process, the throttling valve [23], hydraulic transformer [24] or the pump controlled system which recovers the energy by torque coupling should be adopted. In the hybrid hydraulic excavator proposed by Paolo, a hydraulic accumulator is connected to the non-rod chamber of the boom's hydraulic cylinder through a proportional throttle valve. The nonlinearity characteristics of the hydraulic accumulator is compensated by adjusting the opening of the proportional throttle valve during the potential energy recovery process. In this scheme, the high pressure oil in the accumulator is introduced to the inlet of the pilot pump and the recovered potential energy is used to assist the engine to drive the pilot hydraulic pump [25]. Shen et al. studied the performance of a hydraulic hybrid excavator based on common pressure rail. The hydraulic cylinder of each actuator is separately driven by one hydraulic transformer. Through the hydraulic transformer, the manipulator's potential energy can be recovered and stored in hydraulic accumulator with high pressure [26]. However, there is no commercial hydraulic transformer currently, and the system is costly and complex [27]. Hippalgaonkar et al. studied the characteristics of a hydraulic hybrid excavator that each actuator is driven by a single pump controlled system. By adding a hydraulic pump/motor coupled with engine, the potential and kinetic energy of the excavator can be recovered by means of torque coupling and stored in hydraulic accumulator. Under the same working condition, the fuel consumption is reduced by 50% [28, 29]. A scheme that the hydraulic excavator's boom is driven by double variable displacement pump controlled system was proposed by Daniel [30]. In this scheme, a hydraulic accumulator is connected with one hydraulic pump to recover the gravitational potential energy. Ge et al. studied a scheme that the hydraulic cylinder of the excavator boom is driven by an asymmetric pump [31]. A hydraulic accumulator is connected with one port of the asymmetric pump to store the high pressure oil of the non-rod chamber of the hydraulic cylinder when the boom falls. The accumulator provides high pressure oil to drive the asymmetric pump when the boom lifts. The test results show that good energy saving effect is obtained. However, the structure of the asymmetric pump is complex, and the flow window area ratio is fixed which makes the asymmetric pump only be suitable for the hydraulic cylinder with special area ratio. In the hydraulic energy recovery schemes, the hydraulic-pneumatic balancing method has the higher energy efficiency due to less energy conversion links [32]. Its basical principle is that independent energy storage cylinder or chamber is connected with hydraulic accumulator to recover and reutilize the gravitational potential energy through the way of balancing the self-gravity of working device. Liang firstly theroretically studied the characteristics of a loglift loader's boom driven by two energy storage cylinders and one working cylinder [33]. In reference [34], a scheme that the hydraulic excavator boom is driven by one energy storage cylinder and two working cylinders is presently, and the energy consumption is reduced by 26.2%. Currently, the scheme adopting the energy storage cylinder has been applied to the boom of material handling machines. To apply this method in the compact installation space manipulator driven by single hydraulic cylinder, a hydraulic-pneumatic balancing scheme using three-chamber cylinder having an energy storage chamber is proposed in reference [35, 36], and good energy saving effect is obtained [37].

Through the above analysis, we can see that, in the existing hybrid hydraulic excavators, a separate hydraulic motor-generator unit is used to recover the gravitational potential energy, which increases the system complexity, cost, and the cost recovery cycle, limiting its popularization and application. Moreover, the gravitational potential energy is recovered through conversion links of the hydraulic motor, the generator, the DC-DC converter and supercapacitor or battery, which lowing the energy recovery efficiency. During the energy reutilization process, there is a large throttling loss because of the original valve controlled system, decreasing the overall energy saving effect. By using the pump controlled system, the gravitational potential energy can be conveniently converted into electrical energy and stored in supercapacitor, or be converted into hydraulic energy through torque coupling and stored in the accumulator. However, there are many energy conversion links, which reduces the recycling efficiency of the gravitational potential energy. Moreover, the variable speed or displacement pump controlled system uses two pumps, the structure of the systems is complex and the cost is high. For the large area difference of the differential hydraulic cylinder, in the single pump controlled system, a filling system with large flow rate is needed which causes large energy loss. In the existing energy recovery schemes, the hydraulic-pneumatic balancing method has a high gravitational potential energy recovery and reutilization rate, but the main hydraulic circuit is still valve control system, resulting in a large throttling loss [34].

Based on the feature that hybrid electric excavator has electric energy storage components such as super capacitors and batteries, to address above issues, an innovative speed variable pump controlled and gravitational potential energy recovery integrated boom driving scheme is proposed in this paper. The core element of the system is a three-chamber cylinder. Two chambers of the three-chamber cylinder are directly connected to the hydraulic pump to drive the excavator boom without throttling loss. The other chamber (called energy storage chamber) of the three-chamber cylinder is connected with a hydraulic accumulator. When the boom is lowered, the high-pressure oil of the energy storage chamber is charged into the accumulator under the gravity of the working device to efficiently recover the gravitational potential energy. When the boom is lifted, the accumulator releases high-pressure oil to the energy storage chamber to drive the boom, which realizes the efficiently reutilization of the recovered energy. The proposed system also has the following advantages. For small area difference between the non-rod chamber and the rod chamber, an oil filling system with small flow rate is needed which reduces the system energy loss. Because the self-gravity of the working device is balanced by the energy storage chamber, the hydraulic pump only needs to drive the load and compensate the inertia force, which greatly reduces the installed power compared with the above mentioned pump controlled system.
The paper is organized as follows. In section two, the working principle of the proposed system is illustrated and the velocity feedforward and displacement feedback (VFDB) compound control strategy is designed. In section three, the energy efficiency mathematic models of the proposed system and the valve controlled single rod cylinder system are built. In section four, the operation performance and energy saving effect of the proposed system is tested and analyzed. In section five, the conclusiton is given.

WORKING AND CONTROL PRINCIPLE

Working principle

The working principle of the proposed system for excavator boom is shown in Figure1. The system consists of a controller, a servo-motor, a servo driver, a hydraulic pump, a filling system, a hydraulic control directional valve, a hydraulic accumulator, and a three-chamber cylinder and so on. As shown in Figure1, by adding a fixed piston and manufacturing the piston rod with hollow, the single-rod hydraulic cylinder can be reformed as a three-chamber cylinder. The three-chamber cylinder has non-rod chamber A, rod chamber B and energy storage chamber C. The chamber A and chamber B are connected with the hydraulic pump, respectively. The velocity and displacement of the boom is controlled by adjusting the rotation speed and direction of the servo-motor, respectively. The energy storage chamber is connected with the hydraulic accumulator. The oil in the energy storage chamber is pressed into the hydraulic accumulator under the action of the working device's self-weight when the boom lowers, and the gravitational potential energy is recovered without throttling loss. When the boom lifts, because of the high oil pressure in the hydraulic accumulator, the energy storage chamber outputs force to assist to drive the boom. By this way, the recovered potential energy can be directly reutilized.

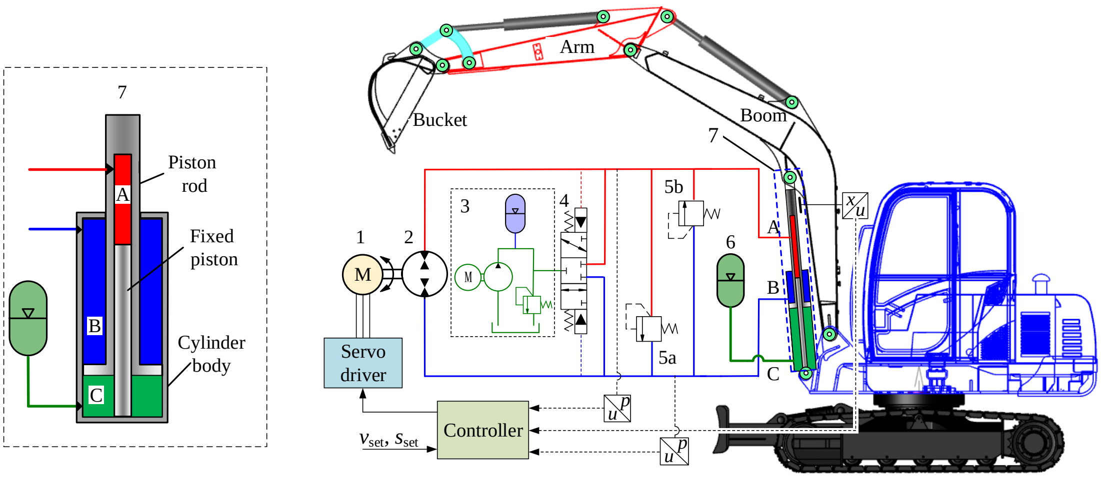

1. Servo-motor 2. Hydraulic pump 3. Oli filling system 4. Hydraulically operated directional control valve
5a, 5b Relieve valve 6. Hydraulic accumulator 7. Three-chamber cylinder
Figure 1 Principle of the proposed system for excavator boom

In the previous study [37], the parameters of the hydraulic accumulator and the three-chamber cylinder has been designed. The capacity of the hydraulic accumulator is selected as 20 L and initial gas pressure is set as 5.5 MPa. Table 1 shows the chamber areas of the hydraulic cylinders. It's known from Table 1 that the area difference between the non-rod chamber and rod chamber of the original working cylinder is about 4900 mm^2 and that of the three-chamber cylinder is about 1500 mm^2. Compared with the original working cylinder, the area difference of the three-chamber cylinder is reduced by 2.26 times, which can greatly reduce the installed power of the filling system. In this paper, the flow rate of the filling system is about 15 L/min and the pressure is 2 MPa. Calculation shows the power of the oil filling system is 0.5 kW. If the single-rod hydraulic cylinder is used, the power of the oil filling system would be 1.6 kW.

Table 1. Areas of hydraulic cylinders

	Chamber A	Chamber B	Chamber C
Three-chamber cylinder	1963.5 mm^2	3141.6 mm^2	7539.8 mm^2
Single-rod hydraulic cylinder	7850 mm^2	3846.7 mm^2	

Control strategy

The proposed system has typical four-quadrant operation characteristics as shown in Figure 2 When the system works in the first quadrant or the fourth quadrant, the pressure of the chamber A is higher than that of chamber B, which makes the chamber A as the control chamber.

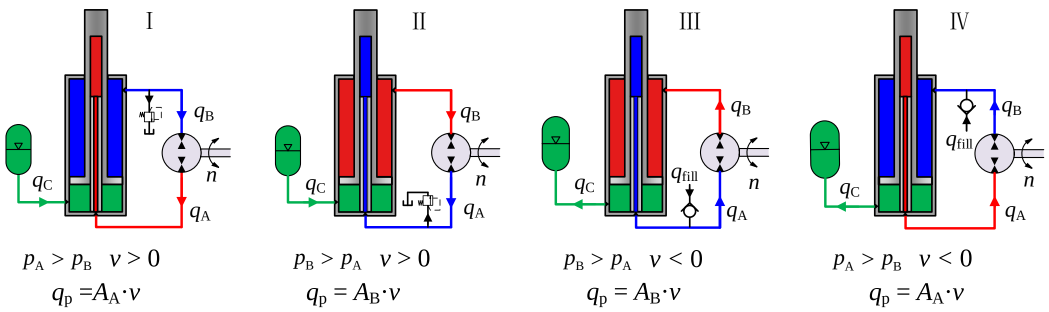

Figure 2 Four-quadrant principle of the proposed system

The output flow of the hydraulic pump is calculated according to the area of the chamber A and the velocity of the three-chamber cylinder.

$$q_p = A_A v \tag{1}$$

where v is the velocity of three-chamber cylinder.

When the system works in the second quadrant or the third quadrant, the pressure of the chamber A is lower than that of chamber B, which makes the chamber B as the control chamber. The output flow of the hydraulic pump is calculated according to the area of the chamber B and the velocity of the three-chamber cylinder.

$$q_p = A_B v \tag{2}$$

The three-chamber cylinder velocity control signal u_s is set as control signal of the velocity feedforward control unit, the rotation speed of the servomotor is shown as follows.

$$n = k_s u_s \tag{3}$$

where n is the servomotor rotation speed, k_s is the gain.

Ignore the leakage of the hydraulic pump, the flow rate of the hydraulic pump is:

$$q_p = nD_p \tag{4}$$

where D_p is the displacement of the hydraulic pump.

According to Eqs. (1), (2), (3) and (4), the relation between the v and u_s is shown as follows.

$$u_s = \begin{cases} \dfrac{A_A v}{D_p k_s} & (p_A \geq p_B) \\ \dfrac{A_B v}{D_p k_s} & (p_B < p_A) \end{cases} \tag{5}$$

In the velocity feedforward control unit, the leakage of the hydraulic pump is not considered. There will be a large deviation of the expected velocity and the actual velocity. Therefore, a displacement feedback closed control unit is added. The integration of the velocity control signal u_s is set as the expected displacement signal s_{in} in the displacement feedback unit. In this way, the comparative value of the expected displacement signal and the actual displacement signal is small. The feedforward control unit plays a major role and the displacement feedback control unit plays an auxiliary regulation role. The three-chamber cylinder can be operated according to set velocity and displacement.

The difference between the actual displacement and the integrated displacement is:

$$\Delta s = \int v dt - s_{\text{act}} \tag{6}$$

where s_{act} is the actual displacement.

The PI controller is used in the displacement feedback control unit, the rotation speed compensation signal of the servomotor is:

$$u_{\text{c}} = k_{\text{p}} \Delta s + \frac{k_{\text{p}}}{T_{\text{i}}} \int \Delta s dt \tag{7}$$

where k_p and T_i are respectively the gain and integration time constant of the PI controller.

Figure 3 shows the principle of the VFDB control strategy. According to the detected pressures, the velocity feedforward control unit determines which chamber is the control chamber, and then outputs the control signal u_s. Meanwhile, the displacement feedback control unit outputs the control signal u_c according to the displacements difference. The controller outputs the sum of u_s and u_c to control the servomotor rotation speed, and then the pump outputs flow according to the demand.

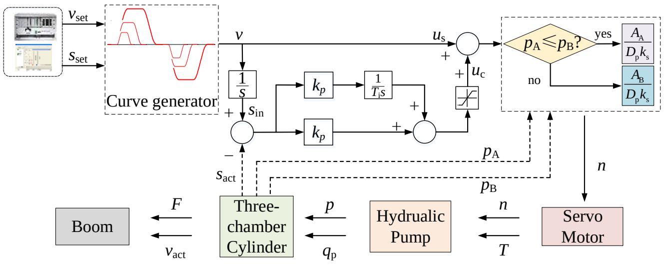

Figure 3 Principle of velocity feedforward and displacement feedback control strategy

Where v_{set} is the setting maximum velocity, s_{set} is the setting object displacement, T is the servomotor torque, p is the pump pressure, F is the three-chamber cylinder force, v_{act} is the actual velocity.

ENERGY EFFICIENCY MATHEMATICAL MODEL

To describe the energy saving effect of the proposed system, the traditional load-sensing system is adopted as a comparison. The pressure difference compensator is used to keep the pressure difference between the inlet and outlet of the directional valve constant, and the output pressure of the hydraulic pump is always about 2-3 MPa higher than the load pressure. Figure 4 shows the working principle of traditional load-sensing system.

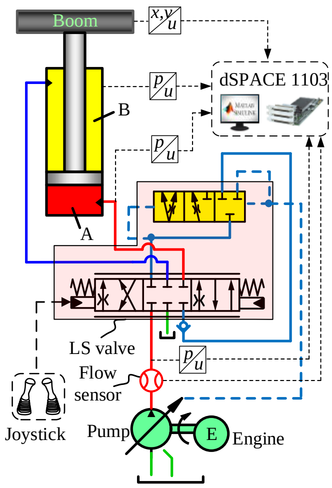

Figure 4 Working and test principle of the traditional load-sensing system

For the traditional load sensing system, the hydraulic pump outputs high pressure oil into the non-rod chamber A through the load sensing valve (LS valve) to lift the boom, and the oil in the rod chamber B flows to the tank. The output energy of the hydraulic pump is :

$$E_{\text{up}} = \int_0^t p_{\text{p}} A_{\text{A}} v dt \tag{8}$$

where A_A is area of the non-rod chamber A, p_p is pressure of the hydraulic pump, t is the boom lifting time;

The energy loss of the system is the throttling loss of the LS valve, which is shown as follows.

$$E_{\mathrm{uploss}} = \int_0^t v(A_{\mathrm{A}}(p_{\mathrm{P}} - p_{\mathrm{A}}) + A_{\mathrm{B}} p_{\mathrm{B}})dt \tag{9}$$

where A_{B} and p_{B} are the area and pressures of the rod chamber B, respectively; p_{A} is the pressure of non-rod chamber pressure.

Similarly, when the boom lowers, the output energy of the pump and the throttling loss of the LS valve are shown respectively:

$$E_{\mathrm{down}} = \int_0^{t_0} p_{\mathrm{P}} A_{\mathrm{B}} v dt \tag{10}$$

$$E_{\mathrm{downloss}} = \int_0^{t_0} (A_{\mathrm{B}}(p_{\mathrm{P}} - p_{\mathrm{B}}) + A_{\mathrm{A}} p_{\mathrm{A}}) v dt \tag{11}$$

where t_0 is the boom lowering time.

The energy consumed by the load sensing system to drive the boom for one cycle is shown as follows.

$$E = E_{\mathrm{up}} + E_{\mathrm{down}} \tag{12}$$

Based on the energy conservation law, the recoverable potential energy of the working device is:

$$E_{\mathrm{p}} = \int_0^{t_0} v(A_{\mathrm{A}} p_{\mathrm{A}} - A_{\mathrm{B}} p_{\mathrm{B}})dt \tag{13}$$

For the proposed system, to lift the boom, the pump only outputs energy in the first quadrant. The energy consumption is:

$$E'_{\mathrm{up}} = \int_0^{t_1} A_{\mathrm{A}} v(p_{\mathrm{A}} - p_{\mathrm{B}})dt \tag{14}$$

where t_1 is the first quadrant time.

During the boom lifting process, the energy loss is the energy discharged to the filling system by the rod chamber.

$$E'_{\mathrm{uploss}} = \int_0^{t_1} v p_{\mathrm{B}}(A_{\mathrm{B}} - A_{\mathrm{A}})dt + \int_0^{t-t_1} (v A_{\mathrm{B}}(p_{\mathrm{B}} - p_{\mathrm{A}}) - v p_{\mathrm{A}}(A_{\mathrm{B}} - A_{\mathrm{A}}))dt \tag{15}$$

Similar to the lifting process, the consumed energy of the proposed system to lower the boom is shown as follows.

$$E'_{\mathrm{down}} = \int_0^{t_2} [(A_{\mathrm{B}} p_{\mathrm{B}} - A_{\mathrm{A}} p_{\mathrm{A}})v + p_{\mathrm{A}}(A_{\mathrm{B}} - A_{\mathrm{A}})v]dt \tag{16}$$

where t_2 is the third quadrant time.

The energy loss is:

$$E'_{\mathrm{downloss}} = \int_0^{t_0-t_2} v(A_{\mathrm{A}}(p_{\mathrm{A}} - p_{\mathrm{B}}) + p_{\mathrm{B}}(A_{\mathrm{B}} - A_{\mathrm{A}}))dt \tag{17}$$

The total pump controlled system energy consumption is shown as follows.

$$E' = E'_{\mathrm{up}} + E'_{\mathrm{down}} \tag{18}$$

During the operating cycle of the boom, the thermodynamic equation of the hydraulic accumulator is shown as follows.

$$p_{\mathrm{x}} V_{\mathrm{x}}^{\mathrm{k}} = p_0 V_0^{\mathrm{k}} = \mathrm{const} \tag{19}$$

where p_{x} is and V_{x} are the gas pressure and volume of the hydraulic accumulator at any time, respectively; p_0 and V_0 are the initial gas pressure and volume of the hydraulic accumulator, respectively; k=1.4 which represents gas index.

When the boom lowers, the energy stored by the hydraulic accumulator is calculated by Eq. (20).

$$E'_{\mathrm{acc}} = \int_0^{t_0} \frac{p_2 V_2^{\mathrm{k}} A_{\mathrm{C}} v}{(V_2 - A_{\mathrm{C}} v t)^{\mathrm{k}}} dt \tag{20}$$

where p_2 and V_2 are the gas pressure and volume of the hydraulic accumulator when the boom begins to lower, respectively.

When the boom lifts, the energy supplied by the hydraulic accumulator is calculated by Eq. (21).

$$E_{\mathrm{acc}} = \int_0^{t} \frac{p_1 V_1^{\mathrm{k}} A_{\mathrm{C}} v}{(V_1 + A_{\mathrm{C}} v t)^{\mathrm{k}}} dt \tag{21}$$

where p_1 and V_1 are the gas pressure and volume of the hydraulic accumulator when the boom begins to lift, respectively.

Besides the potential energy, the energy stored by the hydraulic accumulator also includes the output energy of the hydraulic pump. The recovered potential energy is calculated according to the following equation.

$$E_{\mathrm{r}} = E_{\mathrm{acc}} - \int_0^{t_0} (A_{\mathrm{B}} p_{\mathrm{B}} v - A_{\mathrm{A}} p_{\mathrm{A}} v)dt \tag{22}$$

The potential energy recovery rate is:

$$\eta_{\mathrm{r}} = \frac{E_{\mathrm{r}}}{E_{\mathrm{p}}} \tag{23}$$

By using the proposed system, the reduced energy consumption is:

$$\eta_{\mathrm{s}} = 1 - \frac{E'_{\mathrm{up}} + E'_{\mathrm{down}}}{E_{\mathrm{up}} + E_{\mathrm{down}}} \tag{24}$$

EXPERIMENT RESEARCH

Testing system

The testing platform of a 6-ton hydraulic excavator's boom controlled by the traditional load sensing system was built firstly, and the testing principle is shown in Figure 4. To analyze the feasibility, operation performance and energy characteristics of the proposed system, the testing rig of the proposed system is built, and the testing system is shown in Figure 5. In the testing systems, the Parker flowmeter is used to collect the signals of the pressure and flowrate of the hydraulic pump. The Atos pressure sensor is used to detect the pressures of the hydraulic cylinders. The MTS magneto-strictive displacement sensor is used to detect the displacement and velocity of the hydraulic cylinder. A braking resistor is used to balance the generated electrical energy of the servomotor. The dSPACE 1103 is used as controller and data acquisition.

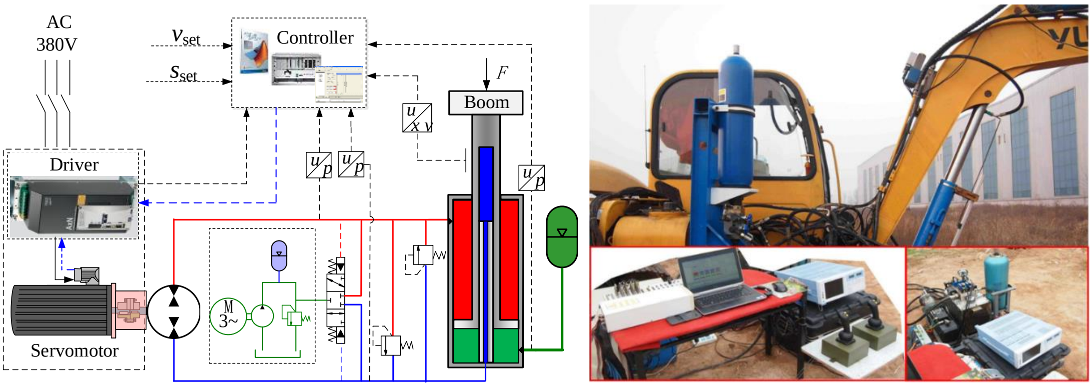

(a) Testing principle (b) Testing picture

Figure 5 Testing principle of the proposed system

Operation characteristics

The influence of the hydraulic accumulator pre-charge pressure on the four-quadrant characteristic was firstly analyzed. Under the same working condition, Figure 6a and Figure 6b show the servomotor bus voltage and the system energy consumption under different hydraulic accumulator pre-charge pressures, respectively. The bus voltage is about 540 V when the servomotor works in motor condition. If the servomotor works under generation condition, the generated electrical energy will make the bus voltage higher than 540 V. When the hydraulic accumulator pre-charge pressure is 10 MPa, the output force of the energy storage chamber exceeds the gravity of the hydraulic excavator working device in the ab section. The energy supllied by the hydraulic accumulator is larger than the required energy to lift the boom. Thus, a part of the supllied energy of the hydraulic accumulator converts into electrical energy through the servomotor, and the bus voltage rises to nearly 600 V. As shown in Figure 6b, the energy consumption of the hydraulic system is the highest. When the initial pressure is 7 MPa, the output force of the energy storage chamber cannot balance the self-gravity of the working device in the cd section. The hydraulic accumulator cannot completely recover the potential energy of the working device and a part of the potential energy is converted into electrical energy and wasted through the braking resistance, and the bus voltage rises to nearly 590 V. The energy consumption of the hydraulic system is about 0.94 of the system under 10 MPa hydraulic accumulator pre-charge pressure.

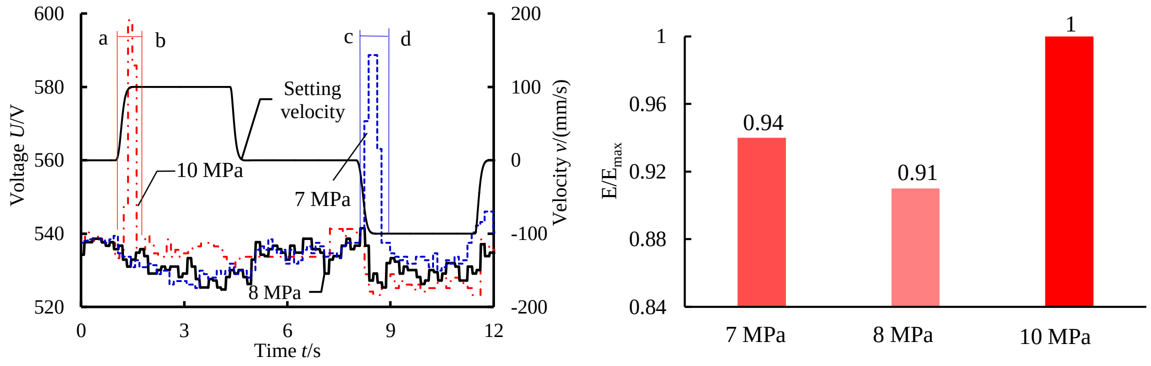

(a) Bus voltage of servomotor (b) Energy consumption of hydraulic system

Figure 6 Characteristics of the proposed system with different accumulator pre-charge pressures

It should be noted that the bus voltage of the servomotor is always about 540 V when the pre-charge pressure is 8 MPa. It means that the servomotor is always working in motor condition and the impact of the negative load on the system can be avoid, which can improve the control performance of the proposed system. It also means that the hydraulic accumulator can recover the potential energy as much as possible and the supplied energy of the hydraulic accumulator isn't wasted. It can be seen in Figure6b that the energy consumption of the hydraulic system is the lowest. To keep the consistency, the following test results of the proposed system are all obtained under 8 MPa pre-charge pressure of the hydraulic accumulator.

Figure7a shows the tested velocity and displacement of the three-chamber cylinder adopting VFDB closed loop control strategy. During the testing process, the set maximum velocity v_{set} is 80 mm/s and the set object displacement s_{set} is 200mm. By using the VFDB closed loop control strategy, the velocity setting value changes along with the displacement difference for the compensation of displacement feedback control unit. The positioning error is 1 mm. Figure 7b shows the pressures and displacement of the three-chamber cylinder. During the boom operation process, the actual displacement of the three-chamber cylinder can meet the requirement of the expected setting displacement, indicating the system has good repeatability. Because of the larger area of the energy storage chamber, when the piston rod extends, the small pressure decreasing in the energy storage chamber makes the pressure of the non-rod chamber increase greatly. Meanwhile, the rod chamber discharges oil into the filling system and the rod chamber pressure equals to the filling system pressure which is about 2 MPa. To lower the boom, the rod chamber pressure keeps high pressure whose mean value is about 6.3 MPa. Because the oil filling system charges oil into the non-rod chamber, the pressure of the non-rod chamber is 2 MPa.

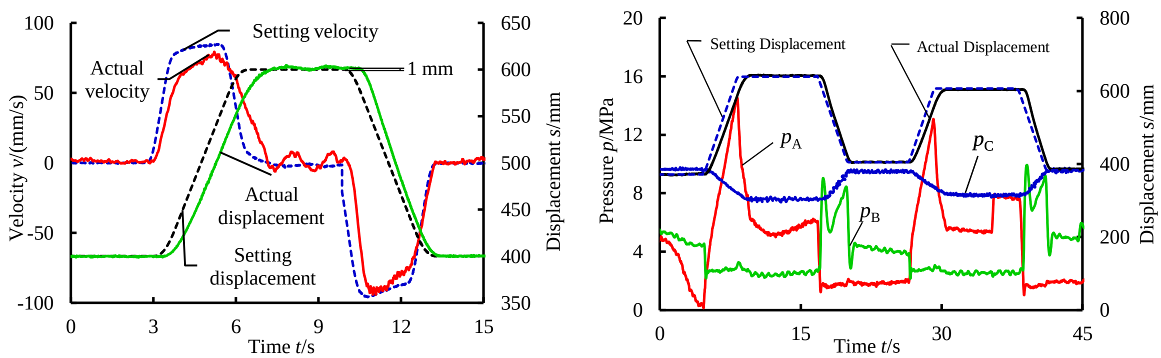

(a) Velocity and displacement (b) Displacement and pressures

Figure 7 Velocity, displacement and pressures of the proposed system

Energy saving characteristics

Figure 8 shows the pressures and energy losses of the different systems when the boom moves 330 mm. The pressures of the traditional load sensing system and the proposed system are respectively shown in Figure 8a and Figure 8b. As shown in Figure 8a, the pressure of the pump outlet port is about 3 MPa higher than that of the hydraulic cylinder in the traditional load sensing system. There are large pressure fluctuation during the lifting process and the non-rod chamber pressure is about 9.5 MPa. To provide enough force to stability drive the boom lowering, the non-rod chamber keeps 7 MPa pressure. The hydraulic accumulator pressure and capacity in the proposed system are selected according to the above pressure values of the single rod cylinder. As shown in Figure 8b, the pressure curves of the proposed system are the same as those shown in Figure 7. For the gas volume of the hydraulic accumulator decreases when the boom lowers, the pressure of the hydraulic accumulator increases which causes the oil pressure rise in the rod chamber of the three-chamber cylinder.

As shown in Figure 8b, the highest pressure in non-rod chamber is about 16.5 MPa under the bucket without load condition. In general, the hydraulic system's maximum pressure of the hydraulic excavator is 28 MPa. Due to the gravity of the load is far lighter than that of the working device, it's known from the previous study [38] that the highest pressure of the non-rod chamber is about 21 MPa under the bucket with full-load condition, which means the pressure level can meet the requirements. Meanwhile, the designed parameters and selected material of the three-chamber cylinder also can meet the structural strength requirements.

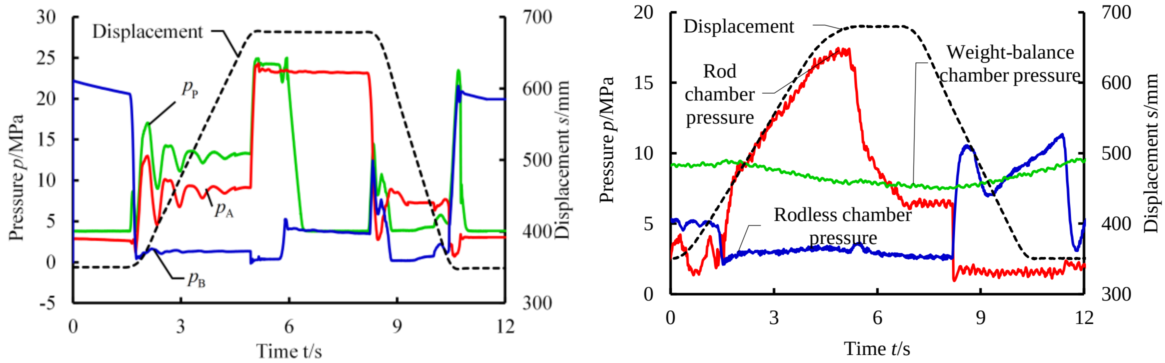

(a) Traditional load-sensing system (b) Proposed system

Figure 8 Pressures of the different systems

Figure 9a and Figure 9b show the energy losses of the traditional load-sensing system and proposed system. As shown in Figure 8a, there is a large pressure loss between the inlet port and outlet port of the control valve due to the throttling effect. It's noted from Figure 9a that a large amount of energy is wasted in the traditional load sensing system. When the boom lifts, the energy loss is mainly the output energy of the hydraulic pump, which is about 12.6 kJ. During the lowering process, the energy loss mainly consists of the output energy of the hydraulic pump and the wasted potential energy, between which the energy loss of the hydraulic pump is about 4.5 kJ. The wasted potential energy of the working device is about 16.5 kJ which accounts for a large parts of the energy loss. Therefore, if the gravitational potential energy can be recovered and reutilized, the energy consumption can be significantly reduced. In the proposed system, the energy loss mainly consists of the discharging energy of the three-chamber cylinder as shown in Figure 9b. Because the discharging flow rate is small and the pressure is low, the energy loss in the proposed system is very small. The energy loss is about 1.2 kJ during the lifting process and 0.1 kJ during the lowering process.

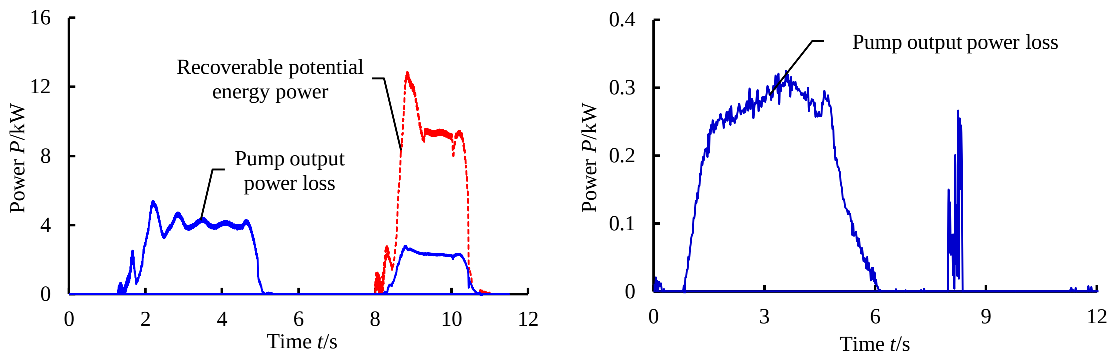

(a) Traditional load-sensing system (b) Proposed system

Figure 9 Energy losses of the different systems

Figure 10a and 10b show the powers and energy consumptions of the traditional load-sensing system and proposed system, respectively. The peak power of the traditional load-sensing system is about 13.5 kW for lifting the boom. Conversely, the peak power of the proposed system is about 3.3 kW for lowering the boom as shown in Figure 10b, which means the peak power is reduced by 76.1% compared with the traditional load-sensing system.

When the boom lifts, the output power of the proposed system is obvious less than that of the traditional load-sensing system as shown in Figure10. The hydraulic pump in the traditional load-sensing system outputs about 11.5 kW mean power and 38.2 kJ energy to lift the boom. During the lifting process, the maximum pump output power of the proposed system is about 2.2 kW and the supplied power of the hydraulic accumulator is about 5.2 kW. The hydraulic pump outputs 6.7 kJ energy and the hydraulic accumulator supports 20.2 kJ energy to lift the boom. The energy supplied by the hydraulic accumulator accounts for 75.4% of the required energy to lift the boom. To lower the boom, the rod chamber pressure of the three-chamber cylinder is high as shown in Figure 8b. The rod chamber outputs large force to fill the oil of the energy storage chamber into the hydraulic accumulator. It is seen from the Figure 10 that the hydraulic power of the proposed system is larger than that of traditional load-sensing system. For the lifting and lowering distances are the same, the supplied energy and stored energy of the hydraulic accumulator are basically identical.

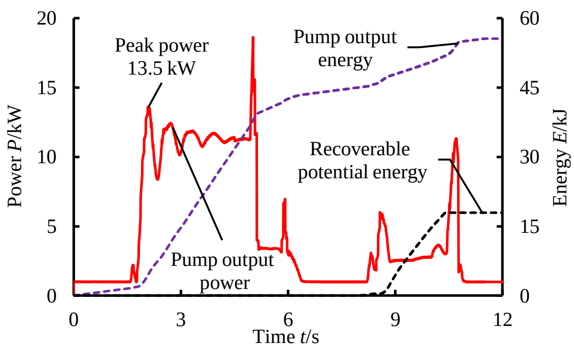

(a) Traditional load-sensing system

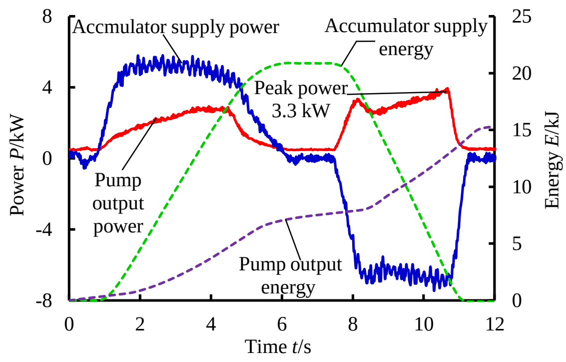

(b) Proposed system

Figure10 Power and energy consumption of different systems

Table 2 shows the testing results of the traditional load-sensing system and the proposed system according to the energy model in section 3 and the testing data.

Table 2 Testing results

	Traditional load-sensing system	Proposed system
Energy loss (kJ)	17.1	1.3
Recoverable potential energy (kJ)	16.5	16.5
Hydraulic accumulator recovered energy (kJ)	0	20.85
Recovered potential energy (kJ)	0	12.35
System peak power (kW)	13.8	3.3
System total energy consumption (kJ)	55.5	15.3

It's known from the Table2 that about 16.5 kJ gravitational potential energy can be recovered when the boom lowers. In the proposed system, the output energy of the hydraulic pump is about 8.5 kJ to lower the boom and the energy stored by the hydraulic accumulator is about 20.85 kJ. According to Eq. (22), about 12.35 kJ gravitational potential energy is recovered by the hydraulic accumulator, which is about 75.3% of the recoverable gravitational potential energy. According to the previous analysis, the gravitational potential energy can be almost completely recovered under 8 MPa hydraulic accumulator pre-charge pressure. However, the test results are not very satisfactory. The main reason is that the friction forces in the three-chamber cylinder and the hinged joints are larger. To drive the boom, the traditional load sensing system consumes about 55.5 kJ energy, and the proposed system consumes about 15.3 kJ energy. Compared with the traditional load-sensing system, the energy consumption is reduced by 72.4%.

In the previous research work, the characteristics of load-sensing system with three-chamber cylinder driving excavator boom were studied [36]. During the period of the boom lifting and lowering 330 mm, the energy characteristics of the different systems are shown in Figure 11. As can be seen, the traditional load-sensing system has the largest energy loss and energy consumption, and the highest peak power. The use of a three-chamber cylinder instead of a single-rod hydraulic cylinder in the load-sensing system significantly reduces the energy consumption, energy loss and peak power of the boom system. It's noted that the proposed system further reduces the boom system energy consumption by 27.5%, energy loss by 69%, and peak power by 28% compared to the load-sensing system with three-chamber cylinder. Since the accumulator volume and the pre-charge pressure are the same, the gravitational potential energy recovery efficiencies of the proposed system and the load-sensing system with three-chamber cylinder are basically the same.

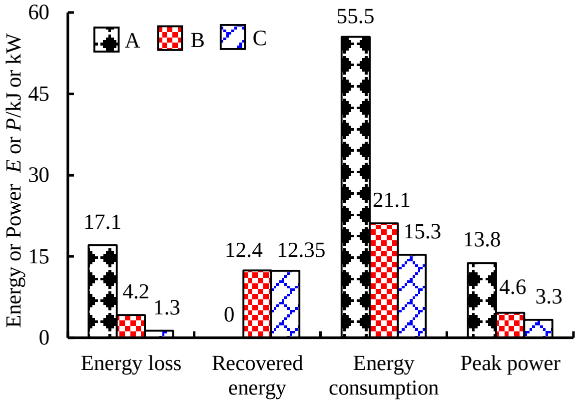

A-Traditional load sensing system, B-Load sensing system with three-chamber cylinder, C-Proposed system
Figure 11 Energy characteristics of different systems

Economic and environmental benefits

Although the energy saving effect of the proposed system cannot directly reflect the reduction of the fuel consumption of the internal combustion engine, the fuel saving effect of the proposed system can be evaluated according to the fuel consumption rate of the engine.

Assuming in the 90° excavation cycle, the distance between the excavation point and the unloading point is 330 mm, meaning that the boom falls and lifts 330 mm, respectively. According to the above calculation, the output energy of the hydraulic pumps is reduced by 33 kJ for one excavation cycle. Considering the efficiency of the hydraulic pump is about 90%, during one 90° excavation cycle, the reduced energy converted onto the engine axis is 36.7 kJ which represents the reduced output energy of the engine.

During the actual operation process, the time for operating a 6-ton hydraulic excavator to complete one 90° excavation cycle is 15 s. Thus, the hydraulic excavator can complete 240 cycles per hour and 8808 kJ energy can be saved per hour. According to that the average fuel consumption rate of the engine is 0.35 L/kWh, the fuel can be saved by 0.86 L per hour. Considering the current fuel price about 7.1 RMB/L in China, it can be estimated that the equivalent fuel cost should be saved about 6.1 RMB per hour by using the proposed system.

The total cost of the prototype of the proposed system is estimated about 23000-25000 RMB, among which the cost of the permanent magnetic synchronous machine and its driver is 14000 RMB, the three-chamber cylinder is 5000 RMB, the hydraulic accumulator is 1200 RMB and the other components accounts for 2800-4800 RMB. If the mass production of the proposed system is realized, the cost can be further decreased. Assuming that the hydraulic excavator is operated for 10 hours per day and 300 days per year, the operation time is 3000 hours per year. By using the proposed system, the running cost of one 6-ton hydraulic excavator can be reduced by 18300 RMB. Thus, after one and a half years, the upfront investment of the proposed system could be recovered by the revenue of fuel saving, and one 6-ton hybrid hydraulic excavator using the proposed system can bring about 18300 RMB per year for customer.

According to the fuel saving per hour and operation time per year, by using the proposed system, the fuel can be saved by 2569 L per year. The carbon dioxide emission of diesel oil is 2.63 kg/L, and one 6-ton hydraulic excavator can reduce the greenhouse gas emissions by 6756.5 kg per year.

Considering the rapid recovery of the upfront investment, the great potential of energy saving and emission reduction, the innovative scheme proposed in this paper can be applied to all heavy-duty manipulators driven by hydraulic cylinder. It not only can be used to manufacture new hydraulic excavators, but also can be used to reform the existing hydraulic excavators through designing the proposed prototype as retrofit kit.

Considering the rapid recovery of the upfront investment, the great potential of energy saving and emission reduction, the innovative scheme proposed in this paper can be applied to all heavy-duty manipulators driven by hydraulic cylinder. It not only can be used to manufacture new hydraulic excavators, but also can be used to reform the existing hydraulic excavators through designing the proposed prototype as retrofit kit.

CONCLUSIONS

The novel scheme of speed variable pump controlled three-chamber cylinder system can realize the integration of the driving and potential energy recovery and reutilization of the hydraulic excavator, and completely eliminate the throttling loss. The scheme has the advantages of shorter energy transfer chain, less energy conversion links, and high gravitational potential energy recovery and reutilization rate. The novel scheme is not only suitable for the speed variable pump controlled system, but also for the displacement variable pump controlled system.

The testing results show that the pre-charge pressure of the hydraulic accumulator has great influence on the four-quadrant characteristics of the proposed system. For the 6-ton hydraulic excavator, when the pre-charge pressure of the hydraulic accumulator is 8 MPa, the servomotor always works in resistance load condition whether the boom lifts or lowers, and the energy efficiency of the system is the highest under above mentioned condition.

The proposed system has good operating characteristics. The VFDB control strategy is used to improve the trajectory tracking precision of the hydraulic excavator boom, and the positioning error is reduced to about 1 mm.

By using the proposed system, the gravitational potential energy recovered by the proposed system can reach to 75.3% of the recoverable energy. To lift the boom, 75.4% of the required energy is supplied by the hydraulic accumulator. Compared with the traditional load-sensing system, the peak power is reduced by 76.1% and the energy saving ratio of the proposed system is 72.4% under the same working condition. This new principle not only reduces the energy used to do useless work, but also greatly reduces the installed power of the main drive circuit.

ACKNOWLEDGMENTS

The authors would like to give their acknowledgment to National Natural Science Foundation of China (No. 51775363, 52105066 and U1910211) for the financial support on the project.

REFERENCES

1. Wang F, Li Z, Zhang K, et al. An overview of non-road equipment emissions in China. Atmospheric Environment 2016; 132: 283-289.
2. Lynch L, Zigler B T. Estimating energy consumption of mobile fluid power in the United States. National Renewable Energy Lab. Golden, CO (United States), 2017. https://www.osti.gov/servlets/purl/1408087.
3. Pei H, Hu X, Yang Y, et al. Configuration optimization for improving fuel efficiency of power split hybrid powertrains with a single planetary gear. Applied Energy 2018; 214: 103-116.
4. Yi C, Epureanu B I, Hong S K, et al. Modeling, control, and performance of a novel architecture of hybrid electric powertrain system. Applied Energy 2016; 178: 454-467.
5. Wang H, Huang Y, Khajepour A, et al. A novel energy management for hybrid off-road vehicles without future driving cycles as a priori. Energy 2017; 133: 929-940.
6. Liukkonen M, Lajunen A, Suomela J. Feasibility study of fuel cell-hybrid powertrains in non-road mobile machineries. Automation in Construction 2013; 35: 296-305.
7. Lin T, Wang Q, Hu B, et al. Development of hybrid powered hydraulic construction machinery. Automation in construction 2010; 19(1): 11-19.
8. Xu B, Cheng M, Yang H, et al. A hybrid displacement pressure control scheme for an electro-hydraulic flow matching system. IEEE/ASME Transactions on Mechatronics 2015; 20(6): 2771-2782.
9. Axin M, Eriksson B, Krus P. A flexible working hydraulic system for mobile machines. International Journal of Fluid Power 2016; 17(2): 79-89.
10. Huang W, Quan L, Huang J, et al. Excavator Swing System Controlled with Separate Meter-in and Meter-out Method. Journal of Mechanical Engineering 2016; 52(20): 159-167.
11. Ding R, Xu B, Zhang J, et al. Self-tuning pressure-feedback control by pole placement for vibration reduction of excavator with independent metering fluid power system. Mechanical Systems and Signal Processing 2017; 92: 86-106.
12. Zimmerman J, Pelosi M, Williamson C, and Ivantysynova, M. Energy Consumption of an LS Excavator Hydraulic System. In: ASME 2007 International Mechanical Engineering Congress and Exposition, Washington, USA, 11-15 November, 2007: 117-126.
13. Quan Z, Quan L, Zhang J. Review of energy efficient direct pump controlled cylinder electro-hydraulic technology. Renewable and Sustainable Energy Reviews 2014; 35: 336-346.
14. Lodewyks J. Variable displacement pump closed loop controlled differential cylinder system. Doctor dissertation, Germany: Rheinisch Westfaelischen Technischen Hochschule Aachen, 1994.
15. Wang T, Wang Q, Lin T. Improvement of boom control performance for hybrid hydraulic excavator with potential energy recovery. Automation in Construction 2013; 30: 161–9.
16. Naruse M, Tamaru M, Kimoto K. Hybrid construction equipment, US Patent No.6708787, 2004-3-23.
17. Riyuu S, Tamura M, Ochiai M, et al. Hybrid construction machine, JP Patent No.2003328397, 2003-11-19.
18. Chen Q, Wang Q, Wang T. A novel hybrid control strategy for potential energy regeneration systems of hybrid hydraulic excavators. Proceedings of the Institution of Mechanical Engineers, Part I: Journal of Systems and Control Engineering 2016; 230(5): 375-384.
19. Yoon J I, Truong D Q, Ahn K K. A generation step for an electric excavator with a control strategy and verifications of energy consumption. International Journal of Precision Engineering & Manufacturing 2013; 14(5): 755-766.
20. Kagoshima M, Komiyama M, Nanjo T, Development of New Hybrid Excavator. Kobelco Technology Review 2007; 27: 39–42.

21. Chen M, Zhao D. The gravitational potential energy regeneration system with closed-circuit of boom of hydraulic excavator. Mechanical Systems & Signal Processing 2017; 82:178-192.
22. Van de Ven J D. Constant pressure hydraulic energy storage through a variable area piston hydraulic accumulator. Applied energy 2013; 105: 262-270.
23. Xiao Y, Guan C, Lai X. Research on the design and control strategy for a flow-coupling-based hydraulic hybrid excavator. Proceedings of the Institution of Mechanical Engineers, Part D: Journal of Automobile Engineering 2014; 228(14): 1675-1687.
24. Shen W, Huang H, Pang Y, et al. Review of the energy saving hydraulic system based on common pressure rail. IEEE Access 2017; 5: 655-669.
25. Casoli P, Riccò L, Campanini F, et al. Hydraulic hybrid excavator—Mathematical model validation and energy analysis. Energies 2016; 9(12): 1002.
26. Shen W, Jiang J, Su X, et al. Control strategy analysis of the hydraulic hybrid excavator[J]. Journal of the Franklin Institute, 2015, 352(2): 541-561.
27. Vukovic M, Sgro S, Murrenhoff H. STEAM–a holistic approach to designing excavator systems. In: Proceedings of the 9th International Fluid Power Conference, Aachen, Germany, March 24-26, 2014: 24-26.
28. Hippalgaonkar R, Ivantysynova M. Optimal power management of hydraulic hybrid mobile machines–part I: theoretical studies, modeling and simulation. Journal of Dynamic Systems Measurement & Control 2016; 138(5): 1-12.
29. Hippalgaonkar R, Ivantysynova M. Optimal power management of hydraulic hybrid mobile machines–Part II: machine implementation and measurements. Journal of Dynamic Systems Measurement & Control 2016; 138(5): 1-10.
30. Daniel B, Claus H, Thomas L. Hybrid-Antriebe bei Raupenbaggern – Konzepte und Losungen. In: 3th Hybridantriebe fur Mobile Arbeitsmaschinen Fachtagung, Karlsruhe, Germany, 2011, 2: 117-124.
31. Ge L, Quan L, Li Y, et al. A novel hydraulic excavator boom driving system with high efficiency and potential energy regeneration capability. Energy Conversion and Management 2018; 166: 308-317.
32. Lin T, Chen Q, Ren H, et al. Review of boom potential energy regeneration technology for hydraulic construction machinery. Renewable and Sustainable Energy Reviews 2017; 79: 358-371.
33. Liang X. On improving energy utilization in hydraulic booms. Ph.D. Thesis Tampere University of Technology, 2002.
34. Hao Y, Quan L, Cheng H, et al. Potential energy directly conversion and utilization methods used for heavy duty lifting machinery 2018; 155(2018): 242-251.
35. Quan L, Xia L, Hao H, et al. Control loop of working device of engineering operation equipment CN, CN105604121A [P]. 2015.
36. Quan L, Dong Z, Hao H, et al. A lifting machinery working device control circuit CN, CN 105523478A [P]. 2015.
37. Xia L, Quan L, Ge L, et al. Energy efficiency analysis of integrated drive and energy recuperation system for hydraulic excavator boom. Energy Conversion and Management 2018; 156: 680–687.
38. Xia L, Quan L, Zhang X, et al. Operating characteristics and energy efficiency of hydraulic-gas combined driving hydraulic excavator boom. Journal of Mechanical Engineering 2017; 53(20): 176-173.

The 11th JFPS International Symposium on Fluid Power HAKODATE 2020 Oct. 12-13, 2021 The Japan Fluid Power System Society

Experimental Validation of Improvement of the Overall Efficiency for Electro-hydraulic Drive System using Efficiency Maps

Ha Tham PHAN* and Yasukazu SATO**

* Graduate School of Engineering Science, Yokohama National University
(E-mail: ha-phan-dz@ynu.jp)
** Faculty of Engineering, Yokohama National University
(E-mail: sato-yasukazu-zm@ynu.ac.jp)
79-5 Tokiwadai, Hodogaya, Yokohama, Kanagawa, Japan

Abstract. In industrial applications, electro-hydraulic drive systems (EHDS) included electric motor driven hydraulic pump are preferred to mechanical and electrical drive system for their advantages. Recently, a crucial research topic in EHDS is to improve the overall energy efficiency. To do so, the valveless EHDS (EHDS without control valve) is proposed by researchers and the advantages of valveless EHDS regarding its energy efficiency is validated. In previous published research, the novel control method of EHDS proposed by authors is to use overall efficiency maps combined from motor efficiency map and pump efficiency map for controlling motor speed and hydraulic pump displacement simultaneously to force EHDS operating at high-efficient points. The simulation results shows that the efficiency of two-degree control system (VS-VP: Variable Speed Motor-Variable Displacement Pump) has improved more than one-degree control system. This paper presents the validation of this method by experiment in actual machines.

Keywords: Electro-hydraulic drive system, Servomotor, Hydraulic pump, Efficiency map

INTRODUCTION

The valveless electro-hydraulic drive system typically includes an electric motor and hydraulic pump to supply hydraulic power to an actuator as shown in Figure 1. The flow rate supplied to actuator will be regulated by changing only the speed of electric motor (VS-FP: variable speed-fixed displacement), controlling only the displacement of hydraulic pump (FS-VP: fixed speed-variable displacement), or changing motor speed and pump displacement simultaneously (VS-VP). Therefore, the efficiency of EHDS depends on the efficiency of electric motor and hydraulic pump.

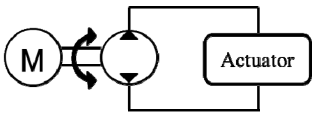

Figure 1. Valveless electro-hydraulic drive system

The formulas to determine the efficiencies of electric motor and hydraulic piston pump have been presented in the previous study as shown in (1) and (2). In case of servo motor, energy efficiency is determined by mechanical power at motor shaft and electrical power supplied to servo amplifier [1].

$$\eta_m = \frac{P_{out}}{P_{in}} = \frac{T_m n_m}{T_m n_m + \Delta P_{Cu} + \Delta P_{Fe} + \Delta P_C} = \frac{T_m n_m}{T_m n_m + 3R_M \left(\frac{T_m}{K_T}\right)^2 + K_{f1} n_m + K_{f2} n_m^2 + K_C \frac{T_m}{K_T}} \tag{1}$$

where, T_m, n_m are torque and speed at motor shaft; ΔP_{Cu}, ΔP_{Fe}, ΔP_C are copper losses, iron losses and current losses at electric motor. R_M is motor winding resistance; K_T, K_{f1}, K_{f2}, and K_C are experimental coefficients.
The total efficiency η_p of variable dipslacement pump such as hydraulic piston pump is determined from volumetric efficiency η_{pv} and hydraulic-mechanical efficiency η_{pm} as expressed in Equation (2) [2,3].

$$\eta_p = \eta_{pv}\eta_{pm} = \left(1 - \frac{C_s \Delta p}{\mu \frac{2\pi}{60} n_p \alpha}\right)\left(\frac{1}{1 + \left\{\left(C_{v1}\alpha^2 + C_{v2}\right)\left(\frac{2\pi}{60}\right)\frac{\mu n_p}{\Delta p} + C_f + \frac{2\pi T_c}{\Delta p D_{\max}}\right\}\frac{1}{\alpha}}\right) \tag{2}$$

where C_s, C_{v1}, C_{v2}, C_f and $\alpha=D/D_{max}$ are non-dimensional quantities. μ, Δp, T_s, n_p and D_{max} are dimensional quantities with the unit of Pa.s, Pa, Nm, rpm and m^3/rev, respectively.
From theoretical formulas (1) and (2), the efficiency of servo motor and hydraulic pump can be determined and used to create the efficiency maps. For variable displacement pump, the number of efficiency maps will depend on the displacement ratio α. The overall efficiency maps of EHDS are combined from servo motor efficiency map and hydraulic piston maps. The theoretical efficiency maps of servo motor and hydraulic piston pump in previous study are shown in Figure 2 and Figure 3, respectively [2].

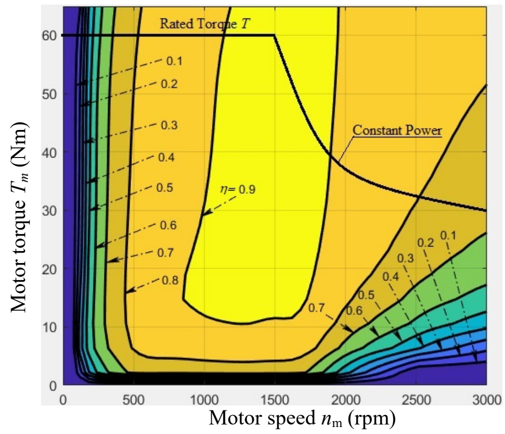

Figure 2. Efficiency map of servo motor

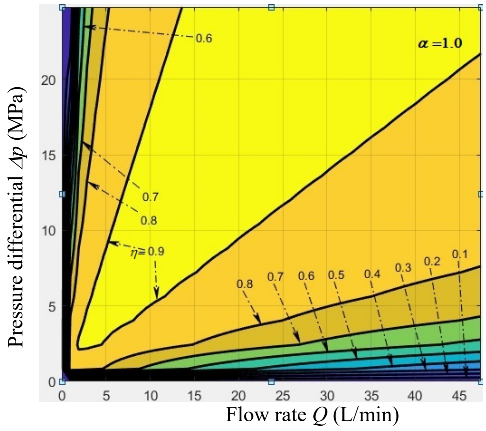

Figure 3. Efficiency map of hydraulic piston pump with α = 1

In previous research [2, 4], the novel control method of EHDS proposed by authors is to use overall efficiency maps combined from motor efficiency map and pump efficiency map for controlling motor speed and hydraulic pump displacement simultaneously to force EHDS operating at high-efficient points. The numerical simulation was conducted for 3 types of EHDS (VS-FP, FS-VP and VS-VP) at different operating points (pressure differential Δp, flow rate Q). The simulation results show that the efficiency of two-degree control system (VS-VP) was improved significantly compared with conventional one-degree control systems (VS-FP, FS-VP). The advantage of VS-VP system was achieved not only separated working points but also entire operating range. In this study, an experimental validation of two-degree control system is conducted in actual machines.

TWO-DEGREE-OF-FREEDOM CONTROL OF EHDS

In EHDS, the flow rate Q supplied to actuator is determined by the following equation:

$$Q = n_m D_{\max} \alpha \eta_{pv} \tag{3}$$

From formula (3), the pump speed n_m and displacement ratio α could be controlled to reach command flow rate Q. However, from formulas (1) and (2), for a given working point (pressure Δp, flow rate Q) the efficiency of electric motor and hydraulic pump are depended on pump speed n_m and displacement ratio α. In other word, the efficiency of EHDS is a function of pump speed n_m and displacement ratio α.

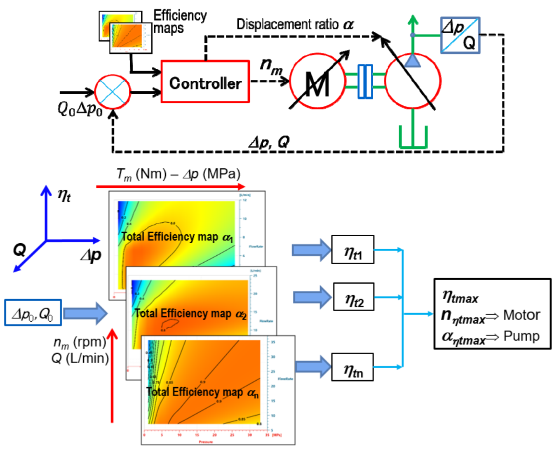

Figure 4. Two-degree-of freedom control system

To control EHDS with high-efficient operation for required pressureΔp and flow rate Q, a two-degree-of-freedom control strategy was proposed in authors' previous research as shown in Figure 4. The target of this system is to optimize overall efficiency of EHDS by using two degrees of freedom (motor speed n_m and pump displacement ratio α) for specified given working conditions (Δp, Q) based on the data of the overall efficiency maps. In other words, for a given value of Δp, Q the controller will determine the value of efficiency in every single overall efficiency map ($\alpha = \alpha_i$) and then compare these values. The working parameters (n_m, α) were determined when the map was at its highest efficiency for the corresponding working point. By two-degree-of-freedom control, the interaction between electric motor efficiency and hydraulic pump efficiency could be considered properly. Compared to one-degree-of-freedom control, the proposed control method is controlled by two control parameters (n_m and α) so it is able to achieve high efficiency for a given working point. Moreover, the flexibility of n_m and α could help the system operate within its permitted working range (motor speed n_m and torque T_m, hydraulic pump speed n_p and pressure Δp) and thus avoid overloading in the servo motor and hydraulic pump.

EXPERIMENTAL VALIDATION

Experiment for establishing overall efficiency maps

To validate the simulation results, the experiment is conducted in EHDS included servo motor and hydraulic axial piston pump as shown in Figure 5. The working points for experiment of servo system and hydraulic piston pump shown in Figure 6 and 7, respectively. The working points are measured at 09 displacement ratio α = 0.2, 0.3, 0.4, 0.5 0.6, 0.7, 0.8, 0.9, 1.0.

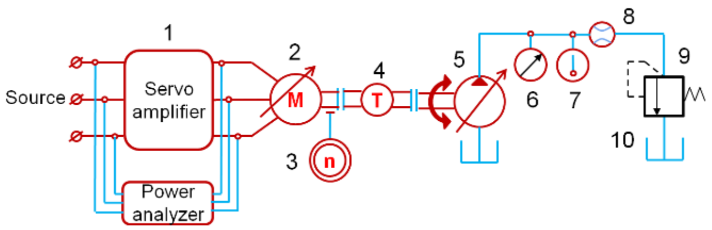

Figure 5. Schematic of hydraulic circuit for measuring the efficiency of system
1. Servo Amplifier; 2.AC Servomotor; 3. Rotation Speed Sensor; 4. Torque sensor; 5. Variable Displacement Pump; 6. Pressure Gauge; 7. Pressure Sensor; 8. Flow meter; 9. Relief Valve; 10. Oil Tank.

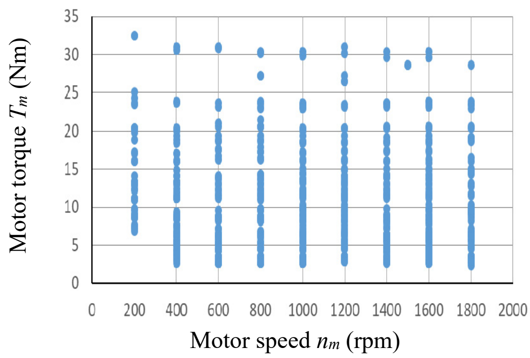

Figure 6. Scatter chart of experiment of servo motor

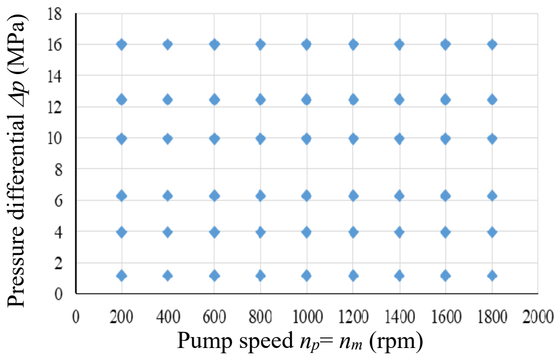

Figure 7. Scatter chart of experiment of hydraulic piston pump

From measured data, experimental coefficients in theoretical formulas (1) and (2) are calculated by the least squares method. Then experimental efficiency maps of servo motor and hydraulic pump are created from formulas with experimental coefficients to build 09 overall efficiency maps of EHDS at 09 displacement ratio α. To validate the advantage of proposed control method, these overall efficiency maps are used to determine overall efficiency of two-degree-of-freedom control (VS-VP) and one-degree-of-freedom control (VS-FP, FS-VP). The efficiency comparison of these system is shown in Figure 8.
In Figure 8, VS-VP unit achieved better overall efficiency than others at almost all given working points because of the flexibility of both n_m and α. The advantage of the VS-VP unit can be seen clearly at a low flow rate range (Q = 2~10 L/min). Considering the work point of Q = 2 L/min; Δp = 16 MPa, the efficiency of the

VS- VP unit is 28% and 10% higher than that of the VS-FP unit and FS-VP unit, respectively. These results in Figure 8 matches with the simulation results as shown in authors' previous research.

Improving the transient efficiency of EHDS using efficiency maps

The results shown in Figure 8 demonstrated the advantage of proposed control strategy in separated working points of EHDS. For applying in actual EHDS, the controller should improve the overall transient efficiency of the system continuously. By using overall efficiency maps, the controller could select the high-efficient working point at any required flow rate Q and pressure differential Δp. The Figure 9 shows the flow rate command with step signal and Figure 10 shows overall efficiency comparison of 3 types of EHDS controls (VS-VP, VS-FP, FS-VP). The results shown that the efficiency of VS-VP system is always higher than VS-FP and FS-VP system. This means that the EHDS with two-degree-of-freedom control could achieve higher efficiency than one-degree-of-freedom control.

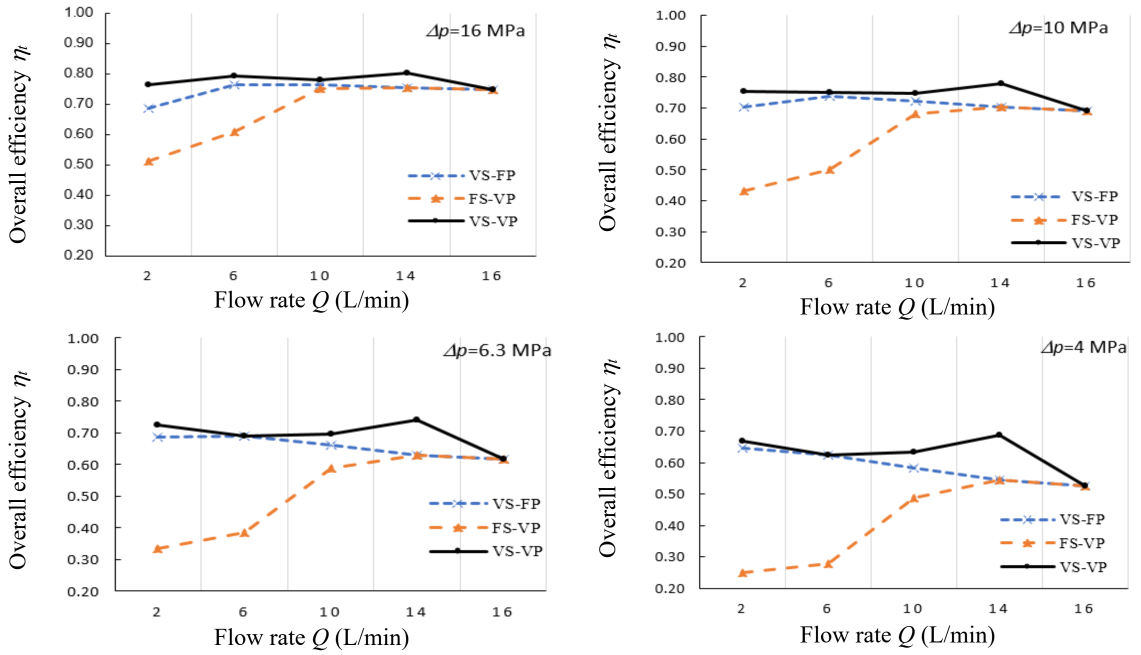

Figure 8. Overall efficiency η_t comparison at pressure differential Δp = 16, 10, 6.3, and 4 MPa

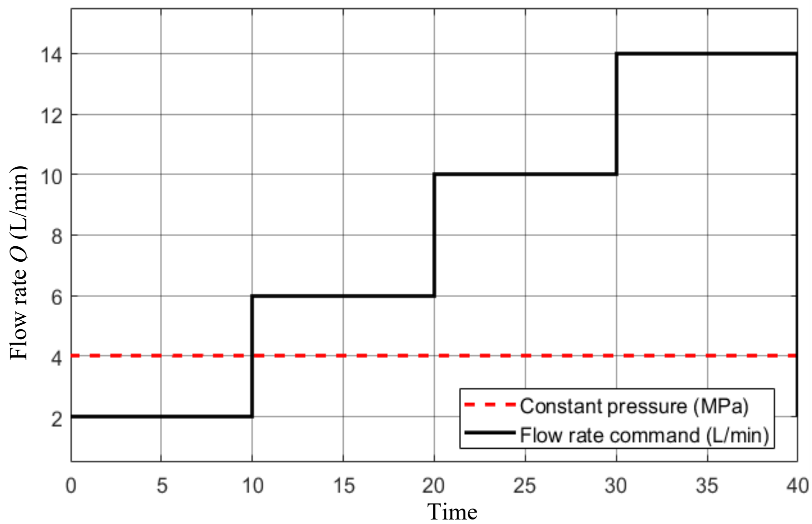

Figure 9. Step flow rate command Q (L/min) at constant pressure Δp = 4 MPa

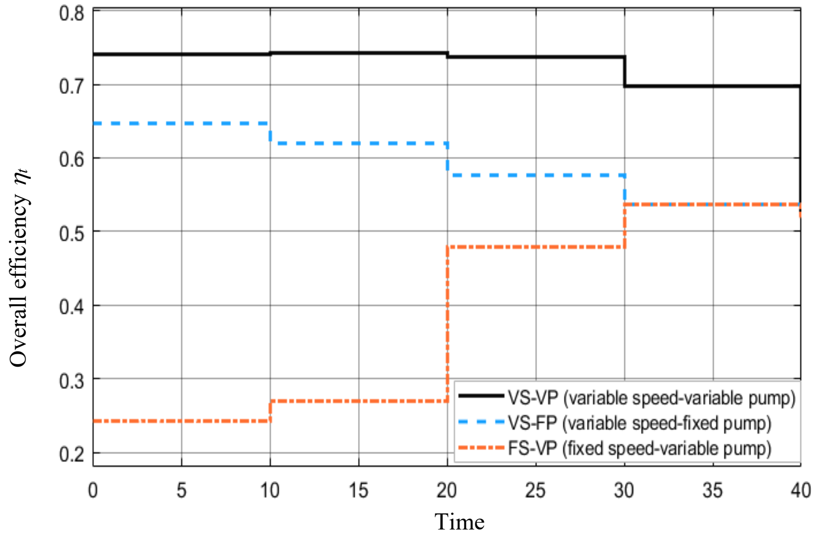

Figure 10. Overall efficiency η_t comparison at output different pressure Δp = 4 MPa

CONCLUSION

This study conducted experiment to validate the simulation results in previous research of authors. The experimental shown that two-degree-of-freedom control could achieve higher efficiency than one-degree-of-freedom control not only at separated working points but also entire operating range with step flow rate command. In next stage, this control will be set up and validated in actual machines.

REFERENCES

1. WILLKOMM, J., et al., Quadratic Programming to Optimize Energy Efficiency of Speed- and Displacement-Variable Pumps, Proceedings of the 8th FPNI Ph.D Symposium on Fluid Power, Lappeenranta, Finland, 2014, V001T05A002, pp.1-10.
2. PHAN, H.T., SATO, Y., Improving the Overall Efficiency of an Electro-Hydraulic Drive System by using Efficiency Maps, JFPS International Journal of Fluid Power System, 2021, Vol.14, Issue 1, pp.10-18.
3. THE JAPAN HYDRAULICS & PNEUMATICS SOCIETY, Oil Hydraulics and Pneumatics Handbook, Ohmsha, Ltd., 1989, pp.205-206. (in Japanese)
4. ITAGAKI, S., PHAN, H.T., SATO, Y., Study on High Efficiency Power Transmission in Servo Motor-Driven Hydraulic System, The Proceedings on Spring Conference of Japan Fluid Power System Society, 2019, pp.45-47. (in Japanese)

Genaral Session | Pneumatics

Medical and Welfare

[GS3-01] Development of Silicone Outer Shell Type Pneumatic Soft Actuator

○Yuma Nakanishi[1], Yasuhiro Hayakawa[1], Keisuke Kida[1], Hiroaki Ichii[1]　(1.National Institute of Technology (Kosen) , Nara College.)

[GS3-02] Development of Pneumatically Driven Verification System for Ophthalmic Needling Operation

Feng Tao[1], ○Maina Sogabe[2], Taro Ito[3], Tetsuro Miyazaki[2], Toshihiro Kawase[4,1], Takahiro Kanno[5], Yoshikazu Nakajima[1], Kenji Kawashima[2]　(1.Tokyo Medical and Dental University, 2.The University of Tokyo, 3.Tottori University, 4.Tokyo Institute of Technology, 5.RIVERFIELD Inc)

[GS3-03] Development of a Whole Body Training Device by Multi-directional Force Input Using Pneumatic Artificial Muscles

Soichiro Ito[1], ○Tetsuro Miyazaki[2], Junya Aizawa[3], Toshihiro Kawase[1,4], Maina Sogabe[2], Takahiro Kanno[5], Yoshikazu Nakajima[1], Kenji Kawashima[2]　(1.Tokyo Medical and Dental University, 2.The University of Tokyo, 3.Juntendo University, 4.Tokyo Institute of Technology, 5.RIVERFIELD Inc.)

[GS3-04] Development of Robotic Forceps Driven by Soft Actuator with Built-In Displacement Sensor

○Osamu Azami[1], Takahiro Kanno[1], Toshihiro Kawase[2,3], Maina Sogabe[4], Tetsuro Miyazaki[4], Kenji Kawashima[4]　(1.Riverfield Inc., 2.Tokyo Medical and Dental University, 3.Tokyo Institute of Technology, 4.Tokyo University)

The 11th JFPS International Symposium on Fluid Power HAKODATE 2020 Oct. 12-13, 2021 JFPS The Japan Fluid Power System Society

Development of Silicone Outer Shell Type Pneumatic Soft Actuator

Yasuhiro HAYAKAWA*, Keisuke KIDA*, Yuma NAKANISHI* and Hiroaki ICHII*

*Department of Control Engineering
National Institute of Technology, Nara College
22 Yata-cho, Yamato-Koriyama, Nara, 639-1080 Japan
(E-mail: hayakawa@ctrl.nara-k.ac.jp)

Abstract. The pneumatic soft actuators have both passive flexibility of the casing and active flexibility through pressurizing and depressurizing. These features are expected to be human-friendly actuators because they enable the approach of using an original soft system by controlling the internal air pressure. The current pneumatic soft actuator has two technical points of interest; control method of driving direction and operating pressure level, requiring an actuator to match these points. In this study, a pneumatic soft actuator with a silicone rubber case, SCSRA (Sponge Core Soft Rubber Actuator) was proposed and developed to respond to the requirement. Thought some experimental results, it is cleared that SCSRA controlled the driving system by realizing a large stroke in the low-pressure region of 30kPa or less as well as peeling and adhering the silicone film.

Keywords: High Performance Insole, Pneumatic, Care Prevention, Walking, Soft Rubber Actuator

INTRODUCTION

There are many types of actuators used in today's industrial, medical, and welfare fields, depending on their operating principles. Even for a simple piston-cylinder system, there are thermal, electric, and fluid types, and they are used in different ways depending on the application and operating object. Among them, pneumatic soft actuators are suitable for applications involving contact with flexible objects such as fruits and human bodies. These actuators, driven by air and mainly using rubber as casing, are referred to as "human-friendly actuators".
This is because pneumatic soft actuators have "two flexibility features[1]" that set them apart from other actuators. First, the flexibility of the case and the compressibility of the air allow the actuator to exhibit passive flexibility as an elastic body even when it is not pressurized. Secondly, the flexibility can be actively controlled by changing the shape and stiffness of the actuator by pressurizing inside of it. This feature makes it possible to realize a unique process in which an original soft system can be strengthened and utilized by control. Furthermore, the system does not require high current or high heat for operation, and even if the case is damaged, the operating energy is harmless air, resulting in minimal impact on the surrounding environment or the object being operated. Because of these features, systems using pneumatic soft actuators have been developed and realized in various fields beyond the existing applications in recent years.
There are two major technical points of interest in the pneumatic soft actuators that have been developed to date. The first is the pressure level to be used. For example, the PBA[2] (Pneumatic Balloon Actuator) performing a bending motion requires an internal pressure of 70kPa for a 7mm-motion stroke, and the twist actuator[3] performing a twist motion, requires an internal pressure of 178kPa for a 70°motion. In the case of pneumatic soft actuators, which are often used in contact with flexible objects, there is a close relationship between the internal pressure and the safety of the operating energy, so from the viewpoint of the impact on the operating object and the surrounding environment, driving at even lower pressure is required. The second is the structure to control the driving direction. In order to generate deformation in a specific direction, the pneumatic rubber artificial muscle[4] uses a sleeve woven with fibers, and the FMA[5] (Flexible Micro Actuator), constrains the deformation direction by installing multiple air chambers. If the drive direction can be controlled with a simpler structure, it will be possible to reduce the cost and space of the actuator.
This study focuses on these improvements and aims to develop a pneumatic soft actuator, SCSRA (Sponge Core Soft Rubber Actuator), that satisfies the following three requirements.

(1) Low-pressure operation
A large internal pressure to motion stroke ratio can be achieved at lower pressure levels (small less than30kPa) than conventional pneumatic soft actuators.
(2) Simple control method for driving direction
By keeping the pressure level low, the deformation direction can be constrained at low cost and with a simple structure.
(3) Both passive and active functions
It is equipped with both pressurized and non-pressurized functions by taking advantage of the "two-

flexibility" characteristic of pneumatic soft actuators.

In this paper, the structure and fabrication method of the SCSRA were described first, and the functions of the SCSRA to satisfy three requirements mentioned above are explained. Next, the characterization experiments show that the specified functions could be achieved under both pressurized and unpressurized conditions, and the parameters affecting the characteristics are clarified.

SCSRA(SPONGE CORE SOFT RUBBER ACTUATOR)

Structure and Features

The structure of SCSRA is shown in Figure1. SCSRA is a pneumatic soft actuator consisting of a core foam sponge surrounded by a case made of silicone rubber and a polyurethane tube for inflow and outflow of air. The combination of three flexible materials and air pressure is suitable for applications involving contact with flexible objects, such as fruits and human bodies.
The difference from conventional pneumatic soft actuators is that the pressurized area is not just a cavity, but a gap between the continuous foam sponges. The presence of the sponge enables the actuator to maintain a certain level of rigidity even when the inside of the actuator is open to the atmosphere, and it also has the advantage that the same internal pressure can be obtained at a lower flow rate than when the inside of the case is simply pressurized.
Since the case is made of two-component RTV rubber, which is liquid before curing, any actuator shape and pressure area can be achieved by changing the shape of the sponge and mold. In addition, the sponge and silicone rubber may be adhered or separated during fabrication, so the functions described in the next section can be used.

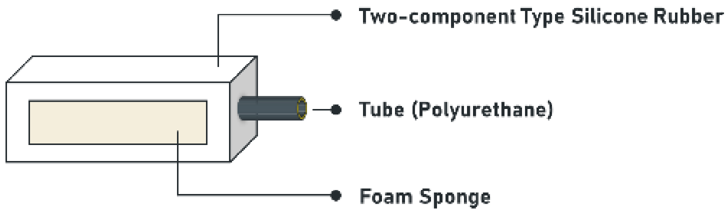

Figure 1. Structure of SCSRA

Fabrication procedure

Figure 2 shows the fabrication procedure of the SCSRA. The procedure is roughly divided into (1)fabrication of the bottom surface, (2)processing and placement of the sponge, (3)fabrication of the side and top surfaces, and (4)installation of the tube. The bonding conditions between the silicone rubber and sponge may vary depending on the timing of the sponge placement. Specifically, in the case of adhesion, the sponge is placed before the silicone liquid on the bottom becoming elastic, and in the case of separation, the sponge is placed after the liquid becoming elastic.
For convenience, SCSRAs in which silicone rubber and sponge are adhered are referred to as "adhesive elements," and SCSRAs in which silicone rubber and sponge are separated are referred to as "separated elements".

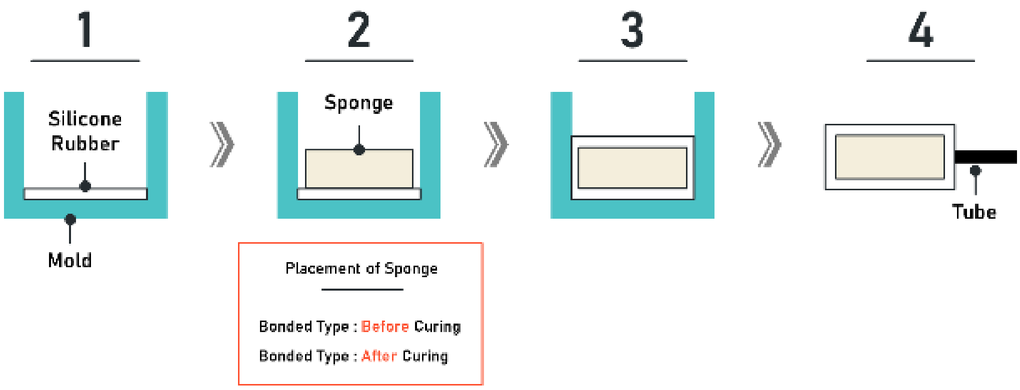

Figure 2. Manufacturing Procedures of SCSRA

Functions

The SCSRA has the following four functions, depending on whether the inside of the actuator is pressurized or unpressurized, and whether the sponge and silicone rubber are adhered or separated.

(1)Force-distribution function (Figure 3(a))
The passive function of the SCSRA is demonstrated by sealing the inside of the actuator with atmospheric pressure. The flexibility of the constituent materials themselves and the compressibility of the air disperse the force applied from the outside in multiple directions.

(2)Force-estimation function (Figure 3(b))
The passive function of SCSRA is demonstrated by sealing atmospheric pressure inside the actuator and connecting a pneumatic sensor to the tube. When an external force is applied to the SCSRA top surface, the pressure-receiving area and the indicated value of the air pressure sensor are substituted into Equation (1) to estimate the applied external force.

$$P=F/A \tag{1}$$

P : Pressure[Pa]
F : Vertical force acting on a surface[N]
A : Force-activated area[m^2]

(3)Rigidity-changing function (Figure 3(c))
The active function of SCSRA is demonstrated by fully adhering the sponge and silicone rubber, and pressurizing the inside of the actuator. Deformation of the silicone membrane under pressure is constrained by the sponge, which rapidly increases its stiffness in response to slight changes in shape.

(4)Shape-changing function (Figure 3(d))
The active function of SCSRA is demonstrated by separating the sponge and silicone rubber only on a specific surface and pressurizing the actuator. Since the silicone rubber other than the separating surface is constrained by the sponge, only the separating surface is deformed significantly under pressure. The driving direction can be controlled by changing the separation surface.

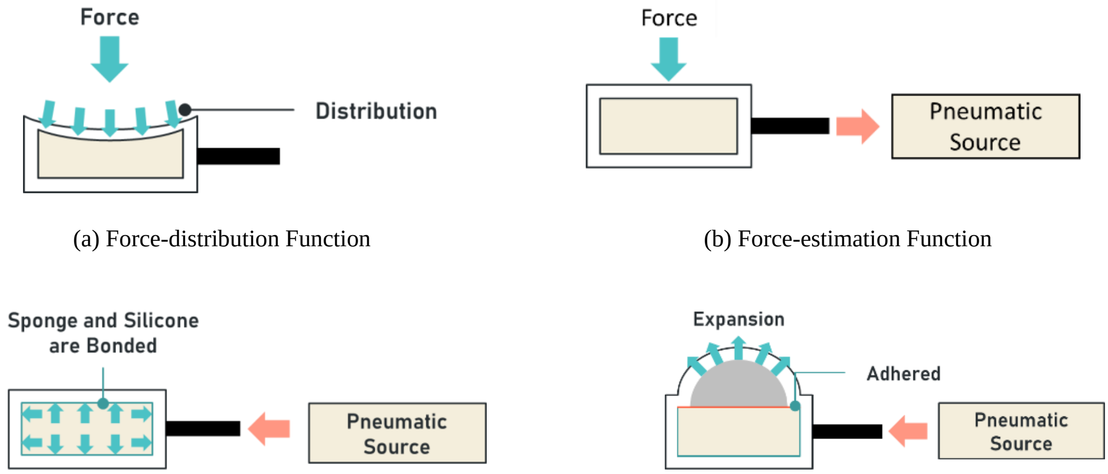

(a) Force-distribution Function (b) Force-estimation Function

(c) Rigidity-changing Function (d) Shape-changing Function

Figure 3. Functions of SCSRA

CHARACTERIZATION EXPERIMENTS

Objective

In order to show that SCSRA satisfies the three requirements described in Chapter 1, characterization experiments were conducted. As explained in Section 2.2, there is a close relationship between the three requirements and the functions of SCSRA. Therefore, by showing that SCSRA can realize the four functions, the purpose of this study is considered to have been achieved.

The function (2), the external force estimation function, has been realized in the previous research in this laboratory, the high-performance shoes system for gait training[6] (Figure 4). The SCSRA is used as an insole element and realizes the function of understanding the subject's gait state through the foot pressure distribution.

In this study, the following functions are demonstrated through characteristic experiments: (1) external force dispersion function, (3) stiffness change function, and (4) shape change function.

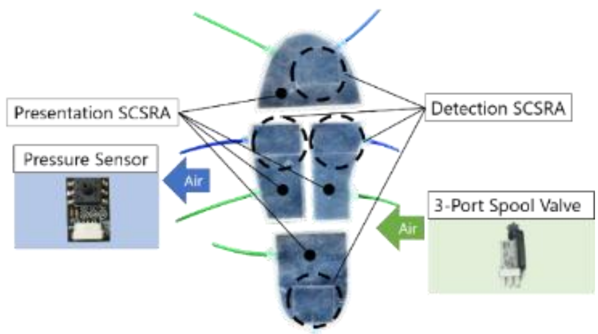

Figure 4. Insole Elements of High-performance Shoes

Use of Devices

Table 1 shows the devices are used for the characteristic experiments.

Table 1 List of Equipment Used in the Experiments

Device Name	Manufacturer	Model Number
DC Stabilized Power Supply	Gwinstek	GPS-3030D
	Gwinstek	GPS-3030D
	METRONIX	512C
Control Circuit	Arduino	UNO R3
AD Converter	ELMOS	RAI-16
Laser Displacement Meter	FASTUS	CD22-35V
Micro Pump	Parker	CTS
Pressure Sensor	Fujikura	AG213-200KG
3-Port Spool Valve	SMC	S070C-RDC-32

Experimental Devices

Figure 5 shows the experimental apparatus used in the characterization experiments. The system is divided into two parts: one is to control the internal pressure of the SCSRA, and the other is to measure the displacement caused by pressurization or load application using a laser displacement meter. The final output value is obtained by converting the analog output of the laser displacement meter to a digital value using an A/D converter. The internal pressure of the actuator is controlled by the electro-pneumatic regulator, and the output of the air pressure sensor is obtained as a voltage value. The breakdown of V1~V7 shown in Figure 5 is as follows.

V1~V3：Supplied by a DC stabilized power supply.

V4~V6：Supplied from each pin of the Arduino, the control circuit.

V7：Supplied from the USB port of the PC.

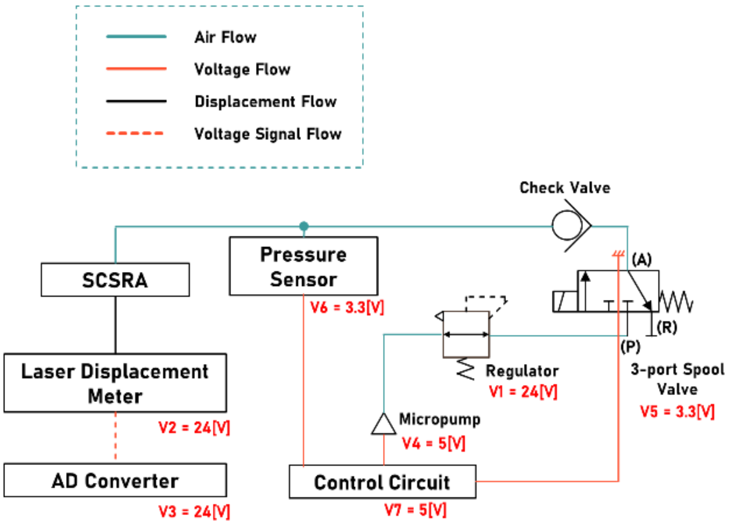

Figure 5. Experiment Equipment for Experiments

SCSRA for the Experiments

The parameters affecting the properties of SCSRA are shown in Figure 6, and the physical properties of the sponge and silicone rubber used in SCSRA are shown in Table 2 and Table 3. In this study, the SCSRA with the parameters shown in Table 4 is used as the reference SCSRA, and we examined how the overall characteristics changed when each parameter is changed.

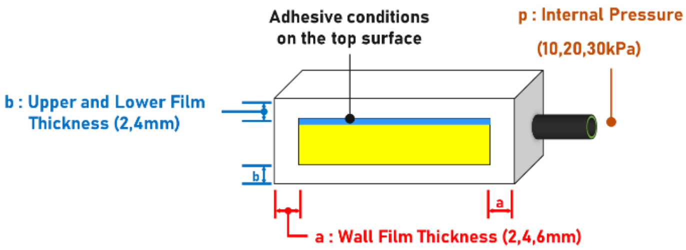

Figure 6. Main Parameters of SCSRA

Table 2 Main Property of Sponge

Sponge	Stiff Urethane Sponge EMO
Density [kg/m³]	50±5
Hardness [N]	12.75≦ [kPa]

Table 3 Main Property of Silicone

Silicone	KE-1316
Hardness [Durometer A]	23
Viscosity [Pa·s]	35
Tensile Strength [MPa]	6.5
Elongation at Break [%]	700
Tear Strength [kN/m]	33
Line Shrinkage Ratio [%]	0.1
Density [g/ cm³]	1.13

Table 4 Parameters of Reference Actuator

External Shape [mm]	50×50×9
Wall Film Thickness [mm]	4
Upper and Lower Film Thickness[mm]	2
Internal Pressure P [kPa]	0
Adhesive conditions on the Top Surface	Separated

EXPANSION CHARACTERISTICS EXPERIMENT

Experimental method

The following procedures are used for the experiment.

(1) Using the experimental setup shown in Figure 5, the internal pressure of the reference SCSRA is set to 0, 5, and 10 kPa.

(2) The relationship between the internal pressure and the amount of expansion is obtained by measuring the top of the expansion shape (the point at which the amount of expansion is maximum) using a laser displacement meter.

From the standard SCSRA, only the bonding condition of the top surface is changed, and the same procedure is performed for the SCSRA in which the silicone film and sponge has completely adhered.

Results and Discussion

The relationship between the actuator internal pressure p and the amount of expansion for the two types of SCSRA is shown in Figure 7. The results can be summarized as follows.

(1) The expansion characteristics of SCSRA followed a quadratic curve:

The correlation coefficients for the quadratic curve approximations were above 0.9 for both the separated and adhered elements, indicating a very strong positive correlation. This is thought to be largely due to rubber elasticity, which is a key property of silicone rubber. From the characteristic curve, it can be seen that the increasing rate of the expansion decreased with raising internal pressure, especially for the reference SCSRA.

(2) The characteristics of separated and adhered elements could be clearly distinguished:
The property curves show that there is a clear difference between the properties of the separated and adhered elements. The first-order coefficient, which is the most important term in the approximation equation, shows a difference of about 24.9 times, and the expansion amount at an internal pressure of 15 kPa shows a difference of about 38.2 times, indicating that the rigidly- and shape-changing functions of SCSRA could be switched depending on the adhesion conditions of the silicone film.

(3) The separate elements had a high internal pressure-to-operating stroke ratio:
Focusing on the reference SCSRA in the expansion characteristic curve, an expansion of approximately 26.0 mm was achieved at an internal pressure of 15 kPa. This indicates that the SCSRA had a shape-changing function. Although it is difficult to compare simply with the bending and twisting motions in the previous studies described in Chapter 1, the internal pressures used were 4.6 and 11.9 times those of the SCSRA, respectively, and the motion stroke was equal to or less than that of the SCSRA. This indicates that the SCSRA achieved higher internal pressure and motion stroke than conventional pneumatic soft actuators.

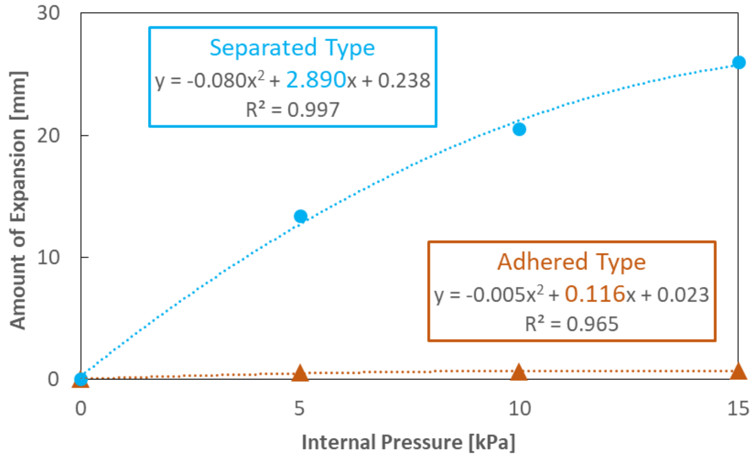

Figure 7. Expansion Amount Characteristic of SCSRA

SPRING STIFFNESS CHARACTERISTICS EXPERIMENT

Experimental method

The following procedures are used for the experiment.

(1) Using the experimental setup shown in Figure 5, the internal pressure p of the reference SCSRA is set to 10, 20, and 30 kPa.

(2) A load of 100, 200, 300, 400, 500, 1000, and 2000 g is applied to the SCSRA top surface, and the amount of sinking is measured by a laser displacement meter to obtain the spring stiffness characteristics.

(3) The internal pressure of the reference SCSRA is set to 0 kPa, and the wall thickness a (Figure 6) is changed to 2, 4, and 6 mm, respectively, and the same measurements are made using the procedure (1)~(2).

(4) The internal pressure of the reference SCSRA is set to 0 kPa, and the upper and lower film thicknesses, b, are changed to 2 and 4 mm, respectively, and the same measurements are made using the procedure (1)~(2).

Results and Discussion

Figure 8 shows the stress-strain curves under different internal pressure “p” from the reference SCSRA. Note that only 100, 200, 300, 400, and 500 g loads are applied to the data because excessive stress under pressure may cause the actuator to break. The results are as follows.

(1) The spring stiffness characteristics of SCSRA followed an exponential function:

In common with each “p”, the correlation coefficient for the exponential function approximation exceeded 0.9, indicating a very strong positive correlation. This characteristic, in which the required stress increased with raising displacement, was extremely similar to the characteristics of air and rubber materials during compression, suggesting that silicone rubber and compressed air formed the spring stiffness characteristics. The effect of the sponge inside wasn't investigated in this experiment, but had been detailed in a previous study conducted by our laboratory[7]. In the experiment using two types of silicone rubber and five types of sponge, it was pointed out that the spring stiffness characteristics changed depending on the combination of silicone rubber and sponge.

(2) The spring stiffness increased with raising internal pressure:

As the “p” increases, the stress required to generate a certain amount of displacement also increases, indicating an increase in spring stiffness. It can be said that the SCSRA realized the rigidly-changing function with the results of extended characterization experiments.

When the initial internal pressure was applied, small deformation was observed as shown in Table 5. Since the deformation was less than 3% of the total SCSRA thickness of 9 mm, it was not considered to be a problem in the experiment.

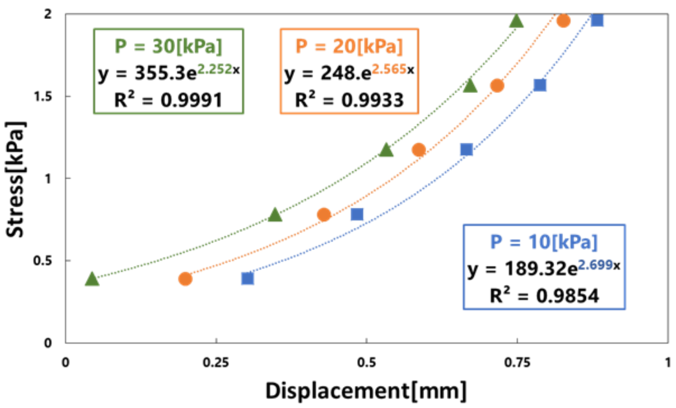

Figure 8. Stiffness Characteristic of SCSRA by P(10.20.30kPa)

Table 5 Initial expansion by pressurization

Initial Internal Preassure “p” [kPa]	Displacement [mm]
10	0.02
20	0.08
30	0.21

Spring stiffness characteristics by wall film thickness A

The stress-strain curves for wall film thickness “a”(Figure 6) different from the reference SCSRA are shown in Figure 9. The results show that as “a” increases, the stiffness of the entire SCSRA decreases. This may be due to the fact that the stiffness of the silicone rubber used in the experiment is less than that of the sponge. In addition, even if the interior of the SCSRA is measured at atmospheric pressure, the characteristics follow an exponential function as in the case of pressurization. This indicates that the SCSRA has the capability to distribute external force due to the passive flexibility of silicone rubber, sponge, and air under non-pressurized conditions.

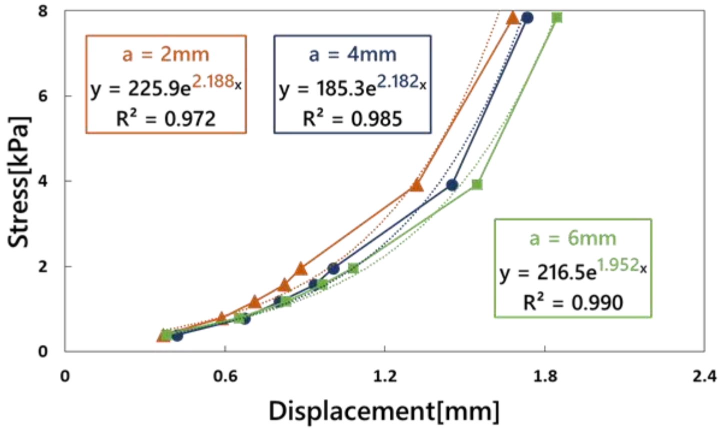

Figure 9. Stiffness Characteristic of SCSRA by A(2,4,6mm)

Spring stiffness characteristics by upper and lower film thickness B

Figure 10 shows that the stress-strain curves for the reference SCSRA and upper and lower film thicknesses "b"(Figure 6). The results show that as "b" increases, the stiffness of the entire SCSRA decreases. This can be attributed to the decrease in the spring stiffness according to the series connection equation (Figure 11) because the increase of the top and bottom film thicknesses corresponds to the addition of a silicone film in series with the reference SCSRA.

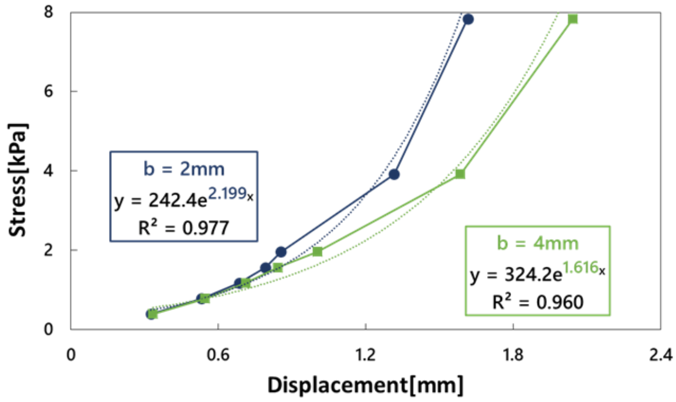

Figure 10. Stiffness Characteristic of SCSRA by B(2,4mm)

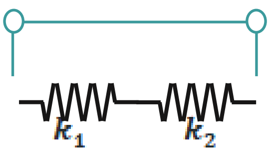

$$\frac{1}{k} = \frac{1}{k_1} + \frac{1}{k_2}$$

Synthetic spring constant k

Figure 11. Rigidity Spring Constant in Series Connection

CONCLUSIONS

In this study, a pneumatic soft actuator, SCSRA, with a sponge core and a silicone rubber case was developed. First, three requirements for SCSRA were defined based on advantages and problems of the previous studies, and then the requirements were specified by passive and active functions. Then, we showed that the SCSRA can realize these functions through characterization experiments.

ACKNOWLEDGMENTS

I would like to express my sincere gratitude to Associate Professor Pak Keunyoung for her english guidance during her busy schedule in conducting this research. I would also like to thank SMC Corporation for providing some of the experimental equipment. Finally, I would like to express my utmost gratitude to all the students who supported my research, both inside and outside the laboratory.

REFERENCES

1. T. Noritugu., Pneumatic Soft Actuator and Human Friendly Mechanism, Journal of Robotics and Mechatronics, Vol.21, No.7, pp. 722-726, 2003
2. Benjamin Gorissen., Michaël De Volder., et al., Theoretical and experimental analysis of pneumatic balloon microactuators, Sensors and Actuators A, Vol.168, pp. 58-65, 2011
3. B.Gorissen., T.Chiskiro., et al., Flexible pneumatic twisting actuators and their application to tilting micromirror, Sensors and Actuators A, Vol. 216, pp. 426-431, 2014
4. S. Kawamura., M. Nokata., et al., Control actuator basics, Corona publishing co., ltd., 2014, pp 49-50
5. K. Suzumori., Flexible Microactuator, *Transactions of the Japan society of mechanical engineers. C,* Vol. 55, No. 518, pp.2574-2552, 1989
6. Y. Hayakawa., Y. Kimata., et al., Study on Human Behavior Classification by using High-Performance Shoes Equipped with Pneumatic Actuators, Journal of Robotics and Mechatronics. Vol.32, No.5, 2020 pp. 1-9
7. T. Minamoto., Y. Hayakawa., Development of a New Rubber Element with Human Compatibility, Graduation Research of Department of Control Engineering, NIT, Nara College. 2020

The 11th JFPS International Symposium on Fluid Power HAKODATE 2020 Oct. 12-13, 2021 The Japan Fluid Power System Society

Development of Pneumatically Driven Verification System for Ophthalmic Needling Operation

Feng Tao*, Maina Sogabe**, Norihiko Ito***, Tetsuro Miyazaki**, Toshihiro Kawase*, ****, Takahiro Kanno***** and Yoshikazu NAKAJIMA*, Kenji Kawashima **

* Institute of Biomaterials and Bioengineering, Tokyo Medical and Dental University
2-3-10 Kanda Surugadai, Chiyoda-ku, Tokyo, 101-0062 Japan
** Department of Information Physics and Computing, The University of Tokyo
7-3-1 Hongo, Bunkyo-ku, Tokyo, 113-8656 Japan
(E-mail: kenji_kawashima@ipc.i.u-tokyo.ac.jp)
** Department of Agriculture, Tottori University
4-101 Koyama-cho Minami, Tottori, 680-8550 Japan
****Institute of Innovative Research, Tokyo Institute of Technology
4259 Nagatsuta-cho, Midori-ku, Yokohama, Kanagawa, 226-8503 Japan
***** RIVERFIELD Inc., Yotsuya Medical Bldg. 5th floor, 20 Samon-cho, Shinjuku-ku, Tokyo, 160-0017 Japan

Abstract. The demand for surgical assist robots is increasing in the field of ophthalmic surgery. However, the patient's movements that occur during surgery increase the difficulty of the operation, and the need for a system that can reproduce and verify the movements has arisen. The proposed system is mainly composed with two parts, needling mechanism and head rotation mechanism. The needling part consist of a remote center of motion mechanism for tilt and roll movements and insertion. The head rotation part is aimed to replicate the posture of the patient eyeball and head. In order to reproduce the smooth motion like a living body, we introduced a pneumatic cylinder with low friction and back drivability. In this study, we used the proposed system to determine the needling point and verified its accuracy. In the future, we plan to use this device to further evaluate the needling task for ophthalmic surgery.

Keywords: Ophthalmic surgery, Surgical assist robot.

INTRODUCTION

The demand for eye surgery increases year by year, and cataract surgery alone exceeds 1 million cases annually [1, 2]. In order to improve the accuracy and prognosis of these operations, research on surgery assisted robotic systems is actively conducted. Surgery assisted robotic systems have many advantages, including enhanced accuracy dexterity, elimination of tremors, capacity for telesurgery, task automation, a rapid learning curve, and alleviating the surgeon’s burden [3-6]. Among them, the issue is the development of surgical techniques that match the body movements of patients during surgery. At the time of surgery, the patient can move the eyeball to some extent with partial anesthesia; it is necessary to have the patient face the front.

However, some patients move their eyes and head due to repellent reactions (Fig. 1). In ophthalmic surgery, such as retinal vein occlusion and cataract, a needle may be inserted into the eye to recanalize the thromboembolic site or to inject drugs [7]. People in the medical field use robust fixation and sedatives to prevent unpredictable movements as much as possible. However, some patients are afraid of being fixed or are resistant to sedatives and may not be able to fix them. Currently, mechanical assist tools in ophthalmic surgery assume that the patient is looking straight ahead, so they do not assume that the head is rotated. Therefore, our goal was to perform the needling operation on the sclera at the corneal edge, which is often performed in ophthalmic surgery, under the eye movement when the head is rotated.

In this case, it is important to have smooth movements that are typical of living bodies. To reproduce this, we chose a pneumatic cylinder, which has less friction and back-drivability than conventional robots using electric motors. In our previous research, we have developed a device that automates the needling operation [8, 9], and as the next step, we aimed at the insertion point of the needle into the eyeball in accordance with the movement. Therefore, we developed a pneumatically driven device that allows us to check the needling operation under the head movement.

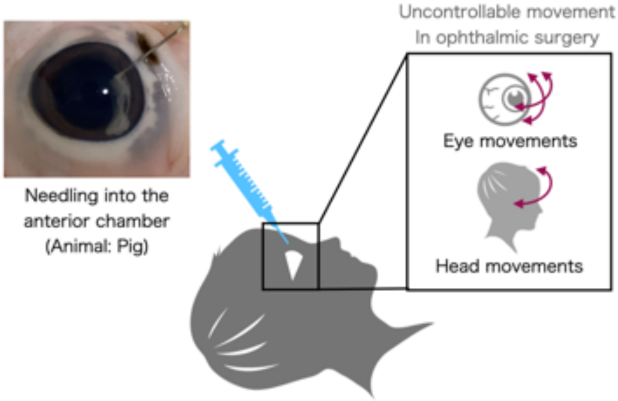

Figure 1. Background about needling for ophthalmic surgery.

CONTROL SYSTEM OF THE PROPOSED SYSTEM

The requirements for this system are that there should be low friction during needling operation, which would interfere with precise movement, and that safety should be ensured when the system is used on a human body in the future. For this reason, we chose a pneumatic drive system that has low friction during operation and also has back drivability. Fig. 2 shows the overview of the proposed system which is mainly composed with two parts, needling mechanism and head rotation mechanism. The needling system consists of two pneumatic cylinders for vertical and horizontal coordinate movement, two pneumatic rotary actuators for pitch and roll rotation, and one soft pneumatic actuator for the insertion of the needle. The head rotation system consists of two pneumatic cylinders for vertical and horizontal coordinate movement and one pneumatic rotary actuator for head tilt.

As shown in the Fig. 3a, the proposed system is actuated by the air pressure. Compressed air supplied from compressor (supply pressure: 0.4 MPa) passes through the regulator and is supplied to the 5-port servo valve (FESTO MPYE- 5-M5-010-B). Flow rate of servo valve depending on its input voltage, which can be controlled by the control PC. The air supplied from the servo valve will drive the actuators used in needling mechanism and head rotation mechanism. Through AD converter, data of position sensors and pressure sensors can be read and control signal will be transferred to the servo valves through DA converter.

Fig. 3 b shows the diagram of real time position control system. In this system, a cascade control system composed with a main loop (position control) and minor loop (pressure control) was adopted. Cascade control has strength in the suppressing of the influence from disturbance and can achieve a high-level of position control. Parameters of cascade control are shown in the Table 1 and 2, where K_{pp} is the proportional gain of position control, K_{pi} is the integrated gain of position control, K_{ap} is the proportional gain of pressure control, K_{ai} is the integrated gain of pressure control, and u is the input voltage of servo valve.

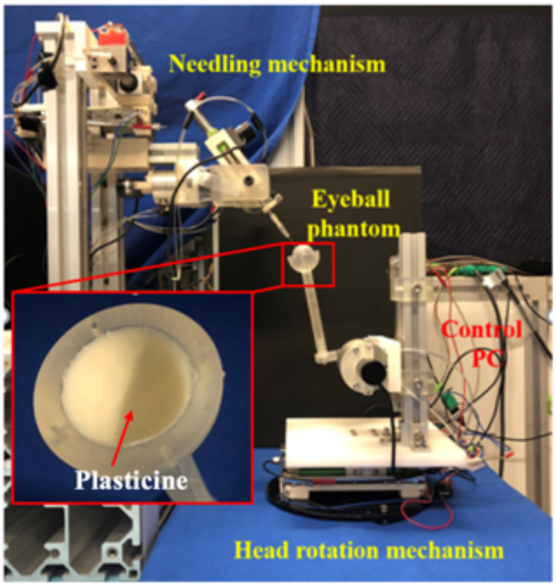

Figure 2. Overview of the proposed system.

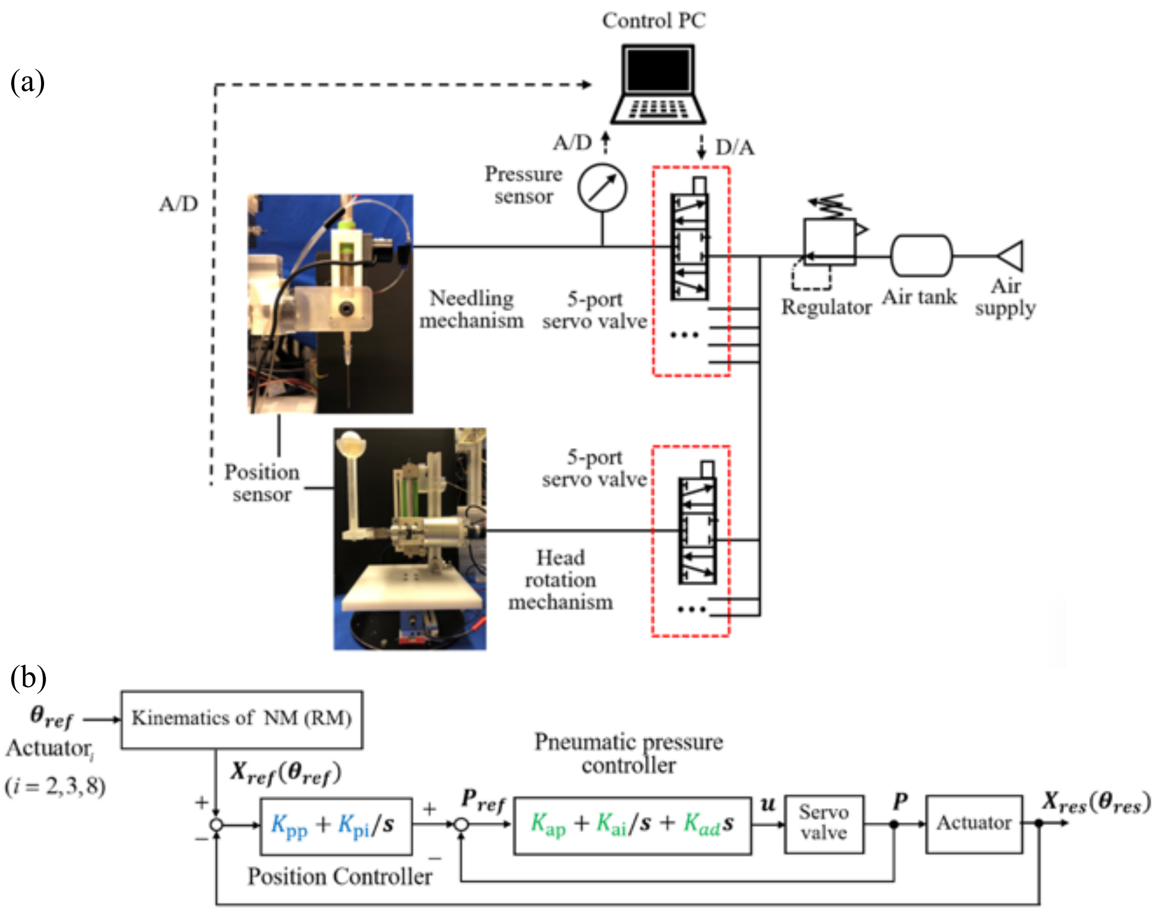

Figure 3. Diagram (a) and block diagram (b) of experimental setting.

Table 1. Parameters of PID gains in needling system

Actuator #	K_{pp}	K_{pi}	K_{ap}	K_{ai}
1	2.5 N/mm	1.5 N/(mm・s)	1.5 V/N	2.5 V/N・s
2	45.0 kPa/mm	25.0 kPa/(mm・s)	0.03 V/kPa	0.05 V/(KPa・s)
3	37.5 kPa/mm	35.0 kPa/(mm・s)	0.03 V/kPa	0.05 V/(KPa・s)
4	35.0 kPa/mm	15.0 kPa/(mm・s)	0.03 V/kPa	0.05 V/(KPa・s)
5	35.0 kPa/mm	20.0 kPa/(mm・s)	0.03 V/kPa	0.05 V/(KPa・s)

Table 2. Parameters of PID gains in head rotation system

Actuator #	K_{pp}	K_{pi}	K_{ap}]	K_{ai}
6	28. 0N/mm	15.0N/(mm・s)	1.5 V/N	0.25 V/(N・s)
7	35.0 kPa/mm	20.0 kPa/(mm・s)	0.03 V/kPa	0.05 V/(KPa・s)
8	25.0 kPa/mm	12.5 kPa/(mm・s)	0.03 V/kPa	0.05 V/(KPa・s)

EXPERIMENTAL PROCEDURE AND RESULT

Needling System

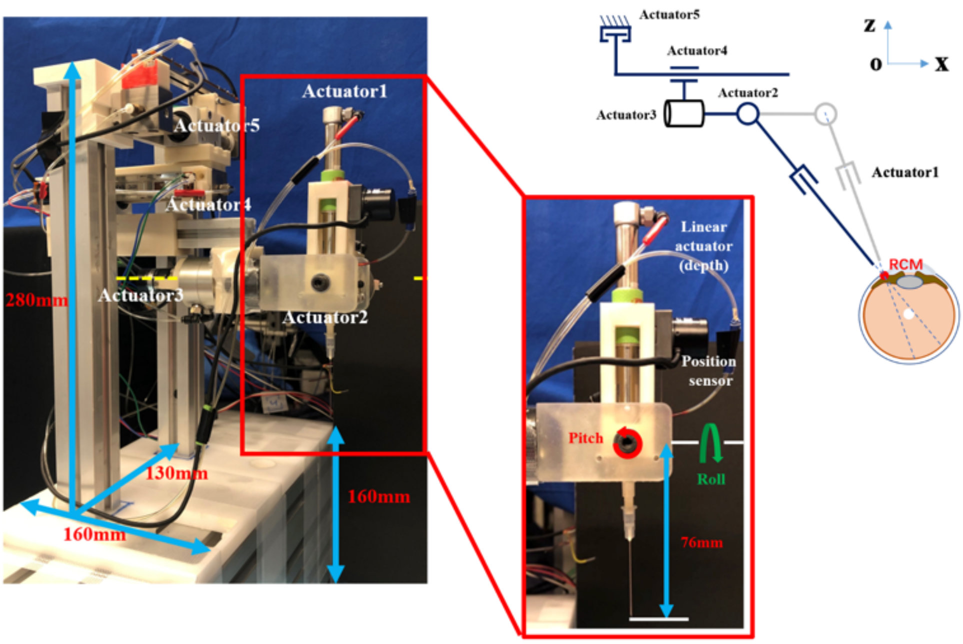

Figure 4. Overview of the needling system.

In the manufacturing of needling mechanism, w two rotary actuators (KURODA PRNA3S-180-90) and two linear actuators (SMC CY3R10-60) are employed for pitch and roll degrees of freedom, and one linear actuator (SMC CJ2XB10- 45Z) is employed for Z-direction (depth) movement. 45Z) for Z-direction (depth) movement. Under a condition of no risk of vision interference and collision with optical device, the needling mechanism is designed and manufactured to realize a 20 degree of workspace in the freedom of pitch and 35 degree of workspace in the freedom of roll. The prototype of needling mechanism is shown as Fig. 4.
According to the data in Fig. 5, we can find that the tip of end effector can move around remote center of motion (RCM) with a range of accuracy error. To the detail, in the freedom of pitch with a motion range of 20 degree, the error in x direction is from -0.25mm to 1mm, the error in z direction is from -2mm to 1.5mm. In the freedom of roll with a motion range of 32 degree, the error in y direction is from -1.75mm to 1.75 mm, the error in z direction is from -1.5mm to 0.25mm. The accuracy error of manipulation mainly comes from the defects in the mechanical design and control system. As for the mechanical design, manufacturing error of the prototype, friction of actuator (especially rod-less linear actuator need to overcome a large friction during manipulation), and the unbalanced gravity effect of needle holder to the actuator 4 and actuator 5 will also influence the accuracy of manipulation. As for the control system, firstly, the accuracy of RCM mechanism adopted (instantaneous type) heavily relies on the control performance of each actuator used in the manipulation (compared with the Parallelogram-based type) and the accumulation of error from each single actuator reduce the accuracy error of the needling mechanism. Secondly, there is an improvement in the parameter tuning of PID control, which will lower the delay in the maximum/minimum value of motion range.

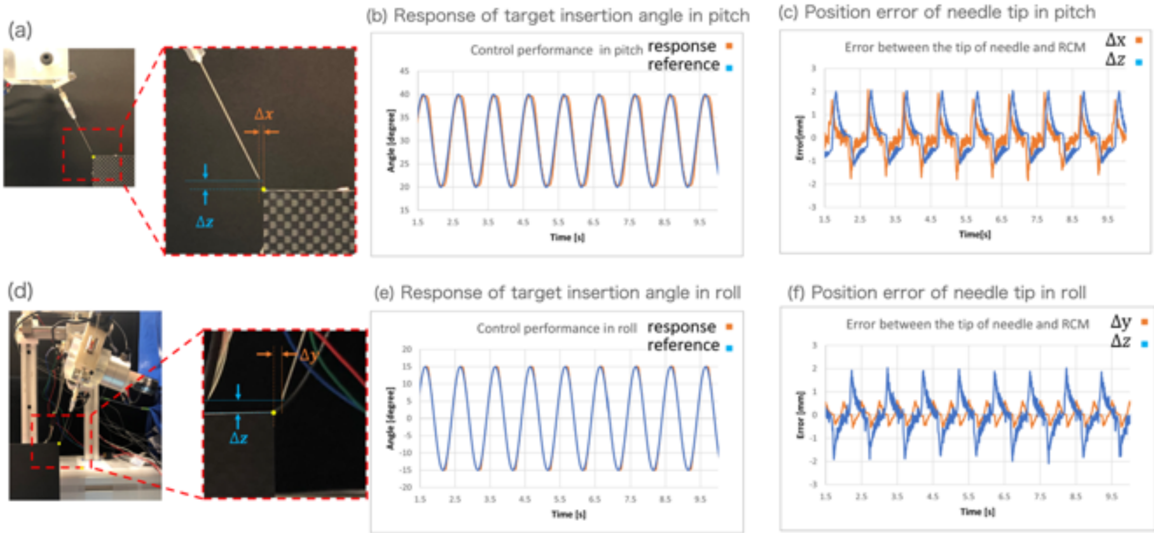

Figure 5. Evaluation experiment of needling mechanism: the error of RCM in the freedom the pitching (a,b,c) and the roll (d,e,f) motion experiments.

Head Rotation System

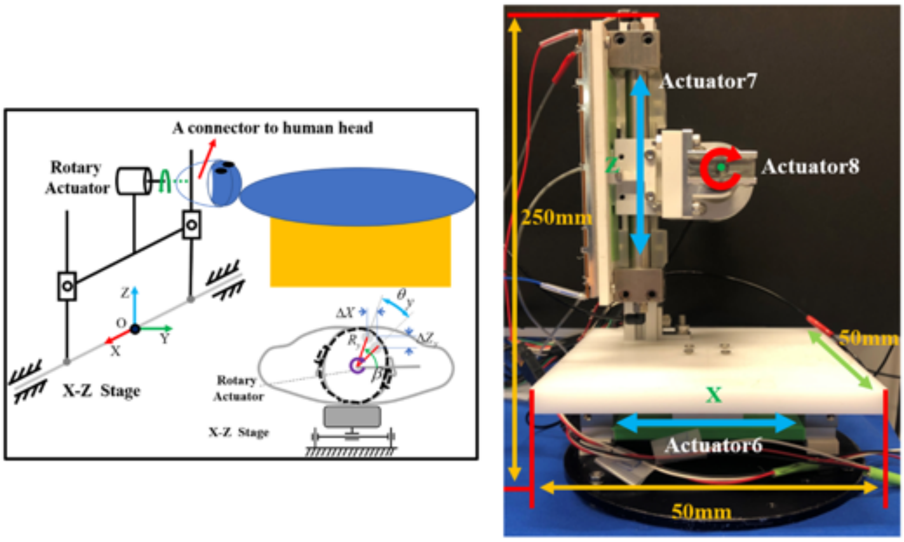

Figure 6. Overview of the head rotation system.

To design the proposed head rotation mechanism, we need to discuss the human head motion and eyeball motion during the operation in the following sections. The motion of human head is based on the motion of cervical spine, which can be divided into three types: Flexion/Extension, Rotation and Lateral Rotation.

Fig. 6 shows the overview of the head rotation system part. Head rotation mechanism is designed to realize a 20-degree head rotation in with Y axis and compensate the associated motion of eyeball center during rotation. In the manufacturing of head rotation mechanism, we adopted one rotary actuator (KURODA PRNA3S-270-45) and two linear actuators (SMC CY3R10-60) to realize the workspace mentioned above. Furthermore, to confirm the feasibility of the proposed robotic system, we developed a human eyeball phantom used for the evaluation experiment. The size of this phantom is mainly based on a commercial skull model.

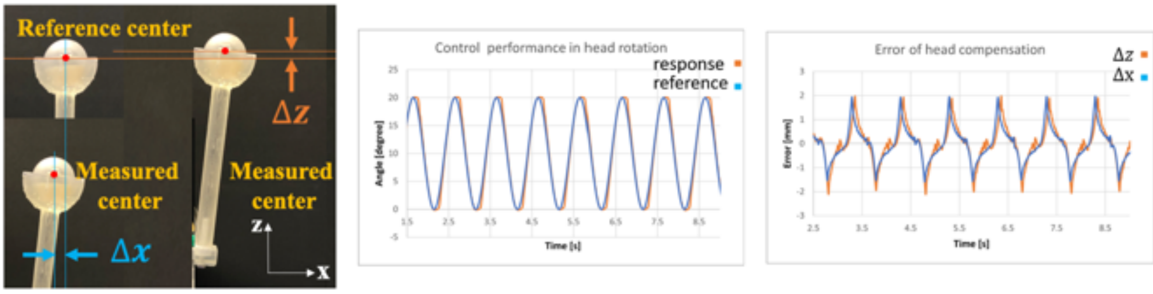

Figure 7. Evaluation experiment; Error of compensation during head rotation.

The control accuracy of head compensation in the process of head rotation, whose performance will decide that if the patient's eyeball keep in the detectable range of other imaging device. The data of this experiment is to measure the error between reference value and measured value of compensation in x and z direction.
Based on the data shown in Fig.7, it is confirmed that the proposed system will have a head compensation ability in x and z direction with a range of accuracy error during a rotation range of 20 degree. To the detail, the error in x direction is from -2.3 to 2mm, the error in z direction is from -1.5mm to 2.0mm. Under this range of error, manipulator can keep the human eyeball in the detective range of observation. However, on the other hand, the error of head compensation is related to the accuracy of needling operation, this is because, kinematics of needling mechanism is based on a reference value of compensation. Therefore, this kind of error should be considered in the improvement of kinematics in the next step.

CONCLUSION

We developed an eye-phantom device that can reproduce the time of head rotation considering the human skeleton and verified the accuracy of the actual needling operation using the proposed system. As a result, it was found that the head rotation could be reproduced using the pneumatic driven proposed system, and the needling operation accuracy could be evaluated. The error of the insertion point setting for needling operation was 2 mm. The error of the head rotation mechanism was up to 2.3mm. Regarding the error, competition for reference bulbs on the needle system side is considered, and it is suggested that it can be solved by improving them.
In future, we plan to improve needing accuracy in real-time using the proposed device and to examine the adaptability of manipulation using an enucleated eyeball instead of the phantom.

ACKNOWLEDGMENTS

This work was supported in part by Riverfield Inc. .

REFERENCES

1. SHARMA, A., D'AMICO, D. J., Medical and surgical management of central retinal vein occlusion. International Ophthalmology Clinics, 2004, 44(1): 1-16.
2. ROGERS, S. et al., The prevalence of retinal vein occlusion: pooled data from population studies from the United States, Europe, Asia, and Australia. Ophthalmology, 2010, 117(2): 313-319.
3. JEGANATHAN, V., SWETHA, E. and SHAH, S., Robotic technology in ophthalmic surgery. Current opinion in ophthalmology, 2009, 21. 75-80.
4. Computer Motion., Available at http://www.computermotion.com. Accessed 2003.
5. DAKIN G. F., GAGNER M., Comparison of laparoscopic skills performance be- tween standard instruments and two surgical robotic systems [abstract]. Accepted for the 8th World Congress of SAGES, New York, NY 2002.
6. HIMPENS J., LEMAN G., CARDIERE G. B., Telesurgical laparoscopic cholecystectomy. Surg Endosc 2003;17:574–9.
7. ASAMI, T. et al., An Endovascular Cannulation Needle with an Internal Wire for the Fragmentation of Thrombi in Retinal Vein Occlusion. Transl Vis Sci Technol. 2016;5(5):9.
8. KANNO T. et al., Soft-material Robot for Ophthalmologic Surgery. Sensors and Materials, 2020 32. 1041.
9. TAO F. et al., Development of a robotic platform for OCT guided retinal surgery. The 38th annual conference of the Robotics Society of Japan (RSJ), 2020.

The 11th JFPS International Symposium on Fluid Power HAKODATE 2020 Oct. 12-13, 2021 JFPS The Japan Fluid Power System Society

Development of a Whole Body Training Device by Multi-directional Force Input Using Pneumatic Artificial Muscles

Soichiro ITO*, Tetsuro MIYAZAKI**, Junya AIZAWA***, Toshihiro KAWASE*, ****, Maina SOGABE**, Takahiro KANNO***** , Yoshikazu NAKAJIMA* and Kenji KAWASHIMA**

* Institute of Biomaterials and Bioengineering, Tokyo Medical and Dental University
2-3-10 Kanda Surugadai, Chiyoda-ku, Tokyo, 101-0062 Japan
** Department of Information Physics and Computing, The University of Tokyo
7-3-1 Hongo, Bunkyo-ku, Tokyo, 113-8656 Japan
(E-mail: Tetsuro_Miyazaki@ipc.i.u-tokyo.ac.jp)
*** Faculty of Health Science, Juntendo University
2-1-1 Hongo, Bunkyo-ku, Tokyo, 113-8421 Japan
**** Institute of Innovative Research, Tokyo Institute of Technology
4259 Nagatsuta-cho, Midori-ku, Yokohama, Kanagawa, 226-8503 Japan
***** RIVERFIELD Inc., Yotsuya Medical Bldg. 5th floor, 20 Samon-cho, Shinjuku-ku, Tokyo, 160-0017 Japan

Abstract. Many of conventional training devices target to train local body parts by repeating simple exercises, and various kinds of training menu will be required to train the whole body. In this paper, we propose a novel pneumatic whole body motion training device by multi-directional force input using pneumatic artificial muscles (PAMs) for total motor system enhancement. PAM is used to actuate the proposed device and gives a trainee flexible and safe force. By using the proposed device, efficient training of the whole body motor system will be realized. The first prototype of the proposed device was developed and applied to a balance board training experiment. In the experiment, we measured floor reaction force and torque in two cases, (i) training with the PAM force, (ii) training without the PAM force. As a result of the experiment, we confirmed that the proposed training will be effective to improve the trainee's core balance performance in a shorter time compared with the conventional training.

Keywords: whole body motion training device, pneumatic artificial muscle, core balance training.

INTRODUCTION

Background

One of major causes that elderly people become patients who need primary nursing care is motor system disorders [1][2], and an appropriate exercise habit is important for realizing a healthy and longevity society. For example, conventional researches have reported that resistance training can improve muscle performance even in elder people [3]–[6]. Due to the fitness boom in recent years, training demand for a wide range of age groups is increasing. In training, a muscular system related to force magnitude and a nervous system related to reaction speed are trained which are main parts of a motor system [7]. For example, as conventional training methods, there are muscle strength training using weights or air pressure [8] and nervous system training that reacts quickly to the external force like a jump training program [9].

Some training devices have the driving source and support specific training which will be difficult by human power alone. For example, an electric treadmill is one of the typical training devices with the driving source, and walking or running training at a target speed set by the trainee is possible by motor control. In addition, various training devices with the driving source have been proposed in conventional researches. Carignan et al. developed an arm curl machine that adjusts the load during operation using a motor [10]. In this machine, the load can be adjusted according to the change of the trainee's elbow angle. The DD System ELITE [11] is a foot press training machine using pneumatic artificial muscle (PAM). The trainee kicks a plate actuated by the PAM while watching the virtual landscape and the data on the display during the exercise. The electric treadmill SKILLRUN [12] has a function to automatically adjust inclination and speed during running, and it has also a function to train kicking force of leg by controlling the rotational resistance of the running belt. The electric training machine series [13] controls the load and allows training both when the muscle contracts and stretches. These training devices can give the desired load of the trainee by driving the actuator instead of the weight block. However, the conventional training devices have many categories according to training courses, and the muscular system and the nervous system require individual training menu. Moreover, many of the conventional devices target to train local body parts by repeating simple exercises, and various kinds of training menu will be required to train the whole body.

Contribution of This Study

Issues of the conventional training devices include (1) individual training of the muscular system and the nervous system are required, (2) trainee's exercise is limited to simple repetitive motion, and (3) various kinds of training are required to train the whole body. In order to solve these issues, we propose a concept of a novel pneumatic whole-body motion training device by multi-directional force input using PAMs for total motor system enhancement. The PAM is used to actuate the proposed device and gives the trainee flexible and safe force. By controlling the contraction force of the PAM and applying an unpredictable load to the trainee, the muscular system and the nervous system are comprehensively trained. By using the proposed device, efficient training of the whole-body motor system will be achieved.
Contributions of this study are as follows.

1. The concept of the novel whole body motion training device for total motor system enhancement is proposed.
2. A first prototype of the proposed device is developed.
3. The prototype device is applied to a balance board training, which is an actual training example. The performance of the prototype device is verified by an experiment of this training.

WHOLE BODY MOTION TRAINING DEVICE

Concept of the Proposed Device

Fig. 1 shows the concept of the pneumatic whole body motion training device proposed in this study. In Fig. 1, a rigid frame fixed on the environment and the trainee's body are connected by multiple PAMs. By using the proposed device and applying multi-directional contraction force of the PAMs to the trainee’s body, the trainee can train the body balance which is important to keep the posture stable against any external force. In addition, it is possible to give rotational force by using long PAM wrapped around the trainee's body, and the proposed device can be also applied to whole body multi axis motion training including torsion, for example, throwing skill practice of judo, etc. Furthermore, by combining the proposed device with VR glasses, it will be possible to construct a whole body motion simulator with force sense presentation function in a virtual space. Information of the trainee during exercise is measured by several sensors, such as electromyogram, pressure sensor, force sensor, force plate, motion capture system, etc. The measured information is used for the device control and the trainee's performance evaluation. As an application example of the proposed device, we mainly assume training for interpersonal competition with collisions such as team sports and tackle sports.
Novel training method using the proposed device will solve the issues of the conventional training devices such as (1) individual training of the muscular system and the nervous system are required, (2) trainee's exercise is limited to simple repetitive motion, and (3) various kinds of training are required to train the whole body. About the issue (1), our research group developed a muscular strength training device actuated by the PAM, and carried out an experiment to give an unpredictable load to the trainee [14]. As a result of the experiment, when the unpredictable load was applied, the trainee's muscle activity increased by more than 1.2 times compared with a case where the predictable load was applied. By applying the unpredictable load, it will be possible to train the nervous system related to the reaction speed as well as the muscular strength system. About the issues (2) and (3), the proposed device in Fig. 1 is possible to apply load to the whole body via the soft PAMs without mechanical limiting the trainee's movement, and the trainee can move spatially and arbitrarily. Therefore, we consider that the proposed device will be able to solve the issues (1) to (3).

Prototype of the Proposed Device

In this paper, an experimental apparatus as shown in Fig. 2 was developed as the first prototype of the pneumatic whole body motion training device. The prototype device shown in Fig. 2 is composed of an aluminum cuboid rigid frame, eight long PAMs, and a force plate. The rigid frame has a width of 1.5 m, a depth

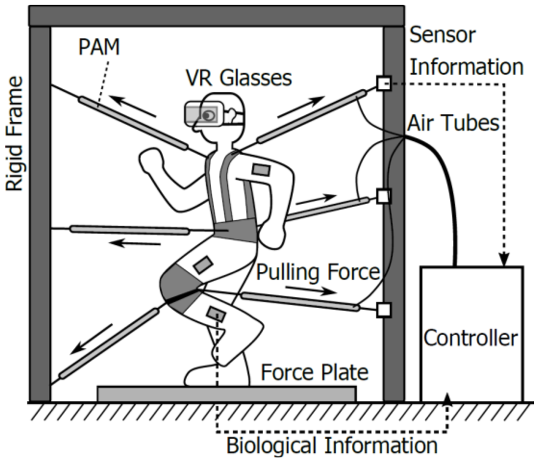

Figure 1. Concept of the pneumatic whole body motion training device.

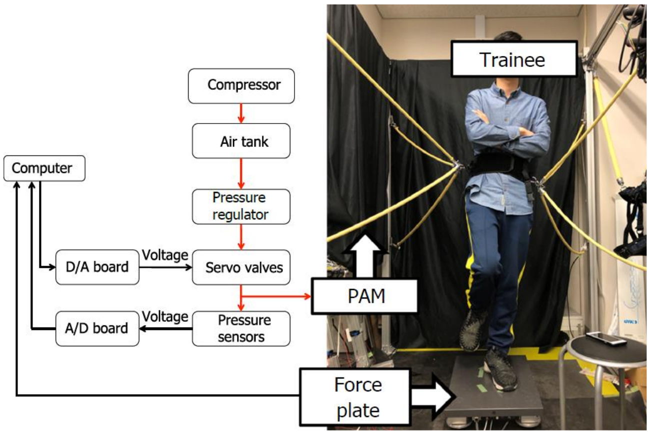

Figure 2. Prototype of the proposed device.

of 1.5 m, and a height of 2.1 m. The trainee stands inside of the frame and its waist is connected to the PAM end, and another end of the PAM is fixed on the frame. The PAM's contraction force in an arbitrary direction is transmitted to the trainee’s body. The positions of the fixing parts that connect the PAMs to the trainee's body can be freely changed according to the exercise task to be performed. In the case of balance board training using the proposed device, the waist part was selected as the fixing position of the PAMs in order to apply an effective external force to the trunk. The waist (pelvis) is the center of the body, and when an external force is applied to this part, it is necessary to move the entire body to balance it. The fixing method of the PAMs is as follows; 1) wrap a soft supporter around the trainee's waist, 2) attach a nylon belt with fixing parts without slack, 3) connect the fixing parts and PAMs. This fixing method can firmly apply the PAM contraction force to the trainee's waist without any pain. The trainee’s ground reaction force during the experiment is measured by the force plate. When measuring myoelectric potential, the trainee wears electromyogram electrodes. The developed device is the first prototype, and eight PAMs are used to exert the load on the trainee’s waist. This physical connection also works as a lifeline and decreases serious accident risks like falling while training. In order to confirm that the prototype device can be applied to actual training, a balance board training was selected as an application example, and we carried out a verification experiment.

The PAM has several unique characteristics. For example, it has a high power-to-weight ratio despite its simple and lightweight structure consisting only of a rubber tube, sleeve, and metal fittings. In addition, the PAM is appropriate for applications that connect to the human body from the safety point of view because it can output flexible and back-drivable driving force. The PAM contains the rubber tube and the outer sleeve knitted with fibers in an oblique direction. When air pressure is applied into the rubber tube, the PAM expands in the radial direction and simultaneously contracts in the long axis direction. Along with this deformation, the contraction force is generated in the long axis direction of the PAM. By controlling the air pressure applied to the PAM, the proposed device gives a variable load to the trainee's muscles. The length of the PAM is 800 mm. The inner diameter of the PAM is φ9.5 mm and generates the contraction force of about 300 N when 400 kPa gauge pressure is applied to the PAMs of the initial length. In this paper, the pressure information is shown as gauge pressure.

Control of the Proposed Device

A pneumatic circuit for driving the proposed device is also shown in Fig. 2. The pneumatic circuit consists of a compressor, air tank, pressure regulator, servo valves (FESTO, MPYE5-1/4-010-B), pressure sensors (SMC, PSE510-M5), a pipeline of air tubes, and PAMs. The pressure in the PAM is measured by the pressure sensor, and its information (voltage) is sent to a control PC. The control voltage for the servo valve is calculated by the computer and is sent to the valve for controlling the pressure in the PAM. A block diagram of the pressure feedback controller is shown in Fig. 3. The proposed training device gives the trainee variable load by controlling the pressure applied to the PAM. In Fig. 3, P_{ref} [kPa] is the target pressure, and P [kPa] is the measured pressure in the PAM. K_p [V/kPa] is the proportional gain, and it was set as 0.05 V/kPa experimentally. K_i [V/(kPa·s)] is the integral gain, and it was set as 0.05 V/(kPa·s). u [V] is the control voltage, G [kg/s] is the mass flow, and s is the Laplace operator.

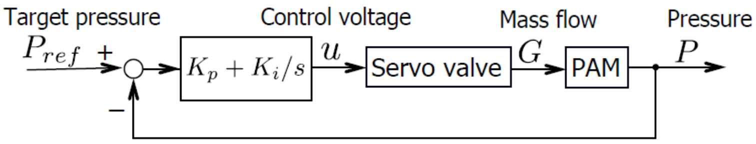

Figure 3. Block diagram of the pressure feedback controller.

In this study, we adopted a simple controller as shown in Fig. 3 because we focused on three main topics as shown in the section of contribution. However, the controller in Fig. 3 is primitive, and in addition, the internal volume of the PAMs is large, so it is expected that the adopted pressure controller will cause a time delay of less than 1 s. In our previous study, we aimed to improve the control performance of power assist devices using PAMs, modeled a pneumatic circuit system including PAMs, and improved the responsiveness of the pressure control [15]. We consider the model in our previous study can also be implemented for the control system of the proposed device. Quantitative evaluation of how the time delay amount due to the difference in control methods affects the training results is an interesting research topic and we consider it to be one of our future works.

APPLICATION TO BALANCE BOARD TRAINING

Experimental Method

In order to confirm that the prototype device can be applied to actual training, we selected a balance board training and carried it out as a verification experiment. In this training, the trainee is required to stand on an unstable board and not to tilt the board largely. There will be various strategies not to tilt largely the balance board for each trainee. For example, there is a general strategy as follows. The trainee keeps its upper body upright from the floor as much as possible so as not to tilt the board largely, and fine-tunes the position of the reaction force on the soles of both legs to maintain the body balance.

We customized our prototype device for the balance board training as shown in Fig. 4. A balance board and rigid frame with four push-button switches are set on the force plate. The trainee stands on the balance board, and force and torque on a contact point between the board and the force plate are measured as time-series data. When the trainee tilts the board largely, the edge of the board pushes one or two buttons, and the PAMs are actuated and support the trainee’s body until the board lifts off from the button. We expect that this control strategy can improve the trainee’s body balance training method as follows. The proposed device can inform the board's inclination state to the trainee by the PAM force, and it makes the trainee can recover to its stable posture quickly. By repeating this training, the trainee will be able to efficiently learn how to keep the body balance does not tilt the board.

We consider the proposed training device can be applied to train the muscular system and nervous system of any part of the whole body by changing the fixing positions of the PAMs. Whether the muscular system or nervous system is intensively trained depends on the exercise task to be performed. For example, in the case of balance board training considered in this study, the external force of the PAMs is used as a force presentation function teaching the correct posture rather than a loading function. In this case, the physical load on the trainee is not large and the training effectiveness on the muscular system is small; however, this training is effective as a nervous system training for improving the trunk balance.

Fig. 5 shows an interlocking relationship between the PAMs and switches. The board inclination direction is distinguished by the combination of pushed switches, and the corresponding PAM is driven in each mode. In Fig. 4 right, upper and lower PAMs in four directions are driven by a common servo valve and contract at the same time. Assuming the upper and lower PAMs as one set as shown in the same colors in Fig. 4 right, the proposed device applies a horizontal force to the trainer's waist using four PAM sets (PAMs 1 to 4). For example, when the board tilts toward the subject's toes and presses the CH 1 switch, the pressure is applied to the PAMs 2 and 3 to raise up the subject's body. When the board presses the two buttons CH 1 and 2, the PAMs 3 is pressurized to reduce the tilt angle of the board. In the PAM control, we set the target pressure value of a step function shape. When the button is not pushed, the PAM target pressure P_{ref} is 0 kPa. While the button is pushed, the corresponding PAM contracts by setting the target pressure value P_{ref} as 300 kPa.

We carried out experimental measurements of two methods, the training using the proposed device and the conventional training without the device, and compared these performances. The number of subjects was five in each group. The experimental procedure is shown in Fig. 6. The experiment is divided into three stages: Pre Test, Test, and Post Test. The trainee stands upright on the board and the line of sight is fixed to the front with the eyes open. In Pre Test and Post Test, holding the above state for 40 s without wearing the PAMs is defined as one trial, and three trials are measured in each of Pre Test and Post Test. In addition, the experiments performed

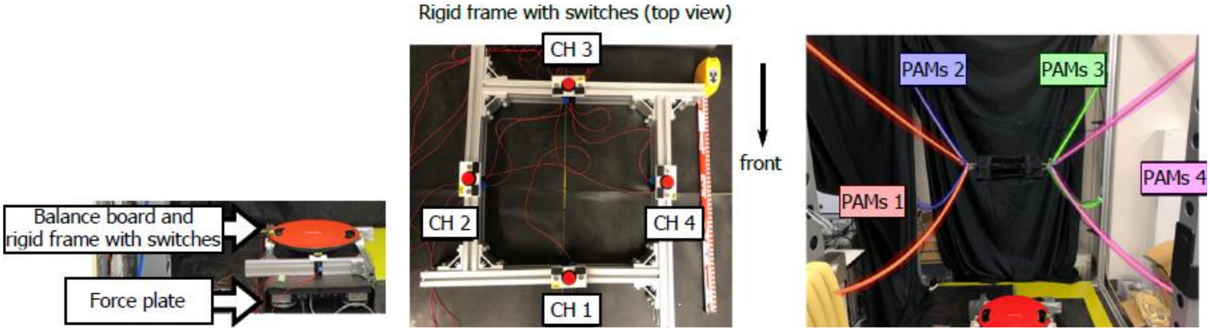

Figure 4. Experimental setup for the balance board training.

	CH 1	CH 2	CH 3	CH 4	CH 1 & 2	CH 2 & 3	CH 3 & 4	CH 4 & 1
PAMs 1			○	○			○	
PAMs 2	○			○				○
PAMs 3	○	○			○			
PAMs 4		○	○			○		

Figure 5. Interlocking relationship between the PAMs and switches.

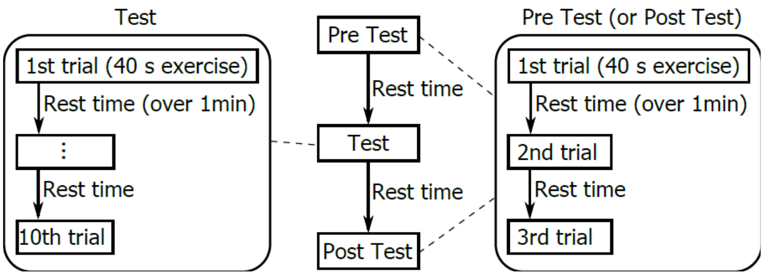

Figure 6. Experimental procedure.

in the Test differ depending on the group. In the group of the proposed method, the external force of the eight PAMs is applied to the waist of the trainee who holds the above state, and in the group of the conventional method, the PAMs are not attached to the trainee. Under these conditions, 10 trials are measured for 40 s in each trial. We set a rest time over one minute between each trial. Time series data of three axes of force and torque are measured in each trial using the force plate. In this experiment, we evaluate the amount of body shake by the standard deviation of the time series data. When the body shake is large, the standard deviation is also large. On the contrary, when the body shake is small, the measured value becomes close to constant and the standard deviation also becomes small. We obtain the measured values of Pre Test and Post Test and compare the training effect in each group. Specifically, we calculate the following index ΔF [%] as:

$$\Delta F = \overline{F}_{pos} / \overline{F}_{pre} \times 100. \tag{1}$$

Where $\overline{F}_{pos}$ is the average value of the standard deviations for three Post Test data, and $\overline{F}_{pre}$ is that for three Pre Test data. This value is calculated for each of the three forces and torques in each trainee. Obtain the average and standard deviation of ΔF from the data of five trainees in each group, and statistically compare the groups using the Student's t-test. Furthermore, for 10 trials of Test data, we calculate the standard deviation for each trial and calculates the slope of the standard deviation with respect to the number of trials. This slope is compared between the groups, and it is clarified whether there is a change in the learning speed of the balance task due to the difference in the training method.

Experimental Results

Fig. 7 shows the average and standard deviation of ΔF in each axis of force and torque. In Fig. 7 left, the bold bar represents the average value and the thin bar represents the standard deviation. The vertical axis shows ΔF

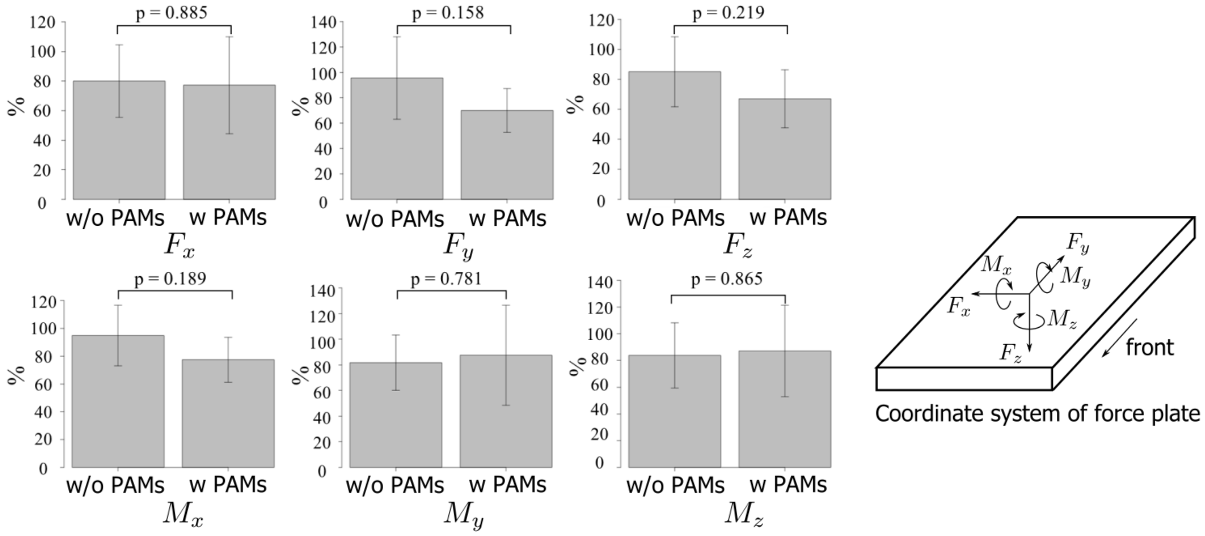

Figure 7. Average and standard deviation of ΔF in each axis of force and torque.

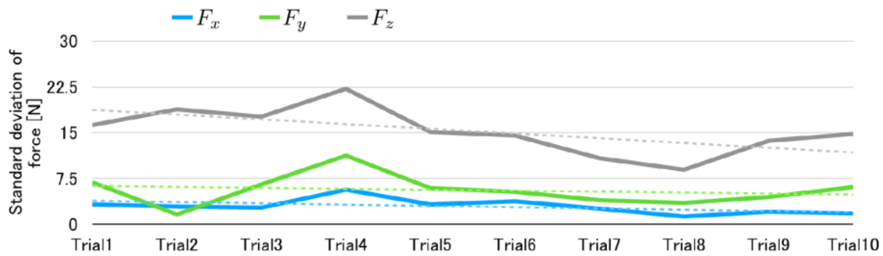

Figure 8. Sample measured Test data.

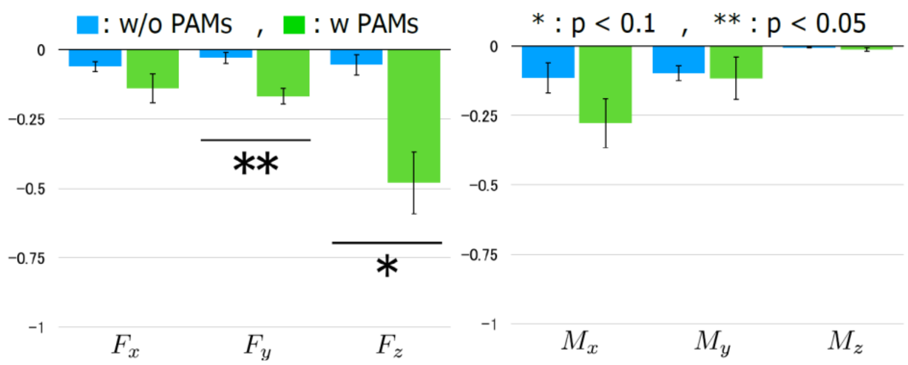

Figure 9. Slopes of the standard deviations of Test data between the groups.

and the horizontal axis shows groups of w and w/o PAMs. p means the p values calculated by the Student's t-test. Fig. 7 right shows the coordinate system of forces and torques measured by the force plate. The origin of the coordinate system was set on the center of the force plate's upper surface.

In addition, Fig. 8 shows the sample measured Test data. The standard deviations of forces and torques are calculated in each trial, and the slope of the standard deviation is obtained by linear approximation. In this figure, the solid lines are the standard deviation of force calculated from the measured value. The dashed lines are the linear approximation of the standard deviation, and we focused on these slopes which will mean learning curves of the trainee. Fig. 9 shows the results of comparing the slopes of the standard deviations of Test data between the groups. In this figure, the bold bar represents the average value and the thin bar represents the standard error. The vertical axis shows the slope value and the horizontal axis represents each axis component of force and torque in each group. The green and blue colors indicate the group of w and w/o PAMs. The symbols * and ** indicate that the values are statistically significantly different at the significance level of 10 and 5% using the two-sided test.

We discuss the results of Fig. 7. For all data, ΔF was less than 100%, and the Post Test value was smaller than the Pre Test value. From these results, it was shown that balance board training is effective for reducing the body shake amount. Regarding the comparison between groups, the values of the proposed method group (w PAMs) were smaller than those of the conventional method group (w/o PAMs) for the three-axis components of forces and torque M_x. Torques M_y and M_z were larger in the proposed method group than in the conventional method group. As an overall tendency, the group of the proposed method tends to have a relatively small ΔF. However, in the experimental results, no significant difference was obtained between the groups in any data. The cause was assumed as that the number of samples (number of trainees) in each group was small of five, and the individual differences in the results were large. As our future work, we consider measuring the larger number of trainee's data and control of athletic ability in the groups.

Next, we discuss the results of Fig. 9. In all the results of force and torque, the slope of the standard deviation of Test was larger in the group of the proposed method than that of the conventional method. In particular, the F_y result showed statistically a significant difference at a significance level of 5%, and the F_z result showed a significant difference at a significance level of 10%. From these results, we considered that the proposed training method may be able to obtain the practice effect more efficiently in a shorter time than the conventional method.

As shown in Fig. 8, the standard deviations of force and torque do not always decrease linearly with the increase in the number of trials. This is a common tendency that is often seen in human experimental measurements, and it is due to the large variation in the measured values for each subject and each trial. To solve this problem, it is effective to set a sufficient number of trials and observe the macroscopic statistical tendency of the data. In this study, we confirmed the significant differences between the groups in 10 trials. A clearer tendency will be observed by increasing the number of trials. However, since an increase in the number of trials leads to an increase in the experiment time and the large burden on the trainee, it is necessary to consider an appropriate number of trials in the future.

CONCLUSION

In this paper, we proposed the novel whole body motion training device by multi-directional force input using PAMs for total motor system enhancement. In addition, we developed the first prototype of the proposed device. The prototype device was applied to the balance board training. The proposed device can inform the board's inclination state to the trainee by the PAM force, and it makes the trainee can recover to its stable posture quickly. By repeating this training, the trainee will be able to efficiently learn how to keep the body balance does not tilt the board. In the experimental validation, we measured floor reaction force and torque in two cases, (i) training with the PAM force, (ii) training without the PAM force. In this experiment, we evaluated the amount of body shake by the standard deviation of the time series data. The experiment was divided into three stages: Pre Test, Test, and Post Test. We obtained the measured values of Pre Test and Post Test and compared the training effect in each case. Furthermore, for 10 trials of Test data, we calculated the standard deviation for each trial and calculated the slope of the standard deviation with respect to the number of trials. This slope was compared between the groups. As a result of the experiment, we confirmed that the proposed training will be effective to improve the trainee’s core balance performance in a shorter time compared with the conventional training.

As our future work, we will observe the change of the trainee's performance when the training using the proposed device is performed over a long period about several months.

ACKNOWLEDGMENTS

This work was supported by the Bridgestone Corporation and KAKENHI (20K19594, 21H04544). This research was also based on the Cooperative Research Project of the Research Center for Biomedical Engineering. The authors would like to thank Shingo Oono, Ryo Sakurai, and Shintaro Yoshida of Bridgestone Corporation for their support.

REFERENCES

1. GOODPASTER, B. H., et al., The Loss of Skeletal Muscle Strength, Mass, and Quality in Older Adults: The Health, Aging and Body Composition Study, Journal of Gerontology: Series A, Vol. 61, No. 10, 2006, p. 1059-1064.
2. IANNUZZI-SUCICH, M., et al., Prevalence of Sarcopenia and Predictors of Skeletal Muscle Mass in Healthy, Older Men and Women, Journal of Gerontology: Series A, Vol. 57, No. 12, 2002, p. 772-777.
3. JOZSI, A. C., et al., Changes in Power with Resistance Training in Older and Younger Men and Women, Journal of Gerontology: Series A, Vol. 54, No. 11, 1999, p. 591-596.
4. FRONTERA, W. R., et al., Strength Conditioning in Older Men: Skeletal Muscle Hypertrophy and Improved Function, Journal of Applied Physiology, Vol. 64, No. 3, 1988, p. 1038-1044.

5. HUNTER, G. R., et al., Resistance Training Increases Total Energy Expenditure and Free-Living Physical Activity in Older Adults, Journal of Applied Physiology, Vol. 89, No. 3, 2000, p. 977-984.
6. ORR, R., et al., Power Training Improves Balance in Healthy Older Adults, Journal of Gerontology: Series A, Vol. 61, No. 1, 2006, p. 78-85.
7. COOK, G., Movement: Functional Movement Systems. On Target Publications, 2012.
8. BALACHANDRAN, A. T., et al., Power Training Using Pneumatic Machines Vs. Plate-Loaded Machines to Improve Muscle Power in Older Adults, Experimental Gerontology, Vol. 98, 2017, p. 134-142.
9. HEWETT, T. E., et al., The Effect of Neuromuscular Training on the Incidence of Knee Injury in Female Athletes, The American Journal of Sports Medicine, Vol. 27, No. 6, 1999, p. 699-706.
10. CARIGNAN, C. R., et al., A Haptic Control Interface for a Motorized Exercise Machine, 2008 IEEE International Conference on Robotics and Automation, 2008, p. 2055-2060.
11. https://jp.ddrobotec.com/en/dd-system-elite/ (accessed on 19 May, 2021)
12. https://www.technogym.com/skillrun.html (accessed on 19 May, 2021)
13. https://www.milon.com/us/milon-world/ (accessed on 19 May, 2021)
14. NAKANISHI, T., et al., Development of an Arm Curl Machine with Variable Resistance Using Pneumatic Artificial Rubber Muscle, 2019 IEEE/RSJ International Conference on Intelligent Robots and Systems, 2019, p. 3830-3835.
15. TAGAMI, T., et al., Pressure Control of a Pneumatic Artificial Muscle Including Pneumatic Circuit Model, IEEE Access, 2020, p. 60526-60538.

The 11th JFPS International Symposium on Fluid Power HAKODATE 2020 Oct. 12-13, 2021 JFPS The Japan Fluid Power System Society

Development of Robotic Forceps Driven by Soft Actuator with Built-In Displacement Sensor

Osamu Azami[*], Takahiro KANNO[*], Toshihiro KAWASE[**,***], Maina SOGABE[****], Tetsuro MIYAZAKI[****] and Kenji KAWASHIMA[****]

[*] Riverfield Inc., 20 Samon-cho, Shinjuku-ku, Tokyo, 160-0017 Japan
(E-mail: osamuazami@gmail.com)
[**] Institute of Biomaterials and Bioengineering, Tokyo Medical and Dental University
2-3-10 Kanda Surugadai, Chiyoda-ku, Tokyo, 101-0062 Japan
[***] Tokyo Institute of Technology, 4259, Nagatsuta-cho, Midori-ku, Yokohama 226-8503, Japan
[****] Tokyo University, 7-3-1, Hongo, Bunkyo-ku, Tokyo 113-8656, Japan

Abstract. We have proposed a pneumatically driven extension-type soft actuator with a built-in displacement sensor. The actuator is constructed by a silicone tube and a metal spring. The displacement is obtained by measuring the change in spring inductance. Furthermore, the force acting on the actuator is estimated from the pressure and the displacement by utilizing the high backdrivability of the soft actuator. In this paper, we proposed and prototyped a robotic forceps using the soft actuator with a built-in displacement sensor. The robotic forceps has a gripper and 2 degrees of freedom joints at the tip. The joints angle and gripper of the robotic forceps are driven by pulling the wire. The pushing force of the soft actuator is transmitting to the pulling force of the wire through the pulley. We evaluate the characteristics of the forceps through experiments. There is a linear relationship between the forceps bending angle and the actuator displacement. The acting force of the forceps tip can be roughly estimated from the supply pressure and displacement of the soft actuator.

Keywords: pneumatic, soft actuator, robotic forceps, built-in sensor

INTRODUCTION

Soft robots and actuators are more flexible and lighter than traditional rigid robots. Therefore, the robots and actuators are safe in contact with human [1]. Soft actuators are being actively studied [2] because the spread of 3D printers has made it easier to prototype. Various shapes of soft actuators have been proposed, and they are applied in various fields such as industrial and medical fields. Regarding the driving method of soft actuators, various methods are used, for example hydraulic, pneumatic and electric. In particular, pneumatic drive is suitable for medical applications because it has the following features: power-to-weight ratio is high and working fluid is clean. Examples of pneumatically driven soft actuators include McKibben type artificial muscle and fiber-reinforced actuators [3][4]. Fiber-reinforced actuator has a large stroke and the relationship between the generated force and the supply pressure is generally linear. It is required sensors to operate the soft actuator precisely. Several actuators with built-in sensors have already been proposed. However, general sensors have the following problems: they are sensitive to heat or water and expensive. Therefore, we have proposed a new pneumatic soft actuator with a built-in displacement sensor [5][6]. The actuator is constructed by a silicone tube and a metal spring. The spring has two roles: reinforcing the outer periphery and sensing displacement. It is able to estimate the actuator displacement by measuring the change in spring inductance. Furthermore, the actuator has high back drivability since it is pneumatically driven. Therefore, the force acting on the actuator can be estimated from the supply pressure and the displacement. We considered that the actuator is suitable for application in the medical field since it has the following characteristic: right weight, low cost, and autoclavable.

In this paper, we proposed and prototyped a robotic forceps driven by the soft actuator. By using the proposed actuator, a lightweight and simple structure forceps can be realized. We proposed a method to estimate the acting force to the forceps tip from the pressure and displacement of the soft actuator. The static and force estimation characteristics of the robotic forceps were examined experimentally.

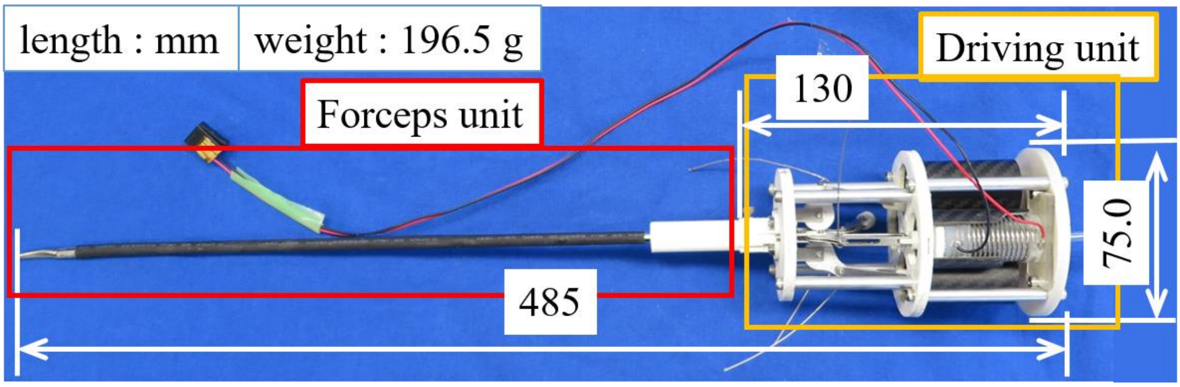

Figure 1. Prototyped robotic forceps driven by soft actuators with built in sensor.

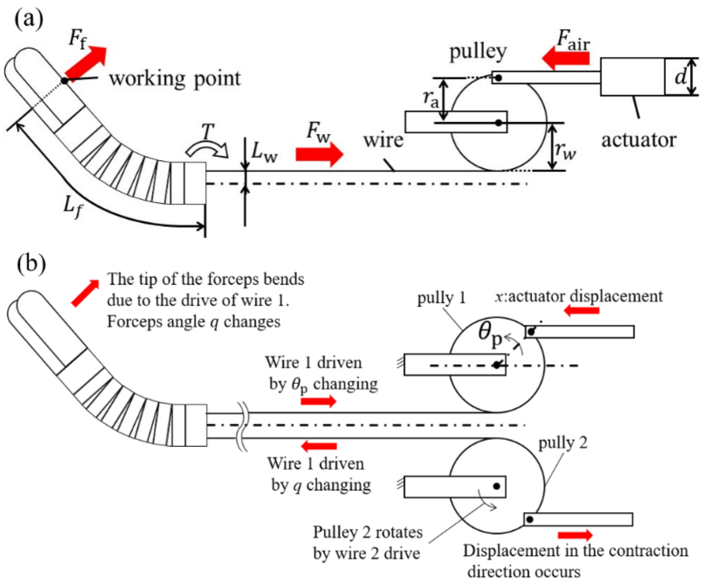

Figure 2. Drive mechanism the robotic forceps.
(a) Crank mechanism. (b) Antagonistic drive.

ROBOTIC FORCEPS

Fig. 1 shows the prototyped robotic forceps. The total length is 485 mm, the drive unit length is 130 mm, and the maximum outer diameter is 75.0 mm. The weight of the forceps is 196.5 g. Fig. 2 shows the schematic drawing of the drive mechanism. The driving force of the actuator is transmitted to the tip joint bending wire via the crank mechanism. As shown in Fig. 2(a), the crank mechanism is necessary to exert a pulling force on the bending wire, since the soft actuator is an expansion type. The forceps mechanism operates by antagonistic drive, and as shown in Fig. 2(b), when an actuator extends, a corresponding actuator (on the opposite side of the same plane) must contract in cooperation. Since the forceps are equipped with two sets of this mechanism, the forceps has two degrees of freedom. The proposed actuator has the minimum length in its natural state. We have set a backlash at the crank mechanism-actuator connection to achieve antagonistic drive. The pulley angle θ_p is 45 ° when the actuator displacement is 0, and the actuator driving force acts on the wire when θ_p is 60 ° or more. The backlash converted to actuator displacement is about 2.3 mm. By geometrically calculating from the dimensions of each part, the acting force F_f of action point at the tip of the forceps can be expressed by Eq. (1).

$$F_f = \frac{L_w}{L_f} F_w = \frac{L_w}{L_f} \frac{r_a}{r_w} F_{air} \tag{1}$$

Here L_w is the length of the moment arm of the bending wire, L_f is the length from the base of the forceps tip joint to the point of action, r_a is radius of the actuator side pulley, r_w is radius of the wire side pulley, F_w is the acting force on the bending wire and F_{air} is the driving force of the actuator.

Table 1. Dimensions of each part of the crank mechanism.

Dimension parameters	Length [mm]
L_w	2.1
L_f	46.5
r_a	9.0
r_w	9.0

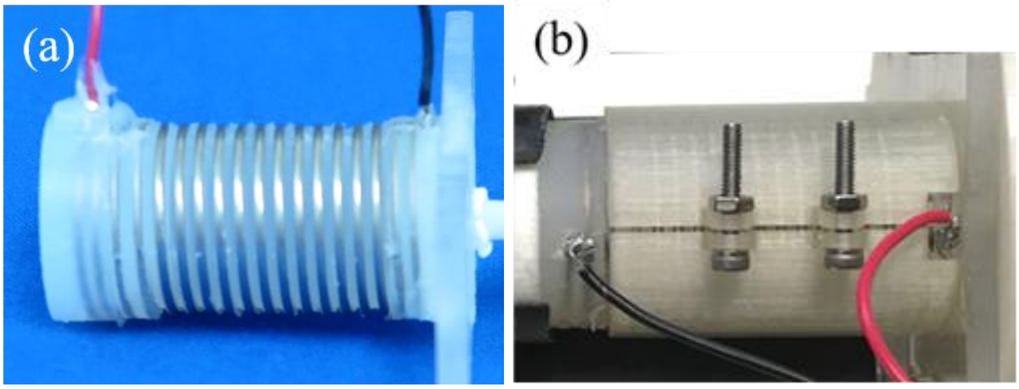

Figure 3. Pneumatically driven extension-type soft actuator
(a) Soft actuator. (b) Soft actuator mounted on the forceps.

Table 1 shows the dimensions of each part of the mechanism. We set the maximum supply pressure to the actuator to be 200 kPa. In our previous study, we have confirmed that the output force of the soft actuator was larger than the pure product of the inner cross-sectional area and the pressure since the rubber wall also transmitted pressure using a thick-walled cylinder model [7]. In the pre-experiment, we measured the supply pressure P and generated force F of the actuator, and calculated the effective cross-sectional area A by assuming $F_{air} = P \times A$. As a result, A is 2.409×10^{-4} m^2. By calculating based on Eq. (1), the maximum value of F_f is determined to be 2.17 N.
Fig.3(a) shows the soft actuator with built-in displacement sensor. The actuator is constructed by a silicone tube and a metal spring. The outer diameter of the actuator is 20mm and the natural length is 40mm. It extends 32.69mm with a pressure of 200kPa. The spring has two roles; reinforcing the outer periphery and sensing displacement. It is able to estimate the actuator displacement by measuring the change in spring inductance. Furthermore, the actuator has high back drivability since it is pneumatically driven. Therefore, it is able to estimate the force acting on the actuator from the supply pressure and the displacement. We have experimentally confirmed that the displacement can be estimated with an error of 5.6%, and the external force can be estimated with an error of 13 % performing experiments with a low frequency sinusoidal input of 0.5 Hz or less [6]. The actuator mounted on the forceps is covered with a pipe with an inner diameter of 21 mm to prevent flexion movement. (Fig.3(b)).
We confirmed that the effects of autoclave sterilization (120 ° C, 30 minutes) were negligible. Therefore, the soft actuator can be used to drive the forceps. It is possible to reduce the weight of the forceps, reduce the cost, and facilitate sterilization by using the actuator for driving the robot forceps.

EXPERIMENTS

Static Characteristics of Tip Joint Angle

We conducted an experiment to measure the static characteristic of the actuator displacement x and the joint angle q at the tip joint. Fig. 4 shows the experimental apparatus. The supply pressure to the actuator was controlled using a servo valve (Valve box). The control signal to the valve was calculated with the PC. The displacement of the actuator was measured from the inductance change of the spring. The joint angle was measured from the image taken by a camera. The relationship between the actuator displacement x_{est} and the joint angle q was derived from the experiments. The target value of the actuator displacement was set as follows: 0.0, 0.5, 1.0, 1.5, 2.0, 2.5, 3.0, 3.5, 4.0, 4.5, 5.0, 5.5 mm. Only one actuator was mounted on the forceps, the antagonistic drive was not implement. The experimental results are shown in Fig. 5. From the results, it can be seen that when x_{est} is less than 2 mm, q remains in initial position, and when x_{est} becomes larger than 2 mm, x_{est} and q have linear characteristics. Furthermore, we derived an approximate equation Eq. (2) to obtain q from x_{est}.

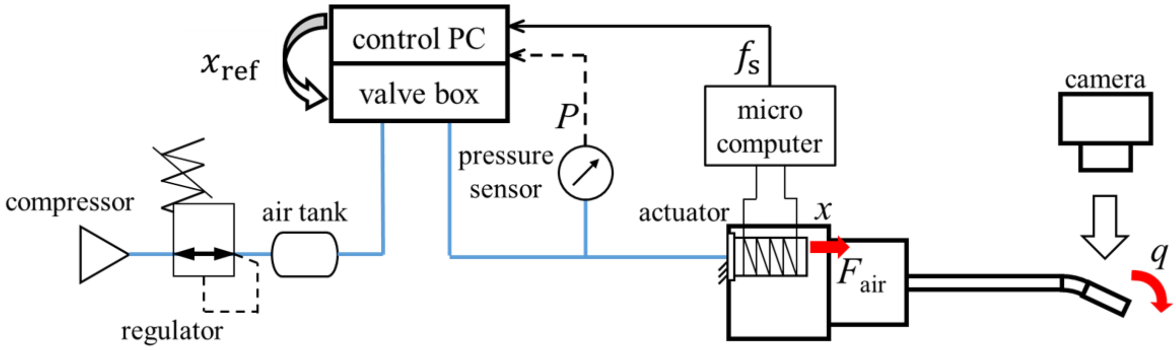

Figure 4. Apparatus for static characteristics experiments of robotic forceps.

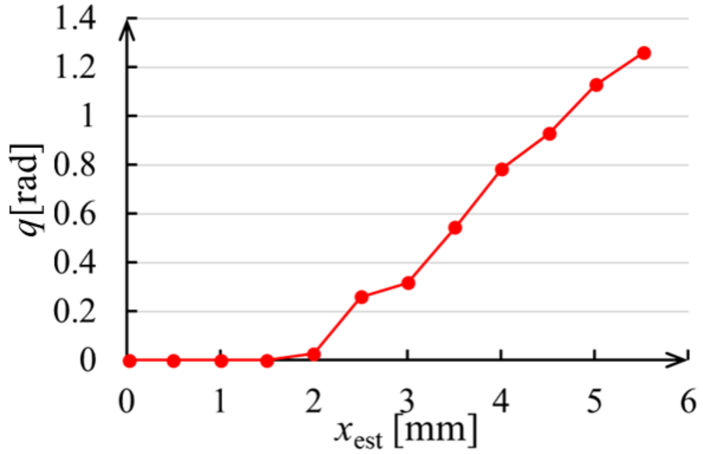

Figure 5. Static characteristics between x_{est} and q of developed robot forceps.

$$\begin{cases} q_{est} = 0.0 \left(x_{est} < 2.0\right) \\ q_{est} = 0.356 x_{est} - 0.681 \left(x_{est} \geq 2.0\right) \end{cases} \tag{2}$$

Force Estimation at the Forceps Tip

We conducted an experiment to estimate the acting force at the tip of the forceps from the state change in the soft actuator. Fig. 6 shows the experimental apparatus. The actuator was driven by position feedback control, and the acting force F_f is measured by a force sensor. We calculated the estimated value F_{fest} of the acting force from the actuator driving force F_{air} using Eq. (1). The joint angle of contact with a force sensor was set as 0 and 10 °, and compared F_f and F_{fest}.

The experimental results are shown in Fig. 7. Fig. 7(a) shows the result of F_f and Fig. 7(b) shows the result of F_{fest}. The waveform of F_f and F_{fest} show a similar trend. However, the average error is 23% at a bending angle of 0 °, and 68% at a bending angle of 10 °. We consider that this error is mainly caused by the friction acting on a bending wire inside the forceps shaft.

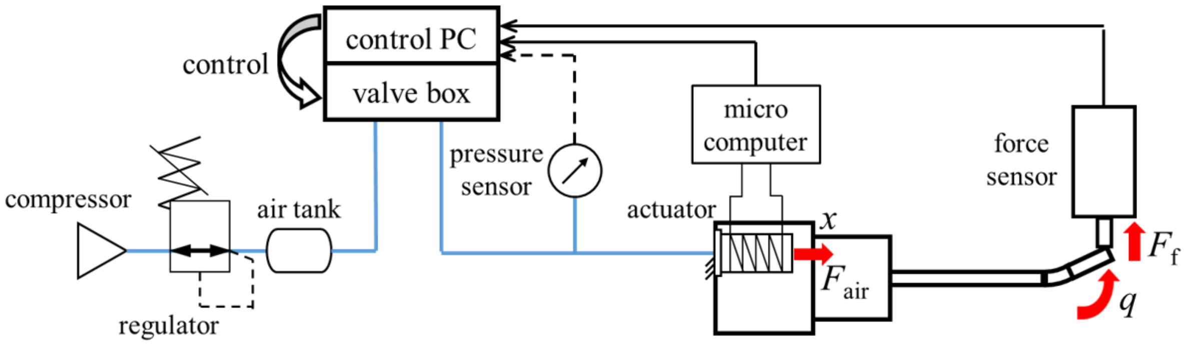

Figure 6. Experimental apparatus for measuring F_f.

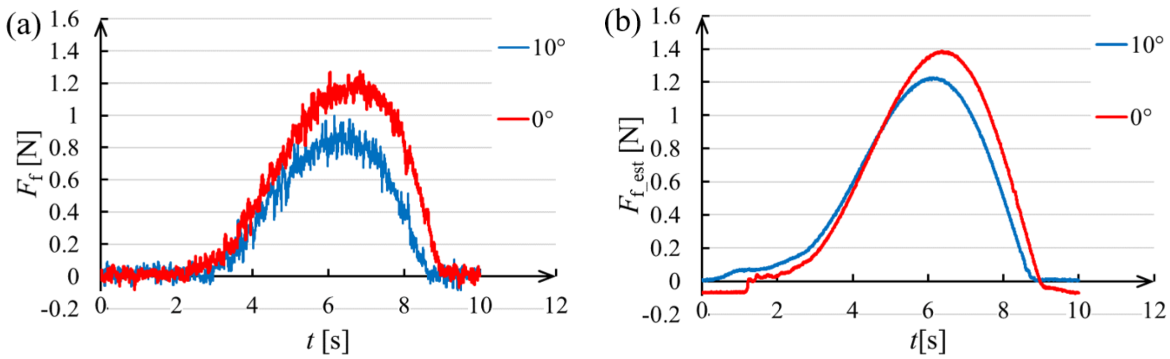

Figure 7. Results of forceps force.
(a) The force measured by a force sensor. (b) The estimated force from the pressure and displacement change of the actuator

CONCLUSION

In this paper, we proposed the robotic forceps driven by pneumatic soft actuator with a built-in sensor. The soft actuator is lightweight, low-cost, and sterilizable by autoclave. Therefore, it is possible to reduce the weight of the forceps, reduce the cost, and facilitate sterilization by using this actuator for driving the robot forceps. We proposed a method to estimate the acting force to the forceps tip from the supply pressure and displacement of the soft actuator. The static and force estimation characteristics of the robotic forceps were examined experimentally. We confirmed that the relationship between estimated value of actuator displacement x_{est} and forceps bending angle q have linear characteristics. We confirmed that the trends of force acting on the tip for each condition are the same between the measured value F_f and the estimated value F_{fest}. The average error is 23% at a bending angle of 0 °. However, the error is not small and increases at the bending angle of 10°. This may be due to the friction between the outer cover and the soft actuator, the friction acting on the wire, and the unintended flexion movement of the actuator. The future work is to reduce the frictions, and increase the flexion rigidity of the soft actuator during operation.

REFERENCES

1. D. Rus and M. Tolley: Nature **521** (2015) 467. https://doi.org/10.1038/nature14543
2. R.F. Shepherd. Multigait soft robot. PNAS. 2011, Volume 108, No. 51, 20400–20403..
3. E. W. Hawkes. Design and Implementation of a 300% Strain Soft Artificial Muscle. In 2016 IEEE International Conference on Robotics and Automation, IEEE: Stockholm, Sweden, 2016; pp. 4022–4029.
4. P. Polygerinos. Modeling of Soft Fiber-Reinforced Bending Actuators. IEEE Transactions on Robotics 2015, Vol. 31, Issue 3, 778-789.
5. O. Azami, Development of the extension type pneumatic soft actuator with built-in displacement sensor. Sensors & Actuators:A 2019, 300. 111623.https://doi.org/10.1016/j.sna.2019.111623.
6. O. Azami. External Force Estimation of Pneumatic Soft Actuator with Built-in Displacement Sensor. Sensors & Materials 2020, Volume 33, No. 2(1), pp. 555–567. https://doi.org/10.18494/SAM.2021.3152.
7. T. Kanno. Model of Coil-Reinforced Cylindrical Soft Actuator. Applied Sciences 2019, Volume 9, Issue 10, 2109

Genaral Session | Oil hydraulics

Tribology, Seals, and Contamination Control

The 11th JFPS International Symposium on Fluid Power HAKODATE 2020 Oct. 12-13, 2021 JFPS The Japan Fluid Power System Society

Effect of Sealing Surface Flatness on Leakage Characteristics of Flange-Type Gasket Model Using Oil Viscosity-Temperature Relations

Song GAO* and Toshiharu KAZAMA**

*Division of Engineering, Graduate School of Muroran Institute of Technology
27-1, Mizumoto-cho, Muroran, Hokkaido, 050-8585 Japan
(E-mail: 19096005@mmm.muroran-it.ac.jp)
**College of Design and Manufacturing Technology, Muroran Institute of Technology
27-1, Mizumoto-cho, Muroran, Hokkaido, 050-8585 Japan

Abstract. Gaskets have a wide range of applications as sealing elements in industry, machinery, and daily life. They prevent fluid leakage between stationary surfaces according to the connected components. Generally, leakage can be restrained by pressing both sides of the sealing surfaces and blocking them up. However, reducing leakage is difficult because roughness and waviness exist on the sealing surface, and deformation may occur due to strong clamping, which can cause partial channels. Therefore, maintaining a flat sealing surface during operation is difficult. In this study, a theoretical model of flange-type gasket is developed using the thermo-hydrodynamic lubrication theory under flat, convex, and concave flange-surface conditions. The concept involves the use of the fluid characteristic that the viscosity increases as the temperature decreases. The effect of flange flatness on the temperature distribution, flow velocity, and leakage was investigated for both conditions of parallel and inclined gap.

Keywords: Seal, Gasket, Temperature, Oil, Viscosity, Flatness

INTRODUCTION

In fluid power and mechanical engineering, sealing elements are vital and indispensable. Gaskets [1-2], as traditional and typical mechanical sealing elements, are widely applied in the industry and factory. Gaskets contain artificial materials that include rubber, copper alloy, and plastic. These materials are installed between the contacting surfaces to enhance the sealing performance of mechanical elements. Normally, leakage is positively correlated to the gap space and is inversely proportional to the flange sealing area. However, excessive clamping can lead to the damage of the sealing surface of gaskets, and elastic deformation may occur due to over extrusion. According to the elastic deformation in theory of elasticity, Persson [3] proposed a theory for estimating a leakage, and sealing performance under both static and dynamic conditions, including plastic deformation, was developed. Lehn et al. [4] analyzed a 3D thermo-elasto-hydrodynamic model of an air-foil thrust bearing by considering the thermal management, the temperature analysis and effect of deformation of the bearing surface on angular velocity were discussed. Furthermore, realizing a flat sealing surface is difficult under practical applications. To achieve outstanding sealing performance, strong clamping is necessary, which can result in surface deformation. Therefore, in the design process of a gasket, we need to investigate the leakage from the gap using theoretical and qualitative analyses of the parameters that affect leakages and apply methods to suppress them. Analysis of a gasket flange with a non-planar sealing surface should also be performed. Gadari et al. [5] numerically and isothermally analyzed an elasto-hydrodynamic lubrication model of seals to estimate the effects of lip deformation assembly and shaft roughness on a revolving lip seal. Shinkarenko et al. [6] developed a theoretical model to investigate practical application of laser-surface texting in the soft elasto-hydrodynamic lubrication. They stated that rigid-counterpart surface testing could increase the load-carrying capacity and reduce friction, which led to an optimal capacity in terms of the aspect ratio and area density with preferred dimples.

In this study, we focus on the lubricant viscosity, particularly that of oil, which is strongly related to temperature. Low temperature corresponds to high fluid viscosity [7]. The fluid viscosity can be increased by cooling the gasket sealing flange. Then, leakage can be reduced. Gao and Kazama [8] proposed the thermo-hydrodynamic lubrication (THL) and iso-viscous methods to control leakage using the characteristics of a flange-type gasket. The flatness of a flange surface is also an important factor that affects the sealing performance. In this paper, the phenomenon between the leakage and solid wall temperature, and the relationship between cooling of sealing flange and leakage reduction is theoretically verified. The THL theory is applied to analyze gap flow, temperature, flow velocity, and leakage, and the effects of temperature control, gap space, and pressure on leakage are calculated using the finite difference method (FDM). The theoretical solution focuses on several types of sealing-surface shapes, e.g., flat, convex, and concave surfaces. The effect of surface flatness on the temperature distribution in the lubricating film, flow velocity, and leakage under both parallel and inclined gap conditions are primarily discussed.

THEORY

Figure 1 shows the schematic diagram of a flange-type gasket model with two circular flanges. P_r is the central recess pressure, P_e is ambient pressure, T_w is the temperature of the solid wall, T_{in} is oil temperature, T'_r is central temperature of disk, T_a is ambient temperature. Flange thickness B is fixed at $r = R_1$. The THL theory is applied to the gap flow with considering the sealing-surface flatness under static conditions of parallel and inclination.

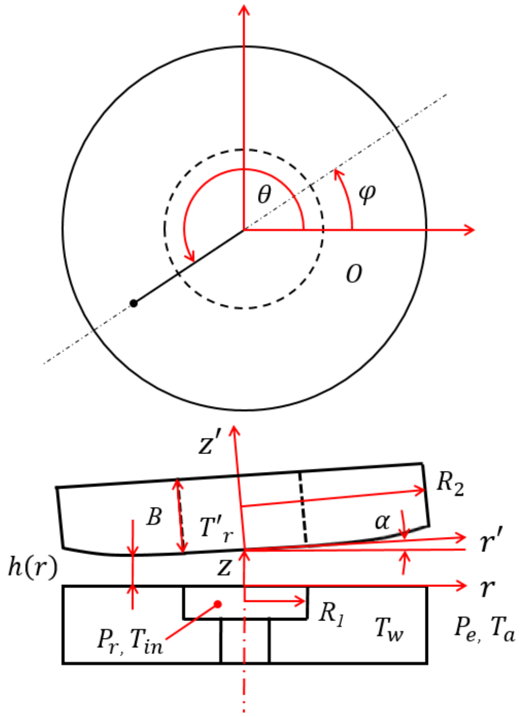

Figure 1. Schematic Diagram of the Flange-Type Gasket Model.

The coupled differential equations contain the generalized Reynolds equation [Eq. (1)], energy equation of the oil film [Eq. (2)], heat conduction equation of upper flange [Eq. (3)], and equations of the lubricant physical properties.

$$\frac{1}{r}\frac{\partial}{\partial r}\left(F_2 r\frac{\partial p}{\partial r}\right)+\frac{1}{r^2}\frac{\partial}{\partial \theta}\left(F_2\frac{\partial p}{\partial \theta}\right)=0 \tag{1}$$

$$\rho c_p\left(u\frac{\partial T}{\partial r}+\frac{v}{r}\frac{\partial T}{\partial \theta}+w\frac{\partial T}{\partial z}\right)=\frac{\partial}{\partial z}\left(\lambda\frac{\partial T}{\partial z}\right)+\mu\phi \tag{2}$$

$$\frac{1}{r\prime}\frac{\partial}{\partial r\prime}\left(r'\frac{\partial T\prime}{\partial r\prime}\right)+\frac{1}{r\prime^2}\frac{\partial^2 T\prime}{\partial \theta^2}+\frac{\partial^2 T\prime}{\partial z\prime^2}=0 \tag{3}$$

where c_p is the specific heat capacity of lubricating oil and λ is the thermal conductivity. Functions of F_0, F_1, F_2, dissipation function ϕ, and boundary conditions of pressure and temperature coincide with those in Reference [8]. Gap space h, flow velocity u, and leakage Q_{out} from the gap at the edge of disk ($r = R_2$) are expressed as follows:

$$h = h_c + \alpha r\cos(\theta-\varphi)+\delta\left(\frac{r-R_1}{R_2-R_1}\right)^2 \tag{4}$$

$$u=\frac{\partial p}{\partial r}\left(\int_0^z\frac{z}{\mu}\mathrm{d}z-\frac{F_1}{F_0}\int_0^z\frac{\mathrm{d}z}{\mu}\right) \tag{5}$$

$$Q_{out}=\int_0^{2\pi}\int_0^h uR_2\,\mathrm{d}z\,\mathrm{d}\theta \tag{6}$$

where α is the inclination angle of the gap space and δ is the surface-flatness coefficient. $\delta < 0$ indicates that the flange surface is concave. $\delta = 0$ indicates a flat surface. $\delta > 0$ indicates the convex flange surface. The viscosity–temperature relationship in the lubricating oil is expressed as

$$\nu = \nu_0 \exp[-\beta(T - T_0)] \tag{7}$$

where β is the oil viscosity–temperature index, which is a constant associated with temperature T_0. In this study, viscosity is a single function of temperature, and the other oil physical properties, including density, coefficients of specific heat, and thermal conductivity, can be considered constant. The Reynolds, energy, and heat conduction equations, are coupling solved using FDM, and the equations are calculated by iteration.
The upper and lower disks are classified as A5052 in JIS and SUS303, respectively. The selected disk parameters are as follows: inner and outer radii are $R_1 = 60$ and $R_2 = 100$ mm, and disk thickness $B = 10$ mm at position $r = R_1$. The lubricant property is selected as that of ISO VG32 oil using calculation. The other input parameters are as follows: $\rho = 869\ \mathrm{kg/m^3}$, $\nu_0 = 32.6 \times 10^{-6}\ \mathrm{m^2/s}$, $\beta = 0.02969\ [1/°\mathrm{C}]$ at $T_0 = 40$ °C, $c_p = 1860$ J/(kg · K), $\lambda = 0.130$ W/(K · m), $\mu = \rho\nu$, $\lambda' = 16.3$ W/(K · m), $h_t = 50$ W/(m^2 · K), and $T_{in} = T'_r = T_a = 20$ °C. The effects of the surface shape on gasket sealing performance such as the temperature distribution, flow velocity, and leakage are presented in the Results and Discussion section.

RESULTS AND DISCUSSION

Theoretical Solutions of the Effect of δ on the Temperature Distribution

Figure 2 shows that the gap space h changes with three kinds of flatness coefficient δ along radius under parallel gap with a central gap of $h_c = 0.15$ mm. We observe that clearance increases with a larger value of δ along the r direction. In this study, all theoretical calculations are performed under the conditions of $h_c = 0.15$ mm and $P_r = 1.4$ kPa. The effect of δ on the gasket sealing performance with circular flanges is discussed relative to these three types of sealing surface as shown in Fig. 2.

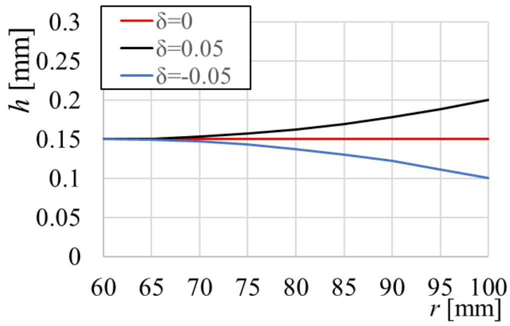

Figure 2. Variation in Gap Space h with Radius r under a Parallel Gap Condition ($h_c = 0.15$ mm).

Temperature Solutions under a Parallel Gap Condition

Figures 3–5 show the theoretical results of the temperature contour map in the section of upper flange and oil film for parallel flange with flat ($\delta = 0$), convex ($\delta = 0.05$), and concave ($\delta = -0.05$) sealing surfaces, respectively. The upper and lower parts indicate the flange and oil domains. The temperature in the abscissa ($z = 0$) represents the solid wall temperature ($T_w = 5$ °C). Although the temperature values at each grid node in the lubricant film are slightly different, they can be feasibly controlled by T_w in all three cases.

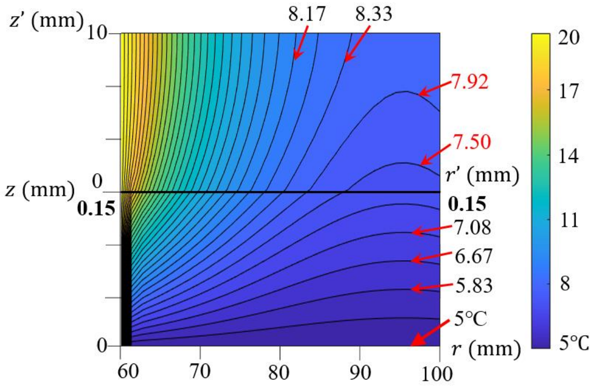

Figure 3. Theoretical Result of T and T' with a Flat Flange Derived by the THL Theory ($\delta = 0$).

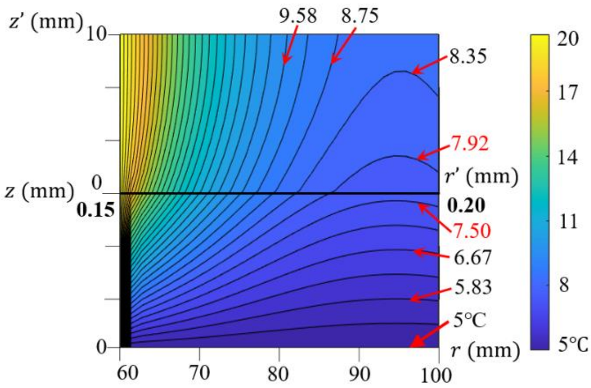

Figure 4. Theoretical Result of T and T' with a Convex Flange Derived by the THL Theory ($\delta = 0.05$).

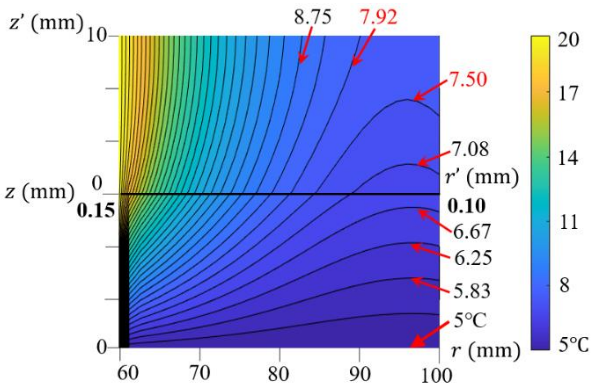

Figure 5. Theoretical Result of T and T' with a Concave Flange Derived by the THL Theory ($\delta = -0.05$).

Figure 3 shows the temperature distribution for a flat flange ($\delta = 0$). Figure 4 shows the convex flange condition ($\delta = 0.05$). The gap space increases to $h = 0.2$ mm at the edge of disk at $r = R_2$. It decreases to $h = 0.1$ mm in the concave flange ($\delta = -0.05$), as shown in Fig. 5. We need to mention that in order to intuitively observe the temperature contour in the cross section of flange and oil film, disk thickness B and gap space h are plotted at equidistant positions in Figs. 3–5. However, the gap space changes along the radial direction at $\delta \neq 0$. Therefore, we show the specific values of the gap space at the oil inlet ($r = R_1$) and outlet ($r = R_2$) in Figs. 3–5.
Figures. 3–5 show the contour line of $T = 7.50$ °C and 7.92 °C, which is marked in red, to indicate the positions of the same contour in three cases. By comparing the result with the flat flange case, the locations of the marked contours point downward in the convex flange ($\delta = 0.05$), and the overall temperature in the oil film is relatively deviated from target value T_w. These values shift upward in the concave flange case ($\delta = -0.05$), and the oil film temperature approaches T_w. In other words, the temperature of oil film area can be easily controlled by the solid wall using a flange with a concave sealing surface.

Temperature Solutions under the Condition of Gap with an Inclination Angle

Figures 6–8 show the temperature contour in the interface between the gap and the upper flange, i.e., $T_{z=h}$ ($T'_{z'=0}$) under an inclined flange condition ($\alpha = 0.057°$) with flat ($\delta = 0$), convex ($\delta = 0.05$), and concave ($\delta = -0.05$) sealing surfaces, respectively. The solid wall temperature is set at $T_w = 5$ °C. Although the gap–disk interface is not a flat circle because of the axial deformation at $\delta \neq 0$, as shown in Figs. 7 and 8, they are still expressed in a circular form for comparison with the flat case shown in Fig. 6.
We can observe that the small variations in temperature exist in the gap–disk interface, which is affected by the different values of flatness coefficient δ. The temperature at the interface agrees with that of the solid wall, and the temperature point near the minimum gap position (h_{min}) the most coincides with T_w in all the three cases. In comparison with the flat flange, the overall temperature at the interface is generally deviated from the solid wall temperature T_w in the gap with the convex flange. However, it is closer to T_w in concave case, as shown in Fig. 8. The overall temperature values in the oil film was much more theoretically agrees with the target value T_w in the smaller gap space condition.

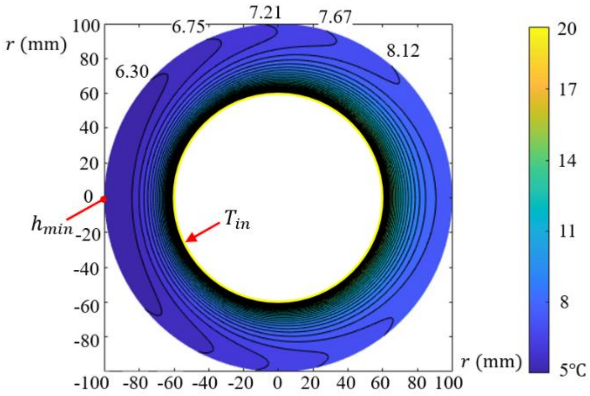

Figure 6. Temperature Contour in the Gap–Disk Interface in an Inclined Gap with a Flat Flange ($\delta = 0$).

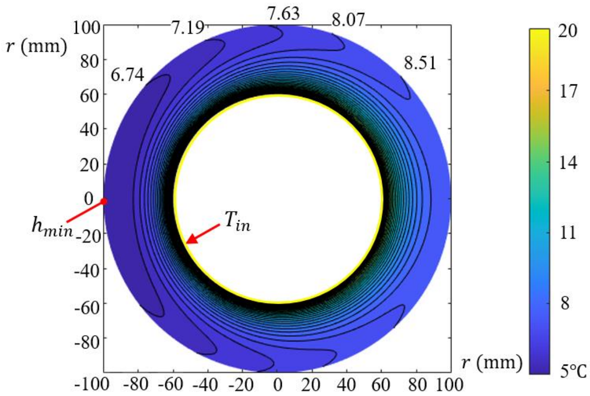

Figure 7. Temperature Contour in the Gap–Disk Interface in an Inclined Gap with a Convex Flange ($\delta = 0.05$).

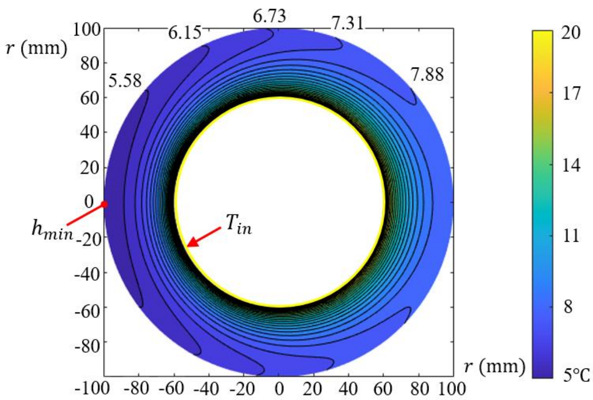

Figure 8. Temperature Contour in the Gap–Disk Interface in an Inclined Gap with a Concave Flange ($\delta = -0.05$).

Theoretical Solutions of the Flow Velocity and Leakage

Flow Velocity under a Parallel Gap Condition

Figures 9–11 show the distribution of flow velocity u along the radius in terms of the z value under parallel gap using flange with flat ($\delta = 0$), convex ($\delta = 0.05$), and concave ($\delta = -0.05$) sealing surfaces, respectively. The solid wall temperature is $T_w = 5$ °C. The specific values of the gap space at the oil inlet and outlet are also shown. Compared with the flat flange case as shown in Fig. 9, the flow velocity of with convex sealing surface decreases near the oil outlet, as shown in Fig. 10, and the closer the surface is to the outlet, the larger is the decrease in the gradient. Meanwhile, the flow velocity of with concave sealing surface increases, as shown in Fig. 11. The velocity difference in three cases can be mainly attributed to the difference in the rate of change in gap along r direction.

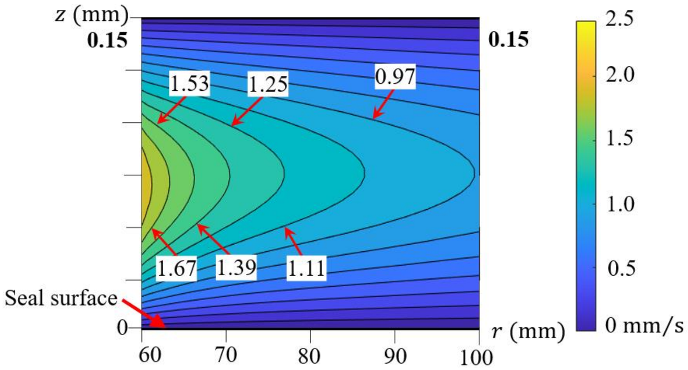

Figure 9. Distribution of Velocity u for a Flat Sealing Surface ($\delta = 0$).

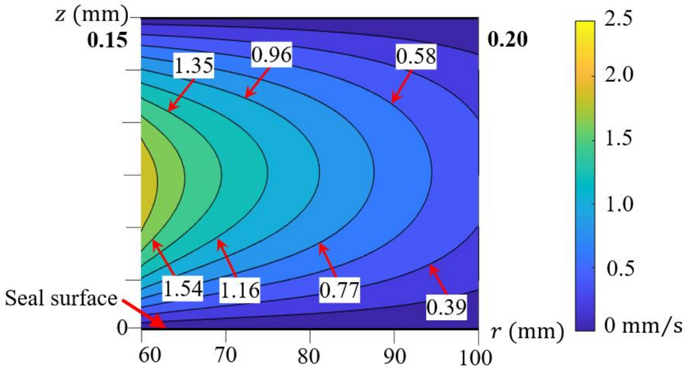

Figure 10. Distribution of Velocity u for a Convex Sealing Surface ($\delta = 0.05$).

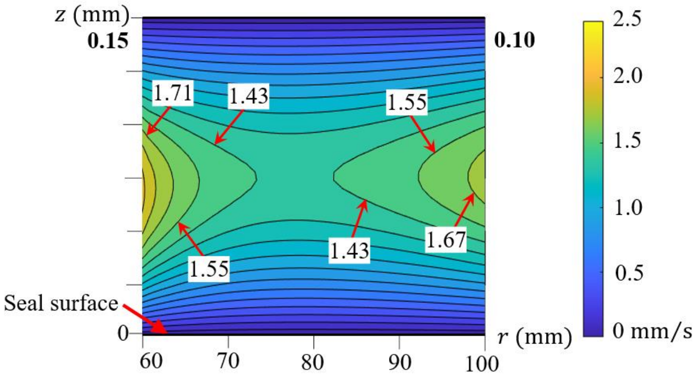

Figure 11. Distribution of Velocity u for a Concave Sealing Surface ($\delta = -0.05$).

Leakage Flow under Both Conditions of Parallel and Inclined Gap

Figure 12 shows the effects of flatness coefficient δ of the flange surface on the leakage flow under parallel gap condition. Figure 13 shows the effects of δ on the leakage flow under the inclined gap with $\alpha = 0.057°$. Solid wall temperature T_w is varied from 5 ℃ to 45 ℃, and the temperature interval is 10 ℃.
Comparison of the parallel and inclined gap cases reveals that the leakage increases under the inclined case at the same values of h_c and P_r. The leakage also increases with larger flatness coefficient δ, and the leakage–restraint phenomenon is most obvious in the flange with concave surface in both cases of parallel and inclination, as shown in Figs. 12 and 13. The main reason is that the a larger flatness coefficient corresponds to a larger gradient in gap space along the r direction, i.e., the gap space is larger at the edge of disk ($r = R_2$) while the center gap remains the same. Another reason is that when the gap is larger, controlling the oil film temperature by solid wall is more difficult. However, although the leakage increases with a larger flatness coefficient, it still can be suppressed by lowering the temperature in the flanges with different types of sealing surfaces under parallel and inclined gaps.

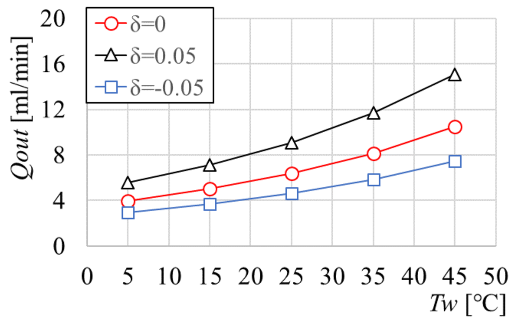

Figure 12. Effect of δ on the Leakage Flow under Parallel Gap Conditions (α = 0°).

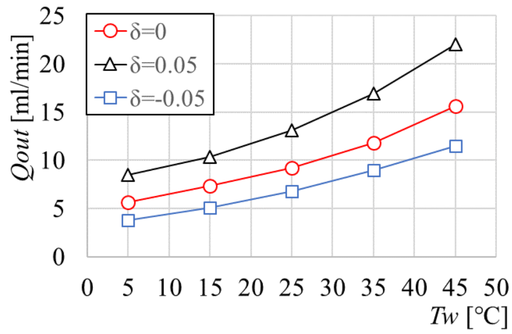

Figure 13. Effect of δ on the Leakage under Inclined Gap Conditions (α = 0.057°).

CONCLUSIONS

In this study, a theoretical model for analyzing the temperature, flow velocity, and leakage of a flange-type gasket was developed using the viscosity–temperature relationship. The THL theory was applied to the gap flow under the sealing surface of installed flat, convex, and concave flanges. The leakage and oil film temperature were theoretically calculated using the surface flatness coefficient and inclination angle were considered as the main parameters. When the temperature of the sealing flange was controlled, the leakage varied under the range of the flatness coefficient and inclination angle. The conclusions of this study are presented as follows:

(1) The oil film temperature could theoretically agree with that of solid wall under various conditions independent of the shape of sealing surface and parallel configuration of the gap.

(2) Comparing to flat flange, the flow velocity in the concave flange theoretically increased along radius for both conditions of parallel and inclined gap. The closer the outlet was, the larger was the gradient increase.

(3) Irrespective of the inclination angle, the leakage could be most obviously restrained by lowering temperature of the sealing parts by using a flange with a concave surface.

REFERENCES

1. JIS B0116, Glossary of Terms of Packing and Gaskets, 2015.
2. ASTM F118, Standard Definitions of Terms Relating to Gaskets, American Society for Testing and Materials, 1985.
3. PERSSON, B. N., Leakage of Metallic Seals: Role of Plastic Deformations, Tribology Letters, Vol.63, 2016, 42.
4. LEHN, A., MAHNER, M., SCHWEIZER, B., A Thermo-Elasto-Hydrodynamic Model for Air Foil Thrust Bearings Including Self-Induced Convective Cooling of the Rotor Disk and Thermal Runaway, Tribology International, Vol.119, 2018, pp.281-298.
5. GADARI, M. E., FATU, A., HAJJAM, M., Shaft Roughness Effect on Elasto-Hydrodynamic Lubrication of Rotary Lip Seals: Experimentation and Numerical Simulation, Tribology International, Vol.88, 2015, pp.218-227.
6. SHINKARENKO, A., KLIGERMAN, Y., ETSION, I., The Effect of Surface Texting in Soft Elasto-Hydrodynamic Lubrication, Tribology International, Vol.42, 2009, pp.284-292.
7. KAZAMA, T., GAO, S., Gap Flow Between Two Circular Plates with Temperature-Controlled Wall: Application of Thermohydrodynamic Lubrication Theory and Comparison with an Iso-Viscous Model, Mechanical Engineering Letters, Vol.6, 2020, 20-00292.
8. GAO, S., KAZAMA, T., Leakage Control for a Flat Flange Model with a Gap Based on Sealing Liquid Viscosity, Journal of Advanced Mechanical Design, Systems, and Manufacturing, Vol.15, No.3, 2021, 21-00065.

The 11th JFPS International Symposium on Fluid Power HAKODATE 2020 Oct. 12-13, 2021 JFPS The Japan Fluid Power System Society

Experimental Analysis of Rotational Motion of Pistons and Slippers of a Swashplate Axial Piston Pump Using Visualization Technique

Takumi FURUYA*, Toshiki HAGA*, and Toshiharu KAZAMA**

*Division of Production Systems Engineering, Graduate School of Muroran Institute of Technology
27-1 Mizumoto-cho, Muroran, Hokkaido, 050-8585 Japan
**College of Design and Manufacturing Technology, Graduate School of Muroran Institute of Technology
27-1 Mizumoto-cho, Muroran, Hokkaido, 050-8585 Japan
(E-mail: kazama@mmm.muroran-it.ac.jp)

Abstract. The spinning motion of the pistons and slippers of a swashplate-type axial piston pump was investigated using a visualization technique. The pump casing was partially replaced with transparent acrylic resin plates. The pistons and slippers with the cylinder block and the swashplate were visualized using a high-speed video camera. Images were extracted from the video and were analyzed, and their behavior was also examined experimentally. The shaft rotational speed and discharge pressure were as high as 1500 rpm and 5 MPa, respectively. By changing the pump's mounting posture, the motion of the pistons and slippers were observed from almost all circumferential directions to cover both discharge and suction ports. The experimental results revealed that the changes in the slipper spin exceeded those in the piston spin.

Keywords: Hydraulic pump, Piston assembly, Spin, High-speed camera, Tribology

INTRODUCTION

A swashplate-type piston pump can handle high pressures while ensuring a high degree of safety, compactness, and efficiency [1]. The piston assembly of the pump comprises pistons and slippers, which are connected with a ball joint. The piston reciprocates in a cylinder bore with the swashplate [2], and the slipper is attached to the other end of the piston to support high and fluctuating loads while sliding at low to high speed on the swashplate's sliding surface [3].
The pistons and slippers also rotate around the main driving shaft while spinning around the cylinder-bores' axis. The rotation and spin behaviors of the pistons and slippers influence the pump's reliability and performance. Few studies have investigated this subject theoretically and experimentally [4]. However, the motion of these parts remains sufficiently unclarified.
Herein, the spinning motion of the piston and slipper is visualized using a high-speed video camera, and their behavior is experimentally examined.

EXPERIMENT

Test Apparatus and Method

Figure 1 shows the hydraulic circuit of the test apparatus [5], which comprises a test pump, a three-phase induction motor (7.5 kW), an electric inverter, a torque transducer (20 N·m), a flow meter, pressure sensors, thermometers, an oil cooler, hydraulic valves, and a reservoir.
The test pump was developed by modifying the commercial swashplate axial piston pump of a rotating cylinder-block type. The basic specifications of the original pump were as follows: maximum pressure = 21 MPa, maximum rotational speed = 1800 rpm (30 s^{-1}), theoretical discharge = 10 ml/rev, and number of pistons = 9. Also, transparent acrylic windows were installed in the revamped casing to observe the motion of the pistons and slippers. The piston assemblies were numbered from one to nine to differentiate between each piston and slipper. Moreover, each piston and slipper were marked with a permanent marker pen to track the rotating motion.
Mineral oil-type hydraulic fluid (density: 869 kg/m^3 at 15°C; kinematic viscosity: 32.6 mm^2/s at 40°C and 5.49 mm^2/s at 100°C) was used as the test oil.

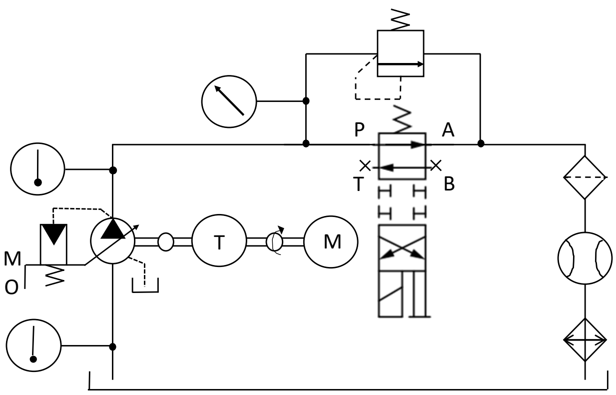

Figure 1. Schematic representation of apparatus' hydraulic circuit.

Image Analysis and Test Conditions

A high-speed video camera and two metal halide lamps were used to record the motion. The distance between the video camera's lens and the test pump's window was set as 310 mm, and the lamps were placed at both sides of the camera. The frame rate was 4000 fps, and the shutter speed was 1/20000 s.
The oil temperature was maintained at 30°C. The pump's rotational speed and discharge pressure were set up to 1500 rpm (25 s^{-1}) and 5 MPa, respectively. The motion of the pistons and slippers was observed and recorded at the center of the discharge (0 rad) and suction (π rad) ports and at postures of $-\pi/4$, $\pi/4$, $3\pi/4$, and $5\pi/4$ rad.
Because a reference location was required to analyze the motion, a jig of a metallic stick was used before recording the motion (Fig. 2). Different images were extracted from the video, which enabled reading the position coordinates (Fig. 3). The images were extracted for every 1 and 10 frames of the conditions at 150 and 1500 rpm, respectively. To avoid errors based on the objects' curvature, the data when the pistons and slippers were crossing at the centerline of the main shaft were adopted. Thus, the number of frames for the image analysis was 12–18 each.

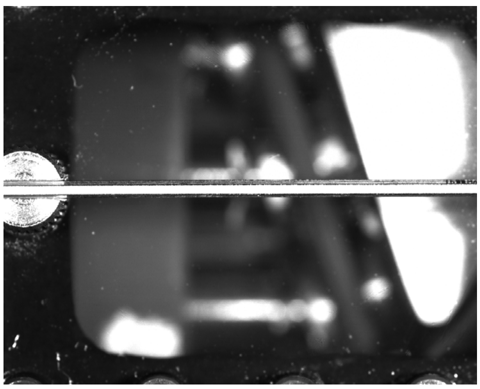

Figure 2. Reference position indexing in images.

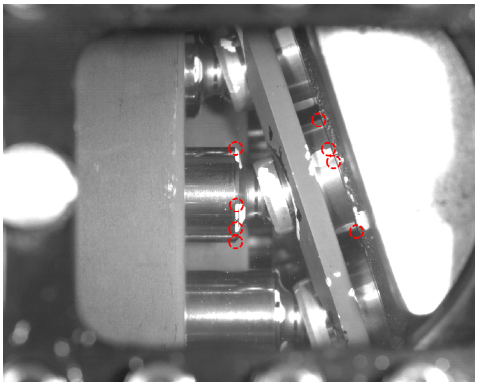

Figure 3. Measuring points of pistons and slippers extracted from a video frame (unloaded, 300 rpm (5 s^{-1}), full swashplate angle, and 0°-pump posture).

RESULTS AND DISCUSSION

Figures 4 and 5 show the rotational motion of the pistons and slippers under the conditions of full and half swashplate angles, respectively. The pump's rotational speed was set as 2.5 and 25 s^{-1}, and the discharge pressure was set at unloaded (slightly > atmospheric pressure) and 5 MPa. The parameter is the ratio of the spinning speed of the pistons and slippers to the rotational speed of the pump's main shaft. Thus, a zero value of the ratio indicates that the spinning speed coincides with the shaft speed, and a positive value implies that the spinning speed exceeds the shaft speed and vice versa. In Figs. 4 and 5, the left (pump angle from $-\pi/2$ to $\pi/2$) and right (pump angle from $\pi/2$ to $3\pi/2$) halves approximately correspond to the discharge and suction ports, respectively.

For all conditions, the fluctuation of the ratio of the slippers exceeded that of the pistons. Comparing Figs. 4 and 5, the fluctuation of the full angle (Fig. 4) was much marked than that of half-angle (Fig. 5). Besides, the ratios and their fluctuations became higher at the centers of both the discharge and suction ports, especially for the slippers under full swashplate angle condition.

Moreover, the slippers' spinning motion of the unloaded condition and that of the 5 MPa condition almost coincided in the half-angle case (Fig. 5, right-hand side), implying that the discharge pressure less affected the slippers' spinning. Overall, for conditions of full and half swashplate angles, the mean values of the ratios of the slippers were positive, whereas the values of the pistons were almost zero.

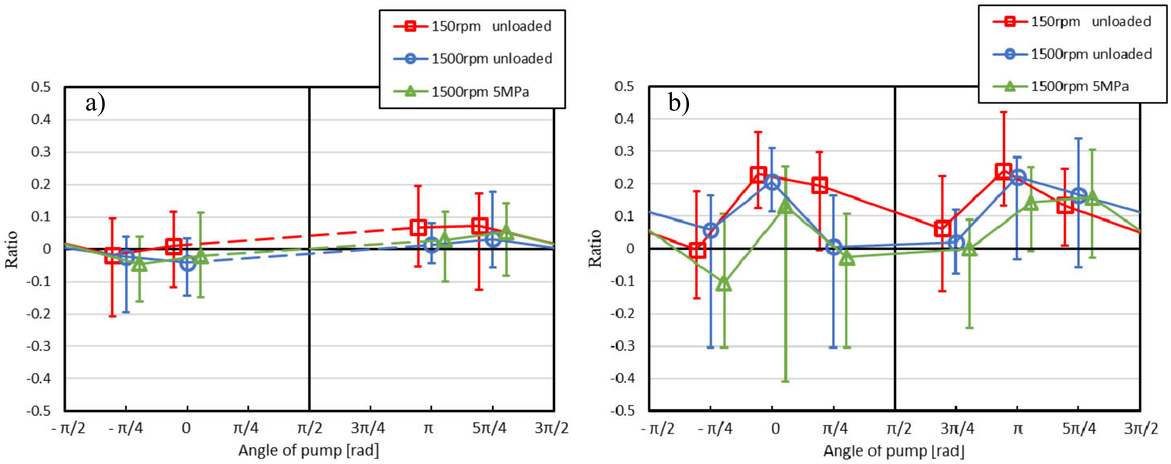

Figure 4. Spin ratio comparison of pistons and slippers for maximum swashplate angle (a: piston; b: slipper).

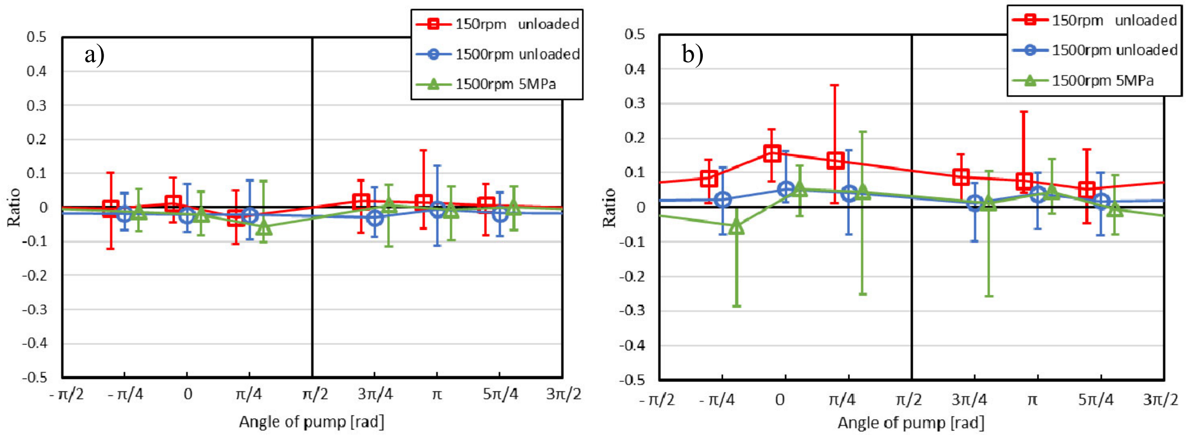

Figure 5. Spin ratio comparison of pistons and slippers for half swashplate angle (a: piston; b: slipper).

CONCLUSIONS

The motion of the pistons and slippers was measured using a visualization technique. Under the present conditions, the variation of the slippers' rotation exceeded that of the pistons, and the rotational speed of the slippers was slightly higher than that of the shaft over the entire circumference.

ACKNOWLEDGMENTS

The authors are grateful to Yuken Kogyo Co., Ltd. for supplying the test pump.

REFERENCES

1. YAMAGUCHI, A., TANAKA, H., Hydraulics and Pneumatics, 1986, Corona Pub. Co., Ltd. (in Japanese)
2. KAZAMA, T., Comparison of Temperature Measurements and Thermal Characteristics of Hydraulic Piston, Vane, and Gear Pumps, Mechanical Engineering Journal, 2015, 2-3, pp.14-00542.
3. KAZAMA, T., SUZUKI, M., SUZUKI, K., Relation between Sliding-Part Temperature and Clearance Shape of A Slipper in Swashplate Axial Piston Motors, JFPS International Journal of Fluid Power System, 2015, 8-1, pp.10-17.
4. CHAO, Q., WANG, Q., XU, B., CHEN, Y., LI, Y., Experimental Investigations of the Slipper Spin in an Axial Piston Pump, Measurement, 2017, 102, pp.112-120.
5. HAGA, T., KAZAMA, T., Visualization Measurement of Rotational Motion of Pistons and Slippers of A Piston Pump (Preliminary Experiment), Proceedings of MoViC2019, 2019, C102. (in Japanese)

The 11th JFPS International Symposium on Fluid Power HAKODATE 2020 Oct. 12-13, 2021 JFPS The Japan Fluid Power System Society

Feasibility and Precision Analysis of a Test Rig with Adjustable Oil Film Thickness

Haiji WANG* and Guanglin SHI *

* School of Mechanical Engineering, Shanghai Jiaotong University
800 Dongchuan Rd, Shanghai, 200240 Japan
(E-mail: glshi@263.net)

Abstract. In the present study, a test rig with adjustable oil film thickness for the slipper is proposed. The mathematical model of the oil film thickness, pressure and temperature is demonstrated. The mechanism of the test rig including the test system, hydraulic system, control system and data collection is shown. The feasibility of the test rig shows that the oil film thickness of the slipper can be precisely adjusted. It's found that the relative errors of the reacting force, torque and temperature in the experiment and simulation are mainly due to the deformation of the retainer. The secondary cause is the pressure fluctuation and temperature increasing from the input oil. The relative errors of the characteristics are less when the simulation is modified. Based on the test rig, further works such as testing the optimized slipper and finding the minimum energy consumption of different operating conditions are prepared to fulfill.

Keywords: Feasibility and precision, Adjustable oil film thickness, Slipper, Test rig.

INTRODUCTION

Slipper/swash-plate pair is the most significant lubricating interface in the piston pump. A suitable oil film forms to separate heavily loaded relatively movable parts in each other[1]. Many researches and optimizations of the piston pump mentioned the importance of the lubrication characteristics[2-5]. Therefore, a test rig for detecting the lubrication characteristics is valuable.

Before 21st Century, Hooke and Kakoullis fulfilled a test rig to measure the oil film thickness with the capacitance displacement sensor[6]. They analyzed the influence of centrifugal force and friction of ball joint between piston and slipper on the lubrication of slipper/swash-plate pair. Based on this test rig, Koc measured the oil film thickness of slipper/swash-plate pair with different sizes of orifice, eccentricity and overclamp ratio[7-10].

After 21st Century, more researchers carried out excellent works on lubrication of slipper/swash-plate pair. Ai designed a test rig which is different from Prof. Hooke's test rig[11-13]. They can continuously measure the thickness since the displacement sensor placed on the retainer of the slipper. Torque loss of the slipper can be measured based on Canbulut's test rig in order to evaluate the oil film thickness[14,15]. Manring placed three pressure sensors on the swash-plate, in order to describe the pressure distribution of the slipper/swash-plate pair[16]. In order to carry out the oil film thickness and torque resulting from the tilting slipper, Rokala used three displacement sensors and force sensor in the test rig[17,18]. This kind of test rig is improved by Xu[19-23]. Displacement sensor, torque sensor and pressure sensor are all placed to find out the slipper motion in axial piston pump. Schenk finished a test rig with six displacement sensors o the swash-plate in order to get the instantaneous oil film thickness[24].

From now on, there are two methods to measure the oil film thickness. The displacement sensor can be placed in the swash-plate or it can be placed in the retainer of the slipper. Assume that the measurement rig is a system, the size of the slipper and the operating condition are the input of this system, and the lubrication characteristics such as oil film thickness, pressure distribution, torque even temperature are the output. However, oil film thickness has great effect on the other lubrication characteristics. Therefore, the oil film thickness should be the input of measurement rig. In the above test rigs, the oil film thickness can be measured, but it can't be controlled. In this paper, authors propose an adjustable oil film thickness test rig. The oil film thickness can be adjusted by three couples of step motor and universal joint coupling. The accuracy of the test rig is determined by a three-coordinate measuring machine and three displacement sensors. The simulation of lubrication characteristics is finished in Matlab. The results from test rig are compared with the results from the simulation. The reasons for the errors between the experiment and simulation are analyzed. It's found that the main cause of the errors is the deformation of the retainer. After the modification of the simulation, the relative errors between the experiment and modified simulation reduce. Compared with authors' last research[25], the temperature effect on the test rig is considered in this paper.

DESCRIPTION OF OIL FILM

Oil Film Thickness

The thickness distribution of oil film of slipper/swash-plate pair is the basic characteristics. The effect of overturning moment makes a tilt when the slipper slides on the swash-plate. Therefore, the thickness of each point of the slipper sealing land is different. Oil film thickness is determined by the height of three points. Figure 1 shows the location and height of three points. Point A, point B and point C are located on the outermost side of the slipper sealing land. The angle between these points is 120° . The heights of each point are h_1, h_2 and h_3 separately. Since the coordinates of three points are $(0,R,h_1),(\frac{\sqrt{3}}{2}R,-\frac{1}{2}R,h_2),(-\frac{\sqrt{3}}{2}R,-\frac{1}{2}R,h_3)$, Eq. (1) shows the equation of oil film.

$$\begin{vmatrix} x & y & z & 1 \\ 0 & R & h_1 & 1 \\ \frac{\sqrt{3}}{2}R & -\frac{1}{2}R & h_2 & 1 \\ -\frac{\sqrt{3}}{2}R & -\frac{1}{2}R & h_3 & 1 \end{vmatrix} = 0 \tag{1}$$

The oil film thickness distribution in Cartesian coordinate and Polar coordinate is described in Eq. (2) and Eq. (3).

$$h(x,y)=\frac{\sqrt{\frac{1}{3}}}{R}(h_2-h_3)x+\frac{1}{3R}(2h_1-h_2-h_3)y+\frac{1}{3}(h_1+h_2+h_3) \tag{2}$$

$$h(r,\theta)=\frac{\sqrt{\frac{1}{3}}}{R}(h_2-h_3)r\cos\theta+\frac{1}{3R}(2h_1-h_2-h_3)r\sin\theta+\frac{1}{3}(h_1+h_2+h_3) \tag{3}$$

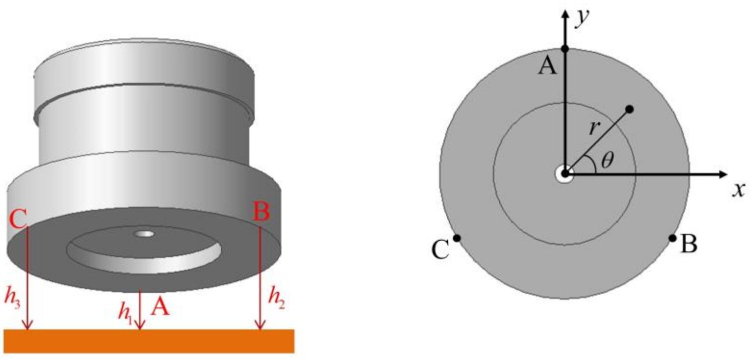

Figure 1. Oil film thickness model 1.

In Figure 2, the oil film thickness distribution can also be described by the center height of the slipper h_c , the tilt angle α and the phase angle ϕ . Eq. (4) shows the thickness distribution by this approach. The thickness and shape are clearly demonstrated. Referred to Eq. (1) and Eq. (4), the relationship between the height of three points and the center height of the slipper, the tilt angle and the phase angle is shown in Eq. (5). The thickness and shape of oil film can be determined by Eq. (4). The height of three points can be adjusted by three step motors of test rig. Therefore, it's realized that the thickness and shape of oil film can be determined by the test rig. The lubrication characteristics in different conditions are measured by the test rig.

$$h = h_c + R\tan\alpha\cos(\theta - \phi) \tag{4}$$

$$\begin{aligned} h_1 &= h_c + R\tan\alpha\cos(\frac{\pi}{2} - \phi) \\ h_2 &= h_c + R\tan\alpha\cos(-\frac{\pi}{6} - \phi) \\ h_3 &= h_c + R\tan\alpha\cos(\frac{7\pi}{6} - \phi) \end{aligned} \tag{5}$$

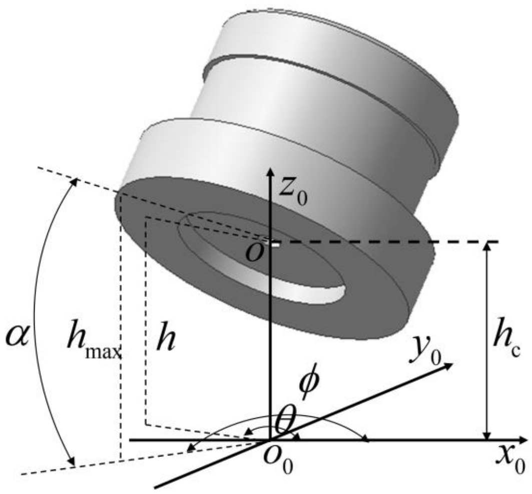

Figure 2. Oil film thickness model 2.

Oil Film Pressure

Researchers studied a lot on oil film pressure distribution. An incompressible Reynolds equation models the distribution of pressure under the slipper sealing land. Eq. (6) shows the Reynolds equation in Polar coordinate. The hydrostatic effect is illustrated on the left hand side of Eq. (6). On the right hand side, the first two parts express the hydrodynamic effect meanwhile the third part expresses the squeeze effect.

$$\frac{1}{r}\frac{\partial}{\partial r}\left(rh^3\frac{\partial p}{\partial r}\right) + \frac{1}{r^2}\frac{\partial}{\partial \theta}\left(h^3\frac{\partial p}{\partial \theta}\right) = 6\mu\left(v_{sr}\frac{\partial h}{\partial r} + v_{s\theta}\frac{\partial h}{\partial \theta} + 2\frac{\partial h}{\partial t}\right) \tag{6}$$

The lubrication characteristics such as reacting force and torque are determined by the pressure distribution. Eq. (7), and Eq. (8) show the lubrication characteristics separately[26].

$$F = p_r \pi r_0^2 + \int_0^{2\pi}\int_{r_0}^{R_0} prdrd\theta \tag{7}$$

$$Tor = \int_0^{2\pi}\int_{r_0}^{R_0} R\left[\left(\frac{h}{2}\frac{\partial p}{\partial r} + \frac{\mu v_{sr}}{h}\right)\cos\theta + \left(\frac{h}{2r}\frac{\partial p}{\partial \theta} + \frac{\mu v_{s\theta}}{h}\right)\sin\theta\right] \times rdrd\theta \tag{8}$$

Eq. (9) shows the power loss. The first part on the right hand of Eq. (9) is the power loss of the leakage. The second part is the power loss of the torque. *Tor* is the integral of pressure gradient $\frac{\partial p}{\partial r}$, $\frac{\partial p}{\partial \theta}$ and viscosity friction $\frac{\mu v_{sr}}{h}$, $\frac{\mu v_{s\theta}}{h}$ from r_0 to R_0 and 0 to 2π.

$$\dot{W} = p \times q + Tor \times n \tag{9}$$

Oil Film Temperature

The oil film is regarded as a control volume[27]. The heat generation results from the power loss[23]. The conductive heat transfer is occurred between the oil film and solid parts such as the slipper and swash-plate. The radiative heat transfer is occurred between the solid parts and ambient air. Assume that the oil is incompressible, Eq. (10) expresses the dynamic temperature of oil film[28].

$$\frac{\mathrm{d}T}{\mathrm{d}t} = \frac{1}{\rho c_{\mathrm{p}} V}\left(\rho c_{\mathrm{p}} q\left(T_{\mathrm{in}} - T\right) + \dot{Q} - \dot{W}\right) \tag{10}$$

Figure 3 demonstrates the temperature status between the oil film, slipper and swash-plate. According to Newton's law of cooling, the relationship of the temperature between the oil film, slipper, swash-plate and ambient air is expressed in Eq. (11) and Eq. (12) separately.

$$\frac{T - T_{12}}{R_{\mathrm{c1}}} = \frac{T_{11} - T_{12}}{R_{\mathrm{c2}}} = \frac{T_{12} - T_0}{R_{\mathrm{c3}}} \tag{11}$$

$$\frac{T - T_{21}}{R_{\mathrm{c4}}} = \frac{2_{11} - T_{22}}{R_{\mathrm{c5}}} = \frac{T_{22} - T_0}{R_{\mathrm{c6}}} \tag{12}$$

In Eq. (12), $R_{\mathrm{c1}} = \left(k_0 2\pi r_0 H_1\right)^{-1}$, $R_{\mathrm{c2}} = \ln(R_0 / r_0) / \left(k_1 2\pi r_0 H_1\right)$, $R_{\mathrm{c3}} = \left(k_0 2\pi R_0 H_1\right)^{-1}$. In Eq. (13), $R_{\mathrm{c4}} = \left(k_0 A_{\mathrm{s1}}\right)^{-1}$, $R_{\mathrm{c5}} = H_2\left(k_2 A_{\mathrm{s1}}\right)^{-1}$, $R_{\mathrm{c6}} = \left(k_0 A_{\mathrm{s2}}\right)^{-1}$. Therefore, the heat transfer ratios of between the oil film and ambient air through the slipper and swash-plate are expressed in Eq. (13) and Eq. (14). The rate of heat rejection between the oil film and ambient air is expressed in Eq. (15). Therefore, the entire rate of heat rejection of the control volume is expressed in Eq. (16).

$$\dot{Q}_1 = \frac{T - T_0}{R_{\mathrm{c1}} + R_{\mathrm{c2}} + R_{\mathrm{c3}}} \tag{13}$$

$$\dot{Q}_2 = \frac{T - T_0}{R_{\mathrm{c4}} + R_{\mathrm{c5}} + R_{\mathrm{c6}}} \tag{14}$$

$$\dot{Q}_3 = k_0 2\pi R_0 h_{\mathrm{c}}\left(T - T_0\right) \tag{15}$$

$$\dot{Q} = \dot{Q}_1 + \dot{Q}_2 + \dot{Q}_3 \tag{16}$$

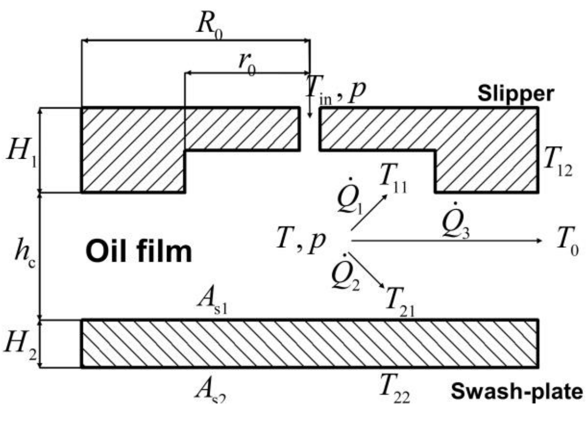

Figure 3. Oil film temperature model.

INTRODUCTION OF TEST RIG

Mechanism of Test Rig

Figure 4 and Figure 5 show the main mechanism of the test rig. Servo motor on the left hand side controls the rotating rate of swash-plate. Two couplings and torque sensor are placed between them. Tapered rolling bearing and thrust rolling bearing are utilized in the end case. They can resist the torque and force resulting from the slipper to the swash-plate separately.

On the right hand side, three step motors control the movement of the retainer. Three couples of bar, universal joint coupling and force sensor are placed between them. The slipper in blue connected with the piston is clamped in the center of the retainer by a circlip. Three eddy current displacement sensors in yellow are distributed over the circumference of the slipper. The laser temperature sensor in red can measure the surface temperature of the slipper.

The schematic of the test rig is built as shown in Figure 6. It mainly includes hydraulic system, cooling system, test system, control system and data logging system. The black curve shows the oil path of the test rig. Meanwhile the red curve and blue curve show the control system and data collection. The test system is driven by a servo motor. The hydraulic system including the servo motor, gear pump, valves and so on offers high pressure oil to the test system. The relief valve and throttle valve adjust the pressure and flow rate of the inlet flow. The unloaded valve protects the hydraulic system when the pressure is too high. All signals obtained from the sensors are collected by a group of ADVANTECH DAQ modules. A Labview program is utilized to control the system and record the data. Besides, the status of test rig is shown in the monitor. Figure 7 shows the test rig in real.

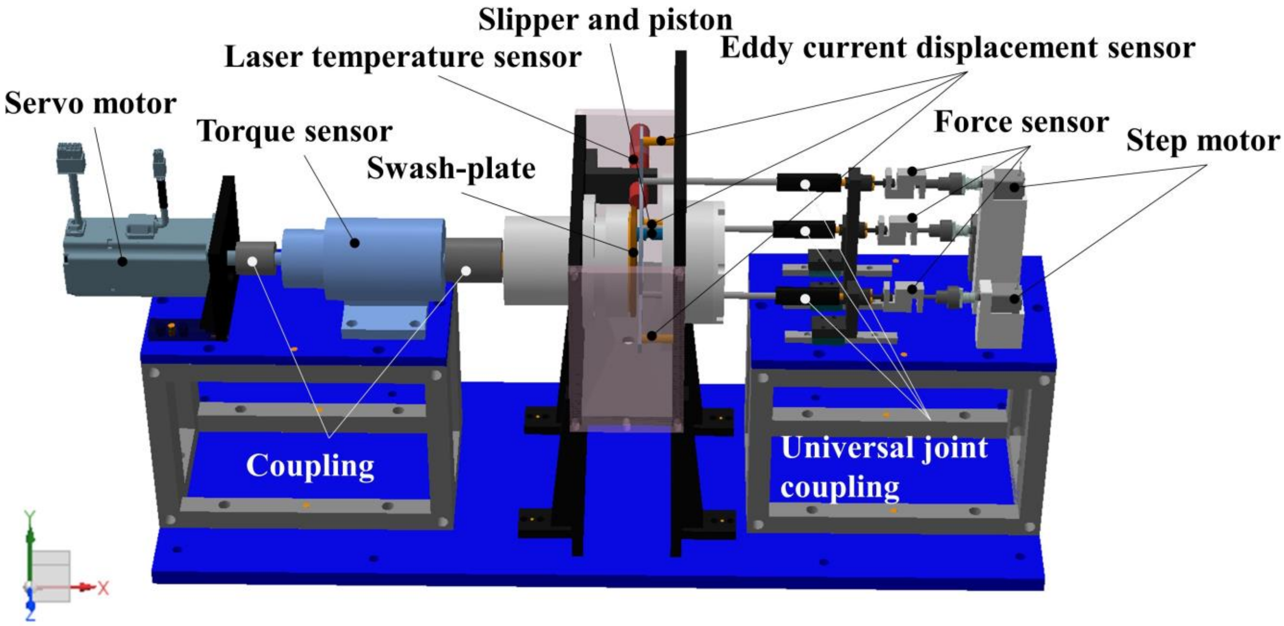

Figure 4. Configuration of test rig.

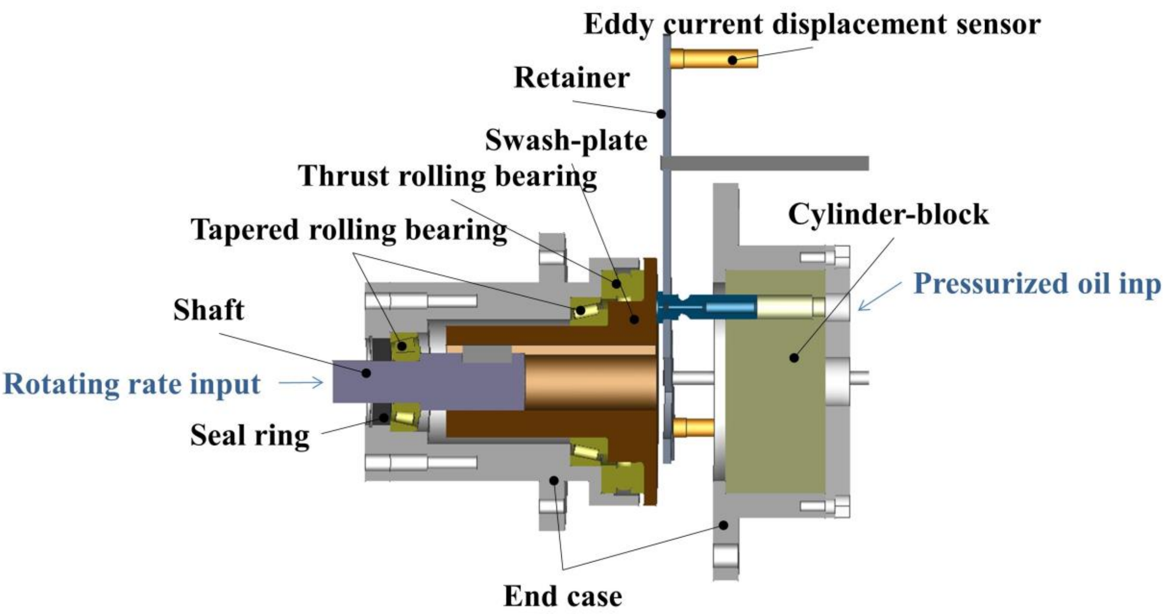

Figure 5. Cross section of key components.

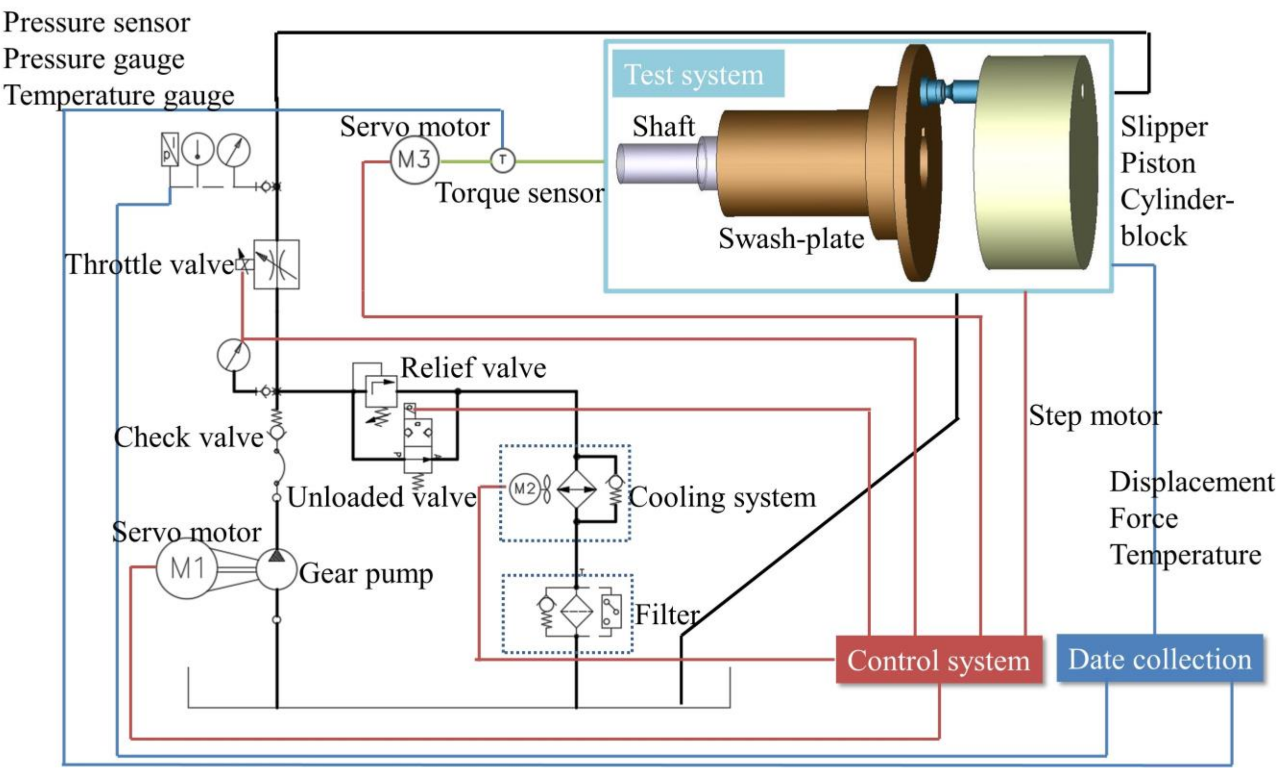

Figure 6. Schematic of measurement.

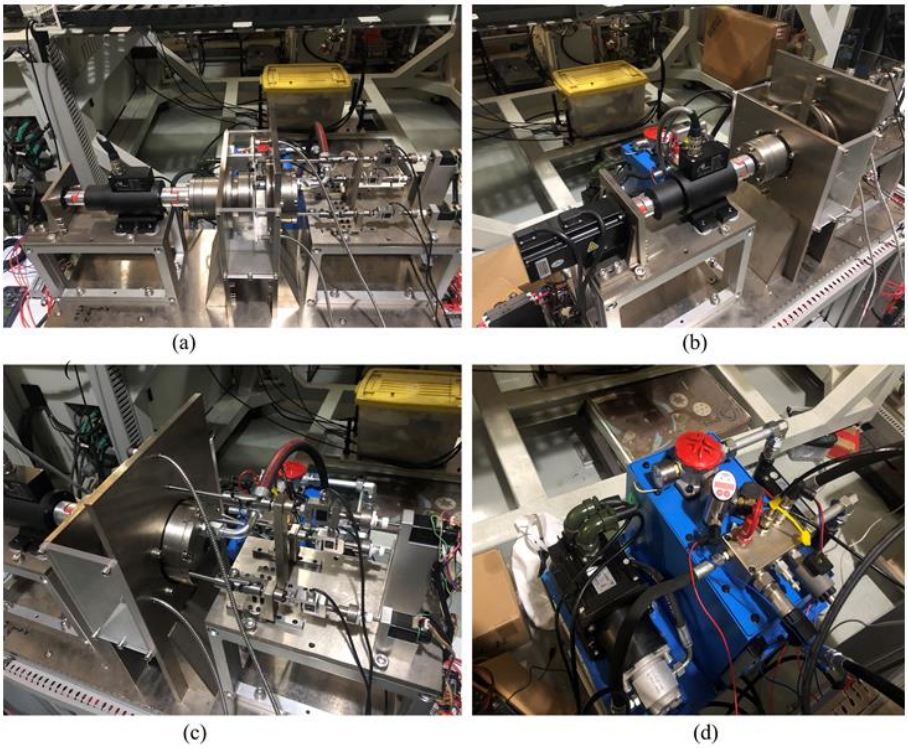

Figure 7. Test rig and components a) shows the entire test rig, b) shows the key components on the left hand side, c) shows the key components on the right hand side, d) shows the hydraulic system.

Table 1 lists the key components of the test rig and their main index. The key components of the hydraulic system are listed on the left hand side. On the right hand side, the range and accuracy of sensors are listed.

Table 1. Parameters of objective axial piston pump.

Description	**Index**	
Servo Motor M1	2000 r/min	
Servo Motor M3	3000 r/min	
Gear Pump	0.66 mL/r	
Relief Valve	Max 20 MPa	
Throttle Valve	Max 1 L/min	
Unloaded Valve	Max 25 MPa	
	Range	**Accuracy**
Torque Sensor	0-0.5 Nm	0.0015 Nm
Pressure Sensor	0-30 MPa	0.03 MPa
Temperature Sensor	0 – 200°C	2°C
Force Sensor	0-500 N	0.5 N
Displacement Sensor	0-5 mm	1 µm
Step Motor	0.3 mm	1.5 µm

Feasibility of Test Rig

The slipper is clasped by the retainer. Meanwhile the retainer, universal joint coupling and step motor can be regarded as a spatial mechanism in 3D coordinate system. The feasibility of motion is decided by the input of system (hereinafter referred to as ʻInput') and the degree of freedom (hereinafter referred to as 'DOF'). Grubler analyzed the relationship between Input and DOF[29]. The mechanism doesn't work when Input is more than DOF; The position of motion can't be guarantee when Input is less than DOF; When Input is equal to DOF, the movement and rotation can be precisely controlled.

Figure 8 shows a brief spatial mechanism of test rig. According to Figure 4 and Figure 5, the number of Input is 3. Seven parts are placed in this mechanism, which are three couples of L-shaped slider and step motor, three universal join coupling and a retainer with bars. L-shaped slider forms sliding pair with ground. Universal joint coupling forms spherical pair with L-shaped slider and retainer separately. Table 2 lists DOF and constraint of this spatial moving mechanism.

Eq. (17) shows the DOF of spatial mechanism. $\sum_{i=1}^{g} f_i$ is the sum of DOF of each pair. For example, DOF of each spherical pair is 3 and there are 6 spherical pairs in this spatial mechanism. Therefore, the entire DOF of spherical pair is 18. Based on Eq. (17), DOF of the proposed spatial mechanism is 3, which is equal to the number of Input. Refer to Figure 4, the movement of retainer along the X axis and the rotation along the Y axis and Z axis can be precisely controlled by three step motors.

$$\begin{aligned} M &= 6\times(N-g-1)+\sum_{i=1}^{g} f_i \\ &= 6\times(7-9-1)+\sum_{i=1}^{9} f_i \\ &= 3 \end{aligned} \tag{17}$$

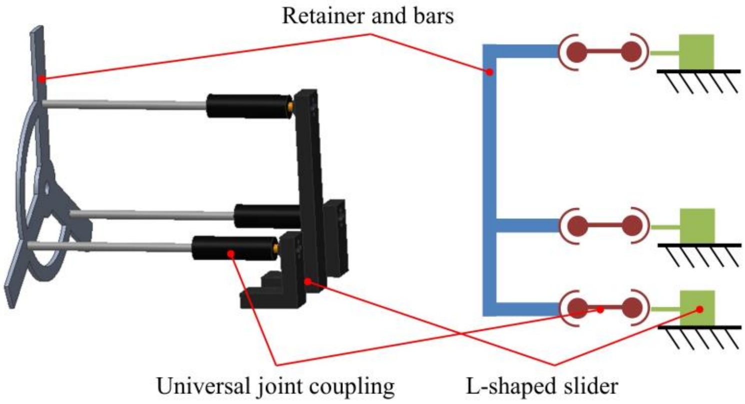

Figure 8. Spatial mechanism.

MEASUREMENT RESULTS

Experiment Introduction

Figure 9 presents the process of simulation and experiment. The simulation is fulfilled in MATLAB. The process of experiment is more complex. It has four steps. In the first step, the thickness between the slipper and swash-plate (oil film) is adjusted by three step motors. After that, run the servo motor of test rig. Record the results from torque sensor and displacement sensor. In this time, the torque is caused by bearing. Therefore, the torque resulting from oil film is the difference between the torque in step 4 and torque in step 2. In the third step, run the servo motor of hydraulic system. The pressurized oil flows to the test system. There’s the reacting force from the slipper sealing land. Since there are very small gaps in universal joint couplings, the shape and thickness of oil film should be adjusted again slightly by the step motors. Finally, all the results such as force, torque and so on can be achieved.

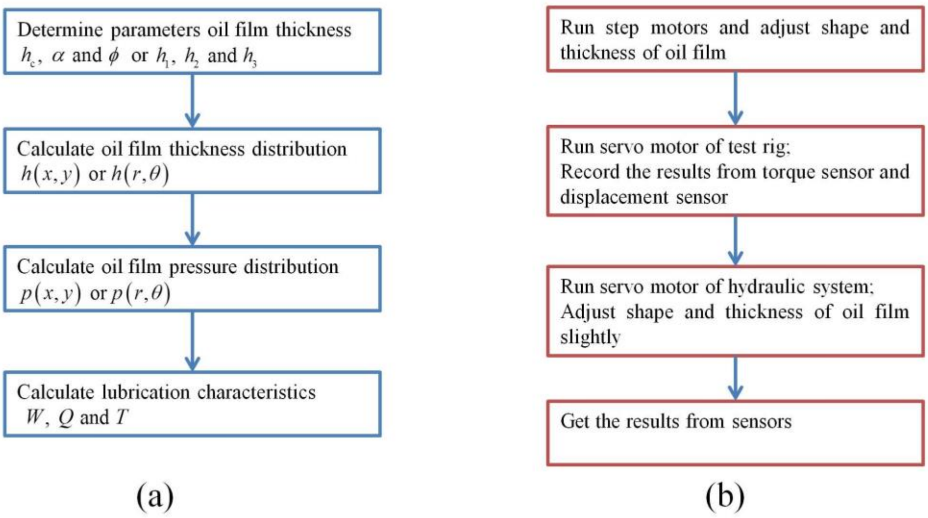

Figure 9. Process of simulation and experiment a) shows the process of simulation, b) shows the process of experiment.

Results Comparison

The experiment results and simulation results are compared. Temperature, viscosity, reacting force and torque are shown in Figure 10. The oil film thickness is set to 5 μm . The operating pressure and rotating rate are set to 5 MPa and 1000 r/min separately. The running time of the test is 10 minutes. The oil film temperature can't measure directly. However the slipper outer surface temperature T_{12} can be measured by the laser temperature sensor. Based on Eq. (12), the oil film temperature can be evaluated.

In Figure 10, the red curves show the results from the simulation meanwhile the blue curves show the results from the experiment. According to Figure 10, the tendency of the evaluated oil film temperature is similar with the simulated one, but the increasing rate is lower. The maximum relative error is about 13.4% when the experiment is end. The accounts of the reacting force from the experiment and simulation are close. The maximum relative error is about 1.2%, which is quite small. Temperature has no effect on the reacting force. Higher temperature reduces the viscosity. Therefore, the torque from the experiment and simulation both decreases. The maximum relative error of torque is about 10% when the experiment is beginning. With time goes on, the decreases rate from the experiment is lower than the one from the simulation. The reason is that the temperature increasing rate from the experiment is lower than the one from the simulation.

The error of the reacting force is small. However other errors are larger than 10%. The reasons are from many aspects. In the next section, the reasons for the errors are analyzed. The simulation model is modified in order to meet the true status of the test rig.

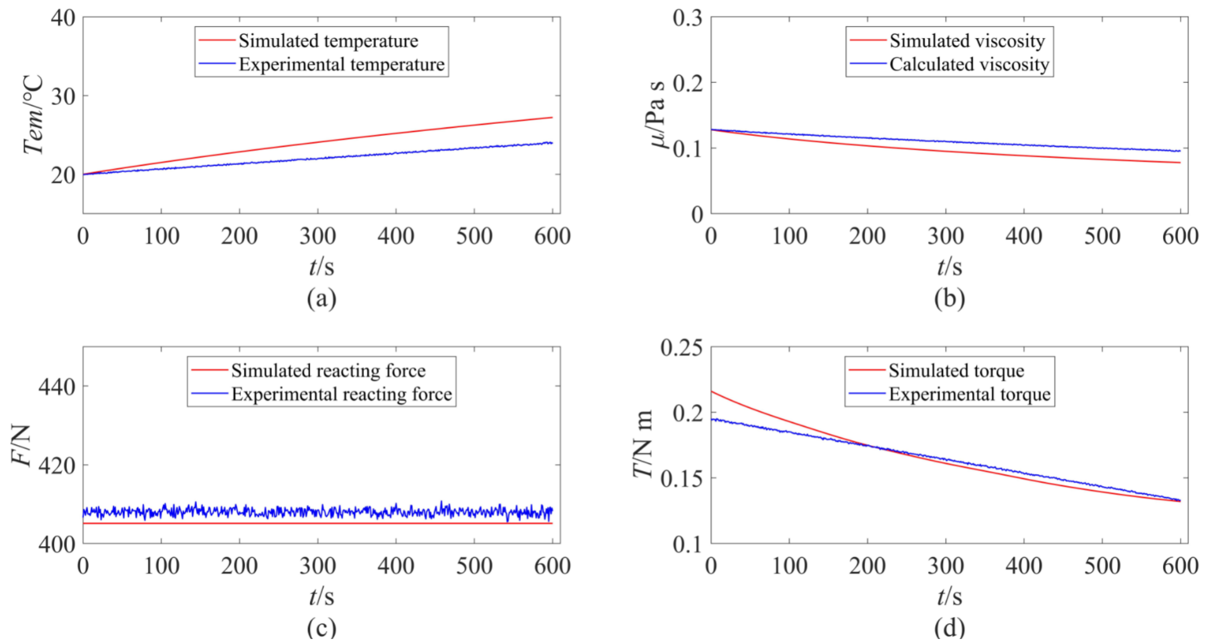

Figure 10. Results comparison between the experiment and simulation a) shows the oil film temperature, b) shows the oil film viscosity, c) shows the reacting force, d) shows the torque.

ERROR DISCUSSION

Test Rig Assembly Error

All parts of the test rig are turned, drilled and milled. With the development of the manufacturing technology, the accuracy and quality of parts are getting higher and higher. However, the errors in assembly are unavoidable. They have great impact on the accuracy of the test rig. Referred to Figure 4, the errors in assembly along the Y axis and Z axis should be focused. No matter where the errors occur in assembly, they eventually lead to concentricity errors of two end cases. Therefore, relative position between swash-plate and slipper in test rig is changed. Figure 11 shows the ideal and wrong relative position between swash-plate and slipper. The error between ideal position and wrong position causes wrong radial shear velocity and wrong circumferential shear velocity. The pressure distribution and reacting force are wrong as well. Therefore, the effect of the errors along the Y axis and Z axis should be calculated.

Based on the results from three-coordinate measuring machine. The maximum errors along the Y axis and Z axis are 0.0654 mm and 0.0143 mm separately. Therefore, the maximum eccentricity error is 0.0669 mm, which influences the pitch radium . Table 2 lists the maximum relative errors between the experiment and different simulations.

Based on Table 2, the difference of the maximum temperature relative error between the experiment and modified simulation is larger. However, other relative errors are almost same. According to the results, the test rig assembly error is not the main cause of the characteristics errors.

Table 2. Maximum relative errors between the experiment and different simulation 1.

Description	Without Eccentricity	With Eccentricity
Temperature	11%	13.6%
Reacting force	1.7%	1.7%
Torque	10%	10.1%

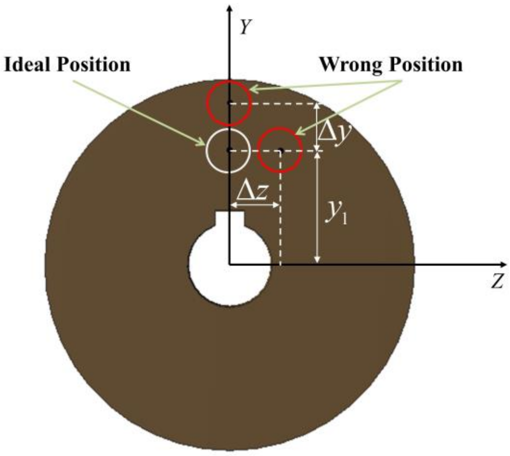

Figure 11. Ideal position and wrong position between the slipper and swash-plate.

Operating Condition Error

In the simulation, the pressure and temperature of the input oil are constant. In the experiment, the operating pressure is generated by the hydraulic system. Although the gear pump is utilized since it can generate low fluctuating pressurized oil, the fluctuation of operating pressure leads to the errors of the characteristics. Besides, the temperature of the input oil from the gear pump increases linearly. Therefore, import the experimental pressure and temperature data into the simulation. The results are shown in Table 3.
Based on Table 3, the maximum relative error of the reacting force and temperature is larger since the input pressure data for the modified simulation is overshoot sometimes. Therefore, operating condition error is the secondary cause of the characteristics errors.

Table 3. Maximum relative errors between the experiment and different simulation 2.

Description	Constant Operating Condition	Real Operating Condition
Temperature	11%	13.6%
Reacting force	1.7%	5.1%
Torque	10%	10%

Retainer Deformation

The retainer withstands the force from the slipper. It deforms the center of retainer along the X axis, which leads to the tested displacement error. In order to reduce the effect of the deformation, multiple thickness retainers are simulated in ANSYS. The maximum deformation is about 8 μm when the thickness of the retainer is 3 mm. It reduces to 0.9 μm when the thickness is 6 mm, which is smaller than the accuracy of the eddy current displacement sensor. Considering the deformation of the retainer in the simulation, the characteristics are shown in Table 4.
Based on Table 4, the main reason of the difference between the experiment and simulation is the deformation of the retainer. The oil film thickness of the experiment and simulation is set to 5 μm . However, because of the deformation, the oil film thickness raises to about 5.9 μm . Therefore, when it' set to 5.9 μm in the simulation. The errors of the characteristics reduce.

Table 4. Maximum relative errors between the experiment and different simulation 3.

Description	With Deformation	Without Deformation
Temperature	11%	5.8%
Reacting force	1.7%	1.7%
Torque	10%	6.7%

CONCLUSIONS

A novel oil film thickness adjustable test rig is proposed. The mathematical models of the oil film thickness, pressure and temperature are illustrated. It’s characteristics such as the reacting force, torque, and temperature from the experiment and simulation are compared.
The mechanism of the test rig including the hydraulic system, cooling system, control system and data logging system are introduced. The feasibility of the mechanism is calculated that the thickness and shape of the oil film can be precisely controlled by the mechanism.
Based on the initial results from the experiment and simulation, the error of the reacting force is less than 10%. However, the errors of other characteristics are larger. The simulation is modified in order to match the real situation of the experiment.
The assembly error of the test rig is taken into account in the simulation. However, it’s not the main cause of the characteristics errors. The main cause is the retainer deformation and the secondary cause is the pressure fluctuation and input oil temperature increasing. The characteristics errors reduce when the retainer deformation and real operating condition are considered in the simulation.

FURTHER WORK

A novel oil film thickness adjustable test rig is made for testing oil film characteristics in the different operating conditions. The optimized slipper is designed in the simulation and it can be tested in this test rig. After that, based on the results from the test rig, an oil film thickness adjustable valve-control axial piston pump is designed which can work with minimum energy consumption in the different operating conditions.

NOMENCLATURE

A_{s1} : Swash-plate inner area
A_{s2} : Swash-plate outer area
c_p : Heat capacity
F : Reacting force
g : DOF of each pair
H_1 : Slipper thickness
H_2 : Swash-plate thickness
h_{1-3} : Oil film thickness in each point
h_c : Central oil film thickness
k_0 : Coefficient of oil heat transfers
k_1 : Coefficient of slipper heat transfers
k_2 : Coefficient of swash-plate heat transfers
M : Degree of freedom
N : Number of parts
n : Rotating rate
p_r : Pocket pressure
q : Leakage
$\dot{Q}$: Rate of heat rejection
R : Pitch radius
R_0 : Slipper outer radius
$R_{c1\text{-}c6}$: Thermal resistance
r_0 : Slipper inner radius
T_0 : External oil temperature

T_{11} : Slipper inner surface temperature
T_{12} : Slipper outer surface temperature
T_{21} : Swash-plate inner surface temperature
T_{22} : Swash-plate outer surface temperature
V : Control volume
v_{sr} : Radial velocity
$v_{s\theta}$: Axial velocity
$\dot{W}$: Power loss
α : Tilt angle
ϕ : Phase angle
θ : Rotating angle
ρ : Oil density
μ : Oil viscosity

REFERENCES

[1] CHAO, Q., ZHANG, J., XU, B., WANG Q., Discussion on the Reynolds Equation for the Slipper Bearing Modeling in Axial Piston Pumps, Tribology International, Vol. 118, 2018, pp. 140-147.
[2] CHO, I. S., A Study on the Optimum Design for the Valve Plate of a Swash Plate-Type Oil Hydraulic Piston Pump, Journal of Mechanical Science and Technology, Vol. 29, No. 6, 2015, pp. 2409–2413.
[3] HONG, Y. S., LEE, S. Y., KIM, S. H., LIM, S. Y., Improvement of the Low-Speed Friction Characteristics of a Hydraulic Piston Pump by PVD-Coating of Tin, Journal of Mechanical Science and Technology, Vol. 20, No. 3, 2006, pp. 358–366.
[4] KIM, J. K., JUNG, J. Y., Measurement of Fluid Film Thickness on The Valve Plate in Oil Hydraulic Axial Piston Pumps (I)-Bearing Pad Effects, Journal of Mechanical Science and Technology, Vol. 17, No. 2, 2004, pp. 246–253.
[5] KIM, J. K., KIM, H. E., LEE, Y. B., JUNG, D. Y., SH, O. H., Measurement of Fluid Film Thickness on the Valve Plate in Oil Hydraulic Axial Piston Pumps (Part I Spherical Design Effects), Journal of Mechanical Science and Technology, Vol. 19, No. 2, 2008, pp. 655–663.
[6] HOOKE, C. J., KAKOULLIS, Y. P., The Effects of Centrifugal Load And Ball Friction on the Lubrication of Slipper in Axial Piston Pumps, 6th International Fluid Power Symposium, Cambridge, England, 1981, pp. 179-191.
[7] KOC, E., LI, K. Y., HOOKE, C. J., Slipper Balance in Axial Piston Pumps and Motors, Transactions of the ASME, Vol. 114, No. 10, 1996, pp. 766-772.
[8] KOC, E., HOOKE, C. J., Investigation into The Effects of Orifice Size Offset and Overclamp Ration on the Lubrication of Slipper Bearings, Tribology International, Vol. 29, No. 4, 1996, pp. 299-305.
[9] KOC, E., HOOKE, C. J., Considerations in The Design of Partially Hydrostatic Slipper Bearings, Tribology International, Vol. 30, No. 11, 1997, pp. 815-823.
[10] KOC, E., HOOKE, C. J., An Analysis of the Lubrication Mechanisms of the Bush-Type Bearings in High Pressure Pumps, Tribology International, Vol. 30, No. 8, 1997, pp. 553-560.
[11] AI, Q., ZHOU, H., ZHANG, Z., YANG, H., Development of Lubricating Characteristics Testing System of Friction Pair in Axial Piston Pump, Chinese Hydraulics & Pneumatics, Vol.11, 2004, pp. 22-25.
[12] ZHUANG, Q., ZHOU, J., AI. Q., Development of Experiment Rig for Lubricate Film of the Slipper-Pad in Axial Piston Pumps, Machine Tool & Hydraulics, Vol. 3, 2005, pp. 113-114.
[13] ZHUANG, Q., ZHOU, J., AI. Q., Comparison in Measurements of Lubricating Film of the Slipper-Pair in Axial Piston Pump, Machine Tool & Hydraulics, Vol. 12, 2005, pp. 86-88.
[14] CANBULUT, F., The Experimental Analyses of the Effects of the Geometric and Working Parameters on the Circular Hydrostatic Thrust Bearing, JSME International Journal Series C, Vol. 48, 2005, pp. 715-722.
[15] CANBULUT, F., SINANOGLU, C., KOC, E., Experimental Analysis of Frictional Power Loss of Hydrostatic Slipper Bearings, Industrial Lubrication and Tribology, Vol. 61, No. 3, 2006, pp. 123-131.
[16] CRABTREE, A., MANRING, D., JOHNSON. R., Pressure Measurements for Translating Hydrostatic Thrust Bearing, International Journal of Fluid Power, Vol. 6, No. 3, 2005, pp. 19-24.

[17] ROKALA, M., CALONIUS, O., KOSKINEN, K., Study of Lubrication Conditions in Slipper-Swash Plate Contact in Water Hydraulic Axial Piston Pump, Proceeding of the 7th JFPS International Symposium on Fluid Power Toyama, Japan, 2008.
[18] ROKALA, M., CALONIUS, O., KOSKINEN, K., Tribological Conditions between Swashplate and Slipper Pad in Variable Displacement Water Hydraulic Axial Piston Unit, Proceeding of the 6th International Fluid Power Conference Dresden, Germany, 2008.
[19] LI, Y., XU, B., Axial Piston Pump Slipper Pad Dynamic Characteristics of Wedge Oil Film, Chinese Hydraulics & Pneumatics, Vol. 9, 2010, pp. 87-91.
[20] LI, Y, Study on Characteristics of Oil Film for Slipper Pair of Axial Piston Pumps, Master Thesis, Zhejiang University, Hangzhou, China, 2001.
[21] XU, B., LI, Y., ZHANG, B., ZHANG. J., Numerical Simulation of Overturning Phenomenon of Axial Piston Pump Slipper Pair, Journal of Mechanical Engineering, Vol. 46, No. 20, 2010, pp. 161-168.
[22] XU, B., ZHANG, J., YANG, H., Investigation on Structural Optimization of Anti-Overturning slipper of Axial Piston Pump, Science China Technological Sciences, Vol. 55, No. 11, 2012, pp. 3010-3018.
[23] XU, B., CHAO, Q., ZHANG, J., LI. Y., Slipper Optimization Model Based on Equilibrium Coefficient, Journal of Zhejiang University, Vol. 49, No. 6, 2015, pp. 1009-1014.
[24] SCHENK, A., Predicting Lubrication Performance between the Slipper and Swashplate in Axial Piston Hydraulic Machines, Ph.D Thesis, Purdue University, Indiana, USA, 2014.
[25] WANG, H. J., SHI, G. L., An Adjustable Oil Film Thickness Test Rig for Detecting Lubrication Characteristics of Slipper/Swash-Pair in Piston Pumps, Industrial Lubrication and Tribology, Vol. 73, No.1, pp. 190-198.
[26] WANG, Y. J., Study on Performance of Slipper Bearing in Hydraulic Axial Piston Pump in High-Pressure and High-Speed, Ph.D Thesis, Beijing Institute of Technology, Beijing, China, 2014.
[27] SHI, G. L., WANG, H. J., Thermal-Hydraulic Model FOR Axial Piston Pump with Leakage and Friction and its Application, Industrial Lubrication and Tribology, Vol. 71, No. 6, 2019, pp. 810-818.
[28] BUSQUETS, E., IVANTYSYNOVA, M., Temperature Prediction of Displacement Contrilled Multi-Actuator Machines, International Journal of Fluid Power, Vol. 14, No. 1, 2013, pp. 25-36.
[29] GRUBLER, M., Allgemeine Eigenschaft en der Zwanglaufigen Ebenen Kinematische Kette, Civiling Enieus, Vol. 29, 1883, pp. 167-200.

Genaral Session | Pneumatics

Components and Systems 1

[GS5-1-01] Magnetic Sensor Study for Improving Air Turbine Spindle Performance

〇Vanisara Kaewnamchai[1], Tomonori Kato[1], Kazuki Kawakubo[1], Kazumasa Yamashita[1]
（1.Fukuoka Institute of Technology）

[GS5-1-02] Study on Multi-Cylinder Type Wind Powered Air Compressor Applied Hypocycloid

〇Ryota Tanoue[1], Toshinori Fujita[1] （1.Tokyo Denki University）

[GS5-1-03] Development of Bidirectional Arm Curl Machine Using Pneumatic Artificial Rubber Muscles

〇Toshihiro Kawase[1,2], Tomoya Nakanishi[1], Shintaro Yoshida[3], Shingo Ohno[3], Ryo Sakurai[3], Tetsuro Miyazaki[4], Takahiro Kanno[5], Maina Sogabe[4], Yoshikazu Nakajima[1], Kenji Kawashima[4]
（1.Tokyo Medical and Dental University, 2.Tokyo Institute of Technology, 3.Bridgestone Corporation, 4.The University of Tokyo, 5.RIVERFIELD, Inc.）

[GS5-1-04] Design of a Pneumatic Oscillator for Paper Machine's Doctor Blade Systems

Stefano Colaiuda[1], 〇Michele Gabrio Antonelli[2], Pierluigi Beomonte Zobel[2], Massimiliano Centofanti[1] （1.SMC Italia S.p.A., 2.Department of Industrial and Information Engineering and Economics, University of L'Aquila）

The 11th JFPS International Symposium on Fluid Power HAKODATE 2020 Oct. 12-13, 2021 The Japan Fluid Power System Society

Magnetic Sensor Study for Improving Air Turbine Spindle Performance

Vanisara KAEWNAMCHAI*, Tomonori KATO*,
Kazuki KAWAKUBO*, Kazumasa YAMASHITA*

*Graduate School of Engineering,
Fukuoka Institute of Technology
3-30-1 Wajirohigashi, Higashi-ku, Fukuoka, 811-0295, Japan
(E-mail: ad20102@bene.fit.ac.jp)

Abstract. Air turbine spindle control systems, in conjunction with high-precision quick-response pneumatic pressure regulators, have been developed for various purposes, such as tool wear investigations and medical machine applications. However, some limitations arose in the speed sensor (tachometer) used in the air turbine system. The tachometer cannot function properly in low-speed conditions (less than 1,000 min^{-1}). Therefore, this study aimed to improve the low-rotational-speed measurement system. Moreover, a magneto-rheological fluid (MRF) damper was proposed for preliminary experiments to enhance the air turbine, which will be included in a future reinstallation of the entire system. Two commercial Hall effect sensors are installed to measure the rotational speed of the air turbine spindle shaft and detect the magnetic field density in the MRF damper. The results showed that the Hall effect sensors could be used to achieve the proposed intention.

Keywords: Pneumatics, Air turbine spindle, Hall effect sensor, Functional fluid, MRF damper.

INTRODUCTION

In the past decade, the rotation feedback control system known as the high-precision quick response pneumatic pressure regulator (HPQR) [1] has been used in several applications in conjunction with the air turbine spindle due to its high speed, low vibration, and low friction. Therefore, the air turbine spindle and HPQR system is essential for ultra-high-speed machines, such as milling machines and medical devices. [2-4]

In previous studies [5-6], the authors improved the air turbine spindle to investigate tool wear by milling sample plates. The system showed satisfactory performance when the rotational speed was high. However, the tachometer, a non-contact sensor placed on the air turbine spindle to measure the rotational speed, had an unacceptably significant error for a rotational speed of less than 1,000 min^{-1}.

To solve this problem, we propose a Hall effect sensor for measuring the low rotational speeds of an air turbine spindle. Furthermore, this study focuses on the preliminary experiments of magneto-rheological fluid (MRF) dampers to enhance the air turbine spindle by using a Hall effect sensor to detect oil viscosity inside the damper at various magnetic field densities. Some studies have investigated the viscosity of oil lubricants using Hall effect sensors. For instance, Sriratana and Murayama [7] used a Hall effect sensor to measure lubricant viscosity by varying the weight of metal particles. Similarly, Satthamsakul et al. [8] studied a Hall effect sensor that detected oil lubricant deterioration under variations in the electromagnetic field generated by a ferrite-core solenoid coil. In addition, Li et al. [9] present a rotary MR damper design in which a magnetic field was used to generate electrical and structural parameters that increased the rotor working area and reduced the moment of inertia of the rotor. The electromagnetic field of the MR damper was analyzed using the finite element method in a simulation of the torque-current properties of the MR damper.

In addition, numerous studies have used Hall effect sensors for inspecting non-destructive testing, such as Sriratana and Murayama [10], who investigated the imperfection of a material by comparing different placements of the Hall effect sensor module. Furthermore, other researchers have studied motor control and have detected relevant parameters using Hall effect sensors. For example, Fernandez et al. [11] discuss the control of a permanent magnet synchronous motor (PMSM) using a Hall effect sensor to measure the position. The device commonly used to measure the rotor position in a PMSM is a position sensor or an encoder/resolver, however, these have drawbacks in terms of the costs and space required for installation. In conclusion, Hall effect sensors are broadly used in various applications because of their small size, low cost, high sensitivity, wide temperature range, and high performance.

PRINCIPLES

Hall Effect Sensor

Hall effect sensors rely on the Hall effect theory for applications in various sensing device objectives. The Lorentz force (F) is exerted on an electrically charged particle (q) that is moving with a certain velocity (v) through an electric field (E) and a magnetic flux density (B). The Lorentz force is defined as shown in Eq. (1)

$$F = q[E + (v \times B)] \tag{1}$$

The Hall voltage (V_{Hall}) is generated by the external magnetic field (B) when a constant current (I) passes through the semiconductor plate (Hall element). The thickness of the Hall element is defined by d, and R_{Hall} is the Hall coefficient, as shown in Eq. (2). [12]

$$V_{Hall} = \frac{R_{Hall}}{d} IB \tag{2}$$

In this study, digital and analog Hall effect sensors were applied to the system to overcome the limitations of the air turbine spindle rotational speed control. The commercial Hall vane sensor consists of a permanent magnet and a digital Hall effect sensor fabricated in a sealed plastic package.
The Hall vane sensor provided a digital signal output. Typically, when the magnetic field is not present, the output signal is in an OFF state, as this Hall vane sensor package contains an internal permanent magnet mounted in a twin tower. Therefore, the output signal from this Hall vane sensor is in the ON state when there is no ferrous gear interrupted.
The analog Hall effect sensor provides an analog output voltage proportional to the magnetic field density, when no magnetic field is present, known as a null voltage. When the Hall effect sensor is sensed by the South Pole, the output voltage increases above the null voltage, while the output voltage decreases below the null voltage when the North Pole is sensed.

MRF Damper

The magneto-rheological fluid (MRF) can be changed from a normal liquid to a semi-solid state by applying magnetic fields. The rotor with the cup shape is connected to the rotating shaft of the damper, placed between the MRF and the coil. When the coil inside the damper is excited, a magnetic field occurs around the damper. Subsequently, the metal particles in the MRF performed as the magnetic field undergoes the gap between the damper surface and the rotor. The metal particles generated a force restricting the rotating shaft of the damper. Therefore, the rotating torque can be controlled by generating a current that is applied to the coil. Figure 1 (a) and (b) show the MRF behavior when no magnetic field exists and when the coil generates a magnetic field, respectively.

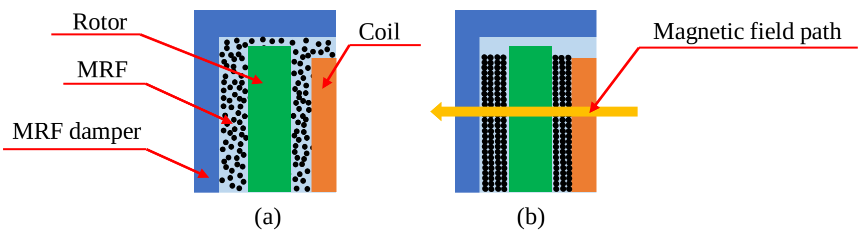

Figure 1. MRF damper behavior.
(a) Magnetic field is not generated.
(b) Magnetic field is generated.

TESTING SYSTEM INSTALLATION

The two different Hall effect sensors are placed in different parts. First, a Hall vane sensor is installed with an air turbine spindle shaft to measure the low-speed control condition. Second, an analog Hall effect sensor is installed with the rotary MRF damper for detecting the magnetic fields.
The diagram of the expected system installation is shown in Figure 2. This diagram will be followed when installing the combination of MRF damper devices after testing this preliminary experiment.

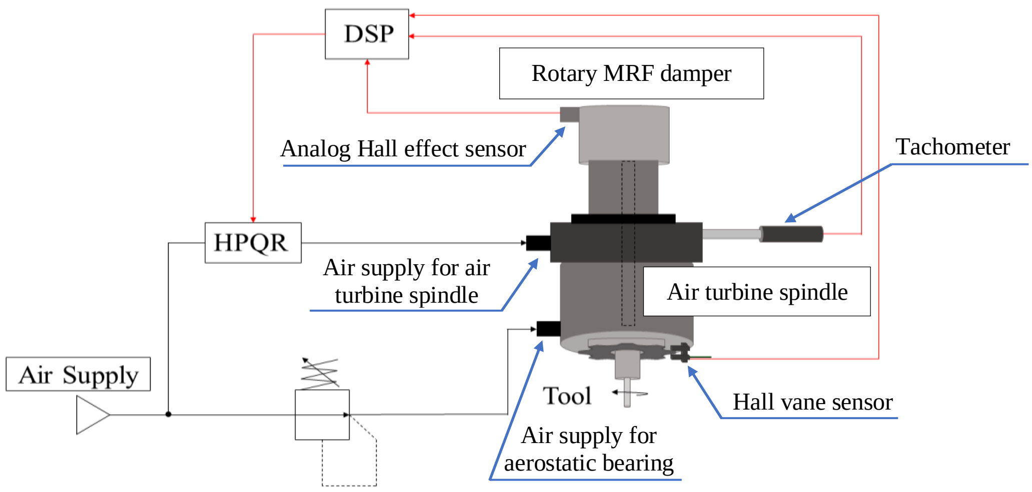

Figure 2. System installation.

Hall Vane Sensor Installed in the Air Turbine Spindle

The installation of the Hall vane sensor with the gear mounted on the air turbine spindle is shown in Figure 3. Figure 4 shows the output voltage square waveform of the Hall vane sensor for a target speed of 1,000 min^{-1}, 0.0601 second per 10 pluses related to the ten teeth of the gear that interrupted the magnetic field density in one cycle. The frequency of the rotation speed is 16.63 Hz, so the rotation speed from the Hall vane sensor is approximately 998 min^{-1}. Therefore, the resolution of the Hall vane sensor is ± 2 min^{-1}. In addition, the operating parameters of the Hall vane sensor with the air turbine spindle are listed in Table 1.

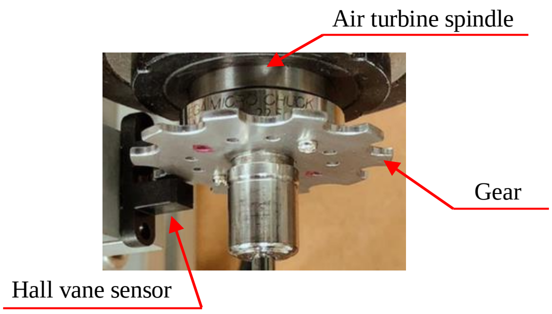

Figure 3. Installation of the Hall vane sensor and the target gear on the air turbine spindle.

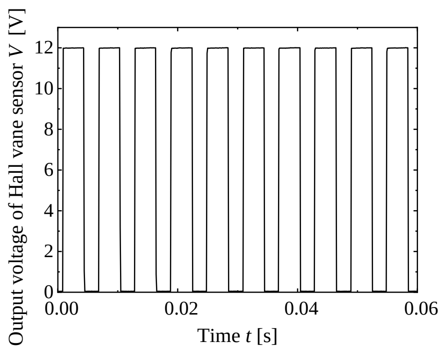

Figure 4. Output voltage waveform of Hall vane sensor for a target speed of 1,000 min^{-1}.

Table 1. Operating parameters of the Hall vane sensor with the air turbine spindle.

Parameters	Value
Rotation speed target	500 min^{-1}
Operating voltage	12 VDC
Operating current (Maximum at 20 ºC)	10 mA
Operating temperature range	-20 to 85 ºC

Analog Hall Effect Sensor Equipped with MRF Damper

The analog Hall effect sensor was installed on the side surface of the MRF damper, where the coil was wound inside. Figure 5 shows the testing installation of the MRF damper, along with the analog Hall effect sensor's shape and size compared to those of a 1 Yen coin.

The operating voltage of this analog Hall effect sensor was 5 VDC, and the output voltage of Hall effect sensor when there is no magnetic field was approximately 50% of the operating voltage (i.e., null voltage). The operating parameters of the analog Hall effect sensor with the MRF damper are shown in Table 2.

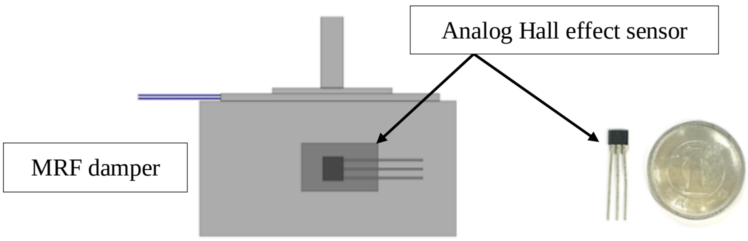

Figure 5. Installation of the analog Hall effect sensor with the MRF damper.

Table 2. Operating parameters of the analog Hall effect sensor.

Parameters	**Value**
Operating supply voltage	5 VDC
Sensitivity (at 25 ºC)	3.125 mV ± 0.125 mV/gauss
Operating temperature range	-40 to 150 ºC
Null (Output @ 0 Gauss, V)	2.50 ± 0.075 V

EXPERIMENTAL RESULTS

The results were divided into two main parts and one additional part. We evaluated the performance between the digital Hall vane sensor and tachometer and the analog Hall effect sensor to clarify the possibility of using a commercial MRF damper with an air turbine spindle system.
The additional capacitive displacement sensor experiment was conducted to measure the amplitude while testing the Hall vane sensor and tachometer when the air turbine spindle is rotating. For the additional experiment, the capacitive displacement sensor was installed along the shaft of the air turbine spindle, leaving a small gap between sensor and shaft.

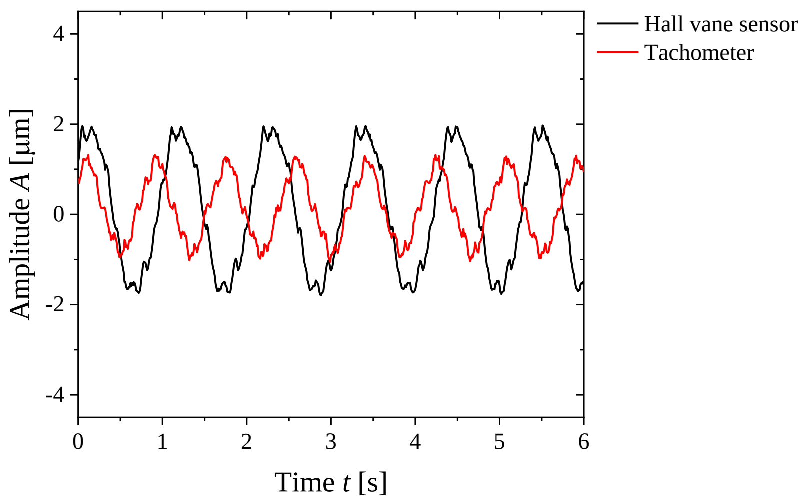

Figure 6. Amplitude of the tachometer and Hall vane sensor.

As shown in Figure 6, the amplitude of the Hall vane sensor is higher than that of the tachometer, which is approximately 1.25 μm. It is found that the Hall vane sensor has little impact on the air turbine spindle shaft due to the magnetic force from the permanent magnet that is placed in the twin tower of the Hall vane sensor.
In the experimental results of the magnetic fields detected by the analog Hall effect sensor, the factors discussed are the output voltage of the analog Hall effect sensor and the supply voltage of the MRF damper to excite the magnetic fields. The experiment started from zero voltage applied to the MRF damper to voltages of 1, 2, 3, …, 22, 23, and 24 VDC. As shown in Figure 7, the output of the Hall effect sensor increases when increases the voltage supply of the damper. Although no voltage to the MRF damper is supplied, the Hall effect sensor output voltage does not change from the null voltage. Note that the results show a linear trend, which would relate to the viscosity of the MRF.

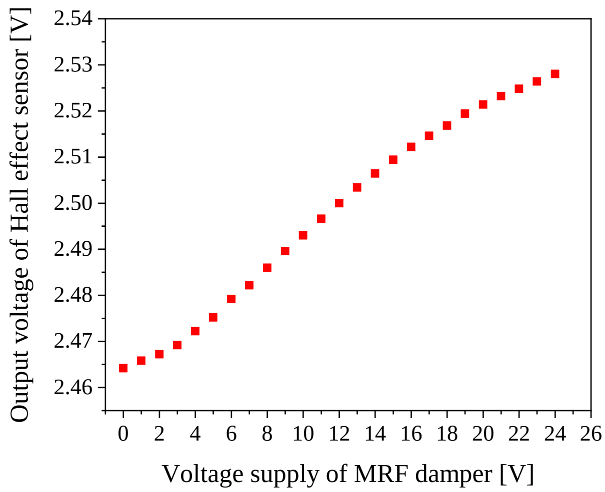

Figure 7. Relationship between the analog Hall effect sensor and MRF damper.

The experimental results in terms of the step response for rotational speed control are shown in Figure 8. The black line represents the control signal of the Hall vane sensor in Figure 8 (a) and (b). The red line represents the control signal of the tachometer in Figure 8 (a). The tachometer used in this experiment is an optical rotation speed sensor type, which is designed for the high-rotation-speed region (up to 300,000 min^{-1}).

As seen in the figure, the Hall vane sensor allows controlling the air turbine spindle when the target speed is 500 min^{-1} even though a peak signal arises between 0 and 100 second. In particular, the peak arises when the rotation speed is lower than 100 min^{-1}, and the rotation control signal from the Hall vane sensor is better than the control signal from the tachometer.

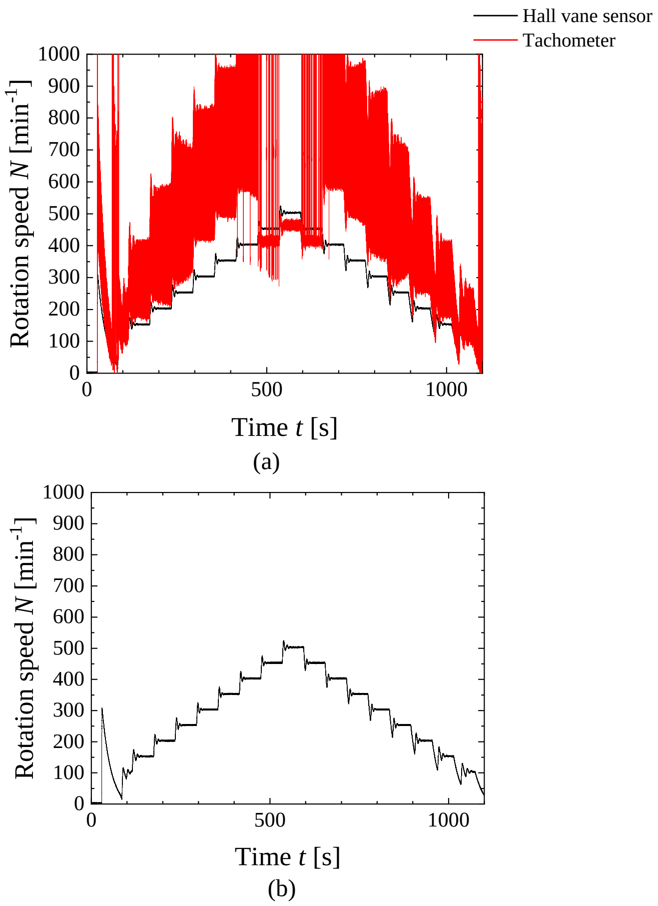

Figure 8. Step response of the rotation speed control.
(a) Control signal of the Hall vane sensor compared with the tachometer.
(b) Hall vane sensor control signal.

CONCLUSION

This study evaluated the air turbine spindle applied with the HPQR. This research implemented a Hall vane sensor to compensate for the limitations of using a tachometer to measure the rotational speed and an analog Hall effect sensor to examine its relationship with the MRF damper. The implement the Hall vane sensor because it is a non-contact type sensor with a compact size that can be used for various purposes at a reasonable cost.

As a result, we found that the Hall vane sensor could be applied with an air turbine spindle to control the rotational speed at a target speed of 500 min^{-1} even though some limitation arose when the speed was lower than 100 min^{-1}. This study, therefore, showed that combining the Hall vane sensor and the tachometer could benefit and work adequately in this type of system. Furthermore, the analog Hall effect sensor could detect the magnetic field of the MRF damper, which is expected to be related to the viscosity measurement of the MRF in future work.

Moreover, we will consider redesigning the position of the Hall vane sensor to develop an air turbine spindle for a milling machine to study the tool wear in the case of the low-speed condition (less than 1,000 min^{-1}). We will install the system following the planned diagram installation and adapting additional algorithms for further enhancement.

ACKNOWLEDGMENTS

This research was supported by JSPS KAKENHI Grant Number 20K04203.

REFERENCES

1. KATO, T., KAWASHIMA, K., FUNAKI, T., TADANO, K., KAGAWA, T., A New High-Precision Quick Response Pressure Regulator for Active Control of Pneumatic Vibration Isolation Tables, Precision Engineering, Vol. 34, 2010, pp. 43-48.
2. KATO, T., A Review of HPR and Its Applications: Control of Air Turbine Spindle and Hybrid Electro-Pneumatic Ultra-Precision Vertical Positioning Stage, International Conference on Fluid Power and Mechatronics (FPM), Harbin, China, Aug. 5-7, 2015.
3. TSUKIYAMA, Y., KATO, T., MATSUO, K., Evaluation of Energy Consumption of Hybrid Electric-Pneumatic Ultra-Precision Vertical Positioning Device, 10th JFPS International Symposium on Fluid Power, Fukuoka, Oct. 24-27, 2017.
4. KATO, T., HIGASHIJIMA, G., YAZAWA, T. et al., Rotation Control of Air Turbine Spindle using High Precision Quick Response Pneumatic Pressure Regulator, Transactions of the Japan Fluid Power System Society, Vol. 45, No.1, 2014, pp. 8-14.
5. KATO, T., OTSUBO, T., SHIMAZAKI, K., et al., Tool Wear Estimation Method in Milling Process Using Air Turbine Spindle Rotation-Control System Equipped with Disturbance Force Observer, International Journal of Hydromechatronics, Vol. 1, No. 4, 2018, pp. 384-402.
6. OKAMOTO, Y., YAZAWA, T., KATO, T., et al., Study on Small-Diameter Ball End Mill Milling of Air Turbine Spindle by Rotation Speed Control, 10th JFPS International Symposium on Fluid Power, Fukuoka, Oct. 24-27, 2017.
7. SRIRATANA, W., MURAYAMA, R., Application of Magnetic Field Method for Measuring Lubricant Viscosity, Materials Science Forum, Trans Technical Publications, Switzerland, Vol. 750, 2013, pp. 116-124.
8. SATTHAMSAKUL, S., SRIRATANA, W., SRIRATANA, L., Empirical Study on Influences of Electromagnetic Field on Hall Effect Sensor for Analysing Oil Lubricant Deterioration, 11th International Conference on Mechatronics and Manufacturing (ICMM), Vol. 895, 2020.
9. LI, J., QIN, C., GUO, S., WANG, J., Magnetic circuit design and performance analysis of a rotary magnetorheological damper with new structure, IEEE 8th International Conference on CIS & RAM, Ningbo, China, 2017.
10. SRIRATANA, W., MURAYAMA, R., Application of Hall Effect Sensor: A Study on the Influences of Sensor Placement, IEEE International Symposium on Industrial Electronics, Taipei, Taiwan, May. 28-31, 2013.
11. FERNANDEZ, D., FERNANDEZ, D., MARTINEZ, M., et al, Resolver Emulation for PMSMs Using Low-Cost Hall Effect Sensors, IEEE Energy Conversion Congress and Exposition (ECCE), Baltimore, MD, USA, Sept. 29-Oct. 3, 2019.
12. RANGAN, C.S., SARMA, G.R., MANI, V.S.V., Instrumentation Devices and Systems, 2nd edition. McGraw-Hill, New Delhi, 2006, pp. 43-45.

The 11th JFPS International Symposium on Fluid Power HAKODATE 2020 Oct. 12-13, 2021 The Japan Fluid Power System Society

Study on Multi-Cylinder Type Wind Powered Air Compressor Applied Hypocycloid

Ryota TANOUE* and Toshinori FUJITA**

* Tokyo Denki Univ. Dept. of Mechanical Engineering.
5 Senju Asahi-cho, Adachi-ku, Tokyo, 120 8551 Japan
(E-mail: 20kmf13@ms.denadi.ac.jp)
**Tokyo Denki Univ. Dept. of Mechanical Engineering.
5 Senju Asahi-cho, Adachi-ku, Tokyo, 120 8551 Japan
(E-mail: tfujita@mail.denadi.ac.jp)

Abstract. Air compressors are machines needed in production lines because of their versatility in compressed air, but they have the problem of high-power consumption. The power consumption of air compressors that produce compressed air is high, and its reduction is required from the viewpoint of greenhouse gas reduction. In this study, we propose a wind powered air compressor that uses wind power, a renewable energy source, to drive the compressor in order to reduce greenhouse gas emissions. In this paper, the principle and structure of the fabricated wind powered air compressor are presented and its characteristics are measured. As a result, a maximum discharge pressure of 0.6 [MPa] and a maximum efficiency of 9 [%] were obtained at an annual average wind speed of 3 [m/s] in Japan. It was found that the system can be put to practical use if the efficiency is improved.

Keywords: Air compressor, Wind velocity, Flow rate, Efficiency.

INTRODUCTION

Compressed air is widely used in production lines for cleaning, conveying and so on. Today, most of the compressed air is produced by electric air compressors. About 80 [%] of the energy consumed in industry is electric energy. About 20 [%] of these are used in electric air compressors, which account for a large proportion. As the reduction of greenhouse gases, which are the main cause of global warming, has become a global issue, there is a need to reduce the power consumption of electric air compressors. For this reason, energy-saving technologies such as inverters and number control have been introduced into electric air compressors. However, there is a limit to the amount of reduction that can be achieved [1]. For this reason, energy-saving technologies such as inverters and number control have been introduced into electric air compressors. However, there is a limit to the amount of reduction that can be achieved.

On the other hand, the use of renewable energy is one of the measures to reduce greenhouse gas emissions, and wind power is becoming increasingly popular due to its cost and simple structure [2]. However, wind power generation is an unstable method of power generation in which the amount of power generated fluctuates greatly depending on the weather. In addition, large wind turbines suffer from power transmission losses, while small ones require inverters and other power transmission equipment, resulting in high prices.

With this background, we proposed a wind powered air compressor that uses wind turbines to power the air compressor for more effective use of wind energy. Compared to the case where the air compressor is driven by wind power generation, this system can be introduced easily and at low cost. In addition, since it does not use electricity, only additional piping is required when it is installed in factories. If a wind powered air compressor can be realized, it can be installed on a vacant space such as the compressed air used, thereby reducing the number of electric air compressors, and leading to a reduction in greenhouse gases.

This study, we proposed and developed an air compressor suitable for a wind powered air compressor, and fabricated a wind powered air compressor.

PROPOSED WIND POWERED AIR COMPRESSOR

Usage Example of Wind Powered Air Compressor

Fig.1 shows an example of compressed air supply in a production line in an industrial plant. Normally, an air compressor is not installed for each machine in a factory, but several compressors are used to supply compressed air to the air pipes that are spread all over the factory. The wind-powered air compressor proposed in this study is not intended to supply all of the compressed air used in the factory, but to be used in conjunction with an electric air compressor as a supplement.

The pressure fluctuates in the range of 0.6 ~ 0.9 [MPa]. Therefore, there is almost no problem even if the discharge pressure fluctuates due to changes in wind speed when a wind-powered air compressor is added. Besides compared to the case where the air compressor is driven by wind power generation, it is obvious that the installation of a wind-powered air compressor is simple and low-cost, as it only requires connection to the air piping, whereas in the case of an electric compressor, the power supply and controller must be reinstalled when adding equipment.

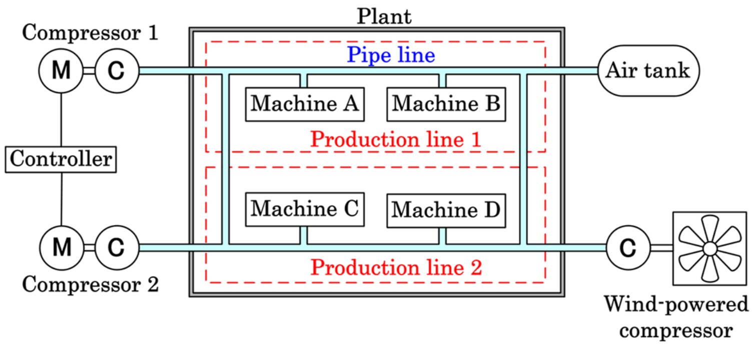

Figure 1. An Example of Compressed Air Supply in a Production Line in an Industrial Plant

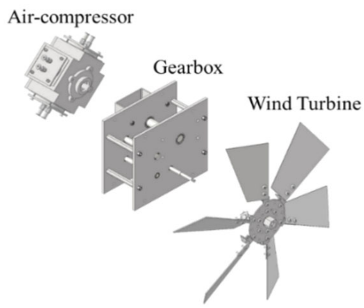

Figure 2. Wind Powered Air Compressor

Structure of Wind Powered Air Compressor

Fig.2 shows wind powered air compressor. Wind powered air compressor consists of a wind turbine, a reduction gear, and an air compressor. Therefore, the driving shaft of the wind turbine is connected to a reduction gear to amplify the torque, and then the air compressor is driven.

Fig. 3 shows the structure of the proposed air compressor based on the hypocycloid. Unlike an electric air compressor, a wind powered air compressor must be able to drive at low speed and low torque due to low air velocity. Screw type air compressors are unsuitable for this driving condition. The reciprocating type has a general piston-crank mechanism that causes pivoting of the piston head motion, which worsens the sealing performance of the packing. Therefore, we adopted a linear-crank mechanism using hypocycloid as shown in Fig. 3(a). The hypocycloid is the trajectory drawn by a fixed point on the circumference of a moving circle that rolls while inscribed on a fixed circle, drawing an ideal straight line when the ratio of the fixed circle to the moving circle is 2:1. Since there is no pivoting motion, this reduces the frictional force and improves sealing performance. If this mechanism were to be realized using gears as is, the mechanism would become complicated. Therefore, as shown in Fig. 3(b), the external gear is replaced with a link, and a guide is attached to the piston rod to constrain the movement of the internal gear. The linkage was extended as shown in Fig. 3(c), and cylinders were arranged with a phase shift of 90[°]. By arranging another pair of cylinders point-symmetrically to the axis of revolution, the four-cylinder system was made possible.

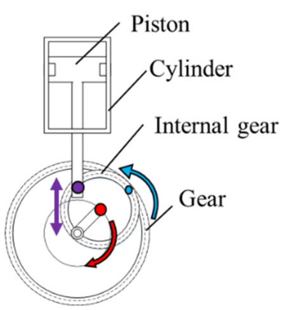

(a) Gear Type

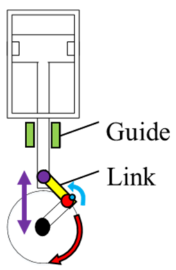

(b) Link Type

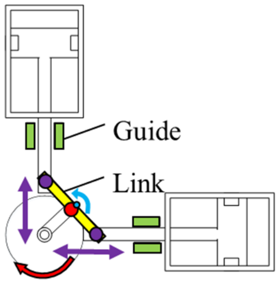

(c) Link Type with Multi-Cylinder

Figure 3. Structure of the Proposed Air Compressor Using Hypocycloid

PROTOTYPE OF WIND POWEREDD AIR COMPRESSOR

Fig.4(a) shows the fabricated wind powered air compressor. The blades of the wind turbine were trapezoidal-shaped flat blades, referring to multi-blade wind turbines, which provide high torque and high output at low rotation speed, and 6 of these blades were used. The pitch angle of the rotor was 60[deg], the diameter was 450 [mm], and the reduction ratio was 60:1. The wind powered air compressor requires a large amount of power to compress the air. The structure of the air compressor is shown in Fig. 4(b). The bore diameter of the compressor cylinder is 40 [mm] and the piston stroke is 12 [mm]. The packing is a low-friction pneumatic cylinder packing.

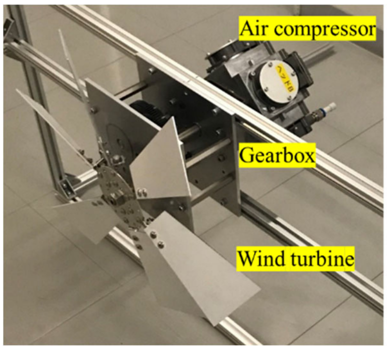

(a) The Fabricated Wind Powered Air Compressor

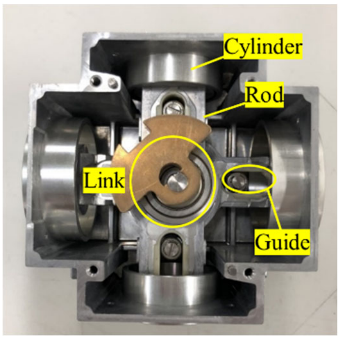

(b) Structure of the Air Compressor

Figure 4. Fabricated Wind Powered Air Compressor

CHARACTERISTIC MEASUREMENT

Measurement of Wind Turbine Characteristics

First, the single wind turbine characteristics were measured. Fig.5 shows the measurement method of the wind turbine. A pulley is attached to the output shaft of the wind turbine and a thread is applied. A weight load was attached to one end of the thread via a pulley, and a scale to the other end. With a constant and uniform wind speed generated in the wind tunnel, the weight load was added in 0.15 [kg] increments until the wind turbine stopped. The number of rotations at this time was measured using an encoder, and the torque generated was measured by multiplying the indicated value on the scale by the pulley radius. The wind turbine efficiency was also calculated from the wind energy, measured torque and revolution speed. The measurement results for wind speeds of 3[m/s], 4[m/s] and 5[m/s] are shown in Fig.6. The theoretical maximum efficiency of wind turbines is 59.3%, and those with 40% efficiency are used for wind power generation. Compared to these, the efficiency obtained was in the low 20% range, which was not good.

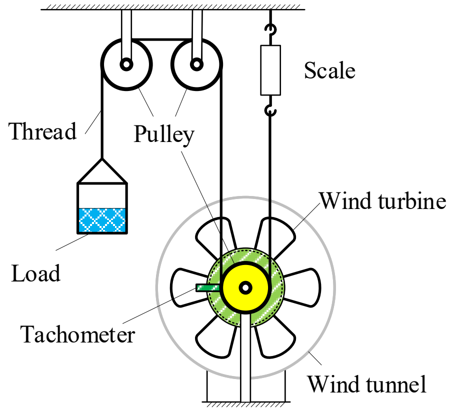

Figure 5. The Measurement Device for Wind Turbine Characteristics

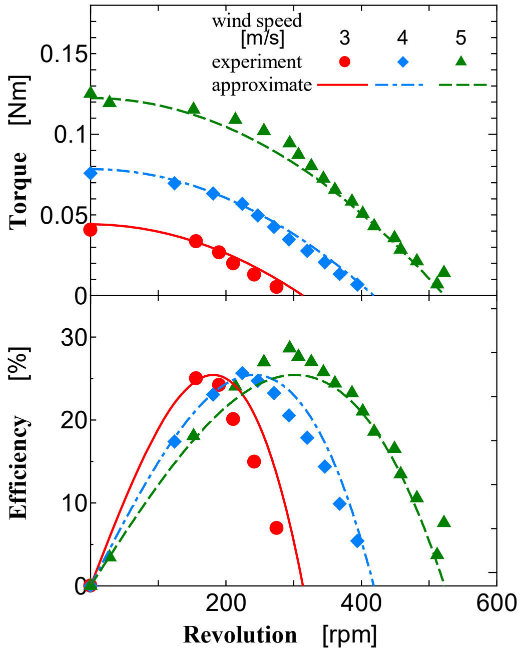

Figure 6. The Measurement Results of Wind Turbine Characteristics

Measurement of Air Compressor Characteristics

The characteristics of the air compressor were investigated in the same way, and the measurement apparatus is shown in Fig.7. The air compressor was revolved at a constant speed by a motor, and the required torque of the compressor was measured by a torque sensor. An isothermal pressure vessel with a volume of 300[cc] was installed at the discharge side of the compressor, and the discharge pressure was read by a pressure sensor. The discharge flow rate was obtained from the equation of state of the gas by differentiating the pressure response of the isothermal pressure vessel. The product of the torque sensor value and the revolution speed was used as the input power, and the exergy of the compressed air was obtained from the discharge pressure and flow rate, and the efficiency was calculated as the output power.

Fig.8 shows the measured pressure flow characteristics and efficiency when the compressor is revolved at a low speed of 5[rpm], as expected in an actual wind turbine compressor. The maximum discharge pressure of the air compressor was 0.6[MPa], and the maximum efficiency was 60[%].

In general, small reciprocating air compressors are said to have about 30[%]. This value includes the motor efficiency, but the motor efficiency is more than 80[%], so even if the motor efficiency is not included, we can say that we have achieved a compressor with a very high efficiency compared to conventional air compressors.

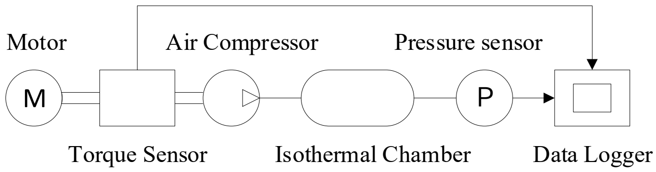

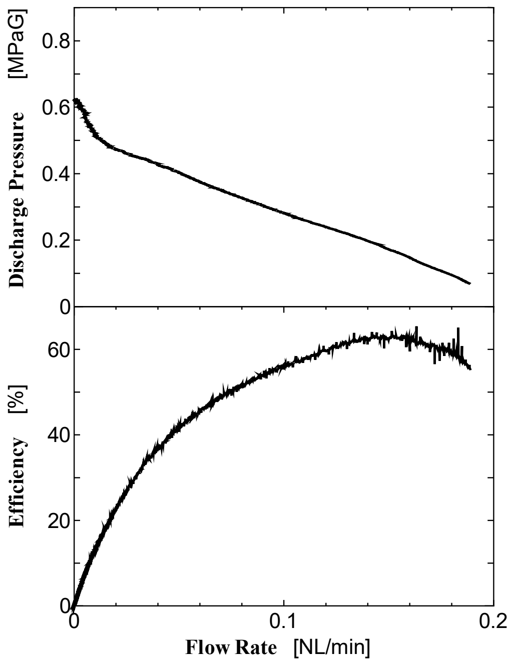

Figure 7. Measured Characteristics of Air Compressor

Figure 8. Measuring Apparatus for Air Compressor Characteristics

Measurement of Wind Powered Air Compressor Characteristics

Fig.9 shows the apparatus used to measure the characteristics of the wind powered air compressor. A constant wind speed was given to the wind powered air compressor by a blower and a wind tunnel, and the compressed air generated at that time was filled into an isothermal pressure vessel. From this pressure response, the pressure flow characteristics were obtained as in the measurement of the air compressor itself. As for the wind speed, the average wind speed in Japan is said to be 3[m/s] [3], so the wind speed was set to 3[m/s] and 5[m/s] for the measurement. Fig.10 shows the characteristics of the obtained wind powered air compressor. The maximum discharge pressure was 0,6 [MPa]. The maximum discharge pressure was 0,6 [MPa], which is slightly lower than the maximum discharge pressure of general air compressors, which is 0,6 to 0,8 [MPa], but still practical. On the other hand, it can be seen that the flow rate increases as the wind speed increases, but the efficiency decreases. This means that it is necessary to match the wind turbine characteristics with the air compressor characteristics so that the maximum efficiency points are the same.

Consider the case where an air compressor is driven by electricity generated by a wind turbine in a remote location. If we assume that the efficiency of the wind turbine is 40[%], the transmission loss of electricity is 20[%], and the efficiency of the compressor is 50[%], the overall efficiency is 16[%]. The maximum efficiency obtained is lower than this value, and it can be said that the efficiency needs to be improved. Since the efficiency of a single wind turbine is low, we believe that it will be possible to improve the efficiency of a single wind turbine and to match the characteristics of wind turbines and air compressors.

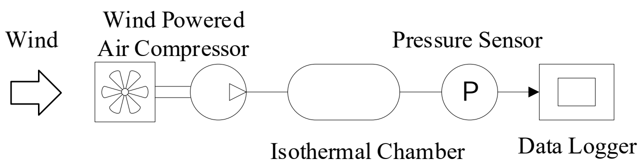

Figure 9. Apparatus Used to Measure the Characteristics of the Wind Powered Air Compressor

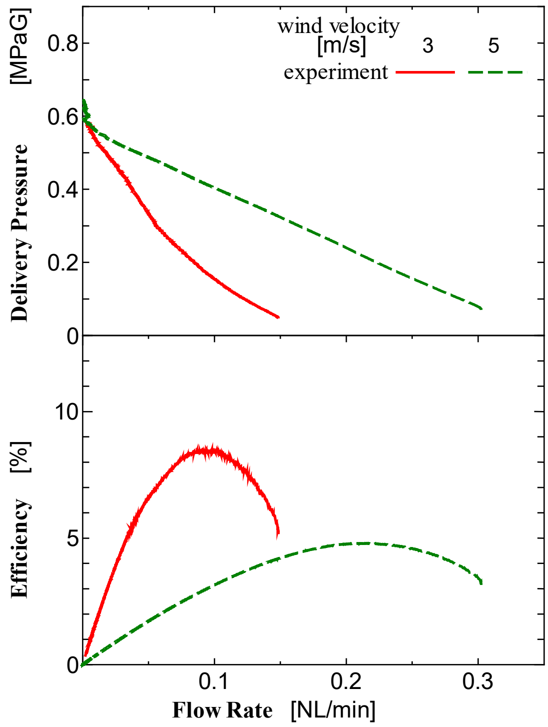

Figure 10. overall efficiency (u=3,5[m/s])

CONCLUSION

We proposed and fabricated a prototype of a wind powered air compressor that utilizes wind energy to reduce greenhouse gas emissions. A compression mechanism using a hypocycloid was shown for that air compressor. The characteristics of the air compressor itself were measured and showed a high efficiency of 60[%]. As a result of measuring the characteristics of the prototype wind powered air compressor, a maximum discharge pressure of 0.6[MPa] and a maximum efficiency of 9[%] were obtained at the annual average wind speed of 3[m/s] in Japan. It was found that the discharge pressure was about the same as that of an ordinary air compressor, and if the efficiency could be improved, it could be put to practical use.

REFERENCES

1. ONEYAMA, N., Energy conservation in pneumatic systems, Energy Conservation Center, 2003, pp.9-12.
2. USHIYAMA, I., Introduction to Wind Turbine Engineering -From Basic Theory to Wind Power Generation Technology-(2nd edition), Morikita Publishing, 2004,pp1-5,139-140,156-162.
3. https://www.data.jma.go.jp/obd/stats/etrn/view/monthly_s3.php?prec_no=14&block_no=47412&year=2019&month=&day=&view=a (accessed on 1 May, 2021)

The 11th JFPS International Symposium on Fluid Power HAKODATE 2020 Oct. 12-13, 2021 JFPS The Japan Fluid Power System Society

Development of Bidirectional Arm Curl Machine Using Pneumatic Artificial Rubber Muscles

Toshihiro KAWASE*,**, Tomoya NAKANISHI*, Shintaro YOSHIDA***, Shingo OHNO***, Ryo SAKURAI***, Tetsuro MIYAZAKI****, Takahiro KANNO*****, Maina SOGABE****, Yoshikazu NAKAJIMA*, Kenji KAWASHIMA****

* Institute of Biomaterials and Bioengineering, Tokyo Medical and Dental University
2-3-10 Kandasurugadai, Chiyoda-ku, Tokyo, 101-0062 Japan
(E-mail: kawase.bmi@tmd.ac.jp)
** Institute of Innovative Research, Tokyo Institute of Technology
4259 Nagatsuta, Midori-ku, Yokohama, Kanagawa 226-8503 Japan
*** Bridgestone Corporation
3-1-1 Ogawahigashi-cho, Kodaira-shi, Tokyo 187-8531 Japan
**** Department of Information Physics and Computing, The University of Tokyo
7-3-1 Hongo, Bunkyo-ku, Tokyo, 113-8656 Japan
***** RIVERFIELD, Inc.
Yotsuya Medical Bldg. 5th floor, 20 Samon-cho, Shinjuku-ku, Tokyo, 160-0017 Japan

Abstract. Physical training with unpredictable perturbations is commonly used to prevent injuries of athletes or older adults. In our previous study, we have developed an arm curl machine that exerts unpredictable loads using a pneumatic artificial rubber muscle (PARM). In this study, we extended the arm curl machine to exert load with unpredictable direction on an elbow. The machine was extended to generate both of flexional and extensional forces with antagonistic actuation of PARMs. Force control of the PARMs was implemented for accurate control of the tension of PARMs. The effect of training using the extended arm curl machine was tested by an experimental training with six healthy participants. The results suggested that the training using load with unpredictable direction generated by the machine had effects on the reduction of extra muscle activation on trunk.

Keywords: Muscle training, Pneumatic artificial rubber muscle, Antagonistic actuation

INTRODUCTION

Physical training with unpredictable perturbations is commonly used to prevent injuries of athletes or older adults [1][2]. In our previous study, we have developed an arm curl machine that exerts unpredictable loads using a pneumatic artificial rubber muscle (PARM) and showed the possibility of effective muscle strength improvement against unpredictable load [3]. In the arm curl machine, the direction of exerted force was only downward as in conventional arm curl machines. In real situations in exercises, the direction of perturbations may also be unpredictable. Generally, the direction of load during movement or posture maintenance is a key factor that determine the pattern of coordinated activity of muscles. Incorrectly coordinated muscle activities under the load may cause dangerous postural change, and training to prevent the hazard, which is caused by load with unpredictable direction, should be considered. In this study, we extended the arm curl machine to exert flexional and extensional force on an elbow with antagonistic actuation using PARMs and confirmed its effect in a training using unpredictable loads by an experiment.

BIDIRECTIONAL ARM CURL MACHINE

Figure 1 shows the developed arm curl machine. The weights of a commercially available arm curl machine (Freemotion Epic Bicep, Icon Health & Fitness, Inc.) were disconnected from its joint, and PARMs (supplied by Bridgestone Corp.) were connected to the joint by wires on flexion (upward) and extension (downward) sides. We used double PARMs on the flexion side for gravity compensation. A rotary encoder (MES-12-1000PST8E, MICROTECH LABORATORY) was attached on the joint of arm curl machine to calculate gravity force on the machine. A force sensor (FGP-50 and FGP-100, Nidec-Shimpo Corp.) was attached to each set of the PARMs and a servo valves (MPYE-5-1/4-010-B, Festo) was connected to each PARM for the control of generated forces.

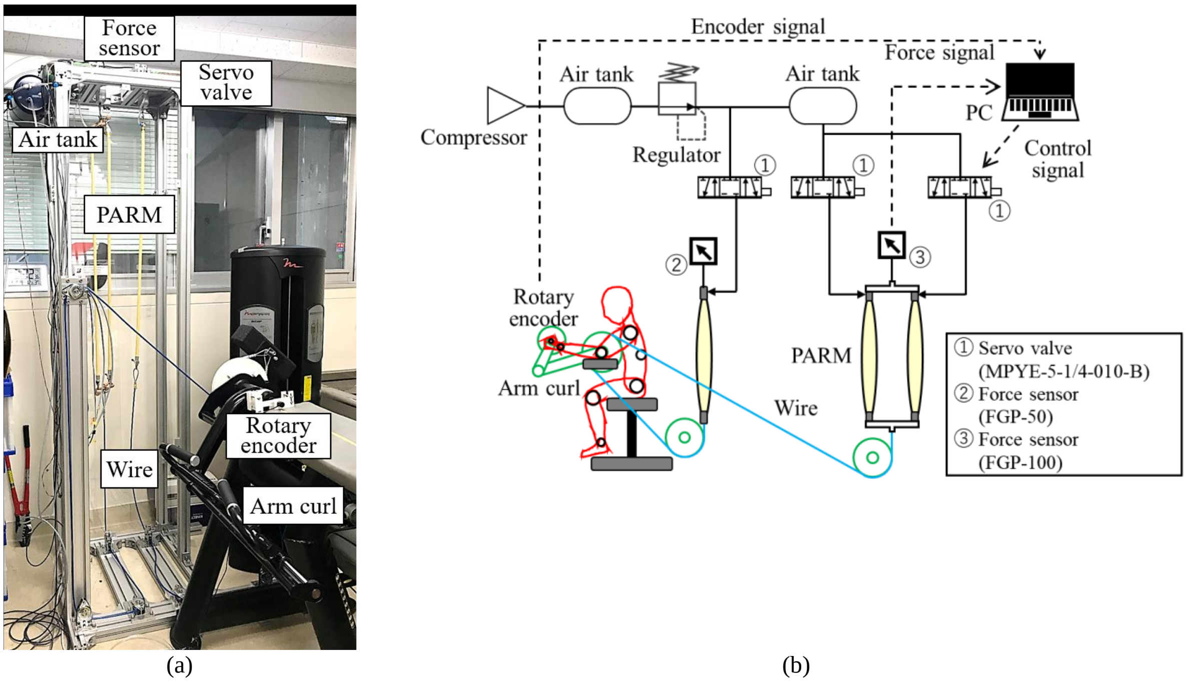

Figure 1. The developed bidirectional arm curl machine. (a) Appearance of the machine. (b) System overview.

The block diagram of the control system is shown in Fig. 2. Force control helped by the force sensors was used to control the tension of PARMs accurately, while the previous version used pressure control [3]. The gain parameters for the force control are shown in Table 1. A PARM on the extension side exerted extensional loads, and two PARMs on the flexion side exerted flexional loads and torque for gravity compensation (Fig. 3). This control system could supply constant force regardless of the posture.

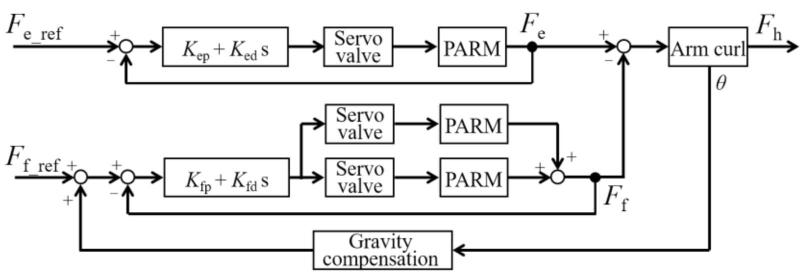

Figure 2. Block diagram of the arm curl machine

Table 1. Gain parameters for force control of PARMs

K_{ep} [V / N]	0.11
K_{ed} [V / (N s)]	0.0001
K_{fp} [V / N]	0.09
K_{fd} [V / (N s)]	0.0001

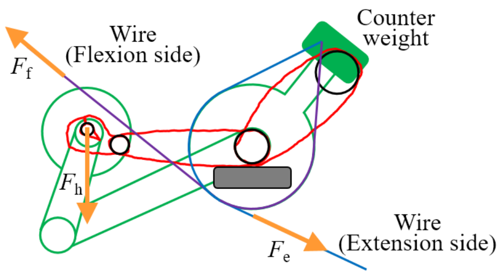

Figure 3. Force on the machine and a trainee

EXPERIMENT

The arm curl machine could present loads with unpredictable direction (extension or flexion), which could not be presented by the previous version. To confirm its effect on physical training, we conducted an experiment with participants.

Six healthy males participated in the experiment. First, the participants maintained their posture under a 1-minute load pattern with randomized amplitude, direction and timing (pre-test task). Second, they trained their posture maintenance under a load pattern with unpredictable direction (Direction pattern; Fig. 4(a)) (training task). The training duration was 3 minutes in total for each participant. Finally, the participants carried out the first 1-minute task again (post-test task). The series of the tasks was conducted with other three load patterns during training without unpredictable direction: load patterns with unpredictable amplitude (Amplitude pattern; Fig. 4(b)), with unpredictable timing (Timing pattern; Fig. 4(c)) and with predictable, cyclic change (Cyclic pattern; Fig. 4(d)).

Through the experiment, we measured surface electromyography (EMG) signals of four muscles: arm muscles (biceps and triceps) and trunk muscles (rectus abdominis and latissimus dorsi). We used EMG measurement system with active electrodes (Bagnoli EMG System, DELSYS) and calculated EMG amplitudes during flexional and extensional load in pre-test and post-test tasks by root-mean-square value of EMG signals. We compared the ratio of EMG amplitude in the post-test task to the amplitude in the pre-test task as an indicator of the change of muscle activity.

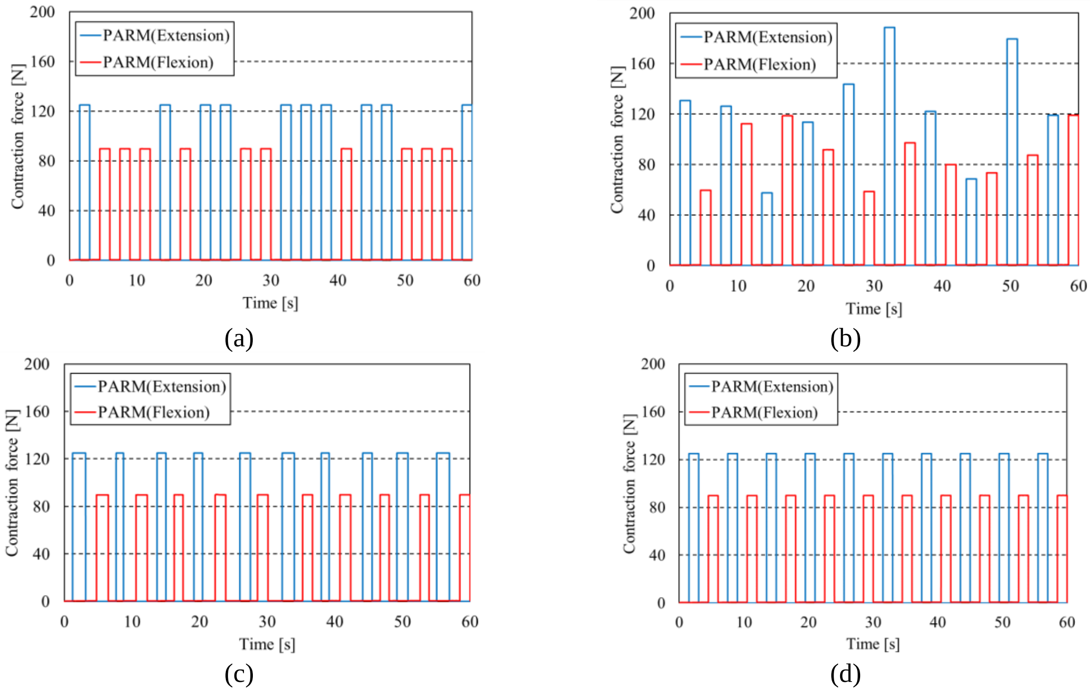

Figure 4. Example of reference force of the PARMs during a training task with four load patterns: Direction pattern (a), Amplitude pattern (b), Timing pattern (c) and Cyclic pattern (d).

RESULT

Figure 5 shows the ratio of EMG amplitude in the post-test task to the amplitude in the pre-test task under the training with four load patterns (means and standard deviations between the participants). In the case of training with Direction pattern (Fig. 5(a)), the EMG amplitude of rectus abdominis showed significant reduction after the training (t-test, $p < 0.05$) in both direction of the load. This phenomenon could not be found in the other training tasks (Fig. 5(b-c)). The rectus abdominis is the muscle that contributes to posture maintenance of upper body; however, in the situation of use of arm curl machine, the activation of rectus abdominis would not be required because the upper arm is fixed on the machine. The results suggest that the training task with unpredictable direction could contribute to restrain over-activation of trunk muscles under unpredictable perturbations.

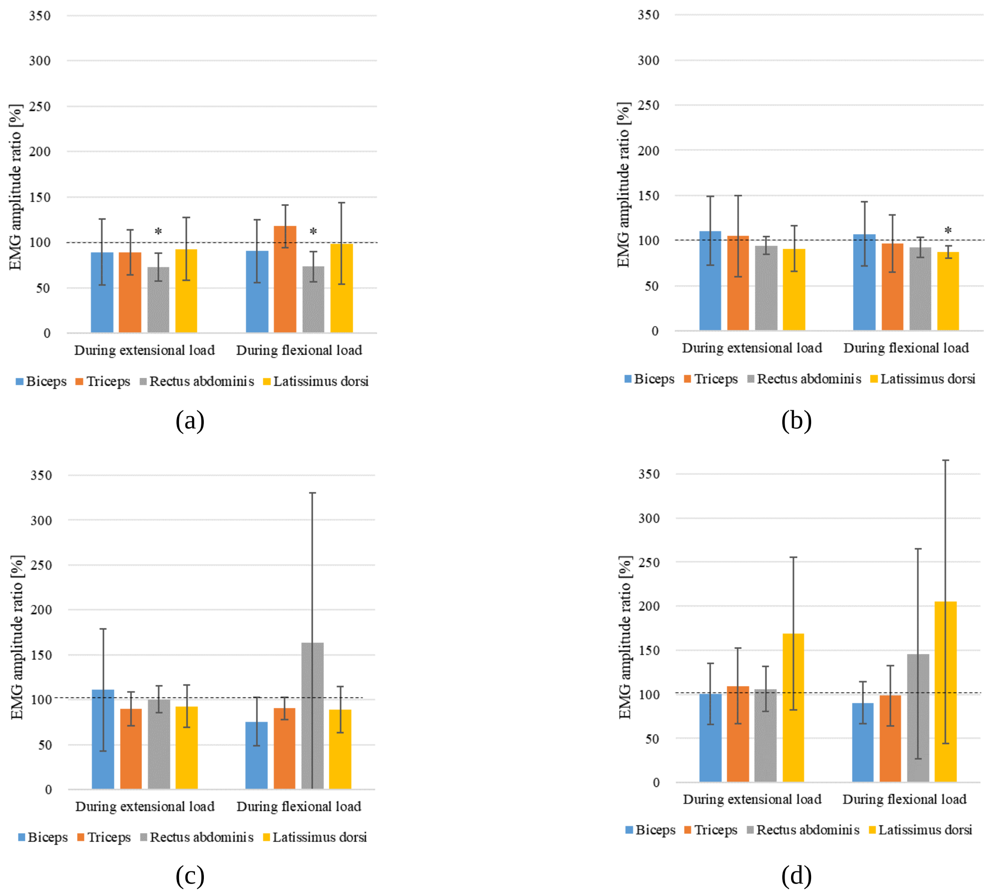

Figure 5. Ratio of EMG amplitude in the post-test task to the amplitude in the pre-test task under the training with four load patterns: Direction pattern (a), Amplitude pattern (b), Timing pattern (c) and Cyclic pattern (d). Means and standard deviations between the six participants are shown. The asterisks show the significant difference of the ratio from 100% ($p < 0.05$).

CONCLUSION

We developed an arm curl machine using PARMs that could exert extensional and flexional loads. We showed that the machine could be used for a training with loads with unpredictable direction, and the training could suppress extra muscle activation under unpredictable perturbations.

ACKNOWLEDGMENTS

This work was supported by the Bridgestone Corporation and KAKENHI (20K19594, 21H04544). This research was also based on the Cooperative Research Project of the Research Center for Biomedical Engineering.

REFERENCES

1. PATERNO. M. V., et al., Neuromuscular Training Improves Single-Limb Stability in Young Female Athletes, Journal of Orthopaedic & Sports Physical Therapy, 2004, 34-6, pp.305-316.
2. MANSFIELD. A., et al., Effect of a Perturbation-Based Balance Training Program on Compensatory Stepping and Grasping Reactions in Older Adults: A Randomized Controlled Trial, Physical Therapy, 2010, 90-4, pp.476-491.
3. NAKANISHI, T., et al., Development of an Arm Curl Machine with Variable Resistance Using Pneumatic Artificial Rubber Muscle, Proceedings of the 2019 IEEE/RSJ International Conference on Intelligent Robots and Systems, 2018, pp.3830-3835.

The 11th JFPS International Symposium on Fluid Power HAKODATE 2020 Oct. 12-13, 2021 JFPS The Japan Fluid Power System Society

Design of a Pneumatic Oscillator for Paper Machine's Doctor Blade Systems

Michele Gabrio ANTONELLI*, Pierluigi BEOMONTE ZOBEL*, Massimiliano CENTOFANTI**, Stefano COLAIUDA**

*Department of Industrial and Information Engineering and Economics, University of L'Aquila
P.le Pontieri, Monteluco di Roio, L'Aquila, 67100 Italy
(E-mail: pierluigi.zobel@univaq.it)
**SMC Italia SpA
Località Recocce, Via delle Industrie, Carsoli (AQ), 67061, Italy

Abstract

In continuous paper machine, the cleaning of the surfaces of the cylinders, adopted for the transformation process of the paper, is essential. The component intended for this scope is the Doctor Blade. It is a steel blade that extends for the total length of the cylinder surface and that can move towards the cylinder and along it. This second motion, transversal with respect to the machine direction, is oscillatory. Hydraulic, pneumatic, and electro-mechanical actuators, commercially available, are typically adopted to carry out this motion. In the present work, a pneumatic oscillator, to be mounted on one end of the Doctor Blade is described. It is made of a pneumatic cylinder equipped with two integrated limit switches. The proposed device was conceived to guarantee the following performances: low cyclic motion, simple and intuitive speed adjustment, ease of assembly and feeding, shielding from external corrosive agents.

Keywords: Pneumatic Oscillator, Actuator Design, Paper Machine, Doctor Blade

1. INTRODUCTION

Pneumatic systems are particularly suitable in environments with moisture problems or the presence of flammable material, in which electrical components are not reliable, and for their low cost and their good power to weight ratio. One of the sectors which requires the use of pneumatic actuators is the paper production sector.

The paper production begins with the supplying of wood from trees, continues with the production of paper coils through the continuous machine with the processing of different cellulose mixtures and ends with the transformation of these large mother coils into finished products.

Neglecting the transformation cycle from the starting wood until the produced cellulose mixtures, once transferred to the paper mill, the latter are spread with water and undergo purging processes, so as to eliminate possible polluting residues, and refining, to give certain mechanical characteristics to the product [1]. In the entrance to the continuous machine there is a suspension of water and fibrous material (concentration less than 1%) from which the paper will be produced. Along the continuous machine, the suspension gradually undergoes a transformation process that consists in a progressive drying, which takes place by a sequence of operations: forming by natural drainage and suction, pressing, evaporation [2] to obtain paper coils with humidity around 5% [3]. In order to perform the sequence of operations, the continuous machine is made of several components: the headbox for conveying the fibrous dough, diluted over 99% of water, into the forming area where the dough, once released on training canvas moved by cylinders, undergoes, in the form of sheet, the phenomenon of drainage in order to remove part of the water from it; presses, made of some cylinders covered by felt, for reducing the residual amount of water; a dry zone, made of the Yankee cylinder and a metal hood, for evaporating the water from 50-60% until a content of about 5%; finally, a cylinder for winding the paper coils until they reach the desired diameter. Coils represent the raw material of the paper works, through which the finished products are produced and packed.

Among the finished products, tissue papers are intended for hygienic and sanitary use with the principal characteristic of softness and bulkiness. These properties are given to the paper thanks to some factors as the degree of adhesion of the paper sheet to the forming cylinders and the difference in speed between the dryer cylinder and the coiler. Another important factor is the action of the Doctor Blades (DBs), steel blades positioned in contact with the cylinders, which have the main tasks of cleaning the surfaces of the cylinders and detaching the sheet leaving a series of small waves imprinted on it [4]. One aspect to be considered is the proper position of a DB with respect to the cylinders that can be adjusted according two modes [5]. The first mode expects the adoption of pneumatic or hydraulic cylinders that approach and move away the DB and its support. The second

mode expects the adoption of a couple of alternatively deformable pneumatic tubes positioned on the sides of a hinge: as pneumatic muscles [6, 7], the radial expansion of the tubes provides for a pushing action on the support of the DB that rotates around the hinge, approaching or moving away the cylinders. Another aspect is the oscillatory motion of the DB (forward and backward) along a cylinder for scraping the external surface of the cylinder. It can be carried out by hydraulic, pneumatic, and electro-mechanical actuators [5]. Pneumatic ones are most common: they can be made by one or more pneumatic air springs with slide mechanism [5, 8] or by pneumatic cylinders [9, 10]. Registered innovations of DB are: new materials as hard carbon and a specially developed epoxy and the equipment of sensors for detecting incorrect settings of the DB [11]; simpler technique of disassembling for a regular maintenance of the pressure tubes, a regular cleaning of the blade pocket and a regular inspection of the top-plate [12]; material water repellent to facilitate cleaning operations while ensuring longer life due to absence of protective treatments [13].
The present research is focused on the development of a pneumatic oscillator to be mounted on a commercial continuous paper machine, for the oscillatory motion of DBs along cylinders. The proposed pneumatic oscillator is made of a pneumatic cylinder equipped with two limit switching systems installed within the two heads of the cylinder. Each system is made of a 2/2 monostable pneumatic valve directly commanded by the piston of the cylinder. Such pneumatic oscillator is mounted at one end of the support of each DB in a continuous machine for the paper production. The concept idea and the design of the pneumatic oscillator are here reported.

2. BACKGROUND

2.1 The doctoring system on the continuous paper machine

An effective and hassle-free cleaning system is essential for the operation of the modern, automatic, and computer-controlled paper machine. The use of good cleaning practices and the best available materials can result in a better machine drivability, safer operations, reduced water consumption, energy savings and an excellent quality of the paper. A very important part of the continuous paper machine is the system of scrape of the cylinders of the forming and pressing processes, made of oscillating blades called DBs. As shown in Figure 1, a DB system expects a blade, that extends for the total length of the cylinder surface, a support beam of the blade equipped with a tank for the containment of processing fluids and a positioner of the support beam. When it is required, the entire system must oscillate along the transverse direction of the machine.

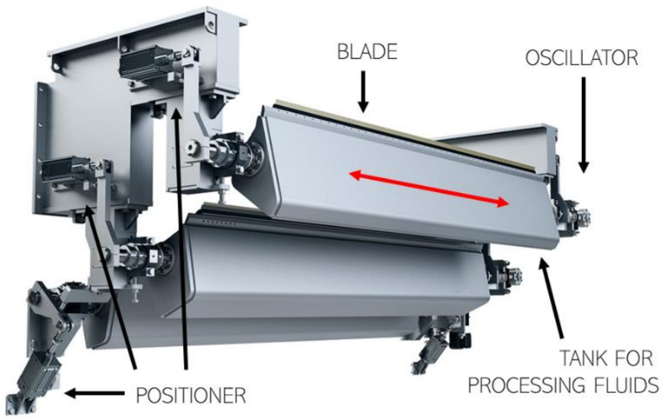

Figure 1. Doctor Blade system with three blades

The DB system has:
- to ensure the proper cleaning of the surface of the cylinder, avoiding the accumulation of foreign material on it, which can compromise the quality of the paper sheet and damage the cylinder;
- to avoid a sanding through the surface of the cylinder and maintain the proper surface roughness for a very long period;
- to ensure the proper detachment of the paper sheet during the forming and pressing process;
- to redirect the paper sheet and prevent it from wrapping around the cylinders.

2.2 Details of the application

The DB system of interest is shown in Figure 2: it is possible to distinguish the blade, the tank for the fluids and the flange interface between the pneumatic oscillator, to be mounted, and the support beam.

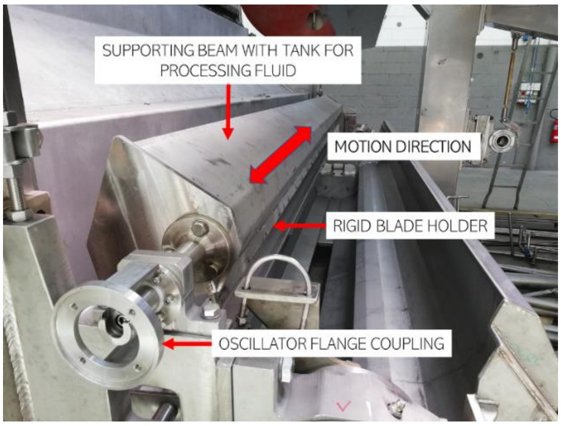

Figure 2. Details of the commercial Doctor Blade system to be moved

The technical requirements are reported in the follow:
- the amplitude of the oscillatory motion can vary in the range 10 - 20 mm;
- the frequency of the oscillatory motion can vary in the range 1 - 10 cycles/min;
- the oscillatory motion has to be linear and fluid.

It means that the cylinder of the oscillator must move at low adjustable speeds. Hence, it must be equipped with an integrated adjustment device. Finally, a low friction pneumatic cylinder (equipped with proper gaskets and greases) must be adopted in order to minimize the stick-slip phenomenon. In addition, no significant backslash in the drive mechanism must be occurred. About the continuous functioning, the pneumatic oscillator must be an automated device. For this reason, it must be equipped with only one inlet port for the compressed air: once connected to the pneumatic line, the oscillator must operate autonomously. Finally, since the oscillator works in a corrosive environment and with a high humidity rate, the external components must be made of stainless steel AISI 304.
The technical specifications of the cylinder of the pneumatic oscillator are reported in Table 1.

Table 1. Pneumatic cylinder technical specifications

Force	11 kN at 6 bar
Stroke	20 ± 1 mm
Number of cycles	1 – 10 cycles/min
Operating pressure	2 ÷ 8 bar
Integrate regulation system	Single air inlet port and a flow regulator for speed adjustment
Suitable for corrosive environments	Material of the outer components: AISI 304

3. MATERIALS AND METHODS

3.1 Preliminary consideration to the design of the pneumatic oscillator

The first step was the definition of the regulation circuit necessary to allow the oscillation of the cylinder. The type of the circuit influences the architecture of the cylinder. Two different solutions were preliminary conceived: the first one is based on timed control pulses of the pilot valve; the second is based on mechanical limit switch valves.
The first solution requires the development of the circuit shown in Figure 3, easily to be integrated on iso/standard cylinder and with a low cost of production. With reference to the Figure, flow regulators S_1 and S_2 are necessary for the speed adjustment; the flow regulators S_3 is connected at one end to the line of the chamber (a) and at the other to the command side of the pilot valve for powering the chamber (b). The current configuration of the circuit expects that compressed air moves to the chamber (a) and provides for the leftward motion of the piston with a speed depending on the throttling level of the regulator S_1; moreover, compressed air moves through the flow regulator S_3 and after a certain time, depending on the throttling level of the regulator, gives the command input (command 14) for switching the pilot valve. When it occurs, both the lines to S_3 are connected to the exhaust and the piston moves rightward. Then the flow regulator S_4 works as S_3, but on the opposite side of the pilot valve, giving the timed pulse command input 12.

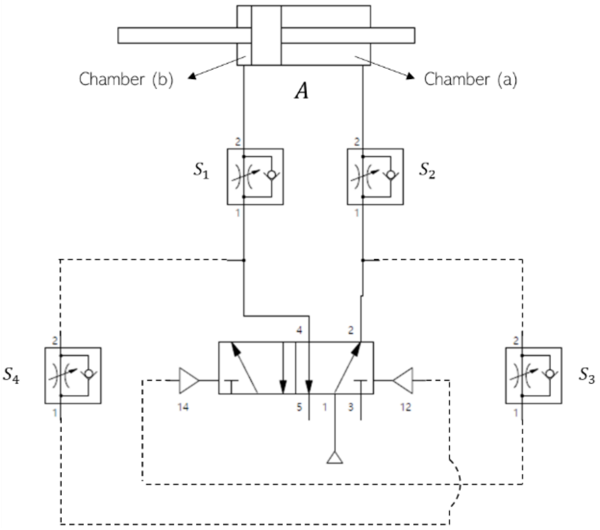

Figure 3. Regulation circuit for the pneumatic oscillator: solution 1

Dimensions of the flow regulator guided the choice to replace the pneumatic timer, bulkier. This solution is time-based and allows the cylinder to move autonomously. Preliminary experimental tests confirmed the described working principle. Nevertheless, to assure the same behavior of the motion along the rightward and leftward stroke, the length of the pneumatic lines should be equal, and the throttling level of the flow regulators should be the same. Moreover, with the change of the desired speed, four manual regulations must be carried out. In addition, synchronization between the speed of the piston and the switching time must be carried out. Finally, due to the low value of the switch pressure of the pilot valve (about 0.03 MPa), flow regulators with a narrow passage section are necessary.

For these critical aspects, the second solution was explored. It requires the development of a circuit that adopts two limit switch valves. With reference to Figure 4, the switch valves a_0 and a_1 are mechanical operated 2/2 monostable pneumatic valves: the pilot valve, a 5/2 monostable pneumatic valve, normally provide for the leftward motion of the piston; when the left rod of the cylinder activates a_0, the latter provides for the 14 command input for switching the pilot valve; hence, the piston rightward moves and the pneumatic line between a_0 and the pilot valve remains pressurized; when the right rod of the cylinder activates a_1, the pilot valve switch to its normal position and the pneumatic line between a_0 and the pilot valve is connected to the exhaust. In order to have a unique point of adjustment of the speed, only one flow regulator is adopted: it is connected to the exhaust ports of the pilot valve.

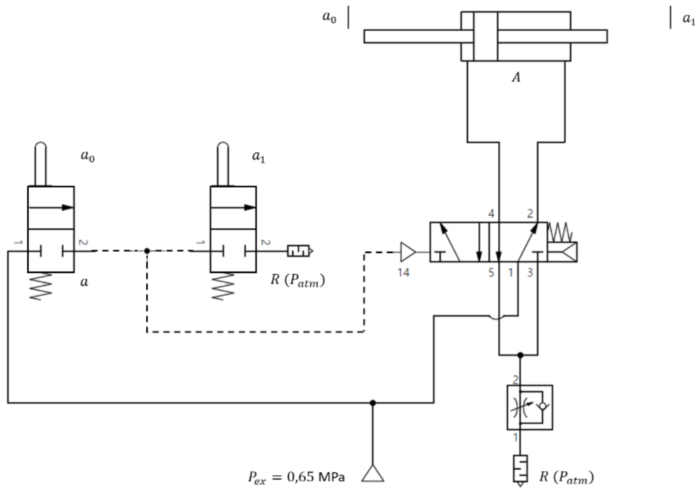

Figure 4. Regulation circuit for the pneumatic oscillator: solution 2

In preliminary experimental tests, 2/2 monostable valves were replaced by 3/2 monostable valves, in which the exhaust ports were capped. For a power supply pressure equal to 0.65 MPa, circuits confirmed the proper functioning. The adjustment of the throttling of the flow regulator was easy to carry out with an improved behavior with respect to the first solution.

3.2 The proposed solution

Figure 5 shows a section view of the cylinder. It is possible to distinguish the two limit switches and how the piston touches and activates the internally integrated valves: if the CHAMBER (A) is powered and the CHMABER (B) unloads, the piston moves downward and touches the limit switch of the lower head. The force exerted on the rod of the limit switch causes air to pass through and the pilot valve, mounted externally of the higher head, to be switched. When the pilot valve switches, the CHAMBER (B) is powered, the CHAMBER (A) unloads and the piston moves upward. When the other limit is operated, the cycle is repeated.

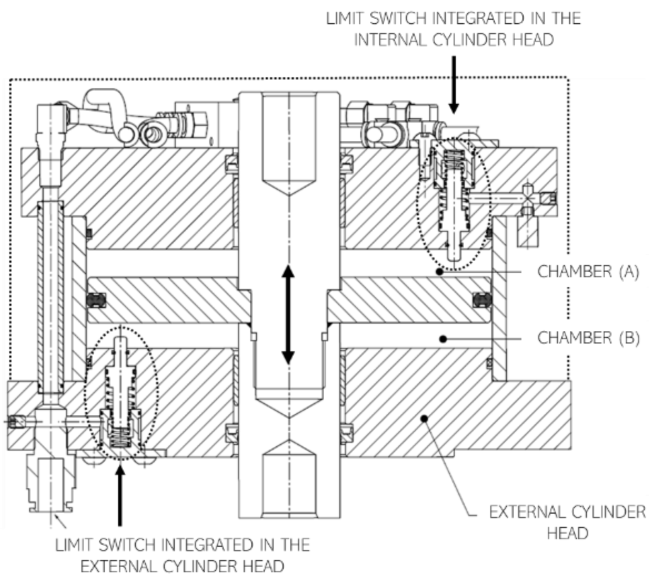

Figure 5. Section view of the cylinder and detail of the two integrated limit switches

The limit switch system is the most important element of the oscillator and is shown in Figure 6. It consists of a movable rod, kept in a resting position by two steel springs EN 10270-1 SH(C) placed in parallel, which moves inside a seat obtained directly in the two heads. The rod is characterized by two lip seals, which isolate the valve body from the inner chamber of the cylinder, and a piston seal that isolates chamber (1) from chamber (2). The system was designed to replicate the operation of a mechanical operated 2/2 (NC) monostable valve: when the piston touches the rod, pushes it and the piston seal downward allowing the passage of air for the switching of the pilot valve.

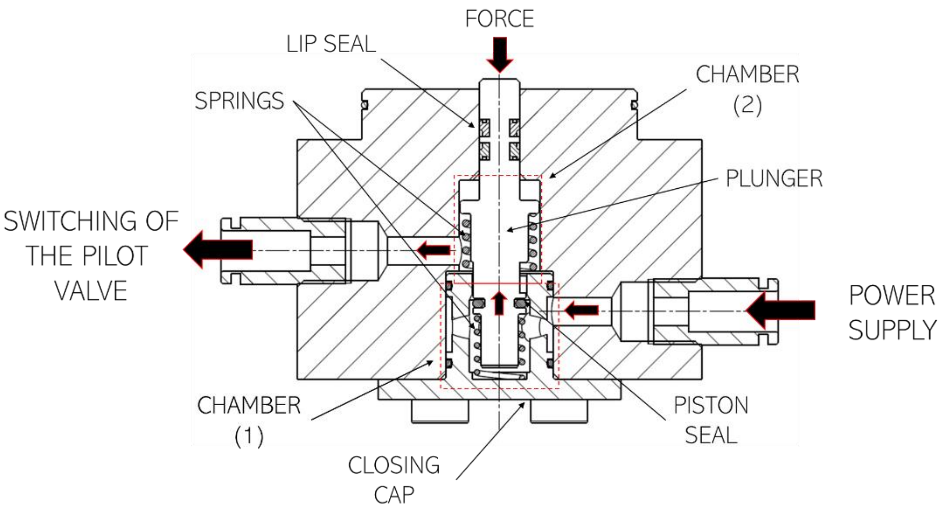

Figure 6. Details of the structure of the limit switch system integrated in the cylinder heads

With reference to Figure 6, the critical area turns out to be the passage section of the fluid, from chamber (1) to chamber (2). This section must be open and closed whenever the piston touches the rod to determine the switching of the pilot valve. The closing cap solved this problem. It was designed not only with the ultimate aim of hermetically closing the system from the outside, but also with the aim of making possible the variation of the section diameter in the passage between the chamber (2) and the chamber (1) and of isolating, between them, the

two chambers. For the latter aim, there is a dynamic seal on the rod: it is not a simple O-ring, but a piston seal. Once mounted, the cap constitutes the chamber (1).
The chamber (1) of the limit switch mounted in correspondence of the CHAMBER (B) is always pressurized: it is directly connected to the main pneumatic line which also provides for the power supply of the pilot valve. During the motion of the rod of the limit switch, due to the exerted force of the piston, the passage section between the chamber (1) and the chamber (2) increases. With reference to Figure 5, as regards the limit switch mounted in correspondence of the CHAMBER (B), the air moves towards the command port of the pilot valve, in the form of a positive command: when the value of the pressure reaches the pilot pressure value, the pilot valve switches, and the piston moves upward. As regards the limit switch mounted in correspondence of the CHAMBER (A), the air moves toward the exhaust port in the form of a negative command, removing the air along the command line of the pilot valve that reaches its normal position. A silencer provides to reduce the noise due the exiting air.
The adjustment system is integrated into the cylinder through a combination of internal and external ducts. In fact, it is necessary to replicate the pneumatic circuit shown in Figure 4 and to integrate it in the cylinder, making the pneumatic cylinder and the adjustment circuit a single and compact body. The main pneumatic branches are shown in the rendered Figure 7a, with different colors:
- in light blue, between the two red lines, the supply branch allows air to be brought from the external supply line to the pilot valve;
- in light blue, in the lower part, the supply/unloading branches of the CHAMBERS (A) and (B);
- in green, the control branch that brings the switching pulses from the integrated limit switching system in the two heads up to the pilot valve, command side;
- in red, the exhaust branch of the two CHAMBERS (A) and (B) and the connection to the pilot valve exhaust ports with the flow regulator (not visible).

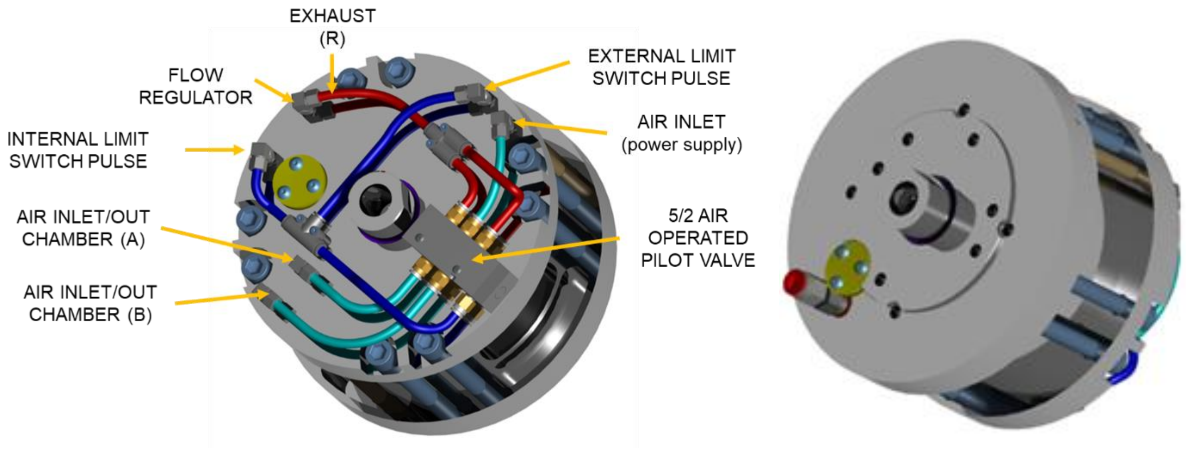

(a) (b)

Figure 7. Definition of the connecting branches of the regulation system

The designed pneumatic oscillator has a construction architecture typical of normal double-effect cylinders with through rod. In the Figure 7b, the cylinder looks like a compact body, in which only one head is visible externally (the one in contact with the external environment). To avoid all the components made of stainless, it was thought to make a watertight protective casing. The head that interfaces both with the machine, by coupling flange, and with the main line of compressed air for the cylinder supply was also conceived to be made of AISI 304, as well as the rod that couples with the DB system to be moved.

4. CONCLUSIONS

In the present paper, the design of a new pneumatic oscillator for a Doctor Blade system was presented. The oscillator is made of a double-effect cylinder with through rod equipped with an internally integrated limit switch in each head. The proposed design will provide for an autonomous pneumatic oscillator with a single air inlet port and a flow regulator for speed adjustment. The next step of the development activity expects the prototyping of the proposed solution and a first campaign of experimental tests to validate the working principle and to achieve the performances of the overall system. Improvements could be introduced in order to reach and industrial and marketable product.

REFERENCES

1. DE ASSIS, T., REISINGER, L. W., PAL, L., PAWLAK, J., JAMEEL, H., GONZALEZ R. W., Understanding the Effect of Machine Technology and Cellulosic Fibers on Tissue Properties – A Review, BioResources, Vol.13, No.2, 2018, pp.4593-4629.
2. AXELSSON, B., Pulp for high absorption tissue products, Paper Technology, Vol.42, No.7, 2001, pp.24-26.
3. KULLANDER, J., NILSSON, L., BARBIER, C. Evaluation of furnishes for tissue manufacturing; suction box dewatering and paper testing, Nordic Pulp & Paper Research Journal, Vol.27, No.1, 2012, pp.143-150.
4. BERNI, A., MENNIG, M., SCHMIDT, H. Doctor Blade. In: Aegerter M.A., Mennig M. (eds) Sol-Gel Technologies for Glass Producers and Users. Springer, Boston, MA, 2004, pp. 89-92.
5. https://www.valmet.com/globalassets/media/downloads/white-papers/process-improvements-and-arts/wpp_doctoring.pdf (accessed on 1 June, 2021)
6. ANTONELLI, M. G, BEOMONTE ZOBEL, P., DURANTE, F., RAPARELLI, T. Numerical modelling and experimental validation of a McKibben pneumatic muscle actuator, Journal of Intelligent Material Systems and Structures, Vol.28, No.19, 2017, pp.2737-2748.
7. DURANTE, F., ANTONELLI, M. G., BEOMONTE ZOBEL, P., RAPARELLI, T. Development of a Straight Fibers Pneumatic Muscle, International Journal of Automation Technology, Vol.12, No.3, 2018, pp. 413-423.
8. WAKE, H. D., Oscillating Doctor-Blade Mechanism, United States Patent 3,750,228, August, 7, 1973.
9. https://www.valmet.com/media/articles/all-articles/valmet-doctor-oscillators-for-reliable-maintenance-free-service/ (accessed on 1 June, 2021)
10. https://dcf.kadant.com/it/prodotti/raschiatura/oscillatore-varimatic (accessed on 1 June, 2021)
11. https://voith.com/corp-en/papermaking/doctor-and-creping-blades.html (accessed on 1 June, 2021)
12. https://www.clouth.com/en/ticker/2020/06/23/clouthr-topslide-the-innovative-doctor-blade-holder-with-patented-quick-top-system (accessed on 1 June, 2021)
13. https://www.flexofem.com/en/doctor-blade-system/ (accessed on 1 June, 2021)

Genaral Session | Oil hydraulics

Components and Systems 2

[GS5-2-01] Leakage Characteristics of a 3-port Pressure Reducing Valve

〇Haroon Ahmad Khan[1], Byeong-Il Choi[2], Jung-Ho Park[2], So-Nam Yun[2] (1.University of Science and Technology, Korea, 2.Korea Institute of Machinery and Materials)

[GS5-2-02] Generation Mechanism of Flow Force Acting on Spool Valve

〇Fumio Shimizu[1], Kazuhiro Tanaka[1] (1.Kyushu Institute of Technology)

[GS5-2-03] The Effect of the Spline Coupling on the Rotating Assembly Tilt Behavior in a High-speed Axial Piston Pump

〇Haogong Xu[1], Junhui Zhang[1], Weidi Huang[1], Bing Xu[1], Fei Lyv[1], Xiaochen Huang[1] (1.State Key Laboratory of Fluid Power and Mechatronic Systems, Zhejiang University)

[GS5-2-04] First-order Trajectory Sensitivity Analysis of Multi-level Pressure Switching Control System

Jing Yao[1,2,3], 〇Pei Wang[1], Xinhao Li[1], Yuwang Cheng[1], Xiaoming Cao[1] (1.School of Mechanical Engineering, Yanshan University, 2.Key Laboratory of Advanced Forging &Stamping Technology and Science of Ministry of Education of China, 3.Hebei Key Laboratory of Heavy Machinery Fluid Power Transmission and Control)

[GS5-2-05] A Study on the Pulse Analysis and Vibration Characteristics of Hydraulic System for Prediction of Check Valve Behavior

〇Jeong-Woo Park[1,2], So-Nam Yun[1], Young-Bog Ham[1], Eun-A Jeong[1] (1.Korea Institute of Machinery &Materials, 2.Chungnam National University)

[GS5-2-06] Research on an Oil-hydraulic Component to Reduce Pressure Pulsation

〇Yasuo Sakurai[1], Misaki Hashimoto[2], Moritaka Maehara[3], Norikazu Hyodo[4] (1.Ashikaga University, 2.MITSUBA Corporation, 3.SAWAFUJI ELECTRIC CO., LTD., 4.TOKYO KEIKI INC.)

The 11th JFPS International Symposium on Fluid Power HAKODATE 2020 Oct. 12-13, 2021 JFPS The Japan Fluid Power System Society

Leakage Characteristics of a 3-port Pressure Reducing Valve

Haroon Ahmad KHAN*, Byeong-Il CHOI**, Jung-Ho PARK** and So-Nam YUN**

*University of Science and Technology
217 Gajeong-ro, Gajeong-dong, Yuseong-gu, Daejeon, Korea
(E-mail: ysn688@kimm.re.kr)
** Korea Institute of Machinery and Materials,
156 Gajeongbuk-ro, Jang-dong, Yuseong-gu, Daejeon, Korea

Abstract. Leakage in hydraulic system is directly related to power losses in the system which is undesirable in any application. Pressure reducing valves have two ports or three ports depending on application. Leakage study on oil-hydraulic pressure reducing valves cannot be found in prior research work which makes this study quite significant. An experimental equipment was setup for testing the valve that included a data acquisition system and pressure sensors. The test results were recorded and analyzed in this study. The leakage of the valve was measured in a steady state with a stop watch and a beaker with volume markings. Instead of a flow sensor, a more basic approach of volume per time was followed because of the inaccuracy of flow sensors at extremely small flow rates. The valve was actuated by solenoid with an ability of having different output pressure. The leakage characteristics were obtained for different output pressures.

Keywords: Pressure Reducing Valves, Hydraulic Leakage, Pressure Control Valves, Solenoid Valves

INTRODUCTION

For any hydraulic system leakage is undesirable as it is a cause of power loss. Less leakage is always desirable but leak-free systems are mostly impossible to design in certain hydraulic valves. In some cases, leakage is inevitable if two surfaces are to slide against one another as is the case with spool valves. In a pressure reducing valve, the outlet pressure is controlled by the movement of spool inside the valve sleeve. If pressure is higher than desired pressure, the spool pushed on one side, if it is less than desired then the spool is pushed to the other side. So, using a spool is inevitable in such a valve and it requires some clearance between the spool and sleeve for the sliding movement. Due to such clearance, there a small amount of flow rate that is leaked all the time. Such a flow can be characterized as Poiseuille flow in an annular section whose formula was derived by [1] as shown in equation (1).

$$Q_{leak} = \frac{G\pi}{8\nu}[R_2^{\ 4} - R_1^{\ 4} - \frac{(R_2^{\ 2} - R_1^{\ 2})^2}{\ln(R_2 / R_1)}] \tag{1}$$

Where G is the pressure drop per unit length, R_1 is the inner radius and R_2 is the outside radius. The power loss due to leakage can be determined as:

$$P_{loss,leak} = P_{out} Q_{leak} \tag{2}$$

Where P_{out} is the pressure obtained at the reducing valve outlet. Although this power loss may be less as compared to losses in other parts of the hydraulic system, it still contributes to higher energy loss if operated for a long time.

Leakage can occur during steady state of the valve system or during dynamic state. In this study only steady state leakage was studied. For this purpose, the valve settings were kept constant during the leakage measurements as will be explained in the next sections.

VALVE DETAILS

The valve used in this study was a pressure reducing valve. Pressure reducing valves can have 3-ports or 2-ports as shown in figure 1:

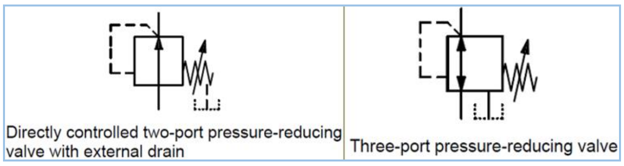

Figure 1. 2-port and 3-port Pressure Reducing Valve [2]

The advantage of using a 3-port pressure reducing valve is that it can allow the pressure at the outlet to drop by connecting the outlet to the reservoir port of the valve. However, a 2-port valve is only used in situations where the pressure at the outlet can never go over the limit set by the spring or the solenoid. In this study a 3-port pressure reducing valve was used and the leakage from outlet port to the reservoir port was tested.

EXPERIMENTAL TESTING

The valve was installed in a hydraulic power unit capable of providing a supply pressure of 50 bars. The inlet port of the valve was connected to the 50 bar pressure. The outlet of the valve was blocked so that leakage flow can be easily measure. A beaker with volumetric markings was used to collect the fluid coming out through the reservoir port. 100ml of liquid was collected and time duration was noted using a stopwatch.

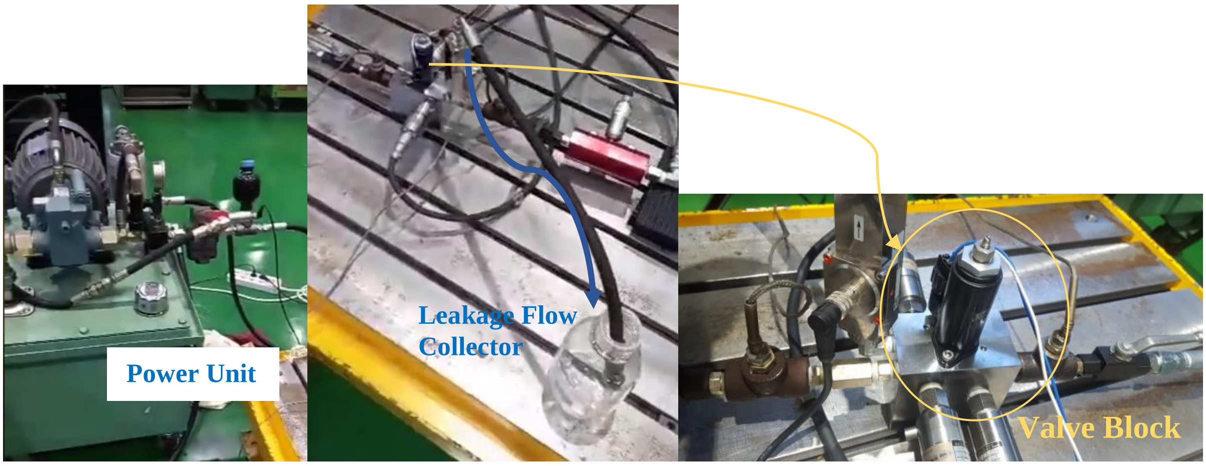

Figure 2. Experimental Details of the Leakage Measurement Equipment used for this study

The details of the hydraulic equipment used in this study is shown in figure 2. The accumulator was used at the outlet of the pressure supply from the pump in order to reduce the fluctuations in the inlet pressure as much as possible in order to have a steady state pressure as close to 50 bars as possible. The valve block was provided with three ports, the inlet port connected to the outlet of the pump, the outlet port blocked with the help of a ball valve and a reservoir port through which the leakage flow was allowed to flow to a beaker. A combination of pressure sensors connected to a data acquisition system for monitoring of the pressure fluctuations in the inlet port was employed as shown in figure 3.

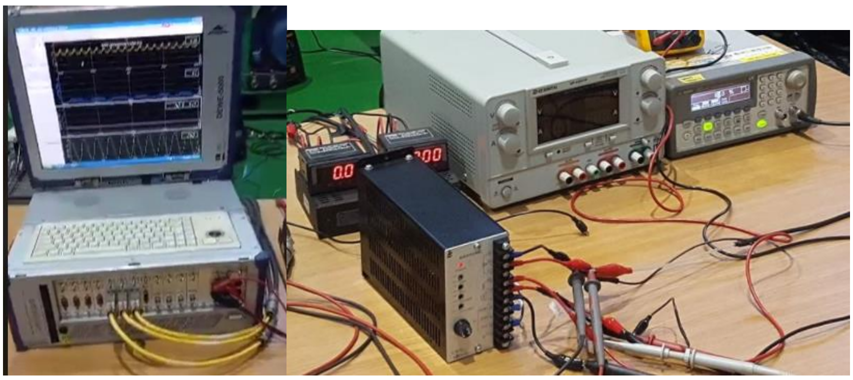

Figure 3. Data Acquisition System for the inlet pressure and Electrical Connections for Solenoid Actuator Input

2

RESULTS AND DISCUSSION

The leakage flow characteristics of the pressure reducing valve were determined by measuring the value of the flow rate that was obtained through the following simple equation:

$$Q_{leak} = \frac{Volume}{Time} = \frac{100\,ml}{Time} \tag{3}$$

When Solenoid was Actuated

When the solenoid actuator was actuated the pressure at the valve's outlet was recorded to be 37 bars. Since the outlet was kept closed through a ball valve, the pressure of 37 bars was successfully achieved without any noticeable fluctuations. The leakage value determined was 9ml/min.

When Solenoid was Turned off

In the absence of the solenoid's actuation force, the outlet pressure was reduced to a value less than 0.4 bars at which the leakage value was determined to be 12 ml/min.

Discussion

Table 1 shows a summary of the leakage-flow results.

Table 1. Leakage flow Results Summary

Solenoid State	Inlet Pressure (bars)	Outlet Pressure (bars)	Flow Rate (ml/min)
On	50	37	9
Off	50	0.4	12

The reason behind the increased flow rate when outlet pressure is increased can be explained by equation (1). At high pressure the leakage is caused by the flow between the inner valve chamber and the reservoir port while at low pressure the leakage is caused by the flow between the inlet, which is at 50 bars and the valve chamber which is at 0.4 bars. Overall the average flow rate turned out to be 10.5 ml/min which for an inlet pressure of 50 bars would result in a power loss of 0.875 watts.

CONCLUSION

The valve tested in this study had an average leakage of 10.5 ml/min. The leakage depends on the pressure. In this study, the pressure at inlet was kept constant at 50bars and fluctuations in its value was minimized by the use of an accumulator allowing us to test the valve for leakage under steady state. Power Loss was 0.875 watts. In future, further details relating leakage with the geometrical construction and inlet pressure can be determined and its effect on the power loss can be evaluated using a similar experimental setup as devised in this study.

ACKNOWLEDGMENT

This research was funded by Korea Institute of Machinery and Materials under the project title "Development of the core equipment for liquid hydrogen supply systems".

REFERENCES

1. SUTERA, S. P.; SKALAK, RICHARD, The History of Poiseuille's Law, Annual Review of Fluid Mechanics, 1993, 25: 1–19.
2. ISO 1219-1:2012, Fluid power systems and components — Graphical symbols and circuit diagrams — Part 1: Graphical symbols for conventional use and data-processing applications, 2012.

The 11th JFPS International Symposium on Fluid Power HAKODATE 2020 Oct. 12-13, 2021 The Japan Fluid Power System Society

Generation Mechanism of Flow Force Acting on Spool Valve

Fumio SHIMIZU* and Kazuhiro TANAKA**

*Department of Physics and Information Technology, Kyushu Institute of Technology
680-4 Kawazu, Iizuka city, Fukuoka, 820-8502 Japan
(E-mail: shimizu@phys.kyutech.ac.jp)
** Kyushu Institute of Technology

Abstract. In hydraulic systems, spool valves play an important role. When the spool in the valve moves to the left or right, the internal flow path changes, and the hydraulic flow rate is controlled by the valve opening. Since high-pressure fluid flows into the valve, it is necessary to predict the behavior of the spool with high accuracy. One of the problems in spool valve is the hydraulic vibration caused by the high-pressure fluid. There is a need for a control valve that can suppress the hydraulic vibration even if it is used alone. The purpose of this study is to visualize the flow field in the spool valve using three-dimensional computational analysis, and to clarify the generation mechanism of the flow force acting on the spool. The jet flow around the spool generates high- and low-pressure regions, and the pressure difference between the two regions generated the flow force.

Keywords: Spool valve, Flow force, Generation mechanism, Validation, Jet flow.

INTRODUCTION

Hydraulic systems are used in various fields, including transportation and construction machinery. The system can be roughly classified as consisting of a tank, pump, piping, hydraulic control valve, and actuator. The hydraulic control valve, such as a spool valve, plays an important role in a hydraulic system. A small spool is installed in the control valve. When the spool moves to the left or right, the flow path in the control valve changes, and the flow rate of hydraulic oil is controlled by the valve opening. A small spool, about 1 [cm] in diameter, controls the operation of a hydraulic circuit with several [MPa] of internal pressure. Therefore, the behavior of the spool needs to be predicted with high accuracy [1]. One of the problems that spool valves have is the hydraulic vibration caused by the high-pressure fluid [2]. The most popular method of vibration damping is to combine multiple control valves [3]. Recently, there is a need to reduce the overall size of the hydraulic machine, and a stand-alone control valve that can suppress hydraulic vibration is required. Therefore, it is necessary to understand the generation mechanism of the flow force acting on the spool, which is the cause of hydraulic vibration, and to study the suppression method of the flow force. The purpose of the present study is to visualize the flow field in a spool valve using three-dimensional computational fluid dynamics (CFD) and to clarify the generation mechanism of flow forces acting on the spool.

COMPUTATIONAL METHODS

In the present paper, numerical analysis was conducted using ANSYS CFX, that was thermal and fluid analysis software [4]. CFX is a commercial software that is widely used around the world. The finite volume method is used as a discretization method, which provides excellent robustness and fluid conservations in numerical calculations. The governing equations are shown below.

$$\nabla \cdot U = 0 \tag{1}$$

$$\frac{\partial U}{\partial t} + \nabla \cdot (U \times U) = -\frac{1}{\rho}\nabla p + \mu \nabla^2 U \tag{2}$$

Equation (1) is the continuity equation for the conservation of mass, and equation (2) is the Navier-Stokes equations for the conservation of momentum.

RESEARCH TARGET AND COMPUTATIONAL CONDITIONS

In the present study, a two-port spool valve was chosen as the target of research. The approximate configuration of spool valve is shown in Figure 1. Figure 1(a) shows the structure and dimensions of the control valve. For the spool valve, one rectangular port was connected to the inlet side and another one to the outlet side. The cross-sections of the inlet and outlet ports were square configuration, with a side length of 10 [mm] on the inlet and 8 [mm] on the outlet. There was a spool with large and small diameter shafts, the diameter size was 16 and 8 [mm], respectively. The flow rate was controlled by the movement of the spool. It had a simple structure. Expressing the valve opening on the inlet side as “S1” and the valve opening on the outlet side as “S2”, the following relationship was obtained,

$$S1 + S2 = 10\ [\mathrm{mm}]. \tag{3}$$

There is an inlet throat ($S1 \leq 5.0$ [mm]) that narrowed the flow path on the inlet side, and an outlet thraot ($S2 \leq 5.0$ [mm]) that narrowed the flow path on the outlet side. In the present paper, numerical analysis was conducted focusing on the inlet throat (S1).

Figure 1(b) shows the overhead view of the computational domain. The computational domain was created by enclosing area of the dashed lines in Figure 1(a). The diameter of the thick shaft of the spool was D=16 [mm], and this length was used as the reference length. The lengths of the inlet and outlet ports were set to 3D for both. In numerical calculations, the spool was treated as having a fixed position. Five types of computational grids with different valve openings S1 were created. The eccentricity and tilt of the spool were not considered. Each computational grid have a total number of about 2 million grid points.

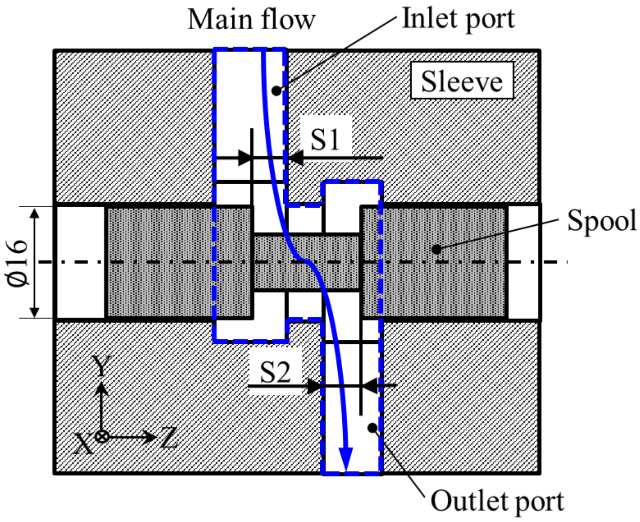

Figure 1(a). Spool Valve Configuration.

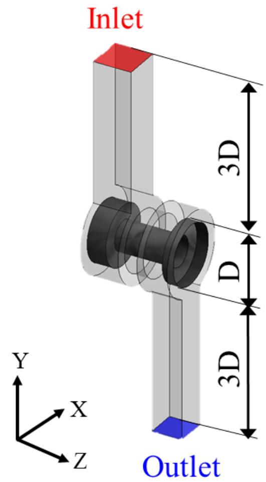

Figure 1(b). Computational Region.

Figure 1. Spool Valve Configuration and Computational Region.

Table 1 summarizes the computational conditions used in the numerical calculations. To explore the possibility of the flow fluctuates with time, an unsteady analysis was performed. The time increments were set so that the CFL condition would be about 10. The working fluid was oil, flowing at 20 [L/min]. The Shear Stress Transport model was used for the turbulence model. Numerical calculations were carried out for five different channel geometries with different inlet throat S1.

Table 1. Computational Conditions.

Analysis type	Transient
Turbulence model	Shear stress transport
Total time	2.0×10^{-2} [s]
Time step	5.0×10^{-5} [s]
Density	850 [kg/m^3]
Viscosity	3.5×10^{-5} [m^2/s]
Inlet	20.0 [L/min]
Outlet	Average static pressure 0.0 [Pa]
Elements	2,000,000 [-]
S1 length	0.2, 0.5, 1.0, 2.0, 5.0 [mm]

PREVIOUS RESEARCH

The flow force acting on the spool can be decomposed into an axial force acting in the direction of the spool axis (Z-axis) and a lateral force acting in the radial (Y-axis) direction. Kondo et al. experimentally measured two types of flow forces acting on a spool [5]. A three-dimensional numerical analysis was also performed using an original numerical code. The flow visualization inside the valve and the flow force acting on the spool were investigated. In the present paper, we compared the experimental and numerical results of Kondo et al. with the computational results obtained by our calculations and confirmed the validity of the present computational method.

COMPUTATIONAL RESULTS AND DISCUSSIONS

Figure 2 shows the results of the present calculations compared with the experimental and numerical results of Kondo et al. Figure 2(a) shows the results of the axial force acting on the spool for five kinds of valve opening S1. Figure 2(b) shows the results of the lateral force. The plotted marks in the figures were all time-averaged values, and the error bars indicated the time variability range of the computational results. In Figure 2(a), the axial force was almost zero for S1≥1.0 [mm]. However, as the inlet throat became narrow, the axial force increased rapidly. The monotonic increase in axial force with decreasing inlet throat was quantitatively good agreement with all three results. The error bars were expanded when the throat was small, so it suggested that time variability occurred. For the lateral forces, present results were compared with the numerical results of Kondo et al. In Figure 2 (b), the value of lateral force was generally smaller than that of axial force. As the throat length decreases, the lateral force tended to increase and then decrease. When the throat length was narrow, unsteady fluctuations appeared in the present results. A comparison of the time-averaged values showed good agreement with the results of Kondo et al., the present numerical analysis is considered to validity.

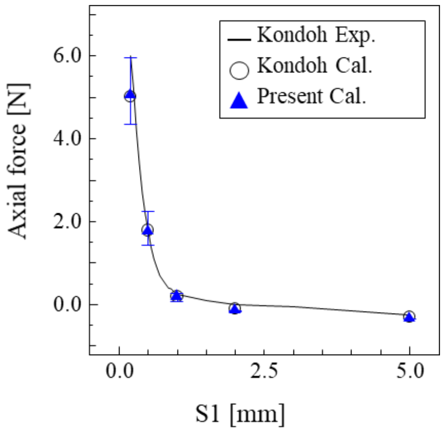

Figure 2(a). Axial Force.

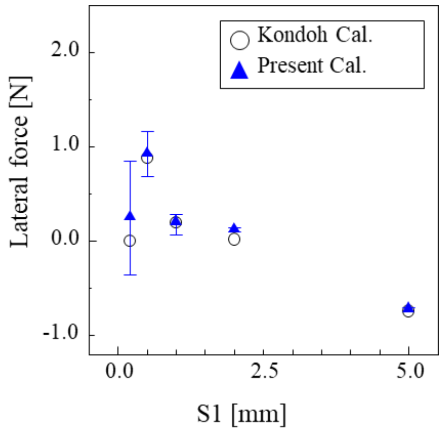

Figure 2(b). Lateral Force.

Figure 2. Flow Force for Inlet Valve Opening S1.

To investigate the generation mechanism of axial and lateral forces, the relationship between the flow pattern inside the valve and the pressure distribution on the spool surface was examined. Figure 3 shows the instantaneous streamlines and the pressure distribution on the spool surface. The case of S1=0.2 [mm] is shown. By observing the streamlines, the flow inside the valve can be explained as follows.

(1) The hydraulic fluid that passed through the inlet throat flowed along the end face of the large-diameter shaft of the spool.
(2) After that, the hydraulic fluid collided with the small-diameter shaft on the inlet side.
(3) The hydraulic fluid traveled downstream along the thin shaft.
(4) The hydraulic fluid collided with the end face of the thick shaft on the outlet side.
(5) The hydraulic fluid flowed out to the outlet port with forming some vortex.

The figure on the right-hand side shows an enlarged view near the inlet throat region. The jet flowed in vigorously. The outer circumference parts of the thick shaft were at the root of the jet, which were a low-pressure region due to the fast velocity of the jet. On the thin shaft, high-pressure region appeared because of the collision of the jet. The pressure difference between low- and high-pressure regions generated the flow force.

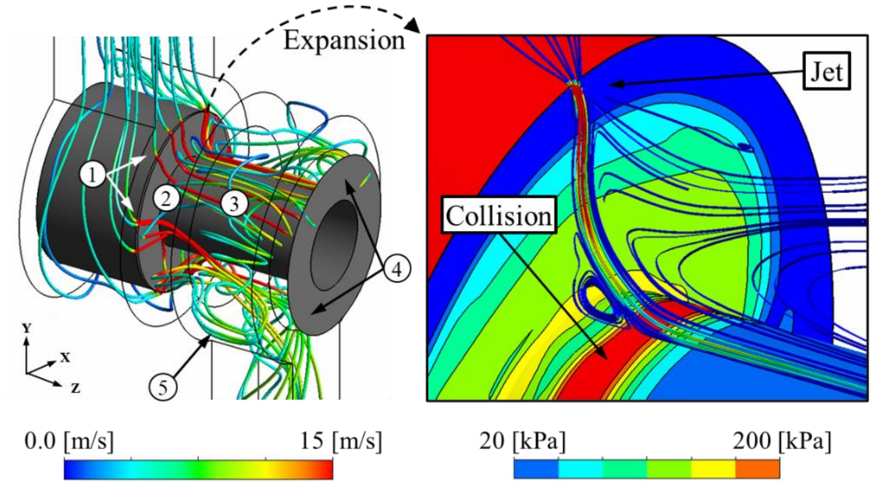

Figure 3. Streamlines and Pressure Distribution for S1=0.2 [mm].

To clarify the mechanism of axial force generation, the flow field inside the valve and the pressure distribution acting on the end faces of the thick shaft were investigated. The results for S1=0.5 [mm] are shown in Figure 4. The velocity vectors in the YZ section and the pressure distribution at the two end faces of the thick shaft are shown. On the left side surface, a low-pressure region was extended by the jet blow. In particular, the pressure was extremely low at the outer circumference part, which was just fast jet area. On the other hand, the right-side end face of the thick shaft was a high-pressure region because the flow along the thin shaft collided with the end face. It was found that the axial force was generated by the pressure difference acting on the left and right end faces.

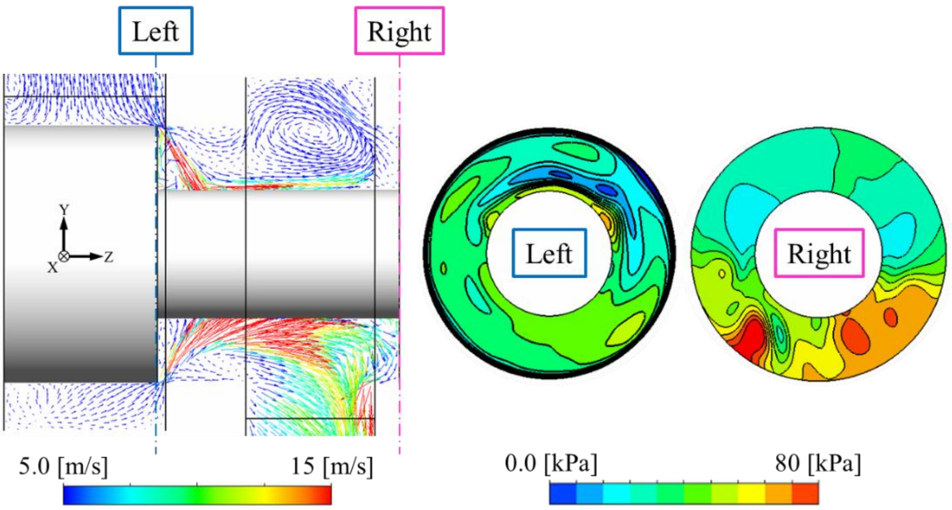

Figure 4(a). Velocity Vectors Plots. **Figure 4(b).** Pressure Distribution on End Faces.
Figure 4. Velocity Vectors Plots and Pressure Distribution for S1=0.5 [mm].

The time variations of the flow field were investigated for S1=0.2 and S1=0.5 [mm]. The velocity distributions at three different times in the YZ section are shown in Figure 5. The high-pressure area on the spool surface was indicated with solid triangle marks, and the low-pressure area was indicated with blank triangle marks. First, we focused on S1 = 0.2 [mm]. The hydraulic fluid that flowed in from the inlet throat became a jet flow and flowed along the end face of the thick shaft and the thin shaft body. The flow formed some vortex near the end face of the thick shaft on the outlet side. Although the jet shape at the upper side remained almost unchanged with time, the jet shape at the lower side changed its direction significantly with time. The lower jet collided with the thin shaft or not collided the shaft. Next, we focused on the pressure distribution acting on the spool. The end face of the thick shaft showed a low-pressure region on the inlet side (indicated by the blank marks), while the outlet side showed a high-pressure region. As a result, there was the pressure difference acting on the left and right surfaces, which acted on an axial force in the +Z (right) direction. The axial force did not change much over time. On the other hand, the pressure on the surface of the small-diameter shaft showed time variation depending on the presence or absence of the jet impact. When the vortex formed on the outlet side collided with the thin shaft, it was observed that a high-pressure region was also formed on the outlet side. The pressure distribution on the thin shaft surface changed significantly with time. Therefore, it was confirmed that unsteady changes in the lateral force occurred.
When S1 = 0.5 mm, the obliquely oriented jet impacted the thin shaft. It was also observed that the flow along the thin shaft changed the direction with time. However, the change was slight, indicating that the unsteady variation was reduced.

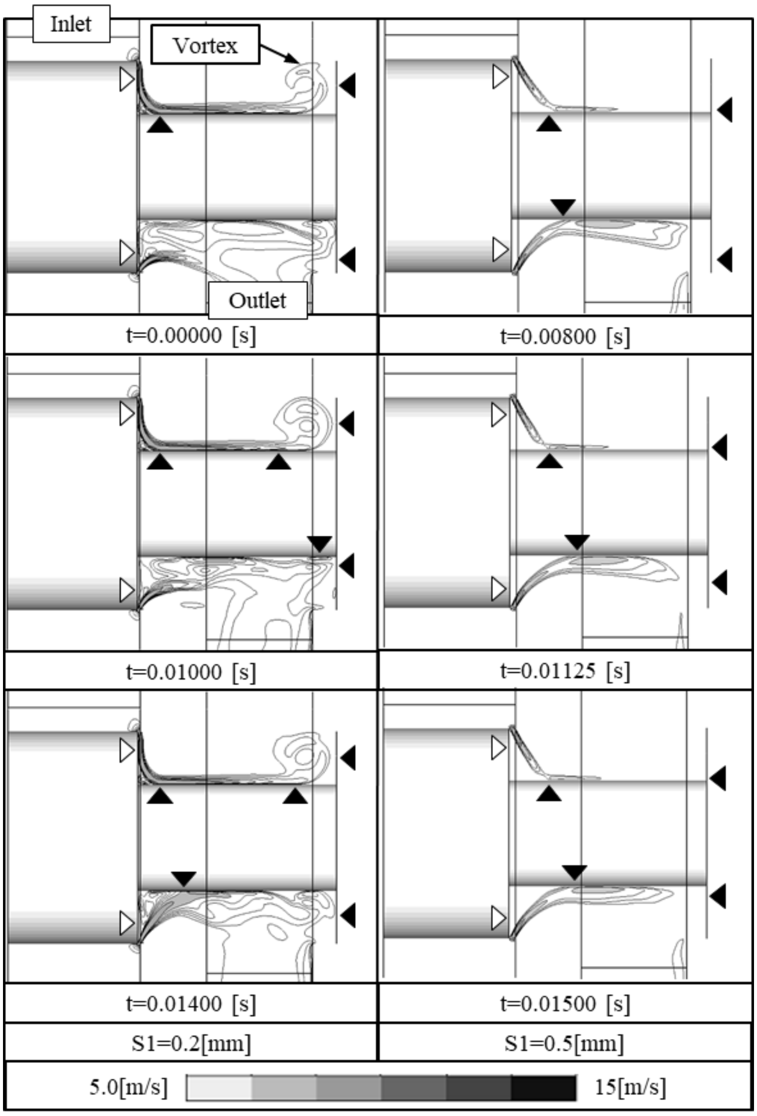

Figure 5. Switching flow at S1=0.2 and 0.5 [mm].

Since the spool position is fixed in the present study, the spool vibration cannot be reproduced. However, spool vibration may occur in actual spool valves due to the action of unsteady flow forces. To investigate the state of spool vibration using CFD, it is necessary to perform fluid/structure coupled analysis that takes spool movement into account.
There is a small gap of several micrometers between the spool and the sleeve. The difference in the gap may cause a change in the flow force. This small gap is not considered at present, but we would like to conduct a numerical analysis taking the gap into account in the future work.

CONCLUDING REMARKS

A two-ports spool valve was numerically investigated using three-dimensional computational fluid dynamics. Flow forces acting on the spool in two directions were investigated. As the results of investigating the magnitude of the flow forces against the change in inlet valve opening, the results of the present calculations were in good agreement with the results of the previous study. The present calculations were confirmed to be valid. It was found that the flow force acting on the spool was caused by the pressure difference between the high-pressure region generated by the impact of the jet and the low-pressure region through which the high-speed jet passed. Fluctuation of the jet flow occurred when the valve opening became narrow. The high-pressure region changed with time due to the time variation in the jet flow direction. It was found that the unsteady fluctuation of the jet flow had a significant effect on the unsteady variation of the flow forces.

ACKNOLWLEDGMENTS

We would like to express our gratitude to Mr. Saiki Tanaka for his great cooperation in the present research.

REFERENCES

1. LEE, S. Y. and BLACKBURN, J. F., Steady-State Axial Forces on Control-Valve Pistons, Transactions of the American Society of Mechanical Engineers, 76, 1952, pp. 1005-1011.
2. KUMAGAYA, H. and MASAKI, K., Your First Hydraulic System (in Japanese), Gijutsu-Hyohron Co., Ltd., 2009, pp. 100-153.
3. ICHIKAWA, T. and HIBI, A., Oil-Hydraulic Engineering (in Japanese), Asakura Publishing, 1979, pp. 88-118.
4. ANSYS Inc, ANSYS CFX-Solver Modeling Guide Release 13.0, 2010, pp. 13-15, pp. 149-152.
5. KONDOH, Y., et al., Analysis of Flow Forces Acting on a Spool Valve (1st Report, Non-Uniformity of Flow Pattern and Momentum Flux in the Azimuthal Direction) (in Japanese), Transactions of the Japan Society of Mechanical Engineers, Series B, 65-639, 1999, pp. 3577-3585.

The 11th JFPS International Symposium on Fluid Power HAKODATE 2020 Oct. 12-13, 2021 The Japan Fluid Power System Society

The Effect of the Spline Coupling on the Rotating Assembly Tilt Behavior in a High-speed Axial Piston Pump

Haogong XU*, Junhui ZHANG*, Weidi HUANG*, Bing XU*, Fei LYV*, Xiaochen HUANG*,

* State Key Laboratory of Fluid Power and Mechatronic Systems, Zhejiang University,
38 Zheda Road, Xihu, Hangzhou, 030027, China
(E-mail: xuhaogong@zju.edu.cn)

Abstract. The rotating speed of the axial piston pump is increasing to meet the requirement of a higher power-to-weight ratio. However, the cylinder block in the pump tilts severely at a high rotating speed, which seriously affects the reliability and efficiency of the pump. The cylinder block is the main component of the rotating assembly, so the tilt behavior of the cylinder block is analyzed through a proposed dynamic model of the rotating assembly in the paper. The elastic deformation of the shaft, the nonlinear bearing characteristics of the oil film, and the reaction of spline coupling are taken into account. Then the tilt angle of the cylinder block and the meshing status of the spline coupling are analyzed. Finally, the influence of the working conditions is investigated to offer an insight into the tilt behavior of the rotating assembly in a high-speed axial piston pump.

Keywords: Rotating assembly, cylinder block, transient behavior, finite element model, spline coupling

INTRODUCTION

The high-speed axial piston pump is widely used in the aerospace industry and the defense industry due to the high efficiency and high power-to-weight ratio. To meet the demand for a higher power-to-weight, the rotating speed and the outlet pressure of the pump are increasing gradually. However, the leakage of the pump increased dramatically at a high rotating speed which reduces the efficiency of the pump. The leakage mainly comes from the three friction pairs: the swash plate/slipper pair, the cylinder block/piston pair, and the valve plate/cylinder block pair. The three friction pairs are shown in **Figure 1**. The cylinder block is driven by the shaft to slide on the valve plate surface. The pistons are forced to rotate around the shaft axis and reciprocate within the cylinder bores at the same time. The slippers slide on the inclined swash plate. The oil film within the three friction pairs plays an important role in the lubrication but generates the leakage which decreases the pump efficiency.

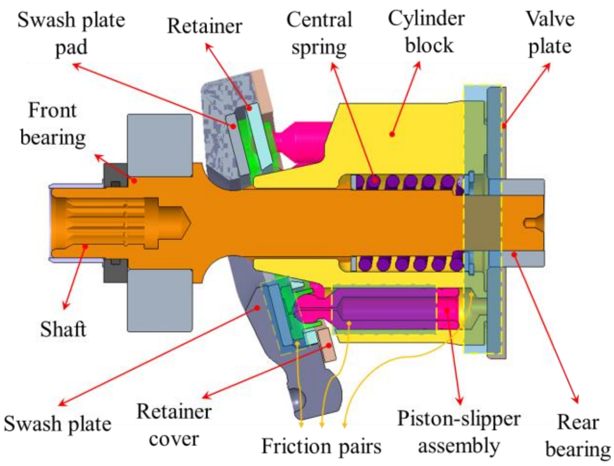

Figure 1. The Inner Structure of the High-speed Axial Piston Pump

The leakage within the friction pairs depends on the pressure and the gap sizes of the friction pairs. In the high-speed pump, the valve plate/cylinder block pair has a larger scale than the other two friction pairs, and it contributes more than 70% of the total leakage of the pump [1]. On the other hand, the oil film thicknesses of the swash plate/slipper pair are limited mechanically by the hold-down mechanism (Retainer cover), while the cylinder bores restrict the oil film thicknesses of the cylinder block/piston pairs. However, the cylinder block is mainly pressed towards the fixed valve plate by the pressurized oil and the central spring, and the maximum oil thickness of the valve plate/cylinder block pair is barely restricted. As a result, the cylinder block is more likely to tilt under high pressure and high rotating speed conditions, which has a noticeable effect on the pump efficiency.

The tilt behavior of the cylinder block determines the oil film shape of the valve plate/cylinder block pair. Many researchers have conducted the thickness distribution measurements of the valve plate/cylinder block pair in industrial axial piston pumps under the actual operating conditions [2–6]. And all the results showed that remarkable tilting of the cylinder block has occurred, and the operating conditions, especially the outlet pressure, affected the tilt behavior of the cylinder block obviously. On the other hand, theoretical analyses have been carried out to investigate the bearing characteristics of the valve plate/cylinder block pair. Many types of the models, such as the analytical model [7,8], elastohydrodynamic model [9–11], and the thermal elastohydrodynamic model [1,12–15], have been established. The oil film thickness, temperature distribution, and the deformations of the sliding surfaces in the valve plate/cylinder block pair were analyzed based on these models. However, these lubrication models mainly focused on the nonlinear bearing characteristics of the oil film but neglected the reactions from other parts in the pump.

Moreover, several researchers paid attention to the interactions between the moving parts in the axial piston pump/motor based on the multi-body dynamic models. The first type of dynamic model was established under the commercial software environment [16–18], and the detailed geometry could be taken into account. The second type was the lumped parameter analytical model [19–21], and the whole pump was modeled as a mass-spring-damper system. However, the movements of the moving parts were over-constrained, and the bearing characteristics of the oil film were always linearized, which would bring obvious errors under a wide operating range.

The cylinder block movement is affected by the connected parts, such as the piston-slipper assemblies, the shaft, and the valve plate. The previous studies mainly focused on the industrial axial piston pump/motor. But in a high-speed axial piston pump, the nonlinear speed-dependent bearing characteristics of the oil film are much more prominent. And the radial force due to the inclined swash plate results in a slight inclination and bending of the shaft, which may affect the meshing status of the spline coupling. However, the underlying interactions between the relative moving parts are still not completely understood. In this paper, a dynamic model of the rotating assembly is proposed to investigate the tilt behavior of the cylinder block in a high-speed axial piston pump. The rest of this paper is arranged as follows: the detailed dynamic model is presented in Section 2; the theoretical results are presented and discussed in Section 3; finally, the conclusion and outlook are drawn in Section 4.

DYNAMIC MODEL OF THE ROTATING ASSEMBLY

The rotating assembly of the high-speed pump is mainly comprised of the shaft, the cylinder block, and 2 bearings. The dynamic model of the rotating assembly is shown in **Figure 2**. The finite element method is adopted to model the shaft and the cylinder block, considering the elastic deformation. A theoretical model is established to investigate the reactions of the spline coupling between the shaft and the cylinder block. The nonlinear bearing characteristics of the oil film are taken into account based on the one-dimensional Reynolds equation.

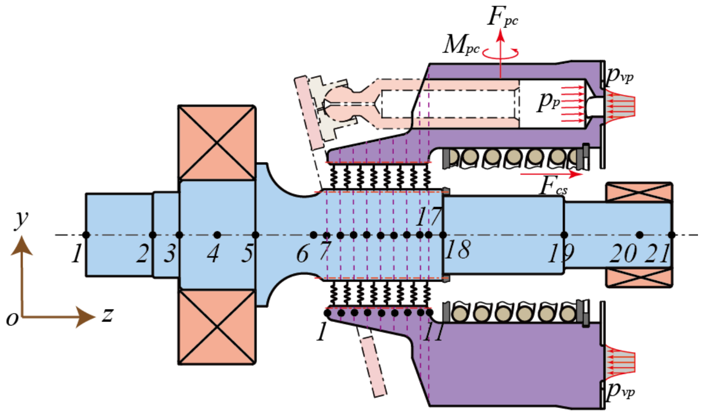

Figure 2. The Finite Element Model of the Rotating Assembly

Finite Element Model of the Rotating Assembly

The finite element model consists of the shaft and the cylinder block. The shaft and the cylinder block are modeled as Timoshenko beam considering their elasticity and inertia. As shown in Figure 2, the shaft is divided into 20 elements by 21 Nodes, in which the spline on the shaft consists of 11 elements. Due to the axisymmetric cross-section of the rotating assembly, the torsional displacement is uncoupled with lateral displacements. The axial movement of the shaft is limited by the preloaded angular contact ball bearing. As a result, each shaft element contains 2 translation degrees of freedom(u,v) and 3 rotary degrees of freedom(θ_x,θ_y, θ_z). According to the non-conservative Lagrange equation, the motion equations of the shaft can be expressed as:

$$\left[M^s\right]\left\{\ddot{q}^s\right\}-\Omega\left[G^s\right]\left\{\dot{q}^s\right\}+\left[K^s\right]\left\{q^s\right\}=\left\{F^s\right\} \tag{1}$$

where superscript 's' denotes the shaft unit, M, G, K are the mass matrix, gyroscopic matrix, and stiffness matrix respectively, Ω is rotating speed, q is the generalized coordinates vector, F denotes generalized force vector exerted on shaft unit.

The contact status of the spline on the cylinder block also should be taken into account, and the cylinder block is divided into 11 elements by 12 nodes. The additional axial movement of each node in the cylinder block is considered compared with the shaft node, since the axial movement of the cylinder block w has an effect on the oil film within the cylinder block/valve plate pair. Therefore, the motion equations of the cylinder block can be obtained

$$\left[M^c\right]\left\{\ddot{q}^c\right\}-\Omega\left[G^c\right]\left\{\dot{q}^c\right\}+\left[K^c\right]\left\{q^c\right\}=\left\{F^c\right\} \tag{2}$$

where superscript 'c' denotes the cylinder block unit. Finally, the motion equations of the rotating assembly can be expressed as

$$\begin{bmatrix} M^s & \\ & M^c \end{bmatrix}\begin{Bmatrix} \ddot{q}^s \\ \ddot{q}^c \end{Bmatrix}-\Omega\begin{bmatrix} G^s & \\ & G^c \end{bmatrix}\begin{Bmatrix} \dot{q}^s \\ \dot{q}^c \end{Bmatrix}+\begin{bmatrix} K^s & \\ & K^c \end{bmatrix}\begin{Bmatrix} q^s \\ q^c \end{Bmatrix}=\begin{Bmatrix} F^s \\ F^c \end{Bmatrix} \tag{3}$$

The Bearing Capacity of the Valve Plate/Cylinder Block Pair

The oil film within the valve plate/cylinder block pair is illustrated in **Figure 3**. According to the geometry, the oil film can be divided into the inner sealing land region, the main kidney land region, and the outer sealing land region. The main kidney land region consists of the pressure ports and the transitional areas of the valve plate, and the pressure in the transitional areas varies periodically as the kidney port of the cylinder block enters and leaves the transitional areas. The pressure in the main kidney land region mainly depends on the pressure in the piston chamber and the pressure port of the valve plate, and it is not affected by the oil film shape.

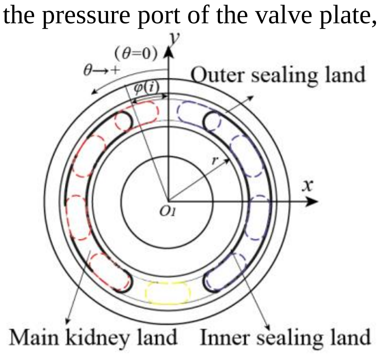

Figure 3. The Oil Film Within the Valve Plate/Cylinder Block Pair

On the contrary, the oil film shape has a significant influence on the pressure distribution in the sealing lands. The two-dimensional Reynolds equation is usually adopted to model the bearing capacity of the oil film, but it can only be solved numerically by the finite element method(FEM) or the finite volume method(FVM), which slows down the calculation efficiency. Fortunately, the width of sealing lands is small enough compared with the radius in the valve plate/cylinder block pair so that the circumferential pressure gradient can be neglected. Then oil film pressure distribution in each sealing land can be obtained based on the one-dimensional Reynolds equation

$$\frac{\partial}{\partial r}\left(rh^3\frac{\partial p}{\partial r}\right)=6\mu\omega r\frac{\partial h}{\partial \theta} \tag{4}$$

where r is the radius of the oil film, h is the oil film thickness, p is the pressure distribution of the oil film, ω is the rotating speed of the cylinder block, μ is the oil viscosity. When neglecting the elastic deformation, the oil film thickness distribution is expressed as

$$h=h_0+\alpha r_m\cos\theta \tag{5}$$

where α is the tilt angle of the cylinder block, r_m is the average radius of the sealing land, the tilt angle α and the central gap height h_0 are related to the movement of the cylinder block. Then the pressure distribution in each sealing land is obtained

$$p_{sl}\left(r,\theta_R\right)=p_{in}\left(\frac{\ln(r/r_{out})}{\ln(r_{in}/r_{out})}\right)+p_{out}\left(\frac{\ln\left(r_{in}/r\right)}{\ln\left(r_{in}/r_{out}\right)}\right)+\frac{3\mu\omega r_m\alpha\sin\theta}{2\left(h_0+\alpha r_m\cos\theta\right)^3}\cdot\left(\frac{r_{out}^2\ln\left(r_{in}/r\right)-r_{in}^2\ln\left(r_{out}/r\right)}{\ln\left(r_{in}/r_{out}\right)}-r^2\right) \tag{6}$$

where the subscript 'in' and 'out' are inner pressure boundary and outer pressure boundary of the sealing land, respectively.

Besides, the asperity contact may occur when the oil film thickness is rather small. The asperity contact pressure can be obtained by the Greenwood –Tripp model [22]

$$p_{\mathrm{c}}=K'E'F_{5/2}\left(\frac{h}{\sigma}\right) \tag{7}$$

where K' is the elastic factor, E' is the composite elastic modulus, $F_{5/2}(h/\sigma)$ is the form function, and σ is the combined standard deviation of the asperities.

Finally, the bearing force and moments of the oil film are given by integrating all the pressure components numerically

$$\begin{cases} F_{\mathrm{vz}}=\iint pr\mathrm{d}r\mathrm{d}\theta \\ M_{vx}=-\iint pr^2\cos\theta\mathrm{d}r\mathrm{d}\theta \\ M_{yx}=\iint pr^2\sin\theta\mathrm{d}r\mathrm{d}\theta \end{cases} \tag{8}$$

The Bearing Capacity of the Spline Coupling

In the high-speed axial piston pump, the shaft and cylinder block are connected by an involute spline coupling, which not only transfers the driven torque but also supports the cylinder block in the radial direction. The radial force exerted on the cylinder block due to the inclined swash plate results in the deformation of the shaft and the cylinder block, and it changes the meshing status of the spline coupling. Therefore, the bearing capacity of the spline coupling is investigated through FEM, and the splines on the shaft and cylinder block are divided into 11 shaft elements, as shown in **Figure 2**. In each spline coupling element, only the parallel misalignment is taken into account, as shown in **Figure 4**.

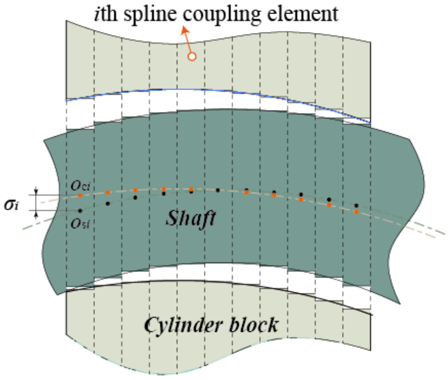

Figure 4. The Misalignment of the Spline Coupling

The meshing status of the spline coupling element is illustrated in **Figure 5**. When the spline coupling is completely aligned, the clearances between all the teeth of the spline are evenly distributed

$$\delta_{\mathrm{initial}}=\frac{1}{2}\Delta\cos\gamma \tag{9}$$

where Δ is the backlash of the spline coupling, and γ is the pressure angle. However, the relative movement of the cylinder block and shaft changes the clearance distribution. The relative movement for each spline coupling element consists of the radial movement and torsional movement, and the additional clearance due to the two types of movements can be obtained

$$\phi_{\mathrm{rij}} = -\sigma_{\mathrm{si}} \cos\left(\frac{2\pi}{n} j + \frac{\pi}{2} - \gamma - \xi_{si}\right); \qquad (j = 1, 2, \ldots n) \tag{10}$$

$$\phi_{\mathrm{ti}} = -r_{\mathrm{s}} \left(\varphi_{si} - \varphi_{ci}\right) \tag{11}$$

where σ_{si}, ξ_{si} are the radial movement and the azimuth angle of the relative movement for the i^{th} spline coupling element, respectively. n is the teeth number, r_{s} is the pitch diameter of the spline. φ_{si} and φ_{ci} are the torsional movements for the i^{th} spline coupling element on the shaft and the cylinder block, respectively. Finally, the clearance distribution is expressed as

$$\delta_{ij} = \delta_{initial} + \phi_{rij} + \phi_{ti} \tag{12}$$

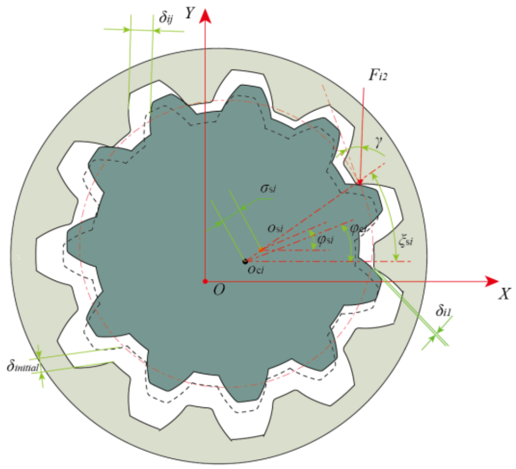

Figure 5. The Meshing Status of the Single Spline Coupling Element

The meshing forces and the relevant force and torque on the shaft can be obtained

$$F_{ij} = \begin{cases} -K_{sp} L \delta_{ij}, \left(\delta_{ij} < 0\right) \\ 0, \left(\delta_{ij} > 0\right) \end{cases} \tag{13}$$

$$F_{xsi} = \sum F_{ij} \cos\left(\frac{2\pi}{n} j - \gamma - \frac{\pi}{2}\right) \tag{14}$$

$$F_{ysi} = \sum F_{ij} \sin\left(\frac{2\pi}{n} j - \gamma - \frac{\pi}{2}\right) \tag{15}$$

$$T_{zsi} = \sum -F_{ij} r \cos\gamma \tag{16}$$

where K_{sp} is the spline tooth constant stiffness, L is the axial length of the spline coupling element.

SIMULATION RESULTS AND DISCUSSION

The Tilt Behavior of the Rotating Assembly

The rotating assembly is mainly subjected to the radial forces and moments from the piston-slipper assemblies and the axial force from the pressurized oil in the piston chambers [23]. The tilt behavior of the rotating assembly under these exerted forces and moments is investigated in a high-speed axial piston pump with 9 pistons.

The tilt behavior of the cylinder block (the bottom surface) under 9000rpm and 6MPa is shown in **Figure 6**. The tilt angle and azimuth angle of the cylinder block fluctuate periodically, and the main wave contains 9 peaks during a cycle, which is consistent with the number of pistons. The azimuth angle varies between 127 and 131 °, and it means the cylinder block tilts towards the area near the outer dead center on the high-pressure port of the valve plate.

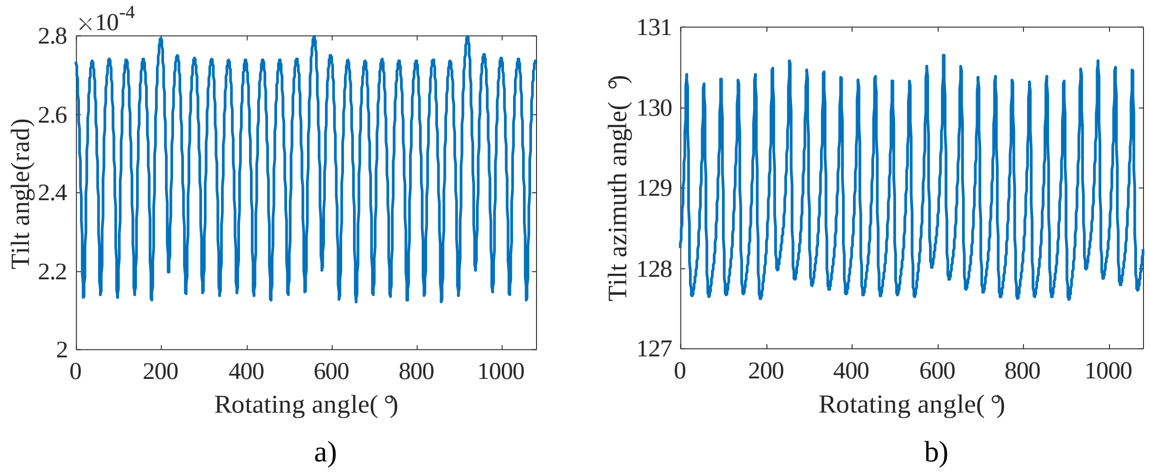

Figure 6. The Tilt Behavior of the Cylinder Block: a).The Tilt Angle; b). The Tilt Azimuth Angle

The tilt behavior of the rotating assembly is obtained based on the average displacement of all the Nodes, as shown in **Figure 7**. It can be seen that the shaft has bending deformation along the *x* and *y* axes, and the deformation along the *y*-axis is significantly greater than that along the *x*-axis. The incline of the shaft also can be found under the external load due to the elastic bearings. And the shaft inclines upward along the *x*-axis and inclines downward along the *y*-axis. The axes of the shaft and the cylinder block spline are obviously out of alignment. The movements of the spline coupling axes are extracted as shown in **Figures 7c** and **7d**. The bending deformation and incline of the cylinder block axis can be found. The relative deflection between the spline centerlines of the cylinder block and shaft is much larger along the *y*-axis than that along the *x*-axis. And the left side of the spline coupling shows the more significant relative movement along the *y*-axis. The clearance distribution of the spline teeth is shown in **Figure 7e**. The negative values indicate that all the teeth are engaged effectively. The spline tooth pairs at node 1 present larger deformations(smaller clearances), and more non-uniform deformation distribution can be found at node 1. It results from not only a larger relative radial movement at the left side of the spline coupling but the largest relative torsion angle at node 1 since it is close to the input torque of the shaft. The maximum deformation of the tooth pair reaches 8.5μm and is located at the tooth pair near the negative *x*-axis at node 1(the tooth number starts from the positive *x*-axis and is numbered anticlockwise). With the node number increasing, the maximum deformation gradually decreases to about 3μm, while the location moves to the positive *x*-axis.

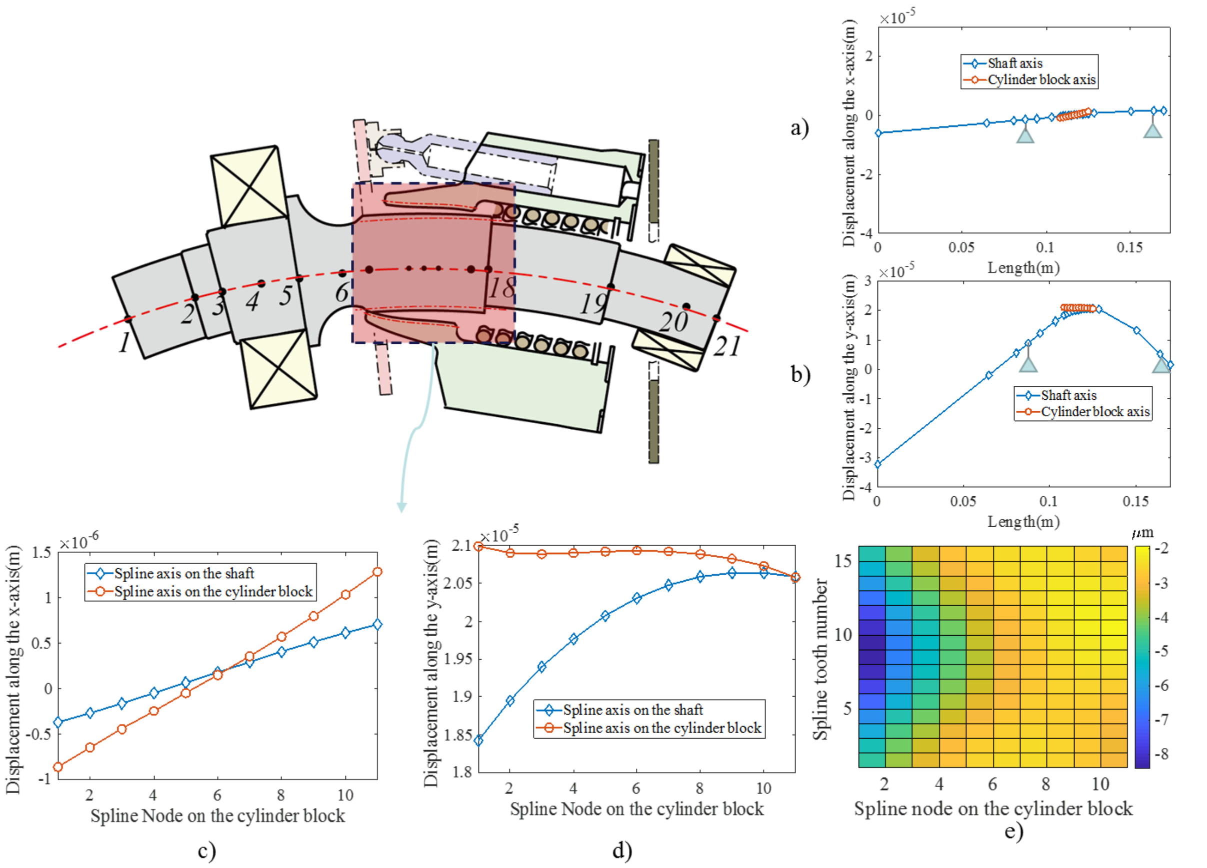

Figure 7. The Tilt Behavior of the Rotating Assembly: a). The Tilt Behavior of the Rotating Assembly along the *x*-axis; b). The Tilt Behavior of the Rotating Assembly along the *y*-axis; c). The Movement of the Spline Coupling Axes along the *x*-axis; d). The Movement of the Spline Coupling Axes along the *y*-axis; e). The Clearance Distribution of the Spline Teeth

The Influence of the Working Condition on the Tilt Behavior of the Rotating Assembly

The influence of working conditions on the tilt behavior of the cylinder block is shown in **Figure 8**. It can be seen that the higher the speed is, the greater the average tilt angle of the cylinder block is. The influence of the rotating speed on the tilt angle is much more obvious under a lower outlet pressure. There is a speed threshold of about 6000 rpm. When the speed is lower than the threshold speed, the pressure increase will significantly enhance the tilt angle of the cylinder block. And the effect of pressure on the tilt angle is opposite when the speed is higher than the threshold speed. In addition, when the outlet pressure increases, the tilt azimuth angle also increases, and it means that the location of the minimum oil film thickness moves to the center of the high-pressure port of the valve plate. And the tilt azimuth angle first decreases then increases with the increasing rotating speed. The minimum oil film thickness of the cylinder block/valve plate pair decreases with the increase of pressure, which indicates that the asperity contact of the valve pair is more severe under high pressure.

On the other hand, the minimum oil film thicknesses under different pressure conditions decrease first and then increase with the rotation speed, as shown in **Figure 8c**. The main reason is that with the increase of rotation speed, the centrifugal forces of the piston-slipper assemblies increase rapidly, and the resulting increased tilt moment intensifies the tilt of the cylinder block. With the further increase of the speed, the hydrodynamic effect of the oil film is enhanced rapidly, which leads to the overall increase of the oil film thickness, and it counteracts the decrease of minimum oil film thickness caused by overturning. Under low outlet pressure, the minimum oil film thickness is larger. It is noticed that the minimum oil film thickness increases sharply at a high rotating speed, especially under the low outlet pressure. At this time, the leakage of the pump will increase sharply, which seriously affects the efficiency of the pump.

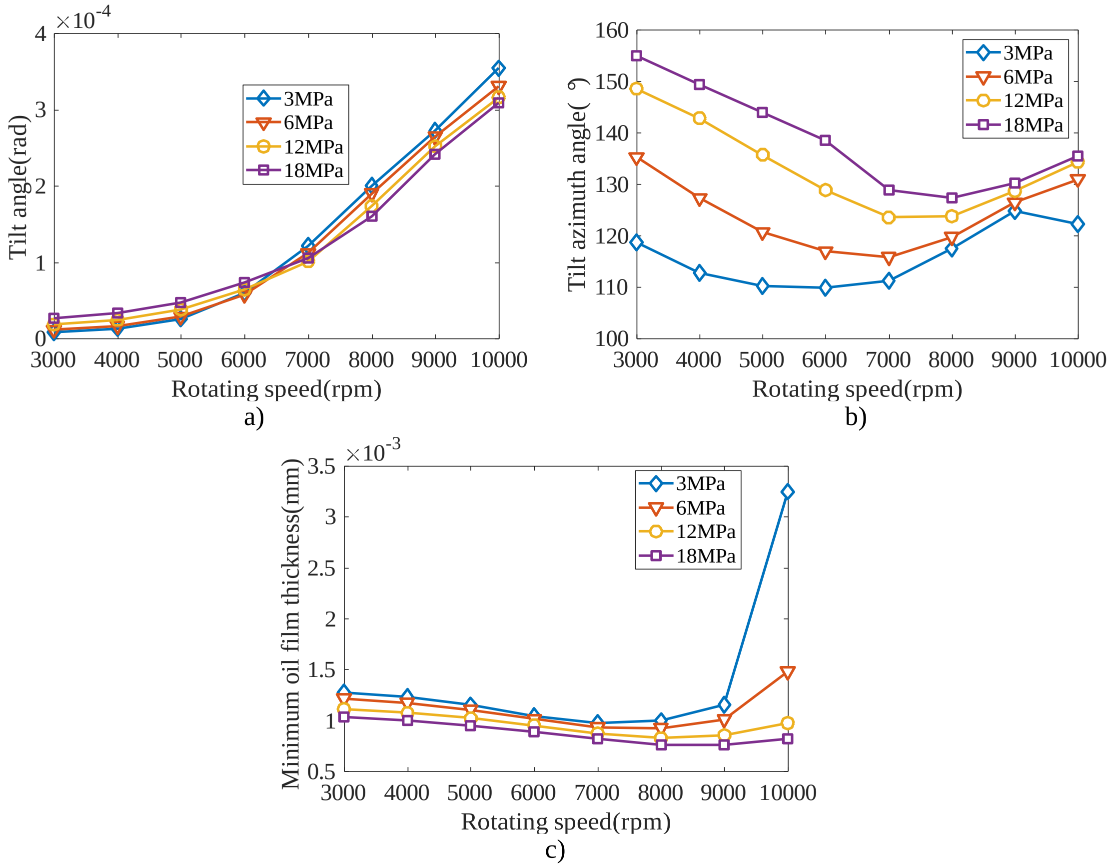

Figure 8. The Tilt Behavior of the Cylinder Block under Different Working Conditions: a). The Tilt Angle; b). The Tilt Azimuth Angle; c). The Average Minimum Thickness of the Oil Film

The effect of the outlet pressure on the spline coupling movement is shown in **Figure 9**. It can be seen that the pressure has little influence on the movements of the spline coupling axes along the *x*-axis. With the increase of pressure, the displacements of all the Nodes on the shaft and cylinder block spline axes decrease, but the change of the relative movement between the axes is not significant. On the other hand, the outlet pressure dramatically affects the spline coupling movement along the *y*-axis. With the increase of pressure, the increasing load on the cylinder block is transferred to the shaft, so the axes movements of both the shaft and cylinder block increase rapidly. Higher outlet pressure leads to a more considerable bending deformation of the shaft, and the relative displacement of the spline axes on the shaft and cylinder block increases obviously, especially the left side Node. The increased relative displacement at the left side node always results in the larger deformation of spline tooth as shown in **Figure 9c** and **9d**. It indicates the increasing meshing force of the tooth pair, which provides a higher anti-tilt moment for the cylinder block. The axes of the shaft and the cylinder block spline gradually separated from the intersection with the increasing outlet pressure, and the spline axis of the cylinder block is entirely above the shaft spline axis under 18MPa. In addition, the driven torque also increases when the outlet pressure rises, and it results in the larger relative twist angle between the shaft and the cylinder block. That's why the deformations, as well as the their distribution, of the spline teeth under high pressure are much larger than that under low pressure.

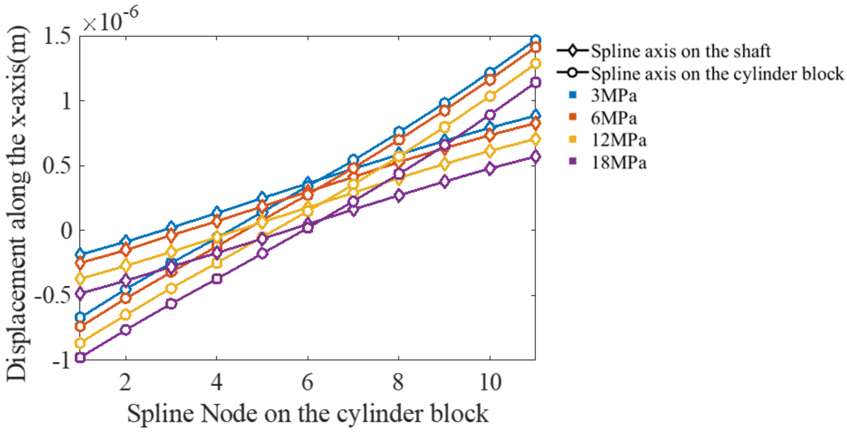

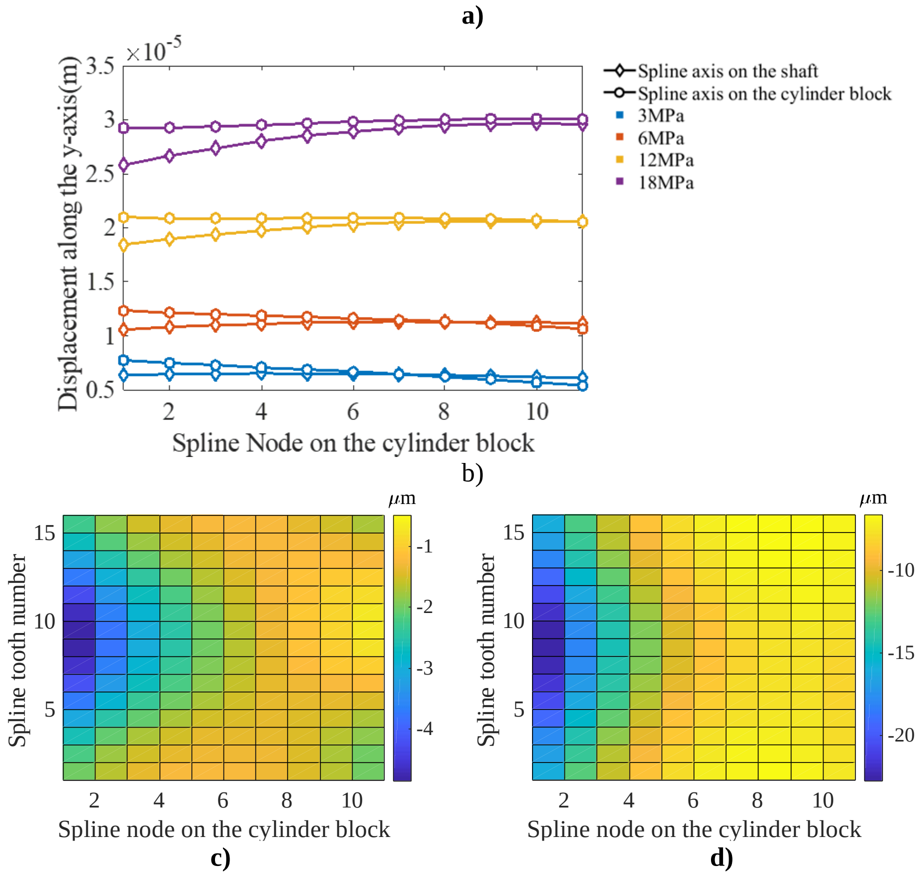

Figure 9. The Effect of the Outlet Pressure on the Spline Coupling Movement: a). The Movement along the *x*-axis; b). The Movement along the *y*-axis c). The Clearance Distribution of the Spline Teeth under 3MPa; d). The Clearance Distribution of the Spline Teeth under 18MPa;

The effect of the rotating speed on the spline coupling movement is shown in **Figure 10**. It can be found that the rotation speed has a noticeable influence on the movements of the spline coupling axes, especially along the *y*-axis. The inclinations along the *x*-axis of the spline coupling axes increase with rotating speed, and the relative inclination between the axes also increases synchronously. In the *y*-axis, with the increase of the rotation speed, the tilt degree of the cylinder block is intensified due to the increased inertia tilt moment of the piston-slipper assemblies and the spline axis of the cylinder block inclines downward. The spline axis of the shaft also inclines downward. At the same time, the axes of the shaft and the cylinder block spline gradually intersect with each other as the rotating speed increases. Comparing **Figure 10c** and **10d**, we can find that the maximum deformation of the spline tooth and the range of the deformation increase slightly with the rotating speed. The location of the maximum deformation on the right side of the spline coupling changes from the negative *x*-axis to the positive *x*-axis when the rotating speed increases to 10000rpm.

The spline coupling mainly balances the radial force along the *y*-axis and the tilt moment around the *x*-axis. When the outlet pressure increases, the radial force increases more significantly than the tilt moment. At this time, all the spline coupling Nodes generate the bearing forces along the negative *y*-axis on the shaft so as to balance the increasing radial force under high pressure. But increasing rotating speed enlarges the tilt moment

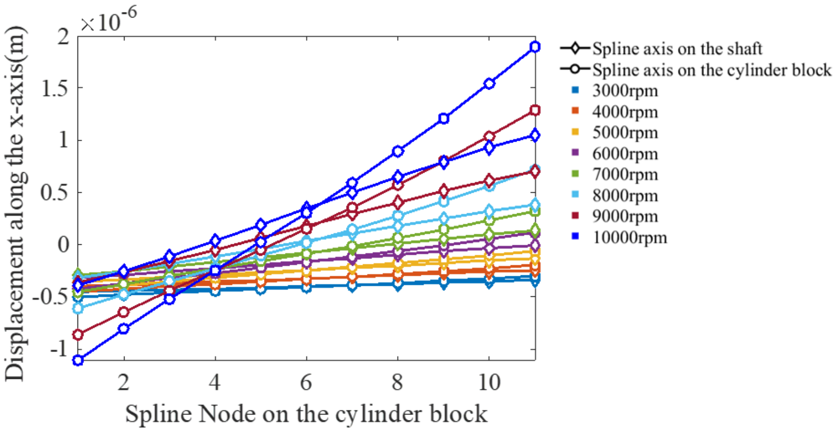

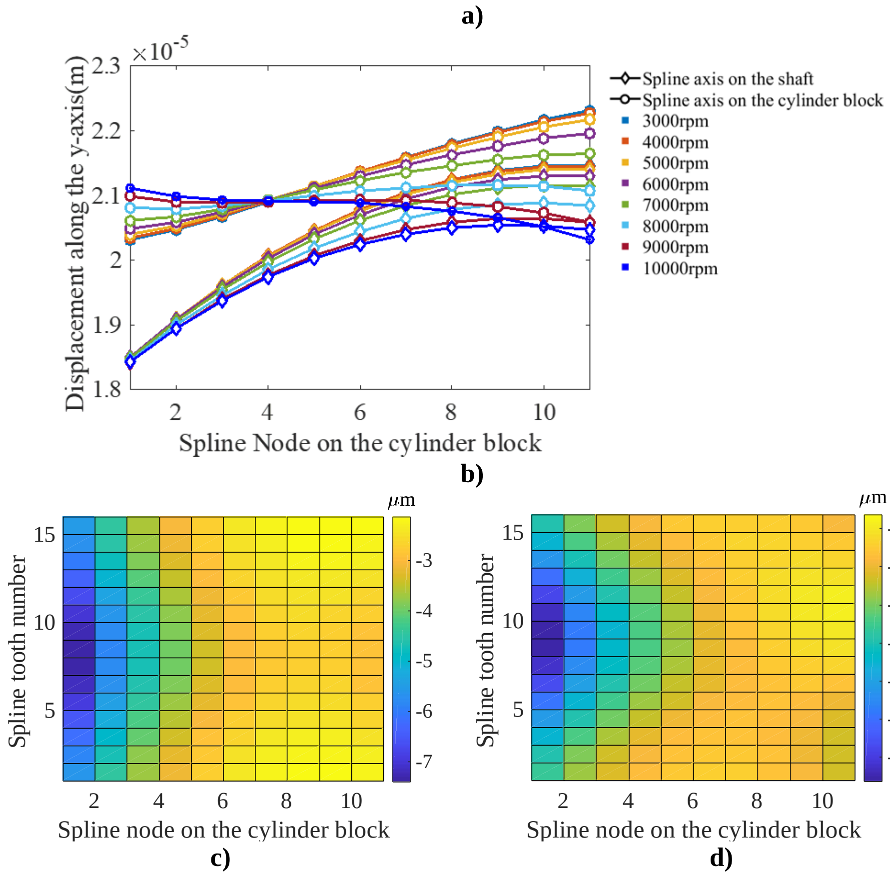

Figure 10. The Effect of the Rotating Speed on the Spline Coupling Movement: a). The Movement along the *x*-axis; b). The Movement along the *y*-axis; c). The Clearance Distribution of the Spline Teeth under 3000rpm; d). The Clearance Distribution of the Spline Teeth under 10000rpm

while barely has an effect on the radial force. As a result, the Nodes of the spline coupling at the left and right sides provide the opposite bearing force to balance the inertia tilt moment at the high rotating speed. On the other hand, the maximum tilt angle of the cylinder block appears under the condition of low outlet pressure and high rotating speed. It means that the ability to balance the tilt moment of spline coupling needs to be further improved to reduce the maximum tilt angle of the cylinder block. Increasing the contact length of spline coupling, or reducing the elastic deformation of the shaft by optimizing the shaft geometry, might be the effective method, which needs to be investigated in the following research.

CONCLUSION

In this paper, a dynamic model of the rotating assembly in a high-speed axial piston pump is presented. In order to investigate the bearing characteristic of the spline coupling, a contact model of the meshing teeth considering the elastic deformation is implemented. Then the dynamic model is adopted to investigate the dynamic behavior of the cylinder block and the rotating assembly.

The simulation results show that the cylinder block mainly tilts towards the area near the outer dead center on the high-pressure port of the valve plate. The elastic deformation and inclination of the shaft can be observed obviously, especially along the *y*-axis. And relative deflection between the spline centerlines of the cylinder block and shaft results in the uniform clearance distribution of the spline coupling, which generates the reaction forces to balance the radial force and tilt moment from the piston-slipper assemblies, and the maximum deformation of the tooth pair is found in the left side of the spline coupling.

The working condition has a significant influence on the tilt behavior of the rotating assembly. The tilt angle of the cylinder block increases with the increasing rotating speed, especially under low outlet pressure. With the increase of pressure, a more considerable bending deformation of the shaft is observed, and the relative displacement of the spline axes on the shaft and cylinder block increases obviously. The axes of the shaft and the cylinder block spline gradually separated from the intersection to balance the increasing radial force under high pressure. With the increase of the rotation speed, the relative displacement of the spline axes on the shaft and cylinder block also increases. And the axes of the shaft and the cylinder block spline gradually intersect with each other as the rotating speed increases to balance the inertia tilt moment at the high rotating speed. The spline coupling node at the left side always has the maximum relative movement, and it is affected by the pressure and rotating speed obviously.

In future work, more detailed models for the rotating assembly will be included, such as the bearing models. And the effect of the geometry parameters of the shaft and the cylinder block will be investigated to help carry out the optimization of the rotating assembly.

ACKNOWLEDGMENTS

The authors gratefully express their appreciation for the financial supports from the National Key R&D Program of China (Grant No. 2019YFB2005101), National Outstanding Youth Science Foundation of China (Grant No. 51922093), and the National Natural Science Foundation of China (Grant No. 51890882), the Natural Science Foundation of Zhejiang Province(Grant No. LQ21E050022).

REFERENCES

1. Han, L., Wang, S., Zhang, C., A partial lubrication model between valve plate and cylinder block in axial piston pumps, Proc. Inst. Mech. Eng. Part C-J. Eng. Mech. Eng. Sci. 229 (2015), 3201–3217.
2. Kim, J.-K.,Jung, J.-Y., Measurement of fluid film thickness on the valve plate in oil hydraulic axial piston pumps (I)-bearing pad effects-, KSME Int. J. 17 (2003), 246–253.
3. Xu, H., Zhang, J., Sun, G., et al., The direct measurement of the cylinder block dynamic characteristics based on a non-contact method in an axial piston pump, Measurement 167 (2021):108279.
4. A. Shorbagy, R. Ivantysyn, J. Weber, An experimental approach to simultaneously measure the temperature field and fluid film thickness in the cylinder block/valve plate gap of an axial piston pump, THMT-18. Turbulence Heat and Mass Transfer 9 Proceedings of the Ninth International Symposium On Turbulence Heat and Mass Transfer., Begel House Inc.,2018.
5. Wegner, S., Gels, S., Jang, D.S., et al., Experimental Investigation of the Cylinder Block Movement in an Axial Piston Machine, Proceedings of the ASME/BATH 2015 Symposium on Fluid Power and Motion Control, Chicago, USA, 2015.
6. Deeken, M., Simulation of the Tribological Contacts in an Axial Piston Machine, ASME International Mechanical Engineering Congress and Exposition. 2004, 47101: 71-75.
7. Manring, N.D., Tipping the cylinder block of an axial-piston swash-plate type hydrostatic machine, J. Dyn. Syst., Meas., Control 122.1 (2000), 216–221.
8. J. M. Bergada, J. Watton, S. Kumar, Pressure, Flow, Force, and Torque Between the Barrel and Port Plate in an Axial Piston Pump, J. Dyn. Syst., Meas., Control 130.1 (2008).
9. Ivantysynova, M.,Baker, J., Power Loss in the Lubricating Gap between Cylinder Block and Valve Plate of Swash Plate Type Axial Piston Machines, International Journal of Fluid Power 10 (2009), 29–43.
10. C HUANG,Ivantysynova, M., A New Approach to Predict the Load Carrying Ability of the Gap between Valve Plate and Cylinder Block, Bath Workshop of Power Transmission and Motion Control PTMC 2003, Bath, UK, 2003.
11. Jihai, J.,Weipeng, Y., An Approach to Predict Wear Distribution of Valve Plate in Elasto-Hydrodynamic Lubrication, IEEE Access 7 (2019), 86789–86797.
12. A. Schenk, M. Zecchi, M. Ivantysynova, Accurate Prediction of Axial Piston Machine's Performance Through a Thermo-Elasto-Hydrodynamic Simulation Model, Proceedings of the ASME/BATH 2013 Symposium on Fluid Power & Motion Control, Sarasota, USA, 2013.
13. CHACON, R.,Ivantysynova, M., An Investigation of the Impact of Micro Surface on the Cylinder Block/Valve Plate Interface Performance, Proceedings of the 8th FPNI Ph.D Symposium on Fluid Power, Lappeenranta, Finland,2014.
14. M. Zecchi, A Novel Fluid Structure Interaction and Thermal Model to Predict the Cylinder Block / Valve Plate Interface Performance in Swash Plate Type Axial Piston Machines, Diss. Purdue University, 2013.
15. Ernst, M.,Vacca, A., Hydrostatic vs. hydrodynamic components of fluid pressure in the tribological interfaces of axial piston machines, Tribology International 157 (2021), 106878.
16. Roccatello, A., Manco, S., Nervegna, N., Modelling a Variable Displacement Axial Piston Pump in a Multibody Simulation Environment, J. Dyn. Syst., Meas., Control 129 (2007), 456-468.
17. ZHANG, B., Xu, B., XIA, C., et al., Modeling and Simulation on Axial Piston Pump Based on Virtual Prototype Technology, CJME 22 (2009), 84–90.
18. Milind, T.R.,Mitra, M., A Study on the Dynamics and Vibration Behavior of an Axial Piston Pump Using Combined MBD/FE Approach, Procedia Engineering 144 (2016), 452–460.
19. Chen, H.X., Chua, P.S.K., Lim, G.H., Dynamic vibration analysis of a swash-plate type water hydraulic motor, Mech. Mach. Theory 41 (2006), 487–504.
20. Ye, S., Zhang, J., Xu, B., et al., A theoretical dynamic model to study the vibration response characteristics of an axial piston pump, Mech. Syst. Signal Proc. 150 (2021):107237.

21. Huang, H., Wu, G., Wu, Y., et al., Identification of acoustic sources for bent-axis axial piston motor under variable loads, J Sound Vib 468 (2020), 115063.
22. N. Patir, Effects of Surface Roughness on Partial Film Lubrication Using an Average Flow Model Based on Numerical Simulation, Ph. D. Thesis, Northwestern University, 1978.
23. Zhang, J., Chao, Q., Xu, B., Analysis of the cylinder block tilting inertia moment and its effect on the performance of high-speed electro-hydrostatic actuator pumps of aircraft, Chin. J. Aeronaut. 31 (2018), 169–177.

The 11th JFPS International Symposium on Fluid Power HAKODATE 2020 Oct. 12-13, 2021 JFPS The Japan Fluid Power System Society

First-order Trajectory Sensitivity Analysis of Multi-level Pressure Switching Control System

Jing YAO * ** ***, Pei WANG *, Xinhao LI*, Yuwang CHENG* and Xiaoming CAO****

* School of Mechanical Engineering, Yanshan University
438, Qinhuangdao, Hebei, China
(E-mail: wpei@stumail.ysu.edu.cn)
** Key Laboratory of Advanced Forging & Stamping Technology and Science of Ministry of Education of China, 438, Qinhuangdao, Hebei, China
*** Hebei Key Laboratory of Heavy Machinery Fluid Power Transmission and Control, Yanshan University
438, Qinhuangdao, Hebei, China
**** CCTEG Coal Mining Research Institute
Beijing, China

Abstract. Some variables have some uncertain influence on the control accuracy of the Multi-level Pressure Switching Control System (MPSCS), but the importance and degree are not known clearly, which adds difficulty to the targeted compensation control for high precision. This paper utilizes sensitivity analysis to explore the output model of MPSCS response to varying fifteen variables and quantifies those variations for control compensation and optimization. The first-order trajectory model of sensitivity based on the state equation of the MPSCS was built to analyze the sensitivity-time history curves of each variable. The indicators of peak sensitivity and mean sensitivity are proposed to quantitatively evaluate the effects of interactions among variables. The simulation and experiments test the influence of model input variables and identify the variable that has the most influence on output characteristics by indicators. Hence, the results serve as a great basis for control optimization and compensation of the MPSCS.

Keywords: Sensitivity analysis, Multi-level pressure, Digital Hydraulic, Quantitatively analysis

INTRODUCTION

Compared with the traditional valve-controlled technique, digital hydraulics is a cutting-edge alternative of fluid power due to the advantages of low cost, high efficiency, control flexibility, and robustness [1-3]. It is composed of several on/off valves actively controlling system outputs [4-5]. Besides, it covers a wide range of applications including digital hydraulic valves, pumps, actuators, and switched hydraulics, as well as digital hydraulic power management systems, which all promise high energy efficiency. Switched hydraulics is a sub-domain of digital hydraulics, including the switching valve-controlled system and the switching hydraulic power supply system. The switching valve-controlled system [6-8], such as the ABS brakes of cars, switching converters, SIHS, etc., is used to adjust or control flow and pressure [9]. The switching hydraulic power supply system [10-12] uses a controller to improve energy efficiency depending on the current load by switch on/off valves. The group at Aalborg University investigated discrete fluid power force systems for wave energy converters (WEC) and analyzed the system configuration [13]. The discrete displacement cylinder (DDC) with several working chambers connected with many pressure supply levels based on Force Switching Algorithm (FSA) to reduce chattering and energy loss [14-16]. The concept of STEAM is introduced in [17], which develops different pressure rails across the on/off valves to match loads and pumps in real-time. The research group at Yanshan University [18-19] applied the two-level pressure to a forging hydraulic press and utilize on/off valves to achieve multi-level pressure independent metering in hydraulic systems.

However, severe pressure fluctuations occur in the switched hydraulic systems, which affect the control accuracy of the system. Some methods were developed to alleviate the pressure fluctuations for high-precision control. The proposed digital hydraulic circuit employed the proper duty cycle to control switching valves and realize an energy-efficient position in [20]. The position control strategy and switching optimization of the digital valve system is investigated in [21], which not only improves positioning accuracy but also optimizes the switching number. Although the advanced control theory has improved the dynamic and static characteristics for the digital switching system, the switching impact is the main issue for switched hydraulic systems and some parameters have a great influence on the output characteristics. Sakai[30] investigated a new structure preserving nondimensionalization for visualization of hydraulic cylinder dynamics to clarify comprehensive relations. The sensitivity analysis is recognized as an effective way to quantify the effect of each parameter, which is beneficial to improve the position accuracy, alleviate pressure fluctuations and optimize control. Due to the development of modern control theory, sensitivity analysis is widely accepted in many fields to study the variables that the influence of parameters upon system performance [22-24]. According to recent studies[25-27], many experts research the valve-controlled system by sensitivity analysis to find the main parameters affecting system characteristics and identify the effect of interactions between variables, such as hydraulic modeling and nonlinearity[31], hydraulic element design.

To achieve the aims outlined above, this paper analyzes the main parameters affecting the system performance of the MPSCS for the controller design and improvement of output characteristics. The outline of this paper is organized as follows: In Section II, the principle and mathematical modeling of MPSCS are described for sensitivity function. In Section III, the first-order tracking sensitivity function is solved and each parameter is analyzed by simulation. In Section IV, the sensitivity analysis theory of MPSCS is validated by experiments. Finally, conclusions are present in Section V.

SYSTEM DESCRIPTION AND MODELLING

Principles of MPSCS

MPSCS [19] mainly consists of accumulator charging circuits, on/off valve matrix, hydraulic transformer, proportional valves and actuators, etc. (Fig. 1). The valve matrix is a rectangular array, arranged in *m* and *n*, ($m \geq 2$, $n \geq 2$). The intersections of rows and columns are usually set in on/off valves. There are many connection methods between the valve matrix and other components (pumps, accumulators and actuators) for different functions. The pumps are only used to supply the average power demand, while the hydraulic accumulators are used for peak power requirements and recovering the surplus energy. In addition to the tank pressure rail, the MPSCS can be classified into p_1, p_2… p_n. Each pressure level needs an accumulator to maintain the system pressure. The different pressure rails are introduced to minimize the throttling losses across the valves and enable energy recuperation by switching the valve matrix. In order to balance the energy among the different pressure levels, the hydraulic transformer is necessary to accomplish the energy transformation

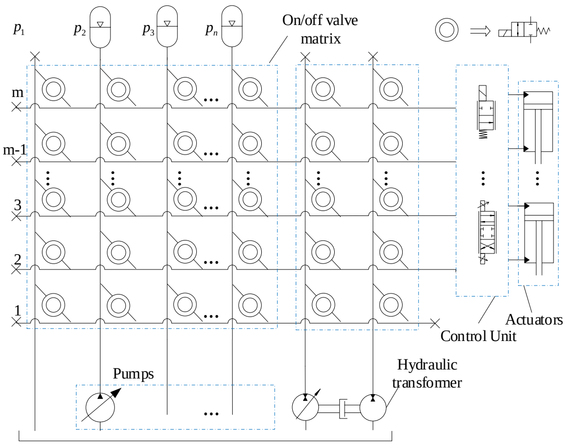

(a) Composition of MPSCS.

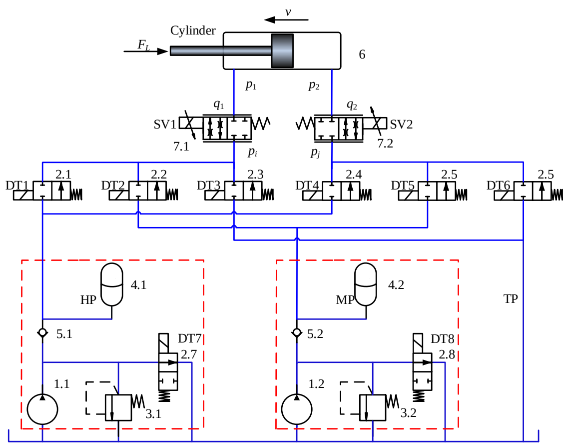

(b) Principle of Three-level Pressure Switching Control System.

Figure 1. Schematic Diagram of MPSCS.

In this study, we take one valve-controlled asymmetric cylinder hydraulic switching system with three-level pressure as the research object. The pumps and accumulators are installed in the columns, and the actuators are connected to the rows. The two chambers of the cylinder can connect independently to any oil circuit of the three-level pressure by on/off valves for different combinations of pressure.

State Equations

To obtain the main parameters influencing the output characteristics of the MPSCS, the mathematical models of the MPSCS were built in detail [28-29]. Based on the model of state variables of modern control theory, all the values of state variables at any time can be obtained, which is helpful to understand the internal state and its dynamic changes and obtain the dynamic characteristics of the system. We select four state variables that are linear irrelevance, $x_1 = y$, $x_2 = \dot{y}$, $x_3 = p_1$, $x_4 = p_2$. The friction F_f, load force F_L, pressure of proportional valves p_i and p_j, and the input voltage of proportional valves U_{g1} and U_{g2} are defined as the input variables $\boldsymbol{u}$. This paper investigates the displacement control characteristics of the MPSCS, so the displacement y is defined as the output variable. The state equations were deduced in Eq. (1).

$$\begin{cases} \dot{x}_1 = x_2 \\ \dot{x}_2 = -\dfrac{K}{m_t}x_1 - \dfrac{B_p}{m_t}x_2 + \operatorname{sgn}(x_2)\dfrac{A_1}{m_t}x_3 - \operatorname{sgn}(x_2)\dfrac{A_2}{m_t}x_4 - \dfrac{F_f + F_L}{m_t} \\ \dot{x}_3 = \dfrac{\beta_e}{V_{g1} + A_1 L_0 + A_1 x_{11}}\begin{Bmatrix} -\operatorname{sgn}(x_2)A_1 x_2 - \left[C_{ip} + C_{ep} - \operatorname{sgn}(x_2)K_{c1}\right]x_3 \\ +C_{ip}x_4 + \operatorname{sgn}(x_2)K_{q1}K_{sv}U_{g1} - K_{c1}p_i \end{Bmatrix} \\ \dot{x}_4 = \dfrac{\beta_e}{V_{g2} + A_2(L\text{-}L_0) - A_2 x_1}\begin{Bmatrix} \operatorname{sgn}(x_2)A_2 x_2 + C_{ip}x_3 - \left[C_{ip} + C_{ep} + \operatorname{sgn}(x_2)K_{c2}\right]x_4 \\ -\operatorname{sgn}(x_2)K_{q2}K_{sv}U_{g2} - K_{c2}p_j \end{Bmatrix} \end{cases} \tag{1}$$

It involves many system parameters, some are the structural parameters and others are the working parameters. Let us introduce them in detail. Y_r represents the displacement input signal. The amplification gain K_{sv} and the flow gain K_{q1} or K_{q2} of the proportional valves is regarded as a constant value. And the K_{c1} and K_{c2} are the flow-pressure coefficient of the proportional valves. The p_i and p_j are the pressure of proportional valves for the rodless and rod cavity of the cylinder. The p_1 and p_2 represent the pressure of rodless and rod cavity. The A_1 and A_2 are the rodless and rod area of the cylinder cavities. The C_{ip} and C_{ep} are the internal and external leakage coefficient of the cylinder, respectively. The stroke of the hydraulic cylinder piston is L, and the initial position of the piston is L_0. V_{g1} and V_{g2} are the channel volume from the rodless and rod cavity to the proportional valve. The β_e is the effective volume modulus subjected to gas content and temperature of the oil. The K_y is the conversion coefficient between actual output displacement Y and displacement sensor voltage U_p. The m_t is the sum mass converted to the rod, and the K is the load stiffness. The B_p is the viscous damping coefficient. The F_L and F_f represent the load force and the friction, respectively.
Therefore, the state equation and output equation are expressed as follow,

$$\begin{bmatrix} \dot{x}_1 \\ \dot{x}_2 \\ \dot{x}_3 \\ \dot{x}_4 \end{bmatrix} = \begin{bmatrix} 0 & 1 & 0 & 0 \\ -\dfrac{K}{m_t} & -\dfrac{B_p}{m_t} & \operatorname{sgn}(x_2)\dfrac{A_1}{m_t} & -\operatorname{sgn}(x_2)\dfrac{A_2}{m_t} \\ 0 & -\operatorname{sgn}(x_2)A_1\dfrac{\beta_e}{V_1} & -\operatorname{sgn}(x_2)\begin{pmatrix} C_{ip} + C_{ep} \\ -K_{c1} \end{pmatrix}\dfrac{\beta_e}{V_1} & C_{ip} \\ 0 & \operatorname{sgn}(x_2)A_2\dfrac{\beta_e}{V_2} & C_{ip} & -\begin{pmatrix} C_{ip} + C_{ep} \\ +\operatorname{sgn}(x_2)K_{c2} \end{pmatrix}\dfrac{\beta_e}{V_2} \end{bmatrix}\begin{bmatrix} x_1 \\ x_2 \\ x_3 \\ x_4 \end{bmatrix} + \begin{bmatrix} 0 & 0 & 0 & 0 & 0 & 0 \\ -\dfrac{1}{m_t} & -\dfrac{1}{m_t} & 0 & 0 & 0 & 0 \\ 0 & 0 & -K_{c1} & 0 & K_{q1}K_{sv} & 0 \\ 0 & 0 & -K_{c2} & 0 & 0 & -K_{q2}K_{sv} \end{bmatrix}\begin{bmatrix} F_f \\ F_L \\ p_i \\ p_j \\ U_{g1} \\ U_{g2} \end{bmatrix} \tag{2}$$

$$y = \begin{bmatrix} 1 & 0 & 0 & 0 \end{bmatrix}\begin{bmatrix} x_1 \\ x_2 \\ x_3 \\ x_4 \end{bmatrix} \tag{3}$$

FIRST-ORDER TRAJECTORY SENSITIVITY SOLUTION

Sensitivity Equation

To analyze the influence of parameters on output displacement characteristics, the state equation of MPCSC can be rewritten as,

$$\dot{x} = \boldsymbol{f}(\boldsymbol{x},\boldsymbol{u},\boldsymbol{\alpha},t) = \begin{bmatrix} \dot{x}_1 \\ \dot{x}_2 \\ \vdots \\ \dot{x}_n \end{bmatrix} = \begin{bmatrix} f_1(x,u,\alpha,\mathrm{t}) \\ f_2(x,u,\alpha,\mathrm{t}) \\ \vdots \\ f_n(x,u,\alpha,\mathrm{t}) \end{bmatrix} \tag{4}$$

where $\boldsymbol{x} = [x_1, x_2, x_3, x_4]^{\mathrm{T}}$, $\boldsymbol{u} = [u_1]^{\mathrm{T}}$, $\boldsymbol{\alpha} = [\alpha_1, \alpha_2, \alpha_3, \alpha_4, \alpha_5, \alpha_6, \alpha_7, \alpha_8, \alpha_9, \alpha_{10}, \alpha_{11}, \alpha_{12}, \alpha_{13}, \alpha_{14}, \alpha_{15}]^{\mathrm{T}}$, $\alpha_1 = K_{q1}$, $\alpha_2 = K_{c1}$, $\alpha_3 = K_{q2}$, $\alpha_4 = K_{c2}$, $\alpha_5 = C_{ip}$, $\alpha_6 = \beta_e$, $\alpha_7 = p_i$, $\alpha_8 = p_j$, $\alpha_9 = L$, $\alpha_{10} = L_0$, $\alpha_{11} = m_t$, $\alpha_{12} = K$, $\alpha_{13} = B_p$, $\alpha_{14} = F_L$, $\alpha_{15} = K_{sv}$.

There are fifteen key parameters that cover the structure parameters, working parameters and control parameters, take the partial to $\boldsymbol{\alpha}$ for the first-order trajectory sensitivity model.

$$(\frac{\partial \dot{\boldsymbol{x}}}{\partial \alpha_i})_n = \frac{\partial \boldsymbol{f}(\boldsymbol{x},\boldsymbol{u},\boldsymbol{\alpha},t)}{\partial \alpha_i} = \begin{bmatrix} \dfrac{\partial f_1(x,u,\alpha,\mathrm{t})}{\partial \alpha_i} \\ \dfrac{\partial f_2(x,u,\alpha,\mathrm{t})}{\partial \alpha_i} \\ \vdots \\ \dfrac{\partial f_n(x,u,\alpha,\mathrm{t})}{\partial \alpha_i} \end{bmatrix} = (\frac{\partial \boldsymbol{f}}{\partial \boldsymbol{x}})_n \cdot (\frac{\partial \boldsymbol{x}}{\partial \alpha_i})_n + (\frac{\partial \boldsymbol{f}}{\partial \alpha_i})_n, (n=4) \tag{5}$$

where, $(\frac{\partial \boldsymbol{f}}{\partial \boldsymbol{x}})_n = \begin{bmatrix} \frac{\partial f_1}{\partial x_1} & \frac{\partial f_1}{\partial x_2} & \cdots & \frac{\partial f_1}{\partial x_n} \\ \frac{\partial f_2}{\partial x_1} & \frac{\partial f_2}{\partial x_2} & \cdots & \frac{\partial f_2}{\partial x_n} \\ \vdots & \vdots & \ddots & \vdots \\ \frac{\partial f_n}{\partial x_1} & \frac{\partial f_n}{\partial x_2} & \cdots & \frac{\partial f_n}{\partial x_n} \end{bmatrix}$, $(\frac{\partial \boldsymbol{x}}{\partial \alpha_i})_n = \begin{bmatrix} \frac{\partial x_1}{\partial \alpha_i} & \frac{\partial x_2}{\partial \alpha_i} & \cdots & \frac{\partial x_n}{\partial \alpha_i} \end{bmatrix}^{\mathrm{T}}$, $(\frac{\partial \boldsymbol{f}}{\partial \alpha_i})_n = \begin{bmatrix} \frac{\partial f_1}{\partial \alpha_i} & \frac{\partial f_2}{\partial \alpha_i} & \cdots & \frac{\partial f_n}{\partial \alpha_i} \end{bmatrix}^{\mathrm{T}}$.

The sensitivity function of the state vector to the parameter vector is defined as,

$$\boldsymbol{\lambda}_0^i = (\frac{\partial \boldsymbol{x}_0}{\partial \alpha_i})_n \tag{6}$$

Then, the sensitivity equation of the MPSCS can be expressed as,

$$\dot{\boldsymbol{\lambda}}^i = (\frac{\partial \boldsymbol{f}}{\partial \boldsymbol{x}})_n \boldsymbol{\lambda}^i + (\frac{\partial \boldsymbol{f}}{\partial \alpha_i})_n \tag{7}$$

where $(\partial \boldsymbol{f} / \partial \boldsymbol{x})_n$ is the coefficient matrix, and $(\partial \boldsymbol{f} / \partial \alpha_i)_n$ is a free item matrix.

Jacobean matrix $(\partial \boldsymbol{f} / \partial \boldsymbol{x})_n$ can be expressed as follow,

$$\frac{\partial f}{\partial x_n}=\begin{bmatrix} a_{1,1} & a_{1,2} & a_{1,3} & a_{1,4} \\ a_{2,1} & a_{2,2} & a_{2,3} & a_{2,4} \\ a_{3,1} & a_{3,2} & a_{3,3} & a_{3,4} \\ a_{4,1} & a_{4,2} & a_{4,3} & a_{4,4} \end{bmatrix} \tag{8}$$

where, $$\frac{\partial f}{\partial x_1}=\begin{bmatrix} 0,-\dfrac{K}{m_t},-A_1\beta_e(V_{g1}+A_1L_0+A_1x_1)^{-2}\begin{Bmatrix}-\mathrm{sgn}(x_2)A_1x_2 \\ -\left[C_{ip}+C_{ep}-\mathrm{sgn}(x_2)K_{c1}\right]x_3 \\ +C_{ip}x_4+\mathrm{sgn}(x_2)K_{q1}K_{sv}U_{g1}-K_{c1}p_i\end{Bmatrix}, \\ A_2\beta_e\left[V_{g2}+A_2(L-L_0)-A_2x_1\right]^{-2}\begin{Bmatrix}\mathrm{sgn}(x_2)A_2x_2+C_{ip}x_3 \\ -\left[C_{ip}+C_{ep}+\mathrm{sgn}(x_2)K_{c2}\right]x_4 \\ -\mathrm{sgn}(x_2)K_{q2}K_{sv}U_{g2}-K_{c2}p_j\end{Bmatrix}\end{bmatrix}^{\mathrm{T}},$$

$$\frac{\partial f}{\partial x_2}=\begin{bmatrix}1,-\dfrac{B_p}{m_t},-\mathrm{sgn}(x_2)A_1\beta_e(V_{g1}+A_1L_0+A_1x_1)^{-1}, \\ \mathrm{sgn}(x_2)A_2\beta_e\left[V_{g2}+A_2(L-L_0)-A_2x_1\right]^{-1}\end{bmatrix}^{\mathrm{T}},$$

$$\frac{\partial f}{\partial x_3}=\begin{bmatrix}0,\mathrm{sgn}(x_2)\dfrac{A_1}{m_t},-\beta_e\left[C_{ip}+C_{ep}-\mathrm{sgn}(x_2)K_{c1}\right](V_{g1}+A_1L_0+A_1x_1)^{-1}, \\ C_{ip}\beta_e\left[V_{g2}+A_2(L-L_0)-A_2x_1\right]^{-1}\end{bmatrix}^{\mathrm{T}},$$

$$\frac{\partial f}{\partial x_4}=\begin{bmatrix}0,-\mathrm{sgn}(x_2)\dfrac{A_2}{m_t},C_{ip}\beta_e(V_{g1}+A_1L_0+A_1x_1)^{-1}, \\ -\beta_e\left[C_{ip}+C_{ep}+\mathrm{sgn}(x_2)K_{c2}\right]\left[V_{g2}+A_2(L-L_0)-A_2x_1\right]^{-1}\end{bmatrix}^{\mathrm{T}}.$$

Jacobean matrix $(\partial \boldsymbol{f}/\partial\alpha_i)_n$ can be expressed as follow,

$$\frac{\partial f}{\partial \alpha_i}=\begin{bmatrix} b_{1,1} & b_{1,2} & \cdots & b_{1,i} & \cdots & b_{1,15} \\ b_{2,1} & b_{2,2} & & & & \vdots \\ \cdots & & \ddots & & & \vdots \\ b_{n,1} & & & b_{n,i} & & \vdots \\ \cdots & & & & \ddots & \vdots \\ b_{4,1} & \cdots & \cdots & \cdots & \cdots & b_{6,15} \end{bmatrix} \tag{9}$$

where,

$$\frac{\partial f}{\partial \alpha_1}=\left[0,0,\mathrm{sgn}(x_2)\beta_eK_{sv}U_{g1}(V_{g1}+A_1L_0+A_1x_1)^{-1},0\right]^{\mathrm{T}},\ \frac{\partial f}{\partial \alpha_2}=\left[0,0,\beta_e\left(\mathrm{sgn}(x_2)x_3-p_i\right)(V_{g1}+A_1L_0+A_1x_1)^{-1},0\right]^{\mathrm{T}}$$

$$\frac{\partial f}{\partial \alpha_3}=\left[0,0,0,-\mathrm{sgn}(x_2)K_{sv}U_{g2}\beta_e\left[V_{g2}+A_2(L-L_0)-A_2x_1\right]^{-1}\right]^{\mathrm{T}},$$

$$\frac{\partial f}{\partial \alpha_4}=\left[0,0,0,-\beta_e\left(\mathrm{sgn}(x_2)x_4+p_j\right)\left[V_{g2}+A_2(L-L_0)-A_2x_1\right]^{-1}\right]^{\mathrm{T}},$$

5

$$\frac{\partial f}{\partial \alpha_5}=\left[0,0,\beta_e\left(-x_3+x_4\right)(V_{g1}+A_1L_0+A_1x_1)^{-1},\beta_e\left(x_3-x_4\right)\left[V_{g2}+A_2(L-L_0)-A_2x_1\right]^{-1}\right]^{\mathrm{T}},$$

$$\frac{\partial f}{\partial \alpha_6}=\left[\begin{array}{l}0,0,\left\{\begin{array}{l}-\operatorname{sgn}(x_2)A_1x_2\\-\left[C_{ip}+C_{ep}-\operatorname{sgn}(x_2)K_{c1}\right]x_3\\+C_{ip}x_4+\operatorname{sgn}(x_2)K_{q1}K_{sv}U_{g1}-K_{c1}p_i\end{array}\right\}(V_{g1}+A_1L_0+A_1x_1)^{-1},\\ \left\{\begin{array}{l}\operatorname{sgn}(x_2)A_2x_2+C_{ip}x_3\\-\left[C_{ip}+C_{ep}+\operatorname{sgn}(x_2)K_{c2}\right]x_4\\-\operatorname{sgn}(x_2)K_{q2}K_{sv}U_{g2}-K_{c2}p_j\end{array}\right\}\left[V_{g2}+A_2(L-L_0)-A_2x_1\right]^{-1}\end{array}\right]^{\mathrm{T}},$$

$$\frac{\partial f}{\partial \alpha_7}=\left[0,0,-K_{c1}\beta_e(V_{g1}+A_1L_0+A_1x_1)^{-1},0\right]^{\mathrm{T}},\frac{\partial f}{\partial \alpha_8}=\left[0,0,0,-K_{c2}\beta_e\left[V_{g2}+A_2(L-L_0)-A_2x_1\right]^{-1}\right]^{\mathrm{T}},$$

$$\frac{\partial f}{\partial \alpha_9}=\left[0,0,0,-A_2\beta_e\left[V_{g2}+A_2(L-L_0)-A_2x_1\right]^{-2}\left\{\begin{array}{l}\operatorname{sgn}(x_2)A_2x_2+C_{ip}x_3\\-\left[C_{ip}+C_{ep}+\operatorname{sgn}(x_2)K_{c2}\right]x_4\\-\operatorname{sgn}(x_2)K_{q2}K_{sv}U_{g2}-K_{c2}p_j\end{array}\right\}\right]^{\mathrm{T}},$$

$$\frac{\partial f}{\partial \alpha_{10}}=\left[\begin{array}{l}0,0,-A_1\beta_e(V_{g1}+A_1L_0+A_1x_1)^{-2}\left\{\begin{array}{l}-\operatorname{sgn}(x_2)A_1x_2\\-\left[C_{ip}+C_{ep}-\operatorname{sgn}(x_2)K_{c1}\right]x_3\\+C_{ip}x_4+\operatorname{sgn}(x_2)K_{q1}K_{sv}U_{g1}-K_{c1}p_i\end{array}\right\},\\ A_2\beta_e\left[V_{g2}+A_2(L-L_0)-A_2x_1\right]^{-2}\left\{\begin{array}{l}\operatorname{sgn}(x_2)A_2x_2+C_{ip}x_3\\-\left[C_{ip}+C_{ep}+\operatorname{sgn}(x_2)K_{c2}\right]x_4\\-\operatorname{sgn}(x_2)K_{q2}K_{sv}U_{g2}-K_{c2}p_j\end{array}\right\}\end{array}\right]^{\mathrm{T}},$$

$$\frac{\partial f}{\partial \alpha_{11}}=\left[0,\frac{K}{m_t^2}x_1+\frac{B_p}{m_t^2}x_2-\operatorname{sgn}(x_2)\frac{A_1}{m_t^2}x_3+\operatorname{sgn}(x_2)\frac{A_2}{m_t^2}x_4+\frac{F_f+F_L}{m_t^2},0,0\right]^{\mathrm{T}},\frac{\partial f}{\partial \alpha_{12}}=\left[0,-\frac{1}{m_t}x_1,0,0\right]^{\mathrm{T}},$$

$$\frac{\partial f}{\partial \alpha_{13}}=\left[0,-\frac{1}{m_t}x_2,0,0\right]^{\mathrm{T}},\frac{\partial f}{\partial \alpha_{14}}=\left[0,-\frac{1}{m_t},0,0\right]^{\mathrm{T}},\frac{\partial f}{\partial \alpha_{15}}=\left[\begin{array}{l}0,0,\operatorname{sgn}(x_2)K_{q1}U_{g1}\beta_e(V_{g1}+A_1L_0+A_1x_1)^{-1},\\-\operatorname{sgn}(x_2)K_{q2}U_{g2}\beta_e\left[V_{g2}+A_2(L-L_0)-A_2x_1\right]^{-1}\end{array}\right]^{\mathrm{T}}$$

It can be considered that at the initial moment, the displacement, velocity and pressure of the hydraulic cylinder are zero, so the initial value of x is x_0=0. Then, the initial value of the sensitivity function λ^{i} can be expressed as follow,

$$\boldsymbol{\lambda}_0^i=\boldsymbol{0},\ (i=1...15) \tag{10}$$

SENSITIVITY ANALYSIS

Sensitivity Indicators

Due to the changing state of the MPSCS in the sampling time, and the value $\boldsymbol{\lambda}$ changes with time as well. Then, the curve of change is defined as a sensitivity-time history curve, which describes the changing process of sensitivity function. The change of parameters vector $\Delta\boldsymbol{\alpha}$ would cause a change in the state vector $\Delta\boldsymbol{x}$, thus we could get the Taylor expansion,

$$\Delta\boldsymbol{x}=\left(\frac{\partial \boldsymbol{x}}{\partial \boldsymbol{\alpha}}\right)_n\Delta\boldsymbol{\alpha}+o(\boldsymbol{\alpha}) \tag{11}$$

It can be seen that the small changes of $\boldsymbol{x}$ will be calculated as long as multiplying the calculated $\left(\partial \boldsymbol{x} / \partial \boldsymbol{\alpha}\right)_n$ by $\Delta\boldsymbol{\alpha}$. There are two indicators[32] to reflect directly the effects of interactions among on state vector $\boldsymbol{x}$.
For displacement step control of MPSCS, both given displacement and initial displacement are the constant value. Therefore, the peak sensitivity S_1 is the percentage for the change of the state vector relative to the difference between the given displacement and the initial displacement, reflecting the impact degree.

$$S_1 = \frac{\Delta x_j}{x_{sj}} \times 100\% = \frac{\lambda_j^i \, \Delta \alpha_i}{x_{sj}} \times 100\% \tag{12}$$

That is, mean sensitivity S_2 represents the overall degree of influence of parameter vector change on the step response to displacement in the dynamic response process.

$$S_2 = \int_o^t \left| \left(\frac{\partial x}{\partial \alpha}\right)_n \right| \Delta \alpha \, \mathrm{d}t \tag{13}$$

This paper selects the step displacement response to analyze the sensitivity, which is easy to observe the rapidity and stability of the MPSCS. And the peak sensitivity and the mean sensitivity of each parameter are calculated and compared in the system to reflect the quantitative analysis results of the influence degree of each parameter change in the system on the displacement output of the system.

Sensitivity Analysis

Based on above sensitivity theoretical model of the MPSCS, the solution of the sensitivity equations need to be synchronously calculated for the real-time variation of the state variables in the system. According to the Eq. (8), there are $n\times(i+1)$ expressions to solve, including n expressions of state equations and $n\times i$ expressions of sensitivity equations. We only investigate the sensitivity of x_1 for parameters $\boldsymbol{\alpha}$. Firstly, the equation of sensitivity function was solved and the programmed Runge-Kutta run in MATLAB/Simulink. Then, the simulation model of the MPSCS is built based on the mathematical model, and the detailed simulation parameters are listed in the Table 1.

Table 1. Simulation Parameters of the MPSCS.

Parameters Name	**Value**
Diameter of Cylinder D	100 mm
Diameter of Rod d	45 mm
Stroke L	400 mm
Load Mass m_t	176 Kg
Frequency of Proportional Valves	40 Hz
Damping ratio of Proportional Valves	0.707
Flow of Proportional Valves	60 L/min
Area of Rodless Cavity A_1	7.85×10-3 m^2
Area of Rod Cavity A_2	6.26×10-3 m^2
Accumulator Volume	40 L

With the difference of the external load force and step displacement, the system response characteristics of the MPSCS in actual work are different. The sensitivity of the system parameters is studied under different load force to analyze the system. The influence of various parameters on the system displacement output characteristics under different load conditions makes the sensitivity analysis results more applicable. The rapidity and stability of the system can be judged more conveniently by the step displacement curve, this paper obtains the sensitivity of each parameter under 5 mm and 10 mm step displacement. The sensitivity-time history curves $\boldsymbol{\lambda}_1^i$ of displacement x_1 to $\boldsymbol{\alpha}_i$ were obtained under 5 mm step displacement and 10 kN load force in Fig.2. Similarly, in other cases, it won't go into detail.

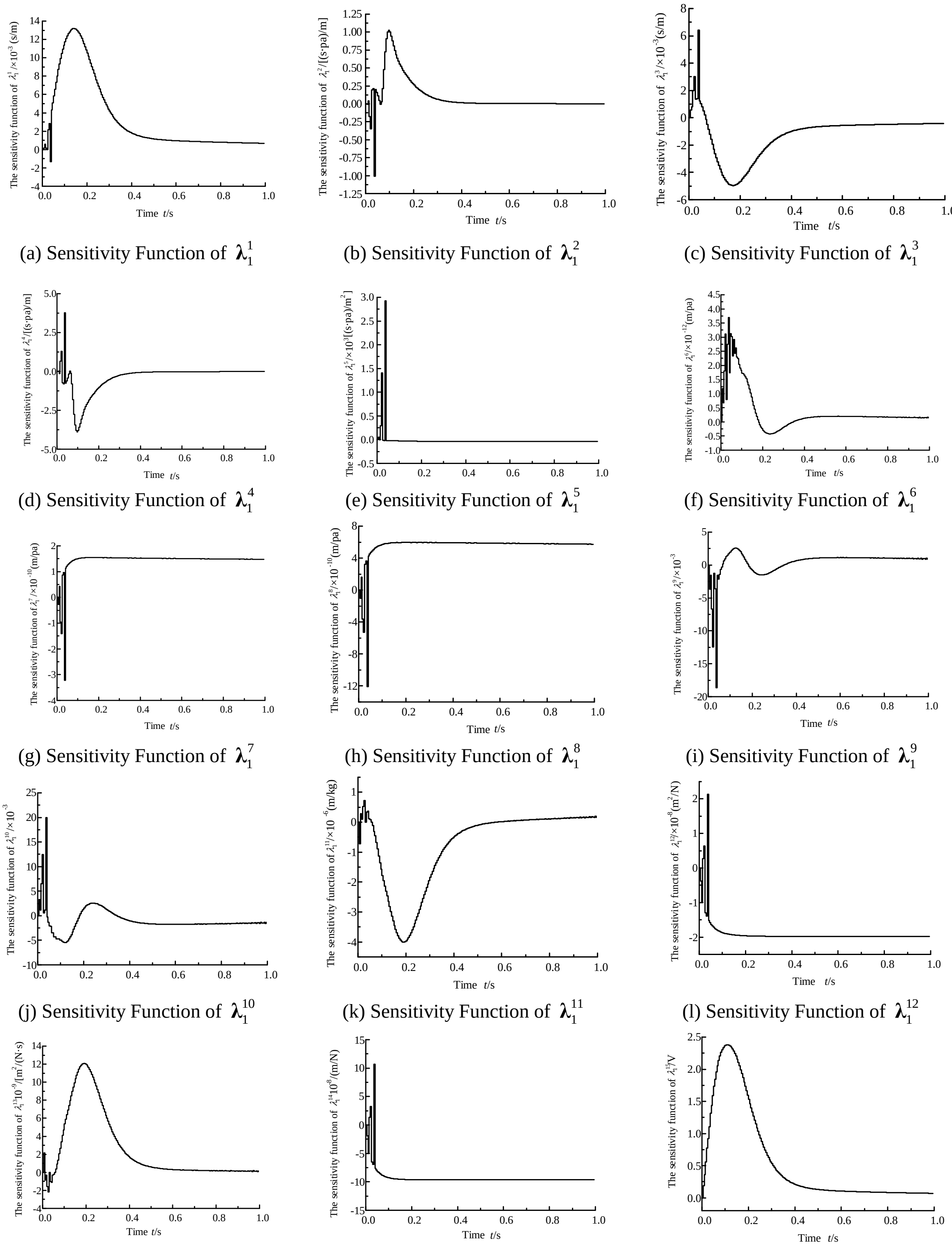

(a) Sensitivity Function of $\boldsymbol{\lambda}_1^1$ (b) Sensitivity Function of $\boldsymbol{\lambda}_1^2$ (c) Sensitivity Function of $\boldsymbol{\lambda}_1^3$

(d) Sensitivity Function of $\boldsymbol{\lambda}_1^4$ (e) Sensitivity Function of $\boldsymbol{\lambda}_1^5$ (f) Sensitivity Function of $\boldsymbol{\lambda}_1^6$

(g) Sensitivity Function of $\boldsymbol{\lambda}_1^7$ (h) Sensitivity Function of $\boldsymbol{\lambda}_1^8$ (i) Sensitivity Function of $\boldsymbol{\lambda}_1^9$

(j) Sensitivity Function of $\boldsymbol{\lambda}_1^{10}$ (k) Sensitivity Function of $\boldsymbol{\lambda}_1^{11}$ (l) Sensitivity Function of $\boldsymbol{\lambda}_1^{12}$

(m) Sensitivity Function of $\boldsymbol{\lambda}_1^{13}$ (n) Sensitivity Function of $\boldsymbol{\lambda}_1^{14}$ (o) Sensitivity Function of $\boldsymbol{\lambda}_1^{15}$

Figure 2. The Sensitivity-Time History Curves of Parameters

It can be seen from Fig.2 that each parameter influences output displacement x_1. The positive and negative mean growth and inhibition, respectively. When the displacement x_1 approaches the steady-state, the sensitivity functions of the parameters α_7, α_8, α_{13}, α_{14} have a non-zero solution and is not close to zero, which have great influence on the state characteristics of displacement. To visually observe the influence of these parameters, dynamic displacement characteristics of 5 mm and 10 mm step under 10 kN and 20 kN loading force were analyzed when 10% parameters change by sensitivity indicators. The pre-pressure of rodless or rod cavity is the switching pressure level, the parameter change in pressure is the change of pressure level actually. The parameters α_7, α_8 would change simultaneously, thus the two parameters merge into one. The results of sensitivity analysis is shown in Fig.3 and Fig.4.

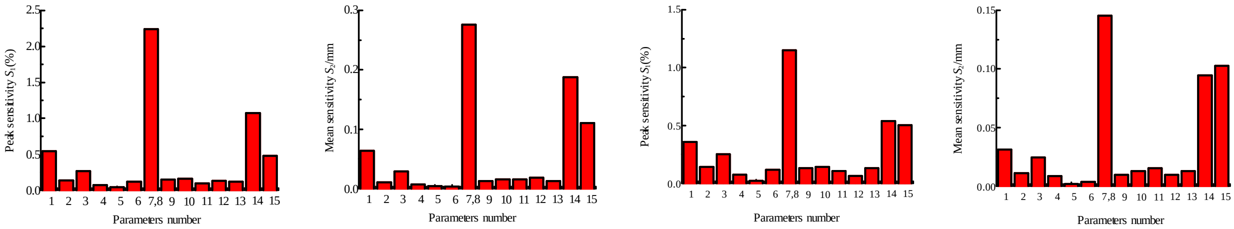

(a) Peak Sensitivity with 5 mm Step Displacement
(b) Mean Sensitivity with 5 mm Step Displacement
(c) Peak Sensitivity with 10 mm Step Displacement
(d) Mean Sensitivity with 10 mm Step Displacement

Figure 3. Sensitivity Indicators under 10 kN Load Force

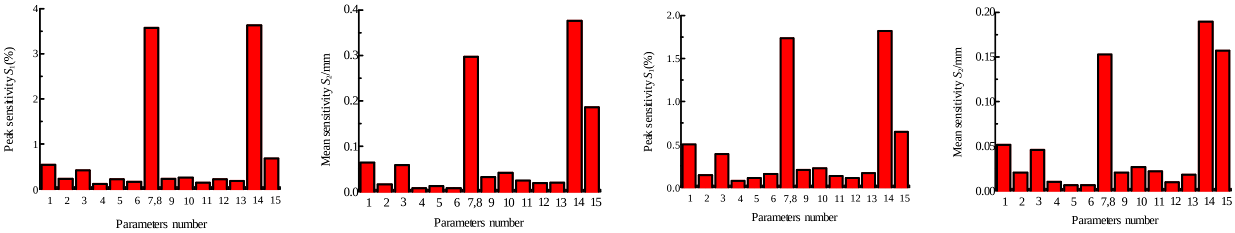

(a) Peak Sensitivity with 5 mm Step Displacement
(b) Mean Sensitivity with 5 mm Step Displacement
(c) Peak Sensitivity with 10 mm Step Displacement
(d) Mean Sensitivity with 10 mm Step Displacement

Figure 4. Sensitivity Indicators under 20 kN Load Force

According to the results of sensitivity analysis, the peak and mean sensitivity indicators of the parameters 1, 2, 3, 4, 5, 6, 9, 10, 11, 12 and 13 are very smaller value compared with the parameters of 7, 8, 14 and 15. The four parameters have a significant influence on the step displacement response in the dynamic characteristics. Under the 10 kN load force, the interaction of parameters 7 and 8 have the most influence on the displacement. The values of peak sensitivity of 5 mm and 10 mm displacement step are 2.24% and 1.15%, respectively. The values of mean sensitivity are 0.28 mm and 0.15 mm, respectively. However, the values of peak sensitivity of 5 mm and 10 mm displacement step with 20 kN are 3.57% and 1.73%, respectively. While, the values of mean sensitivity are 0.30 mm and 0.15 mm, respectively. Therefore, the values of peak sensitivity have a certain increasing trend with the load force increasing under the same displacement step, while the values of mean sensitivity have little change. Besides, both peak sensitivity and mean sensitivity decreased to some extent with the same load force. The parameter 14 is load force, the trend of the change of two sensitivity indicators are the same. The values of the two sensitivity increase dramatically under the same displacement step, while the values decrease under the same load force. For parameter 15, under the different displacement steps, the values of peak sensitivity under 10 kN load force are 0.48% and 0.50%, the values of mean sensitivity are 0.11 mm and 0.10 mm. Under 20 kN load force, the value of S_1 are 0.68% and 0.65%, the value of S_2 are 0.19 mm and 0.16 mm. Hence, the values of two indicators have a little change with the change of displacement step, while it has an obvious increase with load force rising. In conclusion, pre-pressure parameters, load force and proportional action factor have greater influence parameter on the displacement output, especially the pre-pressure.

EXPERIMENT VERIFICATION

To ensure the accuracy and reliability of the sensitivity analysis results, it is necessary to carry out experimental verification on the analysis results. However, many parameters of the MSPCS are difficult to measure, and achieve the experimental verification of the sensitivity analysis results of all parameters. Therefore, this paper verifies the sensitivity analysis results by some measurable parameters through experiments, and prove the analysis conclusions of other parameters by analogy. The parameter 7 and 8, which are changed by switching the pressure levels, the parameter 10 and the parameter 14 are selected to verify the sensitivity theory analysis by experiments.

Experiment Platform

The experiments were carried out on the MSPCS platform, which mainly includes the hydraulic transmission system and the data acquisition and control system, see Figure 5. The servo valve-controlled cylinder system of force closed-loop control is adopted to simulate load force. The multi-level pressure achieve by the connection between the actuator and the pressure level by opening and closing of the corresponding on/off valve in the control valve matrix. Each pressure level is composed of an accumulator with an unloading relief valve and a manual variable pump, the maximum safe working pressure set by the unloading relief valve to compare with pressure level to decide the operation or unloading of the manual variable pump.
The signal control and acquisition system for MPSCS is designed on MATLAB/Simulink software in a personal computer (PC), and the control signals are sent to an industrial personal computer (IPC) to control actuator directly in real-time. Control signals from IPC are sent to the on/off valve matrix to select the corresponding pressure levels. At the same time, the IPC is responsible for signal acquisition, thus the collected pressure and displacement data could processed by the real-time controller with 1 ms sample interval. Moreover, the user interface could help to monitor the data and control process, as well as adjust some system parameters. The components and used transducers are listed in Table 2.

(a) Hydraulic Transmission System (b) The Signal Control and Acquisition System
Figure 5. MPSCS Platform

Table 2. Main Parameters of Experimental Components

Parameters Name	Value
Manual variable pump	0-31.5 MPa; 0-25 mL/rev
Proportional variable pump(MOOG-RKP)	0-28 MPa; 19 mL/rev
Accumulator	40 L
Cylinder	Ø100 mm/45 mm-400 mm
Hydraulic motor	940 mL/rev
Displacement sensor	400 mm; 0.1%FS
Force sensor	20 kN; 0.05%FS
Speed torque sensor	2000 r/min; 5000 N•m; 0.5%FS
Pressure sensor	25 MPa; 0.5%FS
Flow sensor	60 L/min; 2%FS

Results and Discussion

The H pressure level is set as 60 bar, and the M pressure level is set as 30 bar. The initial position of rod L_0=200 mm. Besides, the 5 mm and 10 mm displacement step under 10 kN and 20 kN load force were given and shown in Fig. 6 and Fig.7.

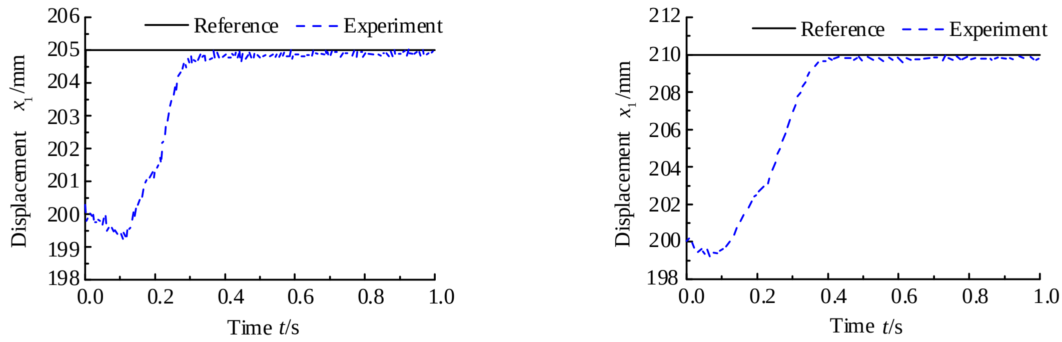

(a) Step Response of 5 mm under 10 kN (b) Step Response of 10 mm under 10 kN

Figure 6. Displacement Step Response under 10 kN

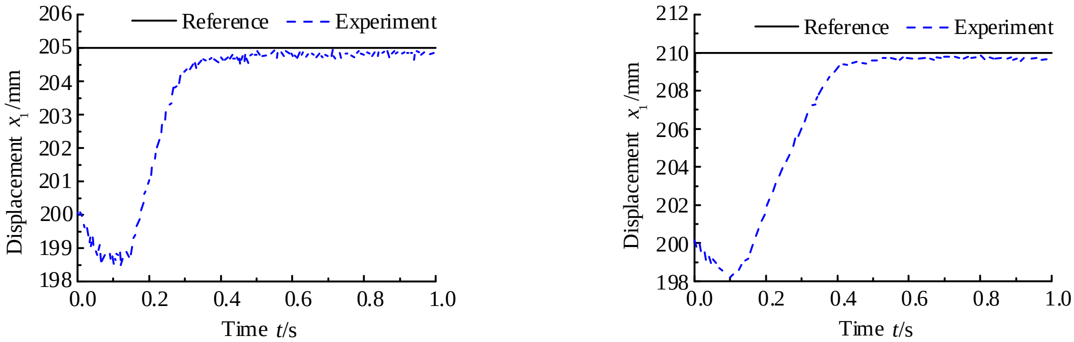

(a) Step Response of 5 mm under 20 kN (b) Step Response of 10 mm under 20 kN

Figure 7. Displacement Step Response under 20 kN

With 10 % variations of above parameters, the comparison between the experiment and theoretical simulation analysis of two indicators are shown in Fig.8

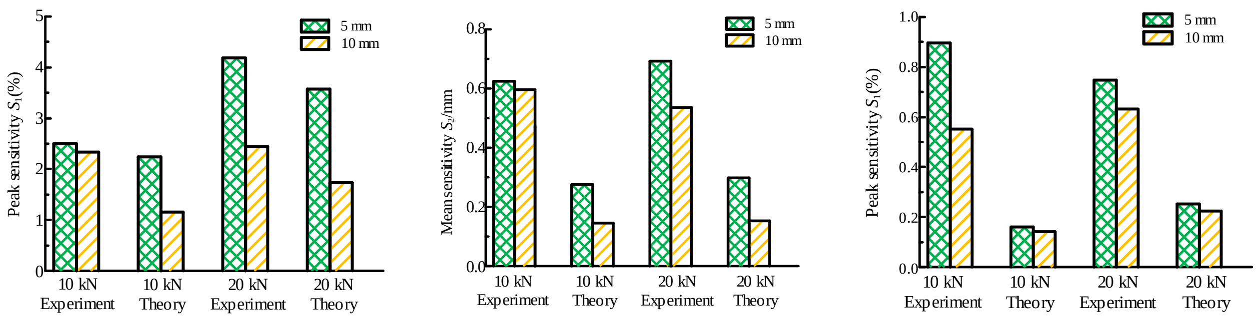

(a) Peak Sensitivity of Parameters 7, 8 (b) Mean Sensitivity of Parameters 7, 8 (c) Peak Sensitivity of Parameter 10

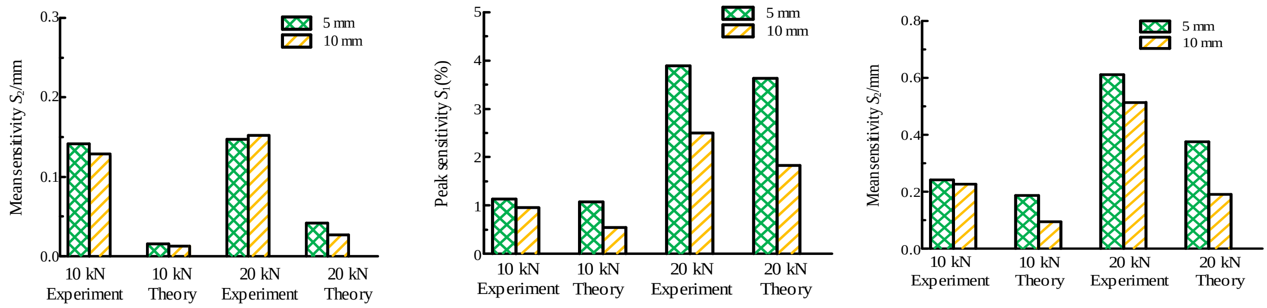

(d) Mean Sensitivity of Parameter 10 (e) Peak Sensitivity of Parameter 14 (f) Mean Sensitivity of Parameter 14

Figure 8. Sensitivity Indicators with 10% Changes of Parameters

The experimental results demonstrate that the two sensitivity parameters almost consistent with the theoretical analysis. The parameter 10 has very little influence on the displacement, but it is susceptible to other factors easily. Thus, the results show the some difference value between simulation and experiment measure. Similarly,

the load force also has a difference due to the impact of transient force, which enhances the change range of load force, thus the experiment indicators of load force is greater than the simulation results. The main reason for value deviation is that it is difficult to describe all the state characteristics based on the current mathematical model, which affects the sensitivity analysis of parameters. It makes the unavoidable deviation between theory and experiment.
Based on above theoretical calculation and experimental verification, the influence of each variation parameter on the output of the MPSCS is quantitatively analyzed. The results show that the front pressure of proportional valve, load force and amplification coefficient of proportional valve significantly affected the displacement output characteristics, especially the front pressure of the proportional valve that has the most influence on output characteristics. This can provide a theoretical basis for MPSCS control optimization and compensation.

CONCLUSION

To address the switching impact and optimize control to obtain better compensation for the Multi-level Pressure Switching Control System (MPSCS), this paper develops the sensitivity analysis method to quantify the influence of the main parameters on the MPSCS characteristics. The first-order trajectory models of sensitivity were established based on the mathematical models of MPSCS and the state equations. We solved the sensitivity function of the fifteen parameters and got the sensitivity-time history curves of each parameter under 5 mm step displacement and 10 kN load force based on the simulation model built by MATLAB/Simulink. The parameter 7, 8, 12 and 14 have great influence on the state characteristics of output displacement.
The influence degree of each parameter on the displacement output dynamic characteristics of the MPSCS was quantitatively analyzed by the proposed peak sensitivity and mean sensitivity. The parameters 7, 8, 14 and 15 have a significant influence on the step displacement response in the dynamic characteristics under 10% parameters change, especially the parameters 7 and 8. The experiments were carried out on the MPSCS platform to validate the feasibility of sensitivity theory by some measurable parameters 7, 8, 14. The experimental results demonstrate that the two sensitivity indicators almost consistent with the theoretical analysis. Though there is a small deviation between theory and experiment, it is unavoidable due to the current mathematical models are not accurate entirely to describe all the state characteristics of the MPSCS. Next, the nondimensionalization would be tried to apply on sensitivity analysis for more general result. Future work will be carried out on the control optimization and compensation for the MPSCS based on the results of the sensitivity analysis.

ACKNOWLEDGMENTS

The authors thank the anonymous reviewers for their critical and constructive review of the manuscript. This study was co-supported by the National Natural Science Foundation of China (No.51975507).

REFERENCES

1. PAN, M., PLUMMWER, A., Digital Switched Hydraulics. Frontiers of Mechanical Engineering, 2018, 13-2, pp.225-231.
2. SCHEIDL, R., LINJAMA, M., SCHMIDT, S., Is the Future of Fluid Power Digital Proceedings of the Institution of Mechanical Engineers. Part I, Journal of Systems and Control Engineering, 2012, 226-6, pp.721– 723
3. YANG, H. Y., PAN, M., Engineering Research in Fluid Power: A Review. Journal of Zhejiang University. Science A, 2015, 16-6, pp.427–442.
4. LINJAMA, M., LAAMANEN, A., VILENIUS, M., Is It Time for Digital Hydraulics? In: Proceedings of the 8th Scandinavian International Conference on Fluid Power. Tampere, 2003, pp.347–366.
5. LINJAMA, M., Digital fluid power: State of the art. In: Proceedings of the 12th Scandinavian International Conference on Fluid Power. Tampere, 2011, pp.18–20.
6. JOHNSTON, D. N., A Switched Inertance Device for Efficient Control of Pressure and Flow, In Proceedings of the ASME 2009 Dynamic Systems and Control Conference - DSCC2009, Hollywood, USA, 2009, pp.589-596.
7. DE, NEGRI, V. J., WANG, P., PLUMMER, A., JOHNSTON, D. N., Behavioural Prediction of Hydraulic Step-up Switching Converters, International Journal of Fluid Power, 2014, 15-1, pp. 19.
8. KOGLER, H., SCHEIDL, R., Two Basic Concepts of Hydraulic Switching Converters. In Proceedings of the First Workshop on Digital Fluid Power, Tampere, Finland, 2008, pp. 113128.
9. PAN, M., HILLIS, A., JOHNSTON, N., Active Control of Fluid-bome Noise in Hydraulic Systems Using In-series and By-pass Structures, 2014 UKACC International Conference on Control. IEEE, 2014, pp.355-360.
10. VUKOVIC, M., MURRENHOFF, H., The Next Generation of Fluid Power Systems, Dynamics and Vibroacoustics of Machines, 2014, pp.1-7.

11. MURRENHOFF, H., SGRO, S., VUKOVIC, M., An Overview of Energy Saving Architectures for Mobile Applications, In Proceedings of the 9th International Fluid Power Conference, Aachen, Germany, 2014b, pp.374-385.
12. VUKOVIC, M., SGRO, S., and MURRENHOFF, H., STEAM – A Mobile Hydraulic System with Engine Integration, In Proceedings of the ASME/BATH 2013 Symposium on Fluid Power & Motion Control, FPMC 2013, Sarasota, Florida, USA.
13. HANSEN, R. H., ANDERSEN, T. O., PERDERSEN, H. C., Analysis of Discrete Pressure Level Systems for Wave Energy Converters, International Conference on Fluid Power and Mechatronics, 2011, pp.552-558.
14. HANSEN, A. H., PEDERSEN, H. C., Optimal Configuration of a Discrete Fluid Power Force System Utilized in the PTO for WECs. Ocean Engineering, Aalborg East, Denmark, 117, 2016, pp.88-98.
15. HANSEN, A. H., ASMUSSEN, M. F., BECH, M. M., Energy Optimal Tracking Control with Discrete Fluid Power Systems Using Model Predictive Control. In Proceedings of the Ninth Workshop on Digital Fluid Power, Aalborg, Denmark, 2017, pp.7-8.
16. LIN, Y., XU, J., LIU, H., et al., Pressure Matching of Wave Energy Device Based on Digital Hydraulic Cylinder Group, Journal of Zhejiang University (Engineering Science), 2019, 53-10, pp.1892-1897.
17. LEIFELD, R., VUKOVIC, M., and MURRENHOFF, H., STEAM – the Best of Both Worlds, The Seventh Workshop on Digital Fluid Power, Linz, Austria, 2015.
18. YAO, J., Li, B., KONG, X.D., Energy Saving and Control of Hydraulic Press Fast Forging System Based on the Two_Stage Pressure Source, Journal of Mechanical Engineering, Vol. 52, No. 10, 2016, p.199-206.
19. YAO, J., CAO, X., WANG,P., et al., Multi-level Pressure Switching Control and Energy Saving for Displacement Servo Control System, in BATH/ASME 2016 Symposium on Fluid Power and Motion Control, Bath, UK, 2016, pp.7-9.
20. SAEEDZADEH, A., REZAEI, S. M., ZAREINEJAD, M., Energy-efficient Position Control of an Actuator in a Digital Hydraulic System Using on/off Valve, The 4th International Conference on Robotics and Mechatronics (ICROM). IEEE, 2016, pp.234-239.
21. GAO, Q., LINJAMA, M., PALONIITTY, M., et al., Investigation on Positioning Control Strategy and Switching Optimization of an Equal Coded Digital Valve System, Proceedings of the Institution of Mechanical Engineers, Part I: Journal of Systems and Control Engineering, 2019.
22. SONG, X. M., KONG, F. Z., ZHAN, C. S., et al., Parameter Identification and Global Sensitivity Analysis of Xin' anjiang Model Using Meta-modeling Approach. Water Science and Engineering, 2013, 6-1, pp.1-17.
23. HALL, J. W., BOYCE, S. A., WANG, Y. L., et al., Sensitivity Analysis for Hydraulic Models, Journal of Hydraulic Engineering, 2009, 135-11, pp.959-969.
24. WEI, P., SONG, J., LU, Z., Global Reliability Sensitivity Analysis of Motion Mechanisms, Journal of Risk and Reliability, 2016, 230, pp.265-277.
25. BA, K., YU B., KONG X., et al., The Dynamic Compliance and Its Compensation Control Research of the Highly Integrated Valve-controlled Cylinder Position Control System, International Journal of Control, Automation & Systems Journal of Dynamic Systems, 2017, 15-4, pp.1814-1825.
26. BA, K., YU, B., Parameters Sensitivity Analysis of Position-based Impedance Control for Bionic Legged Robots' HDU, Applied Sciences, 2017, 7-10, pp.1035.
27. ANTON, I, LOAN, S., Numerical Modeling of Cavitation Characteristics and Sensitivity Curves for Reversible Hydraulic Machinery. Engineering Analysis with Boundary Elements, 2014, 41, pp.18-27.
28. CAO, X., GUO, B., WANG, P., et al., Multi-level Pressure Switching Displacement Servo Control Systems, China Mechanical Engineering, 2017, 28-20, pp.2447-2454.
29. WANG, P., Control Strategy and Design of Multi-Level Pressure Independent Meter-In and Meter-Out Control System, Yanshan University, China, 2018.
30. SAKAI, S., STRAMIGIOLI, S., Visualization of Hydraulic Cylinder Dynamics by a Structure Preserving Nondimensionalization, IEEE/ASME Transactions on Mechatronics, 2018, 23-5, pp. 2196-2206.
31. KHALIL, H. K., Nonlinear Systems. Englewood Cliffs, NJ, USA: Prentice-Hall, 1996.
32. NURMI, J. and MATTILA, J., Detection and Isolation of Leakage and Valve Faults in Hydraulic Systems in Varying Loading Condition, Part 1: Global Sensitivity Analysis, International Journal of Fluid Power, 2011, 12, pp. 41–51.

The 11th JFPS International Symposium on Fluid Power HAKODATE 2020 Oct. 12-13, 2021 The Japan Fluid Power System Society

A Study on the Pulse Analysis and Vibration Characteristics of Hydraulic System for Prediction of Check Valve Behavior

Jeong-Woo PARK*, ** Eun-A JEONG*, Young-Bog HAM* and So-Nam YUN*

*Department of Thermal Systems, Energy Systems Research Division,
Korea Institute of Machinery & Materials, Daejeon, 34103, Korea.
** Department of Convergence System Engineering, Chung Nam National University, Korea.
(E-mail: ysn688@kimm.re.kr)

Abstract. The check valve is a basic type of valve. The poppet shaped check valve has been studied for decades and is still a topic of discussion to improve performance. However, most of the papers were based on experiments to predict valve performance and theoretical parts such as valves or pipelines, but few papers evaluated hydraulic vibration characteristics by simultaneously analyzing pressure-flow pulsation from pumps. Therefore, in this study we propose an experimental circuit that simulates the action of the check valve by generating positive pressure through a well-controlled pump system.

Keywords: Check Valve, Flow Pulsation, Pressure Fluctuation, Set Pressure.

INTRODUCTION

In order to predict the behavior of the check valve, a model of hydraulic circuit was devised to investigate the pulsation and vibration characteristics of the hydraulic system. The speed of the motor connected to the circuit is set to 100 [rpm], and the overflow valve was set to 10 [bar] for consecutive set pressure values, so that pressure changes can be interpreted. The pulsation of pressure and flow was obtained from the inlet of the hose and the inlet of the check valve. The behavior of the check valve was analyzed from the data obtained.

VALVE SYSTEM ANALYSIS AND RESULT GRAPHS

Fig. 1 shows a circuit used to perform experiment for finding characteristics of the check valve. The check valve (No. ①) was installed and the experimental hydraulic unit (No. ②) was used to supply hydraulic oil to the check valve. In this study, hydraulic pump (No. ③) installed in Fig. 1 (No. ②) was modeled and analyzed to predict valve behavior by generating a load at the check valve. Based on Fig. 1 circuit, the Simulation X tool was used to complete the modeling was divided into pump, hose and valve parts. The results were used to compare the pressure pulsation and flow pulsation at the front end of the hose with the pressure and flow pulsation in the check valve.

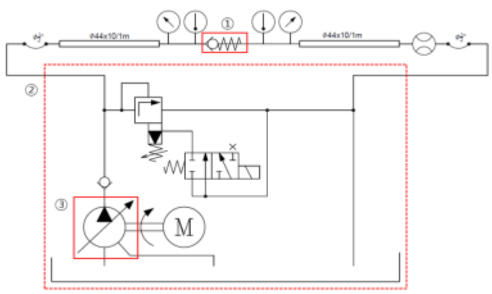

Figure 1. Hydraulic circuit for behavior prediction of check valve

Figures numbered 2 to 5, shows the pulsation change when the pressure of the overflow valve is set to 10 [bar],

20 [bar], 30 [bar], 40 [bar] and 50 [bar]. Fig. 2 and Fig. 4 show the difference between the minimum and maximum values of normal pressure pulsation and Fig. 3 and Fig. 5 show the difference between the minimum and maximum values of normal flow pulsation.
Fig. 2 shows a pressure difference of 0.32 [bar], 2.56 [bar], 5.91 [bar], 9.82 [bar] and 13.48 [bar] for consecutive set pressure values of 10bars to 50 bar. It can be predicted that the greater would be the set pressure, the greater the difference in pressure pulsation.

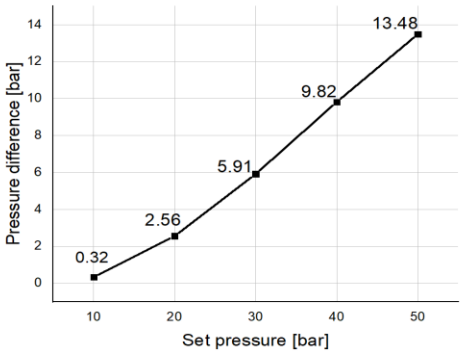

Figure 2. Pressure fluctuations amplitude versus set pressure at the hose inlet

Fig. 3 is a comparison of the magnitude of the flow pulsation difference for different pressure values. It can be seen that there are differences of 0.66 [lpm], 4.33 [lpm], 6.22 [lpm], 7.60 [lpm] and 8.96 [lpm] for consecutive set pressure values. Thus, the greater the pressure, the greater the pulsation of the flow rate. It can be seen that as set pressure is increased by 10 [bar], the average increase in flow rate difference turned out to be about 2[lpm].

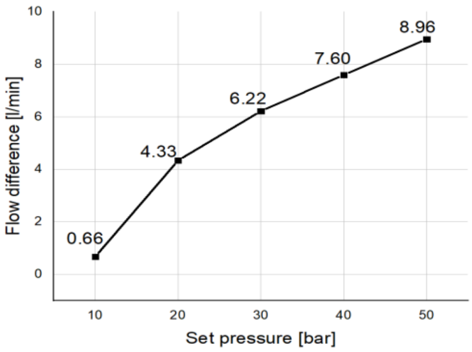

Figure 3. Flow pulsation amplitude on set pressure across the hose

Fig. 4 shows the pressure pulsation difference in the orifice. It can be seen that 0.52 [bar], 3.61 [bar], 6.66 [bar], 10.14 [bar] and 13.81 [bar] remain for consecutive set pressure values. Therefore, it can be said that the vibration from the valve appears as vibration in the pressure pulsation.

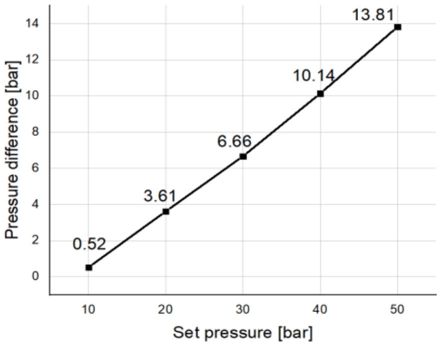

Figure 4. Pressure fluctuations amplitude versus set pressure at the check valve

Fig. 5 shows the difference in flow pulsation in the orifice, and summarizes the difference in flow pulsation by

2

pressure. Based on the difference in flow rate of 0.09 [lpm], 0.38 [lpm], 1.06 [lpm], 1.55 [lpm] and 1.71 [lpm] for consecutive set pressure values, which means the higher the pressure, the greater the flow pulsation. Also because of the hose the pulsation characteristics are better than Fig. 3.

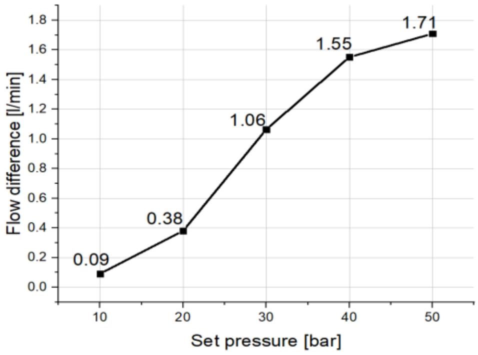

Figure 5. Flow pulsation amplitude on set pressure across the check valve

CONCLUTION

The purpose of this work was to investigate the effect of pressure-flow pulsation on the pump in hydraulic system to predict check valve behavior. The results are summarized as follows.

1. As a method proposed in this study, it is confirmed that the pressure-flow pulsation of the hydraulic pump can be copied and the pressure-flow pulsation increases with the circuit setting pressure.
2. It is considered necessary to use an appropriate hydraulic hose in order to clearly replicate the action of the pre-fill valve in the future because the pulsation generated by the pump varies depending on the pipeline conditions and whether or not the hydraulic hose is installed.

ACKNOWLEDGMENTS

This paper was supported by the Korea Institute of Industrial Technology (P0013851, 2021 Commercial Vehicle Industry Innovation Growth and Future Industrial Ecosystem Construction Project).

REFERENCES

1. J. E. FUNK, Poppet Valve Stability, Journal of basic Engineering ASME, pp.207-212, 1964.
2. A. AMINI, I OWEN, A Practical Solution to the Problem of Noise and Vibration in a Pressure-Reducing Valve, Experimental Thermal and Fluid Science, 0894-1777, pp. 136-141, 1995.
3. C. LI, F. LIEN, E. YEE, M. DONG, Multiphase Flow Simulations of Poppet Valve Noise and Vibration, SAE paper 2015-01-0666, 2015.

The 11th JFPS International Symposium on Fluid Power HAKODATE 2020 Oct. 12-13, 2021 The Japan Fluid Power System Society

Research on an Oil-hydraulic Component to Reduce Pressure Pulsation

Yasuo SAKURAI*, Misaki HASHIMOTO**, Moritaka MAEHARA***, Norikazu HYODO****

* Department of Innovative Engineering
Ashikaga University
268-1 Oomaecho, Ashikaga, Tochigi, 326-8558 Japan
(E-mail: ysakurai@ashitech.ac.jp)
** MITSUBA Corporation
1-2681 Hirosawa-cho, Kiryu-shi, Gunma 376-8555, Japan
*** SAWAFUJI ELECTRIC CO., LTD.
3, Nittahayakawa-cho, Ota City, Gunma 370-0344 Japan
**** TOKYO KEIKI INC.
Sakaecho, Sano-shi, Tochigi, 327-0816 Japan

Abstract. Pressure pulsation in oil-hydraulic system is generated due to the use of a positive displacement pump and it causes oscillation, noise and so on. An accumulator is generally employed to suppress the pressure pulsation. However, accumulator needs regular maintenance to prevent its performance deterioration due to gas leakage from it. Furthermore, there is a case where it is difficult to make the size of oil-hydraulic system compact due to the size of accumulator. Therefore, it seems to be necessary for innovation of an oil-hydraulic system to develop a new oil-hydraulic component to reduce pressure pulsation, and then its size is compact and regular maintenance to keep its performance is not necessary. In this study, an oil-hydraulic component to reduce pressure pulsation is proposed. The component is fabricated and some experiments are carried out to verify the mechanism to reduce pressure pulsation and to make clear its basic characteristics.

Keywords: Oil-hydraulics, Component, Pressure pulsation, Rubber

INTRODUCTION

In oil-hydraulic system with positive displacement pump, the pressure pulsation is generated [1], [2] and it causes vibration and noise [3]-[5]. For example, it is necessary to suppress pressure pulsation in order to finish surface of metal product precisely in a machine tool [6]. Hence, it is important to reduce the pressure pulsation so as to make the quality of an oil-hydraulic system higher.

To make the pressure pulsation smaller, an accumulator filled with pressurized gas is usually employed. However, it is necessary to carry out regular maintenance of the accumulator to prevent its performance deterioration caused by gas leakage [7]. On the other hand, it seems to be significant to reduce the size of accumulator when making the size of oil-hydraulic system more compact. To cope with these problems, it is desirable to develop a new oil-hydraulic component to reduce pressure pulsation with small size and without maintenance.

To realize this, some of the authors had proposed innovative components using the elasticity of rubber [8], [9]. However, in these components, it is difficult to improve durability, to adjust the gap width which is important parameter in the performance and to cope with the leakage from the component.

In this study, the component to reduce pressure pulsation is improved, which is able to overcome the above-mentioned problems. Some experiments are carried out to confirm the mechanism to suppress pressure pulsation and to investigate the basic characteristics of the improved component. In addition to it, through some experiments varying the gap width and the hardness of urethan rubber tube, the influence of these design parameters on the performance of the component are made clear.

MECHANISM TO REDUCE PRESSURE PULSATION

The mechanism of the component to reduce pressure pulsation is shown in Fig.1. The feature of this component is that the elastic tube is inserted and a part of the tube is exposed to the atmosphere through the gap. When the pressure is increased, a part of the tube expands and prevents the increase of the pressure by the increase of the inside volume of the tube. On the other hand, when the pressure is decreased, a part of it contracts and prevents the decrease of the pressure by the decrease of its inside volume. Namely, such movement are assumed to suppress the pressure pulsation.

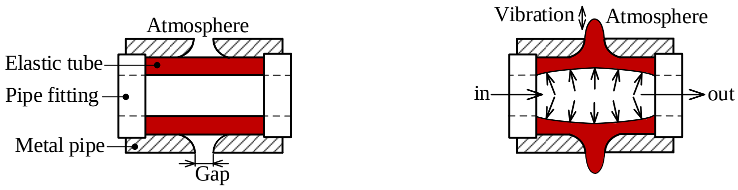

(a)Basic structure (b)Mechanism

Figure 1. Mechanism of the component to reduce pressure pulsation

STRUCTURE OF IMPROVED COMPONENT

The structure of the improved component is shown in Fig.2. In this study, a urethan rubber tube is employed as an elastic tube since urethan rubber has excellent resistance to chemicals and has stable characteristics over a wide range of temperatures. The inner diameter and thickness of the urethan rubber tube were 24mm and 10.5mm, respectively. This component mainly consists of two metal pipes, three pipe spacers, two flanges, a urethane rubber tube and two rubber packings. After attaching the flanges and metal pipes to the pipe fittings, the urethane rubber tube is inserted into the metal pipes. By attaching the pipe spacer between the flanges, the width between the flanges is determined, that is, the length of this component. Owing to adopting this structure, it becomes easy to determine the position of the metal pipes. By adjusting the position of the two metal pipes, the gap width between them can be determined between 0mm and 9 mm. The periphery of the metal pipe is chamfered with R8.0 to ensure the durability of the urethan rubber tube by forestalling stress concentration on the tube when a part of the tube expands. To stop leakage between the urethane rubber tube and the metal pipe, the rubber packings are newly installed. Its thickness was 2.0mm.

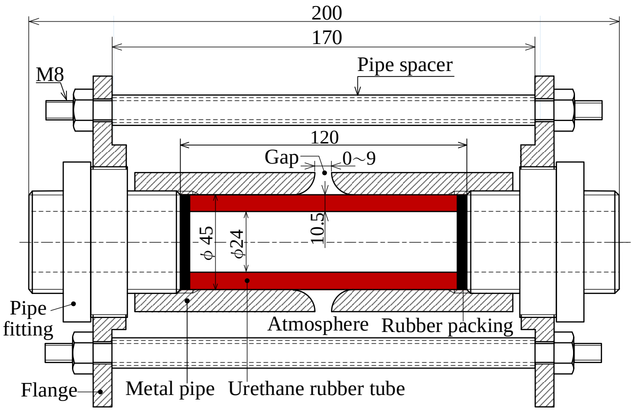

(a)Assembly drawing

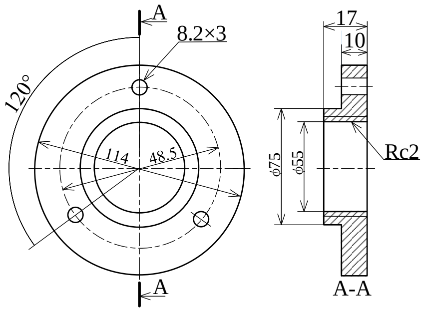

(b)Flange

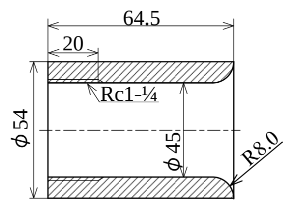

(c)Metal pipe

(d)Photo of component

(e)Photo of parts

Figure 2. Oil-hydraulic component to reduce pressure pulsation

PERFORMANCE OF COMPONENT TO REDUCE PRESSUR PULSATION

Confirmation of Mechanism to Reduce Pressure Pulsation

To confirm the mechanism to reduce pressure pulsation, the experiment was carried out when the pump discharge pressure was low, that is, 1.5MPa.

The experimental apparatus is illustrated in Fig.3. The experimental apparatus is composed of a piton pump, a relief valve, the component to reduce pressure pulsation, a metering valve and a bubble eliminator to reduce the influence of air in oil. The displacement of the pump was 4.0×10^{-5}m^3/rev and its angular velocity was 157rad/s (1500rpm). By adjusting the setting pressure of the relief valve and the opening area of the metering valve, the average pressure at the pump discharge port set about 1.5MPa and the flow rate through the component set about 2.5×10^{-4}m^3/s (15L/min). Then, oil temperature was set at about 25℃, and both upstream pressure P_1 and downstream pressures P_2 of the component were measured by semiconductor strain gauge pressure transducers. The output voltage from these transducers were recorded on a data logger for 10 seconds with sampling time of 0.1ms.

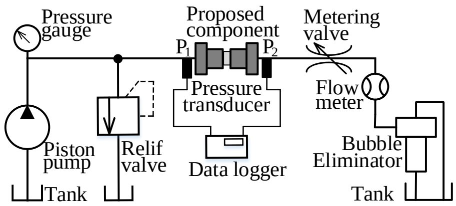

Figure 3. Experimental apparatus

Experimental results are shown in Fig.4. In this experiment, the gap between the two metal pipes was 2mm and the hardness of the urethane rubber tube was A50. As seen from this figure, the variation width of the pressure pulsation of the upstream side of the component is about ±0.146MPa, and that of the downstream side of it is about ±0.071MPa. Namely, the pressure pulsation of the downstream side of the component becomes about 48% of that of the upstream side of it. As a result, it is known that this component is effective to reduce pressure pulsation. The average pressure at the upstream side of the component and that at the downstream side of it are 1.45 MPa and 1.40 MPa, respectively, and the difference is 0.05 MPa. Therefore, in this experimental condition, the pressure drop of this component is sufficiently small.

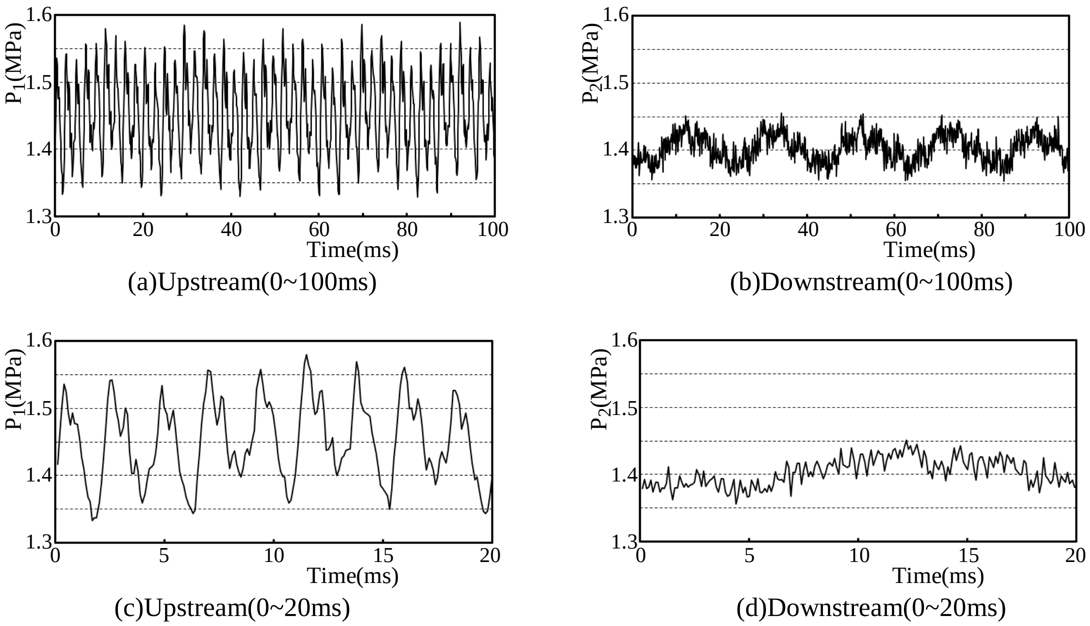

Figure 4. Experimental results

The results of frequency analysis for the experimental results in Fig.4 are shown in Fig.5. In this experiment, a piston pump was used and its rotational frequency was 25Hz and its piston number was 9. As can be seen from Fig.5 (a), there are peaks at almost the integral multiplication of frequency 225Hz, which is the product of its rotational frequency and its piston number. The relation between the frequency and the amplitude are shown in Table 1. From this table, it is known that the amplitude at 447Hz is 0.55MPa in the upstream side, which is the largest and the amplitude at 447Hz becomes about 94% smaller in the downstream side. In addition to it, it is known that the amplitude at other frequencies is also small in the downstream side.

Photos of the urethan rubber tube are shown in Fig.6. As seen from this figure, the urethan rubber tube is expanded when P_1=1.5MPa. Then, displacement X of this part of the urethan rubber tube was measured by using a laser sensor. The results are illustrated in Fig.7. In this figure, X=0.0mm means the position when the pressure in the tube is 0.0Pa. As can be seen from this figure, it is vibrating around 3.346mm. Hence, it is deduced that the inside volume of the tube is change due to this vibration and the variation width of the pressure pulsation of the downstream side of the component becomes small.

Consequently, it becomes clear that the proposed component and its mechanism are effective to reduce the pressure pulsation.

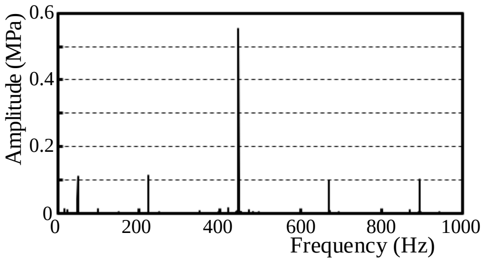

(a)Upstream side

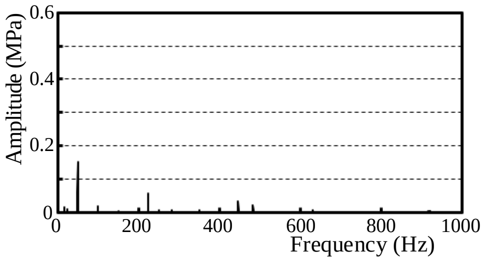

(b)Downstream side

Figure 5. Frequency analysis results

Table 1. Frequency and amplitude

Frequency (Hz)	Amplitude (upstream) (MPa)	Amplitude (downstream) (MPa)
223	0.11	0.06
447	0.55	0.035
670	0.10	6.3×10^{-4}
893	0.10	4.3×10^{-4}

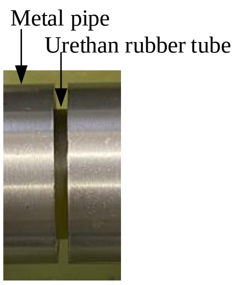

(a)P_1=0.0MPa

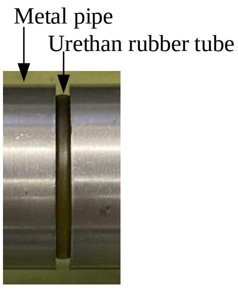

(b)P_1=1.5MPa

Figure 6. Photos of urethan rubber tube

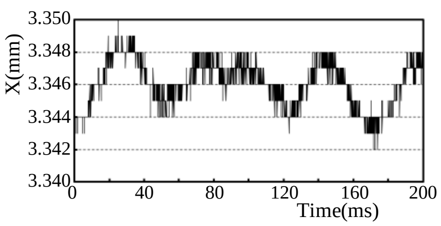

Figure 7. Displacement of the urethan rubber tube

Investigation of Performance of the Component to Reduce Pressure Pulsation at Practical Pressure

In a machine tool such as an NC lathe, an oil-hydraulic system is often used at 3.5MPa [10]. In this section, the experimental results are described when the average pressure at the pump discharge port is a practical value, that is 3.5MPa. On the other hand, it is necessary to investigate the relation between its design parameters and performance. Therefore, some experiments were carried out by varying the gap width between the metal pipes and the hardness of the urethan rubber tube.

Experiment was conducted by using the experimental apparatus shown in Fig.3. Then, the average pressure at the pump discharge port was set about 3.5MPa by adjusting the relief valve setting pressure and the flow rate through the component was set about $2.5\times10^{-4}m^3/s$ (15L/min) by adjusting the opening area of the metering valve.

The typical experimental results are illustrated in Fig.8, where the gap between the two metal pipes is 4.0mm and the hardness of the urethane rubber tube is A50. Then, as shown in Fig.9, the urethane rubber tube expands to the outside of the metal tube. As seen from Fig.8, the variation width of the pressure pulsation of the upstream side of the component is about ±0.19MPa, and that of the downstream side of ±0.11MPa. Namely, the pressure pulsation of the downstream side of the component becomes about 56% of that of the upstream side of it.

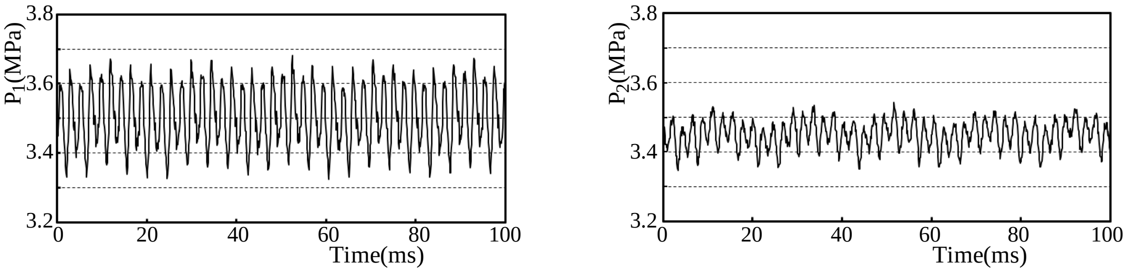

(a)Upstream (b)Downstream

Figure 8. Typical experimental results at 3.5MPa

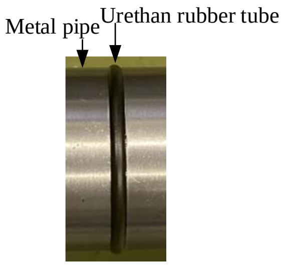

Figure 9. Photos of urethan rubber tube at 3.5MPa

Figure 10 shows the results of frequency analysis for the experimental results in Fig.8. From Fig.10 (a), it is known that there are peaks at almost the integral multiplication of frequency 225Hz. The relation between the frequency and the amplitude are shown in Table 2. This table describes that the amplitude at 444Hz is 0.91MPa in the upstream side, which is the largest and the amplitude in the downstream side at 444Hz is becomes about 41% smaller than the amplitude in the upstream side. Furthermore, it is known that the amplitudes in the downstream side at 665Hz and 887Hz are about 28% smaller than the amplitudes in upstream side. As a result, this component reduces the pressure pulsation by about 56% of the pressure pulsation of the upstream side of it.

Consequently, it is confirmed that this component works effectively to reduce pressure pulsation when the average pressure at the pump discharge port is 3.5 MPa which is a practical pressure in a machine tool.

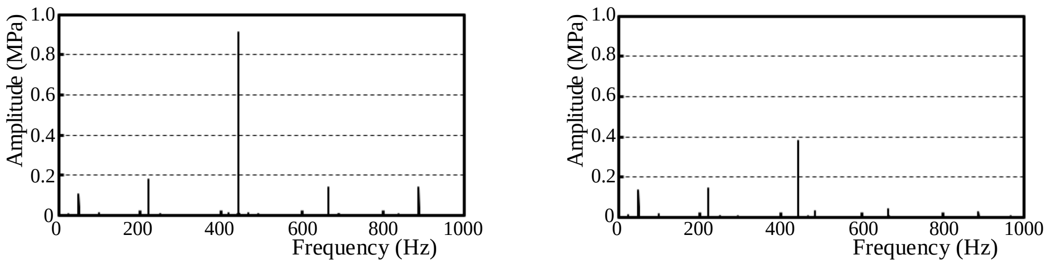

(a)Upstream side (b)Downstream side

Figure 10. Frequency analysis results

Table 2. Frequency and amplitude

Frequency (Hz)	Amplitude (upstream) (MPa)	Amplitude (downstream) (MPa)
222	0.18	0.14
444	0.91	0.38
665	0.14	0.04
887	0.14	0.03

In Figs 4 and 9, there is a larger peak at about twice the integral multiplication of frequency which is the product of its rotational frequency and its piston number. The reason is that the component to reduce pressure pulsation is installed. To verify this point, the experiment was conducted when the component was replaced with a straight pipe in the experimental apparatus shown in Fig.3. Then, the average pressure at the pump discharge port was set about 3.5MPa and the flow rate through the metering valve was set about 2.5×10^{-4}m^3/s (15L/min). The result of frequency analysis for pressure P_2 is shown in Fig.11. This figure shows that there is a large peak at the integral multiplication of frequency. Hence, it is known that the amplitude of twice the integral multiplication of frequency becomes larger than the amplitude of the frequency due to the installation of the component.

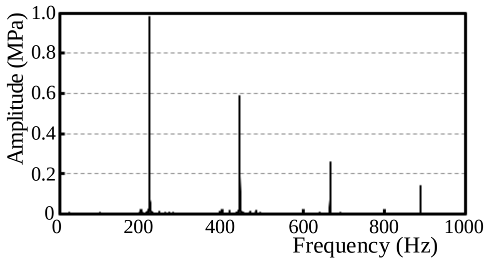

Figure 11. Frequency analysis results when the component is replaced with a straight pipe

Table 3 shows the experimental results when the gap width between the metal pipes and the hardness of the urethan rubber tube were varied. In this table, ΔP_1 is the variation width of the pressure pulsation of the upstream side of the component and ΔP_2 that of its downstream side. As can be seen from this table, the performance to reduce pressure pulsation is improved with an increase in the gap width between the metal pipes and a decrease in the hardness of the urethan rubber tube. In this study, the performance of the component becomes maximum in the combination of gap width 4.0mm and hardness A50. In this component, the gap width can be increased up to 9.0 mm as shown in Fig.2. And the thickness and the internal diameter of the urethan rubber tube are important design parameters. Therefore, in next step, it is necessary to investigate the influence of these parameters on the performance of the component to find suitable combination of the design parameters.

Table 3. Experimental results varying gap width and hardness

Gap width (mm)	Hardness	ΔP_1 (MPa)	ΔP_2 (MPa)	$\Delta P_2/\Delta P_1\times100$ (%)
2.0mm	A50	±0.185	±0.12	63
2.0mm	A70	±0.195	±0.14	71
4.0mm	A50	±0.190	±0.11	56
4.0mm	A70	±0.183	±0.11	58

CONCLUSIONS

In this study, the structure of the improved component to reduce pressure pulsation was described. And the effectiveness of the mechanism to reduce pressure pulsation and the performance of the component were made clear through some experiments. Consequently, it is confirmed that the component can reduce the pressure pulsation by 56% when gap width and hardness of the urethan rubber tube are suitable. Since there are other design parameters, next step is to investigate their influence on the performance of the component. Especially when the gap width is larger than 4mm, it seems to be expected that the performance of the component is improved. In addition to it, it is necessary to develop the mathematical model of the component to determine the suitable design parameters effectively.

ACKNOWLEDGMENTS

This work was supported by JSPS KAKENHI Grant Number 19K04152. The authors thank Mr. Ryuto Suzuki who was a student in Ashikaga University and Mr. Taichi Sakato who is a student in Ashikaga University for their cooperation with the experiments.

REFERENCES

1. ITO, Y., Thought-Evoking Approaches in Engineering Problems, Springer International Publishing, 2014, pp.167-168.

2. LI, B., GUO, S., CAI, B. SHI, Z., Study on Pressure Pulsation Suppression of Reciprocating Pump, Journal of Physics: Conf. Series, Vol.1187, Issue 3, 2019.
3. GHAZALI, M.H., HEE, L.M., LEONG, M.S., Piping Vibration due to Pressure Pulsations: Review, Advanced Materials Research, Vol.845, 2014, pp.350-354.
4. ICHIYANAGI, T., KURIBAYASHI, T., NISHIUMI, T., Design Criteria of a Helmholtz Silencer with Multiple Degrees of Freedom for Hydraulic Systems, Journal of Fluid Science and Technology, Vol. 8, No.3, 2013, pp. 277-293.
5. UMEDA, T., NISHIMURA, T., TSUTA, T., Fujiwara, M., Dynamic Response Analysis of a Tandem Type Hydraulic Piston Pump with Swash Plate, Transaction of the Japan society of Mechanical Engineers, Part C, Vol.64, No.617, 1989, pp.126-133. (in Japanese)
6. LOW, S. K, NAKANO, Y., KATO, H., Suppression of Chatter Marks due to Pulsation of Hydraulic Oil Pressure in Surface Grinding, Journal of the Japan Society for Precision Engineering, Vol. 55, No.3, 1989, pp.514-519, 1989. (in Japanese)
7. LINIGER, J., SEPEHRI, N., SOLTANI, M., PEDERSEN, H. C., Signal-Based Gas Leakage Detection for Fluid Power Accumulators in Wind Turbines, Energies, Vol.33, No.10, 2017, en10030372.
8. SAKURAI, Y., ETINOT, B., HYODO, N., AIBA, K., Proposal of a Component to Reduce Pressure Pulsation in Oil-hydraulic System, Proc. of the 11th JFPS International Symposium, 2017.
9. HASHIMOTO, M., SAKURAI, Y., HYODO, N., AIBA, K., Proposal of Innovative Oil-hydraulic Component to Reduce Pressure Pulsation, Proc of The 8th International Conference on Manufacturing, Machine Design and Tribology, 2019.
10. Practical hydraulic pocket book, Japan Fluid Power Association, 2021, pp.364. (in Japanese)

Genaral Session | Oil hydraulics

Construction, Components and Systems

[GS6-01] Operating Information Presentation for Hydraulic Construction Robot

○Hironao Yamada[1], Takahiro Ikeda[1], Satoshi Ueki[1], Kazuma Shinkai[2], Katsutoshi Ootsubo[3]
（1.Gifu University, 2.Sumitomo Heavy Industries, Ltd., 3.Kinjo Gakuin University）

[GS6-02] Frequency Response Analysis of Parallel Link Mechanism using Oil-hydraulic Cylinders of Tunnel Boring Machines

Ryo Yamamoto[1], ○Kazushi Sanada[1], Shigeaki Ashikaga[2] （1.Yokohama National University, 2.Komatsu Ltd.）

[GS6-03] A Power-Split Hybrid Transmission to Drive Conventional Hydraulic Valve Controlled Architectures in Off-road Vehicles: The Case of a Mini-Excavator

○Mateus Bertolin[1], Andrea Vacca[1] （1.Purdue University）

[GS6-04] Control of Air Bubble Content in Working Oil by Swirling Flow

Sayako Sakama[2], ○Yutaka Tanaka[1], Yasuhiro Kodera[3], Yoshiaki Kitamura[3] （1.Hosei University, 2.National Institute of Advanced Industrial Science and Technology, 3.KYB Corporation）

[GS6-05] Pulse Tests on Additive Manufactured Valve Blocks – Damage Analysis and New Design Possibilities

○Sebastian Deuster[1], Stefan Aengenheister[1], Gunnar Matthiesen[1], Katharina Schmitz[1] （1.RWTH Aachen University, Institute for Fluid Power Drives and Systems (ifas)）

[GS6-06] The Potential in Fluid Power Systems for a Sustainable Future

○Katharina Schmitz[1] （1.RWTH Aachen University, Institute for Fluidpower Drives and Systems (ifas)）

[GS6-07] New Intelligent Hydraulic Power Control System

○Takahiro Urai[1], Ken Shindo[1] （1.Bosch Rexroth corporation）

The 11th JFPS International Symposium on Fluid Power HAKODATE 2020 Oct. 12-13, 2021 The Japan Fluid Power System Society

Operating Information Presentation for Hydraulic Construction Robot

Hironao YAMADA*, Takahiro IKEDA*, Satoshi Ueki*,
Kazuma SHINKAI**, Katsutoshi OOTSUBO ***

*Department of Mechanical Engineering, Faculty of Engineering, Gifu University
1-1 Yanagido, Gifu City, Gifu 501-1193, Japan
(E-mail: yamada@gifu-u.ac.jp)
** Sumitomo Heavy Industries, Ltd.
ThinkPark Tower, 1-1 Osaki 2-chome, Shinagawa-ku, Tokyo 141-6025 Japan
*** Department of Human Life and Environment, Kinjo Gakuin University
2-1723 Omori, Moriyama-ku, Nagoya, Aichi 463-8521 Japan

Abstract. Teleoperation system for construction robot is effective to work in hazardous environment. However, it is a problem to be solved that the work efficiency is inferior to the operation performed directly using a construction machine. The purpose of this study is to improve the operation feeling for teleoperation. In this research, we have developed a "Risk level warning system for avoiding approaching hazardous object" that warns the operator with force and sound when the fork claw approaches a hazardous object. Furthermore, we conducted subject experiments based on multiple force sense presentation methods, and clarified the optimal presentation method from the viewpoint of risk avoidance performance and worker burden.

Keywords: Construction Robot, Remote Control, Operating information, NASA-TLX

INTRODUCTION

Teleoperation system for construction robot is effective to work in hazardous environment [1][2]. However, it is a problem to be solved that the work efficiency is inferior to the operation performed directly using a construction machine. In our research, we have been developing an intuitive teleoperation system for a construction robot in order to perform highly efficient and accurate work. This system is powered by hydraulic actuators and provides force feedback using a hydraulic pressure sensor attached to a cylinder. Recently, we developed an AR presentation system that supports 3D recognition of the work field for an operator, and confirmed its effectiveness for improving the work efficiency and accuracy [3], [4].
The purpose of this study is to improve the operation feeling for teleoperation. In particular, remote control work is assumed in an environment where hazardous or fragile objects exist around the construction robot at a disaster site. We will develop a "Risk level warning system for avoiding approaching hazardous object" that warns the operator by presenting force and sound when the fork claw approaches a hazardous object. Furthermore, through subject experiments, we will examine the optimal presentation method from the viewpoint of risk avoidance performance and worker burden.

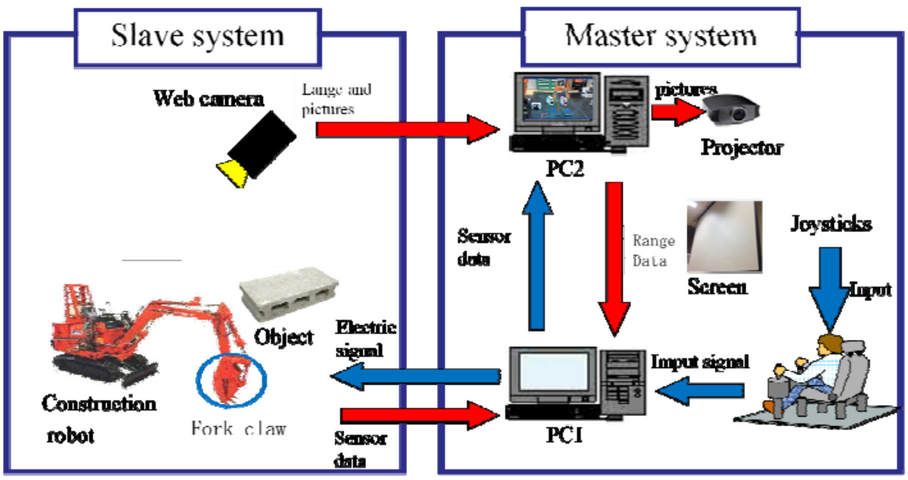

Figure 1. Teleoperation system

TELEOPERATED CONSTRUCTION ROBOT SYSTEM

The teleoperated construction robot system used in this research is shown in Figure 1. This system consists of joysticks (JS), a construction machine, a video camera, a construction machine control computer (PC1), and an image presentation computer (PC2). The master-slave control system is constructed by changing the hydraulic cylinder speed of the construction machine according to the input joystick displacement. The image of the remote place acquired by the video camera is presented to the PC2, and the operator watches the image and performs the work.

The operator operates the joystick based on master-slave control. The displacement of the joystick is detected as a voltage signal by the potentiometer and input to PC1 via the A/D converter. Then, the calculated control input is input to the servo amplifier as a voltage signal via the D/A converter. The servo amplifier converts the given voltage signal into a current signal and drives the hydraulic servo solenoid valve. As a result, the piston operates, and its displacement is detected by the potentiometer and input to PC1 via the A/D converter. The configuration diagram of this system is shown in Figure 2. However, the parts not related to this study are omitted.

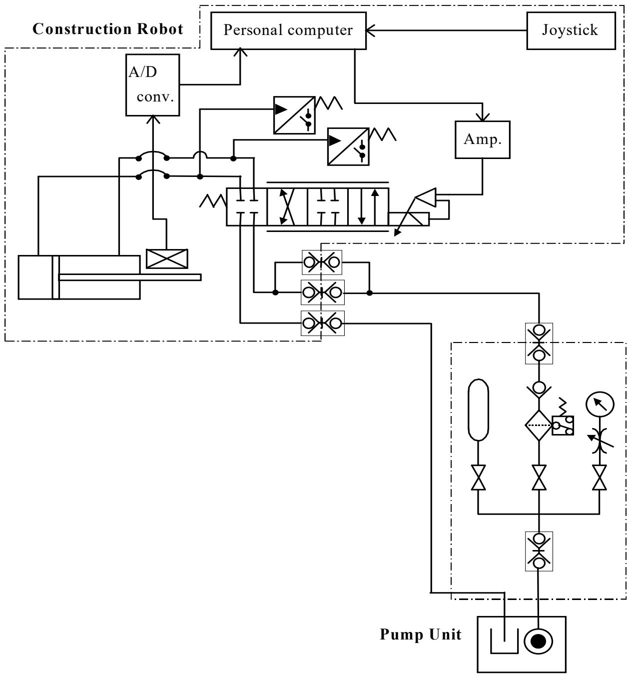

Figure 2. Schematic diagram of the hydraulic system

OPERATING INFORMATION PRESENTATION SYSTEM

In this system, the risk level is judged from the positional relationship between the fork claw's hand coordinates P_o, the contact judgment points P_a to P_d (the bottom point when the fork claw is a rectangular parallelepiped), and the hazardous object. Then, the force sense and sound are presented according to the positional relationship (Figure 3, Figure 4). Here, these coordinates are based on the Cartesian coordinate system with the swing joint of the construction machine as the origin. In addition, it is assumed that the hazardous object is defined as a rectangular parallelepiped shape composed of planes parallel to the coordinate system plane, and the coordinates are known.

In addition, the space around the hazardous object that is expanded by 100 mm in each coordinate axis direction is defined as the hazardous space, and the space is divided into 5 spaces in 20 mm increments as shown in Figure 4. In this system, the risk level is defined in the reverse order of proximity to the hazardous object for the hazardous space and its external space. Then, the operator is presented with a sense of force according to the risk level and the distance to the hazardous object.

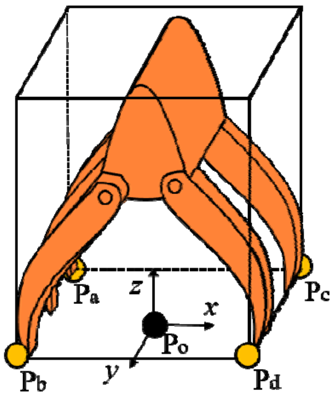

Figure 3. Fork claw

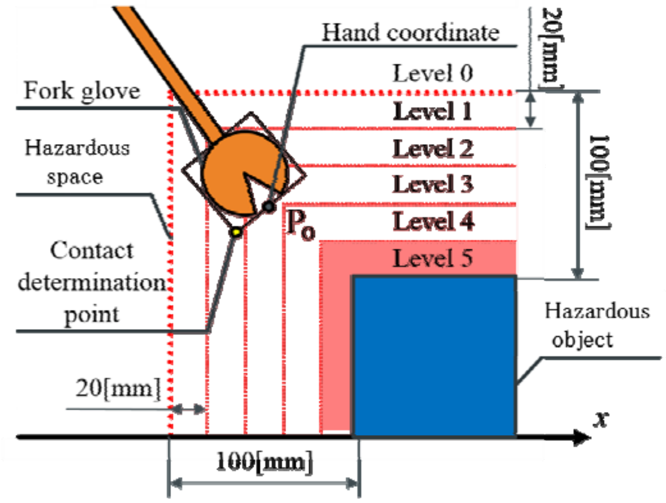

Figure 4. Hazardous space (top view)

The risk level is L (an integer from 0 to 5), the distance to contact is D [mm], and the haptic value is F. The force sense value calculated by any of the equations (A) to (D) is presented in the direction opposite to the input for all axes of the joystick operation. When the risk level L is 0, the distance D to contact is fixed at 100 mm.

$$F = 0.1 \times L \tag{A}$$

$$F = 0.03 \times L^2 \tag{B}$$

$$F = 0.005 \times (100 - D) \tag{C}$$

$$F = 0.000075 \times (100 - D)^2 \tag{D}$$

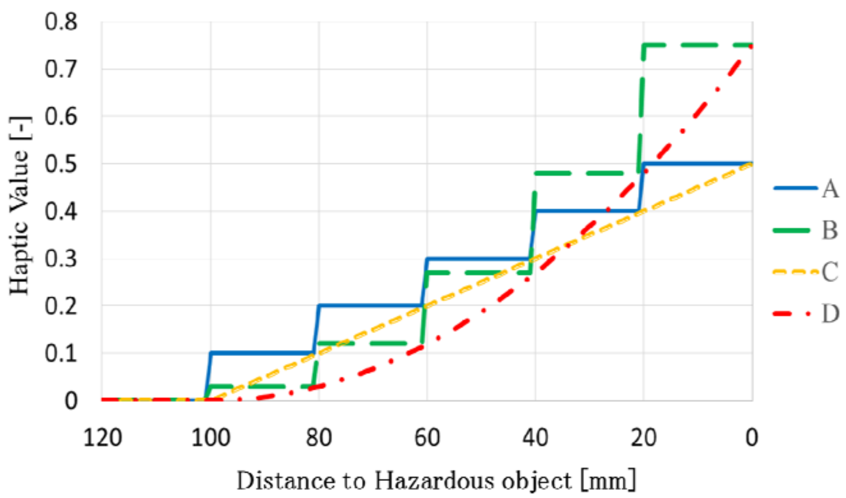

Figure 5. Haptic presentation pattern

Presentation patterns A and B using the force sensory equations (A) and (B) are presented step by step according to the risk level consisting of 6 levels. On the other hand, the presentation patterns C and D using equations (C) and (D) perform stepless presentation. In addition, patterns B and D, which are the squares of each variable, change based on the exponential function. On the other hand, patterns A and D change based on linear functions.

The haptic values calculated by the following patterns (A) to (D) as shown in Figure 5 are presented to the control lever. In addition, a warning sound is presented at the presentation cycle T [s] calculated by equation (E). When presenting a warning sound, a wav file with a length of about 0.2s is read.

$$T = (6 - L) / 5 \qquad \text{(E)}$$

EXPERIMENT

As an evaluation experiment of this system, a subject experiment was conducted for the gripping work of an object. The work environment is shown in Figure 6. In the work environment, three cardboard boxes assuming hazardous objects, a wooden block that is the gripping object to be transported, and one wooden stand that is the transporting point of the gripping object are installed. Figure 7 shows a layout diagram of the work field. Six subjects were asked to carry the wooden block 2 to the transport point 3 so as not to touch the hazardous object 1. The subject works while watching a video showing the work environment. The experiment is performed by five presentation methods including E: sound presentation in addition to four types of force sense presentation based on the calculation methods A to D. The subjects performed the prescribed operations twice for each pattern, and measured the work time T_f [s], risk index R, and mental burden index. In addition, the evaluation was performed by a questionnaire after the experiment. Here, when the risk level at each time is L_t, the risk index R is expressed by Eq. (1), which is the sum of the risk levels divided by the working time.

$$R = \sum_{t=0}^{T_f} L_t / T_f \qquad (1)$$

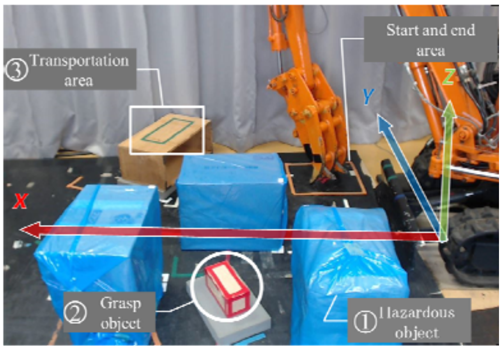

Figure 6. Work field

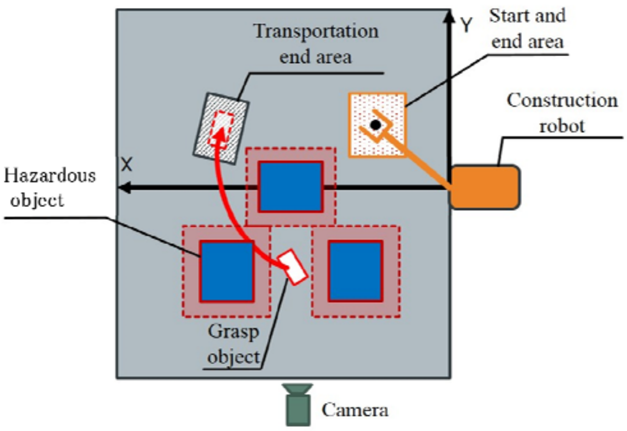

Figure 7. Work field (Top view)

In the experiment, sufficient practice is performed in advance to reduce the influence of proficiency on the experimental results. The subjects were 5 males and 1 female aged 21 to 25 years, with an average age of approximately 22.8 years. Four of them have experience in operating construction machinery, and the remaining two have no experience in operating construction machinery. In addition, considering the order effect, the experiments were conducted in a different order for all the subjects.

EXPERIMENTAL RESULTS AND DISCUSSION

Figure 8 shows the results of the subject average of the risk index based on the results of the experiment. From the figure, it can be seen that the risk index of B is the lowest. In addition, when multiple comparisons were performed by the Turkey test (single-step multiple comparison procedure and statistical test), a significant difference (*) with a significance level of 5 [%] was observed between patterns A-B, B-C, and B-E. Therefore, the presentation method using pattern B is considered to be optimal from the viewpoint of risk avoidance. Although no significant difference was confirmed, the risk index was also lower in pattern D than in patterns A, C, and E. This suggests that the method of increasing the force sense value exponentially is suitable for presentation.

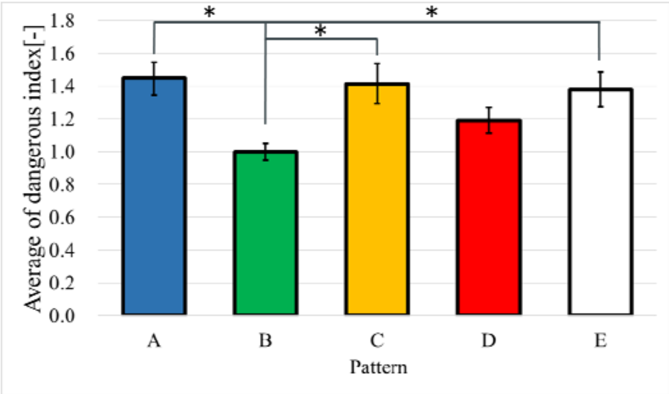

Figure 8. Average of risk index

In general, the magnitude of human sensation increases in proportion to the logarithm of the intensity of the stimulus [1]. Therefore, even when a large force sense value is presented, it is easy to intuitively grasp the change in force sense due to approaching a hazardous object. It is considered that this prevented further approach and contact. In addition, although no significant difference was confirmed, the risk index of pattern B, which changes stepwise, was lower than that of pattern D, which changes the force sense value steplessly. Discrete changes cause the force sense value to rise suddenly at the moment the risk level rises. Therefore, the operator could intuitively grasp that the fork claw was approaching a hazardous object. Therefore, it is considered that the risk index was suppressed. In this study, we used "NASA-TLX" [5] for the assessment of the mental task load. The index is given subjectively, and the task load is divided into six indices: Mental Demand (MD), Physical Demand (PD), Temporal Demand (TD), Performance (OP), Effort (EF) and Frustration (FR). The larger values correspond to larger mental task loads.

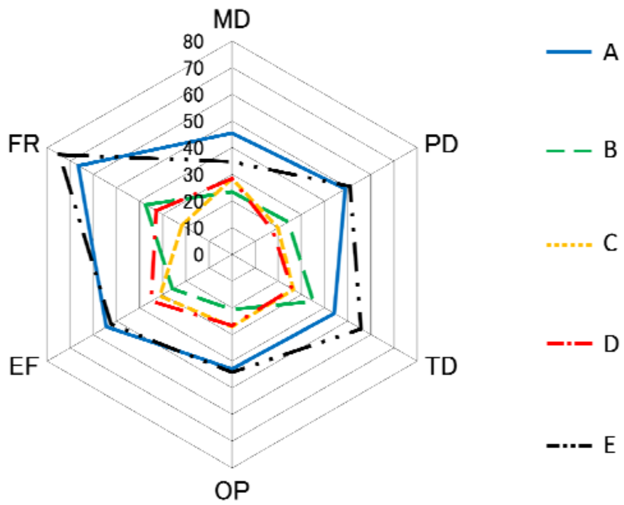

Figure 9. Average of NASA-TLX

Figure 9 shows the result of averaging the six evaluation indexes of NASA-TLX. From the results of Figure 9, it can be seen that the overall mental burden increases in the cases of patterns A and E. In the presentation method using pattern A, the force sense value changes rapidly when the risk level rises. For this reason, it is likely that the work will be burdensome at low risk levels. Similarly, in the case of pattern E, it is considered that it was a burden on the operator that the warning sound was constantly emitted when trying to grasp the grasped object surrounded by hazardous objects. On the other hand, the results showed that the overall mental burden was lower in patterns B, C, and D. Comparing the patterns C and D in which the force sense value was increased steplessly from the results, no significant difference could be confirmed in MD, PD, OP, and EF. However, in FR, pattern D had a slightly higher mental burden than pattern C. This is thought to be because pattern D has a higher maximum force sense value. It can be said that the larger the force sense value, the more stress the worker feels. In addition, pattern B, in which the force sense value is gradually increased, has a higher degree of mental burden in PD and FR than in patterns C and D. However, the mental burden was lower in MD, OP, and EF. When the risk level rises, the sudden rise in the force sense value becomes a physical burden and stresses the worker. However, since the operation information is easy to understand, it is easy to be satisfied with the work results and the mental burden is considered to be low.

CONCLUSION

In this research, we have developed a "Risk level warning system" that warns the operator with force and sound when the fork claw approaches a hazardous object. Furthermore, we conducted subject experiments based on multiple force sense presentation methods, and clarified the optimal presentation method from the viewpoint of risk avoidance performance and worker burden. In the experiment, the blocks were transported by 6 subjects twice for each pattern, for a total of 10 times. As a result, among the proposed methods, the stepwise presentation pattern based on the exponential function is considered to be the most effective presentation method comprehensively.

REFERENCES

1. J. Xue, L. Zhang, T. E. Grift, “Variable field-of-view machine vision based row guidance of an agricultural robot”, in Journal of Computers and Electronics in Agriculture, 84, 2012, pp. 85–91.
2. C. L. Perkinson, M. E. Bayraktar, I. Ahmad, “The use of computing technology in highway construction as a total jobsite management tool”, in Journal of Automation in Construction, 19(7), 2010, pp. 884–897.
3. Support System for Slope Shaping Based on a Teleoperated Construction Robot, Katsutoshi Ootsubo, Daichi Kato, Takuya Kawamura and Hironao Yamada, Journal of Robotics and Mechatronics, Vol. 28, No. 2, pp.149-157, 2016.
4. Teleoperated Construction Robot Using Visual Support with Drones, Hironao Yamada, Naoyuki Bando, Katsutoshi Ootsubo, and Yuji Hattori, Journal of Robotics and Mechatronics, Vol. 30, No. 3, pp.406-415, 2018.
5. S. Hart, L. Staveland, “Development of NASA-TLX (Task Load Index): Results of empirical and theoretical research”, in Advances in Psychology, Human mental workload, 52, North Holland, 1988, pp. 139–183.

The 11th JFPS International Symposium on Fluid Power HAKODATE 2020 Oct. 12-13, 2021 JFPS The Japan Fluid Power System Society

Frequency Response Analysis of Parallel Link Mechanism using Oil-hydraulic Cylinders of Tunnel Boring Machines

Ryo YAMAMOTO*, Kazushi SANADA**, and Shigeaki ASHIKAGA***

* Department of Mechanical Engineering, Materials Science, and Ocean Engineering,
Graduate School of Engineering Science, Yokohama National University
** Faculty of Engineering, Yokohama National University
79-5, Tokiwadai, Hodogaya Yokohama city, Kanagawa, 240-8501 Japan
(E-mail: sanada-kazushi-sn@ynu.ac.jp)
*** Komatsu Ltd.

Abstract. Frequency responses of a parallel link mechanism using six oil-hydraulic cylinders of tunnel boring machine are analyzed in this study. Each oil-hydraulic cylinder is driven with a constant-displacement oil-hydraulic pump whose rotational frequency is controlled by an AC servo motor. The six cylinders generate force for digging the ground. A mathematical model of the parallel link mechanism of six oil-hydraulic cylinders is used in this study. Statics of the parallel link is described with Jacobian matrix. A dynamic model of the oil-hydraulic cylinder and oil-hydraulic pumps is built based on the equation of motion of cutter head, compressibility of oil, and pump characteristics. A model of the tunnel boring machine is obtained by combining the models of parallel link and oil-hydraulic circuit. Frequency responses of the model are useful to investigate control methods of the tunnel boring machine.

Keywords: Cylinder, Parallel link, Frequency response, Mathematical model, Oil-hydraulics

INTRODUCTION

Tunnel boring machines are heavy-duty machines which are used for boring tunnels. An important recent trend in research and development is automatic control of tunnel boring machine. The tunnel boring machine is required to follow planed path of tunnel. Accuracy of tunnel boring is influenced by various factors, for examples, non-uniform hardness of bedrock and machine performance. The tunnel machine treated in this study consists of a parallel link mechanism of 6 oil-hydraulic cylinders driven by pump control. Statics of parallel link was studied by ARAI [1]. Link lengths, forces, and torques are related each other by Jacobian matrix. TSUCHIYA, et al. investigated a parallel link mechanism with 6 oil-hydraulic cylinders controlled by servo valves [2][3]. Combining statics of the parallel link mechanism and dynamics of the servo-valve controlled cylinder drive system, results of frequency responses were compared with experimental results. A simple inertia load was considered in the studies. When the tunnel boring machine is investigated, various forces and torques due to non-uniform hardness of bedrock are necessary to be considered. Path control of cutter head is a main task for automatic control system. In addition, instead of servo-valve controlled cylinder drive system, one-pump one-cylinder drive system is applied. A fixed-displacement oil-hydraulic pump, whose rotational frequency is determined by an AC servomotor, directly drives one cylinder. Final goal of this project is to develop automatic control system for the tunnel boring machine to follow pre-specified path. In this study, as the first step, modeling and frequency response analysis are investigated.

NOMENCLATURES

A_2	area of piston bottom
B	viscous damping coefficient
${}^0\boldsymbol{B}_m = [\ {}^0B_{mx},\ {}^0B_{my},\ {}^0B_{mz}\ ]^T$	position vector of *m*-th joint of base platform with respect to the origin of base platform
$\boldsymbol{C} = [x, y, z, \alpha, \beta, \gamma]^T$	position and attitude angle vector of cutter head
D	pump displacement
${}^e\boldsymbol{E}_m$	position vector of *m*-th joint of end effector with respect to the origin of end effector
${}^0\boldsymbol{E}_m = [\ {}^0E_{mx},\ {}^0E_{my},\ {}^0E_{mz}\ ]^T$	position vector of *m*-th joint of end effector with respect to the origin of the base platform
$\boldsymbol{F} = [F_x, F_y, F_z, T_x, T_y, T_z]^T$	force and torque vector of cutter head
F_x, F_y, F_z	forces acting on the center of gravity of cutter head
$\boldsymbol{f} = [f_1, f_2, \cdots, f_6]^T$	cylinder force vector

h	function relating $\boldsymbol{C}$ and $\boldsymbol{l}$
J_x, J_y, J_z	moment of inertia of cutter head
$\boldsymbol{J}_1$	Jacobian matrix
$\boldsymbol{J}_2$	coefficient matrix
K	bulk modulus of oil
l_m	length of m-th link
$\boldsymbol{l} = [l_1, l_2, \cdots, l_6]^T$	vector of link length
M	mass of cutter head
$\boldsymbol{M} = diag[M, M, M, J_x, J_y, J_z]$	matrix of mass and moment of inertia of cutter head
$\boldsymbol{p}_h$	position vector of the origin of end effector with respect to the origin of base platform
$\boldsymbol{p}_2 = [p_{21}, p_{22}, \cdots, p_{2m}]^T$	bottom pressure vector
$\boldsymbol{q}_2 = [q_{21}, q_{22}, \cdots, q_{2m}]^T$	pump flow rate vector
$\boldsymbol{R}_c$	demand signal of position and attitude angle vector $\boldsymbol{C}$
$\boldsymbol{R}_l$	demand signal of link length vector $\boldsymbol{l}$
${}^0_e\boldsymbol{R}_{X'Y'Z'}(\alpha, \beta, \gamma)$	rotation matrix
s	Laplace variable
T_x, T_y, T_z	Torques acting on the center of gravity of cutter head
t	time
V_2	oil volume of bottom side of cylinder and pipe/hose
x, y, z	coordinate system of base platform (gripper)
x_e, y_e, z_e	coordinate system of end effector (cutter head)
α, β, γ	attitude angle of cutter head
η_v	volumetric efficiency
*	operating point
$\hat{}$	small variation

TUNNEL BORING MACHINE

A tunnel boring machine which is investigated in this study is shown in Figure 1. It consists of a cutter head, 6 cylinders, and a gripper. The cutter head is rotated by an oil-hydraulic motor. Disk cutters of the rotating cutter head break bedrock, and tunnel boring is performed. The cutter head is pushed by a parallel link consisting of 6 cylinders. The gripper maintains machine position inside a tunnel. Roof support, side support, and vertical support are used to cover the tunnel wall and support a body of the tunnel boring machine. One-pump one-cylinder drive system is applied to drive the 6 cylinders. Control of the parallel link determines direction of tunnel which is dug by the tunnel boring machine. The aim of this study is research and development of automatic control system for the tunnel boring machine. Because the tunnel boring machine consists of the parallel link of 6 cylinders and the oil-hydraulic circuit of one-pump one-cylinder drive system, a mathematical model is built by combining each sub-system in the next chapter.

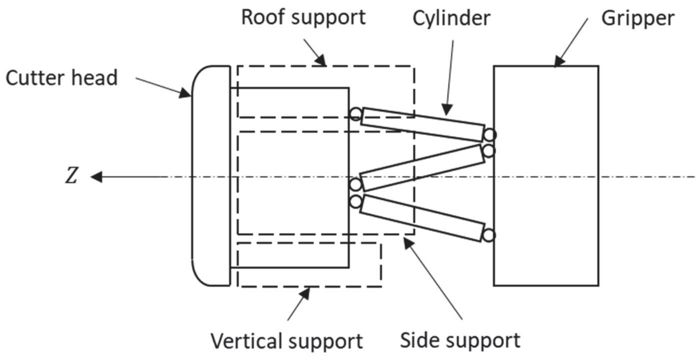

Figure 1. Tunnel boring machine: Six cylinders push a rotating cutter head to break bedrock in the Z-direction.

MATHEMATICAL MODEL

Parallel Link Mechanism

The parallel link mechanism consists of end effector (cutter head), base platform (gripper), and 6 links (cylinder No.1, 2, …, 6) as shown in Figure 2. Coordinate system xyz and $x_e y_e z_e$ are fixed on base platform and end effector, respectively. Position of the origin of the end effector $x_e y_e z_e$ with respect to the origin of the base platform xyz is presented by a position vector $\boldsymbol{p}_h = [x, y, z]^T$. Six broken lines represent six cylinders. ${}^0\boldsymbol{B}_m$ and ${}^e\boldsymbol{E}_m$ are position vectors of cylinder joints of the base platform and the end effector, respectively.

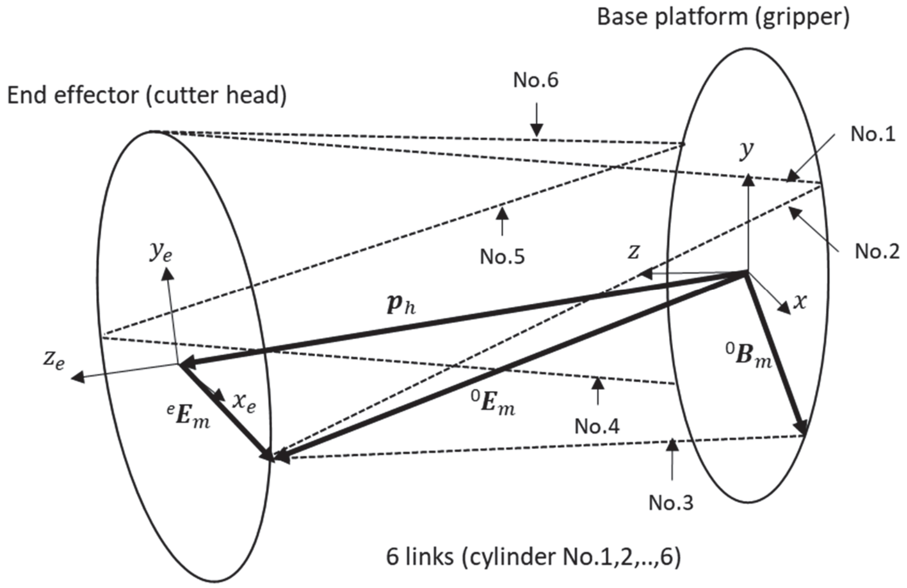

Figure 2. Parallel link consisting of end effector, base platform, and 6 links

Equation of Motion of Cutter Head

Cutter head motion is a combination of transrational and rotational motions. The equation of motion of the cutter head is written as:

$$\begin{cases} F_x = M\ddot{x}, & F_y = M\ddot{y}, & F_z = M\ddot{z} \\ T_x = J_x\ddot{\alpha}, & T_y = J_y\ddot{\beta}, & T_z = J_z\ddot{\gamma} \end{cases}, \tag{1}$$

where position of the center of gravity of the cutter head x, y, z, and attitude angle of the cutter head α, β, γ. A vector $\boldsymbol{C}$ is used to represent the variables:

$$\boldsymbol{C} = [x, y, z, \alpha, \beta, \gamma]^T . \tag{2}$$

Forces and moments are written by a vector $\boldsymbol{F}$:

$$\boldsymbol{F} = \left[F_x, F_y, F_z, T_x, T_y, T_z\right]^T . \tag{3}$$

The equation of motion can be rewritten in a vector form:

$$\boldsymbol{F} = \boldsymbol{M}\ddot{\boldsymbol{C}} . \tag{4}$$

Statics of Parallel Link Mechanism

Statics of parallel link [2][3] was applied to build a mathematical model of the tunnel boring machine. The position vector of the *m*-th joint of the end effector with respect to the origin of the base platform, ${}^0\boldsymbol{E}_m$, is written as:

$$ {}^{0}\boldsymbol{E}_{\boldsymbol{m}} = [x \;\; y \;\; z]^T + {}^{0}_{e}\boldsymbol{R}_{X'Y'Z'}(\alpha,\beta,\gamma)\,{}^{\boldsymbol{e}}\boldsymbol{E}_{\boldsymbol{m}} \,, \tag{5} $$

where a rotation matrix of Euler angle of the end effector, ${}^{0}_{e}\boldsymbol{R}_{X'Y'Z'}(\alpha,\beta,\gamma)$, is written as:

$$ {}^{0}_{e}\boldsymbol{R}_{X'Y'Z'}(\alpha,\beta,\gamma) = \begin{bmatrix} \cos\beta\cos\gamma & -\cos\beta\sin\gamma & \sin\beta \\ \sin\alpha\sin\beta\cos\gamma + \cos\alpha\sin\gamma & -\sin\alpha\sin\beta\sin\gamma + \cos\alpha\cos\gamma & -\sin\alpha\cos\beta \\ -\cos\alpha\sin\beta\cos\gamma + \sin\alpha\sin\gamma & \cos\alpha\sin\beta\sin\gamma + \sin\alpha\cos\gamma & \cos\alpha\cos\beta \end{bmatrix}. \tag{6} $$

Joint distance of m-th link, l_m, is calculated by:

$$ l_m = \sqrt{({}^{0}E_{mx} - {}^{0}B_{mx})^2 + ({}^{0}E_{my} - {}^{0}B_{my})^2 + ({}^{0}E_{mz} - {}^{0}B_{mz})^2} \,. \tag{7} $$

Link length vector $\boldsymbol{l}$ is a function of a vector $\boldsymbol{C}$:

$$ \boldsymbol{l} = h(\boldsymbol{C}) \,. \tag{8} $$

Assuming an operating point (denoted by *), small variation (denoted by $\widehat{\ }$) about the operating point is considered, then:

$$ \boldsymbol{l}^* + \hat{\boldsymbol{l}} \cong h(\boldsymbol{C}^*) + \left.\frac{\partial h(\boldsymbol{C})}{\partial \boldsymbol{C}}\right|_{\boldsymbol{C}=\boldsymbol{C}^*} \widehat{\boldsymbol{C}} \,. \tag{9} $$

The partial-differentiation coefficient is defined as Jacobian matrix $\boldsymbol{J}_1$ which is a 6×6 matrix:

$$ \boldsymbol{J}_1 = \left.\frac{\partial h(\boldsymbol{C})}{\partial \boldsymbol{C}}\right|_{\boldsymbol{C}=\boldsymbol{C}^*} . \tag{10} $$

Small variation of link length is calculated from small variation of the position and attitude angle vector multiplied by the Jacobian matrix:

$$ \hat{\boldsymbol{l}} = \boldsymbol{J}_1(\boldsymbol{C}^*)\widehat{\boldsymbol{C}} \,. \tag{11} $$

Small variation of demand signal of link length is calculated from small variation of the position and attitude angle vector multiplied by the Jacobian matrix:

$$ \widehat{\boldsymbol{R}}_{\boldsymbol{l}} = \boldsymbol{J}_1(\boldsymbol{C}^*)\widehat{\boldsymbol{R}}_{\boldsymbol{c}} \,. \tag{12} $$

According to the virtual work principle, a force and torque vector of the end effector (cutter head) $\boldsymbol{F}$ is related with a cylinder force vector $\boldsymbol{f}$ using a transposed matrix of Jacobian matrix, $\boldsymbol{J}_1^T(\boldsymbol{C})$, then:

$$ \boldsymbol{F} = \boldsymbol{J}_1^T(\boldsymbol{C})\boldsymbol{f} \,. \tag{13} $$

Linearizing the above equation:

$$ \boldsymbol{F}^* + \widehat{\boldsymbol{F}} \cong \boldsymbol{J}_1^T(\boldsymbol{C}^*)\boldsymbol{f}^* + \left.\frac{\partial\{\boldsymbol{J}_1^T(\boldsymbol{C})\boldsymbol{f}\}}{\partial \boldsymbol{f}}\right|_{\substack{\boldsymbol{f}=\boldsymbol{f}^* \\ \boldsymbol{C}=\boldsymbol{C}^*}} \hat{\boldsymbol{f}} + \left.\frac{\partial\{\boldsymbol{J}_1^T(\boldsymbol{C})\boldsymbol{f}\}}{\partial \boldsymbol{C}}\right|_{\substack{\boldsymbol{f}=\boldsymbol{f}^* \\ \boldsymbol{C}=\boldsymbol{C}^*}} \widehat{\boldsymbol{C}} \,. \tag{14} $$

Small variation $\widehat{\boldsymbol{F}}$ is written as:

$$ \widehat{\boldsymbol{F}} = \boldsymbol{J}_1^T(\boldsymbol{C}^*)\hat{\boldsymbol{f}} + \boldsymbol{J}_2(\boldsymbol{C}^*)\widehat{\boldsymbol{C}} \,, \tag{15} $$

where a coefficient matrix of the second term in the right-hand side is

$$ \boldsymbol{J}_2(\boldsymbol{C}^*) = \left.\frac{\partial\{\boldsymbol{J}_1^T(\boldsymbol{C})\boldsymbol{f}\}}{\partial \boldsymbol{C}}\right|_{\substack{\boldsymbol{f}=\boldsymbol{f}^* \\ \boldsymbol{C}=\boldsymbol{C}^*}} . \tag{16} $$

Oil-hydraulic Circuit

Schematic diagram of one-pump one-cylinder drive system is shown in Figure 3. The tunnel boring machine of our interest has six sets of the one-pump one-cylinder drive system for each link of the parallel link mechanism shown in Figure 2. A cylinder (a) is driven by a pump (b) whose rotational frequency is determined by an AC servo motor (c). Maximum outlet pressure of pump is limited by relief valves (d). When the cylinder extracting, suction flowrate of pump is shortage, and a check valve (e-1) will open to fulfil the suction oil flow of the pump (a). When the cylinder retracting, the cylinder receives force from bedrock, and bottom pressure p_2 is generated with a counter-balance valve (f-2). Pump suction flowrate from the bottom side is larger than flowrate to the rod side of the cylinder. An excess of the suction flowrate over the rod-side flowrate will relieve through a shuttle valve (g) to tank. The m-th cylinder generates cylinder force f_m. A cylinder force vector is written as:

$$\boldsymbol{f} = [f_1, f_2, \cdots f_6]^T \,. \tag{17}$$

The cylinder force is equal to the amount of pressure force minus viscous damping force:

$$\boldsymbol{f} = A_2 \boldsymbol{p_2} - B \frac{d}{dt} \boldsymbol{l} \,, \tag{18}$$

where piston area A_2 and viscous coefficient B on the assumption that 6 cylinders have the same piston. Bottom pressure vector is $\boldsymbol{p}_2$, and link length vector is $\boldsymbol{l}$. Linearization of this equation and substitution of Eq.(11) for link length result in:

$$\hat{\boldsymbol{f}} = A_2 \hat{\boldsymbol{p}}_2 - B \frac{d}{dt} \hat{\boldsymbol{l}} = A_2 \hat{\boldsymbol{p}}_2 - B \frac{d}{dt} \left[\boldsymbol{J}_1(\boldsymbol{C}^*) \hat{\boldsymbol{C}} \right] . \tag{19}$$

A pump flowrate vector of the hydraulic pump, $\boldsymbol{q_2}$, is determined by a rotational frequency vector, $\boldsymbol{\omega}$. The pump has displacement, D, and volumetric efficiency, η_v:

$$\boldsymbol{q_2} = \eta_v D \boldsymbol{\omega} \,, \tag{20}$$

Linearizing this equation:

$$\hat{\boldsymbol{q}}_2 = \eta_v D \hat{\boldsymbol{\omega}} \,. \tag{21}$$

Bottom pressure is determined by pump flowrate and piston velocity according to compressibility of oil:

$$\frac{d}{dt} \boldsymbol{p_2} = \frac{K}{V_2} \left(\boldsymbol{q_2} - A_2 \frac{d}{dt} \boldsymbol{l} \right) . \tag{22}$$

Linearizing the above equations and substituting Eq.(11) for $\hat{\boldsymbol{l}}$:

$$\frac{d}{dt} \hat{\boldsymbol{p}}_2 = \frac{K}{V_2} \left(\hat{\boldsymbol{q}}_2 - A_2 \frac{d}{dt} \hat{\boldsymbol{l}} \right) = \frac{K}{V_2} \left(\hat{\boldsymbol{q}}_2 - A_2 \frac{d}{dt} \boldsymbol{J}_1(\boldsymbol{C}^*) \hat{\boldsymbol{C}} \right) . \tag{23}$$

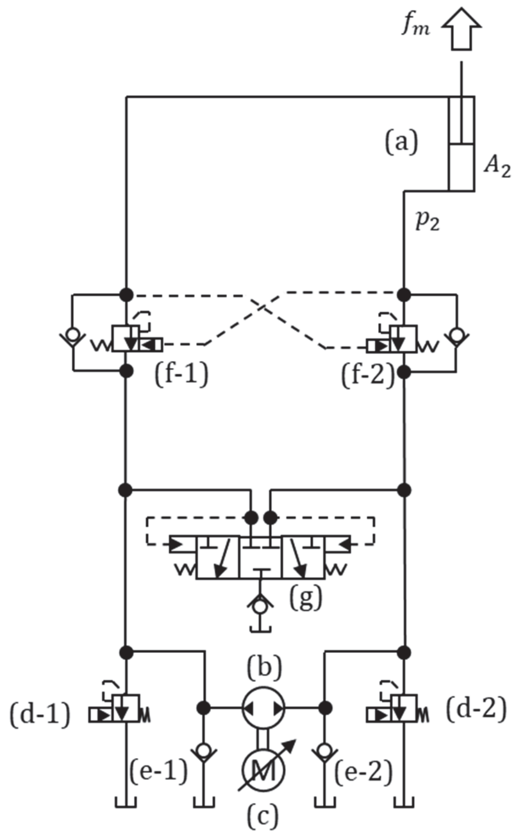

Figure 3. One-pump one-cylinder drive system

Block Diagram of Tunnel Boring Machine

A block diagram of the tunnel boring machine is drawn in Figure 4, which are obtained based on the linearization of fundamental equations. Pump flowrate $\hat{\boldsymbol{q}}_2$ is determined by rotational frequency $\boldsymbol{\omega}$, pump displacement D, and volumetric efficiency η_v, Eq.(21). Bottom pressure $\hat{\boldsymbol{p}}_2$ changes based on the amount of pump flowrate $\hat{\boldsymbol{q}}_2$ minus piston-velocity induced flowrate $A_2\boldsymbol{J}_1(\boldsymbol{C}^*)s\hat{\boldsymbol{C}}$ according to compressibility of oil, Eq.(23). Cylinder force $\hat{\boldsymbol{f}}$ is equal to the amount of pressure force $A_2\hat{\boldsymbol{p}}_2$ minus viscous damping force $B\boldsymbol{J}_1(\boldsymbol{C}^*)s\hat{\boldsymbol{C}}$, Eq.(19). Force and torque acting on the cutter head is the sum of cylinder force component $\boldsymbol{J}_1^T(\boldsymbol{C}^*)\hat{\boldsymbol{f}}$ and link mechanism component $\boldsymbol{J}_2(\boldsymbol{C}^*)\hat{\boldsymbol{C}}$, Eq.(15). According to the equation of motion of cutter head, Eq.(4), the vector of displacement and attitude angle of the cutter head, $\hat{\boldsymbol{C}}$, is derived. Finally, link length $\hat{\boldsymbol{l}}$ is calculated from the vector $\hat{\boldsymbol{C}}$, Eq.(11).

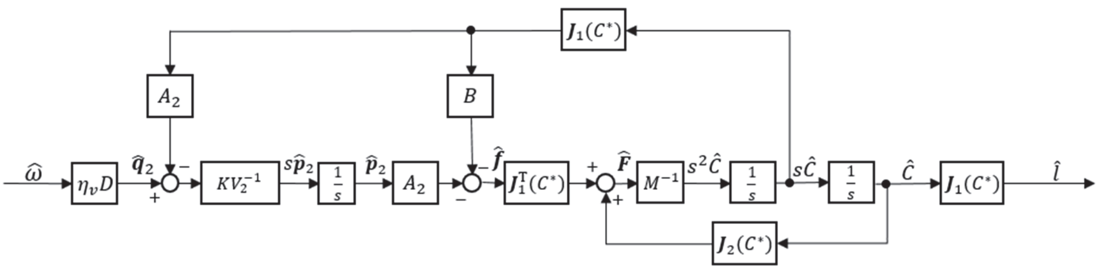

Figure 4. Block diagram of linearized model of the tunnel boring machine

Frequency Response Analysis

Frequency responses from demand signal of rotational frequency of AC servo motor to link length are calculated using the block diagram of Figure 4. The results are shown in Figure 5. Horizontal axis is frequency from 0.01 to 10 Hz. Upper plot is gain plot in dB, and lower plot is phase plot in degree. The system has six demand signals of rotational frequency as input signal and six displacements of cylinder as output signal. Considering all combinations from 6 input signals to 6 output signals, the number of transfer functions becomes 36. In Figure 5, only 6 sets of frequency responses from an input signal of one of AC servo motors of the cylinder No.1 to output signals of 6 cylinders are plotted in Figure 5. The solid line “from 1 to 1” means autocorrelation, which is frequency response of a demand signal of rotational frequency of AC servo motor to displacement of cylinder which is directly connected with a pump driven by the AC servo motor whose rotational frequency is taken as the input signal. In lower frequency region less than 0.4 Hz, the gain plot shows a slope of -20dB/decade and phase of -90 degree. In higher frequency region, the phase decreases gradually to -180 degree. It can be suggested that an integral element is included in the transfer function. Other lines “from 1 to 2”, “from 1 to 3”, “from 1 to 4”, “from 1 to 5”, and “from 1 to 6” are frequency responses of transfer functions representing mutual interference from cylinder No.1 to other cylinders, No.2, No.3, No.4, No.5, and No.6, respectively. In lower frequency region less than 0.4Hz, the gains are much smaller than gain of “from 1 to 1”. In higher frequency region, the differences become relatively small. Phases of the mutual interference begin as 90 degree and 270 degree in lower frequency region. It can be seen when considering complex plane, the “90” degree and “270” degree are identical to the -270 degree and -90 degree, respectively. Phase decrements of the mutual interferences are larger than that of “from 1 to 1”.

It can be said that bandwidth of the system is almost 0.4 Hz. In frequency region less than 0.4 Hz, a transfer function of “from 1 to 1” can be approximated by an integral element, $1/s$. Then, proportional control strategy can be applied to feedback control of link length. When designing control system of the parallel link mechanism, it is desired to consider the mutual interference among cylinders.

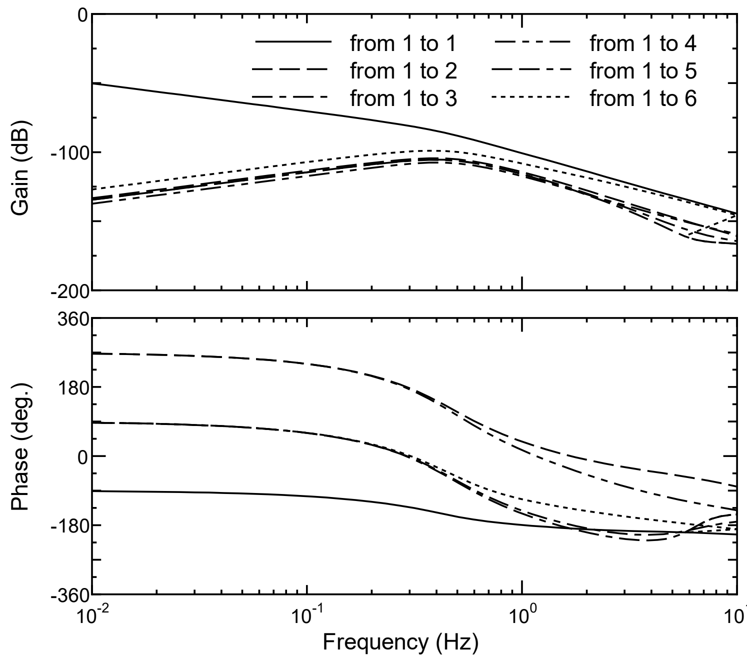

Figure 5. Frequency responses of a cylinder from rotational frequency of pump to length of link

CONCLUSION

Frequency response was calculated using a block diagram of mathematical model considering statics of the parallel link mechanism and the one-pump one-cylinder drive system. The main transfer function of interest can be approximated as an integral element in low frequency region of less than 0.4Hz. Proportional control can be a candidate for control strategy. A possible future work is feedback control of link length for the tunnel boring machine.

REFERENCES

1. ARAI, T., Analysis and Synthesis of a Parallel Link Manipulator Based on Its Statics, Journal of the Robotics Society of Japan, 1992, 10-4, pp.526-533.
2. TSUCHIYA, K. et al., Dynamic Characteristics of Parallel Link Mechanism with Six Degrees of Freedom Using Hydraulic Cylinders, 1st Report Frequency Response Analysis of a Servomechanism, Transactions of the Japan Fluid Power System Society, 2006, 37-1, pp.1-7.
3. TSUCHIYA, K. et al., Dynamic Characteristics of Parallel Link Mechanism with Six Degrees of Freedom Using Hydraulic Cylinders, 2nd Report: Characteristic Analysis by Nonlinear Simulation and Experiment, Transactions of the Japan Fluid Power System Society, 2008, 39-1, pp.1-6.

The 11th JFPS International Symposium on Fluid Power HAKODATE 2020 Oct. 12-13, 2021 The Japan Fluid Power System Society

A Power-Split Hybrid Transmission to Drive Conventional Hydraulic Valve Controlled Architectures in Off-road Vehicles: The Case of a Mini-Excavator

Mateus BERTOLIN* and Andrea VACCA*

*Maha Fluid Power Research Center, Purdue University
1500 Kepner Dr., Lafayette, IN, United States
(mbertoli@purdue.edu and avacca@purdue.edu)

Abstract. In recent years, several disruptive solutions for off-road vehicles hydraulic implements were proposed to increase energy efficiency, many focusing on the reduction of throttling losses. However, the market has showed a limited adoption of such solutions due to high implementation costs and operator's acceptance. Considering these limitations, this paper proposes to adopt a hybrid power-split hybrid transmission between the supply pump and the prime mover, while still using state-of-the-art hydraulic actuation. Such approach results in an independent control of the engine and pump speeds, therefore improving the efficiency of both. The paper describes the potential application of the proposed solution to a small excavator equipped with a load sensing system. The authors developed a simulation model, which was validated against experiments of the baseline machine. The model was used evaluate fuel efficiency gains achieved with the proposed solution, which are estimated in up to 16% for a truck-loading cycle.

Keywords: Hybrid, excavator, power-split transmission, load-sensing system.

INTRODUCTION

Typical hydraulic architectures commonly found in off-road vehicles are well known for two main characteristics: precise motion control, and low energy efficiency associated with the inherent throttling losses of their valve-controlled systems. Especially in machines with multiple simultaneous actuations like excavators, losses caused by the valves are inevitable when a centralized hydraulic supply is used. This is because each pump in the machine usually supplies more than one actuator at the same time. In addition, many vehicles today available in market operate in not optimal conditions for the engine and the pumps. This happens because the faster dynamics and the high installed power capacity of the hydraulic pumps force the engine to operate at high speeds to avoid stall. Additionally, the power and torque limitation of the engine usually results in partial displacement operation of the hydraulic pumps, leading to lower volumetric efficiency. Consequently, during high-power demanding cycles the system operates with two of its most important components at low efficiency conditions.

Literature has been consistent with two approaches to improve fuel efficiency of off-road vehicles. When possible, hybridization is a good solution to improve engine efficiency and to reduce the maximum engine power requirement. In addition, a lot of focus has also been given to minimization or elimination of throttling losses with solutions such as independent metering and de-centralized displacement-controlled (DC) architectures.

Among the most successful systems proposed in literature are the ones that can achieve both a better engine management and a reduction of throttling losses. Vukovic, Sgro, and Murrenhoff [1], [2] proposed the STEAM excavator, which uses two accumulators to maintain three different pressure levels in the machine. The concept is known as constant pressure rails, even though in reality the pressures can vary considerably in each accumulator during the machine operation. On/off valves are used to connected different pressure levels to each actuator chamber. A controller was developed to select the proper pressure level and chamber connection with the goal of minimizing throttling losses and the actuator motion is controlled with proportional valves. The large accumulators adopted in the STEAM allow meeting high flow demands decoupling the actuators flow request from the engine speed. A 55% increase in efficiency during an air grading cycle was reported in the mentioned work.

In a similar fashion, Heybroek and Sahlman [3] also propose different pressure rails with large accumulators to minimize throttling losses and decouple flow request from engine speed. In their proposal, two pressure levels are used in combination with multi-chamber cylinder with 4 chambers, achieving up to 35% reduction in fuel consumption for a truck-loading cycle.

The author's research lab has followed the de-centralized approach to eliminate completely throttling losses. It has been shown by Zimmermann, Busquets and Ivantysynova that only by replacing the state-of-the-art hydraulics with displacement control actuation it is possible to reduce fuel consumption by 40% [4]. Later, the machine was modified to a series-parallel hybrid solution and achieved extra 10% in fuel savings in simulation [5], [6]. However, this solution keeps the DC pumps mechanically connected to the engine shaft. In this scenario, whenever the engine speed is kept constant and the flow request is low, the pumps are forced to operate at low displacements where the volumetric efficiency is low. Williamson [7] showed that by varying the engine speed this problem can be solved, but nevertheless, the engine is forced to constantly vary its speed moving away from its optimal operating point during high flow-demand. To address this issue, a power-split hydraulic hybrid transmission between engine and hydraulic pumps was first proposed by the authors in a recent work [8]. With this approach, DC pumps and engine speeds can be controlled independently, leading to fuel consumption improvements of up to 60% when compared to the baseline Load-Sensing system or extra 11% when compared to the previous version of the hybrid system.

Despite the reduction in fuel consumption achieved in the past mentioned works, it must be considered that the market has showed a limited acceptance of DC based solutions. Besides implementation costs, there are challenges associated with reproducing all the machine requirements and expert operator feelings that are achieved by the current state-of-the art hydraulic architectures, such as load-sensing and open-center systems.

To overcome these limitations, this paper proposes a solution that can be considered as less disruptive when compared to the above-mentioned work, but that is able to achieve reduction in fuel consumption without compromising the current operator experience and market acceptance of the hydraulic system architecture. The rationale is to design a system with high engine-hydraulics integration with limited implementation costs. In addition, the proposed solution aims at keeping the same motion control quality and user feeling of the state-of-the-art hydraulic implements.

The paper structure is as follows. In the next section, the reference machine is introduced and followed by a description of the proposed solution. Then, the modeling approach used to model the baseline load-sensing system is described. Next, the reference working cycle used in this study is presented and simulation results are validated against measurements. Following the model validation, the design of the proposed transmission is discussed, and the simulation approach used to model the transmission is presented. Afterwards, the proposed power-management controller is presented, followed by a discussion on the possible integration of the swing actuator in the transmission. Lastly, simulation results are presented and discussed, followed by conclusions.

REFERENCE MACHINE

The reference machine used in this study is a Bobcat 435 mini-excavator, which in its baseline version uses a post-compensated load-sensing (LS) system with a single pump, like the one shown in Figure 1. The main machine parameters are shown in Table 1.

Table 1. Reference Machine Main Parameters

Machine Parameter	Symbol	Value
Engine Power	P_e	36 kW
Operating Weight	-	5 tons.
Engine Operating Speed (High Speed Mode)	n_e	2400 rpm
LS Pump Displacement	V_p	48 cm^3/rev
LS Pump Margin	s	23 bar
LS Compensator Margin	s_c	4 bar

In this architecture, the highest user pressure is picked-up by the LS line through each actuator pressure compensator. The pump adjusts its displacement to keep its outlet pressure at the level of the LS line plus a fixed margin (s). Pressure compensators ensure a constant pressure differential across each flow control valve. This pressure differential is equal to $s - s_c$ and ensures that the flow is directly proportional to the valve opening area, therefore eliminating any load interference on actuator speed. A fixed orifice bleeds out any trapped pressure in the LS line, while a relief valve in the same line limits the pump maximum pressure. Pilot lines and local actuator relief valves are omitted in Figure 1 for clarity.

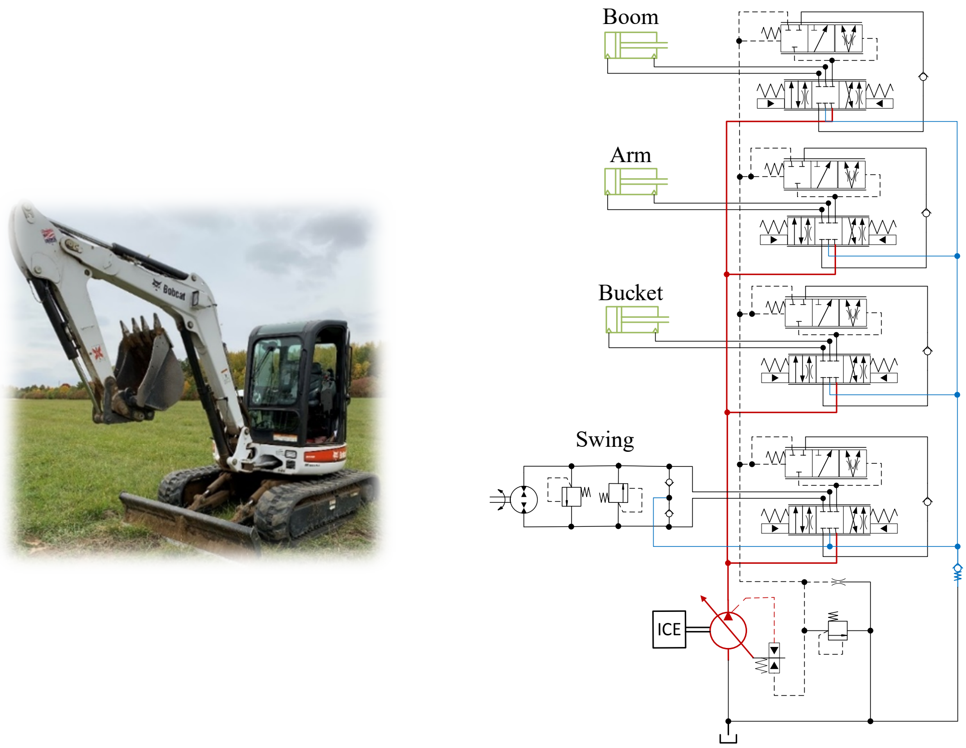

Figure 1. Reference Machine and its baseline hydraulic schematic.

PROPOSED SOLUTION

The proposed solution consists in using a power-split transmission between the engine and the load-sensing pump, like shown in Figure 2.The idea is to improve the overall system fuel consumption, without major changes to the hydraulic actuation of the baseline machine. In addition, another solution including a hybrid swing integrated in the transmission hydraulic path using secondary control will also be introduced and analyzed later in this paper. Despite the proposed solution can be applied with any centralized fluid power architecture, this work demonstrates its application on an excavator equipped with a LS system. It should be noted that a LS system is used here exclusively because it was the original configuration of the baseline machine, for which data was available. However, implementation with an open-center system is also possible.
The widely known power-split transmission has the characteristic of a series hybrid, in which engine and pump speeds are completely decoupled, but with a higher efficiency, since most of the power is still transmitted mechanically through the planetary gear train (PGT). Another advantage is on the size of the transmission units needed. While a series hybrid transmission would have both units sized for maximum system power, the selected power-split system requires smaller units since it relies on mechanical power transmission as well.
The planetary gear used has three shafts. One can be connected to the engine, one the primary hydraulic unit and another connected to the main user, in this case is a LS pump.

Transmission Power Flow

At the PGT, the torque relationship between the shafts is constant. On the other hand, the speed relationship between the three shafts is given by

$$n_{sun} - i_0\, n_{ring} - (1 - i_0\,)n_{carrier} = 0 \tag{1}$$

where i_0 is the PGT standing gear ratio. Therefore, The PGT gear configuration enables independent speed control of 2 out of 3 shafts, as clear from the expression stated in equation (1). Consequently, power can be split between two paths according to the ratio of the selected speeds. In this way, while part of the engine power is transmitted to the LS pump through the mechanical path, the remaining power is transmitted through the hydrostatic path of

the transmission. The ratio between inlet and outlet flows in the transmission hydraulic path determines the accumulator state-of-charge, allowing for energy storage/release.
With this approach, the primary unit is used to load the engine with the desired torque, while the secondary unit uses secondary control to regulate the speed of the LS pump. The engine speed is then controlled by adjusting the engine throttle, with a setpoint determined by a power-management controller. Therefore, compared to the original system the engine is operated in a much steadier way, with nearly constant torque and speed, while the accumulator and the secondary unit handle the severe load transients that occur during a digging operation. In addition, the output shaft speed can be quickly adjusted over time such that the LS pump is forced to continuously operate close to its maximum displacement, hence increasing its volumetric efficiency. Additionally, when the mechanically transmitted power is higher than the demand from the LS pump, the secondary unit serves as hydrostatic brake, also charging the accumulator. Additional relevant information on the behavior of hydraulic power-split transmissions can be found in [9] and [10].
Besides the freedom in engine speed selection, the proposed architecture also brings the typical benefits of hybrid systems, such as the potential for engine downsize. The added energy storage device allows the designer to use a smaller engine such that it is constantly operated closer to its maximum torque, where engine efficiency is maximum, while peak power demand is achieved with a hydraulic boost from the hydraulic accumulator.

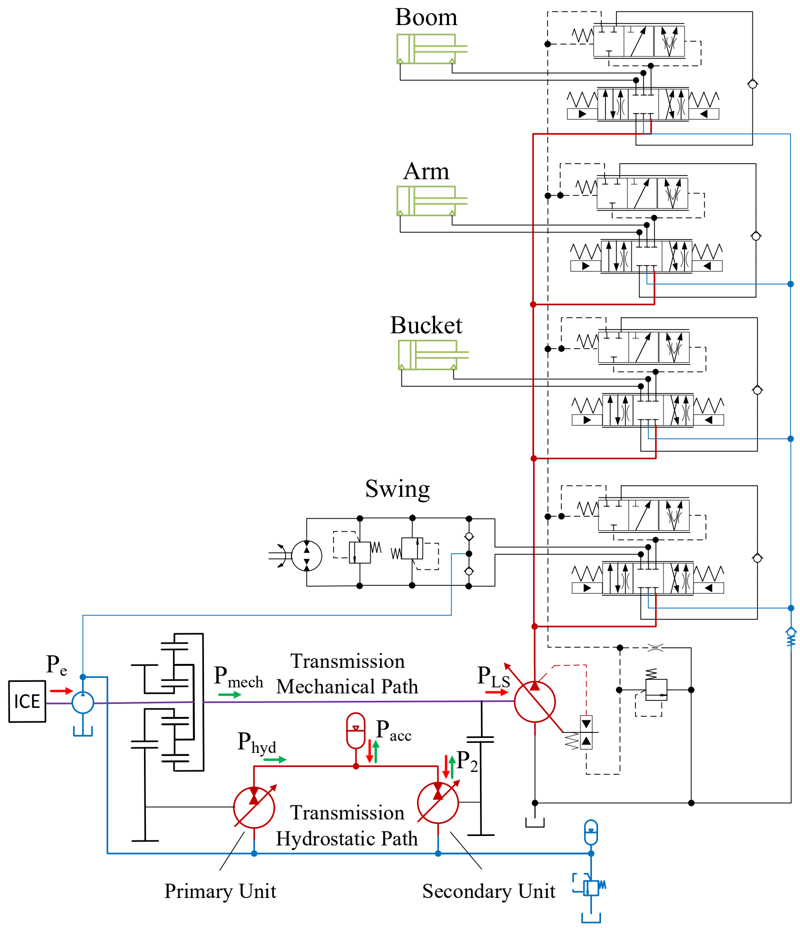

Figure 2. Proposed power-split hybrid excavator with load-sensing implements.

SIMULATION MODEL

The design of the proposed transmission is based on a numerical simulation model that is able to reproduce the behavior of the baseline LS system and achieve a good estimate of its power consumption. Such model is used to characterize the loads that would be seen by a power-split transmission, and to provide important information in the design process. In addition, it is also used to obtain a fair comparison between proposed and baseline systems.

Load-Sensing Implements Model

The Load-Sensing system model is developed in Matlab/Simulink and it can be divided into six different sub-models as shown in the top-level block diagram presented in Figure 3. Since the kinematic model has been presented and validated in previous publications [11] [12], its description will be left out of this paper, but the reader is encouraged to refer to mentioned references for more details. The operator model is a PI controller that generates valve position commands based on a reference cycle profile. Additional inputs to the model include the external load (F_{Ext}), which is estimated based on measured pressures, and the measured engine speed (n_e). The hydraulic components are modeled as follows:

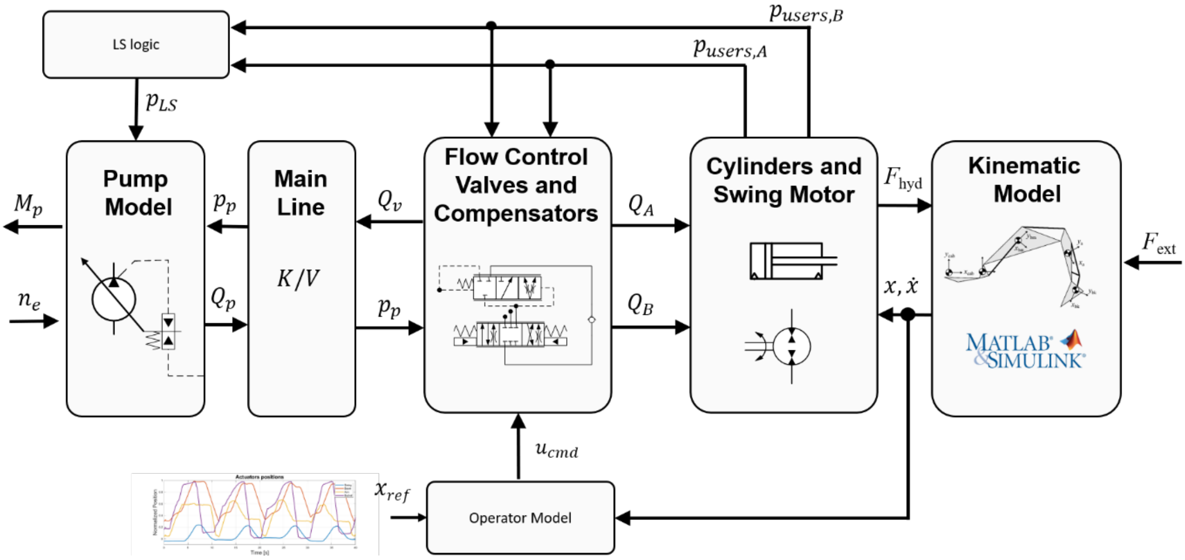

Figure 3. Load-sensing model top-level block diagram

Pump and Main Line Models

The pump model is used to evaluate the effective flow and torque of the LS pump. The pump effective flow rate is obtained with eq. (2):

$$Q_p = n_e V_p \beta_p - Q_s, \qquad Q_s = f(n_e, p_p, \beta_p) \tag{2}$$

where the V_p is the pump maximum volumetric displacement, β_p is the normalized fractional displacement and Q_s accounts for the volumetric losses. The last term is obtained with an empirically derived loss model obtained with steady-state measurements and is a function of pump speed, pressure differential and displacement. Similarly, the pump effective torque is obtained with:

$$M_p = \frac{V_p \beta_p p_p}{2\pi} + M_s, \qquad M_s = f(n_e, p_p, \beta_p) \tag{3}$$

where M_s accounts for the hydromechanical losses. In both cases of eq. (2) and (3) the losses are estimated according to the method proposed by Ivantysynova [13]. The pump fractional displacement can be obtained with a force balance in the pump control piston. If dynamic effects are neglected,

$$\beta_{cmd} = \frac{x_p}{x_{p,max}} = \frac{p_{ls}A_p - p_p A_p + F_{spring}}{K_{spring} x_{max}} \tag{4}$$

where F_{spring} is the spring pre-load, A_p is the control piston area, K_{spring} is the spring constant and $x_{p,max}$ is the control piston maximum stroke. The LS pressure (p_{ls}) is the highest user pressure among the lines connected to the pump. To reduce the number of parameters to be tuned, the above equation can be simplified to a proportional pressure controller such that:

$$\beta_{cmd} = \frac{x_p}{x_{p,max}} = k_p \cdot (p_{ls} - p_p + s) \tag{5}$$

where s is the so-called pump margin given by the spring pre-load. To avoid unrealistic dynamic behavior, a first order transfer function is used to slow down transients. In this way

$$\dot{\beta}_p = \frac{1}{\tau_p}\beta_{cmd} + \frac{1}{\tau_p}\beta_p \tag{6}$$

where τ_p is the transfer function time constant. In addition, the pump displacement can be limited depending on the simulated pump pressure, to mimic torque limiting controls usually implemented in these pumps to avoid engine stall. The pump outlet pressure, is obtained with the pressure build-up equation accounting for all the flows in and out of the line

$$\dot{p}_p = \frac{K}{V} \cdot \left(Q_p - Q_{v,swing} - Q_{v,boom} - Q_{v,arm} - Q_{v,bucket}\right) \tag{7}$$

where $Q_{v,swing}$, $Q_{v,boom}$, $Q_{v,arm}$, and $Q_{v,bucket}$ are the flows to each actuator out of the pump line.

Flow Control Valves and Compensators

The flow through work-port of the flow control valves is obtained considering the turbulent flow orifice equation. Since the goal of this paper is to estimate power consumption, compensator dynamics are neglected. This can be done because compensator dynamics are considerably faster than the actuator dynamics. In this way, the pressure differential across the main spool is always equal to $\Delta p_v = p_p - p_{ls} - s_c$ where s_c is the compensator spring setting. In this way,

$$Q_v = k_v A_v(x_v)\sqrt{\Delta p_v} \tag{8}$$

where k_v is a constant flow coefficient, $A_v(x)$ is the opening area, which is a function of the spool position. To reproduce the effect of the non-return check valve, the value of Δp_v is saturated to zero when it becomes negative. Similarly, for the case of the return line

$$Q_{v,r} = -k_{v,r} A_{v,r}(x_v)\sqrt{p_{act} - p_{return}} \tag{9}$$

where the return pressure is assumed constant and equal to 4 bar and p_{act} is the pressure in the actuator line connected to the return line, according to the operator command.

Cylinders and Swing Motor

Similarly to the case of the pump outlet pressure, the pressure in actuator lines are also obtained with the pressure build-up equation. In the case of the linear actuators, the pressure in the bore chamber (p_A) and in the rod chamber (p_B) are evaluated as follows:

$$\dot{p}_A = \frac{K}{V_A}\left[Q_A - A_A\,\dot{x} - K_L \cdot (p_A - p_B) - Q_{R,A} - Q_{bo,A}\ \right], \quad V_A = A_A \cdot x + V_d \tag{10}$$

$$\dot{p}_B = \frac{K}{V_B}\left[Q_B + A_B\,\dot{x} + K_L \cdot (p_A - p_B) - Q_{R,B} - Q_{bo,B}\ \right], \quad V_B = A_B \cdot (x_{max} - x) + V_d \tag{11}$$

where Q_A and Q_B can be either Q_v or $Q_{v,r}$ depending on the sign of the user command. K_L is the internal leakage coefficient, $Q_{R,A}$, $Q_{R,B}$ are the relief valve flows (considered proportional to the chamber pressure when above the relief setting) and $Q_{bo,A}$, $Q_{bo,B}$ are the laminar flows through the bleed orifice in the LS line. In this way, for the case of the bore chamber:

$$Q_{bo,A} = \begin{cases} k_{bo} \cdot p_A, & p_A = p_{ls} \\ 0, & otherwise \end{cases} \tag{12}$$

Each actuator force can be obtained based on simulated chamber pressures and respective areas. In addition, a Coulomb friction model is used to account for both static and dynamic friction.
The pressures in the swing motor line are modeled in a similar way, therefore:

$$\dot{p}_{A,sw} = \frac{K}{V_{A,sw}}\left[Q_A + Q_{sw,A} - Q_{R,A} - Q_{bo,A}\ \right] \tag{13}$$

$$\dot{p}_{B,sw} = \frac{K}{V_{B,sw}}\left[Q_B + Q_{sw,B} - Q_{R,B} - Q_{bo,B}\ \right] \tag{14}$$

where $Q_{sw,A}$, $Q_{sw,B}$ are the swing motor effective flow rates to/from lines A and B, respectively. These effective flow rates are calculated as follows:

$$Q_{sw,A} = \begin{cases} n_{sw} \cdot V_{sw} - Q_{sw,s} & ,\Delta p_{sw} \geq 0 \\ n_{sw} \cdot V_{sw} & ,\Delta p_{sw} < 0 \end{cases} \tag{15}$$

$$Q_{sw,B} = \begin{cases} -n_{sw} \cdot V_{sw} & ,\Delta p_{sw} \geq 0 \\ -n_{sw} \cdot V_{sw} - Q_{sw,s} & ,\Delta p_{sw} < 0 \end{cases} \tag{16}$$

where $Q_{sw,s} = f(\Delta p_{sw}, n_{sw})$. Similarly, the swing motor effective torque, is given by:

$$M_{sw} = \frac{V_{sw}\Delta p_{sw}}{2\pi} - M_{sw,s}, \qquad M_{sw,s} = f(n_{sw}, \Delta p_{sw}) \tag{17}$$

Reference Cycle and Model Validation

To verify the validity of the model of the hydraulic system, comparisons on measured kinematic quantities and pressures of the simulated machine are presented. A 90 degrees truck-loading cycle performed by an expert operator has been selected. In this cycle, the machine digs into the ground, rotates 90 degrees while raising the boom and dumps the bucket content into a truck. The rationale for the selection of this cycle is twofold: first, it has been widely used both in academia and industry for fuel consumption evaluation of excavators. Second, it reproduces the most demanding operating conditions for the machine, in which four actuators are used simultaneously with maximum power demand.
Based on the available data, it is chosen to look at the actuators measured positions and pump outlet pressure. In short, by comparing measured and simulated positions, it is guaranteed that the pump is delivering a similar flow rate in both experiments and simulation. Additionally, the validation of the pump outlet pressure ensures that the loads and throttling losses are well captured with the model. Therefore, it is inferred that the developed model is representative of the LS pump power consumption.
Actuator positions are shown in Figure 4. Simulated results show a good agreement with measurements, therefore demonstrating that the operator model is able to track the reference cycle well. The Load-sensing pump outlet pressure validation is shown in Figure 5. A perfect match between measured and simulated LS pump outlet pressure is somewhat challenging to obtain with the proposed model since even a small difference in operator command can connect a different chamber to the LS line. Nevertheless, simulation results show a good agreement with measurements.

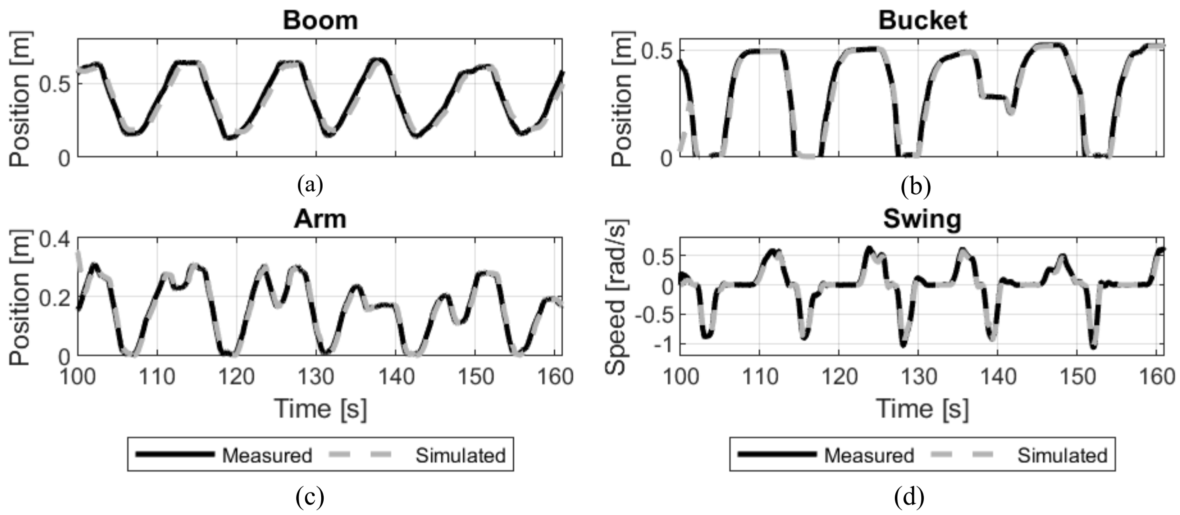

Figure 4. Simulated actuators positions with LS model. Boom (a), Bucket, (b), Arm (c), Swing (d)

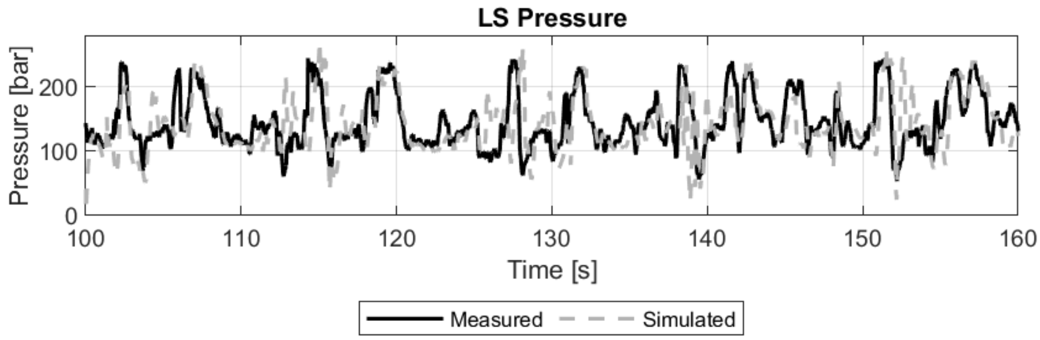

Figure 5. Load-sensing pump outlet pressure validation

PLANETARY GEAR CONFIGURATION SELECTION AND SYSTEM SIZING

Engine Downsizing

Although the proposed system allows any engine to be operated at the desired combination of torque/ and speed, fuel efficiency can be further improved when smaller engines are used. This because a downsized engine will tend to operate more often close to its peak torque, where fuel efficiency is higher and because the hydraulic accumulator can be used to energy storage/release. Therefore, the starting point in the design process is to evaluate the required engine size as well as the optimal engine torque/speed, such that the transmission can be designed to operate the engine at the desired operating point.

To evaluate the required engine size, the developed model is used to evaluate the typical LS pump power demand over a highly demanding cycle, as shown in Figure 6. From these results, it is clear the large variations in power demand over time and therefore it is possible to size the engine to provide only the average power demand and use the energy storage device to handle the heavy transients. For the cycle in analysis, the average demand is 22.8 kW, which is 37.5% lower than the original engine rated power of 36.5 kW. However, such a large engine size reduction is not desired for three reasons: first, there is no guarantee that the cycle in analysis – even if it was an aggressive expert operator cycle – is the most demanding a machine will ever face in real life, meaning different conditions and operators could require a larger average power. Second, this analysis considers only the LS power demand and does not leave any extra power to accelerate the engine, for example should its speed drop during a sudden load increase. Lastly, other functions in the machine like the tracks usually require a constant power supply, and therefore it is not always possible to rely on the accumulator to achieve a higher power supply.

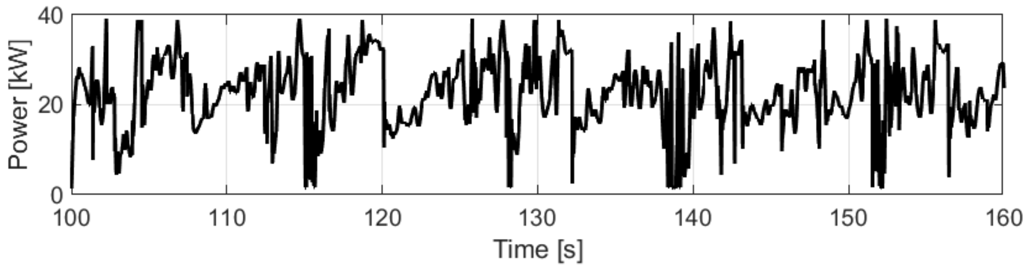

Figure 6. LS Pump power Demand

The aforementioned reasons leave the room for the question on how to properly select the engine size. To answer this, a proposed reasonable approach can be derived from the engine fuel consumption map. Diesel engines typically operate with higher efficiency (or break-specific fuel consumption) near its peak torque, and not near its peak power. Therefore, an engine can be selected to deliver the average power of the studied cycle at its peak efficiency point. This ensures optimal engine operation for a typical cycle, while also leaving some room to operate at higher power demands should the operator require it. Nevertheless, this approach still requires ensuring all the machine requirements are met, such as the power requirements of functions with constant demand like the tracks.

A typical Diesel engine fuel consumption map is shown in Figure 7. In this work, this map is scaled to the specifications of the original engine in the baseline machine. The Figure shows that the peak engine power is at 2300 rpm, while the peak efficiency (and peak torque) is at around 1800 rpm. Therefore, assuming the smaller engine will have similar characteristics, it is desired to select an engine capable of providing 22.8kW at 1800 rpm, resulting in an engine with a maximum power of 29.2 kW, a 20% reduction when compared to the baseline machine. Evidently, different engines will have different fuel consumption maps and the proposed approach may not be as straightforward as presented here, requiring some iterations and analysis of different engines. Nevertheless, it is reasonable to expect that other engines will share similar characteristics.

Besides operating the engine at its peak efficiency, the proposed approach also leaves the possibility of achieving higher power demands. The selected engine can achieve up to 28% more power than what is seen on average in the analyzed cycle, therefore ensuring that more demanding cycles can also be met, and that the accumulator can be quickly charged. In addition, the reduction in power availability to the tracks is not as significant.

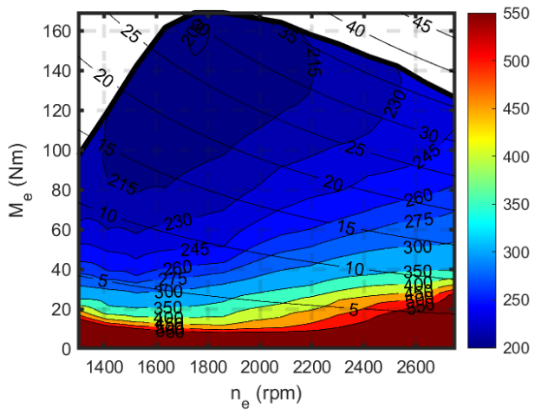

Figure 7. Typical Diesel Engine Fuel Consumption Map. Colormap is Break-specific Fuel Consumption (g/kWh)

Planetary Gear Configuration Selection

With the engine size and preferred engine speed defined, it is desired to select the transmission components. A challenge when designing any power-split transmission is to select the most appropriate configuration, meaning to which one of the PGT shafts should engine, primary and secondary units be connected. Such selection is usually done such that the primary unit speed is as close as possible to the full mechanical point, where the primary unit speed is zero. Therefore, in this condition, most of the power is still be transmitted mechanically through the PGT. The rationale for that approach is based on the fact that mechanical power transmission tends to be more efficient than using a hydrostatic path, where the power flow is subject to total efficiencies of 2 hydrostatic units [14]. In the case of the proposed application, the job of placing the full mechanical point is simplified given the fact that the baseline machine runs with a constant engine speed. In this way, assuming no changes will be made to the LS pump size, it is straightforward to select a configuration that will place the full mechanical point at an engine speed of 1800 rpm and a pump speed of 2400 rpm. This can be done in an iterative process using equation (1) in which different gear ratios and configurations can be plugged in until the solution with the primary unit speed as close to zero as possible is found for the given operating condition. It should be noted that different combinations of configurations and gear ratios may lead to similar primary unit speeds. In that case, the PGT that requires smaller hydrostatic units is preferred, which in the studied case led to the selection of the configuration shown in Figure 2. In this case, the carrier is connected to the engine, the sun is connected to the primary unit and ring is connected to the load. The sizing procedure for the hydrostatic units and accumulator is left out of this paper for brevity, but the reader is invited to refer to [8] for details on the sizing method. However, it is important to highlight that the system is sized such that the power of the original system can always be delivered to the LS pump, even when the accumulator pressure is minimum. As a consequence, the proposed powertrain will have higher power availability than the baseline machine. The final sizing is presented in Table 2. The table contains also other key parameters of the system that will be detailed in the next sections.

Table 2. Sizing Results

Machine Parameter	**Value**
Engine Power	29.2 kW
Planetary Gear Standing ratio	-2.5
Primary Unit Displacement	12 cm^3/rev
Secondary Unit Displacement	21 cm^3/rev
HP Accumulator Volume	6 L
HP accumulator pre-charge	180 bar

ENGINE AND TRANSMISSION MODELS

In the case of the baseline system, the engine speed was measured and then used as an input to the model. On the other hand, in the case of the hybrid system it is desirable to develop a model that includes engine dynamics such that engine torque, speed and fuel consumption can be more accurately predicted. Applying a torque balance in the engine shaft, the engine speed is obtained with

$$\dot{\omega}_e = \frac{1}{I_e}\left(M_e - M_{cp} + M_{carrier}\right) \tag{18}$$

where $M_{carrier}$ is the torque at the carrier gear and M_{cp} is the torque applied by the charge pump. The engine torque is commanded by the engine governor, which in this case is represented by a PID controller trying to follow a reference speed. To represent the dynamics associated with the turbocharger inertia and fuel injection delay, a second-order transfer function is used to reproduce the results obtained by Tsai and Goyal [15]. In addition, maximum engine torque is limited according to the engine wide-open-throttle curve and minimum torque is limited to $M_{fric} = f(n_e)$ where the function was empirically derived by Heywood [16].

The transmission modeling followed the same approach used by Bertolin and Vacca in [8] but is reproduced here for completeness. The nomenclature used in the modeling description is shown in Figure 8. The transmission output shaft speed is evaluated with a torque balance, therefore

$$\dot{\omega}_p = \dot{\omega}_2 = \frac{1}{I_{out}}\left(M_{ring} - M_2 - M_p\right) \tag{19}$$

where M_{ring} is the torque at the ring gear, and M_p is the load torque from the LS pump. Since $n_2 = n_{ring}$, and $n_e = n_{carrier}$, equation (1) can be re-organized to evaluate n_1, therefore defining all the speeds in the PGT.

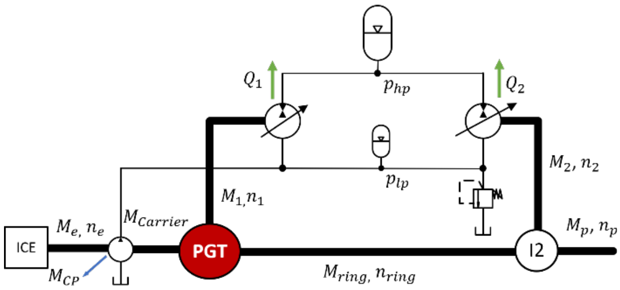

Figure 8. Transmission Model Variables

The torques at the carrier and ring gears are obtained based on the torque of the primary unit. Since the torque relationship in the PGT is fixed,

$$M_{carrier} = (i_0 - 1)M_{sun} = (i_0 - 1)M_1 \tag{20}$$

$$M_{ring} = -i_0 M_{sun} = -i_0 M_1 \tag{21}$$

However, the above equations do not consider any torque losses in the gearing. To account for those, an efficiency map generated based on information provided by a partner company was used. The losses in the PGT are torque and speed dependent. In this way, $M_{carrier} = f(M_1, n_e, n_{ring})$ and $M_{ring} = f(M_1, n_e, n_{ring})$.
The model of the hydrostatic path of the transmission evaluates the high-pressure accumulator pressure, accounting for its capacitance which is dependent on the current pressure. Therefore:

$$\dot{p}_{hp} = \frac{1}{\left[\frac{V_0}{\gamma}\left(\frac{p_0^{\gamma}}{p_{hp}^{\frac{\gamma+1}{\gamma}}}\right).+\frac{V_{line}}{K}\right]}(Q_1 + Q_2). \tag{22}$$

where γ is the gas polytropic coefficient, p_0 is the accumulator pre-charge pressure and V_0 is the accumulator total volume. In a similar way, the approach described by equation (22) is used to evaluate the pressure in the low-pressure side of the transmission (p_{lp}). The effective flow-rates of the primary and secondary units, Q_1 and Q_2, are obtained with a similar approach to the one described in equation (2). Similarly, the effective torques are evaluated with the same approach shown in (3).

Secondary Unit Displacement Control System

One of the challenges of the proposed architecture is the speed control of the output shaft. The common shaft connecting secondary unit and LS pump has very low inertia when compared to the engine fly-wheel, but it can be submitted to large and fast load variations as the LS pump displacement and outlet pressure rapidly change over the cycle. Therefore, high-bandwidth is desired in the speed control of the secondary unit. However, such bandwidth will be limited to how quickly the secondary displacement can be adjusted. To model these dynamics, a method proposed by Grabbel and Ivantysynova [17] is used, which neglects swashplate inertia. In this way,

$$\dot{\beta}_2 = \frac{1}{x_{p,max,2} A_{p,2}} y_{sv} k_{sv} \sqrt{p_{hp}}. \tag{23}$$

where $x_{p,max,2}$ is the control piston stroke, $A_{p,2}$ is the control piston area, y_{sv} is the servo-valve position and k_{sv} is the servo-valve flow gain. The servo-valve dynamic response is modeled with a second-order model. In addition, it should be noted that to increase the system response, the high-pressure line is used as power supply to the control piston.

SUPERVISORY POWER-MANAGEMENT CONTROLLER

The proposed architecture has the advantage of independent control of engine torque, speed and the LS pump speed. The purpose of the supervisory power-management controller is to control these states such that the state-of-charge of the accumulator is kept within the desired range, while ensuring that the LS pump can deliver the required flow in the most efficient way possible.
The controller is designed such that the LS pump shaft speed is varied over time. The rationale for that is twofold: first, it forces the pump to operate at higher displacements, making it is more efficient. Second, it allows an increase in the speed of the primary unit, which results in a quicker charge of the accumulator during low power demand moments of the cycle. To achieve that, it is proposed to use a closed-loop pressure control to determine the desired output shaft speed. Therefore:

$$n_{2,ref} = k_{p,2}(p_{ref} - p_p), \; p_{ref} = p_{ls} + s \tag{24}$$

where $k_{p,2}$ is a proportional gain. It is worth mentioning that the proposed system still considers a typical LS pump with hydro-mechanical pressure feedback. In this scenario, the proposed approach has the following advantages:

- With the proper gain selection, the reference speed will always be close to the minimum required to ensure that $p_p = p_{ref}$, which then forces the LS pump to operate at higher displacements.
- Since two independent controllers act on different control inputs, the proposed controller achieves a faster response when guaranteeing good tracking of the desired pump outlet pressure.
- E-LS can be implemented without any changes to the LS pump, since the supervisory controller can automatically reduce the pump margin by forcing the LS pump to flow saturate.
- The only sensors required for implementation are LS pressure and pump outlet pressure.

To ensure that the accumulator is properly charged, the supervisory controller also changes the commanded power to the engine. Using the derived simulation model, the following set of rules is proposed:

$$P_{e,\,cmd} = \begin{cases} 5\;kW, \; p_{hp} > 310\;bar \\ 17\;kW, \quad 275\;bar \leq p_{hp} \leq 310\;bar \\ 27\;kW, \quad p_{hp} < 275\;bar \end{cases} \tag{25}$$

The idea behind this approach is to command an engine power above the average requirement for two reasons. First, because the engine now also needs to provide power to account for the transmission losses. Second, because it guarantees a quick recharge of the accumulator ensuring power availability. Once the pressure reaches a certain level, then the power command is lowered to avoid constant high-pressure in the HP line, which can increase the volumetric losses in the units. On the other hand, it should be said that this simplified approach is most-likely not optimal, and improvements could be made.
Once the desired engine power is selected, an online optimization algorithm is used to find the optimal combination of torque and speed that delivers the request. Based on the desired torque engine torque, the required primary unit is torque is

$$M_{1,cmd} = \frac{M_{e,cmd} - M_{cp}}{(i_0 - 1)} \tag{26}$$

From (26), an inverse loss model is used to obtain the displacement $\beta_{1,cmd} = f(M_{1,cmd}, n_1, p_{hp})$ needed to achieve the required torque. To avoid sudden changes in the engine load, the displacement command signal to the primary unit is filtered with a low-pass filter. In addition, the displacement of the secondary unit is limited in the case the pressure in the HP line drops below the minimum threshold of 200 bar. A top-level block diagram of the control approach is shown in Figure 9.

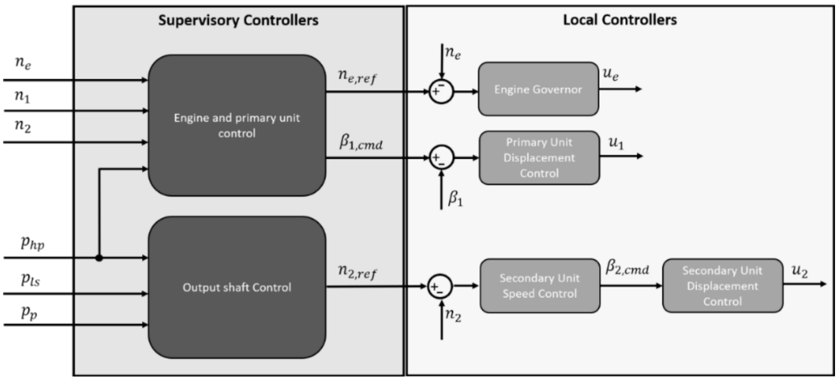

Figure 9. Transmission System Control Top-level Block Diagram

IMPLEMENTATION WITH HYBRID SWING

Another benefit of hybridization is the storage of recovered energy, which is not possible with traditional LS actuation. Based on the proposed architecture, a straightforward solution is to integrate the swing motor in the hydraulic path of the transmission, as presented in Figure 10. The swing is selected since it is the only actuator that can be switched to secondary control. The benefits of such approach are twofold: first, it allows the recovery of kinetic energy from the swing system. Second, it eliminates the throttling losses associated with the swing function in the LS line. Therefore, it is proposed to replace the fixed displacement swing motor with a variable displacement motor with secondary control. To quantify the benefits of the idea, the previously described model was modified to include the swing motor in the hydrostatic path of the transmission.

SIMULATION RESULTS

Before evaluating the fuel consumption improvements of the proposed system, it appropriate to verify that it can actually deliver the same performance of the baseline machine. Ideally, this would be done experimentally by evaluating the machine productivity in tons/liter, but in this simulation study this is done by evaluating how well the proposed architectures follow the baseline cycle. The simulated outlet pump pressures are shown in Figure 11 from which is seen that for most of the cycle, the LS pump outlet pressure is the same. This shows that even though the pump speed is being varied over time, it does not change the ability of the LS pump to track the desired load-pressure and therefore no significant changes in operator perception should be seen.

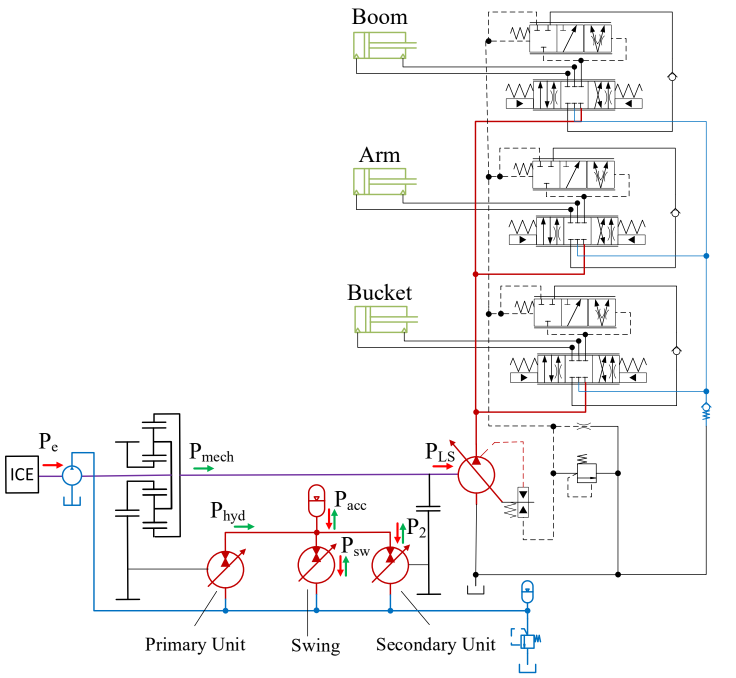

Figure 10. Proposed architecture with hybrid swing

13

The discrepancies seen at 104s and 114s are most likely due to slight differences in the simulated operator command, which may cause different chambers to connect to the LS line, for example if the command to valve position becomes larger than the valve dead-band. Nevertheless, the results in Table 3 show that that all three simulated systems present a nearly identical performance in terms of delivered energy.

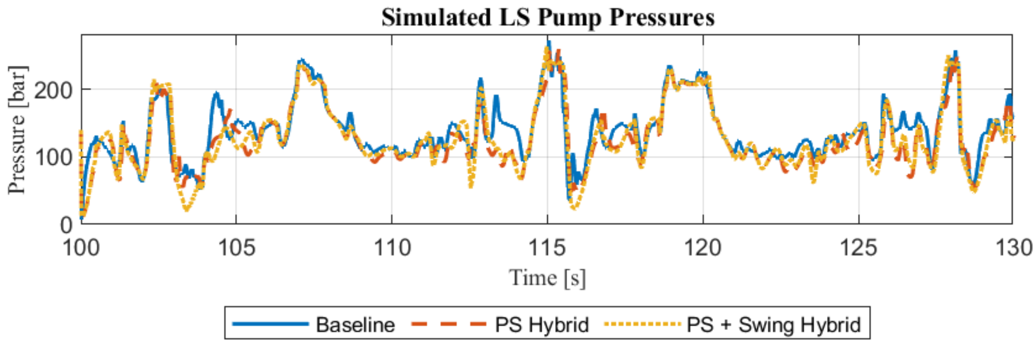

Figure 11. Simulated LS pump outlet pressure

A comparison between the two proposed architectures is shown in Figure 12 and Figure 13. From Figure 12 it is seen that some swing kinetic energy is possible, although it is not that significant due to unit losses and friction. Perhaps, more benefits would be seen in machines with larger inertia, but nevertheless it is clear from the simulated pressures that recovery occurs, especially at 140s and at 152s when the pressure is clearly higher in the system with integrated swing, even though both systems were using the same power-management strategy. Another important aspect to be highlighted in the transmission pressures is that both hybrid systems started and ended the cycle with nearly the same pressure. Therefore, no free energy coming from an initial condition in the accumulator pressure was used to accomplish the cycle and reduce fuel consumption estimation.

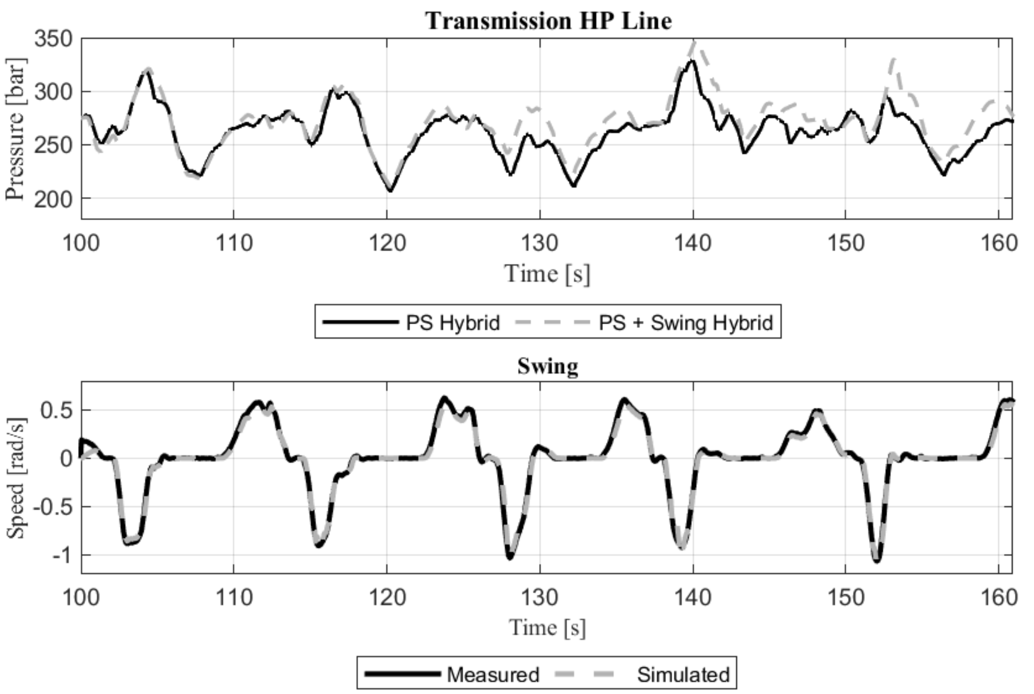

Figure 12. Simulated Transmission pressure differential and swing speed

The LS pump speed is shown in Figure 13. When the swing motor is in use, the pump speed is lower in the system with integrated swing (i.e., at 110s and 116s) therefore demonstrating the ability of the proposed controller to reduce properly slow-down the pump speed under low flow demand. It must also be pointed out that the speed controller used is able to track the reference speed, despite low inertia and sudden load changes. Nevertheless, some spikes in speed are still seen (i.e., at 120s) when the LS pressure suddenly decreases, quickly reducing the load in the shaft.

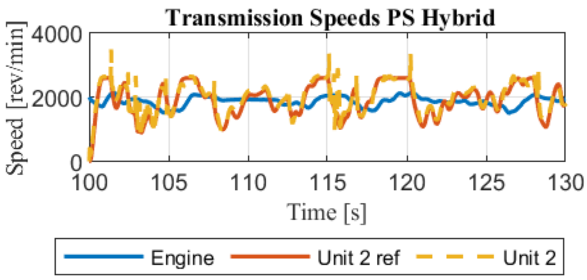

(a)

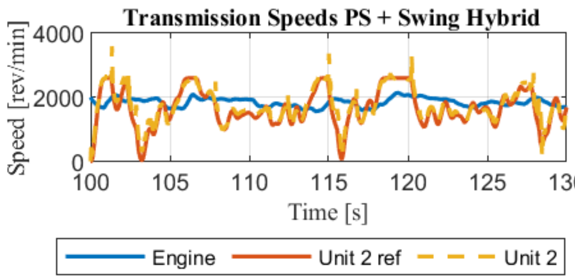

(b)

Figure 13. Simulated Transmission Speeds for Power-Split Hybrid (a) and Power-Split + Swing Hybrid (b)

A summary of the simulation results is shown in Table 3. Results show that the proposed transmission can reduce the fuel consumption in up to 11.2%. This value can be extended up to 16.4% in the analyzed cycle when the swing is integrated in the hydrostatic path of the transmission, while respecting the same expert operator cycle.
The results can be supported by Figure 14 which shows the engine operating points. A significant change in engine operating conditions allows the prime mover to always operate at peak efficiency. The average displacement of the supply pump is also higher due to the implemented controllers, thereby increasing their efficiency. Nevertheless, it should be noted that these gains are not that significant given the fact that the pump in the baseline LS system also operated at a high average displacement. Lastly, the integration of the swing in the transmission allows some energy recovery of the kinetic energy available, while also eliminating the associated throttling losses.

Table 3. Summary of Simulation Results

Parameter	**Baseline**	**PS Hybrid**	**PS + Swing Hybrid**
Engine Downsizing	-	-20%	-20 %
Average LS Pump Displacement	85.3%	93.7%	90.2 %
Delivered Positive Work	388.6 kJ	377.0kJ	388.2 kJ
Fuel Consumption	91.27 g	81.08 g	76.34 g
Difference in Fuel Consumption	-	**-11.2 %**	**-16.4%**

CONCLUSIONS

This work introduced a novel hydraulic architecture by combining an efficient power-split transmission with state-of-the-art hydraulic actuation for high engine/hydraulics integration in an excavator. A simulation model has been developed and validated for the baseline LS system of the reference machine, a 5 ton mini excavator. The model was then used to design and evaluate the benefits of the proposed transmission in simulation.
Simulation results showed the feasibility of developing a design with high integration between engine and hydraulics for off-road vehicles. By allowing the engine to operate at its peak efficiency, up to 11.2% improvement in fuel consumption can be achieved, while still maintaining the reliability and user experience of state-of-the-art hydraulics. The proposed architecture should also result in a lower up-front cost when compared to more radical approaches. It should be noted that, even though this analysis considered a load-sensing architecture, similar approach could also be followed with different architectures such as open-center systems.
In addition, the proposed system can be especially attractive to engine manufacturers, as it would allow an engine design focused on a single point of operation. In this scenario, higher improvements can be expected.
Another advantage of the proposed system is the possibility of swing integration, which increases efficiency improvements by reducing throttling losses and allowing energy recovery. When such approach is used, improvements of 16.4% in fuel consumption are estimated for the reference cycle.

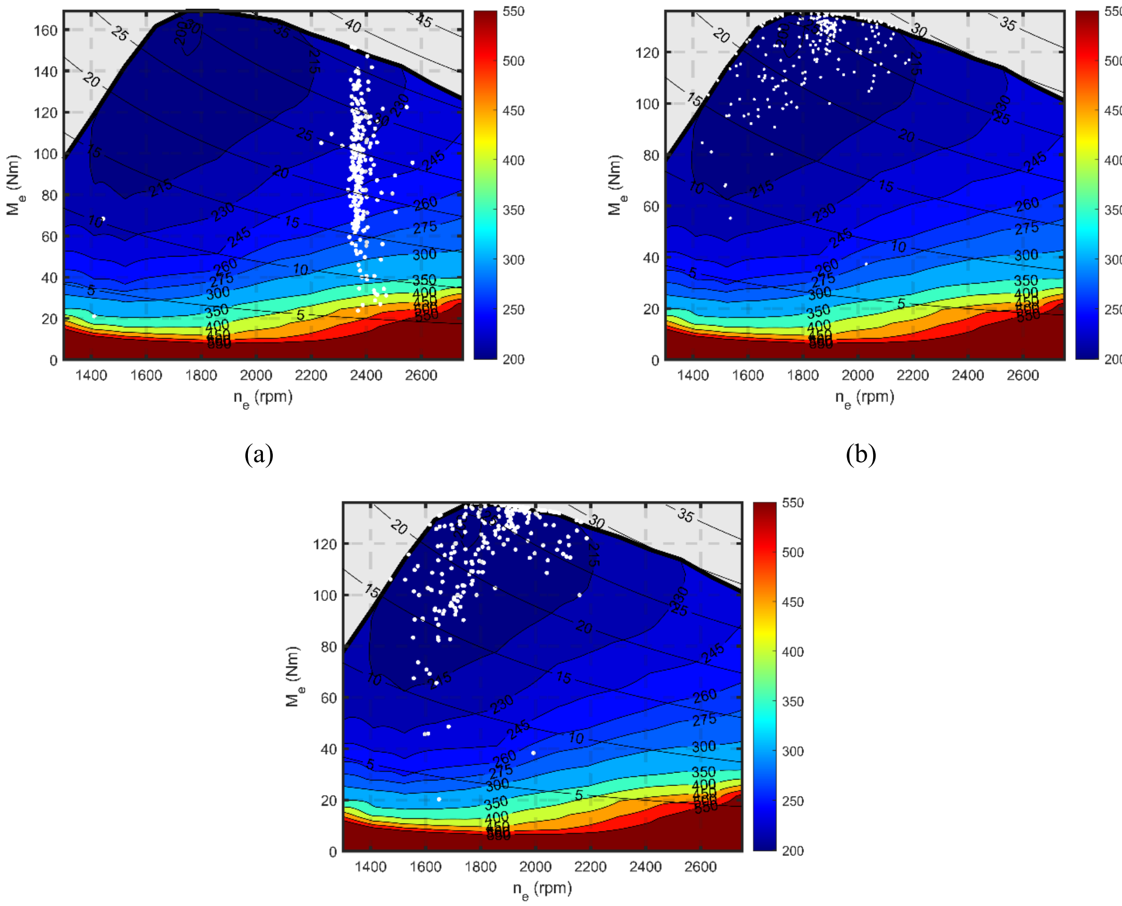

(a) (b)

(c)

Figure 14. Simulated Engine Operation of baseline system (a), Power-split Hybrid (b) and Power-split + Swing hybrid (c)

REFERENCES

[1] M. Vukovic, S. Sgro, and H. Murrenhoff, "Steam - A mobile hydraulic system with engine integration," *ASME/BATH 2013 Symposium on Fluid Power and Motion Control, FPMC 2013*, no. October 2013, 2013.

[2] M. Vukovic, R. Leifeld, and H. Murrenhoff, "STEAM – a hydraulic hybrid architecture for excavators," *Proceedings of the 10th International Fluid Power Conference*, pp. 151–162, 2016.

[3] K. Heybroek and M. Sahlman, "A hydraulic hybrid excavator based on multi-chamber cylinders and secondary control – design and experimental validation," *International Journal of Fluid Power*, vol. 19, no. 2, pp. 1–15, 2018.

[4] J. Zimmerman, E. Busquets, and M. Ivantysynova, "40% Fuel Savings By Displacement Control Leads To Lower Working Temperatures - a Simulation Study and Measurements," in *Proceedings of the 52nd National Conference on Fluid Power*, 2011.

[5] J. Zimmerman and M. Ivantysynova, "Hybrid Displacement Controlled Multi-Actuator Hydraulic Systems," in *The Twelfth Scandinavian International Conference on Fluid Power*, 2011, pp. 952–978.

[6] R. Hippalgaonkar and M. Ivantysynova, "Optimal power management of hydraulic hybrid mobile machines - Part I: Theoretical studies, modeling and simulation," *Journal of Dynamic Systems, Measurement and Control, Transactions of the ASME*, vol. 138, no. 5, 2016.

[7] C. Williamson, "Power Management for Multi-Actuator Machines with Displacement Controlled Hydraulic Actuators," Purdue University, 2011.

[8] M. Bertolin and A. Vacca, "An Energy Efficient Power-Split Hybrid Transmission System to Drive

Hydraulic Implements in Construction Machines," *ASME Journal of Dynamic Systems, Measurement and Control*, 2021.
[9] R. Resch and K. T. Renius, "Continuously Variable Tractor Transmissions," in *Agricultural Equipment Technology Conference*, 2005, no. 29, pp. 1–37.
[10] R. Kumar, M. Ivantysynova, and K. Williams, "Study of energetic characteristics in power split drives for on highway trucks and wheel loaders," *SAE Technical Papers*, vol. 116, no. May 2021, pp. 227–237, 2007, doi: 10.4271/2007-01-4193.
[11] J. D. Zimmerman, M. Pelosi, C. A. Williamson, and M. Ivantysynova, "Energy Consumption of a LS Excavator Hydraulic System," in *Proceedings of the International Mechanical Engineering PCongress and Exposition*, 2007, pp. 1–10.
[12] E. Busquets and M. Ivantysynova, "Adaptive Robust Motion Control of an Excavator Hydraulic Hybrid Swing Drive," *SAE International Journal of Commercial Vehicles*, vol. 8, no. 2, pp. 568–582, 2015, doi: 10.4271/2015-01-2853.
[13] M. Ivantysynova, "Energy Losses of Modern Displacement Machines - A New Approach of Modeling," in *The seventh Scandinavian International Conference onFluid Power (SICFP'01)*, 2001.
[14] B. Carl, M. Ivantysynova, and K. Williams, "Comparison of Operational Characteristics in Power Split Continuously Variable Transmissions," *SAE Technical Paper Series*, no. 2006-01–3468, 2006.
[15] S. Tsai and M. R. Goyal, "Dynamic Turbocharged Diesel Engin Model for Control Analysis and Desig," vol. 95, no. 1986, pp. 81–86, 2019.
[16] J. B. Heywood, *Internal Combustion Engine Fundamentals*, 1st editio. MCGraw-Hill, 1988.
[17] J. Grabbel and M. Ivantysynova, "An Investigation of Swash Plate Control Concepts for Displacement Controlled Actuators," *International Journal of Fluid Power*, vol. 6, no. 2, pp. 19–36, 2005.

NOMENCLATURE

A_A	Linear actuator effective area in the bore chamber
A_B	Linear actuator effective area in the rod chamber
$A_{p,2}$	Secondary unit control piston area
A_p	LS pump control piston area
$A_{v,r}$	Effective flow area in the return port of the flow control valve
A_v	Effective flow area in the inlet port of the flow control valve
F_{spring}	LS pump control piston spring pre-load
I_e	Engine moment of Inertia
I_{out}	Output shaft moment of inertia
K_L	Cylinder internal leakage coefficient
K_{spring}	LS pump control piston spring constant
$M_{1,cmd}$	Desired primary unit torque
M_2	Secondary unit effective torque
$M_{carrier}$	Carrier gear torque
M_{cp}	Charge pump torque
$M_{e,cmd}$	Commanded engine torque
M_e	Engine torque
M_{fric}	Engine friction torque
M_p	LS pump effective torque
M_{ring}	Ring gear torque
M_s	LS pump hydromechanical losses
M_{sun}	Sun gear torque
$M_{sw,s}$	Swing motor hydromechanical losses
M_{sw}	Swing motor effective torque

$P_{e,cmd}$	Commanded engine power
Q_1	Effective flow from/to primary unit
Q_2	Effective flow from/to secondary unit
$Q_{A,sw}$	Swing motor effective flow rate in/out line A
Q_A	Flow from/to the control valve from the A line
$Q_{B,sw}$	Swing motor effective flow rate in/out line B
Q_B	Flow from/to the control valve from the B line
$Q_{R,A}$	Flow through the relief valve connected to the bore chamber
$Q_{R,B}$	Flow through the relief valve connected to the rod chamber
Q_S	LS pump volumetric losses
Q_{bo}	Flow to the LS line
Q_p	LS pump effective flow
$Q_{sw,s}$	Swing motor volumetric losses
$Q_{v,r}$	Flow control valve return flow.
Q_v	Flow from the pump to the users through the flow control valve
V_0	Accumulator total volume
$V_{A,s}w$	Total volume in the swing line A
V_A	Total instantaneous volume in the linear actuator bore chamber
$V_{B,sw}$	Total volume in the swing line B
V_B	Total instantaneous volume in the linear actuator rod chamber
V_d	Cylinder dead volume
V_{line}	Transmission high-pressure line volume
V_p	LS pump maximum volumetric displacement
V_{sw}	Swing motor displacement
i_0	PGT standing gear ratio
$k_{p,2}$	Secondary unit LS pressure control proportional gain
k_p	LS pump adjustment system effective proportional gain
k_{sv}	Servo-valve flow-gain
$k_{v,r}$	Flow control valves flow coefficient in the return port.
k_v	Flow control valves flow coefficient in the inlet port.
n_1	Primary unit speed
$n_{2,ref}$	Secondary unit reference speed
$n_{carrier}$	Carrier gear speed in rpm
n_e	Engine speed
n_{ring}	Ring gear speed in rpm
n_{sun}	Sun gear speed in rpm
n_{sw}	Swing motor rotational speed
p_0	Accumulator pre-charge
p_{hp}	Pressure in the transmission high-pressure side
$p_{A,s}w$	Swing pressure in line A
p_A	Linear actuator bore chamber pressure
$p_{B,sw}$	Swing pressure in line B
p_B	Linear actuator rod chamber pressure
p_{act}	Actuator chamber pressure
p_{ls}	Pressure in the load-sensing line
p_p	LS pump outlet pressure

p_{return}	Pressure in the return line
$x_{p,max,2}$	Secondary unit control piston stroke
$x_{p,max}$	LS pump control piston maximum stroke
x_p	LS pump control piston
x_v	Flow control valve normalized position
y_{sv}	servo-valve normalized position
$\beta_{1,cmd}$	Desired primary unit displacement.
β_2	Secondary unit normalized displacement
β_{cmd}	LS pump fractional displacement for mechanical equilibrium at the control piston
β_p	LS pump normalized fractional displacement
τ_p	LS pump displacement time constant
ω_2	Secondary unit rotational speed in rad/s
ω_e	Engine speed in rad/s
ω_p	LS pump rotational speed in rad/s
Δp_{sw}	Pressure differential across the swing motor
Δp_v	Pressure differential across flow control valves
K	Fluid bulk Modulus
s	LS pump margin
s_c	Compensator spring pre-load
V	Volume at LS pump outlet
γ	Ideal gas polytropic coefficient

The 11th JFPS International Symposium on Fluid Power HAKODATE 2020 Oct. 12-13, 2021 JFPS The Japan Fluid Power System Society

Control of Air Bubble Content in Working Oil by Swirling Flow

Sayako SAKAMA*, Yutaka TANAKA**, Yasuhiro KODERA***, Yoshiaki KITAMURA****

* National Institute of Advanced Industrial Science and Technology
1-1-1 Umezono, Tsukuba-shi, Ibaraki 305-8560, Japan
** Department of Engineering and Design, Hosei University
2-33 Ichigaya-Tamachi, Shinjuku-ku, Tokyo 162-0843, Japan
(E-mail: y_tanaka@hosei.ac.jp)
*** Automotive Components Operations, KYB Corporation, Tokyo 105-6111, Japan
**** Basic Technology R&D Center, KYB Corporation, Tokyo 105-6111, Japan

Abstract. Mixing of air bubbles in the hydraulic oil in hydraulic power transmission systems causes deterioration of the dynamic characteristics of the system, erosion of component, accelerated deterioration of the hydraulic oil, reduction of heat dissipation, and vibration noise. In this paper, a method for control air bubble content by a swirling flow of working oil has been proposed and developed. The amount of air bubbles in the oil flowing out of a bubble separation device is adjusted by controlling the opening and closing of the valve on a vent port of the device. The air bubble content from an output port of the bubble separation device is controlled by the opening time of the vent valve. The validity of the proposed method was experimentally and numerically verified.

Keywords: Air bubble, Bubble separation device, CFD, Hydraulic oil, Swirling flow, Vent port

INTRODUCTION

A few percent of air are dissolved in hydraulic working oils under atmospheric pressure. When the pressure drops locally in hydraulic power transmission circuits, the dissolved air appears in the working oil. Small bubbles due to cavitation stagnate in the hydraulic working oil for a certain period of time, and it takes long time to dissolve again at high pressure or to float and defoam. Air is also mixed from the surface of the hydraulic oil due to the sloshing phenomenon caused by the vibration of the hydraulic circuit and reservoir. Therefore, in the hydraulic working oil in hydraulic power transmission circuits of automobiles, there are many opportunities for air to be mixed in, so 10% to 30% or more of air bubbles are mixed in the working oil. These air bubbles in the hydraulic working oil cause many troubles in hydraulic equipment and are called the third contamination that follows the solid fine particles and water in the oil [1].

Air bubbles in the hydraulic oil reduce the rigidity of the oil and the system response due to sponge effect [2]. It also causes vibration noise [3] and equipment damage [1]. In our previous studies [4], the amount of dissolved air in hydraulic oil can be reduced by actively removing the air bubbles in the oil. As a result, it has been confirmed that the occurrence of cavitation can be reduced. Since one of the causes of failure of hydraulic elements is erosion due to cavitation, reduction of the air bubble content in hydraulic oil prevents damage to the equipment. However, to reduce the performance of the system, the quantitative index of how much air bubbles are contained in the hydraulic oil and how long it takes to reach a failure has not been experimentally clarified. The reason is that it is extremely difficult to accurately measure and control the air bubble content in the hydraulic working oil in real time. To measure the amount of air bubbles in oil, mechanical, optical or electrical methods are available. Schrank et al. [5] compared several methods to determine the amount of mixed air in oil in terms of difficulty of application, accuracy and influence of the measuring systems on the flow in the circuit. Sakama et al. [6] was proposed and evaluated the method for calculating the air volume fraction from measurements of the fluid's effective bulk modulus.

Conventional techniques for removing air bubbles in the hydraulic oil have been passive methods such as releasing air from the surface of oil in the reservoir and adding anti-foaming agents to the hydraulic oil. However, in recent automobiles, the frequency of intermittent operation including stopping the engine is increasing to improve fuel efficiency. The hydraulic pump connected to the engine is also required to start and stop frequently, and the air bubbles in the hydraulic oil stagnant at various parts of the hydraulic circuit and gather to form a large air mass. These air bubbles cause noise at the beginning of startup and instability of the operation of the hydraulic system. Quantitative elucidation of the effect of air bubble content in the hydraulic oil on the hydraulic component is an urgent issue.

In this paper, a method for control air bubble content by a swirling flow of working oil has been proposed and bubble content adjustment system has been developed. A bubble separation and elimination device from the working oil [7][8] has been used to control the air bubble content. The amount of air bubbles in the oil flowing out of the bubble separation device is adjusted by controlling the opening and closing of the valve on a vent port of the device. The air bubble content from an output port of the bubble separation device is controlled by the opening time of the vent valve. The validity of the proposed method is experimentally and numerically verified.

BUBBLE SEPARATION DEVICE BY SWIRLING FLOW

Structure and principle of the bubble separation device is shown in Figure 1. Working oils with entrained air bubbles tangentially flow into a tapered tube chamber from two inlet ports and form swirling flows that circulate the fluid through the flow passage. The swirling flow accelerates to the downstream. Small bubbles are trapped and collected near the vicinity of the central axis in the tapered tube in a short time of about 100 ms by the swirling flow [9]. When some back pressure is applied on the downstream side of the device, the collected bubbles are pushed out from the opposite side through a vent port. The amount of air bubbles to be separated and removed from the working oil can be adjusted by providing a valve for opening and closing at downstream side of the vent port and controlling the opening and closing time of the valve. By using this principle, it is possible to construct a system that controls and adjusts the bubble content in the hydraulic oil on the downstream side of the device.

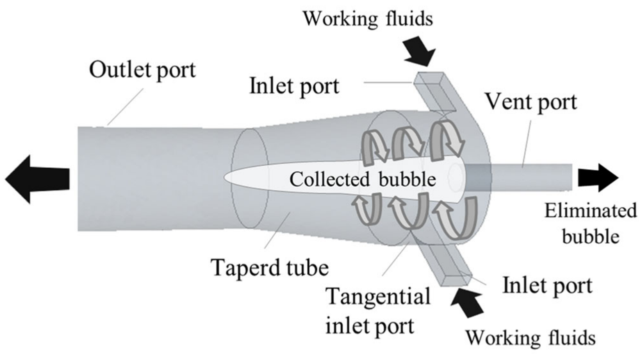

Figure 1. Principle and structure of bubble separation device

DESIGN AND MANUFACTURE OF BUBBLE SEPARATION DEVICE

The goal of the method verified in this study is to adjust the air bubble content in the oil in the range of 1 to 40%. The performance of the bubble separation device must be sufficiently ensured within this bubble content range. The performance of the device depends on the shape and dimensions of the inlet ports and the diameter of vent port [10]. In the design of the bubble separation device, the selection of shape parameters under the flow conditions is very important to realize the method of adjusting and controlling the bubble content in the working oil.
The numerical simulation for the swirl flow in the bubble separation device was carried out using CFD software STAR-CCM+. Geometry of the bubble separation device is shown in Figure 2. To select the optimum shape parameters of the bubble separation device, the numerical analysis was performed under the conditions of air particle diameter of 0.1 mm, bubble content in the hydraulic oil of 20%, 30% and 40%. A density of the oil is 0.85 g/cm^3, a kinematic viscosity is 9.19 mm^2/s, and a flow rate is 30 L/min.

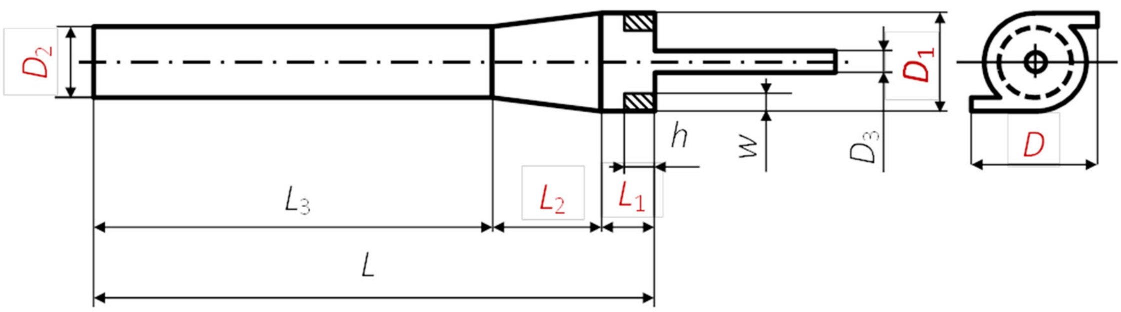

Figure 2. Geometry of bubble elimination device

Figure 3 shows typical simulation results of air particle content in the bubble separation device for bubble content of 20%, 30%, and 40% respectively. It was confirmed that the air particles ware separated and removed from the vent port side of the bubble separation device under all conditions. As a result of numerical analysis, the optimum shape parameters of the bubble separation device ware selected as tabulated in Table 1.

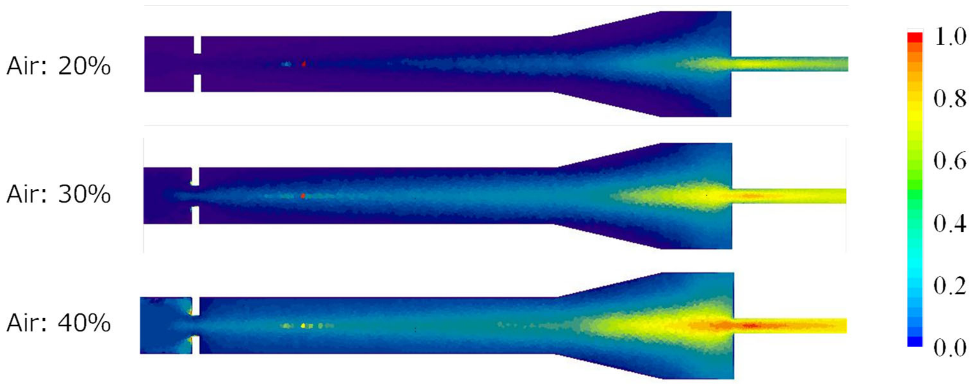

Figure 3. Numerical simulation of air particle content in bubble separation device

Table 1. Shape parameters of the bubble separation device

Shape parameters	Dimensions [mm]
Inner diameter of tapered tube D_1	30.0
Inner diameter of downstream D_2	16.0
Inner diameter of vent port D_3	4.4
Total length L	150.0
Inlet tube length L_1	20.0
Tapered tube length L_2	30.0
Downstream tube length L_3	100.0
Width of inlet port w	2.18
Height of inlet port h	4.35

Figure 4 (a) shows the structure and dimensions of the bubble separation device designed and manufactured for the experiment, and Figure 4 (b) shows a photo of the transparency device manufactured. The experimental bubble separation device was designed separately so that the dimensions of the inlet ports and the diameters of the outlet

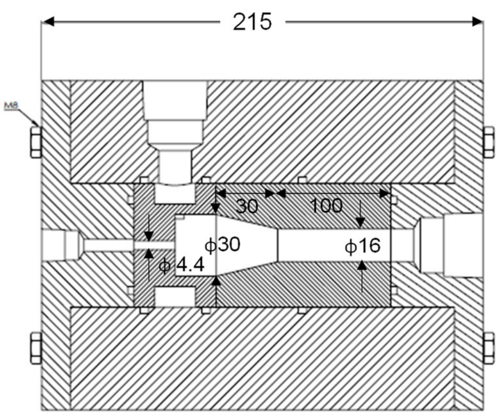

(a) Dimensions of experimental bubble separation device

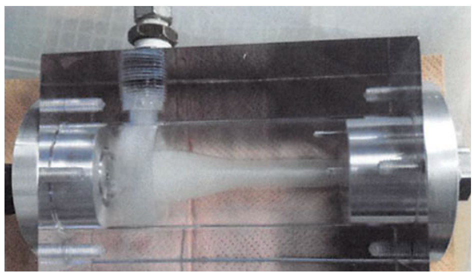

(b) Transparency type of bubble separation device

Figure 4. Bubble separation device designed and manufactured for the experiment

tube and the vent port could be adjusted according to the experimental conditions. Each element designed by dividing was inserted into a transparent housing, fixed from both sides, and integrated. To visualize the flow inside the device, the housing and some of the elements were made of transparent acrylic.

PRELIMINARY EXPERIMENT

Preliminary experiments were carried out to confirm and verify the performance of the bubble separation and the bubble content control method of the manufactured device.
Figure 5 shows a configuration of hydraulic circuit used in the preliminary experiment. The bubble separation device was installed in the oil circulation circuit, and a manual needle valve was installed on the vent port side of the device and a Coriolis flow meter was installed on the outlet side of the device. Air bubbles were forcibly blown into the working hydraulic oil from the delivery side of the pump by an air compressor. The pressure at the inlet line was set at 0.5 MPa. The needle valve was manually adjusted while mixing air into the oil. The density of the oil on the downstream side of the bubble separation device was measured with respect to the opening rate of the needle valve and the air content rate in the oil was estimated by the Coriolis flow meter. The volumetric flow rate was 12.4 L/min in case of closed the needle valve. The oil temperature was kept at 40 ± 1 ℃.
Figure 6 shows the results of the preliminary experiment. Due to the specifications of the needle valve, it is difficult to precisely adjust the flow rate to the vent port depending on the valve opening. The bubble removal rate of the bubble separation device increased by slightly opening the needle valve. As a result, the air bubble content on the outlet line of the device sharply decreased with respect to the opening rate of the needle valve. However,

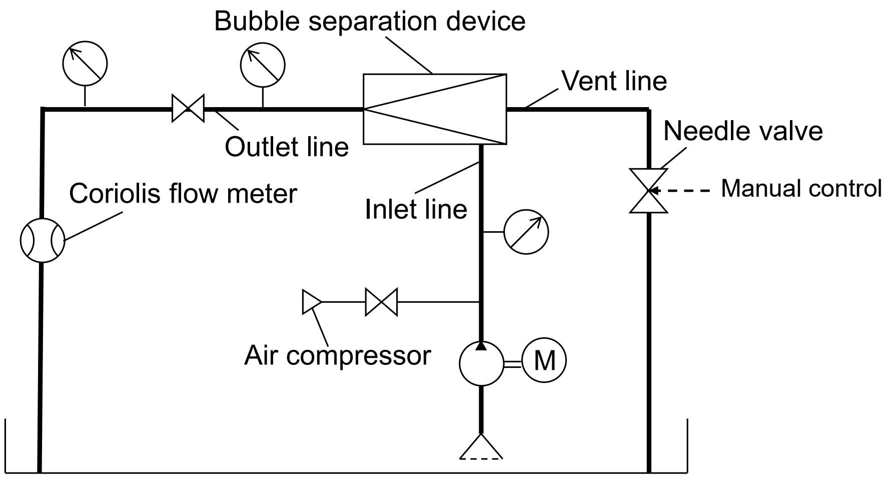

Figure 5. Experimental hydraulic circuit for manual control of air bubble content

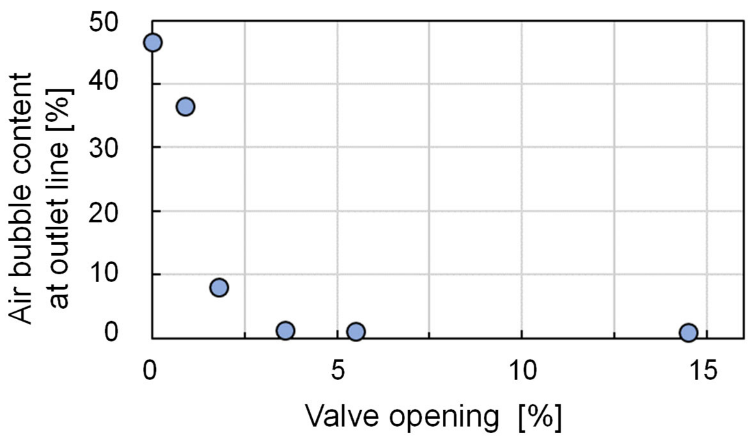

Figure 6. Air bubble content at outlet line by manual control of the needle valve at the vent line

the validity of the basic method of controlling the amount of air bubbles on the outlet side was confirmed by adjusting the opening of the valve on the vent port side of the device.

BUBBLE CONTENT ADJUSTMENT EXPERIMENT

Based on the results of the preliminary experiment, an on-off solenoid valve was installed on the vent port and experiments were carried out to adjust the air bubble content in the oil on the outlet line by controlling the valve switching time and timing.
Figure 7 shows the configuration of the hydraulic circuit used in the adjustment experiment. A bubble separation device was installed in the same circulation circuit as in Figure 5, and the Coriolis flow meter was installed on the inlet line and an in-line impedance type of the bubble content measurement sensor was installed on the outlet line. The bubble content of each of the inlet and outlet lines of the device was measured in real time and stored in a data logger. Air was mixed into the oil by opening the suction side of the pump to the atmosphere. The on-off solenoid valve was installed on the vent line of the bubble separation device. The opening and closing time of the on-off solenoid valve was controlled by a sequencer using a relay according to the deviation between the output value of the bubble content sensor on the outlet line and the target value of the bubble content.

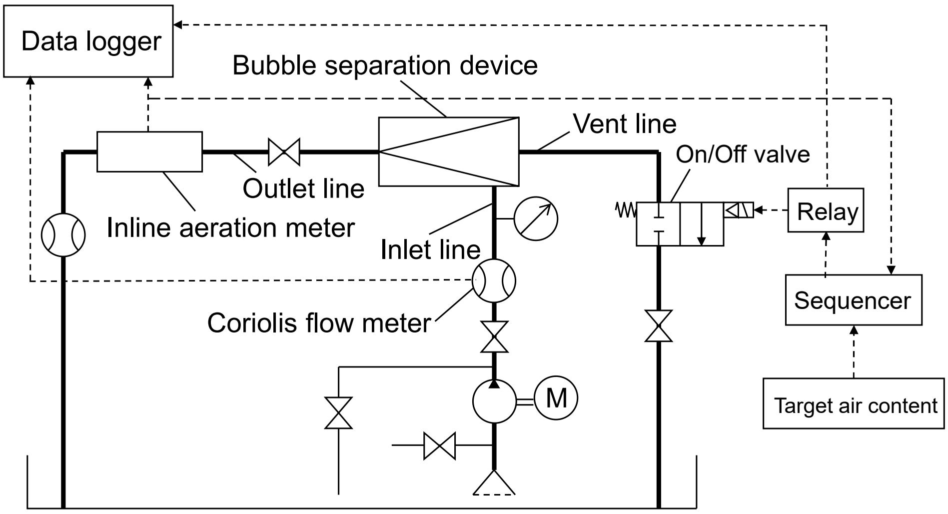

Figure 7. Experimental hydraulic circuit for automatic control of air bubble content

Figure 8 shows a typical example of the adjustment results of the air bubble content. The measured pressure and volumetric flow rate at the inlet line were 0.4 MPa and 11 L/min, respectively. The air bubble content of the inlet line was set to about 9%, the air bubble content of the outlet line when the vent line was closed was set to about 28%, and the target value of the bubble content was set to 18%. The oil temperature was kept at 37 °C. The cycle of opening and closing time of the on-off solenoid valve was adjusted to 1 s, and the duty ratio was adjusted in the range of 10% to 100%. From the measurement results, if the duty ratio was small, the adjustment accuracy and response slightly decreased. On the other hand, the average value of the adjustment results from 19.2 s to 25 s after settling near the target value is 16.8% to 19.7% at each duty ratio. This indicates that the relative error with respect to the target value is within ± 9.4%.

CONCLUSIONS

In this paper, we proposed and developed a bubble amount control system that can arbitrarily adjust the amount of bubble contained in hydraulic oil using the technique of separating air bubbles in oil by swirling flow. We also experimentally verified the validity of the control method. It was experimentally confirmed that the air bubble content on the outlet line of the device can be controlled by adjusting the flow rate on the vent line of the bubble separation device. In these experiments, it was also confirmed that precise adjustment according to the duty ratio was difficult because the response of the on-off solenoid valve on the vent line was slower than the response of the separation performance of the bubble separation device. In the future, it will be necessary to consider countermeasures using high-speed proportional valves instead of the on-off solenoid valve.

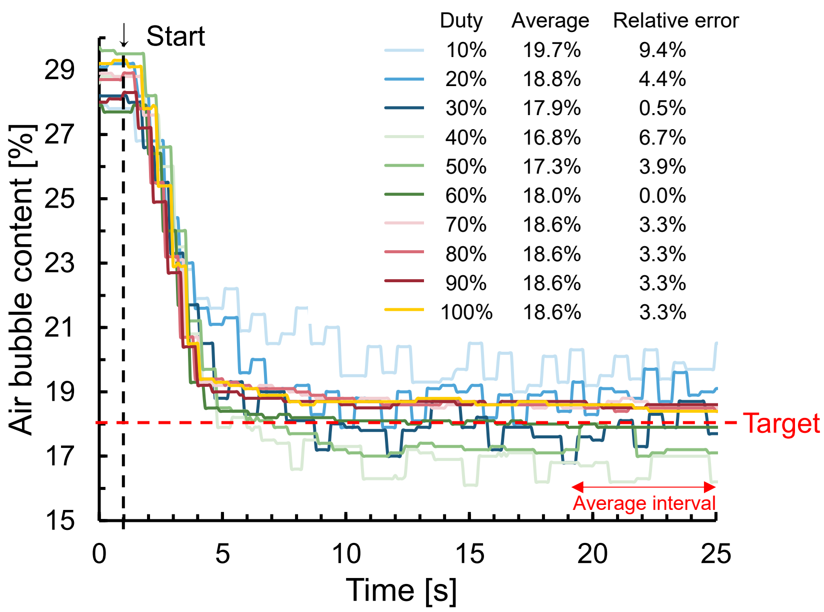

Figure 8. Adjustment results of air bubble content at outlet line by automatic control of vent line

ACKNOWLEDGMENTS

We express appreciation the technical support, Mr. Iori Masuhara of the master course student in the Graduate School of Hosei University. This research was supported by the JSPS KAKENHI Grant Number 26420086 and 18K03916, the Precise Measurement Technology Promotion Foundation the MIKIYA Science and Technology Foundation, and a grant-in-aid from the Ministry of Economy, Trade and Industry, Japan. The numerical simulation was carried out by using the facility and software at the Research Center for Computing and Multimedia Studies, Hosei University.

REFERENCES

1. CANTER, N., Foam, Dealing with a Persistent Problem, Tribology & Lubrication Technology, December 2015, pp.24-38.
2. GHOLIZADEH, H., BURTON, R., SCHNOENAU, G., Fluid Bulk Modulus: A Literature Survey, International Journal of Fluid Power, 2011, Vol.12, No.3, pp.5-15.
3. ERICSON, L., PALMBERG, J., Measurement of Free Air in the Oil Close to a Hydraulic Pump, Proc. 7th International Symposium on Fluid Power TOYAMA, 2008, P2-12.
4. GOTO, H., SAKAMA, S., SUZUKI, R., TANAKA, Y., Reduction of Cavitation Damage by Elimination of Bubbles in Oil Reservoir, Proc. FLUCOME2013, 2013, OS1-02-4.
5. SCHRANK, K., MURRENHOFF, H., STAMMEN, C., Investigation of Different Methods to Measure the Entrained Air Content in Hydraulic Oils, ASME/BATH 2014 Symposium on Fluid Power and Motion Control, Bath, United Kingdom, 2014.
6. SAKAMA, S., KITAZAWA, Y., SUGAWARA, Y., TANAKA, Y., Estimating the Air Volume Fraction in Hydraulic Oil by Measuring the Effective Bulk Modulus, 11th IFK International Conference Proceedings, 2018, Vol.3, pp.79-85.
7. SAKAMA, S., GOTO, H., HIGASHI, H., SUZUKI, R., TANAKA, Y., Air Bubble Separation and Elimination from Working Fluids for Performance Improvement of Hydraulic Systems, Proc. IFPE 2014, 2014, Paper No. 27.1.
8. TANAKA, Y., KISHI, Y., SAKAMA, S., Selective Separation of Air Bubbles from Working Oil by Bubble Elimination Device, Proceeding of the 10th International Conference on Fluid Power Transmission and Control (ICFP2021), Hangzhou in China, 2021, S2401, pp.703-706.
9. TANAKA, Y., SUZUKI, R., ARAI, K., IWAMOTO, K., KAWAZURA, K., Visualization of Flow Fields in a Bubble Eliminator, Journal of Visualization, 2001, Vol.4, No.1, pp.81-90.
10. SAKAMA, S., TANAKA, Y., SUZUKI, R., Optimization of Bubble Eliminator by Numerical and Experimental Investigation, International Journal of Automation Technology, 2012, Vol.6, No.4, pp. 418-425.

The 11th JFPS International Symposium on Fluid Power HAKODATE 2020 Oct. 12-13, 2021 JFPS The Japan Fluid Power System Society

Pulse Tests on Additive Manufactured Valve Blocks – Damage Analysis and New Design Possibilities

Sebastian DEUSTER*, Stefan AENGENHEISTER*, Gunnar MATTHIESEN*, Katharina SCHMITZ*

*Institute for Fluid Power Drives and Systems
RWTH Aachen University
Campus-Boulevard 30, Aachen, 52074 Germany
(E-Mail: sebastian.deuster@ifas.rwth-aachen.de)

Abstract. Additive manufacturing processes are currently experiencing an enormous upswing in different areas. The demand for more efficient and powerful hydraulic systems has risen rapidly in recent years. Due to cost savings and resource conservation, there are always efforts to reduce the power-to-weight ratio of hydraulic components. Especially in areas where weight savings lead to large performance savings, such as the aerospace industry, additively manufactured components in hydraulic systems are becoming increasingly popular. This paper deals with the testing of additively manufactured hydraulic manifold blocks with regard to their strength values. For this purpose, the components are experimentally loaded with pressure pulses until they fail. Subsequently, the cause of fracture is to be determined by means of a surface examination and thus a statement made about the suitability of additively manufactured components in hydraulic systems. These considerations show the potential of additive manufacturing for weight and material savings in hydraulic applications.

Keywords: additive manufacturing, pulse tests, material testing, design optimization, fatigue strength

INTRODUCTION

Due to their potential in lightweight construction and the possible component complexity, additive manufacturing processes are currently experiencing a tremendous upswing in all possible areas. The demand for increasingly efficient and powerful hydraulic systems has risen rapidly in recent years. As a result of cost savings and resource conservation efforts are constantly being made to reduce the power-to-weight ratio of hydraulic components. Especially in areas where weight savings lead to large power savings, such as the aerospace industry, additively manufactured components are experiencing a growing popularity in hydraulic systems. In addition to the material savings which can be achieved, the advantages of additive manufacturing also lie in the freedom of design. In its current state, additive manufacturing is an established tool especially for rapid prototyping. Nonetheless, series production is realized in some applications which are exposed to operational stress such as valve blocks in aerospace. The most common method for manufacturing additive components is selective laser melting (SLM), which is based on using a laser to melt layers of metal powder.
In hydraulic line systems, for example, pressure loss savings can be achieved by adapting the geometry to the fluid flow. However, material parameters such as fatigue strength of these products are difficult to record due to their selective design and are therefore often not sufficiently known.
The task in this paper is to test and compare additively and conventionally manufactured hydraulic distributor blocks with respect to their strength values. For this purpose, the components are experimentally loaded with pressure pulses until their failure. Afterwards the cause of the fracture is determined by means of a surface investigation and thus a statement is to be made about the suitability of additively manufactured components in hydraulic systems. These considerations demonstrate the potential of additive manufacturing for weight and material savings in hydraulic applications. It is also possible to investigate whether the strength of the additively manufactured blocks can be increased by minor geometry optimizations.
All blocks are tested simultaneously in a developed test rig. The additive manufactured blocks are produced by selective laser melting (SLM). A machining of the threads and holes of these components is necessary to achieve the same function and functional surfaces as the components of the conventionally manufactured blocks. To cover statistical uncertainty three versions of the manifold block, nine units are tested. Initially, the blocks are loaded with static pressure. The pressure is increased by 10 bar at fixed intervals until a maximum pressure of 700 bar is reached. The pulse loading of the specimens follows the static tests. As test methods for the pressure pulse, standards DIN EN 2624 [10] and DIN EN ISO 19879 [12] are applied. The pressure level of the pulses is above the range of conventional hydraulics between 500 and 600 bar. The test is stopped at block failure, caused by visible damage or leakage due to small cracks in the component. The damage is detected by means of a visual inspection.

Another damage analysis is carried out after the dynamic tests. Material tests are conducted to evaluate the material structure of the components. Non-destructive and destructive methods are used. In addition, the geometry changes resulting from the pulse loads are examined. The goal is to analyze the differences between the additively and conventionally manufactured valve blocks with regard to material failure. This allows studies to be carried out in subsequent investigations on process optimization in the manufacturing of additive manufactured hydraulic components, which deal with the design and structure.

STATE OF THE ART

Currently, conventionally manufactured components are mostly made from wrought material using cutting methods. This type of process induces a high loss of non-reusable material. In this aspect, additive processes have the advantage of involving minimal post-processing that could lead to loss of material. In accordance with DIN 8580 [1], additive manufacturing is considered a primary shaping process. Additive manufacturing is established as a reliable method for *rapid prototyping*.

Another advantage of additive manufacturing is the use of high-temperature resistant materials such as Inconel 718 [2]. This material is very difficult to form and machine so that shaping by conventional manufacturing methods is only possible to a limited extent. In addition, a functional integration of components can be carried out. This can reduce the assembly complexity and the number of joints in an assembly.

For loaded components however, additive manufacturing has not been applied until recently due to the lack of corresponding data and experience [3]. In hydraulic applications, the potential exists above all to achieve a reduction in weight and optimizations of flow with the aid of components manufactured using additive manufacturing. To this end, suitable components in applications are constructively optimized with regard to the possibilities of additive manufacturing in order to exploit the advantages. Notable applications in recent years include a valve block in the *Airbus A380* and the series production of additively manufactured components at *Liebherr-Aerospace* [4],[5]. Another example is an additive manufactured cartridge valve from *Parker Hannifin*. An additive geometry optimization in this example led to a weight reduction of 42% and at the same time the flow rate was increased by 35% while maintaining the pressure drop of the valve. [6]

Among various methods of additive manufacturing, selective laser melting (SLM) is most commonly used. Therefore a laser is used to melt layers of metal powder. After one layer is melted and thereby bonded, more powder is added, and the melting process is repeated for the next layer. At the end of the process, excess powder can be removed and reused [3], [7]. Possible materials for the SLM process include titanium, aluminum, magnesium, and stainless steels [7]. In comparison to injection molding, SLM is advantageous because it avoids the costly manufacturing of a mold. Further notable benefits are the automated manufacturing on the basis of a CAD file and various options for reducing material usage. Some possible options to reduce material usage are the afore-mentioned removal of excess material, lightweight design for the interior structure, and taking advantage of the design flexibility to reduce material usage in specific locations of the component [8].

Up to this point, mechanical experiments on additively manufactured components have been limited to tensile and notch impact testing. Predominantly, titanium alloys as well as steel-, nickel-, and aluminum-based alloys were tested. As evident from Figure 1, the manufacturing method has a significant influence on the dynamic durability of the component. The component quality is dependent on layer thickness, laser power, and the selected post-processing method. Furthermore, it has been shown that pre-heating the powder can reduce manufacturing defects in the final product. [9]

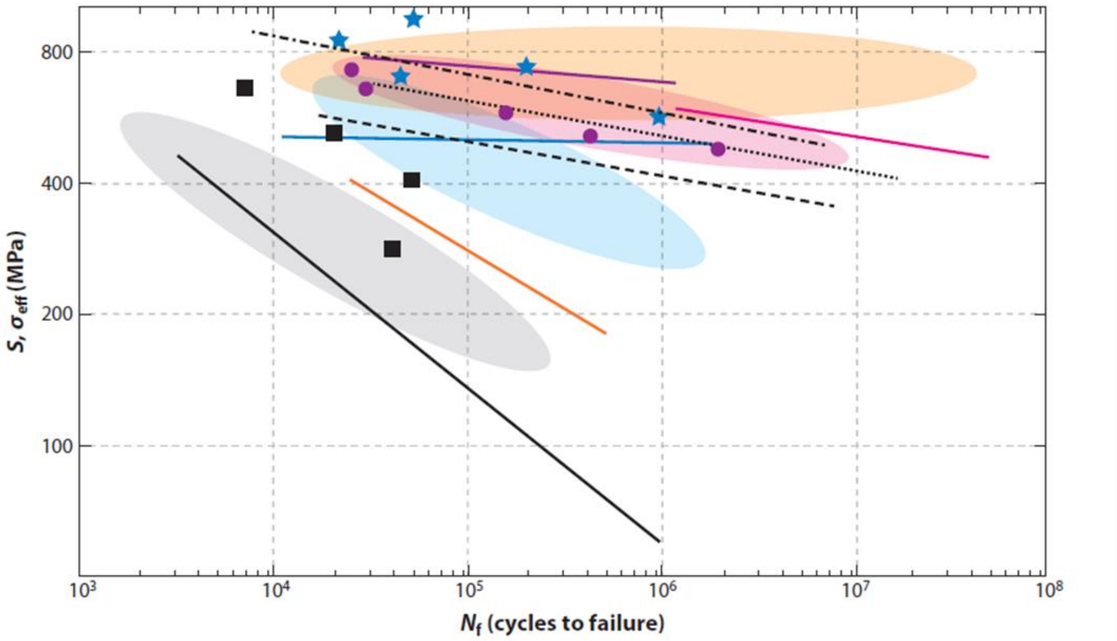

Laser: HIP at 920°C/2 h/100 MPa, processed surface
Laser: no treatment, unprocessed surface
Laser: 3h at 650°C, unprocessed surface , R = 0,1
Laser: no treatment, processed surface
Laser: 4h at 650°C, processed surface
MMPDS 2010: 3 inch cast, processed surface, R = 0,1
MMPDS 2010: forged, annealed, processed surface, R = 0,1
MMPDS 2010: forged, precipitation hardened, processed surface, R = 0,1
EBM: no treatment, processed surface
EBM: no treatment, unprocessed surface
EBM: HIP at 920°C/ 2h, processed surface
Laser metal forming, laser wire feed: heat treated and unprocessed surface
EBM: optimized, no treatment, unprocessed surface, R = 0,1
EBM: optimized, processed surface, R = 0,1
EBM: no treatment, processed surface, R = 0,1

Figure 1. Tensile strength dependency on manufacturing method [9]

Standardization of Pulse Testing

Concerning pulse testing, several standardizations exist. The following three standardizations will be outlined more closely: DIN EN 2624 [10], DIN ISO 6772 [11], and DIN EN ISO 19879 [12].
Experiments based on DIN EN 2624 are designated for the testing of passive components. A pressure increase rate is defined between two points (10% and 90% of maximum pressure respectively) that may not exceed 14,000 bar/s. One test consists of 300,000 cycles at a rate of one to five cycles per second. A constant fluid temperature equivalent to ambient temperature is maintained throughout the experiment. Testing is concluded by inspecting the component for fissures and structural failures.
DIN ISO 6772 is a standardization for the testing of tubes, pipes, and screwed components. DIN ISO 6772 differs from DIN EN 2624 in regard to pressure profile and fluid temperature. One pressure maximum above 110% of the operating pressure is permitted within the first 15% (timewise) of each cycle. The maximum pressure in relation to the operating pressure and depends on the pressure class and the nominal outside diameter and is defined within the standardization. The pressure increase rate is defined in the same way as in DIN EN 2624 and its upper and lower limits are likewise defined within DIN ISO 6772. Before any test, it is necessary to keep the system at testing temperature for one hour. Throughout the testing cycle, the temperature is varied in a defined sequence.

DIN EN ISO 19879 serves as a standardization for the testing of metallic pipe connections, screw-in parts, and flanges. The basic requirement is for the tested component to be uncoated and have a hardness between 35 HRC and 45 HRC. The maximum pressure may not exceed 133% of the operating pressure and the pulse frequency must have a value between 0.5 Hz and 1.25 Hz.

APPROACH AND TESTING

For the investigations on the test bench, three different variations of the aluminum valve blocks were examined. Figure 2 shows the different types. A conventionally manufactured block (1), an additively manufactured replica of the conventionally block (2) and an additively manufactured version with reduced material usage (3) were subject of the testing.

Figure 2. Tested valve block variants

Block 1 was made from 6061-T651 aluminum at *SUN Hydraulics* [13]. Blocks 2 and 3 were additively manufactured at *Aachen University of Applied Sciences (FH Aachen)* using an AlSi10Mg alloy with a layer thickness of 50 µm. The parts were produced by a selective laser melting process.
Due to the limited amount of available valve blocks, an initial static test was conducted. Using this test, a preliminary estimation of the upper pressure limit for the subsequent dynamic testing could be obtained.
In Figure 3 the test rig is shown. A radial piston pump (1) provides the necessary static pressure. The suction line is prefilled by a gear pump. Pipes guide the oil to the test specimen carrier where the fluid flow is distributed between up to six test blocks (3). The correct pressure and a uniform pressure load distribution are ensured by the use of three pressure sensors and two pressure limitation valves within the valve block.
The pump (1) provides a steady fluid flow. In order to maintain a constant pressure, it is necessary to lead the accumulating oil back to the tank in a controlled manner. Pressure oscillations are damped by the accumulator (4).
The static pressure has an initial value of 70 bar that is maintained for ten minutes. After each test pressure that is conducted without any mechanical failure, the pressure is increased by 10 bar. This procedure is carried out until mechanical failure of the block or as soon as the defined upper limit of 700 bar is reached. Pressures above 700 bar would put the remaining components of the test rig at risk and must therefore be avoided.
The locations of the sensors are indicated in Figure 3. A 3/2 directional valve (2) controls the pressure pulses by connecting the tested blocks to the tank and accumulator (4) in alternation. Pressure sensors (Z1, Z2) on the bottom of the pulse block are used to monitor the intensity of the pressure pulses. Pressure sensor S determines the pressure in the accumulator and defines the connection between pump and test blocks.
The returning line from the directional valve to the tank includes a filter (6) that removes contaminations. The pulse block contains a pressure relief valve (5) to ensure that the pressure does not exceed the maximum permitted value. The pressure at the back end of the test specimen is measured in Z2 and continuously compared with the values from Z1. This ensures that all blocks are exposed to the same pressure. The flow directions as well as the motor speed can be controlled. Most of the components are connected by flexible hoses, whose deformation enables the compensation of the pressure variations.

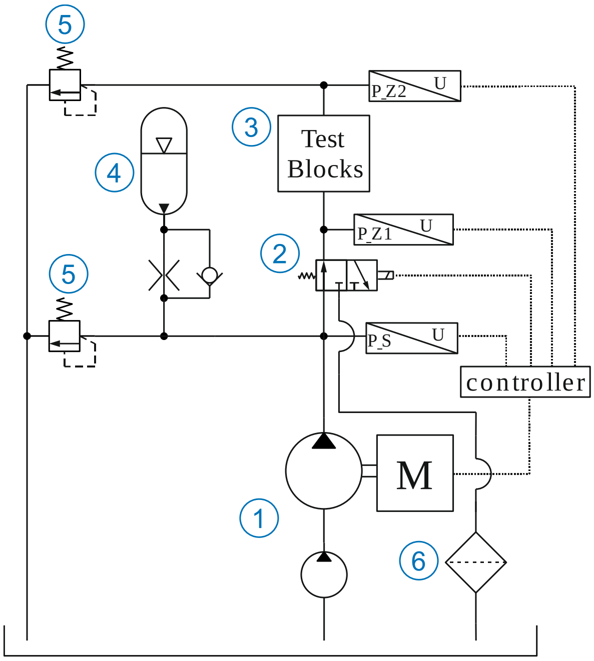

Figure 3. Test bench setup

Among the afore-mentioned standardizations, DIN EN 2624 [10] was selected. This standard was used because the blocks to be tested correspond to the passive hydraulic components described in the standard. Components such as liquid distributors are mentioned here. Furthermore the pressure curve can be represented by the test bench. The pulse frequency can also be covered by the test bench.
The corresponding pressure profile is given in Figure 4. The framework conditions of the standard have already been described in the section ‘standardization of pulse testing’.

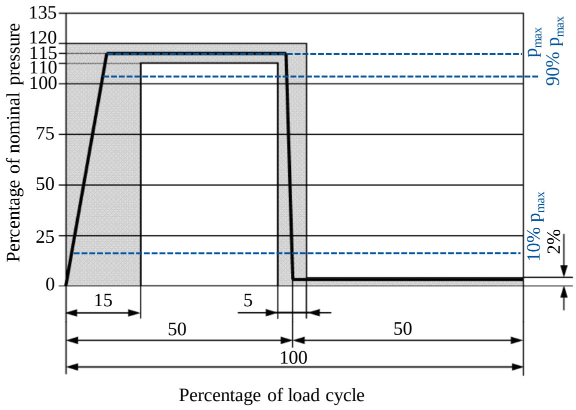

Figure 4. Pressure profile DIN EN 2624 [10]

Because the pulse frequency is not well defined within the standardization, a frequency of 1 Hz was chosen so that all three standardizations previously described are satisfied. An HLP ISO VG 46 was used as the pressurized fluid [14]. To calibrate the test bench and remove air from the system, approximately 100 pulses at 50% of the testing pressure were applied before the experiment. The initial pressure of the dynamic test was defined in accordance with the results of the static test. To achieve control of the system, the sensor measurements are evaluated with the measurement computer. The sensors S and Z2 provide the current pressure in pulse block, accumulator, and distributor block. As soon as sensor S indicates that the testing pressure has been reached in the accumulator, the accumulator is connected to the tested valve blocks for 50% of one impulse duration. At the end of this time interval, pulse block and valve block are separated again. Pressure builds up in the accumulator and the cycle is repeated. The testing pressure can be adjusted by changing the pressure at which the pulse block switches the flow direction. The frequency is a function of the pressure build-up time and increases as the motor speed increases. [10]
Figure 5 illustrates the pressure course during the pulse test. Recorded are the pressure of the end of the test specimen carrier (Z2) and the accumulator pressure (S). In the upper diagram respectful 20 seconds of the pulse

testing are shown. The pulse pressure was 550 bar. It can be seen that a uniform and constant course of the pulse length and frequency was achieved. The average pulse frequency of this recording is 0.95 Hz.
The figure below shows a detailed representation of the pressure curve over a period of one second. It can be seen how the pressure in the accumulator drops abruptly when the directional control valve is opened and the accumulator is connected with the test blocks. Immediately afterwards a pressure peak (Z2) of 564 bar in the test specimen carrier occurs. The oil volume of the accumulator fills the test specimen carrier and the test blocks, before the valve opens in the direction of the tank. The pulse length is about 0.5 seconds. The pressure build up time is 28,305 bar/s and is therefore within the validity range of DIN EN 2624 [10].

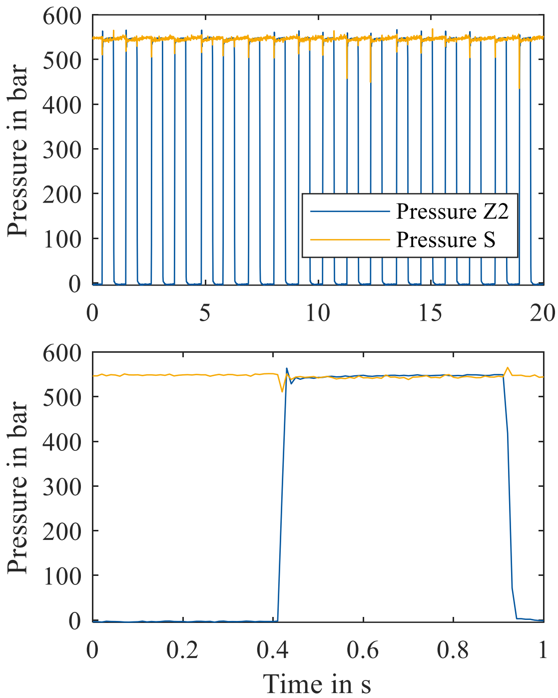

Figure 5. Pressure distribution and close up

INTERPRETATION OF TEST RESULTS

The purpose of the static tests was to estimate the stress limit of additive manufactured in comparison to conventionally manufactured valve blocks. All three test specimens were able to withstand the upper limit of 700 bar under static pressure. From this test, it was concluded that the initial dynamic pressure could be increased to a larger value than the preliminary limit of 210 bar. [13]
For the dynamic tests, it is essential to consider the geometrical boundary conditions. The threads on the upper part of the valve block are incomplete as they are interrupted by the fluid duct. To ensure the sealing of the threads, a stopper must be inserted. The stopper is at risk of unfastening under dynamic stress, so a thread-locking fluid was employed to increase the time until the sealing was breached.
During the test cycle, it proved to be impossible to maintain the desired frequency of 1 Hz. The volume flow of the pump could not refill the accumulator within a short enough time, so it took longer to regain the testing pressure after each impulse. Other factors such as oil temperature, amount of simultaneously tested valve blocks, and residue air in the system can complicate the matter. The complication was solved by manually controlling the pump during the test cycle. The frequent changing of the valve blocks caused more air to enter the system and further complicated a reliable pressure control. Ultimately, the valve blocks were loaded with frequencies between 0.7 Hz and 1.1 Hz. As for the peak pressure, a sufficient accuracy was achieved. For a target pressure of 550 bar, the actual pressure had a value between 548.1 bar and 553.1 bar.
The static tests showed that an initial pressure far greater than the stress limit is necessary to cause a failure. Therefor for the first pulse tests, a pressure of 600 bar was selected. The additively manufactured valve block with optimized geometry lasted for less than 5% of the impulses of the additively manufactured valve block without optimization and was therefore excluded from test series 2 and 3. Test series 2 and 3 were carried out at 550 bar and 500 bar respectively.
The conventionally manufactured valve block exhibited the expected behavior; as the pressure was decreased, the amount of impulses endured increased. For the additively manufactured valve block however, the mount of

endured was roughly the same for all tested pressures. The results were summarized in a Wöhler diagram in Figure 6.

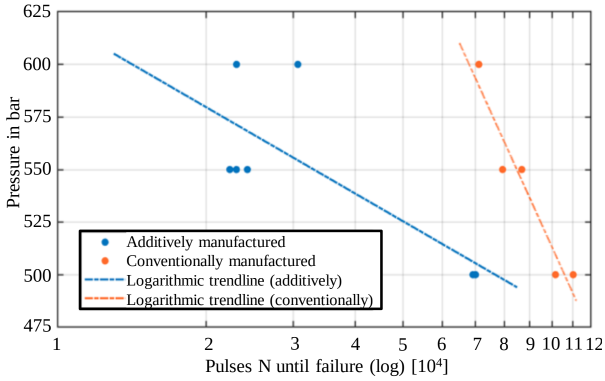

Figure 6. Wöhler diagram

All tests concluded with the same mechanical failure. The damage pattern is shown in Figure 7. In the lower picture, the crack formation has been visualized in red using a crack detection agent. Each failure started with a fracture at the incomplete section of the threads which grew inwards after each subsequent impulse. Differences between the different test specimens could be found regarding the consequences from the failure. For the conventionally manufactured valve block and the additively manufactured valve block without optimization, the fracture eventually reached the uppermost section of the threads and the fluid began to leak. For the additively manufactured valve block with optimized geometry, the fracture experienced rapid growth and caused the fluid to be sprayed from the leakage.

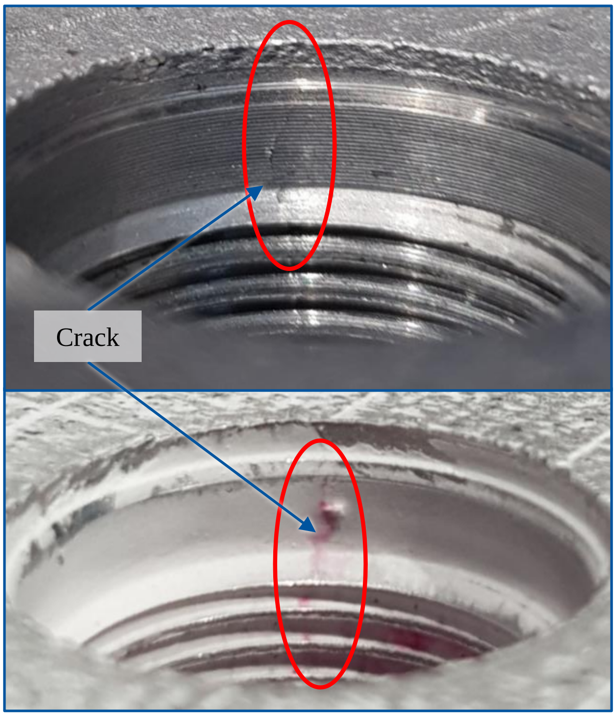

Figure 7. Damage pattern

CONCLUSION AND OUTLOOK

The project goal was to determine the differences between conventionally and additively manufactured valve blocks and to conclude a statement on the suitability of additive manufacturing in hydraulics.
The experiments showed that an additively manufactured component has a lower stress tolerance than its conventionally manufactured counterpart with identical geometry. This result is in accordance with the initial

expectations. It is worth mentioning that exploiting the advantage of material saving by using an optimized geometry further increases the risk of component failure.
Nonetheless, additive manufacturing can be advantageous. The pressures that were used in the tests were larger than the pressures typically encountered in hydraulic systems. At commonly lower pressures, the difference between conventional and additive manufacturing may potentially be neglected. Another advantage is the possibility of post-processing which can eliminate cause of failure. Material usage can also be reduced by employing a FEM analysis to identify points of mechanical failure. Given that all of the valve blocks exhibited damage in the same location, this appears to be a promising option. Using additive manufacturing, it may be possible to reinforce the critical locations and thus prevent crack propagation and enable a better fatigue strength.
The next step is the closer examination of the afore-mentioned aspects. The experiment has shown that additively manufactured components can withstand loads in the same order of magnitude as conventional components. Further research may enable an improvement upon conventional manufacturing.

REFERENCES

1. DIN 8580: 2020, Manufacturing processes - Terms and definitions, division.
2. VDM METALS INTERNATIONAL GMBH: VDM Alloy 718: Nicrofer 5219Nb. https://www.vdm-metals.com/fileadmin/user_upload/Downloads/Data_Sheets/Datenblatt_VDM_Alloy_718.pdf, 02.04.2020.
3. SCHMID, M.: Additive Fertigung mit selektivem Lasersintern (SLS): Prozess- und Werkstoffüberblick, Springer Vieweg, Wiesbaden, 2015.
4. LIEBHERR-AEROSPACE & TRANSPORTATION SAS: World Premier: First Ever 3D Printed Primary Flight Control Component from Liebherr-Aerospace Flown on an Airbus Aircraft. https://www.liebherr.com/shared/media/corporate/news/news-2017/04/13/aer/liebherr-airbus-first-flight-3d-flight-control-actuator-april2017.pdf, 01.04.2020.
5. LIEBHERR-AEROSPACE & TRANSPORTATION SAS: Liebherr-Aerospace Starts Serial Production of 3D Printed Components. https://www.liebherr.com/shared/media/corporate/news/news-2019/01/17/liebherr-press-information-liebherr-start-3d-printed-series-production-jan2019.pdf, 01.04.2020.
6 Parker Hannifin Corporation: Slip-in Cartridge Valves: Pressure Control, Throttle, Check. https://www.parker.com/literature/Hydraulic%20Valve%20Division/Catalogs/Catalog%20PDFs/Cat%20MSG14-3200_Slip-In%20Cartridge%20Valves.pdf, 11.05.2021.
7. GEBHARDT, A.; KESSLER, J.; THURN, L.: 3D-Drucken: Grundlagen und Anwendungen des Additive Manufacturing (AM), Hanser, München, 2016.
8. BUCHMAYR, B.; PANZL, G.: Eine SWOT-Analyse zum Einsatz der Additiven Fertigung für metallische Bauteile. In BHM Berg- und Hüttenmännische Monatshefte, 2015, 160; S. 15–20.
9. LEWANDOWSKI, J. J.; SEIFI, M.: Metal Additive Manufacturing: A Review of Mechanical Properties: Annual Rewiev of Materials Research; S. 151–186.
10. DIN EN 2624: 2008, Aerospace series - Pressure impulse testing of hydraulic system components.
11. DIN ISO 6772: 2018, Aerospace - Fluid systems - Impulse testing of hydraulic hose, tubing and fitting assemblies.
12. DIN EN ISO 19879: 2019, Metallic tube connections for fluid power and general use - Test methods for hydraulic fluid power connections.
13. SUN HYDRAULICS CORPORATION: Data sheet: Model FAV Ninety degree Cavity: T-10A. https://www.sunhydraulics.com/model/FAV, 01.04.2020.
14. DIN 51524-1: 2017, Pressure fluids - Hydraulic oils - Part 1: HL hydraulic oils, Minimum requirements.

The 11th JFPS International Symposium on Fluid Power HAKODATE 2020 Oct. 12-13, 2021 JFPS The Japan Fluid Power System Society

The Potential in Fluid Power Systems for a Sustainable Future

Katharina SCHMITZ

RWTH Aachen University, Institute for Fluid Power Drives and Systems (ifas)
Campus-Boulevard 30, 52074 Aachen, Germany
(E-mail: Katharina.Schmitz@ifas.rwth-aachen.de)

Abstract. Climate change due to human made greenhouse gas emissions is the key challenge for the next decades. Within the next years, the emission of climate active gases have to be reduced globally, requiring enormous changes in all aspects of industry and daily life. In addition, all technologies need to get more sustainable, meaning not only to allow for less greenhouse gas emissions but also respectfully treat all resources of our earth. Fluid power drives and systems are an important technology in many industrial and mobile applications and have to take part in this transformation process. In this paper, some potentials are pointed out to give a first impression on how fluid power systems can help in developing a more sustainable future.

Keywords: Sustainability, Efficiency, Manufacturing, Tribology, Fluid Power Components, Mobile Systems

INTRODUCTION

Since more than three decades, researchers are aware of human made global warming, induced by greenhouse gases in the atmosphere. With the first Kyoto Protocol adopted in 1997 and coming into effect in 2005 and 2012 respectively, first achievements to stop the ever rising exhaust of greenhouses gases were made. In the Paris Agreement of 2016, most nations agreed on the long-term goal to keep the rise in global average temperature below 1.5°C to max. 2°C. To reach this goal, the nations would have to reduce their greenhouse gas emissions. Many ideas on how to achieve this ambitious goal in decreasing greenhouse gas emissions near to zero until 2038 and latest 2050 exist. They are based on high penalties for industry or prizing of CO_2-emissions, the expansion of renewable energies like solar power, wind power, wave and water power, more usage of hydrogen technologies, climate friendly mobility and higher standards in the building sector for new buildings and many more.
Fluid power technology plays an important role in many industrial applications and branches. Due to its high power density and its good controllability, the need for fluid power drives and systems is unchanged. Therefore, the question must be asked and answered: What can fluid power contribute to a more sustainable future? Some answers are given in the following paper with, of course, no claim to be complete. In contrast, more ideas for a sustainable future in general and in fluid power in detail are needed, requiring more creative engineering work.

POTENTIAL FOR SUSTAINABLITIY IN FLUID POWER COMPONENTS

When analyzing the potential for more sustainability in fluid power technology, it makes sense to start at component level. Fluid power components are manufactured, leading to greenhouse gas emissions and the usage of other environment-impairing materials and processes.
The determination of emitted greenhouse gases in the production process is a complex procedure with many unknowns. In a preliminary research project at ifas, the greenhouse gas emissions during material production, component production, distribution, operation and end-of-life were analyzed for pneumatic and hydraulic cylinders and translated in values for CO_2 equivalents. Exemplary results of a pneumatic cylinder are shown in Fig. 1. One observation is that the operation of the exemplary cylinder, as well as in all the other examples, is responsible for the largest amount of greenhouse gas emissions. Therefore, extra effort must

be placed in energy efficient system designs and operation strategies of hydraulic and pneumatic systems as discussed later on.
Nevertheless, the emissions during material procurement and production can not be neglected. Depending on the origin of the used material and the country of production, the values vary significantly. Therefore, measures have to always be based on a company and product individual analysis. However, it can be stated that there still is enormous potential for greenhouse gas emission savings.

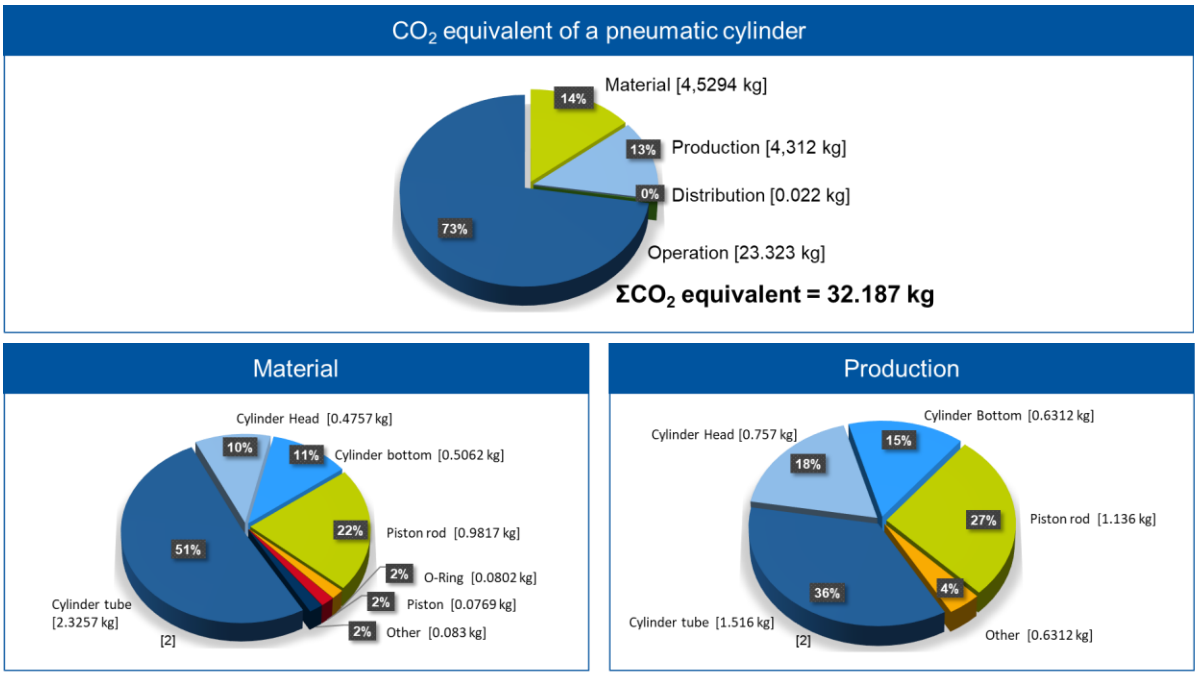

Figure 1. Greenhouse gas emission during the lifetime of a pneumatic cylinder, data given in CO_2 equivalents [see 1, 2]

One opportunity for a more sustainable manufacturing process is the use of digital possibilities in the manufacturing process. With a consistent use of data from development and design stages to the use and end-of-use stage, development costs, reject costs, material costs, transport emissions and energy can be saved [3].

A different challenge in hydraulic components are tribological contacts and the need for leaded material. Since lead is toxic, the reduction of these materials is important. Together with partners from research and industry, ifas is researching new materials and coatings to allow the use of lead free material in hydraulic displacement machines. In Fig. 2 left, the layout of a disc-on-disc tribometer is shown that is amongst others used for this research. On the right side, exemplary measurement results are shown with different special alloys used for the stator. The rotor is made of standard steel with a lapped surface. All materials are technical lead free special alloys with a fine grinded surface with exception of the blue curve, OF2212. This material is a reference material with a lead content of about 0.4% and is regularly used in valves plates of displacement units.

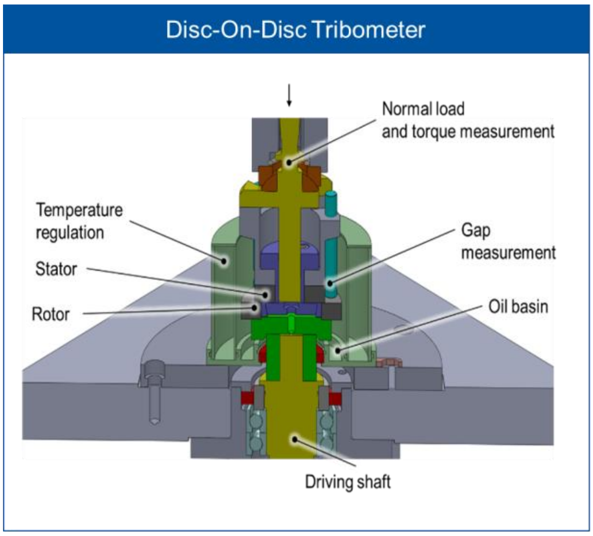

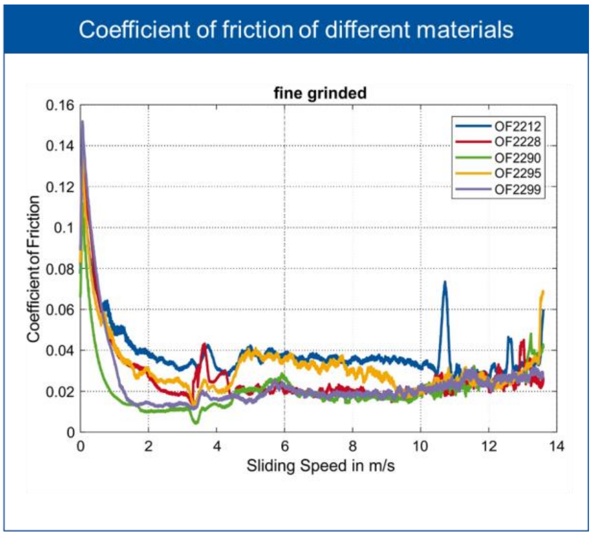

Figure 2. Disc-on-disc tribometer and Stribeck-curve of different special alloys (OF2212 is the leaded reference material) [see 4]

From the measurements it can be seen, that several lead free special alloys have a good potential for an even lower coefficient of friction with comparable strain properties.

Additive manufacturing brings an additional potential to allow for new coating materials and coating processes. One example is the EHLA-process (Extreme high speed laser welding) [5]. In addition, additive manufacturing can significantly help to reduce energy losses in fluid power systems and components by optimized fluid flow inside the components in the future.

Another important role in a more sustainable fluid power is the used pressure media. Pneumatic systems have the advantage of an environmental friendly fluid, but in hydraulic systems, more effort must be taken to find alternatives to mineral oil. Pure water or water based fluids can be part of the solution but definitely not for all applications. The same applies to biodegrable oils. But when looking at greenhouse gas emissions of the fluid used, it is worth thinking about alternatives. McManus, Hammong and Burrows presented a life-cycle assessment of mineral oil and rapeseed oil, see [6]. They came to the conclusion that for the production of 1 kg of mineral oil 3.56 kg CO_2 equivalent greenhouse gases are emitted. For rapeseed oil only 0.3 kg applies.

POTENTIAL FOR SUSTAINABLITIY IN FLUID POWER SYSTEMS

As seen before, fluid power components bare diverse potential for more sustainable approaches. When looking at systems level, two main pillars can be identified – measures for more energy efficiency in the fluid power transmission system and measures for an increase in productivity in the machine or application.

Energy Efficiency

Potential for more energy efficiency in fluid power systems can be found in various examples, such as reduced throttling losses due to multi-pressure systems or displacement controlled systems to enable recuperation, see [7, 8]. Often, energy saving measures are up to now more expensive in aquisition compared to the saved cost in energy. However, when the

emitted greenhouse gases are taken into account, the reduction in systematic pressure losses is crucial. The same applies for electrified machines like mobile construction machines. By lowering the energy consumption of the hydraulic system, the required amount of energy stored in an accumulator is significantly reduced and therewith costs for the electric accumulator and installation space.
New power supplies of mobile construction machines additionally allow the integration of electric drives as well as the design of completely new hydraulic system architectures with unprecedented degrees of freedom in size, rotational speed, control strategy, amount of hydraulic pumps and therewith the whole hydraulic system. For a 9 t open-center compact excavator, Opgenoorth presents possible system adaptations to improve energy efficiency, see Fig. 3. By integrating variable motor speeds, variable pump displacements, electric valve actuations and an electric swing, the energy efficiency of the excavator is increased by 42%. [9]

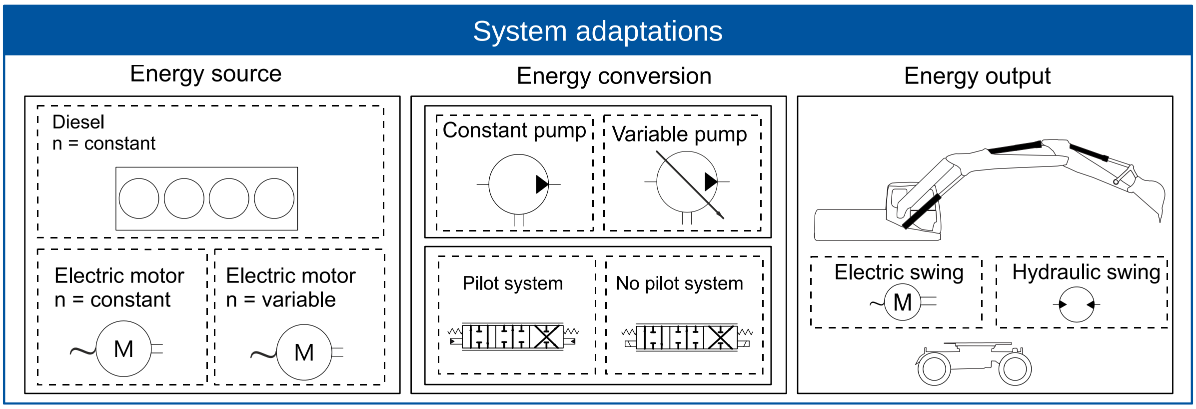

Figure 3. Possible system adaptations based on an example of an excavator [9]

In pneumatic systems, energetic losses are a controversial discussed matter. They exist, but since energy is up to now, relatively cheap, cost consuming measures are not developed nor produced. One promising new approach to save energy in pneumatic cylinder drive applications without significantly increasing system cost, is the combined throttling. It combines the advantage of the downstream throttling of load independent stationary speed and the advantage of the upstream throttling of load dependent air demand. The challenge in this new approach of ifas lies in the required binary control and the delayed start of motion due to pressure adjustments in the downstream chamber.

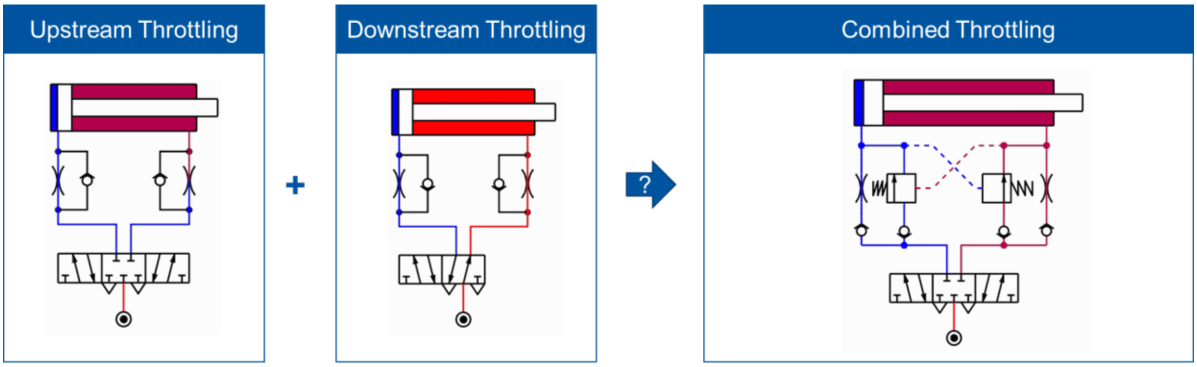

Figure 4. Potential for more energy efficiency in pneumatic systems with combined throttling [see 10]

Increasing Productivity

The second pillar to more sustainability with regard to fluid power systems is the increase in productivity. One example can be found at the construction site. In the last decades, the productivity in all industrial sectors increased (world GDP +13% in last 20 years) due to more automation. In contrast, in the construction sector productivity stagnated [11]. One key for more productivity in this sector can be found in a higher automation – starting with autonomous functions of machines and ending with completely autonomous operated construction machinery. In first, assisting systems like semi-autonomous functions have to be fully developed and implemented. Challenging hereby are the design, accuracy and dynamics of the controller. Potential solutions can be found in new controller design methods like artificial intelligence methods or reinforcement learning methods [12].

Figure 5. Potential in assistance systems in excavators to increase productivity

For fully automated excavating functions, more research is needed and the integration of multiple sensors is required. With that, enormous potential exists for significant productivity increase on construction sites and with that high potential for reducing greenhouse gas emissions onside and in materials etc. Autonomous operating machines can also help reducing the high number of human accidents and people being injured at work on construction sides.

Another potential for fluid power systems to help the overall machine in operating more efficiently is by the use of data from the fluid power system for condition monitoring purposes. On one hand this allows , a good monitoring of the overall machine status and work performance, and on the other hand the ability to predict machine or process failures before a damage or breakdown occurs [13]. One new approach for a better understanding of the system is by using so called soft sensors. In a new research project at ifas, a virtual volume flow sensor is developed. Up to now, flow rate sensors are expensive and relatively difficult to handle. The new approach is, to use two precise pressure sensors and a pipe in-between. By the measurement of the dynamic pressures and a mathematical extension of the Hagen-Poiseuilles law for the transient time domain and turbulent flow, the volume flow rate can be determined dynamically and with relatively low costs [14]. This virtual sensor allows a power monitoring of a whole machine or individual actuators.

SUMMARY

The preservation of the resources of nature and our earth for the next generations is one of the most important tasks for the next years and decades all over the world. By significantly reducing the greenhouse gas emissions within the next years near to zero, global warming can hopefully be limited to less than 2°C. To achieve this goal, all drive technologies have to provide the best effort they can to do so.

In this paper, several ideas and new approaches were presented to show a way how to implement the sustainability aspect in the development of future fluid power systems and components. Still, much more effort has to be placed in this field of research and development, leading to expedient solutions in the future.

ACKNOWLEDGMENTS

This paper shows work of several researchers at the Institute for Fluid Power Drives and Systems. The author thanks the whole team at ifas, with special thanks to J. Duensing, S. Geffroy, C. Haas, A. Holzer, A. Opgenoorth, O. Reinertz, and M. Rueckert for their contribution.

REFERENCES

1. MERKELBACH, S., Analysis of the Economic and Ecological Properties of Pneumatic Actuator Systems with Pneumatic Transformers, PhD thesis, RWTH Aachen, 2019
2. DUENSING, Y., RICHERT, O., SCHMITZ, K., Berechnungstool zur Bestimmung des CO2-Fussabdrucks, O+P Fluidtechnik, 2021/06, Vereinigte Fachverlage GmbH, Mainz, 2021
3. www.awk-aachen.com (accessed on 31 May, 2021)
4. HOLZER, A., SCHMITZ, K., Effizienzsteigerung von Verdrängereinheiten durch optimales Einlaufen, final report of govermental fundated research project, AiF No. 20083 N/1, 2021
5. HOLZER, A., et al., Tribological Investigations on Additively Manufactured Surfaces using Extreme High-Speed Laser Material Deposition (EHLA) and Laser Powder Bed Fusion (LPBF), Proceedings of the 12th International Fluid Power Conference, IFK 2020, Dresden
6. M. C. MCMANUS, G. P. HAMMOND, C. R. BURROWS, Life-Cycle Assessment of Mineral and Rapeseed Oil in Mobile Hydraulic Systems, Journal of Industrial Ecology, Volume 7, Number 3-4, 2004, pp. 163-177
7. VUKOVIC, M., Hydraulic hybrid systems for excavators. PhD thesis, RWTH Aachen, 2017
8. WILLIAMSON, C., IVANTYSYNOVA, M., Power Optimization for Multi-Actuator Pump-Controlled Systems, Proceedings of the 7th International Fluid Power Conference, IFK 2010, Aachen, pp. 91–102
9. OPGENOORTH, A., QUABECK, S., DONCKER, R. W. de; SCHMITZ, K., Challenges and possibilities of the integration of electric drives in mobile machinery, Proceedings of the 12th International Fluid Power Conference, IFK 2020, Dresden, pp. 471–480
10. REINERTZ, O., SCHMITZ, K., Optimized Pneumatic Drives Through Combined Downstream and Adaptive Upstream Throttling, Proceedings of the ASME/BATH Symposium on Fluid Power and Motion Control, 2020
11. MCKINSEY GLOBAL INSTITUTE, Reinventing construction: A route to higher productivity, 2017
12. DADHICH, S., BODIN, U., ANDERSSON, U., Key challenges in automation of earth-moving machines, Automation in Construction 68, 2016
13. DUENSING, J., RODAS RIVAS, A., SCHMITZ, K., Machine Learning for failure mode detection in mobile machinery, Proceedings of the 11. Kolloquium Mobilhydraulik, Karlsruhe Institute for Technology, 10. September 2020, pp. 1-26
14. https://www.ifas.rwth-aachen.de/cms/IFAS/Forschung/Digitalisierung-und-Automatisierung/~nqfoo/Virtueller-Volumenstrom-Sensor/?lidx=1 (accessed on 31 May, 2021)

The 11th JFPS International Symposium on Fluid Power HAKODATE 2020 Oct. 12-13, 2021 The Japan Fluid Power System Society

New Intelligent Hydraulic Power Control System

Takahiro URAI*, Ken SHINDO**

*Sales Business Development, Marketing department, Bosch Rexroth Corporation
3-6-7 Shibuya, Shibuya-ku, Tokyo, 150-0002 Japan
(E-mail: Takahiro.Urai@boschrexroth.co.jp)
** Engineering industrial Hydraulics, Sales department, Bosch Rexroth Corporation
3-6-7 Shibuya, Shibuya-ku, Tokyo, 150-0002 Japan
(E-mail: Ken.Shindo@boschrexroth.co.jp)

Abstract. With the newly developed, intelligent hydraulic power control system, Rexroth combines the benefits of hydraulics with low energy consumption and software-based functions. The integrated IoT service ensures higher availability and avoids unplanned downtimes. With this IoT service, operators can monitor operating statuses and plan maintenance in a cost-effective manner. As a result, fluid technology has taken a further step towards the factory of the future.
Keywords: Industry 4.0, factory of the future, predictive maintenance, IoT

1. INTRODUCTION

The digitalization of mechanical and plant engineering means more than decentralized intelligence, integrated sensors and connectivity. This applies to hydraulics too. With its power density and immunity to impacts and vibrations, hydraulics plays a central role as an important drive technology in Industry 4.0 too. The compact intelligent hydraulic unit is revolutionizing hydraulic pressure supply. This unit is a modular hydraulic power unit for the medium performance range from 7.5 kW to 30 kW. It comprises optimally tailored, impressively compact components. Compared to previous units, considerable amounts of space can be saved.

2. PERFORMANCE DESCRIPTION

One of this system's unique selling points is it compactness. This is possible because the hydraulic power unit can be integrated into a factory like a control cabinet, i.e. upright. The tank no longer supports all other components – Rexroth developed a special supporting structure for this purpose. In addition, a degassing flow-optimized tank is used. On the basis of extensive CFD simulations, the developers improved the tank geometry so skillfully that the new unit needs only a quarter of the oil required by classic designs: instead of 600 liters, 150 liters are now enough – with at least the same service life. The drive unit – a component which usually takes up a large amount of space in hydraulic power units – is equally compact. The asynchronous servo motor has been replaced by a synchronous servo motor. This is the most efficient motor design, producing the same torque even though it is 80 to 90% smaller. The manifold too was redesigned: thanks to 3D printed sand cores, the block including the internal flow geometry is now cast. As a result of this flow-optimized inner structure, less material and space are required. Thanks to all these measures, this unit has a footprint of just 0.5 square meters instead of one and a half to two square meters（Fig.1）. This represents a saving of up to 75%. On top of this, there are energy savings of up to 80% as well as a 10 dB(A) reduction in noise emissions. As a result, noise emissions are lower than 75 dB(A). Refer Table.1 for technical feature..

3. CONNECTED FOR THE FACTORY OF THE FUTURE

In this unit, machine manufacturers will find a ready-configured drive controller with numerous integrated functions. Various sensors provide information on the current filter, oil or drive status. The collected sensor data are bundled via IO-LinkMaster and pre-processed by the drive controller so that they can be integrated flexibly into modern machine designs. This means that this intelligent unit is IoT-ready.

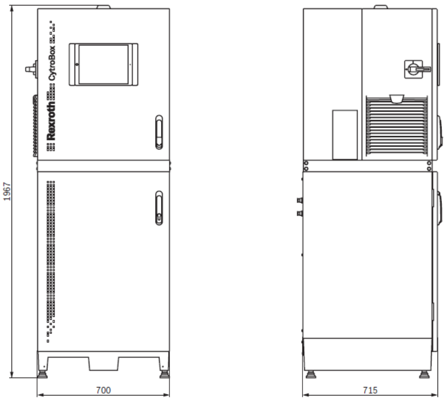

Figure 1. Dimensions

Table 1. Technical feature

Pressure	Up to 31.5MPa
Hydraulic power	30kW
Flow rate	Up to 160L/min
Oil volume	150L
Drive	Servo motor, water-cooled
Cooling system	Plate heat exchanger
Cooling water	20L/min
Noise	<75dB(A)

4. IoT SYSTEM MONITOR SERVICE

With the IoT digital service, operators have all information regarding this system at their fingertips at all times – whether it be information regarding the standardized visualization of the component and operating status or chargeable IoT services such as forthcoming maintenance work and predictive maintenance analyses using Rexroth's Online Diagnostics Network (ODiN).
The data collected are transferred to the browser-based Monitor web dashboard via Multi-Ethernet or 4G-LTE. As a result, operators can be kept up to date regarding the current operating status and key status indicators on any end device (tablet, smartphone, PC). This plug and play service is free of charge and can be used without additional installation work. This IoT monitor service system is implemented in this unit as standard.

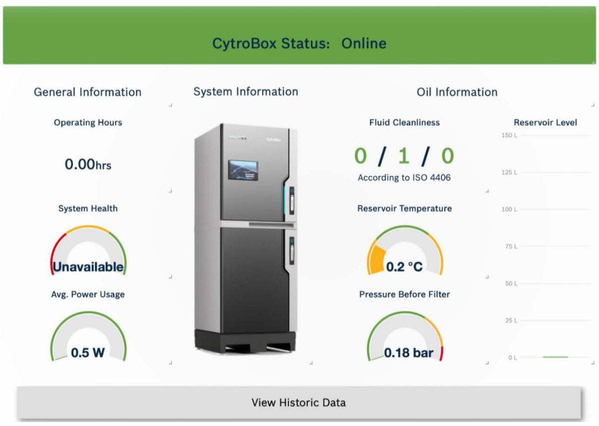

Figure2. IoT system monitor example

5. ADDITIONAL ANALYSIS FUNCTIONS

In addition to this unit's automatic status monitoring, maintenance personnel and maintenance managers can add extra solutions for various applications as add-ons. These pay-per-use payment models include additional IoT analysis tools and can be subscribed to on a monthly basis.
For optimizing maintenance processes, Maintain module in this IoT system monitor service offers access to historical sensor data as well as messages if maintenance is required or in the event of critical operating statuses. Pre-defined and custom rules allow customers to improve their maintenance strategy on an ongoing basis. Customers benefit from scalable software solutions from the Bosch IoT portfolio such as the Nexeed Production Performance Manager and the integrated know-how of the Rexroth domain specialists. The Nexeed Production Performance Manager is a condition monitoring software solution for systematic production optimization.
With Maintain module, data concerning the most important components for reliability and operating life (the hydraulic oil and the drive unit) are assessed. Comprehensive insights into the correlation between the speed of the servo motor and the flow allow the monitoring of system leakage, while correlations between motor data and the operating pressure allow conclusions regarding drive behavior. The leakage sensor, temperature and level sensor, particle sensor, water sensor and oxygen sensor are additional data sources which can be used to make a status diagnosis.

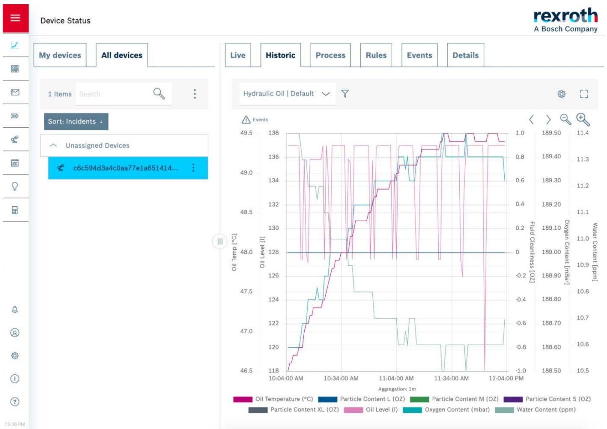

Figure3. Maintain module example

6. PLANNING PREDICTIVE MAINTENANCE EFFIFIENTLY

A further add-on, in Predict module, uses the machine learning algorithms of the Rexroth Online Diagnostics Network (ODiN) for a predictive analysis of the system. With this IoT service, the power curves for a wide range of components are recorded for data analysis purposes. In the event of deviations, the system automatically calculates the expected remaining operating life of the relevant component and informs the operator immediately via a push message. As a result, predictive maintenance application cases can be taken into account predictively in the operator's maintenance plans, thus ensuring maximum availability.

7. CONCLUTION

This new form of hydraulics is energy-efficient, quiet, space-saving and intelligent. With the integrated IoT system monitor service, this intelligent unit offers anything from transparent, efficient machine monitoring to intelligent predictive maintenance measures. Thanks to this unit, fluid technology is now one step closer to the factory of the future.

